

Frontiers in Optics and Photonics 2011

XXXVI OSI Symposium

Editors

Bishnu Pal • Anurag Sharma
M R Shenoy • Joby Joseph



Preface

Frontiers in Optics and Photonics (FOP11) is thirty-sixth in the series of annual symposia of the Optical Society of India. This Symposium is being organized by the Indian Institute of Technology Delhi, which has significantly contributed to the growth of the field of optics and photonics in several ways since its inception in 1961. This Symposium being organized at IIT Delhi, especially to as a part of the Golden Jubilee celebrations of the Institute.

Established as College of Engineering in 1961, the Institute was later declared an Institution of National Importance under the "Institutes of Technology (Amendment) Act, 1963" and was renamed "Indian Institute of Technology Delhi". HRH Prince Philip, the Duke of Edinburgh, laid the foundation stone of the Institute on January 27, 1959. The academic activities of the Institute started on August 16, 1961 with the arrival of first batch of students on campus and the formal inauguration of the teaching activity was done by Prof. Humayun Kabir, the then Union Minister for Scientific Research and Cultural Affairs on August 17, 1961. The main academic complex of the Institute was opened by Dr. Zakir Hussain, the then President of India on March 2, 1968. The Institute celebrated its silver Jubilee during 1985-86 and the Silver Jubilee Convocation was addressed by Shri Rajiv Gandhi, the then Prime Minister on December 19, 1985. The Institute has made a notable mark in higher technical education and research. It has been ranked very high among national and international institutions of higher learning. The Institute is celebrating its Golden Jubilee Year during 2010-2011. The Golden Jubilee Year was inaugurated by the Hon'ble President, Smt. Pritibha Devisingh Patil on August 16, 2010. This Symposium is part of the Golden Jubilee celebrations.

This Proceedings contains summaries of the papers that are being presented at the Symposium in two plenary sessions, 18 technical sessions and 3 poster sessions, comprising of 4 plenary talks, 41 invited talks, 42 oral presentations and 150 poster presentations. These presentations cover a wide variety of topics from optical design and instrumentation to fiber lasers, sensors and nonlinear optics.

We would sincerely like to thank all the authors for their contributions and the members of the Technical Committee for their efforts and support in selecting papers and drawing up the technical programme. We would also like to record our sincere thanks for the support and continuous encouragement from Prof. S. Prasad, former Director and Prof. R.K. Shevgaonkar, Director of our Institute. We would also like to thank our colleagues of the Department for their support and guidance. We are grateful to Mr. Prakash Kedia, Mr. Jagadeesh K.S., Mr. Sachin Kumar Srivastava, Mr. Arun Vinod, Mr. Deepak Gunwant, Ms. Mamta Uppal, Mr. Ambarish S Kumar, Ms. Varinder Pal Kaur and Mr. Vikram Kamaljith in the preparation of this Proceedings.

December 3, 2011
New Delhi

B.P. Pal
Anurag Sharma
M.R. Shenoy
Joby Joseph

Frontiers in Optics and Photonics (FOP-11)

Symposium Executive Committee

Conference Chairs:	Bishnu P Pal and Anurag Sharma
Conference Vice Chairs:	Enakshi K. Sharma and Arun Kumar
Secretary/Convener:	Joby Joseph and G.Vijay Prakash
Treasurer:	R.K. Varshney
Members:	K. Thyagarajan, B.D. Gupta, M.R. Shenoy, R.K. Soni, P. Senthilkumaran

Advisory Committee

Co-Chairs: A.K. Ghatak and Kehar Singh

A. Basuray, <i>Calcutta Univ.</i>	D. Narayana Rao, <i>Hyderabad C. Univ.</i>	Pawan Kapur, <i>CSIO Chandigarh</i>
Ajoy Ghosh, <i>Calcutta Univ.</i>	G. Rajeswaran, <i>Moser Baer, Noida</i>	P.D. Gupta, <i>RRCAT, Indore</i>
A.K. Gupta, <i>IRDEDehradun</i>	G.R.C. Reddy, <i>NIT Warangal</i>	P.K. Sen, <i>SGSITS Indore</i>
A.K. Maini, <i>LASTEC Delhi</i>	I. Manna, <i>CGCRI Kolkata</i>	R.K. Shevgaonkar, <i>IIT Delhi</i>
A.K. Saxena, <i>IAP Bangalore</i>	K. Chalapati, <i>SAMEER Mumbai</i>	R.M. Vasu, <i>IISc Bangalore</i>
A.K. Sood, <i>IISc Bangalore</i>	K.C. Rustagi, <i>IIT Bombay</i>	R. Simon, <i>IMSc Chennai</i>
Anurag Sharma, <i>IIT Delhi</i>	K. Thyagarajan, <i>IIT Delhi</i>	R.S. Sirohi, <i>Invertis Univ. Bareilly</i>
Asit K. Datta, <i>Calcutta Univ.</i>	L.N. Hazra, <i>Calcutta Univ.</i>	S.S. Sundaram, <i>IRDE Dehradun</i>
B.M. Arora, <i>IIT Bombay</i>	Manjit Singh, <i>TBRL Chandigarh</i>	Suresh Nair, <i>NEST Cochin</i>
B.P. Pal, <i>IIT Delhi</i>	M.P. Kothiyal, <i>IIT Madras</i>	T.K. Alex, <i>ISRO Bangalore</i>
B.R. Singh, <i>IIIT Allahabad</i>	M.S. Sodha, <i>Lucknow Univ.</i>	V. Bande, <i>Quanta Laser, Indore</i>
Chris Dainty, <i>President OSA</i>	N. Shroff, <i>DIT New Delhi</i>	V.P.N. Nampoori, <i>CUSAT Cochin</i>
D.D. Bhawalkar, <i>RRCAT Indore</i>	P.K. Gupta, <i>RRCAT Indore</i>	

Technical Programme Committee

A. Bhatnagar, <i>SAMEER Mumbai</i>	Joby Joseph, <i>IIT Delhi</i>	Rajiv Jindal, <i>Moser Baer, Noida</i>
A. Bhattacharya, <i>TIFR Mumbai</i>	Kamal Dasgupta, <i>CGCRI Kolkata</i>	Ranjan Sen, <i>CGCRI Kolkata</i>
A.K. Razdan, <i>LASTEC Delhi</i>	K. Bhattacharyya, <i>Calcutta Univ.</i>	Reji Philip, <i>RRI Bangalore</i>
A.K. Shukla, <i>IIT Delhi</i>	K. Porsezian, <i>Pondicherry Univ.</i>	R.K. Sinha, <i>DTU Delhi</i>
Alika Khare, <i>IIT Guwahati</i>	Krishna Kumar, <i>OPTIWAVE Hyderabad</i>	R.K. Soni, <i>IIT Delhi</i>
Aloka Sinha, <i>IIT Delhi</i>	K Srimannarayana, <i>NIT Warangal</i>	R.K. Varshney, <i>IIT Delhi</i>
Anurag Sharma, <i>IIT Delhi</i>	K. Thyagarajan, <i>IIT Delhi</i>	R.P. Singh, <i>PRL Ahmedabad</i>
A.R. Ganesan, <i>IIT Madras</i>	Manpreet Singh, <i>TBRL Chandigarh</i>	S. Asokan, <i>IISc Bangalore</i>
Arun Kumar, <i>IIT Delhi</i>	M.R. Shenoy, <i>IIT Delhi</i>	S.K. Saha, <i>IAP Bangalore</i>
Ashok Kaul, <i>IRDE Dehradun</i>	Nawal Kishore, <i>GJUS&T Hisar</i>	S. Mujumdar, <i>TIFR Mumbai</i>
Balaji Srinivasan, <i>IIT Madras</i>	Naveen Nishchal, <i>IIT Patna</i>	S.C. Jain, <i>CSIO Chandigarh</i>
B.D. Gupta, <i>IIT Delhi</i>	N.K. Mohan, <i>IIT Madras</i>	S.K. Bhadra, <i>CGCRI Kolkata</i>
B.K. Das, <i>IIT Madras</i>	N.S. Mehla, <i>CSIO Chandigarh</i>	Sanjay Kher, <i>RRCAT, Indore</i>
Chandra Shaker, <i>IIT Delhi</i>	P. Radhakrishnan, <i>CUSAT Cochin</i>	S. Dutta Gupta, <i>Hyderabad C. Univ.</i>
C.S. Narayanamurthy, <i>IIST Thiruvananthapuram</i>	P. Roy Choudhary, <i>IIT Kharagpur</i>	Somnath Sarkar, <i>Calcutta Univ.</i>
D. Goswami, <i>IIT Kanpur</i>	P.C. Devara, <i>IITM Pune</i>	Suchandan Pal, <i>CEERI Pilani</i>
D. Datta, <i>IIT Kharagpur</i>	P.K. Mondal, <i>Osmania Univ. Hyderabad</i>	Subrat Kar, <i>IIT Delhi</i>
D. Ranganathan, <i>IIT Delhi</i>	P. Palai, <i>Tejas Networks, Bangalore</i>	Sudipto Maiti, <i>TIFR Mumbai</i>
D.S. Mehta, <i>IIT Delhi</i>	P.P. Sahu, <i>Tezpur Univ.</i>	Sukhdev Roy, <i>DEI Agra</i>
Enakshi K. Sharma, <i>UDSC Delhi</i>	P. Senthilkumaran, <i>IIT Delhi</i>	Sunil K. Khijwania, <i>IIT Guwahati</i>
G.S. Singh, <i>CSIO Chandigarh</i>	P.T. Ajithkumar, <i>Light Logics, Thiruvananthapuram</i>	S.V. Ramagopal, <i>CSIO Chandigarh</i>
Gufran Khan, <i>IIT Delhi</i>	R. Ghosh, <i>JNU New Delhi</i>	T. Srinivas, <i>IISc Bangalore</i>
G.V. Prakash, <i>IIT Delhi</i>	R. Vijaya, <i>IIT Kanpur</i>	Vipul Rastogi, <i>IIT Roorkee</i>
H.C. Kandpal, <i>NPL Delhi</i>	S.A. Ramakrishna, <i>IIT Kanpur</i>	Vishnu Priye, <i>ISM Dhanbad</i>
Hitesh Mehta, <i>FIBER OPTIKA</i>	Rajib Chakraborty, <i>Calcutta Univ.</i>	N. Viswanathan, <i>Hyderabad C. Univ.</i>
Ikbāl Singh, <i>IRDE Dehradun</i>		V. P. Mahadevan Pillai, <i>Univ Kerala Thiruvananthapuram</i>
J. Nayak, <i>RCI Hyderabad</i>		D.P. Ghai, <i>LASTEC Delhi</i>

Local Organizing Committees

Publications Committee

M.R. Shenoy, E.K. Sharma, D. Ranganathan

Exhibition Committee

R.K. Soni, G.V. Prakash, Chandra Shaker, D.S. Mehta

Technical Planning & Registration Committee

B.D. Gupta, A.K. Shukla, Aloka Sinha, Anurag Sharma

Reception and Hospitality Committee

P. Senthilkumaran, Gufran Khan, R.K. Varshney

Finance Committee

R.K. Varshney, B.P. Pal, Anurag Sharma, J. Joseph

FRONTIERS IN OPTICS AND PHOTONICS – 2011

Overview of Technical Sessions

Date & Time	Room – A	Room – B	Room – C
SATURDAY, DECEMBER 3, 2011			
08:00 – 09:30	REGISTRATION		
09:30 – 11:00	Inaugural Session (Seminar Hall) Keynote Address: Christopher Dainty : <i>Adaptive Optics in Vision Science</i>		
11:00 – 11:30	Inaugural Tea (Foyer of the Seminar Hall)		
11:30 – 13:00	1A1 Optical Instrumentation-I	1B1 Optical Networks	1C1 Sensors-I
13:00 – 15:00	Poster Session-1P and Lunch		
15:00 – 16:30	1A2 Optical Design-I	1B2 Optical Fibers	1C2 Sensors-II
16:30 – 17:00	Tea		
17:00 – 19:00	OSI GBM and Panel Discussion		
19:00 – 20:00	Cultural Programme		
20:00 – 21:30	Symposium Dinner Sponsored by OSA-The Optical Society		
SUNDAY, DECEMBER 4, 2011			
09:00 – 09:45	Plenary: Prem Kumar : <i>All-Optical Switching for Quantum Applications</i>		Room-A
09:45 – 10:30	Plenary: P K Gupta : <i>Biophotonics – Studies at RRCAT</i>		
10:30 – 11:00	Tea		
11:00 – 13:00	2A1 Optical Design-II	2B1 Fiber Lasers and Amplifiers	2C1 Photonic Crystals
13:00 – 15:00	Poster Session-2P and Lunch		
15:00 – 16:30	2A2 Optical Instrumentation-II	2B2 Integrated Optics	2C2 Optical Fields
16:30 – 17:00	Tea		
17:00 – 19:00	2A3 Optical Systems and Applications	2B3 Nanophotonics	2C3 Holography
19:00 – 20:30	Dinner		
MONDAY, DECEMBER 5, 2011			
09:00 – 09:45	Plenary: D. Narayana Rao : <i>Plasmonics for SERS and NLO Studies</i>		Room-A
09:45 – 10:30	Plenary: M P Kothiyal : <i>Interferometry with Broadband Light</i>		
10:30 – 11:00	Tea		
11:00 – 13:00	3A1 Waveguide Devices	3B1 Nonlinear Optics	3C1 Biophotonics
13:00 – 15:00	Poster Session-3P and Lunch		
15:00 – 15:45	Concluding Session		
15:45 – 16:15	Tea		

CONTENTS

PREFACE

COMMITTEES

OVERVIEW OF TECHNICAL SESSIONS

KEYNOTE ADDRESS :

Adaptive Optics in Vision Science

Christopher Dainty

PLENARY TALK :

1. ***All-Optical Switching for Quantum Applications***
Prem Kumar
2. ***Plasmonics for SERS and NLO Studies***
D. Narayana Rao
3. ***Biophotonics - Studies at RRCAT***
P. K. Gupta
4. ***Interferometry with Broadband Light***
M. P. Kothiyal

ORAL SESSIONS :

DAY - I

1A1. OPTICAL INSTRUMENTATION – I

1. INVITED: ***Advances in Optical Remote Sensing Methods: Application to Climate Studies***
P.C.S. Devara
2. INVITED: ***Trends in Infra-Red Systems for Defence Applications***
S. S. Sundaram
3. ***Comparative Study of Various Automated Collimation Testing Techniques in Talbot Interferometry***
Jitendra Dhanotia and Shashi Prakash
4. ***Performance Estimation of Intensified CCD Spectrometer System for UV Laser Induced Fluorescence Standoff Biological Warfare Sensor***
Deepak Kumar, Ramesh C. Sharma and A. K. Maini

1B1. OPTICAL NETWORKS

1. INVITED: ***FTTH Distribution System for Multi Level Dwelling Units***
K.R.Suresh Nair
2. ***Performance Analysis of Multiplexed Signal Distribution Fiber Networks for Radar Applications***
Meena.D, LGM Prakasam, D.C.Pandey, Sujitha, Yadunath.T.R, E. S. Shivaleela and T.Srinivas
3. ***Performance Enhancement of SAC-OCDMA System Using Msequence Codes***
Syed Tajammul Ahmad, Gausia Qazi, G. M .Rather and H. Najeeb- ud- Din Shah.

1C1. SENSORS-I

1. INVITED: ***Novel Optical Fiber Sensors for Nuclear Radiation Monitoring and Radiotherapy***
Sanjay Kher
2. INVITED: ***From Technology to Instrument – Distributed Anti-Stokes Raman Thermometry***
B. Srinivasan, Uvaraj Gajendran and Amitabha Datta
3. ***Current Status of Calibration-Free Tunable Diode Laser Spectroscopy Techniques for Industrial Gas Monitoring***
Arup Lal Chakraborty
4. ***Photonic Crystal Surface Plasmon Waveguide Sensors for High and Accurate Temperature Measurement***
Rajan Jha, Triranjita Srivastava and Ritwick Das
5. ***A Localized Surface Plasmon Resonance Based Fiber Optic Hydrogen Gas Sensor***
S.Prabhakar, Sachin K. Srivastava, Banish D. Gupta and Bodh R. Mehta

1A2. OPTICAL DESIGN – I

1. INVITED: ***Adaptive Optics in Imaging and Vision Science***
A. R. Ganesan
2. INVITED: ***Optical Lithography for Nano-Structural Patterning: Resolution Enhancement Techniques***
Samit Barai

3. **Design of a 2x-6x Zoom Telescope for Low Vision Patients**

G. S. Singh

1B2. OPTICAL FIBERS

1. INVITED: ***Refractive Index and Mode Field Profiling of Optical Fibers using Lensed Fiber Probe***

Anuj Bhatnagar

2. ***'Single Mode-Coaxial-Single Mode Fiber' Module as a Band Reject Filter for Gain Flattening in Erbium Doped Fibers***

Jyoti Anand, Jagneet Kaur Anand and Enakshi K. Sharma

1C2. SENSORS – II

1. INVITED: ***Fiber Optic Sensors Development Programme at CSIO for Structural Health Monitoring***

Subhash C.Jain

2. ***Multi-Measurand Process and Health Monitoring of Fibre Reinforced Composites***

A.K. Nair, V.R. Machavaram, R.S. Mahendran, D. Harris, G.F. Fernando and B.D. Gupta

3. ***Optical Fiber Sensor Based Testing Module for Analysis of Tank T-72 Armament***

B.B.Padhy, A.D.Shaligram and R.B.Sharma

4. ***High Performance Bragg Plasmon Coupled Waveguide Sensor***

Triranjita Srivastava, Ritwick Das and Rajan Jha

5. ***Surface Plasmon Resonance Based Optical Fiber Humidity Sensor Using Gold Nanoparticle Film***

R. Aneesh, Abhinav Rastogi and Sunil K. Khijwania

6. ***Fiber Bragg grating sensors- Some recent applications***

S Asokan

DAY - II

2A1. OPTICAL DESIGN – II

1. INVITED: ***The Riddle of Chromatism***
Lakshminarayan Hazra
2. INVITED: ***Hypertelescope Approach: A Novel Method for Imaging of Stellar Objects***
Swapan K. Saha
3. INVITED: ***Development of IR Zoom Lens: An Overview***
Ikbal Singh
4. INVITED: ***Design Challenges In Optical System Design for See Through Displays***
P.P. Bajpai
5. ***Alignment Strategies and Optical Design of 50/80cm Modified Baker-Nunn Super-Schmidt Astronomical Telescope for 4D Field***
K. G. Gupta

2B1. FIBER LASERS AND AMPLIFIERS

1. INVITED: ***Optical Fiber with Rare-Earth Doped Dielectric Nano-Particles for Efficient Fiber Laser***
Mukul Chandra Paul, Arindam Haldar and Shyamal K. Bhadra
2. INVITED: ***Nonlinear Dynamics of Fiber Laser***
R.Vijaya
3. ***XPM and SPM Induced Crosstalk in Multi-Pumped Distributed Raman Amplifier***
Anamika and Vishnu Priye
4. ***Study of Multipulsing Phenomena in Q-Switched Fiber Lasers***
Manas Srivastava, Deepa Venkitesh and Balaji Srinivasan
5. ***All-Fiber Thullium Doped Fiber Laser by Utilizing Pump at 980 nm***
Atasi Pal, Shyamal Das, Shu Ying Chen, Tong Sun, Kenneth T. V. Grattan and Ranjan Sen
6. INVITED: ***Rare Earth Doped Optical Fiber Fabrication by MCVD Process***
Ranjan Sen

2C1. PHOTONIC CRYSTALS

1. INVITED: ***Supercontinuum Generation in Photonic Crystal Fibers***
K. Porsezian
2. INVITED: ***Slow light Induced SOI Photonic Crystal Waveguides & Devices***
R. K. Sinha
3. INVITED: ***A Simple and Complete Formulation to Compute Propagation Constants of Photonic Crystal Fibers and Predict Total Dispersion***
Dipankar Kundu and Somenath Sarkar
4. ***The Interplay between Order and Disorder in Photonic Crystals***
Rajesh V. Nair and B. N. Jagatap
5. ***Numerical Analysis of Nonlinear Pulse Propagation in Chalcogenide As_2Se_3 Glass Photonic Crystal Fiber Using RK4IP Method***
Bhawana Dabas, Monika Rajput and R. K. Sinha

2A2. OPTICAL INSTRUMENTATION – II

1. INVITED: ***Prospects and Technical Challenges of High Efficiency Solid State Lighting***
Rajeev Jindal, Subrata Dutta
2. ***White Light Interferometry for Surface Profiling with Colour CCD***
U. Paul Kumar, Wang Haifeng, N. Krishna Mohan and M.P. Kothiyal
3. ***Scanning Optical Microscope with Enhanced Signal to Noise Ratio Performance***
Abhijit Das and Bosanta R. Boruah
4. INVITED: ***Optical Technologies for ISRO's Space Programmes: Current and Future Trends***
C L Nagendra and P. Chakraborty

2B2. INTEGRATED OPTICS

1. INVITED: ***Comparative Study of Directional Coupler and Two-Mode Interference Coupler Based on Tooth Shaped Grating Assisted Structure***
Bidyut Deka, Nilima Gogoi and Partha Pratim Sahu
2. INVITED: ***Silicon Photonics in SOI Platform: Problems with Waveguide Dispersion and Birefringence Effects***
B.K. Das, Sujith C., G.R. Bhatt, U. Karthik and R. Sharma
3. ***Simulation of Integrated Optics Structures using a Bidirectional Beam Propagation Method***
Debjani Bhattacharya and Anurag Sharma
4. ***Inline Excitation of Optomechanical Oscillations***
Muhammad Umar Khan and Thomas F. Krauss

2C2. OPTICAL FIELDS

1. INVITED: ***Isolated Polarization Singularities***
Nirmal K. Viswanathan
2. INVITED: ***Role of Surface Plasmons in Modulating Spectral and Coherence Properties of the Incident Field***
H.C. Kandpal, Bhaskar Kanseri and Manish Verma
3. ***Rendering of Underwater Lightfield Using Radiative Transfer Model***
V.B. Sundarabalan and P. Shanmugam

2A3. OPTICAL SYSTEM AND APPLICATIONS

1. INVITED: ***Advances in Photonics for Defence Applications***
A. K. Gupta
2. INVITED: ***Development of Optical Components in a Modern High Performance Fiber Optic Gyroscopes (HiFOG)***
Jagannath Nayak
3. ***Virtual Prototypes for Product Development***
R. Sudhakar Rao and Prof. Chandra Lingam

4. ***Optical Grade Plastics Based Precision Bi-Aspheric Lenses for Indirect Ophthalmoscopy***

G. S. Singh, S. V. Ramagopal and Pawan Kapur

2B3. **NANOPHOTONICS**

1. INVITED: ***Broadband Extra-Ordinary Transmission in Checkerboard Plasmonic Films***

S Anantha Ramakrishna

2. INVITED: ***Statistical Fluctuations in Coherent Emission from Disordered Nanostructured Amplifying Materials***

Ravitej Uppu, Anjani Kumar Tiwari and Sushil Mujumdar

3. ***Temperature Insensitive Refractive Index Sensor Based on Concatenated Linearly Chirped LPGs***

Saurabh Mani Tripathi, Wojtek J. Bock, Arun Kumar and Predrag Mikulic

4. ***Femtosecond Laser Micromachining for Ultrafast Optofluidic Devices***

Nicola Bellini, Tersilla Virgilli and Roberto Osellame, Guglielmo Lanzani, Roberta Ramponi and Krishna Chaitanya Vishnubhatla

5. ***Generation of Nanoscale Focal Hole with Extended Depth of Focus for Trapping Array of Nanoparticles***

K. Lalithambigai, K. Prabakaran, V. Ravi, Z. Jaroszewicz, K. B. Rajesh and P. M. Anbarasan

6. ***Resonant Mode-Coupling at Anti-Crossing Points in THz Regime***

Ritwick Das, Rajan Jha and Triranjita Srivastava

7. ***H-Structure Left Handed Material for Violet Light: Imaging and Nanoantenna Application***

Monika Rajput, Bhawana Dabas and R. K. Sinha

2C3. HOLOGRAPHY

1. INVITED: ***Unification of Coherence and Polarization of Light Beams in Holography and Speckle Experiments***
C. S. Narayanamurthy
2. ***Design & Fabrication of IR Phase Grating in Lithium Niobate Substrate***
U. S. Tripathi, Ajay Mishra, B. P. Dimri, Thigulla Srikanth and A. N. Kaul
3. ***Digital Watermarking to Prevent Hologram Piracy***
Naveen K. Nishchal, Tomi Pitkaaho and Thomas J. Naughton
4. ***Tailored 3D Twister Vortex Superlattices: Tuning the Threads of Absolute Darkness***
Jolly Xavier, Sunil Vyas, Paramasivam Senthilkumaran and Joby Joseph
5. ***Holographic Image Rendering for Laser Doppler Imaging***
Nicolas Verrier, Benjamin Samson and Michael Atlan

DAY -III

3C1. WAVEGUIDE DEVICES

1. INVITED: ***Quasi Bloch Oscillations in a Fibonacci Spaced Waveguide Array***
S. Dutta Gupta
2. INVITED: ***Coupled Mode Configurations in Optical Fibers for use as Band Reject Filters***
Enakshi K Sharma, Sangeeta Srivastava and Jyoti Anand
3. INVITED: ***Large-Mode-Area Guided-Wave Optical Structures***
Vipul Rastogi
4. ***Localization of Light in a Disordered Waveguide Lattice with Longitudinally Modulated Refractive Index***
Somnath Ghosh, R.K. Varsheny and B.P.Pal

3C2. NONLINEAR OPTICS

1. INVITED: ***Zno Modified MoO₃ Nano- Rods, Wires, Belts and Tubes: Non-Linear Optical and Gas Sensing studies***
V.P. Mahadevan Pillai, I. Navas and Heinz Kohler
2. INVITED: ***All-Optical Switching in Protein-Coated Ultrahigh-Q Microresonators and its Application to Low Power Computing***
Sukhdev Roy
3. ***Temperature-Dependent Second Harmonic Generation at 532 nm in Periodically Poled LiNbO₃***
O. P. Naraniya, Ajay Mishra, A. N. Kaul, A. K. Gupta, M.R.Shenoy and K. Thyagarajan
4. ***Nonlinear Compression of Raman-Induced Kink Similariton Pulses in Nonlinear Fibers***
Thokala Solomon Raju, Choragudi Nagaraja Kumar and Prasanta K. Panigrahi
5. ***Super Continuum Generation under Exponential Saturable Nonlinear Response***
R. Vasantha Jayakantha Raja, K. Nithyanandan, T. Uthayakumar and K. Porsezian
6. ***Two-Crystal, Optical Parametric Oscillator to Generate CW, Dual-Wavelength Radiation with Arbitrary Tunability***
G. K. Samanta and M. Ebrahim-Zadeh

3C3. BIOPHOTONICS

1. INVITED: ***Micro-Opto-Electro-Mechanical Systems for Biosensor Applications***
Srinivas Talabattula, Malathi Sathish and Nivesh Mangal
2. INVITED: ***Femtosecond Spatiotemporal Control Approach to Microscopic Super-Resolution and Optical Trapping***
Debabrata Goswami
3. ***Biosensor Based on Plasmon Resonance Energy Transfer for Real Time H₂O₂ Detection***
S. Dutta Gupta, G. Suarez, C. Santschi, L. Juillerat and O. J. F. Martin
4. ***Magnetomotive Molecular Nanoprobes for Biomedical Imaging Applications***
Renu John and Stephen A. Boppart
5. ***Raman Spectroscopy for the Detection of Antibiotic in Honey***
K. M. Khan, H. Krishna, S. K. Majumder and P. K. Gupta
6. ***Monitoring Blood Glucose using Polarization Sensitive Optical Coherence Tomography***
Jitendra Solanki, Joseph T. Andrews and Pratima Sen

POSTER SESSIONS- 1P

1. ***Designing of All-Optical Four-Valued Ordinary Inverter***
Tanay Chattopadhyay and Jitendra Nath Roy
2. ***Characterization of Micro Lens Array using Interferometric Analysis and MTF Evaluation***
L M Pant, K K Pant, M P Singh and A Ghosh
3. ***Stress Analysis and Fabrication of High Aspect Ratio Infrared Lenses***
K K Pant, N Pandey, M P Singh, B Singh and A Ghosh
4. ***Measurement of Thickness of Transparent Specimens using Wedge Plate Lateral Shearing Interferometry***
Satyaprakash Trivedi and Shashi Prakash
5. ***Small Tilt Angle Measurement using Coherent Gradient Sensing***
Reena Disawal and Shashi Prakash
6. ***Fabrication of Large Si Window of 180 mm Diameter***
M P Singh, N Pandey, B Singh, S Mishra, K K Pant and A Ghosh
7. ***Performance Evaluation of a Visible Wavelength Range Fabry-Perot Interferometer***
S. K. Dhara, J. Paul, B. Ravindra and Ravinder Kumar Banyal
8. ***Speckle Interferometry to Study the Rough Emery Sheets***
Kapil Singh Kundu, Sunny Gulati, Shephali Gulati, Deepak Sharma and David Joseph
9. ***Binary Hologram based Beam Scanning with Equal Step Size***
Abhijit Das and Bosanta R. Boruah
10. ***A Remote Controlled Optical Periscope for Core Viewing in Prototype Fast Breeder Reactor (PFBR)***
Sanjiva Kumar, D. V. Udupa, R. V. Sakrikar, A.M. Kadu and N. K. Sahoo
11. ***Initial Correction of Randomly Aberrated Deformable Mirror Surface for Adaptive Optics System***
Vikash Porwal, Dinesh K. Meena, Sanjay K. Mishra, and D. Mohan
12. ***Generation and Detection of Lower Order Zernike Aberrations***
Sanjay K. Mishra, Geeta Kandhol, Awakash Dixit, D. Mohan and Anurag Sharma
13. ***Self Referencing Cyclic Path Interferometer***
Sanjukta Sarkar, N.Ghosh and K.Bhattacharya

14. ***Single Shot Off-Axis Low Coherence Interference Microscopy for Quantitative Phase Imaging***
Vishal Srivastava and Dalip Singh Mehta
15. ***Frequency Analysis of Indoor Convective Turbulences with Various Receiving Apertures***
Aditya K Mamgain, Awakash Dixit, Sanjay K. Mishra, D. Mohan and A K Gupta
16. ***Design consideration of the Projection Lens for Head-up Display System***
Yashpal, G.S. Singh and Rakesh Dhar
17. ***Color Correction Techniques in MWIR Thermal Imaging Lens***
J. V. Choudhary, Manish Uniyal and P.K. Sharma
18. ***Optical Design of 16x Continuous Zoom Lens in MWIR Band***
Manish Uniyal, Ranabir Mandal and Ikbal Singh
19. ***Structural Design of Regular Type Mechanically Compensated Zoom Lenses***
S. Pal and L. N. Hazra
20. ***Super Resolution by Concentric Unequal Area Phase Filters***
N. Reza and L. N. Hazra
21. ***Total Aberrations of Paraxial and Non Paraxial Higher Order Kinoform Lenses***
U. Dutta and L. N. Hazra
22. ***Random Lasing from an Array of Microdroplets***
Anjani Kumar Tiwari, Ravitej Uppu and Sushil Mujumdar
23. ***W-Shaped Resonator of a Thin Disk Yb:YAG Laser***
Zh. Osgoui, M. Shayganmanesh, M.H. Daemi and Sh. Kazemi
24. ***Analysis of Yb:Yag Thin Disk Laser Resonator Considering Thermal Lens Effects: Experimentally and by LASCAD***
M. Asl Dehghan, M. H. Daemi, S. S. Seyed Zamani, M. Shayganmanesh and Zh. Osgoui
25. ***Stability Analysis of Active Mode-Locked Fiber Lasers using a Distributed Model***
Anish Bekal and Balaji Srinivasan

26. ***Asymmetric Detuning in Active Mode Locked Fibre Lasers***
S. Thiruthakkathevan, D. Jayavel and A. Prabhakar
27. ***Synthesis and Characterization of TiO_2 - SiO_2 Composites***
S. Divya, Indu Sebastian, V. P. N. Nampoori, P. Radhakrishnan and A. Mujeeb
28. ***Nonlinear Optical Characterization of Ge-Ga-Se Glass Solution***
Indu Sebastian, S. Divya, V. P. N. Nampoori, P Radhakrishnan and Sheenu Thomas
29. ***Design Parameters for The Annual Performance of Dye-Sensitized Solar Cells***
Divya Jyoti, Devendra Mohan, Rakesh Dhar, Purnima and S.K. Ghoshal
30. ***Emission Analysis of Eu^{3+} and Tb^{3+} : CdO - Bi_2O_3 - B_2O_3 Glasses***
C. Nageswara Raju, C. Adinarayana Reddy, S.Sailaja and B. Sudhakar Reddy
31. ***Spectroscopic Ellipsometry Study of In_2O_3 Thin Films Grown on Different Substrate***
Chaman Singh and Shyama Rath
32. ***Optical Limiting in Nickel-Complex Dye Doped Self-Protecting Geometry***
Devendra Mohan, Purnima, Divya Jyoti and Amrik Singh
33. ***Doped $Na_2O.Bi_2O_3.B_2O_3$ Glass as Neutral Density Filter***
Meena Rani, Ajay Shankar and Ashish Agarwal
34. ***Study of Third Order Nonlinear Optical Parameters of Chalcogenide As_2S_3 Thin Film and Ge Irradiated As_2S_3 Thin Film at 532nm***
Sunita Rani, Devendra Mohan, Nawal Kishore and Purnima
35. ***Spectroscopic Properties of Nd^{3+} in Novel Heavy Metal Contained Zinc Silicate Glasses***
Inder Pal, Ashish Agarwal, Sujata Sanghi and Sunil Bhardwaj
36. ***Optical Absorption and Fluorescence of Er^{3+} Doped Lead Bismuth Silicate Glasses***
S. Bhardwaj, R. Shukla, S. Sanghi, A. Agarwal and Inder Pal
37. ***Effect of Oxygen Flow Rate on Structural and Optical Properties of Ta_2O_5 Thin Films Prepared by DC Sputtering Method***
Kanta Rathee, Mukesh Kumar and B P Malik
38. ***Digital Photonic Switching in Gold Nanoparticle Doped SiO_2 - TiO_2 Sol-Gel Films***
Parag Sharma
39. ***Optical Non-Linearity in Amorphous $Ge_{30}Se_{70-x}As_x$ Thin Films***
R. Chauhan, A. Tripathi and K. K. Srivastava

40. ***Yb-Doped Optical Fiber Through Vapour Phase Doping Technique***
Maitreyee Saha, Archi Bhattacharya, Atasi Pal and Ranjan Sen
41. ***Modeling of All-Optical Flip-Flop based on Coupled Semiconductor Optical Amplifiers***
Yogesh Kumar and M. R. Shenoy
42. ***A Semi-Analytical Reflectance Model for Oceanic Waters***
Surya Prakash Tiwari and Palanisamy Shanmugam
43. ***Computation of Fresnel Diffraction by VHDL***
Arindam Banerjee, Atin Mukherjee, Prabir K. Saha and Debesh Choudhury
44. ***Susceptibility of Double Random Phase Encryption to the Point Spread Function Attack***
Pramod Kumar, Arvind Kumar, Joby Joseph and Kehar Singh
45. ***Optical Interrogation of Optical MEMS Pressure Sensor - Analysis and Designing***
Bhawna Dhingra, K.Thyagarajan and Sudhir Chandra
46. ***Determination of Phase of Quasi Monochromatic Light in Time Domain by Young's Double Slit Experiment***
Manish Verma, S. Joshi, N. S. Bisht, H. C. Kandpal, P. Senthilkumaran and Joby Joseph
47. ***Lidar Studies on the Optical Properties of Aerosols in the Upper Troposphere and Lower Stratosphere at a Low Latitude Tropical Station Gadanki (13.5⁰ N, 79.2⁰ E), India***
S.R Radhakrishnan, M.Satyanarayana, Leena Raj, V.Krishnakumar,Reji K Dhaman, G.S.Motty , V.P Mahadevan Pillai and K Raghunath
48. ***Investigation of Effective Interaction Area for Second Harmonic Generation in Photonic Crystal Fiber***
Ritapa Bhattacharjee
49. ***A Bidirectional Directly Modulated Radio over Fiber Transport Systems Employing SOA and RSOA***
A.S.Patra ,A. Das, B. Bag and Hai-Han Lu
50. ***Tunneling Effects on Optical Solitons in an Erbium Doped Fiber***
M.S.Mani Rajan, A.Mahalingam
51. ***Response of a Human Eye to Periodic Bar Targets in the Presence of SCE-I***
P K Mondal and Sumit Ghosh

POSTER SESSIONS-2P:

1. ***UV-Vis Up-Conversion Luminescence of Tm^{3+}/Yb^{3+} Doped Modified Yttrium-Germanium-Aluminium-Phospho-Silicate Glass based Optical Fibers Under Excitation at 980 Nm***
Arindam Halder, Mukul C. Paul, Mrinmay Pal, Shyamal Das and Shyamal K. Bhadra
2. ***Design of Segmented Cladding Fiber for Femtosecond-Pulse Laser Beam Delivery***
Babita and Vipul Rastogi
3. ***Simulation and Experimental Characterization of SOA/EDFA Hybrid Amplifier***
Umesh Tiwari, K Thyagarajan and M R Shenoy
4. ***Fundamental Noise Limits in Distributed Anti-Stokes Raman Thermometry Systems***
Amitabha Datta, Deepa Venkitesh and Balaji Srinivasan
5. ***Fiber Bragg Grating as an Optical Limiter***
Santosh Pawar, S. Kumbhaj, P. Sen and P. K. Sen
6. ***Fluorescence Chemo Sensor for the Measurement of Fluoride Ion Concentration in Potable Water***
Lokesh Jain, Shubhada Kumbhaj and P. K. Sen
7. ***Temperature Insensitive Fiber Optic Devices using Multimode Interference Effect***
Arun Kumar, Saurabh Mani Tripathi and Manoj Kumar
8. ***Design and Analysis of Dual-Core Leaky Waveguide Gain Flattening Filters for Erbium Doped Waveguide Amplifier***
N. Ashok and Vipul Rastogi
9. ***Characterization of Buried Channel Waveguides from the Diffraction Pattern Under Transverse Illumination***
Ruchi Garg, M. R. Shenoy and K. Thyagarajan
10. ***Optimal Design of LPWG for Flattening ASE Spectrum of EDFA using Adaptive Particle Swarm Optimization***
Girish Semwal and Vipul Rastogi
11. ***Performance Limitations in 10 Gb/s ITU-T G.653 Fiber Based All Optical WDM System in Presence of Combined Nonlinearities and ASE Noise***
Sridhar Iyer, Shree Prakash Singh and Subrat Kar

12. ***Numerical Analysis of SNR Performance of 1.55 μ m inline TWSOA under WDM Signal Transmission***
P.Manimaran and M.Ganesh Madhan
13. ***Experimental Analysis of 900mhz RF Signal Transmission Through Commercial CATV Fiber Optic Link***
S.Piramasubramanian, M.Ganesh Madhan and J.Sankar
14. ***An Efficient Fast (Parallel) Connection Recovery Strategy for Survivable WDM Optical Network***
Dharmendra Singh Yadav, Santosh Rana and Shashi Prakash
15. ***MPR Codes Offer Higher Throughput in O-CDMA Networks***
Shrikant S. Tangade and Shivaleela E. S.
16. ***Design of an Edfa based WDM Distribution Network with 1:64 Split for Radar Applications***
Abdul Hameed P P and Shivaleela E. S.
17. ***Greening the IP over Optical WDM Network***
T. Srinivas and R. Krishnamurthy
18. ***Performance Evaluation of Optical OFDM Communication System***
Varun Srivastava and Gireesh G. Soni
19. ***Performance Characterization of High Speed Point to Point Dual Broadcast Service PON System without using any Source at Onus***
Ambrish kumar, Jiten Boruah and R. K. Sinha
20. ***Tunable Mid-Infrared Radiation with Mercury Thiogallate Crystal***
S Das
21. ***Spectral and Optical Limiting Applications of Sol-Gel Derived Lead Chloride Crystals***
Rejeena.I, Lillibai, V.P.N.Nampoori and P.Radhakrishnan
22. ***Second and Third Order Nonlinear Optical Susceptibility Studies and Laser Damage Threshold Studies on Gamma Glycine Single Crystals for Photonic Applications***
G. Peramaiyan, P. Pandi and R. Mohan Kumar

23. ***Ultrafast Degenerate Pump-Probe Studies of Si-GaAs***
P.T. Anusha, Debasis Swain, Surya P. Tewari and S. Venugopal Rao
24. ***Modulational Instability in Optical Fibers Near the Zero Dispersion Point for a Relaxational Kerr Medium***
K. Nithyanandan, R. Vasantha Jayakantha Raja, T. Uthayakumar and K. Porsezian
25. ***Plasmonic Cavity Made of Defect in an Array of Asymmetric T-Shaped Structures***
Mohammed Nadhim Abbas, Yia-Chung Chang and M. H. Shih
26. ***Long Range Plasmonic Bragg Grating based Refractive Index Sensor***
Prabhat Behere, M. R. Shenoy and K. Thyagarajan
27. ***Imaging Surface Plasmon Resonance Polarimeter***
Shankar Pidishety and Nirmal K. Viswanathan
28. ***Tight Focusing of Hypergeometric-Gaussian Type-II Optical Mode Beam with High NA Lens Axicon***
K. Prabakaran, P.Suresh, Mohamed Musthafa.A, Z.Jaroszewicz and K. B. Rajesh
29. ***Surface Plasmon Propagation in Asymmetric Metal Strip Waveguides with Anisotropic Substrates***
Anju Babu, C Bhagyaraj, Jesly Jacob and Vincent Mathew
30. ***Plasmon Polariton Modes of a Metal Strip Embedded in Uniaxial Dielectric Materials***
Ajith R, Anju Babu, Jesly Jacob and Vincent Mathew
31. ***Quantum Confinement Effect in the Silicon Nanostructures***
Vivek Kumar and A.K. Shukla
32. ***Raman Study of Disorder in the Polycrystalline Graphite***
Kapil Saxena, B L Sueeval and A K Shukla
33. ***Surface Plasmon Resonance based Sugar Concentration Sensor using a CD-R***
Neha Gupta, Babita and Vipul Rastogi
34. ***Synthesis and Optical Characterization of Strong Red Light Emitting $KLaF_4:Eu^{3+}$ Nanophosphors***
Shahzad Ahmad, Subrata Das, A. Amarnath Reddy, R. Nagarajan and G. Vijaya Prakash

35. ***Design and Analysis of Plasmonic Bend Waveguide Band Pass Filter***
Venus Dillu, Shruti, Tiranjita Srivastava and R.K Sinha
36. ***A Simple Experiment for Studying Correlation in Surface Plasmons***
Stuti Joshi, Manish Verma and H. C. Kandpal
37. ***SPR Based Optical Waveguide Refractive Index Sensors***
Saurabh Mani Tripathi, Arun Kumar, Manoj Kumar and Wojtek J. Bock
38. ***Effects of Arbitrary Phase Shift on the Higher- Order Self-Diffraction in Absorptive Optically Active Photorefractive Crystal***
Neha Katyal, Natasha, Amitava Roy and Avinashi Kapoor
39. ***Polarization Shift Keying Systems***
Ram Soorat and Ashok Vudayagiri
40. ***High Power Mid-IR Generation using PPLN based OPO***
Rouchin Mahendra, O. P. Naraniya, Nimish Dixit, A. N. Kaul and A. K. Gupta
41. ***Modulational Instability in an Optical Fiber with Varying Dispersion and Nonlinearity Driven by an External Potential***
A.Uthayakumar, A.Mahalingam and Rajapriya
42. ***Propagation of Two Soliton in an Erbium Doped Inhomogeneous Lossy Fiber with Phase Modulation***
A.Mahalingam, M.S.Manirajan and A.Uthayakumar
43. ***Supercontinuum Emission from Water Soluble Dyes***
S. Sreeja, S. Venugopal Rao, P. Radhakrishnan, Surya P. Tewari and P. Prem Kiran
44. ***Wigner Distribution Function for Optically-Polarized Schrodinger-Cat States***
Ravi S. Singh, Sunil P. Singh, Lallan Yadava and Gyaneshwar K. Gupta
45. ***Analysis of Tunable Terahertz Generation in DAST using Difference Frequency Mixing***
Maria Farooqui, Kuldeep Meena, Nimish Dixit, A. N. Kaul and A. K. Gupta
46. ***Coherent Interaction of Off-Axis Vortex Solitons in Strongly Nonlocal Nonlinear Media***
Pravin Vaity, R. P. Singh, Ashok Kumar, A. Aadhi and S. G. Reddy
47. ***Probing Cold Atoms in Optical Lattice using Atom-Photon Interaction***
Jasleen Lugani, Sankalpa Ghosh and K. Thyagarajan

48. ***Supercontinuum Generation in All-Solid Photonic Crystal Fiber***
Manish Tiwari and Vijay Janyani
49. ***Generation of Optical Phase Conjugation Properties in Dye Sensitised Silver Halides using DFWM***
K. Kochunarayanan, Krishnakumar V. and V.P. Mahadevan Pillai
50. ***Competition Between Field Strength and D-D Interaction in Two Two-Level Atoms***
Shaik Ahmed, V.S. Ashoka and P. Anantha Lakshmi
51. ***Studies on Sol-Gel Coated Polycarbonate Bi-Aspheric Lenses for Indirect Ophthalmoscopy***
Neeraj Kumar, Vinod Mishra, Keshvanand, G S Singh, S V Ramagopal, Pawan Kapur
52. ***Error Compensation in Sol-Gel Coated Polycarbonate Bi-Aspheric Lenses***
Vinod Mishra, Neeraj Kumar, Keshvanand, G S Singh, S V Ramagopal, Pawan Kapur
53. ***Thermal Issues in Precision Machining of Polycarbonate Optics***
Keshvanand, Vinod Mishra, Neeraj Kumar, G S Singh, S V Ramagopal, Pawan Kapur

POSTER SESSIONS-3P:

1. ***Use of Holographic Optical Element in Laser Doppler Anemometry***
Abhijit Ghosh, Kingshuk Bose and H.L.Yadav
2. ***Application of Thick Phase Transmission Hologram Recorded in Dichromated Gelatin Film for Maximum Data Storage***
Abhijit Ghosh, R.Ranjan and H.L.Yadav
3. ***Holographic Multiplexing of Digital Holograms using Orthogonal Phase Encoding Method***
Samsheerali P T and Joby Joseph
4. ***Holographic Live Measurement of Stress in Photopolymer Film During Hologram Recording***
Shaji Sam TL, Abhishek Pathak, Abhay Jith, Sreebha AB and Ajith Kumar P T
5. ***Characterization of a Phase SLM for Enhancement of Resolution in Microscopic Imagery***
S. Mukhopadhyay, K. Bhattacharya and L.N.Hazra

6. ***Electromagnetically Induced Transparency in a Doppler Broadened Y-type System***
Azeem Baig Mirza and Suneel Singh
7. ***FDTD Modeling of Photonic Crystals for OLED Light Extraction***
Manish Kumar, Rajeev Jindal and Joby Joseph
8. ***Slow Light Symmetric Directional Coupler with Elliptical Cell***
Nagesh Janrao and Vijay Janyani
9. ***Modulational Instability Induced by Cubic–Quintic Nonlinearity and Higher Order Dispersive Effect in Nonlinear Metamaterials***
Manirupa Saha and Amarendra K. Sarma
10. ***Design of 2D Silicon Carbide based Photonic Crystal Waveguide***
Yogita Kalra, Jiten Boruah and R.K. Sinha
11. ***All-Optical Pulse Switching in Twin Core Photonic Crystal Fiber***
T. Uthayakumar, R. Vasantha Jayakantha Raja, K. Nithyanandan and K. Porsezian
12. ***ITO Coated Long Period Fiber Grating Sensor with Enhanced RI Sensitivity***
Nidhi, Umesh Tiwari, Vandana Mishra, RS Kaler, Subhash C.Jain, Nahar Singh and Pawan Kapur
13. ***Radiation Response Behavior of Carbon Doped Aluminosilicate Glass based Optical Fibre for Use as Radiation Sensor***
S. Ghosh, M. C. Paul, S.Das, K.Dasgupta, D. Bohra, H. S. Chaudhary, L. Panwar and P. K. Bhatnagar and S. G. Vaijapurkar
14. ***Fiber Optic Alcometer using PVA Chitosan Polymer Blend***
J. Linesh, M.C. Bobby, T. M. Libish, P. Radhakrishnan and VPN Nampoori
15. ***Modeling of Silica Fibers Immersed in Acetonitrile for Optical Sensing***
Mohammad Mohebbi, Rasul Rezaei and Hadi Khormaei
16. ***Single Mode Etched Fiber Coupler for Temperature Sensing***
Geeta Gupta, Ajay Kumar, Arun Mallik and Anuj Bhatnagar
17. ***Self-Sensing Fibre Reinforced Composites***
L. Wang, D. Harris, V.R. Machavaram, A Tomlin, B.D. Gupta and G.F. Fernando
18. ***Real Time Interaction Analysis of Immobilized Biomolecules over SU8 Polymer Waveguide***
Indrajit Boiragi, Roshan Makkar, Alok Verma and K. Chalapathi

19. ***Long Range Surface Plasmon Resonance Sensor using Silicon and Graphene: Sensitivity Enhancement***
Roli Verma and B.D.Gupta
20. ***Comparison of Sensitivities of SPR based Fiber Optic Sensor Utilizing High Index Dielectric Layers***
Priya Bhatia and B.D. Gupta
21. ***Surface Plasmon Resonance based Fiber Optic Refractive Index Sensor utilizing Cu/TiO₂ layer***
Sarika Singh, Satyendra K.Mishra and B.D. Gupta
22. ***Polarization Structuring of Nondiffracting Beams***
Geo M. Philip and Nirmal K. Viswanathan
23. ***Selective Edge Enhancement using Shifted Anisotropic Vortex Filter***
Manoj Kumar Sharma, Joby Joseph and P. Senthilkumaran
24. ***Generation of Reshaped Hollow Gaussian Beam***
Brijesh Kumar Singh, Manoj Kumar Sharma, Joby Joseph, D. S. Mehta and P. Senthilkumaran
25. ***Coherency Matrix of Polarized Optical Vortex Beams***
V.K. Jaiswal, H.C. Kandpal, R.K. Sinha and R.P. Singh
26. ***Near/Far Field Propagation of Custom Designed Wavefronts***
Awakash Dixit, Nilesh Goyal, Akshay Singh and Sanjay K Mishra
27. ***Generation of Longitudinal Magnetic Probe with Extended DOF for Near Field Magneto Optical Recording***
G.Threse Anita, C.Amala Prathiba Janet, S.Sumathi, K.Gokulakrishnan, Z.Jaroszewicz and K.B.Rajesh
28. ***Non-Conventional Joint Transform Correlator for Security Applications***
Sudheesh Kumar Rajput and Naveen K. Nishchal
29. ***Study of Birefringence in Polymeric Flexible Substrate used for Display Application by Mach-Zehnder Interferometry and Fourier Transform Fringe Analysis***
Gyanendra Singh and D. S. Mehta
30. ***Generation of Focal Shift with Large Depth of Focus using High NA Lens Axicon***
P.Suresh, C.Mariyal, C.Kanchana Devi, K.B. Rajesh, Z.Jaroszewicz and T.V.S.Pillai

31. ***Synchronous Fluorescence Spectroscopy for Extraction of Intrinsic Fluorescence from Human Cervical Tissues***
Seema Devi, Meghdoot Mozumder, Nirmalya Ghosh and Asima Pradhan
32. ***Testing of Handheld Probe for Early Detection of Cervical Cancer Through Polarized Fluorescence Spectroscopy***
Ravi Kumar , Srinivasa B S, Jaidip Japtap, Dr. Asha Agarwal, Dr. Kiran Pandey and Dr. Asima Pradhan
33. ***Optical Coherence Tomography for Non-Invasive Assessment of Wound Healing Response in P.Aeruginosa Infected Excisional Wounds Subjected to Photodynamic Treatment***
K. Sahu, Y. Verma, M. Sharma, K. Divakar Rao, A. Dube and P. K. Gupta
34. ***Depth-Sensitive Raman Spectroscopy Combined with Optical Coherence Tomography for Analysis of Layered Tissue***
K. M. Khan, H. Krishna, K. Divakar Rao, S. K. Majumder and P. K. Gupta
35. ***Studies on the Influence of Tobacco Habit on the Fluorescence Spectra of Healthy Oral Mucosa***
H. Krishna, S. K. Majumder, M. Sidramesh, P. Chaturvedi and P. K. Gupta
36. ***Numerical Aperture of Index-Guiding Microstructured Optical Fibers: An Analytical Study***
Dinesh Kumar Sharma and Anurag Sharma
37. ***FDTD Simulation of Two Photon Absorption in Silicon Waveguide and Realization of All Optical Logic Gates***
Anirban Roy Chowdhury, Ivy Dutta, Kousik Mukherjee and Dharmadas Kumbhakar
38. ***Phase Retrieval from Fourier Modulus- A Numerical Simulation***
Senthil Kumar.M, A.S.Kiran Kumar and C.S. Naryanamurthy
39. ***Design and Modelling of Sub-Wavelength Diffractive Structures using Rigorous Coupled Wave Analysis***
Raj Bahadur Yadav, Unnikrishnan G. and A. K. Gupta
40. ***Low Velocity Soliton Propagation in Photonic Crystals***
Swati Rawal and R.K.Sinha
41. ***Imaging Exoplanet Transits with Hypertelescopes***
A.Surya, S.K.Saha and A.Labeyrie

42. ***Visualizing Vector Field Structures using the Helmholtz Hodge Decomposition***
Monika Bahl, S.Chopra and P.Senthilkumaran
43. ***High Performance SiGe Metal Semiconductor Field Effect Transistor (MESFET) based IR Photodetector***
Rajni Gautam, Manoj Saxena, R.S.Gupta and Mridula Gupta
44. ***Redundancy in Cantor Diffractals***
Rupesh Verma, Varsha Banerjee and Paramasivam Senthilkumaran
45. ***Goos-Hanchen and Fedorov-Imbert Shift for Hermite-Gauss Beam***
Chandra Prajapati and D.Ranganathan
46. ***Optimization of Power Confinement in a Silicon Slot Waveguide***
Kanchan Gehlot, D. M. H. Leung, A. Agrawal and B. M. A. Rahman
47. ***Design of Compact Polarization Rotator Exploiting Silicon Slot Waveguides***
Ajanta Barh, B. M. A. Rahman, D. M. H. Leung, B. P. Pal and R. K. Varshney
48. ***Design and Development of CCD Optical Sight for Tracking Real Time Objects***
R. Sudhakar Rao and Prof. Chandra Lingam

ADAPTIVE OPTICS IN VISION SCIENCE

Christopher Dainty
School of Physics
National University of Ireland, Galway, Ireland
email: c.dainty@nuigalway.ie

Abstract In this talk I shall describe how adaptive optics can be used to produce better images of the fundus of the eye, provide improved vision, and be used as a simulator for the development of improved intra-ocular lenses.

Introduction Adaptive optics (AO) was first suggested in 1953 by an astronomer, Horace Babcock, as a means of compensating for the deleterious effects of atmospheric turbulence, or “seeing”. All of the World’s large ground-based telescopes are equipped with AO systems, and AO is an integral part of the next generation of ground-based optical telescopes of diameter 30-40m.

Adaptive optics finds application wherever there are unknown aberrations to be corrected, including the human eye. As an optical system, the eye is very imperfect when the pupil is dilated, typically having around 0.5 micron rms aberration (the Strehl tolerance for a “perfect” optical system is around 40nm in visible light). Thus images of the fundus taken through a dilated pupil are significantly degraded due to the eye’s aberrations. Adaptive optics enables diffraction-limited imaging, at least in principle.

One problem is translating adaptive optics from astronomy to vision is the system cost: astronomical AO systems have an astronomical cost, running to many millions of dollars. For AO in the eye, we need low cost components. Both the wavefront sensor (based, for example, on the Shack-Hartman device) and the control system can be very inexpensive. However the deformable mirror or liquid crystal (LC) spatial light modulator still are a significant cost, \$20K being typical. LC spatial light modulators are particularly attractive for some applications in the eye.

“Super-vision” with Adaptive Optics Early articles on the application of adaptive optics to improved vision showed that, under rather artificial circumstances (dilated pupils at high light level), it was possible to improve visual acuity to 20/12, i.e. letters roughly 60% of the angular size for “normal” vision. This “super-vision” is however of no practical value for most subjects, since at high light levels the pupil is small, around 2mm diameter, and correction of only focus and astigmatism (for example with glasses) provides diffraction-limited angular resolution. At low light levels – when the

pupil is naturally dilated – spatial averaging of the photoreceptor signals by ganglion cells means that higher order aberrations are less important, at least at the level that occurs in most subjects.

Adaptive Optics for Vision Simulation Cataract surgery, in which the aging lens of the eye is replaced by an intra-ocular lens (IOL), is the World’s most frequently performed surgical procedure (>14m operations per year). New designs of IOL are constantly being invented (for example, lenses with added spherical aberration, multifocal lenses, etc), but these have to be tested: clinical trials are very expensive and require ethical approval. Adaptive optics can be used to simulate the optical effects of a new type of IOL, and, importantly, can be used to observe the effects of misalignment or insertion errors. This application has led to the development of commercial vision simulators that use adaptive optics.

Adaptive Optics for Improved Retinal Imaging Since the pioneering work of Roorda and Williams in 1999, in which they unambiguously recorded in vivo images of the S-, M- and L-cone photoreceptors, there has been intense activity in adaptive optics assisted retinal imaging.

Three types of imaging system have been enhanced using adaptive optics: flood imaging fundus cameras, the scanning laser ophthalmoscope (SLO) and optical coherence tomography (OCT).

Recently, extremely high quality images of rod photoreceptors have been observed by Dubra and colleagues, and by others, using an optimally-designed adaptive optics assisted SLO.

In this talk, I will review all of these applications of adaptive optics in vision science.

Acknowledgement The author is grateful to Science Foundation Ireland for financial support.

All-Optical Switching for Quantum Applications

Prem Kumar*

Center for Photonic Communication and Computing
Department of Electrical Engineering and Computer Science
and Department of Physics and Astronomy
Northwestern University
2145 Sheridan Road, Evanston, IL 60208-3118, USA

A key challenge for quantum information processing is the implementation of networked quantum communications between the nodes of a distributed quantum processor. To date, most demonstrations of quantum communications have utilized point-to-point links. A distributed quantum processor, however, must also incorporate one-to-many and many-to-one quantum links; in other words, it must execute networked quantum communications. Since photonic quantum signals cannot be split without introducing decoherence and noise, quantum networking requires the ability to route entangled single photons. Recently we have developed an ultrafast all-optical switch for such networked quantum communications [1, 2]. This switch is capable of routing entangled single photons at high speeds, with minimal loss and added in-band noise, and—most importantly—without disturbing the photons’ quantum state. In this paper I will summarize the performance characteristics of this switch and describe some of its potential applications in all-optical quantum processing. Moreover, I will show that its behavior quantitatively agrees with the quantum theory of all-optical switching in nonlinear optical fibers, wherein the important effects of cross- and self-phase modulation as well as spontaneous Raman scattering have been taken into account [3].

* This work is done in collaboration with Yu-Ping Huang, Joseph B. Altepeter, Monika Patel, Neal N. Oza, and Matthew A. Hall.

- [1] M. A. Hall, J. B. Altepeter, and P. Kumar, “Ultrafast Switching of Photonic Entanglement,” *Phys. Rev. Lett.* **106**, 053901 (2011).
- [2] M. A. Hall, J. B. Altepeter, and P. Kumar, “All-optical switching of photonic entanglement,” *New J. Physics* **13**, 105004(24) 17 October 2011.
- [3] Y.-P. Huang and P. Kumar, “Quantum Theory of All-Optical Switching in Nonlinear Sagnac Interferometers,” submitted to *New J. Physics*.

PLASMONIC NANO STRUCTURES FOR SERS AND NLO STUDIES

D. Narayana Rao*, K. Shadak Alee, G. Sriram
School of Physics, University of Hyderabad, Hyderabad – 500046 (India)

*e-mail: dnrsp@uohyd.ernet.in; narayanarao.desai@gmail.com

Abstract: We will be discussing on the localized plasmon resonances occurring in metallic nanoparticles of single as well as cluster of nanoparticles, focusing on the generation of confined light fields enabling enhancement of Raman-scattering and nonlinear processes. I will also discuss the various other applications of plasmonics.

1. INTRODUCTION

Metal nanostructures have attracted considerable attention both fundamentally and technologically because of their unique physical and chemical properties and functionalities compared to their bulk counterparts. One of the most fascinating aspects is their optical properties. On the nanoscale, many metals, e.g., silver and gold, exhibit strong absorption in the visible region of the spectrum, with rich colors, e.g., yellowish for silver and burgundy for gold spherical particles. The origin of this absorption is attributed to collective conduction band electron oscillation in response to the electrical field of the electromagnetic radiation of light. This optical absorption is termed surface plasmon, partly because net charges are displaced transiently on the particle surface during electron oscillation. The surface plasmon absorption of metal nanoparticles depends on its size, shape and surrounding environments. Whereas highly symmetric spherical nanoparticles exhibit a single absorption peak, anisotropic shapes such as rod, triangular prism and cubes exhibit multiple scattering peaks in the visible wavelengths due to highly localized charge polarizations at corners and edges [1, 2]. The controllable and tunable optical properties of metal nano structures are highly desired for many applications that rely on light absorption of metal, including surface plasmon resonance (SPR), surface-enhanced Raman scattering (SERS), sensing, imaging, therapy, photo catalysis and optical limiters.

Nonlinear optical (NLO) materials are essential for high speed optical network systems dealing with a large amount of data. In particular, organic third-order NLO materials such as conjugated polymers are powerful candidates for developing photonic devices, due to their fast response and easy chemical modification in comparison to the inorganic systems. Due to the local field enhancement with surface plasmon resonance, larger third-order nonlinearity of composite films has been observed in the presence of metal nanoparticles [3, 4]. These materials with large nonlinearities have been considered to be good candidates for all optical and electronic devices [5]. The surface plasmon resonance (SPR), which plays an important role in enhancing the optical nonlinearities, can be altered by changing the size, shape, and

volume of the particle. From the practical point of view, these metal composites can be optimized to meet the requirements of the optical device operation. Lasers with high intensity output pose a major problem to the safety to the sensors and human eye due to laser induced damage. It is therefore essential to develop a device that exhibits a linear transmittance at lower input fluencies and a damped transmission above it. These devices are termed as optical limiters. The optical nonlinearity of metal nanoparticles in dielectrics is of special interest because of their high polarizability and ultrafast response that can be utilized in potential device applications [6-8] and some of our results which exploits Ag-PVA thin films as good optical limiters will be discussed.

The well known Raman spectroscopic technique provides information on vibrational energies of molecules which are the finger print for unique chemical identification. Despite its small interactive cross-section (10-30 to 10-25 cm²/molecule) the Raman scattered signal is very sensitive to the changes in the crystal structure due to impurities, doping, phase transformations etc. These cross-sections can be enhanced through the unique property of surface plasmon field enhancement of metal nanoparticles (NPs) which leads to the field of SERS. SERS occurs by either placing the molecule close to the surface of the metal nanoparticles (electromagnetic enhancement) or by attaching the molecule to the surface of the nanoparticle through a chemical reaction (chemical enhancement). The electromagnetic mechanism mainly depends on the optical properties of the metal NP while chemical mechanism results from the electronic charge transfer between the investigated molecule and metal NP which in turn results of the increasing the polarizability of the molecule and effectively increasing the Raman cross section [9]. One of the major challenges in the field of SERS is the difficulty in producing efficient SERS substrates with large enhancement factors with reproducibility and uniformity over the whole substrate. It is also desirable that the substrates are easy to fabricate and store. The most commonly used SERS-active substrates are aggregated Ag and Au colloids [10-12]. These metal colloid solutions of Ag or Au particles of

nanometer sizes have shown high SERS enhancement factors. The SERS of a single R6G molecule was reported [13], where the molecule gets adsorbed on the silver nanoparticle surface. However, the stability of the colloidal solution and reproducibility of aggregation are two major problems for nano-Ag/Au substrate [14,15]. Highly reproducible substrates can efficiently be used as SERS based sensors for chemical, biological and medical analysis [16, 17]. To meet this challenge the present work is carried out to fabricate a substrate using a magnetron cluster deposition method and to show these substrates play an important role in reproducibility and highly efficient SERS.

We will discuss a novel way to enhance the SERS signals using inverse silica opal structures along with Au nanoparticles. Localized surface plasmon resonance of gold nanoparticles and photonic band gap (PBG) of inverse silica colloidal crystal are unified by the fabrication of metal-dielectric colloidal crystal structure (MDCS) by a simple chemical route. Intense electric field strength owing to the excitation of high density of states (DOS) at the edges of PBG of MDCS is employed for the Raman-scattering study of adsorbed Raman active Benzenethiol (BT) molecule on the MDCS. Huge enhancement of Raman signal compared to other metallic structures depicts the structure's effectiveness for the micro level detection of analyte.

We will also present some of our recent studies on the in-situ formation of Ag nanoparticles through (synthesized by low power CW lasers) Raman scattering technique.

2. MAJOR SECTIONS

1. Optical limiting studies in Ag-PVA thin films

Different sizes of Ag nanoparticles were generated by heating the Ag-PVA/PS thin films by heating them in a hot air oven with the temperature range between 50-90 °C. Fig. 1a shows TEM (transverse electron microscope) image of the roughly spherical silver nanoparticles in PVA matrix obtained by heating the films (Ag/PVA = 0.042) at 90 °C. The corresponding absorption spectra of silver nanoparticles with different heating times are shown in Fig. 1b. The detailed fabrication process can be found in our earlier published paper [18]. We have examined the nonlinear absorption characteristics of the Ag-PVA/PS films using Z-scan measurements. Second harmonic (532 nm) of an Nd:YAG laser (10 Hz, 6 ns) was used in $f/24$ geometry. Films of 5 μm thick, with a linear transmission of 84% at low laser intensities, show strong reverse saturable absorption at higher intensities (Fig 1c). Plot of the output fluence versus the input fluence (Fig 1d) shows

appreciable optical limiting with a threshold ($I_{1/2}$) of 0.83 J cm^{-2} and output clamped at 0.35 J cm^{-2} ($I_{1/2}$ is defined as the input fluence at which the transmittance reduces to half of the linear transmittance). The dynamic range estimated [18] from the damage and limiting thresholds is approximately 2. Ag-PVA films showed similar behavior, however the damage threshold was lower. It is significant that this first report of optical limiting with silver nanoparticle-embedded polymer thin films indicates thresholds which are comparable or superior to those obtained earlier [19, 20] for silver nanoparticles in colloidal medium with 1–2 mm path lengths. Investigations directed at optimizing the film characteristics to achieve even better optical limiting and unraveling the basic mechanisms involved are under way.

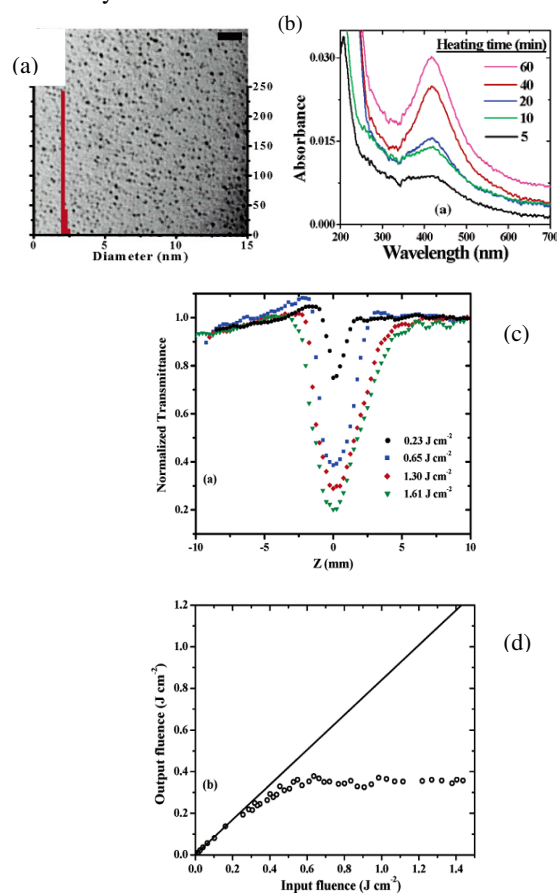


Fig. 1 (a) TEM images of Ag-PVA films heated at 90 °C (b) Plasmon absorption of Ag-PVA heated at 90 °C for different periods of time. (c) Z-scan curves at different input fluences, and (d) optical limiting response; the full line represents 84% linear transmission.

2. Novel plasmonic structures for SERS studies:

Two kinds of plasmonic structures were fabricated with a motivation towards field of sensing. One was fabricated by magnetron nanocluster (NC) deposition

system and the other by a simple chemical technique. These structures were treated with various kinds of organic and bio-molecules to study the efficiency as suitable SERS substrates.

Using the magnetron NC deposition system first a thin silver film will be obtained. In the next stage a precise heating treatment will be followed to obtain silver NCs of approximately 100-200nm in size (Fig 3). The complete details of fabrication parameters could be found in our published report [21]. The structure was treated with very low concentrations (4×10^{-14} to 3.2×10^{-18} M) of crystal violet (CV) molecule to study the efficiency of Raman scattering.

Another plasmonic structure, MDCS is prepared by the immobilization of gold nano particles (Au NPs) through the selective amino group ($-\text{NH}_3^+$) functionalization to the silica network of inverse silica opal (ISO). Hence, with the fabrication of MDCS we have successfully unified the LSPR of AuNPs and PBG of ISO. The optical and structural properties characterization depicts the confirmation and more details on our protocol could be found in our previous reports [22]. Fig 2 shows the protocol followed for the fabrication of our novel MDCS.

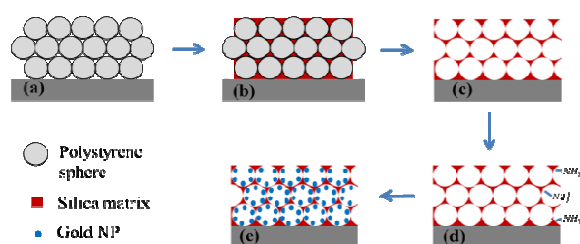


Fig. 2: The schematic diagram shows the protocol for the fabrication steps of a metal-dielectric inverse colloidal structure: (a) self-assembled polystyrene colloidal crystal; (b) silica solution infiltrated polystyrene colloidal crystal structure; (c) an inverse silica opal (ISO) structure obtained by annealing and sintering processes; (d) $-\text{NH}_3^+$ functionalization of the ISO structure with 3-aminopropyltriethoxysilane (APTES); (e) immobilization of Au Nps on the silica network.

With the inherent LSPR features, MDCS could be an effective SERS substrate. We studied the SERS mechanism in our novel MDCS by adsorbing Benzenethiol (BT) molecule, which can covalently bound to the Au NPS of MDCS.

2.1 Plasmonic NC SERS substrate:

In our earlier report we observed that an annealed substrate of 8 minutes deposition with a NC size in the range 100-200 nm is ideal for SERS studies with 514.5 nm excitation wavelength. These substrates were used in the present study to achieve single molecule detection (SMD). Crystal Violet (CV) was used as a probe molecule due to its large Raman scattering cross section. Aqueous solutions of CV

different molar concentrations were prepared by sequential method from decimole to attomole. The SERS spectra were recorded with an excitation wavelength of 514.5 nm which is helpful for studying both the localized surface plasmon resonance (SPR) and resonant Raman scattering (RRS).

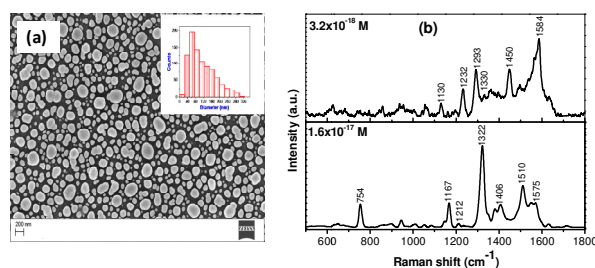
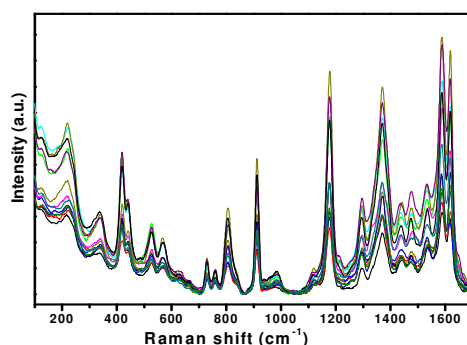


Fig .3: (a) FESEM image of silver NCs and the inset shows the distribution of NCs, (b) shows the Raman spectra of CV for lower molar concentration of CV 1.6×10^{-17} and 3.2×10^{-18} M.

Field Emission Scanning Electron Microscope (FESEM) images were recorded using Carl- Zeiss Ultra 55 system. Fig. 2a shows FESEM image of the substrate. The particle size distribution was obtained using Image J software and estimated to be 112 ± 65 nm sizes (shown in the inset of Fig. 3a). The wide size distribution of Ag NC's on glass is thought to be responsible for SPR broadening. Fig. 2b shows the Raman spectra of CV for lower molar concentration of CV 1.6×10^{-17} and 3.2×10^{-18} M. The observed concentration of CV is 2 orders of magnitude lower than the previously reported limit of detection, which is 10^{-16} M.

From the spectral features seen from Fig. 4, it can be understood that the SERS spectra differ with each other at low concentrations and some of the peaks are shifted either to lower or to higher wavenumbers. This lack of peak to peak amplitude correlation and shift in Raman peaks is ascribed to SMD with different molecular orientations and varying distances with respect to hot spots of NC's. This observation is an indication of SMD. In general the SMD can be done either through limiting of the probe volume or the use of ultra low concentrations of analytes (say 10^{-12} M to as low as possible). CV concentrations of 10^{-14} to 10^{-18} M used in the present study could be a characteristic of SM SERS because at these molar concentrations there is on an average less than 1 molecule of CV within the area of laser spot.

The analytical enhancement factor (AEF) of Ag NC's/glass substrate was found to be $\sim 6.7 \times 10^{12}$. Because of the roughness of the substrate, the Ag NC's can be thought of as forming a 3D structure resulting in a large number of the hot spots. From FESEM image, one can see that both the small and large NC's uniformly spread out on the substrate that



result in a uniform distribution of the hot spots. These

Fig. 4: The reproducible SERS spectra of CV 10^{-6} M

observations confirmed the efficacy of the present SERS substrate fabricated using NC deposition technique. The reproducible SERS spectra of CV 10^{-6} M are shown in Fig. 3. At 10^{-6} M CV, all the Raman peaks are highly reproducible at any location of the probe area on the substrate.

2. 2. Effectiveness of MDCS as SERS substrate:

Wavelength scanned Raman-scattering spectra depicts an intense Raman signal for the 632.8 nm and 785 nm excitations with the former leading to more intense spectra than the later (Fig. 5a). The Raman-scattering with 514.5 nm excitation shows very low intensity signal (Fig. 4a) and deviates from the well-known ω^4 Raman scattering cross-section, where ω is incident frequency [1]. The spectra collected on gold film (not reported here), treated with the BT molecule as same as that of MDCS, shows the validity of ω^4 scattering cross-section dependency. Intense signals are observed for 514.5 nm excitation compared to 632.8 nm and 785 nm. No specific features of BT Raman bands are observed for 785 nm wavelength of excitation.

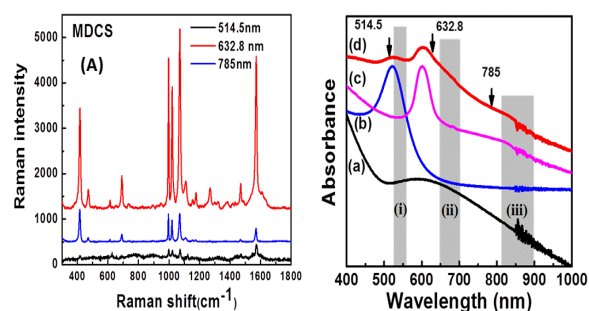


Fig. 5: Wavelength scanned Raman-scattering of $5\mu\text{M}$ BT molecule collected over (A) MDCS-20h, (B) location of 514.5, 632.8, 785 nm wavelengths of excitation on optical absorbance spectra of (a) Gold thin film, (b) Au NPs solution, (c) ISO, (d) MDCS.

Considering the location of the excitation wavelengths in the optical absorption spectra of MDCS (Fig. 5b), the Stokes Raman bands will be on their respective longer wavelength side indicated by the bands in the Fig. 4b. For the excitation wavelength

of 632.8 nm, which is falling on the red band edge, the MDCS will have more density of states due to its fascinating PBG feature compared to homogenous system [23].

According to electromagnetic variational theorem for PhCs [24], it has been well known that low frequency modes concentrate their energy in high dielectric (ϵ) or refractive index (n) regions, and the high frequency modes have a larger fraction of their energy in the low refractive index (n) regions. In 2D and 3D PhCs these mediums being high index dielectric material and low index air medium, the bands above the band gap and below the band gap are labeled as “air band” and “dielectric band” respectively. With this in mind, the modes below the band gap which are corresponding to the 632.8 nm and 785 nm wavelengths of excitation and their respective Raman scattered modes will locate in the dielectric medium [25]. Here the dielectric medium in our MDCS system is a very thin silica matrix with immobilized Au NPs. The 514.5 nm wavelength of excitation and their Raman scattered modes fall on the higher frequency side of the band gap and have their energy concentrated in the air medium [25], which are the air voids of $\sim 325\text{nm}$ in diameter of the inverse opal system. As a consequence, the 514.5 nm excitation above the band edge has low probability to interact with Au NPs resulting in low probable excitation of LSPR and Raman-scattering. On the other hand the 632.8 nm wavelength of excitation below the band edge has the field localized in the dielectric whose thickness will be just few nanometers leading to high probability for excitation and enhancement of LSPR and Raman-scattering of BT molecule which is adsorbed to the Au NPs. The excitation line 785 nm being at much below the band gap, will confine in the dielectric medium like for 632 nm excitation line and will experience moderate response for the excitation of LSPR compared to 632.8 nm. Thus the Raman-scattering probability of BT should be intermediate compared to other two excitation lines. One more important aspect is that the reduced group velocity at the band edge of PBG leads to large light-matter interaction and enhancement of DOS at the band gap edges of the PhC. The experimentally observed (Fig. 5a) more intense Raman signal with the excitation line of 632.8 nm compared to 514.5 nm and 785 nm could be ascribed to two factors: one is the high DOS at band edges of PBG for the excitation line and Raman scattered modes (shaded region (ii) in Fig. 5b) [26] and the second plasmonic effect due to possible field confinement in dielectric medium and excitation of LSPR of Au NPs. The calculation of enhancement due to individual contribution is quite complex since one factor depends on the other. Hence, for the explanation of huge enhancement with 632.8 nm wavelength of excitation the two contributions were considered. From the enhancement factor calculations

the enhancement of 110 times for MDCS under red band edge 632.8nm excitation, compared to 514.5nm excitation, reveals the photonic band edge effects along with plasmonic effect on the enhancement of Raman-scattering.

The observations made for MDCS in analogy to gold thin film shows the confirmation that the modes confinement in the specified dielectric and air band and high DOS avail at photonic band edge could play a massive role in the enhancement of field strengths and there by the spontaneous Raman-scattering.

3. In-situ investigation of the formation of silver nanoparticles in polyvinyl alcohol through Raman spectroscopy:

Though there are many techniques available in the literature for SERS studies, here we developed a novel and simple technique for detecting molecules with large enhancements. The Raman spectrum of the freshly prepared PVA + AgNO₃ films was recorded using Raman spectrometer (HORIBA Jobin Yvon: HR800). CW 514 nm was used as the excitation wavelengths and they were focused by a 50X microscopic objective. The energy used for irradiation was 20 mJ. Laser irradiation with the same CW excitation source and the Raman spectral data collection were done simultaneously. The Raman spectrum was periodically collected at finite time intervals. This was continued till laser damaged the film. With each irradiation the Raman bands of PVA were found to increase as shown in Fig. 6a.

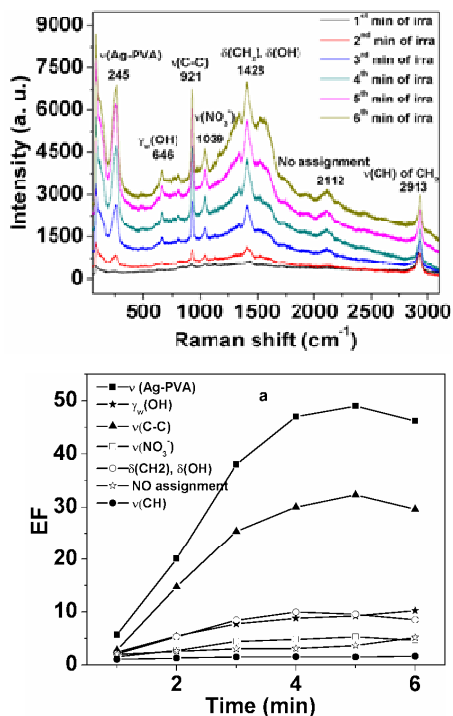


Fig. 6 (a) Raman spectra of PVA+AgNO₃ film recorded with subsequent irradiations using the

excitation wavelength of 514 nm at a power level of 3mW. b) EF for each band calculated with subsequent irradiations using the excitation wavelengths of 514 nm. ν = stretching, δ = bending, γ_w = wagging.

Formation of metal nanoparticles through laser induced heating is a renowned technique [27]. Hence the enhancement of different bands correspond to PVA and PVA-Ag composite [28] (as shown in Fig 6b) is expected due to the formation of Ag nanoparticles. The surface plasmon absorption of these nanoparticles is confirmed by taking the absorption spectra of irradiated spot with successive irradiations. As we did not observe any band corresponding to Ag-O (200 cm⁻¹) stretching vibration, this method provides oxidation free Ag nanoparticles for SERS studies, where the molecules of our interest can be mixed with the PVA solution.

ACKNOWLEDGEMENT

This work carried with financial support from CSIR BRNS and ITPAR. The authors K.S.A and G.S would like to acknowledge the financial support from CSIR-SRF.

REFERENCES

- [1] S. A. Maier, "Plasmonics: Fundamentals and Applications" (Springer, 2007)
- [2] P. N. Prasad, "Nano photonics" (Wiely, 2004)
- [3] Q. Q. Wang, S. F. Wang, W. T. Hang, Q. H. Gong, J. Phys. D: Appl. Phys. **38**, 389 (2005).
- [4] R. F. Haglund, L. Yang, R. F. Magruder, J. E. Wittig, K. Becker, R. A. Zuhr, Opt. Lett. **18**, 373 (1993)
- [5] N. N. Lepeshkin, W. Kim, V. P. Safonov, J. G. Zhu, R. L. Armstrong, C. W. White, R. A. Zuhr, V. M. Shalaev, J. Nonlinear Opt. Phys. Mater. **8**, 91 (1999)
- [6] D. Ricard, Ph. Roussignol, C. Flytzanis Opt. Lett., 10 511 (1985)
- [7] T. Tokizaki, A. Nakamura, S. Kaneko, K. Uchida, S. Omi, H. Tanjai, Y. Asahara, Appl. Phys. Lett. **65**, 941 (1994).
- [8] U. Kreibig, M. Vollmer, Optical properties of metal clusters (Springer, Berlin, 1995).
- [9] E. C. LeRu and P. G. Etchegoin, Principles of surface enhanced Raman spectroscopy and related plasmonic effects, (Elsevier, Amsterdam, 2009).
- [10] T. H. Reilly, S. H. Chang, J. D. Corbman, G. C. Schatz, K. L. Rowlen. J. Phys. Chem. C, **111**, 1689 (2007).
- [11] K. Chou, C. Ren. Mater. Chem. Phys., **64** 241 (2000).
- [12] J. G. Fan, Y. P. Zhao, Langmuir, **24** 14172 (2008).
- [13] S. Nie, S. Emory, Science, **275** 1102 (1997).
- [14] A.M. Michaels, J. Jiang and L. Brus. J. Phys.

- Chem. B*, **104** (2000), p. 11965.
- [15] S.P. Chen, C.M. Hosten, A. Vivoni, R.L. Birke and J.R. Lombardi. *Langmuir*, **18** 9888 (2002).
- [16] S. Shanmukh, L. Jones, J. Driskell, Y.P. Zhao, R. Dluhy and R.A. Tripp. *Nano Lett.*, **6** 12630 (2006), p.
- [17] G. Das *et al.*. *Biosens. Bioelectron.*, **24** 1693 (2009).
- [18] S. Porel, S. Singh, S. S. Harsha, D. N. Rao, T. P. Radhakrishnan, *Chem. Mater.* 17, 9 (2005).
- [19] Y. Sun, J. E. Riggs, H. W. Rollins, R. Guduru, J. *Phys. Chem. B*, **103**,77 (1999).
- [20] R. G. Ispasoiu, L. Balogh, O. P. Varnavski, D. A. Tomalia, T. Goodson, *J. Am. Chem. Soc.* 122 11005 (2000).
- [21] G. Upender, R. Satyavathi, B. Raju, K. Shadak Alee, D. Narayana Rao, C. Bansal, *Chem. Phys. Lett.* **511** 309 (2011).
- [22] Sriram Guddala, A. Chiappini, G. Alombert-Goget, C. Armellini, M. Ferrari, K. Shadak Alee, D. Narayana Rao, A. Chiasera, E. Moser, S. Berneschi, G. Nunzi Conti, G. C. Righini, P. Féron *Proc. of SPIE Vol.* **8173**, 817317-1 (2011).
- [23] S. V. Gaponenko *Phy. Rev. B* 65, 140303 (2002).
- [24] J. D. Joannopoulos, S. G. Johnson, J. N. Winn, and R. D. Meade, "Photonic Crystals: Molding the Flow of Light", 2nd ed. (Princeton U. Press, 2008).
- [25] Ovidiu Toader and Sajeev John, Kurt Busch *Opt. EXPRESS*, Vol. 8, No. 3, 217-222.
- [26] Tetsuyuki Ochiai, Kazuaki Sakoda, and Tsutomu Sawada *Phys. Rev. B* **77**, **245** 101 (2008).
- [27] V. Resta, J. iegel, J. Bonse, J. Gonzalo, C. N. Afonso E. Piscopiello and G. V. Tenedeloo, *J. Appl. Phys.* **100**, 084311 1-6 (2006).
- [28] Y. A. Badr and M. A. Mahmoud, *J. Appl. Poly. Sci.* 99, 3608 (2006).

Biophotonics - studies at RRCAT

P. K. Gupta

Laser Biomedical Applications and Instrumentation Division
Raja Ramanna Centre for Advanced Technology, Indore 452013, India.

pkgupta@cat.ernet.in

Biophotonics, the science of the interaction of light (photons) with biological matter, is playing an important role in the pursuit of two major objectives of quality health care; to detect the disease at a very early stage before it becomes difficult to manage and secondly to treat it with high selectivity that is with no or minimal adverse effect on the normal tissue. In the present talk I shall provide an overview of the work being carried out by us in this area. I shall first describe the use of optical techniques like optical coherence tomography (OCT) for minimally invasive, in-situ biomedical imaging with resolution down to a few micrometers. Some representative applications of OCT like imaging of microstructures of eye; non-invasive monitoring of the healing of wounds and ethanol-induced developmental abnormalities in Zebrafish embryos will be briefly discussed. Next I shall discuss the advantages of the use of optical spectroscopic techniques for the diagnosis of cancer and describe the results of our recent study carried out at Tata Memorial Hospital, Mumbai for *in vivo* diagnosis of cancer of oral cavity. The use of light for the treatment of cancer with minimal damage to the normal tissue and for photodynamic inactivation of antibiotic resistant bacteria will also be briefly touched upon. Finally, I shall discuss the use of light to trap single cells or intracellular objects and for transportation, orientation or rotation of these using only light induced forces. The use of these techniques for spectroscopic studies on single cells or measurement of the visco-elastic parameters of single red blood cells and the role these can play in biomedical diagnosis will also be briefly touched upon.

INTERFEROMETRY WITH BROADBAND LIGHT

M. P. Kothiyal
Applied Optics Laboratory
Physics Department, IIT Madras
Chennai 600 036, India
e-mail : kothiyal@physics.iitm.ac.in

Abstract: A broadband light interference pattern provides phase information corresponding to a range of wavelengths simultaneously. In the recent times a variety of applications such as 3D surface profiling, film thickness measurement, dispersion measurement, optical coherence tomography have been developed by extracting the phase information from the interferogram. Some of these procedures have been discussed here.

1. INTRODUCTION

A broad band light produces a spectacular coloured interference pattern. Interference in the films produced by the sunlight have always been fascinating. The credit for an early application of white light fringes goes to A. Michelson. In the recent times several applications of broadband light interference have been investigated [1-13]. One may look at the interferogram as an incoherent superposition of large number of monochromatic interferograms. This superposition results in a unique intensity distribution in the interferogram with a maximum at zero path difference such that the identification of equality of path difference in the two arms of an interferometer becomes a simple matter. This equality of path difference is extensively used for profiling applications by locating this maximum. In fact this principle was used by Michelson in 1881 in one of the pioneering experiment using interference of light for the calibration of a standard meter. In yet another approach to get useful information from a white light interferogram is to decompose in its individual constituents which may be accessed at the output of a spectrograph, if the interferogram is imaged at the entrance slit of the spectrograph[14-24]. The interference signal may also be Fourier transformed to get the individual monochromatic components[11]. An important advantage of a broad band light source is that it can overcome the ambiguity problem associated with monochromatic interferometry. In a broadband light source such as a filament lamp (white light) or Super Luminescent Diode (SLD), a range of wavelengths are simultaneously present. Alternatively, the broad band effect can also be achieved by the use of lasers at multiple wavelengths, tunable diode laser, or color CCD camera or multiple chips with different filters used with white light.

Extraction of useful information from an interferogram requires careful fringe analysis and techniques that are fast and can be automated. This is important from the point of view of eliminating errors. The development of fringe analysis techniques have played an important role in improving the resolution and accuracy. Procedures such as temporal and spatial phase shifting technique, heterodyne interferometry, Fourier and Hilbert transform techniques have been

employed. Phase shifting has been the most used approach. Temporal phase shifting most frequently makes use of a PZT to introduce phase shift. Polarization phase shifting is another useful method of producing phase shift between the interferograms. From the point of view of stability and dynamic measurement a single shot procedure, which can produce several frames in one go, are of great value. Polarization phase shifting technique has recently been found very useful in this respect[13]. The other possibility is the use of color CCD with its three channels. In the following sections we discuss various measurement techniques developed, including our own results using broad band light.

2. INTERFERENCE WITH BROADBAND LIGHT

A broadband light source is small coherence length, the actual value depending on the bandwidth. For white light source such as a tungsten halogen lamp, it is in the range of a few micrometers. The fringes localize in the vicinity of the test object when the paths between the test and measurement arms of an interferometer match closely. The contrast of the fringes is maximum here. In other words, the fringe contrast function (coherence envelope) peaks at zero path difference.

2.1 Interference Equation

For a broad band light source the intensity distribution in the interference pattern is given by the equation[4]

$$I = I_r + I_t + 2\sqrt{I_r I_t} \gamma_{11}^r(\tau) \quad (1)$$

where I_r and I_t are respectively the intensities of the reference and test beams of the interferometer. $\gamma_{11}^r(\tau)$ is the real part of $\gamma_{11}(\tau)$, the complex degree of coherence of the light source, and τ is the time delay between the two optical paths. A broad band light source may be assumed to have a Gaussian power spectral density function. The value of $\gamma_{11}(\tau)$ is given by

$$\gamma_{11}(\tau) = \exp[-(\pi\tau\Delta\nu)^2] \exp(-i2\pi\bar{\nu}\tau) \quad (2)$$

where $\bar{\nu}$ is the central frequency and $\Delta\nu$ is the spectral width. Eq. (1) can be rewritten as

$$I = I_r + I_t + 2(I_r I_t)^{1/2} g(z) \cos(\phi(z) + \phi_0) \quad (3)$$

where $g(z) = \exp[-(\pi\tau\Delta\nu)^2]$ is the coherence envelope or the fringe contrast function and $\phi(z) = 2\pi\bar{\nu}\tau$. ϕ_0 is the phase shift which accounts for phase changes such as phase shift on reflection. In Eq. (3) $2z$ is the round trip path difference suffered by the interfering beam in a double pass interferometer such as Michelson, Linnik or Mirau in which the actual difference of the arm lengths from the beam splitters is z . z is related to τ as $\tau = 2z/c$; hence

$$\phi(z) = \frac{2\pi}{\lambda} (2z) \quad (4)$$

Equation (3) can be rewritten as

$$I = I_0 (1 + G(z) \cos \phi(z)) \quad (5)$$

where $G(z) = Vg(z)$, $I_0 = I_r + I_t$ and $V = 2\sqrt{I_r I_t} / I_0$, V is the visibility or contrast. The simulation of variation in intensity with z calculated using Eq (3) is shown in Fig.1 for a non zero value of ϕ_0 .

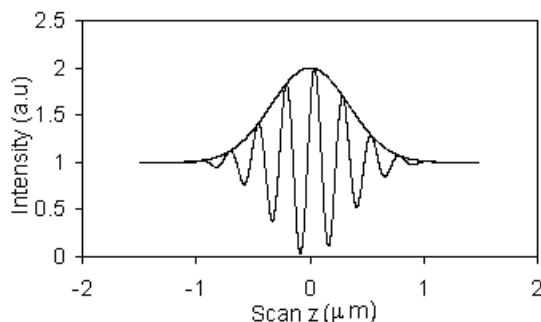


Fig. 1. Simulated white light interference pattern using Eq. (3). ϕ_0 is assumed to be $\pi/2$.

The envelope in Fig.1 is the fringe contrast or the visibility curve and has peak at $z = 0$. The fringe contrast decreases rapidly as the path difference is increased from zero. The peak of the fringe contrast function (the correlation peak) represents zero path difference condition between the object and reference beams. This capability of a white light interferometer to show the zero path condition without any phase ambiguity, as against a monochromatic interferogram where same value maximum and minimum repeats itself, is of great value in optical metrology with broadband light.

2.2 Monochromatic Interferometry using Phase Shifting (PSI)

In the process of analyzing broadband interference, we need to analyze monochromatic fringe patterns as well in some procedures. Here we discuss how monochromatic interferograms are evaluated using

phase shifting methods. For monochromatic light the Eq. (5) can be written as

$$I(x,y) = I_0(x,y) [1 + V(x,y) \cos[\phi(x,y) + \alpha]] \quad (6)$$

where $G(z) = V$ as $g(z) = 1$ for monochromatic illumination and ϕ_0 is assumed zero. In PSI the phase of one of the arms of the interferometer is shifted in steps α and the new intensity at various points (x,y) in the interferogram is recorded at each step.

There are several algorithms available to determine $\phi(x,y)$ and $V(x,y)$ from Eq.(6) [25]. Since there are three unknowns in Eq (6), a minimum of three interferograms are required to solve for the wave front phase and contrast. With steps being $-\alpha$, 0 and α Eq(6) can be solved for the unknown wave front phase as

$$\phi(x,y) = \tan^{-1} \left\{ \frac{1 - \cos \alpha}{\sin \alpha} \left(\frac{I_1 - I_3}{2I_2 - I_1 - I_3} \right) \right\} \quad (7)$$

There are however several errors compensating algorithms that are less sensitive to reference phase shift calibration and other errors [8,25,26]. A five step algorithm with phase shift values as -2α , $-\alpha$, 0 , α , 2α with α , usually being close to $\pi/2$, gives

$$\phi(x,y) = \tan^{-1} \left\{ 2 \sin \alpha \left(\frac{I_2 - I_4}{2I_3 - I_5 - I_1} \right) \right\} \quad (8)$$

$$\sin^2 \alpha = \frac{4(I_2 - I_4)^2 - (I_1 - I_5)^2}{4(I_2 - I_4)^2} \quad (9)$$

The visibility (contrast function) is given as

$$V(x,y) = \frac{[4(I_2 - I_4)^2 + (2I_3 - I_1 - I_5)^2]^{1/2}}{I_1 + 2I_3 + I_5} \quad (10)$$

3. SCANNING WHITE LIGHT INTERFEROMETRY (WLI)

Fig. 2 shows a microscope based version of a broad band light interferometer. It is configured as a spectral interferometer discussed later. For scanning WLI the CCD will be placed at the ES plane (the entrance slit of the spectrometer). The scanning white light interferometer for surface metrology commonly makes use of a Mirau interference objective to scan the object [8]. Broad band light from a halogen lamp is directed to the objective. The objective is mounted on a piezo electric translator (PZT), to translate the objective along the optic axis. The interferogram is imaged on to a CCD camera. Each frame is transferred to the host computer which performs the acquisition and analysis functions and controls the PZT scan rate.

The Mirau objective has the disadvantage that it requires a long working distance microscope objectives to accommodate the two plates, which consists of the reference surface and the beam splitter plate. A Linnik interference microscope can be used to avoid this difficulty [8].

If the PZT is moved in a continuous manner the output at any pixel will go through the sequence as shown in

the Fig. 1. Signal processing can be carried out to determine the peak position as a function of the scan position z . This is usually possible when measurement along z -axis alone it required as done in optical coherence tomography (OCT) as discussed later. To get a 3D picture $z(x,y)$ as in surface metrology, the scanning along the z axis is done insteps. In practice the PZT is moved in steps (usually $\bar{\lambda}/8$ where $\bar{\lambda}$ is the mean wavelength) starting from some reference position and data is available at discrete frame positions.

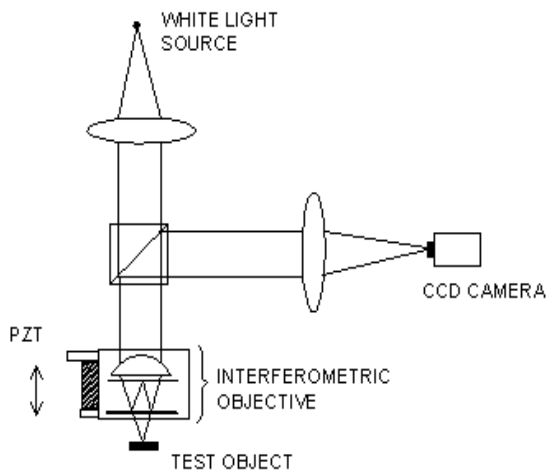


Fig.2 Scanning white light interferometer.

3.1 Computation of Coherence Envelope by Phase Shifting Technique

It has been shown in Sec 2.2 that PSI can be used to determine both the phase and the fringe contrast (visibility). The fringe contrast is practically constant in monochromatic interferometry and its calculation is not of much interest. The white light interference pattern is expressed by Eq.(3) in which $g(z)$ is the fringe contrast function which is not constant but varies with z , the scan position. The application of phase shifting technique to determine the fringe contrast function of a white light interferogram poses problems if the commonly used phase shifting method of translating the reference mirror with PZT is used. Firstly, the phase shift is not same for all the wavelengths. Secondly $g(z)$, the quantity to be determined is not same for all the steps. This will lead to error in the measurement. Nevertheless the phase shifting technique has been applied to white light interferometry using PZT phase shifter, as well as, the phase shifters based on polarization components which can be made achromatic[13].

A successful error compensating 5-step algorithm is by Larkin[10].Using this algorithm, the fringe contrast function $G(z)$ is given by

$$2G(z) \sin^2\alpha = [(I_2 - I_4)^2 - (I_1 - I_3)(I_3 - I_5)]^{1/2} / I_0 \quad (12)$$

For α close to $\pi/2$ for the central wavelength, $\sin^2\alpha/2 \approx 1$ and $G(z)$ can be evaluated by

$$G(z) = [(I_2 - I_4)^2 - (I_1 - I_3)(I_3 - I_5)]^{1/2} / 2I_0 \quad (13)$$

In this equation I_3 represents the intensity of the central frame($\alpha=0$). This algorithm by far gives the best agreement with the ideal coherence envelope.

4. FREQUENCY DOMAIN WLI

We may think of the scan history of the intensity modulation for an individual pixel in a white light interferogram as a sum of single wavelength (monochromatic) fringe patterns superposed incoherently one upon other[5]. The output intensity for a monochromatic constituent of wavelength λ can be expressed as(Eq.(3) with $g(z)=1$)

$$I(z, \lambda) = I_r + I_s + 2(I_r I_s)^{1/2} \cos[\phi(\lambda) + \phi_0] \quad (14)$$

$$\text{where } \phi(\lambda) = \frac{4\pi z}{\lambda} \quad (15)$$

and ϕ_0 may be any additional phase shift for a given z . We may write $\sigma = 1/\lambda$ then $\phi(\sigma) = 4\pi\sigma z$. The variation in $\phi(\sigma)$ with σ is linear and z may be obtained by a slope calculation if $\phi(\sigma)$ can be determined for a series of σ values, i.e.

$$z = \frac{\Delta\phi(\sigma)}{4\pi\Delta\sigma} \quad (16)$$

Each fringe pattern constituting the broad band light interferogram has a unique magnitude, phase and spatial frequency or wave number k defined here as the rate of change of phase with scan position. Peak fringe contrast occurs at a scan position for which the phases of these constituent patterns all agree. Knowledge of the relative phases of the patterns at any given position in the scan tells us where we are with respect to the zero position. The information about the magnitude and phase ϕ of each constituent pattern can be extracted mathematically by means of a Fourier Transform of scan history of the white light interference pattern [11]. The normalized Fourier transform of the intensity $I(z)$ is given by

$$P(k) = \int_{-\infty}^{\infty} I(z) \exp(-ikz) dz \quad (17)$$

In practice at any pixel intensity values I_i taken at equally spaced OPD positions z_i during scanning. The Fourier transform of the scanned intensity may be represented as

$$P_j = |P_j| \exp(-i\phi_j) \quad (18)$$

The transformed interferogram now represents for each pixel, relative strength $|P_j|$ and interferometric phase ϕ_j corresponding to the constituent wave of white light having the wave number k_j . The phase is given by

$$\phi_j = \tan^{-1} \{ \text{Im}(P_j) / \text{Re}(P_j) \} \quad (19)$$

As seen earlier the slope of the ϕ - k line gives the local height z . The modulus of P_j represents the coherence envelope of the white light interferogram. The region

where $|P_j|$ is large has the most useful information. This region in the FT data can be identified and a series of pairs (ϕ_j, k_j) from this region used for obtaining $\phi_j - k_j$ least square linear fit whose slope gives z . For the least square fit the phase data is weighted by $|P_j|^2$. The modulo 2π ambiguities in the phase data are removed by a unwrapping procedure.

5. SPECTRAL INTERFEROMETRY

The white light interferogram can be spectrally decomposed (Spectrally Resolved White Light Interferometry, SRWLI) by a spectrometer which will produce a series of N monochromatic intensities modulated by a cosine function as described by Eq. (18). The number N is determined by the number of pixels in the detection unit such as a CCD array. Each pixel along the chromaticity axis (the direction of dispersion) corresponds to a different σ . The aim is to determine $\phi(\sigma)$ at each pixel and use Eqn. (20) to determine z . These values can be extracted at each pixel (σ value) by Fourier transform technique[17] or by phase shifting technique[12,17]. In phase shifting technique one may use spatial phase shifting or temporal phase shifting.

5.1 Temporal Phase Shifting with PZT Phase Shifter

For a white light source a phase shift of $\pi/2$ with a PZT can be exact at only one wavelength such as the mean wavelength of the source. In SRWLI, in which interferograms are obtained over a range of wavelengths, the phase shift will vary with the wavelength. Nevertheless a PZT phase shifter performs remarkably well in SRWLI in spite of its poor achromaticity. It has been seen that the errors introduced in the calculations of phase as a function of wavelength is oscillatory in nature and get averaged out when ϕ vs σ line is obtained from a least square fit [18]. Further the magnitudes of the error is quite small with error compensating algorithms such as Eq.(8) and practically zero with Eq.(21).

5.2. Experimental Setup

The experimental setup to carry out surface profiling and film thickness is shown in Fig. 3. The test surface is observed through a Mirau-type interferometric microscope objective. The light source is a halogen lamp, which presents a broad continuous spectrum. At the exit plane of the microscope, the white-light interferogram of the surface is passed through the entrance slit (ES) of a direct-vision spectroscope. The ES selects a line of the test surface for profiling. The output of the spectroscope is received on a CCD camera. The camera is aligned such that the ES is parallel to the columns of pixels, so that the rows represent the chromaticity axis because the dispersion is perpendicular to the slit. To implement the phase shifting technique the objective mount is fitted with a PZT. The camera (Pulnix 1010) gives a 10-bit digital

output. The interferograms are transferred to the PC through an image acquisition board (NI PCI 1422). The control voltage to shift the PZT for phase shifting is produced by a digital to analog card (NI DAQ). For calibration of the CCD camera we used the cadmium (Cd) spectral lamp.¹⁹

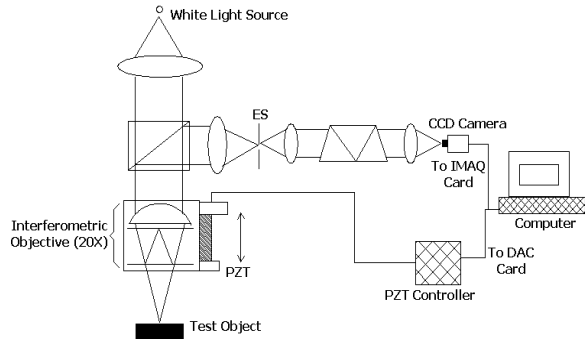


Fig. 3 Schematic of a spectral interferometer

5.2.1 Experimental Results

5.2.1.1 Surface profiling

For this application the phase varies linearly with wave number as

$$\phi(\sigma) = 4\pi\sigma z \tag{20}$$

where $2z$ is the round trip optical path difference and is related to the surface height. The surface height z can be obtained from Eq.(16)

For the calculation of phase $\phi(\sigma)$ we used the temporal phase shifting interferometry. In order to avoid phase calculation error due to the phase shift error at wavelength other than the mean wavelength, we have used the error compensating eight step algorithm given by [25]

$$\tan\phi = \frac{-I_1 - 5I_2 + 1I_3 + 15I_4 - 15I_5 - 1I_6 + 5I_7 + I_8}{I_1 - 5I_2 - 1I_3 + 15I_4 + 15I_5 - 1I_6 - 5I_7 + I_8} \tag{21}$$

where I_1, I_2, \dots, I_8 are the phase shifted spectral interferogram. Fig. 4 shows the spectral interferogram of a plane surface which is observed through the experimental setup shown in Fig. 3. In the fringe pattern any cyclic variation of intensity along the chromaticity (horizontal) axis is due to phase difference as a result of wavelength change only. Similarly any variation in intensity along the vertical axis is due to change in optical path (due to air wedge, for example) as the wavelength is constant along any column of pixels. In any other arbitrary direction, there is contribution due to both. Eight such phase shifted interferograms are needed to calculate the phase $\phi(\sigma)$.

The height value z determined from Eq. (16) is less precise. This value of z is used as a first approximation to the true value and can be improved with the help of the available more precise monochromatic phase value using the equation given by [12,15,19,20]

$$z' = \frac{1}{4\pi\sigma} \left[\phi' - 2\pi \text{int} \left(\frac{\phi' - 4\pi\sigma z}{2\pi} \right) \right] \tag{22}$$

where $\text{int}(x)$ rounds off to the nearest integer to x .

Figure 5 shows the line profile of a $1.76 \mu\text{m}$ standard step obtained using Eq. (22). The step height was found to be $(1761 \pm 2) \text{ nm}$.

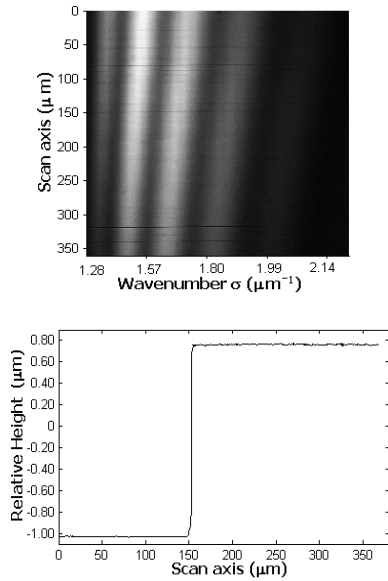


Fig. 4 A typical spectral interferogram (top). Line profile of a $1.76\mu\text{m}$ standard step (bottom).

5.2.1.2 Film Thickness Profiling

When a transparent film is deposited on a substrate as shown in Fig. (1). The reflection coefficient of the system is given by [21,22]

$$R = \frac{r_{01} + r_{12} \exp(-i2\beta)}{1 + r_{01}r_{12} \exp(-i2\beta)} \quad (23)$$

where r_{01} and r_{12} represent the Fresnel reflection coefficients of the top and bottom surfaces of the film respectively, and β is given by the relation $\beta = 2\pi\sigma d n_2$, where d and n_2 are the thickness and refractive index of the transparent film respectively. The reflection coefficient R is complex. The reflected beam due to the presence of the film, therefore, has a phase ψ .

The phase $\phi(\sigma)$ in this application can be written as [21,22]

$$\phi(\sigma) = 4\pi\sigma z + \psi(\sigma, d, n_2) \quad (24)$$

Since $\psi(\sigma, d, n_2)$ is a function of thickness d , $\phi(\sigma)$ is also function of d . The first term $(4\pi\sigma z)$ on the RHS of Eq. (24) is due to the air gap between the reference plane and the top of the transparent film. For the determination of surface height z and film thickness d we used the measured value of $\phi_{\text{measure}}(\sigma)$ to minimized the error function

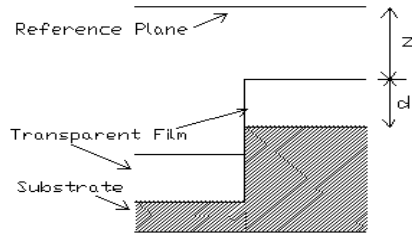


Fig. 5: Cross section of a patterned surface

$$\eta(z, d) = \sum_{\sigma_c - \Delta\sigma/2}^{\sigma_c + \Delta\sigma/2} [\phi_{\text{model}}(\sigma, z, d) - \phi_{\text{measure}}(\sigma)]^2 \quad (25)$$

for a particular value of z and d . where σ_c and $\Delta\sigma$ are the central wave number and the band width of the white light source.

Experiment was carried out with a patterned silicon wafer on which a SiO_2 film was deposited. fringe were recorded. The phase at a series of points along the wave number axis was determined and used to determine the surface height and the thickness of the layer at each point, as given by Eq. (24), were then modeled so as to minimize the error function η given by Eq. (25). Initially we used a linear fit to the experimental data, the slope of this phase $\phi(\sigma)$ vs wave number line gives us an approximate value of $(z + n_2d)$ since $(z + n_2d) = \text{slope}/(4\pi)$. We then used the Levenberg–Marquardt nonlinear least-squares fitting algorithm (Matlab) for thickness modeling. This algorithm requires an initial guess for d and z , which we can get from the above calculation. With these values of d , z and the refractive index as inputs, we obtain, as the output, independently adjusted values of d and z which yield the best fit to the experimental values of the phase. Figure 6 shows film and substrate profiles obtained for the top surface of the film and the substrate for the sample used.

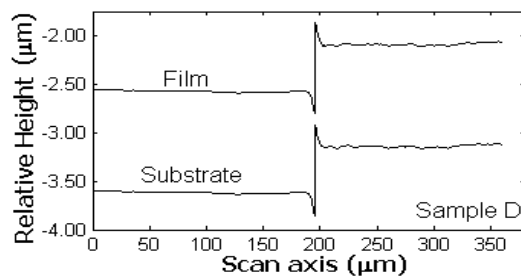


Fig. 6: Line profiles of the top surface of the film and the substrate.

5.2.1.3 GVD measurement

In the presence of a dispersive sample in one arm of the interferometer such as a Michelson interferometer shown in Fig. 7, the phase vs. wave number curve shows a stationary point as shown in Fig.9. At the stationary point the phase $\phi(\sigma)$ is quadratic with σ and is given by [24]

$$\phi(\sigma) = 4\pi^2 L k'' c^2 (\sigma - \sigma_0)^2 = A\sigma^2 + B\sigma + C \quad (26)$$

where L is the thickness of the sample, c is the velocity of the light and k'' is the group velocity dispersion(GVD) of the sample at $\sigma = \sigma_0$, which can be written as

$$k'' = \frac{\lambda_0^3}{2\pi c^2} \frac{d^2 n}{d\lambda_0^2} \quad (27)$$

where n is the refractive index of the sample. From Eqs. (26) and (27) we have $\sigma_0 = -B/2A$ and $d^2 n/d\lambda^2 = -B^3/16LA^2$. It can be clearly seen from Eqs. (26) and (27) that, knowing the sample thickness L and the quadratic fit coefficients A , B , and C from the $\phi(\sigma)$ vs. σ plots, we can calculate the GVD ($\propto d^2 n/d\lambda^2$) of the sample at any wavelength within the lamp spectrum.

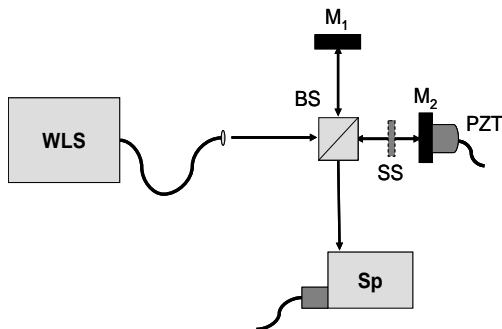


Fig.7: Schematic of the experimental setup for GVD measurement of a plate sample (SS).

To demonstrate the effectiveness of this technique for fast and accurate measurement of GVD we inserted a 1.60 mm thick silica glass slide in the sample arm of the interferometer shown in Fig. 7. Figure 8 shows one of the spectral interferogram with the sample. Using Eq.(21) we calculate the spectral phase. A line scan of the phase $\phi(\sigma)$ versus σ around the stationary phase point σ_0 is shown in Fig.9 (trace b). We can displace the stationary point along the σ axis by appropriately delaying the interferometer arm and obtain a new phase $\phi(\sigma)$ versus σ for around a different σ_0 along the chromaticity axis. Figure 9 shows the line scans of the phase plots around different stationary points. Applying a quadratic fit to each curve and using Eqs. (26) and (27), we calculated $d^2 n/d\lambda_0^2$ for the corresponding $\lambda = \lambda_0$. Figure 10 shows the values of $d^2 n/d\lambda_0^2$ as a function of wavelength of the silica sample. The curve in the figure is a theoretical curve calculated using the Sellmeier dispersion equation with experimental points shown on it by circles.

The arrangement like Fig.7 can as well be used for refractometry of liquid samples, measurement of dispersion curves, or effective thickness of samples with known dispersion[27-29]

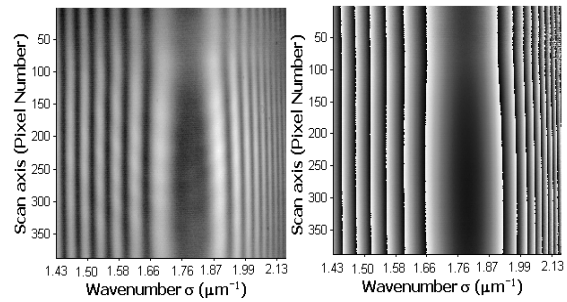


Fig. 8 Spectral interferogram of the sample (left) with the corresponding wrapped phase map (right)

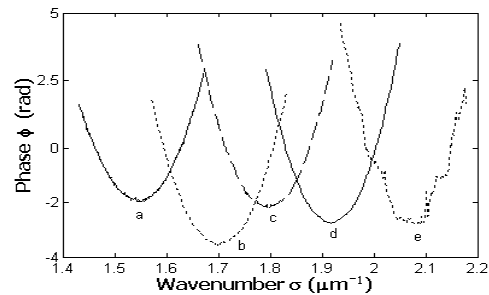


Fig.9 Phase vs. wave number for different stationary points on calculated curve for silica sample.

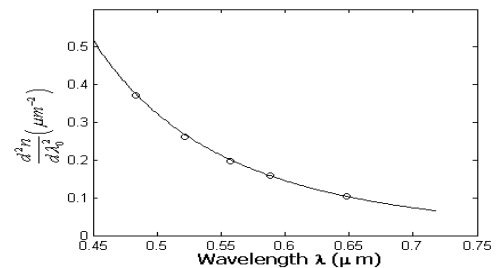


Fig. 10: Experimental values(circles) of $d^2 n/d\lambda_0^2$

6. MULTIPLE WAVELENGTH INTERFEROMETRY

The half a wavelength unambiguous measurement range of monochromatic interferometry is overcome by use of broadband light and spectral interferometry. It is therefore possible to carry out a similar procedure with limited number of wavelength. Use of two wavelengths, resulting in larger equivalent wavelength, and hence the unambiguous range, was proposed [30]. Likewise use of three wavelengths has been studied [31,32]. Since the phase vs wave number relationship is linear, the measurement process involves adding/subtracting multiples of 2π to the wrapped phase data at the three wavelength such that the phase vs wave number graph is linear (Eq. (20)). Figure 11 shows a typical result. The top profile is by equivalent wavelength method which amplifies the noise.

7. OPTICAL COHERENCE TOMOGRAPHY

The vertical scanning interferometry with low coherence light makes use of discrete steps to scan

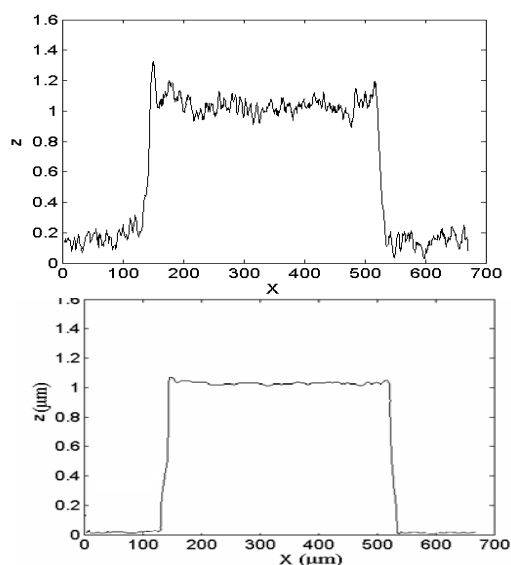


Fig.11 Step profile obtained by multiple wavelengths. Two wavelength (top); three wavelengths (bottom). $z = 1.125\mu\text{m}$.

the reference or object beam to produce 3D imaging. The property of interferometric localization can be used to carry out 3D imaging by combination of scanning in lateral and axial directions [35]. The scanning in the axial direction is continuous. The technique is known as Optical Coherence Tomography (OCT) and is suitable for imaging/profiling multi-layered structures by measuring the interference signal and depth of each layer boundary. The image is constructed point by point. Fig. 12 shows schematic of a fibre optic based OCT arrangement. The detector will produce a signal that will appear as in Fig. 1. Different layers of the medium produce such peaks as the axial scanning is done. The axial distance between the peaks gives the depth information. The axial resolution is determined by the coherence length in the medium and is given by $0.44(\lambda^2/n\Delta\lambda)$ where λ is the wavelength of light, $\Delta\lambda$ the band width and n the refractive index of the medium. Super luminescent light emitting diodes (SLD) commonly used in OCT have $\Delta\lambda \sim 100\text{nm}$ and at $\lambda \sim 800\text{nm}$. With $n = 1.3$, the resolution is $2\mu\text{m}$. This is superior to ultrasonic imaging in which the resolution of tens of micrometer.

7.1 Spectral Domain OCT:

If instead of scanning the path difference (z) we vary the frequency (ω) of the light source such as a tunable laser (swept frequency source), the phase will continuously vary (Eq.(20)) resulting in a sinusoidal interference signal. The frequency of such a signal is a function of depth (z) [36]. Hence two layers at two

different depths will produce different frequencies which are determined by Fourier transformation.

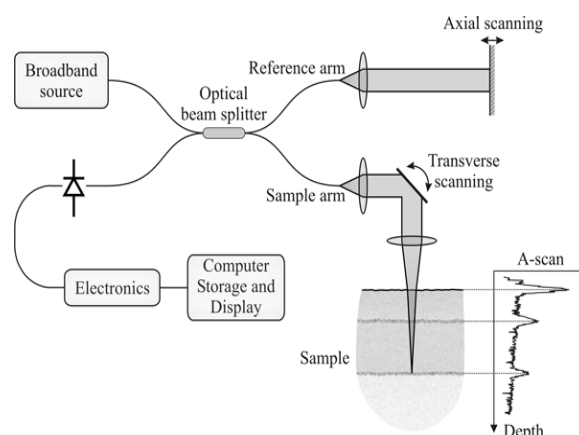


Fig. 12 Schematic of an OCT arrangement [34].

An alternative to recording the interferogram with swept source, we can use a broadband light source and separate frequency components by a dispersive device at the output as in SRWLI (Fig. 3). Now the frequency of the signal along the chromaticity axis is a measure of z .

7.2 Applications:

OCT is a powerful non-contact, noninvasive low power optical imaging technique in clinical medicine, particularly ophthalmology. It has also found use in nondestructive testing (NDT).

References

- 1 Lee B.S, Strand T.C, "Profilometry with a coherence scanning microscope" *Appl. Opt.*, **29**, 3784-3788 (1990).
- 2 Dresel T, Häusler G and Venzke H, "Three dimensional sensing of rough surfaces by coherence radar", *Appl. Opt.*, **31**, 919-925 (1992)
- 3 Caber P.J, "Interferometric profiler for rough surfaces", *Appl. Opt.*, **32**, 3438-3441 (1993).
- 4 Sandoz P and Tribillon G, "Profilometry by zero order interference fringe identification", *J. Mod. Opt.*, **40**, 1691-1700 (1993)
- 5 de Groot P, de Lega X.C, Kramer J, Turzhitsky M, "Determination of fringe order in White-Light interference microscopy", *Appl. Opt.*, **41**, 4571-4578 (2002).
- 6 Sandoz P, Devillers R, Plata A, "Unambiguous profilometry by fringe-order identification in white-light phase-shifting interferometry", *J. Mod. Opt.*, **44**, 519-534 (1997).
- 7 Harasaki A, Schmit J, Wyant C, "Improved vertical-scanning interferometry" *Appl. Opt.*, **39**, 2107-2115 (2000)
- 8 Malacara D, Phase Shifting Interferometry, "Optical Shop Testing" 2nd, John Wiley & Sons.
- 9 Kino G.S and Chim S.C, "Mirau correlation microscope," *Appl. Opt.*, **29**, 3775-3783 (1990)

- 10 K. G. Larkin, "Efficient nonlinear algorithm for envelope detection in whitelight interferometry," *J. Opt. Soc. Am. A* **13**, 832–843 (1996).
- 11 P. de Groot and L. Deck, "Surface profiling by analysis of white light interferograms in the spatial frequency domain," *J. Mod. Opt.* **42**, 389–401 (1995).
- 12 P. Sandoz, "An algorithm for profilometry by white light phase shifting interferometry," *J. Mod. Opt.* **43**, 1545–1554 (1996).
- 13 S. Suja Helen, M. P. Kothiyal, and R. S. Sirohi, "Phase shifting by a rotating polarizer in white-light interferometry for surface profiling," *J. Mod. Opt.* **46**, 993–1001 (1999).
- 14 J. Schwider and L. Zhou, "Dispersive interferometric profilometer," *Opt. Lett.* **19**, 995–997 (1994).
- 15 A. Pfortner and J. Schwider, "Dispersion error in white-light Linnik interferometers and its implications for evaluation procedures," *Appl. Opt.* **40**, 6223–6228 (2001).
- 16 P. Sandoz, G. Tribillon, and H. Perrin, "High resolution profilometry by using phase calculation algorithms for spectroscopic analysis of white light interferograms," *J. Mod. Opt.* **43**, 701–708 (1996).
- 17 J. Calatroni, A. L. Guerrero, C. Sainz, and R. Escalona, "Spectrally resolved white-light interferometry as a profilometry tool," *Opt. Laser Technol.* **28**(7), 485–489 (1996).
- 18 S. Suja Helen, M. P. Kothiyal, and R. S. Sirohi, "Analysis of spectrally resolved white light interferograms: use of a phase shifting technique," *Opt. Eng.* **40**, 1329–1336 (2001).
- 19 S. K. Debnath, and M. P. Kothiyal, "Optical Profiler based on spectrally resolved white light interferometry" *Optical Engineering*, **44**, 013606(2005).
- 20 S. K. Debnath, and M. P. Kothiyal, "Improved optical profiling using spectral phase in spectrally resolved white light interferometry", *Applied Optics*, **45**, 6965 – 6972 (2006).
- 21 S. W. Kim and G. H. Kim, "Thickness profile measurement of transparent thin-film layers by white-light scanning interferometry," *Appl. Opt.* **38**, 5968-5973 (1999).
- 22 S. K. Debnath, M. P. Kothiyal, J. Schmit, and P. Hariharan, "Spectrally resolved white-light phase shifting interference microscopy for thickness-profile measurements of transparent thin – film layers on patterned substrates", *Optics Express*, **14**, 4662 – 4667 (2006).
- 23 S. K. Debnath, Nirmal K. V, and M. P. Kothiyal, "Spectrally-resolved phase-shifting interferometry for accurate group velocity dispersion measurements", *Optics Letters*, **31**, 3098 – 3100 (2006).
- 24 S. K. Debnath, Nirmal K. V, and M. P. Kothiyal, "Spectrally-resolved phase-shifting interferometry for accurate group velocity dispersion measurements", *Optics Letters*, **31**, 3098 – 3100 (2006).
- 25 J. Schmit and K. Creath, "Extended averaging technique for derivation of error-compensating algorithms in phase-shifting interferometry," *Appl. Opt.* **34**, 3610-3619 (1995).
- 26 Hariharan P, Oreb B.F, Eiju T, "Digital phase-shifting interferometer: a simple error-compensating phase calculation algorithm", *Appl. Opt.*, **26**, 2504-2506 (1987).
- 27 C. Sainz, J E Calatroni and G Tribillon, "Refractometry of liquid samples with spectrally resolved white light interferometry," *Meas. Sci. Technol.* **1**,356-361 (1990).
- 28 C. Sainz, P. Jourdain, R. Escalona and G Tribillon, "Realtime interferometric measurement of dispersion curves," *Opt. Commun.* **110**, 381-390 (1994)
- 29 P Hlubina, " White light spectral interferometry to measure effective thickness of optical elements of known dispersion," *Acta Physics Slovaca*, **55**, 387-393 (2005)
- 30 Y Y Cheng J C Wyant , "Two wavelength phase shifting interferometry," *Appl Opt* **24**,804-807 (1985)
- 31 A Pfortner and J Schwider, "Red-blue green interferometer for the metrology of discontinuous structures" *Appl. Opt.*, **42**, 667-673 (2003)
- 32 U. Paul Kumar, N. Krishna Mohan, and M.P. Kothiyal, "Measurement of discontinuous surfaces using multiple-wavelength interferometry," *Optical Engineering*, **48**, 073603,1-8, (2009).
- 33 U. Paul Kumar, N. Krishna Mohan, and M.P. Kothiyal, "Red-Green-Blue wavelength Interferometry and TV holography for surface metrology".*Journal of Optics*, (In-Press)
- 34 <http://obel.ee.uwa.edu.au/research/oct/intro/>
- 35 B Saleh, " Introduction to subsurface imaging," Cambridge University Press (2011)
- 36 Takeda and H Yamamoto, "Fourier transf M orm speckle interferometry: three-dimensional shape measurements od diffuse objects with large height steps and or isolated surfaces" **33**, 7829-7837 (1994).

ADVANCES IN OPTICAL REMOTE SENSING METHODS: APPLICATION TO CLIMATE STUDIES

P.C.S. Devara

Indian Institute of Tropical Meteorology, Dr. Homi Bhabha Road, Pune 411 008 Email: devara@tropmet.res.in

Compared to direct measuring techniques, which provide reasonably reliable information at a specific location, more representative values can be obtained with remote sensing techniques. Remote sensing schemes, on the other hand, have made considerable progress in the recent past. Of the latest optical remote sensing techniques, the active methods such as Laser Radar (lidar) and passive methods such as Solar Radiometry (sun photometer) have been recognized to be powerful and versatile tools for studying atmospheric composition and dynamics for better understanding of climate system and its variability. These techniques have been refined recently. While passive optical remote sensing techniques have a longer history of operation for atmospheric and oceanic studies, including operation in space for a number of years, active remote sensing systems are playing an increasing role in these studies. Existing ground-based and airborne lidar systems yield measurements with super space-time resolution.

Satellite-borne sensors basically follow passive techniques, hence they cannot provide data that are as finely resolved in time and space as lidar measurements, but they offer an unparalleled capability to monitor atmospheric and oceanic states on a global scale for longer time periods. The recent satellite-based active (lidar) and passive (hyper-spectral radiometers) sensors extended this capability further. This presentation provides an overview of different active and passive remote sensing techniques that have been in use, for the past several years, at the Indian Institute of Tropical Meteorology (IITM), Pune, India for weather and climate diagnostics involving (i) earth-atmosphere radiation balance, (ii) environmental pollution and (iii) hydrological cycle. It will also highlight the current gap areas in the field and some directions for future research work.

TRENDS IN INFRA RED SYSTEMS FOR DEFENCE APPLICATIONS

S S Sundaram

Instruments Research & Development Establishment, Dehradun – 248008

ssundaram@irde.drdo.in

The emerging trends in the battlefield scenario, threat perceptions & low intensity conflicts/counter insurgency have led to rapid technological advancement in the development of InfraRed (IR) systems. These are force multipliers as they allow weapons & equipments to operate in day & night with efficiency & desired terminal effects. IR Systems are finding wide range of applications in military environment performing number of missions extending from surveillance to high performance target search, track, acquisition, guidance and missile warning Systems.

Presently three IR spectral bands i.e. (i) Short Wave InfraRed (SWIR) (ii) Medium Wave InfraRed (MWIR) (iii) Long Wave InfraRed (LWIR) are being exploited for military systems.

For reconnaissance, surveillance and target acquisition (RSTA) missions, recent advancement in IR Technology has led to the development of the state of the art 3rd generation TI systems having long range compact systems based on higher no. of detectors in single band or multiband. Currently LWIR sensors are based on 2nd gen. 288 X 4 or 480 X 4 linear MCT FPA (Focal Plane Array) or 3rd gen. 384X288 or 640X512 staring MCT FPA whereas MWIR sensors are based on 3rd gen. 320 X 240 or 640 X 512 InSb/MCT FPAs. 3rd generation Thermal Imagers operating in the LWIR band based on staring 640 x 512 QWIP FPAs or Type 2 Super Lattice are also becoming commercially available. To meet long range & large FOV requirements, there is a need to have mega pixel detectors with smaller pixel size of ~ 12 μm , thermal sensitivity < 10mK. Considering the varying atmospheric conditions, MWIR systems are used for long range applications. For better identification the MWIR or LWIR IR systems are to be complemented by SWIR.

These high performance cooled imagers can be deployed on high value platforms whereas LWIR uncooled imagers, which are also part of 3rd generation family, can be used for short range applications in micro UAVs & Rifle sights. In addition, dual band sensors will be used for missile detection and warning and dual band sensors will be used for better target discrimination capability utilizing image processing/ data fusion.

Real time image processing techniques such as contrast enhancement, edge enhancement, automatic target detection, alerting is being incorporated in the EO system to improve the target recognition and engagement. Change detection and automatic tracking techniques are also being developed to detect the change in scene for observing any movement and follow the moving target. As IR/EO sensors operating in different bands have certain advantages and limitations under different environment condition, image fusion which use the complementary information from different IR/EO sensors are also being developed to enable decision makers to deploy the available assets efficiently, reliably and rapidly.

The growth profile & latest trends of Infrared Systems will be covered along with futuristic systems such as Multi / Hyper-spectral Imagers and Integrated sensor network having Multi-Sensor Data Fusion (MSDF) and three IR bands system having common optical aperture for Laser Receiver.

Keywords:

Thermal Imager (TI), Focal Plane Array (FPA), Short Wave InfraRed (SWIR), Medium Wave InfraRed (MWIR), Long Wave InfraRed (LWIR), Quantum Well Infrared Photodetector (QWIP), Type 2 Super Lattice(T2SL), Multi-Sensor Data Fusion (MSDF)

COMPARATIVE STUDY OF VARIOUS AUTOMATED COLLIMATION TESTING TECHNIQUES IN TALBOT INTERFEROMETRY

Jitendra Dhanotia and Shashi Prakash*

Photonics Laboratory, Department of Electronics and Instrumentation Engineering, Institute of Engineering & Technology, Devi Ahilya University, Indore-452001, INDIA

*Email: sprakash_davv@rediffmail.com

Abstract: In present communication, the applicability of Phase shifting and Fourier transform method for checking the collimation position in Talbot interferometer has been proposed. The interferometric fringes at in-focus, at-focus and out-focus positions has been recorded and analyzed separately using Phase shifting and Fourier transform method for direct phase measurement. The detailed comparative analysis of both techniques is presented.

1. INTRODUCTION

Beam collimation is an important parameter affecting the measurement accuracy in almost all the optical measurements. Wide range of methods based on such as phenomena such as parallel and wedge plate shearing interferometry, Talbot interferometry, Lau interferometry, spatial coherence etc. have been proposed. Among these, Talbot interferometry has been most widely investigated technique for collimation testing because it is in-expensive, simple and offers good measurement characteristics in terms of accuracy and precision.

Various kinds of gratings have been used for collimation testing in Talbot interferometry. Towards this, Kothiyal and Sirohi [4] used the dual field grating. They also tested various other kinds of gratings in Talbot interferometry for collimation testing. A comparative study of collimation testing using dual field linear gratings, evolute gratings and spiral gratings was also reported [2]. Mehta and Kandpal [3] suggested collimation testing using a grating comprising of concentric equilateral triangles and reported that the same accuracy is obtained as with other Talbot interferometric methods. Shakher et al [4] investigated collimation testing using circular gratings based on self-imaging phenomenon.

In recent years, due to the rapid advances in the optoelectronic detection, vast storage and fast processing speed of computers, tremendous improvement has been made in the field of automatic interferogram analysis. Also, the errors due to various factors such as human intervention, environmental perturbations, etc. are reduced and hence high level of accuracy and precision is achieved. Various techniques to appraise phase information embedded in an interference fringe pattern have been demonstrated. Some prominent among them being Phase Shifting Technique (PSD), Fourier Fringe Analysis, Direct Phase Demodulation and Wavelet Transform etc. Out of these, Phase shifting and Fourier transforms technique have been used extensively.

Direct phase measurement using phase shifting technique has been reported by Prakash et al. [5]. The

phase ϕ in case of phase shifting procedure is obtained by four step phase shifting algorithm. Similarly, The details of the Fourier transform method is discussed by Dhanotia et al [7].

In present communication, a comparative analysis of Phase shifting and Fourier transform techniques for collimation testing in Talbot interferometry has been undertaken. the results compared. The performance analysis helps understanding the potential, advantages and limitations of the two techniques.

2. BASIC PRINCIPLE

The Talbot effect is a near field diffraction effect that has been observed both with light and atom optics. When a plane parallel wavefront illuminates a grating G1 it is observed to generate the self-image of the grating at certain well defined planes called Talbot planes. These planes are located at a distance d , also called Talbot distance.

$$d = \frac{2mp^2}{\lambda}$$

where m , p , and λ represent an integer, the pitch of the grating and wavelength of the light used, respectively.

If another identical grating G2 is placed at the Talbot plane corresponding to grating G1, the characteristic moiré pattern is formed. This set-up has been named as Talbot interferometer and has been used extensively for applications in Science and Engineering. The interferometer provides the slope information of the phase object placed between the two gratings and the intensity profile of the fringes at the image plane is triangular. It has been reported elsewhere that the recorded output may be converted to a co-sinusoidal variation if first order filtering is undertaken beyond the image plane.

Collimation testing using phase shifting test procedure in Talbot interferometer involves recoding four images of the resultant fringe pattern during which the interferometric phase has been varied. The calculation/estimation of phase directly using standard mathematical procedure retrieves the

unknown phase. Because of the decollimation effects the interferometric phase varies in a typical fashion, clearly indicating the state of collimation of the input beam. In Fourier Transform method (FTM) the interferometric phase is estimated using standard Fourier Transform algorithm. Because of interferometric phase variation across the wavefront the spatial frequency of the fringe pattern varies. Using standard Fourier transform algorithm the phase information is retrieved back.

3. EXPERIMENTAL ARRANGEMENT

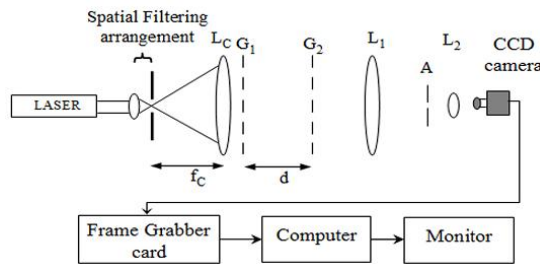


Fig. 1: Experimental arrangement for collimation testing using Talbot interferometer.

The schematic of the experimental arrangement for checking the collimation of a laser beam in Talbot interferometry is shown in Fig. 1. The light from 15mW He-Ne laser is incident on microscopic objective of magnification 40X and is used to focus the beam at the focal point of the collimating lens. A pinhole of $5\mu\text{m}$ diameter is placed at the focus of the microscope objective to serve as spatial filter. The precision achromatic doublet lens PAC088 supplied by Newport Corporation, USA, having a focal length of 250mm, has been used as collimating lens LC. The collimating lens is placed on the translation stage to translate it along the optic axis. The beam is then incident on a set of two identical gratings. One of the grating is placed on the precision translation device. The beam from the collimating lens LC impinges on the grating G1, having a 0.2mm pitch. This results in the formation of the self-image of the grating G1 at certain well-defined planes, called "self-imaging planes". Grating G2 of period same as that of grating G1, is placed at the first self-image plane of grating G1, resulting in the generation of typical shearing moire fringes. The sheared interferogram were recorded using CCD camera supplied by Artray Company, Japan, having 1392×1040 pixels with each pixel sized $4.65 \times 4.65\mu\text{m}$. For image acquisition, Artray 150PIII software supplied by the Artray company, Japan was used and the results were displayed on-line via the computer monitor.

Initially, the collimating lens LC was mounted on the precision translating stage to translate it along the optical axis, making it possible to introduce a known amount of de-collimation. The gratings G1 and G2 were placed in such a way that the grating lines are

parallel to each other. At the image plane uniform illumination was obtained. Now the gratings G1 and G2 are rotated in clockwise and anticlockwise direction, so that the lines of the gratings make small but equal and opposite angles with the vertical. This introduces error corresponding to tilt of the wavefront. When the incident optical beam is collimated, equidistance parallel fringes, perpendicular to grating lines were observed at the image plane. To achieve this condition, the collimating lens was adjusted in such a manner that the fringes were aligned parallel to the set reference line. These horizontal fringes were indicative of collimation position as shown in Fig. 2(b) and the position of collimating lens recorded using attached micrometer screw. Also, on moving the collimating lens corresponding to in-focus or out-of-focus position, the fringes get inclined. It is indicative of setting in of the de-collimation position as shown in Fig. 2(a) and 2(c). This may correspond to a coarse setting of collimation position by visual inspection. In case of phase shifting method for each position of collimating lens, four interferograms were recorded by translating the grating G1 in steps. For fine setting of collimation position, a series of interferogram near the collimation position were recorded and analysed using algorithm in Fig. 3 and Fig. 4. The algorithm in Fig. 3 and Fig. 4 correspond to the phase determination using phase shifting and Fourier transform, respectively.

The recorded patterns have been analyzed using phase shifting and Fourier Transform algorithm and the phase determined in each case. The minimum slope value indicates the most appropriate collimation position.

4. RESULTS AND DISCUSSION

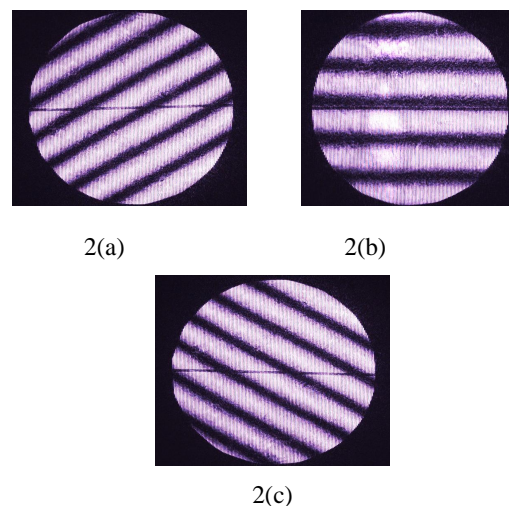


Fig. 2: Fringe pattern recorded using CCD camera at 2(a) in-focus, 2(b) at-focus and 2(c) out-of-focus position of collimating lens of focal length 250mm.

Fig.2 shows the recorded interferogram at in-focus, at-focus and out-focus positions of the collimating lens. During the experiment, for each position, four interferograms were recorded, but in the results only a single interferogram at each position is shown.

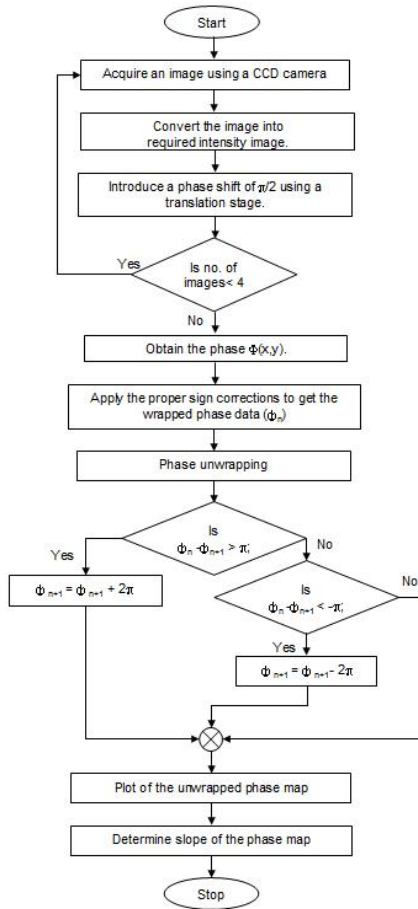


Fig. 3: Flow chart for phase shifting algorithm.

In the next step, the recorded interferograms at each position have been separately analysed using phase shifting and Fourier transform method based algorithms as shown in Fig. 3 and Fig. 4 respectively.

Fig.5 shows the plot obtained at in-focus, at-focus and out-focus positions of the collimating lens using phase shifting technique. Similarly, Fig.6 shows the same positions using Fourier transform method. The analysis shows that the Fourier transform based method is better than Phase shifting technique regarding the ease of experimentation; however it requires more computationally involved algorithm. The phase map obtained in case of phase shifting technique is quite noisy and the precision of measurement lower.

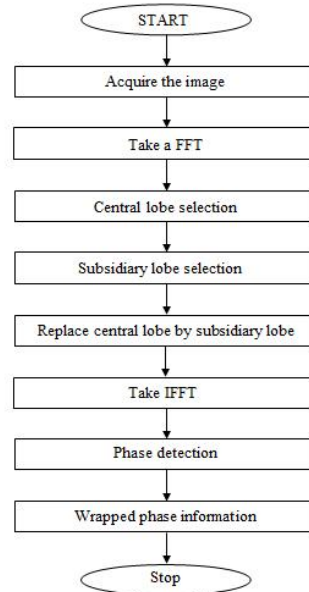


Fig. 4: Flow chart for Fourier transform algorithm

By incorporating the phase shifting technique in Talbot interferometry and using four step algorithm we could achieve the value of accuracy of 6 m. It has been observed that as the collimation position is approached, the noisiness in the interferogram increases. Under the conditions, for different portions of the same wavefront, the slope of the phase varies arbitrarily because of the noise, resulting in ambiguity in measurement.

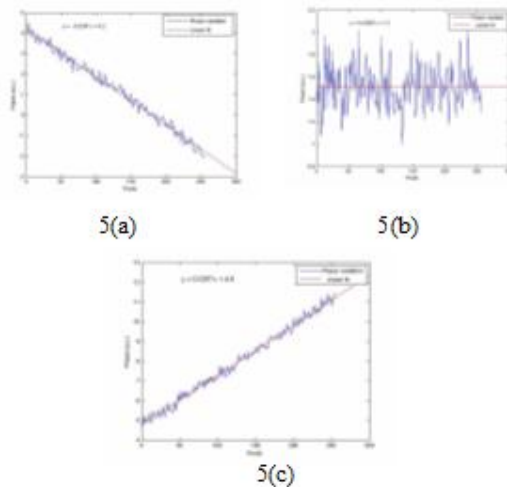


Fig. 5: Variation of phase with respect to x-axis for the fringe pattern corresponding to 5(a) in-focus, 5(b) at-focus and 5(c) out-of-focus position of collimating lens of focal length 250mm. Results obtained using Phase shifting technique)

Similarly by incorporating the Fourier transform method in Talbot interferometry we could achieve the value of accuracy of 1 μ m. It has been observed that the Fourier transform method provides the better measurement characteristics. It is evident by the comparison of the phase plots as shown in Fig. 5 and Fig. 6, the phase plots obtained using phase shifting method are very noisy and Fourier transform method provides the noiseless phase plots. Thus the collimation position can be accurately and precisely achieved.

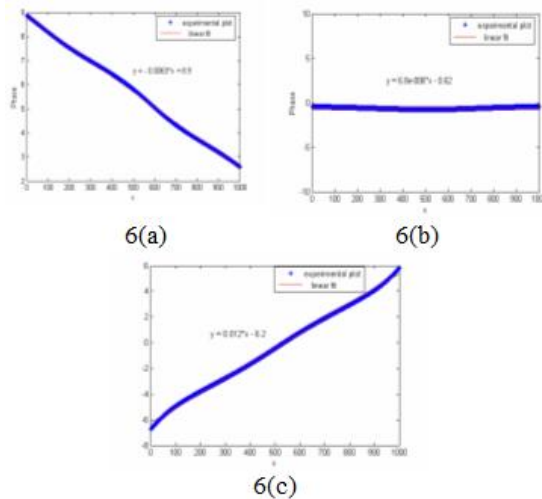


Fig. 6: Variation of phase with respect to x-axis for the fringe pattern corresponding to 6(a) in-focus, 6(b) at-focus and 6(c) out-of-focus position of collimating lens of focal length 250mm. (Results obtained using Fourier transform method)

The discussion regarding the comparisons of various interferogram analysis techniques seems pertinent. The Phase Stepping technique requires either three or four images to extract the phase information, depending on the magnitude of calibrated phase step needed. It has been observed that, the phase plots obtained using phase shifting technique are very noisy. The phase shifting method works well with low frequency grating, while for the high frequency gratings, the method becomes more tedious. The technique requires precision translation stage which is relatively costly. Comparatively, Fourier transform method requires a single interferogram to extract the phase information and offers high accuracy and precision in measurement. However, the algorithm used is computationally more involved in this case.

5. CONCLUSIONS

The comparative analysis of the automated interferogram analysis techniques has been proposed and evaluation has been done successfully. The PSI

technique provides the noisy phase plots which results in lower value of the accuracy. The noise due to the presence of higher harmonics in the intensity limits capability of the technique. Thus suitable modifications to improve the results have been incorporated in FTM. The FTM provides the higher accuracy with noiseless phase plots. Also PSI requires a precision translation device to introduce a phase shift.

REFERENCES

- [1] M. P. Kothiyal and R. S. Sirohi, "Improved collimation testing using Talbot interferometry," *Applied Optics* 26, 4056-4057 (1987).
- [2] K. V. Sriram, M. P. Kothiyal and R. S. Sirohi, "Collimation testing with linear dual-field, and evolute gratings: a comparative study," *Applied Optics* 33, 7258-7260 (1994).
- [3] D. S. Mehta and H. C. Kandpal, "A simple method for testing laser beam collimation," *Optics & Laser Technology* 29, 469-474 (1998).
- [4] C. Shakher, S. Prakash, D. Nand and R. Kumar, "Collimation testing with circular gratings," *Applied Optics* 40, 1175-1179 (2001).
- [5] S. Prakash, S. Rana, S. Prakash and Osami Sasaki, "Automated collimation testing using a temporal phase shifting technique in Talbot interferometry," *Applied Optics* 47, 5938-5943 (2008).
- [6] S. Rana, S. Prakash and S. Prakash, "Automated collimation testing in Lau interferometry using phase shifting technique," *Optics and Lasers in Engineering* 47, 656-661 (2009).
- [7] J. Dhanotia and S. Prakash, "Automated collimation testing by incorporating Fourier transform method in Talbot interferometry," *Appl. Opt.*, 50, 1446-1452 (2011).

Performance Estimation of Intensified CCD spectrometer system for UV Laser Induced Fluorescence Standoff Biological warfare Sensor

Deepak Kumar, Ramesh C Sharma*, A K Maini

Laser Science & Technology Centre, Metcalfe House, Delhi, India

Corresponding author email: rameshsharma@lastrec.drdo.in

Abstract: This paper discusses performance estimates for Gated ICCD (Intensified Charge Coupled Device) spectrometer for Laser based Standoff biological sensor. Ultraviolet Laser Induced Fluorescence (UV-LIF) standoff technique is considered. ICCD based spectrometer parameters are drawn for the biological detection. Analysis of Signal to Noise ratio (SNR) for the ICCD spectrometer detector is carried out for daylight and twilight. Detectable concentration and range for the detector from target range up to 2 kilometer is analyzed.

Introduction: Biological warfare attack poses a serious threat to mankind and other living species. The biological threat can be in the form of aerosolised bacteria, fungi or virus and also it may be spread by vectors and other routes like water and air supply in civilian or defence establishments [1]. In this study aerosolized form of biohazard agents is considered. The Laser Induced Fluorescence (LIF) lidar for remote monitoring of these threats has been explored as one of the valuable technique to detect and discriminate these threats from a standoff distance. Researcher has claimed to detect biological agent simulants from a standoff distance up to 5 kilometres. The detection and discrimination both in the same sensor simultaneously have primarily be reported using LIF technique. Researchers are also using Infra red based DIAL, Long wave infra red differential (LWIR) scattering and infrared Depolarization measurement for biological threat warning but these techniques are far behind LIF in terms of selectivity and sensitivity [2]. All biological organisms emit fluorescence when illuminated by ultraviolet light. Fluorescence can be primarily attributed to the biochemicals, tryptophan and tyrosine (amino acids), Nicotinamide Adenine Dinucleotide (NADH), and riboflavin [3, 4]. At present most trial versions of LIF Lidar use either 266 or 355nm UV light, both these wavelengths being easily derived from an Nd: YAG laser. 266nm UV excites fluorescence primarily from the tryptophan within the bacterial cell wall and tyrosine also 355nm UV excites fluorescence primarily from NADH. [5, 6, 7]. We have not considered 355nm as it is suitable for detecting bacteria in growth phase whereas 266nm can be used for spore: dormant form of bacteria, having Tryptophan as the main fluorescence species. Spore attack is more likely as compared to bacteria attack. Fluorescence cross sections for bio-aerosols are roughly 10^3 to 10^5 times less than the corresponding elastic-scattering cross sections [8]. The greatly reduced cross-section requires fluorescence-based sensors to utilize higher-power optical sources, more sensitive photodetectors, and optical systems that are more efficient at collection of the particle signal, relative to elastic-scattering-based sensors. Aim of the study is to estimates performance of ICCD (Intensified charge coupled device) spectrometer for Ultraviolet Laser Induced Fluorescence (UV-LIF) sensor considering the range, target concentration and atmospheric conditions.

UV Laser Induced Fluorescence Standoff Biological Sensor:

Figure 1 shows typical Schematic of Standoff biological Sensor (UV LIF LIDAR). A fourth harmonic of Nd: YAG laser beam 266nm wavelength excitation pulse is emitted toward the bioaerosol cloud. A small amount of the scattered light is collected by the telescope and spectrally separated by dichroic mirror is directed into a spectrograph separated by a dichroic mirror and detected by a gated ICCD camera.

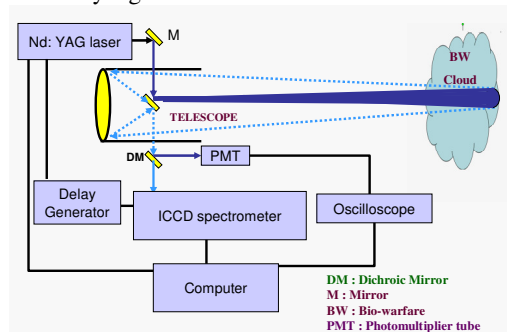


Figure1: Schematic of Standoff biological Sensor

Experimental: The fluorescence spectra of bacteria agents are primarily due to tryptophan fluorescence as the dry weight of bacteria comprises approximately 4-14% of Tryptophan protein. Fluorescence spectra of tryptophan in water (fig 2) having concentration (10^{-5} molar) is carried out using a CCD based spectrometer (Ocean Optics, QE65000). Fluorescence spectra of tryptophan are required for modelling of theoretical parameters in this study.

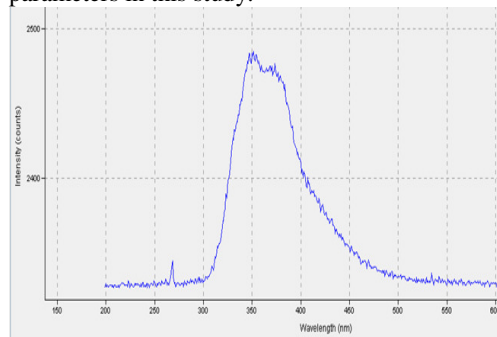


Figure 2. Single-shot LIF spectrum of Tryptophan excited at 266nm

ICCD Detector: SNR Formulation

ICCD detector combines an image intensifier and a CCD camera via fibre coupled systems. An image intensifier typically consists of three components, a photocathode, a MCP and a phosphor screen. The photocathode is photosensitive and can convert the incident photons into electrons. The electrons are then accelerated toward the MCP. Under the high voltage applied to the MCP, the incident electrons gain sufficient energy to knock off additional electrons and hence amplify the original signal at the phosphor screen. [12, 13]

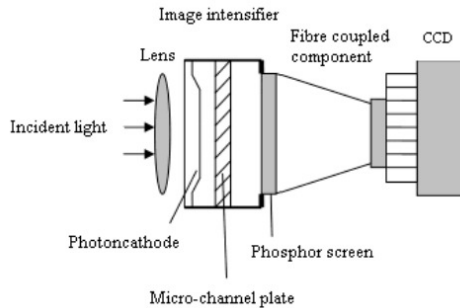


Fig 3. Schematic diagram of an ICCD Detector
Noise contribution of ICCD:

- Intensifier Noise N_i : Photocathode Noise, MCP Noise and Phosphor screen Noise
- CCD Noise N_{ccd} : CCD dark current, CCD read-out noise and CCD controller noise A/D counts

Photocathode Noise:

The noise from photocathode consists of photon shot noise and Equivalent Background Illumination (EBI), which are the two dominant noise contributions to the system. Photon shot noise is the noise associated with the random arrival of photons at any detector. It is a fundamental property of the quantum nature of light and unavoidable in imaging systems. Both photon shot noise and EBI obey the Poisson statistics

$$N_{PC} = \sqrt{t.(P.\eta_{PC} + N_{EBI})} \dots(1)$$

P is the signal photon/pixel/sec, η_{PC} is the quantum efficiency of Photocathode. N_{EBI} is the equivalent background luminance in electron/pixel/sec, t is the integration time.

MCP Noise:

Noise component originating from amplification is represented by Noise factor

Noise factor $F_m = 1.6$ to 2.2 for Gen II ICCD

$$F_m^2 = \frac{\delta_{out}^2}{M^2.\delta_{input}^2}$$

where δ_{out} and δ_{input} are the

variances of input and output signals respectively.

Phosphor Screen Noise:

Phosphor screen usually emit green light with decay times of a few hundred nanoseconds to a few milliseconds. Both the decay times and uncertainty in phosphor screen quantum efficiency contributes to phosphor screen noise.

It is represented here as N_s

$$N_i = \sqrt{N_{PC}^2.G^2.F_m^2 + N_s^2} \dots(2)$$

CCD Noise:

CCD dark current noise:

Dark current is caused by thermally generated electrons in the silicon substrate of the CCD. It is strongly temperature dependent. It also scales with integration time. Dark current noise is the square root of dark current:

$$N_d = \sqrt{D.t} \dots(3)$$

Where D is the dark current and t is the integration time.

Readout Noise: N_r

Readout Noise is generated by the output amplifier and subsequent electronic circuitry, including KTC noise, 1/f noise and quantization noise. It increases with readout frequency and becomes dominant noise at high frame rates for conventional CCDs.

CCD controller noise A/D counts:

$$N_{AD} = N_{AD} = \frac{N_{well}}{2^n.\sqrt{12}} \dots(4)$$

Where N_{well} is the full well capacity for single pixel/ binned pixels and n is the bit for A/D converter. Typically for example a N_{well} of 10^6 electrons and 16 bit A/D the $N_{AD} = 4.4$ electrons.

Total Noise Contribution:

The total noise contribution can be written as a quadrature sum of Intensifier noise and coupling CCD noise plus the read out noise and CCD controller noise A/D counts

$$N = \sqrt{(N_i.\eta_{ccd})^2 + N_{ccd}^2} \dots(5)$$

$$\text{Where } N_{ccd}^2 = N_d^2 + N_r^2 + N_{AD}^2$$

$$\text{Implies } N = \sqrt{(N_i.\eta_{ccd})^2 + N_d^2 + N_r^2 + N_{AD}^2} \dots (6)$$

$$N_{ICCD} = \sqrt{((N_{PC}^2.G^2.F_m^2 + N_s^2).\eta_{ccd})^2 + N_d^2 + N_r^2 + N_{AD}^2} \dots(7)$$

Now the fluorescence signal photons P can be written in terms of signal

$$S_{ICCD} = P.G.\eta_{PC}.\eta_{ccd}.t \dots(8)$$

In the presence of solar background photons 'B' there will be contribution to photon shot noise due to solar background as well as fluorescence photons.

The SNR can now be expressed as

$$SNR_{ICCD} = \frac{S_{ICCD}}{N_{ICCD}} = \frac{PG\eta_{PC}\eta_{ccd}.t}{\sqrt{(t((P+B)\eta_{PC} + N_{EBI})G^2.F_m^2 + N_s^2)\eta_{ccd}^2 + N_d^2 + N_r^2 + N_{AD}^2}} \dots(9)$$

For sufficiently higher gain above equation reduces to

$$SNR_{ICCD} = \frac{P.\eta_{PC}.t}{\sqrt{(t((P+B)\eta_{PC} + N_{EBI}).F_m^2)}} \dots(10)$$

In case the pixels are binned vertically as spectral

information is required in this case not the spatial (in case of imaging).

Let P_x be the number of pixels binned together in that case the above equation will reduce to $\frac{P}{\sqrt{P_x}}$ times the

above value. As for binning case the noise is added in square root of sum of noise squared and signal is added linearly.

$$SNR_{ICCD} = \frac{P_x \cdot P \cdot \eta_{PC} \cdot t}{\sqrt{t \cdot ((P + B) \cdot \eta_{PC} + N_{EBI}) \cdot P_x \cdot F_m^2}} \dots(11)$$

P is the signal photon/pixel/sec, but in the case of gated imaging in conjunction with an active laser source for illuminating the target/cloud. We can consider P and B to the number of photons/pixel/gating interval for a single pulse averaging. In that case N_{EBI} value has also to be deduced for gating interval in every case for different pulse averaging. For averaging of 'N_p' number of pulses the above equation becomes

$$SNR_{ICCD} = \frac{P_x \cdot P \cdot \eta_{PC} \sqrt{N_p}}{\sqrt{((P + B) \cdot \eta_{PC} + \Delta t_g \cdot N_{EBI}) \cdot P_x \cdot F_m^2}} \dots(12)$$

Δt_g is the gating time interval.

Gated ICCD spectrometer

Let us consider the case of a commercially available ANDOR DH720-25F-03 ICCD (Gen II intensifier) having 960x256 pixel. The fluorescence signals when excited by 266nm are obtained starting from 300nm. The spectral resolution of a spectrograph is given by

$$\Delta\lambda = D \cdot \frac{\partial\lambda}{\partial x} = D \cdot \frac{\cos\beta}{k \cdot f \cdot g} \dots(13)$$

where λ is the wavelength, $\Delta\lambda$ is the resolution in wavelength, D is the width of the slit, β is the angle between the grating normal and the exit beam, k is the diffraction order, f is the focal length of the system (assumed to have magnification = 1 in the direction perpendicular to the slit), and g is the grating frequency in rules/mm. The dispersion of the spectrograph, $d\lambda/dx$, is a measure of how fast the wavelength changes with distance at the exit aperture of the spectrograph.

The spectrograph considered in this work is a commercial spectrometer (ANDOR 303) has f = 400 mm and, and a grating with 600 rules/mm with a 500 nm blaze angle (wavelength of maximum diffraction efficiency ~ 0.5). The diffraction order of maximum efficiency is k = 1. The dispersion with this grating is stated to be 5.25 nm/mm. A slit width of 200 μ m is taken to ensure a nominal resolution and throughput. Using these values, we find that $\Delta\lambda = 1.05$ nm. This provides a band pass of 130nm, Band pass = CCD size x dispersion = 960x 0.026mmx 5.25nm/mm = 130nm.

The light at the exit face of the spectrograph is captured by the ICCD camera (ANDOR DH720-25F-03 ICCD). The pixel size (or rather center-to-center distance of the pixels) of this camera is 26 μ m (25 mm/960 pixels). Since the spectrograph has a magnification of 1 in the

direction perpendicular to the slit and the 200 μ m width of the slit is the limiting resolution of the system, it turns out that the camera sampling can be reduced by a factor of 7.7 without reducing the information available in the system. This can be done by horizontal binning blocks of 7 pixels. Also as the system is operated in the spectral dispersion mode the complete vertical of 256 pixels can be done.

Evaluation of LIF LIDAR signal:

The factors that influence on the detection process in a lidar can be composed in lidar equation. This is given below, and describes the spectrally distributed inelastic scattering, by a single type of inelastic scattered, collected by the instrument (before the detector) [14,15]

$$E_f = E_T \cdot T(R) \cdot K_0(\lambda) \cdot \xi(R) \cdot \frac{A}{R^2} \cdot N^f \cdot (\Delta R) \cdot \left\{ \frac{d\sigma^f}{d\Omega} \right\} \dots(14)$$

- E_f = Energy received
- E_T = Energy transmitted = 100mJ
- $T(R)$ = Atmospheric attenuation
- $K_0(\lambda)$ = Receiver Transmission efficiency = 0.8
- ξ = Overlap factor of receiver and transmitter = 1
- A = Aperture area = 0.0707m²
- R = Range: cloud distance
- N^f = Number of fluorescence species
- ΔR = Cloud depth = 50 meter

$\left(\frac{d\sigma^f}{d\Omega} \right)$ = Total differential cross section = 10⁻¹⁶ m²/bacteria-stredian
 Moderate visibility of 10 km is taken to calculate the atmospheric attenuation. $T(R) = \exp(-2 \cdot \alpha \cdot R)$ where α is average of attenuation coefficient for laser and received radiations

$$\alpha(km^{-1}) = \frac{3.91}{V} \cdot \left(\frac{0.550}{\lambda} \right)^{0.585 \cdot V^{1/3}} \dots(15)$$

V is the visibility (km) and λ the wavelength in micron

Parameters of UV LIF Lidar system:

- Lasers: 266nm Nd: YAG Laser
- Laser Energy: 100 mJ @ 266nm
- PRF : 10 Hz
- Pulse Width ~ 6ns
- Target Location : Up to 2 kms.
- Peak emission wavelength : 350nm
- Fluorescence cross section of bacteria= 10⁻¹⁶ m²/stredian/ particle (typical value)
- Receiver Diameter: 30 cm
- Field Of View: 0.83 milli-radian
- Grating efficiency 50%

Operation parameters

- Sky background 0.0001- 0.1 watt/m².nm
- Atmospheric visibility 10 km (moderate)
- Bio-aerosols Bacillus Globiggi
- Concentration 10⁴ to 10⁶ bacteria/litre of air

Solar background contribution:

The challenge in UV LIF based biological sensor is that the fluorescence band and the solar spectra are overlapping with each other. Figure 7 shows the typical Solar spectrum outside the earth's atmosphere. Total power received at the top of the earth's atmosphere from the Sun is 1366W/m^2 (radiant flux). Corresponding an Albedo of 0.7 the radiant flux on earth surface is $\sim 960\text{W/m}^2$.

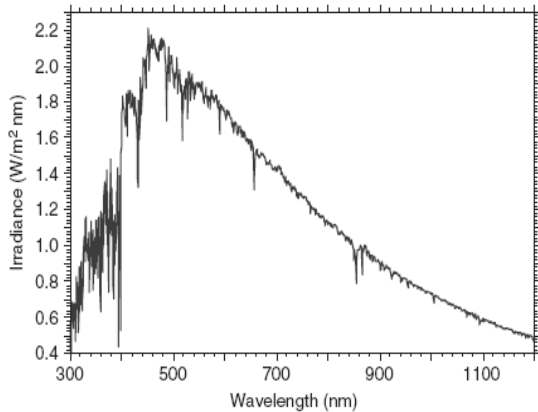


Figure 4. Solar spectrum outside the earth's atmosphere [16]

Spectral irradiance is the irradiance at a given wavelength per unit wavelength interval. In the case of our system the Diffuse Irradiance is important as the sensor is looking towards the sky not any topographic target. The 5-min averaged value diffuse irradiance, centred at 1120 hrs is 267W/m^2 [16]. Spectral irradiance at earth surface to be about 0.7 of the values

as shown the figure 4. Also as the global diffuse irradiance is $1/3.6$ times the radiant flux on earth, the

diffuse spectral irradiance will approximately $1/5$ times of the value shown in figure 4. Average Diffuse spectral irradiance value is taken $0.1\text{ watt/m}^2.\text{nm}$ for 300-500nm band. During the twilight condition (onset of day and night) the solar irradiance is ~ 1000 of its value in daytime. Therefore for twilight average diffuse spectral irradiance value is taken $0.0001\text{ watt/m}^2.\text{nm}$ for 300-500nm band

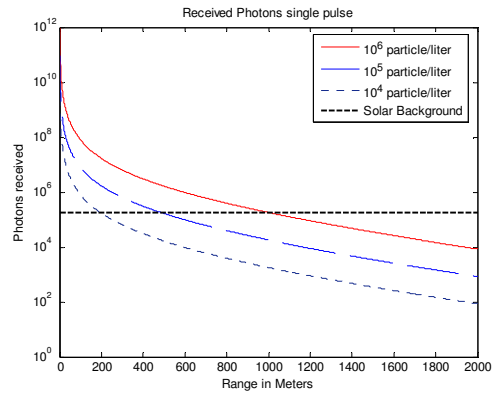


Figure 5 Received fluorescence photons and solar background photons vs. range

Results: Figure 5 shows Received fluorescence photons and solar background photons vs. range at different particle concentration derived from LIDAR equation 14. For the above LIDAR parameters the solar background photons corresponding to an integration time 333ns, FOV of system 0.83milliradian and a spectral bandwidth of 100nm corresponds to 1.8×10^5 photons as received by the optical receiver/telescope. We can see that the daylight will have a severe impact on the threshold resolution due to shot noise generated in the detector.

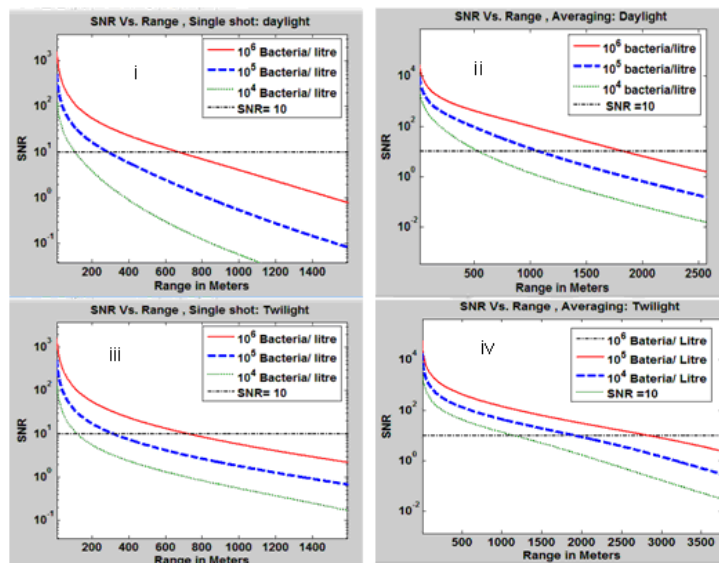


Fig 6. Single shot and Averaged SNR vs. Range for daylight and twilight ICCD

Detector	Maximum Range(Km) for 10 ⁶ bacteria/liter Daylight Condition		Maximum Range(Km) for 10 ⁶ bacteria/liter Twilight Condition		Minimum Detectable concentration (bacteria/litre) at 2 Km for 1 min. averaging	
	Single shot	1 minute Averaging	Single shot	1 minute Averaging	Daylight	Twilight
Gated ICCD	0.7	1.8	0.75	2.8	2x 10 ⁶	10 ⁵

Table: 1

Conclusion:

The table 1 summarizes the result of Detector performance. An optimal SNR value of 10 is taken for the sensor system for standoff detection. Figure 6 shows the SNR plots for gated ICCD detector under different pulses averaging and solar background daylight and twilight. Gated ICCD is able to record the fluorescence spectra from a distance of 1.8 Km in daytime and 2.8 Km at twilight condition for 10⁶ bacteria/litre concentrations for averaging time of 1 minutes (corresponding to 600 pulses). At 2 kilometres range the minimum detectable concentration during daytime for Gated ICCD is 2x 10⁶ bacteria/litre for 1 minute averaging.

Acknowledgement: Author acknowledge Dr. Lalita Gupta and Mr. Subodh Kumar for helping in recording the fluorescence spectra of bio-molecules for this study. Authors are also thankful to Ms. Lalita Dasgupta for providing the Nd:YAG laser facility.

References:

- Henderson, D. A., "The looming threat of bioterrorism," *Science*, **283**, 1279-1282 (1999).
- Sylvie Buteau*, et al, Final Report For Task Group (Rtg-55) On Laser Based Stand-Off Detection Of Biological Agents, NATO Research and Technology Organisation (RTO), Sensors And Electronics Technology (Set-098), 2008
- J. R. Lakowicz, *Principles of Fluorescence Spectroscopy*, 2nd ed. (Kluwer Academic/Plenum Publisher, New York, 1999).
- F. W. J. Teale And G. Weber "Ultraviolet Fluorescence of the Aromatic Amino Acids" *Bioch.* 1957, 65, pp 476-82
- Hill S.C. Pinnick R.G., Niles S., Pan Y.L., Holler S., Chang R.K., Bottiger J., Chen B.T., Orr C.S. and Feather G., "Real-time measurement of fluorescence spectra from single airborne biological particles." *Field Analytical Chemistry and Technology*, **3**, 221-239, 1999
- Seaver M., Roselle D.C., Pinto J.F. and Eversole J.D., "Absolute emission spectra from *Bacillus subtilis* and *Escherichia coli* vegetative cells in solution." *Applied Optics*, **37**, 5344-5347, 1998
- Karen Baxter, Michael Castle, Steve Barrington, Philip Withers, Virginia Foot, Andrew Pickering, and Nicola Felton "UK small scale UVLIF lidar for standoff BU detection" *Proc. of SPIE Vol. 6739 67390Z* pp-1-10, 2007
- Sivaprakasam V.; Huston A. L.; Scotto C.; Eversole J. D. Multiple UV wavelength excitation and fluorescence of bioaerosols. *Optics Express* **2004**, *12*, 4457-4466.
- Sylvie Buteau et al, Joint Biological Standoff Detection System increment II: Field demonstration SINBAHD performances report, DRDC Valcartier TM 2006-140 December 2007
- P. J. Hargis et al, ARES Upgrade: Time-resolved Spectral Measurements of Bio-aerosols, *Research Brief* 2007, pp 22-23
- J R Simard, G Roy, P Mathieu, V Larochelle, J McFee, and J Ho. Standoff sensing of bioaerosols using intensified range-gated spectral analysis of laser-induced fluorescence. *IEEE Transactions on Geoscience and Remote Sensing*, *42*: 865-874, 2004.
- Digital camera fundamentals. www.andor.com
- Wenwen Zhang, Qian Chen, Signal-to-Noise Ratio Performance Comparison of Electron Multiplying CCD and Intensified CCD Detectors 978-1-4244-3986-7/09/ ©2009 IEEE
- Ove Steinvall, Per Jonsson, Fredrik Kullander "Performance analysis for a standoff biological warfare agent detection lidar." *Proc. of SPIE Vol. 6739 673912-1-14*
- Gunnar Rustad and Øystein Farsund Standoff detection of biological aerosols by UV-laser induced fluorescence FFI-rapport 2008/02025
- T. Muneer "Solar Radiation and Daylight Models" IInd edition, 2004, Elsevier

FTTH DISTRIBUTION SYSTEM FOR MULTI LEVEL DWELLING UNITS

K.R.Suresh Nair

NeST Group, Plot 43, Cochin Special Economic Zone, Kochi-682037.

Suresh.nair@nestgroup.net

Abstract: Fiber To The Home (FTTH) systems are recently finding wide installations and the architecture of such systems varies from one country to the other. These distribution system designs call for innovation to meet added features, and functionalities, reduced installation time and easiness of operation. The paper describes development of such system and its applications.

1. INTRODUCTION

As the demand for more bandwidth is unending, copper and wireless network fail to deliver such bandwidths and the future solution will be fiber based. More and more flexible services are now becoming available like the interactive TV, IPTV, globally played online video games, instant downloading of films, live monitoring of offices, houses and establishments. This calls for fiber to reach every home (FTTH). Also over the same fiber, all three basic services namely telephone, video and data are available and known as Triple Play services. The FTTH system design suitable for Multilevel Dwelling Units (MDU) calls for consideration of various aspects like, provision to facilitate services by different service providers, easiness of installation, configurability, reliability and easiness of maintenance, etc.

2. FTTH Distribution System for MDUs.

A series of various subsystems in the FTTH System are designed and manufactured. All these are pre-connectorised MDU plug and play solutions requiring no splicing at field. The strong features of these systems are the reduction in installation time and these are designed to be of installation fool proof.

The major subsystems are 12 Fiber MT connectors, Fiber Distribution Hub, MT cable Assembly and Fiber Distribution Terminal. Many innovations are implemented in every subsystem to excel their performance over global competitors[1]. These systems are manufactured and undergone all related regulatory and reliability tests at Telcordia laboratories. These are now finding good market in US, Europe, Middle East and India. A special process has been developed to achieve 0.3 dB Insertion loss and >65dB Return Loss for 12 fiber MT connector, which is used in this FTTH subsystem.



Fig.1. FTTH Subsystems developed and their locations in MDUs

3. VOLUME MANUFACTURING FACILITY

The product development has undergone proto, pilot and production phases and a facility has been established to do volume manufacturing, complying with TL9000 standards. Special setups were designed to handle such bulky systems.



References:

- [1] K.R.Suresh Nair, et.al, "US Patent Application,US2010/0166376 A1", (2010).

PERFORMANCE ANALYSIS OF MULTIPLEXED SIGNAL DISTRIBUTION FIBER NETWORKS FOR RADAR APPLICATIONS

Meena.D^(a), Yadunath.T.R^(b), Sujitha.P^(b), Abdul Hameed.P.P^(b), E.S.Shivaleela^(b), T.Srinivas.^(b)
LGM Prakasam^(a)

(a)Electronics and Radar Development Establishment (LRDE),Bangalore

(b)Department of ECE, Indian Institute of Science, Bangalore

meenad@ece.iisc.ernet.in

Abstract: Multiple transmit receive modules of Active phased array Radars require various kind of signals for synchronous operation in real time. If the signal distribution can be achieved through optical networks by using Wavelength Division Multiplexing (WDM) methods, it results in a distribution scheme with less hardware complexity and leads to the reduction in the weight of the antenna arrays. This paper discusses about four multiplexed distribution network architectures for Radars. It also gives an insight towards a comparative analysis performed on these schemes by considering the factors like signal levels, loss parameters etc. Thus it aids us in the selection of suitable optical network architecture based on the radar application requirements.

1. INTRODUCTION

In modern radars, multiple receive module's complex video signals are communicated via optical distribution network. But the required clock and Local Oscillator (LO) signals are distributed through conventional heavy Radio Frequency (RF) cables. High capacity existing fiber network used for the distribution of complex video can be further extended for the distribution of above signals using WDM technique. This paper briefs about four different distribution network architectures [2] supported with its performance analysis.

2. ARRAY DISTRIBUTION AND NATURE OF SIGNALS

An array consists of 40 receiver modules arranged in 5 rows X 8 columns structure is considered for analysis purpose. All these receiver modules require LO, Clock and other synchronization signals for the operation. Some cases transmit signals are routed via these receive modules. In addition, also complex video from receive modules are distributed to the next sub system via optical network. Seven different signals which are in Analog, Digital and RF format are considered for distribution purpose. Four different Optical network architectures are derived for distribution of the signals by using WDM techniques [2]. All these structures use various combinations of components like splitters, multiplexers, Erbium doped fiber amplifier (EDFA), demultiplexers etc. Even though the total distance of the fiber to be laid in the arrays is of smaller order, to compensate the losses incurred with splitters EDFAs are used in the networks.

3. SELECTION CRITERIA FOR THE WAVELENGTHS

The introduction of EDFAs in the network results in signals of various gains at the output of EDFA depending on the wavelength values. In this case, the number of wavelengths required depends on the

number of signals to be multiplexed. As per the requirements of the application, 7 different signals are required to be distributed to receiver modules in real time which are in digital, analog and RF in nature. An analysis has been done to identify the region of nearly flat gain for the selection of wavelengths[3]-[5]. So seven different wavelengths in this region with a spacing of 0.8 nm are identified to have less gain variation at the output of EDFA. The gain Vs wavelength plot for selected wavelength ranging from 1542.14nm to 1558.17nm is shown in the Fig:1. In this paper, the comparison has been done between the distribution schemes by selecting the same set of wavelengths for WDM multiplexer input and same gain for EDFAs.

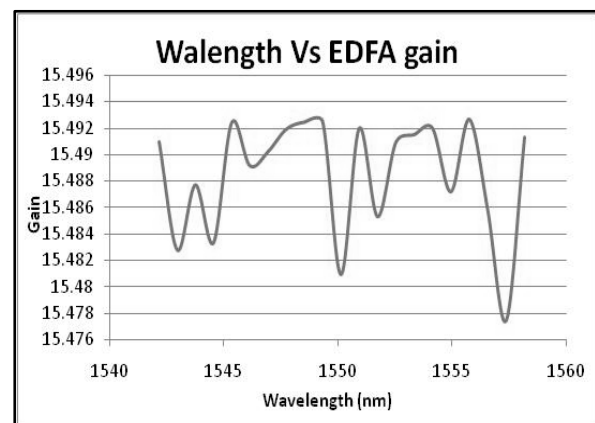


Fig: 1 Wavelength Vs EDFA gain plot

Fig:4 shows the simulation set up used for evaluating the performance of EDFA in the Optiwave environment. In this case for comparative study purpose continuous wave lasers are used as sources for all 7 wavelengths instead of using external modulators for high frequency analog and RF signals. Source power for each wavelength has been taken as 0dBm for all 7 Signals. This reference input of 0dBm helps in analyzing the final output variation before feeding the signal to each of the receiver modules. If

required, necessary amplification can be provided to each of the signals in the electrical domain based on these variation factors.

The selection of wavelength for study is chosen based on minimum variation in EDFA gain ranging from 1547.72nm to 1552.52nm.

4. OPTICAL SIGNAL DISTRIBUTION NETWORK SCHEMES

Following sections prescribe about four different signal distribution schemes with its performance analysis in detail. First 3 schemes employ fully optical network and the last hybrid scheme employs a combination of optical and conventional distribution methods [2]. To have a better comparison in all these distribution architectures, EDFA gain is set to 18dB used by taking into account of receiver sensitivity in the order of -25dBm.

4.1 Evaluation-Optical Distribution N/W Scheme 1

In this scheme first splitting is done row wise and later 5 O/P signals are demultiplexed individually to obtain 7 different signals. These signals are further splitted to 8 different paths based on the number of columns. (Refer Fig: 2). Thus it helps to distribute 7 different signals to 40 receiver modules.

Other parameters considered for the simulation are insertion losses of the splitters, Multiplexers and Demultiplexers. The insertion losses of the different components used are given in the Table: 1. [1]-[6]

Table:1 Insertion Losses of different components

Component	Insertion Loss(dB)
Multiplexer	2.5
Demultiplexer	2.5
<u>Power splitter</u>	
1 X 8	10
1 X 40	20

We observed that the output power is varying around -25dBm before the detector with a min and max variation of -25.071dBm and -25.085dBm respectively (Refer Fig: 3).[4]

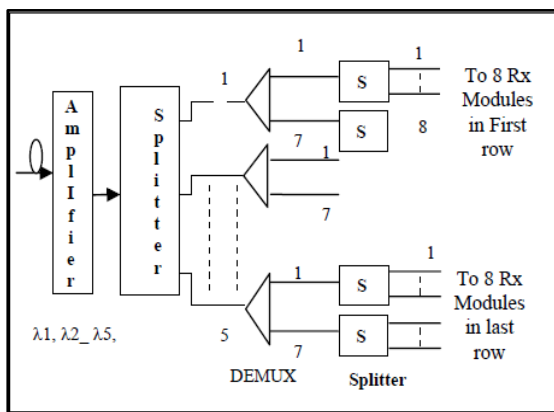


Fig:2 Block diagram of Scheme 1

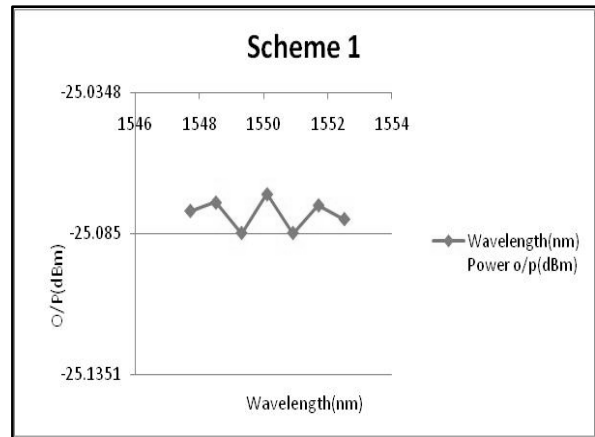


Fig:3 Wavelength Vs Output Power

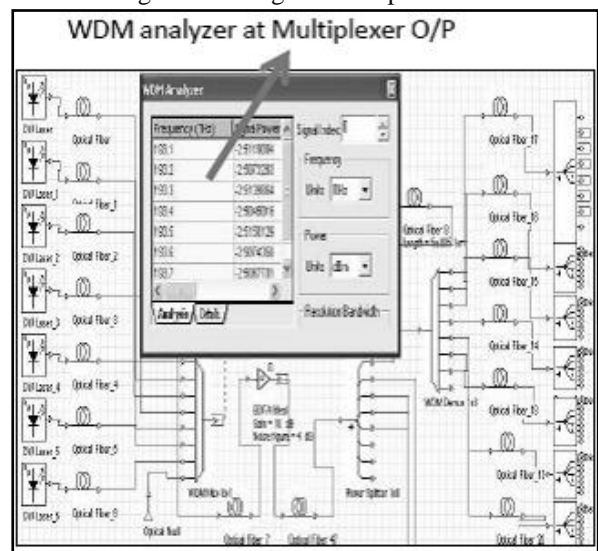


Fig:4 Simulation set up – Scheme 1 (Optiwave environment)

4.2 Evaluation - Optical Distribution Network 2

Here initially itself signals are splitted based on the total number of receiver modules and further these signals are demultiplexed to obtain the individual signals. But splitter of higher order output ports is required in this case. (Refer Fig: 5). More number of demultiplexers are used. [1]-[6]

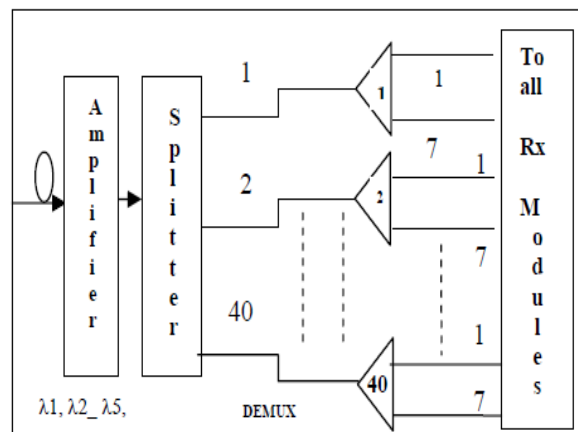


Fig:5 Block diagram of Scheme 2

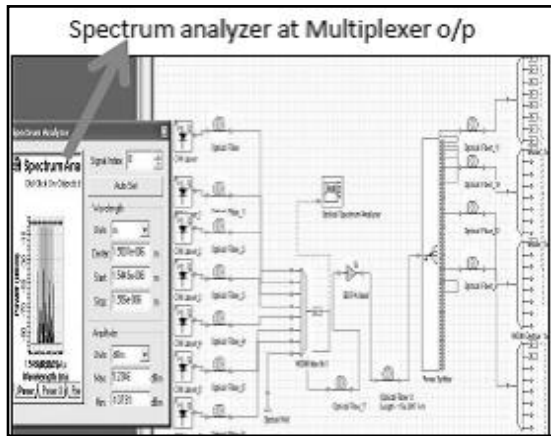


Fig: 6 Simulation set up – Scheme 2 (Optiwave environment)

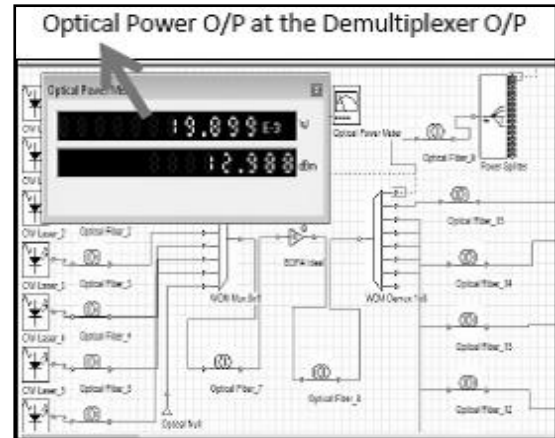


Fig: 9 Simulation set up – Scheme 3 (Optiwave environment)

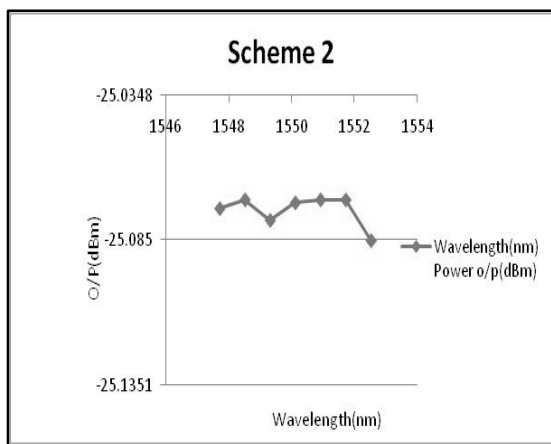


Fig:7 Wavelength Vs Output Power (before detector)

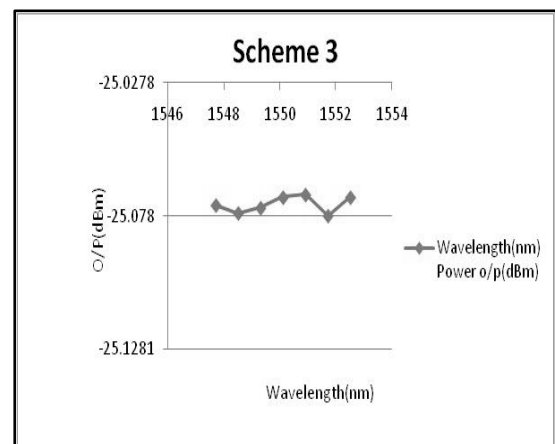


Fig:10 Wavelength Vs Output Power (before detector)

We observed that the output power is varying around -25dBm before the detector with a min and max variation of -25.071dBm and -25.085dBm respectively (Refer Fig 7).[4].

We observed that the output power is varying around -25dBm before the detector with a min and max variation of -25.07dBm and -25.08dBm respectively (Refer Fig 10).[4]

4.3 Evaluation - Optical Distribution Scheme 3

In this case signals are demultiplexed and further each of the signals is splitted based on the total number of receiver modules. (Refer Fig: 8) [1]-[6]

4.4 Evaluation - Optical Distribution Scheme 4

Here all 7 signals are multiplexed and fed through a single fiber (Refer Fig:11). Since generation of these signals does not happen within the array, multiplexed signals can easily be taken through an optical rotary Joint in contrast to the feeding of various signals through slip ring, RF and Optical Rotary Joints. in all these cases, the output signal strength is comparatively high. Since distribution of signals is achieved through normal conventional methods compared to the usage of splitters in Optical domain. The effect of splitters and demultiplexers has been seen in the other three cases. In othree schemes, each component introduces its own losses in the optical network path.

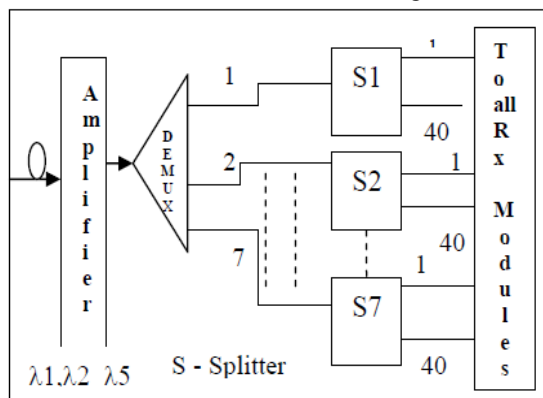


Fig:8 Block diagram of Scheme 3

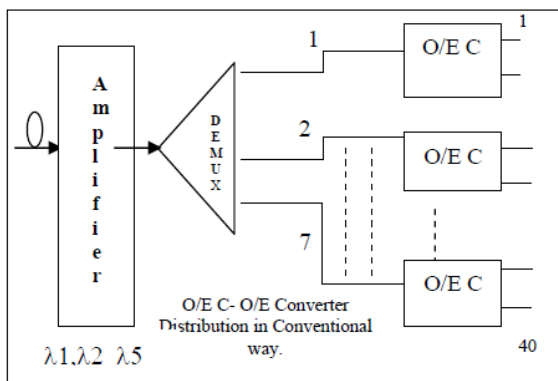


Fig:11 Block diagram of Scheme 4

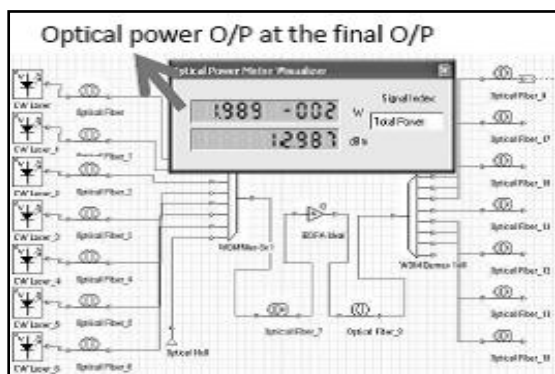


Fig: 12 Simulation set up – Scheme 4 (Optiwave environment)

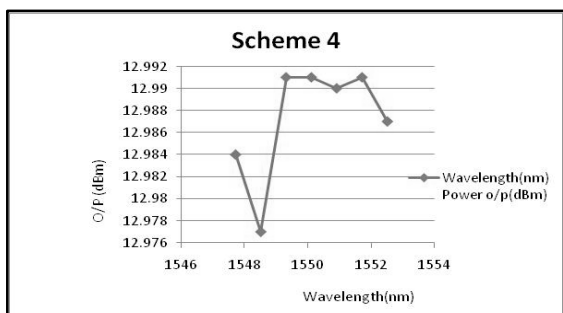


Fig:13 Wavelength Vs Output Power (Before detector)

In this case the signal strength is comparatively at high order of 12.9dBm with min and max variation 12.977dBm and 12.991dBm due to the non usage splitters and demultiplexers. But in RF domain some other path loss get introduce during distribution.(Refer Fig 13.)

5. RESULTS AND COMPARISON

The above analyses gives an insight towards the variation of the output power levels in each scheme. The final output has been analysed by feeding appropriate values for various parameters such loss parameters for multiplexer, demultiplexer and splitters and gain of EDFA etc. To have a realistic comparison, these values are derived from the commercially available similar components of WDM optical networks. It is observed that in the first three schemes the output power level varies based on the various components used in the

schemes. But it can be seen that some scheme uses more number of multiplexers compared to splitters in the network which are more costly. This results in additional cost implication. But fully Optical network schemes will provide better quality signal distribution with a solution free from Electromagnetic interference. Additionally, these schemes, by avoiding cumbersome RF cabling result in the reduction of the total weight and hardware complexity of the array.

6. CONCLUSIONS

This paper brought out four different optical signal distribution networks suitable for Radar application. Basically the number of the wavelengths to be used in the WDM schemes is decided based on the number of signals to be distributed. In all these cases to have a better comparison same input power has been considered against same set of fixed wavelengths. It is also observed that EDFA gain varies with the selection of wavelength. So the selection of wavelengths is very important in the case of multiplexed WDM optical networks. With the variation in the utilization of components in the distribution schemes power levels at the output also varies. But we observed that these variations are not significant in fully optical distribution schemes. So it is suggested that based on the actual requirement, by taking other factors like cost, complexity and weight suitable scheme should be adopted for realization.

ACKNOWLEDGEMENT

The authors wish to acknowledge K.T. Udayanarayana and Dr.D.C.Pandey of Electronics and Radar Development Establishment (LRDE)for their support.

REFERENCES

- [1] G.P.Agarwal, "Fiber-Optics", 3rd Edition, Wiley, 2007
- [2] Meena.D, LGM Prakasam, D.C.Pandey, E.S. Shivaleela, T.Srinivas, "Multiplexed Signal Distribution Using Fiber Network For Radar Applications", AIP Conf. Proc. -- October 20, 2011 -- Volume 1391, pp. 413-415
- [3] Lidia Jordanoval and Valentin Topchiev2, "Amplification of the Multi-Wavelength Signal by using EDFA with Constant Gain" IJCSNS
- [4] Optiwave, *Optisystem -4 Users Manual*
- [5] Li Qian, "Experiment on Erbium-Doped Fiber Amplifiers", Advanced Labs for Special Topics in Photonics (ECE1640H), University of Toronto, 1998.
- [6] Rajiv Ramaswami, Kumar N Sivarajan and Galen Sasaki, *Optical Networks: A practical Perspective*, 3rd Edition, Morgan Kaufmann Publishers, Elsevier, USA, 2009

PERFORMANCE ENHANCEMENT OF SAC-OCDMA SYSTEM USING M-SEQUENCE CODES

Syed Tajammul Ahmad *, Gausia Qazi and Ghulam Mohd Rather

Electronics & Communication Engineering Department National Institute of Technology Srinagar (J&K), INDIA

*Corresponding Author, email: taiju_66@rediffmail.com

Abstract: The optical code division multiple access (OCDMA) is an efficient technique for better utilization of wider bandwidth of optical fiber. The two methodologies i.e., multiplexing and spreading can be employed in OCDMA technique to achieve efficiency, privacy and antijamming. The spectral amplitude coded OCDMA system set up is implemented and simulated. The m-sequence codes are used to design the fiber bragg gratings (FBGs). The FBGs are used as encoders and decoders. The simulation results revealed that an error free transmission ($BER < 1 \times 10^{-9}$) is achieved up to a data rate of 622 Mbps and 1.2 Mbps for a fiber length of 35 km and 10 km respectively.

I. INTRODUCTION

Fiber optic communication technology has changed the landscape of telecommunications, and is still doing so at an extreme pace. Because of the telecommunication appetite for capacity, the bandwidth of commercial systems has increased by orders of magnitude. The information carrying capacity of a single optical fibre channel is estimated at 50 terabits per second (Tbps) but from a practical point of view, commercial links have transmitted far fewer than 100 Gbps. This is an astounding data rate that cannot be achieved with any other transmission medium. So the full advantage of the high data rate in optical fibers can be achieved by allowing several users to transmit data simultaneously over the same communication channel. This is called multiplexing. Two major technological advances i.e. wavelength division multiplexing (WDM) and Erbium Doped Fiber Amplifier (EDFA) have boosted the capacity of existing optical fiber communication systems. The third technique is optical-code division multiple access (OCDMA). OCDMA combines the large bandwidth of the fiber medium with the flexibility of the CDMA technique to achieve high speed connectivity. OCDMA technique is an attractive candidate for next generation broadband access networks [1]. In this paper, focus is on the use of spectral amplitude coding, which can be achieved using fiber Bragg gratings (FBG) in transmission [2]. FBG is an ideal component used as encoder and decoder. Also, the multiple access interference (MAI) which is the limiting case in OCDMA systems can be cancelled by the use of balanced detectors. In [3], a system operating at 622 Mb/s showed a BER floor of 2.7×10^{-8} with only seven active users and achieved an error free transmission ($BER < 1 \times 10^{-9}$) up to five simultaneous users. However in this work, an error free transmission up to seven simultaneous users has been achieved at the data rates of 622 Mb/s and 1.2 Gb/s using fiber lengths of 35 km and 10 km respectively. The shapes of FBG spectral response need to be optimized to achieve this improvement in performance.

The use mode-locked lasers and nonlinear thresholders in OCDMA systems can achieve high data rates, but are quite complex and expensive [4]. So, the broadband sources are used because of their low cost and large emission bandwidth compared to the coherent sources. The reflected spectral chip width from FBG is taken at an optimum value, in order to have better performance in terms of BER or, for fixed BER, could accommodate more users for greater capacity. The Optisystem9 simulator is used as a design tool to numerically trade off the MAI and intensity noise by selecting the bin bandwidth (reflected pulse width) of FBGs.

The remainder of the paper is organised as follows. In Section II, we describe the principle of operation of SAC-OCDMA system. Section III discusses the m-sequence codes. In Section IV, we present our simulation results and BER measurements for the optimized system. Finally, we conclude with suggestions for further improvement in performance that might be attained.

II. SAC-OCDMA SYSTEM

The block diagram of transmitter and receiver part of the OCDMA system using m-sequence codes is shown in figures 1(a) and (b) respectively. The system design is simulated in optisystem9 simulator [5].

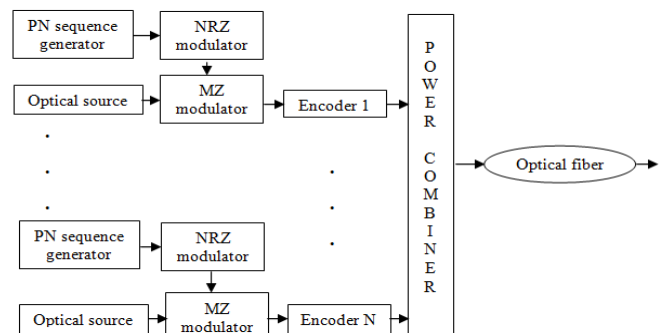


FIG 1(a): 7-User OCDMA system (Transmission part)

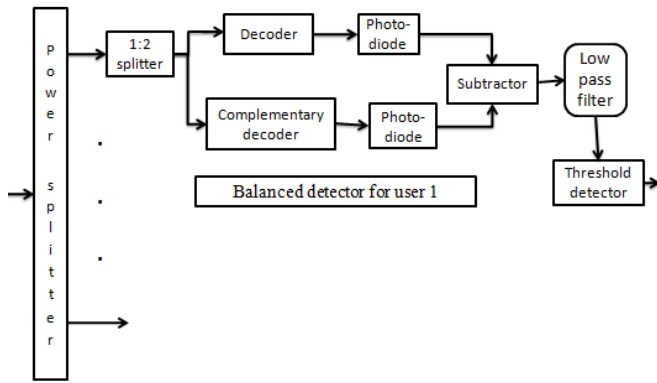


FIG 1(b): 7-User OCDMA system (Balanced detection)

The above setup is based on the star topology. Each transmitter is composed of a broadband source followed by an optical modulator which modulates the source signal with the user data. The full wave half maximum width of the broadband light pulse is chosen to be greater than total number of required spectral slices i.e., the chosen bin bandwidth of FBG [6]. The optical pulses are then encoded by unique spectral encoder consisting of FBGs using m-sequences. The spectrally encoded optical pulses from each user are combined using optical power combiner, and then passed through the standard optical fiber. At the receiver end, the signal is passed through the power splitter in order to broadcast the signal to each user at the receiver end. The received signal is first split into two parts using a 1: 2 splitter. After dividing into two parts, the optical signals are decoded by two complementary decoders. The direct decoder has the same spectral distribution as that of the intended spectral encoder. The complementary decoder has the complementary spectral characteristics as that of the direct decoder. The decoded signals are detected by two photo-detectors connected in a balanced manner at the receiver block. The power of two signals is subtracted using an electrical Subtractor and the impact of MAI can be cancelled after balanced detection. So, here balanced detector is used to eliminate MAI. The original data can be recovered after passing through the Bessel low pass filter and the threshold detector at the receiver end.

III M-SEQUENCE CODES

The m-sequence is a pseudorandom sequence, which can be generated by feedback-shift-registers as shown in figure 2 and has the maximal period. Therefore, it is called the maximal linear feedback-shift-register sequence. The period of an m-sequence does not only depend upon the number of stages of shift-registers, but is also related to the linear feedback logic. Based on this logic, the 3-bit, 7-bit, 15-bit m-sequence codes can be generated which can support 3, 7 and 15 active users respectively. In this work, 7-bit m-sequence codes have been used in order to support 7 active users. Be-

yond this there is huge interference which results in high BER.

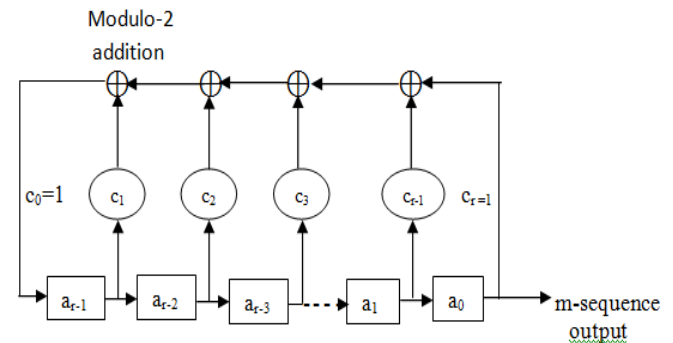


Figure 2: r -stage linear feedback shift-register

The various properties of m-sequences are as follows [6];

- i. The m-sequences are generated by an r -stage shift-register and the period is $2^r - 1$ i.e., 3 bit, 7 bit, 15 bit sequences, etc.
- ii. The number of “1” is only one more than the number of 0s in an m-sequence.
- iii. The m-sequences satisfy run property.
- iv. The auto and cross- correlation is unity.

The Table 1 shows the 7-bit m-sequence codes used for each user.

Table 1: M-sequence codes for 7 user system ($L=7, w=4, \lambda=1$)

No. of Users	Encoder or Decoder	C - Decoder
1	1110010	0001101
2	0111001	1000110
3	1011100	0100011
4	0101110	1010001
5	0010111	1101000
6	1001011	0110100
7	1100101	0011010

Based on these codes, the FBGs are designed and each user is assigned an FBG having different spectral chips. The number of spectral chips present in an encoded signal will be determined by the number of 1s present in a particular code. So each user will have different combination of frequency components.

IV RESULTS AND DISCUSSIONS

The spectral width of the reflected pulses from FBGs is first selected at a value where the BER value is minimum. So, the graph is drawn between the bin bandwidth of FBG and BER for m-sequence coded system at 10 km fiber length in order to find the optimum value of spectral width. This is shown in figure 3. The graph shows that at 3 nm bin bandwidth, the BER value is minimum. At this optimum value the system shows the improvement in performance.

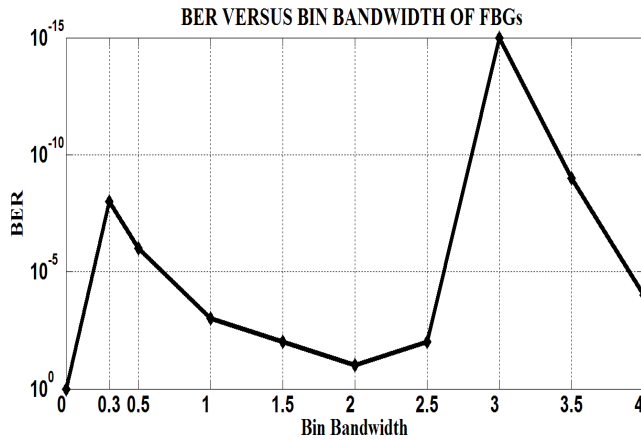


Fig 3: BER versus Bin bandwidth at 10 km fiber length

Now the system is operated at 0.3 nm and 3 nm bin bandwidths using different data rates. The figure 4 shows the graph between BER and data rate for various bin bandwidths of FBGs i.e. at 0.3 nm and 3 nm using 7 user OCDMA system. The optical fiber length used here is also 10 km.

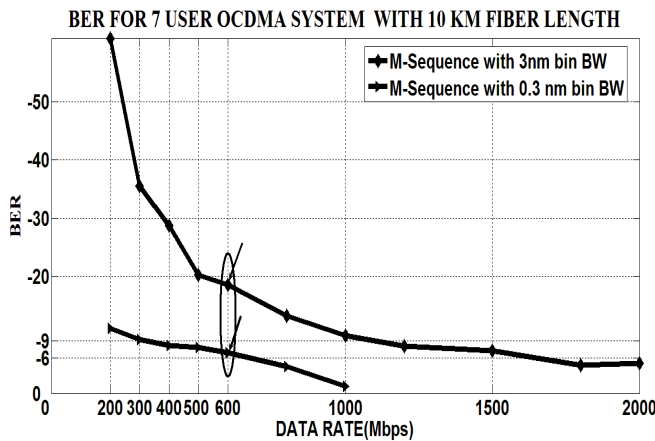


Fig 4: BER versus data rate for 7 user system with 10 km fiber length

The graph shows that an error free transmission can be achieved ($BER < 10^{-9}$) up to 500 Mbps using 0.3 nm bin bandwidth with 7 active users. However an error free transmission can be achieved up to a data rate of 1.2 Gbps using 3 nm bin bandwidth. Also, the BER of 10^{-7} and 10^{-15} can be achieved at a data rate of 600 Mbps for 0.3 nm and 3 nm bin bandwidths respectively.

The error free transmission is also achieved for the above system at a data rate of 622 Mb/s but with a fiber length of 35 km. This is shown in the figure 5. Here the graph is drawn between the BER and the fiber length at a constant data rate of 622 Mb/s. Here the improvement in performance is achieved by the optimization of bin bandwidth of FBGs from the previous one [4].

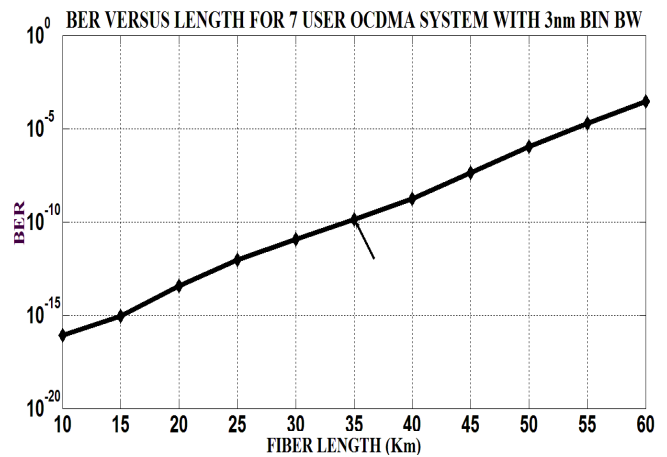


Fig 5: BER versus length for 7 user system at a data rate of 622 Mb/s

The OCDMA system using m-sequence codes is now examined at this optimum value (i.e. 3 nm) but at different fiber lengths. The graph of BER versus data rate at different fiber lengths is shown in figure 6.

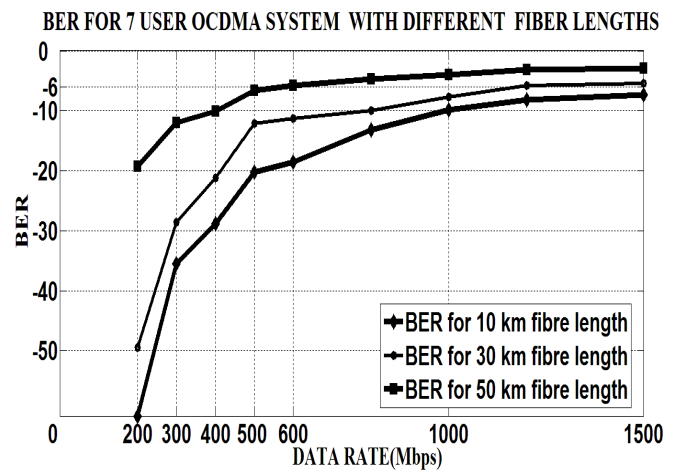


Fig 6: BER versus data rate for 7 user system at different fiber lengths

Figure 6 shows the optimum data rate that can be achieved for an error free transmission in a 7 user OCDMA system at fiber lengths of 10 km, 30 km and 50 km using m-sequence coding. Thus the graph indicates that with the increase in fiber length, the BER also increases but the data rate at which error free transmission can be achieved is decreased.

V CONCLUSION

In this paper the optimization of FBG encoders is examined for SAC-OCDMA systems using m-sequence codes. The conclusion drawn from the simulation results have been summarized as follows:

- 1) The simulation results revealed that the m-sequence codes provide much better improvement in performance than the previous one [3, 8]. In [3], the BER achieved for 7 user system was 2×10^{-8} and an error free transmission was achieved for 5 simultaneous users at a data rate of 622 Mbps. However the proposed system achieves an error free transmission up to 1.2 Gbps and 622 Mbps for 7 simultaneous users at fiber lengths of 10 km and 35 km respectively with the optimized bin bandwidth of 3 nm. This improved performance is due to reduction in intensity noise and the increase of spectral bandwidth. The wider bandwidth will then have wider frequency bins thus reducing interference.
- 2) Hence, it is concluded that the m-sequence codes give an improvement in performance and are most suitable for Ethernet and Gigabit passive optical networks.

Future work will focus on use of coding techniques that will increase the number of active users to match the passive optical network requirements and the examination of low cost optical equipments for that system.

REFERENCES

- [1] M. Abrams, P. C. Becker, Y. Fujimoto, V. O'Byrne, and D. Piehler, "FTTP deployments in the United States and Japan—Equipment choices and service provider imperatives," *J. Lightwave Technology*, vol. 23, no. 1, pp. 236–246, Jan. 2005.
- [2] R. P. Scott, W. Cong, C. Yang, V. J. Hernandez, N. K. Fontaine, J. P. Heritage, B. H. Kolner, and S. J. B. Yoo, "Error-free, 12-user, 10 Gb/s/user O-CDMA network test bed without FEC," *Electron. Lett.*, vol. 41, no. 25, pp. 1392–1394, Dec. 2005.
- [3] J. Penon, Z. A. El-Sahn, L. A. Rusch, S. LaRochelle, "Spectral-amplitude-coded OCDMA optimized for a realistic FBG frequency response," *Journal of lightwave technology*, vol.25, pp. 1256-1263, 2007.
- [4] Jawad A. Salehi, "Code Division Multiple-Access Techniques Optical Fiber Networks-Part I: Fundamental Principles", *IEEE transaction on communications*, vol. 37, no. 8, august 1989, pp. 824-833.
- [5] Optisystem 9, a simulation package by *Optiwave Systems Inc.*, Ottawa, Canada.
- [6] Othonos, K. Kalli, "Fiber Bragg grating: Fundamentals and applications in telecommunications and sensing", Artech House Inc., (1999).
- [7] Mohammad Reza Salehi, Ebrahim Abiri, Mehran Dezfouli, Keyvan Kazemi, "Performance of different code families in SAC-OCDMA systems impaired by gvd," *IEEE GCC Conference and Exhibition (GCC)*, Feb 2011.
- [8] S. Ayotte, M. Rochette, J. Magné, L. A. Rusch, and S. La-Rochelle, "Experimental verification and capacity prediction of FE-OCDMA using superimposed FBG," *J. Lightwave. Technology*, vol. 25, no. 2, pp. 724–731, Feb. 2005.

NOVEL OPTICAL FIBER SENSORS FOR NUCLEAR RADIATION MONITORING AND RADIOTHERAPY

Sanjay Kher,
 Fiber optics Lab, SSLD, RRCAT, Indore, kher@rrcat.gov.in

Abstract: The fiber optic nuclear radiation sensors of high sensitivity and large measurement range are under development at RRCAT, Indore. Specialty long period fiber gratings in different types of single mode fibers have been designed and characterized for high dose sensing applications. I will address various aspects and physical processes related to radiation induced effects in optical fibers and describe our recent results for innovative use of specialty gratings for radiation dosimetry.

1. INTRODUCTION

Optical fiber sensor technology offers a unique capability for remote monitoring of nuclear radiation in difficult-to-access and/or hazardous locations. Dedicated optical fibers and specialty gratings are being fabricated with prospects for wide range of applications such as monitoring of nuclear waste storage, dose measurements at electron accelerators, fusion reactors, accidental environmental leakage, and cancer therapy [1, 3, 5]. Such applications cover a broad dose range from 0.5 Gy to few MGy. Radiation induced darkening due to defect formation in specialty optical fibers have been investigated for low dose regime while specialty long period gratings have been studied for high dose range [2, 3, 4].

2. EXPERIMENTAL DETAILS AND RESULTS

Long period gratings have been fabricated using an automated CO₂ laser system. The gratings were characterized by using an optical spectrum analyzer. All grating based sensors were analyzed off line after irradiation for a specified dose in a gamma chamber. The photo-darkening effect was studied in-situ with gamma dose using lasers operating at 1.06 micron and 633 nm. Table 1 shows the characteristic wavelength dip shifts of long period gratings due to gamma irradiation. Table 2 shows the effect of radiation induced attenuation in specialty single mode optical fibers.

Table 1
 Effect of gamma dose on resonance dip wavelength shift (dose 65 kGy)

Fiber Type	Resonance wavelength(nm)	RDWS (nm)
Smf-28(Fiber Logix)	1522.4	3.0
Photo-sensitive high Ge fiber	1435.2	4.1
B-Ge doped INO fiber	1361.6	9.6

Table 2
 Effect of gamma dose on induced attenuation

Fiber Type	Induced Attenuation at 1.06 micron	Remarks
Smf-28	.01 dB/ m	30 kGy dose
B-Ge doped fiber	0.025 dB/m	30 kGy dose
Rare earth doped double clad fiber	10 dB/m	2 kGy dose

3. CONCLUSION/SUMMARY

Optical fiber sensors provide a unique opportunity to perform radiation dosimetry under a variety of environmental conditions due to small size and flexibility. A combination of sensors described here can provide the entire dose range of interest, 0.5 - 10⁶ Gy. Specialty gratings offer the potential for very sensitive wavelength encoded detection.

REFERENCES

- [1] Sanjay Kher, P.Joshi, R.K.Sharma, Radiation effects on pure silica multimode fibers, Nucl. Inst. Methods in Phys. Res. A 578 (2007) 345.
- [2] Shailesh K.Khamari, V.K.Dixit, Sanjay Kher, S.M.Oak, effect of ⁶⁰Co gamma ray irradiation on electrical properties of GaAs epilayer and GaAS p-i-n diode, Nucl. Inst.Methods in Phys. Res. B 269 (2011) 272.
- [3] Smita Chaubey, P.Joshi, Sanjay Kher, Design and development of long period grating sensors for temperature monitoring, Sadhana, Vol. 32, part 5, Oct. 2007, 513.
- [4] V.N.Rai, Sanjay Kher, S.K.Deb, Effect of gamma ray irradiation on optical properties of Nd-doped phosphate glass, J. Lumin., 130 (2010) 582, issue 4, April 2010.
- [5] A.L.Huston, B.L.Justus et al, Remote optical fiber dosimetry, Nucl. Inst.methods in Phys. Res. B 184 (2001) 55.

FROM TECHNOLOGY TO INSTRUMENT – DISTRIBUTED ANTI-STOKES RAMAN THERMOMETRY

B. Srinivasan, Uvaraj Gajendran, and Amitabha Datta
Department of Electrical Engineering, Indian Institute of Technology Madras
balajis@ee.iitm.ac.in

Abstract: Distributed Anti-Stokes Raman Thermometry (DART) is a well known technique for carrying out distributed temperature sensing which is based on spontaneous Raman scattering in optical fibers. In this paper, we discuss the issues related to realizing a compact, portable instrument from a benchtop demonstration of the technology. Key issues such as calibration, repeatability and packaging are discussed.

Distributed sensing of temperature is a critical requirement for several applications such as monitoring of oil/gas pipelines, power transmission cables, and fire detection in tunnels. Optical fibers are well suited for the above applications as they are amenable to distributed sensing owing to low losses, are not susceptible to electromagnetic interference (EMI), have the ability to be deployed around corners without significant signal loss, and are light weight. Specifically, a fiber-based sensing technique called Distributed Anti-Stokes Raman Thermometry (DART) is a well-established technique for distributed temperature sensing [1]. The DART technique relies on the spontaneous Raman scattering, in which the anti-Stokes scattered signal is much dependent on the temperature compared to the Stokes component. By taking the ratio of the two components (Fig. 1) and marrying the technology with the well-known optical time domain reflectometry (OTDR), one can determine the temperature at a particular location with high precision and spatial resolution.

We have previously demonstrated the distributed temperature sensor based on the above principle over a distance of 10 km with 8 m spatial resolution and 2 deg C temperature measurement error [2]. In this paper, we will focus on the development of a portable instrument that provides the above performance.

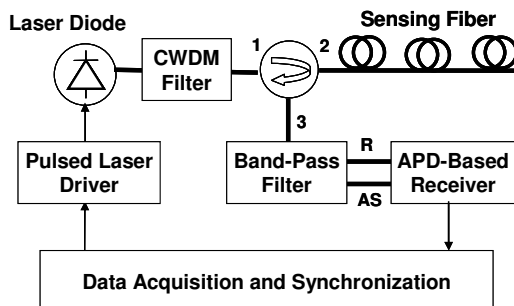


Fig. 1. Schematic diagram of the DART system.

2. INSTRUMENTATION ISSUES

Developing a technology into a reliable instrument is a non-trivial task. Several issues that are not considered for the proof-of-principle experiments can

haunt the instrument development. Take for instance the choice of the source laser itself. Since the above technique relies on spontaneous scattering, one would like to use high power (several Watt output) laser sources which are typically bulky and are available with free space output beams. Although one can carry out demonstrations involving free space coupling into the optical fiber, this is not a reliable approach for an instrument requiring repeatable performance over a long period of time. The tradeoff could be using a relatively lower power fiber pigtailed semiconductor laser, where the performance burden is shifted to the receiver and signal processing sections.

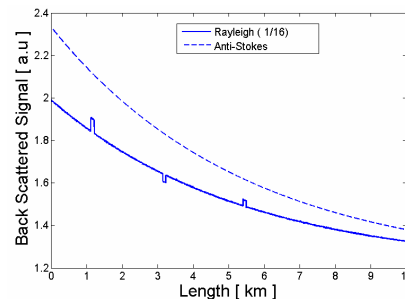


Fig. 2. Sample traces of anti-Stokes and Rayleigh signals.

Another important issue is the calibration of the measurement unit. Due to the attenuation in the sensing fiber, the backscattered anti-Stokes signal degrades over the length of the fiber and needs to be referenced with a similarly varying signal. Here the Rayleigh backscattered signal is preferred over the Stokes signal since the spectral separation is not large. Such issues will be discussed in more detail.

ACKNOWLEDGMENT

The authors wish to acknowledge financial support from the Department of Information Technology, GoI.

REFERENCES

- [1] Alan Rogers, "Distributed optical-fibre sensing" *Meas. Sci. Technol.* 10, R75–R99 (1999).
- [2] A. Datta, B.K. Lagishetty, B. Srinivasan, "Performance Evaluation of Temperature Sensing System Based on DART", Paper # JThA4, Proceedings of the Optical Sensors Conference, Karlsruhe (2010).

CALIBRATION-FREE APPROACHES IN TUNABLE DIODE LASER SPECTROSCOPY OF GASES FOR INDUSTRIAL APPLICATIONS

Arup Lal Chakraborty

Department of Electrical Engineering, Indian Institute of Technology Gandhinagar, Ahmedabad –
382424, Gujarat, India
arup@iitgn.ac.in

Abstract: Industrial gas monitoring applications have greatly benefited from recent developments in tunable diode laser spectroscopy which is the industry standard in non-invasive, real-time measurement. *Calibration-free* wavelength modulation spectroscopy (WMS) techniques have obviated the need for signal calibration. This paper presents a comparison of some of the significant recent developments in this field.

1. INTRODUCTION

Tunable diode laser spectroscopy (TDLS) of infrared rotation-vibration absorption lines of gases is ideal for high-sensitivity, high-specificity and real-time measurements of gas parameters such as concentration, pressure and temperature [1,2]. Modern industries need to adopt adequate process control measures to make them operationally optimized and safe. Inefficient processes lead to high long-term running costs and high emission levels of toxic and greenhouse gases. Over the last few decades TDLS has emerged as the preferred technology in a wide variety of industrial, environmental and medical applications of gas detection. The ability to remotely detect specific gas species in a physical or chemical processes, and more importantly, to be able to make quantitative measurements of critical process parameters is a significant advantage. The ever-widening spectral coverage attainable with compact, frequency-agile and spectrally bright diode lasers makes it possible to achieve multi-species detection in which several absorption lines of target gases are simultaneously recovered with a single tunable laser source. In other applications, very high-resolution spectroscopy of a single, well-isolated rotational-vibrational absorption line of a target gas is performed to extract gas parameters with high speed and accuracy. The rapid advances in this field have been spurred by the development of narrow-linewidth, widely tunable lasers in the near-infrared and mid-infrared (up to 20 μ m) regions of the optical spectrum. These laser sources include conventional distributed feedback edge-emitting lasers, newer varieties of low-power VCSELs, the much more recent quantum cascade lasers (QCLs) and difference frequency generation (DFG) sources.

Conventional gas detection techniques such as electrochemical sensors, gas chromatography (GC), pellistors and non-dispersive infrared (NDIR) sensors are no match for TDLS because these techniques have major drawbacks such as slow response, limited sensitivity and poor selectivity due to cross-sensitivity to different species, and bulky size of instruments.

2. BASICS OF WAVELENGTH MODULATION SPECTROSCOPY

A distributed feedback (DFB) diode laser's centre wavelength can be tuned very conveniently by varying the injection current or the temperature. Temperature tuning is coarse but allows a wider spectral region to be scanned and is often preferred for the detection of multiple species and particularly at high pressures. Current tuning covers a much smaller range, but has better precision and is the preferred method. TDLS essentially involves tuning the emission wavelength of a narrow linewidth laser diode across one or more absorption lines of a gas by varying its injection current with a ramp signal of several tens of milliamperes for telecom-grade diodes, and several milliamperes for VCSELs. Under atmospheric conditions the width of a typical near-infrared absorption line is 1-2 GHz which is fairly straightforward to cover. The incident laser intensity is attenuated by the spectrally-varying absorption of the gas. The relative transmission, obtained by normalizing the transmitted intensity by a baseline fit to the non-absorbing spectral wings, is a function of the product of the absorbance of the gas and the optical path length in accordance with the Beer-Lambert law. For a known path length the absorbance can be calculated. The gas parameters can then be inferred by fitting a Voigt profile (for typical industrial applications) with spectral parameters taken from the HITRAN database and fitting the parameters of interest to the experimental data in a least squares sense. This method is known as direct absorption spectroscopy and is often the first method to be tried essentially because of its simplicity. However the sensitivity of direct detection can be limited by the need to detect a small absorption-dependent change on a large background signal. This is typically the case in the near-infrared region where overtones of fundamental absorption lines are probed. The availability of mid-infrared sources in recent times has made it possible to probe fundamental lines and make this method viable in many applications.

To increase measurement sensitivity TDLS is often used with an additional modulation impressed on its injection current. When the laser's injection current is modulated there is a wavelength modulation (WM) as well as a synchronous intensity modulation (IM) of the laser output [1, 2]. The IM and the WM are separated by a modulation frequency-dependent phase angle ψ . The expressions for the instantaneous values of frequency and intensity are given by the expressions below.

$$v(t) = v_c + a \cos \omega t \quad (1)$$

$$I(t) = I(v_c) + \Delta I(v_c) \cos(\omega t + \psi) \quad (2)$$

Here $I(v_c)$ is the mean laser intensity, $\Delta I(v_c)$ is the IM amplitude, v_c is the slowly-varying centre wavelength of the laser, a is the WM amplitude. This approach, known as modulation spectroscopy, leads to much higher sensitivity than direct detection. For most gas sensing applications the frequency of modulation (f_m) is on the order of a few tens to a few hundreds of kHz and does not demand a lot of either the laser or the detection electronics. This regime of operation is known as wavelength modulation spectroscopy (WMS) as opposed to frequency modulation spectroscopy (FMS) where f_m is on the order of the absorption linewidth (GHz). The interaction of the doubly modulated laser output with the absorption line can be viewed as a spectral modulation of the absorption feature. The absorption line can be viewed as a highly nonlinear transfer function which immediately suggests that the output should contain signal components at various harmonics of f_m in accordance with the Fourier theory. The various Fourier components of the spectrally-modulated transmission coefficient $\tau(v)$ are given by [2],

$$H_0(v_c, a) = -\frac{PxL}{2\pi} \int_{-\pi}^{\pi} S\tau(v_c + a \cos \theta) d\theta \quad (3)$$

$$H_k(v_c, a) = -\frac{PxL}{\pi} \int_{-\pi}^{\pi} S\tau(v_c + a \cos \theta) \cos k\theta d\theta \quad (4)$$

where, P is the total gas pressure, x is the mole fraction of the absorbing species, L is the interaction length with the laser light, S is the line strength of the absorption feature and τ is the line shape function. WMS signals are characterized by the modulation index defined as $m = a/\gamma$, where γ is the half-width-half-maximum value of the linewidth of the absorption feature being studied. The m -value is a very important parameter in WMS because it determines the form and amplitude of the Fourier coefficients and therefore the amplitude of the recovered harmonic signals. The variation of the first three Fourier coefficients with m is shown in Figure 1. The strong dependence of H_1 and H_2 on m suggests

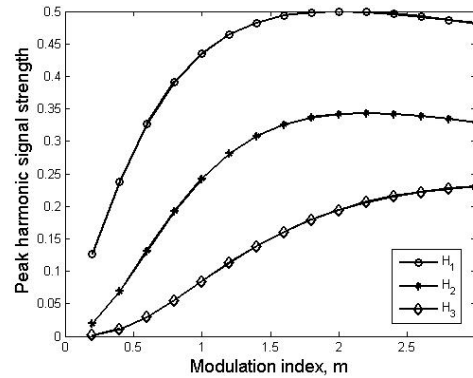


Fig. 1: Variation of the first three Fourier coefficients with modulation index, m , for a Lorentzian absorption feature.

that the laser should be operated at a fixed and optimized m -value. For $1f$ and $2f$ WMS the optimum m turns out to be 2 and 2.2 respectively. At these values H_1 and H_2 are maximized and are relatively insensitive to small variations in m that would inevitably occur in practice. Signal recovery is usually performed at a specific harmonic of f_m , but $2f$ WMS is by far the more popular approach. It turns out that the n^{th} harmonic signal is heavily dominated by the intensity-dependent n^{th} Fourier coefficient, but is distorted by the IM-dependent $(n-1)^{\text{th}}$ and $(n+1)^{\text{th}}$ Fourier coefficients. For example the net $2f$ signal is given by,

$$I_{2f} = \Delta I(v_c)H_1(v_c, a) + I(v_c)H_2(v_c, a) + \Delta I(v_c)H_3(v_c, a) \quad (5)$$

where, for simplicity the phase shift ψ has been assumed to be negligible. Figure 2 shows the various signal components and the net $2f$ signal.

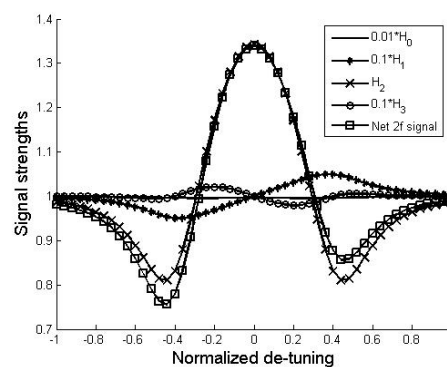


Fig. 2: $2f$ WMS signal components scaled by the laser intensity and intensity modulation amplitude. The distortion of the $2f$ signal due to the IM is evident

The linear IM has been assumed to be 10% of the intensity, which is reasonable, along with a nonlinear IM of 1%. The form of the net $2f$ signal is that of H_2 (with added distortion of the troughs caused by the IM) because $I(v_c)$ far exceeds $\Delta I(v_c)$. It is important to

note that since the line-centre values of H_1 and H_3 are zero the line-centre value of the $2f$ signal is not significantly changed. The distortion due to nonlinear IM is not significant for lasers that have highly linear power-current characteristics and high current tuning efficiency (GHz/mA). Other Fourier coefficients therefore do not enter the picture. The nonlinear IM may, however, be significant for VCSELs for instance, particularly if the wavelength scan is large range. The WMS literature is replete with reports of gas detection using 1st harmonic ($1f$) and 2nd harmonic ($2f$). Higher harmonics are rarely used.

In $2f$ WMS the concentration of the target gas is proportional to the line-centre value of the signal [2]. The only parameter relevant for the extraction of concentration in this case is the peak height of the signal at line centre. Pressure measurements are related to the separation of the maximum and the minimum of a 1st derivative signal in $1f$ WMS, while in $2f$ WMS the pressure is related to the two zero crossings of the signal.

3. CHALLENGES IN WMS – CALIBRATION

It is important to bear in mind that TDLS is often used in harsh environments where the gas parameters are unknown and widely varying. A persistent problem with traditional WMS is the need for signal calibration due to variable parameters such as gas pressure [1]. In industrial applications the pressure of the gas often varies significantly and may be unknown. This in turn means that ν , and therefore m , is also variable. Consequently, even if the WM amplitude of the laser is held constant by constant amplitude of the modulation current, the m -value is liable to vary significantly as a result of the variation of ν caused by pressure variations. The resultant variation in the amplitude of the detected harmonic signal could be wrongly interpreted as a change in concentration. Until a few years back the harmonic WMS signals required to be calibrated against the signal from a control sample of the same gas maintained under accurately known conditions.

In addition to the variation of the pressure that must also be measured there are other spurious systematic effects that vary unpredictably with time. These include the possible variation in laser power, the optical throughput of the system due to poor and variable coupling possibly due to mechanical vibrations and beam steering effects and the contamination of windows and optical surfaces by the environment. The cumulative effect of these factors is that the recovered electrical signal level is liable to vary significantly due to reasons other than the variation of the properties of the gas. This is what made calibration necessary in traditional WMS applications. Although this may be acceptable in laboratory environments, it is clearly an impractical and undesirable requirement in field measurements.

4. CALIBRATION-FREE WMS

Two distinct calibration-free quantitative approaches have recently been demonstrated. The fundamental difference between them is in the choice of detection harmonic. The first approach is based on $1f$ WMS and recovers the absolute absorption lineshape directly from which the gas parameters may be extracted by a method similar to that in direct absorption method. These $1f$ calibration-free WMS techniques are of two types, namely the Residual Amplitude Modulation (RAM) method and the Phasor Decomposition (PD) method [Ref]. Both techniques make use of the signal components that bear the signature of H_0 and H_1 coefficients. The $1f$ WMS signal is given by,

$$I_{1f} = \Delta I(\nu_c)H_0(\nu_c, a) + I(\nu_c)H_1(\nu_c, a) + \Delta I(\nu_c)H_2(\nu_c, a) \quad (6)$$

The aim in these two approaches is to use the phase-sensitive harmonic detection capability of the lock-in amplifier (LIA) to isolate and recover the IM-dependent first term i.e. $\Delta I(\nu_c)$ that follows the absorption lineshape and is separated from the second terms by ψ . For simplicity these details have been omitted here but the interested reader is referred to Ref [1]. The PD method has higher signal-to-noise ratio because it recovers the full absorption-dependent signal before normalization, while the RAM method is able to recover only a projection of the same signal.

The second approach is based on $2f$ WMS in which the recovered $2f$ signal is compared with the simulated $2f$ signals to extract gas parameters [2]. For low absorbance, the line-centre value of the $2f$ signal is essentially given by the coefficient H_2 and is shown to be directly proportional to the species concentration. This component however is intensity-dependent and would therefore require calibration unless appropriate measures are taken.

In either case signal normalization is achieved using the linear IM signal, $\Delta I(\nu_c)$, of the laser. In the $1f$ approach the $\Delta I(\nu_c)$ component is readily available from a baseline fit to the non-absorbing spectral wings of the recovered signal, or by tapping off a known but small fraction of the laser output. In the $2f$ approach one utilizes the very stable ratio of $\Delta I(\nu_c)$ to $I(\nu_c)$, that varies very little at various points in the measurement system. Robust measurement is therefore possible in harsh field conditions. The m -value is optimized at 2.2 so slow variations (see Fig. 1) in it do not greatly effect on the detected signals.

5. $1f$ and $2f$ RAM NULLING

The detection sensitivity of the two $1f$ techniques is limited by a high concentration-independent background RAM signal that arises due to the linear

IM. In $2f$ WMS the nonlinear IM introduces a smaller background signal that but that can vary significantly over a wavelength scan particularly for lasers that have highly nonlinear power-current curves. A recent fiber-optic technique to optically eliminate the $1f$ and $2f$ RAM in real-time [3, 4]. The experimental arrangement to implement a generic fiber-optic RAM nulling technique at any given harmonic is shown in Fig. 3. The principle of operation is to split the intensity-modulated output of a DFB diode laser approximately equally using a fiber-optic 3-dB coupler, with the two outputs going to the gas cell and the fiber delay line respectively. The value of f_m (delay) is so chosen as to introduce a relative phase shift of π between the two IM components on the two beams. The outputs of the gas cell and the delay fiber, after attenuation by a fiber-optic variable optical attenuator (VOA), pass through two fiber-optic polarization controllers to establish orthogonal polarization states for the two signals to minimize optical interference noise when they are recombined through a second 3dB coupler.

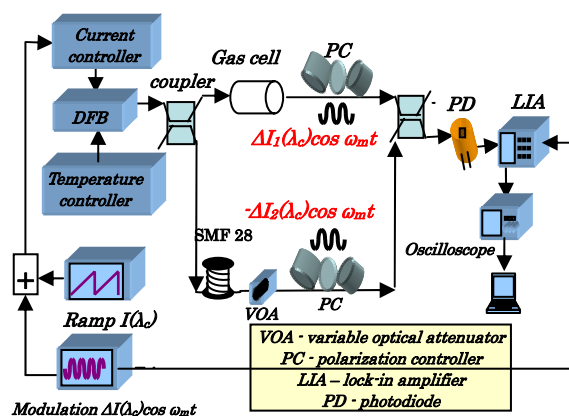


Fig. 3: Generic experimental setup for RAM nulling

When the system is balanced in the absence of gas the two sinusoidal IM components at f_m cancel. The resulting dc signal due to the addition of the two average intensity levels is rejected by the LIA, making the output zero and thus eliminating the background RAM signal. In imbalance due to the presence of gas gives rise to concentration-dependent signal due to the absorption. The generic nature of the RAM nulling strategy has also been demonstrated by implementing $2f$ RAM nulling [4]. This is important in high-pressure $2f$ calibration-free WMS where high m -values lead to high levels of $2f$ RAM. It is also potentially useful for WMS with non-telecom lasers such as VCSELs that have significantly nonlinear power-current characteristics. The elimination of the $1f$ RAM is shown in Fig. 4a in which the absorption signal appears on a zero background. This should be contrasted with the non-nulled case in Fig. 4b where the high background signal is evident. The accurate

recovery of an infrared absorption line of methane at 1651 nm is shown in Fig. 5 for 10% and 1% methane using the RAM and PD methods. Clearly the agreement between theory and experiment is excellent thereby validating the approaches.

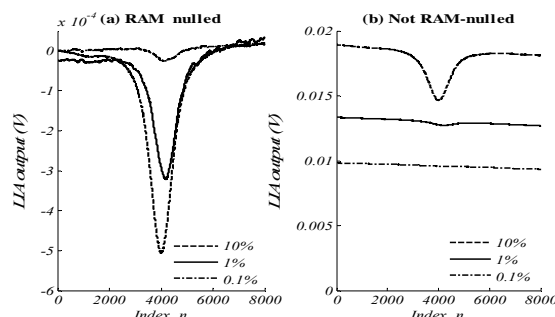


Fig. 4: LIA signals for 10.13%, 1.02% and 0.1017% CH_4 in N_2 for (a) RAM-nulled case, and (b) Non-nulled case.

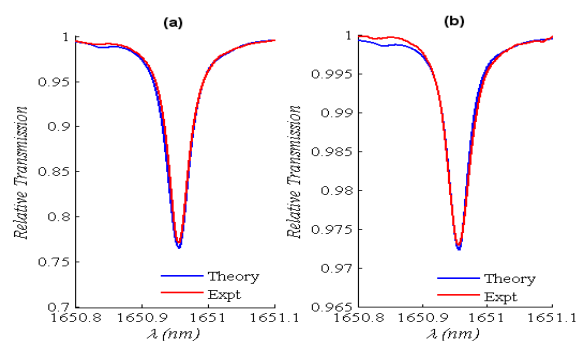


Fig. 5: Relative transmission for methane for (a) concentration 10.13%, pressure 1.067 bar temperature 22.6°C, and (b) concentration 1.02%, pressure 1.082 bar and temperature 23.6°C.

REFERENCES

- [1] W. Johnstone, A. J. McGettrick, K. Duffin, A. Cheung, G. Stewart, "Tunable diode laser spectroscopy for Industrial Process Applications: system characterization in conventional and new approaches," *IEEE Sensors J.*, **8**, 1079 (2008).
- [2] G. B. Rieker, J. B. Jeffries, R. K. Hanson, "Calibration-free wavelength-modulation spectroscopy for measurements of gas temperature and concentration in harsh environments," *Appl. Opt.* **48** (29), 5546-5559 (2009).
- [3] A. L. Chakraborty, K. Ruxton, W. Johnstone, M. Lengden and K. Duffin, "Elimination of residual amplitude modulation in tunable diode laser wavelength modulation spectroscopy using an optical fiber delay line", *Opt. Exp.*, **17**, 9602 (2009).
- [4] A. L. Chakraborty, K. Ruxton, W. Johnstone, "Suppression of intensity modulation contributions to signals in second harmonic wavelength modulation spectroscopy", *Opt. Lett.*, **35**, 2400 (2010).

PHOTONIC CRYSTAL SURFACE PLASMON WAVEGUIDE SENSORS FOR HIGH AND ACCURATE TEMPERATURE MEASUREMENT

Rajan Jha¹, Triranjita Srivastava² and Ritwick Das³

¹School of Basic Sciences, Indian Institute of Technology Bhubaneswar, Toshali Plaza, Bhubaneswar

²Department of Applied Physics, Delhi Technological University, Delhi-110042

³School of Physical Sciences, National Institute of Science Education and Research, Bhubaneswar

Author email address: rjhaphy@iitbbs.ac.in

Abstract: We propose a temperature sensor based on photonic crystal surface plasmon waveguides (PCSPWs) based on surface plasmon resonance optical techniques. We have used standard coupled mode theory for the calculation and have found that the proposed sensor can be used for high temperature application with sensitivity as high as ~ 66 pm/K in the telecommunication window. This will open a new window for sensing application in harsh environment.

1. INTRODUCTION

Surface plasmon polaritons (SPPs) are p -polarized electromagnetic (em) surface waves propagating along the metal-dielectric interface. Due to maximum field strength at interface, they are highly sensitive to any surface phenomenon. This feature has been exploited for various applications in the field of sensors and microscopy. However, the excitation of SPP is usually achieved by employing bulky prisms (Kretschmann scheme [1]) which render the configurations unsuitable for integrated photonic circuits. A crucial variant of SPPs is long-range SPPs (LRSPPs) supported by a thin metal stripe embedded in a symmetric dielectric medium [2]. It is found that the LRSPPs exhibit appreciable enhancement in surface fields and long propagation lengths, which interestingly manifests into narrower angular resonances. However, the major drawback associated with LRSPP applications is the complicated and bulky configuration required to excite the LRSPPs. Also, the requirement of highly symmetric configuration to support LRSPPs limits the flexibility in choice of materials.

Efficient excitation could also be realized using mode-coupling of dielectric waveguide mode to SPP mode [3]. Though, miniaturization is achieved by this approach, the phase-matching between conventional dielectric waveguide mode and SPP mode still remains a challenge, owing to high refractive index of typical waveguide core (~ 1.45) at optical frequencies. One attractive route for efficient SPP excitation is to employ the bandgap-guided of photonic crystal geometry to excite SPP modes. Due to the inherent nature of bandgap guidance mechanism, the effective mode indices of guided modes is appreciably smaller than the core indices and could be substantially tuned using suitable photonic crystal geometries, thus facilitating flexibility in the realization of phase-matching [4,5]. However, the fundamental criterion to be adopted for designing such structure for various application such as refractometer, high temperature

sensor etc depends on geometrical and material parameters of the overall wave-guiding configuration. In the present work we have proposed a temperature sensor for harsh environment. Sensing in harsh environments such as high power lasers, fire alarm systems, monitoring of furnace operation or volcanic events, requires reliable sensors at high temperature. In general, the most of the temperature sensors available in the market are based on gratings or interferometers. We report a wave -guide sensor hereafter referred as; photonic crystal surface plasmon waveguide (PCSPW) based on surface plasmon resonance (SPR) for high and accurate temperature measurement up to 800 K.

The SPR condition is given by the following expression:

$$K_0 n_p \sin \theta_{SPR} = K_0 (\epsilon_{mr} n_a^2 / (\epsilon_{mr} + n_a^2))^{1/2} \quad (1)$$

K_0 is free space wave vector.

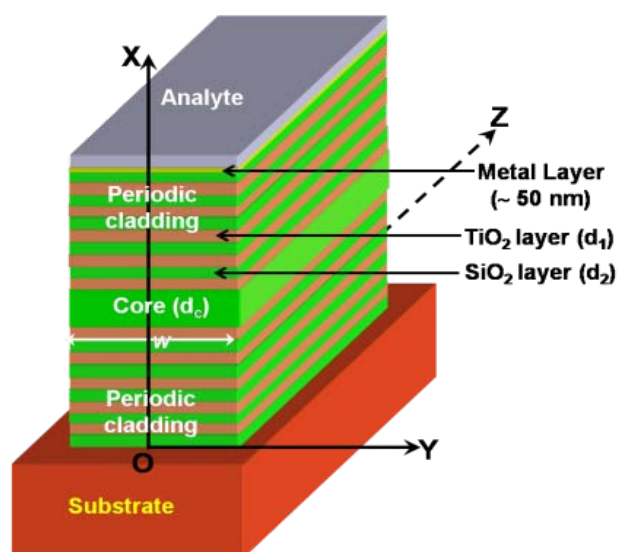


Fig. 1 Schematic of Photonic crystal surface plasmon waveguide (PCSPW) in vertical stack configuration

The term on the left hand side is the propagation constant of the p-polarized light incident at a resonance angle θ_{SPR} through the light coupling prism. The right hand side term is the real part of the SPW propagation constant. If there is change in refractive index of the sensing medium, the value of θ_{SPR} has to change in order to satisfy the resonance.

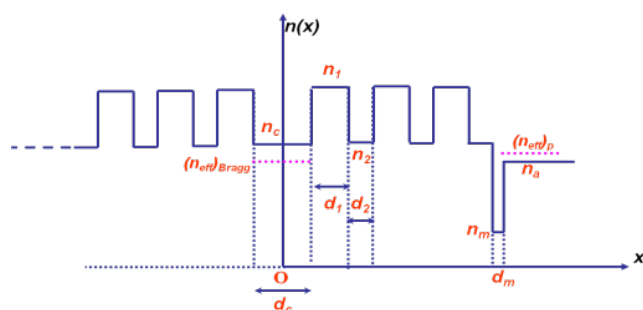


Fig. 2: Refractive index profile of PCSPW

2. PRINCIPLE OF OPERATION

The proposed SPR sensor based on 1-D photonic crystal waveguide as shown in Fig. 1, consists of vertically stacked layer of 1D-PCW and a plasmonic waveguide. The PCW essentially comprised of a silica-based PCW with core refractive index n_c symmetrically sandwiched between periodically stratified cladding (refractive index n_1 & n_2 , of thicknesses d_1 and d_2 respectively) in a vertical stack configuration. Refractive index profile of the planar counterpart is shown in fig. 2 The plasmonic metal layer (~ 50 nm thick) which can be deposited using e-beam technique, followed by an analyte layer ($n_a \approx 1.330$) is placed on top of the PCW.

Employing suitable optical equipments e.g. polarizer, microscope, etc., light from a highly stable tunable laser is launched into the core of a PCSPW which is comprised of silica-PCW followed by a plasmonic waveguide consisting of a 50 nm thick gold (Au) layer and analyte (n_a) in a vertical-stack configuration. The PCW is based on widely used lithographic and nano-fabrication compatible materials like SiO_2 and TiO_2 , such that silica core refractive index n_c and thickness d_c is symmetrically sandwiched between periodically stratified cladding ($n_1 \cdot \text{TiO}_2$ & $n_2 \cdot \text{SiO}_2$, of thicknesses d_1 and d_2 respectively). The transmitted light is measured using appropriate detector, exhibiting a minimum in the transmission spectrum at a particular wavelength; known as resonance wavelength (λ_{res}), implying resonant excitation of SPP wave at metal/analyte interface. Physically, at λ_{res} the effective index of SPP mode ($n_{sp} = \sqrt{\epsilon_m \epsilon_a / (\epsilon_m + \epsilon_a)}$; $\epsilon_m = -\epsilon_{mr} + i\epsilon_{mi}$ and ϵ_a are the dielectric constants of metal and analyte, respectively) is equal to that of the PCW mode (n_{PCW}) and hence, the power which is launched into PCW core gets

transferred to the SPP mode. It is known that λ_{res} and full width at half minima (FWHM) of the transmittance curve determines the sensitivity and accuracy of the sensor, which is highly sensitive to any change in the physical measurable parameter, such as refractive index or temperature of the ambient region. The shift ($\Delta \lambda_{res}$) in the resonance wavelength caused due to temperature change (ΔT) determines the sensitivity of temperature sensor and the accuracy of detection of λ_{res} further depends on the FWHM of the transmittance curve. Narrower the transmittance curve, higher is the sensor accuracy. Thus in order to realize a high performance sensor the product of $\Delta \lambda_{res}$ and FWHM should be as high as possible [6]. In order to quantify the characteristics of a sensor we define the performance parameters as follows.

2.1 Performance parameter of sensor

In general, the performance of a sensor is quantified in terms of two characteristics: sensitivity and detection accuracy (DA). Increasing the refractive index by Δn_a shifts the resonance wavelength by $\Delta \lambda_{res}$. Thus, the sensitivity of a sensor is defined as

$$S_n = \Delta \lambda_{res} / \Delta n_a \quad (2)$$

On the other hand, DA of a SPR sensor depends on how accurately and precisely the sensor can detect the resonance wavelength and hence, the refractive index of analyte. This accuracy of detection of λ_{res} essentially depends on the width of transmittance curve. If FWHM is full width at half minimum of transmittance curve, the DA of SPR sensor is defined as

$$DA = FWHM^{-1} \quad (3)$$

It is to be noted that, for realizing a high performance sensor both these sensor characteristics, i.e. sensitivity and DA, should be as high as possible. In the present study, we considered silica-based wave-guiding geometry as an example keeping in mind the highly matured nano-micro fabrication technology in this area. Also, the simulations are carried out by taking into account the material dispersion of all the constituents of PCSPW. In the following we obtain the thicknesses of different layers of the proposed PCSPW.

3. Design parameter of PCSPW

It is important to note that in photonic crystal based waveguides and devices the waveguidance is achieved by the bandgap guidance mechanism where the waveguide parameters, such as, core (d_c) and cladding thicknesses (d_1 and d_2), should be such that PCW mode falls within the photonic bandgap of periodic cladding region [7]. Thus, to obtain the optimum thicknesses of different layers, we first choose an

arbitrary resonance wavelength (λ_{res}) at which coupling between bandgap guided PCW mode and SPP mode is to be realized. Assuming the silica-PCW and Au/water based plasmonic waveguide to be non-interacting, we calculate the mode effective index of SPP mode ($n_{eff}SPP$) at λ_{res} , which is equal to that of PCW mode ($n_{eff}PCW$). Since at λ_{res} , $n_{eff}PCW = n_{eff}SPP$, we obtain the core thickness (d_c) and the cladding thicknesses (d_1 and d_2) using Eq. (31) and Eq. (24), respectively of Ref. [7]. Following this recipe, we choose an arbitrary $\lambda_{res} = 1.5 \mu m$ and evaluated the core and cladding thicknesses to be $d_c = 1.352 \mu m$, $d_1 = 0.1875 \mu m$ and $d_2 = 0.676 \mu m$ (the temperature and wavelength dependent refractive indices for Au, water, SiO_2 and TiO_2 are taken from Ref. [8] - [11] respectively) at room temperature. Moreover, the results presented hereafter are calculated by choosing 8 unit cells in periodic cladding, substrate refractive index $n_s = 1$ and metal thickness 50 nm.

4. RESULTS AND ANALYSIS

Further, to study the sensor performance we employed widely used coupled mode theory [12] to evaluate the transmittance through the proposed sensor. Figure 3 illustrates the transmittance through the PCW, as a function of wavelength for the proposed PCSPW at $T = 300$ and 600 K for interaction length equal to coupling length at λ_{res} . This figure shows a narrower transmission curve (FWHM = 2.2 nm and 3.8 nm at 300 and 600 K, respectively) at the lower temperature. The narrower FWHM is essentially due to weaker dispersion of SPP mode at lower temperature thereby, exhibiting high contrast in the dispersion slopes of PCW mode and SPP mode.

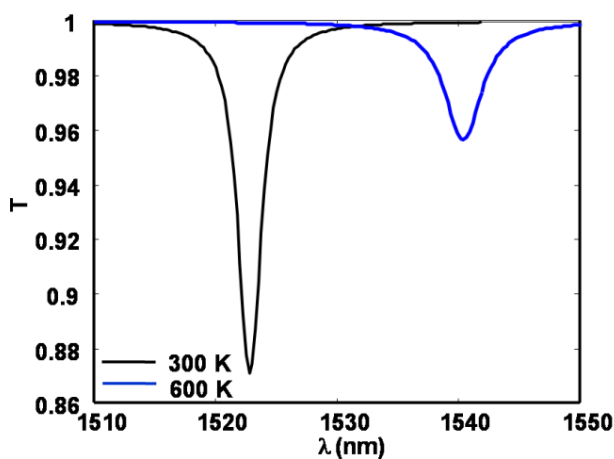


Fig. 3: Transmittance through the PCW, as a function of wavelength for the proposed PCSPW at $T = 300$ and 600 K for interaction length equal to coupling length at λ_{res}

At the resonance wavelength the modal power which is launched into the core of the PCW gets transferred

to the Au/analyte interface hence, for the illustration purpose the fig. 4 illustrates the unity-normalized magnetic field profile (H_y) of the fundamental mode of the PCSPW. It is observed that below λ_{res} the modal power which is mainly concentrated in the core of the PCW gets transferred to the Au/analyte interface beyond λ_{res} . A complimentary behavior is found for the first higher order mode (due to sake of brevity is not shown here), indicating a overall minimum transmittance at the resonance wavelength.

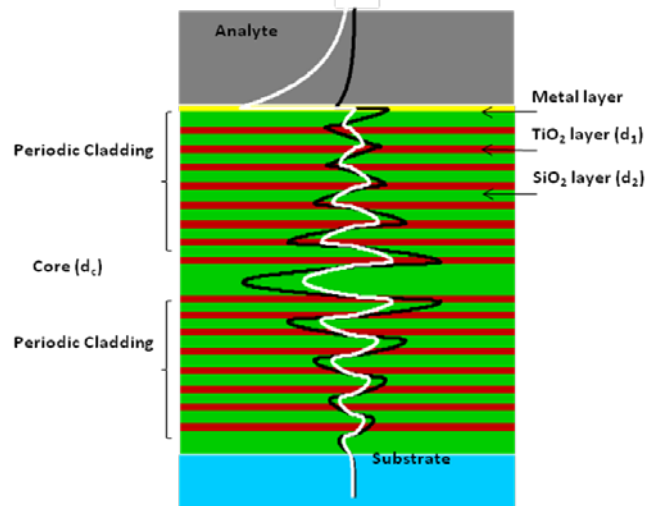


Fig. 4: The unity-normalized magnetic field profile (H_y) of the fundamental mode of the PCSPW

In order to quantify the sensor performance we obtained the variation in the resonance wavelength (λ_{res}) with respect to temperature of the ambient region as illustrated in Fig. 5

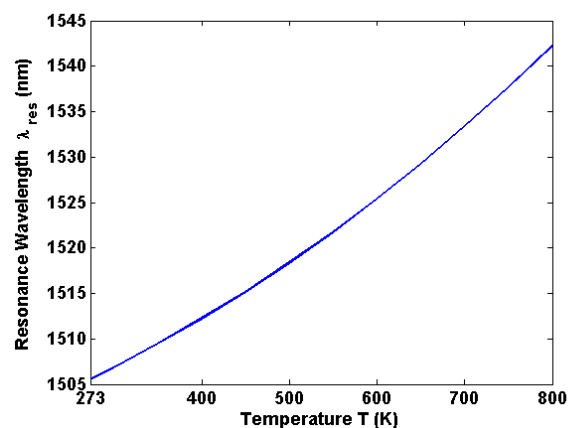


Fig. 5: Variation of resonance wavelength as a function of temperature for the proposed PCSPW.

It is to be noted that the shift in resonance wavelength (λ_{res}) increases non-linearly with temperature, exhibiting $\Delta \lambda_{res} = 35$ nm (approx) for $\Delta T = 527$ K, which results into sensitivity of 66 pm/K. The large

sensitivity is due to large shift in resonance wavelength with increase in temperature. The proposed PCSPW has been optimized for 880 K owing to the melting point of gold, which in principle may be utilized for much higher temperature measurement. Thus the findings show that the proposed sensor can be widely used in petrochemical industry control, aircraft industry, space security and control, air-conditioning control, fire detection and any harsh environment in general.

REFERENCES

- [1] E. Kretschmann *et al.*, *Z. Naturforsch.* **23A**, pp. 2135 (1968).
- [2] A. Boltasseva *et al.*, *J. Lightwave Technol.*, **23**, pp. 413 – 422 (2005).
- [3] J. Dostalek *et al.*, *Sens. Actuators B*, vol. **76**, pp. 8 (2001).
- [4] V. N. Konopsky *et al.*, *Opt. Lett.* **34**, pp. 479 (2009).
- [5] B. Gauvreau *et al.*, *Opt. Express* **15**, pp. 11413 (2007).
- [6] Rajan Jha and Anuj Sharma, *Opt. Lett.* **34**, pp. 749, (2009).
- [7] R. West and A. S. Helmy, *J. Opt. Soc. Am. B* **23**, pp. 1207, (2006).
- [8] Anuj K. Sharma and Banshi Dhar Gupta, *Appl. Opt.*, **45**, pp. 151, (2006).
- [9] P. Schiebener, J. Straub, J. M. H. Levelt Sengers and J. S. Gallaghen, *J. Phys. Chem.. Ref. Data*, **19**, (1990).
- [10] Gorachand Ghosh, Michiyuki Endo and Takashi Iwasaki, *Journ. Lightwave Technol.*, **12**, pp. 1338, (1994).
- [11] T Toyoda and M Yabe, *J. Phys. D: Appl. Phys.*, **16**, L251 (1983).
- [12] A. Yariv, *J. Quant. Electron.*, vol. QE-9, pp. 919, (1973).

A LOCALIZED SURFACE PLASMON RESONANCE BASED FIBER OPTIC HYDROGEN GAS SENSOR

S. Prabhakar, Sachin K. Srivastava, Banshi D. Gupta* and Bodh R. Mehta
Indian Institute of Technology Delhi, New Delhi, India
*bdgupta@physics.iitd.ac.in

Abstract: A fiber optic sensor utilizing the localized surface plasmon resonance of palladium (Pd) nanoparticles has been fabricated and characterized for the detection of hydrogen (H₂) gas. The sensing is based on the adsorption of H₂ by Pd, which changes the refractive index of nanoparticle, resulting in a change in absorption. The LSPR spectra were obtained for 100% nitrogen as well as a mixture of 4% hydrogen and 96% nitrogen. The present sensor has very small response time and reusable after desorption of H₂.

1. INTRODUCTION

There is an increasing demand of research and development for the use of hydrogen as one of the next generation energy sources, which are clean and renewable and can easily reduce our dependence on fossil fuels [1]. Hydrogen gas (H₂), being the smallest in atomic size, can migrate easily and change the surface properties of the host material. This gas is highly combustible and has a lower explosive limit of 4.65% at room temperature and pressure. Since it is the lightest element and explosive too, one of the main challenges of its usage is to overcome its leakage and rapid and accurate detection of leakage, if any. Hence due to security issues, very fast, accurate and reliable sensors are needed for immediate detection of any leakage of hydrogen, otherwise it may cause explosions, if lower explosion limit is reached. There are certain metals which have the uncommon ability to absorb up to 900 times its own volume of hydrogen at room temperature [2, 3]. Many research groups have used palladium (Pd) for hydrogen gas sensing [1-6].

Localized surface plasmons (LSPs) are the quanta of charge density oscillations in metal nanoparticles and they get resonantly excited when the wavelength of the incident light is equal to the characteristic wavelength of the metal nanoparticle, determined by the LSPR extinction condition [7]. At the resonance, the metal nanoparticles show a strong absorption. The resonance wavelength as well as absorbance is highly dependent on the shape and size of the nanoparticle in addition to the refractive index of the surrounding medium [8]. Thus, unlike surface plasmon resonance (SPR), LSPR does not require a phase matching technique for excitation. The collaboration of metallic nanoparticles with optical fiber makes the sensor very cheap and compact. Recently, we have theoretically modeled a fiber optic SPR sensor utilizing metal nanoparticles. It has been shown that the LSPR based fiber optic sensor with intensity modulation scheme along with a light emitting diode as a light source has many advantages such as wide sensing range, low cost, and miniaturization [9]. The plasmon resonances of metal

nanoparticles are primarily characterized by extinction cross-section. The extinction cross section of a nano-sized metal particle is derived by using Mie theory under quasi-static approximation [8]. It primarily depends upon the shape and size of the metal nanoparticle and the refractive index of the surrounding medium. The extinction cross section of a spherical metal nanoparticle of radius R is calculated under dipole approximation and is given by [8]

$$C_{ext}(\omega, R) = \frac{\omega}{c} \frac{12\pi R^3 \epsilon_m^{3/2} \epsilon_2(\omega, R)}{[(\epsilon_1(\omega, R) + 2\epsilon_m)^2 + \epsilon_2^2(\omega, R)]} \quad (1)$$

where ϵ_m is the dielectric constant of the surrounding medium, given by $\epsilon_m = n^2$, n being the refractive index of the surrounding medium, c is the speed of light in vacuum, and ϵ_1 and ϵ_2 are the real and imaginary parts of the metal nanoparticle dielectric functions, respectively. The resonance occurs when ϵ_1 becomes equal to $-2\epsilon_m$.

In the present paper, we have fabricated and characterized a LSPR based fiber optic sensor utilizing palladium (Pd) nanoparticles. Pd has widely been used in sensing of hydrogen (H₂) gas. The present sensing scheme is different from other LSPR sensors, in which the sensing is based on the refractive index change of the sensing medium around the nanoparticle. In present sensor, it is the refractive index (real and imaginary parts of the metal dielectric functions) of the nanoparticle itself which gets changed due to adsorption of H₂ gas.

2. EXPERIMENTAL

A schematic of the fabricated sensor is shown in figure 1.

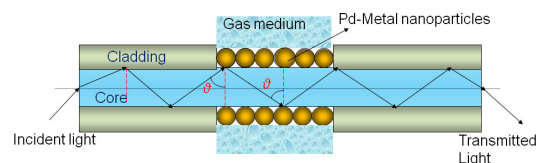


Fig.1 Schematic of the proposed fiber optic probe

One cm. cladding was removed from the middle of a plastic clad silica optical fiber of 600 μm core diameter and 0.37 numerical aperture. The unclad portion of the fiber was then cleaned with acetone before it was coated with spherical Pd nanoparticles. The coating was performed in a vacuum chamber having the facility of thermal evaporation technique. A schematic of the coating unit chamber is shown in figure 2. The principle of vacuum deposition technique is based on the fact that solid materials get vaporized when heated to a sufficiently high temperature and thin film forms by recondensing it on a cooler substrate. In the resistively heated thermal evaporation technique, a charge of the material to be evaporated is placed in a container (usually in shape of basket, boat or crucible), which has a finite electrical resistance. The heating is carried out by passing a high current (10-100A) through a filament container (usually in shape of basket, boat or crucible), which has a finite electrical resistance. An electric resistance heater heats this charge after the chamber has been evacuated to about 10^{-6} Torr. As the temperature of the charge rises, its vapour pressure rises and a significant evaporation rate develops. The evaporant then condenses on the cooler substrate. We have used indirect heating of the charge in which, the heating element does not come into direct contact with the coating material. The evaporation source relies on resistive heating of the thin folded strip (boat) of tungsten which holds a small amount of charge (coating material).

Good vacuum is a prerequisite for producing contamination free deposits and hence one should start deposition only when there is good vacuum. Once the metal is evaporated, its vapour undergoes collisions with the surrounding gas molecules inside the evaporation chamber. As a result a fraction is scattered within a given distance during their transfer through ambient gas. The mean free path of air at 25°C is approximately 45 and 4500 cm at pressure of 10^{-4} and 10^{-6} Torr respectively. Therefore, pressures lower than 1 Torr are necessary to ensure a straight line path for most of the evaporated species and for substrate to source distance of approximately 10 to 50 cm in a vacuum chamber. A quartz crystal oscillator measures the mass of a deposit as a function of time. The mass of material that deposits on the crystal changes its resonant frequency. This change in the resonant frequency is sensed by the electronic package and is converted to a display of deposition rate and coating thickness.

Prior to deposition, the growth chamber has been evacuated to 10^{-6} Torr. And repeated argon purging was carried out to minimize the oxygen concentration in the growth chamber. High deposition pressure (10^{-4} – 10^{-3} Torr of Ar), low substrate temperature ($T_s = 30^{\circ}\text{C}$, and high flow rate of Argon (FR= 20 SCCM) (SCCM denotes cubic

centimeter per minute at STP) resulted in the formation of Pd nanoparticles. High pressure results the Lower average size of nanoparticles and Low Pressure Broad size distribution.[35] AFM results have shown (fig 6.14) for the mean particles size distribution of the nanoparticle structures given below. Through the AFM sectional analysis we came to know the average size of the nanostructures deposited is 15 nm approximately.

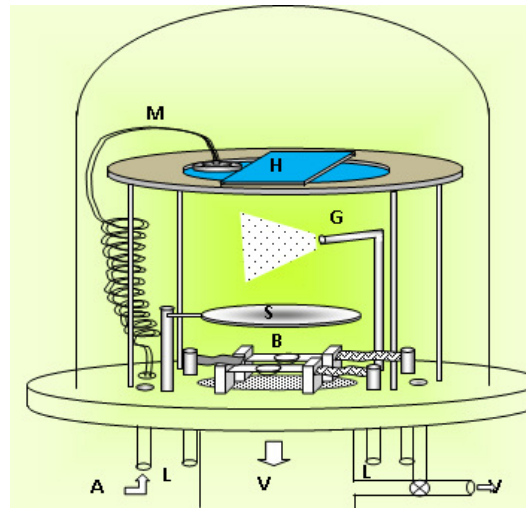


Fig. 2 Schematic diagram of inert-gas evaporation set up (B: dual boat arrangement, S: shutter, G: inert gas inlet, H: substrate holder, M: thickness monitor, A: air-inlet valve, L: LT connections, V: to vacuum pumps).

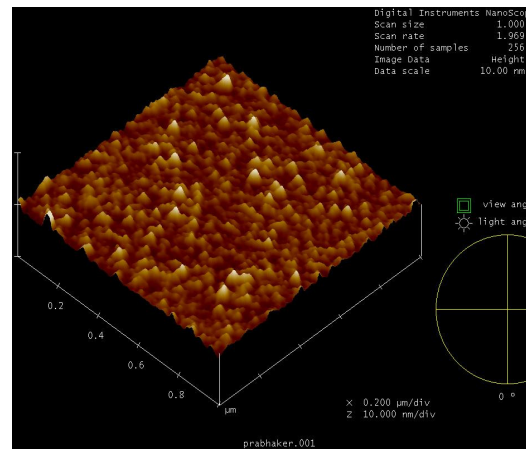


Fig. 3 Atomic force microscopic (AFM) micrograph of the Pd nanoparticle film coated on optical fiber

After the sensor was fabricated, it was fixed in a gas flow cell. The flow-cell has facilities of inlet and outlet of gas. The design and components of the flow-cell are so prepared that it is fully leak proof. The gas supply cylinders consist of 100% nitrogen and 4% hydrogen in 96% nitrogen. These cylinders

were connected to gas chamber using steel piping and these can be used separately using shut-off valves. A schematic of the experimental setup is shown in figure 4.

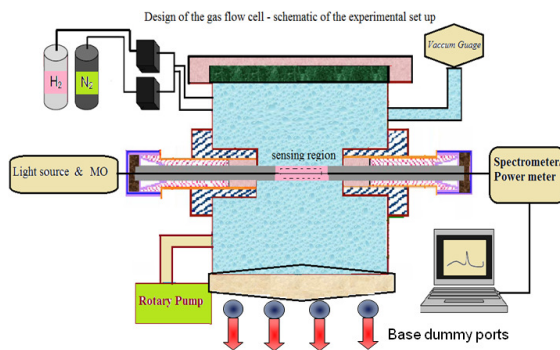


Fig.4 Schematic diagram of the experimental setup

Light was launched from one end of the fiber with the help of a microscope objective and a three dimensional translation stage. It propagates by the phenomenon of total internal reflection (TIR) at the core-cladding interface. The evanescent field of the guided ray interacts with the metal nanoparticles, which results in the wavelength dependent absorption. The absorption spectrum is determined from the spectral analysis of transmitted power recorded at the output end of the sensing probe. The wavelength corresponding to peak absorption (λ_{res}) in the absorption spectrum depends on the refractive index of the medium surrounding the nanoparticles and the refractive index of the metal nanoparticle.

3. RESULTS AND DISCUSSION

Figure 5 shows the LSPR spectra of the present sensor for N_2 and H_2 gases. The chamber is filled with N_2 gas and the corresponding transmitted LSPR spectrum is recorded. The chamber is then evacuated with the help of a rotary pump, filled with H_2 and the corresponding absorbance spectrum is recorded.

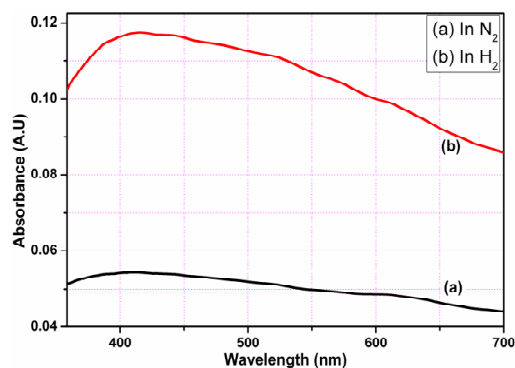


Fig. 5 LSPR spectra for N_2 and H_2 gas

It is observed from the figure that for both the gases, a peak is observed in the absorbance spectrum. This

peak in the LSPR spectrum is a characteristic of the gas. The refractive indices of the two gases (N_2 and N_2+H_2 mixture) are almost the same. Hence the shift in the resonance wavelength is negligible. There is, however, a change in absorbance with the introduction of the H_2 gas in the flow cell. The reason behind this change is understood as follows: when hydrogen comes in contact to the Pd nanoparticles, it gets adsorbed. Due to the adsorption of H_2 , the refractive index of the nanoparticle changes. This change in refractive index of the nanoparticle leads to a change in the evanescent absorbance of the nanoparticle. The reusability of the sensor must be checked, as a natural question arises that after H_2 is adsorbed in the Pd nanoparticle, will it respond the same. To check the reusability and response time of the sensor, we have plotted the variation of transmitted power with time by repeating the introduction and vent of the both the gases.

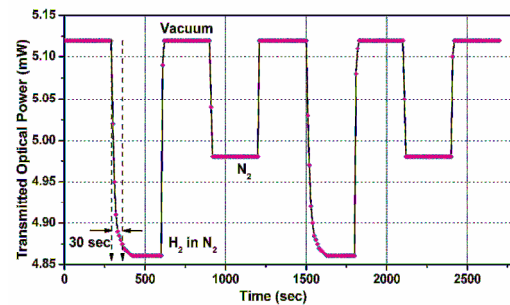


Fig.6 Variation of transmitted power with time

After the gas mixture was flushed out of the gas chamber, the same spectrum was regained. Figure 2 shows the time response of the sensor. It is clearly observed that the sensor takes only 30 seconds to reach a stable response and the transmitted power remains constant. This means that the absorption of H_2 by Pd is complete within 30 seconds. While in case of N_2 the transmitted power stabilized immediately. The transmitted power for the three cases, vacuum, N_2 gas and H_2 remains the same for a number of repeated observations. This confirms the repeatability and reproducibility of the sensor response.

4. CONCLUSIONS

We have fabricated and characterized a LSPR based fiber optic hydrogen gas sensor. The adsorption of hydrogen by Pd nanoparticles leads to a change in the absorbance. The response time of the sensor is 30 seconds and it can be reused after flushing hydrogen gas out of the flow cell. Other advantageous features of the sensor have been discussed throughout the article.

ACKNOWLEDGEMENTS

Sachin K. Srivastava is thankful to the CSIR for research fellowships. The present work was partially supported by the DST, India.

REFERENCES

- [1] Chadwick, B., Tann, J., Brungs, M. And Gal, M., "A hydrogen sensor based on the optical generation of surface plasmons in a palladium alloy," *Sens. Act. B* 17, 215-220 (1994).
- [2] Bevenot, X., Trouillet, A., Veillas, C., Gagnaire, H. And Clement, M., "Hydrogen leak detection using an optical fibre sensor for aerospace applications," *Sens. Act. B* 67, 57-67 (2000).
- [3] Zalvidea, D., Diez, A., Cruz, J. L. and Andres, M. V., "Hydrogen sensor based on a palladium-coated fibre-taper with improved time response," *Sens. Act. B* 114, 268-274 (2006).
- [4] Sutapun, B., Tabib-Azar, M. And Kazemi, A., "Pd-coated elastooptic fiber bragg grating sensors for multiplexed hydrogen sensing," *Sens. Act. B* 60, 27-34 (1999).
- [5] Kim, K. T., Song, H. S., Mah, J. P., Hong, K. B., Im, K., Baik, S. J. and Yoon, Y., "Hydrogen sensor based on palladium coated side-polished single-mode fiber," *IEEE Sens. Journal* 7, 1767-1770 (2007).
- [6] Butler, M. A., "Micromirror optical-fiber hydrogen sensors," *Sens. Act. B* 22, 155-163 (1994).
- [7] E. Hutter and J. H. Fendler, "Exploitation of Localized Surface Plasmon Resonance," *Advanced Materials* 16, 1685-1706 (2004).
- [8] P. Mulvaney, "Surface Plasmon Spectroscopy of Nanosized Metal Particles," *Langmuir* 12, 788-800 (1996).
- [9] S. K. Srivastava, R. K. Verma, and B. D. Gupta, "Theoretical modeling of a localized surface plasmon resonance based intensity modulated fiber optic refractive index sensor," *Appl. Opt.* 48, 3796 (2009).

ADAPTIVE OPTICS IN IMAGING AND VISION SCIENCE

A.R.Ganesan
Department of Physics
Indian Institute of Technology Madras
Chennai 600036, INDIA
arg@iitm.ac.in

Abstract: Adaptive Optics is a technology which provides a correction mechanism to wavefront aberrations, which in turn improves the image quality. The paper discusses the development of an indigenous wavefront measurement and compensation system, as well as the new methodologies developed. The application of this in Vision Science is also presented, along with experimental results.

1. INTRODUCTION

Adaptive Optics (AO) is an emerging branch of Optics wherein the optics modifies itself to changing environmental conditions to provide high resolution imagery [1,2]. Adaptive Optics concepts started with astronomical imaging with a view to compensate for the image degradation caused due to the atmospheric distortion of light from a far-off object with ground-based telescopes. With the new generation of Very Large Telescopes entering into operation, the role of AO system is extremely important. The applications of Adaptive Optics range from Astronomical imaging to laser beam steering in free space satellite optical communication, high resolution imaging of the retina of the human eye, etc.

A typical AO system includes a Wavefront sensor, a deformable mirror, tip-tilt mirror and the control computer unit which significantly improves the imaging performance. In this paper, we report the design and development of an indigenous Shack-Hartmann Wavefront Sensor, which can measure wavefront phase profiles in real-time. Wavefront measurements upto 4th order Zernike polynomials have been carried out. The system can measure wavefront tilts to an accuracy of 19 μ rad. and surface profiles down to $\lambda/50$. Also, a dynamic closed loop system, which does phase compensation for global as well as local tilts has been established. Experimental results of wavefront measurements and compensation are presented. Further, the indigenous wavefront sensor was used to measure the higher order aberrations of the human eye, whose results are also presented.

2. WAVEFRONT SENSING

Wavefront sensing is the measurement of the phase of the propagating light beam. Shack-Hartmann wavefront sensing is the most commonly used method for AO, since it is a non-interferometric way, escaping the constraints of vibration isolation and monochromatic source requirement. Noise properties of this sensor are well determined [3].

The Shack-Hartmann wavefront sensor basically consists of a micro-lenslet array that spatially samples the incoming wavefront and focuses it into an array of spots, each corresponding to the sub-aperture sampled. These light spot patterns are recorded by a CCD camera and then processed by image processing algorithms. The centroids of sub-aperture images formed by each lens of lenslet are determined as a set of $\{x, y\}$ spot positions.

The centroid position formulae are expressed as [1],

$$X_c(K) = \frac{\sum_{i=1}^I \sum_{j=1}^J x(i, j) s(i, j)}{\sum_{i=1}^I \sum_{j=1}^J s(i, j)} \quad (1)$$

$$Y_c(K) = \frac{\sum_{i=1}^I \sum_{j=1}^J y(i, j) s(i, j)}{\sum_{i=1}^I \sum_{j=1}^J s(i, j)} \quad (2)$$

where $x(i,j)$ and $y(i,j)$ is the co-ordinate position of the (i,j) th pixel in the k^{th} sub aperture, $s(i,j)$ is the input wavefront signal of the (i,j) pixel on the square sub-aperture that has $I \times J$ pixels. With the formulae, the centroid position of the input wavefront at the K^{th} sub aperture could be calculated as $(X_c(K), Y_c(K))$. When there is a wavefront distortion, the positions of the spot-centres are changed. The displacement of the spot center x_{ij}^c, y_{ij}^c within the sub-aperture with respect to a reference position x_{ij}^r, y_{ij}^r is measured and the local gradient of the wave-front $\Phi(x,y)$ is obtained according to

$$\partial\phi/\partial x = S_x/f \quad (3)$$

$$\partial\phi/\partial y = S_y/f \quad (4)$$

where $S_x = x^c - x^r$, $S_y = y^c - y^r$, and f is the focal length of the lenslet.

From the slope values of each sub-aperture, the wavefront reconstruction is performed using the relation,

$$S=Aa \quad (5)$$

where A is the gradient rectangular matrix with M columns and $2N_xN_y$ rows. N_x, N_y are the number of focal spots along x direction y direction respectively. As a result we obtain Zernike coefficients:

$$a=B \cdot S \quad (6)$$

where , $B=(A^T A)^{-1} A^T$.

Now, when Zernike coefficients are obtained, a map of the surface is created in a number of equally spaced points, and displayed on the screen. All the measured Zernike coefficients have a clear physical sense like tilt, focus, astigmatism, coma, spherical aberration. From the Zernike phase map, the RMS and peak-to-valley (P-V) can be estimated [4]. The trade off between the number of lenslets, their pitch and focal length have been discussed well [5].

3. WAVEFRONT SENSOR SETUP

The schematic of the developed WFS layout is shown in figure 1. The system consists of a He-Ne laser source with collimating optics for providing reference plane wavefront and it is spatially sampled by the microlens array. The shutters S1 and S2 are used to select one of the beams (reference or test). To begin with, the shutter S1 is open and S2 is kept closed. The well-collimated plane wavefront from the He-Ne laser now gets focused as a set of spots on the CCD array. The centroids of these spots are taken as reference co-ordinates and stored as the values for a zero tilt beam. Once this is done, S1 is closed and S2 is opened which allows the external test beam for wavefront measurement. The shutters S1 and S2 are fitted on stepper motors and automatically controlled by the Wavefront Sensing software. The new positions of the centroids are then estimated. By measuring the positional shift of the centroids with respect to the reference data, the local tilt or slope of the sub-aperture wavefronts are calculated.

4. WAVEFRONT RECONSTRUCTION

From these slope or gradient measurements, the wavefront profile is obtained through wavefront reconstruction algorithms [6,7]. We have used linear integration (Southwell method) for phase reconstruction, and Zernike decomposition to estimate the required phase compensation for global as well as local tilts. The Southwell reconstructor is a Zonal technique while, the Zernike is Modal reconstructor. We have carried out Zernike terms estimation up to the 4th order (i.e. Z_0 to Z_{14}).

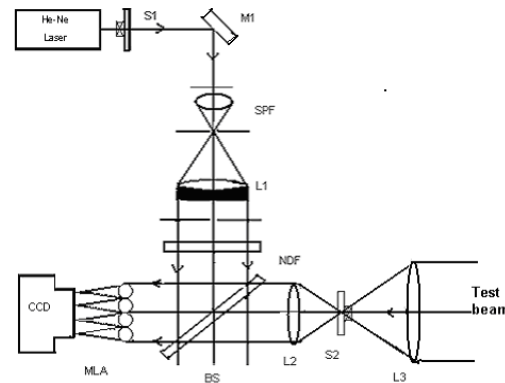


Figure 1 Schematic of the Optical Setup S1,S2 micro controlled stepper motor shutters, M1 –Mirror, L1,L2,L3, - lenses, SPF-Spatial Filter, NDF-Neutral density filter, BS-Beam splitter, MLA-Microlens Array.

5. RESULTS AND DISCUSSION

In the WFS developed by us, a microlens array of 417 μm pitch and 45 mm focal length was used for spatial sampling of the wavefront. A 1/2" monochrome CCD camera (Hitachi KP-M2E) was used for imaging the Hartmann spots. The image data acquisition was done using a general purpose PCVISON frame grabber from Coreco Imaging Inc. Custom made software was developed for processing a 10x10 sampling of the wavefront and other functions. The wavefront sensing and mapping worked at 25 frames per second with a P-IV computer having a 1.6 GHz processor. Wavefront tilt measurements up to 1.9 μ radians and phase profiles up to $\lambda/50$ accuracy have been achieved.

5.1 Tip tilt compensation for Laser beam steering:

The Global tilt correction for laser beam steering was carried out at the laboratory level in a closed loop fashion by driving a tip-tilt mirror using the wavefront sensor data. The optical setup of Fig.2(a) was used for this study. A test beam from a second laser was reflected off two tilt mirrors and made to enter the Wavefront Sensor. The first tilt mirror was used to introduce a tilt. This tilt was measured by the WFS computer, which drives the second tilt mirror for compensating the same. The tilt was introduced by a two axis tilt-mirror (from Piezo-Jena, Germany) having a tilt range of 2 milliradians corresponding to 0-10 V driving voltage. The tilt compensation signals for driving the tilt mirror control unit were generated using a DT 332 D/A converter card from Data Translation Inc. The tilt correction of the laser beam was carried out through another two axis tilt mirror (from Madcity Inc.) which had a resolution of 0.02 microradians. The tilt compensator receives the compensation signal from the WFS computer and nullifies the tilt using adaptive control algorithms. Fig. 2(b) shows the

wavefront profile when a known tilt of 240 μ rad was introduced in both X and Y directions. The compensation of the tilt along both axes could be visualized in Fig. 2(c) when the tilt compensator was activated.

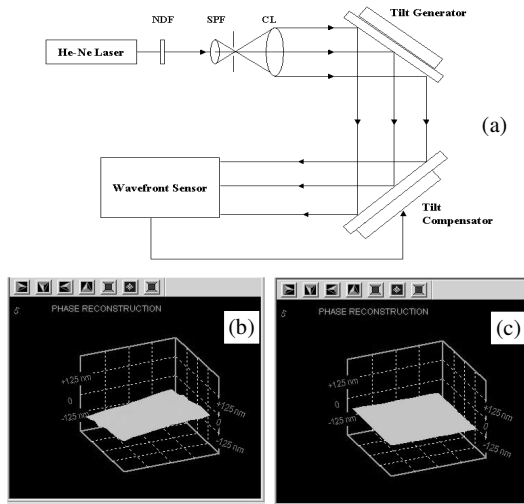


Figure 2 (a) Schematic of closed loop tip-tilt correction (b) 2-axis 240 micro rad tilt and (c) corrected wavefront

5.2 Deformable mirror control

Phase compensation for local phase variations was carried out by fitting the Wavefront sensor data to control a deformable mirror. The experimental setup of Fig.2(a) was used, by replacing the tilt compensating mirror with a deformable mirror. We used a 37-Channel Micro-machined deformable mirror (from OKO Technologies Inc.) for our phase compensation studies. To verify the system performance, a known static aberration (measured using a conventional interferometer) was introduced in the test beam path. The wavefront correction estimated using our Shack-Hartmann sensor values were used to provide the drive signal to 19 electrodes through control driver for real time phase compensation. From the slope values and the actuator spacing distance, we developed an influence matrix for actuator control voltage, which mapped the entire slope values into a central region of 12mm on the deformable mirror. Both direct digital control from slope values as well as modal control were performed for static and dynamic correction. Figure.3(a) shows the wavefront when a static aberration was introduced in the optical path of the beam, while Fig.3(b) shows the aberration compensated wavefront using the deformable mirror.

In our present system, wavefront measurement and display works at 90 frames per second with fast camera and high speed processors. We have also incorporated wavelet based methods for centroid estimation. A closed loop system of 100 Hz is currently being envisaged.

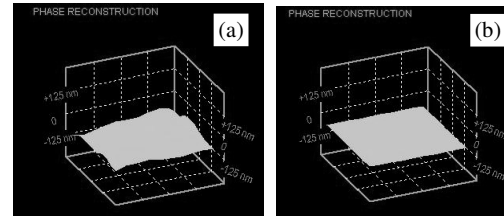


Figure 3 Wavefront Phase maps (a) before and (b) after correction

6. ABERRATION MEASUREMENT IN HUMAN EYES

The aberrations of human eye have been one of the areas of interest. It is well known that aberrations hinder image quality and the aberrations increase with the increase in age. The lower order aberrations namely, defocus and astigmatism could be measured with ophthalmic slit-lamps and corrected with spectacles or contact lenses. But these contribute only to about 92% of aberration content. The remaining 8% of the aberrations is due to higher order aberrations such as coma, spherical, trefoil etc. which cannot be measured with traditional methods. This needs the use of a wavefront sensor [8]. We have used our indigenous Shack-Hartmann Wavefront Sensor for measurement of these higher order aberrations in a batch of young adults between ages of 20 and 30 years [9].

6.1 Experimental method

The Experimental arrangement is as shown in Fig. 4. Collimated beam from a 2mW, 632.8 nm, He-Ne laser is allowed through variable beam splitter and neutral density filter to the eye. The beam reflected to the eye subtends an angle approximately 0.3' of arc at the retina. The illumination on the retina was kept at 3-5 μ W, which is far below than the permissible exposure level prescribed by ANSI [10].

The light reflected from retina is transmitted on to the lenslet array by the beam splitter. The 2D Lenslet image the array of focused spots onto a CCD chip. We have used two afocal lens systems to image the wavefront from pupil plane to the lenslet array (L2&L3, L4&L5). An Iris introduced at the focal point of each afocal system to filter the unwanted reflections. The Sensor estimates the wavefront aberration with reference to a perfect plane wave at eye's entrance pupil.

6.2 Results of Ocular aberration study

We estimated the aberration of human eye for a group of young University students of age group 20 to 30 years. There were 20 subjects, all of whom had normal vision (6/6). Their acuity was tested with Snellen chart prior to the investigation. Subjects

were dilated with 1% Tropicamide eye drops. Zernike coefficients upto fourth order was calculated. First 15 values of Zernike modes are enough to represent sufficiently higher order aberrations.

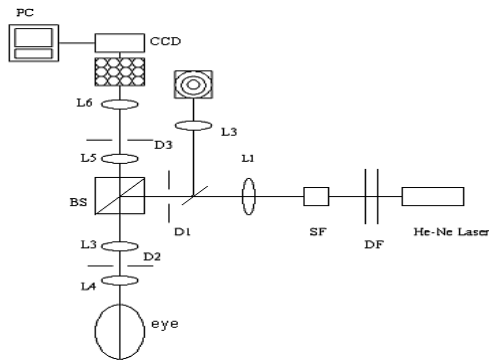


Figure 4. Setup for aberration measurement of human eye

It is found that defocus and astigmatism are the dominant factor in contributing to nearly 92% of the aberrations. We calculated the RMS error corresponding to the Lower order (i.e., first and second) and from third- through the higher –orders [11]. The total aberrations increased with defocus, specifically myopia. The plot between RMS error and age shows the trend, an increase of aberrations with age, a positive correlation, as shown in Fig.5. It was also found that the higher order aberrations increase with the increase of pupil size as shown by the decrease in Strehl ratio depicted in Fig. 6.

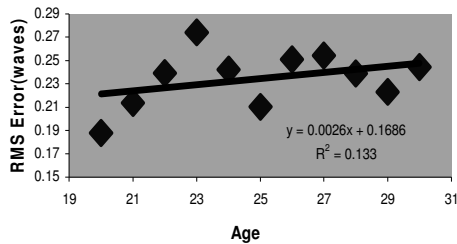


Figure 5. Plot of RMS error in the age group of 20 to 30 years

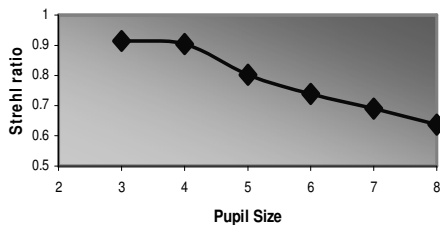


Figure 6. Plot showing the Strehl Ratio decreasing with increase of pupil size meaning that the higher order aberration increases

7. CONCLUSION

The design and development of a closed loop Adaptive Optics system for wavefront sensing and

control has been presented. This low-cost system has been developed with commonly available optical and electronic systems. The system could be used for static and dynamic correction for a 10 cm telescope system for imaging applications in visible region with a resolution of $\alpha_n=1.342$ arc sec seeing conditions. The use of the Shack-Hartmann Wavefront sensor for the measurement of higher order aberrations of the human eye has been demonstrated. This kind of study will help clinicians in surgical evaluation and also forms an analysis tool for the visual aberration measurement and correction methodology.

ACKNOWLEDGEMENT

This work was carried out under a funding by DRDO, India.

REFERENCES

- [1] R. R. Parenti, "Recent Advances in Adaptive Optics methods and Technology", *Proc.SPIE - Laser Wavefront Control*, **1000**,101-108 (1988).
- [2] R. K. Tyson, "Adaptive Optics Engineering Hand Book", Marcel Dekker Inc., New York (2000)
- [3] "Hartmann Wavefront Analyzer Tutorial", by *Spiricon Inc*, (2001).
- [4] J.Y.Wang and D.E.Silva, "Wavefront interpretation with Zernike Polynomials", *Applied Optics*, **19** (9), 1510-1517 (1980)
- [5] A.R. Ganesan, P. Arulmozhivarman, D. Mohan, Ashok Kumar and A.K. Gupta, "Design and development of a closed loop Adaptive Optics system for wavefront sensing and control", *J. Opt. Soc. India*, **34**, 67-81 (2005)
- [6] R.J. Noll, "Phase estimation from slope-type Wavefront Sensors", *J. Opt. Soc. Am*, **68**(1), 139-140 (1978).
- [7] W.H. Southwell," Wavefront estimation from wavefront slope measurements", *J. Opt. Soc. Am.*, **70**, 998-1006 (1980).
- [8] J. Liang, B. Grimm, S. Goelz and J.F. Bille, "Objective measurement of wave aberrations of the Human eye with the use of Hartmann – Shack Wavefront sensor," *JOSA A*, **11**, 1949-1957 (1994).
- [9] M. Jesson, P. Arulmozhivarman and A.R. Ganesan, "Higher Order Aberrations of the Human eye in Indian Young Population" *Asian Journal of Ophthalmology*, **6** (2) 10-16 (2004)
- [10] ANSI, American National Standard for the safe use of Lasers, *ANSI Z136.1-1993* (Laser Institute of America, Orlando, FL, 1993).
- [11] M. Jesson and A.R. Ganesan, "Analysis of Refractive Errors in the eyes of Young Indians", *J. Mod. Opt.*, **54**, 1349-59 (2007)

OPTICAL LITHOGRAPHY FOR NANO-STRUCTURAL PATTERNING: RESOLUTION ENHANCEMENT TECHNIQUES

Samit Barai

Computational Lithography Division, Semiconductor Research and Development Center, IBM, Manyata Tech
Park, Nagawara, Bangalore, India 560045

E-mail: sambarai@in.ibm.com

Abstract: Over the past decade resolution enhancement techniques have become an essential component of lithography process in semiconductor integrated circuit manufacturing. The lithography community is continuously working towards meeting the expected resolution improvement in a given timeline. The difference between the required image resolution and what available optical hardware can offer is ever widening. In order to bridge this gap various computation-assisted resolution enhancement techniques (RET) have successfully been implemented in past few years and the term “computational lithography” been coined. Some of the most widely used RETs are- off-axis illumination, phase-shifted mask, double patterning, optical proximity correction (OPC), source mask co-optimization and inverse lithography. A theoretical as well as industrial perspective of some of these promising resolution enhancement techniques for 22nm and 14nm node is presented.

1. INTRODUCTION

Ever since the inception, the semiconductor industry is moving towards lower technology nodes in order to fulfill the continuous demand of high performance integrated circuits. The integrated circuits are realized using a wide range of highly accurate physical and chemical processes. One of the important steps in the manufacturing flow is the process of creating three-dimensional relief structures on the substrate corresponding to a design aperture (also known as mask). This process is known as lithography and the most favorite variant of it is optical projection lithography. The resolution capacity of projection optical imaging system can be defined by the Rayleigh criterion [1]

$$\text{Minimum Feature} = k_1 \frac{\lambda}{NA} \quad (1)$$

Similarly, the depth of focus is given by

$$\text{Depth of focus} = k_1 \frac{\lambda}{NA^2} \quad (2)$$

here, λ is the wavelength of the optical source, NA is the numerical aperture of the imaging system and k_1 is the reduction factor. An obvious choice to enhance the resolution is reducing the wavelength or increasing numerical aperture (NA) of the imaging system. However, optical lenses for wavelength below 193nm have serious manufacturing challenges and yet not mature enough for industrial applications. On the other hand with the invention of immersion lithography, NA is very close to its physical limit. Moreover, increased NA causes a lower depth of focus resulting in a tight tolerance for the lens. Therefore, over the past several years there has been a strong drive to find other alternatives to reduce the minimum feature while retaining good depth of focus. A number of computation-assisted resolution

enhancement techniques (RET) have successfully been implemented in past few years. Some of the most widely used RETs are- off-axis illumination, phase-shifted mask, double patterning, optical proximity correction (OPC), source mask co-optimization and inverse lithography. Some of these techniques involve rigorous analysis encompassing branches of imaging theory, optimization techniques and high performance computing. There are efforts from both optical and resist development community to improve the print performance. The improvement in resolution using optical component may involve manipulating and optimizing angle of illumination, phase of light and modifying the aperture design using wave-front engineering.

2. IMAGE FORMATION IN PROJECTION LITHOGRAPHY

The aerial image intensity at the wafer plan in the projection optical lithography system can be described by the Hopkins partial coherent imaging model [1]

$$I(x) = \iint u(x')u^*(x'')K(x-x')K^*(x-x'')T(x'-x'')dx'dx'' \quad (3)$$

Here, $I(x)$ is the image intensity at location x in the wafer plane, $u(x')$ is the intensity of the input image at u' , K is the impulse response of the imaging system and T is the mutual intensity of the illumination system. The mutual intensity function is used to account for the coherence characteristics of the extended source of the projection system. For a point source the mutual intensity function is given by $T=1$, whereas for infinitely extended source the mutual intensity function is given by Dirac delta function. However, the lithography system is partially coherent and falls between coherent and incoherent systems. To calculate the aerial image in partially coherent

systems we define

$$W(\xi, \xi') = K(\xi)K^*(\xi')T(\xi' - \xi) \quad (4)$$

using Eq. 3 and Eq. 4

$$I(x) = \iint u(x')W(x - x', x - x'')u^*(x'')dx' dx'' \quad (5)$$

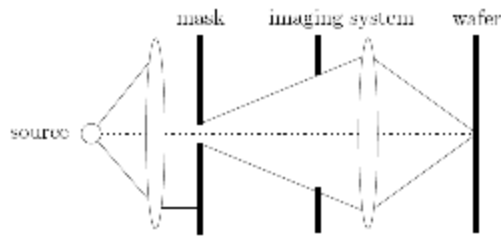


Figure 1. Schematic diagram of projection optical lithography system

In practice, the image calculations are carried out at discrete points at the wafer plane. One can speed up the calculations multiple folds by approximating W with a corresponding low rank matrix [2]. This can be done by expressing W by a series expansion over a set of eigenvector basis as

$$W(\xi, \xi') = \sum_{k=1}^r \lambda_k \psi_k(\xi) \psi_k^*(\xi') \quad (6)$$

Here, first r significant eigenvalues and corresponding eigenvectors are used in the series expansion. Further, scaling the eigenvectors as $\phi_k = \sqrt{\lambda_k} \psi_k$, the intensity can now be written as

$$I(x) = \sum |\phi_k * u(x)|^2 \quad (7)$$

The basis ϕ_k 's can be thought of as different coherent system responses and the intensity as incoherent summation of these coherent responses of the system. This approximation has significant implications when used to calculate aerial images on full chip designs which typically have billions of edges. The basis functions or the set of coherent point spread functions can be calculated and stored beforehand, aerial image calculation is then done easily by convolving the design with the basis functions and adding all the resulting responses incoherently.

3. BASIC RESOLUTION ENHANCEMENT TECHNIQUES

The aerial image at the wafer plan is essentially a superposition of various diffracted waves from the mask. The amplitudes, phases and directions of these waves can be engineered to enhance the print performance.

3.1 Amplitude optimization

The simplest and most common method of manipulating the amplitude of diffracted orders is to manipulate the design in such a way that the overall contrast of the image improves. This technique is known as optical proximity correction (OPC) [2]. Figure 2 shows an example of correction in the mask shape

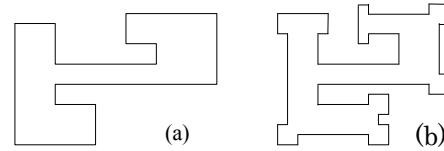


Figure 2. (a) Input design, (b) Post OPC shape

The basic idea is to retain as much diffraction orders as we can from the edges of the design. Typically, a predictive model is used to estimate the print image for a given mask shape and iteratively edges are manipulated in a way that the print image is as close as possible to a given target. Other important techniques in OPC are the use of sub-resolution assist patterns. These patterns are so small that they do not print on wafer but help manipulate the diffraction orders in a way that the resolution and depth of focus improve significantly [3].

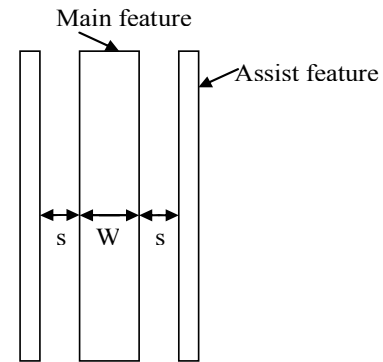


Figure 3. Sub-resolution assist patterns

3.2 Direction optimization

The resolution can be improved by a factor of two using off-axis illumination compared to conventional illumination. It is clear from the Fig. 4 that off-axis illumination can be used to collect more diffraction orders compared to the nominal illumination. Using the basic shift properties of Fourier transform one can obtain a set of best illumination conditions [4]. Some of the modified sources are shown in Fig. 5. These sources are customized for a given layer, for example separated source is customized for gate layer whereas QUASAR source is better for the contact layers.

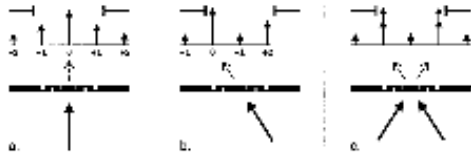


Figure 4. (a) Only two independent orders are collected (b) Three independent orders are collected (c) Focus symmetry through depth is restored using bidirectional illumination.

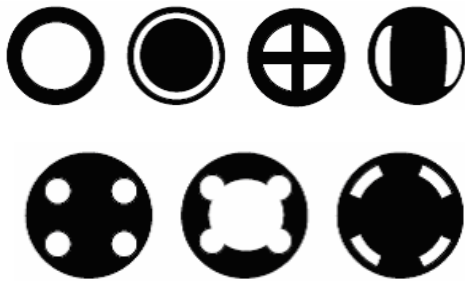


Figure 5. Various source maps ordered from left to right: conventional, annular, fourfold, separated, quadrupole, CQUEST and QUASAR

4. RECENT RESOLUTION ENHANCEMENT TECHNIQUES

Significant development in the mask making capability along with the advent of pixilated projection optics facilitated a new variety of RET techniques by converting source and mask into pixilated versions. In these sources every pixel can be treated as an optimization parameter [4].

4.1 Source Mask Optimization

The distribution of diffracted orders from the mask determines the characteristics of the final image. The aerial image at a given point can be obtained as a quadratic series expansion of the diffracted orders. Further, the optimum intensity for a given design can be obtained by solving a convex optimization problem [4] as

$$\text{Minimize } \Phi_j(\mathbf{a}) = \mathbf{a}^T \mathbf{A}_0 \mathbf{a} \quad (8)$$

subject to

$$\mathbf{a}^T \mathbf{A}_u \mathbf{a} \geq 1 \quad (\forall u | 1 \leq u \leq u_{Max})$$

The symmetric matrices A_u and A_0 are the system matrices that takes into account all the collected diffraction orders from the points where intensity should be as high as possible and as low as possible, respectively. The vector \mathbf{a} consists of all the collected diffraction orders and their superposition. The optimum diffracted orders are then used to calculate

the source intensity distribution by using wave front engineering techniques. Figure 6 show a few examples of source maps obtained using this technique.

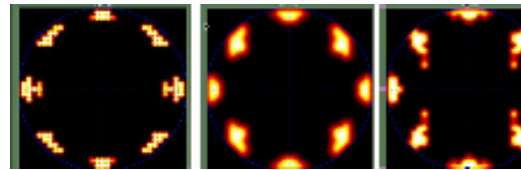


Figure 6. Examples of optimized pixilated sources

The source and the mask optimization can be done concurrently to maximize the process window; this technique is widely known as source mask co-optimization.

4.2 Inverse lithography

In this technique the mask design is decomposed into pixels and every pixel is allowed to take a bright or dark polarity. An optimization framework is developed such that the print image is as close as possible to the target. The lithography process can be considered as a system and can be represented using a transfer function as [5,6]

$$z(x, y) = T\{m(x, y)\} \quad (9)$$

here, $m(x, y)$ is the mask function and $z(x, y)$ is the output image intensity. In a forward problem the mask function is optimized in a way that the output intensity is as close as possible to the target image $z^*(x, y)$. On the other hand, inverse problem formulation takes the target $z^*(x, y)$ as an input and a mask solution is obtained which is as close as possible to the mask function as shown in Fig. 7.

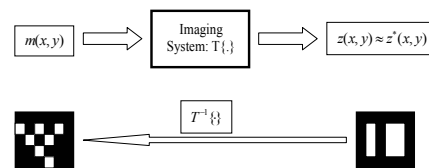


Figure 7. Inverse lithography schematic

It is clear that the inverse solution of the mask have very little resemblance with the original design. However, on wafer this design yields a pattern which is very close to the input design.

The area of computational lithography has been a very active area of research and development as the hardware capability is not expected to improve adequately. Optical lithography augmented with the RETs appears to be the technology solution in a foreseeable future.



Figure 8. (a) Input layout (b) Modified layout using inverse lithography technique

5. REFERENCES

- [1] Born M. and Wolfe E, Principles of optics, Cambridge University Press, 1999
- [2] Cobb N. B., "Fast optical and process proximity correction algorithm for integrated circuit manufacturing," PhD thesis, UC Berkeley, 1998.
- [3] Ma Xu, Gonzalo R. "Computational lithography," Wiley Series in Pure and Applied Optics (Vol. 1), 2010.
- [4] Rosenbluth A. E., Bukofsky S., Fonseca C., Hibs M., Lai K., Molles A., Singh R. N., Wong A. K., "Optimum mask and source patterns to print a given shape," PhD thesis, UC Berkeley, 1998.
- [5] Poonawala A., Milanfar P., "Fast and low-complexity mask design in optical microlithography – An inverse imaging problem," *IEEE Trans. on Image Processing*, 16:3, 774-788, Mar 2007.
- [6] Yu P., Pan D. Z., "TIP-OPC: A new technology invariant paradigm for pixel based optical proximity correction," ICCAD 2007, IEEE/ACM International Conference, pp. 847-853.

DESIGN OF A 2X-6X ZOOM TELESCOPE FOR LOW VISION PATIENTS

G S Singh

CSIR-Central Scientific Instruments Organisation,
Sector-30C, Chandigarh 160030

drgssr@gmail.com

A telescope is an optical instrument that helps in viewing a distant object by increasing the apparent angular size of object on the eye of observer. In its simplest form it consists of an achromatic doublet of long focal length, f_o , known as objective and another achromatic doublet of short focal length, f_e , known as eyepiece. These lenses are separated by a distance equal to the sum of their focal lengths. Therefore, a complete system formed from the combination is afocal that is light enters and exist parallel from the telescope. The angular magnification m is defined as $m = -f_o/f_e$. If both f_o and f_e are positive, astronomical telescope, we obtain a real and inverted image but if f_o is positive and f_e is negative, terrestrial or Galilean telescope, the image is erect and virtual. Galilean telescope is much compact than astronomical telescope and is widely used for observation of distant object on earth. This type of telescope has a fixed imagination as defined above. In order to have a variable magnification we need to have a zoom telescope.

Low vision patients (LVP) have a requirement of a telescope which should has an adequate zooming effect to fulfill their day to day needs of in house and outdoor viewing. In this paper we consider a design of a zoom telescope having a magnification range of 2X to 6x. This zoom range will allow LVP to watch TV in their drawing room at 2X magnification as well as it will allow them to walk outside and

read the number of a city bus at bus stop to make their life comfortable.

In order to make zoom telescope lighter and compact the lenses are made from optical grade plastics and aspheric surfaces are used to reduce the number of lens elements and to improve the image quality and larger field of view.

We have used a four component mechanically compensated zoom configuration to achieve desired zoom ratio $R = 3 = (6X/2X)$. A typical four component mechanically compensated zoom configuration uses second group, known as variator, which move linearly and change the magnification from 2X to 6X. In order to keep the total system afocal throughout the zoom range another group, called compensator, is moved non linearly. The third group performs this task. Second and third groups are linked with the help of a cam system to coordinate their movements. Normally LVP are unable to afford an expansive zoom telescope therefore we have decided not to use third group as compensator. We have used fourth group as compensator as well as focusing unit. The movement of fourth group will be similar to the focusing of an eye piece in an ordinary telescope and can be managed easily manually. The first and third group remains stationary. These approaches make the zoom telescope cost effective, light weight and compact converging large field of view with good quality image.

REFRACTIVE INDEX AND MODE FIELD PROFILING OF OPTICAL FIBERS USING LENSED FIBER PROBE

Anuj Bhatnagar
SAMEER, IIT Campus, Powai, Mumbai-400076
anuj@sameer.gov.in

Abstract: THE refractive index profile (RIP) of optical fiber determines the modal characteristics of guided light. The RIP of optical fibers can be tailored to control mode field, dispersion and polarization characteristics. Measuring index profile of fiber preform can provide an indirect estimate of RIP of drawn fiber. The index profile obtained from experimental measurements can subsequently be used for fiber modelling, designing the guiding medium and validation of measured modal characteristics.

Several methods have been reported to measure the RIP of optical fibers. The near field scanning technique for fiber refractive index profiling [1], refracted near-field (RNF) method [2] and propagation mode near-field scanning [3] are some of the earlier reported methods. Recently, nondestructive method for simultaneous measurement of RIP and cross section geometry of optical fiber preform [4], differential interference contrast microscopy [5], differential near-field scanning optical microscopy [6], nonresonant four-wave mixing microscopy [7], specially resolved fourier transform spectroscopy [8] and reflection-type confocal microscope [9-11] have been reported for RIP measurements. Alternative methods involve near-field guided intensity measurement and use of numerical techniques to reconstruct RIP of guiding medium [12].

Techniques demonstrated so far highlight the need for simple, rapid, accurate and spectrally resolved RIP measurements that are reliable and can be performed on guiding mediums like optical fiber or waveguide, irrespective of their material composition. Direct measurement of RIP is preferred with minimal use of numerical calculations. The reflection-type confocal scanning technique [11] has been demonstrated for profiling photonic crystal fiber (PCF), and ideally suited for RIP application owing to simple experimental configuration.

All fiber optic components based modified reflection and transmission scanning technique, currently being developed in our laboratory is described here for simultaneous measurement of refractive index and mode field profile. RIP measurements on single mode (SM), multimode (MM) and photonic crystal fiber are presented.

REFERENCES

- [1] Sladen, et..al., "Determination of optical fiber refractive index profiles by a near field scanning technique", *Appl. Phys. Lett.*, vol. 28, no. 5, pp. 255-258, 1976.
- [2] K. I. White, "Practical application of refracted near-field technique for the measurement of optical fibre refractive index profile", *Opt. Quant. Electron.* **11**, 185 (1979).
- [3] Katsumi Morishita, "Refractive index profile determination of single mode optical fibers by a propagation mode near field scanning technique", *J. Lightwave Technol.*, **1**, 445 (1983).
- [4] Yucheng Zhao, Simon Fleming, Katja Lyytikainen, and Leon Poladian, "Nondestructive measurement for arbitrary RIP distribution of optical fiber preform", *J. Lightwave Technol.* **22**, 478 (2004).
- [5] Nicoleta M. Dragomir, Eric Ampem-Lassen, Shane T. Huntington, Greg W. Baxter, Ann Roberts, and Peter M. Farrell, "Refractive index profiling of optical fibers using differential interference contrast microscopy", *IEEE Photon. Technol. Lett.*, vol. 17, no. 10 pp. 2149-2151, 2005.
- [6] Wan-Shao Tsai, Way-Seen Wang, and Pei-Kuen Wei, "Two dimensional refractive index profiling by using differential near-field scanning optical microscopy", *Appl. Phys. Lett.*, 91, pp. 611231, 2007.
- [7] Isobe et. al., "Three dimensional profiling of refractive index distribution inside transparent materials by use of nonresonant four-wave mixing microscope", *Appl. Phys. Express*, 1, pp. 22006, 2008.
- [8] Andrew D. Yablon, "Multi-wavelength optical fiber refractive index profiling by specially resolved fourier transform spectroscopy", *J. Lightwave Technol.*, pp. 11628, 2009.
- [9] Young Chun Youk and Dug Young Kim, "Reflection-type optical waveguide index profiling technique", *J. Opt. Society of Korea*, vol. 9, no. 2, pp. 49-53, 2005.
- [10] Young Chun Youk and Dug Young Kim, "A simple reflection-type two dimensional refractive index profile measurement technique for optical waveguides", *Opt. Commun.*, **262**, 206 (2006).
- [11] Youk et. al., "Refractive index profiling of a core-doped photonic crystal fiber", *IEEE Photon. Technol. Lett.*, vol. 19, no. 11 pp. 810-812, 2007.
- [12] Samit Barai and Anurag Sharma, "Inverse algorithm with built-in spatial filter to obtain the 2-D refractive index profile of optical waveguides from the propagating mode near-field profile", *J. Lightwave Technol.*, vol. 27, no. 11, pp. 1514-1521, 2009.

‘Single mode-Coaxial-Single mode’ fiber module as a band reject filter for gain flattening in erbium doped fibers

Jyoti Anand¹, Jagneet Kaur Anand¹ and Enakshi K. Sharma²

¹Department of Electronics, Keshav Mahavidyalaya, University of Delhi, INDIA

²Department of Electronic Science, University of Delhi South Campus, New Delhi-110021,INDIA
jyotianad75@gmail.com, jagneetkaur@gmail.com, enakshi54@yahoo.co.in

Abstract: We propose the use of an Erbium Doped Fiber (EDF) terminated with a coaxial fiber and EDF in coaxial configuration for gain flattening in EDF Amplifiers. The latter gives gain enhancement along with gain flattening.

1. INTRODUCTION

In this paper, we have proposed the use of coaxial fibers [1] (Fig. 1) for gain flattening in an EDF Amplifier. Erbium doped coaxial fibers for inherent gain flattening has also been proposed earlier [2]. However the erbium doped coaxial fiber analysis in [2] assumed the excitation of only the LP₀₁ supermode of the coaxial fiber whereas for the reported parameters, the fiber also supports LP₀₂ and LP₀₃ supermodes. In an earlier paper [3], we have considered a similar coaxial fiber which supports LP₀₁ and LP₀₂ supermodes. We have shown that if such a coaxial fiber is spliced to a single mode fiber at the input end in an actual transmission system, in general both the supermodes get excited. When the output of the coaxial fiber is spliced to another single mode fiber, the amplified signal power coupled into it can be a very sensitive function of the length of coaxial fiber used due to the two mode interference, especially around the phase matching wavelength. If the phase matching wavelength is chosen around 1510 or 1560nm, the power spectrum becomes insensitive to the coaxial EDF length in the entire C band of operation but no inherent gain flattening is seen.

In this paper, we have considered both, the coaxial fiber as an external gain flattening filter and EDF in coaxial configuration. In coaxial fibers, the rod and tube form two independent waveguides, each supporting its individual modes. These non-identical individual waveguides can be chosen to be single moded and synchronous at a phase matching wavelength $\lambda = \lambda_{ph}$. The rod and tube waveguide modes get evanescently coupled and hence coupled mode analysis [4] can be used to calculate the supermodes of the coaxial configuration.

When a single mode fiber carrying a DWDM signal is spliced to such a coaxial fiber, both its supermodes get excited, each with its excitation coefficient strongly dependent on wavelength. If the end of the coaxial fiber is spliced to another output single mode fiber, due to interference between the two supermodes, the output has the characteristics of a band reject filter at the phase matching wavelength, with attenuation and bandwidth strongly depending

on the fiber parameters.

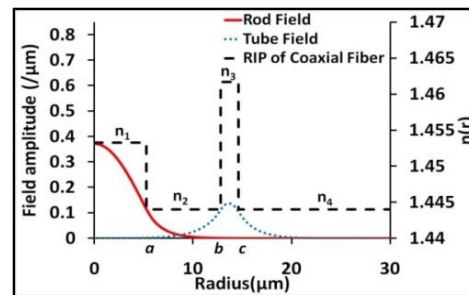


Fig.1. Refractive index profile of coaxial fiber along with the rod and tube field profiles.

2. COUPLED MODE ANALYSIS FOR COAXIAL FIBERS

Various numerical methods have been suggested in literature [5-7] to characterize the complete coaxial fiber in terms of its supermodes and their propagation characteristics. To get a better insight into the propagation characteristics of the coaxial fiber we have used coupled mode analysis [4].

The total field of the coaxial fiber can be written as the superposition of the fields of the inner rod, $\psi_1(r)$ and outer tube, $\psi_2(r)$ waveguides as

$$\Psi(r, z) = a(z)\psi_1(r) + b(z)\psi_2(r) \quad (1)$$

where amplitudes $a(z)$ and $b(z)$ are functions of z . Using the conventional ‘slowly varying’ coupled mode theory one obtains the solutions in the form of two supermodes of the coaxial waveguide:

$$\Psi_s(r, z) = \psi_s(r)e^{-j\beta_s z}$$

$$\Psi_a(r, z) = \psi_a(r)e^{-j\beta_a z} \quad (2)$$

with the field profiles given by

$$\psi_s(r) = \frac{1}{\sqrt{1+b_s^2}}[\psi_1(r) + \bar{b}_s\psi_2(r)]$$

$$= \frac{1}{\sqrt{1+a_s^2}}[\bar{a}_s\psi_1(r) + \psi_2(r)] \quad (3a)$$

$$\psi_a(r) = \frac{1}{\sqrt{1+b_a^2}}[\psi_1(r) + \bar{b}_a\psi_2(r)]$$

$$= \frac{1}{\sqrt{1+\bar{a}_a^2}} [\bar{a}_a \psi_1(r) + \psi_2(r)] \quad (3b)$$

where \bar{b} and \bar{a} are given by

$$\bar{b}_s = \frac{\beta_s - \beta_1}{\kappa_{12}}, \quad \bar{a}_s = \frac{\beta_s - \beta_2}{\kappa_{21}}, \quad \bar{b}_a = \frac{\beta_a - \beta_1}{\kappa_{12}}, \quad \bar{a}_a = \frac{\beta_a - \beta_2}{\kappa_{21}} \quad (4)$$

with β_1 and β_2 being the propagation constants of the individual rod and tube waveguides and β_s and β_a the propagation constants of the two supermodes which are given by

$$\beta_{s,a} = \frac{1}{2}(\beta_1 + \beta_2) \pm \left[\frac{1}{4}(\beta_1 - \beta_2)^2 + \kappa^2 \right]^{\frac{1}{2}} \quad (5)$$

with $\kappa = (\sqrt{\kappa_{12}\kappa_{21}})$, κ_{12} and κ_{21} representing the strength of interaction between the two waveguides defined as

$$\kappa_{12} = \frac{k_0^2}{2\beta_1} (n_1^2 - n_2^2) \int_0^a \psi_1 \psi_2 r dr, \quad (6)$$

$$\kappa_{21} = \frac{k_0^2}{2\beta_2} (n_3^2 - n_2^2) \int_b^c \psi_1 \psi_2 r dr$$

When we excite the coaxial fiber from a single mode fiber (same as the rod waveguide) spliced at the input end, both the supermodes get excited with excitation coefficients

$$a_1 = (1 + \bar{b}_s^2)^{-1/2}$$

$$a_2 = (1 + \bar{b}_a^2)^{-1/2} \quad (7)$$

The variation of excitation coefficients with wavelength is plotted in figure 2. It is quite intuitive from the geometry of the coaxial fiber (Fig. 1) that below the phase matching wavelength more power gets coupled to the LP₀₂ supermode as compared to the LP₀₁ supermode and vice versa .

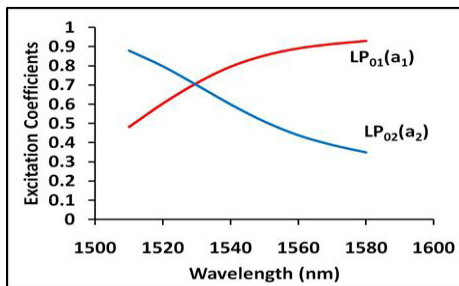


Fig. 2 Variation of the excitation coefficients of the two supermodes of the coaxial fiber with wavelength.

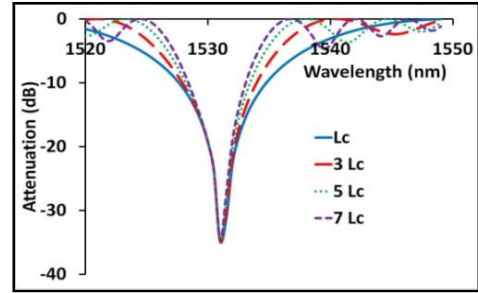
After a propagation length z_L , the power coupled into a similar single mode output fiber (assuming unit input power) is given by

$$P_{out} = 1 - \frac{\kappa^2}{\frac{1}{4}\Delta\beta^2 + \kappa^2} \sin^2 \left[\left(\frac{1}{4}\Delta\beta^2 + \kappa^2 \right)^{\frac{1}{2}} z_L \right] \quad (8)$$

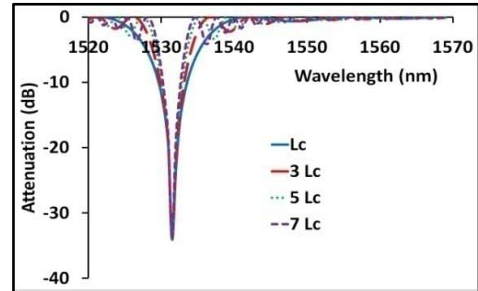
where $\Delta\beta = \beta_1 - \beta_2$. At $\lambda = \lambda_{ph}$ $\Delta\beta = 0$ and no

output power is obtained for $z_L = (2n + 1)L_c$ where $L_c = \pi/2\kappa$ is the coupling length and the output spectrum is shown in Fig. 3.

The resonance dip becomes sharper as length increases in odd multiples of L_c as depicted in Fig. 3; however, side lobes start appearing.



(a)



(b)

Fig. 3 Output Spectrum for different lengths for two different inter waveguide separation for a fiber with $n_2=1.4440236$, $\Delta_1 = 0.00643$, $\Delta_3 = 0.01232$ and

(a) $a = 5.25\mu\text{m}$, $b = 15\mu\text{m}$, $c = 16.8\mu\text{m}$ and $L_c = 3.1\text{cm}$

(b) $a = 5.22\mu\text{m}$, $b = 16\mu\text{m}$, $c = 17.8\mu\text{m}$ and $L_c = 5.5\text{cm}$.

3. EDF IN COAXIAL CONFIGURATION

For an amplifier in this coaxial fiber configuration, we consider the fiber doped with erbium ions in the inner core (rod), i.e. , over a region $0 < r < a$. As seen in section 2, the signal power in the wavelength range 1500-1650nm excites both the supermodes LP₀₁ and LP₀₂ of the coaxial EDF. For the pump power at wavelength 980nm, only the LP₀₁ supermode is excited. The steady state population density N_2 and N_1 in the upper and lower state respectively, can be written as [8]

$$N_2(r, z) = \frac{W_a(r, z)}{W_a(r, z) + W_e(r, z)} N_{Er}$$

$$N_1(r, z) = N_{Er} - N_2(r, z) \quad (9)$$

where $N_{Er} (= 10 \times 10^{24} m^{-3})$ is the total erbium ion density; W_a and W_e , which represent the total

absorption rate and the total emission rate respectively, are given by

$$W_a(r, z) = \left[\frac{\sigma_a(\vartheta_s)}{h\nu_s} \right] I_{ST}(r, z) + \left[\frac{\sigma_a(\vartheta_p)}{h\nu_p} \right] I_p(r, z)$$

$$W_e(r, z) = \left[\frac{\sigma_e(\vartheta_s)}{h\nu_s} \right] I_{ST}(r, z) + A_{sp}$$
(10)

where σ_a and σ_e are the wavelength dependent absorption and emission cross-sections respectively [8], A_{sp} ($= 1/t_{sp}$) is the spontaneous emission rate, ϑ_s and ϑ_p are the signal and pump optical frequencies, I_p is the intensity profile of the pump and I_{ST} is the total intensity profile of the signal.

The given length z_L of the coaxial EDF is divided into small segments of length Δz and propagation is considered in terms of local gain/loss through each segment.

The total field and, hence, the total intensity after a length z can be expressed as a sum of two supermodes as

$$\Psi_{ST}(r, z) = A_1 \psi_s(r) e^{-j\beta_s z} + A_2 \psi_a(r) e^{-j\beta_a z}$$

$$I_{ST} = A_1^2 \psi_s^2 + A_2^2 \psi_a^2 + 2A_1 A_2 \psi_s \psi_a \cos((\beta_s - \beta_a)z)$$
(11)
(12)

where A_1 and A_2 are given by

$$A_1(z) = a_1 e^{\gamma_1(\vartheta, 0)\Delta z} e^{\gamma_1(\vartheta, \Delta z)\Delta z} \dots \dots \dots e^{\gamma_1(\vartheta, z)\Delta z}$$

$$A_2(z) = a_2 e^{\gamma_2(\vartheta, 0)\Delta z} e^{\gamma_2(\vartheta, \Delta z)\Delta z} \dots \dots \dots e^{\gamma_2(\vartheta, z)\Delta z}$$
(13)
(14)

and $\gamma_1(\lambda, z)$ and $\gamma_2(\lambda, z)$ are the gain coefficients of the LP_{01} and LP_{02} supermodes given by

$$\gamma_1(\lambda, z) = \frac{1}{2} \left[\int_0^a \{\sigma_e N_2 - \sigma_a N_1\} \psi_s^2(r) r dr \right]$$

$$\gamma_2(\lambda, z) = \frac{1}{2} \left[\int_0^a \{\sigma_e N_2 - \sigma_a N_1\} \psi_a^2(r) r dr \right]$$
(15)

The pump loss coefficient $\alpha_p(\lambda, z)$ can be evaluated using

$$\alpha_p(\lambda, z) = \frac{1}{2} \int_0^a \sigma_a N_1(r, z) \psi_p^2(r) r dr$$
(16)

The pump power and signal power after each small segment in the LP_{01} and LP_{02} supermodes is given by

$$P_{s1,2}(z + \Delta z) = P_{s1,2}(z) e^{2\gamma_{1,2}(\lambda, z)\Delta z}$$

$$P_p(z + \Delta z) = P_p(z) e^{-2\alpha_p(\lambda, z)\Delta z}$$
(17)
(18)

where subscripts 1, 2 in (17) stand for the LP_{01} and LP_{02} supermodes respectively. The total amplified signal power at the output end z_L of the coaxial EDF is the sum of the powers of the LP_{01} and LP_{02} supermodes given by

$$P_{sout}(z_L) = A_1^2(z_L) + A_2^2(z_L)$$
(19)

The power coupled to the output single mode fiber (P_{out}) is given by

$$P_{out} = [a_1^2 A_1^2 + a_2^2 A_2^2 + 2A_1 A_2 a_1 a_2 \{\cos(\beta_s - \beta_a) z_L\}]$$
(20)

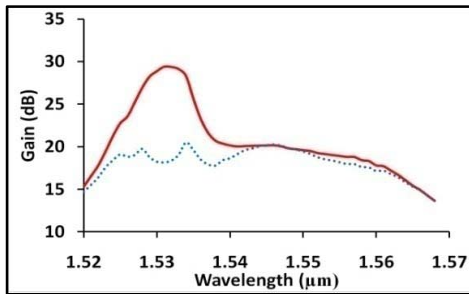
The two mode interference term $\{\cos(\beta_s - \beta_a) z_L\}$ varies between -1 and +1, the power coupled into the output SMF oscillates between $(a_1 A_1 - a_2 A_2)^2$ and $(a_1 A_1 + a_2 A_2)^2$, as the length of coaxial fiber z_L changes.

4. DESIGN OF AN EFFICIENT GAIN FLATTENING MODULE

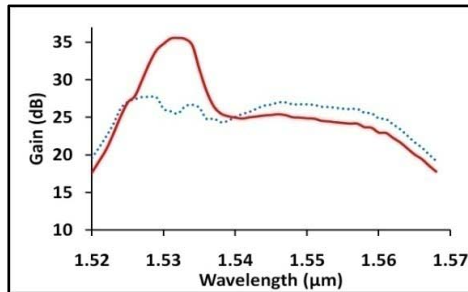
The band reject filter described in section 2 with $\lambda_{ph} = 1530\text{nm}$ can be used at the end of an amplifying EDF to reject the excess gain around 1530nm region. The parameters of the coaxial fiber can be tailored to give an appropriate attenuation and bandwidth. Fig. 4a shows the flattened gain spectrum obtained by using a coaxial fiber of $\sim 3.7\text{cm}$ length at the end of a single core EDF of length 3m (dotted line). It shows a $\pm 1.36\text{dB}$ flat gain over a band of 40nm ranging from 1525nm to 1565nm. In comparison the gain variation obtained in single core fiber of same length is $\pm 4.68\text{dB}$ in the same range.

Alternately, an erbium doped coaxial fiber with doping only in the rod can be used for inherent gain flattening. For such a configuration, the power at λ_{ph} , chosen to correspond to gain peak, couples back and forth between the rod (which has amplification) and the tube as it propagates along the length of doped coaxial fiber.

When a large number of wavelengths propagate through the EDF, the population inversion is reduced due to stimulated emission at each wavelength. The coaxial fiber couples in and out the wavelength corresponding to the gain peak (1530nm) which reduces the corresponding stimulated emissions around 1530nm and hence, the population inversion is available to other wavelengths. This results in inherent gain flattening as well as increase in the average gain across the 1540 – 1560nm band as shown in Fig. 4b, in the case of long period grating written in erbium doped fibers [9]. Fig. 4b shows the flattened gain spectrum by using a coaxial fiber of $\sim 3.66\text{m}$ length after a length of 1m of single core EDF (dotted line). It shows a gain flattening of $\pm 1.68\text{dB}$ over a band of 40nm ranging from 1525 to 1565nm. In comparison the gain variation obtained in single core fiber of same length is $\pm 5.36\text{dB}$ in the same range.



(a)



(b)

Fig. 4 Comparison of the gain spectra of the EDF with simultaneous propagation of 50 different wavelengths each carrying $1 \mu\text{W}$ power (solid line) with (a) external coaxial fiber gain flattening filter of length $\sim 3.7\text{cm}$ (dotted line) (b) EDF in coaxial configuration of length $\sim 3.66\text{m}$ (dotted line).

4. CONCLUSION

The parameters of a coaxial fiber can be tailored to give an appropriate attenuation and bandwidth for use as a gain flattening filter. The excess gain around 1530nm can be reduced by terminating it with an external coaxial fiber gain flattening filter. Alternatively, EDF itself can be used in coaxial configuration for inherent gain flattening. The latter gives gain enhancement in 1540 – 1560nm region along with gain flattening in 1525 – 1565nm region.

ACKNOWLEDGEMENTS

The authors would like to acknowledge the financial support from University Grants Commission, India for their research work.

REFERENCES

- [1] Boucouvalas A C, "Coaxial optical fiber coupling", *J. Lightwave Technol.* LT-3, 1151-1158 (1985).
- [2] Thyagarajan K and Kaur J, "A novel design of intrinsically gain flattened erbium doped fiber", *Opt. Comm.*, 183, 407-413 (2000).
- [3] Jyoti Anand, Jagneet Kaur Anand and Enakshi K. Sharma, "Study of the amplification characteristics of a coaxial EDF with varying coupling conditions", *Optics & Laser Tech.*,

Vol.44, No.3, 688-695, (2012).

- [4] Ghatak AK, Thyagarajan K., *Introduction to Fiber Optics*, Cambridge University Press, (1999).
- [5] Boucouvalas A C and Xin Qian, "Mode dispersion and delay characteristics of optical waveguides using equivalent T-L circuits", *IEEE J. Quantum Electron.*, JOE-41, 951-957 (2005).
- [6] Papageorgiou C D and Boucouvalas A C, "Propagation constants of cylindrical dielectric waveguides with arbitrary refractive index profile using 'resonance' technique", *Electron. Lett.*, 18, 786-788 (1982).
- [7] Morishita K, "Numerical analysis of pulse Broadening in graded index optical fibers", *IEEE Trans. Microwave Th. and Tech.*, MTT-29, 348-352 (1981).
- [8] Pedersen B, "Small signal erbium-doped fiber amplifiers pumped at 980nm: a design study", *Optical and Quantum Electron.*, 26, S273-S284 (1994).
- [9] Rashmi Singh, Sunanda and Enakshi K. Sharma, "Gain flattening with long period gratings in erbium doped fibers", *Optics Commun.*, 240, 123-132 (2004).

FIBER OPTIC SENSORS DEVELOPMENT PROGRAMME AT CSIO FOR STRUCTURAL HEALTH MONITORING

Subhash Chander Jain,
Chief Scientist,
Central Scientific Instruments Organization (CSIR-CSIO), Sector 30, Chandigarh-160030
Email: scj_42@rediffmail.com

Civil Structures such as buildings, bridges, dams, tunnels, ports etc are most expensive assets of the modern society that need to be functional for a very long time under complex conditions, thus their constant monitoring is pivotal to prevent catastrophe and ensure safety. Health monitoring of civil structures used to involve strict periodic maintenance procedures, regular visual inspections and use of conventional sensors i.e. electric strain gages (ESGs). Their Maintenance is expensive (especially when not required) while visual inspection mostly miss critical problems. As far as ESGs are concerned they have number of limitations: (i) prone to get detached from the surface (ii) difficulties with embedding into composites & metallic materials. (iii) there are many input and output wires required for quasi-distributed sensing which may compromise the strength of the structure, and are thus susceptible to electromagnetic interference(EMI), (iv) not suitable for multiplexing and long distance applications and (v) they have limited life span.

Development of fiber optics has led to a significant growth in the field of sensors as they offer several advantages like small size, light weight, immunity to EMI, non-corrosive, chemical inertness, ability to work in harsh environment, suitability for embedding, multiplexing and remote sensing, which make them perfect alternative to ESGs. If protected from breakage they can operate without degradation for decades. Amongst various fiber sensing technologies developed in the recent years, Extrinsic Fabry Perot Interferometer (EFPI) and Fiber Bragg Grating (FBG) sensors for structural health monitoring applications have become popular for their use in structural health monitoring. Whereas EFPIs are point sensors but FBGs are best for distributed sensing. They offer all the advantages of optical fibers with some added advantages as well which includes self-referencing feature as the information is wavelength encoded and can be produced in cost effective way. Multiple FBGs can be surface mounted and/or embedded for distributed sensing in structures to measure strain, temperature,

cracks & vibrations. FBGs are generic sensors which work through creation of strain and other parameters can also be measured by designing appropriate coatings or transducers. This can specify when and what corrective action is needed to repair the structure thereby large expenditure on unnecessary repair is saved and timely warning can save damage. Experiments on FBG sensors for real time health monitoring of various civil structures are underway in advanced countries during the last decade, whereas in Indian context this technology is still in a nascent stage. Practical implementation of these sensors requires immediate attention and constant efforts for their development.

The proposed use of FBGs and EFPI in structural health monitoring improves sensing technique as it helps to achieve surface strain in structures for their long term monitoring. Minimal disturbances to the structure are expected as the diameter of the optical fiber which will carry the response signal from these sensors to the Interrogator would reduce substantially compared with conventional wires from the ESGs.

CSIO has been actively engaged in the R&D of Fiber Optics and Photonics for the last more than 30 years and a good expertise and latest infrastructural facility have been created in these areas. Some of the recent significant R&D achievements include design and development and characterization of EFPI and FBG sensors for structural health monitoring applications. FBG sensors writing facility has been recently established and different configurations of sensors have been designed, fabricated and performance found satisfactory. Laboratory and field studies based on indigenously fabricated EFPI and FBG sensors have been carried out for health monitoring of concrete as well as metal structures and results are encouraging. The talk discusses the status of the work undertaken for structural health monitoring application at CSIO using both EFPI and FBG sensors and results obtained in this area.

MULTI-MEASURAND PROCESS AND HEALTH MONITORING OF FIBRE REINFORCED COMPOSITES

A.K. Nair¹, V.R. Machavaram¹, D. Harris¹, R.S. Mahendran¹,
 G.F. Fernando¹, ²C. Paget and B.D. Gupta³

¹School of Metallurgy and Materials, University of Birmingham, Birmingham. UK.

² Airbus, Filton, UK.

³Department of Physics, IIT Delhi. India.

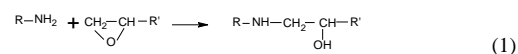
g.fernando@bham.ac.uk

Abstract: Advanced fibre reinforced composites are used extensively in areas where weight is at a premium, for example, aerospace, automotive and marine. The processing of this class of material can be influenced by a number of factors including temperature, chemical integrity of the resin system and the coefficients of thermal expansion of the various constituents. This paper presents an overview of the design and deployment of a novel multi-measurand optical fibre sensor (MMS). The MMS is capable of simultaneously monitoring strain, temperature, refractive index and cross-linking chemistry.

1. INTRODUCTION

Advanced fibre reinforced composites are composed of three key components: the reinforcement (fibres, particulates), a matrix (resin system) and the interface (region between the fibre and the matrix [1]). The manufacturing of composites, using thermosetting matrices, starts with the impregnation of the reinforcement by the matrix; this is followed by consolidation (vacuum and external pressure) of the preform, and cross-linking of the matrix, generally by the application of heat [2]. Generalised representations of the cross-linking reactions are presented in Figure 1 (Equations 1 and 2) for a typical epoxy/amine resin system. Equation 1 shows the initial reaction between the epoxy and amine functional groups; here the primary amine is converted to a secondary amine. This secondary amine (Equation 2) is thus capable of reacting with a further epoxy functional. Cross-linking reactions of this nature result in the conversion of the liquid or semi-solid monomer to a highly cross-linked and infusible solid.

(i) Primary amine-epoxy addition



(ii) Secondary amine-epoxy addition

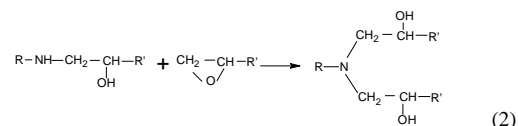


Figure 1 Generalised reaction scheme for an epoxy/amine resin system.

With reference to the design of sensor systems to facilitate real-time process monitoring of composites, Equations 1 and 2

illustrated in Figure 1 can be used to define the basic requirements. (i) Quantitative versus qualitative process monitoring: Data on the quantitative depletion of the epoxy and amine functional groups can be obtained by transmission, reflection or evanescent wave near-infrared spectroscopy. On the other hand, qualitative data on the rate of conversion can be obtained by tracking the refractive index of the resin system. Here, as the molecular weight of the resin system increases as a function of cross-linking, the optical density increases in proportion. Hence, quantitative data on the “molecular weight” can be inferred from the refractive index of the resin system.

(ii) Shrinkage: Since the chemical reactions result in the formation of covalent bonds between the reacting species, the resin system shrinks during cross-linking.

(iii) Temperature: The cross-linking reactions are exothermic and hence it is necessary to monitor and manage the thermal gradients within the composite.

(iv) Residual fabrication strain: Since the reinforcing fibres and the matrix have different coefficients of thermal expansion, when the composite is cooled from the process temperature, residual fabrication stresses will develop. To-date, the majority of the fibre optic-based sensor systems have been single or at the most, dual measurand systems. This paper presents a sensor design that is capable of monitoring four independent measurands: strain, temperature, the relative concentration of specified functional groups in the resin system and refractive index.

A unique feature of this sensor system is that a conventional fibre-coupled near-infrared spectrometer is used monitor the four

independent parameters.

2. SENSOR DESIGN AND INTERROGATION

A schematic illustration of the MMS is presented in Figure 2. This sensor design is based on the extrinsic fibre Fabry-Perot interferometer, where a pair of cleaved optical fibres are housed in a precision-bore fused silica capillary. The cleaved optical fibres are secured to the capillary tube via a pair of fusion joints. The gauge length of the sensor is defined as the distance between the fusion joints; the “cavity length” or the gap between the cleaved optical fibres is interrogated using white-light interferometry. Since the gauge length is known, the strain can be calculated. The inscription of a Bragg grating towards the end of the cleaved optical fibres was demonstrated previously [3]. In this configuration, the grating is in a strain-free state and hence, it responds only to temperature.

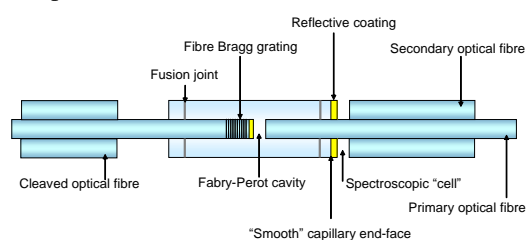


Figure 2 A schematic illustration of the multi-measurand sensor design (simultaneous monitoring of: strain, temperature, refractive index and cross-linking chemistry).

The chemical sensing element in Figure 2 consisted of the following: one of the cleaved faces of the capillary was gold-coated and annealed prior to the construction of the EFPI sensor. A pseudo-cavity was created by bonding additional secondary fibres onto the primary fibre, whereby the gap between the gold-coated capillary end-face and the cleaved secondary fibres served as a reservoir for the resin system. Thus it was possible to conduct transmission/reflection spectroscopy of the resin system that was contained in the secondary cavity. Finally, a pair of cleaved secondary fibres was positioned at a suitable distance away from the gold-coated end-face of the capillary; these optical fibres served as a Fresnel reflection sensor.

With reference to Figure 2, the MMS was interrogated using a conventional Fourier transform near-infrared spectrometer (MATRIX™-F, Bruker Optics Ltd, UK). The

primary EFPI-FBG sensor was illuminated using an ASE (amplified spontaneous emission) light source and connected to the spectrometer via 2 x 2 single-mode couplers. The secondary sensors, namely, chemical and Fresnel reflection sensors were illuminated using the FTIR light source and connected to the spectrometer via 2 x 2 multi-mode couplers.

3. EXPERIMENTAL

The above-mentioned sensors, within the MMS, were embedded in-between the fourth and fifth plies of an eight-ply E-glass fabric laminate (PD-Interglas Technologies, UK). A commercially-available thermosetting epoxy/amine resin system, LY3505/XB3403 (Mouldlife, UK), was mixed in the ratio of 100:35 (by weight) and the fabric layers were impregnated and laminated manually. A schematic illustration of the location of the sensors is shown in Figure 3. The optical fibre sensors were connected to a fibre-coupled FTIR spectrometer. The parameters used for the interrogation of the MMS are given in Table 1.

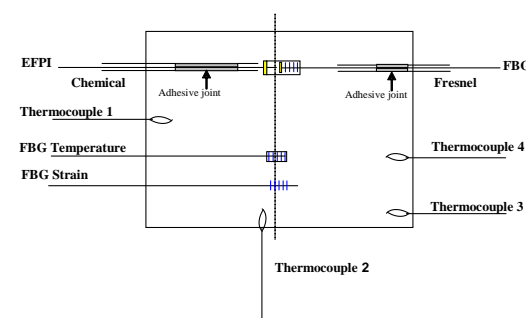


Figure 3 A schematic illustration of the location of the MMS (chemical, EFPI, FBG-temperature and Fresnel reflection sensors) between the fourth and fifth plies of an eight-ply fabric laminate. The locations of the independent FBG-temperature, FBG-strain and conventional thermocouples are also indicated.

Table 1 Parameters used for the interrogation of the MMS using the FTIR spectrometer.

Sensor	Light source	Resolution	Number of scans
EFPI	ASE	4 cm ⁻¹	16
FBG	ASE	1 cm ⁻¹	16
Chemical	FTIR	4 cm ⁻¹	64
Fresnel	FTIR	4 cm ⁻¹	64

A separate FBG (strain and temperature) sensor was also embedded along with the MMS to enable comparison between the

sensors. The independent FBG (strain and temperature) sensor was interrogated using an FBG interrogation unit (FiberPro IS7000).

4. TYPICAL RESULTS AND DISCUSSION

Figure 4 shows typical spectra that were obtained during the cross-linking of the resin system at 120 °C.

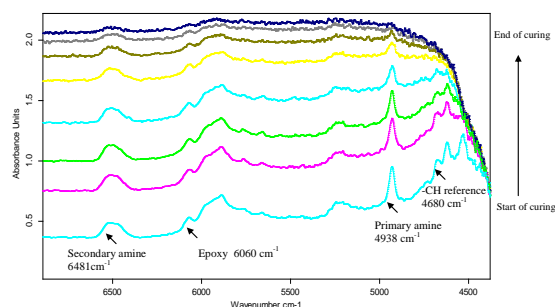


Figure 4 Typical NIR spectra of the resin system during cross-linking at 120 °C.

With reference to Figure 1, the depletion of the amine and epoxy functional groups as a function of processing time is readily apparent in the spectra shown in Figure 4. The degree of conversion data shown in Figure 5 was calculated from the spectra shown in Figure 4 using the following equation:

$$\alpha = 1 - \left(\frac{A_{EP,t} / A_{ref,t}}{A_{EP,0} / A_{ref,0}} \right) \quad (3)$$

where α is the conversion, $A_{ref,0}$ and $A_{ref,t}$ refer to the areas of the “inert” reference peak at the start of the reaction ($t=0$) and after time, t , respectively. $A_{EP,0}$ and $A_{EP,t}$ are the areas of the epoxy peak for the uncured and partially cured resin at a specified time respectively. The relative rate of conversion of the primary amine is faster than that observed for the epoxy group; this may be attributed to the evaporation of this low molecular weight component at the elevated processing temperature. Nevertheless, the MMS was successful in tracking the depletion of the active functional groups in the resin system.

The evolution of strain during processing (heating) was calculated from the change in the primary Fabry-Perot cavity length and the gauge length of the EFPI sensor. The residual fabrication strain was also measured using an independent FBG strain sensor; this sensor was interrogated using a different interrogation unit

(FiberPro). The data from the two sensor systems are presented in Figure 6. As the temperature was increased from ambient, a tensile strain was recorded, presumably due to thermal expansion. However when the temperature recorded in the laminate during the heating phase reached 45 °C, a compressive strain was recorded and this continued until the temperature reached 90 °C ; after this period, a tensile strain was recorded up to the isothermal temperature dwell (120 °C). The reasons for this discontinuity in the strain are not known at present but the following factors may have been responsible: (i) The glass transition temperature (T_g) of the acrylate coating on the optical fibre was measured via a differential scanning calorimeter to be 78.6 °C (the heating rate was 20 °C min⁻¹). Therefore, loss of coupling efficiency between the optical fibre and the resin (matrix) may occur above the T_g of the acrylate coating; (ii) Deformation of the acrylate coating during the period when the pressure was applied and the subsequent relaxation above its T_g . A detailed study is currently underway to ascertain the reasons for the discontinuity in the measured strain during the heating phase. The shrinkage of the resin is unlikely to be a primary factor because this behavior was observed when the cured laminate was reheated and cooled twice (without pressure or vacuum in the autoclave).

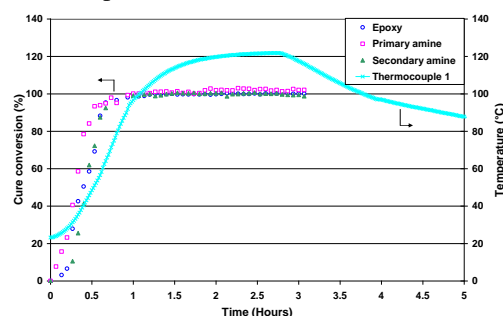


Figure 5 The degree of conversion of the epoxy, primary amine and secondary amine functional groups via the multi-measurand chemical sensor. The cross-linking was carried out at 120 °C.

With reference to the FTIR data presented in Figure 5, the conversion attained 95% after 40 minutes. Hence it can be assumed that the stripped regions (capillary for the EFPI sensor and the stripped region where the FBG was inscribed) were bonded to the matrix. During the cooling phase, a reduction in the previously recorded strain was observed as expected. The residual fabrication strain recorded at 32 °C, due to the thermally-induced resin shrinkage and the thermal expansion mismatch between

the woven E-glass fabric and the epoxy resin, measured using EFPI (MMS) and FBG (independent sensor) sensors were found to be $-203 \mu\epsilon$ and $-357 \mu\epsilon$ respectively.

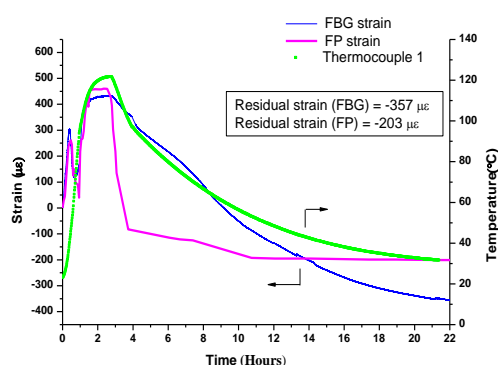


Figure 6 The evolution of strain during the processing of the eight-ply woven fabric preform. The strain data were measured using the EFPI sensor and FBG sensor.

The correlation between the data recorded by the FBG in the MMS (in a strain-free condition) and the K-type thermocouple is presented in Figure 7. The temperature measured using the two sensing devices show excellent correlation.

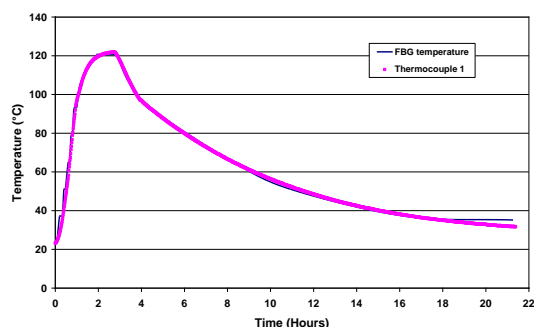


Figure 7 Temperature measured using an FBG sensor and a thermocouple during the processing of the glass fibre fabric laminate.

In situations where inferring the extent of cross-linking reactions will suffice (as opposed to the requirement for quantitative kinetic data via infrared spectroscopy), the Fresnel sensing element shown in Figure 2 provides a route for inferring the refractive index of the resin system. The amplitude of the interferogram of the FTIR data can be used to quantify the magnitude of the reflected Fresnel signal. Figure 8 shows the correlation between the conversion shown in Figure 5 and the amplitude of the interferogram.

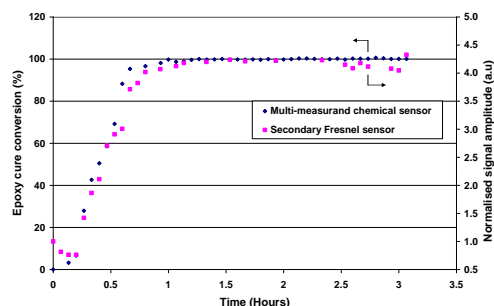


Figure 8 Correlation between the conversion presented previously in Figure 5 and the magnitude of the amplitude of the FTIR interferogram measured using a secondary Fresnel reflection sensor.

CONCLUSIONS

A multi-measurand sensor system that is capable of monitoring strain, temperature, specified chemical functional groups and refractive index was demonstrated. The above-mentioned parameters were interrogated using a conventional fibre-couple near-infrared spectrometer. The sensor design is based on an extrinsic fibre Fabry-Perot interferometer. Good correlation was observed between the MMS and the independent sensors that were used: FBG; Fresnel reflection; temperature; and transmission infrared spectroscopy.

REFERENCES

- [1] Wang, L., Pandita, S. D., Machavaram, V. R., Malik, S. A., Harris, D. and Fernando, G. F., "Characterisation of the cross-linking process in an E-glass fibre/epoxy composite using evanescent wave spectroscopy", *Composite Science and Technology*, 69 (13), 2069-2074, (2009).
- [2] Fernando, G. F. and Degamber, B., "Process monitoring of fibre reinforced composites using optical fibre sensors", *International Materials Reviews*, 51 (2), 65-106, (2006).
- [3] Fernando, G. F., Liu, T., Crosby, P. A., Doyle, C., Martin, A., Brooks, D., Ralph, B. and Badcock, R. A., "A multi-purpose optical fibre sensor design for fibre reinforced composite materials", *Journal of Measurement Science and Technology*, 8, 1065-1079, (1997).

ACKNOWLEDGEMENTS

The authors wish to acknowledge the financial support provided by EPSRC/TSB Airbus and The Royal Society.

OPTICAL FIBER SENSOR BASED TESTING MODULE FOR ANALYSIS OF TANK T-72 ARMAMENT

¹B.B.Padhy, ²A.D.Shaligram and ¹R.B.Sharma

¹Defence Institute of Advanced Technology (DU), Girinagar, PUNE - 411025

²Dept. of Electronic Science, University of Pune, PUNE - 411007

bbpadhy2@yahoo.com

Abstract: Optical fiber sensor based testing module has been designed, developed and experimented for the analysis of 125 mm Tank T-72 barrel wear and burst. The developed system is based on extrinsic intensity modulated fiber optic displacement sensor with self-referencing technique and promises to be suitable for field employment by field troops.

1. INTRODUCTION

The Indian Army is facing a major challenge in arresting or preventing the barrel burst of the 125 mm gun fitted on Tank T-72. The increasing number of barrel burst cases since 2003 has been an issue of major concern for the field troops. Several attempts, including the autofrettage and modified chemistry have been made in past to prevent such barrel bursts, but have not yielded satisfactory results. As on date, the method used for barrel wear or crack examination is based on inspection of the gun, passing of a gauge plug bore limiter of 124.95 mm diameter and the boroscopic inspection using a video/VGA camera.

The purpose of this study is to develop a testing module for inspection of the barrel with respect to wear. The analysis of these data can be vital for arresting and/or preventing the barrel burst cases and reducing fatal accidents for the field troops.

2. SENSOR TEST MODULE

The test module is a multimode optical fiber based extrinsic intensity modulated displacement sensor [1]-[2]. PMMA fiber of 1000 μm diameter, laser diode at 660 nm and Thorlab make powermeter have been used for the experimentation. The photograph of the developed test set up is shown in Figure 1.

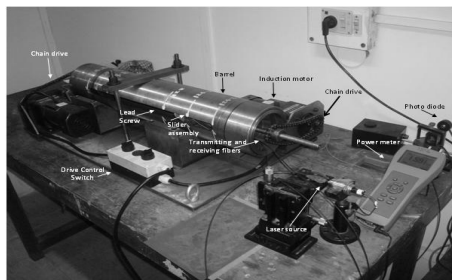


Figure 1. Photograph of test set up.

2.1 Sensor Design and Working

Experimentation has been carried out with two fiber geometry and also with self-referencing technique [3]. The source, detector and set of fibers are mounted on a movable plate and set of motors provide the lateral and rotational movements. The testing module is

supported on a base plate to hold the barrel of 125 mm inner diameter. The test assembly slides and rotates the laser and detector inside the barrel for measurements. Variations in the inner diameter of the barrel in terms of depth (made during manufacture) and measured displacements are compared.

3. RESULTS AND DISCUSSION

The barrel was examined using two fibers placed parallel to each other and equidistant from the barrel surface. The sensor has a sensitivity of 1.44 $\mu\text{W}/\text{mm}$, which is higher than that required for the actual use.

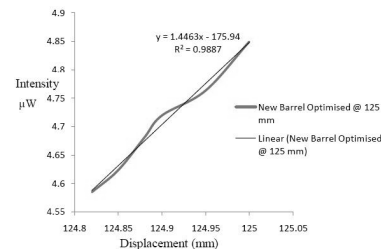


Figure 2. Response of the two-fiber configuration.

Similar trend with higher sensitivity are obtained for self-referenced sensor. Since there is a linear relationship between the inner diameter (ID) and the power detected, this system can be used to examine and detect wear in the barrel. In practice, a new barrel can be used as a reference and ID of an worn out barrel can be compared in terms of the change in ID to decide on a threshold wear after which further use of the barrel may be prohibited and thus reduce the barrel burst cases and fatal accidents.

REFERENCES

- [1] B. P. Pal, *Fiber Optics in Telecommunication and Sensor Systems*, Wiley Eastern, New Delhi, 1992.
- [2] S.A.N. Murthy and B.B.Padhy, "Fiber optic displacement sensor", *Journal of Optics*, **29** (4), 179-191, (2000).
- [3] B.B. Padhy, N. Chandrashekhara, J K Barui and C S Joseph, "Effects of varying source power on sensor performance in self-referenced fiber optic displacement sensor", *Journal of Optics*, **35** (3), 136-143, (2006).

BRAGG PLASMON COUPLED WAVEGUIDE SENSOR

Triranjita Srivastava¹, Ritwick Das² and Rajan Jha³

¹Department of Applied Physics, Delhi Technological University, Bawana Road, Delhi-110042

²School of Physical Sciences, National Institute of Science Education and Research, Bhubaneswar

³School of Basic Sciences, Indian Institute of Technology Bhubaneswar, Toshali Plaza, Bhubaneswar

Author email address: triranjita@gmail.com

Abstract: We present high performance ultra-stable Bragg-plasmon coupled waveguide sensor based on intermodal coupling and modal power transfer around resonance wavelength leading to sensitivity of 7500 nm/RIU and accuracy of 350/ μm for lab on chip. We found that an ultra thin (3 nm) layer of gold (Au) over aluminum (Al) protects aluminum (Al) from oxidation and exhibits better sensor performance.

1. INTRODUCTION

In the last decade or so, the phenomenon of surface plasmon resonance (SPR) has become a highly efficient mechanism for sensor technology, spectroscopy, microscopy and miniaturized nanophotonic components for integrated circuit [1-4]. The conventional SPR sensor structures are based on Kretschmann's attenuated total reflection (ATR) configuration [5], where a thin metal film is deposited on the prism base and a *p*-polarized incident light excites a surface plasmon wave (SPW) along the metal-dielectric interface by satisfying certain resonance condition. The metallic layer used in SPR measurements consists of either silver (Ag) or gold (Au). Ag displays a narrower resonance curve but, is prone to oxidation there by deteriorating the performance of the sensor significantly. On the other hand, Au demonstrates a larger shift in the resonance wavelength with change in refractive index of the analyte, and is chemically stable. However, the conventional route to excite surface plasmon (SP) modes i.e. Kretschmann configuration, deploy various types of high-index prisms for achieving resonance/phase-matching between the incident-wave and SP wave, thereby making them unsuitable for miniaturized applications like lab on chip for different sensing applications [4]. Moreover, the use of bulky prisms in Kretschmann configuration leads to substantially high costs and large size, thereby confining such systems mostly to laboratory. A crucial variant of SPs is long-range SPs (LRSPs) supported by a thin metal stripe embedded in a symmetric dielectric medium [6]. It is found that the LRSPs exhibit appreciable enhancement in surface fields and long propagation lengths, which interestingly manifests into narrower angular resonances. However, the major drawback associated with LRSP applications is the complicated and bulky configuration required to excite the LRSPs. Moreover, the requirement of highly symmetric configuration to support LRSPs limits the flexibility in choice of materials. Efficient excitation could be realized using mode-coupling of dielectric waveguide mode to SPP mode. However, owing to high refractive index

(~ 1.45) of dielectric waveguide core, the proposed schemes are extremely complicated. One attractive route for efficient SPP excitation is to employ the bandgap-guided modes of photonic crystal geometry to excite SPP modes [7]. In this work we present high performance ultra-stable Bragg-plasmon coupled waveguide (BPCW) sensor based on intermodal coupling by riding on the advantage of low absorption coefficient of Al as compared to Au. We also analyze its performance with respect to various metals, such as Au and Al. The oxidation problem of an Al-based SPR sensor has been addressed by coating it with an ultrathin Au layer. The proposed BPCW is considered to be composed of SiO_2 and TiO_2 , which are the widely used materials in the photonics industry due to its compatibility with latest nanofabrication technique. We believe that such design will pave a new route for realizing lab on chip for ultra sensitive and accurate bio-chemical sensors.

2. THEORY AND WORKING PRINCIPLE

We considered a planar BPCW comprised of a silica-based Bragg reflection waveguide (BRW) with refractive index n_c ($\equiv \text{SiO}_2$) symmetrically sandwiched between periodically stratified cladding ($n_1 \cdot \text{TiO}_2$ & $n_2 \cdot \text{SiO}_2$, thicknesses d_1 and d_2 respectively).

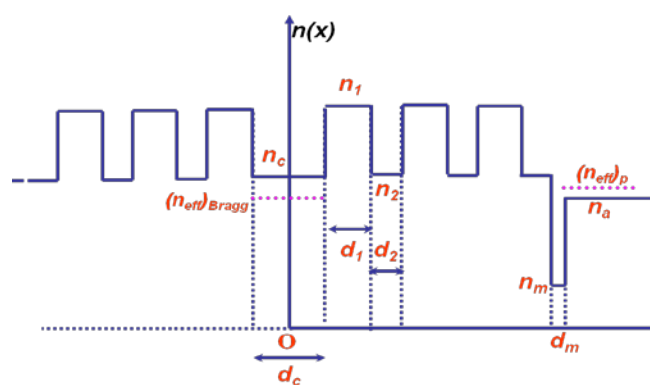


Fig. 1: Refractive index profile of proposed BPCW

Thin metal layer (~ 50 nm thick) followed by an analyte layer ($n_a \approx 1.330$) is placed on top of BRW. The refractive index profile for the same is shown in

fig.1 The suitable thicknesses of different layers were calculated using quarter wave stack conditions [8]. In the refractive index sensing measurement technique, light wave from a highly stable tunable laser is launched into the core of a BPCW using suitable optics and the transmitted light is analyzed employing appropriate diagnostics (power meter, wavelength meter etc.). It is observed that the obtained transmission spectrum exhibits minima at a particular wavelength; known as resonance wavelength (λ_{res}), implying the resonant excitation of the SPP wave the metal/analyte interface. Physically, at the resonance wavelength the mode effective index of the SPP mode ($n_{spp} = \sqrt{\epsilon_m \epsilon_a / (\epsilon_m + \epsilon_a)}$; $\epsilon_m = -\epsilon_{mr} + i\epsilon_{mi}$ and ϵ_a are the dielectric constants of the metal and analyte respectively) is equal to that of the BRW mode and hence, the power which is launch into the core of the BRW gets transferred to the SPP mode and hence, exhibiting a minima in the transmittance curve. Figure 2 illustrates a schematic plot of transmittance as a function of wavelength of the incident light for sensing layers with refractive indices n_a and $(n_a + \delta n_a)$. It is observed that the resonance wavelength is highly sensitive to any change in the refractive index of the analyte, which leads to shift in the resonance wavelength, which is the measure of the sensor performance.

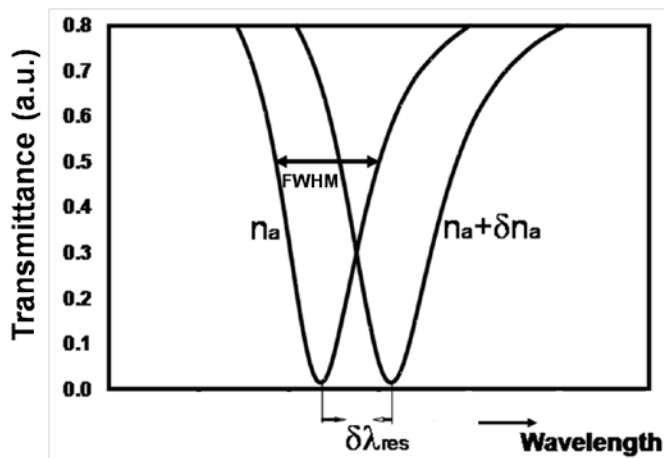


Fig. 2: Variation of normalized transmittance with respect to wavelength for two different refractive indices n_a and $n_a + \delta n_a$ of the analyte

In general, the performance of a sensor is quantified in terms of two characteristics: sensitivity, and detection accuracy (DA). The sensitivity of a SPR sensor depends on the shift in the resonance wavelength with a change in refractive index of the analyte. Increasing the refractive index by δn_a shifts the resonance wavelength by λ_{res} . On the other hand, DA of a SPR sensor depends on how accurately and precisely the sensor can detect the resonance wavelength and hence, the refractive index of the sensing layer. This accuracy of detection of resonance wavelength further depends on the width of the transmittance curve.

2. RESULTS AND DISCUSSION

In order to design a high performance sensor, we first obtain the suitable thicknesses of different layers. We assume the BRW and SPP waveguide (Au/water) to be non-interacting and calculate the mode effective index of SPP mode ($n_{SPP}=1.345$) at a wavelength say, $\lambda_0=1.486 \mu\text{m}$. For the resonant excitation of SPP wave, we use the condition $n_{BRW} = n_{SPP}$ and obtain the core thickness (d_c) of BRW using the Eq. (31) of Ref. [8] which has been derived assuming quarter-wavelength stack (QWS) condition being satisfied at λ_0 . The cladding layer thicknesses (d_1 and d_2) are calculated by using QWS condition i.e. Eq. (24) of Ref. [8]. In the calculations, the refractive indices for SiO_2 and TiO_2 are taken from Ref. [9] and [10] respectively. Following this recipe, we calculated the core and cladding thicknesses to be $d_c = 1.400 \mu\text{m}$, $d_1 = 0.182 \mu\text{m}$ and $d_2 = 0.700 \mu\text{m}$. Now, we obtain the mode effective index of the fundamental mode of the BRW by employing the standard transfer matrix method [4]. The dielectric constants of Au and Al are taken from Ref [1]. It is found that the resonance wavelength (λ_{res}) for the refractive index of 1.330 and 1.331 are 1.4687 and 1.4651 μm , respectively for Au and 1.4993 and 1.4962 μm , respectively for Al and hence, Au (λ_{res} -shift=3.6 nm) exhibits larger shift as compared to Al (λ_{res} -shift=3.1 nm), which shows that Au is more sensitive to the refractive index change.

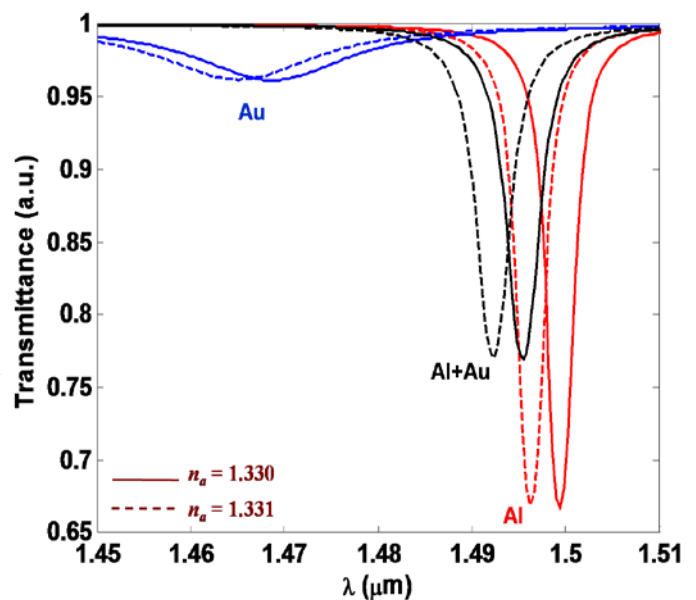


Fig. 3: SPR transmittance curve obtained from the proposed BPCW for analyte refractive index $n_a = 1.330$ and 1.331 with various metals (Au, Al and Al + Au (47 nm Al and 3 nm Au)).

Fig. 3 illustrates the transmitted power from the BRW

with respect to the wavelength, when the analyte refractive index changes by 0.001 (1.330 to 1.331) for Au, Al and bimetallic combination of Al and Au (47 nm of Al and 3 nm of Au). The couple mode theory has been implemented to obtain the transmittance through PCW [11]. This figure shows a narrower transmittance curve for Al based sensor ($FWHM = 3.2$ nm) as compare to Au based sensor. The narrower $FWHM$ is attributed to the strong coupling strength at the resonance wavelength. On the other hand, for the bimetallic combination of Al and Au, the shift in the resonance wavelength ($\Delta\lambda_{res} = 3.2$ nm) and the $FWHM$ (4.0 nm) is almost the same as that of the Al based sensor. Hence, the few nanometer Au layer over the Al, not only protects the Al from oxidation and also keeps the sensor performance close to that of Al.

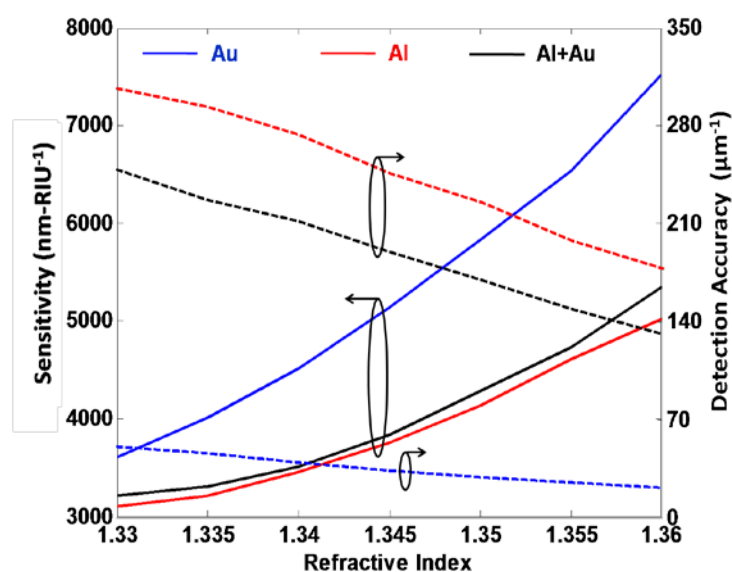


Fig. 4: Variation of the Sensitivity and Detection accuracy of the proposed sensor consisting of various metals; Au, Al and Al + Au (47 nm Al and 3 nm Au).

In order to quantify the sensor performance, we obtained the sensitivity and DA of the proposed sensor for various metals (Au, Al and Al + Au) as shown in Fig. 4. This figure shows that the sensitivity increases non-linearly, which is due to strong dispersion of BRW. It is found that Au based sensor exhibits highest sensitivity (~ 7500 nm-RIU $^{-1}$), which is 1.5 times higher than that of Al based sensor; whereas, the sensitivity of the Al and bimetallic combination based sensor is almost same. However, DA of Au based sensor is smallest (~ 6 times smaller than Al). This indicates that though the Au based sensor can exhibit larger shift in the resonance wavelength, but it cannot be so accurate in determining in resonance wavelength (refractive index of analyte) as compared to Al based sensor. On the other hand, the poor chemical stability of Al limits its usage. Thus, the best possible way to circumvent

this issue is to coat the Al with a few nanometer Au layer.

Fig. 4 shows the sensor overall characteristics. It is found that Au based sensor exhibits highest sensitivity (~ 7500 nm-RIU $^{-1}$ at $n_a = 1.36$), but smallest DA (~ 20 μm^{-1}). However, Al based sensor has smallest sensitivity (~ 5000 nm-RIU $^{-1}$) but largest DA (~ 180 μm^{-1}), i.e. high accuracy. On the other hand, the bimetallic combination (Al+Au) based sensor has moderate DA (~ 130 μm^{-1}) and almost same sensitivity (~ 5330 nm-RIU $^{-1}$) as that of Al.

Thus the bimetallic combination of Al+Au has advantage of high chemical stability, high sensitivity and moderate accuracy over Al.

3. CONCLUSIONS

In conclusion, we proposed a high performance BRW based SPR sensor, whose high sensitivity upsurge in a vicinity of more than 100% for a refractive index difference of 0.030 will be very useful for different biomolecule sensing applications and detection. The proposed design may be very useful in opening a new route for designing lab on chip for ultra sensitive and accurate bio-chemical sensors.

REFERENCES

- [1] J. Homola, S. S. Yee and G. Gauglitz, Surface plasmon resonance sensors: review, *Sens. Actuators B* 54 (1999) 3-15.
- [2] A. K. Sharma, R. Jha, and B. D. Gupta, "Fiber-Optic Sensors Based on Surface Plasmon Resonance: A Comprehensive Review," *IEEE Sens. J.* 7 (2007) 1118-1129.
- [3] E. Ozbay, Plasmonics: Merging Photonics and Electronics at Nanoscale Dimensions," *Science* 311 (2006) 189-189.
- [4] Anuj K. Sharma and Rajan Jha, SPR based gas sensor with chalcogenide glass and bimetallic alloy nanoparticles layer, *Journal of Applied Physics*, 106 (2009) 103101-107.
- [5] E. Kretschmann and H. Reather, Radiative decay of non-radiative surface plasmons excited by light. *Naturforsch.* 23 (1968) 2135-2136.
- [6] A. E. Craig, G. A. Olson and D. Sarid, Experimental observation of the long-range surface-plasmon polariton, *Opt. Lett.* 8, (1983) 380-382.
- [7] T. Srivastava, R. Das, and R. Jha, "Design consideration and propagation characteristic of channel bragg plasmon coupled waveguide," *Appl. Phys. Lett.* 97, 213104-3 (2010).
- [8] B. R. West and A. S. Helmy, "Properties of the quarter-wave Bragg reflection waveguide: theory," *J. Opt. Soc. Am. B* 23, 1207 (2006).

- [9] E. D. Palik, Handbook of Optical Constants of Solids. New York: Academic.
- [10] J. R. DeVore, "Refractive indices of Rutile and Sphalerite," J. Opt. Soc. Am **41**, 416 (1951).
- [11] A. Yariv, "Coupled-mode theory for guided-wave optics," J. Quant. Electron. QE-9, 919 (1973).

SURFACE PLASMON RESONANCE BASED OPTICAL FIBER HUMIDITY SENSOR USING GOLD NANOPARTICLE FILM

R. Aneesh, Abhinav Rastogi and Sunil K. Khijwania*

Department of Physics, Indian Institute of Technology Guwahati, Guwahati-781039, India

*e-mail: skhijwania@iitg.ernet.in

Abstract: Surface Plasmon Resonance (SPR) based optical fiber humidity sensor using gold nanoparticle film is reported. For the sensor fabrication, U-bend region of a plastic-clad-silica fiber has been coated by gold nanoparticle film which is followed by nanostructured dielectric film. Sensor is characterized by exposing it to different humid environments. A linear and reversible response is observed over a dynamic range of 12-80%RH.

1. INTRODUCTION

During past two decades, optical sensors based on SPR have been studied as a useful tool for chemical and biological sensing. A surface plasmon resonance is a charge density oscillation existing along the boundary between a metal and a dielectric. For the excitation of surface plasmon, energy as well as momentum of the incident light should match to that of the surface plasmon wave (resonance condition). This will result in a sharp dip in the reflected light spectrum. The resonance condition depends on the angle of incidence, wavelength of the light beam and the dielectric functions of metal as well as the dielectric [1]. SPR has also been exploited in conjunction with fiber optics. For this, the cladding over a certain length of the fiber is removed. Uncladded region is coated with metallic layer. Interaction of evanescent wave of the propagating light with plasmon mode results in SPR excitation. Dependence of resonance wavelength on dielectric constant of the surrounding medium is used for sensing applications. This paper reports a SPR based optical fiber humidity sensor using a gold nanoparticle film for plasmon excitation. Preliminary result shows a linear response over the observed dynamic range with a good sensitivity.

2. EXPERIMENT AND RESULTS

Colloidal gold nanoparticles were prepared by the reduction of hydrogen tetra-chloro-aurate (HAuCl_4) with sodium citrate. Suitable volumes of HAuCl_4 and that of sodium-citrate were mixed at a specific temperature. Sodium-citrate reduces Au ions to nanoparticles of Au metal. Plastic-clad-silica multi-mode fiber of pre-researched [2] core diameter ($125\mu\text{m}$) was used for the sensor development. About 5cm length of a centrally decladded fiber was carefully bent into a U-shape by exposing it to a propane flame. Afterwards, U-shaped region of the fiber was dipped in amino-propyl-tri-ethoxy-silane (APTES) for silanization. Afterwards, a dried probe was dipped in colloidal gold nanoparticles to realize metal nanoparticle film. Inset in Fig. 2 shows the SEM image of gold nanoparticles film on the fiber. A dielectric nanostructured film of pre-researched thickness using

TiO_2 nanoparticles was then synthesized over the metal layer. U-shaped sensing probe was carefully fixed inside a humidity chamber for its characterization. Light from a Broad Band Source (BBS) was coupled to one end of the sensing probe and the other end was coupled to a spectrometer (Ocean Optics-HR4000) (Fig. 1). A commercial (electronic) RH sensor was used for calibration. Figure 2 depicts sensor's response. As can be observed, peak absorption wavelength shifts towards higher wavelength upon increasing the humidity. This is due to the increase in *r. i.* of the dielectric film with an increase in the humidity. Importantly, sensor response is linear throughout a wide dynamic range ($\sim 12\%RH - \sim 80\%RH$). Also, an excellent sensitivity of $0.018\text{nm}/\%RH$ is achieved.

Fig. 1: Schematic diagram of experimental setup for sensor calibration

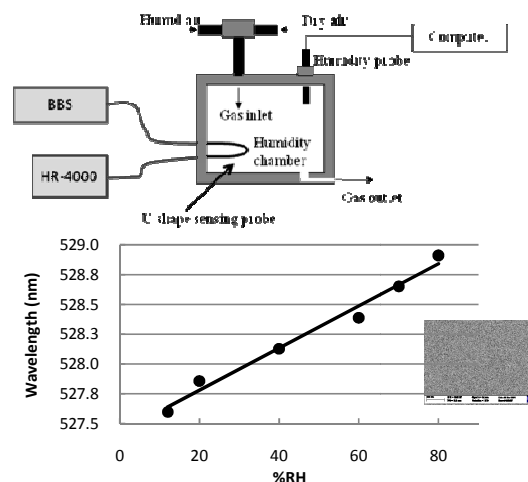


Fig. 2: Experimentally observed sensor response. Inset: SEM image of gold nanoparticles film onto the optical fiber.

REFERENCES

- [1] J. Homola, S. S. Yee, G. Gauglitz, "Surface plasmon resonance sensors: review", *Sens. Actuators B*, **54**, 3 (1999).
- [2] S. K. Khijwania and B. D. Gupta, "Fiber optic evanescent field absorption sensor: effect of fiber parameters and geometry of the probe," *Opt. & Quantum Electron.*, **31**, 625-636 (1999).

Fiber Bragg Grating sensors-Some Recent applications

S. Asokan,

Department of Instrumentation and Applied Physics

Applied Photonics Initiative

Robert Bosch Centre for Cyber Physical Systems

Indian Institute of Science, Bangalore 560012

Abstract

Fiber Bragg Gratings (FBGs) are wavelength dispersive refractive index structures inscribed in the core of a photo sensitive germano silicate optical fiber through ultra-violet (UV) exposure. In the past, they have found use in wavelength division multiplexing filters, dispersion compensators & fiber laser resonators for telecommunication applications and point or distributive sensors for a variety of applications. The present talk will highlight some of the recent applications of FBG sensors in chemical sensing, bio sensing and structural health monitoring.

THE RIDDLE OF CHROMATISM

Lakshminarayan Hazra
Department of Applied Optics and Photonics
University of Calcutta
92 Acharya Prafulla Chandra Road
Kolkata 700009

Email: lnhaphy@caluniv.ac.in, lakshminarayanahazra@gmail.com, lnhazra@sify.com

Abstract: This talk dwells upon the intricacies involved in accurate analysis and understanding of paraxial chromatism, and of different techniques employed for assessment of chromatic aberrations of various orders for non-paraxial rays in both axial and extra-axial imagery.

Design and development of high quality optical instruments call for a synergetic approach involving both ray and wave optical treatments. Parameters like equivalent focal length, magnification etc. can be related with the system variables by using suitable paraxial ray tracing, but diffraction-based image evaluation criteria like point spread function or optical transfer function cannot be related directly with the constructional parameters of an optical system. It is necessary to make use of aberrational analysis based on finite ray tracing for obtaining a link between the two. Over the years several pitfalls in this analysis were discovered; subsequently, most commercial optics design software have incorporated suitable measures by taking recourse to pupil exploration and appropriate normalization of coordinates of the entrance/exit pupil and object/image. For monochromatic systems, it has led to substantial reduction in variation of image evaluation criteria across the software platforms.

A direct extension of this approach for the treatment of optical systems operating under polychromatic or broadband illumination is not straightforward. The chromatic variation of paraxial parameters gives rise

to image defects of the same order as monochromatic aberrations, and needs to be tackled accordingly. The widely held concepts of axial color and lateral color, and their corrections are usually based on simplistic thin lens model that overlooks the chromatic variation of unit or principal planes.

On the other hand, chromatic variation of the entrance/exit pupil needs to be considered appropriately for proper analysis of chromatic variation of the monochromatic aberrations. For evaluation of image evaluation criteria like polychromatic PSF or polychromatic OTF it is necessary to use object space associated rays while tracing rays at the discrete wavelengths to obtain values of wave aberrations at the corresponding wavelengths. It should be noted that Conrady (D-d) formula provides first order estimates for chromatic variation in wave aberration, but the value refers to image space associated rays.

For the sake of better analysis and synthesis of optical systems operating in broadband light, this talk will make an attempt to dispel commonly held misconceptions in this area by unfolding the mysteries of chromatism in optical systems.

Hypertelescope Approach: A Novel Method for Imaging of Stellar Objects

Swapan K Saha
 Indian Institute of Astrophysics,
 Bangalore - 560 034, India
 sks@iiap.res.in

Abstract: The diffraction limited phase retrieval of a degraded image is an important subject that is being implemented in other branches of physics too, for example, electron microscopy, wavefront sensing, and crystallography. A third-order moment (bispectrum) analysis yields the phase allowing the object to be fully reconstructed. This can be extended from the single aperture speckle interferometry to the multi-aperture long baseline interferometry as well. However, in order to obtain snapshot images of the astronomical sources, many-aperture optical array with arbitrarily diluted apertures is required to be built, what is known as Hypertelescope approach. A major challenge for building such a system is the development of adaptive phasing system. Modified wave sensing techniques such as dispersed speckle analysis are planned to be used with these systems. But development and installation of such advanced methods are not available at present. In such a scenario, speckle mode observations with hypertelescope becomes a viable alternative. A study of speckle techniques with such systems is thus of great interest. This lecture is aimed to describe some of these techniques and methods.

Introduction

The diffraction limited resolution of celestial objects viewed through the atmospheric turbulence can be achieved by employing post-detection processing of a large data set of short exposure images using Fourier domain methods. Certain specialized moments of the Fourier transform of a short exposure image contain diffraction limited information about the object of interest. This post-processing method, what is referred to as speckle interferometry [1], has made impacts in several important fields in astrophysics. Following its success, astronomers focused their efforts on developing post-detection image processing techniques and applied them to improve the resolution of astronomical images [2 and references therein]. In the last few decades or so, adaptive optics system that compensates in real time of the wavefront perturbations by incorporating a controllable phase

distortion in the light path which is opposite to that introduced by the atmosphere, has become part and parcel of many large telescopes. However, since the resolution of any large telescope is limited by its diameter, diluted aperture interferometry became necessary to achieve high angular resolution information in optical astronomy. Some interferometers using diluted apertures equipped with adaptive optics system have been successful in producing results, but a new generation array, based on the concept of densified pupil imaging, has the potential of obtaining high angular resolution images. This article discusses the reconstruction ability using the aforementioned technique.

Tomographic Speckle Imaging

Several algorithms have been developed to retrieve the diffraction limited phase of a degraded image, of which the triple correlation technique [3], is a third-order moment (bispectrum) analysis yielding the phase allowing the object to be fully reconstructed. It is a generalization of closure phase technique where the number of closure phases is small compared to those available from bispectrum. This algorithm is insensitive to: (i) the atmospherically induced random phase errors, (ii) the random motion of the image centroid, and (iii) the permanent phase errors introduced by telescope aberrations; any linear phase term in the object phase cancels out as well. The images are not required to be shifted to common centroid prior to computing the bispectrum. The other advantages are: (i) it provides information about the object phases with better S/N ratio from a limited number of frames, and (ii) it serves as the means of image recovery with diluted coherent arrays. The disadvantage of this technique is that of demanding very severe constraints on the computing facilities with 2-dimensional data since the calculations are 4-dimensional. It requires extensive evaluation time and data storage requirements, if the correlations are performed by using digitized images on a computer.

Tomographic methods using Radon transform offer better alternatives since they are computationally efficient. Surya and Saha [4] have developed both Direct Bispectrum and Radon transform based triple correlation algorithms to process the speckle frames. Figure 1 displays the reconstruction of a close binary star, HR5747. The specklegrams of this object were obtained from the 2.34 m Vainu Bappu Telescope (VBT), situated at the

Vainu Bappu Observatory, Kavalur, India. Also, the developed algorithms were applied to the simulated speckle images from IMAGIN, which is a numerical simulation developed for multi-aperture imaging in cophased and speckle mode. The mode of beam combination used was Fizeau mode.

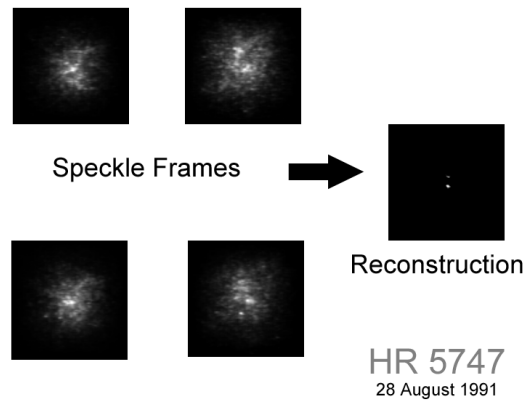


Figure 1: The reconstructed image of HR5747; the separation was found to be 0.23 arcseconds.

Speckle Imaging with Hypertelescope

Interferometric imaging through aperture synthesis with many baselines to reconstruct images, have been highly successful at radio wavelengths and also demonstrated at optical wavelengths. But it has been only recently that it was realized that many-aperture optical arrays can provide snapshot images, with arbitrarily diluted apertures. This hypertelescope approach to imaging may be viewed as a simple modification of the classical Fizeau interferometer by employing pupil densification. In order to obtain direct images, many apertures are needed, for a better sampling of the incoming wavefront. The coherent imaging thus achievable improves the sensitivity with respect to the incoherent combination of successive fringed exposures, heretofore achieved in the form of optical aperture synthesis. For efficient use of highly diluted apertures, this can be done with pupil densification. It has a vast potential, particularly since large arrays of relatively small apertures are easy to implement. Prototypes of such systems already have been developed [5] and large scale versions like CARLINA2 are under development.

A major challenge for these type of hypertelescopes is the development of adaptive phasing system. Modified wave sensing techniques such as dispersed speckle analysis are planned to be used with these systems. But development and installation of such advanced techniques will take time. In such a scenario, speckle mode observations with hypertelescopes becomes a viable alternative. Even in table top versions of hypertelescopes [6] speckle images have been observed due to phase variations in the subapertures. However, for imaging with hypertelescope, the incomplete output pupil filling provides a serious limitation. It is shown with the help of numerical simulations that even with smaller pupil filling rate in output pupil, high resolution imaging can be done with these interferometers by utilizing aperture rotation through the night.

Although best done with adaptive phasing, concentrating most energy in a dominant interference peak for a direct image of a complex source, such imaging is also possible with random phase errors such as caused by turbulent "seeing", using methods such as speckle interferometry and speckle imaging. We have simulated such observations using an aperture which changes through the night, as naturally happens on Earth with fixed

grounded mirror elements, and found that the reconstructed images of star clusters and extended objects are of an unprecedented high quality. As with cophased imaging with these telescopes, speckle imaging is also constrained by the field of view limitations. Also it is shown that with utilizing the aperture rotation of the diluted array through night, reconstruction quality could be increased substantially. The results of the simulations of image reconstructions (see Figure 2) show that the tomographic speckle imaging provides a computationally efficient alternative to Direct Bispectrum technique with Fizeau imaging optical

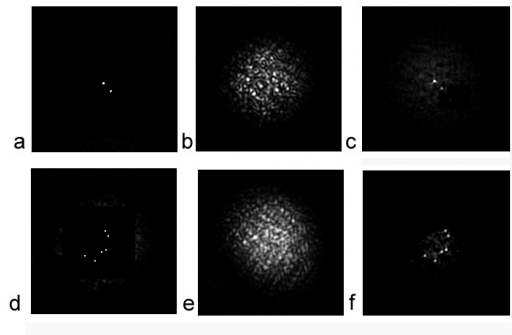


Figure 2; Bispectrum recovery from simulated speckle images of a binary system and a cluster of 6 objects of a hypertelescope: 40 frames of speckle simulations were taken for analysis: (a) binary system (brightness ratio 3:1), (b) a convolved speckle frame of the binary, (c) reconstructed image through speckle masking, (d) cluster of 6 objects of equal brightness, (e) a convolved speckle frame of the cluster, and (f) reconstructed cluster image [7].

interferometers. The bispectrum computes direct bispectrum of images. The speckle PSF (Point Spread Function) was convolved with the object distribution for object speckles. The simulation used 200 random apertures inside a disk, which was further densified with densified aperture diameter: disk diameter ratio is taken as 1:5.

Conclusion

The future of high resolution optical astronomy lies with the new generation arrays but its implementation is a challenging task. With improved technology, the interferometric arrays of large telescopes may provide snapshot images at their recombined focus and yield improved images, spectra of quasar host galaxies, and astrometric detection and characterization of extra-solar planets. Although the Large Binocular Telescope (LBT), in which the mirrors are co-mounted on a fully steerable alt-az mount, offers unprecedented spatial resolution of the order of 8-9 mas at the near IR (1 micron), its baseline is limited to 22 m. In this system, the information in the (u, v)-plane can be continuously combined or coadded. In this respect, developing an array based on the hypertelescope technique, though it is a subtle technique, will have far reaching impact on astrophysics, thus offering the possibilities for direct measurement of all the basic physical parameters for a large number of stars. With instruments as powerful as the current generation of working or planned interferometers, the element of serendipity will bring many surprises to astronomy.

Acknowledgement: The author acknowledges the services rendered by A. Surya in terms of developing the Bispectrum code and obtaining images.

References:

- [1] Labeyrie A., 1970, *Astron. Astrophys.*, **6**, 85.
- [2] Saha S. K., 2007, *Diffraction-limited Imaging with Large and Moderate Telescopes*, World-Scientific, New Jersey.
- [3] Lohmann A., Weigelt G., Wirtitzer B., 1983, *Appl. Opt.*, **22**, 4028.
- [4] Surya A., Saha S. K., 2011, 'Image Processing of Stellar Objects by interferometry', Presented at the 'International Conference on Contemporary Trends in Optics and Opto-Electronics', during January 17-19, 2011, at Trivendrum.
- [5] Le Coroller H., Dejonghe J., Arpesella C., Vernet D., Labeyrie A., 2004, *Astron. Astrophys.*, **426**, 721.
- [6] Pedretti E., Labeyrie A., Arnold L., Thureau N., Lardi\ere O., Boccaletti A., Riaud P., 2000, *Astron. Astrophys. Suppl.*, **147**, 285.
- [7] Saha S. K., 2010, *Aperture Synthesis: Methods and Applications to Optical astronomy*.

DEVELOPMENT OF IR ZOOM LENS: AN OVERVIEW

Ikbal Singh

Instruments Research and Development Establishment, Dehradun
ikbalsingh@irde.res.in

Abstract:

Thermal imager produces image by capturing IR radiations emitted by objects irrespective of availability of reflected visible light and therefore can be used for day as well as night applications. The thermal imager work either in 3-5 μm (MWIR) or 8-12 μm (LWIR) wavelengths bands, because of the good atmospheric transmission of these wavelength bands. A thermal imager mainly consists of four components: an imaging lens, an IR detector, amplifier & signal processing electronics, and a display. Objective lens of a thermal imager is usually designed to work either in single or two discrete field of view modes. But, for surveillance type applications, always a continuous zoom lens system is preferred. In two discrete field of view system, different fields of view are achieved either by inserting an additional lens in the form of flip-in flip-out magnification change over unit or by finite axial movement of a particular lens group, while in continuous zoom lens two/three group of lenses called “variator” and “compensator” continuously move to magnify the scene from wide field of view to narrow field of view and this makes the design difficult. In continuous zoom, lens has to be aberration corrected for all zoom positions.

Development of IR zoom lens involves optimum optical design, mechanical design, design of encoded steppers motors and calibration of moving optical elements. Optical design is an important part of IR zoom lens, which should cater not only for aberration correction at all zoom positions, but also the optimization for temperature range from -30°C to $+60^{\circ}\text{C}$. The design should also cater for near and far distance focus. World wide many companies like M/s ELOP, Israel, M/s Ophir, Israel, M/s TAMEK, Israel, M/s Controp, Israel, IR Zoom Lens, USA, WASCAM, USA have come out with IR zoom lenses, which have been used in various Electro-optic systems. IRDE, Dehradun, is also engaged in the development of IR zoom lenses in 3-5 μm based on cooled IR detectors, for last few years. As the detector is cooled one, the entrance pupil of the lens should match with the cold filter position of the detector, which in turn makes the front element large in diameter if cold stop is not matched with entrance pupil. To avoid this, reimaging type of configuration is used and the focal length of such a configuration can be obtained by multiplying the focal length of first focusing group and the linear magnification of the reimaging group (see Fig. 1).

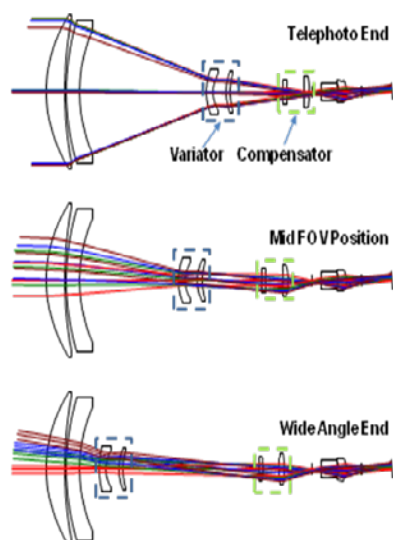


Fig. 1 Optical Layout of a typical IR zoom lens

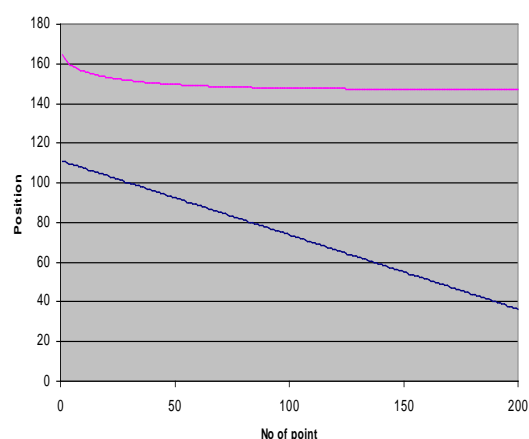


Fig. 2 CAM Profile of this IR zoom lens

In this process, several zoom lenses have been designed with 5X, 16X and 20X zoom ratio for different focal length ranges. One of the typical 20X zoom lens designed, is shown in Fig. 1 with its CAM profile in Fig. 2 [Design I]. This design uses Si and Ge as lens materials with few aspheric surfaces used to control the aberrations. The first two elements are of Si and Ge respectively, which were used in such combination in order to control the color. Since, this design uses two big size elements at the front, the weight of the optics is on the higher side and that has been reduced drastically in another design by making the second surface of the front Si element diffractive, which reduced the need of second Ge element for controlling the color along with reducing the length and relaxing many opto-mechanical tolerances [Design II]. The design-I uses '+', '-', '+' scheme in the front focusing group, but we have also used '+', '-', '+', '+' scheme instead of this scheme in a different design as this removed the second Ge element, by assigning the role of this element to the last positive group mentioned in this scheme [Design III]. We have also succeeded in designing one 16X zoom lens that uses '+', '-', '+', '+' scheme with re-imaging group and each group containing single element of Si with diffractive surfaces except the second group which is a single element of Ge with diffractive surface. This design has three moving groups in place of two, which can be linked by means of a CAM and a single motor can be used to drive them [Design IV]. This basic zoom lens along with the range extenders (afocal optics) has been used for producing different zoom ranges, while keeping the zoom ratio fixed [Design V]. Finally, our aim is to design an all Si element zoom lens in MWIR with diffractive surfaces used for color correction, which also reduces the number of elements in design along with reducing the cost and weight of the optics. The design shown in Fig. 1 is an example of a mechanically compensated zoom, in which the variator moves linearly, while the motion of the compensator is linked to it by means of a non-linear CAM. One can use independent encoded stepper motors for moving zooming elements to avoid fabrication of cam. As, the length of these cooled detector is large (of the order of 140mm), folded zoom lenses have been designed to make the thermal imager compact. [Design VI]. In all these designs the re-imaging group is used for athermalization and focusing.

REFERENCES

- [1] Allen Mann, *Infrared Optics and Zoom Lenses*, v. TT83, SPIE Press, 2nd Edition, 2009.
- [2] A D Clark, *Zoom Lenses*, Monograph in Applied Optics, No. 7, Adam Hilger Ltd., London, 1973.

DESIGN CHALLENGES IN OPTICAL SYSTEM DESIGN FOR SEE THROUGH DISPLAYS

P P Bajpai

Central Scientific Instruments Organisation (CSIR-CSIO), Chandigarh
e-mail: p_p_bajpai@yahoo.co.in

Optical system of a See Through Display like Head up Display (HUD) is essentially a collimating lens system which is used to project an infinitely distant image of the display source. This image is superimposed, with the help of a semi reflecting beam combiner, on a direct view of the scene, seen through the combiner. A folding mirror is used in the optical module to facilitate beam path fold to make it reach to the beam combiners. The available field of view is determined by the dimension of the exit pupil of the lens system and its distance from the pilot's eye position. The performance criteria which are of utmost importance to obtain desired performance from the HUD systems include aberrational performance; FOV performance and photometric performance.

The optical system is normally folded, extended and shaped to suit a particular aircraft installation in order to improve FOV performance. The aperture stop is external to the system, located at the pilot's eye, and eye relief is quite large. This restricts the IFOV available to the pilot, but a vertical head movement is allowed to cover the Total Field of View (TFOV) within the prescribed "Head Motion Box (HMB)". Further both eyes are involved in seeing the object; hence collimator optics of HUD is biocular. Conventionally this biocular is designed by considering the stop at the exit lens so as to simplify the design procedure. A system optimized with such an assumption, however, may not perform satisfactorily in actual use, because in real situation, the stop is at the pilot's eye, which is at considerable distance from the exit lens. In biocular, the eye pupil does not lie on the axis and eye pupils are shifted from the optical axis depending on the pupillary separation between two eyes (approx. 65 mm). The performance of biocular must be evaluated by decentering the eye pupil on both sides of the axis. The parallax or binocular disparity could be evaluated only by decentering the eye pupil in a biocular.

The Instantaneous field of view (IFOV) is limited by the size of the collimator exit lens and the distance between the latter and the pilot eye location. Thus it cannot be increased beyond a limit defined by the available space and geometry of the aircraft. The requirement of higher IFOV elevation necessitates the adoption of dual beam combiners. This also necessitates the use of petzval lens type of design to obtain the desired corrections for accuracies, resolution, parallax/collimating error. The Petzval

lens configuration comprises two positive power groups separated by an air gap. The air gap enables a mirror to be introduced to fold the system such that light from the CRT is projected into the beam splitting combiner glass which contains a reflecting surface.

The use of dual Beam Combiners (DBC) enhances the vertical IFOV by providing another path to the main ray to pass through the same aperture which otherwise is limited by the lens aperture. The increase in the size of Vertical Field of View (IFOV-EL) is determined by the spacing between the two beam combiners. However, there is a limit and again vertical FOV is limited by the size of lenses, so a balance has to be ensured between these two factors for optimum FOV.

In binocular overlap region, where both eyes are able to see the same object point, the vertical image points for both eyes must coincide within specified angular tolerances. Any departure from these results in parallax, and the images will not be properly fused. Binocular disparity is basically an error between the two optical axes of oculars in a binocular.

Image Doubling arises because of the fact that some of the object points are viewed by a single eye through a single combiner as well as through both combiners. The eye views the same field point through different parts of the pupil which may result in blurring of the image or in image doubling if the system is not properly optimized.

The pilot sees the projected imagery of the symbols on the display source superimposed on the outside scene through the Lower Beam Combiner (LBC) and the Upper Beam Combiner (UBC). The UBC and part of LBC are reflecting for the display source wavelength and transmitting for the rest of visible region. The remaining part of LBC is not coated for reflection and it is transmitting for the visible region. In case of sharp boundaries, the pilot will see a line in his FOV, which will give him impression of a false horizon.

The fabrication of optical components with stringent tolerances is a tricky affair as the stress developed during fabrication process could impart weak areas in the fabricated glass parts which could widen during thermal cycling. The assembly of optical components requires precise positioning of the fabricated optical components axially and radially with respect to each other and their integrated interfacing with CRT in the mechanical housing.

ALIGNMENT STRATEGIES AND OPTICAL DESIGN OF 50/80CM MODIFIED BAKER-NUNN SUPER-SCHMIDT ASTRONOMICAL TELESCOPE FOR 4D FIELD

K. G. Gupta

Aryabhata Research Institute of Observational Sciences (ARIES), Nainital-263129

Email: kkg@aries.res.in

Abstract: Out of the total 12 such original Baker-Nunn Satellite Tracking Cameras all over the world, one got installed at UPSO [now ARIES] in 1955 for optical tracking of artificial earth satellites, which has been renovated since 2005 for wide field [four degree / 4D] optical astronomical imaging of various interesting objects, depth of focus being only 2.4 micron, implying ultra precision focusing mechanism.

1. INTRODUCTION

Opto-mechanical and optical alignment process options, approaches, strategies and practical methods being used for final commissioning of ARIES Baker-Nunn Schmidt telescope in optically & equatorially renovated version at a new site at Manora Peak will be discussed in this presentation on behalf of various engineers, scientists, national and international agencies & experts, other technically competent ones who continue to be associated actively in this unique indigenous telescope technology development initiative programme initiated in April 2005.

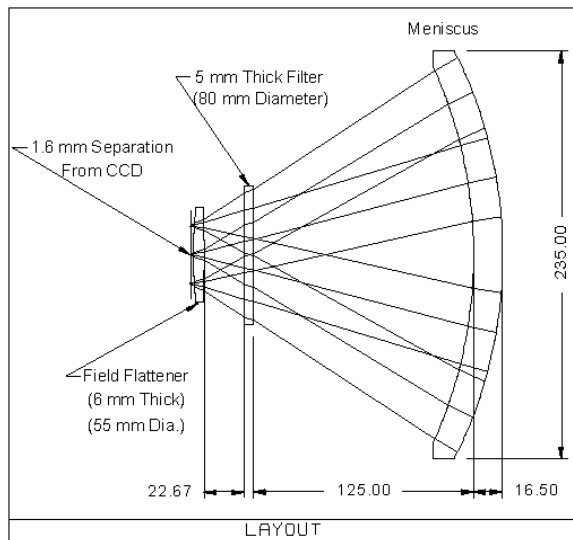


Figure 1. Detail of Field Corrector / Flattener , designed in consultation with Dr MJMacFarlane USA.

Above Figure 1 shows schematically the modifications implemented to the original standard & patented version of Baker-Nunn optical system, available in Reference [1].

Variouly modified equatorial telescope is likely to receive first light towards the end of 2011-12.

ACKNOWLEDGEMENT

Prof Ram Sagar, Director ARIES initiated and consistently nurtured the Project, so we thank him. Similar projects at Australia-UNSW, Canada-Calgary and Spain-Barcelona TFRM were our technical guides, so experts like Prof Octavi Fors require a word of deep thanks for their constant consultancy. Authors in the list of references below, technicians & consultants have generously contributed to the Project execution at various stages, hence acknowledged. Nearly 100 international references/reports/websites have been studied and indirectly used, just to mention thankfully.

REFERENCES

- [1] Soumen Mondal, K. G. Gupta, Sneha Lata, Biman J. Medhi, Tarun Bangia, T. S. Kumar, Shobhit Yadav & S. K. Singh "Development of ARIES Baker-Nunn camera to a wide-field Imaging Telescope with CCD" has been at International Conference on *Trends in Optics and Photonics (IconTOP)*, March 2009.
- [2] S. K. Singh, K. G. Gupta, Sneha Lata, Tarun Bangia, S. B. Pandey and B. B. Sanwal "Development, design and image quality analysis of different modern telescopes at ARIES" has been presented in *National Space Science Symposium (NSSS) during 26-29 February 2008 at Ooty (Tamilnadu)*.
- [3] K. G. Gupta, T. Bangia, T. S. Kumar, Sneha Lata, N. Sharma and V. Shukla: Development of 50-cm B-N Schmidt Telescope at ARIES, Poster presented at *25th ASI conference 2007*.
- [4] Sneha Lata, K. G. Gupta and S. K. Singh: Science goals with ARIES 50-cm Schmidt Telescope, Poster presented at *25th ASI conference in February 2007*.
- [5] K. G. Gupta, R. K. S. Yadav, T. Bangia, T. S. Kumar and N. Sharma: Redesigning ARIES Baker-Nunn Camera for Wide Field Imaging, Poster presented at *23rd ASI conference 2005*.

OPTICAL FIBER WITH RARE-EARTH DOPED DIELECTRIC NANO-PARTICLES FOR EFFICIENT FIBER LASER

Mukul Chandra Paul, Arindam Haldar and Shyamal K Bhadra*
CSIR-Central Glass & Ceramic Research Institute
Kolkata-700032
Email: *skbhadra@cgcric.res.in

Abstract: Major challenges for high power fiber laser are thermal management, efficient coupling of pump power to the active core and long term stability with less photo-darkening effect and nonlinearity. We have developed a fiber composed of Yb_2O_3 doped yttria-alumino rich silica nano-particles (DNP) in D-shaped low RI coated large core having diameter around 30.0-35.0 micron. Lasing experiments of the fibers demonstrate high slope efficiency of ~80% and low noise (ASE) factor, at in-core 975-nm pumping. Photodarkening effect at high power lasing appears to be low compared to conventional fiber.

The conventional modified chemical vapour deposition (MCVD) with solution doping (SD) technique is used for fabricating Yb_2O_3 doped yttria-alumino rich silica nano-particles (DNP) in D-shaped low RI coated large core fiber. Y_2O_3 ceramics has possessed excellent thermal property and possessed low phonon energy.

DNP are created during drawing of optical fiber from the modified preform which was annealed at 1450-1550 $^\circ\text{C}$ for 3-5 hours of heating and cooling rate was precisely controlled at 20 $^\circ\text{C}/\text{min}$. The size of the nano-particles was maintained within 5-10 nm with doping small quantity of fluorine. There is a great need to engineer the composition as well as doping levels of different elements within the core glass during the preform making stages to generate phase-separated Yb_2O_3 doped yttria-alumino rich silica nano particles in the fiber core. Interestingly such DNP containing fiber shows 20% less photodarkening effect compared to standard alumino-silica glass fiber under identical condition. These specialty fibers (core diameter: 30-35.0 micron, NA: 0.07-0.08) shows 17-18 W output power having 81.0 % lasing efficiency [Fig. 1].

Another new Ytterbium doped zirconium-germanium-alumino (ZGA) silica nano-particles based optical fibers are developed where the increase of sizes and numbers of nano-particles formed in the host glass depends on increasing Zr/Yb ratio. ZrO_2 serves as a nucleating agent facilitating the formation of such kind of phase-separated nano-particles with better thermal properties. Laser experiments with these fibers demonstrate high slope efficiency of ~75% and low noise (ASE) factor ($\sim 10^{-4}$), at in-core 975-nm pumping. Photodarkening effect at high power lasing is being studied.

This type of DNP containing rare-earth doped fiber has great potential as possible solution to counter

photodarkening effect under high power lasing application as well as for fiber amplifiers for intrinsic gain flattening and minimal spectral hole burning.

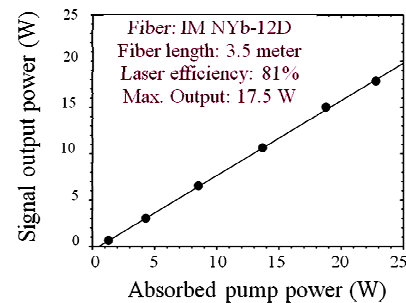


Fig-1: Lasing performance of Yb_2O_3 doped large core (35.0 μm) nano-engineered optical fiber

ACKNOWLEDGEMENT

The authors wish to thank Prof. Indranil Manna, Director CSIR-CGCRI for constant support and encouragement. They also wish to thank DST-Delhi and CSIR-Delhi for financial grant. Part of the work was carried out through Indo-Mexican collaborative project.

REFERENCES

- [1] J. Kong, D. Y. Tang, C. C. Chan, J. Lu, K. Ueda, H. Yagi and T. Yanagitani, *Opt. Letts.*, **32(3)**, 247-249 (2007).
- [2] J. Kong, J. Lu, K. Takaichi, T. Uemastu, K Ueda, D. Y. tang, D. Y. Shen, H. Yagi, T. Yanagitani and a. A. Kaminskii, *App. Phys. Letts.*, **82(16)**, 2556-2558 (2003).
- [3] B. N. Samson, P. A. Tick and N. F. Borrelli, *Opt. Letts.*, **26(3)**, 145-147 (2001).

NONLINEAR DYNAMICS OF FIBER LASER

R.Vijaya

Department of Physics, IIT Kanpur, Kanpur 208 016, India
rvijaya@iitk.ac.in

Abstract: An erbium-doped fiber ring laser when subjected to loss modulation exhibits features similar to that of a nonlinear oscillator. Resonance features measured in the regime of the relaxation oscillation frequency of the laser, under the variation of modulation frequency and driving amplitude, are analyzed to study this behavior.

1. INTRODUCTION

An exotic application of chaotic lasers is the generation of truly random numbers at GHz rates [1-2]. This is unlike the software-based approaches where the random number generation is only pseudorandom. The photonic noise in a chaotic laser can add unpredictability to the deterministic pseudo-random sequence in the optical approach. However, the software approach can generate these numbers as fast as their processor will allow, while the laser-based physical approach will be limited in its speed.

In lasers, the spontaneous emission is the precursor to stimulated emission and is the major source of unavoidable noise. But its fluctuating contribution settles down to a steady state during repeated amplification within the laser resonator. If the laser is made to operate in its nonlinear oscillator mode, such as by modulating the loss in its cavity, interesting features such as sub- and super-harmonic generation as well as chaotic output and bistability are possible.

2. ERBIUM-DOPED FIBER LASER

Fiber lasers which belong to the category of class B lasers are characterized by faster polarization decay as compared to the decay times of electric field amplitude and the population density. These lasers are capable of rich dynamical features. The dynamics of a laser is governed by the main laser resonance which is related to the relaxation oscillation frequency. In recent years, the dynamics of an erbium-doped fiber laser with a Fabry Perot cavity under harmonic pump modulation has been studied to a great extent [3]. As opposed to this, the dynamics in an erbium-doped fiber ring laser (EDFRL) under harmonic *loss modulation* is addressed here.

2.1 Experimental arrangement

An erbium-doped fiber (EDF) of suitable length is pumped by a semiconductor laser diode operating at 980 nm. Wavelength division multiplexers are used on either side of the EDF to couple power into and out of the fiber. A lithium niobate based electro-optic modulator is introduced in the ring cavity to provide loss modulation. An isolator in the cavity ensures unidirectional operation. A directional coupler is used to feed 99% of the signal power back into the cavity.

The remaining 1% of the power is monitored for obtaining the spectral- and time-domain features.

2.2 Dynamical features

Keeping the pump power fixed at a value above the threshold, and the driving amplitude of modulator very low, the frequency response of the laser showed a single peak indicating the linear nature of the system. At a higher driving amplitude, the main resonance was found to occur at a lower frequency with secondary sub- and super-harmonic resonances. A further increase in the driving amplitude shifted the main resonance further to a lower frequency and the resonance features are clearly more complicated than the two previous cases. The nonlinearity in the system is thus evident at the higher driving amplitudes.

The time series of the laser output clearly showed the rich dynamical features of period-1, period-2 and period-4 states as well as chaos when the modulation frequency is changed. These have been analyzed both from the time-domain data and the associated spectral-domain data using FFT. At the higher driving amplitude, bistability is also observed in the region of harmonic resonance. The ease with which these features have been obtained in a fiber laser indicates their suitability for more exotic applications such as random number generation and secure data communication.

ACKNOWLEDGEMENT

The author acknowledges Ms. Aditi Ghosh at IIT Bombay for the experimental work. The equipment used in the work is from the sponsored funding of Dept of Information Technology, Govt of India.

REFERENCES

- [1] T. E. Murphy and R. Roy, "The world's fastest dice", *Nature Photonics*, **2**, 714 (2008)
- [2] A.Uchida *et al.*, "Fast physical random bit generation with chaotic semiconductor lasers", *Nature Photonics*, **2**, 728 (2008)
- [3] A. N. Pisarchik, A. V. Kir'yanov, Y. O. Barmenkov, and R. Jaimes-Reategui, "Dynamics of an erbium-doped fiber laser with pump modulation: theory and experiment," *J. Opt. Soc. Am. B* **22**, 2107 (2005)

XPM and SPM Induced Crosstalk In Multi_Pumped Distributed Raman Amplifier

Anamika and Vishnu Priye

Electronics Engineering, Indian School of Mines
Dhanbad -826004, IndiaE-mail id: anamika.ece.ism@gmail.com, vpriye@hotmail.com

Abstract – Closed form formulae are derived analytically to study Cross-Phase modulation (XPM) and Self –Phase Modulation induced crosstalk in multi-pumped distributed Raman amplifier (DRA). The formulae are applied to study the sensitivity of XPM and SPM with respect to input power, interchannel separation and bit rate prevalent in optical transmission system. Performance of XPM and SPM induced crosstalk for various pumping scheme of DRA is also evaluated. Results show that backward pumped DRA suffers minimum crosstalk.

I. INTRODUCTION

Cross-Phase modulation (XPM) and Self-Phase modulation (SPM) are two nonlinear effects also known as optical Kerr effects [1,2]. The change in phase of channel is proportional to its own intensity in SPM and to the intensity of other channels in XPM.

The attenuated signals in optical transmission system are amplified using optical amplifiers such as distributed Raman amplifiers. In distributed Raman amplifiers, high power pump provides continuous gain to signals along the transmission length of fiber [3, 4]. In order to achieve broad and flat gain multiple pumps separated by a few nanometers are used. This technique is known as ‘WDM pumping scheme’. When a large number of signals simultaneously propagate in a single mode fiber (SMF), due to high power confinement, nonlinear effects are greatly enhanced.

Optical nonlinearities such as cross-phase modulation (XPM) and self phase modulation (SPM) gives rise to many effects in optical fibers which can be detrimental in optical communications. The transmission capacity of a wavelength division multiplexing optical system can be increased by increasing the data rate per wavelength or increasing number of wavelength channels. The first method has been illustrated by the recent increase in data rate per wavelength from 2.5 to 10 and then to 40 Gb/s. In the second method, the number of wavelengths in a fixed optical band is significantly increased by decreasing the spacing between adjacent wavelengths. Both methods suffer from system limitations due to XPM and SPM induced fiber nonlinearity.

In this research article using statistical method close form formulae have been derived to evaluate XPM and SPM induced crosstalk in WDM system employing bi-directional

pumped DRA. We investigate the limitations imposed by fiber nonlinearities in DRA. Impact of XPM and SPM on individual channels due to remaining N-1 channels has been investigated. Dependence of fiber nonlinearity such as XPM and SPM induced crosstalk on average input power, decreases in the spacing between adjacent wavelengths and increase in data rate per wavelength has also been assessed. Performance of XPM and SPM induced crosstalk for various pumping scheme of DRA is also evaluated.

The paper is organized as follows. In section 2 closed formed formulae has been developed to study crosstalk in WDM system employing bi-directional pumped DRA. Section 3 uses the closed formed formulae to evaluate crosstalk performance in a typical configuration of WDM system. Section 4 concludes the paper.

II. THEORY

In this section, crosstalk variance is derived in a distributed Raman amplifier for bi-directional pumping scheme. A single span of DRA of length L with no repeater is considered. In N-channel WDM systems, the phase modulation of i^{th} channel induced by j^{th} channel due to XPM is given as [5]

$$\Phi_{ij}(t) = 2\gamma \int_0^L P_j(0, t - d_{ij}z') e^{-\alpha z'} \cdot g_F(z) \cdot g_B(z) dz \quad (1)$$

Where $P_j(z,t)$ is the power of j^{th} channel as a function of length z and time t . $P_j(0,t)$ is the launched power at the transmitter, γ is the nonlinear co-efficient, α is the fiber attenuation co-efficient, d_{ij} ($= 1/v_j - 1/v_i$) is propagation time difference between the two different channels (i, j) during a unit length transmission.

In DRA, forward amplification gain [6] is

$$g_F(z') = \exp\left(\frac{g(\sum_{\lambda_p} \frac{\lambda_s}{\lambda_p} P_{so} + P_{po})}{A_{eff}\alpha} (1 - e^{-\alpha z'})\right) \quad (2)$$

where peak Raman gain $g = 6.5 \times 10^{-14}$, P_{po} and P_{so} are the initial pump and signal power respectively, λ_s (λ_p) is Signal (Pump) Wavelength.

Backward amplification gain [6] is

$$g_B(z') = \exp\left(\frac{g(\sum_{\lambda_p} \frac{\lambda_s}{\lambda_p} P_{so} + P_{PL})}{A_{eff}\alpha} (e^{\alpha(z'-L)} - 1)\right) \quad (3)$$

where P_{PL} is initial Pump power, L is the length of DRA and other parameters are same as (2).

Power spectral density of $\varphi_{ij}(t)$ is found by taking the Fourier transform of auto-correlation function and is given as

$$S_{\varphi_{ij}}(\omega) = S_{P_{ij}}(\omega) |H_{ij}(\omega)|^2 \quad (4)$$

Where

$S_{\varphi_{ij}}(\omega)$ = Power spectral density of $\varphi_{ij}(0, t)$

$S_{P_{ij}}(\omega)$ = Power spectral density of $P_j(0, t)$ which depends on pulse shape $p(t)$.

A rectangular NRZ pulse is given as $p(t) = \begin{cases} 2P_0 & (|t| < \frac{T}{2}) \\ 0 & (|t| > \frac{T}{2}) \end{cases}$

Fourier transform of $p(t)$ is given as $|P(\omega)| = 2P_0 T \frac{\sin \frac{\omega T}{2}}{\frac{\omega T}{2}}$

An RZ pulse of duty cycle τ_b is given by same equation as above with T replaced by $\frac{T}{\tau_b}$

$\tau_b = 2$ for 50% duty cycle

$= 3$ for 33.3% duty cycle

$H_{ij}(\omega) =$

$$2\gamma \int_0^L e^{-jd_{ij}z'\omega} e^{-\alpha z'} e^{K'(1-e^{-\alpha z'})} e^{(K''(e^{\alpha(z'-L)} - e^{-\alpha L}))} dz'$$

$$\text{Where } K' = \frac{\gamma(\sum_{\lambda p} P_{so} + P_{Po})}{\alpha A_{eff}}$$

$$\text{and } K'' = \frac{\gamma(\sum_{\lambda p} P_{so} + P_{PL})}{\alpha A_{eff}}$$

After some algebraic manipulation we get

$$H_{ij}(\omega) = 2\gamma \left[\frac{1 - e^{-(\alpha + jd_{ij}\omega)L}}{\alpha + jd_{ij}\omega} \right] - 2\gamma K' \left[\frac{1 - e^{-(2\alpha + jd_{ij}\omega)L}}{2\alpha + jd_{ij}\omega} \right] + 2\gamma K'' e^{-\alpha L} \left[\frac{1 - e^{-(jd_{ij}\omega)L}}{jd_{ij}\omega} \right] \quad (5)$$

The variance of XPM induced crosstalk is given by

$$\sigma_{XPM}^2(i, j) = \frac{1}{2\pi} \int_{-\infty}^{\infty} S_{\varphi_{ij}}(\omega) d\omega \quad (6)$$

The expression of $S_{\varphi_{ij}}(\omega)$ is substituted in equation of variance (σ_x^2). The infinite integral is performed using table of integral and series [9] and the final form is given in Appendix.

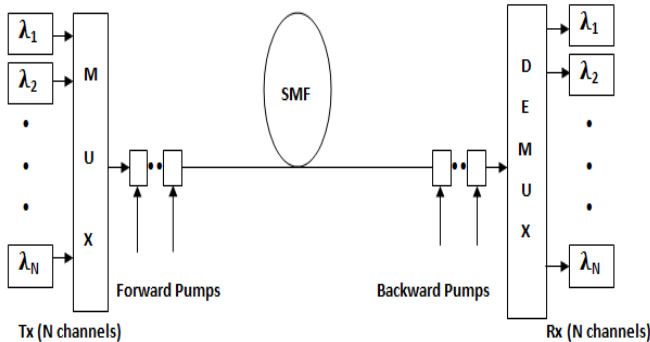


Fig. 1: Schematic diagram of bidirectional multi-pumped DRA

In N-channel WDM system, each channel is modulated independently by random data. Thus, the variance can be approximated as

$$\sigma_{XPM}^2(i) = \sum_{j=1}^N \sigma_x^2(i, j) \quad (j \neq i) \quad (7)$$

The variance of SPM induced crosstalk is calculated by taking the interchannel separation ($\Delta\lambda$) equal to zero in the expression of variance of XPM. This is due to the fact that in SPM change in phase of the signal is proportional to its own intensity. Hence,

$$\sigma_{SPM}^2 = (1/4)\sigma_{XPM}^2(\Delta\lambda = 0)$$

The factor of 1/4 comes from the fact that phase shift induced by XPM is twice as large as SPM for the same intensity of the signal.

Thus total variance of XPM and SPM induced crosstalk is given as $\sigma_x^2(i) = \sigma_{SPM}^2 + \sigma_{XPM}^2(i)$.

III. RESULTS AND DISCUSSION

Fig.1 shows the DRA configuration considered for our analysis. The interacting channels of WDM system are assumed to transmit 0 dBm power in wavelength range of 1515 – 1575 nm with inter – channel separation of 1 nm. The multi – pumps consisting of 6 pumps are in wavelength range of 1430 -1480 nm, separated by 10 nm and each having power of 20 dBm yielding wideband and flat gain spectrum in signal wavelength range of 1515 – 1575 nm. Each pump provides peak Raman gain to signal at a shifted wavelength of 100 nm from pump wavelength and has a gain spectrum of 10 nm. Other parameters used for calculation are given in Table 1.

Fig. 2 shows the variation of XPM and SPM induced crosstalk with signal wavelength for bit rate of 2.5Gbps, 10 Gbps and 40 Gbps. It can be seen from the figure that with the increase in bit rate of the signals, crosstalk decreases and minimum crosstalk is observed for 40 Gbps signal. This is because walk-off length $L_w (= \frac{T}{|D\Delta\lambda|})$, the distance at which two i^{th} and j^{th} pulses of length T becomes completely walk-off [11], varies inversely with fiber dispersion co-efficient and bit rate of the system. Hence it can be concluded from the analysis that in DRA; variance of crosstalk varies with L_w and hence decrease with the increase in bit rate of the system, other parameters remaining constant. We have neglected the impact of collision rate between the pulses and have only considered walk-off length (which is actually the inter collision distance).

TABLE I: Parameters of SMF for evaluating crosstalk variance

A_{eff} (Effective Area)	80 μm^2
Zero Dispersion Wavelength	1265.5 nm
Dispersion Slope	0.058 x 10 ³ ps/nm/nm/km
α (attenuation co-efficient)	0.2 dB/km
L (length)	80 km
γ (Nonlinear Co-efficient)	1.18 W ⁻¹ km ⁻¹

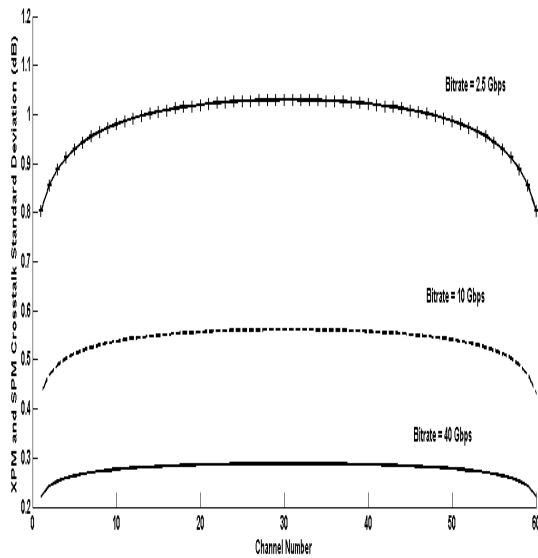


Fig. 2: Variation of crosstalk with channel number for different bit rate of the system.

Further studies were done to investigate the effect of interchannel separation and input power on XPM and SPM crosstalk. It is observed from the Fig. 3 that with the increase in interchannels separation crosstalk decreases. It is also observed that smaller channels suffer greater increase in crosstalk compared to middle and longer channels. It is also observed that there is a greater percent increase when interchannel separation is increased from 1 nm to 1.5 nm than from 1.5 nm to 2 nm. The reason for this nature of crosstalk comes from the fact that with the increase in interchannel separation keeping number of channel constant, the wavelength range increases in the WDM system. Hence crosstalk suffered by WDM system decreases as the XPM induced crosstalk varies inversely with the interchannel separation. Fig. 4 shows the variation of power penalty with channel number for power input of 0 dBm, 5dBm and 10 dBm. Other parameters assumed are same as the previous

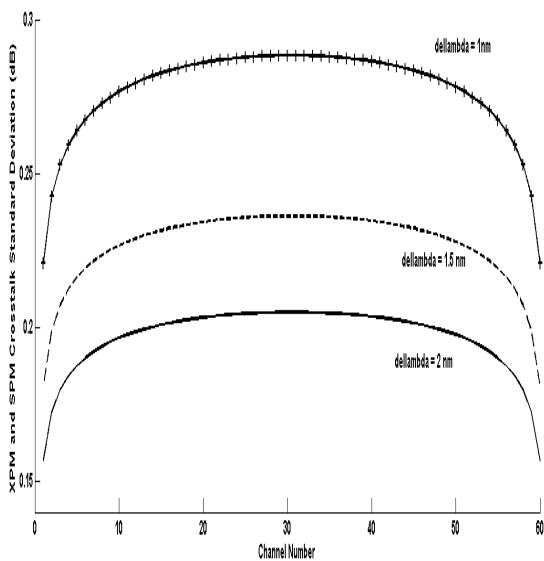


Fig. 3: Variation of crosstalk with channel number for different interchannel separation of the system.

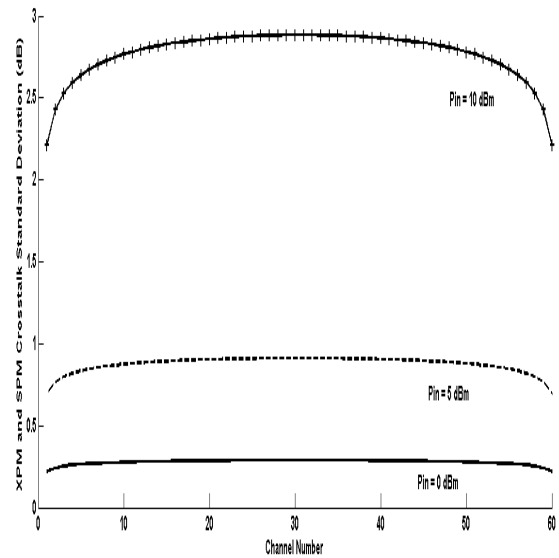


Fig. 4: Variation of crosstalk with channel number for different power input of the system.

analysis and configuration of fiber links is as shown in Fig.1. It is observed that with the decrease in input power of the signals crosstalk decreases. This is clearly evident from the equation of crosstalk variance which is directly proportional to the input power of the signal.

Using the above observation, variation of crosstalk with channel number for various pumping configurations of DRA. The expression of variance of SPM and XPM induced crosstalk can be used to investigate crosstalk in forward pumped DRA by making backward pump P_{PL} strength equal to zero. Similarly to study crosstalk in backward pumped DRA, the strength of forward pumps P_{P0} is made equal to zero. It can be observed from the Fig. 5 that backward pumping scheme suffers minimum crosstalk and is best suited for optical communication among all the possible choices mentioned above from SPM and XPM induced crosstalk point of view.

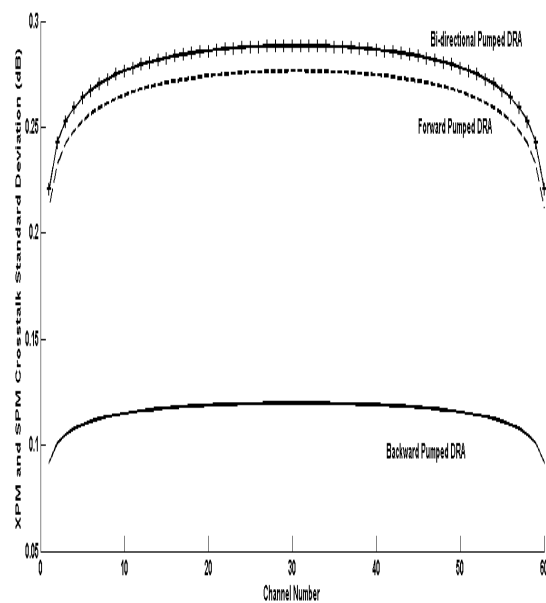


Fig. 5: Variation of crosstalk with channel number for different pumping scheme of DRA.

IV. CONCLUSION

XPM and SPM induced crosstalk has been evaluated in multi-pumped distributed Raman amplifier (DRA). It is observed that maximum crosstalk is suffered by the central channel of WDM system and crosstalk increases with increase in wavelength separation, input power of the signal and bit rate of the signal. Backward pumped DRA suffers minimum crosstalk among the three pumping schemes available.

ACKNOWLEDGMENT

One of the author (Anamika) wishes to acknowledge ISM Dhanbad for encouragement and financial support in conducting the present research work.

APPENDIX

$$\begin{aligned} |H_{ij}(\omega)|^2 &= |M + N + O|^2 \\ &= (M + N + O) \times (M + N + O)^* \\ &= |M|^2 + |N|^2 + |O|^2 + 2 \times \text{Re}(MN^*) + 2 \times \text{Re}(MO^*) \\ &\quad + 2 \times \text{Re}(NO^*) \end{aligned}$$

Substituting the values of M, N and O from equation of $H_{ij}(\omega)$ and simplifying we get the final expression of $|H_{ij}(\omega)|^2$.

The expression of $H_{ij}(\omega)$ and $S_{P_{ij}}(\omega)$ (assuming rectangular NRZ pulse shape) is substituted in equation of variance (σ_x^2). On performing the infinite integration using Tables of Integral and Series [9], we get the expression of variance (σ_{XPM}^2).

$$\sigma_{XPM}^2 = (F(T) + F_1(T) + F_2(T) + F_3(T) + F_4(T) + F_5(T))$$

Where

$$\begin{aligned} F(T) &= \frac{C^2 P_0^2}{\alpha^3 L_w} \{ (1 - e^{-\alpha L})^2 P_1(\alpha) + e^{-\alpha L} P_2(\alpha) \} \\ F_1(T) &= \frac{C^2 K'^2 P_0^2}{8\alpha^3 L_w} \{ (1 - e^{-2\alpha L})^2 P_1(2\alpha) + e^{-2\alpha L} P_2(2\alpha) \} \\ F_2(T) &= \frac{8C^2 K'^2 P_0^2 e^{-2\alpha L}}{3d_{ij}^2 T} \min\left(\frac{T^2}{4}, \frac{d_{ij}^2 L^2}{4}\right) \left\{ 3 \max\left(\frac{T}{2}, \frac{d_{ij} L}{2}\right) - \right. \\ &\quad \left. \min\left(\frac{T}{2}, \frac{d_{ij} L}{2}\right) \right\} \\ F_3(T) &= \frac{-C^2 K' P_0^2}{\alpha^3 L_w} \left[(1 + e^{-3\alpha L} - e^{-2\alpha L} - e^{-\alpha L}) \left(\frac{P_1(\alpha)}{3} + \right. \right. \\ &\quad \left. \left. \frac{2P_1(2\alpha)}{3} \right) + \frac{1}{2} (e^{-\alpha L} + e^{-2\alpha L}) (P_2(\alpha) + \frac{2P_2(2\alpha)}{3}) \right] + \\ &\quad \frac{C^2 K' P_0^2}{24\alpha^3 L_w} \left(\frac{P_3(2\alpha)}{4} - P_3(\alpha) \right) \\ F_4(T) &= \frac{C^2 K'' e^{-\alpha L} P_0^2}{\alpha^3 L_w} [(1 + e^{-\alpha L}) P_2(\alpha) - (1 - e^{-\alpha L}) P_3(\alpha)] + \\ &\quad \frac{C^2 K'' e^{-\alpha L} P_0^2 T}{\alpha d_{ij}} [(1 - e^{-\alpha L}) P_4(T, d_{ij} L)] \\ F_5(T) &= \frac{C^2 K'' e^{-2\alpha L} P_0^2}{8\alpha^3 L_w} [(1 + e^{-2\alpha L}) P_2(2\alpha) - (1 - e^{-2\alpha L}) P_3(2\alpha)] + \\ &\quad \frac{C^2 K'' e^{-2\alpha L} P_0^2 T}{2\alpha d_{ij}} [(1 - e^{-2\alpha L}) P_4(T, d_{ij} L)] \end{aligned}$$

And

$$P_1(\alpha) = (e^{-\alpha L_w} + \alpha L_w - 1)$$

$$P_2(\alpha) = 2(e^{-\alpha L_w} + e^{-\alpha L} - 1) - (e^{-\alpha|L+L_w|} + e^{-\alpha|L-L_w|} + \alpha(|L+L_w| - |L-L_w|))$$

$$P_3(\alpha) = [\text{sign}(d_{ij} L)(2 - 2e^{-\alpha L}) + \text{sign}(T - d_{ij} L)(1 - e^{-\alpha|L-L_w|}) - \text{sign}(T + d_{ij} L)(1 - e^{-\alpha|L+L_w|})]$$

$$P_4(T, d_{ij} L) = \text{sign}(d_{ij} L + 2T) \left(\frac{(d_{ij} L)^2}{8} + \frac{(d_{ij} L)T}{2} + \frac{T}{2} \right) - \text{sign}(d_{ij} L) \frac{(d_{ij} L)^2}{4} + \text{sign}(-d_{ij} L + 2T) \left(\frac{(d_{ij} L)^2}{8} + \frac{(d_{ij} L)T}{2} - \frac{T^2}{2} \right)$$

$$L_w = \frac{T}{|d_{ij}|}$$

REFERENCES

- [1] G.P. Agrawal, Nonlinear Fiber Optics, 3rd ed. San Diego, CA: Academic, 2001.
- [2] J.Toulose, "Optical Nonlinearities in Fibers: Review, Recent Examples and System Applications, *IEEE J. of Lightwave Technology*, Vol.23, pp.3625-1498, 2005.
- [3] M.N.Islam, "Raman amplifiers for telecommunications", *IEEE J. of Sel. Topics in Quantum Electronics*, Vol. 8, pp. 548-558, May/Jun. 2002.
- [4] S. Namiki and Y. Emori, "Ultra Broad Band Raman Amplifiers pumped and gain equalized by Wavelength-Division Multiplexed High-Power Laser Diodes", *IEEE J. of Sel. Topics in Quantum Electronics*, Vol. 7, pp. 3-16, Jan/Feb. 2001.
- [5] Keang-PoHo, "Error probability of DPSK Signal due to Cross-Phase Modulation Induced Nonlinear Phase Noise", *IEEE J. of Sel. Topics in Quantum Electronics*, Vol. 10, pp. 3421-427, Mar/Apr. 2004.
- [6] M. S. Kao and J.Wu, "Signal light Amplification by Stimulated Raman Scattering in an N-Channel WDM Optical Fiber Communication System", *IEEE J. of Lightwave Technol.*, Vol.9, No.9, pp. 1290-1299, Sep.1989.
- [7] A. H. Gnauck, G. Raybon, S. Chandrasekhar, J. Leuthold, C. Doerr, L. Stulz, and E. Burrows, "25 40-Gb/s co polarized DPSK transmission over 12 100-km NZDF with 50-GHz channel spacing," *IEEE Photon. Technol. Lett.*, vol. 15, no. 3, pp. 467-469, 2003.
- [8] C. Rasmussen, T. Fjelde, J. Bennike, F. Liu, S. Dey, B. Mikkelsen, P. Mamyshev, P. Serbe, P. van de Wagt, Y. Akasaka, D. Harris, D. Gapontsev, V. Ivshin, and P. Reeves-Hall, "DWDM 40G transmission over trans-Pacific distance (10,000 km) using CSRZ-DPSK, enhanced FEC and all-Raman amplified 100 km Ultra-Wave fiber spans," in *Optical Fiber Commun. Conf. (OFC '03)*, postdeadline paper PD18.
- [9] I.S.Gradshetyn and I.M.Ryzhik, "Tables of integrals, Series and Products," 6th Edition, San Diego, CA: Academic 2000.

STUDY OF MULTIPULSING PHENOMENA IN Q-SWITCHED FIBER LASERS

Manas Srivastava*, Deepa Venkitesh, Balaji Srinivasan
 Department of Electrical Engineering, IIT Madras, Chennai 600036, India
 *ee10s044@ee.iitm.ac.in

Abstract: We have studied the multi-pulsing phenomena in Q-switched fiber lasers using a finite difference time domain (FDTD) model. Our studies show that such phenomena occurs for switching times smaller than the cavity round-trip times and is attributed to residual population inversion after one round trip. Addition of a suitable length of fiber in the cavity aids in reducing multi-pulsing, while retaining smaller pulse widths.

1. INTRODUCTION

High energy pulses with short durations find applications in material processing, laser based ranging and distributed sensing [1]-[3]. Q-switching is a commonly used technique to generate such laser pulses by introducing a suitable loss-modulator in the laser cavity. The gain medium and the cavity itself are modeled as bulk systems in the conventional models of Q-switched lasers [4]. Since the cavity length in a fiber laser is comparatively large, it is essential to understand the spatial evolution of pulses in the cavity in order to understand the complete pulse dynamics. This is possible with a finite difference time domain (FDTD) model.

In this paper, the results of FDTD simulation model of an Erbium doped fiber amplifier (EDFA) based Q-switched fiber ring laser are presented. Simulations are carried out for various combinations of modulation parameters such as switching time (τ) and length of the cavity. It is found that for switching rates comparable to the cavity roundtrip time, the phenomenon of multipulsing is observed. This is further analyzed in this work and suggestions to suppress multipulsing have been provided.

2. SIMULATION MODEL

The gain medium in the cavity is Erbium, which is modeled as a three level system. The energy gap between the ground state and the upper excited state corresponds to a wavelength of 980 nm, which is used as pump wavelength. This energy state has a very short lifetime, and the electrons in this level undergo non-radiative decay and relax to the metastable state which has a lifetime of 10 ms. The energy gap between the metastable state and ground state corresponds to a wavelength range of 1520 nm to 1570 nm and these two energy states constitute the lasing level. Hence, Erbium can be modeled as a two-level system.

The ring cavity of total length 8 m (cavity-roundtrip time (t_r) of 40 ns) shown in Fig. 1 is modeled. The gain medium is a 1.5 m long EDFA with pump absorption 9 dB/m. An isolator is included in the cavity to ensure unidirectional propagation of signal power and for the suppression of backward propagating amplified spontaneous emission (ASE). A

Wavelength division multiplexer (WDM) is used to combine the pump power with the signal power. A 3-dB coupler is used as the output coupler. The acousto-optic modulator (AOM) is introduced in the cavity to switch the cavity losses from high value to low value.

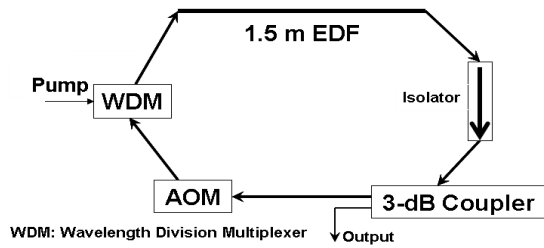


Figure 1. Schematic of the Q-switched ring laser cavity

The following differential equations are used to model the laser system:

$$\frac{dN_1}{dt} = -R_{13}P_pN_1 - R_{12}P_sN_1 + R_{21}P_sN_2 + \frac{N_2}{\tau_f} \quad (1)$$

$$\frac{\partial P_p}{\partial z} + \frac{1}{v} \frac{\partial P_p}{\partial t} = b_p P_p \quad (2)$$

$$\frac{\partial P_s}{\partial z} + \frac{1}{v} \frac{\partial P_s}{\partial t} = b_p P_p \quad (3)$$

$$\frac{dP_{ASE}}{dz} = b_s P_{ASE} + \sigma_{es} N_2 P_{ASE}^0 \quad (4)$$

$$P_{ASE}^0 = 2h\nu\Delta\nu \quad (5)$$

Equation (1) is the population rate equation where N_1 and N_2 are the ground state and excited state populations (in m^{-3}) respectively and total Erbium concentration in the EDF is $N_0 = N_1 + N_2$. P_p and P_s are the pump and signal powers (in W) respectively. R_{13} is the rate of pump absorption, R_{12} is the rate of signal absorption at ground state and R_{21} is the rate of stimulated emission at signal wavelength (in $\text{W}^{-1}\text{s}^{-1}$). These rates are defined as follows:

$$R_{13} = \frac{\sigma_{ap}}{A_{eff} h\nu_p} \quad (6)$$

$$R_{12} = \frac{\sigma_{as}}{A_{eff} h\nu_s} \quad (7)$$

$$R_{21} = \frac{\sigma_{es}}{A_{eff} h \nu_s} \quad (8)$$

A_{eff} is the effective area of cross-section area of core of EDF, ν_p and ν_s are the pump and signal frequencies. σ_{ap} , σ_{as} and σ_{es} are the absorption cross section for pump, absorption cross section for signal and emission cross section of signal wavelengths respectively.

Spontaneous emission lifetime of excited state is τ_f . Equations (2) and (3) are the pump and signal propagation equations respectively. The velocity of light in the fiber is given as v and the gain coefficients for pump and signal are given as b_p and b_s . Equation (4) gives the spatial variation of ASE in the forward direction, where P_{ASE} is the total forward propagating ASE, σ_e is emission cross section of the signal and P_{ASE}^0 is the noise power in the bandwidth $\Delta\nu$ around the signal frequency ν .

The equations (1)-(4) are solved in tandem using the FDTD technique. The stability factor of the finite difference scheme is chosen as 0.9 to avoid numerical oscillations. Size of the space step is chosen to be 0.03 m and the corresponding size of time step is 0.135 ns. The tolerance limit of error is taken as 2%.

Within the EDF, the interaction between the pump (980 nm) and the signal at 1530 nm with amplified spontaneous emission (ASE) noise bandwidth of 5 nm is modeled through the standard rate equations. The

Erbium doping concentration N_0 of $2.65 \times 10^{25} \text{ m}^{-3}$ and τ_f of 10 ms is used for the simulations. The EDF has a core radius of 2.2 μm and numerical aperture 0.29.

In order to model the Q-switching effect, the loss of AOM is varied from 50 dB to 2 dB over a switching duration (τ). The nature of variation is considered to be sinusoidal [5]. When the Q-factor of the cavity is high, the total cavity loss including the AOM loss (2 dB) is 5.9 dB. The simulation is done for a pump power of 300 mW, switching repetition rate of 10 kHz, with the low loss duration of 500 ns. The AOM switching duration is varied to observe and analyse multipulsing in the output pulse.

3. RESULTS AND DISCUSSION

The typical design requirement of a Q-switched laser is to achieve short pulses of high peak powers. This is typically possible by increasing the Q-factor of the laser cavity rapidly. However, the switching transient of the AOM plays an important role in deciding the nature of the Q-switched pulse. For certain cases the output is found to be multipulsing. The multipulsing behaviour of the Q-switched laser pulse and its relation with the switching transient time is established in this section. Subsequently, methods to suppress multipulsing and to limit the output to a single narrow pulse are discussed.

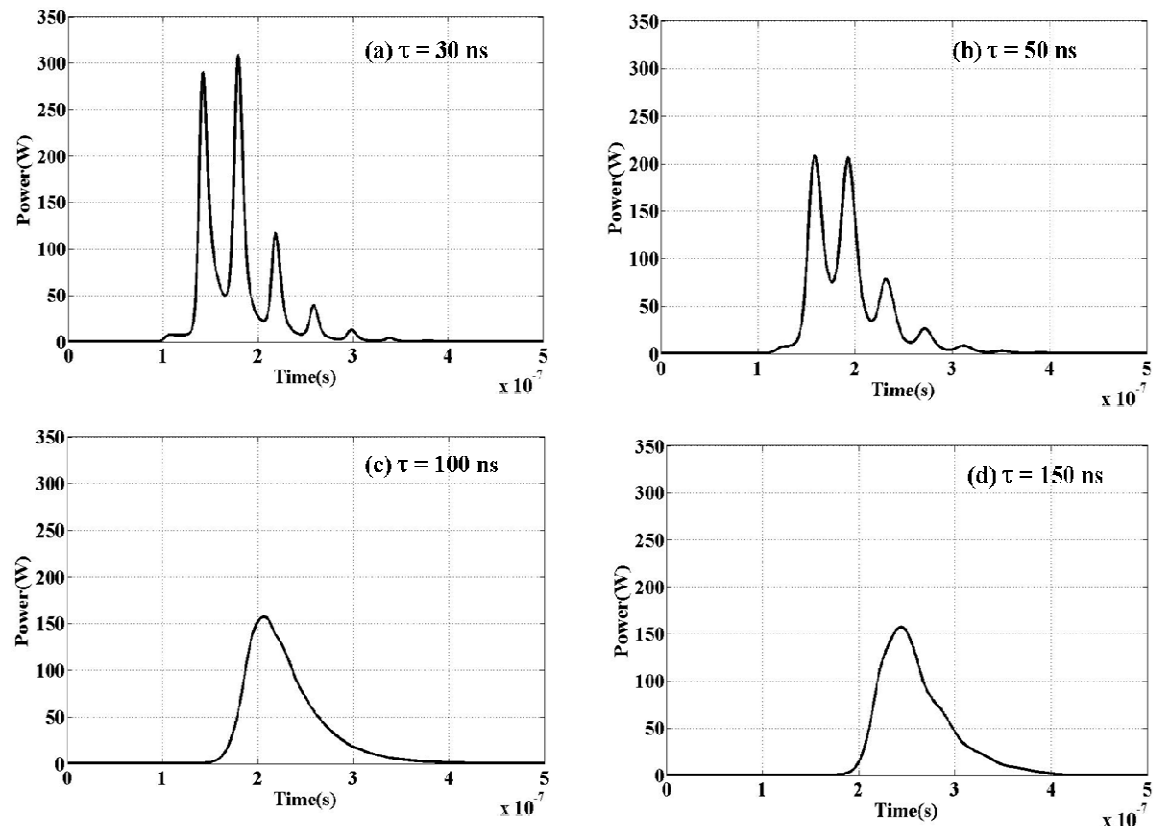


Figure 2. Output power from the Q-switched cavity for AOM switching time varying from 30 ns to 150 ns

3.1 Variation of switching duration

The simulation was done for switching duration (τ) varying from 30 ns to 150 ns. It is seen that for τ less than the cavity roundtrip time, the output pulse consists of several peaks. As τ increases, the ripples in the output also decrease. For τ considerably larger than (4 times) the roundtrip time, the output is found to be a smooth pulse.

Fig. 2 shows the output pulse in the steady state, for τ of 30 ns, 50 ns, 100 ns and 150 ns. The origin indicates the time at which AOM is switched ON. It is evident from fig. 2(c) and 2(d) that when the switching is slow (100-150 ns), a smooth pulse is obtained, whereas in case of fast switching (30 ns) the output pulse breaks into multiple pulses, as shown in fig. 2(a).

When the switch (AOM) starts closing (represented by time = 0 in the plots), the power fed back to the EDF gradually increases. Initially, the noise due to spontaneous emission, which is of the order of nano-Watts, is fed back to the cavity. This noise power gets amplified over several roundtrips and then appears at the output as a pulse. This explains the delay between the beginning of switching duration and building up of the pulse.

The reason for multipulsing can be understood by observing the dynamic output of the simulation. When the switch is closed rapidly (within one roundtrip time), noise power is fed back to EDF as a single

bunch of photons generated during the switching transient time, which is further amplified in the EDF, resulting in the formation of a pulse. However, this power generated is not sufficient to deplete the excited state population in a single roundtrip. It takes several roundtrips to deplete the upper lasing level. This results in the ripples at the output, which are found to be separated exactly by cavity round-trip time (40 ns).

In contrast, in the case when the switching time is much greater than the cavity round trip time, the arrival time of the seed photons is spread over several cavity round-trips and hence results in a smooth pulse. This is because the feedback power increases gradually and is amplified continuously, forming a smooth rising edge. The inversion is depleted during the rising edge; hence the pulse decays continuously, thus forming a smooth trailing edge. The pulse width (FWHM) is observed to be 70 ns.

In case of slow switching, the loss variation takes place over a longer period of time. In this duration, some of the energy stored in the EDFA is lost. Hence, for slower switching, the peak power is found to be smaller than that in case of faster switching.

3.2 Methods to suppress multipulsing

One method of limiting the output to a single pulse can be to switch the cavity loss from low to high value as soon as the first large pulse of the multipulse (say,

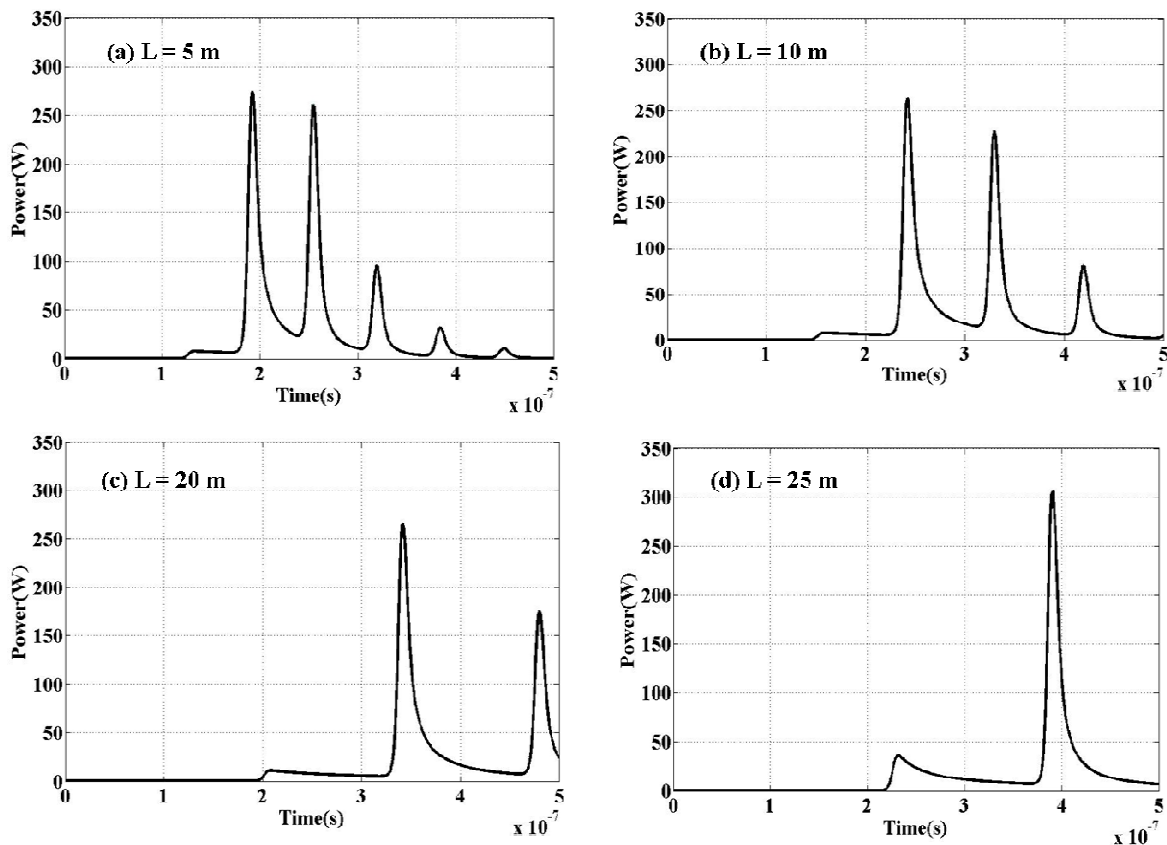


Figure 3. Output power from the Q-switched cavity including buffer fiber of length L .

at 160 ns in case of the output corresponding to fig.2 (a) is obtained. This is possible by reducing the duty cycle of the loss modulation. However, reducing the duty cycle results in the increase of pumping duration, hence the gain built up in the EDF is larger. Also, the cavity is switched back to high loss state when the gain in the EDF is not completely depleted, and considerable amount of residual inversion is left in the cavity. So the output during the subsequent Q-switch can be very different from expected. Hence this requires a very fine control over the duty cycle of loss modulation.

A practical solution is to introduce a delay between the adjacent ripples of the output and to switch the cavity off during this delay. This can be achieved by adding a certain length of standard single mode fiber in the cavity, to act as a buffer which increases the cavity roundtrip time. The buffer fiber is introduced between the output coupler and the AOM. The residual pulse undergoes a propagation delay in the buffer fiber, and before it reaches the EDF, the AOM is switched off. Hence the output is limited to a single, large pulse with a much smaller pulse width.

The length of the buffer fiber can be estimated by analyzing the inter-relationship of the low-loss duration, switching duration and cavity round-trip time. The low-loss duration should accommodate 2-3 cavity round-trips, during which, the pulse with high peak power is obtained. Thereafter, the AOM should be switched off during the subsequent round-trip, before the residual signal power reaches the EDF again. Considering a low-loss duration of 500 ns and τ of 30 ns, a suitable value of cavity round-trip time is 150 ns, which corresponds to a total cavity length of 30 m. This can be realized using a buffer fiber of length 22 m in the 8 m ring cavity.

FDTD simulations for the cavity are done after including the buffer fiber for 300 mW pump power, 10 kHz repetition rate, 500 ns low loss duration and 30 ns switching duration. The length of buffer fiber is taken to be 5 m, 10 m, 20 m and 25 m. The steady state results for the same are shown in fig.3.

It is evident from the results that the separation between the subsequent ripples increases when the length of the buffer fiber increases, owing to the increase in cavity roundtrip time. Buffer fiber length as long as 25 m (fig. 3(d)) introduces sufficient delay between the pulses to eliminate multiple pulses. The residual signal power decays in the cavity due to switching off of the AOM. Thus it is prevented from undergoing amplification in the EDF. Hence the output is limited to a single pulse with large peak power (300 W) and small pulse width (12 ns).

It is observed that the peak power obtained from the cavity having 25 m of buffer fiber is higher. This is because the delay caused by the buffer fiber is longer, and hence the inversion built up in the EDF during this delay is higher. So, the initial ASE power is

amplified to higher levels. Further investigations to validate this understanding are currently being done.

4. CONCLUSION

The analysis of multipulsing behaviour of Q-switched fiber laser pulses is done using the FDTD model for fiber ring cavity. Multipulses or ripples in the output are attributed to the small switching duration of the loss modulator (AOM) when compared to the propagation time in the cavity. With fast switching, high peak power pulses with ripples are obtained. In case of slower switching, the pulse is smoothed out but the peak power is low due to slow loss variation. In order to limit the output to a single short pulse, a buffer fiber is introduced in the cavity to increase the delay between two successive peaks in the multiple pulse structure. It is found that a proper choice of length of the buffer fiber results in a short pulse of high peak power. Efforts to validate the simulation results through experimental implementation are underway.

ACKNOWLEDGEMENTS

The authors are grateful to Anish Bekal, PhD scholar, Department of Electrical Engineering at IITM for fruitful discussions on the theory and simulations of fiber lasers.

REFERENCES

- [1] U. Sharma, C.-S. Kim, and J. U. Kang, "Highly stable tunable dual-wavelength q-switched fiber laser for dial applications," *IEEE Photonics Technology Letters* **16**, 1277-1279 (2004).
- [2] Y. Kaneda, Y. Hu, C. Spiegelberg, J. Geng, and S. Jiang, "Single-frequency, all-fiber q-switched laser at 1550-nm," *Advanced Solid-State Photonics* (2004).
- [3] G. Lees, A. Hartog, A. Leach, and T. Newson, "980nm diode pumped erbium³⁺/ytterbium³⁺ doped q-switched fibre laser," *Electronics Letters* **31**, 1836-1837 (1995)
- [4] C. Gaeta, M. Dignonnet, and H. Shaw, "Pulse characteristics of q-switched fiber lasers," *Journal of Lightwave Technology* **LT-5** 1645-1651 (1987).
- [5] S. Adachi and Y. Koyamada, "Analysis and design of q-switched erbium-doped fiber lasers and their application to otdr," *Journal of Lightwave Technology* **20** 1506-1511 (2002).

ALL-FIBER THULLIUM DOPED FIBER LASER BY UTILIZING PUMP AT 980 nm

Atasi Pal^a, Shyamal Das^a, Shu Ying Chen^b, Tong Sun^b, Kenneth T V Grattan^b, Ranjan Sen^a

^aCSIR-Central Glass & Ceramic Research Institute, 196, Raja S.C. Mullick Road, Kolkata, India.

^bSchool of Engineering & Mathematical Sciences, City University London, UK

atasi@cgcri.res.in

Abstract: A compact and economic all-fiber laser in the 2 μm wavelength range has been developed by utilizing commercial pump source at 980 nm.

1. INTRODUCTION

The broad emission spectrum (~ 1.7 to ~ 2.1 μm) of Thulium (Tm) in silica glass under excitation at 800 nm and 1600 nm [1] provides wide flexibility in laser operating wavelength and overlaps with a strong water absorption band and absorption signature of many toxic gases that allows for bio-molecule sensing and toxic gas detection. Such applications require a compact and stable source.

The present work focuses on the development of fiber Bragg grating (FBG) based Tm doped fiber laser in the 2 μm wavelength range by utilizing commercial pump source at 980 nm.

2. EXPERIMENTS AND RESULTS

The schematic of the FBG based laser system is shown in Fig.1. Composition of Erbium (Er) doped and Tm doped fiber has been standardized for emission at 1.6 μm and 2 μm range respectively.

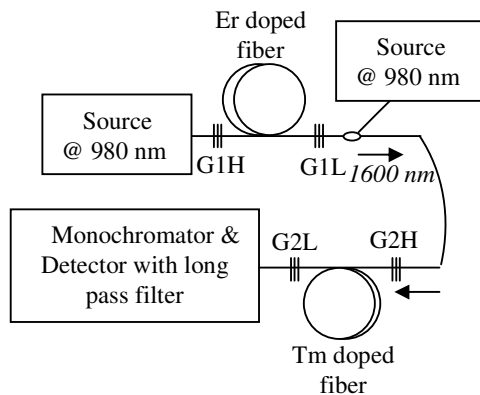


Fig.1. Schematic of the FBG based laser system. G1H and G1L: FBG @ 1600 nm with High and Low reflectivity respectively. G2H and G2L: FBG @ 1874 nm with High and Low reflectivity respectively

The intermediate Er doped fiber laser at 1600 nm is effective for direct excitation of Tm for emission in the 2 μm range.

The absorption and fluorescence spectrum as well as the laser spectrum with peak at 1874 nm is shown in Fig.2 (a) while Fig.2 (b) indicates the variation of laser power with launched pump power at 980 nm. The obtained laser output power of 6 mW with high

spectral purity is effective for toxic gas (like CO_2 , NO, CO) sensing.

Incorporation of grating pair within the emission wavelength range can provide lasing in the range of 1.65 μm to 2 μm . The linear increment of laser power with pump indicates that the laser power can be scaled up by utilizing higher pump power. Further work on the power scaling and efficiency enhancement is going on.

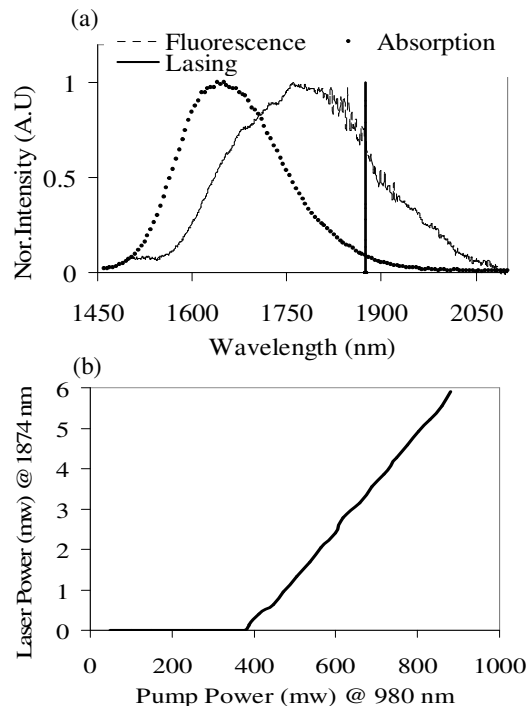


Fig.2. (a) Absorption, Fluorescence and Lasing spectrum from Tm doped fiber (b) Variation of laser power with launched pump power

ACKNOWLEDGEMENT

The authors wish to acknowledge the support of CSIR, India and EPSRC, UK for funding

REFERENCES

- [1] S. D. Jackson and T. A. King, "High-power diode-cladding-pumped Tm doped silica fiber laser," *Opt. Lett.* 23, 1462–1464 (1998)

RARE EARTH DOPED OPTICAL FIBER FABRICATION BY MCVD PROCESS

Ranjan Sen*

CSIR - Central Glass & Ceramic Research Institute, 196, Raja S.C. Mullick Road, Kolkata, India.

*rsen@cgcri.res.in

Abstract: The key issues involved in fabrication of rare earth doped fibers by solution doping and vapor phase doping techniques have been reviewed to assess their suitability for making fibers for various applications.

1. INTRODUCTION

Rare earth (RE) doped optical fiber is now the key component behind the success of a number of enabling technologies in Photonics. Elements such as erbium (Er), ytterbium (Yb), neodymium (Nd), thulium (Tm) and europium (Eu) are the optically active ingredients at the heart of many lasers, optical amplifiers and phosphors. There has been rapid progress in this field during the last few years. The increasing demand of the fibers led to intensive R&D effort to improve the fiber performance. In contrast to the standard telecommunication fibers, active fibers demand a greater variety of materials and structures in order to realize superior characteristics of amplification and lasing at a variety of operating wavelengths.

Conventionally, the REs are impregnated into the core by solution doping or vapor phase doping process. The majority of RE doped fibers for various applications are currently prepared by MCVD (modified chemical vapor deposition) and solution doping technique, an established method for fabricating Er doped fibers for amplifiers. However, because of limitations in developing a large core by this method as required for laser fibers, the vapor phase method is gaining importance. The main issues behind fabrication of fibers by each method along with their suitability will be reviewed in this article.

2. SOLUTION DOPING PROCESS

The solution doping process involves two major steps viz. deposition of porous core layer within a silica tube by MCVD process and impregnation of the porous deposit with a solution containing salts of RE and a codopant, mostly Al (Fig. 1). The soaked layer is subsequently dehydrated and sintered to obtain the RE doped core. The tube is finally collapsed to produce the preform and draw the fibers conventionally in a fiber drawing tower. The main advantage of this method is simplicity and flexibility in doping various REs or their combinations by changing the solution composition.

The critical step in this process is the deposition of uniform soot layer of suitable composition and porosity which serves as the precursor for solution impregnation. The variation in porosity as well as pore size distribution leads to poor control over RE

incorporation and inhomogeneity along the length of the preform/fiber. Unless the soot layer morphology is analyzed and controlled by suitably adjusting the deposition conditions, the fiber performance cannot be improved. On the other hand the composition of the soaking solution, the Al/RE proportion, the nature of solvent, dipping period etc. are the controlling factors during the solution doping step to achieve the desired properties in the fiber. Thus, optimization of the process parameters is essential to achieve the preferred fiber properties in a reproducible manner.

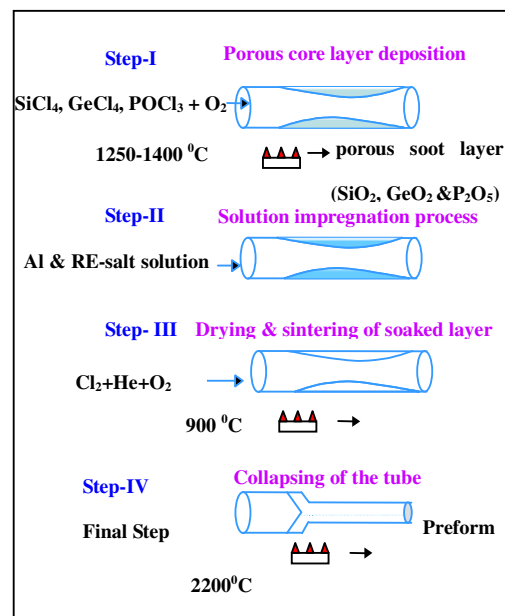


Fig 1: Schematic diagram of solution doping process

A systematic investigation carried out in this context by our group [1,2] reveals that for fabricating an Er doped germanosilicate core fiber with numerical aperture of 0.20 or above, a process condition where the porous core is deposited at 1250-1260°C, the soaking solution contains 0.3 M AlCl_3 + 0.01 M ErCl_3 made in ethanol and dipping time is selected as 45 minute, is observed to be optimum and the fiber core is found to contain around 650 ppm of Er^{3+} ion with appreciably good doping uniformity along the length. An important effect first time observed is the interdependence of Al ion concentration with the RE incorporation into the core because of a cooperative

phenomenon. It offers a new approach of controlling RE concentration in the fiber. A process reproducibility of about 80% has been achieved by maintaining the optimized fabrication conditions.

3. VAPOR PHASE DOPING TECHNIQUE

In this process, volatilized RE precursors are transported and delivered directly to the hot reaction zone by a system of heated sublimators so that RE doping takes place simultaneously with the deposition of SiO₂ and other dopants [3-5]. The MCVD system consists of one main gas cabinet which delivers Silicon Tetrachloride (SiCl₄) and other refractive index modifying reagents while one high temperature vapor delivery unit is used for the sublimation and delivery of AlCl₃ and RE chelate compounds. The advantages of the technique lie in the “in-situ” RE incorporation which reduces impurities in the preform, better control over the process parameters, ability of fabricating large mode area (LMA) fibers by increasing number of layers during core deposition and enhanced repeatability over solution doping method. However, condensations of precursor materials, decomposition of RE chelate compounds, variation in RE concentrations over the preform length etc. were the main critical experimental challenges which restricted proper utilization of the process to its full potential. In addition, there was

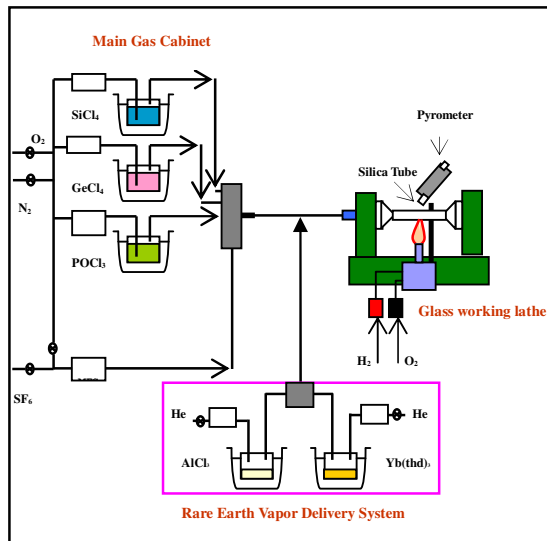


Fig 2: Schematic of vapor phase doping technique

lack of availability of a reliable system that can ensure smooth transportation of volatilized RE precursors during deposition step.

A state-of-the-art facility has recently been established in our Institute (OFC-12 MCVD system of Nextrom Technology, Finland) for this purpose, a schematic of which is shown in Fig.2. The system has been utilized successfully to fabricate Yb-doped aluminosilicate

fibers of various designs by optimizing the process parameters.

Preforms with length up to 400 mm and diameter of 10.5–14.6 mm were produced with numerical aperture (NA) in the range of 0.08-0.24. The maximum core diameter achieved in the preform is 4.2 mm. For the first time, the Al⁺³ could be increased beyond 22 mol% in the core. The core diameter of 36 μm (w.r.t 125 μm) has been achieved with NA of 0.11. The Yb⁺³ concentration has been varied in the range of 0.10 to 1.3 mol%. A number of good quality preforms of different designs and compositions have been successfully fabricated with good repeatability.

4. CONCLUSION

Both solution doping and vapor phase doping techniques have unique advantages which make them widely acceptable for making RE doped preforms and fibers. The challenges to achieve the desired fiber properties as well as reproducibility by each method have been discussed along with recent advances. The selection of a particular technique depends on its suitability to fabricate the targeted fiber structure and composition needed for a specific application.

ACKNOWLEDGEMENT

The author wishes to acknowledge the financial support of CSIR, India and DIT, India.

REFERENCES

- [1] Dhar, A., Paul, M. C., Pal, M., Mondal, A. Kr., Sen, S., Maiti, H. S. & Sen, R. (2006), Characterization of porous core layer for controlling rare earth incorporation in optical fiber, *Optics Express*, Vol. 14, No. 20, (October 2006), pp. 9006-9015, ISSN 1094-4087.
- [2] Dhar, A., Paul, M. C., Pal, M., Bhadra, S. K., Maiti, H. S. & Sen, R. (2007), An improved method of controlling rare earth incorporation in optical fiber, *Optics Communication*, Vol. 277, (September 2007), pp. 329-334, ISSN 0030-4018.
- [3] Sekiya, E.H., Barua, P., Saito, K., Ikushima, A.J., “Fabrication of Yb-doped silica glass through the modification of MCVD process”, *J. Non-Cryst. Solids* 354(2008) p 4737.
- [4] Kveder, M., Lenardic, B., “Advanced Vapor-Phase Doping Method Using Chelate Precursor for Fabrication of Rare Earth - Doped Fibers” *OSA* (2009).
- [5] Sahu, J. K. et al., “Rare-Earth Doped Optical Fiber Fabrication Using Novel Gas Phase Deposition Technique”, *OSA* (2010).

SUPERCONTINUUM GENERATION IN PHOTONIC CRYSTAL FIBERS

K. Porsezian
Department of Physics
Pondicherry University
Pondicherry 605 014.
India

Supercontinuum generation (SCG) using photonic crystal fiber (PCF), which relies on high nonlinearity and adjustable zero group velocity dispersion of PCF, is the technology of choice for the next generation of ultrabroadband sources of coherent light. SCG in a PCF was discovered by Ranka as a means to generate a broad spectrum with two octave width at unprecedentedly low input pulse energies. Since then it has attracted extensive attention for both its fundamental and application aspects which was mainly motivated by its nonlinear applications in spectroscopy, telecommunication, optical frequency technology, optical coherence tomography and sensors. SCG is a process which dramatically broadens the spectral shape from the narrow initial spectrum, mainly induced by soliton fission and pulse breaking arising due to higher-order effects of soliton-related dynamics such as higher-order linear dispersion terms, Raman soliton self-frequency shift and spectral recoil. We will discuss the nonlinear propagation of femtosecond pulses in liquid-core photonic crystal fibers (LCPCF) filled with CS₂. The effect of slow nonlinearity due to reorientational contribution of liquid molecules on broadband SCG in the femtosecond regime is studied using appropriately modified nonlinear Schrodinger equation.

To analyze the quality of the pulse, we perform the stability analysis and study coherence of supercontinuum pulse numerically. We also show that the response of the slow nonlinearity not only enhances broadening of the pulse and changes the dynamics of the generated solitons, but also increases coherence of the pulse. Then, we will explain the SCG on the basis of modulational instability (MI) in liquid-core photonic crystal fibers (LCPCF) with CS₂-filled central core. The effect of saturable nonlinearity of LCPCF on SCG in the femtosecond regime is studied using appropriately modified nonlinear Schrodinger equation. We also compare the MI induced spectral broadening with SCG obtained by soliton fission. To analyze the quality of the pulse broadening, we study the coherence of SC pulse numerically. I will also demonstrate that the response of the saturable nonlinearity suppresses the broadening of the pulse. We also conclude that the MI induced SCG in the presence of saturable nonlinearity degrades the coherence of the SCG pulse when compared to unsaturated medium.

SLOWLIGHT INDUCED SOI PHOTONIC CRYSTAL WAVEGUIDES & DEVICES

R. K. Sinha

TIFAC-Centre of Relevance and Excellence in Fiber Optics and Optical Communication,
Department of Applied Physics, Delhi Technological University (Formerly Delhi College Of Engineering,
University of Delhi), Bawana Road, Delhi-110042, India

Abstract: Slow light in photonic crystals offers a promising solution for buffering and time-domain processing of optical signals. It also offers the possibility for spatial compression of optical energy and the enhancement of linear and nonlinear optical effects.

Photonic crystals (PhCs) with photonic bandgap (PBG) properties have attracted much attention as a possible platform for densely integrated photonic circuits and novel photonic functionality. By carefully engineering the photonic dispersion relationship, one may obtain unique opportunities for realization of devices that exploit slow light effects. PhC channel waveguides can be used as defect mode slow light structures. Slow light, which refers to reduction of the group velocity, leads to increased light-matter interaction, thereby enabling increased time-delay for optical signals, which is a key functionality for the processing, storing and buffering desired for all-optical communications and information processing systems. Slow light in PhC waveguide structures is typically accompanied by large amounts of dispersion, which can remove much of the advantage of operating in the slow light regime - because it limits the bandwidth that can be utilized. This bandwidth-dispersion issue can be overcome by tuning the structure towards dispersion-free behaviour. Recently we have demonstrated the feasibility and benefits of using an elliptical air-hole based photonic crystal structure to obtain slow light behaviour [1]. However the tunability of PhC lattices can further be extended and controlled by filling their segments with certain types of liquid crystal (LC) material. This combination offers the possibility of shifting the frequency of the defect modes and tuning the dispersion curves, in order to obtain flat slow modes with low group velocity dispersion. Propagation losses and their dependence on group velocity are another matter of concern. There is little justification in exploring the slow light regime if any advantage obtained is immediately counteracted by excessive losses. These losses include losses due to inefficient coupling which occurs due to the large mismatch at the interface between the slow light PhC waveguide that results from large changes in group index. One way of overcoming the problem of impedance mismatch is to introduce a finite region that firstly couples the light from a ridge or stripe waveguide into a fast mode PhC waveguide and then into the slow mode PhC waveguide [2]. The response of a given material to an incident electromagnetic wave is characterized by the study of induced polarization of the medium. The linear response of the

medium is valid only if the incident radiation is weak. However, if the intensity of incident light increases, polarization of the medium is no longer linear but becomes nonlinear. Therefore in such media, light propagation is controlled by light itself. The concept of nonlinear photonic crystals can be employed by taking the advantage of slow group velocities of light achievable in such structures. In this frame of work, we next, report the effect of slow light on two photon absorption (TPA), free carrier absorption (FCA) and self phase-modulation (SPM) processes in silicon-on-insulator (SOI) photonic crystal (PhC) channel waveguides. It is found, that, in the slow light regime, these nonlinear effects are enhanced and the resulting increase in the induced phase shift can be used to decrease the size and power requirements needed to operate devices such as optical switches, logic gates, etc. However soliton dynamics will dominate the propagation of femtosecond pulses in PhC waveguides when group velocity dispersion (GVD) is strongly anomalous because of large waveguide dispersion. Keeping above facts in view, we have investigated the propagation of light in a nonlinear slow light medium formed by a channel SOI PhC structure having elliptical holes in silicon core. This type of slow light structure has considerable potential for use in photonic device applications such as optical switches, logic gates etc.

REFERENCES

- [1] S. Rawal, R. K. Sinha and R. M. De La Rue, "Slow Light Miniature Devices with Ultra-Flattened Dispersion in Silicon-on-Insulator Photonic Crystal", *Optics Express*, vol. 17, pp. 13315-13325, August 2009
- [2] S. Rawal, R. K. Sinha and R. M. De La Rue, "Slow Light Propagation in Liquid-Crystal Infiltrated Silicon-on-Insulator Photonic Crystal Channel Waveguides" *IEEE/OSA Journ. Light. Tech.*, vol. 28, 2560-2571, September 2010

A SIMPLE AND COMPLETE FORMULATION TO COMPUTE PROPAGATION CONSTANTS OF PHOTONIC CRYSTAL FIBERS AND PREDICT THEIR TOTAL CHROMATIC DISPERSION

(Invited)

¹Dipankar Kundu, ²Somenath Sarkar

¹Department of Electronics and Communication Engineering, St. Thomas' College of Engineering and Technology, 4, Diamond Harbour Road, Kolkata-700 023, India.

^{2,1}Department of Electronic Science, University of Calcutta, 92, A. P. C. Road, Kolkata-700 009, India

E-mail: ¹dipan_kar_k@rediffmail.com

²snsarkar_50@yahoo.com

Abstract: Within the scalar framework, we present a simple and complete formulation of the normalized propagation constants of infinite cladding region of a photonic crystal fiber (PCF) with triangular lattice of air-holes, dependent only on the relative air-hole size. The accuracy of our proposed relationships is depicted by comparing our results with those obtained by Russell. An equivalence between two approaches of Russell and Saitoh is also sought. Then we evaluate the refractive indices of the fundamental space-filling mode (n_{FSM}) in the cladding region of the PCF from Russell's equation and our proposed relations and see two indices to match quite excellently for different values of relative air-hole size and wavelength. Now, we apply our proposed relations to evaluate the total chromatic dispersion in a PCF, treating it as a conventional step index fiber having its core and cladding indices as those of silica and n_{FSM} respectively. On comparison with the available results of Saitoh, we observe our results to match nicely.

Key Words: Photonic crystal fibers, Effective cladding index, Normalized propagation constant, Waveguide dispersion, Chromatic dispersion.

1. INTRODUCTION

Photonic crystal fibers (PCFs) with periodic microstructures in the transverse direction are low loss waveguides[1]. Various numerical simulations have been developed to predict the propagation constants of PCFs. But those are deeply involved, time-consuming and expensive, employing plane wave expansion method[2], finite element method(FEM)[3], multipole method[4] and other intricate methods. However for practical and pedagogic purposes, we need to have a simple and complete formalism to understand and predict the characteristics of PCFs.

If we can easily compute the effective refractive index of the fundamental space filling mode (FSM) in the infinite photonic crystal cladding without any defect in the air-hole and glass matrix, we can have a PCF whose one air-hole is replaced by glass as defect and can treat this PCF as analogous to a conventional

step index fiber (CSF) with cladding refractive index equal to the effective index of FSM. In a formalism [1] in the recent past, an approximate formula of the concerned PCF for a fixed diameter of air-holes and their separation is given for this purpose.

But, it would have been more useful if we had a simple and complete formulation to calculate the effective index of PCFs over the entire range of relevant geometrical parameters in the endlessly single moded region. In this paper, we develop and present such a formulation for the propagation constants of infinite photonic crystal cladding, dependent only on two fundamental geometrical parameters- the air-hole diameter and the hole pitch.

We show the accuracy of our proposed relations by comparing the results for arbitrary PCF parameters, computed from our approach with those from [1].

In addition to the formalism of Russell, there are empirical relations, given by K. Saitoh and M. Koshiba [5], which are obtained from full vector finite

element method. While analyzing PCF characteristics using these two well-known approaches, we are able to see their equivalence.

However, it will be more judicious and acceptable if one uses our complete formulation for the propagation constants as an alternative and simple solution to determine PCF characteristics so that it is easily accessible to the experimentalists. In this connection, we evaluate the effective indices of the fundamental guided mode in PCFs from our proposed relations, treating the PCFs as equivalent CSFs with core and cladding refractive indices replaced by those of silica and n_{FSM} respectively and hence the total chromatic dispersion in PCFs from the evaluated indices. Comparing our results with those obtained from the empirical relations in [5], we observe them to match nicely for arbitrary values of relative air-hole size and wavelength.

2. ANALYSIS

2.1 Normalized Propagation Constant of Infinite Cladding of PCF.

We consider an all-silica PCF with triangular lattice of air-holes of diameter d , running along the whole length of the fiber. The holes are placed symmetrically around a central defect acting as the fiber core which consists of a solid silica region, i.e. an omitted air-hole. The air-hole matrix has lattice constant or hole-pitch Λ . This region acts as the cladding of the PCF like a CSF. This fiber structure remains invariant in the longitudinal direction. Since the core index is greater than the cladding index, the fiber can guide light by total internal reflection as in case of a CSF for longer wavelengths and photonic band gap mechanism for shorter wavelengths.

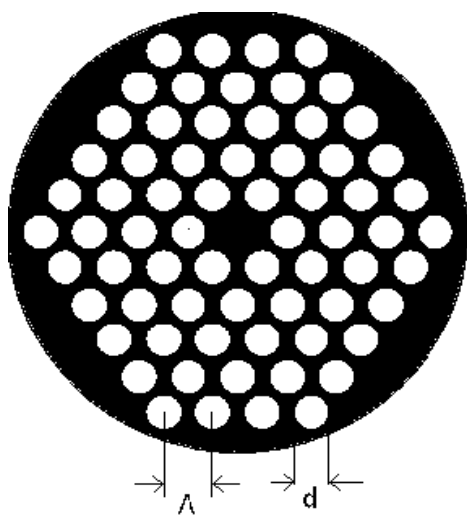


Fig.1 Index-guided photonic crystal fiber

Following Russell's approach, we know that the

propagation constants β of the guided modes in the core of the PCF are governed by the following relation [5]:

$$kn_{co} > \beta > \beta_{FSM} \quad (1)$$

where $k = 2\pi / \lambda$, n_{co} is the index of silica (the core material), β_{FSM} is the propagation constant of the fundamental space-filling mode (FSM) which is the fundamental mode in the infinite photonic crystal cladding without the core or defect. The quantity β_{FSM} is the maximum β allowed in the cladding of the concerned PCF.

The effective cladding index or the refractive index for the FSM is given by

$$n_{FSM} = \frac{\beta_{FSM}}{k} \quad (2)$$

Now, the normalized parameters v and u for the infinite cladding region of the chosen PCF are defined as [1]:

$$v = k\Lambda(n_{co}^2 - 1)^{1/2} \quad (3)$$

$$u = k\Lambda \left(n_{co}^2 - \frac{\beta^2}{k^2} \right)^{1/2} \quad (4)$$

$$\text{with } u^2 + w^2 = v^2 \quad (5a)$$

$$\text{and } \sqrt{b} = \frac{w}{v} \quad (5b)$$

where b is the normalized propagation constant in the defect free infinite photonic crystal cladding.

For any value of v , the value of u can be determined from Russell's equation [1], as given below:

$$wI_1(a_n w) [J_1(b_n u) Y_0(a_n u) - J_0(a_n u) Y_1(b_n u)] + uI_0(a_n w) [J_1(b_n u) Y_1(a_n u) - J_1(a_n u) Y_1(b_n u)] = 0 \quad (6)$$

$$\text{where } a_n = \frac{d}{2\Lambda}, \quad b_n = \left(\frac{\sqrt{3}}{2\pi} \right)^{1/2}.$$

Though, using Eq.(6), Russell has presented only one polynomial fit to u for $d / \Lambda = 0.4$ and $n_{co} = 1.444$, this polynomial fit should be more simple and available for all d / Λ values of practical interest in

endlessly single moded region, where d/Λ is less than 0.45.

We take $n_{co}=1.45$ and find the roots of Eq.(6) for different d/Λ and λ values to determine the values of constant b , and hence propose to write a simple expression as follows :

$$\sqrt{b} = A - \frac{B}{v} \quad (7)$$

where A and B are two different optimization parameters, dependent only on the relative air-hole size d/Λ .

Thus, for each value of d/Λ with variations of λ , we obtain b from the corresponding v values and then using Eq.(6) and Eq.(5). By least square fitting of b in terms of v to Eq.(7) for a particular d/Λ , we generate values of A and B . The various A and B are simulated for various d/Λ in the single mode regime and then empirical relations of A and B in terms of d/Λ are sought as follows :

$$A = a_0 + a_1 \left(\frac{d}{\Lambda}\right) + a_2 \left(\frac{d}{\Lambda}\right)^2 + a_3 \left(\frac{d}{\Lambda}\right)^3 + a_4 \left(\frac{d}{\Lambda}\right)^4 \quad (8)$$

$$B = b_0 + b_1 \left(\frac{d}{\Lambda}\right) + b_2 \left(\frac{d}{\Lambda}\right)^2 + b_3 \left(\frac{d}{\Lambda}\right)^3 + b_4 \left(\frac{d}{\Lambda}\right)^4 \quad (9)$$

where the values of the coefficients a_i (for $i=0$ to 4) and b_i (for $i=0$ to 4) are given in TABLE 1 in the next section.

Now, the effective index of FSM, obtained from Eq.(4) is used to find the V parameter of the PCF which is expressed as [5]:

$$V = \frac{2\pi a_{eff}}{\lambda} (n_{co}^2 - n_{FSM}^2)^{1/2} \quad (10)$$

where λ is the operating wavelength, n_{co} is the core index, a_{eff} is the effective core radius which has been

assumed to be $\Lambda/\sqrt{3}$ [6] with

$$U = \frac{2\pi a_{eff}}{\lambda} (n_{co}^2 - n_{eff}^2)^{1/2} \quad (11)$$

$$W = \frac{2\pi a_{eff}}{\lambda} (n_{eff}^2 - n_{FSM}^2)^{1/2} \quad (12)$$

$$\text{and } V = \sqrt{U^2 + W^2} \quad (13)$$

n_{eff} being the effective index of the fundamental

guided mode and the parameters U and W are called the normalized phase and attenuation constants of the PCF under consideration.

2.2 Equivalence of Two Approaches

Now, our aim is to show the equivalence between two well-known approaches.

According to Russell, the normalized parameters in the infinite PCF cladding are given by Eq.(3) and Eq.(4). The effective V value is given by [6]

$$V = \frac{2\pi\Lambda}{\lambda} (n_{co}^2 - n_{FSM}^2)^{1/2} \quad (14)$$

whereas according to Saitoh and Koshiba [5], the V parameter is given by Eq.(10).

Therefore, there is a difference between the core radii of the two equations by a factor of $1/\sqrt{3}$. So, the hole pitch Λ (same as the core radius approximately) in Eq.(14) has been replaced by $\Lambda/\sqrt{3}$ in Eq.(10). This means the V parameter, given in [5], [7] is $1/\sqrt{3}$ times the value of effective V parameter in [6].

2.3 Chromatic Dispersion in PCFs

Then, we use Eq.(10) to compute the total chromatic dispersion of the aforesaid PCF. Treating the PCF as a CSF, we take the effective index n_{FSM} of the infinite cladding of PCF as the refractive index of cladding of the equivalent CSF and n_{co} of the PCF as the refractive index of the core of CSF.

The corresponding V parameter is given by,

$$V = \frac{2\pi a}{\lambda} (n_{co}^2 - n_{FSM}^2)^{1/2} \quad (15)$$

where a is the radius of core of the equivalent CSF, which we take to be $\Lambda/\sqrt{3}$.

The effective refractive index of the fundamental guided mode n_{eff} of the equivalent CSF is obtained from the roots of the concerned equation for that mode in a CSF in usual way.

The waveguide dispersion parameter D_w at a particular wavelength is found from the following equation:

$$D_w = -\frac{\lambda}{c} \frac{d^2 n_{eff}}{d\lambda^2} \quad (16)$$

where c is the velocity of light in vacuum.

The material dispersion parameter D_m is obtained from the well-known Sellmeier relation [8], given below :

$$n(\lambda) = C_0 + C_1\lambda^2 + C_2\lambda^4 + \frac{C_3}{\lambda^2-1} + \frac{C_4}{(\lambda^2-1)^2} + \frac{C_5}{(\lambda^2-1)^3} \quad (17)$$

where C_0, C_1, C_2, C_3, C_4 and C_5 are constants, given by

$$C_0 = 1.4508554, C_1 = -0.0031268, C_2 = -0.0000381, C_3 = 0.0030270, C_4 = -0.0000779, C_5 = 0.0000018.$$

Then we find the total chromatic dispersion D in PCFs from the addition of these two contributions.

3. RESULTS AND DISCUSSIONS

We take different values of λ , ranging from 0.7 to 2 μm in steps of 0.1 μm and calculate the values of ν using Eq.(3). Then the corresponding u values as roots of Eq.(6) are determined. Then we find the values of A and B in Eq.(7) from the values of ν and corresponding \sqrt{b} using least square fitting method. The polynomials of A and B in terms of d/Λ involve coefficients a_0 to a_4 and b_0 to b_4 , given in TABLE 1.

TABLE 1

VALUES OF COEFFICIENTS

	$i=0$	$i=1$	$i=2$	$i=3$	$i=4$
a_i	1.0164	-0.2064	0.9887	-1.872	1.3653
b_i	-0.0411	0.5502	2.1164	-3.8187	5.504

We check the accuracy of Eq.(7) for any two

arbitrary values of d/Λ in the single moded region.

For these two d/Λ , first we find the roots of Eq.(6) or corresponding values of u at a particular $\lambda=1.55\mu\text{m}$. Then we determine the respective values of effective cladding index n_{FSM} from Eq.(4), where β/k is same as the index n_{FSM} .

Again, we determine the values of u using the polynomials of A and B [Eq.(8) and (9)] and then using Eq.(7) and Eq.(5a) for those two d/Λ values. From the two u values we compute the indices n_{FSM} using Eq.(4). The results obtained from two different approaches are depicted in TABLE 2 for comparison. We see that the results obtained from our approach match excellently with those from [1].

TABLE 2

COMPARISON OF DATA

d/Λ	from Russell's Equation	from Our Approach
0.34	$u = 2.5135$ $n_{FSM} = 1.4352$	$u = 2.5037$ $n_{FSM} = 1.4353$
0.38	$u = 2.7409$ $n_{FSM} = 1.4324$	$u = 2.7335$ $n_{FSM} = 1.4325$

Then for different values of λ , ranging from 0.7 to 2 μm in steps of 0.1 μm , we calculate the refractive indices n_{FSM} from our proposed relations. We determine the corresponding effective refractive indices of the fundamental guided mode of the PCF from the equation of the equivalent CSF for those λ values as said earlier and hence the corresponding waveguide dispersion parameters D_w , from Eq.(16). The material dispersion parameters D_m in ps/km-nm are found out from Sellmeier relation, given by Eq.(17). We obtain the total chromatic dispersions D for the chosen PCF as a function of λ for $\Lambda=3\mu\text{m}$ and $d/\Lambda=0.3$ and 0.4, as typical cases in the

single mode regime .

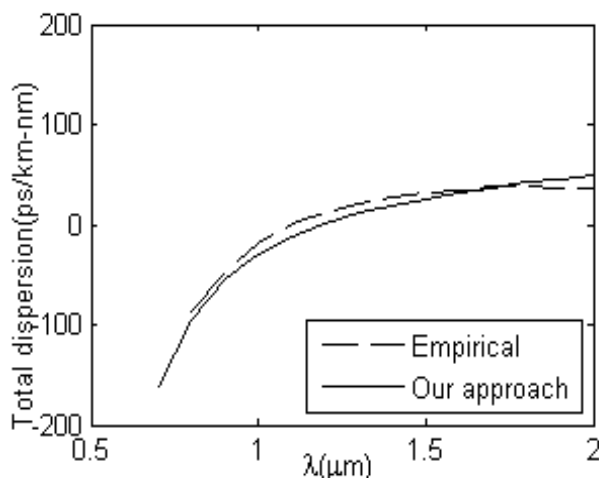


Fig. 2. Chromatic dispersion as a function of wavelength for $\Lambda = 3 \mu\text{m}$, $d / \Lambda = 0.3$.

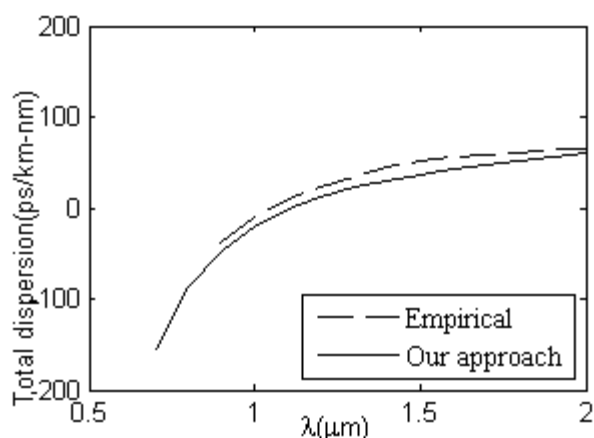


Fig. 3 Chromatic dispersion as a function of wavelength for $\Lambda = 3 \mu\text{m}$, $d / \Lambda = 0.4$.

The solid curves represent the variation of total dispersion as function of λ in Fig. 2 and 3 for $\Lambda = 3 \mu\text{m}$ and $d / \Lambda = 0.3$ and 0.4 respectively. On the other hand, these curves are compared with the dotted ones drawn from the empirical relations obtained from FEM in the same figures. Thus our simple formulation is seen to work fairly excellently for practical purposes in studies of propagation

characteristics of PCF with a typical example of dispersion of PCF. We will use our formulation to compute other propagation characteristics of PCF as our next scheme of study.

4. CONCLUSIONS

We have presented a simple and complete formulation to find normalized propagation constants in the infinite photonic crystal cladding and have shown that they can be used to compute the propagation constants of a PCF with triangular lattice of air-holes and the total chromatic dispersion for typical values of relative air-hole size and wavelength.

5. ACKNOWLEDGEMENT

The authors acknowledge the financial support of the Centre for Research in Nanoscience and Nanotechnology, University of Calcutta.

REFERENCES

- [1] Philip St. J. Russell, "Photonic-crystal fibers", *Journal of Lightwave Technology*, vol. 24, No. 12, 2006, pp.4729 .
- [2] S.G. Johnson and J. D. Joannopoulos, "Block-iterative frequency-domain methods for Maxwell's equations in a planewave basis", *Opt. Express* 8, 173-190 (2001).
- [3] M. Koshiba, "Full-vector analysis of photonic crystal fibers using the finite element method." *IEICE Trans. Electron.* E85-C, 2002, pp.881-888 .
- [4] T. P. White, B. T. Kuhlmeiy, R. C. McPhedran, D. Maystre, G. Renversez, C. M. de. Sterke, L. C. Botten, "Multipole method for microstructured optical fibers. I. Formulation", *J. Opt. Soc. Am. B* 19, 2002, pp. 2322-2330.
- [5] K.Saitoh and M. Koshiba, "Empirical relations for simple design of photonic crystal fibers", *Optics Express*, vol. 13, No. 1, 2004,

pp. 267-274.

- [6] T. A. Barks, J. C. Knight and P. St. J. Russell, “Endlessly single-mode Photonic crystal fiber”, *Optics Letters*, vol. **22**, No. 13, 1997, pp.961-963.
- [7] M.Koshiha and K. Saitoh, “Applicability of classical optical fiber theories to holy fibers, *Opt. Lett.* **29**, 2004, pp. 1739-1741 .
- [8] A. Ghatak and K. Thyagarajan, “ Introduction to Fiber Optics”.

THE INTERPLAY BETWEEN ORDER AND DISORDER IN PHOTONIC CRYSTALS

Rajesh V. Nair and B. N. Jagatap

Atomic and Molecular Physics Division, Bhabha Atomic Research Centre, Mumbai, 400 085 India

Email: rvnair@barc.gov.in

Abstract: We report experimental results of the affect of extreme order and disorder on the optical properties of photonic crystals. The superior ordering results in Bragg wave coupling at certain conditions of the incident wave vector. We also study the characteristics of photonic stop gap as a function of controlled disorder in photonic crystals.

1. INTRODUCTION

Photonic crystal structures offer unprecedented control over light propagation and emission. They are characterized by a periodically varying refractive index along three-orthogonal directions. The underlying periodicity can open stop gaps, in dispersion relation, along certain directions similar to semiconductors. At the stop gap frequency the density of states is zero and that result in an extreme control over the light propagation and emission.

Synthesis of photonic crystals with thickness (t) larger than the Bragg length (L_B) is a challenge due to constrains imposed by the fabrication conditions. When $t > L_B$, the finite size effects are eliminated and that results in rich physics and optical properties. We present here our results on the impressive optical properties exhibited by photonic crystals with $t > L_B$. Angle-resolved photonic stop gap shows well-resolved Bragg wave coupling which is one of the most beautiful phenomena exhibited by three-dimensional (3D) photonic crystals. We also engineer disorder in photonic crystals in a controlled way to illustrate the stop gap at different level of disorder.

2. EXPERIMENTAL

3D ordered photonic crystals are synthesized using self-assembling techniques. We used polystyrene sphere of different diameters to realize photonic stop gap in different spectral ranges. Disorders are introduced through controlling the self-assembling process using electrolytes of different concentrations. Photonic stop gap is characterized using a spectrophotometer with an unpoalrized light. Diffuse intensity spectra are measured at each level of disorder in order to account for the generated disorder.

3. RESULTS AND DISCUSSIONS

Field emission scanning electron microscope (SEM) image of the photonic crystals is given in Fig. 1(a). The well-ordering of spheres on the surface of the crystal is evident. This image represents the (111) plane of the face centered cubic (*fcc*) lattice. The photonic stop gap measured at near-normal incidence of light from the (111) plane is given in Fig. 1(b). The peak in reflectivity spectra is in good agreement with

the trough in transmission spectra indicates the signature of photonic stop gap. An angle-resolved reflectivity measurement shows the shift of the stop gap towards the shorter wavelength region in accordance with Bragg's law. At high angles of incidence we observe extremely well-resolved Bragg wave coupling as seen in Fig. 1(c). Experimentally observed Bragg wave coupling is in good agreement with theoretical calculations. The new diffraction peak, appearing at the Bragg wave coupling, is due to the (200) diffraction peak.

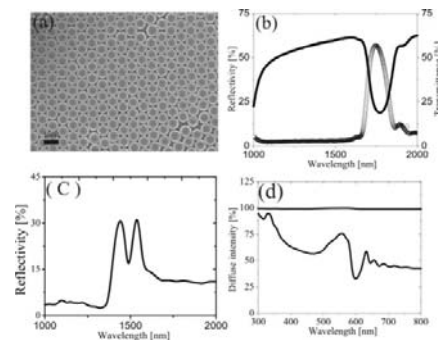


Figure 1. (a) SEM image of the photonic crystals indicate the (111) plane of the *fcc* lattice. (b) The reflectivity (symbol) and transmittance (line) at near-normal incidence shows the signature of photonic stop gap. (c) The Bragg wave coupling occur at an angle of incidence of 53° shows the well-resolved diffraction peaks. (d) The diffuse scattered intensity for 0% disorder (black line) and 100% disorder (gray line) indicate the signature of controlled disorder.

The signature of the induced disorder can be appreciated in Fig. 1(d). For nearly-perfect photonic crystals (0% induced disorder), the diffuse intensity shows trough at the stop gap and increases towards the shorter wavelength ranges. But for completely disordered photonic crystals (100% induced disorder), stop gap disappears in addition to the 100% diffuse scattering of light inside the photonic crystal. In this manner, we can engineer photonic crystals with any amount of disorder between these two extreme conditions. We also discuss the resonant characteristics in the multiple scattering of light.

Numerical analysis of nonlinear pulse propagation in chalcogenide As_2Se_3 glass Photonic Crystal Fiber using RK4IP method

Bhawana Dabas, Monika Rajput and R. K. Sinha

TIFAC-Centre of Relevance and Excellence in Fiber Optics and Optical Communication, Department of Applied Physics, Delhi Technological University (Formerly Delhi College of Engineering, Faculty of Technology, University of Delhi), Bawana Road, Delhi-110042, India.

Telephone No. - +91-11-27871017, Fax No. +91-11-27871023

Email: dabas_bhavna@yahoo.co.in, dr_rk_sinha@yahoo.com.

ABSTRACT: Pulse propagation in chalcogenide As_2Se_3 Photonic Crystal Fiber (PCF) is numerically investigated using Fourth-Order Runge-Kutta in the Interaction Picture (RK4IP) method. The RK4IP method is used to demonstrate soliton pulse generation and soliton collision in As_2Se_3 PCF. The numerical value of collision length ($L_{col}=51.3L_D$) using RK4IP method, is found to be in good agreement with the theoretical value of collision length ($L_{col}=51.408L_D$) obtained from inverse scattering transform method.

1. INTRODUCTION

In recent years, intensive investigation of Photonic crystal fibers (PCFs) has brought a major revolution in nonlinear optics. PCFs are a new class of fiber, usually designed and fabricated with solid pure silica core surrounded by an air hole lattice in the cladding region [1-3]. A number of various numerical methods have been developed to analyze the propagation characteristics of PCF [4-7]. But to achieve more accurate dispersion results, fully vectorial version of EIM (Effective Index Method) was proposed [6] and known as Fully Vectorial Effective Index Method (FVEIM). FVEIM has the advantage of high speed and greater accuracy over the conventional EIM.

On the other hand, very recently, research work is focused on different types of PCFs having solid or hollow core, regular as well as irregular geometries and using different materials. Non-silica compound glasses like chalcogenide, soft glasses have been effectively used in PCFs for investigation of non-linear propagation in PCFs [8-12]. Chalcogenide glasses are based on sulphur, selenium, tellurium and the addition of other elements such as arsenic, germanium, antimony, gallium, etc. Chalcogenide glasses are promising nonlinear materials especially in the longer wavelength infrared (IR) region. The large refractive index of chalcogenide glasses (compared to other glasses) of 2.4 to 3.0 opens up the possibility of achieving compact nonlinear devices [13-14]. Non-linearity (n_2) in chalcogenide glasses is 100–1000 times as high as the non-linearity of silica at 1.55 μm . The most common and widely known method in the field of optics to solve Generalized Nonlinear Schrödinger Equations (GNLSE) is the symmetric Split Step Fourier Method (SSFM) [15] which has an accuracy of the second order in the step size. However, in recent literature, a more sophisticated method has been considered, which has an accuracy of fourth order, is known as the Fourth order Runge-Kutta in Interaction Picture (RK4IP) method [16, 17]. It has applications for studies of

nonlinear pulse propagation and spectral broadening in optical fibers. The accuracy of RK4IP method has been tested by comparing it with number of conventional methods [17].

In this paper, RK4IP method is implemented to investigate the soliton pulse propagation and soliton collision in chalcogenide As_2Se_3 PCF, which gives an accuracy of fourth order. Effective refractive index, effective area and non-linear coefficient (γ) of the proposed chalcogenide As_2Se_3 glass PCF, is calculated by Fully Vectorial Effective Index Method (FVEIM) method. Next, parameters obtained by FVEIM are used for the study of RK4IP method to solve the NLSE. The value of wavelength for distortion less ($L_{NL}=L_D$) propagation of the soliton pulse is also evaluated for different value of Λ ($2\mu\text{m}$ to $6\mu\text{m}$) with fixed value of $d/\Lambda=0.9$. It is found that the soliton collision length is in good agreement between the numerical ($L_{col}=51.3L_D$) value obtained by RK4IP method and theoretical ($L_{col}=51.408L_D$) value obtained by inverse scattering transform method for the proposed design of As_2Se_3 PCF. It is also exhibited that the solitons repel each other, for non-unity amplitude and non-zero phase difference between them in As_2Se_3 PCF, whereas the repulsion between solitons is more for $\theta=\pi/2$ in comparison of $\theta=\pi/4$. This confirms the validity of the RK4IP method so developed for studying soliton evolution and collision in As_2Se_3 PCF.

2. RESULTS AND NUMERICAL CALCULATIONS

The PCFs are designed with small core to get a high nonlinear coefficient (γ). For this purpose fixed value of $d/\Lambda=0.9$ with different value of Λ is considered. From figure 1, it is concluded that, anomalous dispersion region ($\beta_2 < 0$) is obtained when $\Lambda=2\mu\text{m}$ and $d/\Lambda=0.9$ for the designed PCF and hence with these parameters all the requirement (i. e. low A_{eff} , high γ and $\beta_2 < 0$) are fulfilled to obtain solitary wave

solutions. These parameters obtained by FVEIM are used for solving the NLSE using RK4IP method.

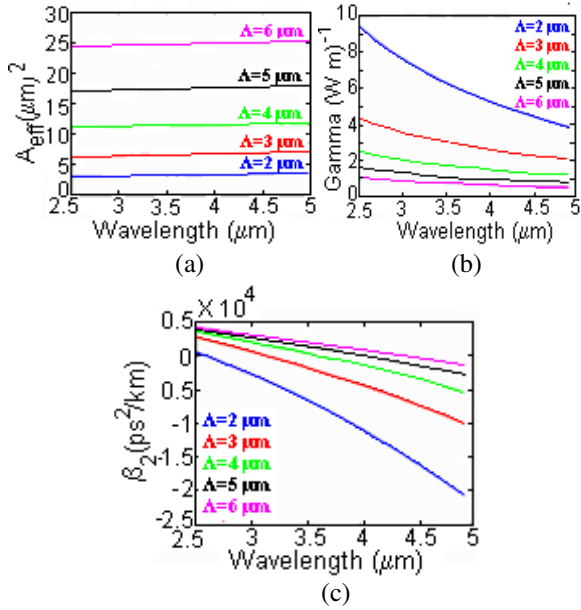


Figure1: Variation of (a) A_{eff} , (b) Gamma (γ) and (c) GVD parameter (β_2) with wavelength for As_2Se_3 PCF at $d/\Lambda=0.9$ for different Λ values.

2.1 OPTICAL SOLITON

The physical process of the evolution of the fundamental soliton propagation can be explained by considering the effect of SPM and GVD. The dispersion length and nonlinear length of the optical

soliton are defined as $L_D = \frac{T_0^2}{|\beta_2|}$ and $L_{NL} = \frac{1}{\gamma P_0}$.

When the fiber length L is longer or comparable to both L_D and L_{NL} , dispersion and nonlinearity are simultaneously dominating factor as the pulse propagates along the fiber. The parameter (N) can be

determine as, $N^2 = \frac{L_D}{L_{NL}} = \frac{\gamma P_0 T_0^2}{|\beta_2|}$, which is related

to the soliton order. Dispersion dominates for $N \ll 1$ while SPM dominates for $N \gg 1$. For value of $N \approx 1$ both SPM and GVD play an equally important role during pulse evolution. In the anomalous dispersion regime, where $\beta_2 < 0$, the fiber can support soliton propagation. Distortion less propagation of the soliton pulse is achieved at the wavelength corresponding to $N \approx 1$ for a given pitch, as the nonlinear and dispersion effects are almost balanced. The variation of pitch with different values of wavelength of least distortion ($L_{NL} = L_D$) for the soliton propagation is as shown in figure 2(a). From the figure it is observed that the variation of pitch against the wavelength for minimum distortion is almost a linear one.

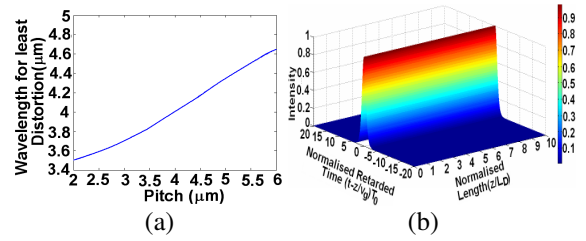
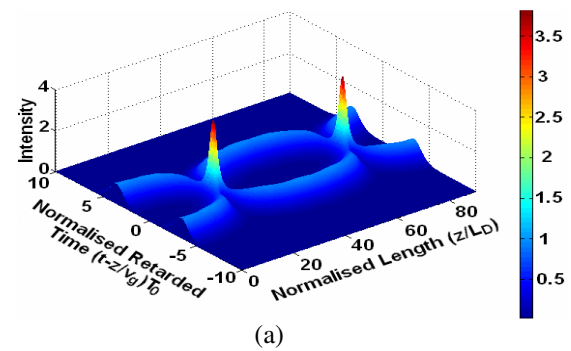


Figure2: (a) Variation of pitch with least distortion wavelength for fixed value of $d/\Lambda=0.9$ in As_2Se_3 PCF and (b) Evolution of first order soliton in time domain at $3.5\mu m$.

We have simulated the pulse evolution for the first order ($N=1$) soliton for fixed value of air hole size $d/\Lambda=0.9$ and different value of pitch ($\Lambda=2\mu m$ to $6\mu m$). To investigate soliton propagation in PCF, we have numerically solved the NLSE using RK4IP method with initial envelope of the soliton at $z=0$ given by $U(0, \tau) = \text{sech}(\tau)$, where τ is the normalized retarded time ($\tau = (t - z/v_g)/T_0$). P_0 is suitably selected in order to let the soliton order be $N = 1$. In figure 2 (b), we show the time and frequency domain evolution of a fundamental soliton for $d/\Lambda=0.9$ with $\Lambda=2\mu m$ at $\lambda=3.5\mu m$. The values of the parameters β_2 and γ is such that $N \approx 1$, which is the condition for generating a first order soliton.

2.2 SOLITON COLLISION

The case of two soliton pulses interacting with each other is studied through numerical algorithm and verified analytically [18]. It is observed that, for the case of equal amplitudes ($r=1$) and same phase ($\theta=0$), the two solitons will attract each other and collide periodically along the length of the fiber as shown in figure 2(a). Solitons repel each other, for a non-zero phase (θ) difference between them as shown in figure 2 (b) and when the relative amplitude of the soliton deviates slightly from unity ($r=1.1$), in this case the solitons will not collide but oscillate periodically



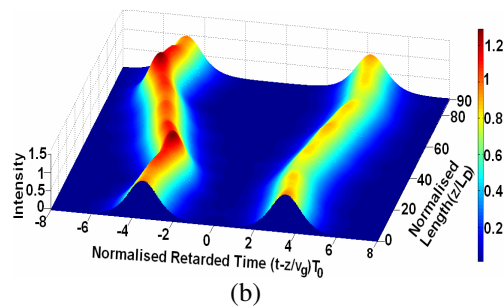


Figure 2: Soliton collision in As_2Se_3 PCF (a) for $\theta=0$ and $r=1$ and (b) for $\theta=\pi/4$ and $r=1$ when $L=2\mu\text{m}$ and $d/L=0.9$ at $\lambda=3.5\mu\text{m}$.

Hence, our algorithm reveals that RK4IP is very nifty and precise for future research work in PCF.

CONCLUSION

In this paper, we have analyzed the dynamics of the pulse propagation in designed chalcogenide As_2Se_3 glass PCF using the RK4IP method with FVEIM. The effective area (A_{eff}), non-linear coefficient (γ) and dispersion are computed for the designed As_2Se_3 glass PCF. A linear variation of pitch with different values of wavelength of least distortion ($L_{NL}=L_D$) for the soliton propagation is evaluated for the reliable optical communication application. The RK4IP method is implied to demonstrate the soliton pulse generation and collision in the proposed As_2Se_3 PCF, under the influence of nonlinear Kerr effects and Group Velocity Dispersion (GVD). The numerical value of collision length ($L_{\text{col}}=51.3L_D$) obtained by RK4IP method for soliton collision is in good agreement with the theoretical value ($L_{\text{col}}=51.408L_D$) obtained by inverse scattering transform method. Comparison of the result obtained through numerical simulation with that for theoretical data (vis-à-vis soliton collision length), shows that our algorithm for implementing RK4IP is valid and reliable for further study of this type of fibers.

ACKNOWLEDGEMENTS

The authors gratefully acknowledge the initiatives and support towards establishment of “TIFAC Centre of Relevance and Excellence in Fiber Optics and Optical Communication at Delhi College of Engineering, Delhi” through “Mission REACH” program of Technology Vision-2020, Government of India.

REFERENCES

- [1] E. Yablonovitch, Inhibited spontaneous emission in solid state physics and electronics”, *Physical. Review Letter.* **58**, 2059–2062 (1987).
- [2] J. C. Knight, T. A. Birks, P.St.J. Russell and D. M. Atkin, “All-silica single-mode optical fiber

with photonic crystal cladding”, *Opt. Lett.* **21**, 1547–1549 (1996).

- [3] K. Saitoh, and M.Koshiba, “Leakage loss and group velocity dispersion in air-core photonic band-gap fibers”, *Opt. Exp.***11**, 3100–3109 (2003).
- [4] S. K. Varshney, M. P. Singh, R. K. Sinha, “Propagation Characteristics of Photonic Crystal Fibers”, *J. of Opt. Commun.* **24**, 856 (2003).
- [5] R.K.Sinha, Anshu D.Varshney, “Dispersion Properties of Photonic crystal Fiber: comparison by scalar and fully vectorial effective index methods”, *Opt. Quantum Electron.* **37**, 711-722 (2005).
- [6] Y. Li, C. Wang, and M. Hu, “A fully vectorial effective index method for photonic crystal fibers: application to dispersion calculation”, *Opt. Commun.* **238**, 29–33 (2004).
- [7] Vasantha Jayakantha Raja and K.Porsezian, “A fully vectorial effective index method to analyse the propagation properties of microstructured fiber”, *Photonics and Nanostructures.* **5**, 171-177 (2007).
- [8] Sourabh Roy and Partha Roy Chaudhuri, “Supercontinuum generation in visible to mid-infrared region in square-lattice photonic crystal fiber made from highly nonlinear glasses”, *Opt. Commun.* **282**, 3448-3455 (2009).
- [9] Bhawana Dabas, R.K. Sinha, Dispersion Characteristic of Hexagonal and Square Lattice Chalcogenide As_2Se_3 Glass Photonic Crystal Fiber, *Opt. Commun.* **283**, 1331-1337 (2010).
- [10] Bhawana Dabas, R.K. Sinha, Design of Highly Birefringent Chalcogenide glass PCF: A simplest design, *Opt. Commun.* **284**, 1186-1191 (2010).
- [11] S. K. Varshney, K. Saitoh, K. Iizawa, Y. Tsuchida, M. Koshiba, and R. K. Sinha, “Raman amplification characteristics of As_2Se_3 photonic crystal fibers”, *Opt. Exp.* **33**, 2431-2433 (2008).
- [12] D. -I. Yeom, E. C. Mägi, M. R. E. Lamont, M. A. F. Roelens, L. Fu, and B. J. Eggleton, “Low-threshold supercontinuum generation in highly nonlinear chalcogenide nanowires”, *Opt. Lett.* **33**, 660-662 (2008).
- [13] E. C. Mägi, L. B. Fu, H. C. Nguyen, M. R. Lamont, D. I. Yeom, and B. J. Eggleton, “Enhanced Kerr nonlinearity in sub-wavelength diameter As_2Se_3 chalcogenide fiber tapers”, *Opt. Exp.* **15**, 10324-10329 (2007).
- [14] M. R. Lamont, B. Luther-Davies, D. Choi, S. Madden, and B. J. Eggleton, “Supercontinuum generation in dispersion engineered highly nonlinear ($\langle\gamma\rangle = 10 \text{ /W/m}$) As_2Se_3 chalcogenide planar waveguide”, *Opt. Exp.* **16**, 14938-14944 (2008).

- [15] Z B Wang, H Y Yang and Z Q Li, “The Numerical Analysis of Soliton Propagation with Split-Step Fourier Transform Method”, *Journal of Physics: Conference Series*. **48**, 878–882 (2006)
- [16] Zhongxi Zhang, Liang Chen, and Xiaoyi Bao, A fourth-order Runge-Kutta in the interaction picture method for numerically solving the coupled nonlinear Schrödinger equation, *Opt. Exp.* **18**, 8261-8276 (2010) .
- [17] Johan Hult, “A Fourth-Order Runge–Kutta in the Interaction Picture Method for Simulating Supercontinuum Generation in Optical Fibers”, *J. Lightwave Technol.* **25**, 3770-3775 (2007).
- [18] G. P. Agrawal, “Nonlinear Fiber Optics, 4th ed. San Diego”, CA: Academic, 2007.

PROSPECTS AND TECHNICAL CHALLENGES OF HIGH EFFICIENCY SOLID STATE LIGHTING

Rajeev Jindal, Subrata Dutta
Corporate R&D, Moserbaer India Ltd, 66 Udyog Vihar , Greater Noida, UP
rajeev.jindal@moserbaer.in

Abstract: The talk describes the technology behind Solid State Lighting, the paradigm shift it is introducing to conventional lighting design, energy advantages it offers and the two categories of lighting viz LED & Organic LED.. The relative advantages and technical challenges are discussed.

1. INTRODUCTION

With the world moving towards green technologies, lighting industry and lighting in general is also changing its shape very fast. While it took mankind, more than millions of years to develop a non-fire based light source (so called EDISON bulb) a transition from that to a more efficient light in form of solid state lighting i.e. LED and OLED is happening within a matter of ~ 100 years and we are sure to move to these much better lightings in almost immediate future.

While burning fire for light to incandescent technology solved the purpose of anytime-anywhere light, the main thrust in the next hundred years has to be beyond this basic necessity.

2. SOLID STATE LIGHTING

The technology which shaped 20th & 21st century is electronics and all the conventional lighting technologies such as incandescent, fluorescent etc uses very little of this technology and hence is inefficient from photometric, colorimetric and intelligent control point of view. With the next generation lighting system we are now looking for lighting efficiency, lighting quality, intelligent interface etc. This is where Solid State Lighting has burst into the scene, a semiconductor product driven by semiconductor electronics.

In spite of all the potential it has, a LED based lighting device is actually a complex mix of semiconductor technology, optics, electronics and heat management. The talk will focus on various technology challenges related to these areas and especially on associated optical challenges which are necessary to be solved / improved for more efficient lighting. It would be described through example that how light can be utilized better by distinguishing between useful light and un-useful light and how a good optical system can convert so called unused light into useful light. Further, electronic and thermal management challenges will also be discussed to cover overall product development aspects.

The talk would further look into next generation of solid state lighting i.e. OLED technology which is a counterpart of LED technology and has the potential to change the landscape for general illumination lighting, provided a number of technical and market

barriers can be overcome. Certain challenges associated with OLED technology will also be briefly mentioned.

The presentation will end by providing a view on how both LED and OLEDs can coexist to handle different challenges associated with lighting industry.

ACKNOWLEDGEMENT

The authors wish to acknowledge the management of Moserbaer India Ltd for allowing to publish this work.

REFERENCES

- [1] E. Fred.Schubert, "Light Emitting Diode & Solid State Lighting", *Department of Physics, Applied Physics, and Astronomy, Rensselaer Polytechnic Institute, Troy, NY 12180*
- [2] "Luminaires & Light Distribution," chapter 7, *Advanced Lighting Guidelines*. www.algonline.org.
- [3] Steffen, *The CELMA Guide to LED Luminaire Design*., European Lamp Companies Federation , 2010
- [4] "Thermal Design of LED Luminaires" www.vossloh-schwabe.

WHITE LIGHT INTERFEROMETRY FOR SURFACE PROFILING WITH COLOUR CCD

U. Paul Kumar, Wang Haifeng

Department of Physics, National University of Singapore, Singapore 119260.

N. Krishna Mohan and M.P. Kothiyal

Department of Physics, Indian Institute of Technology Madras, Chennai 600036, India.

e-mail: upaul.k@gmail.com

Abstract: In several applications accurate surface profile height measurement is an important requirement. Laser based interferometer is routinely used for this purpose. In laser based interferometry, the unambiguous measurement range is limited to half a wavelength. Multiple wavelength or white light interferometer is used to overcome this difficulty. In this paper a white light interferometry with color CCD camera is discussed. We access interference intensity information from the three channels of the color CCD simulating three-wavelength measurement. This makes the data acquisition as simple as in single wavelength interferometry. The usefulness of the proposed method is demonstrated on a micro-sample.

1. INTRODUCTION

Interferometry using phase shifting technique is a widely used tool for precision surface metrology [1,2]. A laser is usually employed as a light source. Due to the monochromaticity of the laser, the unambiguous measurement range is limited to half a wavelength. The unambiguous range can be increased using multiple wavelength techniques [3-8]. However this requires two or three lasers for the measurement. White light interferometry (WLI) is a state-of-the-art technique for measuring discontinuous surface profiles [9,10]. WLI combining with advanced CCD cameras, computers, image processing cards, and software packages has given an extremely powerful measurement tools. Extremely short coherence length of the white light source results in high contrast fringe occurs only when the optical path difference (OPD) is close to zero. The 3-D plot of the axial positions of the zero OPD along the optical axis represents the surface profile of the object under test. Compared to single wavelength phase shifting interferometry, the white light interferometry is rather slow, because the number of frames to be recorded and evaluated is rather large. It is a time consuming process. The spectrally resolved white light interferometry (SRWLI) [11,12], on the other hand gives only a line profile of the object, although the requirement on number of frames is similar to the single wavelength phase shifting interferometry.

In this paper, we describe a single shot white light microscopic interferometry with colour CCD camera for surface profile analysis on micro-specimens. For recording of

interferograms a three-chip or a single-chip colour CCD cameras can be used. Maximum resolution will be achieved by using 3-chip colour CCD. In this investigation, however, a single chip colour CCD camera is used. Typically more than three frames are required to use phase shifting algorithm for phase calculation. Thus the data acquisition is as simple as in single wavelength case. Each RGB phase shifted fringes thus stored are then separated into its R, G, B components. The phase at individual wavelength is calculated using phase shifting algorithms. The combination of white light interferometry with colour CCD camera makes the measurement faster, simple and cost effective. There is a practical issue in implementing this approach with a phase-shifting technique. The single chip-CCD has three separate spectral bands called R-band, G-band, and B-band centered at Red ($\lambda_1=620$ nm), Green ($\lambda_2=540$ nm) and Blue ($\lambda_3=460$ nm) wavelengths respectively. The phase shifts are usually produced by using a piezoelectric transducer (PZT) to change the length of one of the optical paths. The phase step produced at single wavelength can be set precisely at 90° , but the same motion of the PZT introduces a phase-step miscalibration at the other wavelengths. We use phase step value $\alpha_2=90^\circ$ at $\lambda_2=540$ nm. Hence $\alpha_1=(\lambda_2/\lambda_1)90^\circ=78.4^\circ$ for $\lambda_1=620$ nm and $\alpha_3=(\lambda_2/\lambda_3)90^\circ=105.7^\circ$ for $\lambda_3=460$ nm. The phase shift error introduced at λ_1 and λ_3 are 14.8% and 14.9% respectively. This problem can be overcome in various ways [8]. The phase at individual wavelengths is calculated using the higher order (8-step) phase shifting algorithm which has a higher tolerance of $\pm 20\%$ for phase-shift miscalibration error [13]. Use of this

approach combining white light interferometer with colour CCD camera increases the unambiguous range for surface profile measurement. Experimental results on a micro-specimen are presented.

2. OPTICAL INSTRUMENTATION

The schematic of the microscopic white light interferometric arrangement shown in Fig.1 is used for the measurements. The white light beam is collimated using a collimating lens (CL). The collimated beam illuminates the micro-specimen via the beam splitter (BS) and the Mirau objective. The specimen is mounted on a 3-axis stage for alignment. The microscopic imaging system consists of a 5X, 10X, 20X microscopic objectives. The Mirau interference pattern is stored using a JAI BB-500GE 2/3" GigE vision camera. It is a color progressive scan camera with 5 million pixels resolution and GigE Vision interface. These are single-chip colour sensors which contain the primary colours red, green, and blue and are used in most single-chip digital image sensors used in digital cameras to create a color image. It has 2456(H) X 2058(V) active pixels with a 3.45 μm square pixel. The camera is interfaced to PC with NI PCIe-8231 card. A PZT is attached to the Mirau objective for phase shifting. The PZT is driven by an amplifier which is interfaced to a PC with a DAQ (NI6251) card. LABVIEW based programs suitable for colour CCD camera have been developed for real time visualization of fringes and storing the phase shifted frames for fringe analysis.

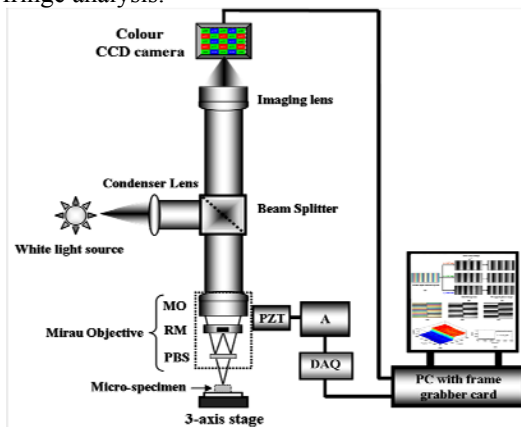


Fig.1 Schematic of the white light microscopic interferometric system: MO, Microscopic objective; RM, Reference mirror; PBS, Plate beam splitter; A, Amplifier; PZT, Piezo electric transducer; DAQ, Data acquisition system.

3. THEORY OF MEASUREMENT OF LARGE DISCONTINUITIES USING FRINGE ORDER METHOD

The intensity distribution of the phase shifted frames corresponding to any one wavelength of the white light interferogram can be expressed as

$$I_{in} = I_o(1 + V \cos(\phi_i(z) + (n-1)\alpha_i)) \quad (1)$$

where I_o is the bias intensity, V , the visibility ϕ_i , the phase; n , the frame number and α_i , the phase shift for wavelength λ_i with $i=1,2,3$.

To evaluate the phase, we use the 8- step ($n=8$) algorithm [13], which gives the phase as

$$\phi_i = \arctan\left(\frac{-I_{i1} - 5I_{i2} + 11I_{i3} + 15I_{i4} - 15I_{i5} - 11I_{i6} + 5I_{i7} + I_{i8}}{I_{i1} - 5I_{i2} - 11I_{i3} + 15I_{i4} + 15I_{i5} - 11I_{i6} - 5I_{i7} + I_{i8}}\right) \quad (2)$$

The surface profile phase is governed by the following equation

$$\phi_i = 4\pi\sigma_i z \quad (3)$$

where wavenumber $\sigma_i=1/\lambda_i$, and z is the profile variation. $z \leq \lambda_i/2$ can be measured unambiguously with single wavelength. From the Eq. (3), it is clear that the variation of ϕ_i with σ_i is linear. With the phase values at three wavelengths, it is possible to adjust the wrapped phase data at any pixel such that they lie on a best fit line by addition or subtraction of multiples of 2π . The slope of this line gives the absolute height at the pixel as

$$z_a = \frac{1}{4\pi} \left(\frac{\Delta\phi}{\Delta\sigma} \right) \quad (4)$$

The value of z_a obtained from Eq. (4) is less precise but it is quite close to the actual value. The ambiguity-free phase can be expressed as

$$\Phi_i = \phi_i - 2\pi \text{round}\left(\frac{\phi_i - 4\pi\sigma_i z_a}{2\pi}\right) \quad (5)$$

The function round () gives the nearest integer. The total profiles height with single wavelength resolution can be obtained as

$$z = \frac{\lambda_i}{4\pi} \Phi_i \quad (6)$$

Thus the fringe order method helps to increase the measurement range and to retain the single wavelength resolution of the surface profile of a test object.

4. EXPERIMENTAL RESULTS

Fig.2(a) shows the white light tilt fringes generated on reflective surface stored using the system shown in Fig.1. The dimensions of the stored RGB image are 2456 X 2058 X 3. Each pixel contains the information regarding the red, green, blue wavelengths. It is then separated into its monochrome R, G, and B components of dimensions 2456X2058. The decomposed components at Red ($\lambda_1=620$ nm), Green ($\lambda_2=540$ nm), and Blue ($\lambda_3=460$ nm) are shown in Fig.2(b). Multiple frames are recorded to use phase shifting algorithms for quantitative phase evaluation. Each phase shifted frame is decomposed and processed separately. Fig.2(c) shows the wrapped phase maps generated for each wavelength using 8-step equation (Eq.(2)). The position of zero-order fringe, identified by a dotted line is independent of the wavelengths. Here the fringe centers for all the wavelengths match. It occurs once within the coherence envelope of the white light source.

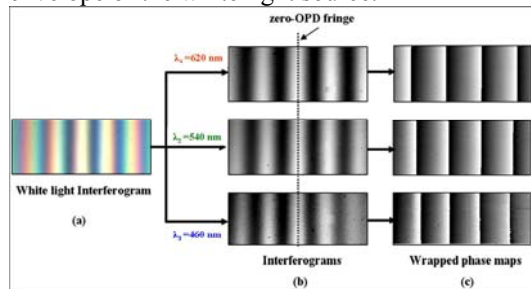


Fig.2 Flow chart for white light interferometric fringe analysis: (a) White light interferogram (RGB image), (b) interference patterns, and (c) wrapped phase maps at individual wavelength. Dotted line indicates the location of the center of zero-order fringe.

Fig.3 shows the experimental results on an etched silicon sample with large discontinuities. Fig.3(a) shows the recorded RGB white light interferogram. The RGB images thus recorded are separated into its individual components. The fringe pattern and wrapped phase maps evaluated at $\lambda_1=620$ nm wavelength obtained following the procedure explained above are shown in Fig. 3(b) and 3(c) respectively. Similarly phase maps can be obtained at λ_2 , and λ_3 . The wrapped phase maps thus evaluated can be used to increase the unambiguous range in two ways: (a) Phase Subtraction Method (PSM) [3,8], and (b) Fringe Order Method (FOM) [6,8]. In phase subtraction method, phase maps at individual wavelengths are subtracted to generate effective wavelength

phase map. The profiles measured at effective wavelengths are noisy due to the fact that the signal-to-noise ratio (SNR) increases with the wavelength used for measurement (i.e. error amplification effect) [3,8]. Whereas the fringe order method (Section-3) can provide surface profile with the resolution of single wavelength and it can extend the measurement range of the interferometer. Fig.3(d) shows the ambiguity removed 3-D profile using fringe order method for $\lambda_1=620$ nm. The profile height measured is 1.12 μ m. The profile shown in Fig.3(e) has the usual smoothness of single wavelength phase shifting interferometry.

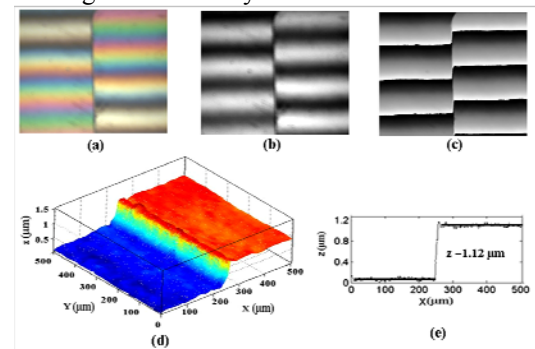


Fig.3 3-D Surface profile analysis using the fringe order method: (a) white light interferogram, (b) interferogram at λ_1 , (c) wrapped phase map at λ_1 , (d) $2m\pi$ ambiguity corrected single wavelength 3-D surface profile of an etched silicon sample using 620 nm phase data, and (e) line scan which shows a profile height of 1.12 μ m.

5. CONCLUSIONS

We have demonstrated a white light interferometer system using a single-chip colour CCD for 3-D surface profiling on micro-samples. White light phase shifted frames are stored using the color CCD and then decomposed into individual R,G, B images. In the proposed method the data acquisition and phase evaluation procedures are as simple as in case of single wavelength method. The application of 8-step algorithm provides error free phase for quantitative measurements. The use of colour CCD camera in white light interferometry makes the measurement faster, simple and cost effective which is very much useful for industrial applications.

REFERENCES

- [1] J.E. Greivenkamp and J.H. Bruning, Phase shifting interferometry, D.

- Malacara Ed., *Optical Shop Testing*, 2nd edition, Chap.14, John Wiley & Sons Inc, New York, 1992.
- [2] K. Creath, "Phase-measurement interferometry techniques" *Progress in Optics*, E. Wolf, Ed., Vol. XXVI, pp. 349-393, Elsevier, Amsterdam, 1988.
- [3] K. Creath, "Step height measurement using two-wavelength phase-shifting interferometry," *Appl. Opt.*, **26**, 2810(1987).
- [4] J. Schmit and P. Hariharan, "Two-wavelength interferometry profilometry with a phase-step error compensating algorithm," *Opt. Eng.*, **45**, 115602-1 (2006).
- [5] C. Polhemus, "Two wavelength interferometry," *Appl. Opt.*, **12**, 2071(1973).
- [6] A. Pfortner and J. Schwider, "Red-green-blue interferometer for the metrology of discontinuous structures," *Appl. Opt.*, **42**, 667(2003).
- [7] Y.Y. Cheng and J.C. Wyant, "Multiple wavelength phase shifting interferometry," *Appl. Opt.*, **24**, 804(1985).
- [8] U. Paul Kumar, N. Krishna Mohan, and M.P. Kothiyal, "Measurement of discontinuous surfaces using multiple-wavelength interferometry," *Opt. Eng.*, **48**, 073603-1(2009).
- [9] P. de Groot and L. Deck, "Surface profiling by analysis of white-light interferograms in the spatial frequency domain," *J. Mod. Opt.*, **42**, 389(1995).
- [10] P. de Groot and L. Deck, "Three-dimensional imaging by sub-Nyquist sampling white-light interferograms," *Opt. Lett.*, **18**, 1462(1993).
- [11] P. Sandoz, G. Tribillon, and H. Perrin, "High resolution profilometry by using phase calculation algorithms for spectroscopic analysis of white light interferograms," *J. Mod. Opt.*, **43**, 701(1996).
- [12] S.K. Debnath, and M.P. Kothiyal, "Experimental study of the phase-shift miscalibration error in phase shifting interferometry: use of a spectrally resolved white-light interferometer," *Appl. Opt.*, **46**, 5103(2006).
- [13] J. Schmit, and K. Creath, "Windows function influence on phase error in phase shifting algorithms," *Appl. Opt.*, **35**, 5642(1996).

SCANNING OPTICAL MICROSCOPE WITH ENHANCED SIGNAL TO NOISE RATIO PERFORMANCE

Abhijit Das and Bosanta R. Boruah
Indian Institute of Technology Guwahati, Guwahati, Assam
Email: ab.das@iitg.ernet.in

Abstract: A scanning optical microscope is proposed where the illumination beam intensity can be controlled in real time during the scanning over the sample plane. Here the scanning of the beam is achieved using a computer controlled liquid crystal spatial light modulator (LCSLM). The LCSLM device can be made to act like a binary diffraction hologram by displaying an appropriate pattern on the LCSLM panel using a computer generated holography technique. In the proposed scanning microscope the +1 order beam diffracted from the hologram displayed on the LCSLM, is the illumination beam. By displaying a sequence of binary holograms on the LCSLM, the +1 order beam can be made to scan a rectangular area similar to a conventional scanning microscope. The technique provides the complete control of the amplitude and phase profile of the illumination beam. In a conventional scanning microscope the intensity of the illumination beam remains constant for the entire image frame. So when such a conventional scanning microscope is used to get the images of samples having non uniform reflectivity or transmissivity, the image formed will have poor signal to noise ratio (SNR) in the region of weak reflectivity or transmissivity. To improve the SNR in such a region one has to increase the intensity of the illumination beam. But one cannot increase the intensity arbitrarily to increase the SNR in the region of weak reflectivity or transmissivity, since the signals from the region of higher reflectivity or transmissivity may saturate the detector. So, one need to modulate the intensity of the illumination beam in such a way that the intensity of the illumination beam is higher in region of lower reflectivity or transmissivity and vice versa. In the proposed scanning microscope the sample plane is first scanned with a beam having constant intensity for the whole sample to identify the region of weak reflectivity or transmissivity. The holograms are then computed using the recorded image so that the intensity of the illumination beam i.e., the +1 order diffracted beam has the higher intensity in the region of weak reflectivity or transmissivity and vice versa. The image obtained with the modified set of holograms has the superior SNR all over, relative to a conventional scanning microscope. In this paper we present some preliminary results using the proposed microscope.

1. INTRODUCTION

The laser scanning microscope has become important tool for the scientists during the last few decades. It has got applications in the diverse fields such as biological science, medical science, material science etc [1]. In a conventional scanning microscope [2] a collimated laser beam is focused by a lens called objective lens onto the sample plane. The focal spot is then scanned relative to the sample using a beam scanner. The light scattered or reemitted from the sample plane is collected by the same objective lens and relayed to the scan unit and finally focused onto a detector using another lens. For each position of the beam on the sample plane the detector collects signals and stores it. At the end of the scanning the signal collected is converted to a digital image of the scanned area.

In a conventional scanning microscope the intensity of the beam is kept constant throughout the sample plane for the entire image frame. There are number of biological and material samples where the reflectivity or transmissivity of the sample is not uniform. So for such a sample the image obtained using conventional scanning will have poor SNR in the region of weak reflectivity or transmissivity compared to higher reflectivity or transmissivity region. This may lead to loss of information from the region of weak reflectivity or transmissivity. One can increase the signal in such a region by increasing the intensity of

the illumination beam. But at the same time the signal from the region of higher reflectivity or transmissivity may saturate the detector. Therefore the intensity of the illumination beam cannot be increased arbitrarily and one has to modulate the beam according to the reflectivity or transmissivity profile of the sample to get uniform SNR.

In this paper a scanning microscope is described, where the intensity of the illumination beam can be modified according to the sample profile, using a computer generated holography technique [3, 4]. An image is recorded in the conventional way to determine the weak reflectivity or transmissivity region of the sample. This information is then used to modulate the illumination beam intensity such that intensity is maximum in the low reflectivity or transmissivity region and vice versa.

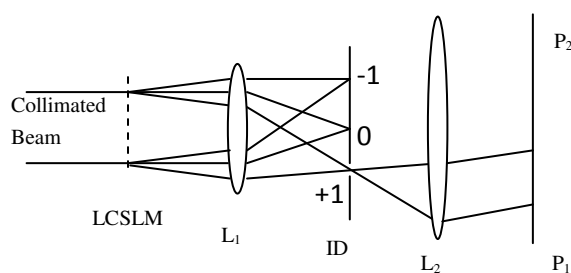


Fig.1. Set up for generating the illumination beam

2. BEAM SCANNING USING BINARY HOLOGRAMS

In the proposed microscope a computer generated hologram technique is employed to deflect the beam as well as to control the intensity of the beam [3, 4]. The basic set up for deflecting the beam using an LCSLM in transmission mode is shown in Fig. 1. An LCSLM is a two dimensional array of liquid crystal pixels whose light transmittance property can be controlled through a PC interface. Thus it is possible to write binary diffraction holograms on the LCSLM panel. Hence by displaying appropriate set of holograms on the LCSLM panel by a PC running Labview program the +1 order beam can be made to scan a rectangular area in a way similar to a conventional scanning microscope. The amount of deflection of the beam along x and y axis are represented by the τ_x and τ_y . Let $\varphi(x,y)$ be the phase on the plane P_1P_2 , where (x, y) are the coordinates along (x, y) . The total phase at the plane P_1P_2 is given by

$$\Phi(x, y) = \varphi(x, y) + x\tau_x + y\tau_y \quad (1)$$

The phase $\Phi(x,y)$ at the point (x,y) on the plane P_1P_2 is described by the pixel value at the corresponding location of the LCSLM. If $p(x,y)$ denotes the pixel values of the LCSLM $p(x,y)$ is given by

$$p(x, y) = \begin{cases} 1, & \text{if } \cos\{\Phi(x, y)\} > 0 \\ 0, & \text{if } \cos\{\Phi(x, y)\} \leq 0 \end{cases} \quad (2)$$

The plot between p and Φ is a square wave. Hence for a collimated laser beam the LCSLM acts as binary amplitude hologram [4]. So the diffracted beam when focused by a lens the diffraction orders $\pm 1, \pm 3, \pm 5 \dots$ along with the undiffracted focal spot appear on the focal plane of the lens. The +1 order beam is taken as the illumination beam for the microscope and is isolated from the other orders using an iris diaphragm. The locations of the +1 order beam with respect to the undiffracted order depends on the number of square waves i.e., the spatial frequency in the described hologram, the focal length of the lens and the wave length of the laser beam. Thus by varying the spatial frequency of the hologram along two orthogonal axes the +1 order beam can be made to scan a rectangular area.

3. MODULATION OF THE INTENSITY OF THE ILLUMINATION BEAM

The same LCSLM is used to modulate the intensity of the +1 order beam. The intensity of the +1 order diffracted beam depends on the duty cycle (dc) of the binary amplitude hologram. The duty cycle of a binary hologram defined as the ratio of the transmittance length to full length of one cycle or period. The relation between the efficiency (η) of the +1 order beam and the duty cycle of the binary amplitude hologram [5] is given by the relation

$$\eta = \left\{ \frac{\sin(\pi \times dc)}{\pi} \right\}^2 \quad (3)$$

from the relation it can be seen that the efficiency of the +1 order beam is highest when the duty cycle is equal to 0.5. So it is possible to vary the intensity of the illumination beam on a pixel to pixel basis by varying the duty cycle of hologram. With the help of the PC running a Labview program the duty cycle of the computer generated binary amplitude hologram can be changed to get the desired variation of the intensity of the beam. Two holograms with different duty cycle along with their diffraction pattern are shown in Fig. 2. (a)-(d). The beam generated by the hologram described in equation (2) has the fixed intensity (say I_m). Now let the desired variable intensity of the beam is I where $0 \leq I \leq I_m$ for the second scanning.

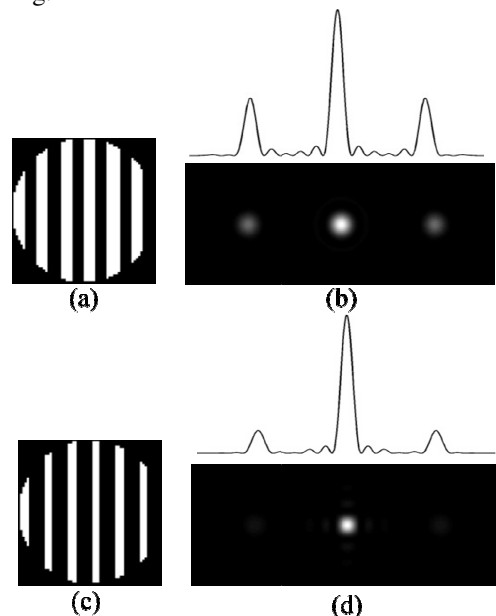


Fig. 2. Holograms (a) with duty cycle=0.5 (c) with duty cycle <0.5. The resulting diffraction orders are seen (b) and (d) along with their intensity profile.

The pixel value of the LCSLM to get the desired intensity of the illumination beam is given by

$$p(x, y) = \begin{cases} 1 & \text{if } \cos\{\Phi(x, y)\} > \cos\{\sin^{-1}(I)\} \\ 0 & \text{if } \cos\{\Phi(x, y)\} \leq \cos\{\sin^{-1}(I)\} \end{cases} \quad (4)$$

If $I=1$, the duty cycle is 0.5 and if $I=0$ the duty cycle is 0. For manipulating the holograms to generate the beam with variable intensity while it scans the sample plan, it is required to have a priori transmissivity profile of the sample plane. This is achieved by recording an image of the sample with fixed intensity of the illumination beam for the entire sample plane.

4. THE EXPERIMENTAL SET UP

The experimental set up for the proposed scanning microscope in the transmissive mode is shown in Fig. 3. Here the beam from a He-Ne laser is expanded and

collimated using the two lenses L_1 and L_2 . The collimated beam is then reflected by a reflective type LCSLM which is interfaced to a PC. A suitable binary amplitude hologram is displayed on the LCSLM. The diffracted beam from the LCSLM panel is focused by another lens L_3 , which is placed at a distance equal to the focal length of L_3 from the LCSLM. On the back focal plane of the L_3 the sample is kept and the +1 order beam is isolated from the other diffraction orders using an iris diaphragm (ID) placed just in front of the sample plane. The light transmitted through the sample is collected by lens L_4 and focused on a CCD camera. The beam on the sample plane is scanned by suitably changing the holograms displayed on the LCSLM so that the duty cycle of the hologram remains constant. As a result the focal spot on the sample plane and its image on the CCD camera describe a rectangular area. To collect the signals for each position of the beam on the CCD camera the program generates a square around the focal spot on the CCD image. During the scanning of the beam, the program generated square is synchronized to move with the beam [6].

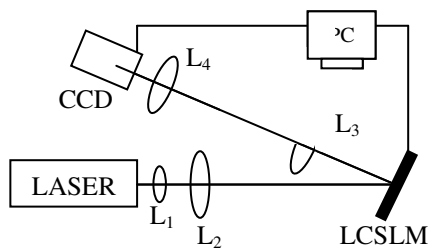


Fig. 3. The experimental setup

Now to vary the intensity of the illumination beam, the program reads the image recorded with constant intensity beam to identify the location of weak transmissivity. Let the image recorded with the fixed intensity beam is $i_1(x,y)$. The weighted intensity $w(x,y)$ of the beam during the second scanning is described by

$$w(x,y) = \frac{\frac{M - i_1(x,y)}{M - m} + \frac{w_m}{1 - w_m}}{1 + \frac{w_m}{1 - w_m}} \quad (5)$$

where M and m are the maximum and minimum pixel values of the image $i_1(x,y)$. The weighted intensities for the most transmittance and the least transmittance regions are taken as 0.25 and 1 respectively.

The program then computes a series of holograms and displays on the LCSLM so that the intensity of the +1 order beam is relatively high in the low transmissive region than the high transmissive region. The second image $i_2(x,y)$ is then recorded with the modified set of holograms. The final image of the sample with better SNR is digitally constructed from the two recorded images using the relation

$$i_3 = \frac{i_1 + i_2}{1 + w} \quad (6)$$

5. RESULT AND DISCUSSION

The image i_1 of a sample is recorded in 128×128 pixels with fixed intensity beam and displayed in Fig. 4(a). From this image the weighted intensity w of beam is calculated and a second image i_2 is recorded with the modified beam and displayed in Fig. 4(b). The final image is constructed digitally from the two images and is shown in Fig. 4(c). A plot of the image pixel values along the line of the images is shown in Fig. 4 (d). The rounded portion of 4(d) is magnified and shown in Fig. 4(e). From the plot it can be seen that the signals from the weak transmissivity region has improved in the second image as well as in third image compared to the first image.

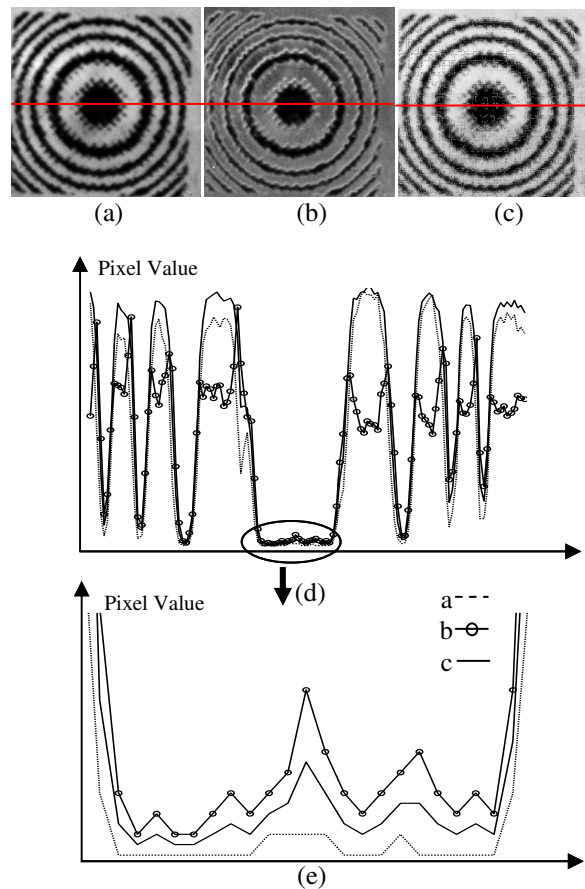


Fig. 4. Recorded images (a), (b) and digitally reconstructed image (c) with their line plot (d). The magnified line plot of the rounded portion in (d) is shown in (e) in arbitrary scale.

6. CONCLUSION

We have presented a scanning optical microscope with variable illumination beam intensity. The scanning is achieved using binary hologram written over a computer controlled LCSLM. Unlike the conventional scanning microscope the proposed microscope has relatively high illumination beam intensity in the regions of the sample plane with weak reflectivity or transmissivity. The proposed system can thus increase the overall SNR especially in the region from where the signals received are weak.

REFERENCES

- [1] J.B. Pawley, ed., *Handbook of Biological Confocal Microscopy*, Springer, 2006
- [2] T. Wilson, ed., *Confocal Microscopy*, Academic Press, 1990
- [3] M. A. A. Neil, M. J. Booth, and T. Wilson, "Dynamic wave-front generation for the characterization and testing of optical systems," *Opt. Lett.* **23**, 1849 (1998)
- [4] B. R. Boruah, "Dynamic manipulation of a laser beam using a liquid crystal spatial light modulator", *Am. J. Phys.* **77**, 331 (2009).
- [5] Robert E. Fischer, Biljana Tadic-Galeb and Paul R. Yoder, *Optical System Design*, McGraw-Hill Companies, 2008.
- [6] Abhijit Das and B. R. Boruah, "Optical sectioning microscope with a binary hologram based beam scanning", *Review of Scientific Instruments* : **82** 043702 (2011).

OPTICAL TECHNOLOGIES FOR ISRO'S SPACE PROGRAMMES: CURRENT AND FUTURE TRENDS

C L Nagendra* and P. Chakraborty
Laboratory for Electro-Optics Systems(LEOS)
Indian Space Research Organization(ISRO)
First Cross, First Phase, Peenya Industrial Estate
Bangalore 5600 58
[*clnagendra@leos.gov.in](mailto:clnagendra@leos.gov.in)

ISRO has made a mark in the areas of remote sensing and weather observation and forecasting by successful launching and use of several state of the art electro-optical payloads on board Indian Remote Sensing (IRS) and weather observation satellites, on operational basis. In all these electro-optical systems, the front end optical systems are 'the eyes' of the electro-optical (E. O) systems. The optical systems' performance, in terms of image quality at the required spatial frequency, radiometric though put, spectral and spatial resolution, stability of image format against thermal and vibration environments, field of view dictate the performance of the E. O. sensors in space. Added to these demanding requirements, the optics is required to be optimized with respect to weight and volume. Over the last two to three decades, several optical systems belonging to reflective, refractive and catadioptic categories have been developed and flown. For this several optical technologies have been developed which are, mirror light weighting design and light weighted mirror development and testing meeting the requirements of very low surface deviations, demonstration of mirror wave front error (WFE) under near zero g condition, precision surface polishing techniques, with micro-roughness close to 0.2nm, thin film coating technologies, comprising of reflective and refractive coatings, and band pass optical filters. In addition to these, opto-mechanical design and fabrication techniques leading to high performance multi-element lens assemblies have given way to successful

development of high resolution lens optics assemblies and their successful use in several wide angle and medium and long focal length high resolution cameras in IRS satellites.

In the coming decade, there will be requirements in enhancing the size of the optics with improved light weight ratio yet maintaining the optical performance close to the theoretical limits, and surface roughness better than 0.1nm to achieve scattering loss of the mirrors close to 1ppm. In order to integrate multiple wavelengths in a single optical system, novel optical band pass filter configurations are required to developed and qualified for applications in future space optics. It will be inevitable to enlarge the field of view of and the operating wavelength range of lens assemblies with enhanced image quality performance at higher spatial frequency. All these demanding requirements call for new optical technologies.

In this invited talk, the authors will present the current technologies which are in use in the development of space optics for ISRO's space programmes and special features of optics flown in IRS, INSAT and science mission satellites. The new investigations which are under progress in the areas of optics for ultraviolet wavelength, super smooth mirror surface for Aditya mission, and retro-reflector tray for laser ranging will be discussed. The presentation will also cover the road map of optics development for future missions of ISRO.

COMPARATIVE STUDY OF DIRECTIONAL COUPLER AND TWO-MODE INTERFERENCE COUPLER BASED ON TOOTH SHAPED GRATING ASSISTED STRUCTURE

Bidyut Deka, Aradhana Dutta, Nilima Gogoi, Partha Pratim Sahu*
Department of Electronics & Communication Engineering, Tezpur University,
Tezpur, Assam-784028 (India)

*Corresponding email: pps@tezu.ernet.in

Abstract: In the paper, comparative study of an ultra compact two mode interference (TMI) couplers and directional coupler (DC) based on tooth shaped grating geometry has been presented using a mathematical model based on sinusoidal mode simple effective index method (SEIM). Using this model, we have shown the transition of grating assisted directional coupler (GA-DC) to grating assisted TMI (GA-TMI) coupler by decreasing coupling gap. It is seen that the beat length of tooth shaped GA-DC and GA-TMI coupler for $\Delta n=5\%$ is $\sim 50\%$ less than that of DC and TMI coupler without grating.

1. INTRODUCTION

Recently, the compact waveguide device components based on grating assisted structures have been a growing interest in the application of integrated optic circuits (IOC) for its compactness property, which is very much essential for high density integration of photonic integrated devices (PID) [1-8]. The basic components of these PIDs are power divider, filter, modulator, ring resonator, and switch based on directional coupler (DC) [1], two-mode interference (TMI) coupler [2], multimode interference (MMI) coupler [3], X-branches [4], Y-branches [4], MZ-structures [5] etc. From the literature review, it is seen that very few studies are made on the comparative study of directional coupler and two mode interference couplers for grating assisted geometry [6-7]. To our knowledge no literature is available, stating transformation relationship for grating assisted directional coupler (GA-DC) and grating assisted TMI (GA-TMI) coupler based on tooth shaped grating structure. We have already shown the transition from DC to TMI coupler without grating [8].

In this paper, a mathematical model based on sinusoidal mode simple effective index method (SEIM) [1,8] has been used for details comparative study of modal power in tooth shaped grating assisted

directional coupler (GA-DC) with grating assisted two mode interference (GA-TMI) coupler. It is also shows the transition of GA-DC with very small waveguides separation gap into GA-TMI coupler.

2. DESIGN AND PRINCIPLES

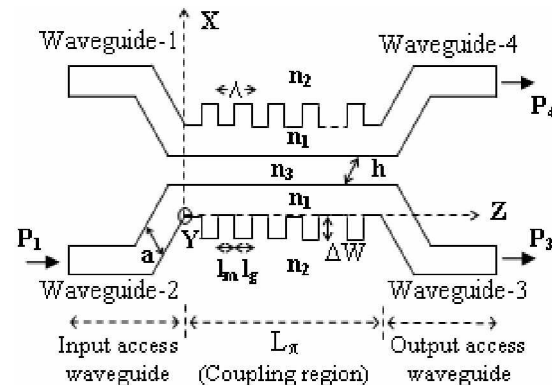


Fig-1: Schematic view of GA-DC with small waveguide separation gap $\sim h$.

The fig-1 shows the two dimensional (2D) cross-sectional schematic view of 2×2 tooth shaped grating assisted directional coupler (GA-DC) with small waveguide separation gap $\sim h$. The channel waveguide of GA-DC consists of two single mode input access waveguides (Waveguide-1 & Waveguide-2) of core width a and thickness b , two single mode output access waveguides (Waveguide-3 & Waveguide-4) of similar core dimensions. The coupling region of length L with alternating guiding width ($W_m=2a+h$)

and grating width ($W_g=W_m+2\Delta W$, where ΔW =tooth width of grating) is consist of N total numbers of grating period, $\Lambda=l_m+l_g$; where l_m and l_g are the length of guiding width ($K=m$) and grating width ($K=g$) in each grating period respectively. n_1 and n_2 are the refractive index of core and cladding region respectively, whereas n_3 is refractive index of the coupling cladding region in the waveguide separation gap. P_1 is the input power launched into lower most input access waveguide and P_3 , P_4 are the output powers as bar state and cross state respectively.

When the input signal mode field of propagation constant $\beta_i(\lambda)$ is incident through input single mode access waveguide (Waveguide-2), even and odd modes are excited in the grating assisted coupling region. At the end of GA-DC coupling region, based on relative phase difference between these modes in both guided and grating region, the light power is either coupled into two single mode output access waveguides (Waveguide-3 and Waveguide-4) or losses out. As fundamental and first order modes hold most of signal power, the beat length (defined as the length for π phase shift) for the directional coupler assisted with total N numbers of grating period is approximated as [6],

$$L_\pi = [(N+1)l_m + Nl_g] = \frac{\pi}{[(\beta_{00}^m - \beta_{01}^m) + (\beta_{00}^g - \beta_{01}^g)]} \quad (1)$$

where $\beta_{00}^m, \beta_{01}^m$ and $\beta_{00}^g, \beta_{01}^g$ are the propagation constants of fundamental and first order modes in the guiding region ($K=m$) and grating region ($K=g$) respectively.

Fig-2 shows the schematic cross sectional view of a tooth shaped grating assisted TMI coupler with the channel waveguide consisting of two input access waveguides of width a, thickness b and two output access waveguides of same dimensions, whereas the waveguides separation gap, $h \sim 0 \mu m$. The coupling region of beat length L_π is consist of total N numbers

of grating period (Λ) where each grating period is consist of guiding width, W_m and grating width, W_g respectively. n_1 and n_2 are the refractive indices of the core and cladding region respectively.

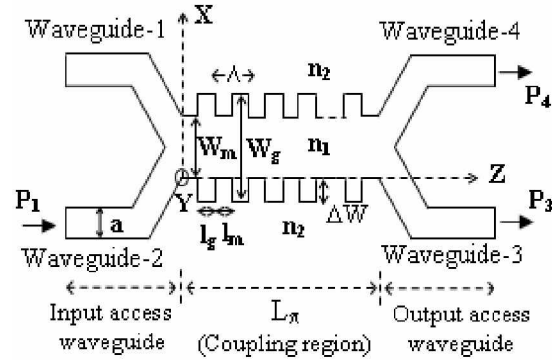


Fig-2: Cross-sectional view of GA-TMI coupler.

At the end of coupling region in the tooth shaped GA-DC, the optical power is either transferred to the output access waveguides or lost out. The mode field of output access waveguides is contributed by all guided modes propagated in grating assisted coupling region. The mode fields at M^{th} access waveguide a distance $z=L$ inside GA-DC region for can be written as

$$H_M(x, L) = \sum_{i=0}^{r-1} H_{M,i}(x, L) = \sum_{i=0}^{r-1} c_{M,i} H_i(x) \exp[j(\beta_0 - \beta_i)L] \quad (2)$$

where $i=0, 1, 2, \dots, (r-1)$ denotes the order of guided modes, β_0 is the propagation constant of fundamental mode ($i=0$) and β_i represents the propagation constant for i^{th} order mode respectively. $L=[(N+1)l_m+Nl_g]$ and $c_{M,i}=(C_{M,i})^{1/2}$ is the i^{th} order mode's contribution coefficient (measure of field contribution) which can be calculated by using a mathematical model based on sinusoidal mode simple effective index method (SEIM) [8] as,

$$\frac{C}{C_0} = \frac{\pi^2 b^3}{64 a^3} \left[\frac{1}{V_1^2} \exp\left(\frac{-2V_1 h}{b}\right) \left\{ \exp\left(\frac{2V_1 a}{b}\right) - \exp\left(\frac{-2V_1 a}{b}\right) \right\} + \frac{1}{V_2^2} \exp\left(\frac{-2V_2 h}{b}\right) \left\{ \exp\left(\frac{2V_2 a}{b}\right) - \exp\left(\frac{-2V_2 a}{b}\right) \right\} \right] \quad (3)$$

where C_0 is the normalization coefficient and

$$V_1 = \frac{b}{2} k \sqrt{n_1^2 - n_2^2}, V_2 = \frac{b}{2} k \sqrt{n_1^2 - n_3^2} \quad (4)$$

Normalized coupling power at the M^{th} output access waveguide for tooth shaped grating assisted directional coupler can be approximated as [6],

$$\frac{P_{M,i}(x,L)}{P_{1,i}(x,0)} \approx \sum_{i=0}^{r-1} C_{M,i} H_i^2(x) + \sum_{i=0}^{r-1} \sum_{j=1+i}^{r-1} \left[2\sqrt{C_{M,i} C_{M,j}} H_i(x) H_j(x) \times \cos \left\{ \sum_{\substack{i=0, j=i+1 \\ K=m, g}}^{r-1} [(N+q_K)(\beta_i^K - \beta_j^K) L_K] \right\} \right] \quad (5)$$

where $i, j = 0, 1, 2, 3, \dots (r-1)$ are order of modes so that $j > i$, $N = \text{Number of grating period}$, $q_K = 0, 1$ for grating width ($K=m$) and guided width ($K=g$) respectively. $C_{M,i}, C_{M,j}$ are the contribution coefficient to M^{th} output access waveguides for i^{th} and j^{th} order modes whereas β_i, β_j are propagation constant for i^{th} and j^{th} order modes that are determined from dispersive equations [5,8].

3. RESULTS AND DISCUSSIONS

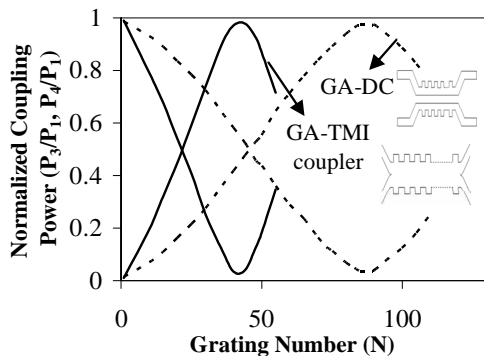


Fig-3: Normalized coupling power vs. number of grating period (N) for GA-DC and GA-TMI coupler with $\Delta n=5\%$, $\Delta W=0.2 \mu\text{m}$.

Fig-3 shows the normalized coupling power (P_3/P_1 and P_4/P_1) vs. number of grating period (N) calculated using eqn. (1)-(5) for the tooth shaped grating assisted

directional coupler ($h=3.0 \mu\text{m}$) and grating assisted TMI coupler ($h=0 \mu\text{m}$) with $\Delta W=0.2 \mu\text{m}$, $\Delta n=5\%$, $a=1.5 \mu\text{m}$, $b=1.5 \mu\text{m}$, $l_m \approx l_g \approx 0.27 \mu\text{m}$, $n_1=1.5$, $n_2=1.45$ and wavelength $\sim 1.55 \mu\text{m}$. From the plot, it is seen that the peak normalized coupling power (P_4/P_1) is obtain at beat lengths (calculated using equ. (1)) $\sim 24 \mu\text{m}$, $48 \mu\text{m}$ respectively, with the corresponding values of N are 44 and 90 for grating assisted TMI coupler and grating assisted DC respectively.

When $h \rightarrow 0$, equation (3) reduces to

$$\frac{C}{C_0} = \frac{\pi^2 b^3}{64 a^3} \left[\frac{1}{V_1^2} \left\{ \exp\left(\frac{2V_1 a}{b}\right) - \exp\left(-\frac{2V_1 a}{b}\right) \right\} \right] \quad (6)$$

which yields similar coupling coefficient to that of a grating assisted two mode interference (GA-TMI) coupler with same parameters.

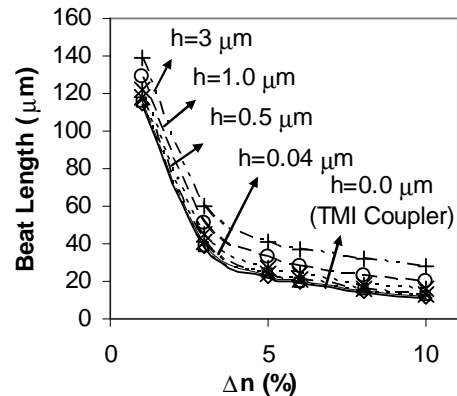


Fig-4: Beat length (L_π) versus Δn (%) for GA-DC with different gap ($h \neq 0$) and GA-TMI coupler ($h=0$) with $\Delta W=0.2 \mu\text{m}$.

Fig-4 shows the beat length (L_π) versus index contrast (Δn) that is estimated from coupling power distribution curves (as shown in Fig-3) using eqn. (1)-(4) and (6) for tooth shaped GA-TMI coupler ($h=0 \mu\text{m}$) and tooth shaped GA-DC with different values of waveguide separation gap, $h=0.04 \mu\text{m}$, $0.5 \mu\text{m}$, $1.0 \mu\text{m}$, $3.0 \mu\text{m}$ and $\Delta W=0.2 \mu\text{m}$, $a=1.5 \mu\text{m}$, $b=1.5 \mu\text{m}$, $n_1=1.5$, $n_2=1.45$ and wavelength $\sim 1.55 \mu\text{m}$. It is seen from the plot that the beat lengths for GA-DC and GA-TMI coupler decreases as Δn (%) increases. The rate of decrease of L_π is smaller for $\Delta n > 5\%$ and lower

values of h . As h becomes nearer to zero coupling gap ($h=0$), the curves become closer and at $h < 0.04 \mu\text{m}$, the curves for GA-DC almost coincide with the curve for GA-TMI coupler ($h=0 \mu\text{m}$). Thus, it is observed that for very small value of coupling gap ($h \sim 0.04 \mu\text{m}$), GA-DC shows equivalent behavior as that of GA-TMI coupler.

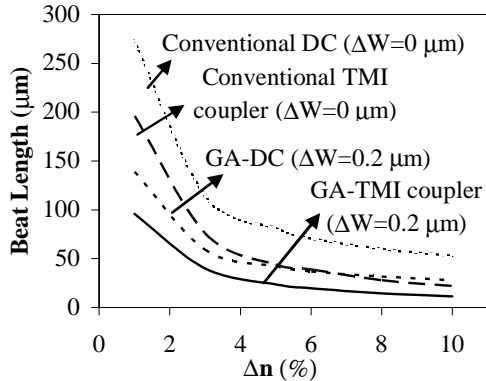


Fig-5: Beat length (L_π) versus Δn (%) for GA-DC, GA-TMI coupler with $\Delta W=0.2 \mu\text{m}$ and conventional DC, TMI coupler ($\Delta W=0 \mu\text{m}$) with $\Delta n=5\%$ and $\lambda \sim 1.55 \mu\text{m}$.

In Fig-5, it shows the beat length (L_π) versus index contrast (Δn) that is obtained using equation (1), (3) and (4) for GA-DC/GA-TMI coupler with $\Delta W=0.2 \mu\text{m}$ and conventional DC/TMI couplers ($\Delta W=0 \mu\text{m}$). It is observed from the plot that the beat lengths with $\Delta n=5\%$ for GA-DC, GA-TMI coupler, conventional DC and conventional TMI coupler are $\sim 48 \mu\text{m}$, $24 \mu\text{m}$, $96 \mu\text{m}$ and $48 \mu\text{m}$ respectively. It is also evident from the figure that beat length for grating assisted geometry has $\sim 50\%$ lower than that of conventional structures. The lower beat lengths in GA-DC/GA-TMI coupler are due to the multiple reflections that takes place in the tooth shaped grating geometry.

5. CONCLUSION

In this paper, we have shown transformation relationship between GA-DC and GA-TMI coupler. It is seen that GA-DC with coupling gap $\leq 0.04 \mu\text{m}$ is

equivalent to GA-TMI coupler and the beat length of GA-DC/GA-TMI coupler is $\sim 50\%$ less than conventional DC/TMI coupler.

REFERENCES

- [1] D. Marcuse, "Directional Couplers Made of Nonidentical Asymmetric Slabs. Part I: Synchronous Couplers", *J. of Lightwave Tech.*, **LT-5**, 113–118 (1987).
- [2] T. Y. Tsai, Z. C. Lee, C. S. Gau, F. S. Chen, J. R. Chen, C. C. Chen, "A novel wavelength-division multiplexer using grating assisted two-mode interference", *IEEE Photonic Tech. Letters*, **16**, 2251-2253 (2004).
- [3] L. B. Soldano, E.C.M. Pennings, "Optical multi-mode interference devices based on self-imaging: principles and applications", *J. Lightwave Tech.*, **13**, 615-627 (1995).
- [4] H.P. Chan, C. K. Chow, A. K. Das, "A wide angle X-junction polymeric thermo optic digital switch with low crosstalk", *IEEE Photonic Tech. Letters*, **15**, 1210-1212 (2003).
- [5] H. Nishihara, M. Haruna, T. Suhara, *Optical Integrated Circuits* (McGraw-Hill, New York, 1989).
- [6] Bidyut Deka, Partha Pratim Sahu, "Tooth-shaped grating-assisted structure for compact multimode interference coupler", *Appl. Opt.*, **50**, E193-E199 (2011).
- [7] T. Y. Tsai, Z. C. Lee, J. R. Chen, C. C. Chen, Y. C. Fang, M. H. Cha, "A novel ultra compact two-mode-interference wavelength division multiplexer for $1.5 \mu\text{m}$ operation", *IEEE J. Q. Elec.*, **41**, 741-746 (2005).
- [8] B. Deka, P. P. Sahu, "Transformation relationship of directional coupler with multimode interference coupler and two mode interference coupler", <http://dx.doi.org/10.1007/s12596-009-0008-7>, *J. of Optics*, **38**, 75-87 (2009).

SILICON PHOTONICS IN SOI PLATFORM: PROBLEMS WITH WAVEGUIDE DISPERSION AND BIREFRINGENCE EFFECTS

B.K. Das, Sujith C, G.R. Bhatt, U. Karthik, and R. Sharma
 Integrated Optoelectronics / Microelectronics & MEMS Labs
 Department of Electrical Engineering, IIT Madras, Chennai – 600 036, India
 E-Mail: bkdas@ee.iitm.ac.in

Abstract: Various SOI based waveguide geometries have been studied in terms of their guided mode birefringence, mode-field distributions, bend-induced waveguide losses, and wavelength dispersions. It has been observed that the major bottleneck of CMOS compatible silicon photonics devices in DWDM applications is the waveguide birefringence and group index dispersion effects.

1. INTRODUCTION

Compact, light-weight, cost-effective, multifunctional and efficient PIC/OEIC can be realized in SOI platform by integrating various photonic and electronic components via low-loss, broad-band and high-speed optical interconnects or tightly confined single-mode optical waveguides [1]. However, these waveguides are found to be highly dispersive as well as polarization dependent and consequently limiting the device performances.

In an effort to eliminate/compensate these discrepancies, we have studied various single-mode waveguide geometries in terms of guided mode birefringence, mode-field distributions, bend-induced waveguide losses, and wavelength dispersions.

2. SINGLE-MODE SOI WAVEGUIDES

Based on literature reports, we have classified four different types of single-mode SOI waveguides (see Table-I): (i) LCRW – large cross-section rib waveguide, (ii) RCRW – reduced cross-section rib waveguide, (iii) PhWRW – photonic wire rib waveguide, and (iv) PhWW – photonic wire waveguide. First two types of waveguides are compatible to microelectronics & MEMS technology whereas the last two types are CMOS compatible.

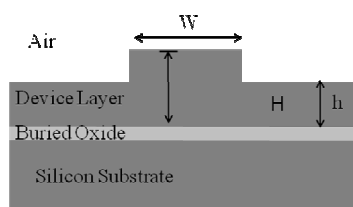


Fig. 1: Typical waveguide cross-sectional view in SOI platform: W – waveguide width, H – device layer thickness, and h – slab height.

Our theoretical investigations reveal that both LCRW and RCRW are nearly polarization independent and dispersion free. However, PhWRW and PhWW are found to be highly polarization sensitive and dispersive. Currently, we are working towards designing a polarization insensitive and

dispersion free silicon photonics devices based on optimized photonic wire waveguide geometry.

Table-I: Various single-mode waveguide parameters and group index dispersion (GID) at $\lambda = 1550$ nm.

	W [μm]	H [μm]	h [μm]	GID [nm^{-1}]	
				TE	TM
LCRW	5.0	5.0	3.2	-2×10^{-8}	-2×10^{-8}
RCRW	1.3	2.0	0.8	-2×10^{-6}	-2×10^{-6}
PhWRW	0.5	0.22	0.05	-6×10^{-4}	-9×10^{-4}
PhWW	0.5	0.22	0	-9×10^{-4}	-1×10^{-3}

3. EXPERIMENTAL RESULTS

We have successfully demonstrated single-mode LCRW and RCRW waveguide structures using conventional microelectronics technology. The LCRW structures were fabricated by single-step RIE process [2], whereas, the RCRW by a multi-step RIE process. As expected, they have been characterized as nearly polarization independent. The wavelength dependent performances of some fabricated integrated optical devices based on these waveguide geometries are being investigated and will be presented during the conference. RCRW structures are found to be technologically rugged in bio-sensing applications.

4. CONCLUSIONS

We have investigated the properties of various single-mode waveguide geometries in SOI platform. Polarization dependencies and wavelength dispersion appear to be the real bottleneck for CMOS compatible silicon optical interconnects. Wavelength dependent device performances will be presented.

REFERENCES

- [1] K. Ohira, et al, "On-chip optical interconnection by using integrated III-V laser diode and photodetector with silicon waveguide", *Opt. Express*, vol. 18, pp. 15440 – 15447, 2010.
- [2] R. Navalakhe, et al, "Fabrication and characterization of straight and compact S-bend optical waveguides on a silicon-on-insulator platform", *Appl. Opt.*, vol. - 48, G125-130, 2009.

SIMULATION OF INTEGRATED OPTIC STRUCTURES USING A BIDIRECTIONAL BEAM PROPAGATION METHOD

Debjani Bhattacharya and Anurag Sharma
Physics Department, Indian Institute of Technology Delhi-110016, New Delhi, India
debjani112@gmail.com, asharma@physics.iitd.ac.in

Abstract: We present a bidirectional beam propagation method using a nonparaxial split-step scheme. The method can model multiple reflecting structures very efficiently. Simulation of fiber Bragg gratings is presented.

1. INTRODUCTION

Analysis and modeling of reflections and transmissions are important for design of photonic structures. Numerical modeling of reflection requires methods, which can model both the forward and backward propagating fields. Methods like the finite difference time domain (FDTD) method are generally used for such modeling but these are computationally very extensive. On the other hand the beam propagation method (BPM) is a highly efficient method. However most BPM's are unidirectional and the prevalent bidirectional BPM's either use an iterative Padé method [1], or solve two paraxial equations for counter propagating fields iteratively [2] and are not very efficient. Recently we have developed a finite difference based split-step nonparaxial (FDSSNP) method which is bidirectional and can be used for treating reflections efficiently. Here we present simulation of a blanch fiber Bragg grating (FBG). More examples and application to volume Bragg gratings (VBG) will be presented later.

2. THE BIDIRECTIONAL FDSSNP METHOD

In our method the second order scalar wave equation is solved directly (without the one-way or paraxial approximations) in direction 'z' using a split step scheme [3]. Both the forward and backward propagating fields are present in the solution. The total field evaluation requires only numerical matrix multiplication. The forward and backward fields at any plane can be obtained from the total field and its z-derivative using the following relation,

$$\begin{bmatrix} \psi_+(z) \\ \psi_-(z) \end{bmatrix} = \begin{bmatrix} \frac{1}{2}\mathbf{I} & \frac{i}{2}\sqrt{\mathbf{S}_z^{-1}} \\ \frac{1}{2}\mathbf{I} & -\frac{i}{2}\sqrt{\mathbf{S}_z^{-1}} \end{bmatrix} \begin{bmatrix} \psi(z) \\ \psi'(z) \end{bmatrix} \quad (1)$$

where $\mathbf{S}_z = \partial^2/\partial x^2 + k_0^2 n^2(x, z)$.

3. MODELING PHOTONIC STRUCTURES

An FBG is a periodic or aperiodic perturbation of the effective refractive index in the core of an optical fiber. They are often used for wavelength filtering, as end mirrors in lasers, rocking filters, as distributed fiber optic sensors among others. We present simulation of a blanch FBG which are widely used as sensors. The incident field is a fundamental mode.

Waveguide parameters: $w_{core} = 3\mu m$, $n_2 = 1.4529$, $n_1 = 1.4579$. FBG parameters: $l = 1cm$, $\Lambda = 0.282\mu m$, $tilt = \theta$, $\Delta n(z) = \Delta n + n_{mod} \sin^2(\pi z/\Lambda)$, $\Delta n = 5 \times 10^{-4}$, $n^2(x, z) = n_2^2 + 2n_1 \Delta n(z) \sec^2(2x/w_{core})$. Fig.1 shows the reflectivity spectrum with variation of tilt angle. Fig. 2 shows the fundamental field coupling to the second mode in an FBG for $\theta = 4^\circ$ at $\lambda = 0.82264\mu m$.

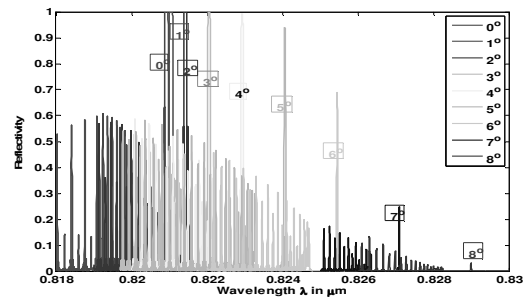


Fig. 1: Spectrum of a tilted FBG

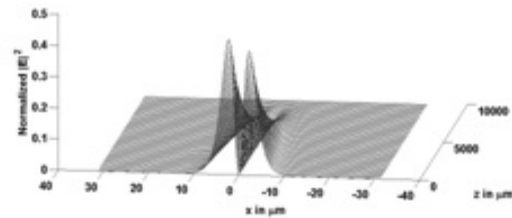


Fig. 2: Reflected field for $\theta = 4^\circ$ at $\lambda = 0.82264\mu m$

ACKNOWLEDGEMENT

One of the authors (DB) would like to acknowledge CSIR (Govt. of India) for financial support.

REFERENCES

- [1] H. L. Rao, R. Scarmozzino, and R. M. Osgood Jr., "A bidirectional beam propagation method for multiple dielectric interfaces," *IEEE Photon. Technol. Lett.*, **11**, 830 (1999).
- [2] H. Shu and M. Bass, "Modeling the reflection of a laser beam by a deformed highly reflective volume Bragg grating," *Appl. Opt.*, **46**, 2930 (2007)
- [3] A. Sharma, A. Agrawal, "Non-paraxial split-step finite-difference method for beam propagation," *Opt. Quantum Electron.*, **38**, 19 (2006).

INLINE EXCITATION OF OPTOMECHANICAL OSCILLATIONS

Muhammad Umar Khan* and Thomas F. Krauss
 School of Physics and Astronomy, University of St. Andrews,
 St. Andrews, Fife KY16 9SS United Kingdom
 *muk@st-andrews.ac.uk

Abstract: In the present paper, we have experimentally demonstrated excitation of optomechanical oscillations at 36.8 MHz using inline end-fire coupling instead of commonly used tapered fibers. Light was coupled to the periodic structures using silicon waveguides fabricated next to the structures in place of plane tapered fibers. Side-coupled structures were simulated, fabricated and characterized to achieve inline optomechanical oscillations.

1. INTRODUCTION

Optomechanics, a combined study of optical and mechanical properties of structures, has become a very important branch of photonics [1, 2]. It combines properties and characteristics of both optical cavities [3] and mechanical resonators [4], which were considered to be two separate subjects earlier. Optomechanical oscillations of the micro-fabricated structures using light have already been observed experimentally by different groups to achieve frequencies ranging from a few kilohertz to hundreds of Megahertz [4, 5]. In this paper, we have used in-plane excitation scheme to excite the optomechanical oscillations instead of using the out of plane tapered fibers. Inline excitation of the optomechanical structures will pave the way for on chip optical processing.

Periodically varying refractive index structures, such as photonic crystals provide very high values of optical quality factor. Coupled light, which is resonant with the cavity is trapped within the cavity, and creates a large circulating power within the cavity because of high value of quality factor. Photons of the trapped light keep on hitting the walls of the cavity and transfer their momentum. Net force equal to the rate of change of momentum will act on the walls of cavity given by;

$$F = \frac{\Delta p}{\Delta t} = \frac{2P}{c} \quad (1)$$

Here, P is the incident average optical power, c is the speed of light and F represents the force acting on the walls. It results in displacement of the walls of the cavity from its equilibrium position and causes the walls to oscillate around its equilibrium position. New roundtrip conditions were formed because of the change in the length of the cavity and two new frequencies named stokes and anti-stokes frequencies corresponding to the extreme positions of the walls are generated. These newly generated frequencies corresponding to the extreme positions are shown in Fig. 1.

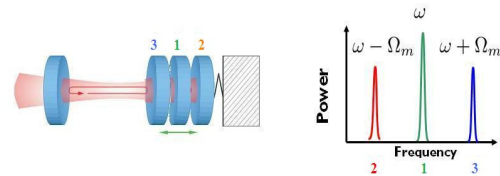


Fig. 1. Extreme positions of oscillating mirror of optomechanical cavity are represented by positions 1, 2 and 3. The sidebands created because of the oscillation of the mirror are marked corresponding to the position generating them.

Generation of these two side frequencies at $\omega - \Omega_m$ and $\omega + \Omega_m$ give rise to optomechanical oscillations.

2. EXPERIMENTAL WORK

We have used the Ladder structure given in [3] to achieve inline excitation of optomechanical oscillations. These ladder structures having waveguides next to them, called side-coupled Ladder structures, were simulated, fabricated and characterized to achieve the final goal of inline optical excitation.

2.1 Simulation

Ladder structure given in [3] was simulated to find the resonance wavelength. The quadratic defect introduced in the periodic Ladder structure forms a cavity within the structure. Resonance wavelength of the cavity was calculated using FDTD software “FullWave RSoft”. Two dimensional ladder structure was modeled and material was assigned the silicon refractive index. Source and a detector were placed inside the cavity to launch and detect optical field inside the cavity, respectively. Intensity of the optical field and its distribution are shown in Fig. 2. Peak at 1.6 μm in Fig. 2(b) gives the resonance wavelength of the cavity. Gaussian distribution of the field at resonance wavelength is shown in figure 2(c).

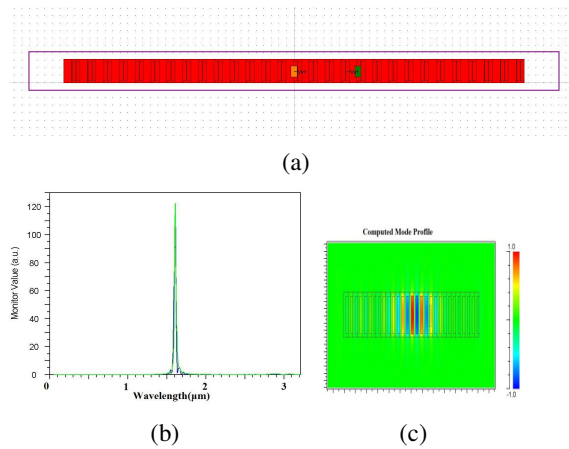


Fig. 2. a) Modeled structure with source and detector placed inside the cavity. b) Calculated resonance wavelength at $1.6 \mu\text{m}$. c) Field calculated inside the cavity.

Three dimensional silicon structures were simulated to find the mechanical resonance frequency of Ladder structure using FEM software “COMSOL Multiphysics 4.0 Values of Young’s modulus and density were assigned to the ladder structure to observe mechanical properties of silicon. Mechanical eigenfrequency of the structure were then calculated generating a fine mesh. Fig. 3(a) shows the modeled three dimensional ladder structure for mechanical simulation. Simulated mechanical frequency of 36.35 MHz provided an estimate of the expected resonance frequencies of Optomechanical oscillations. Calculated mechanical resonance frequency is shown in Fig. 3(b).

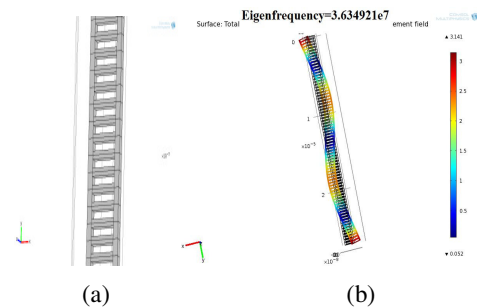


Fig. 3. a) Three dimensional modelling of the ladder structure for mechanical resonance frequency calculation. b) Mechanical resonance frequency of 36.35 MHz calculated using silicon properties $Y= 168.5 \text{ GPa}$ and $\rho= 2330 \text{ Kg/m}^3$.

2.2 Fabrication

Simulated side-coupled structures were fabricated on 220nm Silicon-on-Insulator (SOI) wafers to confirm the simulation results. Structures were fabricated using e-beam lithography. Electron beam

sensitive mask was coated on wafer and was exposed to the e-beam for exposure. Structures were imprinted on silicon after exposure and development using Reactive Ion Etching (RIE). Buffered Hydrofluoric Acid (HF) was used after etching to release structure from the silica to make structures suspend in the air like a bridge. Structures were released from the silica so that silica may not hinder the oscillations. Fig. 4 shows the pictures taken using Scanning Electron Microscope (SEM).

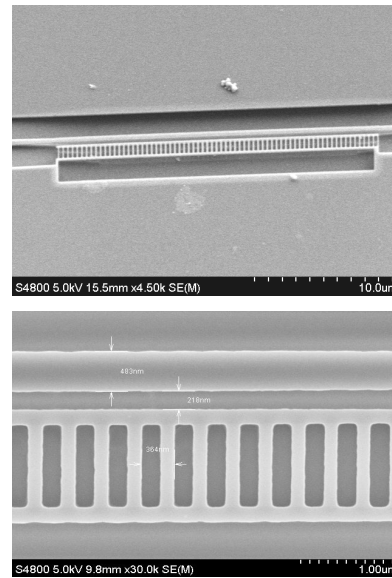


Fig. 4. SEM pictures of the fabricated side-coupled Ladder structures.

2.3 Characterization

Fabricated structures were characterized to observe the resonance wavelength of the cavity experimentally. Fabricated structures were excited using Amplified Spontaneous Emission (ASE) source ranging from 1520nm to 1620nm. Light was coupled to the waveguide fabricated next to the structure and was collected from other end of the waveguide to observe the transmission response. Setup used to characterize the fabricated structure is shown in the Fig. 5.

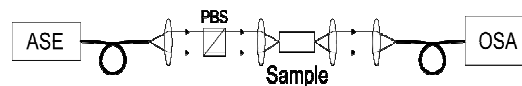


Fig. 5. Setup used for optical characterization.

Beam splitter was used to couple only Transverse Electric (TE) polarization of the light to the sample. Light was focused and collected using lenses shown in the Fig. 5. Optical spectrum analyzer was used to observe the transmission response of the side-coupled

ladder structure. Resonance wavelength of the cavity was found to be lying within the telecom wavelength range. Dips in Fig. 6 at 1543 nm and 1568 nm represent the resonance of the fabricated structure.

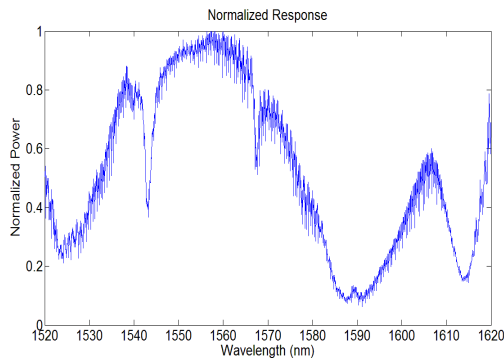


Fig. 6. Normalised transmission response showing the resonance dips at resonance wavelengths.

Same structure was characterized to observe the mechanical behavior of the cavity. Structure was excited at the observed fundamental resonance wavelength with narrow line-width laser to observe the optomechanical resonance. Setup used for mechanical characterization of the fabricated device is shown in Fig 7.

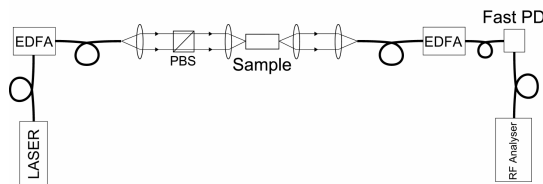


Fig. 7. Setup used for mechanical characterization.

RF spectrum analyzer and fast photo-detector were used to observe the optomechanical oscillations excited with narrow line-width laser. Fast photo-detector converts optical signals to electrical signals as RF spectrum analyzer could detect only the electrical signals. Erbium Doped Fiber Amplifiers (EDFA) were further used to amplify the optical signal so that fast photo-detector which could detect optical power only in mill watts could detect it. Fundamental optomechanical oscillation at 36.8 MHz and its higher harmonics at multiples of 36.8 MHz were observed on RF spectrum analyzer during characterization. Transmission response observed using the mechanical characterization setup is shown in Fig. 6. Peaks represent the fundamental and higher harmonics of the optomechanical oscillations.

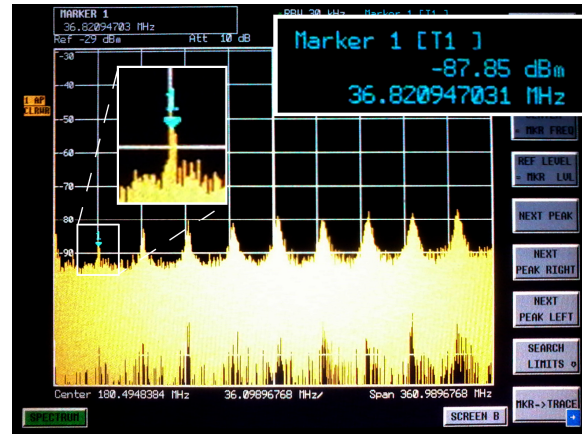


Fig. 8. Experimentally observed optomechanical frequency of 36.8 MHz and its higher harmonics on RF Spectrum Analyzer.

Fundamental mode of the optomechanical oscillation at 36.82 MHz is enlarged in the Fig. 8 and is in agreement with the simulated resonance frequencies.

Optomechanical frequencies of 36.8 MHz and its higher harmonics were observed on RF spectrum analyzer showing the inline excitation of optomechanical oscillations.

3. APPLICATIONS

The devices on semiconductor chips like oscillators [6, 7], optical mixers [8], tunable optical filters, semiconductor lasers [9], optical clocks and all optical switches [10, 11] are some of the future possible applications of the semiconductor optomechanics.

4. CONCLUSIONS

We have experimentally demonstrated inline excitation of optomechanical oscillations using side coupling technique. Optomechanical oscillations with fundamental frequency of 36.8 MHz are observed which confirms the simulation results. This inline excitation will pave the way for on-chip processing of the optical signals.

ACKNOWLEDGEMENTS

We acknowledge the facilities provided by Department of Physics and Astronomy, University of St. Andrews, St. Andrews, United Kingdom. Funding for this project was provided by Erasmus Mundus Master of Photonics consortium.

REFERENCES

- [1] D. Van Thourhout and J. Roels, "Optomechanical device actuation through the optical gradient force," *Nat. Photonics* 4, 211-217 (2010).
- [2] T. J. Kippenberg and K. J. Vahala, "Cavity optomechanics: Back-action at the mesoscale," *Science* 321, 1172-1176 (2008).
- [3] K. J. Vahala, "Optical microcavities," *Nature* 424(6950), 839-846 (2003).
- [4] H. G. Craighead, "Nanoelectromechanical systems," *Science* 290(5496), 1532-1535 (2000).
- [5] M. Eichenfeld, J. Chan, R. M. Camacho, K. J. Vahala & O. Painter "Optomechanical crystals," *Nat.*, **462**, 78-82, 2009.
- [6] T. J. Kippenberg, H. Rokhsari, T. Carmon, A. Scherer, and K. J. Vahala, "Analysis of Radiation-Pressure Induced Mechanical Oscillation of an Optical Microcavity," *Physical Review Letters* 95, 033,901 (2005).
- [7] H. Rokhsari, T. J. Kippenberg, T. Carmon, and K. J. Vahala, "Radiation-pressure-driven micro-mechanical oscillator," *Optics Express* 13(14), 5293-5301 (2005).
- [8] Hossein-Zadeh, Mani and Vahala, Kerry J. (2008) Photonic RF Down-Converter Based on Optomechanical Oscillation. *IEEE Photonics Technology Letters*, 20 (4). pp. 234-236. ISSN 1041-1135.
- [9] T. P. M. Alegre, R. Perahia, and O. Painter, "Optomechanical zipper cavity lasers: theoretical analysis of tuning range and stability," *Opt. Express* 18, 7872 (2010).
- [10] M. L. Povinelli, J. M. Johnson, M. Loncar, M. Ibanescu, E. J. Smythe, F. Capasso, and J. D. Joannopoulos, "High Q enhancement of attractive and repulsive optical forces between coupled whispering-gallery-mode resonators," *Optics Express* 13(20), 8286-8295 (2005).
- [11] M. Eichenfeld, C. Michael, R. Perahia, and O. Painter, "Actuation of Micro-Optomechanical Systems Via Cavity Enhanced Optical Dipole Forces," *Nature Photonics* 1(7), 416 (2007).

ISOLATED POLARIZATION SINGULARITIES

Nirmal K. Viswanathan

Beam Optics and Applications Group

School of Physics, University of Hyderabad, Hyderabad-500046, India

Email: nirmalsp@uohyd.ernet.in

Abstract: Isolated Polarization Singularities - IPSs (*C*-point and *s*-line) in a paraxial ellipse field are generated at the output of a two-mode optical fiber excited by circularly-polarized Gaussian and Laguerre-Gaussian beams. The IPSs, used as markers, enables the study of transverse energy flow in optical beams and the phase and amplitude behavior under different experimental conditions.

1. INTRODUCTION

Singular optics, the study of optical beams with embedded phase and polarization singularities is an important topic of research in modern physics to understand the physics of light [1, 2]. Optical vortices (OVs) are phase singularities in scalar fields due to wavefront dislocations. Polarization singularities in vector fields of paraxial optical beams are known as wavefront disclinations which includes vector singularities and Stokes singularities [3]. In paraxial optics, the general state of field with two orthogonal components resulting in elliptically polarized state leads to two special conditions of Stokes singularities in the observation plane: *C*-point, on which the field is circularly polarized, where the orientation of the major and minor axes of the ellipse are undefined and *s*-line, on which the field is linearly polarized, where the handedness of the ellipse is undefined [4].

The generic paraxial ellipse speckle field generated using a multimode optical fiber was analyzed using singular Stokes polarimetry (SSP) [5]. The SSP measurements of paraxial ellipse field structure and its topology and morphology analyses are promising techniques for both fundamental investigations and technical applications. We recently demonstrated a method to control the IPS characteristics generated at the output of a two-mode optical fiber, excited by offset-tilted circularly polarized Gaussian beam [6]. Here we present our study of the fine structure of the output field to understand the topology, morphology and dispersion characteristics of the IPSs. The characteristic IPS markers are also used to study the transverse energy flow in optical beams and to characterize the phase and amplitude asymmetries under different experimental conditions.

2. EXPERIMENTAL DETAILS

Coherent superposition of the fundamental (HE_{11}) and vector-vortex modes ($CV_{\pm 1}^{\pm}/IV_{\pm 1}^{\pm}$), excited by circularly polarized ($\sigma = \pm 1$) Gaussian and Laguerre-Gaussian (LG) beams, in a two-mode optical fiber results in controlled generation of IPSs [6]. Schematic of the experimental setup used for the

generation and the output beam indicating the presence of singularities are shown in Fig. 1 below:

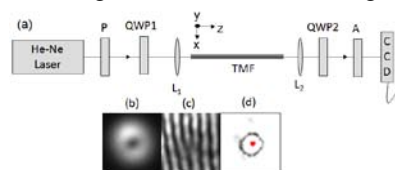


Fig. 1 Experimental setup and results (see text)

3. RESULTS AND DISCUSSION

SSP measurements were carried out on the output beam to identify the well-defined IPSs: *C*-point – red dot and *s*-line: circular contour around it in Fig. 1 (d). The IPSs generated for $\sigma = \pm 1$ Gaussian and LG beams show controllable topology and morphology characteristics. The dispersion of the excited fiber modes changes the IPS characteristics significantly. The transverse energy flows in optical beams without and with angular momentum (AM) are understood in the context of beams with single *C*-point and dipoles. IPSs used to investigate total internal reflection (TIR) and reflection at Brewster angle shows dramatic changes in the behavior of the PS characteristics due to phase and amplitude asymmetries introduced. The results and analysis of the study will be presented in the talk.

4. SUMMARY

Using the isolated polarization singularities generated at the output of a two-mode fiber we study transverse energy flow in optical beams and use them to understand phase and amplitude asymmetries.

ACKNOWLEDGEMENT

The author acknowledges DST for financial support and his research students for all measurements.

REFERENCES

- [1] M.S. Soskin et al., Prog. in Optics **42**, Ch 4, 2001
- [2] M.R. Dennis et al., Prog. in Optics **53**, 293, 2009
- [3] I. Freund, Opt. Commun., **199**, 47, 2001
- [4] J.F. Nye, "Natural focusing and fine structure of light," (IOP Publishing, 1999)
- [5] M.S. Soskin and V. Denisenko, Opt. Lett., **28**, 1475, 2003
- [6] Y.V. Jayasurya et al., Appl. Opt., **50**, E131, 2011

ROLE OF SURFACE PLASMONS IN MODULATING SPECTRAL AND COHERENCE PROPERTIES OF THE INCIDENT FIELD

H.C. Kandpal, Bhaskar Kanseri and Manish Verma
 CSIR-National Physical Laboratory, New Delhi-110012.
 Email: hckandpal@mail.nplindia.org

Abstract: It is shown theoretically that the spatial coherence and also the spectra of the field emerging of a gold double slit can be modified by the generation of surface plasmons along a metal-dielectric interface. The effect of surface plasmons on spectral switching at the observation plane in the far zone of the double slit is also shown.

1. INTRODUCTION

Recently, it was shown that generation of surface plasmons along a metal-dielectric interface of a gold double slit modulate the coherence [1] properties of incident light in the far zone.

In this paper, the modified spectral interference law is derived which results due to modulation of the coherence by the plasmonic effect. The modulations in the spectral density at the observation plane in the far zone of a gold double slit (Fig 2) are shown. Secondly, the influence of the surface plasmons on spectral switching in the far zone is also shown.

2. THEORY

2.1. The spectral interference law: An incoherent field $U(r, \omega)$ from a blackbody (at $T=3000K$) is first made spatially coherent after propagation and is then made incident on a gold double slit (Fig.1). If α is the fraction of the field directly transmitted at the slits, $\alpha\beta$ is the fraction converted into surface plasmons which travel to the other slit where they reappear as a freely propagating field and k_{sp} is the surface plasmon polaritons propagation constant, the net field coming out from each slit can be written as

$$U_1(\omega) = \alpha U_1'(\omega) + \alpha\beta U_2'(\omega) \exp(ik_{sp}d) \quad (1)$$

$$U_2(\omega) = \alpha U_2'(\omega) + \alpha\beta U_1'(\omega) \exp(ik_{sp}d) \quad (2)$$

The cross correlation function $W_{ii}(\omega) = S(\mathbf{r}, \omega) = \langle U_i^*(\omega) U_i(\omega) \rangle$ for $(i=1, 2)$, is given by,

$$W_{12}(\omega) = |\alpha|^2 S'(\omega) \left[\mu_{12}'(\omega) + 2\text{Re}\left\{ \beta \exp(ik_{sp}d) \right\} \right] + |\beta|^2 \mu_{12}^*(\omega) \exp(-2k_{sp}''d) \quad (3)$$

where $\mu_{12}'(\omega)$ is the spectral degree of coherence of the incident light at the two slits and $k_{sp} = k_{sp}' + ik_{sp}''$. In terms of the modified spectral degree of coherence, i. e. $\mu_{12}(\omega) = \left[W_{12}(\omega) / \sqrt{S_1(\omega) S_2(\omega)} \right]$, at the two slits Q_1 and Q_2 , the spectral interference law for the modified field can be expressed as:

$$S(\mathbf{r}, \omega) = S^1(\omega) + S^2(\omega) + 2\sqrt{S^1(\omega) S^2(\omega)} \times |\mu_{12}(\omega)| \cos[\arg \mu_{12}(\omega) - k(R_1 - R_2)]$$

2.2. Spectral switching: If we place a phase shifting electro-optic device before the two slits (Fig.1), the spectral properties of the incident field (e.g. a narrow band Gaussian spectral profile) could be altered [2] as shown in Fig. 3 and this alteration is termed as spectral switching. In this process a considerable intensity variation is seen in the far zone due to plasmonic effect.

3. FIGURES

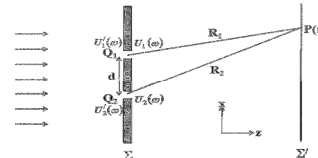


Figure 1: Schematics of the experiment.

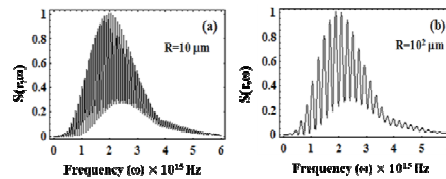


Figure 2: Plots of normalized spectra at an off-axis point, when the double slit is illuminated by radiation from a thermal source

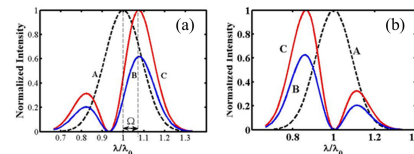


Figure 3: Spectral switching in the far field of a gold double slit for a narrow band polychromatic light having Gaussian spectral profile. A is the spectrum of the incident field B and C are the shifted spectra.

ACKNOWLEDEMENT

The authors thank Director, NPL for encouragement.

REFERENCES

- [1] C. H. Gan, G. Gbur and T. D. Visser, "Surface plasmons modulate the spatial Coherence of light in Young's interference experiment", Phys. Rev. Lett. **98**, 043908-1-4 (2007).
- [2] P. Han, "Electro-Optic modulation for spectral switches and phase singularities of a double-slit in the far-field", J. Opt. **13**, 035713-1-6 (2011).

RENDERING OF UNDERWATER LIGHTFIELD USING RADIATIVE TRANSFER MODEL

VB. Sundarabalan and P. Shanmugam

Department of Ocean Engineering,

Indian Institute of Technology Madras, Chennai – 600036, India

Email: vbsbalanin@gmail.com

Abstract: The objective here is to generalize a system, developed to simulate the underwater light field in the oceanic medium, by presenting an extended form of the radiative transfer equation to incorporate the bottom slope, bottom material, new phase function and inelastic processes. Solutions of this model are able to generate the realistic rendering of underwater light field using radiance information obtained from the model below the water along the depth.

1. INTRODUCTION

Ocean water is arguably the richest participating medium with optically influential constituents which affect the light propagation either by attenuation or by redirection due to various types of interactions such as absorption, scattering and emission that occur in it [1]. The radiative transfer in the coupled ocean-atmosphere system is very important for naval applications, climate forecasting and marine biology, and also special operations require for the prediction of underwater visibility for aircraft observers, divers and cameras using ambient (natural) light or lamps. Realistic simulation of the inwater light field using the underwater radiance mainly depends on the IOP's which incorporated in the radiative transfer equation (RTE) [2]. Apart from the Inherent optical properties, the RTE also depend on the type of the bottom material, bottom slope, phase function and internal source.

2. MODIFIED RTE

RTE is a differential-integral equation which generally has no analytical solution for realistic medium configurations and boundary conditions. The simplest situation of horizontally homogeneous water and time independence in the basic RTE equation is as follows [2]:

$$\cos\theta \frac{dL(z, \theta, \varphi, \lambda)}{dz} = -c(z, \lambda)L(z, \theta, \varphi, \lambda) + S(z, \theta, \varphi, \lambda) + \int_{4\pi} L(z, \theta', \varphi', \lambda) \times p(z; \theta', \varphi' \rightarrow \theta, \varphi; \lambda) d\Omega' \quad (1)$$

Here L is the radiance, p is the new exponential Phase function with modified anisotropy factor G which is calculated as [3],

$$p(\cos\theta) = \frac{1}{2\pi \times G} \times \frac{\exp(-(1-\cos\theta)/G)}{1-\exp(-2/G)}$$

S is internal source in Eq. 1 which includes new chlorophyll fluorescence model based on [4]. It may be expressed as $S_{chl} = FI(\lambda) \cdot h(\lambda)$ based on the traditional Gaussian distribution along with the chlorophyll concentration. The Bottom boundary condition is mainly based on the bottom slope with bottom material reflectance [5] which is also included in the MRTE. The effective reflectance equation with the bottom slope is as follows,

$$\frac{R_{eff}(\lambda)}{R(\lambda)} = 0.5 \times \cos[\theta_z - \theta_b] + 0.5 \times \cos[\theta_z + \theta_b]$$

Here the effective reflectance is based on the θ_b which is the angle of the bottom slope and θ_z is the zenith angle of the irradiance.

3. RESULTS

We found that the MRTE provides approximately around 10% changes after implementing the new models in the RTE which was validated using the Hydrolight model. The results indicate that the underwater radiance changes when only considering bottom slope 8.4% in the surface and 15.09% at the bottom for wavelength of 555 nm, when including slope, phase function and fluorescence. There is a significant change at 685 nm mainly because of the sun-induced chlorophyll fluorescence. Further results suggest that the MRTE is more robust and can be effectively used to simulate the underwater radiance in a variety of waters commonly found in the coastal and clear waters.

REFERENCES

- [1] D. Gutierrez, F.J. Seron, A. Munoz, O. Anson, "Visualizing the underwater ocean optics," Eurographics, **27**, 2 (2008).
- [2] C.D. Mobley, "Light and Water: Radiative Transfer in Natural Waters," Academic Press, Inc, San Diego, 1994.
- [3] A.D. Kim, and M. Moscoso, "Beam propagation in sharply peaked forward scattering media," J. Opt. Soc. Am, **21**, 797 (2004).
- [4] A. Gilerson, J. Zhou, S. Hlaing, I. Ioannou, B. Gross, F. Moshary, and S. Ahmed, "Fluorescence component in the reflectance spectra from coastal waters. II. Performance of retrieval algorithms," Opt. Exp., **16**, 2446 (2008).
- [5] J. Ronald, V. Zaneveld, and E. Boss, "The influence of bottom morphology on reflectance: Theory and two-dimensional geometry model," Limnol. Oceanogr., **48**, 374 (2003).

ADVANCES IN PHOTONICS FOR DEFENCE APPLICATIONS

A.K. Gupta

Instruments Research & Development Establishment, Dehradun-248 008

Email: akgupta@irde.drdo.in

Abstract: Photonic Bandgap structures, Metamaterials, Silicon photonics, Superlattice IR detectors, etc. are the advanced research areas emerging in the field of photonics. There have been recent advances in fabrication technologies which have enabled a flurry of activities in the fields of Micro-optics and Nanophotonics. Thus devices with enhanced capabilities and totally new functionalities have become possible. Micro-optics and Nanophotonics technologies are going to have a tremendous impact on defence systems. A brief overview of the proposed activities being initiated by DRDO in the fields of Micro-optics and Nanophotonics will be presented.

1. INTRODUCTION

Throughout the last few decades, there has been a significant activity in the development of photonic devices that can confine, control, and route light on a scale comparable to modern electronic devices, namely the nanometer scale. Recent advances in fabrication technologies have enabled a lot of activities in the fields of Micro-optics and Nanophotonics [1]. Advances in nanofabrication technologies will have a tremendous impact for defence applications. Some potential applications may take substantial investments and time before they are realized. However, pursuit of these technologies is essential, as it will have an all round impact on various other sectors in addition to national defence needs. The major defence areas, where these technologies will play a dominant role, are surveillance, countermeasures, navigation sensors & seekers, and communication. Chemical and explosive detection is also an important area where plasmonics and Terahertz technologies are going to play a leading role.

2. ADVANCED RESEARCH AREAS IN PHOTONICS

Advanced research areas in photonics like Micro-optics, Diffractive optics, Photonic crystals, Metamaterials, Silicon Photonics, Type II superlattice, etc. have promising defence applications. DRDO has taken up an initiative to accelerate R&D activities in these areas of Micro-optics and Nanophotonics.

Micro-optics comprises of optical components with small dimensions where feature sizes are 100-1000 times the operating wavelength. Micro-optical components –both refractive and diffractive- have led to significant reduction in the size and weight of the optics in many application areas especially imaging systems. For defence applications, reducing system volume and weight is critically important.

Nanophotonics deals with structures having feature sizes of the order of or smaller than the operating wavelength. Photonic crystals are periodic optical nanostructures with low and high refractive indices that are designed to affect the motion of photons in a similar way that periodicity of a semiconductor crystal affects the motion of electrons [2]. They find applications in light generation, light guidance, light control/manipulation and light detection.

Metamaterials [3] or structured composite materials, primarily involving metallic structures, can have electromagnetic or optical properties normally unattainable in natural materials. These materials have structure sizes and periodicity much smaller than the wavelength of light. They can be designed to have large absorption at IR wavelengths that create localized heat spots and can also be designed to cloak an object by deflecting radiation around that object.

Silicon photonics is a technology that offers an ideal platform for integrating various photonic and electronic components for realizing high speed and better controlled multifunctional optoelectronic chips [4].

REFERENCES

- [1] B. C. Kress and P. Meyrueis, *Applied Digital Optics: From Micro-optics to Nanophotonics*, Wiley, 2009.
- [2] J. D. Joannopoulos, S. G. Johnson, J.N. Winn, and R. D. Meade, *Photonic crystals: Molding the flow of light*, Princeton University Press, 2008.
- [3] S. A. Ramakrishna and T. M. Grzegorzczak, *Physics and applications of negative refractive index materials*, CRC Press, 2009.
- [4] B. Jalali and S. Fathpour, 'Silicon Photonics', *IEEE J. Lightwave Technol.* 24, 4600-4615, 2006.

OPTICAL COMPONENTS IN A MODERN HIGH PERFORMANCE FIBER OPTIC GYROSCOPES (HiFOG)

Jagannath Nayak

Scientist, Inertial System Group, Research Centre Imarat, Hyderabad-500069, India
nayak_jagannath@rediffmail.com

Abstract: High performance fiber optic gyros of class 0.01 are required for future inertial navigation system for aircraft and aerospace applications. The design and fabrication of various optical components such as optical source, integrated optic chip, polarization maintaining fiber and so on, required for high performance integrated fiber-optic gyroscopes has been presented in this paper. The current status of these components at Research Centre Imarat, Hyderabad and other laboratories in India has also been discussed.

1. INTRODUCTION

Gyroscopes are the core of the today's inertial navigation, guidance, and control systems for aircraft, missiles, ships, and land vehicles. Autonomous vehicles used in battlefield, aerospace and undersea environments place tough demands on gyroscope technology, including extreme ruggedness, small-size, light-weight, low-cost, and low power operation.

Optical gyroscopes, such as ring laser gyros (RLGs) and fiber-optic gyroscopes (FOGs), are far superior [1,2] to their conventional counterparts because of low reaction time, no 'g' sensitivity drift, wide dynamic range, and high accuracy and reliability, which are the needs for modern inertial navigation systems. FOGs are a highly-desirable navigation solution for the applications in high-dynamic environments with severe thermal excursions, shock and vibration, but high-precision FOGs been too expensive for most volume applications [3]. The optical components of the FOGs play very important role in performance, size, volume and cost of the FOG system [4].

This paper addresses the development and requirement of different types components technology such as optical source, integrated optic chip, polarization maintaining fiber, sensor coil, detectors required for high performance FOG. The development status of the components for FOGs at Research Centre Imarat, Hyderabad and other laboratories in India is presented.

2. FOG TECHNOLOGY

FOGs exploit the Sagnac effect which is the difference in time-of-flight for counter-propagating light in a circular optical path caused by rotational acceleration. Light propagating clockwise through a fiber loop will have the same optical path length as light that propagates counter-clockwise if the loop is at rest. However, if the loop is rotated while the light is propagating through the fiber, the beginning and ending points of the loop are shifted during the optical propagation; with the result that one beam will have

farther to travel than the other, depending on which direction the loop is rotated. The path difference can be measured as a phase difference by interfering the beams from the two directions. Thus a fiber loop can be used as a rotation sensor.

The configuration of a closed loop FOG is shown in Fig. 1.

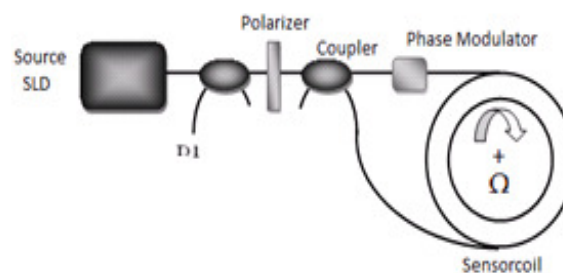


Fig. 1: Configuration of a closed loop FOG

When system is at rest the light propagating in clockwise (CW) and counter clockwise (CCW) directions traverse identical paths and so there is no phase difference between them. When the system rotates at an angular velocity Ω , then CW path will be longer by $(LR/C)\Omega$ and CCW path will be shorter by $(LR/C)\Omega$ i.e $L_{ccw} = 2\pi R - R\Omega t_{ccw}$ and $L_{cw} = 2\pi R + R\Omega t_{cw}$. This yields $\Delta L = c(t_{cw} - t_{ccw}) = 4A\Omega/c$. Thus the phase difference produced between CW and CCW wave is obtained from above expression as

$$\Delta\phi_R = \frac{8\pi NA}{\lambda c} \Omega \quad (2.1)$$

Where $\Delta\Phi_R$ is the phase shift due to rotation rate, $A = \pi R^2$, the area enclosed by the path of radius R , L is length of the coil $L = 2\pi RN$, N being the number of turns of fiber loop and c is the speed of light, λ is source wavelength.

In open loop FOG the DC voltage of the demodulator is proportional to rotation induced Sagnac Phase change, in case of closed loop system

the output of the demodulator is passed through a Servo-amplifier, which drives the electro-optic phase modulator phase modulator, placed at the end of the sensor coil to nullify the Sagnac Phase [5]. The advantages of closed loop system are that the output is independent of the intensity variations of the source and better Scale Factor linearity compared to Open-loop FOG.

In order to increase the precision of a FOG loop, the optical fiber is wound many times to form a coil. In extremely high accuracy applications, several kilometers of fiber may be used in each coil. For each axis, a FOG uses a transmitter to generate a beam of light into a fiber. In high-performance systems, a closed feedback loop is formed in which the light is split into two serrodyne-modulated beams using a lithium-niobate phase modulator. These modulated beams are fed into opposite ends of the PM fiber coil loop and counter-propagate. The returning light passes through the phase modulators again and is then recombined and detected. The phase modulators serve to move the interfered signal away from noise at DC, enhancing the sensitivity of the FOG. By detecting the interference fringes, the FOG measures rotation in that axis, and by combining all three axes, complete information on attitude in space is obtained. FOGs typically use a low-coherence optical source so that noise induced from multiply-reflected light as well as Rayleigh backscatter and non-linear effects are reduced. The use of a lithium-niobate FOG modulator employing the annealed-proton-exchange process creates an inherently strong polarizer which is ideal for interferometric sensing applications. The lithium niobate device also has extremely high bandwidth (~1 GHz), which permits a "closed-loop" electronics implementation which maintains a fixed phase offset on a single interference fringe that is synchronized with the light transit time through the fiber coil. This form of closed loop operation greatly improves the precision of the gyro by linearizing its operation and eliminating many of the effects of deficiencies in the optical circuit

The relatively large size and high cost of the optical components required to realize a closed-loop FOG (transceiver source and detector elements, lithium-niobate optical phase modulators, and polarization-maintaining (PM) fiber) has limited their use to mostly the high-performance applications in low volumes, such as spacecraft and aircraft navigation and attitude control.

A new class of gyroscopes based on optical microcoil resonator (OMR) is drawing much attention now-a-days. The OMR forms a combination of conventional and slow-light propagation. Rotation of slow-light structure modifies the dispersion relation of the counterpropagating waves and generates a rotation-dependent phase shift between them. Thus, the dispersion properties of the medium affect the

phase shift accumulated by the rotating waves. When rotated, the combination of the slow and conventional propagation schemes can significantly enhance the phase difference between the counterpropagating waves [6].

3. FIBER OPTIC GYROSCOPE COMPONENTS

The major components of FOG are a super fluorescent laser source, sensor coil, two fiber directional couplers, a fiber polarizer, a PZT phase modulator and a PIN FET detector. All the optical components are made of single mode fiber in case of all fiber gyro and these discrete components are replaced by integrated optic chip in case of closed loop FOG for inertial grade performance. Fusion splices interconnect the optical components, with splice losses varying from 0.1 to 0.25 dB. The all-fiber phase modulator was developed in our laboratory. The critical components like fiber laser, integrated optic chip, PIN FET, PM fiber and directional couplers are also being developed with joint collaboration of academic institutions and R&D Organizations in our country.

Table 2: Comparison of the components used in conventional and modern FOG

Components	Conventional FOG	Modern high performance FOG
Light source	Super-luminescent Diode	Superfluorescent Fiber Source
Detector	PIN FET	PIN FET
Sensor	PM fiber (PANDA , Bow-Tie)	Photonic crystal fiber
Directional coupler, polarizer & other components	Fiber components in case of open loop FOG and Multifunction Integrated Optic chip(MIOC)	MIOC with Er-doped fiber or Silicon
Signal Electronics	Medium-Precision electronics Open-loop operation	High Precision electronics Closed loop operation-Serrodyne modulation, with modeling and compensation technique
Packaging	Discrete component packaging	Hybrid optical packaging in chip level

3.1 Optical Source

A modern high performance fiber optic gyroscope requires source with high power and stable wavelength with respect to temperature. Such a broadband source suitable for high performance FOG has been simulated, fabricated and tested at our Lab. Broadband light sources are needed to reduce coherent back-scattering noise and Kerr effect in FOG. Erbium doped fiber pumped at 980 nm results in the most efficient 1550 nm fiber source till date. Fiber sources pumped at 980 nm are ESA (excited-state absorption) free. Our design consists of erbium-doped fiber pumped with 980 nm laser diode through a WDM. The emission wavelength is 1550 nm with an output power of 10 mw [7]. The spectral width of the source is 40 nm and wavelength stability of 9 ppm. Figure 2 shows the configuration of the fiber source developed in the lab. It is being pumped at 980nm with 50 mW power. WDM is 2 X 1 coupler with pump and signal insertion loss of 0.08 dB and 0.13dB respectively. Erbium fiber has a core radius of 2.2 μm , NA of 0.23 and absorption coefficient of 5.4 dB at 979 nm. Length of the fiber employed in the source is 16 m.

The optical sources commonly used in FOG are super luminescent diode (SLD), edge light emitting diodes (ELED) etc. These sources suffer from limited output power, poor coupling of output power into a single mode optical fiber and are sensitive to temperature. Power stability of an SLD and fiber source is compared in Fig.4 that confirms the more stable power with fiber source. Fiber lasers developed in house having 10 mW power and a linewidth are used for the three-axis FOG.

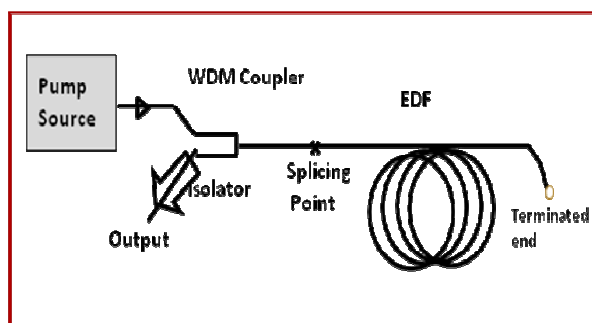


Fig. 2: Configuration of the fiber source

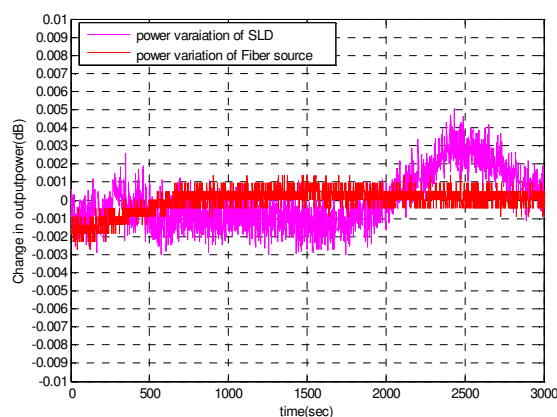


Fig. 3: Power stability of SLD and Fiber source

3.2 Fiber Optic Directional Coupler

Two directional couplers are required for the minimum configuration 'all-fiber gyroscope' one at the source end and another at the sensing coil end. Etched fiber, fused fiber and polished fiber couplers are the three types in common use. But fused directional coupler is more stable under environment conditions specified. Polarization-maintaining (PM) fiber couplers based on fused fiber technology are fabricated and used in modern high performance FOGs. The process parameters of a PM directional coupler are gas flow rate, fusion torch height, fusion temperature, pulling speed of translational stages and birefringent axis alignment [8]. These couplers maintain the state of polarization of input light which is desirable in a gyroscope. Prior to that, in conventional FOGs we had used commercially available single mode fiber couplers at 1550 nm center wavelength, based on 50/50 coupling ratio and 3.6 dB insertion losses. Polarization-maintaining directional couplers are being fabricated at our lab with focus on the size-miniaturization and fool-proof packaging.

3.3 Multifunction Integrated Optics Chip

The MIOC is a solid state waveguide device on an X-cut LiNbO₃ substrate. The MIOC consists of a polarizer, a Y branch, and optical phase modulator. The Y-branch is used for splitting the optical power in the forward direction, while in the reverse direction, it is used for combining. In addition to this, the integrated- optics chip (IOC) is composed of a phase modulator on each branch of the Y junction. Design of IOC for FOG consists of the designs of channel waveguide, directional coupler, and/or Y branch. A combination of the effective index and beam propagation methods is used for the design of directional coupler and Y branch. It is fabricated using the annealed proton-exchange process. MIOCs are

developed in house and are used in FOGs for closed-loop operation [9].

3.4 Detector

Basically there are three types of photodetectors, namely, photoconductors, PIN detectors, and avalanche photodiodes (APDs) available commercially. PIN photodiodes are the best choice for modern high performance FOG because of their high quantum efficiency. The PIN-FET (Field Effect Transistor) hybrid receiver utilizes a high-performance p-i-n photodiode followed by a low-noise preamplifier. When compared with the APD receiver, the PIN-FET hybrid has both cost and operational advantages, especially in the longer wavelength region. The intensity modulated light beam is detected by PINFET, converting into equivalent current. PIN diodes are developed in house and integrated into the control-grade FOG.

3.5 Gyro Sensor Coil

Sensor coil is known to be the heart of fiber optic gyroscope. The sensor coil design starts with fixing the dimensions of the spool and the length of the fiber, considering the input parameters as the sensitivity and dynamic range of the sensor. Then the type of winding and selection of the type of fiber is considered. It is possible to design different types of gyroscopes by simply changing the area of the coil without changing the components and assembly techniques. The length of the optical fiber and diameter of the spool should be large for a better scale factor, but the fiber diameter should be as small as possible to limit the size of the gyroscope. Thus, it remains an interesting choice for the dimension of the fiber and spool to be decided by the designer depending on the different grades of the gyroscopes to be fabricated.

The type of optical fiber coil winding can induce thermal non-reciprocity if there is a time dependent temperature gradient along the different layers of the optical fiber. Two possible methods of reducing the thermally induced non-reciprocity are called dipolar and quadruple winding. Compared to ordinary winding the dipolar winding reduces the effect of the thermally induced non-reciprocity by a factor approximately equal to the number of layers and even better compensation equal to the square of layers is possible with quadruple winding. It has been found that the best choice for spool material is fused silica and silicon carbide. For controlled temperature environment silicon carbide is preferred for sensor coil spool material as it can sustain higher vibration and shock than fused silica [10].

3.6 Packaging

Hybrid optical bench is used for packaging the

device. Optical submounts for components such as superluminescence diode (SLED), P-I-N photodiode with field effect transistor (PIN FET), integrated optical circuit (IOC), are prepared. These mounts are assembled with high precision machine. All the submounts are bonded to ceramic circuit board to which fiber isolator and directional coupler are assembled. The fully equipped CCB is assembled in housing onto thermoelectric cooler. This gives compactness and ruggedness to the device.

4. CONCLUSION

Various optical components such as source, detector, sensor coil, directional coupler, etc. as employed in a high performance gyroscope have been presented. The comparison of the conventional components with the modern ones has also been done.

The main points to be considered for FOG product development are gyro dimension, weight, sensitivity, bias stability, scale factor stability, power consumption, and resistance to perturbations, such as temperature, shocks, vibration. It is necessary to take into account the economic factors, such as component prices and manufacturing time consumption, for gyro production. These factors will be under control if and only if all the components are fabricated in house. In these cases, it will be easy to meet different requirements for optics with various gyro applications.

The critical technologies for FOG development are indigenous development of optical components like optical source, multifunctional integrated optic chip (MIOC), polarization maintaining fiber, miniaturization of optical and electronics components, packaging, winding of optical fiber etc. As regards to the various critical components like the integrated optic chip (IOC), polarization maintaining fiber, directional coupler, PIN detector, indigenous development work has been undertaken with various academic institution and research organizations in our country. We have also undertaken critical components such as integrated optic chip, optical fiber, fiber laser and PIN FET etc. with joint collaboration of academic institutions and R&D Organizations in our country. In past we have developed the complete design package for different grades of FOGs. We have successfully fabricated and tested two prototypes of 10-deg/hr classes of FOGs. The technology knows-how and infrastructure facilities for test and characterization of optical components for 10-100 deg/hr FOGs has been established. Now the challenge before us is to reduce the overall size of the gyro so that it can replace the control and free gyros used in our Missiles, Aircraft and Torpedoes. The flight model is under development for evaluation of mechanical and thermal environment in order to assess the right

fabrication process and optimum packaging. The inertial grade FOG development is under progress.

ACKNOWLEDGEMENTS

I express our sincere thanks to Shri S. K. Ray, Director, RCI and Shri G. Sateesh Reddy, Associate Director for their constant encouragement. I also sincerely thank Prof. A. Selvarajan and FOG TEAM of RCI for their constant interaction and active participation in this work.

REFERENCES

- [1] R. A. Bergh, H. C. Lefevre and H. J. Shaw, "An overview of fiber optic gyroscope", *J. Lightwave Technol.* **2**, 91(1984).
- [2] H. Kajioka, T. Kumagai, H. Nakai, T. Dohsho, H. Soekawa and T. Yuhara, "Commercial applications of mass-produced fiber optic gyros", *Proc. SPIE* **2837**, 18 (1996).
- [3] G. A. Sanders, B. Szafraniec, R. Y. Liu, C. Laskoskie and L. Strandjord, "Fiber optic gyros for space, marine, aviation applications", *Proc. SPIE* **2837**, 61 (1996).
- [4] J. Nayak, "Fiber Optic Gyroscopes: From design to production", *Appl. Opt.*, **50**, E152 (2011).
- [5] G. A. Sanders, B. Szafraniec, R. Y. Liu, M. S. Bielas and L. Strandjord, "Fiber optic gyros development for a broad range of applications", *Proc SPIE.*, **2510**, 1995, pp. 2-11.
- [6] J. Scheuer, "Fiber microcoil optical gyroscope", *Opt. Lett.* **34**, 1630 (2009).
- [7] M. Mapre, J. Nayak, P. Kumar, D. V. K. Sastry and T. Radhakrishnan, "Design and testing of broadband fiber source for high performance fiber optics gyroscopes", International Conference on Optics and Optoelectronics, IRDE, Dehradun, India, 12-15 December, 2005.
- [8] Ch V. V. Satyanarayana, P. Kumar, J. Nayak, "Effect of temperature on packaging of Polarization Maintaining Directional Coupler for Fiber Optic Gyroscope Application", Proc. National Conference on Advances in Sensors for Aerospace Applications, 14-15 December, 2007.
- [9] A. Selvarajan, J. Nayak, T. Srinivas, and P. Banerjee, "Integrated optics for fiber optics gyroscope," Proceedings of the National Conference on Miniaturization in Aerospace Systems, MAERO '98 Research Centre Imarat, Hyderabad, India, pp. CIII.1–CIII.12, January 2-3, 1998.
- [10] P. Kumar, G. Purohit, and J. Nayak, "Analysis of Vibration and Temperature Effects on Sensor Coil Performance of Fiber Optics Gyro", International Conference on Specialty Glass & Optical Fiber: Materials, Technology & Devices. August 4-6, 2011.

VIRTUAL PROTOTYPES FOR PRODUCT DEVELOPMENT

R. Sudhakar Rao

Design & Engineering Division, Bharat Dynamics Limited,
Kanchanbagh, Hyderabad – 500 058, A.P., India
E-mail:rsrbd1@yahoo.com

and

Prof. Chandra Lingam

Dept. of Physics, College of Engineering,
JNTU, Kukatpally, Hyderabad – 500 085, A.P., India.
E-mail:chandra_lingam@yahoo.com

Abstract: Long Range Telescope for real time image capture of target and high speed weapon was designed and developed. Optical, mechanical design software packages are used for virtual prototype modeling, simulation, form, fit and functional verification. The design modeling, development, application of the system and some results obtained are accounted.

1. INTRODUCTION

Computer graphics were once time-consuming and required much hard work and imagination. But now, they have been enriched with technologies that have revolutionized the established standards with a flood of innovations. Being the core of every industry, the designing process and every crucial aspect associated with it has always had top priority. Virtual Reality (VR) graphic tools are helping to generate computer graphics and simulation that one may find difficult even to imagine and swiftly erasing the differences between a design and its prototype. VR techniques are helping design teams make changes to new designs much before the item itself is taken shape. Eventually, collaborations will work with virtual prototypes and it becomes an essential element for all vehicle and complex equipment design. At such a time, our outlook and verification would be more virtually driven and virtual designs would have more realism associated with it. Three Dimensional immerse environments are emerging due to the availability of hardware like microprocessors, PC or TV environments. For more details on the different technologies and their implementation environments, the referenced article [1] provides better information.

Lot of design and development work in Bharat Dynamics Limited, Hyderabad involves in the area of Computer Aided Optical, Electronic and Mechanical Designs using the State-of-the Art digital tools. Optical System theoretical formulas were used to arrive at basic optical systems. Optical Design software ensures to bring out optimized optical layouts. Performance analysis was carried using the optical design software; basing on the design data, the optical components, associated mechanical housings; CCD camera sensor virtual components are modeled. Then the required mounting arrangements are visualized and modeled using IDEAS software on a CAD workstation. All the required virtual modeled components are

integrated on a platform. The aesthetic and outer colour details are verified. Preliminary and critical design reviews are conducted on the virtual prototypes. The functional and constructional aspects are reviewed and then the drawings are finalized and later sent to the shop floor for fabrication. In this approach, fabrication and testing of a prototype could be made rapidly. Such is the precision and power of the digital tools available today.

2. IMPORTANCE OF THE INNOVATION

The importance of a weapon with state of the art features in today's warfare can be assessed from the latest wars in Iraq, Serbia, Afghanistan and Libya. Weapons are the first systems to be used for pre-emptive strikes with lethality. The gradual increase in their importance is evidenced from the elevation of these systems from tactical to strategic and now coined as political weapon. In some areas of the world, the possession of weapons has averted conflicts. However, in the present environment, wherein society has become sensitive to loss of lives, errors in the delivery of weapons have become unacceptable. Also, the need for better precision to avoid collateral damage is inescapable. Thus, there is a need to have weapons, which are lethal and accurate, to achieve the aims of their employment.

A weapon system to achieve desired hit probabilities requires incorporation of different modules such as guidance systems to steer it in flight, control its range by adjusting trajectory, achieve the desired angle of attack by adjusting the trajectory on final descent and detonate the warhead at the desired height along the target or detonate the warhead at the desired depth at the target so as to cause optimum damage as designed. The techniques differ for different class of weapons such as:

- (a) Anti Tank Guided Weapons
- (b) Tactical Weapons
- (c) Intermediate Range Ballistic Weapons and
- (d) Inter Continental Ballistic Weapons.

The discussion is restricted to Anti Tank Guided Weapons (ATGWs) of long range (4 km) only. These are produced in limited series for research and

development and then bulk produced on the requirement.

The scope of the work led us to carry out some innovative research and development to create a new instrument that helped in capturing the weapon flight trajectory in real time as well as keeping the target still in the field of view of the capturing system. It is generally believed that the hit probability of ATGWs is around 60%. The effort to bring down the balance 40% hit probability is not made seriously by many weapon manufacturers. The failure is mainly attributed to the man made errors (operator handling errors) and defective weapon systems. The increase in the hit probability of ATGW is possible by providing prior training and feedback on live firing using suitable instrumentation. To have control over the man made errors, the analysis must distinguish between the failures caused by the pilot and the defective weapon system. Then the findings become effective and useful for the manufacturer to eliminate / reduce the defects arise due to the pilot and the weapon system. With such facility, quality assurance agencies will certify the system performance without ambiguity.

In this research program, a case study was taken up involving a weapon proof firing trials from an Infantry Carrier Vehicle. In these trials, some of the weapons were getting short landed. It was not possible to distinguish the particular errors whether they are handling errors or system errors. After observing the trajectory of the weapons for their good and bad performance cases, a novel idea was conceived. It was decided to build a tool and use it so that the developers shall get to know detailed real time performance information which could be used for detailed scientific performance analysis of the weapon. Such a tool is nothing but a real time video optical system specially made for this requirement, mounted and harmonized to the weapon sight.

During the launch and guiding of the weapon, the weapon is controlled from the launcher and being guided on to the target using a wire link between the launcher and the weapon. In this process, basing on the feedback from the weapon certain correction commands in the form of small increments in azimuth and elevation are given to the weapon and these small increments are recorded by the video system, if the tracking system is co-mounted a the same platform as that of the launcher. Extended application of this new system is also mentioned here. At present, the pilot (s) / gunner (s) is (are) trained in firing the ATGWs using the simulators as firing a live weapon in a real firing range involves elaborate arrangements requiring a number of personnel in addition to expending costly weapons for each firing practice. By using this type of Telescope – CCD Camera system and mounting them on the training

simulator, it would be possible to improve the performance of the pilot / gunner in launching and guiding the long range weapons with such details as of aiming, firing, obtaining the lag & lead details with respect to the target movement, short landing, hit or miss analysis information. Such a simulator could be tied up with a computer to get real time analysis data.

3. DESIGN & DEVELOPMENT DETAILS OF WEAPON & TARGET CAPTURE SYSTEM

Real time motion study of the fast moving objects in flight requires proper instrumentation. Over a period, relevant experience was acquired in the design and developing of the necessary Opto-Electronic instrumentation [2-3]. With such background, for this specific case, a Long Range Telescope (LRT) system was conceived, designed and developed. Basic theoretical study was carried out on various ATGWs trajectory characteristics to establish the relationships for flight path, flight time and deviation from the line of sight in order to arrive at a suitable field of view. Similarly, a study was carried out to estimate the size of the acquired target image on a TV monitor. The study revealed that an Optical System with a Field Of View of $0.55^\circ \times 0.41^\circ$ is an optimum value for long range targets and weapons that are in being produced. Optical System basic layout was initiated with the inputs from the theoretical studies and optical design procedure established by us [4, 5]. Optical System Layout and Optimization (OSLO) optical design software was used to design and optimize the optical system. The resultant optical layout and aberration plots are shown in the Figure. 1.

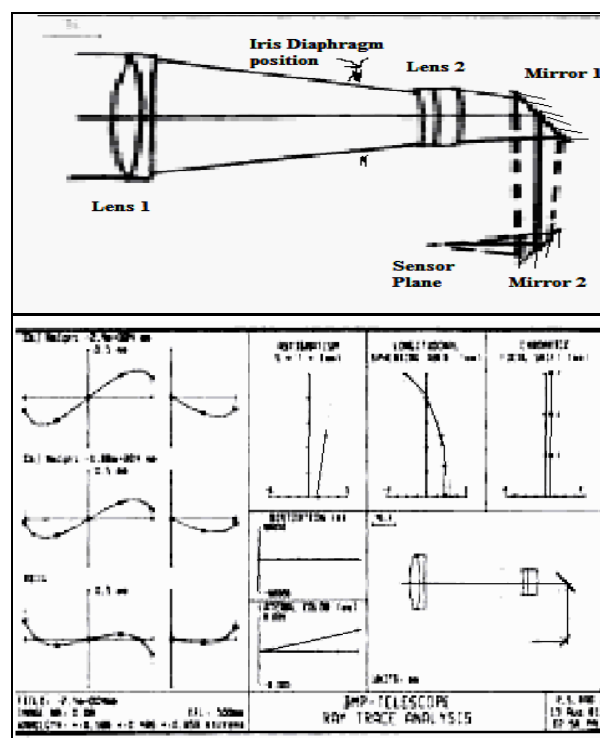


Fig. 1 Optical System layout and Aberration plots

4. VIRTUAL PROTOTYPE DESIGN AND DEVELOPMENT OF A REAL PROTOTYPE

Taking the inputs from the weapon characteristics, optical layout has been arrived at. Mechanical design of the housing, mounting arrangements; electrical and electronic control arrangements for the powering the CCD, focus motor and iris motor movements and acquiring the video and relaying the out put to a TV monitor are made considering the launch platform. Then design of a virtual prototype was modeled using the IDEAS software. Main parts of the models are shown in the Figure 2 in the order of assembly layout. Assembled LRT system in CAD modeled form can be seen in Figures 3(a) and 3(b).

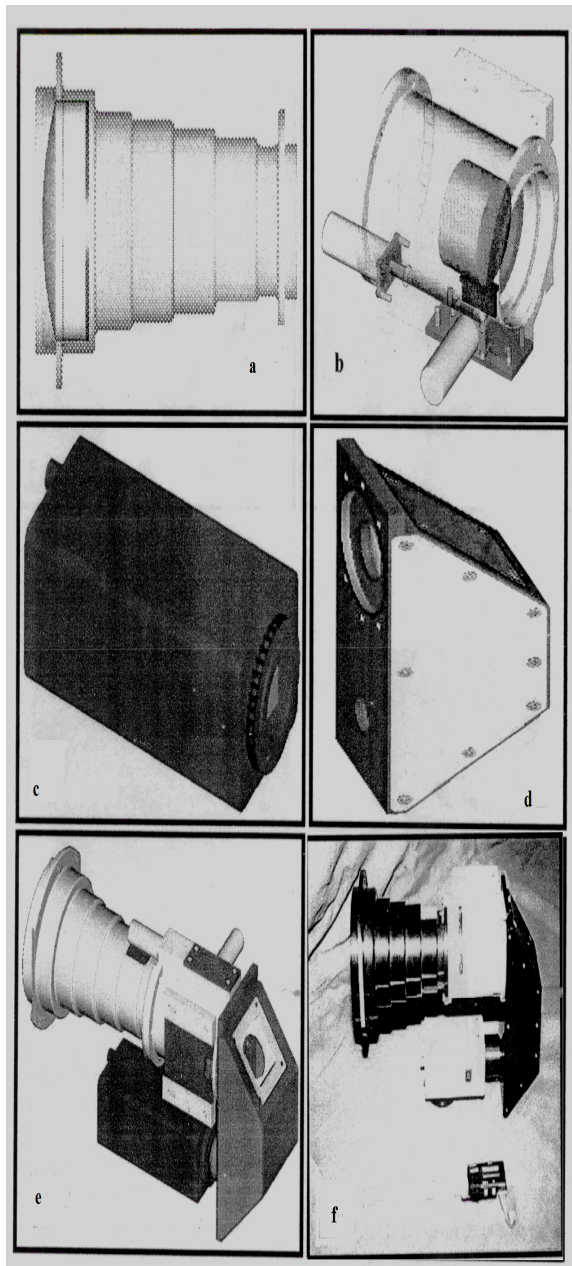


Fig. 2 CAD modeled subassemblies of LRT (a – e); f – is the fabricated unit

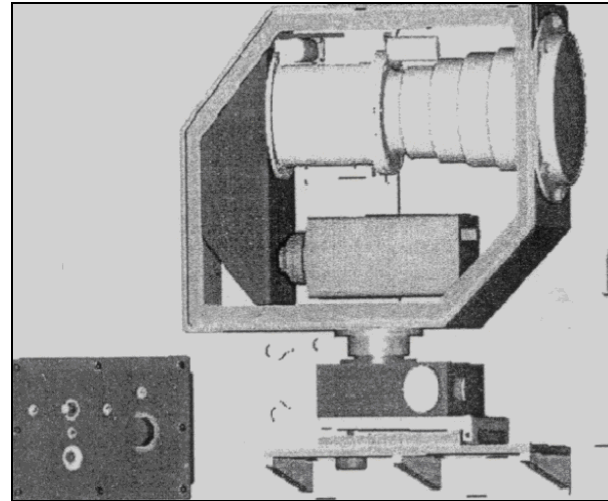


Fig. 3(a). Assembled LRT system in CAD model (Side cover open condition)

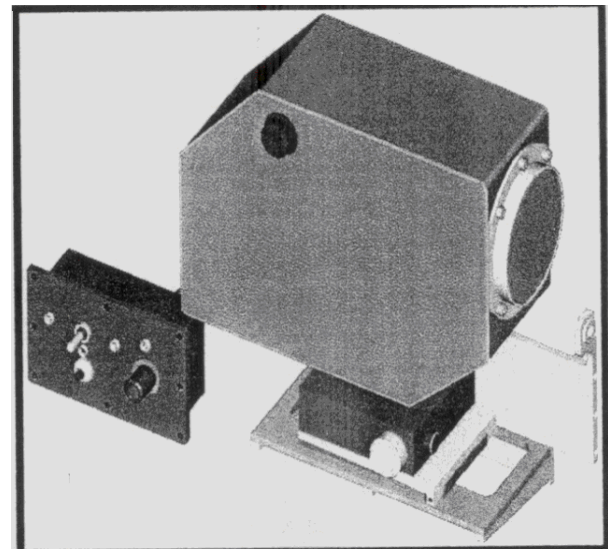


Fig. 3(b). Virtual Prototype LRT system in CAD model

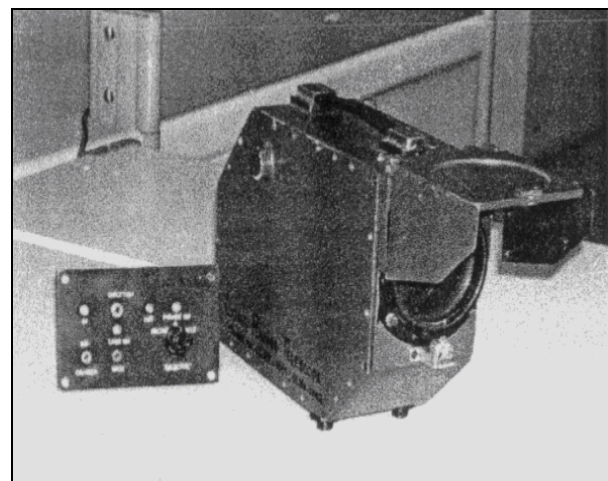


Fig. 4. Fabricated Prototype LRT in assembled form



Fig. 5 LRT system mounted on an ICV

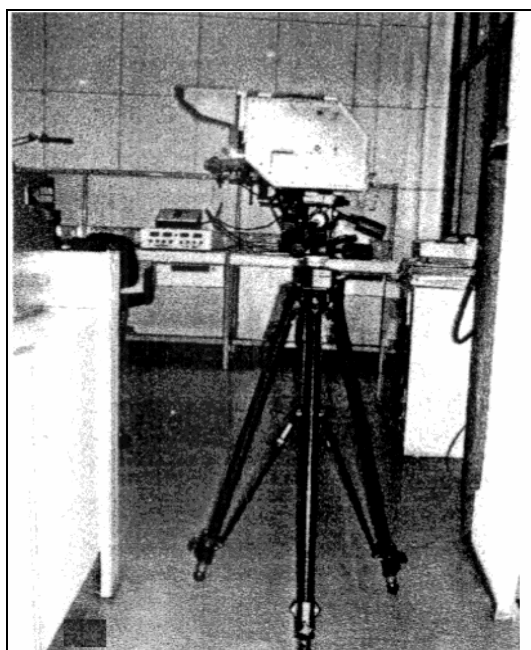


Fig. 6 LRT mounted on a stand alone Tripod

A virtual prototype model was modeled in the Computer by following the steps given here:

- (a) finalization of design input data
- (b) layout of preliminary optical, mechanical, electronic and electrical subsystems
- (c) computer aided design of optical system, mechanical system, electronic and electrical subassembly finalization
- (d) design detail verification of CAD generated components
- (e) finalization of CAD output
- (f) drawings finalization for assessing the suitability in mechanical fitment and aesthetic look
- (g) production drawings
- (h) fabrication of optical, mechanical elements and electronic and electrical elements
- (i) assembly of optical, mechanical, electronic, electrical parts and wiring harness to make a prototype model (Figure 4) and its mounting

on ICV (shown in the Fig. 5) and on a standalone Tripod (shown in the Figure. 6).

- (j) testing of the prototype model for its functional and fitment on the vehicle and
- (k) acceptance of LRT system for its specified use.

The system was successfully mounted on an ICV to capture the real time flight of the weapon as well as the target. The developed system has catered to the requirements of a long range weapon.

5. DISCUSSION AND CONCLUSION

From the procedure to design VR prototypes explained in this paper, it is clear that one can adapt this method. The procedure also paves the way for improving the prototypes for upgrading or improving the system with additional features at any later stage of the development as the drawings are physically available in the computer. The design and development of LRT system helped us to realize a robust system and this tool was used to record the real time flight trajectory of an ATGW successfully.

ACKNOWLEDGEMENTS

R. Sudhakar Rao is grateful to CMD, Directors, GM (P&A), Head-D&E, BDL for permitting to present this research work. He is also thankful to the colleagues who have associated in the design, development, integration, evaluation and application of the system.

REFERENCES

- [1] Saurabh Kudesia, "Computer Graphics: Illusion Vs Reality", Journal of Information Technology, Page 80-81, January 2004.
- [2] R. Sudhakar Rao et al, "Design and development of a Solid Stage Imaging Telescope CCD Camera for a Weapon Simulator", a paper presented at 26th National Symposium on 'Optics and Optoelectronics', conducted by the Optical Society of India and Regional Engineering College (REC) Warangal during Feb 2-4, 2000.
- [3] R. Sudhakar Rao et al, "Design and development of a Long Range Telescope Coupled with CCD Camera for remote detection application", Journal of Optics, Vol. 31, No. 31, page 145-152, 2002.
- [4] R. Sudhakar Rao et al, "Optical Design considerations of Narrow Field of View optical system for long range imaging application", Proc. Of Conference on Optics and Photonics in Engineering, organized by Optical Society of India and Netaji Subhash Institute of Technology, New Delhi during Jan 6-8, 2003.
- [5] R. Sudhakar Rao et al, "Study of Resolution capabilities of Charge Coupled Devices (CCDs) and Complementary Metal Oxide Semiconductor (CMOS) sensors to match suitably to optical systems for Long Range Imaging", Proc. Of Int. Conf. on Optoelectronics Technology, held jointly by OSI & North Maharashtra University, Jalgaon, 10 -14 January, 2004.

OPTICAL GRADE PLASTICS BASED PRECISION BI-ASPHERIC LENSES FOR INDIRECT OPHTHALMOSCOPY

GS Singh, SV Ramagopal, Pawan Kapur

CSIR-Central Scientific Instruments Organisation (CSIR-CSIO), Sector-30C, Chandigarh 160030

drgssr@gmail.com

With the advent of aspheric design methodologies and availability of fabrication and characterization facilities for realization of aspheric surfaces, aspheric-based optical instrumentation is taking centre stage in many applications, particularly where compact, light weight, high aperture and large fields are needed. To make systems further lightweight, system developers are exploring optical grade plastic aspheric profiles (in place of optical glasses) in numerous commercial products (cameras, CD/DVD lenses etc). Another advantage of using plastic optics is the cost effective large volume production of these lenses by injection molding. These developments brought commercial optics within the reach of customer without compromising on quality.

Indirect Ophthalmoscopy is used for the fundus examination of patients with vision problems. The Indirect Ophthalmoscope is a condensing Bi-Aspheric Lens to form an aerial intermediate real and inverted image of retina at a magnification of around 3.3X. The ophthalmologist studies this image further with the help of a microscope to examine and diagnose retinal problems. A series of high dioptric power (20D, 28D, 78D & 903D) bi-aspheric lenses are used for this purpose. There is a huge demand of these Bi-Aspheric Lenses (especially for 20D and 28D lenses) as they are required by every ophthalmologist (professional and student). The demand is generally

met by imports. Under DST funding, CSIR-CSIO has undertaken a series of projects at its National Aspheric Facility, to explore optical grade plastics for the indigenous development of these lenses.

In the first project of this effort, optical grade PMMA is used to develop Bi-Aspheric lenses (20D and 28D) for Indirect Ophthalmoscopy. The clinical trials of these lenses are held at major national Eye Care Centers: RPC-AIIMS (Delhi), PGIMER (Chandigarh), GMCH (Chandigarh), Venu Eye Hospital (Delhi) and Shankara Netralaya (Chennai). The results thereof are encouraging. Leading ophthalmologists advised CSIR-CSIO to explore high index plastics in this direction, to further improve the peripheral image quality.

Subsequently, CSIR-CSIO continued similar effort with using PolyCarbonate a high refractive index optical grade plastic, as the candidate material. This effort also has given similar encouraging results, with better performance in terms of lower peripheral residual aberrations.

On the recommendation of experts and leading ophthalmologists, CSIR-CSIO has now started working on the Development of Production Technology for Injection Molding of Precision Bi-Aspheric Plastic Lenses using PolyCarbonate. CIPET Chennai and ARCI Hyderabad are CSIR-CSIO's collaborators in this effort.

Broadband extra-ordinary transmission in checkerboard plasmonic films

S. Anantha Ramakrishna

Department of Physics, Indian Institute of Technology Kanpur

email: sar@iitk.ac.in

Abstract: Sub-wavelength sized square holes placed in a checkerboard lattice were fabricated by focused ion beam technologies. These checkerboard structures show an unanticipated broadband extra-ordinary transmission of light with a transmission of over 80% at 650 – 950 nm in the near-infra-red spectrum. Theoretical and computational work confirms this phenomenon that arises due to the unique plasmonic properties of the checkerboard structures.

Extraordinary transmission (EOT) of light through subwavelength sized holes has been a much debated topic since its first report by Ebbesen in 1998 [1]. Small (subwavelength) nanoholes in opaque silver or gold films, which usually show very small transmission, when placed on periodic lattices transmitted unusually large amounts of light at certain resonant frequencies. The resonant frequencies depended on the periodicity and lattice while the band widths usually depended on the material and shape of holes etc. The levels of the transmission across the structured film could be very high – upwards of 90%. The band-widths for EOT typically are about 30-50 nm. Checkerboards of negative refractive index media and plasmonic media have been shown to exhibit very singular photonic properties, including very large local field enhancements and divergences in the density of states [2]. These unique photonic properties of checkerboard systems arise as they are essentially large collections of periodically placed corners between positive and negative refractive (or negative permittivity) media. The corners and edges are expected to dominate all the optical properties of the checkerboards. This naturally prompts the question as to whether plasmonic gold and silver nano-films structured as checkerboards can enable control of light and enhance light transmission through the nano-hole apertures while confining light within the transverse plane.

In this presentation, we will discuss the unexpected observation of broadband EOT through opaque gold films containing through square nanoholes placed in checkerboard fashion [3]. These films were structured using focused ion beam technologies and show EOT throughout the red to the near infra-red spectrum from about 650 nm to beyond 950 nm wavelengths. Calculations using both home-built codes and the COMSOL multiphysics solver obtain excellent agreement with the experimental results and indicate that resonant photonic tunneling through the nanoholes to be the mechanism of the EOT. The unique properties of the checkerboards enable them to support degenerate plasmonic resonances across all frequencies below the bulk plasmon frequency. This principle Physical effect behind the broadband EOT will be discussed in some detail.

REFERENCES

- [1] T. W. Ebbesen, H. J. Lezec, H. F. Ghaemi, T. Thio, P. A. Woff, *Nature*, 391, 667 (1998)
- [2] S. Guenneau and S.A. Ramakrishna, *Comptes Rendus Physique (Paris)*, **10**, 352-378 (2009)
- [3] S.A. Ramakrishna, P. Mandal, K. Jeyadheepan, N. Shukla, S. Chakrabarti, M. Kadic, S. Enoch and S. Guenneau, *Phys. Rev. B (In press)*, (2011)

STATISTICAL FLUCTUATIONS IN COHERENT EMISSION FROM DISORDERED NANOSTRUCTURED AMPLIFYING MATERIALS

Ravitej Uppu, Anjani Kumar Tiwari and Sushil Mujumdar
Tata Institute of Fundamental Research, Homi Bhabha Road, Mumbai 400 005
mujumdar@tifr.res.in

Abstract: We discuss the fluctuations in emission intensity of coherent modes generated by amplification of extended modes in open, disordered, amplifying media. After an initial heuristic treatment, we quantify the fluctuations in terms of Levy exponents, and identify the statistical regimes of fluctuations.

1. INTRODUCTION

That coherent optical emission can be obtained from disordered nanostructured materials is now an amply proven fact. Such emission, termed ‘coherent random lasing’ relies on the amplification of a variety of modes sustained in a disordered medium. For instance, localized modes can be formed in strongly disordered media[1]. In weaker media, resonant modes can occur between two scatterers[2], or even extended modes can exist that undergo avalanche amplification, leading to coherent emission[3].

Owing to the inherent randomness, such systems exhibit a rich statistical character[4]. The disordered structure realizes chaotic fluctuations in the frequency of the coherent mode. The non-deterministic lifetimes of the various modes manifest as intensity fluctuations. Here, we discuss the heuristic statistics of the intensity of coherent modes, and thereafter chalk out the various statistical regimes spanned by such systems.

2. INTENSITY STATISTICS

The path-lengths of the non-resonant modes existing in the disordered system is given by an exponential distribution, $P(L) \propto \exp(-L/l)$. At the same time, the intensity accumulated by the mode is ruled by exponential gain, $P(I) \propto \exp(L/l_g)$. Together, one obtains a power-law distribution of the intensity, the exponent of which is determined by the gain length, and the mean first passage length.

We measured the intensity statistics of coherent modes generated from a sample of Rhodamine 6G dissolved in methanol, into which ZnO nanoparticles were suspended. A wavelength interval of 0.2 nm, which was the resolution of the setup, was chosen for analysis. A set of intensities was created from 2500 spectra, and the Koutrouvelis algorithm was used to fit the power-law decay.

Figure 1 shows two distributions, the Gaussian being the pre-lasing statistics, and the fat-tailed distribution showing the power-law statistics. As a function of pump energy and the sample size, the system crosses over from the Gaussian to the power law (Levy) regime at the random lasing threshold. Interestingly, a

second cross-over occurs at a higher pump energy, where the statistics re-enter the Gaussian regime. The inset in figure 1 indicates the various regimes observed in the experiment.

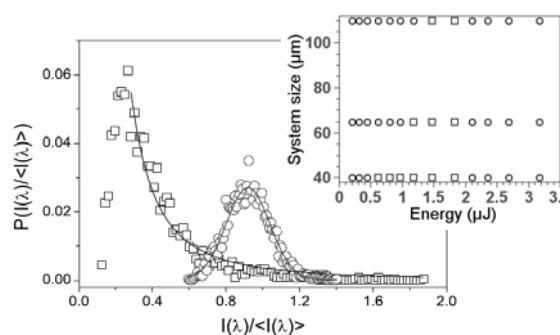


Figure 1. Experimentally observed Gaussian (symmetric) and power-law (fat-tailed) statistics. Inset: Regimes of Gaussian (circles) and Levy (squares) statistics.

In conclusion, we have discussed the important statistical transitions in emission intensity from coherent random lasers. The study reveals the utility of such systems in investigations of non-gaussian statistics.

REFERENCES

- [1] H.Cao Y.G.Zhao, S.T.Ho, E.W.Seelig, Q.H.Wang and R.P.H.Chang, “Random laser action in semiconductor powder,” *Phys. Rev. Lett.* **82**, 2278 (1999).
- [2] X. Wu, Fang W., Yamilov A., Chabanov A. A., Asatryan A. A., Botten L. C., and Cao, H, “Random lasing in weakly scattering systems” *Phys. Rev. A* **74**, 053812 (2006).
- [3] S. Mujumdar, M. Ricci, R. Torre, and D. S. Wiersma, “Amplified extended modes in random lasers”, *Phys. Rev. Lett.* **93**, 053903 (2004).
- [4] R. Uppu and S. Mujumdar, “Statistical fluctuations of coherent and incoherent intensity in random lasers with nonresonant feedback”, *Opt. Lett.*, **35**, 2831 (2010).

TEMPERATURE INSENSITIVE REFRACTIVE INDEX SENSOR BASED ON CONCATENATED LINEARLY CHIRPED LPGs

Saurabh Mani Tripathi,¹ Wojtek J. Bock,¹ Arun Kumar² and Predrag Mikulic¹

¹Centre de Recherche en Photonique, Université du Québec en Outaouais, Gatineau, QC, Canada

²Department of Physics, Indian Institute of Technology Delhi, New Delhi - 110016, India

tripathi.iit@gmail.com, wojtek.bock@uqo.ca, akumar@physics.iitd.ac.in, predrag.mikulic@uqo.ca

Abstract: We propose and demonstrate a novel refractive index sensor based on two concatenated, chirped long period fiber gratings. An inter-grating space (IGS), deliberately introduced between the two gratings, provides an extra phase difference between the core and cladding modes. This makes the device similar to a Mach-Zehnder interferometer with one of its arm phase shifted. Adjusting the thermal induced phase difference of the IGS region (by adjusting its length) to compensate for the thermal induced phase change of the grating region, we show that a temperature independent resonance wavelength can be obtained. The IGS, however, doesn't affect the ambient refractive index sensing characteristics of the sensor. Further, measuring the spectral shifts of two resonance wavelengths, we show that a simultaneous measurement of the refractive index and the temperature can also be done using the present scheme.

1. INTRODUCTION

The precision refractive index (RI) sensing is of prime importance for both the scientific and industrial research sectors. Although, the sensors based on long period gratings [1], surface Plasmon polaritons [2], multimodal interference [3] etc., offer an extremely high sensitivity, often a precise determination of the RI needs temperature calibration since the refractive index of bio/chemical samples is a function of temperature. Studies based on the FBGs combined with LPGs [4], cascaded two LPGs with different periods fabricated in a double cladding fiber [5], and the titled FBGs [6] etc., have been reported to realize it. Although these methods have their own advantages, they cannot avoid using bulky circulators, complex grating writing techniques and special post-processing treatments like etching and polymer coating.

In this paper, we present a novel dual-parameter sensor based on two concatenated linearly-chirped LPGs by introducing an inter-grating space (IGS) between them (Fig.1)). The IGS provides an extra phase difference between the core and cladding modes, adjusting which by judiciously selecting its length to compensate for the thermal induced phase change of the grating region; a temperature independent resonance wavelength can be obtained.

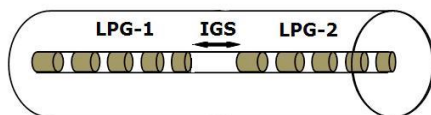


Fig.1. Schematic of the sensor structure.

2. THEORETICAL ANALYSIS

In order to obtain the propagation constant and the field distribution of the modes we use the well known linear polarization (LP) approximation. In this method

the Maxwell's equations reduce to the following scalar wave equation [7, 8]:

$$\frac{d^2\phi}{dr^2} + \frac{1}{r} \frac{d\phi}{dr} + (k_0^2 n_i^2 - \beta^2)\phi = 0 \quad (1)$$

where, k_0 , n , and β are the free space propagation constant, the refractive index distribution and the propagation constant, respectively. The direction of propagation is taken to be along z -axis and the (z, t) dependence of the fields is taken of the form $\exp\{i(\omega t - \beta z)\}$. The propagation constants and the field distributions of the core and the cladding modes are obtained by solving Eq.(1) employing the continuity of ϕ and $d\phi/dr$ field components at every dielectric discontinuity. The continuity conditions can be written, in the Matrix form, as:

$$\begin{bmatrix} \phi \\ \frac{1}{\beta} \frac{d\phi}{dr} \end{bmatrix} = M_m \begin{bmatrix} A_m \\ B_m \end{bmatrix} \quad (2)$$

with the matrix M_m given by,

$$M_m = \begin{bmatrix} Z_m & \bar{Z}_m \\ \frac{u_i}{\beta} Z_m & \frac{u_i}{\beta} \bar{Z}_m \end{bmatrix} \quad (3)$$

here, the index $m = co, cl, se$ represents the substrate, core, cladding, metal and sensing region, respectively; A_m and B_m are field coefficients in the m th region, and Z_m and \bar{Z}_m are signified as follows:

$$\begin{aligned} Z_m &= J_m(u_i r), \bar{Z}_m = Y_m(u_i r), \quad \text{for } u_i^2 = k_0^2 n_i^2 - \beta^2 > 0 \\ Z_m &= I_m(u_i r), \bar{Z}_m = K_m(u_i r), \quad \text{for } u_i^2 = k_0^2 n_i^2 - \beta^2 < 0 \end{aligned}$$

At the junction of the two neighboring regions m and n , therefore, the field amplitudes are connected as:

$$M_n \begin{bmatrix} A_n \\ B_n \end{bmatrix} = M_m \begin{bmatrix} A_m \\ B_m \end{bmatrix} \quad (4)$$

thus, the amplitudes in the substrate and sensing regions will be connected as:

$$\begin{bmatrix} A_{co} \\ B_{co} \end{bmatrix} = M \begin{bmatrix} A_{se} \\ B_{se} \end{bmatrix} \quad (5)$$

where, M is given by

$$M = (M_{co}^{-1} M_{cl})_{r=a} (M_{cl}^{-1} M_{se})_{r=b} \quad (6)$$

Now, since for physically acceptable solutions the fields must be finite in all the regions: the field coefficients B_{co} and A_{se} of the exponentially growing components in core region and the sensing region must be zero. Using this condition in Eq.(6) gives us the Eigen-value equation as:

$$M_{22} = 0 \quad (7)$$

which is solved to obtain the propagation constants of the core and cladding modes. Having obtained the propagation constants, the field coefficients in various regions are calculated by using Eq.(5) and Eq.(6). The fields are then normalized to carry unit power along the z direction [8].

Now, in order to obtain the transmission spectrum of the sensor we again follow the transfer matrix method [9, 10], in which the longitudinal field coefficients of the core mode and the participating cladding mode in every grating sections of uniform period, are connected to the field coefficients of the next section via a transfer matrix as [9, 10],

$$\begin{bmatrix} A_c^i(z) \\ A_{cl}^i(z) \end{bmatrix} = \begin{bmatrix} \cos(\alpha l) + i \frac{\delta}{\alpha} \sin(\alpha l) & i \frac{\kappa_{c-cl}}{\alpha} \sin(\alpha l) \\ i \frac{\kappa_{c-cl}}{\alpha} \sin(\alpha l) & \cos(\alpha l) - i \frac{\delta}{\alpha} \sin(\alpha l) \end{bmatrix} \begin{bmatrix} A_c^{i+1}(z) \\ A_{cl}^{i+1}(z) \end{bmatrix} \quad (8)$$

where,

$$\delta = \frac{1}{2} [\kappa_{c-c} - \kappa_{c-cl} + \beta_c - \beta_{cl} - \frac{2\pi}{\Lambda}], \alpha = (|\kappa_{c-cl}|^2 + \delta^2)^{1/2} \quad (9)$$

β_n is the propagation constant of the n^{th} mode, A_n^m is the field amplitude of the n^{th} mode in the m^{th} grating section, l is the length of uniform grating section, κ_{c-c} and κ_{c-cl} are the self-coupling coefficients of the core and cladding modes, respectively, and κ_{c-cl} is the cross coupling coefficient between the core mode and the cladding mode [10]. Using Eq.(1) the field amplitudes at the output of the first chirped grating is obtained. A phase matrix

$$U = \begin{bmatrix} \exp(i\beta_c L) & 0 \\ 0 & \exp(i\beta_{cl} L) \end{bmatrix} \quad (10)$$

is then used to incorporate the phase introduced by the inter-grating space. Finally, using another set of transfer matrices to incorporate the second chirped grating, the transmission spectrum of the concatenated gratings with an IGS can be obtained.

3. RESULTS AND DISCUSSION

In our analysis we consider the fiber core to be made of 3.1 mole% GeO₂ doped SiO₂ with its

diameter being 9.6 μm , cladding region made of fused SiO₂ and its diameter being 62.5 μm . The wavelength dependent refractive indices of the core and cladding regions have been obtained from the well known Sellmeier equation [11]. The ambient region has been considered to be made of water with its refractive index being 1.33. Employing these fiber parameters and the power coupling between the fundamental core mode and the 6th cladding mode, in Fig.(2) we have shown the transmission spectrum of the sensor for four different IGS.

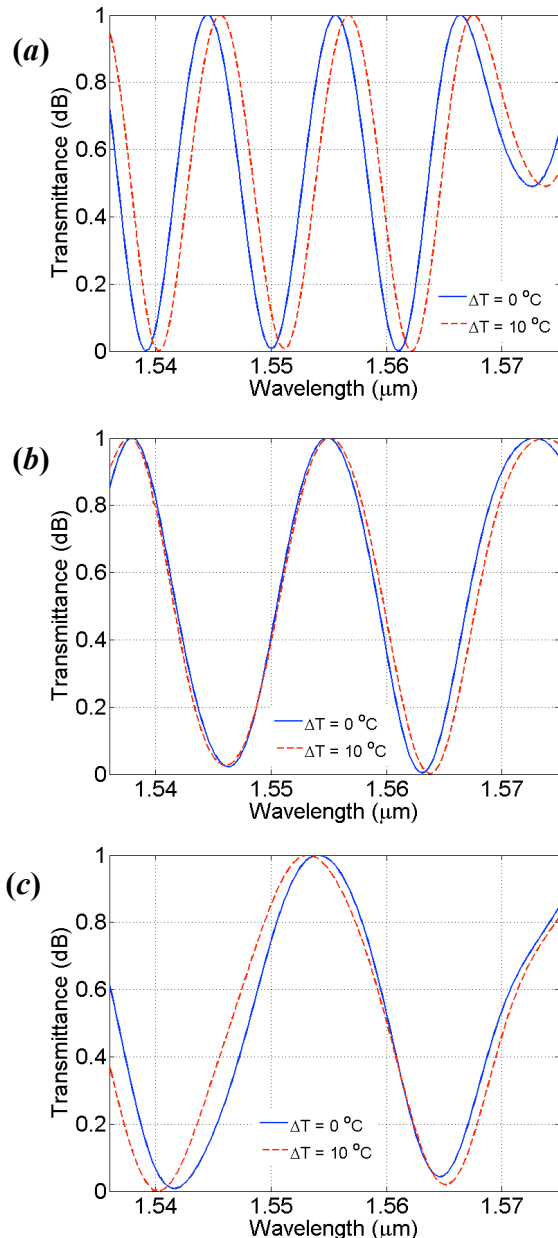


Fig.2 Transmission spectrum for (a) an IGS = 0 cm, (b) IGS = 2 cm and (c) IGS = 3 cm; showing the temperature independence for the wavelength dip near ~ 1.545 μm .

The grating period has been taken as 467 μm , the chirp constant is 3.74×10^{-4} and the grating length has

been taken as 5.14 cm. As can be observed, for zero IGS the structure shows a red (positive) spectral shift with respect to increasing temperatures. As the IGS is increased to 2 cm the transmission minima near 1.545 μm is virtually temperature insensitive (Fig.2(b)), and showing a blue (negative) spectral shift as the IGS is increased further (Fig.2(c)).

To show the ambient refractive index (ARI) sensitivity of the sensor corresponding to an IGS of 2 cm, in Fig.3 we have plotted the transmission spectrum at two different ambient refractive indices, $n_{se} = 1.33$ and $n_{se} = 1.34$. The refractive index sensitivity comes out to be ~ 230 nm/RIU which is similar to the sensitivities reported for the LPG based sensors [1] indicating that the IGS doesn't affect the refractive index sensitivity of the sensor.

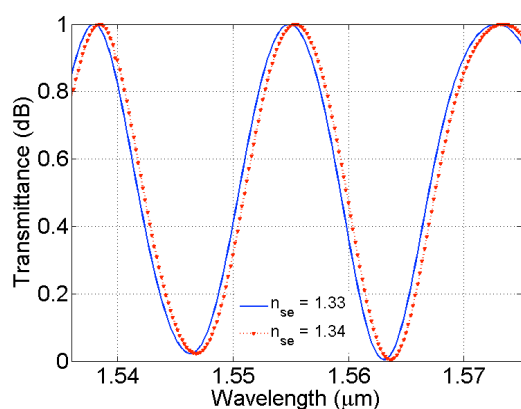


Fig.3 Transmission spectrum of the sensor corresponding to an IGS = 2 cm.

To carry out the experimental study we fabricated the chirped LPGs over a 5 cm length of SMF-28TM fiber (Corning: NY, 14831 USA). For ease of fabrication the photosensitivity of the fibers was increased by hydrogen loading of the fibers at 150 bars in Hydrogen chamber for 15 days. Photosensitive LPGs were then inscribed into the fiber core using a chromium amplitude mask and a high-power KrF excimer laser (LumonicsTM Lasers: Pulse Master[®]-840) emitting at 248 nm at a pulse repetition rate of 100 Hz, pulse duration of 12 ns and peak pulse energy of 10 mJ. Variable length between 0 to 3 cm were then moved forward before inscribing another identical chirped grating over the next 5 cm of the fiber. The inter-grating space was carefully marked during the grating inscription process. The fabricated LPGs were then annealed at 150 $^{\circ}\text{C}$ for 4 hours for the thermal stabilization and the measurements were then carried out.

The presence of macro-bends along the LPG region are the primary cause of measurement errors in LPG based sensors. In order to avoid them we maintained a constant tension along the LPG throughout the experiments by attaching the fiber near one end of the LPG and applying a fixed force near the other end of it. Light was launched into the fiber using an Agilent-

83437A broadband source (BBS) and the transmission spectrum was recorded using an Agilent-86142B optical spectrum analyzer (OSA) with a resolution of 0.02 nm.

In Fig.4 we have shown the absolute value of the resonance wavelength shift (corresponding to an incremental temperature of 10 $^{\circ}\text{C}$) of the transmission minima near ~ 1.545 μm for different IGS. The curve above the IGS axis correspond to a red spectral shift and that on the below of IGS axis corresponds to the blue spectral shift. As can be observed the structure shows nearly zero spectral shift for an IGS ~ 2.3 cm. The small difference between the theoretically predicted IGS and the experimental one can be attributed to the small variations in the theoretical and experimental chirps, the small difference in the LPG lengths and the refractive index modulation within the grating regions.

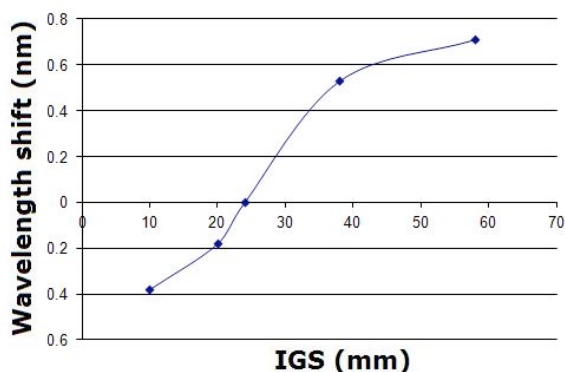


Fig.4 Experimental resonance wavelength shift of the transmission minima near ~ 1.545 μm for different IGS. The incremental temperature difference has been taken as 10 $^{\circ}\text{C}$.

Finally, in Fig.5 we have plotted the variation in the resonance wavelength corresponding to the dip at ~ 1.545 μm .

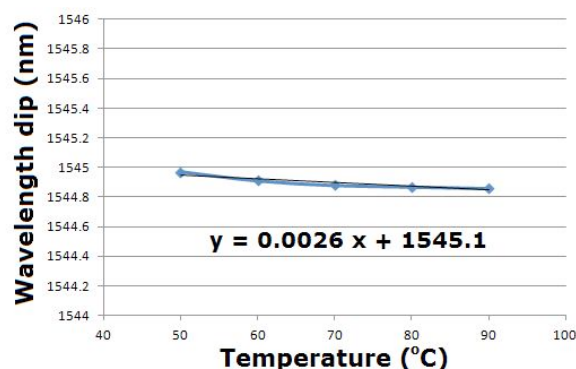


Fig.5 variation in the resonance wavelength corresponding to the dip at ~ 1.545 μm .

The net temperature sensitivity of the dip being ~ 0.0026 nm/ $^{\circ}\text{C}$, which is $\sim 10^{-4}$ times smaller than the typical temperature sensitivity of LPGs [1, 12]. We would like to mention here that an exact temperature insensitive device can be obtained by slightly

modifying the phase matching condition and/or the phase difference between the two chirped gratings by partially etching the grating region and/or the IGS region in between them.

4. CONCLUSIONS

In this paper we have proposed and demonstrated a novel refractive index sensor based on two concatenated, chirped long period fiber gratings. The inter grating space between the two linearly chirped gratings provides an extra phase difference between the core and cladding modes. Adjusting the thermal induced phase difference of the IGS region (by adjusting its length) to compensate for the thermal induced phase change of the grating region, we have demonstrated a temperature independent resonance wavelength near $\sim 1.545 \mu\text{m}$. The IGS, however, doesn't affect the ambient refractive index sensing characteristics of the sensor.

REFERENCES

- [1] V. Bhatia and A. Vengsarkar, "Optical fiber long period grating sensors," *Opt. Lett.*, **21**, 692 (1996).
- [2] J. Homola, ed., *Surface Plasmon Resonance Based Sensors*, Springer, 2006.
- [3] J. Villatoro, V. Minkovich, V. Pruneri, and G. Badenes, "Simple all-microstructured-optical-fiber interferometer built via fusion splicing," *Opt. Express*, **15**, 1491 (2007).
- [4] X. W. Shu, B. A. L. Gwandu, Y. Lin, L. Zhang, and I. Bennion, "Sampled fibre Bragg grating for simultaneous refractive-index and temperature measurement," *Opt. Lett.*, **26**, 774 (2001).
- [5] B. A. L. Gwandu, X. Shu, T. P. Allsop, W. Zhang, and I. Bennion, "Simultaneous refractive index and temperature measurement using cascaded long-period grating in double-cladding fibre," *Electron. Lett.*, **38**, 695 (2002).
- [6] C. L. Zhao, X. F. Yang, M. S. Demokan, and W. Jin, "Simultaneous Temperature and Refractive Index Measurements Using a 3Slanted Multimode Fiber Bragg Grating," *J. Lightwave Technol.*, **24**, 879 (2006).
- [7] A. K. Ghatak and K. Thyagarajan, *Optical Electronics* (Cambridge, 1989).
- [8] K. Okamoto, *Fundamentals of Optical Waveguides* (Academic, 2000), Chap. 2.
- [9] M. Das and K. Thyagarajan, "Wavelength-division multiplexing isolation filter using concatenated chirped long period gratings", *Opt. Commun.*, **197**, 67 (2001).
- [10] R. Kashyap, *Fiber Bragg Gratings*, (Academic Press, 2010).
- [11] M. J. Adams, *An Introduction to Optical Waveguides*, (Wiley, New York, 1981).
- [12] S. Khaliq, S. W. James and R. P. Tatam, "Enhanced sensitivity fibre optic long period grating temperature sensor", *Meas. Sci. Technol.* **13**, 792 (2002).

FEMTOSECOND LASER MICROMACHINING FOR ULTRAFAST OPTOFLUIDIC DEVICES

Nicola Bellini¹, Tersilla Virgili¹, Roberto Osellame¹, Guglielmo Lanzani^{1,2}, Roberta Ramponi^{1,2}, and Krishna Chaitanya Vishnubhatla^{2,*}

1)Istituto di Fotonica e Nanotecnologie - CNR and Dipartimento di Fisica - Politecnico di Milano,

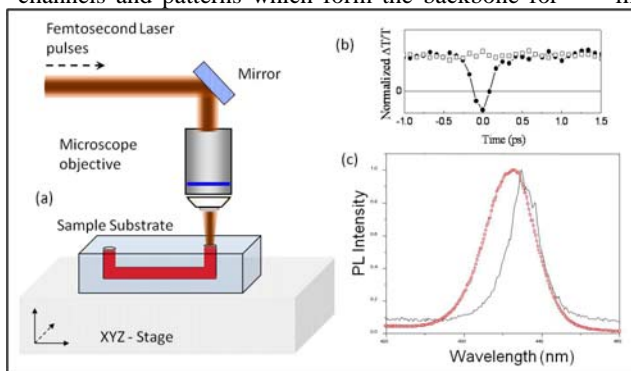
2)Center for Nano Science and Technology @Polimi, Istituto Italiano di Tecnologia, Milan, Italy.

*email presenting author: krishna.vishnubhatla@iit.it

Abstract: We fabricated an embedded microfluidic-channel chip by femtosecond laser irradiation and chemical etching (FLICE) technique. Using the microchannel we demonstrate a polymer based optofluidic amplifier capable of ultrafast switching and by dispersing nanoparticles in the solution we are able to achieve random lasing in the microchannel.

1. INTRODUCTION

Optofluidics is a rapidly emerging field and it culminates the integration of optics and novel microfluidics functions onto a single platform. Optofluidic devices are gaining importance, owing to their advantages over other solid state photonic counterparts; some materials like conjugate polymers have certain beneficial properties, when in solutions as compared to their solid forms [1]. Microfluidic channels and patterns which form the backbone for



(a) The schematic diagram of FLICE (b) Pump-push-probe dynamics (solid circles) and pump-probe dynamics (squares) of 3g/L^{-1} PFO solution at 490 nm; (c) Lasing emission from nanoparticle dispersed solution (solid line) is compared to the normalized photoluminescence from PFO solution (dotted line)

such optofluidic devices can be fashioned by lithographic and chemical-etching techniques, but these approaches are primarily limited to the fabrication of two-dimensional patterns on the surface. In order to create a true 3-D structure several layers of glass substrates need to be patterned, etched and fused together. A relatively new technique of Femtosecond Laser Irradiation and Chemical Etching (FLICE) can add nuance to these fabrication approaches and, thereby, permit the development of directly buried microchannels with various aspect ratios [2]. As this is a maskless technology it enables rapid prototyping of new devices. Moreover, since the same femtosecond laser can be used to produce

low loss optical waveguides, these femtosecond laser based technologies could become one-stop solution for fabrication of microfluidic channels and their integration with optical circuits.

2. EXPERIMENTAL

The FLICE fabrication procedure is a two step process. The first step is femtosecond laser irradiation with intensities below the laser ablation threshold, wherein the design of the microchannels is imprinted into the substrate volume (fig.a) (fused

silica glass). The second step involves etching of the femtosecond laser modified region using HF acid. As an example to demonstrate the practical utility of such embedded microchannels and to develop an optofluidic device, the microchannel was filled with poly(9,9-dioctylfluorene) (PFO) (American Dye Source) in decahydronaphthalene (Sigma-Aldrich), and the gain switching properties were studied.

3. RESULTS/CONCLUSIONS

By the new innovative FLICE technique we demonstrated for the first time that embedded microchannels with access holes reaching the substrate surface can be fabricated. By combining the gain and ultra-fast switching properties (fig.b) of PFO in solution with an optofluidic microchannel in a fused silica substrate we were able to produce an easily integratable all-optical amplifier capable of ultra-fast gain switching providing potential switching rates well into the THz region. Further by dispersing nano-particles we also demonstrate an on chip laser source (fig. C) exploiting the random lasing phenomenon [3].

REFERENCES

- [1] D. Psaltis, S. R. Quake, C. Yang, *Nature*, **442**, 27 (2006).
- [2] Vishnubhatla, K.C., Bellini, N., Ramponi, R., Cerullo, G., Osellame, R., *Optics Express*, **17** (10), pp. 8685-8695 (2009).
- [3] Vishnubhatla, K.C., Clark, J., Lanzani, G., Ramponi, R., Osellame, R., Virgili, T., *Applied Optics*, **48** (31), pp. G114-G118, (2009).

GENERATION OF NANOSCALE FOCAL HOLE WITH EXTENDED DEPTH OF FOCUS FOR TRAPPING ARRAY OF NANOPARTICLES

K.Lalithambigai^a, V.Ravi^a, K.Prabakaran^b, Z.Jaroszewicz^c, K.B.Rajesh^{d*}, P.M.Anbarasan^a, T.V.S.Pillai^b

^aDepartment of Physics, Periyar University, Salem, Tamilnadu, India

^bDepartment of Physics, Anna University of Technology Tirunelveli, India

^cInstitute of Applied Optics, Department of Physical Optics, Warsaw, Poland and National Institute of Telecommunications, Warsaw, Poland

^dDepartment of Physics, Government Arts College, Dharmapuri, Tamilnadu, India

*rajesk@gmail.com

Abstract:

We investigate the focusing properties of a double-ring shaped azimuthally polarized beam by a high NA lens axicon based on vector diffraction theory. We observe that our proposed system generates sub wavelength focal hole of 0.5λ having large uniform focal depth of 48λ without any annular aperture. We also observed that the distribution of the total intensity near the focus has little variation with the degree of truncation β of the incident beam by the pupil. The authors expect such a high intense super long dark channel may find applications in optical, biological, and atmospheric sciences.

Keywords: Axicon, Aberration, Optical engineering, Polarization, Apodization, Diffraction.

1. INTRODUCTION

Optical bottle beams are beams with low or null intensity channels surrounded by three-dimensional (3D) regions of higher intensity. This optical bottle has obvious applications for trapping particles with refractive indices lower than that of the surrounding medium and the single-beam blue-detuned trapping of atoms in a low-intensity region. Over the past years, a variety of techniques have been proposed for generating such beams for applications in optical tweezers and atom traps [1–7]. Stable trapping of a single particle is expected if we can make the bottles small enough and comparable to the particle size. Such “microbottles” were established recently with the volume speckle field [8]. Recently, a sub wavelength focal hole ($\sim 0.5\lambda$) with a quite long depth of focus ($\sim 26\lambda$) was achieved

near the focus by tight focusing of double ring shaped azimuthally polarized beam with annular high NA lens [9]. In this paper we describe a numerical study, based on the vector diffraction theory, of a property of a azimuthally polarized double ring-shaped R-TEM₁₁* mode beam that is tightly focused by a high-NA-lens axicon. We observe that our proposed system generates sub wavelength 0.5λ focal hole with large uniform focal depth 48λ without any annular truncation.

2. THEORY

A schematic diagram of the suggested method is shown in Fig-1. The analysis was performed on the basis of Richards and Wolf’s vectorial diffraction method [14] widely used for high-NA focusing systems at arbitrary incident polarization. In the case of the azimuthally incident

polarization, adopting the cylindrical coordinates r , z, φ and the notations of Ref. [15].

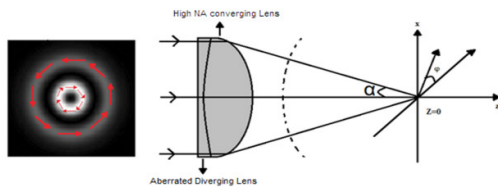


Fig. 1. Scheme for a double-ring-shaped azimuthally polarized beam focused by high NA objective lens axicon.

The electric field $E(r, \varphi, z)$ in the vicinity of the focal region can be written as

$$E(r, \varphi, z) = \begin{bmatrix} E_r \\ E_\varphi \\ E_z \end{bmatrix} = \begin{bmatrix} 0 \\ 2A \int_{\delta\alpha}^{\alpha} \cos^2(\theta) \sin(\theta) A(\theta) J_1(kr \sin \theta) e^{i l \cos \theta} d\theta \\ 0 \end{bmatrix} \quad (1)$$

where δ distinguishes the presence or absence of annulus and $\alpha = \arcsin(NA/n)$. where NA is the numerical aperture and n is the index of refraction between the lens and the sample. $J_0(x)$ and $J_1(x)$ denote the Bessel functions of zero and first order and the function $A(\theta)$ describes the amplitude modulation. For illumination by a double ring-shaped R-TEM₁₁* beam with its waist in the pupil, this function is given by [16]

$$A(\theta) = \beta^2 \frac{\sin \theta}{\sin^2 \theta} \exp \left[- \left(\beta \frac{\sin \theta}{\sin \alpha} \right)^2 \right] L_p^1 \left[2 \left(\beta \frac{\sin \theta}{\sin \alpha} \right)^2 \right] \quad (2)$$

Where β is the parameter that denoted the ratio of pupil diameter to the beam diameter and L_p^1 is the generalized Laguerre polynomial.

3. RESULTS

We perform the integration of Eq.(1) numerically using parameters $\lambda = 1$, NA=0.6 and $\beta = 1.2$ as in

[9]. Here, for simplicity, we assume that the refractive index $n = 1$ and $A = 1$.

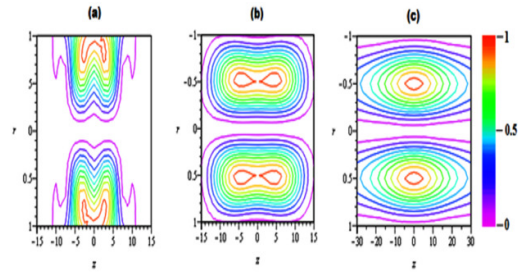


Fig. 2. Intensity distribution of the focused field near focus for the double-ring-shaped azimuthally polarized beam focused with (a) $\delta = 0$ (full aperture lens) (b) $\delta = 0.7575$ (annular lens) (c) High NA lens axicon. The other parameters are $\beta = 1.2$ and NA = 0.6.

The Fig. (2-a) shows the contour plot of the total intensity distribution in the yz plane near the focus for the focusing system without annular aperture ($\delta = 0$). It is observed that depth of focus (DOF) of the dark channel is about 12λ and the radii of the focal holes are not uniform along the dark channel. However, when $\delta = 0.75$, the radius of the focal hole is shown to be uniform along the dark channel, with its FWHM about 0.5λ and its depth of focus about 26λ which is shown in Fig.(2-b). The results are the same as reported in [9]. Hence by using annular aperture, it is possible for us to generate sub wavelength focal hole with large uniform focal depth. However it is estimated that almost 80% of the incident energy is blocked by the annular aperture which results in a poor intensity of the focal channel. We show that it is possible to generate high intense sub wavelength focal hole with large uniform focal depth without any annular aperture by using high NA lens axicon. The high NA lens axicon is a doublet of aberrated diverging lens and a high NA converging lens. Here we consider only systems that comprise a diverging lens that has third-order spherical aberration and a perfect high NA converging lens. The intensity distribution of the lens axicon is

evaluated by replacing the function $A(\theta)$ by the function $A(\theta)T(\theta)$ where $T(\theta)$ is the non-paraxial transmittance function of the thin aberrated diverging lens [10-13].

$$T(\theta) = \exp \left(ik \left(\psi \left(\frac{\sin(\theta)}{\sin \alpha} \right)^4 + \left(\frac{1}{2f} \left(\frac{\sin(\theta)}{\sin \alpha} \right)^2 \right) \right) \right) \quad (3)$$

where $k = 2\pi/\lambda$, f is the focal length and ψ is the aberration coefficient. In our calculation we take $f = 18.4\text{mm}$ and $\psi = 6.67 \times 10^{-5} \text{mm}^{-3}$ [17]. This results in an equiconcave diverging lens which is simple to manufacture.

Fig.(2-c) shows the contour plot of the total intensity distribution in the yz plane near the focus for the high NA lens axicon without any annular aperture ($\delta = 0$). It is observed that the radius of the focal hole is shown to be uniform along the dark channel, with its FWHM about 0.5λ and its focal depth around 48λ . Though the FWHM of the focal hole produced by the high NA lens axicon is equal as that of the annular lens with $\text{NA}=0.6$ and $\delta = 0.75$, the focal depth of the focal hole generated by the high NA lens axicon is almost 46% larger for the assumed set of parameters the focal depth of the focal hole generated by the annular lens. Thus the proposed high NA lens axicon system generates sub wavelength super long dark channel without any annular truncation. Since such a long uniform sub wavelength focal hole segment is generated without any annular aperture, the intensity of the focal hole segment also remains very high when compared to the system proposed in [9].

3.1 EFFECT OF NA OF THE LENS

We have also calculated the electric energy density profiles of the total field near the focus for the focusing system with $\text{NA} = 0.9$, $\beta = 1.2$ and is

shown in Fig.(3) is observed that the focal hole segment generated by the lens without any annular aperture is non uniform in nature with DOF around 6λ which is shown in Fig. (3-a).

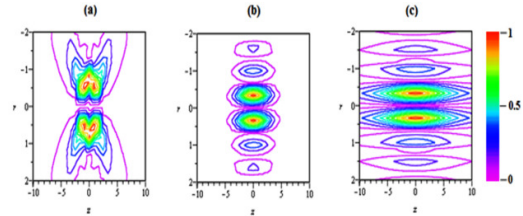


Fig.3. Intensity distribution of the focused field near focus for the double-ring-shaped azimuthally polarized beam focused by a high NA lens with (a) $\delta = 0$ (full aperture lens) (b) $\delta = 0.7575$ (annular lens) (c) High NA lens axicon. The other parameters are $\beta = 1.2$ and $\text{NA} = 0.9$.

However the presence of annular aperture with $\delta = 0.75$ generates uniform intensity focal hole segment with FWHM of 0.342λ and DOF around 6.7λ . The result is identical as in [9] and is shown in Fig. (3-b). Fig.(3-c) shows the focal segment generated by the proposed lens axicon system without any annular aperture. It is observed from the figure that FWHM of the focal hole is 0.332λ and its corresponding focal depth drastically increased to 16λ . It is observed though the FWHM of the focal hole generated by the proposed high NA lens axicon is almost the same as that of the annular aperture lens, its DOF is very large and is almost 58% greater than the annular lens with equal NA and $\delta = 0.75$.

3.2 EFFECT OF PUPIL TO BEAM RATIO OF THE INCIDENT BEAM.

The Fig. (4-a) and (4-b) shows the contour plot of the total intensity distribution in the z plane near the focus of the high NA lens axicon for the incident double ring shaped azimuthally polarized beam with pupil to beam ratio $\beta = 1.3$ and 1.5 respectively.

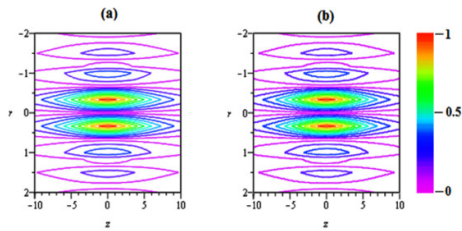


Fig.4. Intensity distribution of the focused field near focus for the double-ring-shaped azimuthally polarized beam focused by a high NA lens for $\beta = 1.3$ and $NA = 0.9$ (a) $\delta = 0$ (full aperture lens) (b) $\delta = 0.7575$ (annular lens)

It is observed from the figures that the FWHM of the focal hole segment for $\beta = 1.3$ is 0.338λ and its corresponding DOF is 16λ . However for $\beta = 1.5$, the FWHM of the focal hole slightly decreased to 0.332λ and its corresponding DOF is 16λ . Hence the degree of truncation of the incident beam has little effect in the case of high NA lens axicon.

Conclusion

The intensity distributions of azimuthally polarized beam that has a double-ring-shaped transverse mode pattern tightly focused by high NA lens axicon were calculated based on vector diffraction theory. It is observed that the distribution of the electric field near the focus has little variation with the degree of truncation of the incident beam by a pupil. We observed that the proposed high NA lens axicon without any annular aperture can generate Sub Wavelength Super-Long Dark Channel with FWHM of 0.5λ and DOF of 48λ . The authors expect such a high intense super long dark channel may find applications in optical, biological, and atmospheric sciences.

Reference

- [1] J. Arlt and M. Padgett, *Opt. Lett.* **25** (2000) 191-193.
- [2] B. Ahluwalia, X. Yuan, and S. Tao, *Opt. Express.* **12** (2004) 5172-5177.
- [3] P. Rudy, R. Ejnisman, A. Rahman, S. Lee, and N. P. Bigelow, *Opt. Express.* **8** (2001) 159-165.
- [4] D. Yelin, B. E. Bouma, and G. J. Tearney, *Opt. Lett.* **29** (2004) 661-663.
- [5] J.X. Pu, X.Y. Liu, and S. Nemoto, *Opt. Commun.* **252** (2005) 7-11.
- [6] L. Isenhower, W. Williams, A. Dally, and M. Saffman, *Opt. Lett.* **34** (2009) 1159-1161.
- [7] P. Xu, X. He, J. Wang, and M. Zhan, *Opt. Lett.* **35** (2010) 2164-2166.
- [8] V.G. Shvedov, A.V. Rode, Y.V. Izdebskaya, A.S. Desyatnikov, W. Krolikowski, and Y.S. Kivshar, *Opt. Express* **18** (2010) 3137-3142.
- [9] B. Tian and J. Pu, *Opt. Lett* **36** (2011) 2014-2016.
- [10] K.B. Rajesh, Z. Jaroszewicz and P.M. Anbarasan *Opt. Express.* **18** (2010) 26799-26805.
- [11] K.B. Rajesh, N. Veera Bagu Suresh, P.M. Anbarasan, and K. Gokulakrishnan, *Opt. Las. Technol.* **43** (2010) 1037-1040.
- [12] K.B. Rajesh, Z. Jaroszewicz, P.M. Anbarasan, T.V.S. Pillai and N. Veera Bagu Suresh, *Optik.* **122** (2011) 1619-1621.
- [13] K.B. Rajesh and P.M. Anbarasan *Chin. Opt. Lett.* **6** (2008) 785-787.
- [14] B. Richards, E. Wolf, *Proc R Soc A. London Ser.* **253** (1959) 358-79.
- [15] K. Youngworth, T. Brown. *Opt. Express.* **7** (2) (2000) 77-87.

RESONANT MODE-COUPPLING AT ANTI-CROSSING POINTS IN THz REGIME

Ritwick Das¹, Rajan Jha² and Triranjita Srivastava³

¹School of Physical Sciences, National Institute of Science Education and Research, Bhubaneswar

²School of Basic Sciences, Indian Institute of Technology Bhubaneswar, Bhubaneswar

³Department of Applied Physics, Delhi Technological University, New Delhi

Email: ritwick.das@niser.ac.in

Abstract: We present a design principle and novel route to excite surface-plasmon (SP) waves using a Bragg-reflection and SP based coupled-waveguide system at terahertz (THz) frequencies. The anti-crossing behavior exhibited by dispersion curves of supermodes due to modal interference gives rise to a novel route to excite THz-SP modes and the splitting leads to sharp change in group-velocity close to resonance wavelength.

1. INTRODUCTION

Guided-wave devices in any region of the electromagnetic (*em*) spectrum are extremely crucial ingredients for transmission as well as signal-processing. The quality of signal transmission mainly depends upon the absorption, scattering and leakage through the waveguide and the useful bandwidth for signal-processing is essentially dictated by the dispersion properties of waveguide. At optical frequencies, the plasmonic geometries comprising metals, like gold and silver offer an attractive route to realize surface plasmon polariton (SPP) based waveguides that exhibit affordable losses and excellent dispersive features for effective signal transmission as well as processing [1]. This is achievable due to the fact that the lower limit for plasmonic activity of metals depends on the plasma frequency which usually lies in visible or near-infrared (IR) region of the *em* spectrum [2]. However, realizing desirable plasmonic waveguides much below the plasma frequency of metals turns out to be a major bottleneck, as extremely large imaginary component of the complex permittivity function strongly prohibits penetration of *em* field in the metal and thus, exciting only loosely bound surface modes [3]. In order to circumvent this bottleneck, there have been attempts to address the issue of SPP mode excitation at terahertz (THz) frequencies [4-6] but still, the challenge remains to develop high performance practical THz plasmonic waveguides which would facilitate the realization of complex geometries.

In order to address this concern, few materials have been synthesized that gives rise to the possibility of plasmon-like behavior at THz frequencies owing to their small plasma-frequencies between 0.1-1.0 THz. One of the materials that exhibit such an attractive feature is polyvinylidene fluoride (PVDF) which is a ferroelectric semi-crystalline polymer with a real but small value of permittivity in the visible and near-infrared (IR) regions [7]. However, the dielectric constant of PVDF in THz regime exhibits frequency dependence given by [7],

$$\epsilon_{PVDF} = \epsilon_{opt} + \frac{(\epsilon_{dc} - \epsilon_{opt}) \omega_{TO}^2}{\omega_{TO}^2 - \omega^2 + i\gamma\omega}$$

where $\epsilon_{opt} = 2.0$, $\epsilon_{dc} = 50.0$, $\omega_{TO} = 0.3$ THz, $\gamma = 0.1$ THz and ' ω ' is angular frequency in THz. The plot depicting the variation of real and imaginary parts of PVDF dielectric constant as a function of wavelength is shown in Fig. 1. By analogy with the behavior of dielectric constant of metals at optical frequencies, it could well be expected that a SPP-mode could be supported at PVDF-dielectric interface in THz range.

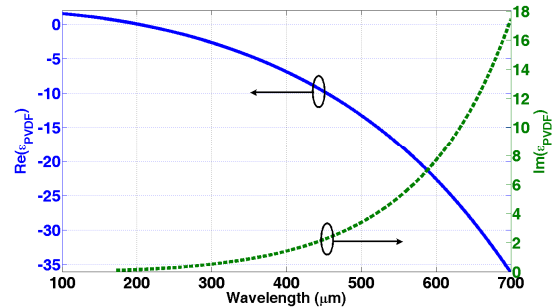


Fig. 1: Variation of real and imaginary part dielectric constant (ϵ) of PVDF as a function of wavelength.

The excitation of SPP waves at THz frequencies offer another critical challenge, essentially due to non-availability of high-index lossless prisms. A promising alternate route is via the deployment of THz-dielectric polymer based Bragg reflection waveguide (BRW) geometry for exciting SPP modes at THz frequencies using the concept of intermodal coupling between bandgap-guided and SPP modes. The present work explores this possibility of excitation via coupling between BRW fundamental mode and THz-SPP mode in a channel waveguide configuration, called Bragg reflection-Surface-plasmon-Coupled-Waveguide (BSCW). The channel BSCW is comprised of solid core made of polymethyl methacrylate (PMMA, $n_c = n_{PMMA} = 1.59$ at 1 THz), symmetrically sandwiched between 8 vertically-stacked bilayers of polycarbonate (PCB) ($n_l = n_{PCB} = 1.65$ at 1 THz) and PMMA (n_2), forming the periodic-cladding of low-index core of BRW. A thin layer of plasmonic material (PVDF) which is ~ 30 μm thick, followed by a low-index analyte layer ($n_a \approx 1.330$) is placed on top

of BRW which forms the SPP waveguide. In order to obtain the appropriate thicknesses of different layers, first we choose a resonance wavelength (λ_{res}) at which coupling between the fundamental BRW and SPP mode is to be realized. Assuming that BRW and SPP waveguide to be non-interacting, we calculate the mode effective index of SPP mode ($n_{(eff)SPP}$) at λ_{res} . Under the constraint that $n_{(eff)SPP} = n_{(eff)PCW}$ at λ_{res} , we calculate the core-thickness ($d_c = \lambda_{res} / (2\sqrt{n_c^2 - n_{(eff)PCW}^2})$) of BRW which has been derived assuming quarter-wavelength stack (QWS) condition being satisfied at λ_{res} [11]. In that case, the thicknesses of periodic bilayers can be evaluated using [11],

$$d_1 = \lambda_{res} / (2\sqrt{n_1^2 - n_{(eff)PCW}^2}) \quad \& \quad d_2 = \lambda_{res} / (2\sqrt{n_2^2 - n_{(eff)PCW}^2}) \dots \quad (2)$$

Due to the weak dispersive behavior of PMMA and PCB in THz frequencies, their impact on overall dispersion of BSCW is negligible and hence, the material dispersion of materials has been neglected in calculations [12]. For illustration purpose, we choose an arbitrary wavelength $\lambda_{res} = 400 \mu\text{m}$ ($\nu_{res} = 0.75$ THz) in order to design the waveguide. However, it is to be noted that the design could be realized for any choice of λ_{res} around which materials exhibit appreciable transparency. For $\lambda_{res} = 400 \mu\text{m}$, we calculated the core and cladding thicknesses to be $d_c = 457.0 \mu\text{m}$, $d_1 = 161.0 \mu\text{m}$ and $d_2 = 228.5 \mu\text{m}$. Without any loss of generality, we assume that the substrate as well as the surrounding medium to be air ($n = 1$) and carry out simulation for the channel BSCW structure with 8 bilayers by implementing widely used effective index method (EIM) [13]. For obtaining TM-polarized mode effective indices along x -direction, we employ standard transfer matrix method.

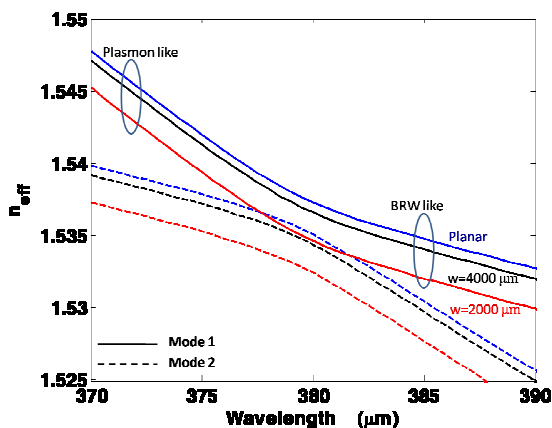


Fig. 2 Variation of real part of mode-effective indices of supermodes for BSCW as a function of wavelength

The variation of n_{eff} for two lowest order supermodes, named mode-1 and mode-2 hereafter, as a function of wavelength for channel BSCW at different channel widths, $w = 2000 \mu\text{m}$, $4000 \mu\text{m}$ and planar geometry are shown in Fig. 2. The figure

illustrates that around a phase-matching wavelength, $\lambda_{pm} = 379 \mu\text{m}$, the curves exhibit an anti-crossing behavior leading to a discernable slope-change.

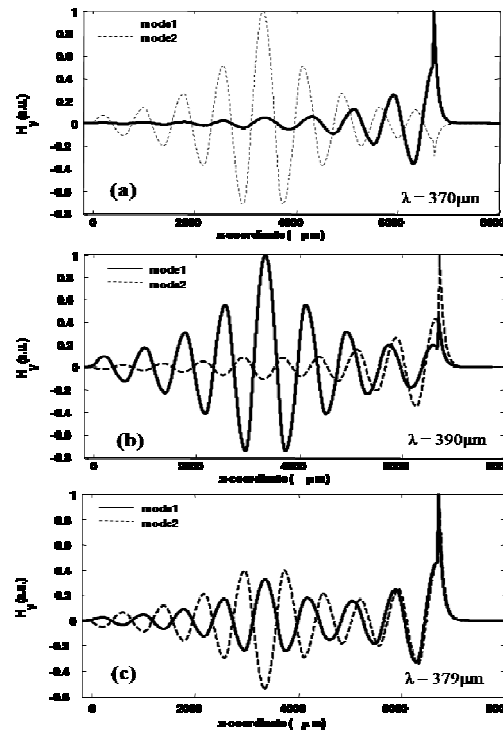


Fig. 3: TM-polarized (H_y) mode-field distribution (along x) of mode-1 and mode-2 at (a) $\lambda = 370 \mu\text{m}$ (b) $\lambda = 390 \mu\text{m}$ (c) $\lambda = 379 \mu\text{m}$

In order to appreciate the physical mechanism leading to this anti-crossing behavior, we plot the TM-polarized field (H_y) in planar geometry at $\lambda = 370 \mu\text{m}$, $390 \mu\text{m}$ and $379 \mu\text{m}$ (λ_{pm}) as shown in Fig. 4. The H_y field for mode-1 is primarily concentrated at the PVDF-analyte boundary in Fig. 3(a), which leads to a similar phase-velocity dispersion as that of a SPP mode (in Fig. 2) close to $\lambda = 370 \mu\text{m}$. The same supermode (mode-1) undergoes discernible redistribution when wavelength changes to $\lambda = 390 \mu\text{m}$ (Fig. 3(b)). The field, in this case, is appreciably confined in BRW region leading to a phase-velocity dispersion resembling to that of BRW mode. Due to this reason, the n_{eff} variation in Fig. 2 has been branched into “plasmon-like” and “BRW-like” arms. It is important to note in Fig. 3(c) that, the mode-fields for mode-1 and mode-2 at $379 \mu\text{m}$ (λ_{pm}) shows significant presence in both BRW and PVDF-analyte boundary but are out-of-phase with respect to each other at BRW core giving rise to the splitting (or anti-crossing) at λ_{pm} . This is a clear signature of modal-interference [14]. Mode-2 in Fig. 2 shows a similar but complimentary behavior with respect to mode-1 which can also be appreciated by observing the mode-field redistribution in Fig. 3 at different wavelengths. There are a few points worth mentioning here: (i) the

chosen $\lambda_{res} \neq \lambda_{pm}$, which is mainly due to smaller number of bilayers (8) than that required to contain entire individual mode-field of BRW and therefore, the perturbation effects tend to shift the λ_{res} to λ_{pm} [11]. (ii) When the channel width (w) decreases, the overall dispersion in Fig. 2 shifts to lower n_{eff} values without substantial change in λ_{pm} . This is essentially due to spreading of modal-field in air ($n = 1$) along y -direction as ' w ' decreases.

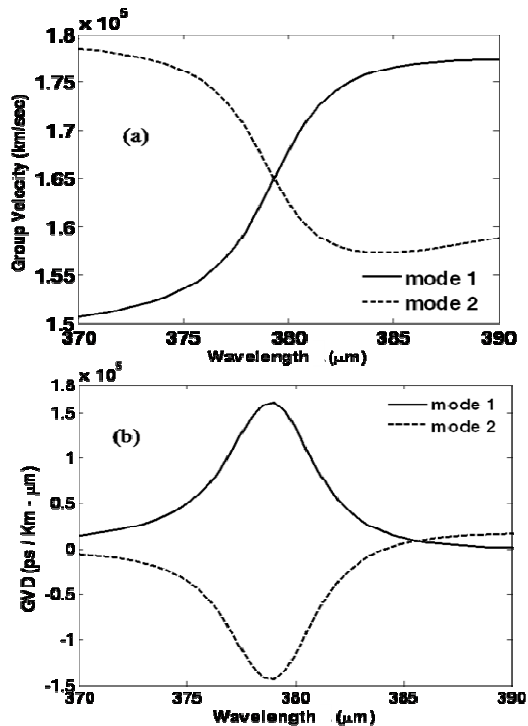


Fig. 4: Variation of (a) group-velocity (b) group-velocity-dispersion (GVD) for mode-1 and mode-2 of BSCW ($w = 2000 \mu\text{m}$) as a function of wavelength

The splitting of dispersion curves in Fig. 2 manifests into an interesting behavior of group-velocity and group-velocity-dispersion (GVD). In Fig. 4(a), the variation of group-index with wavelength (8 bilayers and $w = 2000 \mu\text{m}$) elucidates that group-velocity monotonically increases for mode-1 whereas it monotonically decreases for mode-2. From the dispersion properties of individual BRW and SPP modes, we have found that interaction bandwidth of $52.2 \mu\text{m}$ for $L = 1.0 \text{ cm}$. The extremely narrow interaction bandwidth could be exploited for designing strongly wavelength selective devices at THz frequencies. Further, the group-index variation manifests into a maximum $\approx 1.60 \times 10^5 \text{ ps/Km} \cdot \mu\text{m}$ (for mode-1) and minimum $\approx -1.40 \times 10^5 \text{ ps/Km} \cdot \mu\text{m}$ (for mode-2) at $\lambda = \lambda_{pm}$ in the curve showing GVD variation with respect to wavelength shown in Fig. 4(b). The large GVD could be practically implemented for realizing highly efficient dispersion compensating modules in THz range for time-

resolved spectroscopic measurements. We also observed that the change in channel width (w) has negligibly weak impact on GVD behavior.

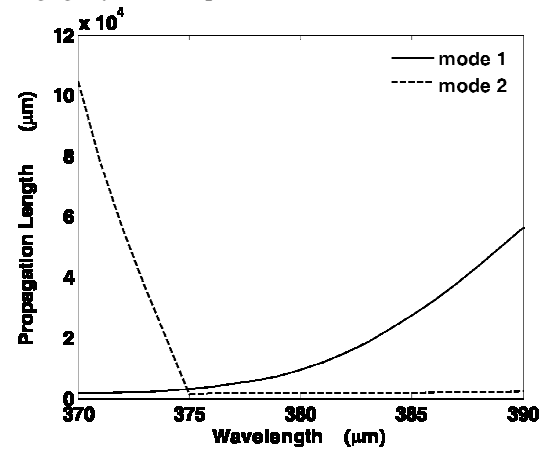


Fig. 5: Variation of (a) group-velocity (b) group-velocity-dispersion (GVD) for mode-1 and mode-2 of BSCW ($w = 2000 \mu\text{m}$) as a function of wavelength

The propagation losses suffered by supermodes (mode-1 & mode-2) are mainly a consequence of modal power absorption by thin PVDF layer which could be obtained from the imaginary part of mode effective index values for supermodes. In general, the propagation loss of mode-1 and mode-2 is measured in terms of their propagation length (l_p), which is defined as the distance over which the modal power falls to $1/e^{\text{th}}$ of its maximum value (at the BSCW input) i.e. $l_p = \lambda / (4\pi n_{(eff)j})$ where $n_{(eff)j}$ is the imaginary part of the mode effective index of the two supermodes. Figure 6 illustrates the variation of propagation lengths (l_p) of mode-1 and mode-2 as a function of wavelength. For mode-1, l_p exhibits a gradual but nonlinear increase due to gradual increase of field in BRW core as wavelength increases. On the other hand, l_p for mode-2 reduces almost linearly as wavelength increases up to $375 \mu\text{m}$ and once the major fraction of mode-field of mode-1 concentrates in SPP mode, the l_p drops below $100 \mu\text{m}$. It is important to note that the variation in l_p is quite asymmetric which is mainly a consequence of marked asymmetry in BSCW geometry leading to unequal modal-field redistribution across different waveguide sections when wavelength changes.

The most attractive feature of BSCW geometry is the possibility of realizing this phenomenon in any desired region of THz spectrum. This is mainly due to bandgap-based guidance mechanism in BRW, which permits the attainment of desired dispersion properties by appropriately choosing the thicknesses of core (d_c) and cladding (d_1 and d_2). However, the freedom of tailoring the dispersion property is limited by the available spectral transparency region of the core, cladding and plasmonic materials at THz frequencies.

In conclusion, we have presented a detailed

analysis of design considerations and propagation features of channel BSCW at THz frequencies employing standard polymers (PMMA and PCB) and a novel plasmonic material (PVDF). The anti-crossing behavior of phase-velocity dispersion curves for the supermodes leading to substantial change in slope has an interesting manifestation in the variation of group-index which results into appreciably large GVD and propagation length. The results obtained are strongly supported by the variation of modal field distribution. Also, we employ PVDF and other organic polymers such as PMMA and PCB to form BSCW-geometry which could be advantageous in fabricating THz devices using established mass production techniques such as microembossing and hence, makes the fabrication process highly suitable for industrial scale-up.

REFERENCES

- [1] A. V. Zayats, I. I. Smolyaninov and A. A. Maradudin, "Nano-optics of surface plasmon polaritons," *Phys. Rep.* **408**, 131-314 (2005).
- [2] M. A. Ordal, L. L. Long, R. J. Bell, S. E. Bell, R. Bell, R. W. Alexander, Jr., and C. A. Ward, "Optical properties of the metals Al, Co, Cu, Au, Fe, Pb, Ni, Pd, Pt, Ag, Ti, and W in the infrared and far infrared," *Appl. Opt.* **22**, 1099-1120 (1983).
- [3] T. I. Jeon and D. Grischkowsky, "THz Zenneck surface wave (THz surface plasmon) propagation on a metal sheet," *Appl. Phys. Lett.* **88**, 061113 (2006).
- [4] R. Mendis and D. Grischkowsky, "Undistorted guided wave propagation of sub-picosecond THz pulses," *Opt. Lett.* **26**, 846-848 (2001).
- [5] J. A. Harrington, R. George, P. Pedersen, and E. Mueller, "Hollow polycarbonate waveguides with inner Cu coatings for delivery of terahertz radiation," *Opt. Express* **12**, 5263-5268 (2004).
- [6] K. Wang and D. M. Mittleman, "Metal wires for terahertz wave guiding," *Nature* **432**, 376 (2004).
- [7] T. Hidaka, H. Minamide, H. Ito, J. Nishizawa, K. Tamura, and S. Ichikawa, "Ferroelectric PVDF cladding terahertz waveguide," *J. Lightwave Technol.* **23**, 2469-2473 (2005).
- [8] C. Rau, G. Torosyan, R. Beigang, and K. Nerkararyan, "Prism coupled terahertz waveguide sensor," *Appl. Phys. Lett.* **86**, 211119 (2005).
- [9] J. F. O'Hara, R. D. Averitt, and A. J. Taylor, "Prism coupling to terahertz surface plasmon polaritons," *Opt. Express* **13**, 6117-6126 (2005).
- [10] A. Hassani, A. Dupuis, M. Skorobogatiy, "Porous polymer fibers for low-loss Terahertz guiding," *Opt. Express* **16**, 6340-6351 (2008).
- [11] B. R. West and A. S. Helmy, "Properties of the quarter-wave Bragg reflection waveguide: theory," *J. Opt. Soc. Am. B* **23**, 1207-1220 (2006).
- [12] Y. S. Jin, G. J. Kim, and S. G. Jeon, "Terahertz dielectric properties of polymers," *J. Korean Phys. Soc.* **49**, 513-517 (2006).
- [13] A. Kumar and T. Srivastava, "Modeling of a nanoscale rectangular hole in a real metal," *Opt. Lett.* **33**, 333-335 (2008).
- [14] D. M. Shyroki, "Mode coupling and conversion at anticrossings treated via stationary perturbation technique," [arXiv:physics/0307128v2](https://arxiv.org/abs/physics/0307128v2) (2003).

H-structure left handed Material for violet light: Imaging and Nanoantenna application

Monika Rajput, Bhawana Dabas and R. K. Sinha

¹TIFAC-Centre of Relevance and Excellence in Fiber Optics and Optical Communication, Department of Applied Physics, Delhi Technological University (Formerly Delhi College of Engineering, University of Delhi), Bawana Road, Delhi-110042, India. Telephone No. - +91-11-27871017, Fax No.-+91-11-27871023(E-mail: monika_scholar@yahoo.com, dr_rk_sinha@yahoo.com)

Abstract: A new design of left-handed plasmonic lens with negligible aberration is presented to focusing of violet light using Dispersion engineering and numerical analysis. Phase index is matched with the incident medium leads to compensating the losses. Values of permeability (μ) and permittivity (ϵ) calculated by applying discrete dipole approximation (DDA). 3-D FDTD results demonstrate imaging application from the designed structure. The far-field resonance spectra also confirm the validity of the structure as a LHM and favoring its potential application as left handed plasmonic optical nano-antenna (LH-PONA).

1. INTRODUCTION

In 1968, Veselago predicted negative index materials (NIMs) with simultaneously negative permittivity ϵ and permeability μ forming a left handed triplet of wave vector \mathbf{k} , the electric field vector \mathbf{E} and the magnetic field vector \mathbf{H} for an isotropic medium, called left-handed materials (LHMs) or double-negative material (DNM) [1]. According to his analysis, the poynting vector of a plane wave is anti-parallel to its phase velocity in DNM. In LHMs light is allowed to bend in a direction opposite to that of ordinary material. This phenomenon is called negative refraction (NR). After more than 30 years, in 1999 Pendry demonstrated a design of NIM with composite structure consisting of rows of split ring resonators and wire strips [2-3]. Subsequently, there has been explosive interest found in the designing and developing different artificial engineered composite structures to achieve the LHM [4-33]. Several studies on linear properties with their application of LHM have been done [4-33]. For the first time, in this paper, we report a new design of LHM demonstrating imaging characteristics in the violet region as per our knowledge. We used Drude model to characterize the embedded metal in the designed structure. Negative real values of both permeability and permittivity with low imaginary values are obtained for the working wavelength centered at 410 nm by employing DDA method [18]. The 3-D finite difference time domain (FDTD) method is applied using commercially available package of RSoft Fullwave to evaluate near-field and far-field spectrum, which reveals its high directionality potential.

2. DESIGN AND ANALYSIS

We consider an artificial engineered structure, with metallic silver double nano-rods immersed in a host matrix with dielectric constant $\epsilon_h=13.25$, radius of nano-rods $r/a=0.20$. The dielectric response of Ag with the wavelength is observed from the Drude model [19].

2.1 Dispersion engineering: Negative index

By the exploring the dispersion properties, various interesting effects that do not exist in conventional materials e.g. Negative refraction can be explained. To study the refraction properties of light, band diagram and equi-frequency surface (EFS) diagram for the proposed structure are obtained by employing Plane Wave Expansion (PWE) method as shown in Fig. 1.

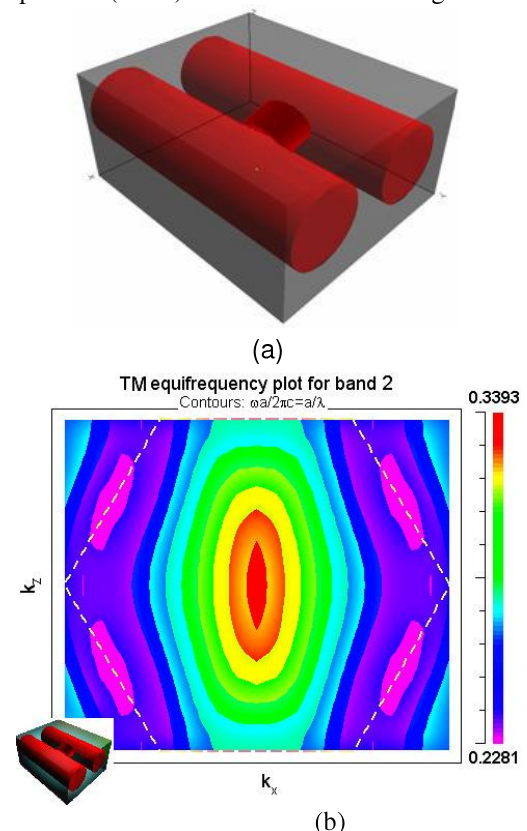


Fig. 1: (a) Schematic of the H-structure and (b) EFS for TM polarization of the 2nd band in the full Brillouin zone.

It is observed that negative refraction can be achieved in the proposed structure. The EFS that move outwards from the center with increasing frequency corresponds to RHM with $v_g \cdot k_f > 0$ and inwards moving EFS corresponds to LHM with $v_g \cdot k_f < 0$ [34,35]. Fig. 1 also shows the elliptical behavior of EFS with some structure modification (H-structure) in LH-PONA. It exhibits its uni-axial anisotropic behavior, which automatically cancelled the spherical aberration for the imaging effect.

2.2 Analysis for effective parameters (ϵ and μ)

In designed structure length of individual nanorods is $2l$, their diameter is $2r$, and the distance between the nanorods in the pair or lattice constant is a . The metallic-nanorods of dielectric constant ϵ_m are embedded into host with dielectric constant ϵ_d . The electric moment and magnetic moment of the individual two-nanorod pair can be deduced using discrete dipole approximation [18]. We get the electric moment and magnetic moment as in the following table for the wavelength 410 nm;

Table 1: Permittivity and Permeability values for fundamental (650 nm) and second harmonic wavelength (325 nm)

Wavelength(nm)	Permittivity (ϵ)	Permeability (μ)
410 nm	-1.81 - 0.015i	-1.1 + 0.00882i

Observed values of permittivity and permeability are negative for the working wavelength with ultralow imaginary values.

3. OPTICAL AND SPECTRAL CHARACTERIZATION

To get more insight about electromagnetic response of the designed LHM, the field map is shown in Fig. 2.

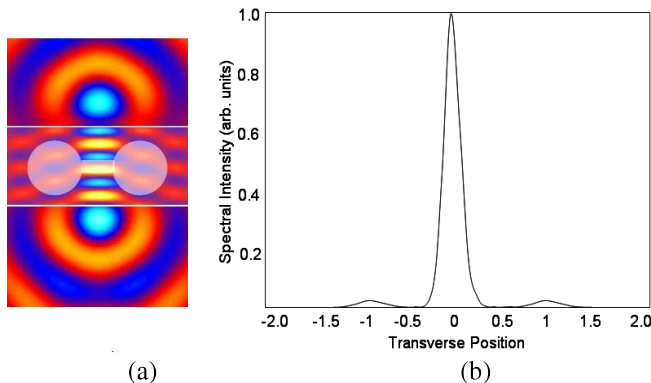


Fig. 2.: (a) Field map of imaging from the designed structure for violet light and (d) Normalized intensity distribution of the image plane along the transverse coordinate for designed lens.

Finally, we show FDTD results demonstrating imaging effect by the designed structure. We consider a TM polarized point source which is centered at one side ($z=-u$) of the lens, while the two

surfaces of the slab are $z=0$ and $z=L$. An image is formed on the other side of the lens as shown in Fig. 2 (a). The image inside the designed structure is not visible due to the small thickness of slab. We also measured the normalized intensity distribution of the image plane along the transverse coordinate for designed lens, shown by Fig. 2(b). The designed lens forms a focal point having a transverse spot size of less than 1 and can be attributed to the reduced spherical aberrations.

3.1 Far-field spectrum

Fig. 3 are the far-field spectrums obtained by employing 3-D FDTD method with incident continuous wave. Angular distribution of intensity at the output of the designed LHM is shown in Fig. 3. It is observed that the transmission peak is obtained in the deep negative side (same side to the normal of second interface), which confirms left-handed transmission in the proposed LHM. The obtained far-field intensity spectrum shows highly left-handed directional emission.

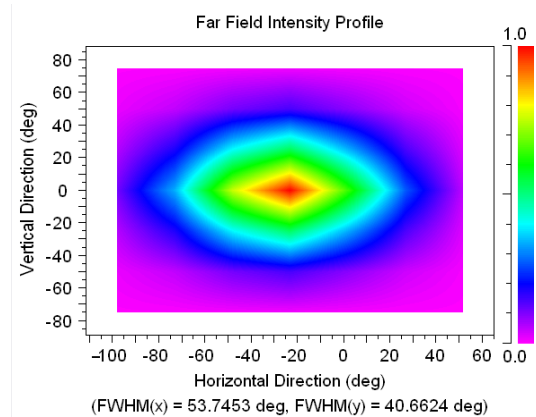


Fig. 3: far-field intensity pattern vs. horizontal direction (deg) of TM mode at $\lambda=410$ nm, which shows negative refraction for designed LHM.

4. CONCLUSION

We have proposed a new design of index matched left handed plasmonic lens for violet light. By exploring the dispersion properties and negative values permeability and permittivity, Near-field demonstration its imaging efficiency with transverse spot size of less than 1 and can be attributed to the reduced spherical aberrations. Far-field spectrum is also investigated to demonstrate highly left handed directional transmission efficiency of the designed LHM. The proposed LHM may show various functionalities such as, optical mirror, optical plasmonic nanoantenna, polarization sensitivity, light ruling and imaging application which can be further extended for broad spectrum covering entire visible range.

Acknowledgement

The authors gratefully acknowledge the initiatives and support towards establishment of "TIFAC Centre of Relevance and Excellence in Fiber Optics and Optical Communication at Delhi College of Engineering, Delhi" through "Mission REACH" program of Technology Vision-2020, Government of India.

References and links

1. V.G. Veselago, "The Electrodynamics of substances with simultaneously negative values of 'ε' and 'μ'," *Soviet Physics Uspekhi*, vol. 10, pp. 509-514, 1968.
2. J. B. Pendry, A. J. Holden, D. J. Robbins and W. J. Stewart, "Magnetism from conductors and enhanced nonlinear phenomena," *IEEE Trans. Microwave Theory Tech.*, vol. 47, pp. 2075-2084, 1999.
3. J. B. Pendry, A. J. Holden, W. J. Stewart, I. Youngs, "Extremely low frequency plasmons in metallic structures," *Phys. Rev. Lett.*, vol. 76, pp. 4773-4776, 1996.
4. R. A. Shelby, D. R. Smith and S. Schultz, "Experimental verification of negative index of refraction," *Science*, vol. 292, pp. 77-79, 2001.
5. C. G. Parazzoli, R. B. Greigor, K. Li, B. E. C. Koltenbah and M. Tanielian, "Experimental verification and simulation of negative index of refraction using Snell's law," *Phy. Rev. Lett.*, vol. 90, pp. 107401-107404, 2003.
6. A. Houck, J. B. Brock and I. L. Chuang, "Experimental observations of a left-handed material that obeys Snell's law," *Phy. Rev. Lett.*, vol. 90, pp. 137401-137404, 2003.
7. M. Notomi, "Theory of light propagation in strongly modulated photonic crystal: Refraction like behavior in the vicinity of photonic band gap," *Phy. Rev. B*, vol. 62, pp. 10696-10705, 2000.
8. C. Luo, S. G. Johnson and J. D. Joannopoulos, "All-angle negative refraction without negative effective index," *Phy. Rev. B*, vol. 65, pp. 201104-01-201104-04, 2002.
9. C. Luo, S. G. Johnson and J. D. Joannopoulos, "All-angle negative refraction in a three dimensionally periodic photonic crystal," *Appl. Phy. Lett.*, vol. 81, pp. 2352-2354, 2002.
10. T. Baba and T. Matsumoto, "Resolution of photonic crystal superprism," *Appl. Phy. Lett.*, vol. 81, pp. 2325-2327, 2002.
11. J.B. Pendry, "Negative Refraction," *Contemporary Physics*, vol. 45, pp. 191-202, 2004.
12. J. D. Joannopoulos, P. Villeneuve and S. Fan, "Photonic crystal: putting a new twist on light," *Nature (London)*, vol. 386, pp. 143-149, 1997.
13. A. Martinez, H. Miguez, J. Sanchez-Dehesa and J. Marti, "Analysis of wave propagation in a two-dimensional crystal with negative index of refraction: plane wave decomposition of the Bloch modes," *Opt. Exp.*, vol. 13, pp. 4160-4174, 2005.
14. E. Cubukcu, K. Aydin, E. Ozbay, S. Foteinopoulou and C. M. Soukoulis, "Electromagnetism waves: Negative refraction by Photonic crystal," *Nature (London)*, vol. 423, pp. 604-605, 2003.
15. E. Schonbrun, T. Yamashita, W. Park and C. J. Summers, "Negative-index imaging by an index-matched photonic crystal slab," *Phy. Rev. B*, vol. 73, pp. 195117-1195117-6, 2006.
16. P. V. Parimi, W. T. Lu, P. Vodo, J. Sokoloff, J. S. Derov and S. Sridhar, "Negative Refraction and Left-Handed Electromagnetism in Microwave Photonic Crystals," *Phys. Rev. Lett.*, vol. 92, pp. 127401-1-4, 2004.
17. P. Vodo, W. T. Lu, Y. Huang, and S. Sridhar, "Negative refraction and plano-concave lens focusing in one-dimensional photonic crystals," *Appl. Phy. Lett.*, vol. 89, pp. 084104-0841043, 2006.
18. V. A. Podolskiy, A. K. Sarychev, V. M. Shalaev, "Plasmon modes and negative refraction in metal nanowire composites," *Opt. Exp.*, vol. 11, pp. 735-745, 2003.
19. L. Wu, M. Mazilu, T. Karle, TF Krauss; "Superprism phenomena in planar photonic crystals"; *IEEE Journal of Quantum Electronics*, vol. 38, pp. 915-918, 2002.
20. J. Zhou, T. Koschny, M. Kafesaki, E. N. Economou, J. B. Pendry, and C. M. Soukoulis, "Saturation of magnetic response of split-ring resonators at optical frequencies," *Phys. Rev. Lett.*, vol. 95, p. 223902, 2005.
21. K. Aydin, Z. Li, L. Sahin, and E. Ozbay, "Negative phase advance in polarization independent, multi-layer negative-index Metamaterials," *Opt. Exp.*, vol. 16, pp. 8835-8844, 2008.
22. J. Yao, Z. Liu, Y. Wang, C. Sun, G. Bartal, A. M. Stacy and X. Zhang, "Optical negative refraction in bulk materials of nanowires," *Science*, vol. 321, p. 930, 2008.
23. C. Yan, Q. Wang, S. Zhuo and Y. Cui, "High transmission negative refraction of discrete rod resonators confined in a metal waveguide at visible wavelengths," *Opt. Exp.*, vol. 16, pp. 13818-13823, 2008.
24. S. A. Ramakrishna and O. J. F. Martin, "Resolving the wave vector in negative refractive index media," *Opt. Lett.*, vol. 30, pp. 2626-2628, 2005.
25. V.M. Shalaev, W.S. Cai, U.K. Chettiar, H.K. Yuan, A.K. Sarychev, V.P. Drachev and A.V. Kildishev, "Negative index of refraction in optical metamaterials," *Opt. Lett.*, vol. 30, pp. 3356-3358, 2005.
26. S. Zhang, W.J. Fan, P.C. Panoiu, K.J. Malloy and R.M. Osgood, "Demonstration of near infrared negative-index metamaterials," *Phy. Rev. Lett.*, vol. 95, pp. 137404, 2005.
27. Y. Gao, J. P. Huang, Y. M. Liu, L. Gao, K. W. Yu, and X. Zhang, "Optical Negative Refraction in Ferrofluids with Magnetocontrollability", *Phys. Rev. Lett.* 104, 034501, 2010.
28. G. Dolling, M. Wegener, C.M. Soukoulis and S. Linden, "Negative-index metamaterial at 780 nm wavelength," *Opt. Lett.*, vol. 32, pp. 53, 2007.
29. H. Chen, L. Ran, J. Huangfu, X. Zhang, K. Chen, T.M. Grzegorzczuk and J.A. Kong, "Left-handed materials composed of only S-shaped resonators," *Phys. Rev. E*, vol. 70, pp. 057605, 2004.
30. U. Algreto-Badillo and P. Halevi, "Negative refraction and focusing in magnetically coupled L-C loaded transmission lines," *J. Appl. Phys.*, vol. 102, pp. 086104, 2007.
31. D. Kwon, D. H. Werner, A. V. Kildishev and V.M. Shalaev, "Near-infrared metamaterials with dual band negative index characteristics," *Opt. Exp.*, vol. 15, pp. 1647-1652, 2007.
32. O. Paul, C. Imhof, B. Reinhard, R. Zengerle and R. Beigang, "Negative index bulk metamaterials at terahertz frequencies," *Opt. Exp.*, vol. 16, pp. 6736-6744, 2008.
33. S. A. Ramakrishna, and J. B. Pendry, "Removal of absorption and increase in resolution in a near-field lens via optical gain," *Phys. Rev. B*, vol. 67, p. 201101, 2003.
34. P. V. Parimi, W. T. Lu, P. Vodo, J. Sokoloff, J. S. Derov and S. Sridhar, "Negative Refraction and Left-Handed Electromagnetism in Microwave Photonic Crystals," *Phys. Rev. Lett.*, 92, 127401-1-4 (2004).
35. P. Vodo, W. T. Lu, Y. Huang, and S. Sridhar, "Negative refraction and plano-concave lens focusing in one-dimensional photonic crystals," *Appl. Phy. Lett.*, 89, 084104-0841043 (2006).

UNIFICATION OF COHERENCE AND POLARIZATION OF LIGHT BEAMS IN HOLOGRAPHY AND SPECKLE EXPERIMENTS

C S Narayanamurthy

Department of Physics, Indian Institute of Space Science and Technology (IIST),
Valiamala (PO), Thiruvananthapuram – 695 547, India

1. INTRODUCTION

Recently, Wolf¹ et.al predicted that the coherence and polarization of light beams are not independent of each other but they are manifestations of the same physical phenomenon due to correlations between fluctuations in light beams. Coherence of light beams arise due to correlation of light fluctuations at two or more points in space where as polarization is manifestation of correlations between fluctuating components of electric field at a single point. This unification of coherence and polarization property of light can be observed in holography and speckle experiments.

2. THEORETICAL EXPLANATION

If we consider the total electric field $\{E(\mathbf{r}, \omega)\}$ represents the statistical ensemble of electric field vector at point $P(\mathbf{r})$ on the detector (CCD/photographic plate) due to contributions from object points at two different times(in case of doubly exposed holography) or two different positions of a diffuse object (in case of speckles) then,

$$E(r, \omega) = k_1 E(\rho_1, \omega) e^{ikR_1} + k_2 E(\rho_2, \omega) e^{ikR_2} \quad (1)$$

Where, R_1 and R_2 are the distances propagated by object and reference beam respectively and from two different points Q_1 and Q_2 from diffuse object in case of speckles. Introducing the spectral density $S(\mathbf{r}, \omega)$ at the detector point $P(\mathbf{r})$,

$$S(r, \omega) = |k_1|^2 S(\rho_1, \omega) + |k_2|^2 S(\rho_2, \omega) + k_1^* k_2 TrW(\rho_1, \rho_2, \omega) e^{ik(R_1 - R_2)} + k_1 k_2^* TrW(\rho_2, \rho_1, \omega) e^{ik(R_2 - R_1)} \quad (2)$$

In Eqn.2, the Tr denotes trace of the cross spectral density matrix $W(\rho, \rho, \omega)$ which is,

$$W(\rho_1, \rho_2, \omega) = \begin{bmatrix} \langle E_x^*(r_1, \omega) E_x(r_2, \omega) \rangle \langle E_x^*(r_1, \omega) E_y(r_2, \omega) \rangle \\ \langle E_y^*(r_1, \omega) E_x(r_2, \omega) \rangle \langle E_y^*(r_1, \omega) E_y(r_2, \omega) \rangle \end{bmatrix} \quad (3)$$

and for coincident points like $(\mathbf{r}_1 = \mathbf{r}_2 = \mathbf{r})$,

$$TrW(r, r, \omega) = \langle E_x^*(r_1, \omega) E_x(r_2, \omega) \rangle + \langle E_y^*(r_1, \omega) E_y(r_2, \omega) \rangle \quad (4)$$

Further, the spectral density term $S(\mathbf{r}, \omega)$ can be re written using complex degree of coherence function μ_{12} as,

$$S(r, \omega) = 2S^{(1)}(r, \omega) \{1 + \text{Re}[\mu(\rho_1, \rho_2, \omega) e^{i\delta}]\} \quad (5)$$

With,

$$\mu(\rho_1, \rho_2, \omega) = \frac{TrW(\rho_1, \rho_2, \omega)}{\sqrt{TrW(\rho_1, \rho_2, \omega)} \sqrt{TrW(\rho_2, \rho_1, \omega)}} \quad (6)$$

The Eqn.5 represents both the coherence and polarization matrix of interfering electromagnetic

beams either from two different diffuse points in case of speckles or from object and reference beams in case of holography.

3. EXPERIMENTAL DISCUSSIONS

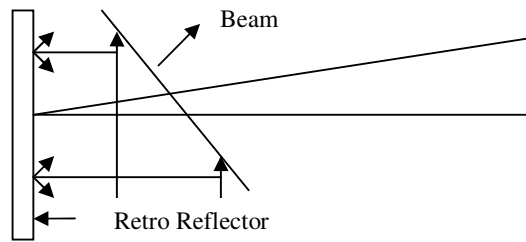


Fig. 1

Fig.1 shows a typical geometry for speckle photography using white light speckle generated using back scattering of a white light beam using retro-reflecting paint². The light beam from source is made to incident normally and the diffuse object is coated with a retro-reflector where the enhanced backscattering of white light creates speckles. The coherence behaviour of these white light speckled beams are similar to partially coherent light and if we assume two different backscattered beam arrive at the detector the spectral density term $S(\mathbf{r}, \omega)$ behaves similar to partially coherent beam resulting in enhanced coherent behavior and a correlation between electric field terms at a same point. Similarly, a doubly exposed hologram³ at two different times has same electric field fluctuation and correlations from fluctuating optical beams at two different times.

4. CONCLUSIONS

It is shown that the unified theory of coherence and polarization proposed by Wolf¹ et.al can be observed in a doubly exposed holographic experiment as well as in a speckle photography experiment using backscattered white light speckles from retro-reflected paint.

REFERENCES

1. E. Wolf, Phys. Lett, A 312 (2003)
2. N Krishna Mohan et.al, Optics Communications (Elsevier), Vol.76, No.3, 222-226(1990)
3. C M West, Holographic Interferometry, John wiley (New York), 1978

Design & Fabrication of IR Phase Grating in Lithium Niobate Substrate

U. S. Tripathi*, Ajay Mishra, B. P. Dimri, Thigulla Srikanth[#] & A. N. Kaul

Instrument Research & Development Establishment, Dehradun

[#] National Institute of Technology, Warangal

*E-mail: ustripathi@gmail.com

Abstract: Fabrication of phase gratings has been achieved in LiNbO₃ substrate for Infra Red (IR) and visible region. These gratings have phase variation inside the substrate which is different from conventional phase gratings on glass or quartz substrates which has groove on the surface. This work has been done by selective refractive index change of the substrate by using proton exchange (PE) technology in X cut LiNbO₃ substrate. Since it is PE technology based phase grating therefore light of only one state of polarization get diffracted.

1 INTRODUCTION

Diffraction gratings are optical component with a regular pattern, which splits and diffracts light into several beams travelling in different directions. The directions of these beams depend on the spacing of the grating and the wavelength of the light so that the grating acts as the dispersive element. These gratings can modulate amplitude as well as phase of the incident light. Gratings with phase modulation rather than amplitude modulation are called phase gratings. Phase gratings are used as dispersers in a variety of spectroscopic imaging instruments. Phase gratings can be used in multiple image formation for integrated circuits and pattern reorganization. Other applications lies in fiber optical communication, optical disc systems and coherent addition of laser beams. Diffraction grating fabrication falls in the domain of integrated optics which is the optical counterpart of integrated electronics and deals with generation, modulation, switching, multiplexing, filtering etc. of optical signals by using miniaturized optical components on an optical chip.

Lithium Niobate (LiNbO₃) is a very important dielectric material because of its wide transparency range i.e 0.4 to 4.5 μm. One of the very attractive and convenient method of fabricating phase modulation in Lithium Niobate is proton exchange (PE) technique. This technique involves the replacement of Li⁺ ion by H⁺ ion and it was first established by Jackel et al in 1982. In this process a substrate is immersed in a melt of an organic acid at a suitable temperature and duration. A variety of organic and inorganic acids have been used, and among these acids benzoic acid and phosphoric acid are most popular proton sources for exchange process. But they are dangerous to use because of their toxic and corrosive nature. In the fabrication of phase grating we have chosen stearic acid (CH₃(CH₂)₁₆COOH) as a proton source because it is nontoxic, noncorrosive and has a high boiling point with respect to above acid. In this technique only extraordinary refractive

index increases which is of the order of ~0.12 at 633nm wavelength. Therefore it will work for only one polarization state of light. Due to the extremely large index change, this technique gives phase gratings with high diffraction efficiency.

2 DESIGN AND SIMULATION

A phase grating was designed and simulated for the wavelength 633 nm & 1550 nm. For this we can assume an infinitely extended diffraction grating as shown in Fig. 1, and use the Fourier expansion series to obtain the value of the Fourier coefficients G_m corresponding to the amplitude of the m^{th} diffraction order. Amplitude can be calculated as

$$(G_m) = (1/p) \int_0^p g(x) \exp\left(\frac{im2\pi x}{p}\right) dx$$

Where

p = period of grating

g(x) = transmittance function which is defined as

$$g(x) = \exp(iA) \quad \text{for } 0 < x < a * p \\ = 1 \quad \text{for } a * p < x < p$$

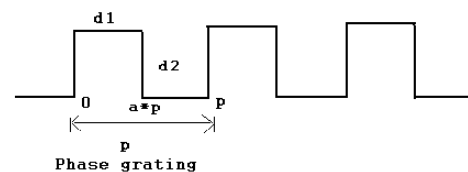


Fig. 1: Schematic of phase grating

$$d_1 = a * p$$

$$d_2 = (1-a) * p \text{ and } d_1 + d_2 = p, a = \text{Duty cycle}$$

$$G_m = \left(\frac{1}{p}\right) \int_0^{a*p} \exp(iA) * \exp\left(\frac{im2\pi x}{p}\right) dx + \left(\frac{1}{p}\right) \int_{a*p}^p (1) * \exp\left(\frac{im2\pi x}{p}\right) dx$$

$$G_m = \left(\frac{i}{2m\pi} \right) (1 - \exp(im2\pi\alpha)) (\exp(iA) - 1)$$

$$I_m = G_m * \text{conj}(G_m)$$

$$I_m = \left[\left(\frac{2}{m\pi} \right) \sin(\pi m \alpha) \sin \left(\frac{A}{2} \right) \right]^2$$

Above expression is for $m = \pm 1, \pm 2, \pm 3, \pm 4$

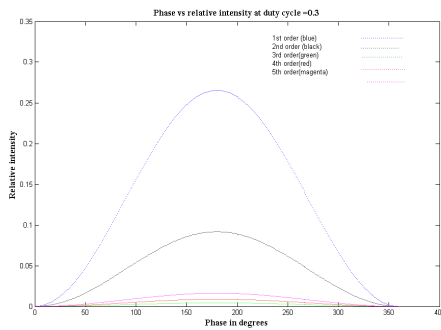


Fig. 2: IntensityVs different phase depth for duty cycle 0.3

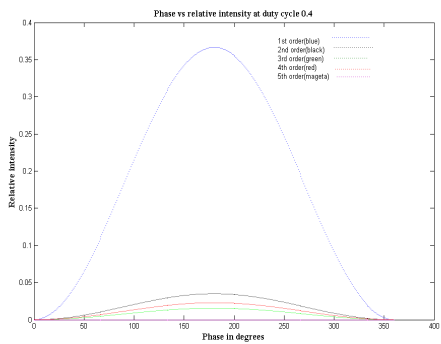


Fig. 3: IntensityVs different phase depth for duty cycle 0.4

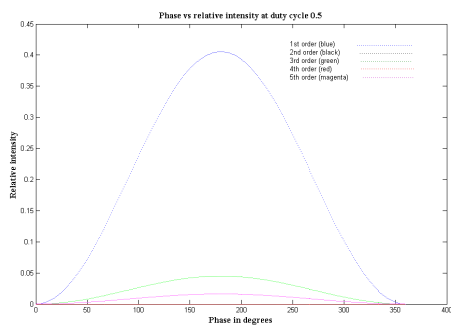


Fig. 4: IntensityVs different phase depth for duty cycle 0.5

The phase grating was simulated for diffraction efficiency of different orders for different duty cycles as well as for different phase changes. Fig. 2, 3 & 4 shows the diffraction efficiency for different phase variation in different order for duty cycle 0.3, 0.4 and 0.5 respectively.

It can be observed through phase grating simulation results that with the increase of phase change, diffraction efficiency in all orders was increasing. The efficiency increases up to phase change of π after that it keep on decreasing on further increment of phase change up to 2π . It can also be concluded through simulated result that increment in duty cycle while keeping phase change constant results in the increment of diffraction efficiency in odd orders i.e. 1st, 3rd and 5th order and decrement of diffraction efficiency in even order i.e. 2nd, 4th and 6th order.

3 FABRICATION OF PHASE GRATING

Phase grating were fabricated by proton exchange technology (mentioned in previous section) for 633 nm wavelength i.e. visible region and for 1550nm wavelength i.e. IR region. X-cut LiNbO₃ wafer from Crystal Technology, USA has been taken as substrate for the fabrication of phase grating. X cut LiNbO₃ substrate was chosen because in PE process refractive index change only for one polarization state. After proper cleaning of this substrate a thin layer of titanium was deposited by E-beam coating system. This was followed by coating of photo resist layer over the Ti coated substrate by spin coating. Subsequently, grating pattern was transferred with the help of grating structured mask and mask aligner. After developing the wafer wet etching of titanium was done to get the desired window as amplitude grating on the wafer. Later the wafer was inspected and the duty cycle of the grating structure was measured.

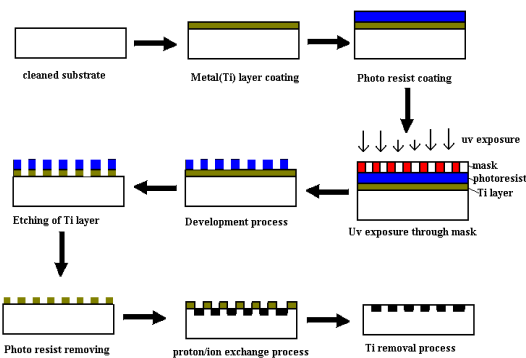


Fig. 5: Steps involved in phase grating fabrication

Then PE was performed in Stearic acid at the

required temperature and duration. In this process, refractive index change occurred in substrate only in the region where titanium layer was absent. After proton exchange the remaining titanium layer was etched out in a suitable etchant to remove titanium layer completely. Schematic of complete fabrication process is shown in Fig.5. Phase grating structure has been obtained after final titanium etching. The fabricated phase grating has been shown in Fig. 6

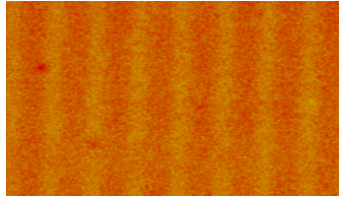


Fig. 6: Fabricated phase grating

For phase depth information, a planar waveguide was also fabricated on the same substrate. It was characterized by prism coupling technique at wavelength 633nm and 1550 nm.

4 CHARACTERISATION

After fabricating the desired phase grating it was characterized in terms of diffracted intensities in different orders with respect to the incident power. For the characterization of phase grating a polarized laser source was incident on the grating surface and light was diffracted in different order. The experimental set-up used for characterization of fabricated phase grating has been shown in Fig. 7.

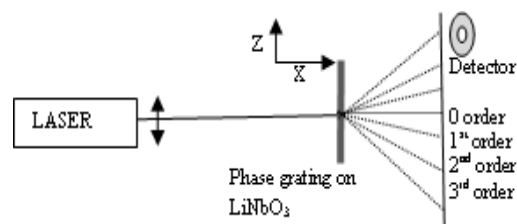


Figure 7: Experimental arrangement for characterisation of phase grating

The observed orders of the phase gratings at wavelengths 633 nm and 1550 nm have been shown in Fig. 8 & Fig. 9 respectively. When the laser (polarization of the light) was rotated by 90 degree the diffracted light was almost negligible as shown in Fig. 10. This confirms that the phase grating diffract the light for only one polarization state of light i.e. vertical polarization as per schematic shown in Fig 7.

The intensities were measured in different orders by using a suitable detector.



Fig. 8: Different order of phase grating at wavelength 633 nm (vertical polarisation)

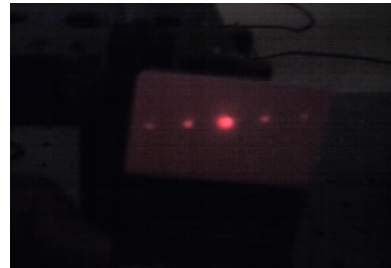


Fig. 9: Order of phase grating at wavelength 1550nm (vertical polarisation)



Fig. 10: Order of phase grating at wavelength 1550nm (horizontal polarisation)

The diffracted intensities at wavelengths 633nm & 1550 nm were compared with theoretical values as shown in the Fig. 11 & 12 respectively. The fabricated phase grating (duty cycle 0.4) is having phase depth 0.8π for visible region and 0.92π for IR region. It is obvious from the Fig. 11 & 12 that the experimentally observed relative intensities in different orders is in good agreement with the theoretical results except for zero order. The intensity at zero order is higher than the theoretical value, which may be because of the improper vertical polarization orientation of the input laser light.

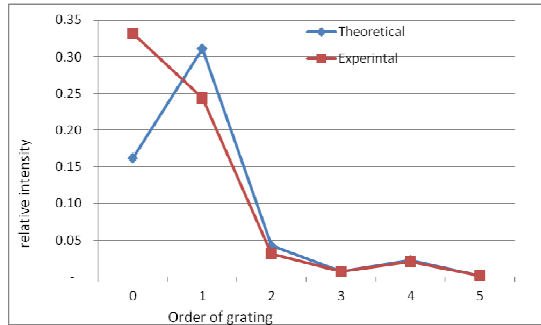


Fig. 11: Diffracted intensities in different order for wavelength 633 nm

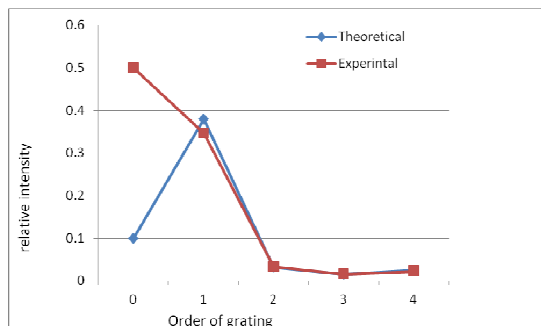


Fig. 12: Diffracted intensities in different order for wavelength 633 nm

5 CONCLUSIONS

Phase grating has been fabricated for a 0.4 duty cycle at wavelengths 633 nm & 1550 nm with a phase depth 0.8π & 0.92π respectively. It can also be concluded from above experimental results that it matches the theoretical values.

ACKNOWLEDGEMENT

The authors wish to acknowledge Director, IRDE for giving permission to publish this paper. Thanks are also due to Deepak Gond for his help during the fabrication process.

REFERENCES

- [1] M del Mar Sánchez-López, Ignacio Moreno and Antonio Martínez-García “Teaching diffraction gratings by means of a phasor analysis”
- [2] Diffractive Optics, Design, Fabrication, and Test by Donald C. O’Shea Thomas J. Suleski Alan D. Kathman Dennis W. Prather, SPIE Tutorial Texts in Optical Engineering.

- [3] J. L. Jackel, C. E. Rice and J. J. Veselka “Proton exchange for high index waveguides in LiNbO_3 ” Appl Phys. Lett., vol. **41**, pp. 607-608, 1982.
- [4] J. M. White and P. F. Heidrich, January 1976, Vol. 15, No. 1, *Applied Optics*

DIGITAL WATERMARKING TO PREVENT DIGITAL HOLOGRAM PIRACY

Naveen K. Nishchal¹, Tomi Pitkäaho², and Thomas J. Naughton³

¹Department of Physics, Indian Institute of Technology Patna, Patna-800 013, India

²R F Media Laboratory, Oulu Southern Institute, Oulu University, Ylivieska, Finland

³Department of Computer Science, National University of Ireland Maynooth, Ireland

E-mail: nkn@iitp.ac.in, tomi.pitkaaho@oulu.fi, tomn@cs.nuim.ie

Abstract: We present a method for preventing the digital hologram piracy by introducing a watermark in a plane at some known distance from the object so that even if a new hologram is generated from the original hologram the watermark can always be traced by propagating the new hologram back to the object and then onto the watermark plane. The watermark is retrieved successfully using the correct encryption parameters. We consider both numerical (full complex field) and optoelectronic (phase-only) reconstruction methods. We obtain the watermark from different windows of the hologram corresponding to different reconstruction perspectives. Also the effect of phase quantization has been studied.

1. INTRODUCTION

Digital holography (DH) can be described as an electro-optical system encompassing the abilities to record an optical wavefield, a hologram, on a charge-coupled device camera, store the captured hologram in a computer memory, and reconstruct the hologram numerically at any point of time [1-3]. In this case, the reconstruction can be performed numerically by simulating the propagation of the wavefield back to the plane of the object. With advances in computer performance and electronic image acquisition devices, DH is becoming more attractive for many applications [1-7]. The technique also makes it possible to record video holograms of a three-dimensional (3D) object. Storage of a hologram in a computer enables us to reduce the noise through image processing techniques and numerically reconstruct the object with arbitrary views. It is possible to generate another hologram with one optically recorded or computer generated holograms by propagating the hologram in free-space at certain distances. Thus, the original holographer may lose his ownership if somebody generates a new hologram and claims his/her right. This allows unwanted use of the holographic information, which we may call *Digital Hologram Piracy*. Piracy of information without appropriate permission from rightful owners deprives the original creators of their rights. It is therefore desirable in some quarters to protect the individual holographer's ownership. A possible solution to protect from *digital hologram piracy* could be embedding a watermark into the hologram. Watermarking of two-dimensional or three-dimensional data has been studied to provide protection for digital image, audio, and video [3-16].

Watermarking is a method for protecting data from unauthorized distribution. A watermark is a visible or invisible identification code that is permanently embedded in the data and remains present within the data after any decryption process. A good watermarking scheme should meet a number of conditions [3-5]. For example, the host data quality

should not be affected in a significant way by the hidden data. Another important issue with watermarking is the level of security. In other words, how hard is to decode the hidden information by an unauthorized user even if the watermarking technique is known [3-16].

A transformation domain is often needed for robustly embedding an invisible watermark, for example the frequency domain. Therefore, the signal energy present in any signal frequency becomes undetectable. Embedding watermark sequences into fractional Fourier domain has an important advantage over embedding in spatial domain or in frequency domain. Watermark in fractional order domain provides extra security against attackers since fractional orders of the transform provides extra degree of freedom [1,8,10,12,13,15]. Properties and applications of the ordinary Fourier transform are special cases of those of the fractional Fourier transform (FRT), which is a generalization of the ordinary Fourier transform with an order parameter α [13]. The generalization of ordinary Fourier transform to the FRT comes at no additional cost in digital computation or optical implementation.

In this paper, we present a method of watermarking a real phase-shift Fresnel digital hologram of a real world 3D scene using the FRT. The watermark is encrypted using the double random phase encoding technique [1-3]. The encrypted watermark is embedded into the digital hologram at a specified location relative to the object and can always be recovered by first propagating the newly generated hologram back to the object location. We consider both numerical (full complex field) and optoelectronic (phase-only) reconstruction methods. We also obtain the watermark from different reconstruction perspectives. To increase the storage and transmission efficiency, the quantization has been applied to the watermarked digital hologram and the watermark is recovered successfully and also it does not affect the numerical reconstruction.

2. PRINCIPLE

We followed the conventional double random phase encoding (DRPE) technique for encryption of the watermark. The random phase masks (RPMs) were placed in the fractional Fourier plane instead of the conventional Fourier plane. Let function $f(x,y)$ represent the watermark to be encrypted by double random fractional Fourier domain encoding scheme. The watermark is multiplied with a random phase mask (RPM1), defined as $\exp[2\pi jr(\zeta,\eta)]$, and its FRT of order α is obtained. A two-dimensional FRT of function $\{f(x,y) \times \exp[2\pi jr(\zeta,\eta)]\}$ of order $(\alpha_1 = p_1\pi/2)$ is given by $g(\zeta,\eta)$ as [1]

$$g(\zeta,\eta) = K \iint f(x,y) \times \exp[2\pi jr(x,y)] \times \exp\left(j\pi \frac{x^2 + y^2 + \zeta^2 + \eta^2}{\tan\alpha_1} - 2j\pi \frac{xy\zeta\eta}{\sin\alpha_1}\right) dx dy \quad (1)$$

Here (x,y) and (ζ,η) represent the space and fractional domain coordinates, respectively. The parameter K is a complex constant. The function $g(\zeta,\eta)$ is multiplied by another mask, RPM2, defined as $\exp[2\pi jr(\rho,\sigma)]$, and an FRT of order $(\alpha_2 = p_2\pi/2)$ is obtained, which gives the encrypted image as

$$e(\rho,\sigma) = K \iint \{g(\zeta,\eta) \times \exp[2\pi jr(\zeta,\eta)]\} \times \exp\left(j\pi \frac{\zeta^2 + \eta^2 + \rho^2 + \sigma^2}{\tan\alpha_2} - 2j\pi \frac{\zeta\eta\rho\sigma}{\sin\alpha_2}\right) d\zeta d\eta \quad (2)$$

The encrypted image of watermark, $e(\rho,\sigma)$, is combined with the Fresnel digital hologram, $h(\rho,\sigma)$. The watermarked image, $w(\rho,\sigma)$, is then given by

$$w(\rho,\sigma) = h(\rho,\sigma) + ae(\rho,\sigma) \quad (3)$$

where a is an arbitrary constant, called the weighting factor of the watermark. This parameter ensures the invisibility of watermarked image and the robustness of the watermarked image against distortions. The value for a is selected by trial and error. It has been shown that the optimal weighting factor produces the least errors in the reconstructed 3D host object and the decoded watermark even in the presence of an occlusion attack [6].

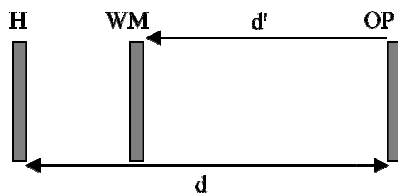


Fig. 1 Schematic to show the different planes. H: hologram plane, WM: watermarking plane, OP: object plane, d : separation between the hologram plane and object, d' : separation between the object and the watermarking plane.

Figure 1 shows the schematic of the different planes. For better security purposes we encoded the watermark in a plane that was a known distance d from the object. One may encode the watermark in the hologram plane but in that case if a new hologram is generated then it is not possible to recover the watermark without an exhaustive search. In this proposal, the search space is reduced to the uncertainty of determining the front of the 3D object in the reconstruction volume.

3. EXPERIMENTAL RESULTS

The results of computer experiment carried out using the MATLAB platform. We used a phase-shift digital hologram of a real world 3D scene recorded with parameters $\lambda = 632.8$ nm, recording distance, $d = 179$ mm, and pixel size = $7.4 \mu\text{m} \times 7.4 \mu\text{m}$. The object, a chip, was used for the study. The recorded Fresnel digital hologram is of size 2048×2048 pixels, as shown in Fig. 2(a).

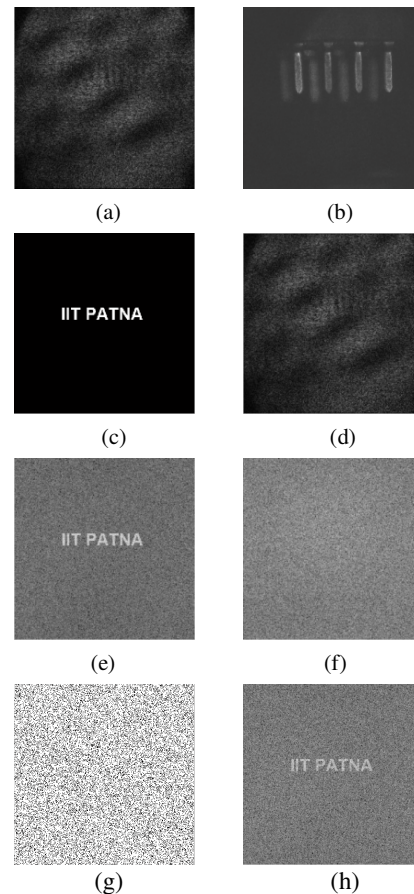


Fig. 2. (a) phase-shift Fresnel digital hologram, (b) reconstructed object, (c) watermark, (d) watermarked digital hologram, (e) recovered watermark, (f) recovered watermark with one of the wrong fractional orders, (g) phase-only of the hologram, and (h) recovered watermark with phase-only hologram.

The numerical reconstruction of the digital hologram is shown in Fig. 2(b). The watermark, as shown in Fig. 2(c) is encrypted with two random phase masks placed at input and the fractional domains, respectively. The fractional orders used for encryption were $p_1 = 0.555$ and $p_2 = 0.355$. The encrypted image of the watermark was embedded ($a = 0.25$) to the regenerated hologram at $d' = 20$ mm distance from the original hologram plane and has been shown in Fig. 2(d). The recovered watermark after using the correct encryption keys is shown in Fig. 2(e). Fig. 2(f) shows the intensity image when we tried to recover the watermark with one wrong fractional order $p_1 = 0.50$ and using other fractional order and phase masks correctly. It is not yet possible to reliably and conveniently modulate a spatial-light modulator with arbitrary complex-values. Phase-modulating devices are often used to optoelectronically reconstruct appropriately modified complex-valued holograms. We consider only the phase of the watermarked complex-valued hologram by setting each amplitude to unity as shown in Fig. 2(g) and successfully recover the watermark from the degraded hologram as shown in Fig. 2(h).

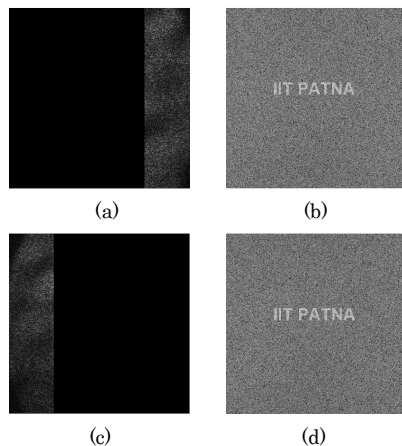


Fig. 3. (a) cropped 25% from right side of the watermarked hologram, (b) recovered watermark, (c) cropped 25% from left side of the watermarked hologram, and (d) recovered hologram.

We also obtained the watermark from different windows of the hologram corresponding to different reconstruction perspectives. The results have been shown in Figs. 3(a-d). We cropped only 25% of the watermarked hologram from the right side, as shown in Fig. 3(a) and recovered the watermark, as shown in Fig. 3(b). The cropping from left side and correspondingly recovered watermark have been shown in Figs. 3(c) and (d), respectively. To increase the storage and transmission efficiency, quantization has been applied directly to the complex-valued holographic pixels [17]. The effect of phase-quantization was also studied. Fig. 4(a) shows the

phase of the phase-only hologram quantized to 1 bit and (b) shows the corresponding recovered watermark. It is to be noted that there is no effect on the reconstruction of the digital hologram.

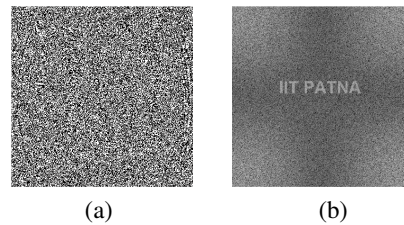


Fig. 4. (a) phase of the phase-only watermarked hologram quantized to 1 bit and (b) recovered watermark.

CONCLUSION

A method to protect from *hologram piracy* has been presented that employs watermarking a digital hologram at a specific plane from the sensed object. We demonstrate the technique with a phase-shift Fresnel digital hologram of a real world 3D scene and the FRT. The watermark can always be recovered by propagating the watermarked hologram back to the object and then to a well-known plane before applying the correct decryption keys. We also recover the watermark from a phase-encoded version of the digital hologram. We obtain the watermark from different windows of the hologram corresponding to different reconstruction perspectives of the 3D scene. The effect of phase quantization has also been studied.

ACKNOWLEDGEMENT

The authors thank Emmanouil Darakis for recording the digital hologram. One of the authors (NKN) acknowledges funding from the Council of Scientific and Industrial Research (CSIR), Government of India, under Grant No. 03/(1183)/10/EMR-II.

REFERENCES

- [1] N. K. Nishchal, J. Joseph, and K. Singh, "Securing information using fractional Fourier transform in digital holography," *Opt. Commun.* **235**, 253 (2004).
- [2] A. Nelleri, J. Joseph, and K. Singh, "Digital Fresnel field encryption for three-dimensional information security," *Opt. Eng.* **46**, 045801 (2007).
- [3] B. Javidi, Ed., *Optical Imaging Sensors and Systems for Homeland Security Applications*, Springer: New York, 2006.
- [4] S. Kishk and B. Javidi, "Watermarking of three-dimensional objects by digital holography," *Opt. Lett.* **28**, 167 (2002).
- [5] S. Kishk and B. Javidi, "3D watermarking by a 3D hidden object," *Opt. Express* **11**, 874 (2003).
- [6] H. Kim and Y. H. Lee, "Optimal watermarking of digital hologram of 3-D object," *Opt. Express* **13**, 2881 (2005).

- [7] X.-F. Meng, L.-Z. Cai, X.-L. Yang, X.-F. Xu, G.-Y. Dong, X.-X. Shen, H. Zhang, and Y.-R. Wang, "Digital color image watermarking based on phase-shifting interferometry and neighboring pixel value subtraction algorithm in the discrete-cosine-transform domain," *Appl. Opt.* **46**, 4694 (2007).
- [8] N. K. Nishchal and T. J. Naughton, "Three-dimensional image watermarking using fractional Fourier transform," *Proc. of Int'l Confer. on Optics and Photonics*, CSIO Chandigarh, Oct. 30-Nov. 1, 2009.
- [9] L. Sun and S. Zhuang, "Watermarking by encrypted Fourier holography," *Opt. Eng.* **46**, 085801 (2007).
- [10] I. Djurovic, S. Stankovic, and I. Pitas, "Digital watermarking in the fractional Fourier transformation domain," *J. Network Computer Appl.* **24**, 167 (2001).
- [11] K. Deng, G. Yang, and C. Zhang, "Burch computer-generated hologram watermarking resilient to strong cropping attack," *Biomed. Opt., OSA Tech. Digest, JMA* **30** (2010).
- [12] N. K. Nishchal, "Optical image watermarking using fractional Fourier transform," *J. Opt.* **38**, 22 (2009).
- [13] J.-T. Wang, P.-C. Wang, and S.-S. Yu, "Reversible fragile watermarking scheme for three-dimensional models," *Opt. Eng.* **48**, 097004 (2009).
- [14] N. K. Nishchal, "Hierarchical encrypted image watermarking using fractional Fourier domain random phase encoding," *Opt. Eng.* **50**, 097003 (2011).
- [15] Q. Guo, Z. Liu, and S. Liucora, "Image watermarking algorithm based on fractional Fourier transform and random phase encoding," *Opt. Commun.* **284**, 3918 (2011).
- [16] A. H. Taherinia and M. Jamzad, "Blind dewatermarking method based on wavelet transform," *Opt. Eng.* **50**, 057006 (2011).
- [17] A. E. Shortt, T. J. Naughton, and B. Javidi, "A companding approach for nonuniform quantization of digital holograms of three-dimensional objects," *Opt. Express* **14**, 5129 (2006).

TAILORED 3D TWISTER VORTEX SUPERLATTICES: TUNING THE THREADS OF ABSOLUTE DARKNESS

Jolly Xavier, Sunil Vyas, Paramasivam Senthilkumaran, and Joby Joseph
Department of Physics, Indian Institute of Technology Delhi, New Delhi, 110016, India
E-mail: jolly.xavierp@physics.iitd.ac.in

Abstract: We computationally simulate as well as experimentally demonstrate tailored vortex embedded tunable complex 3D twister superlattices by the interference of phase engineered non-coplanar plane waves. The generated 3D intertwined helices and vortex spirals are analyzed using various tools. Their possible real-time tunable applications in advanced holographic micro-particle manipulation are also briefly discussed.

1. INTRODUCTION

The tailored superposition of light fields as artificial photonic lattices with periodic or transversely-quasicrystallographic spatial symmetry breakings has channeled the core concepts of optics to concrete applications [1-3]. In such superpositions of scalar optical wave fields, there exists a ubiquitous presence of optical vortices, the singular dislocation points or lines of amplitude nulls: the threads of absolute darkness [1,2,4].

Though diverse geometries of 2D photonic vortex lattices of varying topological charges have been explored, [2, 4] yet a controlled formation of large area complex spiraling clusters of optical vortices and rings of darkness embedded in structured 3D light fields would give insight into many a future application [1]. Here, we present tunable 3D twister vortex superlattice (TVS) structures by means of superposition of the simplest solutions of Helmholtz equations, the plane waves [5, 6]. They are centrally engrafted with independently designable vortex helices surrounded by perturbed dark rings, while along these rings the zeros of real and imaginary parts of the field exactly overlap prior to unfolding [6]. The controlled formation of complex spiraling clusters of optical vortices and rings of darkness embedded in such structured 3D light fields gives insight into many a future application like tunable microparticle manipulation in microfluidics [1, 2].

2. COMPUTER SIMULATIONS

Unlike the superposition of complex scalar wave solutions of the form of Bessel beams, or L-G modes to tailor complex vortex lattice structures [1], we avail the simplest solutions of Helmholtz equation, the plane waves, in order to tailor complex twister vortex superlattices (TVS) [6]. A distribution of N vortices in a Gaussian back ground envelop at $z=0$ could be expressed as a product [6,7],

$$\psi(\mathbf{r}, \varphi, z=0) = \psi_0 \mathbf{E}_{BG}(\mathbf{r}) \prod_{j=1}^N \mathbf{A}(\mathbf{r}_j) e^{-ikz} e^{i\ell_j \varphi_j} \quad (1)$$

where φ is the azimuthal coordinate in transverse plane, ψ_0 is the characteristic amplitude, \mathbf{E}_{BG} is the

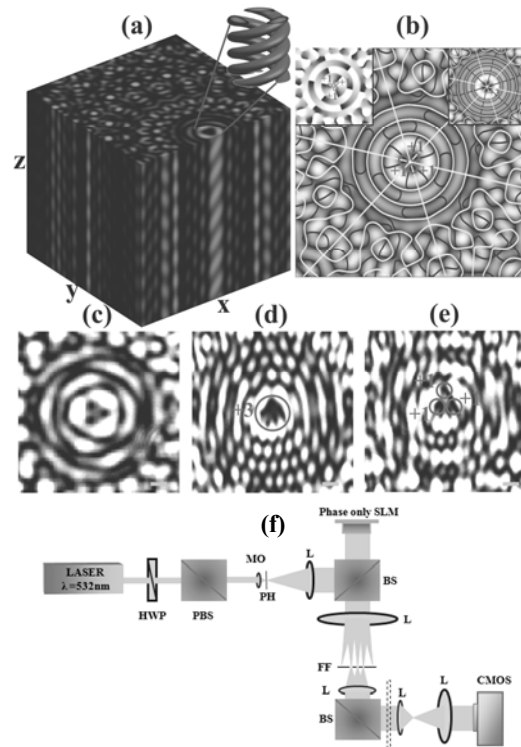


Fig. 1. (a) 21+1 plane wave interference 3D intensity distribution of a spiraling 3D twister vortex superlattice with centrally intertwined triple helices. (b) Zero crossing plot: Zeros of $\text{Re}\psi(\mathbf{r})$ [blue] and $\text{Im}\psi(\mathbf{r})$ [green] (Left Inset: Phase profile and Right Inset: Zero crossing plotting for unperturbed structure). (c) Experimentally recorded Intensity pattern for one of the x-y planes of (a). [All scale bars= $10\mu\text{m}$].(d)-(e) Experimental fork formation while the lattice forming beams are superposed with an additional plane wave launched with a large angle. (d) For an unperturbed complex vortex lattice and (e) For a 3D TVS after perturbation. (f) Schematic representation of the experimental setup for the generation of diverse 3D TVS structures. HWP: half wave plate, PBS: polarizing beam splitter, MO: microscope objective, PH: pin hole, L: lens, BS: beam splitter, FF: Fourier filter. Region of recording is indicated in dotted line.

back ground envelop function, $\mathbf{A}(\mathbf{r}, z)$ is the small localized vortex core function. By an appropriate

wave design of multiple interfering plane waves, diverse geometries of optical vortices similar to the above distribution can be tailored. Dynamically generated axially equidistant coplanar multiple plane waves with designed relative phase are superposed in a controlled manner. This forms a superlattice structure, centrally engrafted with a vortex of higher topological charge. [6]. The choice of the number and the relative initial phase of the coplanar plane waves to form the desired superlattice are primarily based on the required number of dark rings as well as the charge and sign of the higher order vortex at the center. In order to form a (p, q) -TVS which is threaded by p -stranded vortex helix under perturbation, we define axial dislocation strength of 'p' at the center as well as 'q' number of dark rings prior to unfolding [2,6]. Further, in an unperturbed structure the number of 0 to 2π phase changes along a dark ring equals the total strength of the dislocations threading it at the center. Figs. 1a and 1b give the computational analysis of a TVS by $21+1$ noncoplanar plane wave interference. Precisely formed vortex with higher order topological charge at the centre is unfolded into identically signed vortices of unit charge and triply intertwined 3D helices in the presence of a perturbing plane wave [5,6].

3. EXPERIMENTAL ANALYSIS

In Fig 1c-1e, show the experimental results to those of our computations. We realize this by means of a phase only spatial light modulator (SLM) (Holoeye PLUTO-VIS, Holoeye Photonics AG)-assisted single step fabrication approach [5,6]. The schematic of the experimental set up is given in Fig. 1f. In addition to experimentally capturing the intensity distributions (Fig. 1c), the experimental realization of the forks (Fig. 1d and 1e), well matching to the simulated results clearly indicate the position as well as the topological charge and sign of the cyclic phase change around the intensity nodes of designed vortices. The fork formation at the centre in the folded and the unfolded TVS structure gives the inference of the identical sign of the single charged vortices in the presence of a perturbing field [2,6].

4. CONCLUSION

We have computationally simulated and experimentally realized diverse large area spiraling 3D TVS, centrally configured with perturbed tailored dark rings of diverse order threaded by vortex helices, by the designed interference of relatively phase engineered plane waves. Through a programmable SLM-assisted single step fabrication approach, well-defined diverse structures of 3D TVS are experimentally realized and analyzed. These real-time tunable as well as reconfigurable spiraling 3D vortex

superlattice structures by phase engineered plane wave interference are envisaged to find applications in advanced micro-particle manipulation, 3D-stacked micromotors, tunable chiral metamaterials, nulling interferometry etc. [1-3,6].

REFERENCES

- [1] D. L. Andrews, *Structured Light and Its Applications: An Introduction to Phase-Structured Beams and Nanoscale Optical Forces*, Academic Press, London, 2008.
- [2] M. R. Dennis, K. O'Holleran, and M. J. Padgett, "Singular optics: Optical vortices and polarization singularities," *Progr. in Opt.* **53**, 293 (2009).
- [3] J. Xavier, M. Boguslawski, P. Rose, J. Joseph, and C. Denz, "Reconfigurable optically induced quasi-crystallographic three-dimensional complex nonlinear photonic lattice structures," *Adv. Mater.* **22**, 356 (2010).
- [4] Y. F. Chen, H. C. Liang, Y. C. Lin, Y. S. Tzeng, K. W. Su, and K. F. Huang, *Phys. Rev. A* **83**, 053813 (2011).
- [5] J. Xavier, and J. Joseph, *Opt. Lett.* **36**, 403 (2011).
- [6] J. Xavier, S. Vyas, P. Senthilkumar, C. Denz, and J. Joseph, "Sculptured 3D twister superlattices embedded with tunable vortex spirals," *Opt. Lett.* **36**, 3512 (2011).
- [7] G. Indebetouw, "Optical vortices and their propagation," *J. of Mod. Opt.* **40**, 73 (1993).

HOLOGRAPHIC IMAGE RENDERING FOR LASER DOPPLER IMAGING

Nicolas Verrier*, Benjamin Samson, Michael Atlan
 Langevin Institute. PGG Foundation. CNRS UMR 7587, INSERM U 979, UPMC, Paris 7 University. ESPCI ParisTech - 10 rue Vauquelin. 75005 Paris. France
 *nicolas.verrier@espci.fr

Abstract: A brief review of rendering methods of optically-acquired off-axis digital holograms is presented. We report our latest developments in image auto-focusing, adjustable magnification, and video-rate implementation of numerical image reconstruction. Applications to laser Doppler imaging are reported.

1. INTRODUCTION

Frequency-shifting holography was shown to enable spatially-resolved laser Doppler sensing of blood flow contrasts in superficial vessels [1]. In holography, numerical image rendering is of primary importance. It consists of calculating an image from a recorded optical field diffracted by an object. It involves computationally-intensive Fourier transform calculations. Real-time (video-rate) imaging was hindered by technological barriers. Since the advent of commodity graphics processing units (GPU), this issue has been alleviated [2,3]. A brief review of the main numerical reconstruction and optimal refocusing methods is proposed, as well as our latest technological developments in high throughput holographic rendering.

2. RECONSTRUCTION METHODS

Holographic field measurements consist of recording an optical field diffracted by an object under investigation, beating against a reference field on a 2D array sensor. Mixing the object field with a reference field enables recording of both the amplitude and the phase of the optical wavefront radiated by the object. The features and quality of holographic image rendering depends on the choice of the reconstruction algorithm [4].

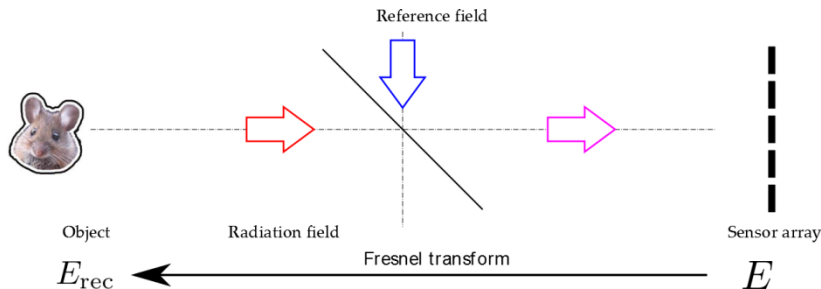


Figure 1. Illustration of holographic recording and reconstruction.

One can reconstruct the object field E_{rec} from the recorded diffraction pattern E by numerical propagation from the sensor plane to the object plane. Propagation is calculated using the integral formulation of the Fresnel transformation

$$E_{\text{rec}}(\xi, \eta) = -i \frac{z}{\lambda} \int_{\mathbb{R}^2} E(x, y) \frac{\exp(ikr)}{r} dx dy. \quad (1)$$

Under the Fresnel approximation, Eq. (1) can be written as [5]

$$E_{\text{rec}}(\xi, \eta) = \frac{\exp\left(\frac{i2\pi}{\lambda}z\right)}{i\lambda z} \int_{\mathbb{R}^2} E(x, y) \exp\left\{i \frac{\pi}{\lambda z} \left[(x - \xi)^2 + (y - \eta)^2\right]\right\} dx dy. \quad (2)$$

Computation of Eq. (2) can be performed considering two different approaches, a convolution-based approach and a Fourier-based approach.

It can be noticed that Eq. (2) can be expressed as the spatial convolution product between the recorded diffraction pattern E and the impulse response of the free-space propagation h_z . It can be expressed, in one-dimension

$$E_{\text{rec}} = E(x) * h_z(x) \tag{3}$$

where $h_z = \exp(i\pi x^2 / (\lambda z))$, and x is the lateral coordinate. This relation can be effectively computed using three fast Fourier transformations. Considering $H_z = \mathcal{F}[h_z] = \exp[2i\pi z(1 - \lambda^2 u^2) / \lambda]$, one can compute Eq. (3) as the propagation of the angular spectrum of the reconstruction beam.

Going back from Eq. (1), propagation from the sensor plane to the object plane can be viewed as a Fourier transformation

$$E_{\text{rec}} \approx \mathcal{F} \left\{ E(x) \exp\left(i\frac{\pi x^2}{\lambda z}\right) \right\} \tag{4}$$

By adequately selecting the reconstruction distance z one can obtain an in-focus image of the object to be analyzed.

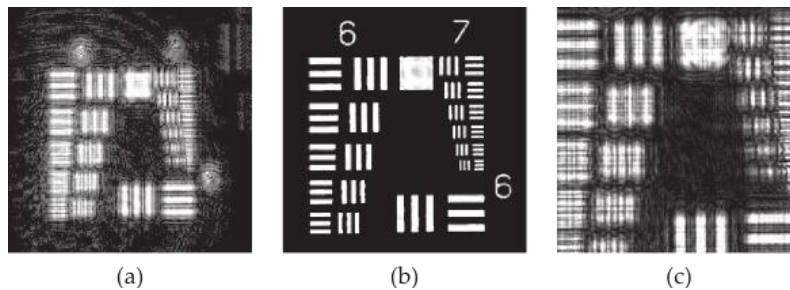


Figure 2. Out-of-focus (a,c) and in-focus (b) intensity rendering of the transmission hologram of a resolution target.

Choice of the optimal reconstruction distance can be realized with an autofocus procedure based on a criterion such as the local variance of the reconstructed hologram [6].

Proposed reconstruction formalisms exhibit different properties. Convolution based approaches will allow

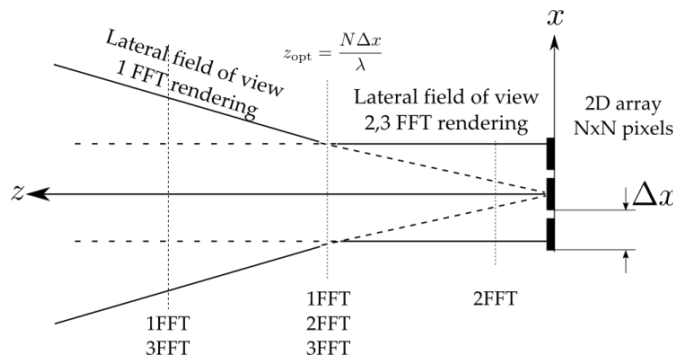


Figure 3. Holographic reconstruction field of view

reconstruction of the hologram with a constant field of view (FOV), whereas in Fourier-based implementation, the FOV will depend on the reconstruction distance.

3. REAL-TIME IMPLEMENTATION

The numerical reconstruction of digital holograms in real-time is an essential feature in imaging applications [7]. The image reconstruction and display algorithm was elaborated with Microsoft Visual C++ 2008 integrated development environment and NVIDIA's Compute Unified Device Architecture (CUDA) software development kit 3.2. FFT calculations were made with the function `cufftExecC2C()` from the

CUFFT 3.2 library on single precision floating point arrays. The program was compiled and run on Microsoft Windows 7 - 64 bit. The computer hardware configuration was based on an ASUS P6T motherboard with a 2.67 GHz Intel core i7 920 CPU and a NVIDIA GeForce GTX 470 GPU.

Image rendering calculations $I \rightarrow H \rightarrow F \rightarrow |f|^2$ are performed sequentially, in the main GPU thread, while video-rate image acquisition is performed in the main CPU thread (Fig. 4).

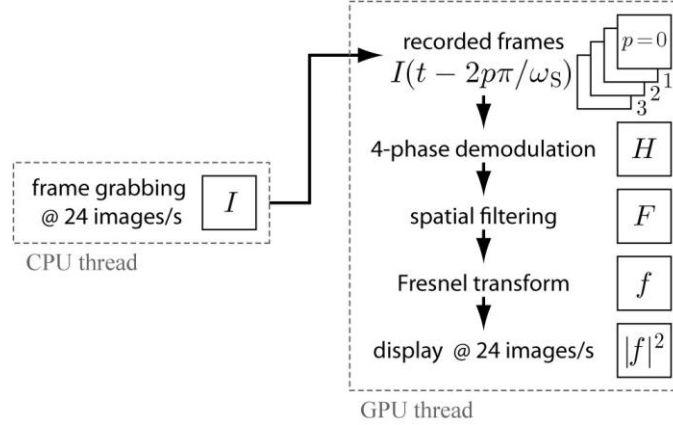


Figure 4. Algorithmic layout of holographic rendering

4. ADJUSTABLE MAGNIFICATION

Presented algorithms are strongly dependent on the hologram recording conditions. To cope with this limitation and to be able to adjust the reconstructed FOV at will, adjustable magnification algorithms have to be considered [8,9]. For instance, Restrepo et al. proposed a convolution-based method which can be described as

$$E_{\text{rec}} = f * g \quad (5)$$

with

$$f = E \exp \left[i \frac{\pi x^2}{\lambda z} (1 - \gamma) \right], \quad \text{and} \quad g = \exp \left(i \frac{\pi x^2}{\lambda z} \gamma \right) \quad (6)$$

Here γ is the ratio between the reconstructed FOV and the array extent. Increasing the value of γ results in zooming in the reconstructed object lateral field (thus reducing the reconstruction FOV), whereas reducing γ increases the FOV.

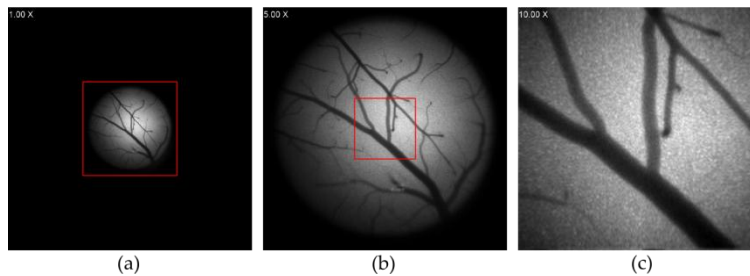


Figure 5. Adjustable magnification reconstruction of the vascular tree of a mouse brain. (a) 1x. (b) 5x. (c) 10x.

Illustration of the adjustable magnification reconstruction is proposed in Fig. 3. Here, reconstruction of the hologram of the vascular tree of a mouse brain is depicted. Figure 3(a) corresponds to the reconstruction using the Fourier-based algorithm. The FOV of the image is too important to image over the details in the vascular tree. A zoom is performed within the red box by setting $\gamma = 5$ and $\gamma = 10$. When $\gamma = 5$

(Fig. 3(b)), the reconstructed FOV is brought to the size of the sensor array. For $\gamma = 10$ (Fig. 3 (c)), details of the smallest vessels can be distinguished.

5. APPLICATIONS

Frequency-shifting holography can be used in Doppler sensing for mechanical vibration assessment [10], fluid mechanics screening [11] and biomedical imaging, with promising applications in medical angiography [12], enabling non-ionizing imaging of blood perfusion in the microvasculature with near infrared laser sources, without any contrast agent.

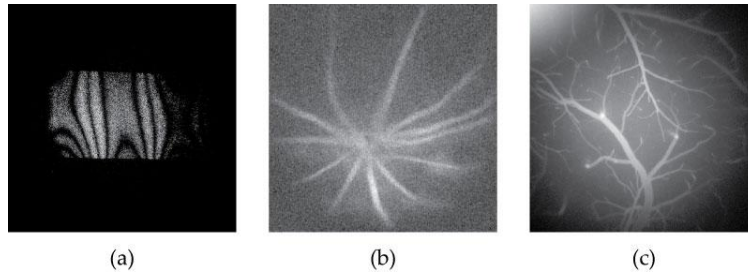


Figure 6 Laser Doppler holographic imaging applied to vibrometry (a), retinal ophthalmoscopy (b), cerebral blood flow imaging (c).

The detection characteristics of holographic imaging offer excellent opportunities to assess blood perfusion non-invasively, where current scanning laser Doppler imaging solutions are in limit of performance.

Illustration of the performances of digital holography for Doppler imaging is reported on Fig. 5. With Doppler sensing, we successfully imaged out-of-plane vibration modes of a mechanical structure in sinusoidal motion and can be applied to non-destructive testing (Fig. 5(a)). It also allows to image blood flow in the eye fundus (Fig. 5(b)) or in cerebral cortex (Fig. 5(c)), in rodent models.

6. CONCLUSION

We have discussed the applicability of digital holography to laser Doppler imaging. After a brief reminder of the main techniques for image reconstruction, we have presented an adjustable magnification scheme allowing to control the FOV of the reconstructed image and to zoom over its details without interpolation losses. Real-time implementation of the holographic reconstruction has been proposed for applications in laser Doppler imaging. Non-destructive mechanical testing, and biomedical imaging may benefit from real-time holographic laser Doppler imaging.

REFERENCES

- [1] M. Atlan *et al.*, *Opt. Lett.* **31**, 2762 (2006).
- [2] T. Shimobaba, *et al.* *Opt. Exp.* **16**, 11776 (2008).
- [3] L. Ahrenberg, *et al.* *J. Disp. Tech.* **5**, 111 (2009).
- [4] N. Verrier, *et al.* *Appl. Opt.* **50**, to be published (2011).
- [5] J.W. Goodman, "Introduction to Fourier optics", *Roberts and Company*, Third edition (2005).
- [6] J.L. Pech-Pacheco *et al.*, *IEEE Int. Conf. Patt. Rec.*, **3**, 3318 (2001).
- [7] B. Samson *et al.*, *Opt. Lett.* **36**, 1449 (2011).
- [8] J-C. Li *et al.*, *Opt. Lett.*, **34**, 572 (2009).
- [9] J. Restrepo *et al.*, *Appl. Opt.*, **49**, 6430 (2010).
- [10] F. Joud *et al.*, *Opt. Express* **17**, 2774 (2009).
- [11] M. Atlan *et al.*, *JEOS:RP*, **1**, 06025 (2006).
- [12] M. Simonutti *et al.*, " *Opt. Lett.* **35**, 1941 (2010).

QUASI BLOCH OSCILLATIONS IN A FIBONACCI SPACED WAVEGUIDE ARRAY

S Dutta Gupta

School of Physics, University of Hyderabad, Hyderabad 500046
sdgsp@uohyd.ernet.in

Abstract: After a brief review of Bloch oscillations and the Wannier-Stark ladder in a periodic array of waveguides with a linear refractive index ramp, we study a quasiperiodic array, where the coupling of the adjacent guides vary as given by a Fibonacci sequence. We report localization as well as self-similarity in the structure.

1. INTRODUCTION

Coupled resonators and coupled optical waveguides have been a very convenient prototype system to test many of the fundamental aspects and predictions of both classical and quantum physics [1-4]. Effects like electromagnetically induced transparency, storage and retrieval of light, time-reversal of a pulse, quantum Zeno effect, Bloch oscillations constitute few of the examples. Bloch oscillations in optical systems is especially attractive because of the clean nature of the corresponding experiments as compared to the solid state counterpart [1,3]. It has been demonstrated by several groups both theoretically and experimentally [3]. Identical guides, spaced evenly, (leading to identical coupling) built on a linear ramp are used in these studies. In this presentation we modify the near neighbor coupling by adjusting the separation between the guides. The separation between the guides are chosen such that the coupling constants form a Fibonacci sequence. We look at the evolution of the field when initially only one central guide is excited. Since the weak localization and self-similarity of Fibonacci structures are well known [5-8], we look for similar signatures in the context of Bloch oscillations. We do see weak localization near the central guide, which would have dispersed completely in absence of the ramp. Moreover, we report self-similar features in the 9-th and 12-generation structures.

2. BLOCH OSCILLATIONS IN A PERIODIC STRUCTURE

Bloch oscillations take place in a system describable by a periodic potential with a built-in linear ramp [2,3]. An applied electric field over and above the periodic potential in a crystal corresponds to such a situation. In the context of an optical system such a potential can be created in a periodic array of waveguides with a linear refractive index ramp as the background [2]. The eigen-energies corresponding to such a system are equidistant and constitute the so-called Wannier-Stark ladder. In absence of the linear ramp, the excitation, initially launched in, say, a central guide, undergoes a diffusive spreading. The presence of the ramp drastically affects the spread of the wave and periodically reconstructs the initial field

pattern. The latter is referred to as Bloch oscillations. It is clear that the reflection of the wave on the edge with lower refractive index is caused by total internal reflection, while the same at the other edge is due to the periodic structure.

Consider a periodic array of single-mode waveguides described by the following equations [2]

$$i \frac{da_n}{dz} + \alpha n a_n + a_{n-1} + a_{n+1} = 0 \quad (1)$$

where α gives the slope of the ramp and a_n is the amplitude of the n -th guide. The propagation direction is along Z and is characterized by the propagation constant $\beta_m = m\alpha$ (m - integer). Thus the progress of the field profile along Z is characterized by equidistant wave numbers (referred to as the Wannier-Stark ladder). Moreover, there is a complete recovery of the initial field after a propagation distance of $2\pi/\alpha$ (referred to as the Bloch oscillation period). The evolution of the field for the excitation of a single guide is shown in Fig.1. The top panel in this figure gives the absolute value of the field amplitude while the bottom panel gives the contour plot of the same.

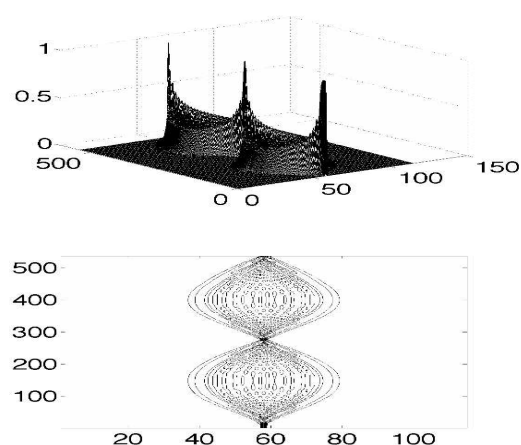


Fig. 1 Two periods of Bloch oscillation

3. FIELD EVOLUTION IN A QUASIPERIODIC STRUCTURE

Consider an array of identical single-mode

waveguides. Now the coupling between the adjacent guides changes following a Fibonacci sequence. Starting with initial generations $S_0 = A$ and $S_1 = B$, any S_{i+i} can be generated as follows

$$S_{i+1} = S_{i-1}S_i \quad (2)$$

Any generation contains the Fibonacci number of elements in it. The optical properties of a Fibonacci layered medium comprising of slabs of two types were investigated in detail and weak localization of light and interesting multifractal scalings were demonstrated [5]. Later studies [6-8] concentrated on nonlinear Fibonacci stacks with a goal to assess the role of nonlinearity in localization. It was shown that nonlinearity hinders localization and reduces localized states to extended ones. The existence of gap solitons as in nonlinear periodic structures was shown.

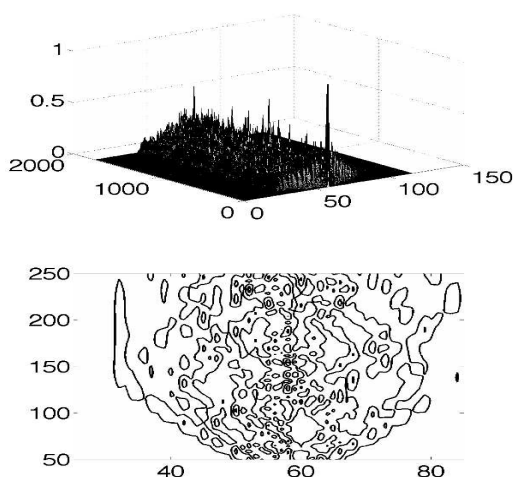


Fig. 2 Propagation of the excitation profile (top) and the corresponding contour plot for ninth generation.

In the context of quasi-reconstruction of the input field profile, rather, quasi-localization, we modify Eq.(1) to the following form, where we have changed the near-neighbor coupling constants to a Fibonacci array

$$i \frac{da_n}{dz} + \alpha na_n + c_{n-1}a_{n-1} + c_{n+1}a_{n+1} = 0 \quad (3)$$

with $A = 1.0$ and $B = 1.5$. Thus, for a fifth generation Fibonacci array, the coupling between guide to guide will be changing as $ABBAB$ (or 1.0,1.5,1.5,1.0,1.5). We excite the central guide in an array of waveguides in a ninth generation structure. The results without the ramp ($\alpha=0$) clearly shows the excitation dispersing away from the central guide to both the sides (not presented here). One has to be careful about the large erroneous values at the edges of the computation

domain, due to the periodic boundary conditions (instead of PML) used in our calculations. In presence of the ramp, as in Bloch oscillations, the character of the propagation of the excitation profile, changes drastically. This is depicted in Fig.2, where the top panel shows the excitation profile, while the bottom one shows the corresponding enlarged contour plot.

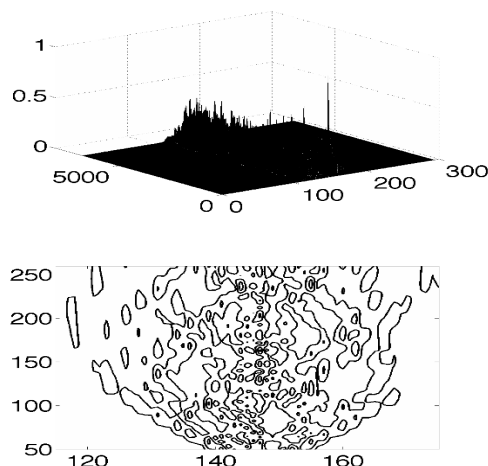


Fig. 3 Same as in Fig.2 but for the twelfth generation

Though one does not have the complete reconstruction of the initial profile, one has the excitation dominantly near the central guide. This, of course, is a signature of the weak localization property of a Fibonacci array. The localization aspects are more pronounced for the 12-th generation of the Fibonacci array (see Fig.3).

Next we compare the enlarged portions of the contour plot of the excitation profile for the ninth and the twelfth generations. These results are shown in the bottom panels of Figs. 3 and 4. The self-similarity features are quite clear from this figure. Note the different scales in the horizontal axis. Thus lower generation features are embedded in a contracted form in the higher generations. Moreover, multifractal nature and the scaling laws are intact in a much more complex scenario like Bloch oscillations.

ACKNOWLEDGEMENT

The author is thankful to the Department of Science and Technology, Government of India for financial support.

REFERENCES

- [1] D. N. Christodoulides, F. Lederer and Y. Silberberg, "Discretizing light behaviour in linear and nonlinear waveguide lattices", *Nature*, **424**, 817 (2003).
- [2] U. Peschel and T. Pertsch and F. Lederer, "Optical Bloch oscillations in waveguide arrays", *Opt. Lett.*, **23**, 1701 (1998).

- [3] R. Morandotti and U. Peschel and J. S. Aitchison and H. S. Eisenberg and Y. Silberberg, "Experimental observation of linear and nonlinear optical Bloch oscillations", *Phys. Rev. Lett.*, **83**, 4756 (1999).
- [4] A. Szameit, F. Dreisow, M. Heinrich, S. Nolte and A. A. Sukhorukov, "Realization of Reflectionless Potentials in Photonic Lattices," *Phys. Rev. Lett.*, **106**, 193903 (2011).
- [5] M. Kohmoto, B. Sutherland and K Iguchi, *Phys. Rev. Lett.*, **58**, 2436 (1987).
- [6] S. Dutta Gupta and D. S. Ray, "Optical multistability in a nonlinear Fibonacci multilayer", *Phys. Rev.* **B38**, Rapid Commun., 3628 (1988)
- [7] S. Dutta Gupta and D. S. Ray, "Soliton like distribution and their self similarity in a nonlinear Fibonacci Multilayer", *Phys Rev.* **B40**, 10604, (1989)
- [8] S. Dutta Gupta and D. S. Ray, "Localization in optics: Nonlinear quasiperiodic media", *Phys Rev.***B 41**, 8047 (1990).

COUPLED MODE CONFIGURATIONS IN OPTICAL FIBERS FOR USE AS BAND REJECT FILTERS

Enakshi Khular Sharma¹, Sangeeta Srivastava² and Jyoti Anand³

¹Department of Electronic Science, University of Delhi South Campus, New Delhi-110021,INDIA

²Department of Electronics, Rajdhani College, University of Delhi, INDIA

³Department of Electronics, Keshav Mahavidyalaya, University of Delhi, INDIA
enakshi54@yahoo.co.in

Spectral filters have very important applications in dense wavelength division multiplexing (DWDM) optical communication systems comprising of optical amplifiers. In particular, specially designed gain flattening filters or amplified spontaneous emission (ASE) suppressors are required for Erbium Doped Fiber Amplifiers (EDFA). Band rejection filters are also required in cascaded Raman amplifiers to remove the unnecessary Stokes orders. Although bulk optical filters are available, it is desirable to have all-fiber configurations, as they can be spliced into the system with very low insertion losses. It is interesting to see that a number of optical fiber configurations, shown in Fig.(1), which act as band reject filters are all based on coupling between two modes and can all be analyzed in a similar manner by the conventional slowly varying coupled mode theory.

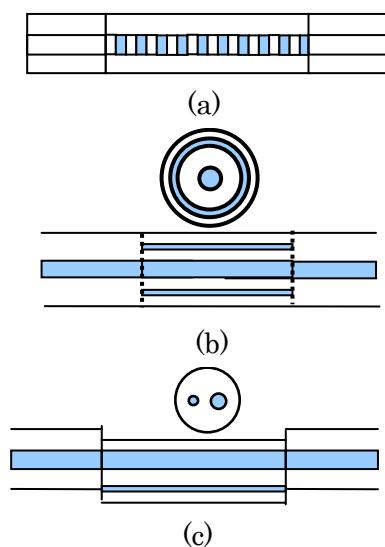


Fig. 1 Band reject optical fiber configurations
 (a) Long Period Grating (b) Coaxial Fiber
 (c) Twin Core Fiber

An early band reject filter in optical fiber configuration was proposed by Vengsarkar et al. [1] in the form of a long period grating in optical fibers (Fig. 1a). The filter action is based on resonant coupling at a phase matched wavelength from propagating core guided mode to a cladding mode due to periodic refractive index changes with period ~500 micron in the core. For a given resonant wavelength, the bandwidth of the filter depends on the choice of the phase matched cladding mode and a desired attenuation can be controlled by the grating length [2]. A coaxial optical fiber [3,4] can also act as a band reject filter (Fig. 1b). The high index central

rod core and the high index tube core, both act as single mode non-identical waveguides which can be designed to be synchronous at a desired wavelength. Coupling between the waveguides results in band reject characteristics. The bandwidth of the filter is decided by the crossing angle of the propagation constant curves and spacing between the waveguides. A twin core fiber [5] with two different cores can also act as a spectral filter (Fig. 1c). The propagation constants of the two cores can be designed to be equal at a certain wavelength. At this phase matched wavelength, strong coupling occurs between the two cores. The bandwidth of the filter can be again be tailored by changing the inter core separation. These filters have been demonstrated as gain flattening filters for Erbium Doped Fiber Amplifiers [6].

ACKNOWLEDGEMENTS

The authors acknowledge the financial support received from UGC, India.

REFERENCES

- [1] A.M. Vengsarkar, P.J. Lemaire, J.B. Judkins, V. Bhatia, T. Erdogan and J.E. Sipe, "Long Period Gratings as Band Reject Filters", *J. Lightwave Technol.*, Vol. 14, No. 1, 58-65, (1996).
- [2] Rashmi Singh and Enakshi K. Sharma, "Tailoring the transmission spectrum of long period grating by variation in the length of the grating", *Proc. of SPIE*, Vol. 646, 64680Y1-6, (2007).
- [3] Jyoti Anand, Jagneet Kaur Anand and Enakshi K. Sharma, "Study of the amplification characteristics of a coaxial EDF with varying coupling conditions", *Optics & Laser Tech.*, Vol.44, No.3, 688-695, (2012).
- [4] S. Fevrier, P. Roy, D. Pagnoux, J.L. Auguste, J.M. Blondy and J. Marcou, "12nm FWHM 20dB stop band filter based on cascaded dual concentric core fiber filters", *Electron Lett.*, Vol 37, No. 18, 1113-1115, (2001).
- [5] B. Ortega and L. Dong, "Characteristics of mismatched twin-core fiber spectral filters", *IEEE Photon. Tech. Lett.*, Vol. 10, No. 7, 991-993, (1998).
- [6] Yi Bin Lu and P. L. Chu, "Gain Flattening by Using Dual-Core Fiber in Erbium-Doped Fiber Amplifier", *IEEE Photon. Tech. Lett.*, Vol. 12, No. 12, 1616-1617, (2000).

LARGE-MODE-AREA GUIDED-WAVE OPTICAL STRUCTURES

Vipul Rastogi

Department of Physics, Indian Institute of Technology Roorkee, Roorkee 247 667, India

Email: vipul.rastogi@osamember.org

Abstract: We have designed large-mode-area optical fibers for various applications including high power lasers and amplifiers, high data rate optical communication, dispersion compensation and high peak power ultra-short laser pulse delivery. The designs are essentially multilayer structure based and have been analyzed by transfer matrix method. Single-mode operation of large-core fiber designs has been attained by higher-order mode discrimination. Dual-core structure with same core indices but different cladding indices has been implemented to design large-mode-area dispersion compensating fibers. Structures having mode-area close to $2000 \mu\text{m}^2$ have been designed for high peak power femtosecond laser pulse delivery.

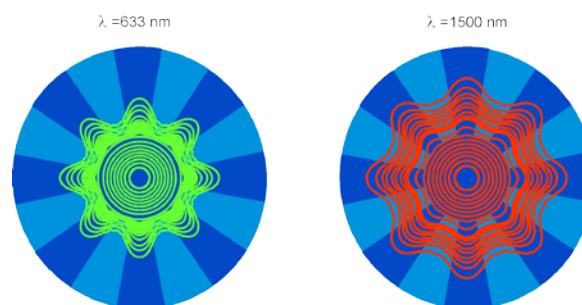
1. INTRODUCTION

Large-mode area optical fibers find applications in high power fiber lasers for industrial applications and beam delivery of high peak power ultra-short laser pulses for micro-machining, laser ablation, femtochemistry and biomedical applications. In optical communication systems employing dense wavelength division multiplexing, the dispersion compensating fiber used should have large-mode-area (LMA) in order to prevent unwanted nonlinear effects and the loss of signal as a consequence of these effects. We have designed large-mode area fibers based on higher-order mode (HOM) discrimination to have effective single-mode operation. Our LMA designs for high power applications include segmented cladding fiber (SCF) consisting of alternate low- and high-index segments arranged periodically in the cladding [1-3]; multi-layer-cladding (MLC) fiber consisting of alternate low- and high-index concentric layers, with varying refractive-index of low-index layers [4,5]; dual core resonant leaky fiber (DCRLF) with two concentric cores set-up in resonance for first higher-order mode to enable efficient HOM stripping [6]; and dual-shape core fiber (DSCF) with perfectly guided fundamental mode and leaky HOM [7]. We have also designed dispersion compensating fibers (DCF) having large-mode area. The fiber employs dual-core resonant structure to achieve high negative dispersion while having large-mode-area [8,9]. We have also investigated the propagation of ultra-short pulse (USP) through the LMA designs and have designed the SCF and a W-fiber for high peak power USP delivery [10].

2. LMA DESIGNS

The LMA designs are based on HOM discrimination. The HOM discrimination has been achieved using SCF, MLC, DCRLF, and DSCF. SCF has been designed to provide single-mode operation with large core size over an extended range of wavelength while keeping the polarization mode dispersion low. The fiber consists of segmented cladding achieved by alternate arrangement of high-

and low-index segments in the angular direction [1,2]. The fiber has been fabricated in PMMA and silver halide glass and has shown single-mode operation with large core [3,11,12]. The SCF has a highly dispersive cladding and is essentially a leaky structure. The single-mode operation of the fiber is ensured by high differential leakage loss between the fundamental and higher order modes. The modal fields of the SCF at 633 nm and 1550 nm wavelengths are shown in Fig. 1. Using SCF, one can achieve LMA single-mode operation over an extended range



of wavelength with $20 \mu\text{m}$ core diameter [1].

Fig.1. Modal field profiles of the SCF at 633 nm and 1550 nm wavelengths.

Like photonic crystal fibers or holey fibers, it is not possible to fabricate an SCF using conventional fabrication techniques such as MCVD. We have therefore, also investigated another leaky design, namely, MLC leaky fiber for large-mode-area high power applications. The refractive index profile of an MLC fiber along with the modal field profile is shown in Fig. 2(a). With MLC we could design fiber having $700 \mu\text{m}^2$ mode area and 0.16 numerical aperture (NA) [4]. The MLC fiber with a few cladding layers was fabricated by MCVD [5]. The low index trenches were obtained by F doping into fused silica. The mode profiles after different lengths of propagation are shown in Fig.3 along with the refractive-index profile of the fiber. The fiber showed the mode filtering effect clearly and single-mode operation could be obtained

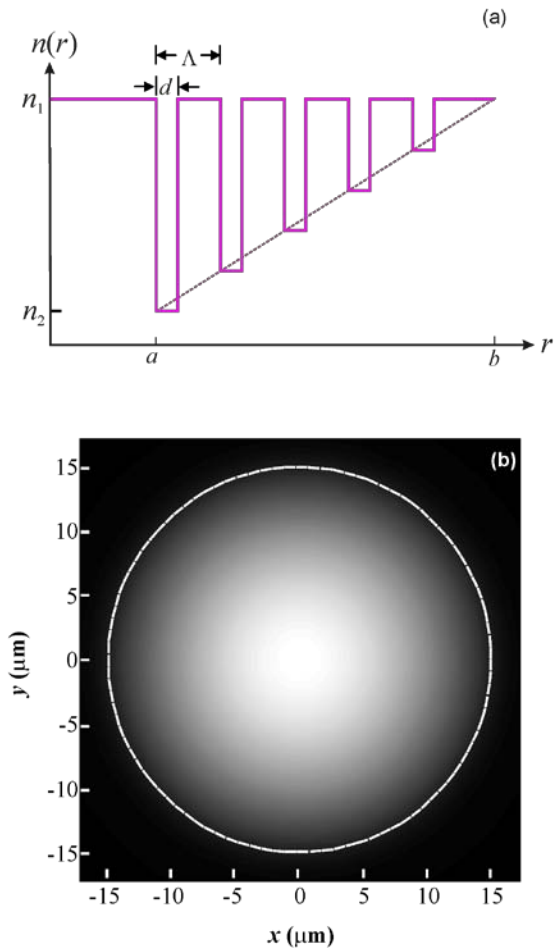


Fig.2. (a) Schematic of the refractive-index profile of the MLC fiber. (b) Modal field profile of the fundamental mode.

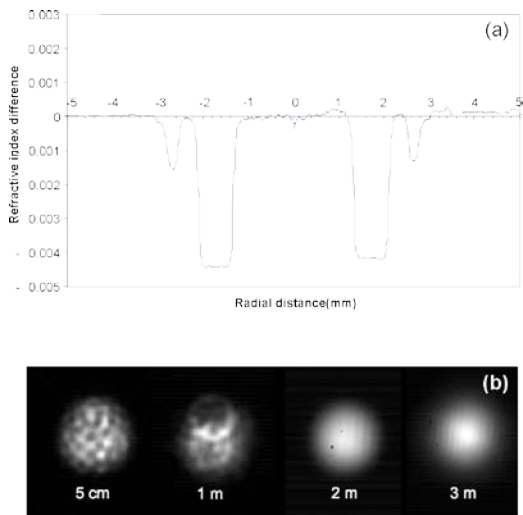


Fig.3. (a) Refractive-index profile of the perform of the leaky fiber. (b) Evolution of mode intensity along the length.

after 2-m length of propagation with 380- μm^2 mode

area and 0.11 NA [5].

A DCRLF design for efficient stripping of higher order modes and to have high NA LMA operation was also proposed. With this design the single-mode operation could be shown within 10 cm length of propagation through the fiber [6]. We also proposed an LMA design with perfectly guided single-mode and leaky HOM. This design employs a dual-shape core consisting of a large-core of high index and a small side core of slightly lower refractive-index. The fiber shows single-mode operation with 580 μm^2 mode area and low bend loss [7].

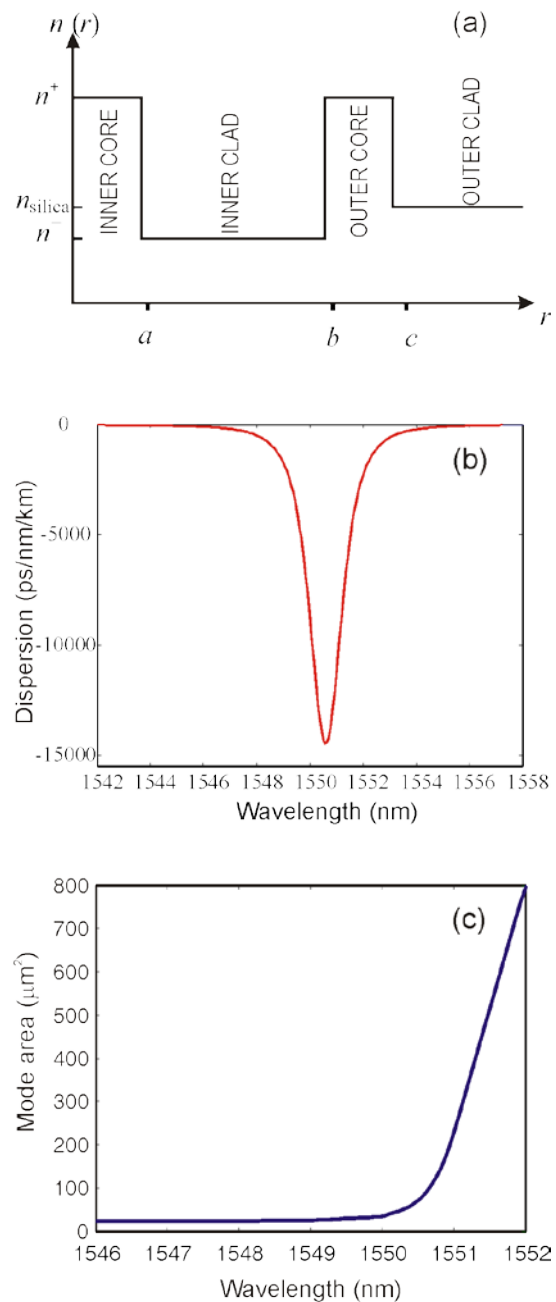


Fig.4. (a) Refractive-index profile of dual-core DCF. (b) Dispersion coefficient. (c) Corresponding mode area.

3. DCF

We have also designed LMA DCF for narrowband

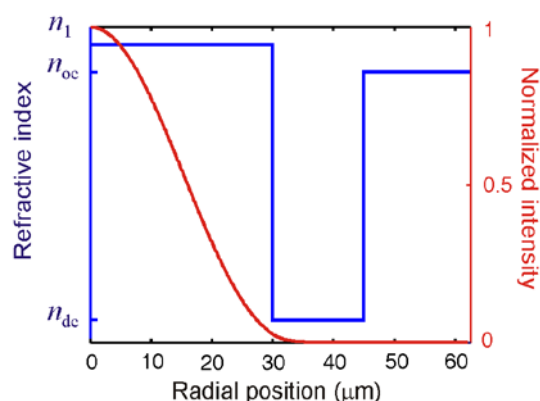


Fig.5. Refractive-index profile and the normalized mode intensity profile of the W-type fiber for ultra-short laser pulse delivery.

and WDM applications. The refractive-index profile along with the dispersion and the corresponding mode-area for the narrowband design is shown in Fig.4. In our narrowband design we could achieve a dispersion of $-14,500$ ps/(nm.km) at 1550-nm wavelength with mode area of $86 \mu\text{m}^2$. Our WDM DCF design shows dispersion ranging between -80 and -280 ps/(nm.km) over a wavelength span of 40 nm, kappa value near 30 nm, figure of merit 1030 ps/(dB.km) and mode area $63 \mu\text{m}^2$ [8,9].

3. FIBERS FOR USP DELIVERY

We have investigated the possibility of delivery of fs duration high peak power laser pulses through the SCF and the W-type fiber. The refractive-index profile

along with the radial intensity profile of the W-type fiber designed for the delivery of femtosecond laser pulses is shown in Fig.5. The fundamental mode of the fiber is perfectly guided and has effective mode area of $1950 \mu\text{m}^2$. The higher-order modes of the fiber are leaky [10]. The difference between the effective indices of the LP_{01} and LP_{11} modes of the fiber is about 1.6×10^{-4} , which is large enough to avoid loss due to mode coupling [13]. The dispersion coefficient of the fiber at 1550-nm centre wavelength is 21.7 ps/(nm.km). The pulse propagation in the fiber has been simulated by solving the nonlinear Schroedinger equation (NLSE) by split step Fourier method [14]. We have considered self-phase modulation, 2nd order group velocity dispersion and propagation loss while solving the NLSE. Figure 6 shows propagation of 56-kW peak power 100-fs 1550-nm wavelength hyperbolic secant pulse over 4-m length of the fiber. We can see distortion-free propagation of the pulses through the fiber. In the SCF we could obtain near distortion-free propagation of 100-fs pulses at 800 nm and 1550 nm wavelengths with mode areas over $1800 \mu\text{m}^2$.

ACKNOWLEDGEMENT

This work has been partially supported by UK-India Education and Research Initiative (UKIERI) major award on "Application specific microstructured optical fibers," and DST sponsored project on "Development of silica-based segmented cladding fiber."

REFERENCES

- [1] V. Rastogi, and K. S. Chiang, "Propagation characteristics of a segmented cladding fiber,"

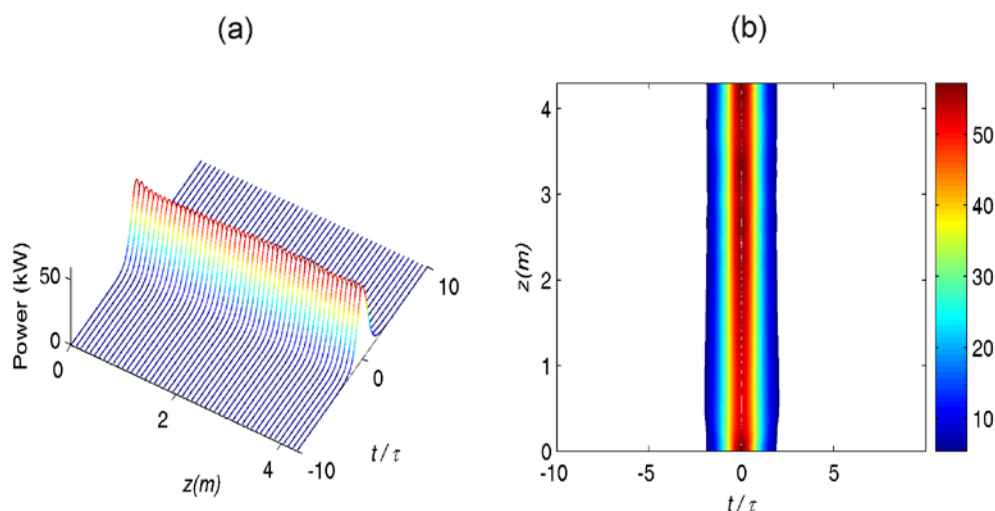


Fig.6. (a) Propagation of hyperbolic secant pulse through the W-type fiber. (b) Corresponding contour plot.

- Opt. Lett.*, **26**, 491 (2001).
- [2] V. Rastogi, and K. S. Chiang, "Analysis of segmented cladding fiber by radial effective index method," *J. Opt. Soc. B*, **21**, 258 (2004).
- [3] A. Yeung, K. S. Chiang, V. Rastogi, P. L. Chu, and G. D. Peng, "Experimental demonstration of single-mode operation of large-core segmented cladding fiber," *Optical Fiber Communication Conference (OFC 2004)*, Los Angeles, Feb. 22-27, 2004.
- [4] A. Kumar, and V. Rastogi, "Design and analysis of a multilayer cladding large-mode-area optical fiber," *J. Opt. A: Pure Appl. Opt.*, **10**, 015303 (2008).
- [5] B. Dussardier, V. Rastogi, A. Kumar, and G. Monnom, "Large-mode-area leaky optical fiber fabricated by MCVD," *Appl. Opt.*, **50**, 3118 (2011).
- [6] A. Kumar, V. Rastogi, C. Kakkar, and B. Dussardier, "Co-axial dual-core resonant leaky fibre for optical amplifiers," *J. Opt. A: Pure Appl. Opt.*, **10**, 115306 (2008).
- [7] A. Kumar, and V. Rastogi, "Design and analysis of dual-shape core large-mode-area optical fiber," *Appl. Opt.*, **50**, E119 (2011).
- [8] R. Kumar, A. Kumar, and V. Rastogi, "Dual core large mode area for dispersion compensating fibre," *15th OptoElectronics and Communication Conference (OECC 2010)*, Sapporo, Japan, July 5-9, 2010.
- [9] V. Rastogi, R. Kumar, and A. Kumar, "Large-effective area all-solid dispersion compensating fiber," private communication.
- [10] Babita, V. Rastogi, and A. Kumar, "Large-mode-area W-type fiber design for femtosecond laser pulse delivery," private communication.
- [11] A. Millo, I. Naeh, Y. Lavi, and A. Katzir, "Silver-halide segmented cladding fibers for the middle infrared," *Appl. Phys. Lett.*, **88**, 251101 (2006).
- [12] A. Millo, I. Naeh, and A. Katzir, "Single-mode segmented cladding fibers for the middle infrared," *J Lightwave Technol.*, **25**, 2115 (2007).
- [13] S. Ramachandran, J. W. Nicholson, S. Ghalmi, M. F. Yan, P. Wisk, E. Monberg, and F. V. Dimarcello, "Light propagation with ultralarge modal areas in optical fibers," *Opt. Lett.*, **31**, 1797 (2006).
- [14] G. P. Agrawal, *Nonlinear Fiber Optics*, Academic, San Diego, 2001.

LOCALIZATION OF LIGHT IN A DISORDERED WAVEGUIDE LATTICE WITH LONGITUDINALLY MODULATED REFRACTIVE INDEX

Somnath Ghosh*, R. K. Varshney and B. P. Pal

Physics Department, Indian Institute of Technology Delhi, Hauz Khas, New Delhi 110016, India
*somnit@rediffmail.com

Abstract: We report the enhancement of the effect of transverse localization of light (TL) in presence of dynamic localization in a longitudinally modulated disordered waveguide lattice. In our chosen lattice, tunneling inhibition along length favors to achieve the diffraction-free propagation. Results can be used to tune the threshold for TL.

1. INTRODUCTION

Engineering the diffraction properties of light which essentially results in broadening of light beam, in discrete photonic structures is possible either by choosing a disordered refractive index profile in the transverse direction in the form of transverse localization of light [1], or inhibiting tunneling among different channels by longitudinally oscillating refractive index which is often referred as dynamic localization [2]. In our chosen specific 1D coupled waveguide lattice configuration, we have incorporated bi-directional modulation of refractive index, i.e. along both transverse and longitudinal directions. In this paper, we address the effect of dynamic localization in the context of transverse localization in our chosen lattice.

2. THEORY AND MODELING

We describe the propagation dynamics of a CW light beam along the z-axis of a modulated disordered waveguide lattice solving the following equation [1]

$$i \frac{\partial A}{\partial z} + \frac{1}{2k} \left(\frac{\partial^2 A}{\partial x^2} \right) + \frac{k}{n_0} \Delta n(x, z) A = 0 \quad (1)$$

whose refractive index profile is assumed to be of the form

$$\Delta n(x, z) = \Delta n(x) [1 + \mu \sin^2(\Omega z)] \quad (2)$$

$$\Delta n(x) = \Delta n_p (H(x) + C \delta(x)) \quad (3)$$

here C is a dimensionless constant, whose value governs the level/strength of transverse disorder; μ represents the longitudinal modulation depth and Ω is the modulation frequency. We solve Eq. (1) numerically through the scalar beam propagation method, which we implemented in Matlab.

3. RESULTS

Our chosen waveguide array consists of 100 evanescently coupled waveguides as shown in Fig.1 (when $\mu = 0$), each of $7 \mu\text{m}$ width and separated from each other by $7 \mu\text{m}$ with other parameters as mentioned in [1]. The results in terms of averaged output beam width are shown in Fig. 2. It can be seen that in the case of a modulated lattice ($\mu = 0.3$ & $\Omega = 0.002$), the width of a localized state is much smaller than its counterpart in unmodulated ($\mu = 0$) lattice. Moreover, inset of Fig. 2 indicates that in a modulated lattice a

faster transition to the localized regime is possible even after a relatively shorter distance of propagation.

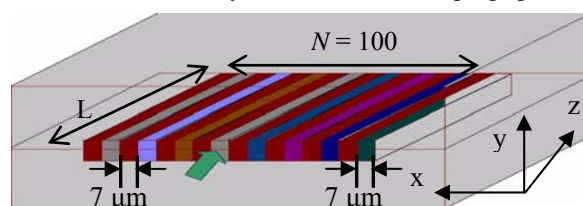


Fig. 1. Schematic of a 1D coupled disordered lattice. Different shades of color signify different refractive indices over an average refractive index.

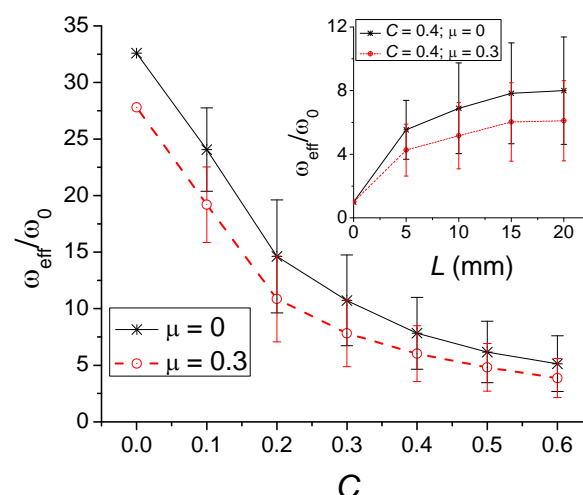


Fig. 2. Variation in the ensemble averaged effective width of the output beam for an input Gaussian beam (FWHM $10 \mu\text{m}$) with different strengths of disorder after a propagation distance of 15 mm . The error bars are the statistical standard deviations of beam widths. Inset shows a faster transition to localization in a modulated lattice.

This work is partially supported by ONRG Grant N62909-10-1-7141 by N.R.L., Washington, D.C.

REFERENCES

- [1] S. Ghosh, G. P. Agrawal, B. P. Pal and R. K. Varshney, *Opt. Comm.* **284**, 201-206, (2011).
- [2] A. Szameit, I. L. Garanovich, M. Heinrich, A. A. Sukhorukov, F. Dreisow, T. Pertsch, S. Nolte, A. Tünnnermann, S. Longhi, and Y. S. Kivshar, *Phys. Rev. Lett.* **104**, 223903, (2010).

ZNO MODIFIED MOO₃ NANO- RODS, WIRES, BELTS AND TUBES: NON-LINEAR OPTICAL AND GAS SENSING STUDIES

V.P. Mahadevan Pillai¹, I. Navas^{1,2} and Heinz Kohler²

¹Department of Optoelectronics, University of Kerala, Kariavattom, Thiruvananthapuram-695581, Kerala, India.

²Institute for Sensorics and Information Systems, Karlsruhe University of Applied Sciences, Moltkestr. 30, D-76133, Karlsruhe, Germany.

MoO₃ nanorods, nanowires, nanobelts and nanotubes have been fabricated by varying ZnO doping levels. On the basis of our systematic analyses by XRD and micro-Raman, we propose a growth mechanism that derives from partial screw dislocations due to the strain effect induced by ZnO doping. The presence of ZnO in MoO₃ with respect to doping levels is ascertained by EDX analysis. The orthorhombic α -MoO₃ structure of the nanostructures is not altered by higher doping concentrations of ZnO, but ZnO induces oxygen vacancies in MoO₃ lattice. The variation of particle size, band gap and refractive index with ZnO concentrations are also analysed. The PL spectra are recorded at two excitation wavelengths 250 and 380 nm. Among the two; the photo emission at 380 nm is the strongest. The PL peak positions do not change with different excitation wavelengths, indicating that there are a few fixed exciton energy levels on the surface of MoO₃ nanostructures, which are possibly related to the surface states resulting from the oxygen vacancies and adsorbed oxygen. The PL intensity is enhanced with ZnO doping levels and the emission band positions show a slight blue shift with increase in doping concentrations. Undoped and 1% doped MoO₃ nanostructures do not give any nonlinear absorptive responses, whereas saturation absorption (SA) behaviour is observed for higher ZnO doping levels ($\geq 3\%$). It is observed that with the increase of ZnO doping level, the contribution of SA behaviour decreases while induced absorption increases and finally the major contribution to the observed nonlinear absorption appears to be from reverse saturation absorption (RSA) due to two-photon absorption (TPA). The observed behaviour is attributed to the change in microstructure and particle size on introducing dopants, which in turn changes the localized defect state density. So by properly adjusting the ZnO doping levels and thereby controlling the microstructure and particle size of these doped oxides, the NLO properties can be "tailored" for potential use of these materials in various applications like optical switching, laser pulse compression and in optical limiting devices for

protecting optical sensors from high power laser pulses.

Pure and ZnO (1, 10, 25 at. wt. %) doped MoO₃ gas sensitive layers on alumina substrates (with inter-digitated electrodes) are realized in nanostructured form by RF magnetron sputtering and controlled post deposition annealing. The structural, compositional and morphological analyses are carried out by using XRD, micro-Raman, EDX and ESEM studies. The four sensors are tested under five gas species, humidity (H₂O), hydrogen (H₂), carbon monoxide (CO), propylene (C₃H₆) and ethanol (C₂H₅OH). The sensor test measurements towards these gas species are carried out in constant (200 and 300 °C) and cyclic temperatures (ramping between 100 and 320 °C) and at different gas concentrations. The ZnO doping concentration has profound influence on the sensitivity towards these gases.

The mechanism of sensing of these gases by MoO₃ layers in non-humid and humid conditions is explained. It is mainly noted that unlike other metal oxides, the gas detection by MoO₃ is mainly directed by the lattice oxygen rather than chemisorbed oxygen. The lattice oxygen from MoO₃ layer catalytically oxidizes the incoming analyte gases and simultaneously reduces. Hence, the change in conductivity is determined by the reduction of MoO₃ to non-stoichiometric levels. Water, CO₂, acrolein and acetaldehyde are the main by-products respectively for the catalytic oxidations of H₂, CO, propylene and ethanol.

The sensors show very poor sensitivity at 200 °C towards these gases except ethanol. The sensors show highly stable signals in humid and non humid conditions at 300 °C and the signals maintain baseline values. The results show that the MoO₃ can be used as a sensing material for humidity detection. The presence of water also influences the sensor performance to other analyte gases; it diminishes the sensor response towards all analyte gases. The MoO₃ sensors show sensitivity towards the analyte gases in the order ethanol > propylene > H₂ > CO. The sensors show good sensitivity, stability and reproducibility with very less selectivity.

ALL-OPTICAL SWITCHING IN PROTEIN-COATED ULTRAHIGH-Q MICRORESONATORS AND ITS APPLICATION TO LOW-POWER COMPUTING

Sukhdev Roy

Department of Physics and Computer Science
Dayalbagh Educational Institute (Deemed University), Agra, India

Email : sukhdevroy@dei.ac.in

The anticipated requirement for ultrafast ultrahigh bandwidth information processing has provided tremendous impetus for realization of all-optical devices and circuits. The advent of nano and bio technologies in the design, synthesis and characterization of novel materials and structures, has opened up exciting new possibilities for generation, manipulation and detection of light, to achieve all-optical information processing¹. The prospect of photonic applications using ultrasensitive natural photoreceptor proteins, discovered in a broad range of plants and organisms that exhibit an efficient nonlinear optical response, which has also been optimized over centuries of evolution, is extremely fascinating. Integration of these photochromic biomolecules with nanostructures provides a powerful capability to meet present challenges to achieve ultrafast low-power all-optical computing.

The talk would focus on some of our recent experimental and theoretical results on all-optical switching in a variety of biomolecules that include the unique bacteriorhodopsin (BR) protein, pharaonis phoborhodopsin, proteorhodopsin, plant-based LOV2 phototropin, chlorophyll-A, and in BR protein-coated ultrahigh-Q microcavities²⁻⁴. A comparison with switching in fullerenes, organometallics, ex. Cu-phthalocyanines and graphene will be presented⁵. We will also present its application in novel designs of a variety of all-optical and opto-electronic low-power biomolecular Boolean, conservative, reversible and reconfigurable computing devices and circuits that include switches, spatial light modulators, Boolean, Fredkin, Toffoli, Feynman and Peres logic gates, half/full adder-subtractors, delays, MUX-DEMUX, flip-flops, ALU and PLA circuits³⁻⁷. The talk would highlight, (i) emergence of a new class of biomolecules for photonic applications, (ii) prospects

for ultrafast femtosecond optical biomolecular computing and (iii) integration of nano, bio and photonic technologies for a new computational paradigm.

REFERENCES

- [1] S. Roy (Ed.), Special Issue on Optical Computing, Circuits, Devices and Systems, *IET Cir., Dev. Syst.* **5**, 73 (2011).
- [2] S. Roy, K. Kulshrestha and M. Prasad, "Switching light with light in chlorophyll A molecules", *IEEE Trans. Nanobiosci.* **8**, 83 (2009).
- [3] S. Roy, M. Prasad, J. Topolancik and F. Vollmer, "All-optical switching with bacteriorhodopsin protein coated microcavities and its application to low power computing circuits", *J. Appl. Phys.* **107**, 053115 (2010).
- [4] S. Roy and M. Prasad, "Novel proposal for all-optical Fredkin logic gate with bacteriorhodopsin coated microcavity and its applications", *Opt. Engg.* **49**, 065201 (2010).
- [5] S. Roy and C. Yadav, "All-optical ultrafast logic gates based on saturable to reverse saturable absorption transition in CuPc-doped PMMA thin films", *Opt. Commun.* **282**, 4435 (2011).
- [6] S. Roy and M. Prasad, "Design of all-optical reconfigurable logic unit with bacteriorhodopsin protein coated microcavities", *IEEE Trans. Nanobiosci.* **10**, 160 (2011).
- [7] S. Roy, P. Sethi, J. Topolancik and F. Vollmer, "All-optical reversible logic gates with bacteriorhodopsin protein coated microresonators", *Adv. Opt. Technol., Special Issue on Nano-Biophotonic Devices: Design, Fabrication and Applns.* **2012**, 727206 (2012).

TEMPERATURE-DEPENDENT SECOND HARMONIC GENERATION AT 532 NM IN PERIODICALLY POLED LiNbO₃

O. P. Naraniya^{a,b,*}, Ajay Mishra^a, A. N. Kaul^a and A. K. Gupta^a

M .R. Shenoy^b and K. Thyagarajan^b

^aPhotonics Division, IRDE, Raipur Road, Dehradun -248008

^bDepartment of Physics IIT Delhi, Hauz Khas, New Delhi-110016

*Email: papps_om@yahoo.co.in

Abstract: We report Type I first-order quasi-phase-matched (QPM) second harmonic generation (SHG) in the $o \rightarrow e$ scheme in periodically poled lithium niobate (PPLN). A Q-switched Nd:YVO₄ laser was used as the pump at the wavelength of 1.064 μ m. By using in-house-fabricated PPLNs of different grating periods, SHG at 532 nm was achieved with $o \rightarrow e$ and $e \rightarrow e$ conversion schemes. The measured temperature tuning bandwidth for the $o \rightarrow e$ conversion was 1.3 $^{\circ}$ C, which is in good agreement with the theoretically obtained value of 1.37 $^{\circ}$ C for PPLN of length 2 cm. The average conversion efficiency for $o \rightarrow e$ and the commonly employed $e \rightarrow e$ schemes obtained are 32% and 9%, respectively.

1. INTRODUCTION

In second harmonic generation (SHG), a fundamental wave with frequency ω_1 interacts with the second-order nonlinear susceptibility of a material to produce a polarization wave at the second-harmonic frequency $\omega_2 = 2 \omega_1$. SHG in nonlinear optical materials is always widely discussed among the researchers because of its application in coherent green and blue lasers, high density data storage etc. [1, 2].

In the commonly employed birefringence phase matching (BPM) scheme, SHG can take place in Type I and Type II configurations. In Type I SHG, two photons of ordinary polarization in the crystal combine to form one photon at double the frequency and of extraordinary polarization. In Type II SHG, two photons of orthogonal polarizations combine to form one photon with double the frequency and extraordinary polarization. An alternative to BPM is quasi-phase-matching (QPM). QPM uses a periodic modulation of the sign of the nonlinear optical susceptibility to compensate for the refractive index dispersion. For a given crystal orientation or grating period, only one of these types of SHG occurs. Periodically poled lithium niobate (PPLN) is widely used to realize high conversion efficiency SHG owing to its high transparency range (down to 0.35 μ m), high effective nonlinear coefficient, and excellent mechanical stability [3]. In this paper we demonstrate QPM schemes in PPLN for the SHG process; first where the fundamental and second harmonic waves have the same polarization ($e \rightarrow e$) and the second where both the waves are orthogonally polarized ($o \rightarrow e$).

In the $o \rightarrow e$ scheme, the d_{31} coefficient is used in place of d_{33} coefficient for $e \rightarrow e$ scheme. Although smaller d_{31} coefficient used in the $o \rightarrow e$ scheme is

expected to result in smaller SHG efficiency, the larger temperature bandwidth and grating uniformity leads to significantly improved conversion efficiency. Also the fabrication of PPLN for $o \rightarrow e$ scheme is much easier in comparison to the $e \rightarrow e$ scheme due to the requirement of large grating periods [4].

In z-cut PPLN we demonstrated first order QPM in the $o \rightarrow e$ scheme and third order QPM in the $e \rightarrow e$ scheme for SHG at 532 nm green light. Average conversion efficiency obtained for the $o \rightarrow e$ scheme was 32% whereas for the $e \rightarrow e$ scheme, it was 9%. Although d_{31} coefficient is involved in $o \rightarrow e$ scheme (in place of d_{33}), conversion efficiency obtained was higher than the $e \rightarrow e$ scheme because of the large acceptance bandwidth and better uniformity of the QPM grating structure.

Temperature acceptance bandwidth measured for the $o \rightarrow e$ scheme was 1.3 $^{\circ}$ C, which is close to the theoretical value of 1.37 $^{\circ}$ C. However temperature acceptance bandwidth for the $e \rightarrow e$ scheme couldn't be obtained, as the very small acceptance bandwidth requires fabrication uniformity of few nm, which couldn't be achieved because of the fabrication difficulties. The main reason for the low conversion efficiency in our experiments is the departure from ideal QPM in periodicity, i.e. the fabrication errors of grating period.

2. THEORETICAL CONSIDERATION

2.1 Quasi Phase Matching (QPM)

In nonlinear interactions that involve frequency conversion, two basic conditions must be satisfied. The first condition is energy conservation of the participating waves and the second is momentum conservation. Momentum conservation is also known as the phase-matching condition between the interacting waves. The phase-matching condition is

achieved by using either BPM or QPM techniques [2]. QPM involves repeated inversion of the relative phase between the forced second-harmonic and free fundamental waves after an odd number of coherence lengths. Thus the phase is “reset” periodically in the manner so that on the average a proper phase relationship is maintained for growth of the second harmonic wave.

In the first order quasi phase matched devices, the nonlinear coefficient is modulated with a period equal to twice the coherence length of the interaction, to offset the accumulated phase mismatch. Whereas for the third order quasi phase matched device, the period will be four times of the coherence length.

The greatest advantage of QPM lies in its ability to design a device for operation at desired wavelengths and temperature. Another important feature is to accomplish phase-matching which would otherwise be impossible: in isotropic materials, or in materials that possess either too little or too much birefringence at the wavelength of interest [2, 4].

Here we report the first order $o \rightarrow e$ and third order $e \rightarrow e$ QPM schemes for SHG. First, the grating periods were designed and fabricated. With the fabricated gratings, SHG conversion efficiency and temperature tuning bandwidth have been studied numerically as well as experimentally for both the schemes. The first order QPM equations for the two schemes are given by [5, 6]

$$\Delta k_{o \rightarrow e} = 2\pi \left(\frac{n_{e,2\omega}}{\lambda_{2\omega}} - 2 \frac{n_{o,\omega}}{\lambda_{\omega}} - \frac{2\pi}{\Lambda_{o \rightarrow e}} \right) = 0$$

$$\Delta k_{e \rightarrow e} = 2\pi \left(\frac{n_{e,2\omega}}{\lambda_{2\omega}} - 2 \frac{n_{e,\omega}}{\lambda_{\omega}} - \frac{2\pi}{\Lambda_{e \rightarrow e}} \right) = 0$$

For the successful use of LiNbO₃ in SHG, a knowledge of this uniaxial crystal's refractive indices as a function of wavelength and temperature is necessary. The temperature dependence of the refractive index for the o - and e - polarizations are obtained by using Sellmeier equations for wavelengths 532 nm and 1064 nm [5].

In the $o \rightarrow e$ scheme, due to the different temperature dependence of the ordinary and extraordinary refractive index, QPM period for the $o \rightarrow e$ scheme becomes temperature dependent. Although, the smaller d_{31} coefficient will be used for $o \rightarrow e$ scheme, larger acceptance bandwidth and grating period in comparison to the $e \rightarrow e$ scheme, assures better optical nonlinear interactions. Temperature dependence of grating period for both the schemes is shown in figure 1 [7].

From figure 1 we see that the $o \rightarrow e$ scheme implies considerably larger QPM periods in comparison to the $e \rightarrow e$ scheme. Also QPM period for the $o \rightarrow e$ scheme is temperature dependent whereas for the $e \rightarrow e$ scheme it's nearly independent of the temperature.

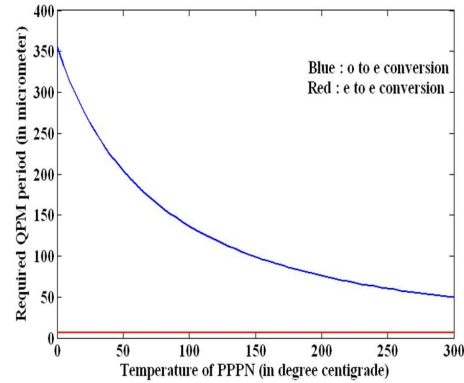


Figure 1. The QPM periods of LiNbO₃ necessary for SHG of Nd: YVO₄ laser (@1064nm) versus temperature for $o \rightarrow e$ and $e \rightarrow e$ process.

3. PERIODIC POLING

An ideal uniform periodic domain structure in PPLN crystal is very important to obtain high frequency conversion efficiency in a QPM nonlinear interaction. In our experiment we have used z-cut congruent LiNbO₃ samples with 20-mm length, 20 mm width and 0.5 mm thickness to fabricate PPLN with grating periods of 115 μ m and 18.5 μ m. Although a variety of methods have been investigated to improve the fidelity of the reversed domains [8-10], the basic technique of domain inversion in PPLN uses a lithographically patterned insulating layer and lithium chloride liquid electrolyte contained in a chuck that sandwiches the sample between two O -rings. Current monitoring in the external circuit allows control of the domain evolution during poling [11, 12].

Congruent LiNbO₃ is subject to photorefractive damage at temperature below 100 $^{\circ}$ C and suffers from high coercive field that limits thickness of polling to about 0.5 mm. So for grating period design, we have used temperature well above this limit, i.e. \sim 125 $^{\circ}$ C for o to e conversion. Also LiNbO₃ samples of 0.5 mm thickness are used for E-field polling.

Z-cut, 0.5mm thick LN wafers were spin-coated with a thick positive photoresist layer followed by photolithography using a Mask Aligner to pattern the periodic electrodes. In this way, a thick layer of photoresist is applied over the wafer, leaving a portion of the wafer exposed. Contact is made to the exposed LN wafer with LiCl liquid electrolyte. Typically the applied e-field value is 21 kV/mm for LiNbO₃ so 12 kV being applied to the 0.5 mm thick samples. PPLN with grating period of 115 μ m was designed and fabricated for first order SHG with $o \rightarrow e$ scheme. Also PPLNs with \sim 18.5 μ m grating periods are fabricated for 3rd order $e \rightarrow e$ scheme (figure 2).

Thus, we have chosen fixed QPM grating periods of 115 μ m and 18.5 μ m (third order QPM \sim 3 \times 6.3) for the SHG experimentations with $o \rightarrow e$ and $e \rightarrow e$

schemes, respectively.

4. RESULTS AND DISCUSSION

The experimental set-up shown in the figure 3 is used for both the SHG conversion schemes i.e. $o \rightarrow e$ and $e \rightarrow e$. We used Nd:YVO₄ laser of wavelength 1064 nm as a pump source (fundamental frequency). For $e \rightarrow e$ scheme, the pump beam was polarized along the z -axis whereas for the $o \rightarrow e$ y -direction has been chosen. The end faces of the samples were polished but without antireflection coating. The PPLN was placed in a micro-oven, in which the temperature can be controlled with an accuracy of 0.1 °C.

The maximum SHG efficiency will be obtained corresponding to the perfect phase matching temperature. Varying the temperature will result in reduced conversion efficiency. Temperature tuning bandwidth is the FWHM for the conversion efficiency with respect to the temperature plot. For the first-order $o \rightarrow e$ scheme measured temperature tuning bandwidth was 1.3°C, which is in good agreement with the theoretically obtained value of 1.37 °C for PPLN of length 2 cm. The experimental results agree well with the calculated result, which also shows the polarization dependence of QPM in PPLN.

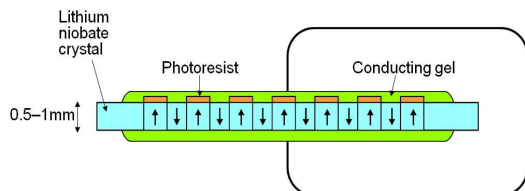


Figure 2. Schematic of experimental setup for E-field polling for fabrication of PPLN

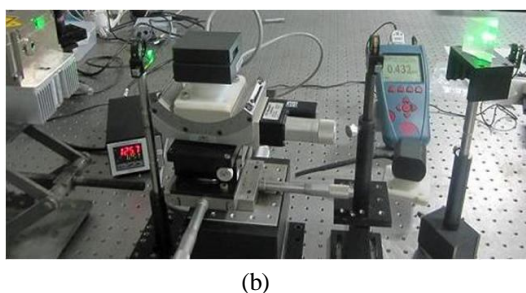
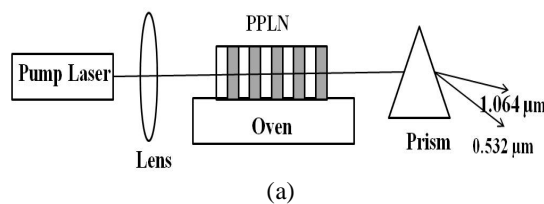


Figure 3. (a) Schematic of experimental setup for SHG and actual photograph of the experimental setup for measuring SHG conversion efficiency

The SHG power from a PPLN sample of fixed QPM period of 115 μm as a function of temperature is shown in figure 4. Also a sinc^2 curve is fitted to the experimental points as shown in figure 4. Theoretically the FWHM of central peak for $o \rightarrow e$ conversion is found to be 1.37 °C for a PPLN of length 2 cm [4]. Experimentally measured temperature bandwidth for $o \rightarrow e$ conversion is 1.3 °C, which is close to the theoretically estimated results.

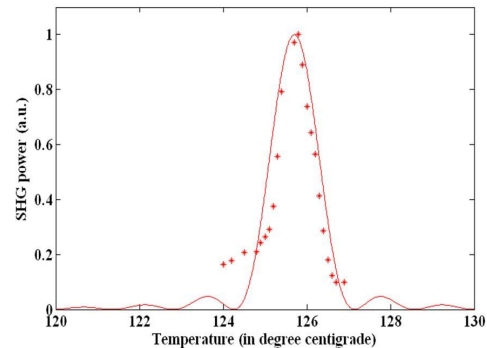


Figure 4. Temperature tuning curve for 20-mm long PPLN for first order QPM ($o \rightarrow e$) conversion. The FWHM acceptance bandwidth is ~ 1.3 °C.

Temperature tuning for the PPLN of period at 118.5 °C for 3rd order QPM was experimentally investigated and the process was repeated for few more fabricated PPLNs, but we could not find the temperature tuning properties as theoretically predicted. That is because the $e \rightarrow e$ scheme requires a grating period uniformity of few nm, which couldn't be achieved in our fabrication process due to fabrication limitations.

SHG conversion efficiency for both the process were measured, and an average conversion efficiency of 32% and 9% has been achieved for the $o \rightarrow e$ and $e \rightarrow e$ schemes, respectively.

ACKNOWLEDGEMENT

The authors wish to acknowledge Director, IRDE for granting his permission to publish this paper. Also help from Deepak Gond in PPLN fabrication is gratefully acknowledged.

REFERENCES

- [1] W.P. Risk et al, , *Compact Blue-Green Lasers*, Chapter 1, Cambridge Univ. Press, U.K., (2003)
- [2] M. M. Fejer, G A. Magel, D. H. Jundt, and R. L. Byer, " Quasi phase matched second harmonic generation: tuning and tolerances," IEEE J. Quantum Electron. 28, 2631-2654 (1992).
- [3] W.K. Burns, W. McElhanon, and L. Goldberg, "Second Harmonic Generation in Field Poled,

- Quasi-Phase- Matched, Bulk LiNbO₃,” IEEE Photon. Technol. Lett. **6**, 252-254 (1994).
- [4] Michele Belmonte, Troben Skettrup and Christian Pedersen “Frequency doubling in LinbO₃ using temperature-dependent QPM” J. Opt. A, Pure Appl. Opt. **1**, 60-63 (1999).
- [5] D. H. Jundt “Temperature-dependent Sellmeier equation for the index of refraction, ne, in congruent lithium niobate” Opt. Lett., **22**(20), 1553-1557 (1997).
- [6] E.J. Lim, M.M. Fejer and R.L. Byer, “Second-harmonic generation of green light in periodically poled planar Lithium Niobate waveguide,” Electron. Lett. **25**, 174-175 (1989).
- [7] Y. Chen, R. Wu, X. Zeng, Y. Xia, X. Cheng “Type I quasi-phase-matched blue second harmonic generation with different polarizations in periodically poled LiNbO₃” Opt. & Laser Tech. **38**, 19-22 (2006).
- [8] W.K. Burns, W. McElhanon, and L. Goldberg, “Second Harmonic Generation in Field Poled, Quasi-Phase- Matched, Bulk LiNbO₃,” IEEE Photon. Technol. Lett. **6**, 252-254 (1994).
- [9] E.J. Lim, M.M. Fejer and R.L. Byer, “Second-harmonic generation of green light in periodically poled planar Lithium Niobate waveguide,” Electron. Lett. **25**, 174-175 (1989).
- [10] M. Yamada and K. Kishima, “Fabrication of periodically reversed domain structure for SHG in LiNbO₃ by direct electron beam lithography at room temperature,” Electron. Lett. **27**, 828-829 (1991).
- [11] L.E. Myers, R.C. Eckardt, M.M. Fejer, R.L. Byer, SPIE, Vol. 2379 (1995)
- [12] L.E. Myers, G. D. Miller, R.C. Eckardt, M.M. Fejer and R.L. Byer, Optics Letters, Vol. No.20, 52 (1995)

We analytically discover chirped kink-similariton pulses induced by stimulated Raman scattering in the case of a generalized nonlinear Schrödinger equation with varying dispersion, nonlinearity, gain or absorption, nonlinear gain, and stimulated Raman scattering. It is demonstrated that these chirped kink-similariton pulses can be precisely piloted by appropriately tailoring the dispersion profile. This fact is profitably exploited to achieve optimal compression of these chirped similaritons. The solution does not develop any side pedestal or deformation in pulse shape as it propagates, making it a promising candidate for this new compression technique. Nonlinear chirping of these kink-similaritons is also demonstrated.

I. INTRODUCTION

Self-similar solutions of the relevant nonlinear evolution equations have become a topic of growing interest in the description of many complicated phenomena, including the scaling properties of turbulent flow [1], the formation of fractals in nonlinear systems [2], and the wave collapse in hydrodynamics [3] over the years. In nonlinear optics, the study of self-similar waves has attracted much attention and has played an important role toward the development of all-optical devices [4–11]. We specially note that exact self-similar solutions of the nonlinear Schrödinger equation with distributed coefficients were found by using symmetry reduction [5]. As reported, these self-similar pulses or solitary waves possess a strictly linear chirp that leads to efficient compression or amplification and thus are particularly useful in the design of optical fiber amplifiers, optical pulse compressors, and soliton-based communication links.

It is well-known that the propagation of picosecond pulses in optical fibers is governed by the nonlinear Schrödinger equation (NLSE). Nonetheless, several higher-order terms become important for the propagation of femtosecond pulses through nonlinear fibers. Then the pulse evolution is governed by the higher order nonlinear Schrödinger equation (HNLSE), which includes the higher-order effects such as third-order dispersion, self-steepening term, and the stimulated Raman scattering (SRS). Many authors have found exact bright solitons in the case of anomalous dispersion region and dark solitons in the normal-dispersion region for the HNLSE. Mathematically, a third kind of soliton known as the kink soliton can exist [12]. Although kink solitons occur in many branches of physics e.g., particle physics and solid

state physics, their occurrence in nonlinear optics is relatively rare. It is only recently that the possibility of kink solitons in optical fibers has been discovered [13]. Kink solitons owe their existence to the phenomenon of SRS.

Recently, Kruglov *et al.* [14] demonstrated high compression of similariton pulses under the influence of higher order nonlinearities in generalized HNLSE. Unfortunately, they could not find exact solution for this model with distributed coefficients. Spurred on by this issue, we report the discovery of chirped kink-similariton pulses induced by stimulated Raman scattering in the case of a generalized nonlinear Schrödinger equation with varying dispersion, nonlinearity, gain or absorption, nonlinear gain, and stimulated Raman scattering. It is demonstrated that these chirped kink-similariton pulses can be precisely piloted by appropriately tailoring the dispersion profile. This fact is profitably exploited to achieve optimal compression of these chirped similaritons. The solution does not develop any side pedestal or deformation in pulse shape as it propagates, making it a promising candidate for this new compression technique. Nonlinear chirping of these kink-similaritons is also demonstrated.

II. SIMILARITON PROPAGATION REGIMES

The modified NLSE with distributed nonlinear gain governing the propagation of the optical field in a single-mode optical fiber can be written as

$$i\partial_z\psi = \frac{\beta(z)}{2}\partial_\tau^2\psi - \gamma(z)|\psi|^2\psi + i\frac{g(z)}{2}\psi + i\chi(z)|\psi|^2\psi + \epsilon(z)\psi\partial_\tau|\psi|^2, \quad (1)$$

where ψ is the complex envelope of the electric field in a comoving frame, z is the propagation distance, τ is the retarded time, $g(z)$ is the gain function, $\chi(z)$ is the nonlinear gain or absorption [15, 16], and $\epsilon(z)$ accounts for the coefficient of SRS. In the absence of last two terms,

*Electronic address: soloman@karunya.edu

this equation has exact self-similar solutions that exhibit a linear chirp. But here, we are concerned with solutions. *Frontiers in Optics and Photonics* 2011 chirp, resulting from the nonlinear gain.

To this end, the complex function $\psi(z, \tau)$ can be written as

$$\psi(z, \tau) = P(z, \tau) \exp\{im_0 \ln[P(z, \tau)] + i\Phi(z, \tau)\} \quad (2)$$

where m_0 denotes the nonlinear chirp parameter, and P and Φ are real functions of z and τ . We look for kink-similaritons of Eq. (1), assuming that the phase has the following quadratic form:

$$\Phi(z, \tau) = a(z) + b(z)[\tau - \tau_p(z)] + c(z)(\tau - \tau_p)^2, \quad (3)$$

where the pulse position τ_p is a function of z . Here, $a(z)$, $b(z)$, and $c(z)$ are the parameters related to the phase offset, the frequency shift, and the phase-front curvature, respectively. It is noteworthy that Eqs. (1)-(3) yield a self-similar form of the amplitude

$$P(z, \tau) = \frac{Q(T)}{\sqrt{\Gamma(z)}} \exp(S(z) - m_0 \Theta(z)), \quad (4)$$

where the scaling variable T is given by

$$T = \frac{\tau - \tau_p(z)}{\Gamma(z)}, \quad (5)$$

where $\Gamma(z) = 1 - 2c_0 R(z)$. And the other functions $R(z)$, $\Theta(z)$, $S(z)$ and $\tau_p(z)$ take the forms

$$R(z) = \int_0^z \beta(z') dz', \quad (6)$$

$$\Theta(z) = -\lambda \int_0^z \frac{\beta(z')}{[1 - 2c_0 R(z')]^2} dz', \quad (7)$$

$$S(z) = \frac{1}{2} \ln \left(\frac{m_0^2 - 2}{2} \rho(0) \right) + \int_0^z g(z') dz', \quad (8)$$

$$\tau_p(z) = \tau_c - b_0 R(z), \quad (9)$$

where b_0 , λ , c_0 and τ_c are the integration constants and $\rho(z) = \beta(z)/\gamma(z)$. In terms of the above functions (6)-(8), the phase parameters $a(z)$, $b(z)$, and $c(z)$ are found to be

$$a(z) = a_0 + \frac{1 + m_0^2}{2} \Theta(z) - \frac{b_0^2}{2} R(z) - \frac{m_0}{2} \ln[|c(z)|] - m_0 S(z), \quad (10)$$

$$b(z) = b_0, \quad (11)$$

$$c(z) = \frac{c_0}{1 - 2c_0 R(z)}. \quad (12)$$

It should be emphasized that the existence of such self-similar solutions is conditional on the following two formulas:

$$g(z) = \frac{1}{2\rho(z)} \frac{d}{dz} \rho(z) + \frac{c_0 \beta(z)}{1 - 2c_0 R(z)} - \frac{\mu \lambda m_0 \beta(z)}{[1 - 2c_0 R(z)]^2}, \quad (13)$$

$$\frac{\chi(z)}{\gamma(z)} = \frac{3m_0}{m_0^2 - 2} \quad (14)$$

where $\mu = 1$ or $\frac{3}{4}$. The former condition describes that the parameter functions in Eq. (1) can not be chosen independently, while the latter condition implies that the nonlinear chirp parameter m_0 in fact be determined by the ratio $\chi(z)/\gamma(z)$. In this paper, it requires that this ratio is a constant. From the physical cases we have considered, we come to the conclusion that $m_0^2 \neq 2$ for arbitrary nonlinear materials.

As a result, for $\mu = 1$, the function $Q(T)$ in Eq. 4 can be determined by solving the elliptic equation

$$\frac{d^2 Q}{dT^2} - \lambda Q - 2\alpha Q^3 + 2\epsilon Q^2 \frac{dQ}{dT} = 0, \quad (15)$$

where $dQ/dT \neq 0$. Then it follows from Eqs. (4)-(15) for the case $\lambda = \tau_0^{-2}$ that a kink-similariton of the following emerges as an exact solution of Eq. (1):

$$\psi(z, \tau) = \left[\frac{(3/2\epsilon) \sqrt{(m_0^2 - 2)(\beta(z)/\gamma(z))}}{\sqrt{2} [1 - 2c_0 R(z)]} \left(1 + \tanh \left[\frac{\tau - \tau_c + b_0 R(z)}{1 - 2c_0 R(z)} \right] \right) \right]^{1/2} \times \exp \left\{ i(m_0/2) \ln \left[(3/2\epsilon) \left(1 + \tanh \left[\frac{\tau - \tau_c + b_0 R(z)}{1 - 2c_0 R(z)} \right] \right) \right] + i\Phi(z, \tau) \right\}, \quad (16)$$

where $\alpha = \epsilon/3$ for $\lambda = -1$.

III. NONLINEAR CHIRPING

In this section, we cite an example of the kink-similariton, illustrative of the fascinating features of

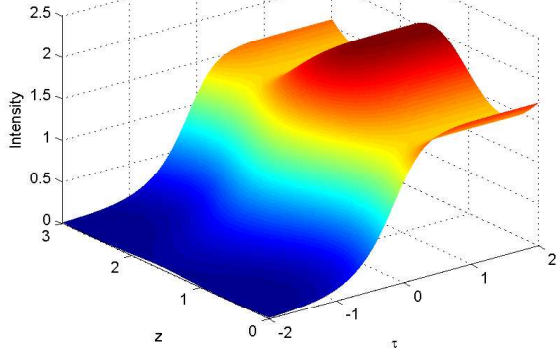


FIG. 1: Surface plot depicting the nonlinear chirping of the kink-similariton solution for $\sigma = 0.5$, $\alpha = 3.45$, $\lambda = -3.34$, and $\epsilon = -2.78$.

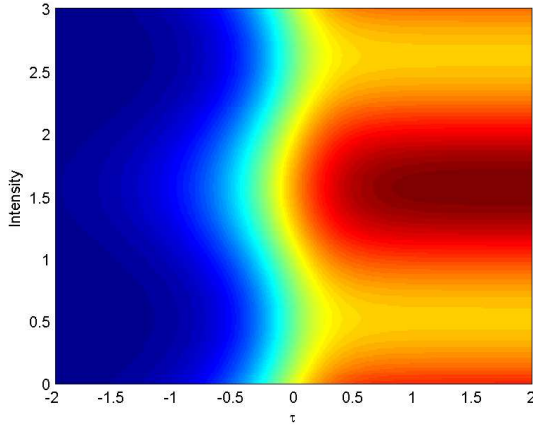


FIG. 2: Density plot depicting the nonlinear chirping of the kink-similariton solution for $\sigma = 0.5$, $\alpha = 3.45$, $\lambda = -3.34$, and $\epsilon = -2.78$.

chirping in optical fibers, by considering the system in which the GVD and the nonlinearity are distributed according to

$$\beta(z) = \beta_0 \cos(\sigma z), \quad \gamma(z) = \gamma_0 \cos(\sigma z), \quad (17)$$

where β_0 , γ_0 and $\sigma (\neq 0)$ are arbitrary constants. In this case, the corresponding gain, and the nonlinear gain of the fiber amplifier are given by

$$g(z) = \frac{\sigma \nu \cos(\sigma z)}{2 - 2\nu \sin(\sigma z)} - \frac{\mu \lambda m_0 \cos(\sigma z)}{(1 - \nu \sin(\sigma z))^2}, \quad (18)$$

$$\chi(z) = \frac{3m_0 \gamma_0}{m_0^2 - 2} \cos(\sigma z), \quad (19)$$

where the parameter $\nu = 2c_0\beta_0/\sigma$ has been introduced for brevity.

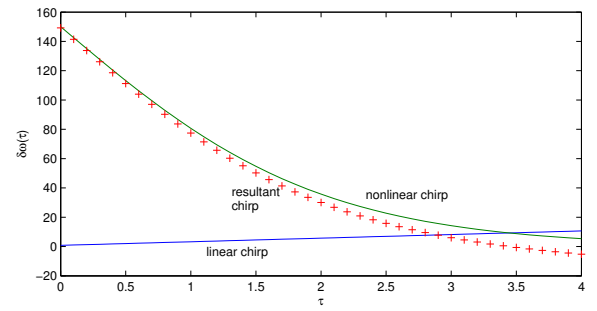


FIG. 3: Plot depicting the linear chirp, nonlinear chirp, and the resultant chirp.

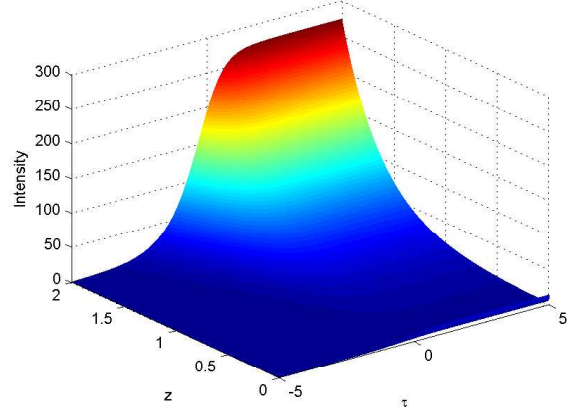


FIG. 4: Surface plot depicting the nonlinear compression of the kink-similariton solution for $\sigma = 1.0$, $\alpha = 3.45$, $\lambda = -3.34$, and $\epsilon = -2.78$.

Hence the amplitude of the similariton pulse is

$$P(z, \tau) = \frac{\sqrt{(m_0^2 - 2)\rho(0)}}{\sqrt{2}(1 - \nu \sin(\sigma z))} \left(1 + \tanh \left[\frac{\tau - \tau_p}{W(z)} \right] \right)^{1/2} \quad (20)$$

where

$$W(z) = \tau_0 [1 - \nu \sin(\sigma z)],$$

and the pulse position τ_p varies with $\tau_p = \tau_c - (b_0\beta_0/\sigma) \sin(\sigma z)$. The resultant chirp consisting of linear and nonlinear contributions are derived as [17]

$$\delta\omega(\tau) = \frac{m_0 \left[1 - \tanh \left(\frac{\tau - \tau_p}{W(z)} \right) \right]}{2W(z)} - b_0 - \frac{2c_0\tau_0}{W(z)} (\tau - \tau_p). \quad (21)$$

We notice that the first term in Eq. (21) denotes the nonlinear chirp that results from the nonlinear gain, while the last two terms account for the linear chirp. The propagation of this chirped pulse has been depicted in Fig. 1 and a density plot of the same in Fig. 2, for various parameter values of τ_0 and $\nu = 0.5$. In Fig. 3, we depict the linear chirp, nonlinear chirp, and the resultant chirp for $z = 0$.

Next, we elucidate the compression problem of the pulse in a dispersion decreasing optical fiber. For the purpose of comparison with Ref. [5, 18], we assume that the GVD and the nonlinearity are distributed according to the following relations

$$\beta(z) = \beta_0 \exp(-\sigma z), \quad \gamma(z) = \gamma_0 \exp(\alpha z), \quad (22)$$

where $\beta_0 \leq 0$, $\gamma_0 \geq 0$, and $\sigma \neq 0$. Then from Eq. (18) the expression for gain can be calculated as

$$g(z) = -\alpha + \nu\sigma \frac{e^{-\sigma z}}{1 - \nu(1 - e^{-\sigma z})} - \frac{\mu\lambda m_0 \beta_0 e^{-\sigma z}}{(1 - \nu(1 - e^{-\sigma z}))^2}. \quad (23)$$

Let us consider the most typical physical situation when the loss in an optical fiber is constant i.e., $\gamma(z)$ is constant. According to Eq. (23), this occurs when $\nu = 1$ and $\alpha > 0$: $g(z) = -\alpha$, hence the gain is negative. It is remarkable that the width of the solutions presented here tend to zero when $z \rightarrow \infty$. We apply the above insights to nonlinear compression of the kink-similariton solution given by Eq. (16). Then the amplitude of the compressed wave is

$$P(z, \tau) = U(z) \left(1 + \tanh \left[\frac{\tau - \tau_p}{W(z)} \right] \right)^{1/2}, \quad (24)$$

where

$$U(z) = \frac{\sqrt{(m_0^2 - 2)\rho(0)\exp[-(\sigma + \alpha)z]}}{\sqrt{2}[1 - \nu(1 - \exp(-\sigma z))]}.$$

And $W(z) = \tau_0[1 - \nu(1 - \exp(-\sigma z))]$. Figure 4 shows that for constant loss the kink-similariton pulse can be compressed to any required degree as $z \rightarrow \infty$, while maintaining its respective original shape.

The analytical findings of the present model suggest potential applications especially in areas such as optical fiber compressors involving asymmetric cores, optical fiber amplifiers nonlinear optical switches, and optical communications. For example, the case $\sigma > 0$, $\alpha = 0$, and $\nu > 1$ implying that the gain

$$g(z) = \nu\sigma \frac{e^{-\sigma z}}{1 - \nu(1 - e^{-\sigma z})} - \frac{\mu\lambda m_0 \beta_0 e^{-\sigma z}}{(1 - \nu(1 - e^{-\sigma z}))^2}. \quad (25)$$

has application to long-haul chirped soliton links where fiber losses are compensated periodically by an amplification system. This long-haul link is based on a distributed dispersion-loss- managed chirped soliton propagation regime and serves as an alternative to loss-managed soliton systems [19]. The main advantage of such systems is the absence of soliton radiation as the kink-solitary waves propagating in this regime are an exact solution of Eq. (1) and hence generate no radiative noise.

V. CONCLUSION

In summary, for a dispersion decreasing fiber amplifier with stimulated Raman scattering term, we have discovered analytically, an exact kink-similariton pulse that undergoes optimal compression, as the length of the fiber $z \rightarrow \infty$. This is the hallmark of this new compression technique based on exact solution of this model. The solution does not develop any side pedestal or deformation in pulse shape as it propagates, making it a promising candidate for this new compression technique. These analytical findings suggest potential applications in areas such as optical fiber compressors, optical fiber amplifiers, nonlinear optical switches, and optical communications.

-
- [1] V. Yakhot, Phys. Rev. Lett. **87**, 234501 (2001).
 [2] N. Korabel and R. Klages, Phys. Rev. Lett. **89**, 214102 (2002).
 [3] D. van der Meer, K. van der Weele, and D. Lohse, Phys. Rev. Lett. **88**, 174302 (2002).
 [4] Z. Xu, L. Li, Z. Li, G. Zhou, and K. Nakkeeran, Phys. Rev. E **68**, 046605 (2003).
 [5] V. I. Kruglov, A. C. Peacock, and J. D. Harvey, Phys. Rev. Lett. **90**, 113902 (2003).
 [6] V. N. Serkin, A. Hasegawa, and T. L. Belyaeva, Phys. Rev. Lett. **98**, 074102 (2007).
 [7] Lei Wu, Jie-Fang Zhang, Lu Li, Qing Tian, and K. Porsezian, Opt. Express **16**, 6352-6360 (2008).
 [8] S. A. Ponomarenko and G. P. Agrawal, Phys. Rev. Lett. **97**, 013901 (2006).
 [9] J. F. Wang, L. Li, and S. T. Jia, J. Opt. Soc. Am. B **25**, 1254-1260 (2008).
 [10] T. Soloman Raju, P.K. Pnaigrahi, and K. Porsezian, Phys. Rev. E **72**, 046612 (2005).
 [11] T. Soloman Raju and P.K. Pnaigrahi, Phys. Rev. A **81**, 043820 (2010).
 [12] R.K. Dodd et al. *Solitons and Nonlinear Wave equations* (Academic Press, Orlando, Fla., 1982).
 [13] G.P. Agrawal and C. Headley III, Phys. Rev. A **46**, 1573-1577 (1992).
 [14] V.I. Kruglov, D. Méchin, and J.D. Harvey, J. Opt. Soc. Am. B **24**, 833-838 (2007).
 [15] S. P. Gorza, N. Roig, Ph. Emplit, and M. Haelterman, Phys. Rev. Lett. **92**, 084101 (2004).
 [16] Z. Li, L. Li, H. Tian, G. Zhou, and K. H. Spatschek, Phys. Rev. Lett. **89**, 263901 (2002).
 [17] M.E. Fermann et al., Phys. Rev. Lett. **84**, 6010-6013 (2000).
 [18] S. Chen and L. Yi, Phys. Rev. E **71**, 016606 (2005).
 [19] A. Hasegawa and Y. Kodama, Phys. Rev. Lett. **66**, 161-164 (1991).

SUPER CONTINUUM GENERATION UNDER EXPONENTIAL SATURABLE NONLINEAR RESPONSE

R. Vasantha Jayakantha Raja^a, K. Nithyanandan^b, T. Uthayakumar^b, and K. Porsezian^b
^bDepartment of Physics, Central University of Tamil Nadu, Thiruvarur – 610 001, India.

^aDepartment of Physics, Pondicherry University, Puducherry – 605 014, India.

rjvraja@yahoo.com, nithi.physics@gmail.com, uthayapu@gmail.com and ponzsol@yahoo.com

Abstract: We theoretically investigate the supercontinuum generation (SCG) with the effect of exponential saturable nonlinearity response in liquid-core photonic crystal fibers (LCPCF). We also compare the achieved spectral broadening with that of the conventional type of saturable nonlinear response.

1. INTRODUCTION

The Supercontinuum (SC) is the generation of intense ultrafast broadband high coherent pulses spanning over a few octaves which emerge as the technology of choice for a future generation of broadband source [1,2]. With the rapid advancement in photonic crystal fiber (PCF) technology, SC gains momentum and evolves as one of the most elegant and dramatic effect in optics with a wide range of potential applications in various fields such as frequency metrology, biomedical sensors, optical coherence tomography, wavelength division multiplexing, etc. SCG is typically achieved by two mechanisms, namely, soliton fission (SF) and modulation instability (MI). In the case of soliton fission, the spectral broadening is governed by the transformation of the pump pulse into higher order solitons which break up into N fundamental soliton. The resulting fundamental solitons emit dispersive wave in the normal GVD and achieve phase matching at a specific frequency in the presence of third order dispersion, thereby transfers energy between the soliton and dispersive radiation and completes the spectrum. Latter is the SCG through MI, where pulse breaking and the broadening of the spectrum occurs through noise driven dynamics [3].

Following the introduction about SCG, we are moving on to the objective of the paper by providing a glimpse of the research activities on the SCG in PCF and the motivation of us to go for this problem. SCG through soliton fission is achieved for the first time by Husakou et al., Soon then the concept of soliton fission revolutionized the broadband source and stands out to be the best method for achieving SCG. This is attributed to the fact that the SF route of producing broadband spectrum is of superior spectral purity with high coherence and flat spectrum, which is proven to be impossible by any of the known method including the familiar MI process.

This makes sense to go for SF process instead of the conventional MI process to generate broadband spectrum. In recent times, the concept of saturated nonlinearity has deserved much interest due to its inherent nature in all material and owing to its high

power operation [4]. Recently, Vasanth et. al., analyzed the concept of MI induced SCG with the incorporation of saturable type nonlinearity. Where the authors have used the MI route of achieving broadband spectrum and concluded that MI results in broadband spectrum with poor noise figure. Thus, we in the current paper adopt the SF technique to achieve SCG with saturable nonlinear response. We compare the quality of the generated SCG spectrum with the MI counterpart for the insight picture of SCG through SF.

2. Theoretical Model

The mechanism leading to SCG can be understood by solving the modified nonlinear Schrodinger equation (MNLSE) in the presence of saturable nonlinear effect given by

$$\frac{\partial U}{\partial z} + i \frac{\beta_2}{2} \frac{\partial^2 U}{\partial t^2} - \frac{\beta_3}{6} \frac{\partial^3 U}{\partial t^3} - i \frac{\beta_4}{24} \frac{\partial^4 U}{\partial t^4} - i \gamma \frac{|U|^2}{1 + \Gamma |U|^2} U$$

$U(z,t)$ is the initial pulse envelope in the co-moving frame of reference with pulse centered at frequency ω_0 . β_n and γ are the dispersion coefficient and nonlinear parameter, respectively. Γ is the saturation parameter ($\Gamma = 1/P_s$). P_s is the saturation power of the nonlinear medium.

2.1 Supercontinuum generation through Soliton fission:

Fig.1 SCG for the case of unsaturated kerr nonlinear response with parameters $\beta_2 = -0.01 ps^2/m$, $\beta_3 = -0.00002 ps^3/m$, $\beta_4 = 2.3 \times 10^{-8} ps^4/m$, $P = 10W$, $\gamma = 12.2 W^{-1} m^{-1}$

Fig.1 SCG for the case of SNL response with parameters $\beta_2 = -0.01\text{ps}^2/\text{m}$, $\beta_3 = -0.00002\text{ps}^3/\text{m}$, $\beta_4 = 2.3 \times 10^{-8}\text{ps}^4/\text{m}$, $P = 10\text{W}$, $\gamma = 12.2\text{W}^{-1}\text{m}^{-1}$

To investigate SCG, we numerically solved Eq. (1) using split step Fourier method with initial envelope of the soliton at $z = 0$ given by $U(0, t) = \sqrt{P_0} \text{sech}(t)$. Numerical simulations are carried out for the input pulse at central wavelength $\lambda_0 = 1.04 \mu\text{m}$. The fiber parameters are calculated using scalar effective index method. The pulse propagation in the anomalous dispersion regime is characterized mainly by the higher soliton formation with a soliton order N in the form [5]

$$N^2 = \frac{\gamma P_0 \tau_0^2}{|\beta_2|}$$

The higher order soliton are degenerate unstable solutions and tend to decay by virtue of the higher order dispersion.

The analyze of the spectral broadening mechanism can be illustrated in different stages [6]. In the first stage of the propagation the pulse is compressed and the strong temporal contraction leads to the maximum expansion of the soliton spectrum. The broadened spectrum reaches the resonant radiation frequency of a dispersive wave on the blue side. Further propagation down the fiber leads to the break-up of the higher-order soliton into fundamental single solitons, due to the perturbation from the higher order dispersive and nonlinear effects, especially the third order dispersion (TOD) and stimulated Raman effect. The fundamental soliton leads to the emission of non-solitonic radiation at a specific frequency determined by the third order dispersion [7]. Every time when the soliton spectrum overlaps the resonant frequency of the dispersive wave, there occurs the resonant power transfer between the soliton and the non-solitonic radiation. Then the further spectral broadening is taken care of by the four wave mixing process between the fundamental soliton and the blue shifted radiation. Further propagation down the fiber does not lead to broadening of the spectrum proportionally rather saturates after certain distance.

2.2 Impact of saturable nonlinearity in the SCG

Fig(1) illustrates the pulse broadening through SF process at difference length of the fiber without saturable nonlinearity. It is evident from the figure that one can achieve broadband spectrum at length approximately 0.6 m. Fig(2) portraits supercontinuum generation in high nonlinear fiber with saturable nonlinear response where the spectrum broadened only at a distance of 2 m. Comparing fig 1 and 2, one can conclude that the incorporation of saturable nonlinear response suppresses SCG, this is attributed to the fact that the inclusion of SNL impart additional nonlinear phase shift and thereby requires further propagation down the fiber to satisfy the phase matching condition required to achieve four-wave mixing. Thus the SCG can only be achieved in the case of long fiber.

For better insight into the picture of MI-SCG, we have investigated the evolution of MI for various saturation power as in Fig. 3. In the operating conditions of saturated nonlinearity, the optical modulational frequency not only varies with the input power of pulse but also saturation power as illustrated in Fig. 3. It is observed that the evolution of MI in is certainly suppressed by decreasing saturation power, which implies that while increasing the SNL the MI-SCG gets suppressed. Fig. 3 depicts spectral evolution of MI-SCG in the presence of SNL with different saturation power.

Fig. 3 Variation of spectral output with respect to the saturation power.

Although SNL suppresses the SCG but the output spectrum after the soliton period is fairly broad spanning from 800 to 1500 nm and the spectral density at the peak varies merely less than 10 -dB over the SCG output.

3 COHERENCE ANALYSIS

An important consequence of the noise induced fluctuation is the coherence degradation, which actually determines the quality of the supercontinuum generation. In order to analyze the coherence of the resulting broadband spectrum, a shot-to-shot coherence analysis is performed. The degree of spectral phase stability is qualitatively calculated by the following expression

Our calculation yields fairly a coherent spectrum with coherence value of 0.93, which is regarded as near to the upper coherence limit. Thus ensure that SF means of generating a broadband spectrum result in the highly coherence supercontinuum output.

Conclusion

In summary, we numerically investigated the SCG using SF for a saturable medium by solving modified nonlinear Schrodinger equation. Numerically, we observed that saturable nonlinearity suppress the SF and leads to spectral broadening at longer distance of propagation. In order to analyze the quality of the spectrum, coherence analysis is performed which leads to a fairly coherent spectral output.

Acknowledgements:

KP wishes to thank the DST, DAE-BRNS, and UGC, Government of India, for the financial support through major projects.

ACKNOWLEDGEMENT

KP thanks, DST, DAE-BRNS, and UGC, Government of India, for the financial support through major projects.

REFERENCES

- [1] J.M.Dudley,Goery Genty, and Stephane Coen, "Supercontinuum generation in photonic crystal fiber", *Rev. Mod.Phys.* **78**, 1135-1184 (2006)
- [2] A.V. Husakou and J. Herrmann, "Supercontinuum Generation of Higher-Order Solitons by Fission in Photonic Crystal Fibers" *Phys. Rev. Lett.* **87**, 203901(1-4) (2001).
- [3] R. Vasantha Jayakantha Raja, K. Porsezian, and K. Nithyanandan, "Modulational-instability-induced supercontinuum generation with saturable nonlinear response", *Phys. Rev. A*, **82**, 013825 (1-6) (2010).
- [4] P. Tchofo Dinda and K. Porsezian, "Impact of fourth-order dispersion in the modulational instability spectra of wave propagation in glass fibers with saturable nonlinearity,"*J. Opt. Soc.Am. B* **27**, 1143-1152 (2010).
- [5] A. Demircan and U. Bandelow, "Analysis of the interplay between soliton fission and modulation instability in supercontinuum generation", *Appl. Phys. B.* **86**, 31-39 (2007).
- [6] R. Vasantha Jayakantha Raja, Anton Husakou, Joachim Hermann, and K. Porsezian, "Supercontinuum generation in liquid-filled photonic crystal fiber with slow nonlinear response", *J. Opt.Soc. Am. B*, **27**, 1763 (2010).
- [7] Samudra Roy, S. K. Bhadra, and Govind P. Agrawal, "Dispersive waves emitted by solitons perturbed by third-order dispersion inside optical fibers", *Phys. Rev. A*, **79**, 023824 (2009)

TWO-CRYSTAL, OPTICAL PARAMETRIC OSCILLATOR TO GENERATE CW, DUAL-WAVELENGTH RADIATION WITH ARBITRARY TUNABILITY

G. K. Samanta,^{1,2,*} and M. Ebrahim-Zadeh^{2,3}

¹Theoretical Physics Division, Physical Research Laboratory, Navarangpura, Ahmedabad 380 009, India

²ICFO-Institut de Ciències Fòtiques, Mediterranean Technology Park, 08860 Castelldefels, Barcelona, Spain

³Institució Catalana de Recerca i Estudis Avançats, Passeig Lluís Companys 23, Barcelona 08010, Spain

*corresponding author: gsamanta@prl.res.in

Abstract: We report a novel generic design for an independently tunable, dual-wavelength source based on cw singly-resonant-parametric-oscillators (SROs), providing two signal waves of arbitrary tuning. Using this source we generate two distinct wavelengths with frequency difference 0.556THz.

1. INTRODUCTION

Coherent light sources of arbitrarily tunable dual-wavelength radiation are of great interest for many applications including spectroscopy. While optical parametric oscillators (OPOs) are now established as versatile and practical sources of widely tunable radiation, the generation of a signal-idler pair of truly arbitrary wavelength pairs is not possible due to constrained phase-matching and energy conservation. Here, we present a novel and generic approach for the generation of two truly independently tunable wavelengths, which are unbound by energy conservation and can be independently controlled to provide any arbitrary value using a simple and compact four mirror ring-cavity cw singly-resonant OPO (SRO). Such a novel system can be used to generate tunable THz radiation down to 0.55 THz.

2. EXPERIMENTAL SETUP

The cw two-crystal SRO (T-SRO), as shown in Fig. 1, is designed in a compact ring cavity comprising four concave mirrors, M_1 - M_4 , of same curvature ($r=10$ cm), with high reflectivity ($R>99\%$) for the signal (890-1000 nm) and high transmission for idler and pump (532nm) [1]. Two identical nonlinear crystals X_1 and X_2 (30-mm-long MgO:spPLT crystal, single grating, $\Lambda =7.97$ μm [1], housed in separate temperature oven) are placed at the two foci of the cavity. The T-SRO uses a double-pumping configuration, where both the crystals are pumped separately using Pump 1 and Pump 2 at 532 nm. The phase-matching condition of the crystals is controlled independently resulting arbitrary wavelength tunability. Both the pump beams are focused at the center of the crystals to identical beam radius of $w_{0p}\sim 31$ μm ($\xi=1$).

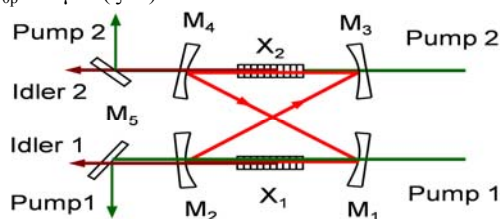


Fig. 1. Experimental design of the two-crystal SRO.

3. RESULTS AND DISCUSSIONS

Although both the crystals are coupled in a single cavity, due to independent pumping, their output characteristics are independent. To verify the independent performance of the output, we pumped both the crystals at same green power (Pump1=Pump2=5 W) and measured the signal spectra at different crystal temperatures, with the typical results shown in Fig. 2. At $T_1=77^\circ\text{C}$ and $T_2=110^\circ\text{C}$, the dual-SRO has resonant signals at 939 nm (idler 1227.3 nm) and 971 nm (idler 1176.7 nm), respectively, with a frequency difference of 10.5 THz. If we increase T_1 and decrease T_2 to bring the oscillator to work as a single SRO, then different combinations of (T_1 , T_2) result in resonant signals of frequency difference 7 THz (82°C , 104°C) and 1.66 THz (88°C , 96°C). Further, increase of T_1 to 91°C and decrease of T_2 to 93.5°C results in coherently-coupled resonant signals at a single wavelength (955 nm), which is verified from the appearance of the Raman shift at ~ 17 nm (~ 204 cm^{-1}) due to the high intracavity power. The same performance can be obtained across the entire SRO tuning range (850-1430 nm) [1] showing the versatility of this design. The difference in crystal temperature ($T_2-T_1=2.5^\circ$) to generate same signal wavelength can be attributed to the difference in crystal heating configurations. Other results including closest possible wavelength pair, power scaling, power stability, theoretical calculations and entire device characterization will be presented.

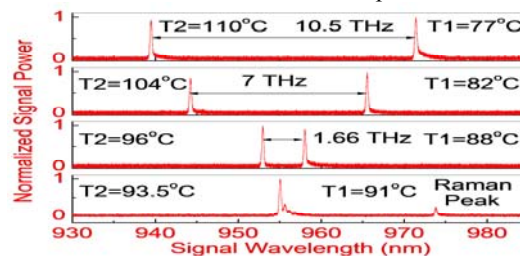


Fig. 2. Signal spectra of the T-SRO at different combination of the crystal temperatures, T_1 and T_2 .

REFERENCES

- [1] G. K. Samanta, G. R. Fayaz, and M. Ebrahim-Zadeh, *Opt. Lett.* **32**, 2623-2625 (2007).

MICRO-OPTO-ELECTRO-MECHANICAL SYSTEMS FOR BIOSENSOR APPLICATION

Srinivas Talabattula, Malathi Sathish and Nivesh Mangal
ECE Dept, Indian Institute of Science, Bangalore
tsrinu@ece.iisc.ernet.in

Abstract: Recently biological applications of micro-opto-electro-mechanical systems have attracted attention. In this paper, a brief review of the topic will be followed by recent work on integrated optic devices such as ridge waveguide and micro ring resonator based optical biosensors. The main idea is to use the biomaterial as cladding layer and measure the change in effective refractive index. In a typical case the response of a SOI slab with Blood Clad with varying Glucose levels is studied and the sensitivity is found 3.2×10^{-2} RIU and 2.9×10^{-1} RIU respectively in the case of bulk sensing. In the case of MRR the sensitivity of 5 μm and 20 μm radius resonators turn out to be 32.5 nm/RIU and 17.5 nm/RIU respectively. Experimental work on these devices will be briefly mentioned.

1. INTRODUCTION

The development of biosensors started in the year 1962 with the demonstration of enzyme electrodes by L.C.Clark and C.Lyons [1]. A bio sensor is a self-contained integrated device, which is capable of providing specific quantity or semi-quantitative analytical information using biological recognition element (biochemical receptor) which is retained in direct spatial contact with a transduction element. They can detect chemical or biological species or a micro organism [2]. They are used to monitor the changes in the in vivo concentration of an endogenous species as a function of a physiological change induced internally or by invasion of a microbe. Or even more recent interest is the use of biosensors to detect toxins, bacteria and viruses because of the danger posed by chemical and biological terrorism. At present, the global market for biosensors is about \$7 billion, with home-use health monitoring devices (e.g., glucose biosensors and pregnancy test strips) being dominant. These devices provide accurate results in no time and at low cost. Evolution of biophotonics- an interdisciplinary field could be schematically represented as shown in Fig.1.

- Clinical diagnosis
- Drug development
- Environmental monitoring
- Food quality control

Biosensors consist of two important features: molecular recognition element and the signal transduction mechanism. The molecular recognition element can take the form of a biomolecules (antibody, enzyme or nucleic acid), biological system (membranes, tissues or whole cells), or biomimetic (synthetic bioreceptors) and imparts specificity to the system. The signal transduction mechanism is the process by which the biochemical event is converted into a measurable signal, the intensity of which is proportional to the analyte concentration. A biosensor in general utilizes a biological recognition element that senses the presence of an analyte and creates a physical or chemical response that is converted by a transducer to a signal. Sensors utilizing electrochemical response succeeded in the field of microsensor. Later fiber optics and integrated optics sensor evolved and became alternative for many applications.

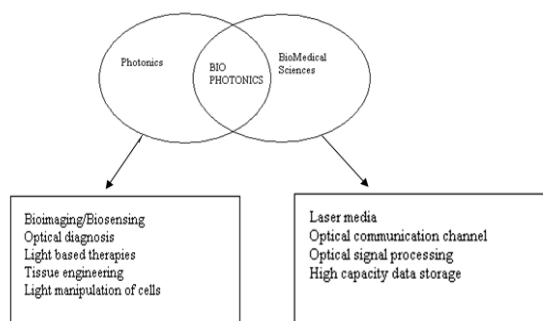


Fig.1. Biophotonics- Engineering solution for Medical Applications

Biosensors thus find a wide range of applications:

2. INTEGRATED OPTIC SENSORS

Planar dielectric waveguides have advantage over Surface Plasmon Resonance (SPR) devices for label free detection, which lies in the enhanced degrees of freedom for sensor design. In both technologies the penetration depth of guided waves at the interface is directly related to the geometrical extent of the measurement volume where sensitivity is high. For SPR system the typical penetration depth is around 200nm[3]. In the case of planar dielectric waveguides, this property could be chosen by design enhancing the application fields to the detection of relatively large objects in the micrometer range such as cells [4].

Silicon photonics wire evanescent field sensors have the highest response to molecular binding event compared with other waveguide

platforms. SOI wafer is an interesting material for high density photonic integrated circuits. Aggressive scaling is possible with SOI technology owing to its extremely high refractive index contrast between the silicon core ($n=3.5$) and silica ($n=1.45$). The waveguide size can be shrunk down to sub micron cross section, while maintaining single mode propagation at 1.3-1.5 μm telecommunication wavelength.

In an optical guiding structure, a shift of propagating optical mode effective index can be induced by two different phenomena:

(1) *Homogenous Sensing*: In this category, effective index of a propagating optical mode changes with a uniformly distributed analyte extending over a distance well exceeding the evanescent field penetration depth. The sample serves as the waveguide cover.

(2) *Surface Sensing*: In the case of surface sensing, the analyte is bound to the surface of the waveguide. The effective index of an optical mode changes with the refractive index as well as the thickness of an adlayer. A thin layer of adsorbed or bound molecules that are transported from liquid or gaseous medium serving as waveguide cover is referred as an Adlayer.

3. WAVEGUIDE BASED BIOSENSORS

A schematic diagram of a slab waveguide biosensor is showed in fig 2. The upper cladding will be the solution, which contains the specific target molecules to be identified. When the analyte interacts with the waveguide and modify the dielectric constant, the modal power contained in the surface volume changes. The waveguide core thickness can be reduced to a point where the mode is less confined. Evanescent tail of the waveguide interacts with solution and the effective refractive index of the mode changes accordingly. We have analyzed the waveguide response as a Homogeneous sensor [5-6].

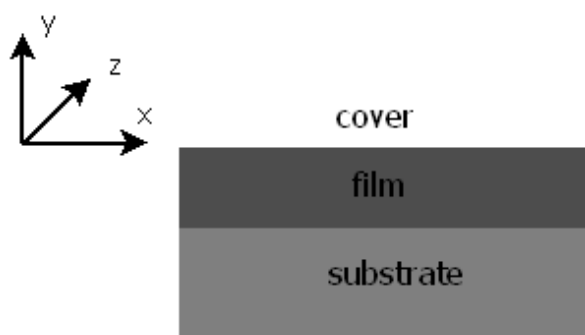


Fig.2.Schematic of a SOI Slab waveguide biosensor-homogeneous sensing

Slab waveguide sensitivity for TE and TM modes are calculated using Finite Difference Mode solver – 3.2×10^{-2} RIU and 2.9×10^{-1} RIU respectively in the case of bulk sensing. Rib waveguide sensitivities are 9.107×10^{-3} and 6.6071×10^{-3} RIU for the TE and TM modes. In the case of Strip waveguide, we obtained

sensitivity of 1.3929×10^{-1} RIU for TE mode and 4.6821×10^{-1} RIU for TM mode. Using a numerical mode solver, we analyzed the waveguide response to the glucose concentration variations. Fig.3. depicts a bulk sensor with strip waveguide configuration. The strip waveguide has a dimension of $500\text{nm} \times 220\text{nm}$. A rib structure would possess two thin slabs of silicon on the top of silica clad. The rib waveguide is optimized which has a width of 500nm, slab height of 500nm and etch depth of 500nm.

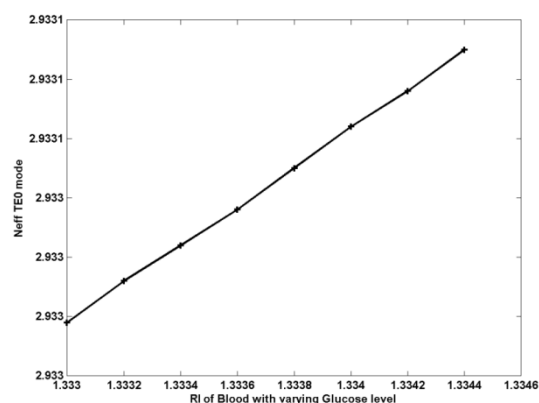


Fig.3.Response of a SOI slab with Blood Clad with varying Glucose level

4. MICRO RING RESONATOR BASED SENSORS

Micro-ring resonator based compact devices make label-free bio-sensing possible with high throughput and sensitivity and enabling various implementations of integrated optic litmus test sensor chips. In bio-sensing applications, waveguides should be long enough to maximize the interaction between the optical signal and biomaterial coating. This acts as a bottleneck for miniaturization of the sensor. Resonator structure overcomes this by allowing longer photon life in the ring that facilitates the evanescent field to interact strongly with cladding material. Whispering gallery modes (WGM) form due to the total internal reflection at the curved boundary surface. This has an evanescent field (EF) outside the ring with a penetration depth of $\sim 100\text{nm}$.

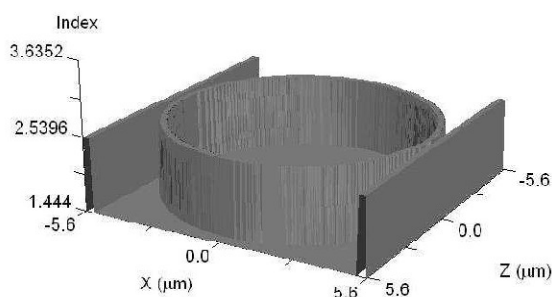


Fig.4.Refractive index profile of a microring resonator

Microring resonator response is simulated both by analytical approach and by RSOFT™ Beamprop package. Refractive index profile of a microring resonator is shown in fig.4.

A homogeneous label-free biosensor design on SOI strip waveguide based ring resonator was simulated and analyzed for the rings of radii 5 μm and 20 μm . The gap of 200 nm was analyzed with scalar approach while 300 nm gap optimization was achieved with full-vectorial approach for the device. The primary concern of a sensor design is the quality factor of the ring resonator. The calculated values of Q factor, Free Spectral range and Wavelength shift are tabulated in Table.1 and Table.2. for two different gaps between bus waveguide and ring structures.

Parameters of ring resonator device for 5 and 20 μm radius and 200 nm gap.

Parameters	Radius = 5 μm		Radius = 20 μm	
	Air	Bio-layer	Air	Bio-layer
Lumped Cross-Coupling Coefficient($/\mu\text{m}$)	0.1637	0.1787	0.1644	0.1794
FWHM(nm)	0.17	0.16	0.085	0.09
Resonant Wavelength(nm)	1574	1563	1555	1553
Quality Factor	9258.82	9768.75	18294.11	17255.5
Free Spectral Range(nm)	31	30	8	7
Wavelength Shift(nm)	11		2	

Table.1. With a gap of 200nm between bus waveguide and ring structure

Parameters of ring resonator device for 5 and 20 μm radius and 300 nm gap.

Parameters	Radius = 5 μm		Radius = 20 μm	
	Air	Bio-layer	Air	Bio-layer
Lumped Cross-Coupling Coefficient($/\mu\text{m}$)	0.2708	0.23701	0.2544	0.21935
FWHM(nm)	0.56	0.4	0.16	0.13
Resonant Wavelength(nm)	1559	1572	1554	1561
Quality Factor	2784	3930	9712.5	12007.69
Free Spectral Range(nm)	40	37	10	9
Wavelength Shift(nm)	13		7	

Table.2. With a gap of 300nm between bus waveguide and ring structure

Though temperature compensation was not taken into account, any anomaly in the results can be rectified by considering a thermo optic ring resonator in parallel with the device which can provide the detuning offset to calibrate the original device. The device will be fabricated and tested wherein bending loss calculations would be instrumental in analyzing the theoretical and practical sensitivity of the device.

The sensitivity of 5 μm and 20 μm radius resonators turn out to be 32.5 nm/RIU and 17.5 nm/RIU respectively [7].

We have fabricated a ring resonator of 20 μm radius at the Nanofabriaction facility , IITB-Mumbai using E-beam lithography. The SEM picture of the fabricated device is shown in fig.5.The process of characteization is underway using Near Field Scanning Optical Microscopy (NSOM) initially with

air cladding, to find the resonant wavelength λ_{res} . when a biolayer is coated on the ring surface, the resonant wavelength shifts depending on the refractive index of the biomolecules.

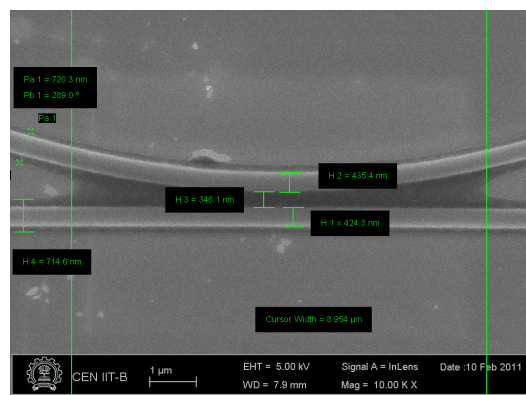


Fig.5.SEM image of fabricated Microring resonator with a gap of 300nm between bus and ring waveguide

5. REFERENCES

- [1] Clark, L.C., Lyons, C., “Electrode Systems for Continuous Monitoring in Cardiovascular Surgery”, Ann. NY Acad. Sci. 1962, 102, 29-45.
- [2] Vo-Dinh,T.,Allain,L. “Biosensor for medical application”,Biomedical Photonics Handbook, Vo-Dinh,T., Ed, CRC press, 2003.
- [3] W.Lukosz, “Principles and sensitivities of integrated optical and surface plasmon sensor for direct affinity sensing and immunosensing,” Biosensors and Bioelectronics, vol.16, pp215-225,1991
- [4] Robert Horvath, “Optical waveguide sensor for on-line monitoring of bacteria,” Optics letters, vol.28, Issue .14, 2003.
- [5] S.Malathi, K.E.Rani,R.Usha and T.Srinivas, “Design and Analysis of SOI based Rib Waveguide Biomedical Transducer”,IEEE ICP 2010, 5-7,July,2010.
- [6] S. Malathi, Usha Raghunath, and T. Srinivas, “Ultra-compact SOI microrings for sensing applications,” Proc. Photonic Global Conference, Singapore (2010).
- [7] S.Malathi, M.Nivseh, A.S.Shafeek,V.H.Rajini and T.Srinivas, “SOI strip waveguide microring resonator for homogeneous biosensing, Proc of SPIE Vol. 8129, SPIE Optics and Photonics ,21-25,Aug,2011.

FEMTOSECOND SPATIOTEMPORAL CONTROL APPROACH TO MICROSCOPIC SUPER-RESOLUTION AND OPTICAL TRAPPING

Debabrata Goswami

Indian Institute of Technology Kanpur, Kanpur -208016
dgoswami@iitk.ac.in

Abstract: Obtaining a resolution beyond the diffraction limit is presently a hot topic in the microscopy research. We explore the simultaneous control of internal and external (i.e. centre-of-mass motion) degrees of freedom, which require the coupling of various control parameters to result in the spatiotemporal control. We discuss some recent studies pursued in our group on several control experiments with important applications in (one-photon) confocal and two-photon fluorescence laser-scanning microscopy and optical trapping with laser tweezers.

1. INTRODUCTION

Pioneered by Arthur Ashkin and his co-workers, optical tweezers use single tightly focused laser beam [1] to trap as well as to manipulate micron to nano sized dielectric and biological particles, which have emerged as a very effective tool to directly measure very tiny forces (\sim pN) present in various physical, chemical and biological systems. Trapping of small particles using CW lasers needs a very high power that in turn can damage the sample. On the other hand, femtosecond pulses, due to their fleeting ultrafast existence, have gigantic peak power that generates ponderomotive force on the particle that results in stable 3D trapping of small nanoparticles at a much lower average power [2].

In microscopy, there are presently two popular approaches to address the issue of obtaining super-resolution (i.e., a resolution beyond the diffraction limit): one is to make new fluorophores having a very high two-photon absorption cross section, so that we get better resolution; and the second is to selectively suppress or excite one of the fluorophores by coherent quantum control using laser pulse shaping [3]. We present an alternate approach of selective spontaneous fluorescence suppression in one of the fluorophores present in the sample through wavepacket interference using pulse-pair or pulse-train excitation with application in microscopy [4], an effect prevailing even after the fluorophore coherence timescale.

2. RESULTS AND DISCUSSIONS

We use a high repetition rate (HRR) femtosecond Ti:Sapphire laser operating 76 MHz and tunable between 770-900 nm for our all our experiments reported here. We take one-color pulse-pair scheme from a Mach-Zancker interferometer where we control the time delay between the two pulses to selectively suppress the two-photon fluorescence of one fluorophore [4]. Figure 1 shows selective fluorescence suppression of Texas Red dye compared to DAPI fluorophore present in slides of bovine pulmonary artery endothelial (BPAE) cells. Detailed study of this two-photon fluorescence suppression is due to one-color stimulated emission depletion.

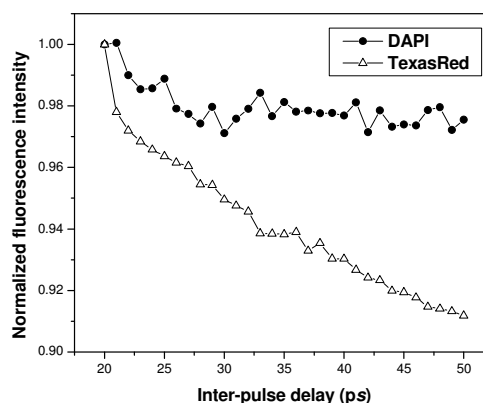


Figure 1: Selective two-photon fluorescence suppression for Texas Red compared with DAPI under pulse-pair excitation

For the HRR femtosecond optical tweezers, the distinguishing feature of the fleeting existence of the pulsed laser would be discussed to show how HRR optical tweezers effectively work. We discuss the detailed study of the effect of HRR femtosecond pulses in the tweezing action.

ACKNOWLEDGEMENT

The author wishes to acknowledge his graduate students: A.K. De and D. Roy for experiments related this work and the funding agency: MHRD for continued support on furthering this research.

REFERENCES

- [1] A. Ashkin, J. M. Dziedzic, J. E. Bjorkholm, S. Chu, "Observation of a single-beam gradient force optical trap for dielectric particles", *Opt. Lett.*, **11**, 288 (1986).
- [2] A.K. De, D. Roy, A. Dutta, D. Goswami, "Stable optical trapping of latex nanoparticles with ultrashort pulsed illumination", *Appl. Opt.*, **48**, G33 (2009).
- [3] D. Goswami, "Optical pulse shaping approaches to coherent control", *Phys. Rep.*, **374**, 385 (2003).
- [4] D. Goswami, "Towards controlling molecular motions in fluorescence microscopy and optical trapping: a spatiotemporal approach", *Intl. Rev. Phys. Chem.*, **iFirst**, 1-25 (2011).

Biosensor based on plasmon resonance energy transfer for real time H₂O₂ detection

S. Dutta-Gupta⁽¹⁾, G. Suarez⁽¹⁾, C. Santschi⁽¹⁾, L. Juillerat⁽²⁾ and O. J. F. Martin⁽¹⁾

⁽¹⁾EPFL, Lausanne, Switzerland;

⁽²⁾IUP, CHUV, Lausanne, Switzerland
shourya.duttagupta@epfl.ch

Abstract: We investigate a new optical biosensor for the detection of H₂O₂ based on absorption enhancement of Cytochrome *c* molecules with gold nanoparticles. H₂O₂ is an important biomolecule since it gives an indication of the oxidative stress in cells. Using this technique we investigate the oxidative stress generated in the mammalian cells caused by various external agents such as nanoparticles. We further demonstrate real time monitoring of H₂O₂ generated by living cells.

1. INTRODUCTION

Plasmonic sensing has been extensively explored for the detection of various biomolecules and biological species in real time and with high specificity. Even though standard LSPR sensing techniques using different plasmonic nanoparticles give highly sensitive specific real time information, they suffer from the drawback that the analyte to be sensed must cause enough refractive index change to be measurable. To circumvent this limitation, other techniques like surface enhanced raman spectroscopy (SERS), surface enhanced infrared absorption spectroscopy (SIERA), fluorescence enhancement using plasmonic structures etc... have been used which do not rely on the shift of the plasmon resonance [1,2]. Liu *et al.* [3] showed that the absorption spectrum of free unbound Cytochrome *c* (Cyt *c*) could be measured in the scattering spectrum of the gold nanoparticle (AuNP) when the distance between them was in the order of a few nanometers. The explanation given was that the absorption of Cyt *c* was enhanced due to the local field enhancement at the plasmon resonance and thus they named the phenomenon plasmon resonance energy transfer (PRET). It should be noted that in the paper by Liu *et al.* the Cyt *c* was not bound covalently to the surface of the AuNP thus the distance between gold and Cyt *c* was not fixed, which is a critical parameter in any energy transfer process. Recently, it was shown that the absorption spectrum of Cyt *c* could also be seen in the scattering spectrum of a dielectric medium which possessed no plasmonic resonances. Thus it is not immediately clear what exactly is PRET and what are the necessary conditions for having PRET.

In the present paper Cyt *c* was chosen as the absorbing molecule (acceptor in PRET process) as it exhibits different absorption spectrum in oxidized and the reduced forms as shown in Fig. 1. The change between the reduced to the oxidized form of Cyt *c* can be brought about by reaction with H₂O₂. Thus by monitoring the absorption of Cyt *c* one can detect the level of H₂O₂ in the surrounding. H₂O₂ is an important biomolecule (reactive oxygen species) because it is

associated with various processes like signaling cascades, protein hydrolysis and maintenance of the redox homeostasis in a cell. An imbalance in the level of H₂O₂ to anti-oxidants is known as oxidative stress. Oxidative stress can be observed in unhealthy and diseased cells. For example in diseases like cancer, Parkinson's, Alzheimer's etc..., there is overproduction of H₂O₂. Thus detection of H₂O₂ becomes important from a medical perspective. Standard plasmonic sensors cannot be used for detection of H₂O₂ because the refractive index change caused due to H₂O₂ is negligibly small and does not cause a measurable shift in the resonance peak.

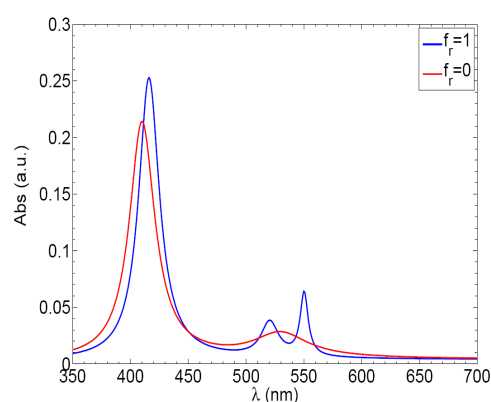


Figure 1. Absorption spectrum of reduced (blue, $f_r=1$) and oxidized (red, $f_r=0$) Cyt *c*.

The experimental results obtained by Liu *et al.* suggest that PRET originates from near field interactions between the plasmon resonance of the AuNP and the absorption bands of Cyt *c*. However, no extensive theoretical investigations have yet been performed on the parameters affecting the energy transfer between Cyt *c* and AuNP. In this paper, we first theoretically study PRET using Green's function formalism and study its dependence on different parameters. Then we elucidate how these two (PRET and enhanced absorption from a scattering medium) methods can be used for detection of H₂O₂ in a biological environment.

2. METHODS

The green's function method was used for studying the interaction between AuNP and Cyt *c* [4]. We approximate Cyt *c* and AuNP to be point dipoles (see Fig. 2) with realistic polarizabilities. AuNP can be approximated as a dipole since for small particles the energy transfer is mediated by the dipole mode of the localized plasmon and higher order modes do not play a major role. Under these assumptions the field at any point in space can be given by the following equation,

$$\vec{E}_i = \vec{E}_i^0 + \sum_{j, j \neq i} \vec{G}_{ij} k_0^2 \Delta \epsilon_j V_j \vec{E}_j + \vec{M}_i k_0^2 \Delta \epsilon_i \vec{E}_i - \vec{L} \frac{\Delta \epsilon_i}{\epsilon_b} \vec{E}_i,$$

where G_{ij} is the green's tensor, $\Delta \epsilon_j$ is the dielectric constant difference between the element j and the background (ϵ_b), V_j is the volume of the j^{th} element and E_i^0 is the electric field at the i^{th} element due to the incident plane wave. In the simulation results presented in this paper, the size of the AuNP and Cyt *c* is taken to be 50 nm and 3.4 nm respectively. The scattering spectra of AuNP is calculated by evaluating

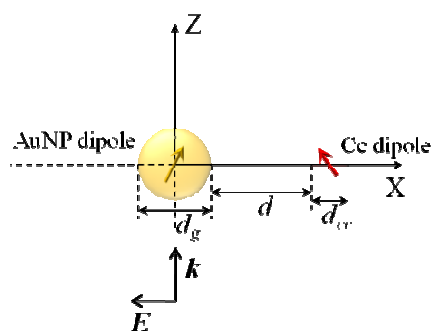


Figure 2. Configuration used in the simulations.

the integral of the intensity of the scattered electric field on a spherical surface with radius 10 microns. The dielectric function of Cyt *c* was modelled using the following equation,

$$\epsilon_{oxi/red} = \epsilon_w + \sum_{i=1}^3 \frac{f_{pi}^2}{f_{oi}^2 - f^2 - i\gamma_i f},$$

where the parameters f_{pi} , f_{oi} and γ_i represent the resonance strength, frequency and damping respectively of the different resonances. f is the frequency and ϵ_w is the dielectric constant of water ($\epsilon_w=1.7689$; since Cyt *c* is generally dissolved in water). For reduced (oxidized) Cyt *c* the Q-band(s) are at 550 nm and 520 nm (530 nm). It should be noted that the parameter f_{pi} is dependent on the concentration of Cyt *c* present.

3. RESULTS

Considering the effect of distance of separation (d) of the two dipoles, it is seen from Fig. 3 that the

absorption of reduced Cyt *c* is enhanced in the near field of the nanoparticle, i.e. when $d < 40$ nm (we obtain analogous results for oxidized Cyt *c* (not shown here)). It can be seen that when the molecule is placed directly on the surface of the gold nanoparticle i.e. $d = 0$ nm, the absorption of reduced Cyt *c* is enhanced by a factor of almost 20. Another interesting observation is that when the separation distance is smaller than 7 nm, the

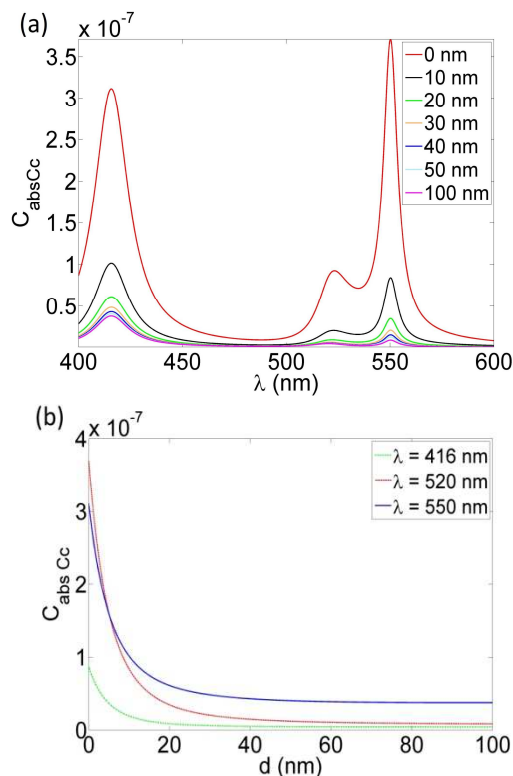


Figure 3. (a) Absorption spectrum of reduced Cyt *c* for different distances of separation from AuNP, (b) Absorption enhancement at the absorption bands of Cyt *c* (Blue- Soret band; red and green- Q bands).

Q-band of reduced Cyt *c* at 550 nm exhibits higher absorption than its Soret band at 416 nm as shown in Fig. 3(b). In experiments dealing with the coupling of nanoparticles and molecules, keeping the number of molecules constant between two different experiments is extremely difficult. Therefore it may be possible to infer the absorption enhancement due to the AuNP by directly taking the ratio between the Q-band and the Soret band. This gives a direct way of quantifying the absorption enhancement in the system. Secondly, considering the effect of the relative orientation of Cyt *c* and AuNP, we observe that the spatial map of the absorption enhancement of the Q-band is very similar to that of the electric field distribution at the localized plasmon resonance itself (figure not shown).

Since we are actually interested in sensing the change of oxidation state of Cyt *c* molecule for sensing H_2O_2 , we now investigate how the absorption enhancement previously discussed can improve the

sensitivity. Fig. 4(a) shows the absorption spectra of both oxidized and reduced Cyt *c* for both enhanced ($d = 0$ nm) and non enhanced case ($d = 1000$ nm). It can be clearly seen that the absorption of both, the oxidized and reduced Cyt *c*, is enhanced because of the plasmon resonance. In most experiments we actually measure the scattering spectrum of the AuNP. By taking the difference scattering spectrum of AuNP in the presence of reduced and oxidized Cyt *c* we observe the signature of the change in the oxidation states (Fig. 4(b)). Moreover, it is seen that this signature is minimal when there is no AuNP. It should be noted that for experimentally validating the absorption enhancement as well as the detection of change of oxidation state of Cyt *c* it is necessary to bind it to the surface of the AuNP. Chemical routes are ideal for conjugating Cyt *c* and AuNP, since the separation distance can be controlled in the angstrom regime by using different linker molecules, which is not possible using standard nano fabrication techniques.

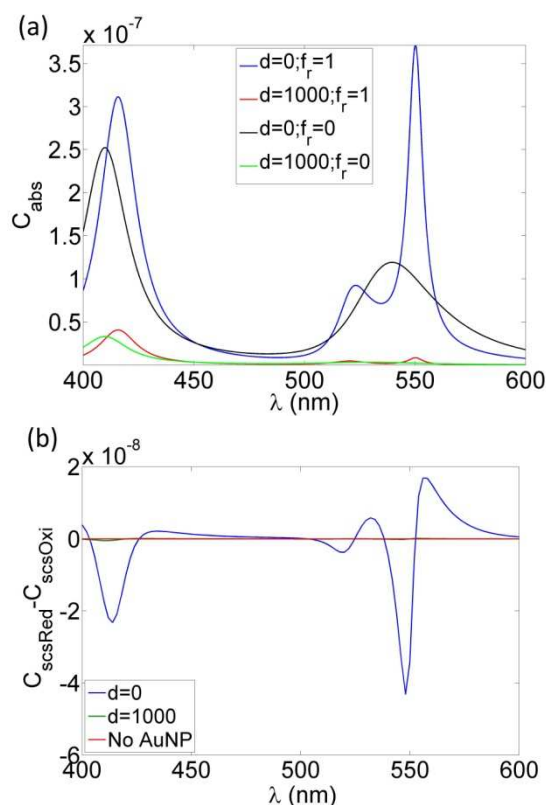


Figure 4. (a) Absorption spectrum of reduced (blue, red) and oxidized (black, green) Cyt *c* for two distances $d=0$ nm and $d=1000$ nm.

An alternative technique similar to PRET is the absorption enhancement of Cyt *c* in a highly scattering medium. As shown in Fig. 5, there is a change in the peak intensity at 550 nm (Q-band of reduced Cyt *c*) as the Cyt *c* in the sample is oxidized by the addition of H_2O_2 . After normalization using a

standard absorption spectrum of Cyt *c*, a reduction coefficient is calculated which represents the amount of reduced Cyt *c*. By monitoring the absorption spectrum continuously, we are able to obtain the reduction coefficient as a function of time, which provides an indication of the kinetics of the phenomenon under study. Figure 6 shows the evolution of the coefficient as a function of time in a system consisting of HL60 (Human Leukemia) cells which are experiencing a temperature shock (the temperature during the measurement was 31° C whereas the standard culture temperature is 37° C). Similar results were obtained with adherent cell line like Human cerebral epithelial cells (HCEC) (not shown here). The main limitation of this technique is that even though it exhibits high sensitivity, it is limited to measurement of the extracellular released H_2O_2 and can not be used to probe the intracellular generation.

This work paves the way for other biosensing schemes that rely on optical coupling between the analyte and a plasmonic nanostructure [5].

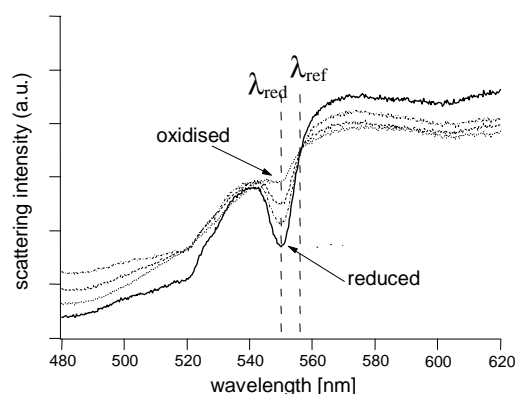


Figure 5. Scattering spectrum showing the absorption dips corresponding to Cyt *c*. The change from the reduced to oxidized is produced by addition of H_2O_2 .

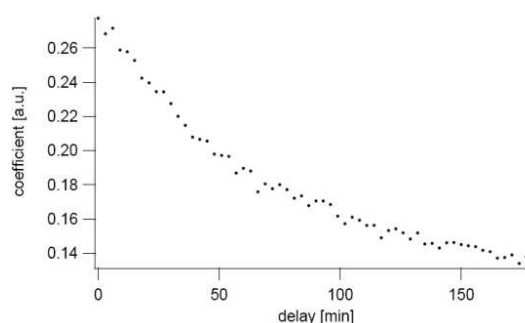


Figure 6. Evolution of the reduction coefficient as a function of time caused by a temperature shock to HL60 cells.

REFERENCES

- [1] X. Qian, *et al.*, “In vivo tumor targeting and spectroscopic detection with surface-enhanced Raman nanoparticle tags ”, *Nature Biotechnology* **26** (1), 83-90 (2007).
- [2] A. Fercher *et al.*, “Intracellular O₂ Sensing Probe Based on cell-Penetrating phosphorescent Nanoparticles”, *ACS Nano*, **5** (7), 5499–5508 (2011).
- [3] G. L. Liu *et al.*, “Quantized plasmon quenching dips nanospectroscopy via plasmon resonance energy transfer”, *Nature Methods*, **4**, 1015-1017 (2007).
- [4] O. J. F. Martin and N. B. Piller, “Electromagnetic scattering in polarizable background”, *Physical Review E*, **58**, 3 (1998).
- [5] S. Dutta-Gupta and O.J.F. Martin, “Strong coupling in a bio-plasmonic system”, *J. Appl. Phys.*, **110**, 044701 (2011).

MAGNETOMOTIVE MOLECULAR NANOPROBES FOR BIOMEDICAL IMAGING APPLICATIONS

Renu John^a and Stephen A. Boppart^b

^aIndian Institute of Technology Hyderabad, ^bBeckman Institute for Advanced Science and Technology, Departments of Electrical and Computer Engineering, Bioengineering, and Medicine, University of Illinois at Urbana-Champaign, 405 North Mathews Avenue, Urbana, IL, USA 61801
Email:renujohn@iith.ac.in

Abstract: In this manuscript, we discuss synthesis, characterization and applications of magnetomotive molecular nanoprobe for coherence optical imaging applications. We demonstrate dynamic contrast using magnetomotive molecular nanoprobe for molecular-specific imaging. Magnetomotive agents are superparamagnetic nanoparticles that can be physically displaced by the application of a small modulating external magnetic field. These magnetomotive displacements of the order of nanometers can be detected as phase changes in a coherent interferometric detection system.

1. INTRODUCTION

Modern trends in the field of biomedical imaging aim at the transformation of anatomical imaging to molecular-specific imaging. High resolution imaging modalities with high penetration depths and sensitivity are very critical in achieving this goal. Development of molecular probes with high specificity is another enabling factor towards imaging at molecular level. Optical coherence tomography (OCT) is a rapidly emerging high-resolution biomedical imaging technique that holds strong promise as a next generation clinical imaging modality at resolutions approaching those of histopathology [1]. Recent developments in nanotechnology have contributed immensely towards the development of novel molecular contrast agents. Target-specific molecular imaging agents combined with OCT has capabilities for providing morphological, spatial, and functional information at the molecular level with high sensitivity and precision, compared to other imaging modalities. In this manuscript, we provide an overview of recent advances in coherence optical imaging and molecular specific contrast agents.

2. MATERIALS AND METHODS

Super paramagnetic iron oxide nanoparticles (MNPs) can be synthesized through coprecipitation method where a mixture of ferrous and ferric ion salts in alkaline medium and an oxygen-free environment yield iron oxide nanoparticles of sizes from 20 to 90 nm [2]. A spectral domain OCT system is used for imaging the samples. The magnetic field can be produced by the introduction of a water-cooled solenoid coil immediately above the sample in the sample arm of the standard Mach Zehnder interferometer [3]. The MNPs under magnetomotion due to an axial magnetic field result in a change in amplitude and phase of the interference pattern in a spectral domain OCT system.

3. RESULTS AND CONCLUSIONS

We introduce a new class of dynamic contrast agents called magnetomotive molecular nanoprobe for molecular-specific imaging. These magnetomotive nanoparticles are conjugated to antibodies for target-specific imaging applications. Using a magnetomotive phase sensitive OCT system, we demonstrate *in vivo* targeted imaging of mammary tumor in preclinical models. Magnetomotive displacements of the MNPs of the order of nanometers can be detected as phase changes in the OCT signals leading to imaging with high specificity and sensitivity. These iron-oxide nanoparticles also exhibit negative T2 contrast in MRI.

ACKNOWLEDGEMENT

The authors wish to acknowledge all members of the Biophotonics Imaging Laboratory and Beckman Institute for Advanced Science and Technology, University of Illinois, Urbana Champaign for supporting this work. More information can be found at www.biophotonics.illinois.edu.

REFERENCES

- [1] D. Huang, E. A. Swanson, C. P. Lin, J. S. Schuman, W. G. Stinson, W. Chang, M. R. Hee, T. Flotte, K. Gregory, C. A. Puliafito and J. G. Fujimoto, "Optical coherence tomography," *Science*, **254**, 1178 (1991).
- [2] A. K. Gupta and S. Wells, "Surface-modified superparamagnetic nanoparticles for drug delivery: Preparation, characterization, and cytotoxicity studies," *IEEE Trans. Nanobioscience.*, **3**, 66 (2004).
- [3] R. John, R. Rezaeipoor, S. G. Adie, E. J. Chaney, A. L. Oldenburg, M. Marjanovic, J. P. Haldar, B. Sutton and S. A. Boppart, "In vivo magnetomotive optical molecular imaging using targeted magnetic nanoprobe," *Proc. National Academy of Sciences, USA.*, **107**, 8085 (2010).

RAMAN SPECTROSCOPY FOR THE DETECTION OF ANTIBIOTIC IN HONEY

K. M. Khan, H. Krishna, *S. K. Majumder and P. K. Gupta

Laser Biomedical Applications and Instrumentation Division, Raja Ramanna Centre for Advanced Technology, Indore - 452013, India
*shkm@rrcat.gov.in

Abstract: We report the use of near-infrared Raman spectroscopy in combination with partial least square (PLS) calibration for quantification of antibiotic level in honey.

1. INTRODUCTION

Antibiotic such as tetracycline is widely used in apiculture as veterinary drug for the treatment of infectious diseases. There are concerns that consumption of honey with residual tetracycline present in it may pose health problems. Therefore, detection of antibiotic levels in honey is an urgent current need. Various methods have been proposed in the literature to detect antibiotic levels in honey based on a variety of chromatographic techniques including solid phase extraction, liquid chromatography (LC), high-performance LC (HPLC), rapid one step assay (ROSA) etc. While the methods have been shown to be very sensitive in detecting trace levels of antibiotic present in honey, all of these require a tedious and time consuming sample preparation. Thus, there remains a need for alternative detection method that does not require any sample pre-treatment and also is simple and quick. In recent years, Raman spectroscopy has been suggested and validated as a powerful alternate tool that can aid current techniques of food authentication [1]. We report results of an exploratory study to assess the applicability of near-infrared Raman spectroscopy for rapid quantitative determination of antibiotic level in honey.

2. EXPERIMENTAL METHOD

Commercial brands of honey were purchased from the local market at Indore, India. Oxy-tetracycline (Pfizer Ltd., Bangalore, India), an antibiotic belonging to the generic tetracycline group, was procured as 500mg capsules from the local medical store. The oxy-tetracycline powder contained within these capsules was used for the study. Four different sets of honey-antibiotic mixtures were prepared with each set containing honey of a particular brand mixed with oxy-tetracycline at various concentrations ranging from 0-25mg/gm. For making honey-antibiotic mixture homogeneous, 1gm of honey was first diluted with 200 μ L of milli Q water (pH-6.85) before adding oxy-tetracycline while preparing each sample. The Raman spectra were measured with a Raman spectroscopy set up that incorporated a 785nm diode laser and a fiber-optic Raman probe to excite and collect the Raman scattered light. For measuring Raman spectra, the tip of the fiber-optic probe was placed normally on the surface of the quartz cuvette

containing the honey samples. For each antibiotic concentration, five different spectra were recorded which were then averaged to get a mean Raman spectrum corresponding to that concentration. Standard normal variate (SNV) transformation was applied to these spectra to offset for any baseline shift. An algorithm based on partial least square (PLS) regression was developed to quantitatively predict the concentration of oxy-tetracycline where this set of preprocessed spectra was used as an input.

3. RESULTS AND DISCUSSIONS

Fig.1a shows the Raman spectra of native honey and honey mixed with three different concentrations of oxy-tetracycline. For comparison's sake the Raman spectrum of oxy-tetracycline is also shown in the same figure. Characteristic Raman peaks of oxy-tetracycline at 1125, 1320 and 1640 cm^{-1} are seen to be clearly visible in the spectra of honey mixed with the antibiotic. The PLS algorithm was validated over the full set of spectra by leave-one-out cross validation. A comparison of the concentration of oxy-tetracycline estimated using the PLS algorithm with that of the reference concentration is shown in Fig.1b. The predictive performance of the algorithm was measured by calculating the R^2 value that was found to be 0.90.

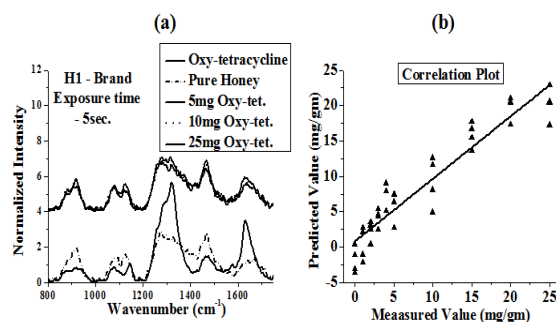


Fig.-1: (a) Honey Raman spectra with oxy-tetracycline adulteration (b) Correlation plot for leave one spectra out

The details of these results will be presented.

REFERENCES

- [1]. W. Wang and J. Paliwal, "Near-infrared spectroscopy and imaging in food quality and safety" *Sens. & Instrumen. Food Qual.* 1:193–207 (2007).

Monitoring Blood Glucose Using Polarization Sensitive Optical Coherence Tomography via Degree of Polarization

Jitendra Solanki, Pratima Sen¹, Joseph Thomas Andrews

Department of Applied Physics, Shri G S Institute of Technology & Science, Indore 452003 India

¹Laser Bhawan, School of Physics, Devi Ahilya University, Indore 452017 India

Abstract: *Scattering and change in the optical property of biological tissues modifies the state of polarization of backscattered light from tissues. Monitoring the degree of polarization of the backscattered light using polarization sensitive optical coherence tomography yields a linear relation. The results are supported with the measurement using tissue phantom as well as with clinical measurements with human subjects.*

1 Introduction

World health organization (WHO) as well as International Diabetics Federation have declared India as the Capitol of Diabetes and ranked India as the country with most diabetics worldwide. An estimation shows that about 1 Million people will be killed in India this year alone by diabetes. While, on one side the statistics is alarming, on the other the monitoring and diagnostic methods available for diabetes mellitus is very painful and is time consuming. Wide varieties of Diabetic monitoring tools based on optical methods are currently adopted. However, all of them are either invasive or minimally invasive. The authors have proposed and demonstrated [1] that the noninvasive monitoring of diabetes could be possible with optical coherence tomography (OCT). Hee et al. also demonstrated use of optical coherence tomography as a tool for biomedical metabolic control in diabetic patients [2]. Another review by Bazaev and Selishchev [3] discuss various noninvasive methods for blood glucose monitoring.

Other existing non-invasive blood glucose monitoring methods work on various modalities such as absorption spectroscopy [4,5], optical activity and polarimetry [6,7], Optical Coherence Tomography [8,9], bioimpedance spectroscopy [9], fluorescence [10], etc. The other optical techniques include Raman spectroscopy [11] and reflectance spectroscopy [12]. However, due to optical interference, poor signal strength, and calibration issues, optical methods still face many challenges [12]. The measurement of blood glucose level using OCT technique exhibits large fluctuations due to motion artifacts or other physiological and environmental conditions [1,7, 8].

Optical coherence tomography is a nondestructive technique that examines the internal structure of superficial layers of biological tissues. It is based on interferometric recording of near-infrared light backscattered from the point of study, which could carry information about the disease. Conventionally, in OCT backscattered light is collected, measured, and integrated to assemble images [13]. Recently, OCT technique applied by Larin et al [8] and Poddar et al [1] to noninvasive monitoring of blood glucose concentration by probing the skin of human. It was found that the light scattering and slope of the scattered signal decrease with increasing blood glucose concentration. The reason is attributed to the fact that the variation of glucose concentration in the extracellular space produces changes in the refractive index mismatch between the Extracellular fluid and the scattering centers, hence, modifying the tissue scattering properties [14]. Despite of these results, the concentration dependent effect of glucose in the near infrared (NIR) spectral range at physiological concentration requires additional study with a more sensitive method.

PSOCT is the functional mode of OCT. Several studies demonstrate PS-OCT's ability to reveal birefringence distribution, reflectivity and retardation of biological tissue, which is unavailable in conventional OCT [15-20]. According to Hitzenberger [18] PSOCT is very useful to measure three parameters backscatter intensity, phase retardation, and fast-axis angle distributions of a specimen were calculated using the amplitude and phase of the interference signal, and provide a greater contrast than is available with conventional OCT system [14, 15].

The other well known mechanism that dominates the changes in the polarization state of the light that propagates through the biological tissue is scattering event. However, birefringence predictably alters the polarization states of photons, whereas scattering randomly affects polarization states, reducing the Degree of polarization (*DOP*) of the incident polarized light. Jarry et al. [25] reorted that despite the application of interferometric low coherence, some scattered light may be coherently detected in a tomographic system and degrade the image.

Various theoretical and experimental model have shown using PSOCT for depolarization of light is caused by optical activity of the glucose and refractive index. Yi and Co-workers [20] reported on how optical activity contributions due to glucose were encoded in Muller matrix patterns of turbid media through the use of a Monte Carlo simulation approach [3]. The amplitude and phase of the interference signals at different depths were determined using the Hilbert transform [14, 15]. In addition, for studying the polarization evolution in highly scattering media, radiative transfer equations have obtained for linearly and circularly polarized light [22].

More recently, Bicout et al. [22] developed a numerical simulation and experimentally verified that depolarization of light as a function of numbers of the scattering events through suspensions and influence of the particle size [23] which Mie scattering regims [24, 25]. From all these studies, it is found that polarized light is highly affected by the birefringence, optically activity, and scattering events caused in the biological tissue. It is well known that the most of the biological tissues are birefringence in nature which participate with polarized light and may affect the *DOP*. Change in the state of polarized light is also caused due to the chiral molecules or optical activity like glucose [26, 27], similarly intraction of polarized light with the biological tissue gets diffuse and scattered, addition of glucose increase the density and refractive index of the medium parallal it decreases the scattering coefficient. Depolarization occurs when the polarized light such as circularly polarized light is incident onto the turbid media such as biological tissues [28].

The present experimental work is performed with circularly polarized light and state of polarization and *DOP* of backscattered OCT signal are analysed.

2 Experiment

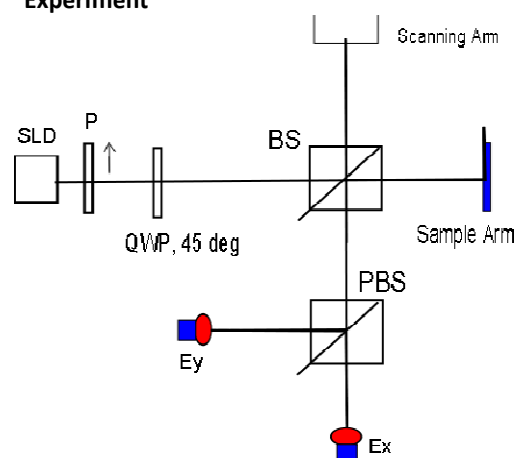


Figure 1: Schematic of the Polarization Sensitive Optical Coherence Tomography setup: SLD - Superluminescent diode, P- Polarizer, QWP – Quarter wave plate, BS-Beam Splitter, PBS-Polarizing Beam Splitter, Ex and Ey are signal amplitude measured using the detectors D_1 and D_2 .

A schematic of free space optical setup PS-OCT using Michel interferometer is shown in Figure 1. A low coherence broad band light source as Superluminescent diode (SLD) with a center wavelength of 835 nm and bandwidth 50 nm is used to understand scattering from sample under study. Large scattering coefficient and low absorption coefficient is achieved using near infrared region when index mismatch occurs between ECF and scatters. In short, a low coherence beam of light emitted from a broad band SLD light source, in which incident beam was vertical polarized by a plane polarizer, and a circularly polarized light was obtained using a quarter-wave plate (QWP) with an azimuth angle set at (45deg), simultaneously and delivered to the a 50-50 beam splitter which provide two modes in which one propagate to the reference arm and other to the examined specimen. On the other hand, the refrence arm, which repetitively scanned at a constant speed of (3 mm/s). Both the reference arm and the sample arm rotate the polarization of the incident light formed an interferogram, which was again delivered to the polarizing beam splitter which again split the interference signal in two modes which are detected by two different photo diodes. The light signal is detected from each photo diode detector or photoreciever was filtered, amplified, and delivered to a personal laptop for further processing. The *DOP* of backscattered light is estimated from the following relation

$$DOP = \frac{\sigma_x - \sigma_y}{\sigma_x + \sigma_y} \equiv \frac{D_1}{D_2}$$

Here, σ_x and σ_y are the amplitude of right and left circularly polarised light, respectively, while D_1 and D_2 are the OCT signal amplitude measured in the experiment.

2.1 Signal Processing

National Instruments Labview Virtual Instruments are used for analysis, display, calculation, and automation. An interference signal detected from each photo diodes was analyzed and display.

2.2 Sample Preparation

The aim of this experiment is to find the linearly change in the state of polarized light by glucose molecules or chiral molecules or optical activity, DOP is also affected by the scattering caused by the tissue phantom as intralipid like RBC in human blood, and decreasing of scattering coefficient with increasing glucose concentrations.

An experimental work was performed with the followings samples: firstly, intralipid based tissue phantom and secondly, Human subjects for blood samples.

2.3 Tissue Phantom

It is well known that by accurate knowledge of optical properties of any biological tissues can be widely use for the diagnosis and the treatment of the diseases. Today, intralipid is widely used in many optical experiments to find the scattering properties of biological tissues and can be use as a good scatterer like RBCs in human blood. Intralipid is an emulsion of soyabean oil, egg phospholipids and glycerin. The major advantages of intralipid are its well known optical properties and the similarity of its microparticles to lipid cell membranes and organelles that constitute the source of scattering in biological tissue. During measurements an intralipid used as a tissue phantom that provides the backscattered component. Average size of scatterers in intralipid measured using laboratory optical confocal microscope is found to be $3.5\mu\text{m}$ with refractive index of 1.42.

The measurement was taken under the hypoglycemics, normal, and hyperglycemics glucose levels of humans as (< 80 mg/dl), (80-110 mg/dl),

and (> 110 mg/dl), respectively. Experiment was done in the followings steps: in the first step fixed volume 1 ml of intralipid (20% w/V) diluted to 100 ml of laboratory distilled water and obtained diluted solution of 0.01% becomes tissue phantom. In the second step 200 mg of glucose dissolved in again 100 ml of laboratory distilled water. In the third steps the concentrations of glucose in 1ml tissue phantom is increased in steps of 20 mg/dl upto 200mg/dl using U-TEK Chromatography syringe with least count of $5\mu\text{l}$. Two minutes of settlement time was given between tissue phantom and every glucose concentrations. Only $10\mu\text{l}$ of whole solution was placed in the sample arm and five measurements of backscattered light from microscopic coverslip $140\mu\text{l}$ in thickness was taken for each concentrations of glucose.

2.4 Blood samples

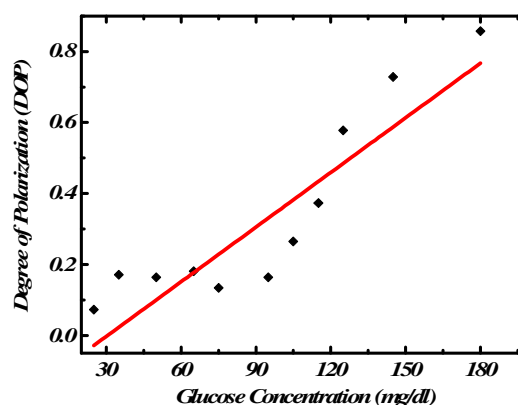


Figure 2: Measured variation in DOP with various glucose concentration in tissue phantom.

Today, commercially available, conventional pathological method known as Oxydised or Peroxydised using semiautomated is widely used to obtain exact value of glucose in human subjects. In order to optimize an optical PSOC setup different human subjects contribute in the measurements. Human tissue was measured in vivo by having a volunteer place his hand in the path of the normal beam. A platform was stabilised to maintain stability in palm of the human hand. Five normal measurements were taken in the thumb region, the measurements were taken under the best comfortable and static position of the hand.

3 Results

It is well known that the biological tissues affects the

polarized light. From the well known optical property of the glucose which easily rotate the state of polarization of the incident polarized light because of its chiral or optically activity property. In Figure 2, an amplitude of the backscattered PSOCT signal is plotted for identification of the change in the state of polarized light with glucose and also in increasing concentration of glucose. This Figure 2 clearly shows that the change in the state of polarization is a linear combination of glucose concentrations.

A scattering events happen in the biological tissue in the accident of polarized light. Any state of polarized light is affected by the change in the pathological tissue which affects the *DOP* of the incident light. Figure 2, It is clear that change in the *DOP* linearly varies with different concentrations of glucose.

4 Conclusions

Optical activity or chiral property of the glucose and scattering in the biological tissues may be useful for measurement of glucose in human. This work is based on the measurement of the DOCP of backscattered PSOCT signal from blood in the presence of tissue phantom scatterer as intralipid like RBC in human blood which can be useful in the world for real time monitoring of glucose in the subjects. Figure 2 clearly shows a linear relation between degree of circular polarization and glucose concentration, which can be useful in practical application for monitoring of glucose in subjects.

The authors thank Prof. P. K. Sen, SGSITS for fruitful discussions. One of the author (JTA) thank financial support received from MPCST, Bhopal.

References

- [1] R. Poddar, S. R. Sharma, J. T. Andrews and P. Sen, *Current Science*, 2008, 95, 2.
- [2] M. R. Hee, D. Huang, E. A. Swanson, and J. G. Fujimoto, *J. Opt. Soc. Am.*, 1992, 9, 903.
- [3] B. D. Cameron, Y. Li, *J. Diab. Sci. and Tech.*, 2007, 1, 6.
- [4] N. A. Bazaev and S. V. Selishchev, *Biomed, Eng*, 2007, 41, 40-48.
- [5] C.F. Amaral, M. Brischwein, B. Wolf, *Sensors and Actuators B*, 2009, 140, 12-16.
- [6] B. Rabinovitch, W. F. March, R. L. Adams, *Diabetes Care*, 1982, 5, 254-258.
- [7] G. L. Cote, M. D. Fox, R. B. Northrop: *IEEE, Trans, Biomed, Eng*, 1992, 39, 752-756.
- [8] K. V. Larin, M. Motamedi, M. S. Eledrisi, R. O. Esenaliev, *Diabetes Care*, 2002, 25, 2263-2267.
- [9] J. C. Pickup, F. Hussain, N. D. Evans, O. J. Rolinski, D. J. S. Birch, *Biosensors and Bioelectronics*, 2005, 20, 2555-2565.
- [10] J. R. McNichols and L. G. Cote, *Journal of Biomedical Optics*, 2000, 5, 5-16.
- [11] S. F. Malin, T. L. Ruchiti, T. B. Blank, S. U. Thennadil, and S. L. Monfre, *Clini. Chem.*, 1999, 45, 1651-8.
- [12] V. Ashok, A. Nirmalkumar, and N. Jeyashanthi, *International Journal of Biological and Life Sciences*, 2010, 6, 3.
- [13] V. V. Sapozhnikova, D. Prough, R. V. Kuranov, 2006, 231, 1323-1332.
- [14] K. V. Larin, T. Akkin, R. O. Esenaliev, M. Motamodi, and T. E. Milner, *Applied Optics*, 2004, 43, 17.
- [15] W. C. Kuo, *Polarization-Sensitive Optical Coherence Tomography in Cardiology*, 2010, 9, 838.
- [16] J. F. D. Boer, T. E. Milner, M. J. C. V. Germert, J. S. Nelson, *Optics Letters*, 1997, 22, 934-936.
- [17] M. J. Everett, K. Schoenenberger, B. W. Colston, Jr, L. B. Da Silya, *Opt. Let.*, 1998, 23, 228-230.
- [18] A. Baumgartner, S. Dichtl, C. K. Hitzemberger, H. Sattmann, B. Robl, A. Moritz, A. F. Fercher, W. Sperr, *Caries Res.*, 2000, 34, 59-69.
- [19] J. F. de Boer, S. M. Srinivas, B. H. Park, T. H. Pham, Z. Chen, T. M. Milner, J. S. Nelson, *IEEE J. Sel. Top. Quantum Electron*, 1999, 5, 1200-1203.
- [20] W. Yi, C. Xiaodong, HU Zhiquiang, LI Qiao, YU Daoyin, *Proc of SPIE*, 2008, 6621, 66211K.
- [21] G. Jarry, E. Steimer, V. Damaschini, M. Epifanie, M. Jurczak and R. Kaiser, *Appl. Opt.*, 1998, 37, 7357.
- [22] D. Bicout, C. Brosseau, A. S. Martinez, and J. M. Schmitt, *Phys. Rev. E*, 1994, E 49, 1767-1770.
- [23] R. L. T. Cheung and A. Ishimaru, *Appl. Opt.*, 1982, 21, 3792-3798.
- [24] D. Bicout, C. Brosseau, *J. Phys. (France)*, 1992, 12, 2047-2043.
- [25] G. Jarry, E. Steimer, V. Damaschini, M. Epifanie, M. Jurczak, and R. Kaiser, *Applied Optics*, 1998, 37, 31.
- [26] N. Ghosh, M. F. G. Wood, S. Li, R. D. Weisel, B. C. Wilson, R. Li, and I. A. Vitkin, *J. Biophoton*, 2009, 2, 145-156.
- [27] A. D. Kim, and M. Moscoso, *Phys. Rev.*, 2001, 64, 026612.
- [28] D. A. Zimnyakov, Y. P. Sinichkin, P. V. Zakharov, and D. N. Agafonov, *Waves Random Media*, 2001, 11, 395-412.

POLARIZATION ENCODED FOUR-VALUED ORDINARY INVERTER

Tanay Chattopadhyay and Jitendra Nath Roy *

Department of Physics, National Institute of Technology, Agartala, 799055, Tripura, India. Email: tanay2222@rediffmail.com, jnroys@yahoo.co.in

Abstract: The principle and possibilities of design of an all-optical four-valued ordinary Inverter circuit with the help of ultra-fast all-optical interferometric switch is proposed and described. Different polarized state of light represents the different 4-valued logical states. Simulation result confirming described methods and conclusion are given in this paper.

1. INTRODUCTION: Multi-valued logic is positioned as a technology that can execute arithmetic functions faster and with less interconnect than binary logic and can provide considerable relief of capacity constraints [1-18]. In binary logic there is just one inverter that changes a state into another state. An arithmetical approach to inverters in an m-valued logic in the literature is provided by the formula: $x = (m-1)-y$ where y is the 'original' value and x is the 'inverted' value of y. There are 4! four-valued reversible inverters. In this present paper we propose and describe the all-optical circuit of polarization encoded one self reversing inverter (also known as ordinary inverter) with the help of Terahertz Optical Asymmetric Demultiplexer (TOAD) based interferometric switches.

2. TOAD BASED OPTICAL SWITCH

Terahertz Optical Asymmetric Demultiplexer (TOAD) based gate has added a new momentum in the field of all-optical logic and data processing [19-23]. It consists of a loop mirror with an additional, intra-loop 2x2 (ideally 50:50) coupler. The loop contains a control pulse (CP) of other wavelength of light than the incoming pulse and a semiconductor optical amplifier (SOA) that is offset from the loop's midpoint by a distance Δx as shown in fig.1. In this present communication we have tried to take the output from both the transmitting (port-1) and reflecting (port-2) mode of the device. The output power at port-1 & 2 can be expressed as [13-16]

$$P_{out}(t) = \frac{P_{in}(t)}{4} \cdot \left\{ \frac{G_{cw}(t) + G_{ccw}(t)}{\mp 2\sqrt{G_{cw}(t) \cdot G_{ccw}(t)} \cdot \cos(\Delta\phi)} \right\} \quad (1)$$

where, $G_{cw}(t), G_{ccw}(t)$ are the power gain and the phase difference between cw and ccw pulse $\Delta\phi = -1/2 \cdot \ln(G_{cw}/G_{ccw})$, α is line-width enhancement factor. In the absence of a control signal, the incoming signal enters the fiber loop, pass through the SOA at different times as they counter-propagate around the loop, and experience the same unsaturated amplifier gain G_0 of SOA, recombine at the input coupler i.e. $G_{ccw} = G_{cw}$.

Then, $\Delta\phi \approx 0$. So expression for $P_{out,1}(t) \approx 0$ and $P_{out,2}(t) = P_{in}(t) \cdot G_0$. It shows that data is reflected back toward the source.

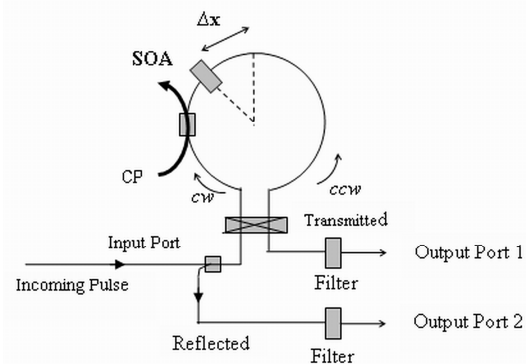


Fig-1: TOAD based interferometric switch.

When a control pulse is injected into the loop, it saturates the SOA and changes its index of refraction. As a result, the two counter-propagation data signal will experience a differential gain saturation profiles i.e. $G_{ccw} \neq G_{cw}$. Therefore they recombine at the input coupler, and then $\Delta\phi \approx \pi$ the data will exit from the output port-1 and $P_{out,2}(t) \approx 0$. A filter may be used at the output to reject the control and pass the incoming pulse. Now it is clear that in the absence of control signal, the incoming pulse exits through input port of TOAD and reaches to the output port-2. In this case no light is present in the output port-1. But in the presence of control signal, the incoming signal exits through output port of TOAD and reaches to the output port-1. In this case no light is present in the output port-2. In the absence of incoming signal, port-1 and port-2 receives no light as the band pass filter (BPF) blocks the control signal.

3. DESIGNING OF ALL-OPTICAL QUATERNARY INVERTER CIRCUIT

A quaternary Inverter truth table is shown in the Table-1 and the optical circuit is shown in Fig-2. The QNOT gate consists of two TOAD based switch S_1 and S_2 respectively. Here, the control signal (X) is taken as the quaternary input, which can take any one of the four

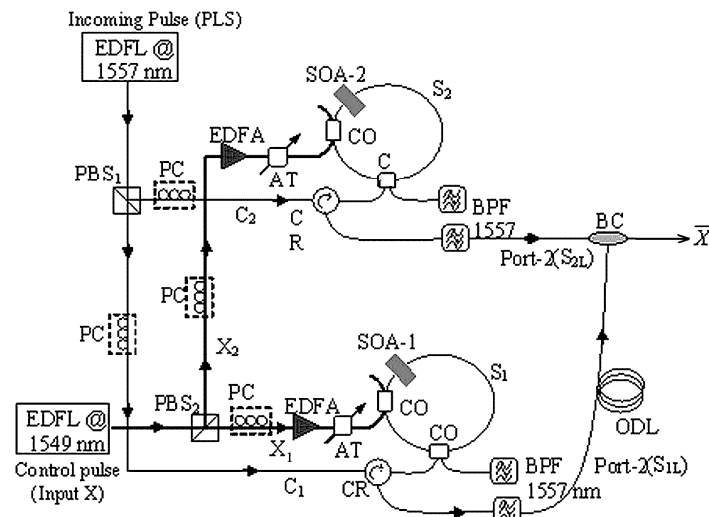


Fig-2: Physical model of the QNOT circuit

quaternary logic states. It falls on a polarizing beam splitter PBS₂. When vertically polarized light (\uparrow) is incident on PBS₂, it goes straight along X₁. If horizontally polarized light (\bullet) is incident on PBS₂, it goes along X₂. When light consisting of vertical and horizontal polarization (\diamond) is incident on PBS₂, one component i.e. the vertically polarized light (\uparrow) goes straight along X₁ and the other component i.e. the horizontally polarized light (\bullet) goes along X₂. Vertically polarized light (\uparrow) that comes out from PBS₂ is connected with S₁. It acts as a control signal to S₁. Whereas the horizontally polarized light (\bullet) that comes out from PBS₂ is connected with S₂. It acts as a control signal to S₂. Er³⁺ doped fiber laser source of 1549 nm and 1557 nm wavelength act as control signal and incoming signal respectively. Here, PC is polarization controller, AT is variable attenuator, CO is 2×2 3 dB coupler; CR is optical circulator, BPF is band pass filter; BC is beam combiner; OD is Optical delay line.

Case-I: Now at the first time, when input X is absent (i.e. X=0) then no control signal is present at S₁ and S₂. Then X₁ = 2 (\bullet) and X₂ = 1 (\uparrow), so the output become \bar{X} = 3 (\diamond).

Case-II: For When X = 1 (\uparrow), X₁ = 0 (no light) and X₂ = 1 (\uparrow). Then we get all the light from S₁ switch goes to the reflected port (S_{1L}) and all light of the switch S₂ goes to the transmitted port (upper port). Hence output (\bar{X}) gets light only from S_{1L} i.e. we find horizontally polarized light i.e. logical state '2'.

Case-III: When X = 2 (\bullet), X₁ = 2 (\bullet) and X₂ = 0 (no light). Then we get all the light from S₂ switch goes to the reflected port (S_{2L}) and all light of the switch S₁ goes to the transmitted port (upper port). Hence output

(\bar{X}) gets light only from S_{2L} i.e. we find vertically polarized light i.e. logical state '1'.

Case-IV: When X = 3 i.e. mixed polarized light then X₁ = 2 (\bullet) and X₂ = 1 (\uparrow). Hence according to the switching principle of the TOAD based interferometric switch, light through both switch goes to the transmitted port i.e. S_{1L} = S_{2L} = 0 (no light). Hence output \bar{X} = 0 (no light).

Table-1: Truth table of ordinary quaternary inverter.

Input (X)	Output (\bar{X})
0	3
1	2
2	1
3	0

3. RESULT AND DISCUSSION

Simulation is done for input bit pattern "0123 0123" and the corresponding output bit pattern is "3210 3210" and the data rate is 10.53 Gb/s (shown in Fig-3). Here we use parameter for MQW-SLA (Injection current of SOA = 300 mA, unsaturated single-pass amplifier gain = 29.6dB, line-width enhancement factor of SOA = 4, gain recovery time = 95 ps, saturation energy of the SOA = 2084 fJ, eccentricity of the loop of TOAD = 30ps, Control pulse energy = 708.56 fJ, full width at half maximum of Gaussian control pulse = 2 ps and Incoming pulse energy = 6.25 fJ) [21]. From the simulated waveform we get insertion loss $IL|_0$ = 8.33 dB, $IL|_1$ = 10.51 dB, $IL|_2$ = 8.33 dB and $IL|_3$ = 1.90 dB. The output contrast ratio (C.R.) as the minimum peak power when the pulse of the payload is high (1, 2 or 3) and we found maximum contrast ratio (C.R.) = 10.92 dB. The calculated Q-Value is 3.82 dB.

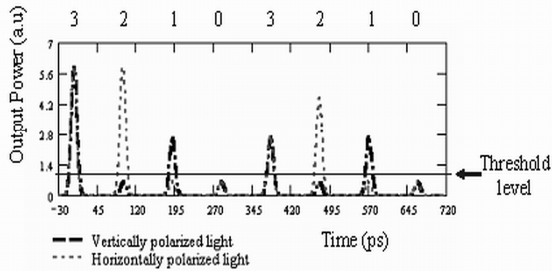


Fig-3: All-optical quaternary inverter output data pattern “3210 3210” at \bar{X} port, when input signal pattern is “0123 0123” at X physical model of the QNOT circuit

4. CONCLUSION

In this paper, the first time to our knowledge, we have proposed and described an optical circuit for quaternary inverter. The significant advantage of this scheme is that the logical operation, which can be performed, is all-optical in nature. Also this quaternary inverter circuit can also be exploited to design multi-valued flip-flop.

REFERENCES

- [1] S.L.Hurst, “Multiple-Valued Logic—Its Status and its Future”, *IEEE Transactions on computers*, C-33 (12), 1160-1179, (1984).
- [2] T.Chattopadhyay, J.N.Roy and A.K.Chakraborty, “Polarization encoded all-optical quaternary R-S flip-flop using binary latch”, *Optics Communications*, 282,1287-1293 (2009).
- [3] T.Chattopadhyay, G.K.Maity and Jitendra Nath Roy, “Designing of all-optical tri-state logic system with the help of optical nonlinear material”, *Journal of Nonlinear Optical Physics & Materials*, 17(3), (2008), 315-328.
- [4] T.Chattopadhyay, C.Taraphdar and J.N.Roy, “Quaternary Galois field adder based all-optical multivalued logic circuits”, *Applied Optics*, (feature issue on ‘optical high-performance computing’), 48(22), (2009), E35-E44.
- [5] T.Chattopadhyay and J.N.Roy, “Polarization encoded all-optical quaternary multiplexer and demultiplexer-a proposal”, *Optik International Journal for Light and Electron Optics*, 120 (2009), 941-946.
- [6] T.Chattopadhyay and J.N.Roy, “All-optical conversion scheme: binary to quaternary and quaternary to binary number”, *Optics & Laser Technology*, 41(3), 289-294, (2009).
- [7] T.Chattopadhyay and J.N.Roy, “An all-optical technique for a binary-to-quaternary encoder and a quaternary-to-binary decoder”, *J.Opt.A:*

Pure Appl. Opt., 11 (2009) 075501 (8pp) doi:10.1088/1464-4258/11/7/075501.

- [8] T.Chattopadhyay, “All-optical quaternary circuits using quaternary T-gate”, *Optik International Journal for Light and Electron Optics*, 121, (2010), 1784-1788, DOI:10.1016/j.ijleo.2009.04.014.
- [9] T.Chattopadhyay and J.N.Roy, Polarization encoded TOAD based all-optical quaternary Literals, *Optik International Journal for Light and Electron Optics*, 121, (2010), 617-622.
- [10] T.Chattopadhyay, “All-optical symmetric ternary logic gate”, *Optics and Laser Technology*, 42, (2010), 1014-1021.
- [11] T.Chattopadhyay and J.N.Roy, “Polarization Encoded All-optical Quaternary Universal Inverter and Designing of Multi-valued Flip-flop”, *Optical Engineering*, 49(3), 035201 (2010), doi: 10.1117/1.3362897.
- [12] C.Taraphdar, T.Chattopadhyay and J.N.Roy, “Designing of an all-optical scheme for single input Ternary logical operations”, *Optik International Journal for Light and Electron Optics*, 122(1), (2011), 33-36.
- [13] T.Chattopadhyay and J.N.Roy, “All-optical quaternary Galois field sum of product (GFSOP) circuits”, *Optik International Journal for Light and Electron Optics*, 122(9), (2011), 758-763.
- [14] T.Chattopadhyay, M.K.Das, J.N.Roy, A.K.Chakraborty and D.K.Gayen, “Interferometric switch based all optical scheme for Conversion of Binary number to its Quaternary Signed Digit form”, *IET Circuits, Devices and system*, (special issue on ‘Optical Computing Circuits, Devices and Systems’), 5(2), (2011), 132-142.
- [15] T.Chattopadhyay and J.N.Roy, “Polarization encoded all-optical quaternary successor with the help of SOA assisted Sagnac switch”, *Optics communication*, 284(12), (2011), 2755-2762.
- [16] T.Chattopadhyay and J.N.Roy, “Semiconductor optical amplifier (SOA)-assisted Sagnac switch for designing of all-optical tri-state logic gates”, *Optik International Journal for Light and Electron Optics*, 122(12), 2011, 1073-1078.
- [17] T.Chattopadhyay and J.N.Roy, “Easy conversion technique of Binary to Quaternary Signed Digit and vice versa”, *Physics express*, 1(3), 2011, 165-174.
- [18] C.Taraphdar, T.Chattopadhyay and J.N.Roy, “Designing of Polarization encoded all-optical ternary multiplexer and Demultiplexer”, *Recent Patents on Signal Processing*, (In press).
- [19] J.P.Sokoloff, P.R.Prucnal, I.Glesk and M.Kane, “A terahertz optical asymmetric demultiplexer (TOAD)”, *IEEE Photon. Technol. Lett.*, 5(7), 787-790, (1993).
- [20] M. Eiselt, W. Pieper and H. G. Weber, “SLALOM: Semiconductor Laser Amplifier in a Loop mirror”, *Journal of lightwave Technology*, 13(10), 2099-2112, (1995).
- [21] B.C.Wang, V.Baby, W.Tong, L.Xu, M.Friedman, R.J.Runser, I.Glesk and P.R.Prucnal, “A novel fast

- optical switch based on two cascaded terahertz optical asymmetric demultiplexers (TOAD)", *Optics Express*, 10(1), 15-23, (2002).
- [22] Y.K.Huang, I.Glesk, R.Shankar and P.R.Prucnal, "Simultaneous all-optical 3R regeneration scheme with improved scalability using TOAD", *Optics Express*, 14(22), 10339-10344, (2006).
- [23] T.Houbavlis and K.E.Zoiros, "Numerical simulation of semiconductor optical amplifier assisted Sagnac gate and investigation of its switching characteristics", *Optical Engineering*, 43(7), 1622-1627, (2004).

CHARACTERIZATION OF MICRO LENS ARRAY USING INTERFEROMETRIC ANALYSIS AND MTF EVALUATION

L M Pant, K K Pant, M P Singh, A Ghosh

Instruments Research and Development Establishment, Dehradun

Email: pant.lalitmohan@gmail.com

Abstract: Due to very small in dimensions micro lens array are fabricated using very specialized techniques. The physical and optical parameters of micro lenses like shape, radius of curvature, focal length, surface quality, as well as optical performance plays very important role in performance of those lenses. Present work focuses on the evaluation and characterization of micro lenses in terms of their physical and optical parameters. A setup is rigged up for the measurement of very short focal length (less than 10 mm) and implemented to micro lens. The microlens array was further evaluated for surface profile with aberration analysis and MTF.

1. INTRODUCTION

de

There are variety of means to manufacture micro lens array viz. lithography [1], molecular stuffing process and ion exchange [2]. To ensure very high accuracy required of a manufactured micro lens array, precise knowledge of its physical and imaging properties like surface geometry, radius of curvature, focal length, surface accuracy and MTF are of fundamental importance. Since there are challenges of small dimensions and precise alignment tolerances, measuring those parameters is of much more complicated process than a normal lens. A micro lenslet array of size 4 x 4 having 1 mm diameter and 1.2 mm pitch obtained from trades to be used in imaging application but this micro lens was not able to produce a sharp imaging. To address the problem, we have evaluated micro lens array for its various fabrication parameters.

2. EXPERIMENTAL SET UPS

The setups for focal length, Interferometric analysis for radius of curvature and aberration analysis including spherical aberration, coma and astigmatism and MTF measurement were rigged up. The experimental setups are described in subsequent paragraphs.

2.1 Setup for Shot focal length Measurement

The schematic diagram of the experimental set up is described in fig 1; the circular target graticule is illuminated by an extended source placed at the focal position of the achromatic objective lens. The lens to be tested is placed on the two dimensional holding stage with the linear accuracy of 1 micron in either direction against the collimated light. This precise holding stage is very important for the accurate measurement of the diameter of focal spot (image of the target plate) formed by the test lens at its focal position, viewed by the microscope.

Using this experimental setup, a number of

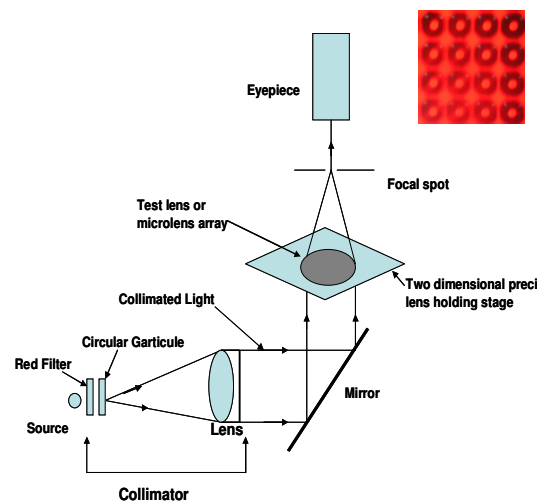


Fig 1 Short focal length measurement set up of micro lens

measurements were taken using standard lenses to determine experimentally the value of instrument constant for focal length up to 35 mm. To experimentally verify the techniques, few numbers of lenses with different optical glasses including BK 7&, SF14, LaF2 and SF16 were designed using Zemax with focal length below 10 mm and it was found that the percentage error of measurement was within 1%. This set up was used for the focal length measurement of the micro lens array which is otherwise not practically feasible by using conventional focometer. The focal length of micro lenses was measured with 0.59% error for complete matrix of 4 x 4 array designed focal length is 3.39 mm. It was found that the percentage error of measurement is below the designed tolerance of 1%. The measured values of the focal length of microlens are given in table 1.

2.2 Interferometric Analysis

Since the measured focal lengths of the micro lenses are in close agreements of their designed

values however their imaging quality was not up to the required performance so to analyse this problem the Interferometric analysis of aberrations and surface accuracy was also carried out. A setup for Fizeau phase shift interferometer at 632.8 nm wavelength is used to conduct present study. A reference transmission sphere of 0.65 numerical apertures was used, being small in size lens array were producing a mess of interference patterns. It was difficult task to get the accurate fringes corresponding to known lens for which a precise 2D stage of 1 micron accuracy was utilized and the lens number and corresponding fringe pattern was ensured to take the observations on surface accuracy of the micro lenses. The interference fringes of the micro lenses were captured for full aperture and analysed for primary aberrations. The interference fringes in figure 2 depicts that there is variations in surface accuracy of each micro lens. Table 2 shows the measured surface accuracy (P-V value) of the micro lens array for full aperture these were found between 695 nm to 997 nm. The shape of the lens is not circularly symmetric but it is slightly elliptical this may be due to the molding or chemical etching process used for the fabrication of the lenses, however for 90% of the aperture of the lens the interference pattern was analysed and observed that the surface accuracies are slightly improved. Fig 3 shows the three dimensional surface plot of each micro lens obtained using interferometry.

695.94	776.68	700.39	807.38
677.79	730.09	730.09	743.37
776.48	772.92	814.38	920.81
742.52	996.31	704.48	706.03

Table 2. surface accuracies of micro lens array (nm)

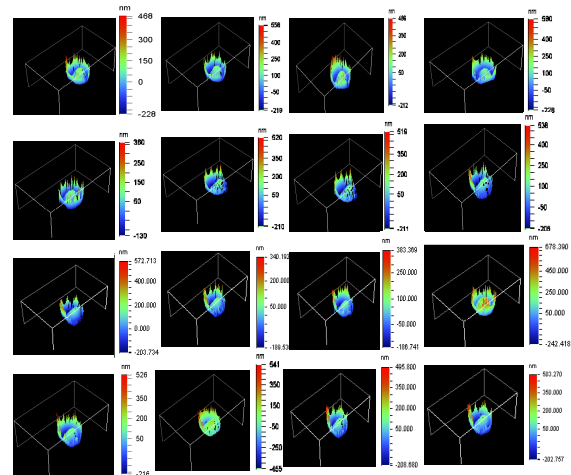


Fig3: 3- D surface plot of micro lens array

3.41	3.41	3.41	3.41
3.41	3.41	3.41	3.41
3.41	3.41	3.41	3.41
3.41	3.41	3.41	3.41

Table 1. Focal lengths of micro lens array (mm)

2.3 MTF Analysis of microlens array

The MTF is a very important parameter to know the detailed imaging characteristics of the imaging system. The MTF test configuration consists of a collimator, test device holder and a CCD camera with a microscopic objective. The data is acquired and processed by a computer, to get the MTF of the micro lens array a precise holding mechanism with three dimensional precise movements of 1 micron was used. The CCD camera used is having 1280 x 1024 pixels and pixel size is 6.45 micron. A highly corrected 50X microscopic objective of high numerical aperture (0.8) is used in front of camera to get the image. The system is placed on a vibration isolation optical table. The system uses the line spread function obtained as the image of a slit of width 15 micron and then computes the modulation transfer functions (MTF). Figure 4 shows the line spread function (LSF) of the micro lens array and Figure 5 shows the MTF curves for the micro lens array. The LSF curves are not symmetric it may be because of asymmetry of aperture and degraded surface accuracies. The MTF curves also depict that the imaging quality of lenses is not consistent as average cut off frequency observed is about 430 lp/mm however designed cutoff is 540 lp/mm.

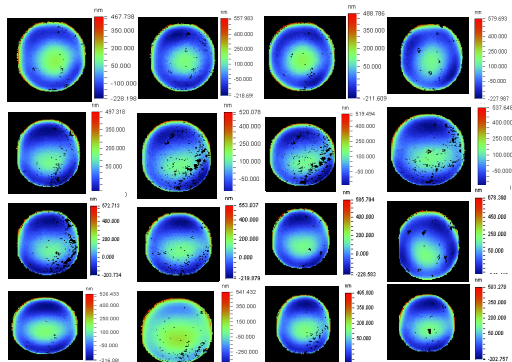


Fig 2: fringe pattern of full aperture micro lens array

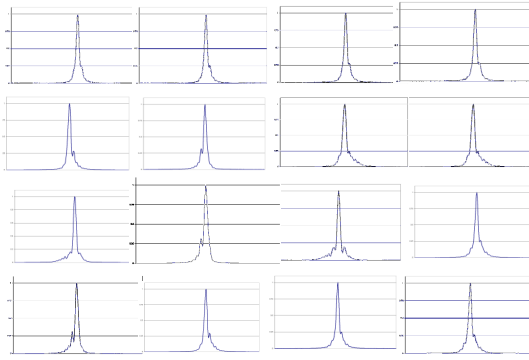


Fig4: Line Spread function of micro lens array

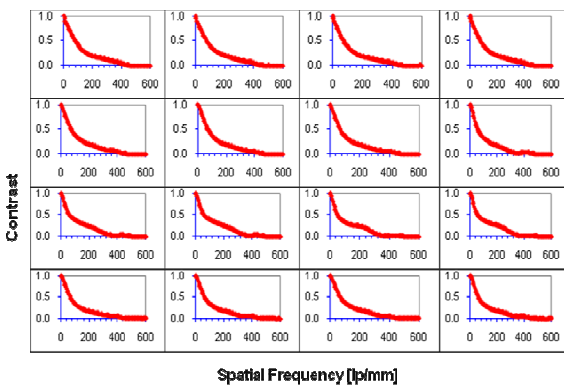


Fig 5: Modulation Transfer Function of micro lens array

CONCLUSION

The micro lens array obtained from trades for imaging application was evaluated for its focal length, surface accuracy and modulation transfer function. The measured focal lengths were very close to their design values and within designed tolerances. The surface accuracy of the micro lenses varies from 650 to 997 nm, There is variation in the surface accuracy of each micro lens may be the due to the fabrication technique used either molding or chemical etching processes. The imaging characteristics of the lenses are also not consistent which is further supported by the MTF values of those lenses. The fabrication parameters surface quality and MTF s can be improved by using the latest fabrication techniques [5], [6], [7].

4. ACKNOWLEDGEMENT:

Authors are thankful to Sh. SS Sundaram director IRDE and Dr. A K Gupta, Sc 'H' for their support and encouragement.

5. REFERENCES:

- [1]. P.H.Nussbaum, R Volke, H P Herzig, M Eisner, Haselbeck, Pure Appl. Opt. 6(1997), 617.
- [2]. A D Pearson, W G French, E G Rawson, Appl PhysLett 15 (1969), 76
- [3] J Bahr, K H Brenner, T Sinzinger, M Testorf, Appl Opt, 33 (1994), 5919
- [4] Gerald C Holst. SPIE press, 2008
- [5] Ming-Hsien Wu and George M Whitesides. J. Micromech. Microeng. 12 (2002) 747–75
- [6] Christopher Altman, FISBA-TU Delft OFT/Applied Physics 2007
- [7] Chia-Nying Hu, et.al. J. Micromech. Microeng. 21 065013, June 2011
- [8] M P Singh et al, ICOP 2009 CSIO Chandigarh

Stress Analysis and Fabrication of High Aspect Ratio IR Lenses

K K Pant, N Pandey, M P Singh, B Singh and A Ghosh
Instruments Research and Development Establishment, Dehradun
Email kpant28@gmail.com

Abstract: Fabrication of high aspect ratio (thickness to diameter more than 1:10) Infrared lenses is a critical and challenging task. In the present work, a method is described for fabrication of these IR lenses and its stress control during the blocking and deblocking stage. Interferometric analysis of the deblocking stress is also carried out using phase shift laser interferometer. By using the method developed for fabrication of these high aspect ratio IR lenses, precision manufacturing tolerances can be maintained over the fabricated components.

1. INTRODUCTION

Inherently, the human visual system is limited to the visible region. However, technological developments in the last century and thereafter have enabled mankind to extend its imaging capability to wavelength either side of the visible spectrum^[1]. The field of IR optics is one of the fastest growing branches of traditional optics. New laser sources, fiber optic communications, thermal imager and a host of new detector technologies make the field of IR optics ripe for further growth^[1,2]. The optical components in IR system create an image of observed objects in plane of the detector (detectors). The major differences between glass and IR optics revolve around the limited number of materials that transmit in the IR and their very different mechanical, chemical, and thermal properties from those of glass. These material differences make some great differences in how IR optics is fabricated. In addition, the optical elements like windows, domes and filters can be used to protect system from environment or to modify detector spectral response. To make these systems lighter, one aspect is to design high aspect ratio (thickness to diameter more than 1:10) lenses and flats in diverse infrared materials i.e. Silicone (Si), Germanium (Ge), Zinc Sulphide (ZnS), Zinc Selenide (ZnSe) etc. The difference between polishing IR materials and glass optics is entirely in the chemistry of the polishing process. Some IR materials are much softer and/or more brittle than glass so more care must be used in the various stages of its fabrication process but the techniques for what size tools and what strokes to use are identical to those used in making glass optics^[2]. Since these materials are costlier than the optical glass so precise calculations of material dimensions is required before starting fabrication process.

In the present work we have discussed the fabrication challenges of such optics and their analysis to maintain the specified tolerances given by optical designer^[3,4].

2. FABRICATION AND STRESS ANALYSIS

A meniscus shape Si lens was designed using following fabrication parameters [Table 1]

Table 1:- Fabrication parameter

Material	R1	R2	Thickne ss	Dia.
Silicon	153.125 ^{±0.1%} (Vex)	305.08 ^{±0.1%} (Cave)	8 ^{±0.01}	82 ^{-0.01}

* All dimensions are in mm

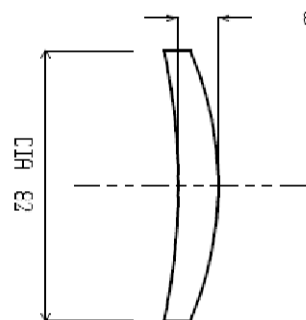


Fig: 1- Meniscus shape Si lens with aspect ratio (diameter to thickness) >1:10

The circular silicon disk of diameter 88 mm and thickness 18 mm (which incorporate the sag for the designed curvature, centre thickness and processing allowances) is trepanned using trepanning machine. The generating imparts dimensionally true surfaces on the work piece so that subsequent operations can be performed accurately and efficiently. With silicon lenses, the generating is done with cup-shaped grinding wheels with a lip of diamond grit in a metal matrix on the curve generating machine with rotating spindle (2000 rpm). The residual machining marks were further processed in the smoothing process with loose abrasive technique, where the particle size of the order of 50-60 micron initially and 10-15 micron at final stage (during smoothing). By doing this, the subsurface damage produced at the initial grinding stages can be minimized. The initial aspect ratio for the meniscus lens was 1:11. After grinding and smoothing, the lens was blocked on a cast iron tool with the help of pitch. The blocked lens was pitch

polished using continuous slurry method with 12 bar pressure exerted on the individual polishing surface for 48 hours. Pitch polishing is one of the most proven and efficient way to achieve high surface finish and surface quality in precision optical components. The excellent chemistry of polishing material Cerium oxide (CeO_2) does not work in IR material to make polished surface with high surface finish and excellent cosmetic quality^[5,6]. So a different polishing material known as linde powder aluminum oxide (Al_2O_3) with particle size of 1 micron is used to achieve high surface finish on the polished surface. The aluminum oxide particle does not have the tendency to embedded on the pitch polisher, so a thin layer of wax is also applied on the pitch polisher to hold these polishing particle so that cutting action retain for relatively longer time. Even a slight contaminated polishing slurry or hardening of pitch polisher causes streaks and scratches on the polishing surface of silicon lens more frequently as compared to glass. To avoid these effects, glycerin was added to the slurry for wetting action and hot water in the place of cold water to make polisher quite warm.



Fig 2(a)

Fig 2(b)

Fig2: Lens blocking (a) after smoothing (b) during blocking with hard pitch as a blocking material

After polishing of first surface, pre inspection was carried out with test plates. Since the surface is convex in nature and edge thickness of the lens is smaller than the centre thickness so the surface was polished in such a way that it remains 2 ring vex with respect to test plate. When the rings were found regular, final inspection was carried out on laser interferometer. The surface accuracy was measured 163 nm PV (peak to valley) over full surface on phase shift laser interferometer at measuring wavelength of 632.8 nm. It was found that surface accuracy was under precision manufacturing tolerance of the order of one wavelength peak to valley. After the measurement, lens was deblocked from the blocking tool and again measured for surface accuracy. The surface became astigmatic and surface accuracy was measured 1.5 micron Peak to Valley.

Figure 3 is the Interferogram before and after deblocking of a high finish convex surface ($R_1=153.125$ designed value).

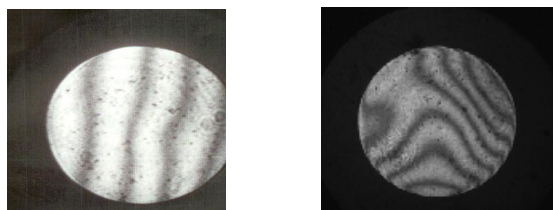


Fig3: Interferogram of polished surface (a) Before Deblocking (PV-163 nm) (b) After deblocking (PV-1.5 um)

Since the aspect ratio was high, and the lens was under constant pressure on the polishing machine, that causes the stress developed on the material. Because of this high aspect ratio, the developed stress was released in an unpredictable manner and made severe degradation on the polished surface in terms of surface accuracy after deblocking. Degradation in the polished surface was the consequence of non uniform softening of pitch due to heat generated during process and causes uneven this stress developed throughout the lens surface. To overcome this problem, the blocking process was modified.

3. CONTROLLING OF STRESS

The blocking pitch was boiled for ½ an hour and making quite hard. Glass piece fixture was fabricated with same diameter and radius of curvature, matched with the blocking side radius of curvature and plane surface on other side. The glass piece was blocked on flat aluminum tool with the help of wax. A thin and uniform layer of pitch boiled above was poured on the glass surface and lens was placed on it for 4 hours at room temperature. The polishing was carried out with lower pressure of 6 bars for 72 hours. During the polishing of meniscus lenses, it is very important to leave the tolerance on surfaces with same nature so that the focal length of polished lenses is under precision manufacturing tolerance^[7].

The radii of curvature R_1 (vex) =153.141mm and R_2 (cave) =304.056 mm was measured before deblocking. The radii of curvature were R_1 (vex) =153.134 mm and R_2 (cave) =304.097 mm after deblocking.

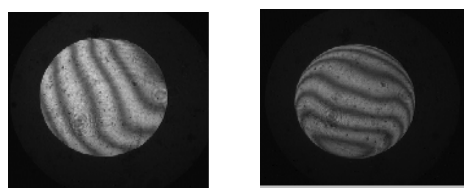


Fig 4 (a)

Fig 4(b)

Fig4: Interferogram of polished surface after modified deblocking process (a) PV-314nm for convex surface (b) PV-493nm concave surface

Since the lens surface is changing on deblocking so irregularity on edges may enhance and severely degrade lens surface. Therefore it must be ensured that the fringes on both the surface should regular so that after deblocking only number of fringes may change rather than their shape.

The surface accuracy was again measured after deblocking and found 314 nm PV over full aperture which is far improved as compared to previous case (1.5 micron PV) on first side(convex surface). Similarly the surface accuracy of concave side is 493 nm PV which is again under stipulated tolerance of one wave at $\lambda=632.8$ nm.

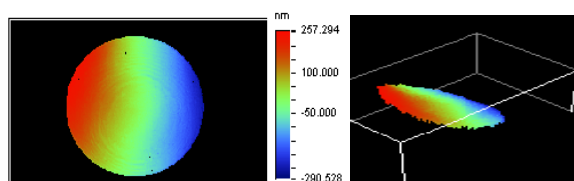


Fig 5 (a) Convex surfaces (R1 153.134 mm)

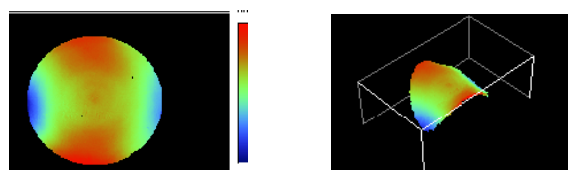


Fig 5 (b) Concave surface (R2 304.097 mm)
Fig.5 Phase map of polished surfaces after deblocking

Figure 5 is the phase map for both the surface after deblocking for full aperture. The changes in the concave surface (shallower) in terms of radius and surface figure was observed higher as compared to convex part (which is deeper), so it is very important to keep in mind that convex surface (deeper radius of curvature) should be polished first and concave surface should polish after to minimize the effect of stress produce during deblocking process. The centering of the lens was done by reflection method on the transferrable spindle using laser. Thereafter the lens was edged at the centered position on the edging machine with diamond wheel to maintain final diameter of 81.99 mm.

4. CONCLUSION

The fabrication of IR meniscus lenses is a challenging task. We have demonstrated a method of fabricating and controlling stress developed during deblocking process of high aspect ratio IR lenses more than 1:10, by using thin layer of hard pitch and wax between lens and a BK7 glass component as an additional attachment. During deblocking the convex surface has the tendency of expanding in concave direction and

concave surface has the tendency towards convex direction. This observation was very helpful to maintain tolerances on outer surface with same nature, which is one of the important aspects to maintain focal length of the lens within tolerance. The surface figure were also improved and under tolerances as compared to conventional blocking process. The described process was also adopted for other IR meniscus lenses in other material like germanium, zinc selenide zinc sulphide etc. Although the rate of variation of fabricated parameters including radius of curvature and surface accuracy after deblocking depends on the mechanical properties of materials viz hardness, tensile strength, coefficient of thermal expansion etc, but the nature of variation was similar as predicted by the described method.

ACKNOWLEDGEMENT

Authors are thankful to Sh. S S Sundaram, Director, IRDE and Dr. A K Gupta, Scientist, H for their support and guidance for the above work.

REFERENCES

- [1] Robert E. Parks, *Fabrication of infrared optics*, Optical Engineering 33(3), 685—691 (March 1994).
- [2] H. H. Karow, *Fabrication methods for precision optics*, John Wiley and Sons Inc, New York, (1993)
- [3] R. Kingslake. *Lens Design Fundamentals*. New York: Academic Press,1978
- [4] R E Parks,optical components specifications, Proc. of SPIE Vol. 0237, May 1980.
- [5]B E. Gillman, F Tinker, *Fun Facts about Pitch & the Pitfalls of Ignorance*, SPIE Vol. 3782, July 1999
- [6] D Golini, and S. D. Jacobs , *The Physics of Loose Abrasive Microgrinding*,” Applied Optics 30 2761 – 2777(1991).
- [7] G. P. Dimri, G. K. Sharma, and V. M. Mudholkar ,*Fabrication of deep curvature meniscus lenses*, Appl. Opt.**28**, 17-17 (1989)

MEASUREMENT OF THICKNESS OF TRANSPARENT SPECIMENS USING WEDGE PLATE LATERAL SHEARING INTERFEROMETRY

Satyaprakash Trivedi and Shashi Prakash*

Photonics Laboratory, Department of Electronics & Instrumentation, Institute of Engineering & Technology-Devi Ahilya University, Khandwa Road, Indore-452017 INDIA

*Corresponding author: sprakash_davv@rediffmail.com

Abstract: We report measurement of thickness measurement of flat transparent glass plate using wedge plate interferometric setup. The specimen is introduced in the interferometer prior to the wedge plate and rotated by a known angle. The variation in the inclination angle of the fringes is related to the thickness of specimen. Relatively high accuracy and precision in measurement is achieved.

1. INTRODUCTION

Lateral Shearing Interferometer (LSI) is an important type of optical interferometer. It has been applied for wide range of applications in optical testing and measurement. It is based on interference of the original wavefront and the displaced wavefront using a shearing device. Various arrangements have been reported based on different optical principles.

In wedge plate LSI, a parallel glass plate or a slightly wedge plate held obliquely to an incident beam, can be used to obtain sheared images. Wedge plate LSI is a sensitive interferometer in which shear fringes align parallel to the shear direction. Defocusing the collimating lens from its collimation position results in the inclination of shear fringes with respect to the shear direction.

2. EXPERIMENTAL ARRANGEMENT

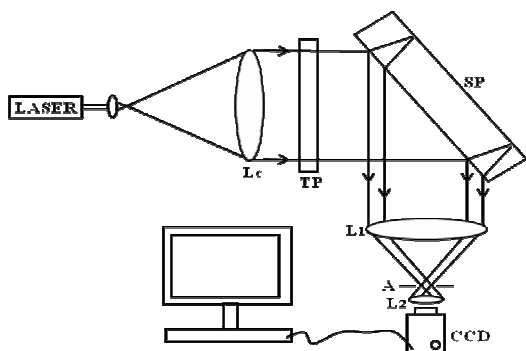


Fig.1: Experimental setup for lateral shear interferometer.

The schematic of the experimental setup is shown in Fig. 1. Light from a 15 mW He-Ne laser of wavelength 632.8 nm is allowed to pass through a spatial filtering arrangement consisting of a microscope objective MO of magnification 60X and an aperture of 5 μm placed at the front focal plane of MO. A collimating lens L_c of 250 mm focal length is used to collimate the laser beam. The collimated beam is incident on a wedge plate at an oblique angle. As a result of beam reflected from the front and back surface of the wedge plate, two laterally sheared

wavefronts are obtained at the image plane. A lens arrangement helps to capture the fringes of the lateral shearing interferometers onto the CCD chip directly.

3. RESULTS AND DISCUSSION

A simple wedge plate shearing interferometric method for the measurement of thickness of flat glass plate has been experimentally demonstrated. For measuring the thickness of the test plate, the collimated beam is first made to pass through the test plate introduced between the wedge plate and collimating lens. It is then rotated by a known angle, and the resulting shift in the fringe orientation is recorded using CCD camera as shown in Fig. 2a. Simple mathematical formulation relates the thickness of the test plate with to the refractive index of the plate, rotation angle of the test plate (TP) and the inclination angle of the fringe pattern. Hence, by measuring the change in the orientation of fringes, the thickness of test plate has been determined.

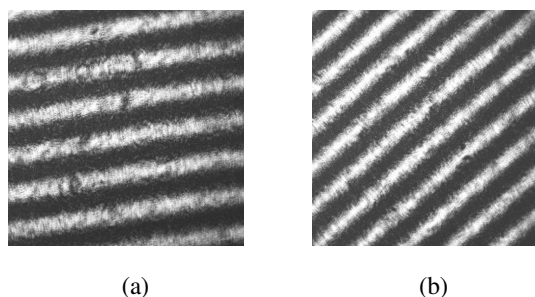


Fig. 2: Shear fringes obtained (a) when test plate is perpendicular to the optic axis, and (b) tilted by an angle θ with respect to the initial position (a).

REFERENCES

- [1] J. Dhanotia and S. Prakash "Collimation testing using wedge plate lateral shearing interferometry and Fourier fringe analysis," *Opt. and Lasers in Eng.* 49, 1025-1031 (2011).
- [2] S. Prakash, S. Singh and S. Rana, "Automated small tilt-angle measurement using Lau interferometry" *Appl. Opt.* 44, 5905-5909 (2005).

SMALL TILT ANGLE MEASUREMENT USING COHERENT GRADIENT SENSING

Reena Disawal , Satyaprakash Trivedi, Shashi Prakash

Department of Electronics & Instrumentation, Institute of Engineering & Technology,

Devi Ahilya University, Khandwa Road, Indore-452017 INDIA

Corresponding author: sprakash_davv@rediffmail.com

Abstract: In the present communication, an application of Coherent Gradient Sensing (CGS) for the tilt angle measurement is proposed. The specularly reflecting specimen is illuminated by a collimated light from the laser. The reflected light from the specimen is incident on the set of two gratings, results in the formation of sheared fringe pattern. The inclination angle of sheared fringe pattern is a function of tilt angle of the specimen.

1. INTRODUCTION

Tilt angle is one of the most important fundamental parameter in optical metrology. Tilt angles have been measured widely using either autocollimator [1] or an interferometer.[2]. An autocollimator measures angle by detecting the lateral displacement of a source beam, reflected from the object that is subjected to the angular displacement. In contrast, the interferometer is based on the principle of interference of two coherent beams that traverse slightly different optical paths whenever an angular displacement occurs. The measurement sensitivity depends on the distance between the gratings. Various configurations have been investigated for improving the accuracy and simplifying the structure of the interferogram [3, 4].

Recently, double grating lateral shearing interferometry called coherent gradient sensing (CGS) has been extensively used in various engineering applications [5, 6]. Similar to Talbot interferometry technique, this technique also uses two gratings in tandem. In this technique any two diffracted orders are separated and selectively superposed to form high contrast fringes at the image plane. This facilitates the fringe formation corresponding to any arbitrary distance between the gratings, thereby alleviating problems associated with the exact location of self-imaging planes. Also the two interfering wavefronts have equal amplitudes; hence excellent visibility of fringes is obtained. As the effects due to Fourier imaging are absent, the contrast of fringes is independent of grating separation.

In present communication, we report our investigations undertaken towards small tilt angle measurement of the specimen surface using coherent gradient sensing interferometer. The technique is based on common path interferometer and hence errors due to extraneous disturbances are minimized. The technique also has potential applicability in environments outside the laboratory conditions. The experimental arrangement is simple, inexpensive and realizes compact geometry.

2. BASIC PRINCIPLE

The basic principle of coherent gradient sensing is shown in fig.1. The expanded and collimated laser beam is incident on the pair of two Ronchi gratings G_1

and G_2 having the same pitch 'p' and an arbitrary separation 'd'. The light passing through the grating G_1 comprises of several diffraction orders. Out of these, let us consider only two orders, say the zeroth and the first (± 1) order, for interferometric analysis. Then the magnitude of the angle between propagation directions of the zeroth and the first order beams is given by the diffraction equation $\theta = \sin^{-1}(\lambda/p)$, where λ is the wavelength, p is the grating period.

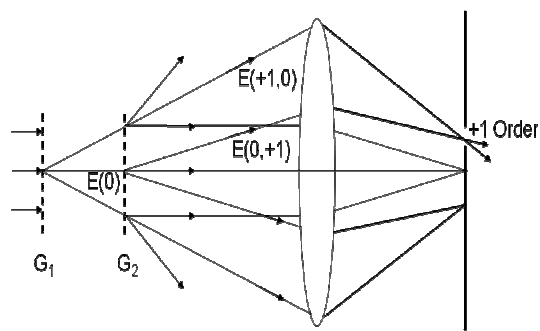


Fig. 1: Basic principle of coherent gradient sensing system

These beams after passing through the second grating G_2 , are again diffracted into several orders such as $E(0, 0)$, $E(+1, 0)$, $E(0, +1)$ and so on. These wavefronts are propagating in different directions. These wavefronts are focused using the filtering lens at the focal plane of the field lens. Hence several diffraction spots corresponding to first order spots [$E(+1, 0)$, $E(0, +1)$] are segregated and allowed to propagate. The rest are blocked using a spatial filter placed at the back focal plane of the field lens. For the automatic detection, recording, storage and retrieval of data a charge coupled device (CCD), a frame grabber card and a computer system have been used.

3. EXPERIMENTAL ARRANGEMENT

Fig.2 shows CGS interferometer developed for the measurement of small tilt angle. Light from 15 mW He-Ne laser is spatially filtered using a combination of pinhole and microscopic objective. The diverging beam so obtained is collimated using a collimating lens and is incident on the specimen which is placed

at 45° angle on precision rotational stage.

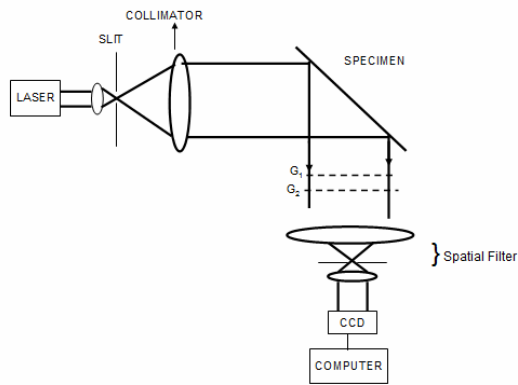


Fig. 2: Experimental arrangement for measurement of tilt angle using coherent gradient sensing system.

The reflected light from the specimen is incident on the set of two gratings G_1 and G_2 . The crossed angle between the gratings G_1 and G_2 is set initially to 3°. The specimen under test is taken to be a mirror of diameter 50mm. Mechanical surfaces grinded by diamond-tool can very well be used as a test specimen. In this technique the emergent light after grating G_2 having various diffraction orders. Out of which the two desired diffracted orders are separated and selectively superposed to form high contrast fringes at the image plane. This facilitates the fringe formation corresponding to any arbitrary distance between the gratings, thereby alleviating problems associated with the exact location of self-imaging planes. The experiment is performed by varying the tilt angle of the specimen and capturing the corresponding sheared fringe patterns using a CCD camera and its subsequent digitization using frame grabber card.

4. RESULTS

Fig.3 shows the image acquired directly from the CCD camera. It is evident that the quality of the image needs to be improved significantly if the accurate measurement of the angle is desired. The noise in the form of grating lines should be significantly reduced or if possible removed completely and the poor brightness should be improved. To fulfill these requirements, image processing software was used to undertake image acquisition and perform various image processing operations such as contrast improvement, low pass filtering etc.

Fig. 3(a-d) show the processed results with different inclination angles of the sheared fringes corresponding to the tilt angle variation of the object surface. From the range of observations it is noticed that there is one to one relationship between inclination angle of the sheared fringe corresponding to the tilt angle variation of the object surface as

shown in Fig.4. Table 1 shows variation of angle of inclination of fringes obtained for different Tilt of the object surface.

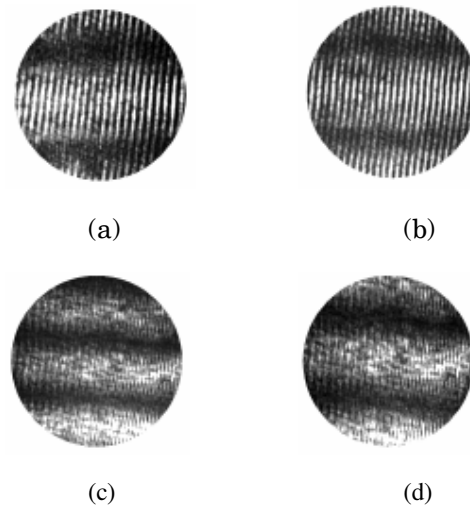


Fig. 3: Recorded fringe patterns at different angle of the specimens for:(a) $\theta = 43^\circ$ (b) $\theta = 45^\circ$, (c) $\theta = 47^\circ$, (d) $\theta = 49^\circ$

Sr. No.	Tilt angle (δ°)	Inclination angle (θ°)
1.	51	6
2.	49	4
3.	47	2
4.	45	0
5.	43	2
6.	41	4
7.	39	6

Table1: Table showing the variation of Tilt angle specimen surface with the inclination angle of shearing interferometric fringes

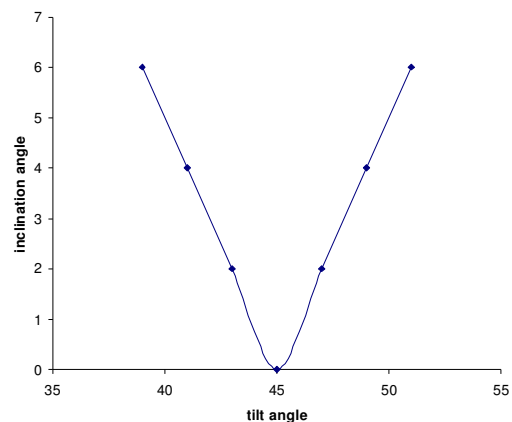


Fig4: Plot showing variation of inclination angle of fringes with the tilt angle of specimen

5. CONCLUSION

We have presented a simple, non contact, online technique for the measurements of small tilt angles of an object. The small tilt angle variation of the object is determined in terms of variation in inclination angle of the sheared fringes. The technique is useful for measuring the tilt angle of various reflecting surfaces, including mechanical surfaces ground by a diamond tool. The technique is inexpensive and uses components such as coarse grating, He-Ne laser, which are widely available. The technique can be used under workshop conditions because the effect of environmental conditions is minimal.

REFERENCES

- [1] P. R. Yoder, E. R. Schlesinger, and J. L. Chickvary, "Active annular-beam laser autocollimator system," *Appl. Opt.* **14**, 1890-1895 (1975).
- [2] D Malacara and O. Harris, "Interferometric measurements of angles," *Appl. Opt.* **9**, 1630-1633 (1970).
- [3] T. Takano and S. Yonehara, "Basic investigations on an angle measurement system using a laser," *IEEE Trans. Aerosp. Electron. Syst.* **26**, 657-662 (1990).
- [4] P.Shi. and E. Stijns, "Improving the linearity of Michelson interferometric angular measurement by a parameter compensation method," *Appl. Opt.* **32**, 44-51 (1993).
- [5] Tippur HV, Krishnaswamy S, Rosakis AJ, "A coherent gradient sensor for crack tip deformation measurements: analysis and experimental measurements," *International Journal of Fracture* **48**, 193-204 (1991).
- [6] Tippur HV, "Simultaneous and real-time measurement of slope and curvature fringes in thin structures using shearing interferometry," *Optical Engineering* **43**, 1-7 (2004).

Fabrication of large Si window of 180 mm diameter

M P Singh, N Pandey, B Singh, S Mishra, K K Pant and A Ghosh
Instruments Research & Development Establishment, Dehradun
Email: mpsy79@gmail.com

Abstract: Silicon (Si) has been recognized as an ideal material for IR imaging application in 3-5 μm regions. The greater hardness, low coefficient of thermal expansion, low refractive index variation with temperature and high specific stiffness of the Si makes it a suitable material for optical windows to be used in this region. It is very difficult to polish large thin windows by conventional method because due to deblocking stress it is very difficult to maintain the surface accuracy. Here we report a technique to minimize deblocking stress so that large thin windows can be polished with high surface accuracy.

1. INTRODUCTION

A window is used in an optical instrument primarily as a transparent interface between the internal components and the outside environment. This is why optical flats/ windows are mostly used in optical instruments to protect the sensitive components and detectors that can be affected by environment^[1,2,3]. Usually, it is a plane-parallel plate of a material that allows the desired radiation to pass through with minimal effect on intensity and image quality, but excludes dirt, moisture, and other contaminants. For IR applications, the window must not radiate due to its temperature in a manner that interferes with its function.

The performance parameters for a window are parallelism, surface figure and transmitted wavefront. The requirements depend, of course, on the specific application and the wavelength used. For example, a visual viewing system may allow a wavefront error as large as one wave peak to valley (p-v) at 0.63 μm . A window for a conventional forward looking infrared (FLIR) sensor operating at 10.6 μm may tolerate 0.1 wave p-v wavefront error at that wavelength (equivalent to 1.7 waves p-v at 0.63 μm). It should be noted that transmitted wavefront errors include contributions resulting from material inhomogeneity, as well as those resulting from residual surface figure errors from fabrication and from mechanical deformations due to mounting or environmental influences. So from the fabricator's point of view, it is most important to control the surface figure errors and for this a precise control over the fabrication process is required.

Silicon (Si) has been recognized as an ideal material for IR imaging application in 3-5 μm regions. Its properties such as greater hardness, low coefficient of thermal expansion, low refractive index variation with temperature and high specific stiffness etc makes it a superior choice over other IR materials in this region. The hardness of the Si makes it a suitable material for optical windows to be used in this region. Ideally these optical windows have aspect ratio 1:10 or smaller to reduce the overall weight of the system. The optical flats/windows with aspect ratio 1:10 or better are

polished using double sided polishing machine or by means of free float polishing. It is very difficult to polish these windows with conventional method because due to deblocking stress it is very difficult to maintain the surface accuracy. Optical flats /windows with such a small aspect ratio always shows a deviation in their surface accuracy when these are deblocked.

2. POLISHING OF Si WINDOWS

The fabrication of a window involves following steps.

- Raw material shaping and trepanning
- Flattening one side of window
- Blocking to tool or runner
- Generating or lapping first side
- Polishing first side
- Re-blocking after protecting first side
- Lapping to thickness and polishing
- Deblocking and cleaning
- Testing surfaces



Fig1:- Si window blocked on a cast iron tool with the help of pitch

The process steps given above are common for any flat/window fabrication. The part is blocked on a tool with the help of pitch or wax and then processed in accordance with the above steps. When the first surface is polished completely and deblocked it is found that the surface figure degrades and becomes highly irregular. This is due to the thermal gradients generated between different areas of the block and thus different amount of holding force between pitch and sample

at different points of the block. Another reason for this is thickness of pitch becoming non uniform during the process due to thermal effects.

Here we report a very simple and effective method to polish optical windows with small thickness where stress during deblocking plays a critical role for large diameter of 180 mm^[1].



Fig2:- (a) Glass plate with circular hole

A method was adopted where pitch buttons are used on the cast iron blocking tool of 180 mm diameter and maintaining nearly uniform gap among pitch balls. To achieve this, a BK-7 glass plate of thickness 10 mm was fabricated and trepanned at different places of hole diameter 20 mm. This plate was rested on the cast iron tool and pitch is apply on that. The pitch is allowed to settle for half an hour at room temperature. Extra pitch from the top of the glass plate was taken out and glass plate was gradually removed.



Fig2:- (b) pitch button with glass plate

This approach allowed to make pitch button of uniform height and nearly uniform gap among them. The Si optics is placed on pitch balls of same height and pressed gently so that it is being blocked on the blocking tool. The blocked Si window was polished using continuous slurry method for 48 hours. The advantage of this modified blocking scheme is that it avoids the local heating of the job as the flow of slurry/coolant from the gap between the pitch buttons to prevent heating and thus the stress is not developed.



Fig2:- (c) Pitch buttons on cast Iron tool

The designed surface accuracy was 6 fringes or 3λ PV (1 fringe = $\lambda/2$, $\lambda=589.3\mu\text{m}$).The reference flat diameter was 110 mm .For smaller test flat and larger test surface, fringe scaling is required to maintain the designed tolerance on the complete polished surface of 180 mm diameter. From the given equation^[1]

$$N1 = N0 \times (D0/D1)^2 \quad (1)$$

Where N1 is number of fringes in D0=110 mm diameter and N0 (=6 fringes) is the number of fringes required in D1=180 mm diameter. N1 was calculated 2.24 fringes.

We have maintained 2 fringes or λ surface accuracy (Peak to Valley) on a part diameter of 110 mm at different points to ensure the regularity of fringes and maintaining tolerance of 6 fringes on overall surface.



Fig3 Polished Si window

3. RESULT

By using the above mentioned techniques Si windows with dia 180 mm and thickness 15mm (aspect ratio 1:12) were polished with surface accuracy $3\lambda/2$ which shows the effectiveness of this method.

4. CONCLUSION

We have developed a systematic and effective method to fabricate thin Si windows. By applying above described systematic approach thin Si windows can be fabricated.

5. REFERENCES

- [1] H. H. Karow, Fabrication methods for precision optics, *John Wiley and Sons Inc*, New York, (1993)
- [2] Twyman F., Prism and lens making, 2nd ed. London: *Hilger and Watts*, 1952. p. 375}80.
- [3] D. F. Home, Optical Production Technology, Second Edition, *Adam Hilger*, Bristol (1983)

PERFORMANCE EVALUATION OF A VISIBLE WAVELENGTH RANGE FABRY-PEROT INTERFEROMETER

S. K. Dhara*, J. Paul, B. Ravindra and Ravinder Kumar Banyal
 Indian Institute of Astrophysics,
 2nd Block Koramangala, Bangalore-560034, India
 Email: *sajal@iiap.res.in

Abstract: Fabry-Perot interferometer has been rapidly evolving and is gradually gaining acceptance for solar observations because of its extremely narrow pass band, high throughput, easy wavelength tunability, and large optical diameter. This paper outlines a method used to evaluate the Fabry-Perot interferometer. Two-dimensional characteristic maps of the Fabry-Perot interferometer, including the bandpass, effective finesse, peak transmission, along with free spectral range and flatness were obtained in a series of experiments. These studies are important for design and fabrication of the instrument for solar observations in future.

1. INTRODUCTION

The magnetic field on the Sun is highly dynamic and it rapidly evolves in space and time that leads to energetic events such as flares and coronal mass ejections. An instrument capable of taking the images of solar atmosphere at desired spectral and spatial resolution is necessary to investigate these highly dynamic processes. A Fabry-Perot based narrow band imager is being developed at Indian Institute of Astrophysics, Bangalore for such types of solar studies.

The current Fabry-Perot (*IC Optical System Ltd., U.K.*) interferometer has high average transmission (>95%) for the wavelength range from 400nm to 700nm. The calculated finesse due to reflectivity is ~ 61 and free spectral range is ~5.4Å at $\lambda = 656.3\text{nm}$. This paper outlines a method used to evaluate the performance characteristic of the Fabry-Perot and check the results against the device specifications given by the vendor.

2. FABRY-PEROT INTERFEROMETER CHARACTERISTICS

2.1 Basic Principles of Fabry-Perot Interferometer

A Fabry-Perot interferometer (FPI) consists of two plates with high surface reflectivity and an enclosing medium of refractive index n . It operates on the principle of multiple beam interference. The ratio of the transmitted intensity I_t relative to the incident intensity I_i can be written as (Born & Wolf 1999),

$$\frac{I_t}{I_i} = \left(1 - \frac{A}{1-R}\right)^2 \frac{1}{1 + \frac{4R}{(1-R)^2} \sin^2 \frac{\delta}{2}} \quad (1)$$

Where, A is the absorption coefficient, R the reflectivity. The phase difference (δ) between two successively transmitted waves is

$$\delta = \frac{2\pi}{\lambda} (2nd \cos \theta) \quad (2)$$

Where, d is the separation between two plates and θ is the incident angle of the beam. The transmission profile of the FPI is periodic. Two key parameters that should be considered carefully before building a narrow band imager using FPI are: a) Free Spectral Range (FSR) and b) the Full Width at Half Maxima (FWHM).

The free spectral range is the distance between two consecutive transmission maxima at a given wavelength. The Free Spectral Range (FSR) and effective finesse can be obtained from the following relations,

$$FSR = \frac{\lambda}{m} = \frac{\lambda^2}{2nd \cos \theta} \quad (3)$$

and
$$F = \frac{FSR}{FWHM} \quad (4)$$

3. LABORATORY EXPERIMENTS

3.1 Experimental Setup

We have characterized the Fabry-Perot using a collimated configuration, shown in Figure 1. A He-Ne laser of a center wavelength 633nm was used as a source to perform the experiment. The laser beam was passed through a spatial filter (a combination of 15 μm pinhole and a 40X microscopic objective) and the expanded beam was collimated by a $f=600\text{mm}$ lens (L1), resulting in a beam of diameter ~50mm to feed Fabry-Perot interferometer.

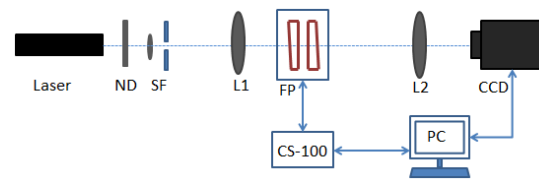


Figure 1. Sketch of the optical set-up to characterize the FPI. ND: Neutral density filter, SF: Spatial Filtering set-up, L1: Collimating

Lens, L2: Reimaging Lens and FP: Fabry-Perot interferometer.

The beam was re-imaged by a $f=225\text{mm}$ lens (L2) on a CCD camera (2KX2K). The plate spacing was controlled via IEEE-488 interface to the CS-100 controller via a PC. The CCD camera was controlled by the same PC to capture images as the cavity spacing was varied in incremental steps.

3.2 Procedure and Results

3.2.1 Bandpass

The FWHM of the bandpass of Fabry-Perot can be measured in the following way by assuming the bandwidth of laser beam is much narrower than the bandpass of Fabry-Perot. The spacing of the FP plates have been changed by 5 steps in order to get different orders of fringes and at the same time CCD camera captures the images at each wavelength steps. The scan is performed in discrete steps from 0 to 4095. In this way, a 3D data cube is generated by the scan. Figure 2 shows the transmitted images of the laser beam through the Fabry-Perot as the cavity spacing was varied from one maximum to other maximum.

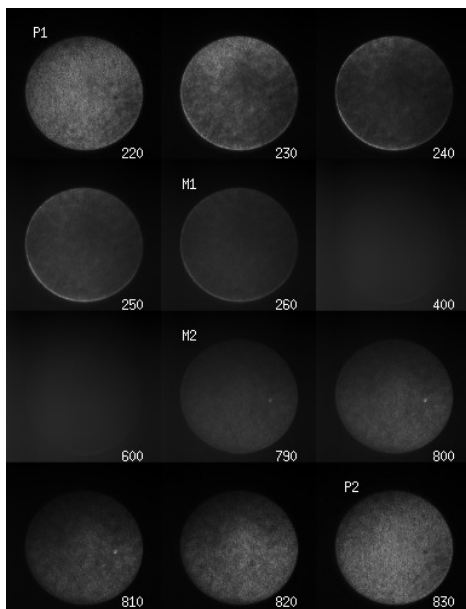


Figure 2. Captured images from the scanning of one transmission peak to other. The FPI steps corresponding to the images are shown in the label below. P1, M1 are the peak position and minimum position images respectively of the first transmission profile and P2, M2 are the peak position and minimum position images respectively of the second transmission profile.

An intensity profile which is the average of intensity in the central part of each images from the data cube, is shown in Figure 3. The effective FWHM

of the bandpass is obtained by fitting a Gaussian profile of the measured intensity values. The effective FWHM is found to be 29 steps, which corresponds to $\sim 23.77\text{pm}$. The conversion factor between wavelength units and discrete steps is given by 0.82 pm/step . In a similar way, a surface plot of the FPI bandpass in 2D space was constructed for each resolution element from the same data cube. Figure 4(A) shows the surface plot of FWHM of the Fabry-Perot bandpass and its corresponding histogram (Figure 4(B)). The figure implies that the bandpass is not homogeneous and most of the values are distributed from 18 steps ($\sim 14.75\text{pm}$) to 39 steps ($\sim 31.97\text{pm}$).

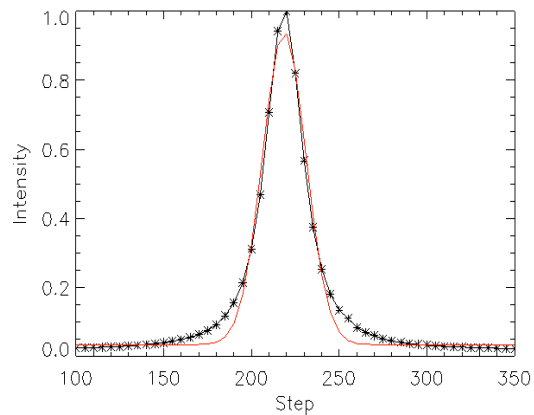
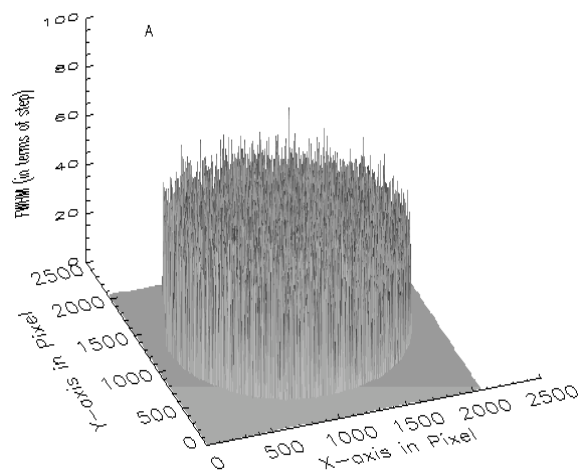


Figure 3. The average intensity profile of one transmission peak. The red line shows Gaussian fitting to the measured intensity profile. The wavelength regime is given in discrete steps (100-350) of the CS-100 controller.



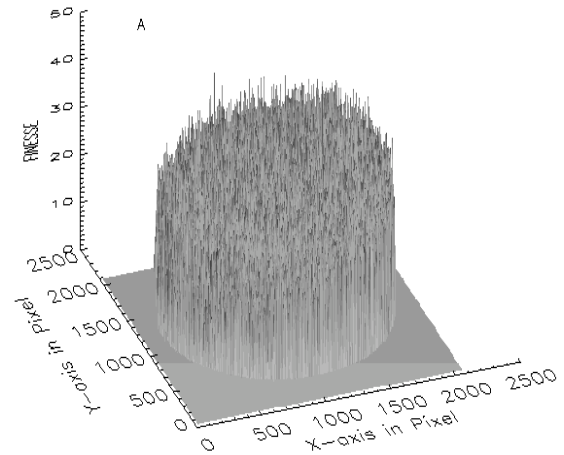
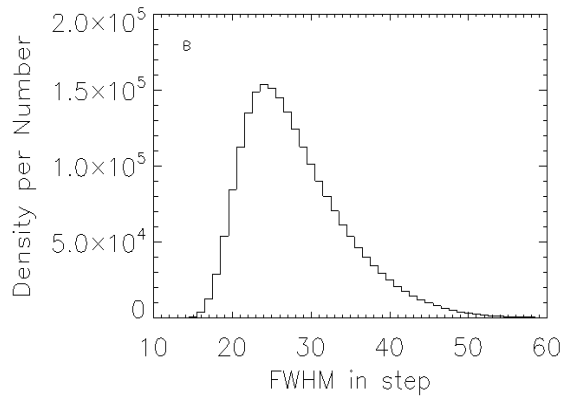


Figure 4. A) The surface plot of the FPI bandpass. B) Histogram of the corresponding frequency distribution.

3.2.2 Free Spectral Range and Finesse

Figure 5 shows the several transmission peaks to illustrate the free spectral range (FSR) of the FPI. The measured FSR is 610 steps ($\sim 499.93\mu m$). Since the nominal spacing between two parallel plates is $400\mu m$, then from the equation (3), the calculated FSR is $500.86\mu m$ at wavelength $633nm$. The total scanning range is $3.356nm$.

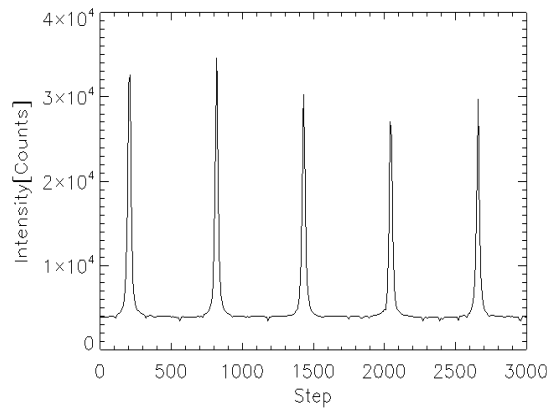


Figure 5. The average intensity profile of several transmission peaks. The wavelength regime is given in discrete steps (0-3000) of the CS-100 controller.

According to Equation (4), the average effective finesse is 21.03. A 2D surface plot of the finesse and its corresponding histogram of the frequency distribution were constructed, shown in Figure 6. The distribution of finesse over the field of view is inhomogeneous as well and most of its values are ranges from 13 to 30 (neglecting some spurious data at extreme edge).

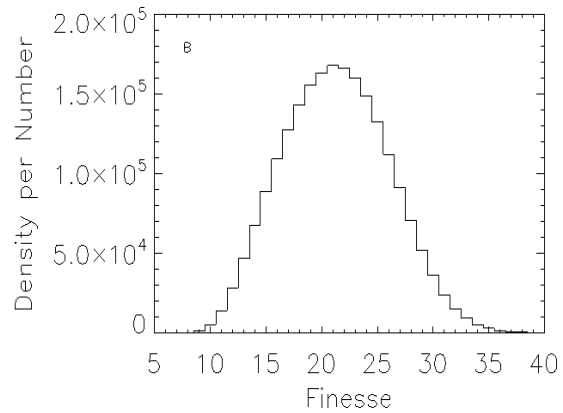


Figure 6. A) The surface plot of the FPI effective finesse. B) Histogram of the corresponding frequency distribution.

3.2.3 Plate Flatness

An appropriate understanding of the flatness of the Fabry-Perot plates is needed as it affects the bandpass and finesse of the system. With measurements of the surface flatness and surface roughness we can estimate the overall finesse of the FPI plates. In this study, from the same data cube (as mentioned in section 3.2) for each resolution element the peak position of transmission maxima is measured. And a 3D map of the surface flatness and its corresponding histogram was constructed as shown in Figure 7. From the maximum and minimum of the histogram we have determined that the surface has a peak-to-valley deviation about 15steps. This implies a surface flatness of about $\lambda/35$. The root mean square surface roughness calculated from the same data by neglecting some lower and upper pathological data is about 7 steps, which implies a surface roughness of $\lambda/74$.

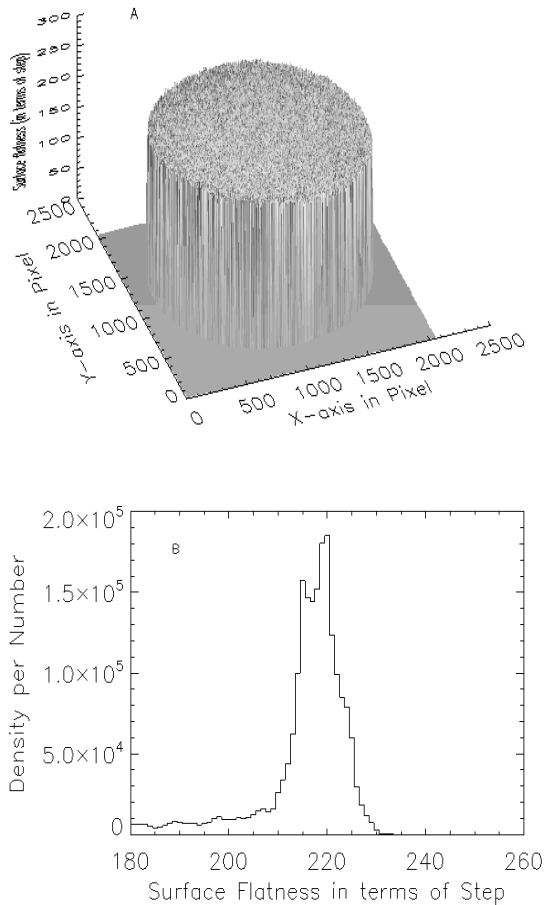


Figure 7. A) The surface plot of the FPI surface flatness. B) Histogram of the corresponding frequency distribution.

3.2.4 Transmission

In this study, we first constructed the peak transmission image from the same data cube as mentioned above. This peak transmission image is finally divided by a reference image which is nothing but an image of the laser beam without Fabry-Perot in the optical path. The measured average transmission of the FPI is about 76%.

4. DISCUSSION

The effective finesse is the most important part for the performance evaluation of Fabry-Perot Interferometer. It is dependent on the finesse (F_R) due to reflectivity, finesse (F_S and F_G) due to plate defects, and the finesse due to the illumination of the plates. In details, the finesse due to plate defects is dependent on overall flatness and roughness of the FP plates and the departure from the parallelism of the two FP plates. Assuming that the expanded beam was perfectly collimated and FP plates were sufficiently

parallel, the effective finesse of a Fabry-Perot can be represented as

$$F = \left(\frac{1}{F_R^2} + \frac{1}{F_S^2} + \frac{1}{F_G^2} \right)^{-1/2} \\ = \left(\frac{(1-R)^2}{\pi^2 R} + \frac{4\delta t_s^2}{\lambda^2} + \frac{22\delta t_G^2}{\lambda^2} \right)^{-1/2} \quad (5)$$

Where, δt_s is the peak-to-valley deviation from perfect flatness, δt_G is the plate rms-deviation. Reflectivity of the FP plate is given by 95%. Hence, we can find out $F_R = 61.24$. And according to section 3.2.1, $F_S = 17.285$ and $F_G = 15.761$. In conclusion, the calculated effective finesse is not in agreement with the measured finesse. The following possible reason might be helpful to interpret the differences between calculated and measured values. a) The measured FWHM for this FP may have been broadened by the finite bandwidth of the laser beam, resulting decreasing of the measured effective finesse (according to Equation (4)). b) The expanded source might not be perfectly collimated to feed the FPI, resulting in lowering the finesse. c) The Fabry-Perot unit is protected from dust etc. by two protective windows (made up of Perspex) which has lots of scratches and dips. Since the entire experiment was done without removing these windows, we suspect this too might have affected the estimation of surface flatness of the plates and caused further degradation of measured effective finesse. d) From the measured finesse, the estimated reflectivity of the FP plates is about 86%, which is not consistent with the vendor supplied values. So we can conclude this might be one of the reasons in degrading the effective finesse.

These experimental results will help to design and fabricate a Fabry-Perot based narrow band imager for solar studies in future.

REFERENCES

- [1] Born, M., & Wolf, E. 1999, Principles of Optics (Cambridge University Press)
- [2] C. Gullixon, "Characteristics of Available Fabry-Perot Filters", Tech. Memo., National Solar Observatory, 1998.
- [3] W. Cao et al., 2004, "Telescopes and Instrumentation for Solar Astrophysics". Edited by Fineschi, Silvano; Gummin, Mark A. Proceedings of the SPIE, **5171**, 307.

SPECKLE INTERFEROMETRY TO STUDY THE ROUGH EMERY SHEETS

Kapil Singh Kundu, Sunny Gulati, Shephali Gulati, Deepak Sharma and David Joseph
Optical Engineering Section, Department of Applied physics
Guru Jambheshwar University of Science and Technology,
Hisar- 125001, Haryana
Mail id: davedjp07@gmail.com

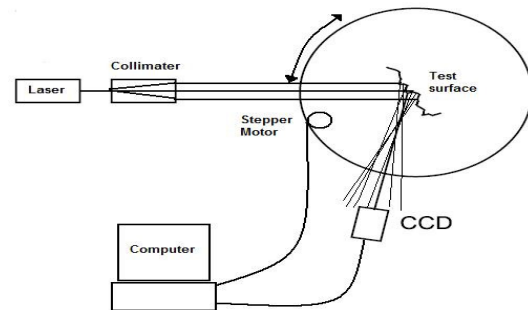
Abstract: Interference phenomenon in scattered light is an important optical phenomena which is extensively used in Speckle interferometry to find out the surface roughness of materials. In the present study we designed a speckle interferometer with a stepper motor card for precise automatic rotation of CCD and a laboratory spectrometer. This setup can be used to find out the surface roughness of the sample given. Image obtained from the CCD are processed using ImageJ Program to find out the correlation of the images.

1. INTRODUCTION

There has been lot of increased interest for surface roughness by the development of the laser in 1960. This technique is of much interest in the paper industry. In the present study, the image obtained by speckle in the given sample surface is considered as a series of images, and therefore image analysis methods are suitable for the characterization of sample surface. This technique has been used widely in sample characterization because it provides not only the correlation of the images but also gives the profile of the surface at each point. In this method, a tightly focused laser beam that is intense enough to induce speckles in the sample is used. As the sample is lightened up by the tightly focused laser, due to different reflections from each surface point the interference phenomenon formed forms a speckle pattern which then can be recorded with the help of CCD. This speckle pattern can be used to find out the surface roughness characteristics.

2. EXPERIMENTAL

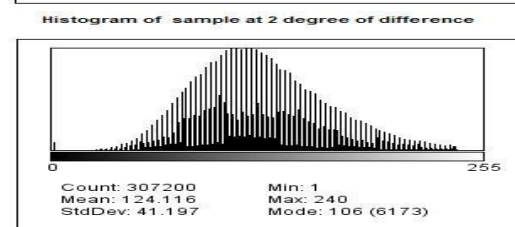
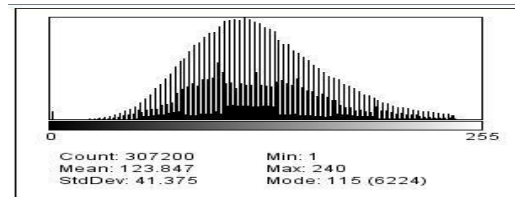
The main components of the setup are the Collimating arm with a Helium-Neon and a beam expander. The CCD (the detector) moved 2 degree approximately in each step. The Collimating arm and the CCD detector arm were both mounted and fixed with a laboratory spectrometer. The movement of the CCD is done by using NMB PMK55L-048 Steeper motor which is controlled by a program through computer. The program is burnt into Microsoft visual macros. The setup is being used to obtain roughness parameters of Emery papers of different roughness grades.



A ImageJ program is used to analyze input data obtained from the setup which read the initial data of a particular speckle scan and calculates the positive and negative functional values [1].

3. RESULTS

Each speckle pattern is recorded for few angles for five different Emery sheets. Typical histograms are shown below. The skewness and Kurtosis values are computed by the Image J Program. Further studies are focused on finding the Correlation functions



4. REFERENCES

[1]. Jan Valcek Vilem Madr, "Utilization of optical methods for determination of surface properties" vol 15. Metal, Ostrava, Czech Republic, (2001).

BINARY HOLOGRAM BASED BEAM SCANNING WITH EQUAL STEP SIZE

Abhijit Das and Bosanta R. Boruah

Indian Institute of Technology Guwahati, Guwahati, Assam

Email: ab.das@iitg.ernet.in

Abstract: In this paper we describe a scanning technique to scan a laser beam with equal step size. The scanning with equal step size is achieved by writing a sequence of binary amplitude hologram on a computer controlled Liquid crystal spatial light modulator (LCSLM). First a binary hologram is computed and displayed on the LCSLM via a Labview program. For a collimated laser beam the LCSLM acts as diffraction grating and diffracts the beam. When the diffracted beam is focused by a lens, ± 1 , ± 3 , ± 5 etc. diffraction orders along with the undiffracted beam appears on the back focal plane of the lens. The location of the diffracted beams relative to the undiffracted beam depends on the spatial frequency of the hologram. Out of the diffracted beams the +1 order beam is taken as the beam to be scanned and is isolated from the other orders by placing an iris diaphragm just in front of the focal plane. A CCD camera is placed on the focal plane of the lens so that the +1 order beam is focused on the CCD sensor plane. By changing the spatial frequency of the hologram along one axis the beam can be made to move along a line on the CCD sensor plane. For each location of the beam on the CCD camera, the beam location is recorded. However the location of the beam is not exactly a linear function of the spatial frequency when the diffraction grating is implemented by a pixelated device. Thus increase in spatial frequency in equal step size is not going to give equal separation of the +1 order beam. Here we show that by constructing a map between the beam location and the corresponding spatial frequency of hologram one can get beam scanning with small but equal step size.

1. INTRODUCTION

The scanning of a laser beam has wide range of applications such as scanning optical microscopy [1] etc particularly. In scanning microscopy a laser beam is scanned relative to the sample plane by a beam scanner. There are number of techniques for scanning a laser beam such as galvo scanner mirrors, micro electromechanical system (MEMS) actuator etc. However such techniques have limited repeatability and accuracy in beam positioning. As a result there is a necessity of beam scanning mechanism that has precise beam positioning ability especially for applications involving long period of operations.

In this paper we describe a beam scanning mechanism where the beam can be scanned with equal steps and with precise beam positioning. The scanning of the beam is achieved by using a computer controlled LCSLM assembly. The LCSLM assembly allows the implementation of a computer generated holography technique to generate a diffracted beam which can be scanned by displaying a sequence of holograms on the LCSLM. Here we show that by generating a map between the beam deflection and the spatial frequency in the hologram, the beam can be made to scan with small but equal step size. We present here proof of concept experimental results.

2. BEAM SCANNING USING BINARY HOLOGRAMS

As stated previously, in the proposed method, the beam scanning is performed by a computer generated holography technique. The working principle of this technique is depicted in the Fig. 1. Figure 1(a) shows a square wave transmission grating comprising of black and white stripes of equal widths. The black

stripe has zero light transmittance while the white stripe has the maximum light transmittance. The focused diffraction pattern due to the hologram in Fig. 1(a) can be computed by taking Fourier transform of the array representing the hologram. The resulting pattern obtained numerically is shown in Fig. 1(c). Figure 1 (b) shows another such hologram with larger spatial frequency of the square wave. The corresponding diffraction pattern is seen in Fig. 1(d). It is seen from the two diffraction patterns that the location of the diffracted orders relative to the undiffracted zero order is a function of the spatial frequency in the hologram. Thus, in principle one of diffracted beams can be made to scan a given line or area by changing the spatial frequency in the grating in a dynamic fashion.

Binary holograms as shown in Fig. 1 can be realized with the help of an LCSLM assembly. The LCSLM is a display device comprising a two dimensional array of liquid crystal pixels. The light transmittance property of each pixel can be controlled individually on application of an electric field. Thus by displaying an appropriate pattern the LCSLM can be made to act as a binary hologram.

The beam scanning mechanism on the basis of the computer generated holography technique implemented with a transmissive type LCSLM is described in Fig. 2. The amount of deflection of the beam along x and y axis is represented by m_x and m_y . Let $\varphi(x, y)$ be the phase of the beam on the plane P_1P_2 , where (x, y) are the coordinates of the plane. The total phase $\Phi(x, y)$ of the beam on the plane P_1P_2 is

$$\Phi(x, y) = \varphi(x, y) + xm_x + ym_y \quad (1)$$

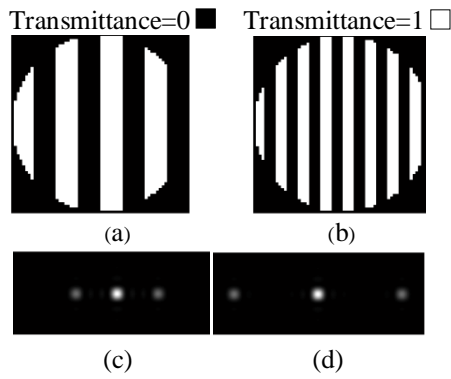


Fig.1 Holograms with their diffraction patterns

The phase $\Phi(x, y)$ of the beam at each point of the plane P_1P_2 is described by the pixel value at the corresponding location of the LCSLM. If $p(x, y)$ is the pixel value of the LCSLM the

$$p(x, y) = \begin{cases} 1, & \text{if } \cos\{\Phi(x, y)\} > 0 \\ 0, & \text{if } \cos\{\Phi(x, y)\} \leq 0 \end{cases} \quad (2)$$

The plot between p and Φ is a square wave. Hence for a collimated laser beam the LCSLM acts as binary amplitude hologram. When a collimated laser beam is diffracted by the LCSLM and then focused by a lens, different diffraction orders $\pm 1, \pm 3, \pm 5 \dots$ etc. along with the undiffracted beam appear in the back focal plane of the lens [2, 3]. The location of the +1 order beam depends on the number of square wave i.e., values m_x and m_y , focal length of the lens and the wavelength of the laser beam. By changing the values m_x and m_y of the hologram, the +1 order beam can be scanned. The location of the +1 order beam can be recorded as the coordinates of a CCD pixel plane placed at the focal plane of the lens L_1

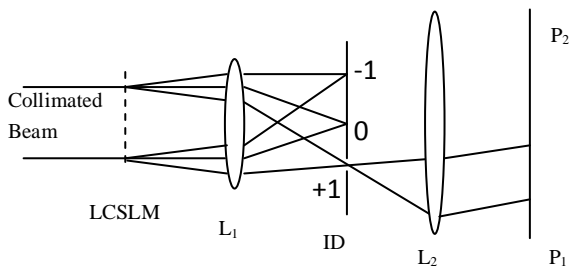


Fig.2. Set up for generating the illumination beam

3. BEAM SCANNING WITH EQUAL STEP SIZE

Suppose a hologram is described over $N \times N$ number of pixels of the LCSLM and let the number of square waves in the hologram along horizontal direction is m . So the hologram will be consists of m numbers of dark and equal number of bright stripes. Each dark or bright stripe will contain $\frac{N}{2m}$ number of pixels provided $\frac{N}{2m}$ is an integer. Such a hologram is shown in Fig. 3(a) with $N=64$ and $m=8$. But such a requirement is always not satisfied and in such a situation the numbers of pixels in dark and bright

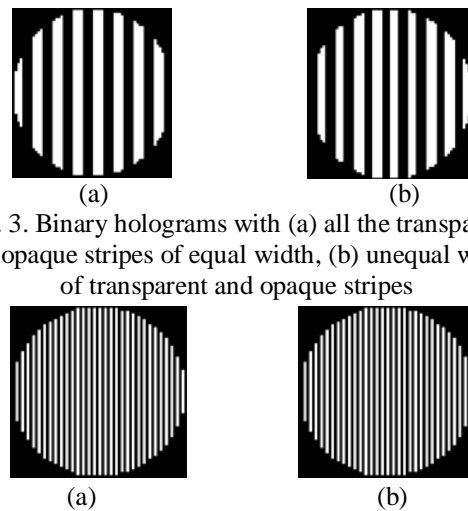


Fig. 3. Binary holograms with (a) all the transparent and opaque stripes of equal width, (b) unequal width of transparent and opaque stripes

Fig. 4. Binary holograms with (a) $m=31.9$, (b) $m=32.0$

stripes are not equal. A hologram with such a condition, i.e., $N=64$ and $m=9$ is shown in Fig. 3 (b). It can be seen that when the number of square waves of the hologram increases or decreases in a certain uniform steps the movement of the beam on the focal plane i.e., on CCD camera is not uniform. Again when we increase or decrease the number of square waves of the hologram programmably in very small steps, the square wave in the hologram does not change its states relative to the previous value of m . Fig. 4 (a) and (b) show two holograms of $N=64$ having same states but different m values such as $m=31.9$ and $m=32.0$. Since both the holograms are similar, when the value of the m changes from 31.9 to 32.0 the location of the +1 beam does not alter its location. Thus when the value of m changes in small steps, the change in the state of the square wave is not uniform and exist discontinuities at some values of m . As a result as m changes in equal but small steps the deflection in the beam is not uniform.

Further, the beam on the CCD camera can be made to travel along a line by uniformly changing the spatial frequency of the hologram in small step. If the displacement of the beam is smaller than the pixel size of the CCD camera, the program will record the identical beam locations for a few consecutive frequencies of the hologram until the beam moves to the next pixel. Such a step like plot is shown in Fig. 5, where the location of the beam is plotted against the spatial frequency of a hologram. Here the location of the beam with respect to the undiffracted beam is found by computing the Fourier transform over 2400×2400 pixels of a hologram described over 600×600 pixels. The graph between beam location and frequency is plotted for the change of frequency from 100 to 110 in step of 0.1.

In order to make the beam move in small but equal step size it is required to construct a mapping between the beam position in the CCD plane and the spatial frequency in the hologram. The beam position as the

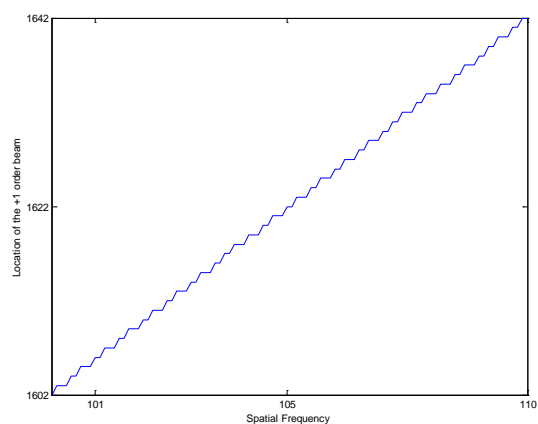


Fig. 5. Numerically computed beam location as function of the spatial frequency

coordinate of CCD pixels and the corresponding spatial frequency of the hologram can be recorded and stored by a computer program. The program then reads the recorded beam coordinates and selects the beam location which lies at the middle of each step and the corresponding frequency. During scanning of the beam for uniformly separated beam locations, the program reads the corresponding spatial frequency from the map and displays an appropriate hologram. As a result the beam will move in steps with step size equal to the pixel size of the CCD camera.

4. THE EXPERIMENTAL SETUP

The proposed beam scanning mechanism setup is shown in Fig. 6. The laser beam from the source is expanded and collimated using two lenses L_1 and L_2 , then allowed to fall on a computer controlled reflective type LCSLM. A Labview program running in a PC computes an appropriate binary hologram and displays over the LCSLM panel. The diffracted beam from the LCSLM is focused by a lens L_3 kept at a distance of focal length of the lens from the LCSLM. A CCD camera is placed on the focal plane of the lens L_3 to detect the +1 order beam. The +1 order is isolated from the other diffraction orders by placing an iris diaphragm (ID) just in front of the CCD camera. The Labview program then computes a sequence of holograms and displays on the LCSLM. As a result, the diffracted +1 order beam on the CCD camera travels in a particular direction. The program records the location of the beam on the CCD camera and corresponding spatial frequency of the hologram.

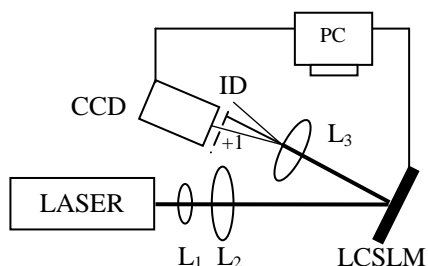


Fig. 6. The beam scanning arrangement

5. RESULT AND DISSCUSION

A hologram of dimension 700×700 is displayed on the LCSLM with initial spatial frequency ($m_x=100$, $m_y=100$) along x and y axis of the hologram. The diffracted beam is focused by a lens of focal length 30cm on the CCD camera so that the only +1 order beam falls on the CCD camera. The CCD camera comprises of two dimensional arrays of 1024×768 pixels. The pixel pitch of the camera is $4.5 \mu\text{m}$. The beam on the camera observed to be very much aberrated the due to LCSLM, and other optics. The aberration is corrected using the aberration correction facility provided by the program [3, 4]. The program changes the spatial frequency of the hologram along the x direction from 100 to 300 in step of 0.05. So the beam on the camera moves over 4001 discrete locations between the pixel number 245 and 834 along x-axis in the camera plane. The program records the beam positions as the pixel coordinates. A portion of the plot between spatial frequency and recorded beam coordinates is shown in Fig. 7(a). From the plot it can be seen that there are some regions where the beam has moved backward. The reason for this is attributed to external vibration. Before starting the scan for equal step size the program corrects these coordinates by assuming that the backward movement has actually not occurred. The corrected beam location as function of spatial frequency is shown in Fig. 7(b). The resulting data is used to construct the map between the beam location and the spatial frequency in the hologram. The beam is then scanned using the constructed map.

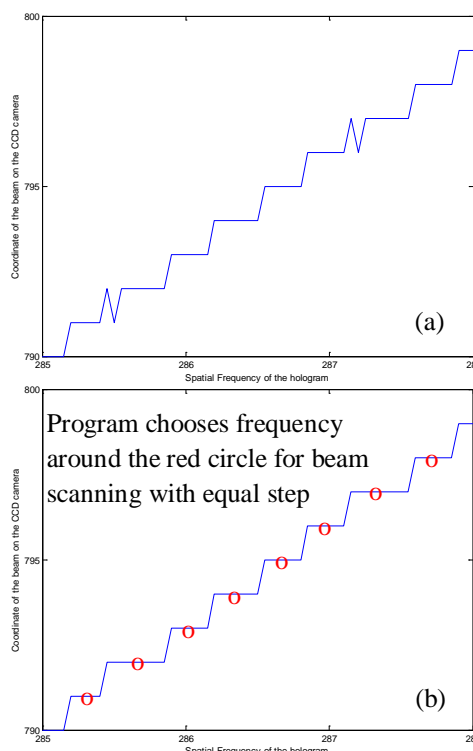


Fig. 7. Plot of (a) recorded beam locations and (b) corrected beam locations

During this scanning, the beam moves only in $(834-245) + 1 = 590$ number of discrete location with step equal to the size of the pixel pitch of the camera. The experiment is repeated by replacing the lens L_3 with another lens with focal length 15 cm. At this time the spatial frequency of hologram is changed from 100 to 300 in step of 0.1 i.e., the beam has 2001 discrete locations on the camera and the beam on the camera moves from pixel number 123 to 440 along x-axis. Thus the beam has $(440-123)+1=318$ discrete locations on the camera.

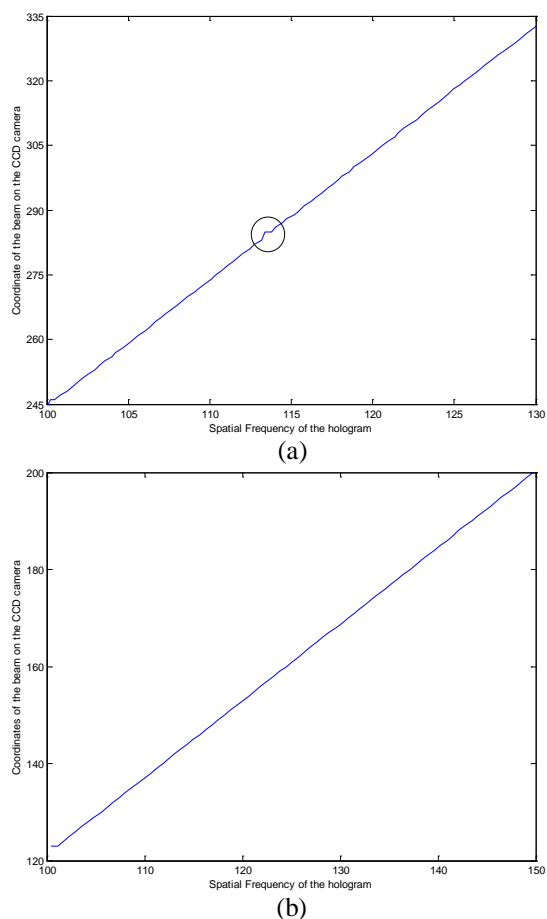


Fig. 8. Plot of the recorded beam locations as the coordinate of the pixel of the CCD camera and spatial frequency with lens focal length (a) 30cm and (b) 15cm

A portion of the recorded beam locations during the scanning for equal step size are shown in Fig. 8(a) and (b) using lenses of focal length 30cm and 15cm respectively. The figures show that the beam moves with equal steps except some locations as can be seen from Fig. 8(a). This is due to external vibrations as mentioned earlier. For checking the repeatability of the scanning mechanism the beam is scanned for 30 times for the both lenses. The variance of the beam at each beam location corresponding to each spatial frequency is calculated. The maximum variances are found to be 0.2576 and 0.1 for lens 30cm and 15cm focal length respectively.

6. CONCLUSION

We have presented a technique to scan a laser beam with equal step size having maximum probable error equal to the pixel pitch of the CCD camera. The error can be reduced by replacing the CCD camera by one with smaller pixel pitch. The anomalous displacement of the beam due to the vibration can also be diminished by using a vibration isolation table. The experimental results have showed that the scanning mechanism provides precise beam positioning and repeatability.

REFERENCES

- [1] J.B. Pawley, ed., *Handbook of Biological Confocal Microscopy*, Springer, 2006
- [2] M. A. A. Neil, M. J. Booth, and T. Wilson, "Dynamic wave-front generation for the characterization and testing of optical systems," *Opt. Lett.* **23**, 1849 (1998)
- [3] B. R. Boruah, "Dynamic manipulation of a laser beam using a liquid crystal spatial light modulator", *Am. J. Phys.* **77**, 331 (2009).
- [4] Abhijit Das and B. R. Boruah, "Optical sectioning microscope with a binary hologram based beam scanning", *Review of Scientific Instruments* : **82** 043702 (2011).

A REMOTE CONTROLLED OPTICAL PERISCOPE FOR CORE VIEWING IN PROTOTYPE FAST BREEDER REACTOR (PFBR)

Sanjiva Kumar, D. V. Udupa, R. V. Sakrikar*, A.M. Kadu* and N. K. Sahoo

Applied Spectroscopy Division, Bhabha Atomic Research Centre, Trombay, Mumbai 400 085

*Division of Remote Handling & Robotics, Bhabha Atomic Research Centre, Trombay, Mumbai
E-mail: sanjivk@barc.gov.in

Abstract: A 10-meter long optical periscope has been developed for viewing and video recording the objects in the core of a Prototype Fast Breeder Reactor (PFBR) during maintenance. The system is capable of viewing the 0.2 mm thick lines separated by spacing of 0.5 mm at an object distance of 4 meter from the objective end. The periscope can be remotely operated for scanning the area of interest, image zooming and rotation.

1. INTRODUCTION

A periscope is an optical instrument that facilitates viewing of objects in a remote or out of line of sight location [1, 2]. In a nuclear reactor, a periscope is an important in-service inspection tool for regular maintenance and other operations in radiation environment under shut down conditions.

We present here the development of 10 meter long periscope for remote viewing of the core of Prototype Fast Breeder Reactor (PFBR) coming up at IGCAR, Kalpakkam.

2. DESCRIPTION

PFBR main vessel core is filled with liquid sodium, which is the coolant for the reactor during operation. The space above this liquid is filled with argon cover gas and has many sub-assemblies that require visual inspection during reactor maintenance. The periscope has been designed for introduction into the reactor from the top roof slab vertically for this inspection. The instrument can operate at ambient temperature of the



Fig.1 Photograph of periscope cover gas, which is 150° C and radiation field of 1.3 R/hr. Additional accessories such as Leak Tight Chamber, Preheating Chamber and Gate Valves ensure periscope introduction and inspection in a leak tight manner. The Periscope is also sealed, purged with Argon and maintained at slightly higher pressure than the reactor cover gas, ensuring no leakage of reactor argon in case of seal failure. The complete assembly consisting of viewing and illuminating

canals is housed in a 10 meter long cylindrical tube of 400 mm diameter.

3. OPTICAL DESIGN

The optical design of the periscope incorporates the facility for scanning the area of interest, zooming arrangement, image focusing and image rotation for proper perspective in viewing, which are motorized and can be remotely operated.

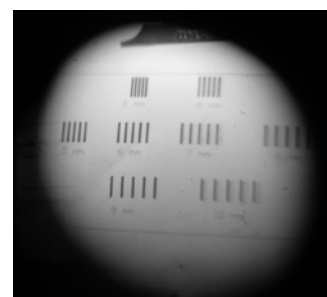


Fig. 2 Image of a test target viewed through the periscope

The Periscope has a set of stationary and movable prism mounted in front for object scanning in vertical direction, a zoom lens objective for primary imaging, six relay lenses and two field lenses for transmission of the image, pechan prisms for image rotation, a beam-splitter and eyepiece [3]. By rotating the prisms, rotating the periscope about its own axis and adjusting the height of the periscope, the operator can survey the complete area of interest. The final image obtained at the eyepiece is erect and non-laterally reversed.

3. CONCLUSION

A remotely controlled optical periscope has been developed for in-service inspection of PFBR. The periscope is possibly the longest such instrument to be used in fast breeder reactors.

REFERENCES

- [1] Francis B Patrick, "Military Optical Instruments" in *Applied Optics and Optical Engineering*, Vol. V Part II, R. Kingslake, ed. Academic Press, New York, pp 209-214 (1969)
- [2] M Born and E Wolf, "*Principles of Optics*," Pergamon Press London, New York, 6th Ed., pp 243 - 245 (1980)
- [3] D V Udupa and Sanjiva Kumar, "Optical Design of a 10 Meter Remote Viewing Periscope using Radiation Hard Glasses," *Proc. of Intl. Conf. on Optics & Photonics*, Chandigarh, Oct. 30 - Nov. 1, p. 226 (2009)

INITIAL CORRECTION OF RANDOMLY ABERRATED DEFORMABLE MIRROR SURFACE FOR ADAPTIVE OPTICS SYSTEM

Vikash Porwal*, Dinesh K. Meena, Sanjay K. Mishra, D. Mohan, and A. K. Gupta
Adaptive Optics Group, Photonics Design Centre, Instruments R & D Establishment (DRDO)
Dehradun 248008, India.
*vporwal26@gmail.com

Abstract: Deformable mirrors are used for controlling the wavefront shape in adaptive optics technology. Deformable mirror needs to be corrected initially for the random surface aberrations before using it in adaptive optics closed-loop. The corrected surface ensures the generation of requisite phase conjugated wavefront. The correction procedure is established and results are presented.

1. INTRODUCTION

In adaptive optics (AO) systems, deformable mirrors (DM) [1, 2] are used to compensate for medium induced dynamic wavefront aberrations. The DM surface dynamically adapts to conjugate the local phase errors consequently compensating the wavefront aberrations.

Earlier, we worked on micro-machined deformable mirror (MMDM), its performance was evaluated for various parameters such as initial mirror surface figure, single and multiple actuator responses, etc. [3].

Presently we are working with the DM from M/s Xinetics, USA. It consists of a 2 mm thin facesheet attached to 37 electrostrictive PMN (lead magnesium niobate) ceramic piezo actuators, bonded to a base and arrayed on a square grid spaced 7 mm apart with 25 μm tolerance. The actuators are capable of delivering 4 μm mechanical stroke at 100V. The facesheet permits the shape of the reflective surface to be modified, thereby changing the phasefront of light reflected from the mirror. A complete mirror system consists of DM, interface cabling, and driver electronics.

DM needs to be corrected for the random surface aberrations before its use in adaptive optics closed-loop. The corrected DM surface ensures the generation of suitable phase conjugated wavefront. It should be noted that it is possible to use DM in AO closed loop without flattening it, because AO closed loop in itself is a convergent iterative process. However, such an approach achieves DM control at the expense of precious bandwidth, and the poor wavefront correction. Therefore corrected DM surface is prerequisite for achieving the optimal performance of adaptive optics system.

2. METHODOLOGY

DM surface was investigated at a wavelength of 633 nm over the full aperture by Zygo phase shift interferometer having 4" aperture. The alignment and mapping of the mirror was defined within the flattening program and it was ensured that the mirror did not move during the flattening process. Interferometer generated the high resolution phase

maps of DM surface driven by Xinetics driver electronics and saved the phase data in binary file format. Digital commands for driver electronics range from -32766 counts to +32767 counts. The dedicated MetroPro software provided the mirror surface statistics in terms of various parameters. A typical MetroPro screenshot showing biased mirror surface is shown in Fig. 1.

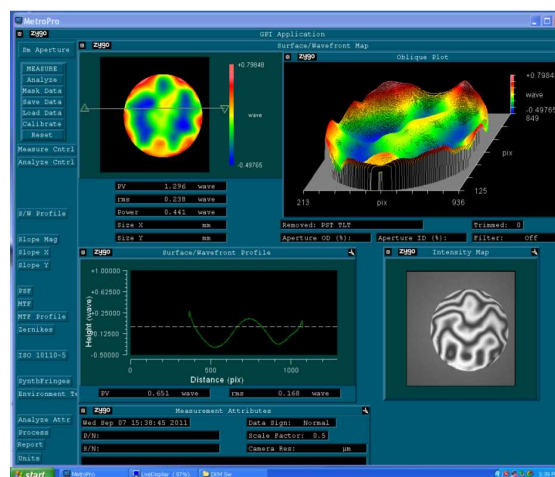


Figure 1. Biased mirror surface

A correction methodology was evolved [4] and MATLAB flattening program was developed for reducing the initial DM surface aberrations. The program included the procedures for mirror alignment within the phase map, estimation of actuator coordinates, calculation of average phase at actuator locations, and finally generation of compatible digital commands for the driver electronics. A few iterations were used to minimize the residual error and hence flatten the mirror surface. A routine was also developed for reading Zygo binary files into appropriate data arrays within the flattening program. The flow chart shown in Fig. 2 elaborates the steps involved in the flattening process. The laser source wavelength and the interferometer scale factor were the most important parameters for determining the conversion of the phase measurements from waves to microns.

The optical path difference (OPD) at actuator locations were converted into a digital command by assuming the following relation for m^{th} actuator.

$$C_m = \frac{32767 \Delta Z_m}{S_{max}}$$

Where; C_m is the command value, ΔZ_m is the average OPD, and S_{max} is the maximum stroke.

The following iteration was then used to reduce the residual error and hence flatten the DM surface.

$$C_{j+1} = C_j - \Delta_j$$

Where; C_j is the j^{th} command frame, Δ_j is the j^{th} measurement made, C_{j+1} is the next set of commands to be applied.

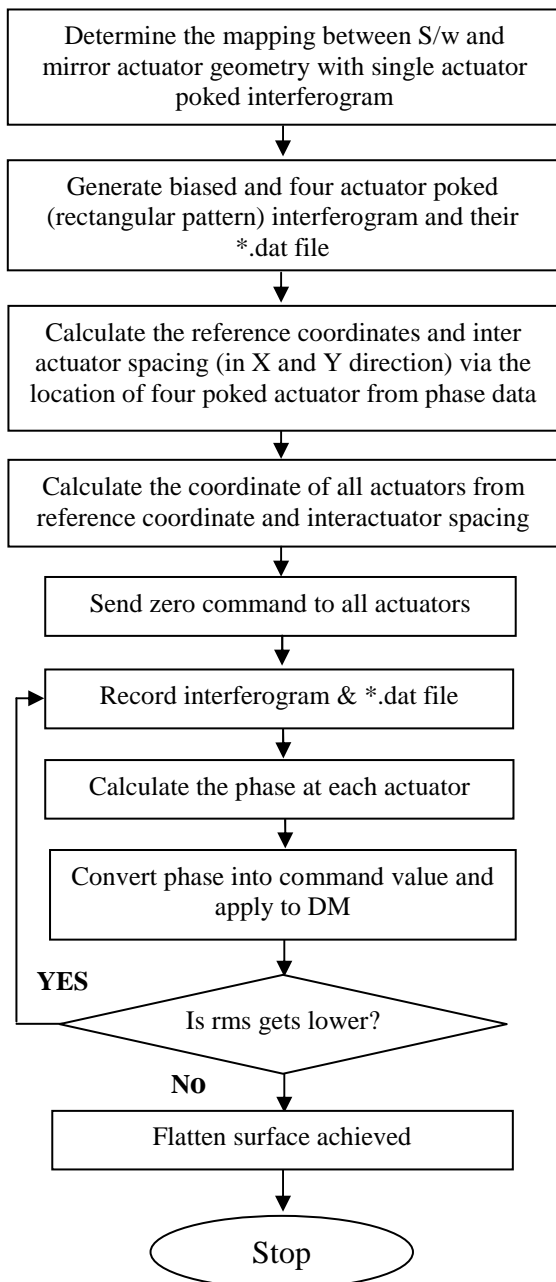


Figure 2. Flow chart for flattening process

3. RESULTS & DISCUSSION

The interferograms showing the PV and rms values were recorded for different procedural steps. The rms value of the powered initial DM surface was found to be 0.238 waves as shown in Fig. 2. For all iterations the rms values of mirror surface were recorded for case 1 and case 2 are shown in Table 1.

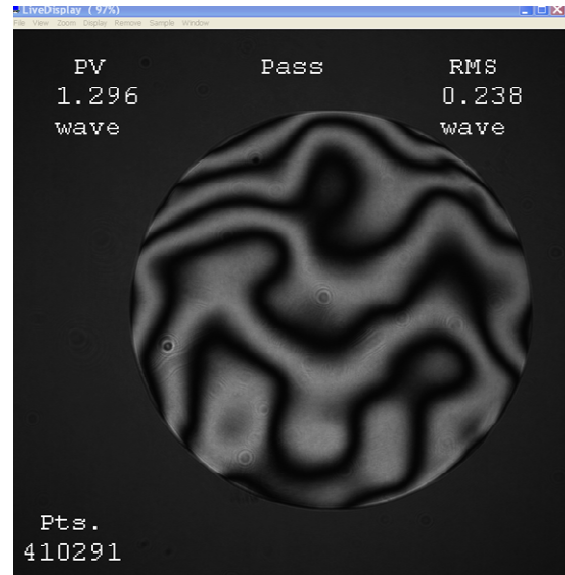


Figure 2. Powered initial DM surface having random aberrations

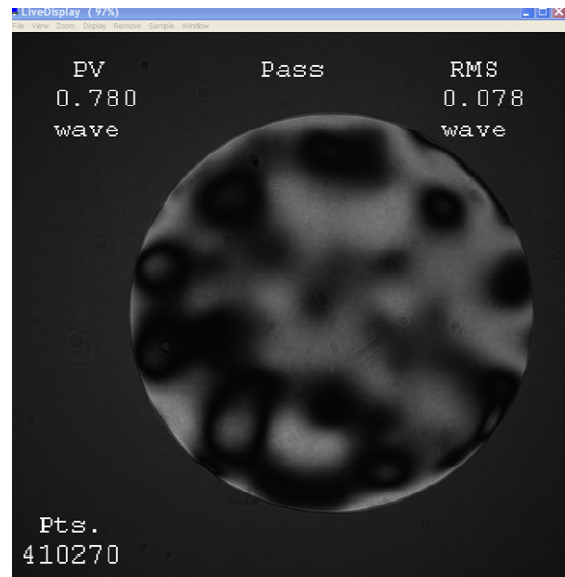


Figure 3. Flattened DM surface after eight iterations

It was found that the rms values in case 2 were converging faster as compared to the values in case 1. Significant improvement was obtained both for rms values and number of iterations for case 2 as shown in Fig. 4. This was attributed to the implementation of improved algorithm in terms of better mapping of actuators onto the

phase map. The final command frame obtained after eight iterations was found to be as shown in Table 2. The flattened mirror surface was found to be of the order of $\lambda/13$ as shown in Fig. 3.

Iteration No.	Surface RMS (Waves)	
	Case1	Case2
0	0.238	0.238
1	0.175	0.163
2	0.141	0.119
3	0.122	0.098
4	0.108	0.089
5	0.102	0.081
6	0.100	0.080
7	0.099	0.078
8	0.095	0.077

Table 1. DM surface rms values (in waves)

0	0	-2526	1247	-9466	0	0
0	-9	-433	2564	-785	-1729	0
0	3315	-681	-1329	4519	3801	395
-2013	3015	860	-597	-194	3847	-1358
-1331	4423	2504	-81	3335	3841	-2323
0	-2069	3792	-1615	1689	1838	0
0	0	-1415	-1280	-1936	0	0

Table 2. DM surface flattening file

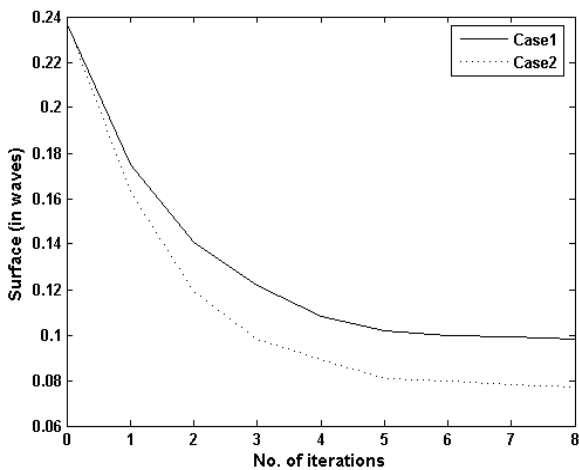


Figure 4. Correction results in flattening process

ACKNOWLEDGEMENT

The authors are grateful to Shri S. S. Sundaram, Director, IRDE for inspiration, Shri H. B. Srivastava for valuable suggestions and Senior General Manager, Ordinance Factory, Dehradun for facilitating the use of Zygo interferometer.

REFERENCES

[1] L. Zhu, P. C. Sun, D. U. Bartsch, W. R. Freeman and Y. Fainman, "Adaptive control of a micromachined continuous-membrane deformable mirror for aberration compensation" *App. Opt.* **38(1)**, 168-176 (1999).

[2] J. A. Perreault, T. Bifano, B. M. Levine and M. Harenstein, "Adaptive optic correction using microelectromechanical deformable mirrors" *Opt. Engg.* **41(3)**, 561-566 (2002).

[3] V. Porwal, A. Dixit, S. K. Mishra, D. K. Meena, D. Mohan, and A. K. Gupta. "Performance evaluation of micro-machined deformable mirror", *Proc. of International Confrence on Contemporary Trends in Optics and Optoelectronics-2010 (Extended abstract)*, 106 (2011).

[4] A. Sivaramakrishnan and B. Oppenheimer "Deformable mirror calibration for adaptive optics systems", *Proc. SPIE*, **3353**, 910-916 (1998).

GENERATION AND DETECTION OF LOWER ORDER ZERNIKE ABERRATIONS

*Sanjay K. Mishra¹, Geeta Kandhol², Awakash Dixit¹, D. Mohan¹, and Anurag Sharma²

¹Instruments Research and Development Establishment (DRDO), Dehradun-248008, India

²Indian Institute of Technology Delhi, New Delhi-781039, India

*skmishra@irde.drdo.in

ABSTRACT: In this paper we report the generation and detection of the lower order Zernike modes in a quantified manner that is required for the testing and performance evaluation of an AO system. We used a phase only SLM for the generation of these modes and a SH-WS for its detection. A MATLAB routine is written for the generation of these modes and the results obtained demonstrate the generation and detection of such modes with good resolution.

1. INTRODUCTION

When wave-front aberration changes unpredictably in real time, correction is not possible with conventional optics. Indeed we need an optical system which would be capable of compensating aberrations in real time. In current technologies adaptive optics (AO) deals with the control of wavefront aberrations in closed-loop fashion in real time. A key component of the AO system is Shack Hartmann wavefront sensor (SH-WS) which can detect the dynamically changing wavefront errors at 1000 frame per second. Such a fast SHWS is developed at Instruments R & D Establishment, Dehradun and is in use with adaptive optical system [1,2].

For performance evaluation of various AO subsystems there is a requirement of simulating the atmospheric turbulence conditions in the laboratory. Motivation behind the work is to simulate atmospheric turbulence conditions of known turbulence strengths. Wavefront errors induced by atmospheric turbulence can be expressed in terms of the combinations of various Zernike modes [3]. Precise generation and detection of standard Zernike aberrations are required for simulating the turbulence conditions. Now days due to availability of the spatial light modulator (SLM) from various firms allows, generating these Zernike modes accurately for wide dynamic range [4].

We generated various wavefront aberrations in terms of the Zernike modes using phase only SLM. As values of any Zernike polynomials is defined over unit circle and lies in the region $-1 \leq Z_i \leq +1$ [5], it needs to be normalized between 0 to 255 grey levels which corresponds to 0 to 2π phase of the SLM. A MATLAB based routine is written to estimate discrete wrapped phase levels for lower order Zernike modes. Single indexing scheme for these Zernike modes were used [5]. For 8-bit gray levels, the Zernike terms were calculated and normalized so that these would generate desired wavefront aberrations.

Earlier we have generated few off-axis aberrations using lens and concave mirror combination and used SH-WS for its detection [6]. Experimentally quantified known strengths of various lower-order Zernike aberrations were generated and further detected with conventional SH-WS accurately. Response curves for the detection of few lower order Zernike modes such as defocus (Z_4), astigmatism (Z_6), and coma (Z_8) were produced. Initial aberrations of the SLM have been also characterized.

2. SHACK-HARTMANN WAVEFRONT SENSOR

SH-WS is now being used in many different fields, from astronomy to industrial inspection. In ophthalmology, this sensor is very popular element of an aberrometer, used to assess the visual quality of eye and vision research, real time surgery monitoring and clinical diagnostics.

SH-WS is an improved version of classical Hartmann test and offers good dynamic range, accuracy, signal-to-noise ratio, and speed. In SH-WS local slope errors are measured and then different techniques are used to reconstruct the wavefront. In modal wavefront reconstruction these slope errors are used to fit into a complete set of Zernike modes. Modal representation has an advantage it provides phase quantization of wavefront in terms of contents of various Zernike aberrations. It involves extensive computation that scales with the spatial resolution of the sensor. In the modal wavefront reconstruction, the aberration $W(x, y)$ is approximated as a linear combination of a finite number of Zernike polynomials as given by eqn. 1.

$$W(x, y) = \sum_{j=1}^J c_j Z_j(x, y) \quad (1)$$

where c_j is strength of the Zernike aberration $Z_j(x, y)$ the orthogonal Zernike basis functions and J is number of Zernike terms used in this truncation representation. Zernike polynomials are widely used

in optics because they are closely related to aberrations introduced in optical systems. Hence individual polynomials describe aberrations such as defocus, astigmatism, coma, and spherical aberrations. The lowest order terms are analogous to the Seidel aberrations. These polynomials are complete set of orthogonal functions that represent balanced aberrations over the circular pupil. Since the polynomials are orthogonal therefore it is possible to separate the various effects, because presence/ or absence of one term does not affect the others. An advantage of using orthogonal set of functions is that the aberrations coefficients are uniquely specified regardless of truncation, although some errors occur due to series truncation. Because of the orthogonality the strength of a specific Zernike mode within $W(x, y)$ can be determined by projection

$$c_j = \int W(x, y)Z_j(x, y)dxdy \quad (2)$$

In the modal reconstruction method, the wavefront surface is described in terms of smoothly varying modes. The key property of these modes is that the analytic derivatives can be obtained that may be fitted to the measured slope errors. Since the modes are continuous and analytic through the first derivative, the wavefront gradient may be written as eqn. 3.

$$\left. \begin{array}{l} \partial W / \partial x \\ \partial W / \partial y \end{array} \right|_n = \sum_{j=1}^J c_j \left. \begin{array}{l} \partial Z_j / \partial x \\ \partial Z_j / \partial y \end{array} \right|_n \quad (3)$$

This provides an analytic description of wavefront slopes at every point, which may be compared to the measurement gradient values to obtain the appropriate set of coefficients c_j by least square fitting or other methods. Modal reconstruction provides a very compact notation for describing the wavefront, since the detailed shape information is contained in the modes $Z_j(x, y)$. In modal reconstruction the fewer the number of Zernike modes that are used in the fit, the smoother the representation will be. On the other hand, when the data is over smoothed, the information is mostly lost, specially the higher order modes.

3. PHASE ONLY SLM

SLMs are being used for various applications such as astronomical instrumentation, ophthalmology, apodization, focus tracking, optical image processing, and high resolution wavefront sensing and compensation [7-8]. For using SLM to any application, the wavefront aberration introduced by SLM has to be investigated. Initial aberration larger than 2λ are common for a given SLM and this would degrade the performance of optical setup for which it

is being employed. Liquid crystal on silicon (LCoS) from M/s Holoeye, Germany (Model: PLUTO HES 6010) is a phase only reflective micro-display of 1920 x 1080 pixel resolution. The electronic circuit controlling the LC is fabricated on a Si chip and since circuit is just behind the pixel therefore does not create any obstruction in the light path ("Screen door" effect). The device is optimized for phase shift $> 3\pi$ in visible spectrum and broadband AR coated. Average reflectivity of the device is ~60%, with high fill factor of 87%, pixel size 8 μm , and 8-bit addressable phase levels. Such phase only SLMs are being used for various applications like beam shaping, CGH, optical tweezers, wavefront manipulation, optical image processing, etc.

A good and complete calibration of SLM is an essential step, particularly if SLM is to be used in applications that require precise wavefront control. The inherent distortion of a reflective SLM may need compensation not only for the back plane curvature but also for other possible non-uniformities caused by thickness variations of the LC layer across the aperture. A method based on multi-point phase calibration of LCoS is discussed in [9]. A grid of elemental square cells onto the SLM aperture is defined and developed a multipoint calibration by means of which the relative phase variations between neighboring cells for uniform gray levels addressed to them are detected. From the measurement of these variations an update map of the inherent phase error can be built and a multi look up table (LUT) can be defined for more complete compensation. The method generates a specific LUT for every element of SLM aperture.

At SLM we need to produce specific lower order Zernike mode corresponding to the Zernike coefficient c_j . Due to pixelated structure of SLM the realized wavefront $\tilde{W}(x, y)$ certainly will not be the continuous one. Instead it will be

$$\tilde{W}(x, y) = \sum_k P_k(x, y)W(x_k, y_k) \quad (4)$$

where P_k is the windowing function associated with the k^{th} pixel of LCoS and (x_k, y_k) is the coordinates of the center of k^{th} pixel. In this representation we choose the pixelated wavefront to match the desired wavefront exactly at the center of each pixel. Thus to determine the Zernike coefficients \tilde{c}_j for the pixelated wavefront $\tilde{W}(x, y)$ we use eqn. 5.

$$\tilde{c}_j = \int \tilde{W}(x, y)Z_j(x, y)dxdy \quad (5)$$

It was shown that \tilde{c}_j is a function of all the continuous Zernike coefficients, not just c_j because the pixelated Zernike no longer form an orthonormal

set, neither are they orthonormal to the continuous Zernike [3]. However, the fractional error in a specific pixilated coefficient that is due only to that pixilated Zernike mode can be evaluated by,

$$err_j = \frac{c_j - \sum_k \int P_k(x, y) Z_j(x, y) Z_i(x_k, y_k) dx dy}{c_j} \quad (6)$$

4. EXPERIMENTAL SETUP

An experimental setup as shown in Fig. 1 has been rigged up to study the quantified generation and detection of wave-front errors for various Zernike modes corresponding to defocus, coma, astigmatism and spherical aberrations, etc.. The setup mainly consists of a phase only SLM and a SH-WS.

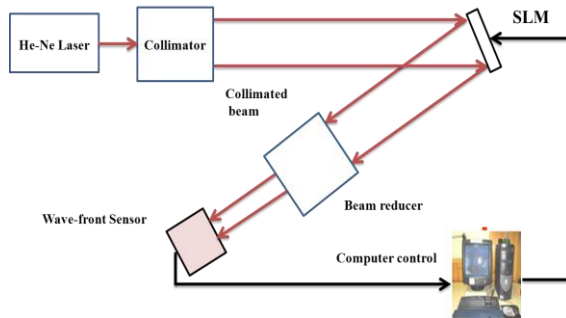


Figure 1. Optical setup

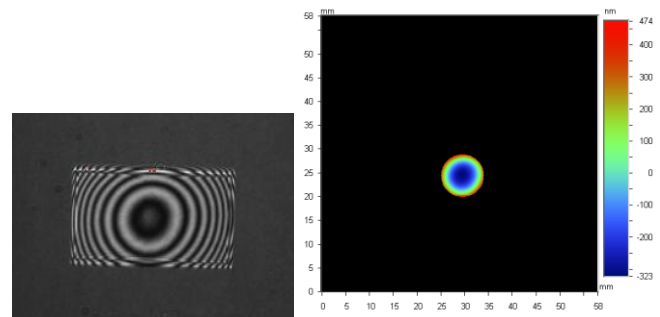
The lower order Zernike modes such as defocus, astigmatism, coma and spherical aberrations have been encoded on SLM in about 4 mm diameter. While illuminating with plane wave after reflection from the SLM, these modes are generated. SLM has been kept at a small tilt with the incident beam; this avoids uses of a beam splitter and the associated energy loss. The tilted incidence affects the phase modulation and diffraction efficiency. For incidence angle less than 6° , the variation in the phase modulation is 1% and for less than 3° the variation in diffraction efficiency is 1% with 16 quantized phase levels. Thus good wavefront detection can be produced with the incident angle of upto 3° [10].

5. RESULTS AND DISCUSSION

Discretised phase patterns for lower order Zernike modes were displayed on the SLM to generate the modes as per the mode strength. Purity of Zernike mode generation with phase only SLM depends on the initial flatness of the SLM and the diffraction pattern due to pixilated structure at the center of the far-field pattern. There are procedures to flatten such initial aberrations [11]. The phase SLM used in the experiment possess spherical aberrations that is due to the polishing of the window used for sandwiching

the LC cells. In the reported work we characterised the initial aberrations of the SLM using Wyko interferometer. In Fig. 2 we illustrate the results obtained from the interferometer. Interferogram of the bare SLM, illuminated with plane wave is shown in Fig. 2(a) and the contour map of the phase profile that is analysed for the central 9 mm aperture of the SLM is shown in Fig. 2(b). The initial aberrations were measured as 194 nm (RMS) and in peak-to-valley it is more than a wave, i.e., 800 nm. Corresponding Zernike coefficients for the Defocus was the dominating aberration and its strength was 335 nm while other third order aberrations were less than 63 nm.

At SH-WS the incident beam is centrally symmetric that is about 4 mm in diameter reflected from SLM. We ignored the initial aberrations on the performance. Initially a reference wavefront of wavefront error (WFE) of 16 nm is stored and with respect to this reference few typical Zernike modes were detected as shown in Fig. 3.



(a) Interferogram

(b) Contour map

Figure 2. Characterisation of bare SLM surface

Few lower order Zernike modes have been generated with the SLM and then detected with SH-WS. For estimating the response of a particular Zernike mode the mode coefficient measured by sensor is tabulated for a set of displayed known mode strengths. Response curve is a plot between values of the displayed Zernike coefficient and the detected one with SH-WS. Detection response curves for these modes were produced by fitting the data set to a quadratic polynomial. Experiments for sensor response have been performed for the detection of few typical Zernike modes such as defocus, astigmatism, and coma. The response curves for the respective modes are illustrated in Figs. (4-6). The accuracy of detection of defocus, astigmatism and coma has been estimated as 17 nm, 14 nm and 13 nm respectively. The procedure can easily be extended

for higher order Zernike modes. Once the setup is calibrated the desired atmospheric turbulence conditions can be easily simulated in laboratory.

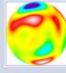

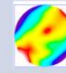
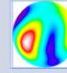
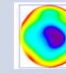
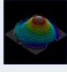
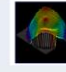
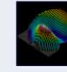
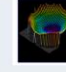
Plane/Reference	Defocus	Astigmatism	Coma	Spherical
				
3D				
Strength (in μm)	0.181	0.102	0.098	0.088

Figure 3. Detected few typical Zernike modes

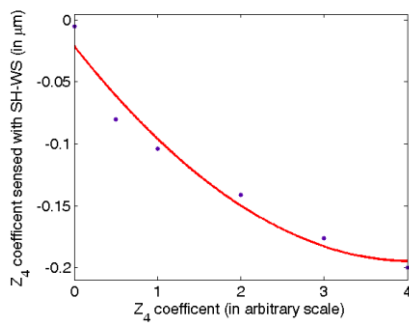


Figure 4. Response curve for Defocus detection

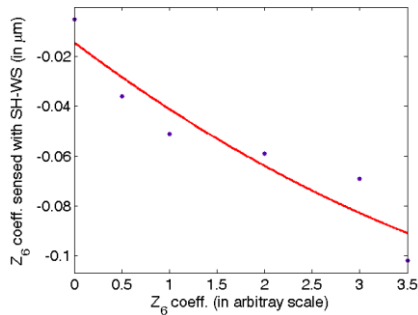


Figure 5. Response curve for Astigmatism detection

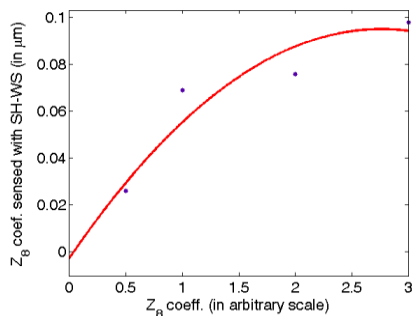


Figure 6. Response curve for Coma detection

ACKNOWLEDGEMENT

The authors wish to acknowledge Sh. S. S. Sundaram, Director IRDE for permitting to publish the work and Dr. A. K. Gupta for inspiration. Authors also thank to Dr. Vikash Porwal and Dr. Amit Agrawal for stimulating discussions.

REFERENCES

- [1] S. K. Mishra, D. K. Meena, D. Mohan, and A. K. Gupta, "FPGA based fast Shack Hartmann wavefront sensor for aircraft vision," National conference on Advances in Sensors for Aerospace applications, RCI, Hyderabad (2007).
- [2] A. K. Gupta and S. K. Mishra, "Development of adaptive optical imaging system at IRDE," Proc. of Int. Conf. on Cont. Trends in Optics and Optoelect., IIST, Trivandrum (2011).
- [3] D. C. Dayton, S. L. Browne, S. P. Sandven, J. D. Gonglewski, and A. V. Kudryashov, "Theory and laboratory demonstrations on the use of a nematic LC phase modulator for controlled turbulence generation and adaptive optics," *Appl. Opt.* 37, 5579-89 (1998).
- [4] G. D. Love, "Wavefront correction and production of Zernike modes with a Liquid crystal spatial light modulator," *Appl. Opt.* 36, 1517-1525 (1997).
- [5] V N Mahajan, "Zernike circle polynomials and optical aberration of system with circular pupils," *Supp. to Appl. Opt.*, 8121-8124 (1994).
- [6] S. K. Mishra, et. al., "Testing of fast wavefront sensor for off-axis aberrations," Proc. of Int. Conf. on Cont. Trends in Optics and Optoelect., IIST, Trivandrum (2011).
- [7] P.M. Prieto, E.J. Fernandez, S. Manzanera, S. Artal, "Adaptive optics with a programmable phase modulation: application to human eye," *Opt. Express* 12, 4059-4070 (2004).
- [8] G. Wirnicke, S. Kruger, J. Kamps, H. Gurber, N. Dermoli, M. Durr, et.al., "Applications of LC display SLM system as dynamic diffractive element in optical image processing." *Opt. Commun.* 25, 141-148 (2004).
- [9] X. Xun and R. W. Cohn, "Phase calibration of spatially non-uniform SLM," *Appl. Opt.* 43, 6400-06 (2004).
- [10] Z. Cao, Q. Mu, L. Hu, Y. Liu, Z. Peng, and Li Xuan, "Reflective liquid crystal wavefront corrector used with tilt incidence," *Appl. Opt.* 47, 1785-89 (2008).
- [11] Wang X., Wang B., Pouch J., Miranda F., Anderson J. E., Bos P. J., "Performance of a LCoS Spatial light modulator," *Opt. Eng.* 2769-2774 (2004).

Self referencing cyclic path interferometer

Sanjukta Sarkar*, N.Ghosh and K.Bhattacharya
Department of Applied Optics and Photonics, University of Calcutta

* Department of Electronics and Communication, Techno India,
EM4/1, Saltlake City, Kolkata-700091, INDIA
Email:ssanjukta07@yahoo.co.in

Abstract: In a cyclic interferometer with rectangular path configuration, the counter propagating wavefronts are mutually folded when traveling within the interferometer arms although they are eventually unfolded after emerging from the interferometer. A phase sample inserted in one lateral half of the interferometer arm therefore results in the phase information being superposed on the two beams in their complementary lateral halves. Polarization phase shifting technique is used to generate four phase shifted interferograms which are utilized to evaluate the phase profile of the phase sample.

Introduction: In a cyclic interferometer an incident beam of light is amplitude-split into two beams which propagate in the cyclic interferometer in the opposite directions. The two counter propagating beams finally emerge at the output, resulting in a stable and rugged interferometer. This type of interferometer was first described by Michelson [1] although it is more commonly associated with Sagnac [2] who carried out an extensive series of experiments with it. Common path cyclic Interferometric systems have long been used for surface and phase characterizations to determine the quality of optical samples both in laboratories and industries. A variety of cyclic shearing interferometers [3] have been constructed along with polarization phase shifting techniques [4-6] by using polarizing beam splitters, half wave plates as well as other polarizing components to incorporate the phase shifting capability. The geometry of the rectangular path cyclic interferometer dictates that the counter propagating wavefronts are laterally folded with respect to each other when traveling within the four interferometer arms. A phase sample inserted in one lateral half of the interferometer arm therefore results in the phase information being superposed on the two beams in their complementary lateral halves. At the output of the interferometer, the two wavefronts emerge laterally unfolded. Thus, for each of the emergent beams, the lateral half that carries the sample information has a plane wave reference in the complementary half of the other interfering beam. This is particularly useful for analyzing figured structures or thin film coatings on transmitting substrates, where the unfigured or uncoated substrate is referenced with respect to the figured and coated substrate, thereby suppressing the uniform substrate phase from the derived phase profile. The sample phase distribution is then extracted applying phase shifting interferometric techniques [7, 8].

Experimental Arrangement: The basic optical setup of the cyclic interferometer is shown in Fig 1. It is not common for a cyclic path interferometer to be used in the angular shearing mode due to the fact that for the two counter propagating beams apparently carry the same phase information and interference between them do not yield any fruitful result. Although this may be true for a triangular path cyclic configuration, a rectangular path cyclic path interferometer, as shown in Fig.1, behaves differently. Expanded and collimated laser beam polarized at is amplitude split through a Cube beam splitter (CBS). The two exist faces of the CBS are masked by the linear polarizers $P(0^\circ)$ and $P(90^\circ)$ oriented such that the reflected and transmitted components consist linearly polarized light A polarization beamsplitter cube (PBS) in place of the polarization masked cube beamsplitter employed, would have served the same purpose. A transparent phase sample is inserted in one lateral half of the beam as shown in Fig.1. A half wave plate (HWP) is inserted in one of the interferometer arms so that the linearly polarized states of the counter propagating beams are interchanged to enable their passage through the masking polarizers during the return path. A quarter wave plate (QWP) is placed at the output of the interferometer so that the two interfering beams are rendered circularly polarized in the opposite sense. Following this is a linear polarizer $P(\theta)$, for visualization of the fringes as well as to facilitate polarization phase shifting. The sample is positioned as close to the mirror M_2 as possible so that the lens L_1 along with the lens L_2 constitute an afocal system and the sample is imaged on the CCD. With the sample positioned at near the focal plane of the lens L_1 , the interference fringes are superposed on a moderately well defined image of the sample.

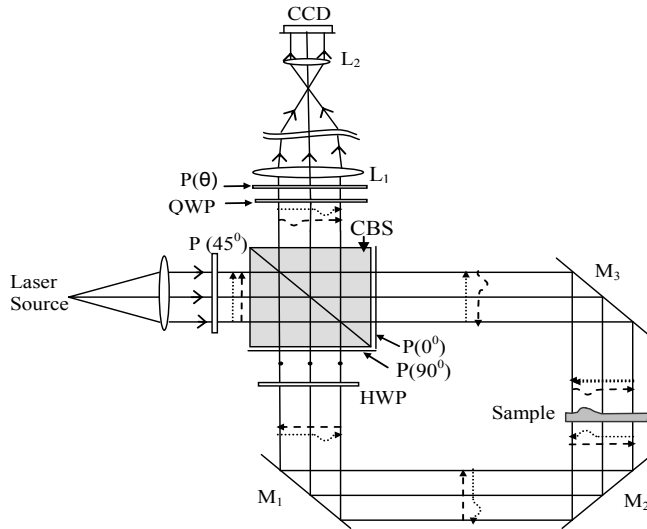


Fig.1. Schematic of the proposed polarization shifting cyclic interferometer. The clockwise and anticlockwise propagating wavefronts are denoted by dotted lines and dashed lines respectively, the arrow heads indicating the lateral orientation of the wavefront.

Theory: Using Jones Calculus formalism for polarized light, the Jones vector for light with an arbitrary state of polarization is given by:

$$\varepsilon_i = \begin{pmatrix} a \\ be^{i\alpha} \end{pmatrix} \quad (1)$$

Where a and b are the amplitudes of the E field along the vertical and horizontal direction and α is the phase difference between them. Assuming a unit amplitude input beam, the anticlockwise propagating wavefront prior to the final polarizer $P(\theta)$ is expressed as,

$$\varepsilon_a = \frac{1}{\sqrt{2}} W(\pi/2, 45^\circ) \cdot P(90^\circ) \cdot W(\pi, 45^\circ) \cdot P(0^\circ) \cdot \begin{pmatrix} 1 \\ 1 \end{pmatrix} \quad (2)$$

where in general, $P(\theta)$ is Jones matrix for the arbitrary oriented linear polarizer.

$W(\gamma, \varphi)$ is the Jones matrix of a retarder of retardation γ , oriented with its fast axis at an angle φ to the reference axis. Using the specific values of $P(\theta)$ and $W(\gamma, \varphi)$ as in Eq.2,

$$\varepsilon_a = \frac{-1}{2} \begin{pmatrix} 1 \\ -i \end{pmatrix} \quad (3)$$

Note that for the wavefront propagating clockwise in the sample arm the X-Y directions are reversed in the arm containing the half wave plate. For this beam the fast axis orientation of the half wave plate is therefore 135° . Taking this into consideration, the amplitude of this beam may

$$\begin{aligned} \varepsilon_c &= \frac{1}{\sqrt{2}} W(\pi/2, 45^\circ) \cdot P(0^\circ) \cdot W(\pi, 135^\circ) \cdot P(90^\circ) \cdot \begin{pmatrix} 1 \\ 1 \end{pmatrix} \\ &= \frac{-i}{2} \begin{pmatrix} 1 \\ i \end{pmatrix} \end{aligned} \quad (4)$$

From Eq.3-4 it seems that the two oppositely circularly polarized beams ε_c and ε_a are in phase quadrature to each other as a result of the polarization phase introduced due to the polarization transformations involved. However, taking into account phase changes on reflection and transmission through the beam splitting interface for the two counter propagating beams, we consider an additional phase of $(\pi + \beta)$ is associated with ε_c . The phase β is accounted for in consideration of the finite thickness of the beam splitting layer. Taking this into consideration,

$$\varepsilon_c = \frac{i}{2} \begin{pmatrix} 1 \\ i \end{pmatrix} e^{i\beta} \quad (5)$$

It may be observed from Eqns. 5 and 7 that the two interfering beams have a phase difference of $|\pi/2 + \beta|$.

If an arbitrary transparent phase sample $\delta(x,y)$ is inserted in one lateral half of the interferometer, as shown in Fig.1, the two beams ϵ_a and ϵ_c pass through the sample and linear polarizer $P(\theta)$ to emerge as ϵ_{a0} and ϵ_{c0} at the output. It is convenient for further analysis to designate the two symmetrical halves these interfering beams separately such that $\epsilon_{a0} = \epsilon_{a0S} + \epsilon_{a0R}$ and $\epsilon_{c0} = \epsilon_{c0R} + \epsilon_{c0S}$, where the additional suffices S and R denote the lateral halves the interfering wavefronts containing the sample information and the plane reference phase respectively. It is obvious from Fig.1 that the sample phase $\delta(x,y)$ is embedded in ϵ_{c0S} as $\delta(-x,-y)$ due to the lateral inversion suffered by the clockwise propagating beam ϵ_{c0} . The different components of the interfering wavefronts may therefore be expressed as follows:

$$\begin{aligned}\epsilon_{a0S} &= -\frac{1}{2}P(\theta) \begin{pmatrix} 1 \\ -i \end{pmatrix} e^{i\delta(x,y)} \\ &= \frac{1}{2}e^{i(\pi-\theta)}e^{i\delta(x,y)} \begin{pmatrix} \cos\theta \\ \sin\theta \end{pmatrix}\end{aligned}\quad (6)$$

$$\begin{aligned}\epsilon_{a0R} &= -\frac{1}{2}P(\theta) \begin{pmatrix} 1 \\ -i \end{pmatrix} \\ &= \frac{1}{2}e^{i(\pi-\theta)} \begin{pmatrix} \cos\theta \\ \sin\theta \end{pmatrix}\end{aligned}\quad (7)$$

and

$$\begin{aligned}\epsilon_{c0S} &= \frac{i}{2}P(\theta) \begin{pmatrix} 1 \\ i \end{pmatrix} e^{i\delta(-x,-y)} e^{i\beta} \\ &= \frac{1}{2}e^{i(\pi/2+\theta)}e^{i\delta(-x,-y)}e^{i\beta} \begin{pmatrix} \cos\theta \\ \sin\theta \end{pmatrix}\end{aligned}\quad (8)$$

$$\begin{aligned}\epsilon_{c0R} &= \frac{i}{2}P(\theta) \begin{pmatrix} 1 \\ i \end{pmatrix} e^{i\beta} \\ &= \frac{1}{2}e^{i(\pi/2+\theta)}e^{i\beta} \begin{pmatrix} \cos\theta \\ \sin\theta \end{pmatrix}\end{aligned}\quad (9)$$

The intensity distribution I_L and I_R on the two lateral halves of the interference pattern may thus be written as

$$\begin{aligned}I_L &= |\epsilon_{c0R} + \epsilon_{a0S}|^2 \\ &= \frac{1}{2}\{1 + \cos(2\theta + \beta - \pi/2 - \delta(x,y))\}\end{aligned}\quad (10)$$

$$\begin{aligned}I_R &= |\epsilon_{c0S} + \epsilon_{a0R}|^2 \\ &= \frac{1}{2}\{1 + \cos(2\theta + \beta - \pi/2 + \delta(-x,-y))\}\end{aligned}\quad (11)$$

Phase shifting is achieved by varying the transmission axis θ of the output polarizer and the interferograms I_{L1} , I_{L2} , I_{L3} , I_{L4} and I_{R1} , I_{R2} , I_{R3} , I_{R4} are recorded for values of θ oriented along 45° , 90° , 135° and 0° respectively, yielding corresponding phase shifts of 0 , $\pi/2$, π and $3\pi/2$ respectively. The phase shifted frames are digitally recorded and the phase $\delta(x,y)$ reconstructed using standard four frame phase shifting algorithm.

$$[\beta - \delta(x,y)] = \arctan \left[\frac{I_{4L} - I_{2L}}{I_{1L} - I_{3L}} \right].\quad (12)$$

$$[\beta + \delta(-x,-y)] = \arctan \frac{I_{4R} - I_{2R}}{I_{1R} - I_{3R}}\quad (13)$$

The characteristics of the reconstructed phase profile, as predicted from Eqs.23 and 24, are as follows:

- i) A phase difference of 2δ exists between the two lateral halves of the reconstructed phase profile.
- ii) The phase profile is centered about the β phase plane.

Experimental Results: As validation of the proposed technique, we present the result that have been experimentally obtained using the proposed cyclic interferometer. It is shown that the unwrapped phase will consist of a positive as well as a negative phase reconstruction of the sample in the same frame. Interestingly, this opens up the possibility of testing optical phase uniformity, e.g., flatness and/or homogeneity, between two halves of a transparent sample. An experimental result showing the typical phase reconstruction obtained with a wedge shaped optical sample is shown in Fig.2.

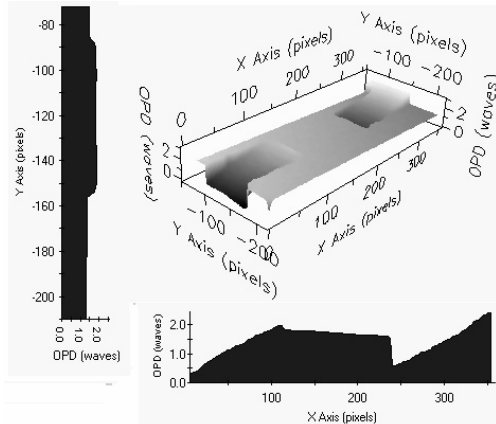


Fig.2. The unwrapped phase obtained for a wedge-shaped phase sample.

Conclusion: From the theory and the results presented it is obvious that rectangular cyclic interferometers may be used in angular shearing mode to evaluate phase distribution in optically transmissive samples that can be accommodated in one lateral half of the beam. In cases where the sample is mounted or coated on a substrate, proper placement of the sample ensures that the substrate phase is completely eliminated in the result. It is also worth noting that a triangular path cyclic interferometer would not have served the same purpose since in this configuration no mutual lateral folding of the propagating wavefronts is observed within the interferometer.

References

1. P. Hariharan "Sagnac or Michelson-Sagnac interferometer?" Applied Optics, Vol. 14, Issue 10, pp. 2319_1-2321 (1975).
2. G. Sagnac, "Comptes Rendus de l'Academie des Sciences (Paris)", 157, 708-710, 1410-1413 (1913).
3. P.Hariharan and D.Sen, "Cyclic shearing interferometer," J. Sci. Instrum., Vol 37, 374 (1960).
4. Mahendra P. Kothiyal and Claude Delisle, "Shearing interferometer for phase shifting interferometry with polarization phase shifter", Appl.Opt. 24 (24), 4439-4442 (1985).
5. J. Huang, T. Honda and N. Ohymaa, "A phase stepping double-focus interferometer using a cyclic design and polarized light", Optics Comm., Vol 76, 297-301 (1990).
6. Y. Pavan Kumar and Sanjib Chatterjee, "Thickness measurement of transparent glass plates using a lateral shearing cyclic path optical configuration setup and polarization phase shifting interferometry", Appl. Opt., 49(33), 6552-6557 (2010).
7. K. Creath, "Phase measurement interferometry techniques Progress in Optics", XXVI, Vol 26 ed E. Wolf (Amsterdam: North Holland Publ.) chapter 5, 349-393 (1988).
8. Malacara D, Servin M and Malacara Z, "Phase Detection Algorithms in Interferogram Analysis for Optical Testing", (New York: Dekker) chapter 6, (1998).

Single shot off-axis low coherence interference microscopy for quantitative phase imaging

Vishal Srivastava and Dalip Singh Mehta^{a)}

Laser Applications and Holography Laboratory, Instrument Design Development Centre,
Indian Institute of Technology Delhi, India

a): E-mail: dsmehta@iddc.iitd.ac.in

Abstract: To quantitatively obtain the phase map we have realized an off-axis low coherence interferometry based Hilbert phase microscopy (HPM). The spatial carrier frequency is introduced into the 2-D spectral interferogram in the lateral direction by using a tilted reference wavefront. HPM is used to investigate dynamic phenomena that take place in transparent structures such as biological cells. Moreover, the slightly-offaxis interferometry owns higher effective bandwidth and more sensitivity than traditional off-axis interferometry. The present method requires a single interferogram to compute the phase map of an object, for which refractive index and height distribution can be computed and have a real-time imaging ability. Results of silicon chip and onion skin are presented

1. Introduction

The phase distribution determines the inner structure and dynamic information in the biological cells and other samples in a completely noninvasive manner [1]. Several well-known microscopy techniques such as the phase contrast and differential interference contrast microscopy [2] has been used so far. However, these general phase microscopy techniques do not yield quantitative phase distribution. To quantitatively obtain the phase image of the biological cells and industrial objects, the interferometric phase microscopy has been proposed [3-5]. The interferometric phase microscopy could provide the quantitative phase images associated with the optical path delays. The optical path delay relates to the cell profile and the refractive index distribution, which can reflect the inner structure and profile of the cells. As a result, the interferometric phase microscopy can make the cellular morphology quantization under real-time condition, and thus can be an important tool for medical diagnostics and cell biology studies [6]. Interferometric phase microscopy is basically of two types: on-axis interferometry [7] and off-axis interferometry [8]. In the case of on-axis interferometry, at least three phase-shifted on-axis interferograms of the sample are required and then the sample phase information is separated through phase-shifting algorithm. However, for dynamic processes, the sample may change between the acquisitions of the multiple frames. In addition, phase noise may increase due to the system fluctuations between the frames. Traditional off-axis interferometry can realize real-time phase imaging, because one can obtain the quantitative phase image from a single interferogram. In the off-axis interferometry large angle is introduced between the reference and sample beams to separate the desired and undesired waves which will lose the sensitivity of interference measurement [9]. Here we are using hybrid method Single shot off-axis low coherence interference microscopy based on HPM, which combines the advantages of slightly-off axis interferometry [10], i.e. high effective bandwidth and HPM, i.e. single-shot nature and details detection ability. The slightly-off-axis interferometry proposed in Ref. [11] is an intermediate solution between the conventional on-axis interferometry and off-axis interferometry; it is a powerful tool for interferometric phase measurements of bio-samples and industrial objects with fine spatial details. Due to its single-shot nature, HPM acquisition time is limited only by the recording device and thus can be used to accurately quantify nanometer-level path-length shifts at the millisecond time scales or less, where many relevant biological phenomena develop [12].

2. Mathematical analysis

According to the HPM theory, only one interferogram I is acquired to extract the quantitative phase image. The intensity of the interferogram can be expressed as follows [13]:

$$I(x) = I_R + I_O + 2 [I_R I_O]^{1/2} \cos[fx + \Phi(x)] \quad (1)$$

where I_R and I_O are the reference and object irradiance distributions, respectively, f is the fringe frequency, and Φ is the spatially-varying phase associated with the measured sample. The interferogram is Fourier transformed, spatially high-pass filtered to isolate the sinusoidal term and eliminate the background components as in equation (2), and then the single-shot Hilbert transform of the filtered signal is performed to yield the wrapped phase.

$$S(x) = 2 [I_R I_O]^{1/2} \cos[f x + \Phi(x)] \quad (2)$$

The Hilbert transform of Eq. (2) can be written as follows:

$$Z(x) = 0.5*[S(x) + j.\{\text{Hilbert}(S(x))\}] \quad (3)$$

Using Eq. (3) the wrapped phase can be obtain as follows:

$$\Phi(x) = \tan^{-1}(\text{Im}z(Z(x)/\text{Real}(Z(x))) \quad (4)$$

The wrapped phase can be unwrapped to obtain the desired information.

3. Experimental Setup

Figure 1 shows the schematic diagram of the off-axis low coherence interferometric microscope based on Michelson Interferometer. In this reference mirror is tilted by a small angle θ to generate high spatial frequency. The compact interferometer is attached with the microscope. A super -luminescent diode (Model No. SLD 371-HP1-DIL-PM-PD, SUPERLUM Diodes Ltd.) having full width half maximum (FWHM) $\Delta\lambda = 48.38\text{nm}$ and center wavelength $\lambda_0 = 842.5\text{nm}$, output power = 7mW is used as low coherence light source.

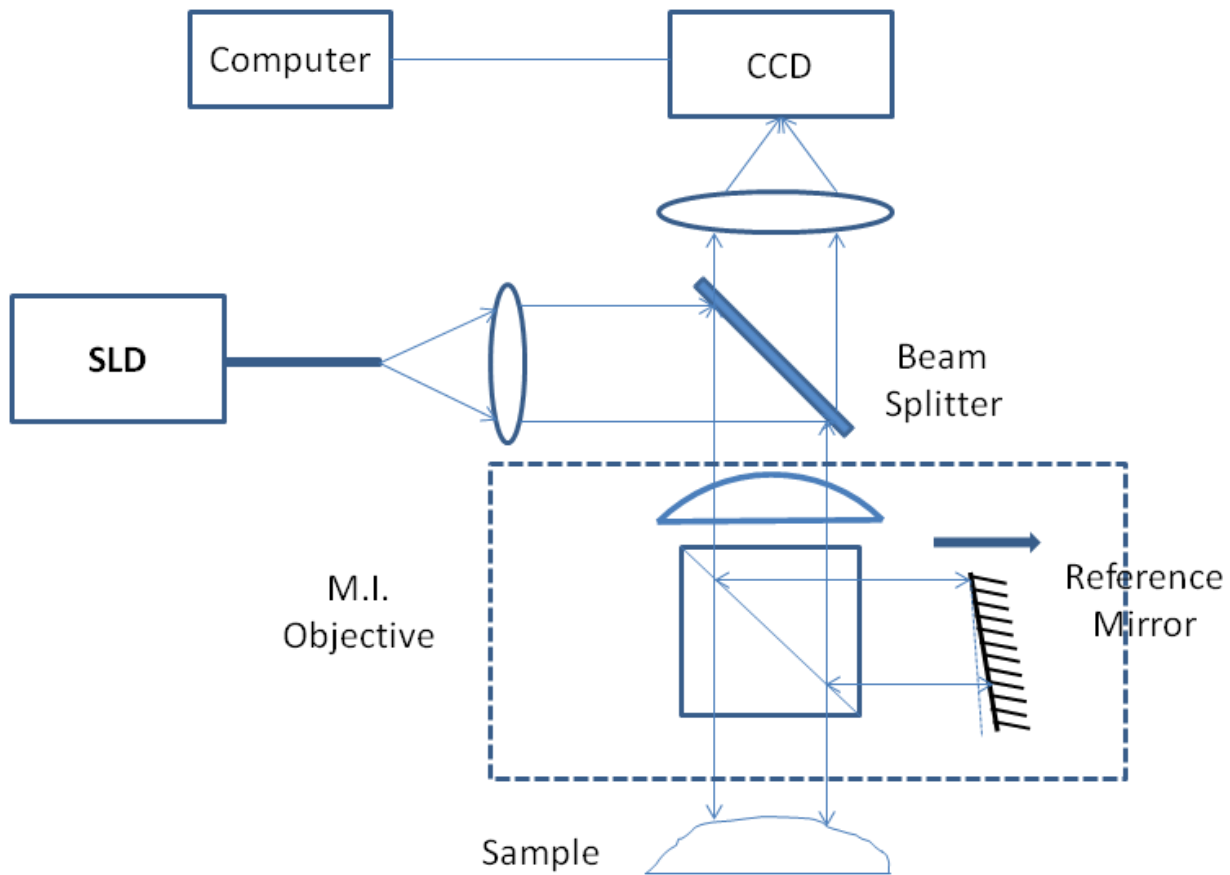


Fig. (1) Shows the schematic diagram of the off-axis low coherence interferometric microscope. In which the reflected mirror is tilted by a small angle θ to generate high spatial carrier frequency.

4. Experimental Results

Single interferogram is recorded and used to obtain the phase distribution of Silicon chip and Onion skin. Figures 2 (a),(b),(c) and (d) respectively shows the high density interferogram of silicon chip, the phase map obtained by Hilbert transform method, unwrapped phase map and mesh plot of unwrapped phase map of silicon chip. Figures 3 (a),(b),(c) and (d) respectively shows the high density interferogram of onion skin, the phase map obtained by Hilbert transform method, unwrapped phase map and mesh plot of unwrapped phase map of onion skin.

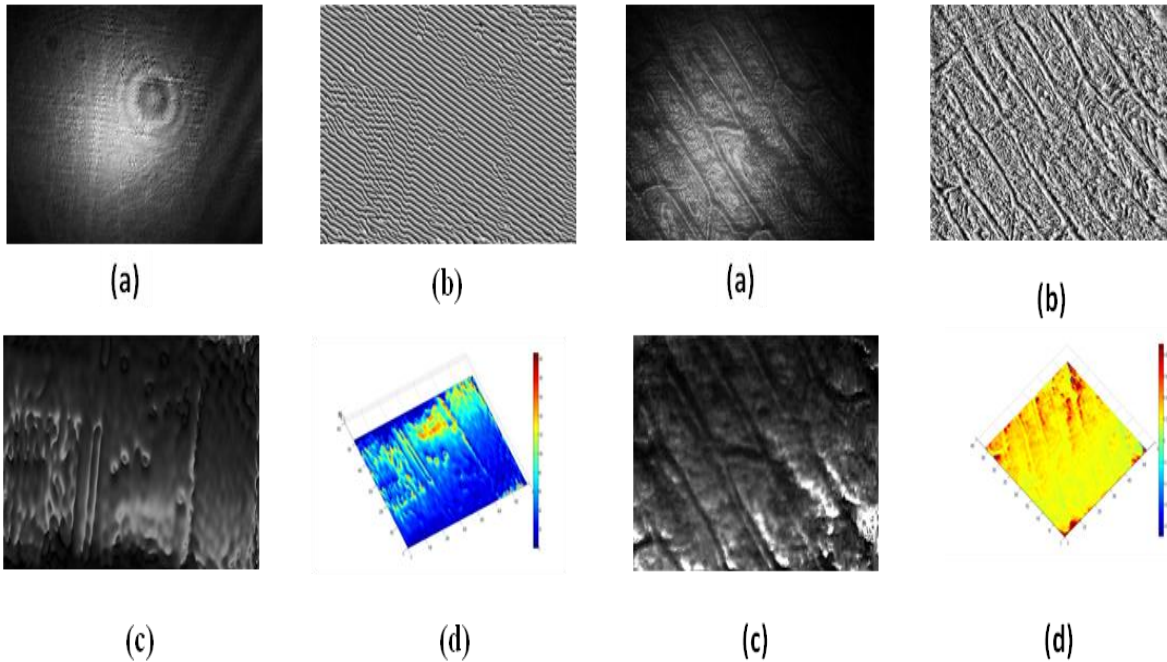


Fig 2) (a) Off-axis interferogram , (b) shows the phase map obtained by Hilbert transform method, (c) represents the unwrapped phase map ,(d) mesh plot of unwrapped phase map of Silicon chip.

Fig 3) (a) Off-axis interferogram , (b) shows the phase map obtained by Hilbert transform method, (c) represents the unwrapped phase map ,(d) mesh plot of unwrapped phase map of onion skin.

Quantitative phase reconstruction based on slightly-off axis interferometry reveals the overall structure of the silicon chip and onion skin as a result of high effective bandwidth ratio, but off-axis mode provides an incomplete outline especially in edges where partial structure is lost.

Conclusions: We have demonstrated Single shot off-axis low coherence interference microscopy for quantitative phase imaging. The HPM needs only single interferogram to extract the phase distribution We believe that the proposed method should be a powerful tool for quantitative phase measurements of dynamic processes, especially for observing live biological cell dynamics and various industrial objects.

Acknowledgments:

Authors gratefully acknowledge the financial assistance from Department of Science and Technology, Delhi, Government of India for the Project No. SR/S2/LOP-0021/2008.

References:

- 1.Zahid Yaqoob, Toyohiko Yamauchi, Wonshik Choi, Dan Fu, Ramachandra R. Dasari, and Michael S. Feld1, "Single-shot Full-field reflection phase microscopy", *Optics Express* 7587 / Vol. 19, No. 8
2. D. J. Stephens and V. J. Allan, "Light microscopy techniques for live cell imaging," *Science* **300**(5616), 82–86 (2003).
3. G. N. Vishnyakov and G. G. Levin, "Interferometric computed-microtomography of 3D phase objects," *Proc.*

SPIE **2984**, 64–71 (1997).

4. Y. Sung, W. Choi, C. Fang-Yen, K. Badizadegan, R. R. Dasari, and M. S. Feld, “Optical diffraction tomography for high resolution live cell imaging,” *Opt. Express* **17**(1), 266–277 (2009).

5. Z. Yaqoob, W. Choi, S. Oh, N. Lue, Y. Park, C. Fang-Yen, R. R. Dasari, K. Badizadegan, and M. S. Feld, “Improved phase sensitivity in spectral domain phase microscopy using line-field illumination and self phasereferencing,” *Opt. Express* **17**(13), 10681–10687 (2009).

6. P. Marquet, B. Rappaz, P. J. Magistretti, E. Cuche, Y. Emery, T. Colomb, and C. Depeursinge, “Digital holographic microscopy: a noninvasive contrast imaging technique allowing quantitative visualization of living cells with subwavelength axial accuracy,” *Opt. Lett.* **30**(5), 468–470 (2005).

7. I. Yamaguchi and T. Zhang, “Phase-shifting digital holography,” *Opt. Lett.* **22**(16), 1268–1270 (1997).

8. E. Cuche, P. Marquet, and C. Depeursinge, “Spatial filtering for zero-order and twin-image elimination in digital off-axis holography,” *Appl. Opt.* **39**(23), 4070–4075 (2000).

9. E. N. Leith and J. Upatnieks, “Reconstructed wavefronts and communication theory,” *J. Opt. Soc. Am.* **52**(10), 1123–1128 (1962).

10. N. T. Shaked, Y. Zhu, M. T. Rinehart, and A. Wax, “Two-step-only phase-shifting interferometry with optimized detector bandwidth for microscopy of live cells,” *Opt. Express* **17**(18), 15585–15591 (2009).

11. T. Ikeda, G. Popescu, R. R. Dasari, and M. S. Feld, “Hilbert phase microscopy for investigating fast dynamics in transparent systems,” *Opt. Lett.* **30**(10), 1165–1167 (2005).

12. G. Popescu, T. Ikeda, R. R. Dasari, and M. S. Feld, “Diffraction phase microscopy for quantifying cell structure and dynamics,” *Opt. Lett.* **31**(6), 775–777 (2006).

13. Xue L, Lai J, Wang S, Li Z., “Single-shot slightly-off-axis interferometry based Hilbert phase microscopy of red blood cells”, *Biomed Opt Express*. 2011 Mar 29;2(4):987-95

FREQUENCY ANALYSIS OF INDOOR CONVECTIVE TURBULENCES WITH VARIOUS RECEIVING APERTURES

Aditya K. Mamgain*, Awakash Dixit, Sanjay K. Mishra, D. Mohan and A. K. Gupta
Adaptive Optics Group, Photonics Design Centre, Instruments R & D Establishment (DRDO)
Dehradun-248008, India

*Email: aditya_mamgain@rediffmail.com

Abstract: Turbulent atmosphere produces random jitter in the laser beam while propagation through it and its dynamics largely depend on the receiving aperture size. In this paper we have described a simple experimental setup for generating various strengths of turbulence. Further we analyzed the frequency spectra of such turbulence-induced Angle-of-Arrival (AOA) fluctuations by varying the aperture sizes and turbulence strengths.

1. INTRODUCTION

Turbulent atmosphere produces phase fluctuations in the laser beam while propagation. Various methods have been adopted to study the temporal spectra of phase-related quantities [1]-[3]. These include measurement of some relevant quantities such as Angle-of Arrival using image centroid motion [1], [2] variances of piston and tilt motions of the mirror segments of the corrector [3]. The temporal behavior of turbulence has extensively been studied theoretically [4]-[6]. This has been employed to determine the bandwidth of an adaptive optics system [4]. Such temporal frequency power spectra have been determined by Zernike expansion coefficients of tilt data for point source with Kolmogorov turbulence [5] and other approaches, viz., fringe motion, image motion differential AOA, etc. [6]. Most of these studies are for stellar observations involving vertical turbulence path and fixed aperture sizes.

However to the best of our knowledge, there is no reported method for the study of the aperture dependency of the frequency spectra for near ground turbulence with horizontal propagation. We employed the frequency power spectra of AOA fluctuations to analyze the temporal behavior of near ground turbulence.

2. EXPERIMENTAL SETUP

The experimental schematic is given in Figure.1. A spatially filtered laser beam (He-Ne laser, $\lambda=632.8\text{nm}$, power 9.0mW) was expanded with a Plano-convex lens ($f=76.5\text{mm}$) and propagated over a distance about 12m. Artificial turbulence was generated using two electric heaters each of 1000 watt of power.

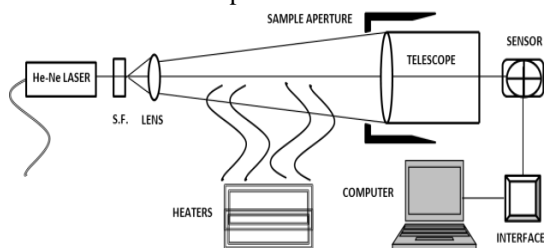


Figure 1- Experimental Schematic

The optical waves propagated about 1m above the heaters and were collected using a telescope (Meade LX-200 ACF) of aperture size 203mm with a central obstruction of 73mm and focal length 2000mm. An optical beam positioner (Newport OPB U-96, Series L3130) was placed at the telescope focus to measure the turbulence induced beam jitter. A snap-shot of actual experimental setup is shown in Figure.2.



Figure 2 - Experimental setup

3. METHODOLOGY

In the proposed method thermally induced turbulence has been taken as representative to the atmospheric turbulence [7]. Three different degrees of turbulence were generated by switching on the heaters. The characterizing temperatures were measured with a mercury thermometer placed along the laser propagation axis that is about 1m above heaters. The turbulences were categorized into three strength cases and the measured temperatures are as follows:

- weak turbulence $\langle T \rangle \sim 21.3^\circ\text{C}$
- moderate turbulence $\langle T \rangle \sim 24.6^\circ\text{C}$
- strong turbulence $\langle T \rangle \sim 27.2^\circ\text{C}$

For each case the turbulence settling time was fixed as 30minutes to obtain isotropic turbulence. Circular apertures of six different sizes viz. 90mm, 115mm, 140mm, 165mm, 190mm and 203mm were placed sequentially in front of the telescope in order to select different turbulence scales. In similar experiment the inner scale was determined to be of the order of a few millimeters [8] while the outer scale was about a hundred millimeters [9].

Thus we have assumed that all our aperture sizes are in inertial range.

The optical beam position sensor measured the instantaneous x-y coordinates of the centroid of the spot. We captured the data at an acquisition rate of 500Hz. Each data set was recorded for 4 seconds, i.e. 2000 sample data were taken in one snap-shot. We captured ten such data sets (each containing 2000 sample data) for each of the five aperture sizes, in each of three degrees of turbulence. Thus a total 20,000 data were obtained for each aperture size in each degree of turbulence. The instantaneous position coordinates were employed to calculate the radial shift of the focal spot. The radial data set was then analyzed by using the Digital Fourier Transform (DFT) at MATLAB platform.

4. RESULTS AND DISCUSSION

We calculated the Fourier spectrum of all the ten records, each containing 2000 data set, for all the six aperture sizes in all the three turbulence strengths. The average of these 10 Fourier spectra was then taken as being representative of a particular aperture size in a given turbulence strength case. Different frequencies were found to be dominant at different turbulence scales corresponding to different aperture sizes. Figure 3(a) - 3(c) represent Fourier spectra for 203mm aperture size for all the three turbulence strength cases.

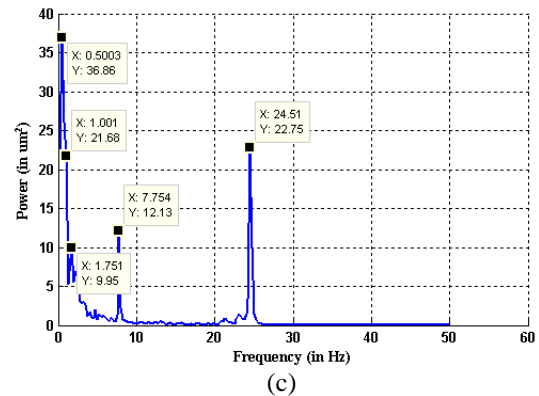
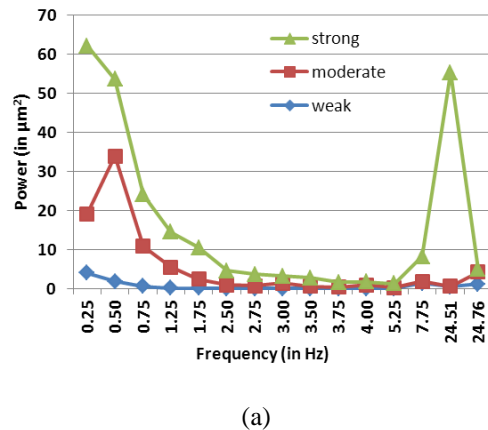
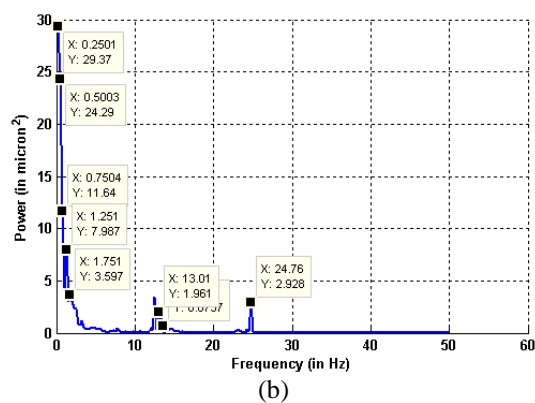
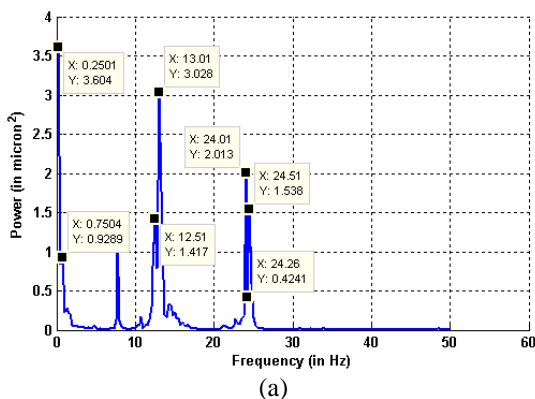


Figure 3 - Frequency power spectrum for 203mm aperture size (a) weak turbulence (b) moderate turbulence (c) strong turbulence

Similarly Fourier spectra were calculated for data corresponding to other aperture sizes for all the three turbulence strength cases. We took into account only those temporal frequencies whose weight was found to be at least 10% of the weight of the most dominant frequency. Thus applying this threshold criterion helped to determine and select the significant frequencies as against the background noise. The temporal frequencies observed as common in all the cases were 1Hz, 2Hz, 3Hz, 4Hz, 8Hz, 13Hz and 25 Hz (all rounded off to nearest integer for simplicity).

We also studied the effect of increasing turbulence strength on frequencies' content for commonly observed frequencies. While keeping the aperture size fixed, the frequencies' weight was plotted against the jitter frequencies while varying the turbulence strength. The effect of various turbulence strengths was thus compared. The curves plotted for the various aperture sizes viz. 203mm, 190mm, 165mm, 140mm, 115mm and 90mm are shown graphically in Figure 4(a) - 4(f).

It is evident that the weight of all the jitter frequencies increases with increasing turbulence strength thereby showing the expected behaviour within experimental errors/limitations.



(a)

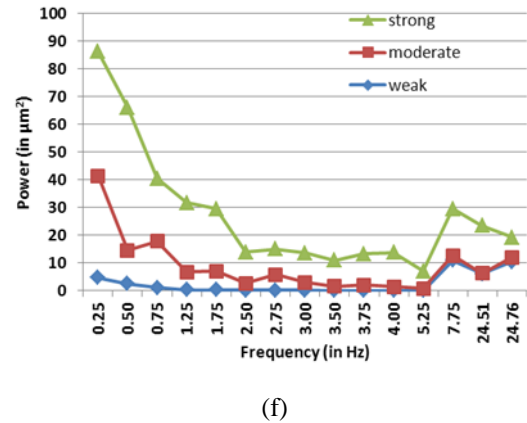
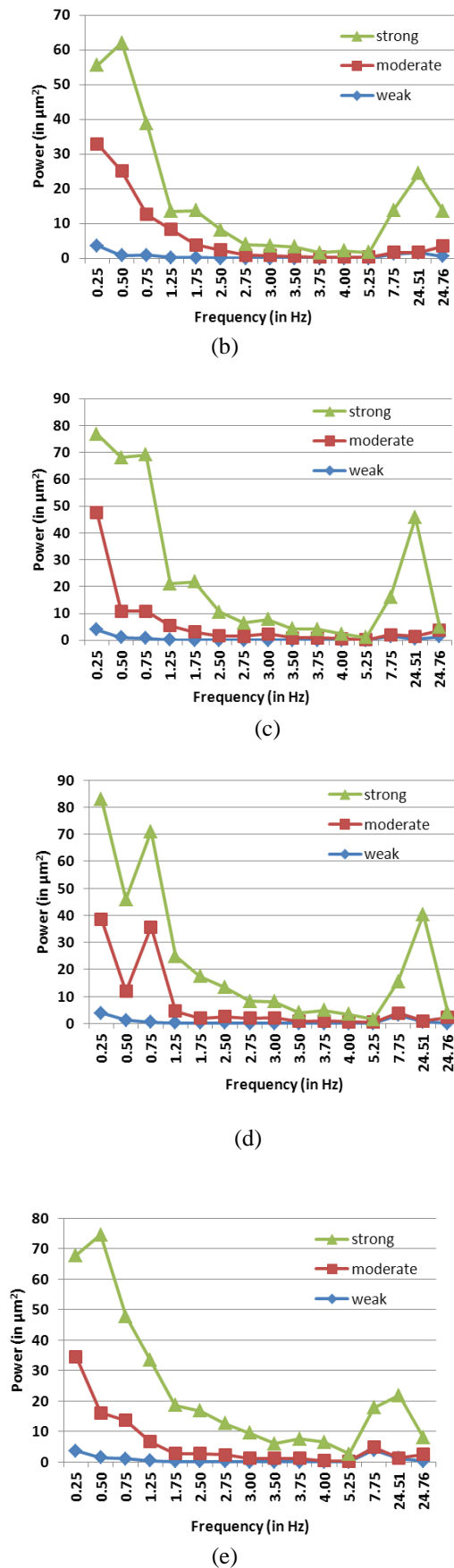


Figure 4 - Comparison of frequencies' content at different turbulence strengths for various aperture sizes (a) 203mm (b) 190mm (c) 165mm (d) 140mm (e) 115mm (f) 90mm

We further studied the effect of change in aperture size on the weight of jitter frequencies while keeping the turbulence strength fixed. Again we selected and compared those jitter frequencies which were observed for all the six aperture sizes. This was done for all the three cases of turbulence strengths. We have adopted best power fit method for estimating the curves. Figure.5 (a)-(c) represents the weight of jitter frequencies as a function of aperture size. It is found that the weight of jitter frequencies decreases with increasing aperture size thereby indicating that in a given turbulence scenario the content of jitter frequencies tends to decrease at higher turbulence scales. Thus it is clear that higher turbulence scales share lesser contributions to jitter frequencies. It appears from Figure 5, that the power spectrum curves become less steep at higher turbulence strengths. e.g. the exponents for the curve of 8 Hz are -0.97, -0.50 and -0.30 for weak, moderate and strong turbulence cases respectively. That is the weight of jitter frequencies fall off with increasing aperture size more rapidly at lower turbulence strengths. Moreover the weight of all the jitter frequencies appears to attain limiting values with increasing aperture size. Beyond a certain aperture size the weight of these temporal frequencies should be independent of the aperture size as long as the aperture size remains below the outer scale. This can be verified by repeating the experiment over a larger aperture size range. Once the aperture size exceeds the outer scale (or reduced below the inner scale) phase dampening effect is set into picture and other effects may be expected. However we could not investigate into this region because of limited size of our telescope aperture. More data and larger aperture range together with controlled turbulence are required to attain significant results. It must be stressed here that all our observations presented are based on two premises. First, all our aperture sizes are in inertial range and second, the

turbulence is isotropic. Moreover we have also ignored the central obstruction of the telescope aperture. The effects of a centrally obstructed aperture may be more than just blocking the contributions from those turbulence scales which are smaller than the obstruction. We did not go into this problem.

and turbulence strengths. In all three cases of turbulence strength jitter frequencies were found to be limited by 25Hz for all the receiving aperture sizes.

ACKNOWLEDGEMENT

The authors wish to acknowledge Sh. S. S. Sundaram, Director IRDE for encouraging pursuing and permitting to publish the work. Also Dr. Vikas Porwal is acknowledged for his valuable suggestions.

REFERENCES

- [1] D. B. Soules, J. J. Drexler, A. H. Waldie, J. A. Qualtrough, F. D. Eaton, W. A. Peterson, and J. R. Hines, "Temporal characteristics of turbulence-induced image motion," *Proc. S.P.I.E.* **115**, 224-231, (1989).
- [2] H. M. Martin, "Image motion as measure of seeing quality," *Pub. Astron. Soc. Pacific*, **99**, 1360-1370, (1987).
- [3] D. P. Greenwood and D. L. Fried, "Power spectra requirements for wave-front-compensative systems," *J. Opt. Soc. Am.* **66**, 193-206 (1976)
- [4] D. P. Greenwood, "Bandwidth specification for adaptive optics systems," *J. Opt. Soc. Am.* **67**, 390-392 (1977)
- [5] C. B. Hogge and R. Russell Butts, "Frequency spectra for the geometric representation of wavefront distortions due to atmospheric turbulence," *IEEE Trans Antennas Propagation*, **AP-24**, 144-154, (1976).
- [6] J. M. Canon, G. Rousset and P. Y. Madec, "Wave-front temporal spectra in high-resolution imaging through turbulence," *J. Opt. Soc. Am. A*, Vol. **12**, No. 7, 1559-1570, (1995)
- [7] A. Consortini and K. A. O'Donnell, "Measuring the inner scale of atmospheric turbulence by correlation of lateral displacement of thin parallel laser beam," *Waves in Random Media* Vol. **3**, No. 2, 85, (1993).
- [8] A. Consortini, Y.Y. Sun, C. Innocenti and Z. P. Li., "Measuring inner scale of atmospheric turbulence by angle of arrival and scintillation," *Opt. Comm.* Vol. **216** (1-3), 19-23, (2003).
- [9] A. Consortini, Y.Y. Sun and C. Paoli, "Estimation method for outer scale of atmospheric turbulence," *Opt. Comm.* Vol. **214** (1-6), 9-14, (2002).

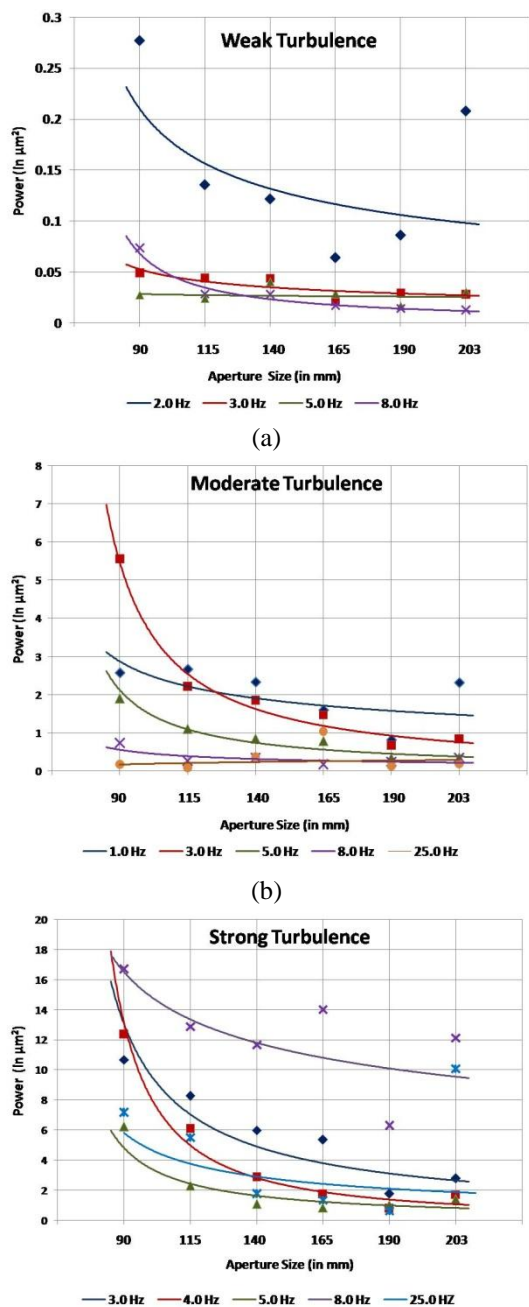


Figure 5 - Variation in different frequencies' weight with various aperture sizes (a) weak turbulence (b) moderate turbulence (c) strong turbulence

Thus we studied the dynamics of jitter motion for the near-ground turbulence with various apertures

Design consideration of the Projection Lens for Head-up Display System

Yashpal, G.S. Singh**, Rakesh Dhar

Optical Engineering, Department of Applied Physics, GJ University of Science and Technology, Hisar, Haryana-125001,

**Optical Design and Spectroscopy, CSIR-CSIO, Sector-30C Chandigarh-160030
yashpal.lather@gmail.com

1.1 Abstract

Head up Display (HUD) systems are semi-transparent electro-optical display devices. In HUD, a projector enables the pilot to see flight information without refocusing on the flight instruments. Projector displays all the information on a beam combiner which is placed in the line of sight of pilot/ Head Motion Box (HMB). The approach followed is designing a Petzval lens configuration for the Projector system which will serve the requirement of HUD using ZEMAX optical design software.

1.2 Introduction

Head up Display (HUD) systems are used for presenting data related to attitude, navigation, guidance, targeting during the flight and also other important information in the pilot's forward field of view through the aircraft glass protection window. All HUD systems have a requirement of an image source for displaying data on screen. For this purpose generally a high-brightness cathode-ray tube (CRT) is used. An optical system is required for projecting the information displayed on CRT face at optical infinity. The displayed data image is seen by the pilot through a reflection/refraction (depending upon the type of HUD system used), that occurs from a semi-transparent element/ or a thin film coating/filter and that element is called the HUD Beam Combiner.

1.3 Specification and layout of Petzval Lens

Specification and consideration should be established before the lens design begins. These may be contradictory. In this case, these are given below:

- Effective focal length (EFL)
- Field of view (FOV)
- F-number (infinite versus working)
- Wavelength range
- Performance (MTF and Distortion)
- Depending on the functional requirement of the system, there may be other performance requirements relating to image quality, point spread function (PSF), control of aberration etc.

Based on the above consideration, an initial system is designed. After the initial design, this system is evaluated on the basis of paraxial data. This evaluation results in the decision of starting point of the design for optimization. After the completion of optimization, one can easily understand the whole system parameters. The performance of that design is examined at each step of optimization using Zemax. After getting the desired performance, following figure shows our system which was actually required according to our set parameters.

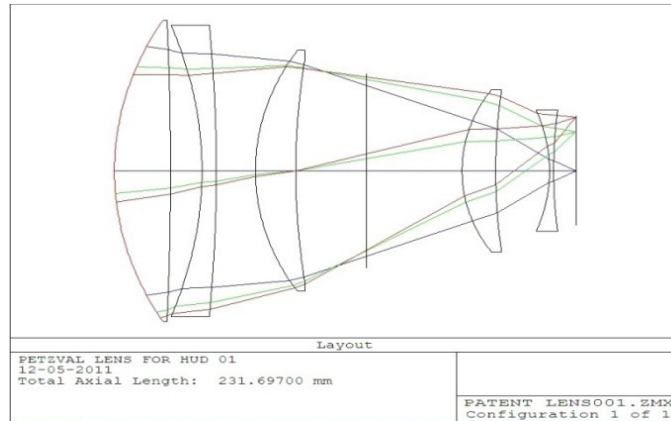


Fig.1 Optical layout of HUD

This designed system is an initial design of this particular Petzval lens configuration. With the help of calculation and optimization technique, we can achieve the more advanced system. Above designed Petzval type projection lens for a refractive type HUD have following parameter specification.

Parameter	Value
Type of HUD	Refractive
Number of Elements	5
Maximum CRT Diagonal	65 mm
Entrance pupil diameter	150 mm
Effective focal length	149.9976 mm
Back focal length	11.7294 mm
Total system track length	231.697 mm
Working F- number (F/#)	0.99415
Spectral Coverage	539-544-559 nm

Fig.2 Parameter Table

1.4 Performance Characteristics

Layout has been prepared with the given specifications and a Total FOV of 32.5 mm radial field. By setting the merit function, the whole design is given to the software for optimization. After optimization process, result plots are made for the performance evaluation of the system. Total length of the system is 231.697 mm. Performance graphs for this Petzval lens includes the graphs which shows the modulation Transfer curve (MTF) curve, Spot diagram, Optical Path Difference (OPD), Ray fan-out, and Field curvature and Distortion curves in a single report diagram.

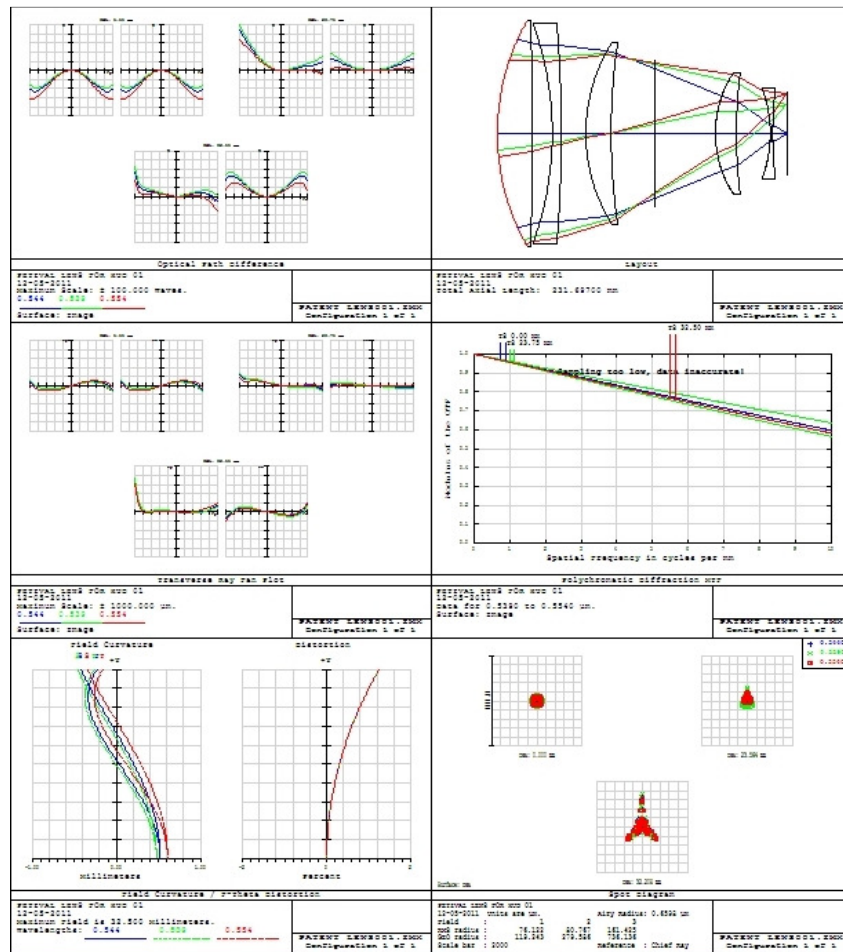


Fig.3 Performance report of layout

Acknowledgement

First author wish to express his gratitude to Dr Pawan Kapur, Director, CSIR-CSIO, Chandigarh for allowing him to carry out his M.Tech Project work at Optical Design and Spectroscopy division, CSIR-CSIO, Chandigarh. Authors also wish to thank Dr Kapur for his kind permission to publish/present this work.

References

1. "Head up display optics" R.A.chorley, AGARD lectcture Series no.71, pp 6-18.
2. "Optical design of dual combiner Head-up Displays" Anthony J. Kirkham, international lens design conference (1990), Pilkington optronics, UK pp 310-315.
3. "Electro-optical display" Book edited by Mohammad A. Karim, pp 337-412.
4. "ENHANCED HEAD-UP DISPLAY FOR GENERAL AVIATION AIRCRAFT" Douglas P. Burch and Michael S. Brmch, Ohio University Avionics Engineering Centre, Athens, Ohio, 2002- IEEE, pp 11.C.6-1 – 11.C.6-11.
5. "Head-up displays -The integrity of flight information" L.L. Dopping-Hepenstal, B.Sc, C.Eng., M.I.E.E, IEEE PROC. VOL.128, Pt.F. No. 7, Dec.1981, pp 440-442 .

COLOR CORRECTION TECHNIQUES IN MWIR THERMAL IMAGING LENS

J. V. Choudhary, Manish Uniyal & P.K. Sharma
 Instruments Research and Development Establishment, Raipur Road, Dehradun-248008
 Email: cjvallabh@gmail.com

Abstract: The lens materials used in MWIR are less dispersive and do not introduce much chromatic aberration as far as focal length requirement is small. As focal length of the lens needs to be designed increases the need to control the chromatic aberration becomes must and one may have to use several techniques to control this menace. Basically there are only two ways to eliminate the effect of chromatic aberration or color in any refractive optical system, 1. Use of combination of various materials with large difference in V values, 2. Use of combination of diffractive and refractive optics (a hybrid approach). In this work three lenses have been designed using the above mentioned techniques to show that both the techniques can be used for color correction in MWIR band. The advantages of one approach over the other have also been discussed.

1. INTRODUCTION

Thermal imagers produce images by capturing IR radiations emitted by all objects instead of visible light and therefore can be used for day as well as night applications. The thermal imagers work either in 3-5 micron (MWIR) or 8-12 micron (LWIR) wavelengths bands, because of the good atmospheric transmission of these wavelength bands [1]. A thermal imager mainly consists of four components: an imaging lens, an IR detector, amplifier & signal processing electronics, and a display [1]. Materials which can be used as lens material in MWIR band are silicon, germanium, zinc sulphide, zinc selenide, gallium arsenide etc, as these materials transmit in this band and can be processed for making lenses [2]. Although, effect of chromatic aberration or color in the lens designed with such materials is not prominent as these are less dispersive materials with very high V values as defined in MWIR band, but this is true only if the focal length of the lens needs to be designed is not very large. As the focal length of the lens needs to be designed becomes large, this aberration starts to affect the image point blur (as longitudinal chromatic aberration = $-f/V$, for object at infinity, where 'f' is focal length of lens and 'V' is Abbe number of material [3]) and the designer may have to use one or several techniques to control this menace. Basically there are only three approaches to eliminate the effect of chromatic aberration or color in any optical system: 1. use of various material combinations with large difference in V values, 2. use of diffractive and refractive optics combination (a hybrid approach), 3. use of reflective optics. In this work three separate lens designs have been discussed, which are designed to find the usefulness of the first two techniques to control the chromatic aberration in MWIR thermal imaging lens. Advantages of one approach over the other have also been discussed. The third approach has not been considered because the reflective optics that consists of mirrors does not disperse and therefore the need to control the chromatic aberration does not arise here.

2. OPTICAL DESIGN

We have considered designing F/5.5 lenses with focal lengths 300.0 mm in MWIR for thermal imaging camera that uses 640 X 512 (pixel pitch $15\mu\text{m}$) InSb based cooled detector, using various color correction techniques. As the detector is cooled one, in order to achieve 100% cold stop efficiency, the aperture stop of the lens has to be placed at the cold shield window of the detector, which in turn makes the front element very large in diameter and increases the weight of the lens. To avoid this, reimaging type of configuration has been used and the total focal length of such a configuration can be obtained by multiplying the focal length of first focusing group and the linear magnification of the reimaging group (Fig. 1) [1, 2]. In 1st case we have used a positive lens of less dispersive material (Si) and negative lens of more dispersive material (Ge) in order at the front doublet of the lens and this resembles the situation of an achromatic doublet design in visible with positive crown element in front with negative flint element at back. In 2nd case a negative element of more dispersive material (ZnS) and positive element of less dispersive material (Si) are used in order at the front doublet and this resembles the situation of an achromatic doublet design in visible with negative flint element in front with positive crown element at back. In 3rd case a hybrid approach has been considered and a single Si element with first surface refractive and second surface diffractive is used in place of front doublet [4].

In this design the focal length is 300mm and thus for correcting the chromatic aberration we need to use materials with reasonably large difference in V values. Here V value is defined for 3- 5 micron according to the relation given below, " $V_{3-5\mu\text{m}} = (n_{4\mu\text{m}} - 1) / (n_{3\mu\text{m}} - n_{5\mu\text{m}})$ " Where $n_{3\mu\text{m}}$, $n_{4\mu\text{m}}$, $n_{5\mu\text{m}}$, are the refractive indices at 3, 4, and 5 micron wavelengths respectively [2]. Generally combination of silicon and germanium is preferred for design of lens in 3-5 micron because of cost and manufacturability factors, but here we

have shown that the combination of silicon and zinc sulphide can also produce the lens with excellent performance. The V values of Si, Ge and ZnS are 250 and 107 and 114 respectively [2], therefore this suggests that the material pairs like (Si, Ge), and (Si, ZnS) can be equally used for controlling the chromatic aberration in MWIR. Since the V value difference between Ge and ZnS is very small these two materials cannot be used in pair for color correction in this wavelength band. The condition for achromatic correction for two lens elements placed in contact is $\Phi_1/V_1 = -\Phi_2/V_2$, where Φ_1 , Φ_2 , V_1 , V_2 are the powers and V values of the elements used respectively [3]. The V values for all materials discussed here are positive, therefore, this suggests that only combination that can give achromatic design is a lens with positive power of high V value material with a lens with negative power of a low V value material. The V value of diffractive optical element is given by the relation " $V = 4 / (3-5)$ " where 4, 3 and 5 are middle short and long wavelengths of the MWIR band in μm [4]. Here negative V value of the diffractive element gives the idea that the conventional optical element with positive lens power and a diffractive optical element with positive lens power can give chromatic correction. Since, the order of various colors present in the dispersion pattern of conventional optical surface and diffractive optical surface are reverse, this gives the idea that a single lens with one surface refractive and second surface diffractive can produce an achromatic design. Such approach is called hybrid approach. The diffractive optical surface does not help in controlling secondary color, one may have to use either combination of three materials or combination of two materials along with diffractive surface to correct this.

3. PERFORMANCE EVALUATION

The performance of the designed lenses can be analyzed and compared from the transverse ray aberration plots, longitudinal spherical aberration and field aberration plots, and MTF plots shown in the figures 2, 3, and 4 respectively. The transverse ray aberration plot reflects that the lens aberrations are well within $\pm 50 \mu\text{m}$ in both the tangential as well as sagittal planes for all the three lens systems. Although the color correction is best in the case in which the Si & Ge combination are used at the front lens position than the other two cases but the order of color correction is nearly same in all cases. The longitudinal spherical aberration plot reflects that the lens aberration is well corrected in all the three cases for on axis point. The axial color is more corrected in lens that uses Si and Ge at front as well as in the lens that uses Si with DOE at the front. The lens that uses ZnS and Si at the front has also good color correction but not as comparable to the other two cases and this is because of the fact that the V value difference of the

materials used in this case is less than that of the other two cases. The distortion for all zoom positions is less than 2%, the astigmatism is less than 0.5 mm for wavelength components, while other aberrations are also within acceptable limit.

4. CONCLUSION

Three lenses have been designed to find the usefulness of various techniques like combination of materials with large difference in V values and the hybrid approach to control the color in MWIR thermal imaging lens design. The 1st and 2nd case tells that the (Si, Ge), (Si, ZnS) pairs in any order can be equally used for color correction in MWIR. The pairs like (Si & GaAs), (Si & ZnSe), can also be used for color correction in MWIR as V values for GaAs and ZnSe in MWIR are 146 and 177 respectively [2], but, the (Si, Ge), (Si, ZnS) pairs provide some extra advantages, because of large V value difference. For very large focal length designs material pair like (Si & ZnSe) will not give very good chromatic correction. As Ge is a high index material and easy to process, 1st case is useful when length of the lens and ease of manufacturability are primarily important. As ZnS is low density material in comparison to Ge, one can choose 2nd solution when light weight design is priority. The hybrid approach removes one big size lens without affecting the design performance and thus reduces the weight along with the cost. This also helps in reducing the length of the lens along with relaxing many opto-mechanical tolerances [4]. Therefore, the suitable combination of materials with large V value difference and the hybrid approach both gives good color correction, but the use of diffractive optics has many added advantages.

5. FIGURES

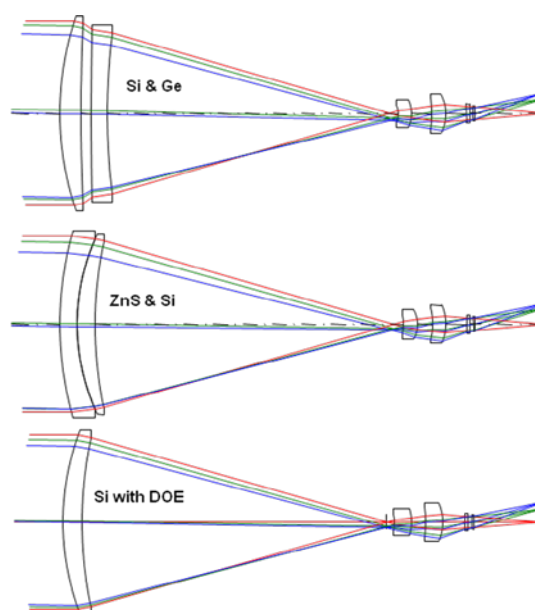


Fig. 1 Optical Layouts

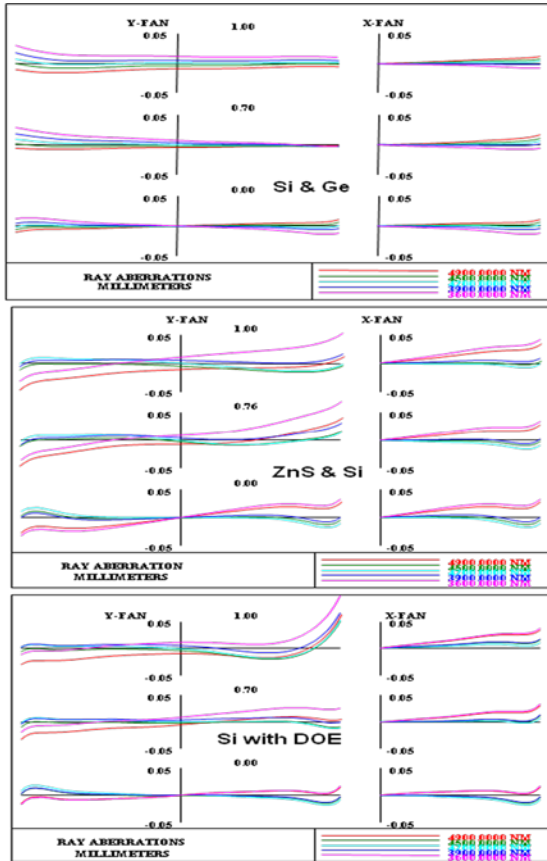


Fig. 2 Transverse Ray Aberration Plots

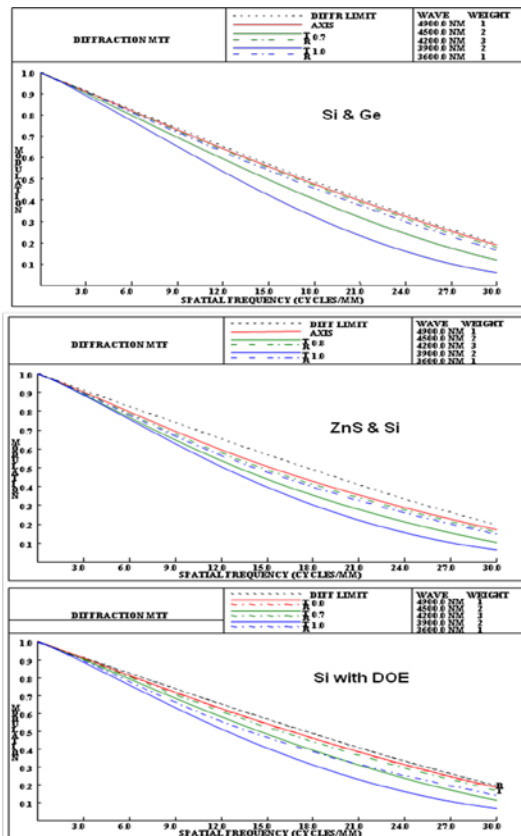


Fig. 3 MTF Plots

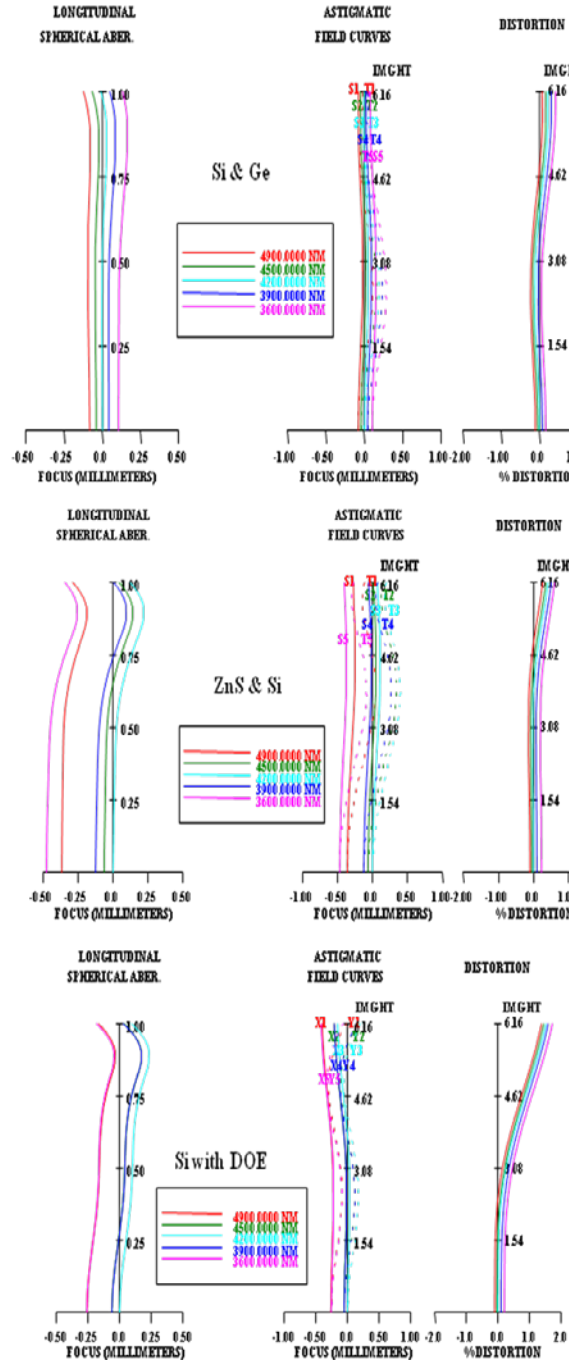


Fig. 4 Longitudinal Aberration and Field Aberration Plots

REFERENCES

- [1] J M Lloyd, Thermal Imaging Systems, Plenum Press, New York, 1975.
- [2] Allen Mann, Infrared Optics and Zoom Lenses, v. TT83, SPIE Press, 2nd Edition, 2009.
- [3] R. Kingslake, Lens Design Fundamentals, Academic Press, 1978.
- [4] Dean Faklis and G. Michel Morris, Diffractive Lenses in Broadband Optical System Design, Photon. Spectra, 131-134, 1991.

OPTICAL DESIGN OF 16X CONTINUOUS ZOOM LENS IN MWIR BAND

Ranabir Mandal, Manish Uniyal, Iqbal Singh

Instruments Research and Development Establishment, Raipur Road, Dehradun-248008

Email: ranabir@irde.drdo.in

Abstract: The zoom system provides continuous changes in the field of view from the narrow field of view to the wide field of view, which is very useful for surveillance application. A compact mid-wavelength infrared zoom objective with a zoom ratio of 16:1 in MWIR band is described in this paper. The movement of the lens groups and the focal length of the system are smooth and continuous. The zoom lens has three moving element for varying focal length and compensating focal plane shift and a reimaging element to focus the image plane onto a cooled focal plane array detector. Hybrid lens (refractive and diffractive) is used to correct aberration and chromatic correction.

1. INTRODUCTION

Thermal imagers produce images by capturing IR radiations emitted by objects, unlike CCD/CMOS/IITube based imagers where reflected/scattered light is used for imaging. Therefore Thermal Imager can be used for day as well as night surveillance, even in no light condition. The thermal imagers work either in 3-5 micron or 8-12 micron wavelengths bands, because of the good atmospheric transmission of these wavelength bands [1]. Thermal Imager mainly consists of four modules: imaging lens ie. IR Objective, IR detector, Signal processing electronics and display. IR Objective is usually designed for either single or two discrete field of view. For surveillance application a continuous zoom lens system is preferred. In discrete field of view system, different fields of view are achieved either by flip-in flip-out of Magnification change over (MCO) unit or by axial movement of a particular group, while in continuous zoom lens two or more group of lenses move continuously[2,3] to magnify the scene from wide field of view to narrow field of view. The lens has to be aberration corrected for all zoom positions and this makes the design more difficult [3].

2. DESIGN LAYOUT AND CAM PROFILE

The designed 16X continuous zoom lens is for a thermal imager working in 3-5 micron wavelength band. The camera has InSb based cooled focal plane array type detector of format 640X512 with a pixel pitch of 15 μ m. As the detector is cooled one, the aperture stop of the lens has to be placed at the cold shield window of the detector, which in turn, makes the front element very large in diameter and hence increases the weight of the lens. To avoid this, pupil imaging configuration has been used where a relay optics matches the entrance pupil of the objective with the cold shield of the detector. The total focal

length of such a configuration can be obtained by multiplying the focal length of objective and the linear magnification of the reimaging group [2]. The zooming is achieved by varying the focal length of the first focusing group by the movement of three moving elements. The first moving element works as the variator while the third and fourth lens compensates the image plane shift. The zooming group uses the basic “+” “-” “+” zooming scheme [4]. The variator (“-” group) moves towards the front elements as lens zooms out from narrow FOV to wide FOV and for this the focal length changes from the high value to the low value. The compensator (“+” group) moves away from the front element to keep the image plane fixed as the lens zooms out from narrow FOV to wide FOV (Fig. 1). Throughout the zoom range the nature of the designed lens is par focal and the image is always formed at the particular position only (on Focal Plane Array). The designed system has only five lenses, out of which only one is germanium and the rest are silicon. Four hybrid (diffractive & aspheric) surfaces are used for chromatic correction. In 3-5 μ m wavelength band, Silicon-Germanium combination is generally used for chromatic correction. Number of lenses in zoom optics is decreased by using diffractive surfaces as along with monochromatic aberrations, diffractive surface helps in chromatic correction also. To achieve the 16X zoom ratio, the focal length of the lens varies from 275 mm to 17.5 mm and the diagonal field of view varies from 2.4° to 38.5°. The designed lens has length of 132 mm which is quite compact in view of the focal length and zoom ratio. Although the diameter and position of exit pupil is fixed, the diameter and position of the entrance pupil vary as the magnification changes with the movement of lenses. It is often required to use range extender for getting longer ranges with the base zoom lens. In view of this requirement, the foot print of the beam should be

maintained minimum at the first lens throughout the zoom, especially towards the wide end of zoom due to high field angle. Otherwise range extender design becomes very difficult. In our design this condition is considered.

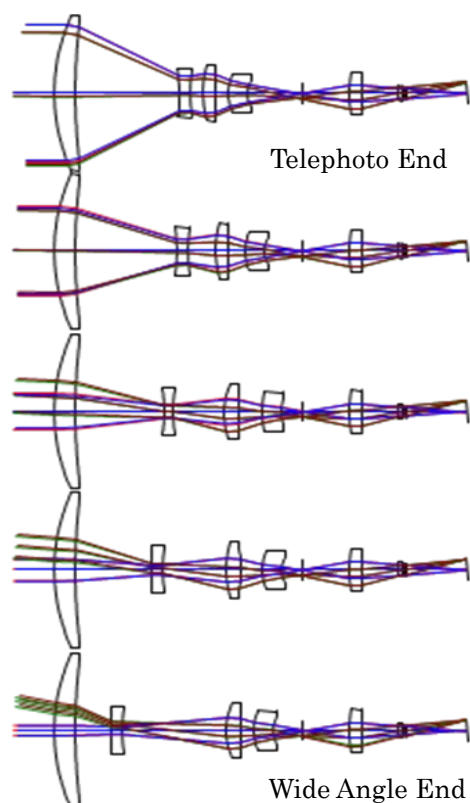


Fig. 1 Optical Layout for Five Positions

The 'zoom' groups are driven to their specific location by means of a cam comprising of a hollow cylinder with three slots in which followers are located. The carriages containing the moving lens groups are driven by the cam followers. Follower follows the slotted path as the cylinder rotates about its axis and the lenses move along the pre-determined path. The diameter of cam cylinder is determined by the diameter of narrow FOV ray cone at the position of variator group in wide FOV position. For high zoom ratio and large focal length range, the cam span (travel of lens) increases. It increases the length as well as diameter of the cam cylinder. The larger is the movement in variator towards the first fixed lens element, larger is the clearance required in cam cylinder in ray path in narrow FOV (larger aperture) position. This makes the opto-mechanical system heavy and big in size. In design, the diameter of the cam and length is also optimized. In the design system, the cam dia is 40 mm and length is 40.2 mm. One can choose the cam profile depending upon the linearity requirement. CAM profile can be plotted by incrementing position of any of the three moving element and corresponding position of the other

moving elements. Fig 2 shows the cam profile where the position of the variator (first moving element) is incremented linearly from its telephoto to wide angle position. In fig 3 the cam is plotted with linear increment of the Effective Focal Length of the lens. The cam profile of designed lens is smooth. The profile shows that the third moving element initially moves away from the first element but near the wide end, it starts moving towards the first element. The relay lens, ie. the fifth element can be used as a compensator for defocus compensation due to change in position of object from infinity to a finite distance (focusing) and temperature change (athermalization).

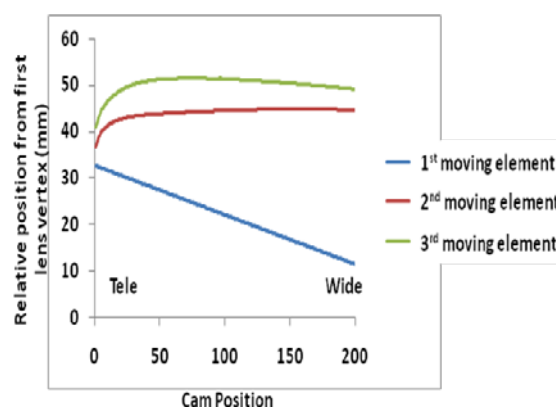


Fig. 2 Cam profile (linear increment in variator)

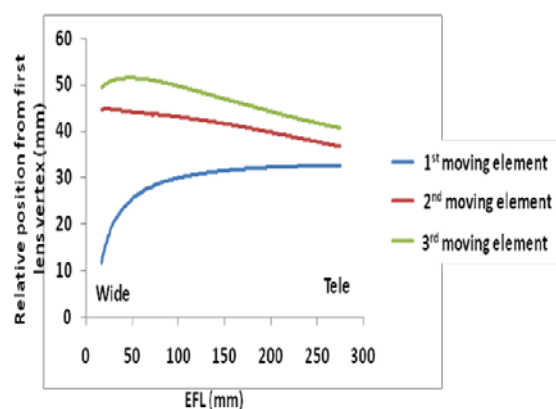


Fig. 3 Cam profile with linear increment in EFL

3. Performance Evaluation

The performance of the designed lens is evaluated for 20 zoom position starting from telephoto to wide angle position. CODEV® software has been used for evaluation of different performance parameters as well as for design optimization. Performance of the lens system has been evaluated for object at infinity with temperatures at 20°C with the help of analysis tools like rim ray plot, spot diagram, modulation transfer function (MTF) etc. Fig 4a and fig 4b shows the RIM ray curve for Telephoto and wide angle position respectively. It shows aberration is very well corrected for all the field for whole wave band.

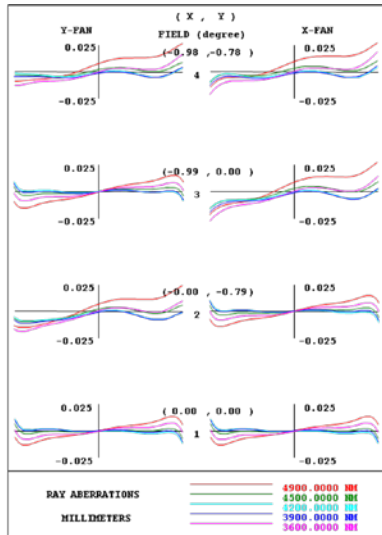


Fig. 4a RIM Ray curve for Telephoto end

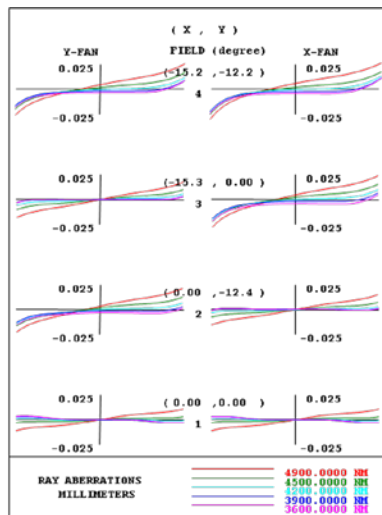


Fig. 4b RIM Ray curve for Wide angle end

Fig 5a and fig 5b shows the polychromatic Modulation Transfer Function (MTF) of the system for Telephoto and wide angle position respectively.

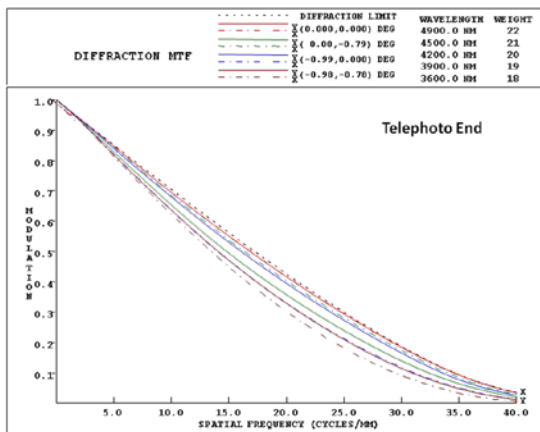


Fig. 5a MTF Plot for Telephoto End

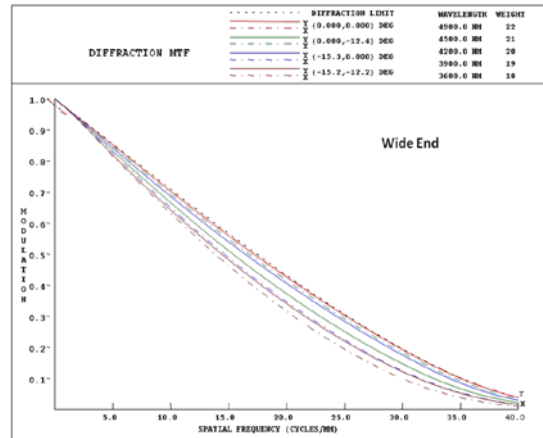


Fig. 5b MTF Plot for Wide Angle End

The MTF of the designed lens is near diffraction limited for all zoom positions. The distortion for all zoom positions is less than 2.5%, while other aberrations are also within acceptable limit.

4. CONCLUSION

This paper describes the design of an 16X Zoom lens for a cooled IR detector. It utilizes hybrid optics for correcting aberration with minimum optical elements.

ACKNOWLEDGEMENTS

The authors are grateful to Shri S S Sundaram, Director, IRDE for the permission to publish this work.

References

1. J M Lloyd, Thermal Imaging Systems, Plenum Press, New York, 1975.
2. A D Clark, Zoom Lenses, Monograph in Applied Optics, No. 7, Adam Hilger Ltd., London, 1973.
3. Allen Mann, "Selected Papers on Zoom Lenses," SPIE Milestone Series, Vol. MS 85, 1993.
4. Allen Mann, Infrared Optics and Zoom Lenses, v. TT83, SPIE Press, 2nd Edition, 2009.

Structural Design of Regular Type Mechanically Compensated Zoom Lenses

S. Pal and L. N. Hazra

Department of Applied Optics and Photonics

University of Calcutta

s.pal@sify.com, lnhaphy@caluniv.ac.in

Abstract: ‘*Ab initio*’ synthesis of thin lens structures for four-component mechanically compensated zoom lenses of Tanaka Regular Type I- IV is reported. This is facilitated by an implementation of evolutionary programming based on Genetic Algorithm. Illustrative results are presented.

1 INTRODUCTION

Optimization of thin lens structures of optically and linearly compensated zoom lenses, using genetic algorithm, has been reported recently [1, 2]. Also, we reported on the feasibility of extending the approach for designing mechanically compensated zoom lenses [3]. This report presents some results of our recent investigations on designing thin lens structures of regular type mechanically compensated zoom lenses. Based on the magnification of the variator, β_V and the compensator, β_C at the wide angle position of the zoom lens, Tanaka [4] classified four-component zoom lenses in four regular types. The values of β_V and β_C for four regular type zoom lenses are listed in Table 1.

Table 1 β_V and β_C at the wide angle position for four regular types zoom lenses.

Regular Type	I	II	III	IV
β_V	< 1	< 1	> 1	> 1
β_C	> 1	< 1	< 1	> 1

An optimization technique, based on genetic algorithm (GA), is developed for the design of regular type mechanically compensated zoom lenses. The algorithm searches a configuration space formed by the design variables, viz. powers of individual components and intercomponent separations for globally or quasi-globally optimal thin lens structures of the zoom lenses.

A brief discussion about the optimization procedure is included in the next section. The third

section presents an illustrative result of our investigation. Concluding remarks are put forward in the next section.

2 STRUCTURAL DESIGN OF REGULAR TYPE ZOOM LENSES

The optimization procedure, which mimics the natural phenomenon of evolution, commences with a population which is updated in successive generations. The population consists of a number of chromosomes each of which represents a particular zoom structure. An individual chromosome has a particular fitness value that depends on the deviation of Gaussian characteristics of the zoom lens from their desired values. Genetic operators namely, crossover and mutation, change the structure of a chromosome in search of a globally or quasi-globally optimal thin lens structure of zoom lens having a high fitness value. The chromosome with the highest fitness value is finally selected as the final result.

2.1 FITNESS CALCULATION

For the design of four-component mechanically compensated zoom lenses, four powers of individual components and three intercomponent separations are the available design variables and thus obtained by decoding a chromosome. These design parameters are used to carry out a paraxial ray trace through the system repeatedly in various stages of optimization process. Paraxial ray trace data are used to evaluate initial focal length (f_{eq}^{mi}) of the zoom lens.

$$f_{eq}^{mi} = \frac{h_1}{u_5} \quad (1)$$

where u_i is the convergence angle of the paraxial marginal ray (PMR) before i th component and h_i is height of the PMR at the i th component.

Initial focal length of the system decides direction of axial shift of the variator. First, the variator, a prespecified component in the zoom system, is given sequentially an axial shift by a small amount ε in both directions, and the resulting focal lengths of the zoom system are calculated. The direction providing a change of the focal length towards the desired wide angle focal length is chosen as the direction of axial movement of the variator. The change in focal length corresponding to the new position of the variator is accompanied by a change in position of the image plane. The compensator, another prespecified component in the zoom system, is then shifted along the axis by small amount ε in both directions. The direction providing a reduction in shift of the image plane is chosen as the preferred direction. The correct position of the compensator for exact compensation of the image plane is then determined by using bi-section search technique. The latter essentially involves repeated halving of the interval within which the compensator needs to be located axially for providing exact compensation. These two processes, the variation of focal length and then the compensation of image plane is repeated till the movement of any component is restricted by the mechanical constraints or when the overall power becomes equal to the desired wide angle power. At the end of this process, the focal length of the system gets its minimum value f_{\min} . Next, a search for axial locations of the variator and the compensator is carried out to achieve the long focal length (f_{\max}) by following a technique similar to the one used for searching the wide angle position of the system. The value of ε used in our computation is typically taken as (1/50) of the minimum value of inter-component separations of the system.

Finally merit function (Φ) is evaluated using following expression.

$$\begin{aligned} \Phi = & \omega_1 \left(1 - \frac{f_{\min}}{f_{WA}} \right)^2 + m^2 \omega_2 \left(1 - \frac{f_{\max}}{f_{Tel}} \right)^2 \\ & + \omega_3 \left(\sum_{i=1}^4 (k_i - K_T) f_{WA} \right)^2 \\ & + \omega_4 \left(\frac{\Delta L_{sys}}{f_{WA}} \right)^2 \end{aligned} \quad (2)$$

where, f_{WA} and f_{Tel} are required values for the zoom lens at its wide angle and telephoto positions respectively, f_{\min} and f_{\max} are the corresponding values achievable with the candidate solution. m is required zoom ratio, and K_T is the target value for the sum of powers to satisfy required Petzval criterion. ΔL_{sys} is the error in the system length.

$$\begin{aligned} \Delta L_{sys} = & L_{sys}^T - L_{sys} & \text{if } L_{sys}^T > L_{sys} \\ = & 0 & \text{if } L_{sys}^T \leq L_{sys} \end{aligned} \quad (3)$$

L_{sys} and L_{sys}^T are achieved and target values for the system length respectively. $\omega_1, \omega_2, \omega_3$ and ω_4 are weighting factors. For usual purposes ω_1, ω_2 are assigned a larger value and smaller values are chosen for ω_3 and ω_4 . A fitness (Ψ) function is then determined using following equation.

$$\Psi = \frac{1}{1 + \Phi} \quad (4)$$

Target of the optimization is to increase the value of fitness function.

3 NUMERICAL RESULTS

Fig. 1 and Fig. 2 present two $5 \times$ four-component Regular Type-I and Regular Type-II mechanically compensated zoom lenses. The zoom lenses are designed for an object at infinity. Powers of individual components are written just under every component. Intercomponent separations can be determine from the scale given at the top of the each image. Focal length of both of these zoom lenses attains a value 1 at the wide angle position.

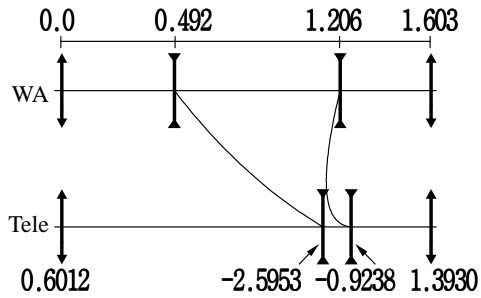


Fig. 1 Four-component Regular Type -I mechanically compensated zoom lens

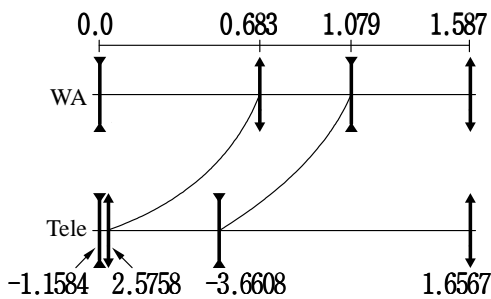


Fig. 2 Four-component Regular Type -II mechanically compensated zoom lens

4 CONCLUDING REMARKS

The zoom lens structures presented in the previous section are one potential solution of Regular Type -I and Regular Type -II zoom lens for the specified zoom range. Useful alternative solutions may be searched by repeated runs of the algorithm.

REFERENCES

1. S. Pal and L. N. Hazra, "Ab initio synthesis of linearly compensated zoom lenses by evolutionary programming", *Appl. Opt.* **50**, 1434 – 1441, 2011.
2. S. Pal and L. N. Hazra, "Structural design of four-component optically compensated zoom lenses: Use of evolutionary programming", *Optik, In the Press*, 2011.
3. L. N. Hazra and S. Pal, "A novel approach for structural synthesis of zoom systems," *Proc. SPIE* **7786**, 778607, 2010.
4. K. Tanaka, "Paraxial analysis of mechanically compensated zoom lenses. 1: Four-component type", *Appl. Opt.* **21**, 2174 – 2183, 1982.

SUPER RESOLUTION BY CONCENTRIC UNEQUAL AREA PHASE FILTERS

N. Reza & L. N. Hazra

Department of Applied Optics and Photonics, University of Calcutta
92 Acharya Prafulla Chandra Road, Kolkata - 700009
nasrin.reza.cu@gmail.com, lnhaphy@caluniv.ac.in

Abstract: In many new imaging paradigms, acquisition of 3D image information necessitates tailoring of the point spread function. Pupil plane filtering provides a straightforward means for tailoring of resolution in optical imaging. This paper reports our investigations on the use of concentric unequal area phase filters for enhancing transverse resolution in the image.

1. INTRODUCTION

Resolution capability of any optical imaging system is limited by several factors. The residual aberrations of the imaging lens severely affect its resolving power. Even for an aberration free objective, diffraction effects on account of the finite aperture of the imaging objective impose a fundamental limit for the least resolvable distance in the object/image. The Rayleigh/Abbe limit on transverse resolution stipulates that, the least resolvable distance on the object/image space is proportional to $(\lambda/n \sin \alpha)$, where $(n \sin \alpha)$ is the object/image space numerical aperture of the imaging objective, and λ is the operating wavelength [1, 2]. It should be noted that the shape and the size of the point spread function are affected significantly in presence of residual aberrations of the imaging lens. A technique for overcoming this fundamental limit is called superresolution. A straightforward tailoring of the point spread function can be performed by appropriate pupil plane filtering. About half a century ago, Toraldo di Francia [3], and subsequently Boivin [4] initiated investigations on pupil plane filtering for exceeding resolution of the imaging system beyond the diffraction limit by means of set of concentric amplitude and/or phase filters on the pupil of an image forming system. For an aberration free objective, the two dimensional point spread function (Airy pattern), consists of a central lobe surrounded by a set of dark and bright rings of gradually decreasing intensity, and the shape of the central lobe effectively determines the least resolvable distance. Use of a central obscuration on the pupil can make the central lobe sharper, but this decrease in intensity of the central lobe of the diffraction pattern is accompanied by an increase in the intensity of the neighboring sidelobes. Thus the apparent gain in resolution obtained by reduction in size of the central lobe is offset by the increase in intensity of the sidelobes. By using pupil with an array of concentric annuli, the point spread function can be tailored in a fashion such that one can get a narrow central lobe surrounded by neighboring lobes of low

intensity, with one or more lobes of high intensity spaced far away from the center.

We have already explored the use of phase annuli as pupil filters in tailoring of both transverse and axial resolution [5, 6]. In this present work we intend to explore the use of concentric unequal area phase filters for the purpose.

2. MATHEMATICAL EXPRESSION

Calculations associated with equal area phase filters have already been discussed in our previous communications [5, 6].

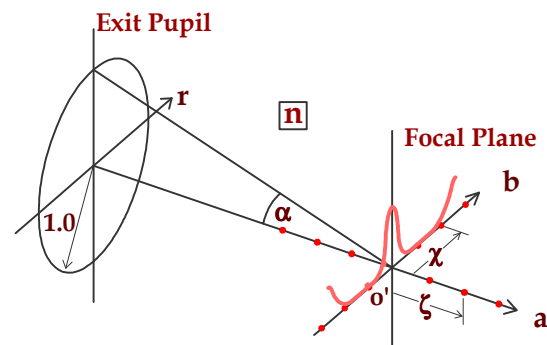


Fig. 1: Image space of an imaging system.

For an axially symmetric pupil [Fig. 1], the farfield amplitude distribution on the paraxial focal plane is given by:

$$F(b) = \int_0^1 f(r) J_0(br) r dr \quad (1)$$

where the reduced diffraction variable b for points on the transverse plane is defined as,

$$b = \frac{2\pi}{\lambda} (n \sin \alpha) \chi \quad (2)$$

χ is the geometrical distance of the point from the axis.

For a uniform transmittance Airy pupil,

$$f(r) = 1, \text{ for } 0 \leq r \leq 1$$

$$= 0, \text{ otherwise.} \quad (3)$$

From equation (1) we get,

$$F(b) = \int_0^1 J_0(br) r dr \quad (4)$$

and,

$$F(0) = \int_0^1 r dr = \frac{1}{2} \quad (5)$$

The normalized amplitude $F_N(b)$ is given by

$$F_N(b) = \frac{F(b)}{F(0)} = \left[\frac{2J_1(b)}{b} \right] \quad (6)$$

Considering a phase filter with M concentric unequal area of annular zones, let,

$$f(r) = \sum_{m=1}^M f_m \mathcal{C}\mathcal{P}_m(r) \quad (7)$$

where, $\mathcal{C}\mathcal{P}_m(r)$ are zero-one functions which can be defined as [7],

$$\mathcal{C}\mathcal{P}_m(r) = 1, \text{ for } r_{m-1} \leq r \leq r_m$$

$$= 0, \text{ otherwise.} \quad (8)$$

Then equation (6) becomes,

$$F_N(b) = \frac{F(b)}{F(0)} = 2 \sum_{m=1}^M f_m \int_0^1 \mathcal{C}\mathcal{P}_m(r) J_0(br) r dr \quad (9)$$

$$= 2 \sum_{m=1}^M f_m \int_{r_{m-1}}^{r_m} J_0(br) r dr$$

This can be expressed as

$$F_N(b) = 2 \sum_{m=1}^M f_m \mathfrak{S}_m(b) \quad (10)$$

where, $\mathfrak{S}_m(b)$ denote

$$\mathfrak{S}_m(b) = \left[\frac{r_m J_1(br_m) - r_{m-1} J_1(br_{m-1})}{b} \right] \quad (11)$$

$$= \left[r_m^2 \frac{J_1(br_m)}{(br_m)} - r_{m-1}^2 \frac{J_1(br_{m-1})}{(br_{m-1})} \right]$$

In the case of phase filters having same phase kW_m over the m^{th} zone,

$$f_m = e^{ikW_m} \quad (12)$$

Substituting from equation (12) and equation (10), we obtain

$$F_N(b) = 2 \sum_{m=1}^M e^{ikW_m} \mathfrak{S}_m(b) \quad (13)$$

The normalized intensity distribution on the paraxial focal plane corresponding to the M zone phase filter is given by

$$I_N(b) = |F_N(b)|^2 \quad (14)$$

$$= 4 \sum_{m=1}^M \sum_{n=1}^M [\cos \{k(W_m - W_n)\}] \mathfrak{S}_m(b) \mathfrak{S}_n(b)$$

To obtain the mathematical expression for farfield diffraction pattern on transverse plane due to an unequal area phase filter at the exit pupil we consider radii of contours of the annuli r_m , $m = 1, \dots, M$, as variables. In each zone, the phase W is also treated as a variable with $2^p = p$ discrete levels over $(0, 2\pi)$.

3. OPTIMUM PHASE FILTERS BY - EVOLUTIONARY PROGRAMMING

We have used evolutionary programming to obtain globally or quasi-globally optimum phase filters for achieving prespecified point spread function. This consists of binary coding of the design variables, an initial population of randomly generated chromosomes or bit strings, and evolution of this population through many generations by successive applications of the three genetic operations, namely, selection, crossover, and mutation [8, 9]. The degrees of freedom are the number of the annuli, phases in the annuli and radii of the annuli.

In this algorithm, each individual in a population is assigned a unique fitness value Φ , and the algorithm aims to maximize this fitness in members of the population in succeeding generations.

Fitness function Φ is inversely related to the merit function ψ by

$$\Phi = \frac{1}{1 + \psi} \quad (15)$$

The merit function ψ is defined as the weighted sum of transverse intensities at a prespecified set of regularly spaced transverse points along an azimuth from the centre of the diffraction pattern.

$$\psi = \sum_{d=1}^D \omega_d I_d \quad (16)$$

where I_d is the intensity at the d^{th} point on the axis, and ω_d is the corresponding weight. Preferred intensity variations are expected to be obtained by suitable choice of relative values of the weighting factors ω_d .

In order to avoid undue stagnation and slow convergence of the algorithm we adopted an approach of 'dynamic merit function' by redefining the merit

function, and correspondingly the fitness function, after each iteration.

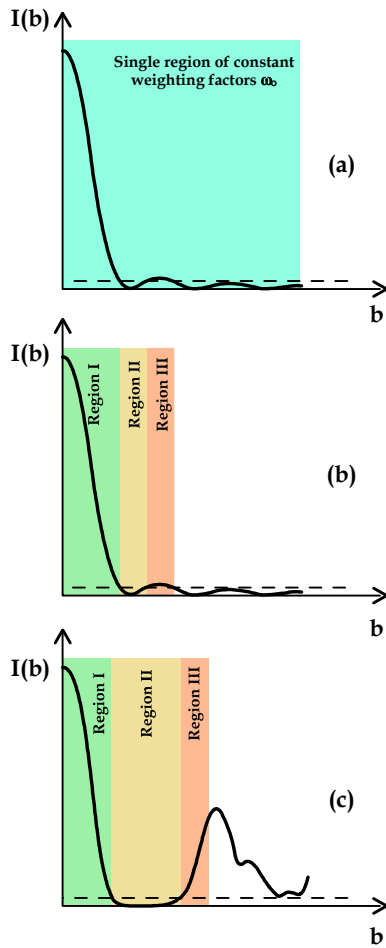


Fig. 2: Change in transverse intensity distribution of the elite members of different generation during the run of our algorithm from (a) first generation, (b) at generation $G_1 > 1$, (c) at generation $G_2 > G_1$.

The merit function ψ is redefined as weighted sum of intensities over equidistant points in three regions along the transverse axis [Fig. 2(b)]. ψ is given by,

$$\psi = \sum_{d=1}^{D_1-1} \omega_1 I_d + \sum_{d=D_1}^{D_2} \omega_2 I_d + \sum_{d=D_2+1}^{D_2+5} \omega_3 I_d \quad (19)$$

Three different weighting factors ω_1 , ω_2 and ω_3 are applied for transverse points lying in the three regions along b. The three regions consist of the central lobe, neighboring sidelobes with low intensity, and region of high intensity lying beyond the second zone.

The evolutionary process is affected significantly by the choice of weighting factors. Numerical checks can show that, in general, convergence is ensured when $\omega_1 > \omega_2 > \omega_3$.

4. ILLUSTRATIVE RESULT

As an illustrative example, Tables 1(a) and 1(b) respectively give the phase and radius information for a concentric unequal area eight zone phase filter. Similarly, Tables 2(a) and 2(b) give the phase and radius information for another concentric unequal area eight zone phase filter. Figures 3 and 4 show the transverse intensity distribution for the phase filters corresponding to Table 1 and Table 2 respectively.

Table 1(a): Optimum phase levels for the eight zones of the 8-Zone phase filters for transverse superresolution (Allowed number of discrete phase levels $P = 4$):

Zone	Phase
1	0.000 π
2	1.000 π
3	1.000 π
4	0.000 π
5	1.000 π
6	1.000 π
7	0.000 π
8	1.500 π

Table 1(b): Optimum radii for the eight zones of the 8-Zone phase filters for transverse superresolution (Allowed number of discrete phase levels $P = 4$):

Radius	Value
r1	0.307
r2	0.520
r3	0.618
r4	0.871
r5	0.934
r6	0.995
r7	0.999
r8	1.000

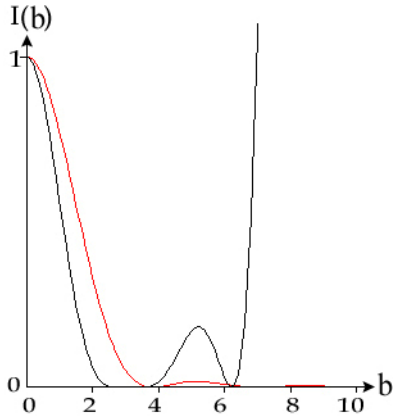


Fig. 3: Normalized transverse distribution of intensity for the optimum eight zone concentric unequal area phase filter, (—) uniform pupil.

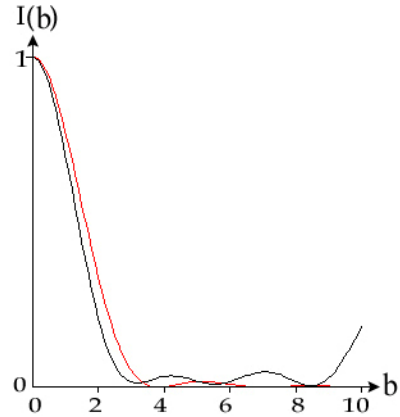


Fig. 4: Normalized transverse distribution of intensity for the optimum eight zone concentric unequal area phase filter, (—) uniform pupil.

Table 2(a): Optimum phase levels for the eight zones of the 8-Zone phase filters for transverse superresolution (Allowed number of discrete phase levels $P = 8$):

Zone	Phase
1	0.000 π
2	1.250 π
3	0.000 π
4	1.000 π
5	0.000 π
6	1.000 π
7	1.750 π
8	1.000 π

Table 2(b): Optimum radii for the eight zones of the 8-Zone phase filters for transverse superresolution (Allowed number of discrete phase levels $P = 8$):

Radius	Value
r1	0.055
r2	0.249
r3	0.556
r4	0.759
r5	0.991
r6	0.998
r7	1.000
r8	1.000

5. CONCLUSION

It is important to observe that the optimum phase filters as obtained by evolutionary programming do not make use of all discrete phase levels permitted in zones for these unequal area multilevel phase filters. This observation validates the inference that there are practical upper limits both in the number of zones and the number of allowable phase levels in synthesis of superresolving filters, beyond which no significant gain in resolution can be obtained. We are still experimenting on this.

REFERENCES

1. Born, M., Wolf, and E., *Principles of optics*, Pergamon, Oxford (1980).
2. Goodman, J. W., *Introduction to Fourier Optics*, Second Edition, McGraw-Hill, Singapore (1996).
3. G. Toraldo di Francia, "Nuovo pupille superresolventi", *Atti Fond. Giorgio Ronchi*, **7**, 366 (1952).
4. A. Boivin, *Théorie et Calcul des Figs de Diffraction de Révolution*, Université de Laval, Quebec, (1964).
5. L. N. Hazra and N. Reza, *SPIE Optics & Photonics Conference*, San Diego, 2 Aug. – 6 Aug. 2010, published in Proc. SPIE 7787, 77870D-1 (2010).
6. L. N. Hazra and N. Reza, *PRAMANA- journal of physics*, **27**, 5, 855 (2010).
7. L. N. Hazra, "Walsh filters for tailoring of resolution in microscopic imaging", *MICRON*, **38**, 129-135 (2007).
8. Rechenberg, I., *Evolutionsstrategie: Optimierung Technischer System nach Prinzipien der Biologischen Evolution*, Frommen – Holzboog Verlag, Stuttgart (1973).
9. D. E. Goldberg, *Genetic algorithm in search, optimization and machine learning*, Addison-Wesley, Reading, 1989.

TOTAL ABERRATIONS OF PARAXIAL AND NON PARAXIAL HIGHER ORDER KINOFORM LENSES

U. Dutta and L. N. Hazra
Department of Applied Optics & Photonics
University of Calcutta
E-mail: ujjal@gmail.com, lnhaphy@caluniv.ac.in

Abstract: Paraxial design of kinoform lenses gives rise to large aberrations and concomitant decrease in quality of image when the lenses are used for small values of $F\#$. The effect is likely to be more pronounced in the case of higher order kinoform lenses. This paper reports on our investigations on these problems.

1. INTRODUCTION

The maximum relief height of a kinoform should correspond to a phase modulation of $2\alpha\pi$, where α is any integer. For a first order kinoform lens, $\alpha = 1$ and the maximum relief height is $\lambda/(\mu - 1)$. However higher order kinoform lenses [1], with greater profile depths result for values of $\alpha > 1$. Again, the location of the phase transition zones in a kinoform lens of focal length f , is given by

$$r_m^2 = 2m\alpha\lambda_0 f + m^2\alpha^2\lambda_0^2 \quad (1)$$

where r_m is the radius of the m^{th} zone, λ_0 is the operating wavelength. The formula for zonal phase transitions given by Eq. (1) is appropriate for non paraxial kinoforms meant for infinite conjugate imaging applications. But for paraxial kinoform lens, $f \gg m\alpha\lambda_0$, and the second term on the right hand side of Eq. (1) may be neglected to obtain the approximate relation

$$r_m^2 = 2m\alpha\lambda_0 f \quad (2)$$

Design considerations of both, a paraxial and non paraxial first order kinoform lens on the

basis of third order aberrational analysis have already been reported [2]. We explore the design of higher order kinoform lenses by an evaluation of their total aberrations. This paper will dwell upon our investigations on aberrational characteristics of higher order kinoform lenses on finite substrates of non-unity refractive index [3].

REFERENCES

1. L. N. Hazra and C. A. Delisle, "Higher order kinoform lenses: diffraction efficiency and aberrational properties," *Opt. Eng.* **36**, 1500–1507 (1997).
2. D. A. Buralli, G. M. Morris and J. R. Rogers, "Optical performance of holographic kinoforms," *Appl. Opt.* **28**, 976-982 (1989).
3. U. Dutta and L. N. Hazra, "Monochromatic primary aberrations of a diffractive lens on a finite substrate", *Appl. Opt.* **49**, 3613-3621 (2010)

RANDOM LASING FROM AN ARRAY OF MICRODROPLETS

Anjani Kumar Tiwari, Ravitej Uppu and Sushil Mujumdar

Nano-optics and Mesoscopic Optics Laboratory, Tata Institute of Fundamental Research,
1, Homi Bhabha Road, Colaba, Mumbai 400 005, India
anjanyumartiwari@tifr.res.in, mujumdar@tifr.res.in

Abstract: We demonstrate coherent random lasing from an array of poly-disperse aperiodic microdroplets made of Rhodamine 6G dissolved in alcohol. Ultra-narrow lasing peaks are observed in the longitudinal direction. The origin of ultranarrow modes is attributed to nonresonant feedback within the array of microdroplets. The threshold behavior of random lasing is also observed.

1. INTRODUCTION

Coherent emission from randomly distributed elastic scatterers dispersed in a gain medium is termed as random lasing [1-2]. The amplification is proportional to the dwell-time of light inside the gain medium. When the dwell-time is sufficient, the amplification can exceed the optical losses and lasing can occur. The system consists of two parts, amplifying medium and randomly distributed scatterers. In most cases, the scatterers and the amplifying medium are different. For example, when nano-particles like polystyrene or TiO_2 are suspended in a laser dye solution, the nano-particles act as scatterers and the dye solution acts as an amplifying medium. On the other hand, ZnO powders, Nd-doped powders or dye-doped scatterers are different in the sense that both the scattering and amplification are provided by the same entity [3]. In these powder lasers, the scatterers are in a random close-packed formation and hence they are strongly correlated. The inter-scatterer separation cannot be increased as it changes the scatterer density, hence affecting the gain and multiple scattering processes. Here, we demonstrate a novel system that overcomes these issues. We show threshold behavior in the emission intensity to confirm random lasing.

2. EXPERIMENTAL SETUP

The experiment deals with the generation of an array of aperiodic random sized microdroplets and observation of their emission under laser pumping as shown in Fig (1). The microdroplets were created from a solution of Rhodamine 6G dissolved in methanol. The solution is contained in a liquid container which is a closed hollow cylinder with two openings, one for the gas and another for the liquid solution. The liquid in this container is pressurized using a non-interacting gas supply (not shown in fig.). This gas pressure pushes the solution and makes it to pass through micro-capillary (M.C.). Under this pressure, the dye emitted through the capillary in the

form of a stream of polydisperse and arbitrary shaped droplets, with a random spacing between them. This stream of microdroplets is pumped by the second harmonic of a 25 ps Nd:YAG Laser.

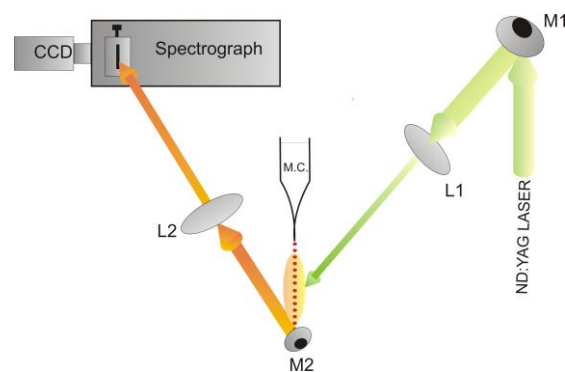


Fig. 1- Schematic of the experimental set-up used for observing random lasing from the stream. M.C. is microcapillary used to produce microdroplets. Lens L1 focuses the beam onto the droplet stream. Mirror M2 redirects the longitudinal emission. Lens L2 focuses the redirected emission into the spectrometer.

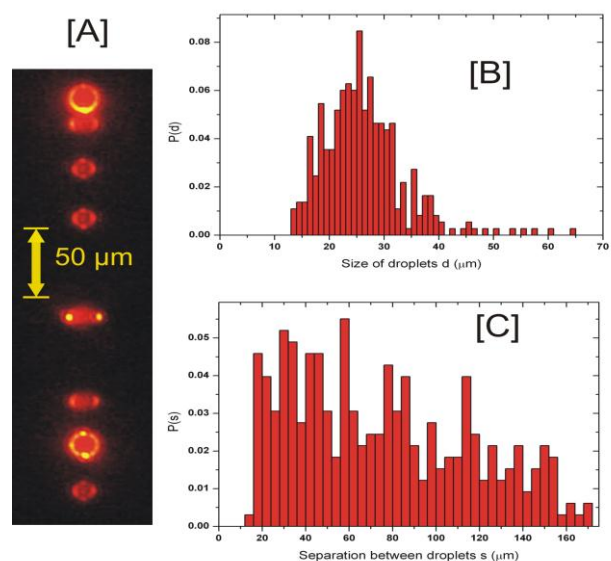


Fig. 2. [A] Image of an array of aperiodic polydisperse microdroplets. [B] The distribution of sizes. [C] Distribution of center to center separation between the droplets.

The array was excited by a focal spot of diameter ~ 1 mm to pump sufficient number of droplets. Mirror M2 was placed at about 40° from the vertical axis to redirect the longitudinal emission. Lens L2 was placed on a XYZ translation stage to collect and focus this longitudinal emission on the entrance slit of 0.5 m focal length spectrometer.

An imaging CCD was employed to image the array, this enables the measurement of the size and the spacing distribution of the droplets. Fig (2) shows the distribution of sizes and center to center separation between the droplets. They are separated from each other by several wavelengths, so they are uncorrelated.

3. RESULT AND DISCUSSION

Two representative longitudinal spectra at pump energy of 100 μJ are shown in Fig. 3. The general characteristic of a coherent random laser like ultra-narrow bandwidth, pulse to pulse intensity fluctuations etc. are observed in the longitudinal emission. The bandwidth of the peaks is measured to be 0.1 nm, which is limited by the resolution of our spectrometer.

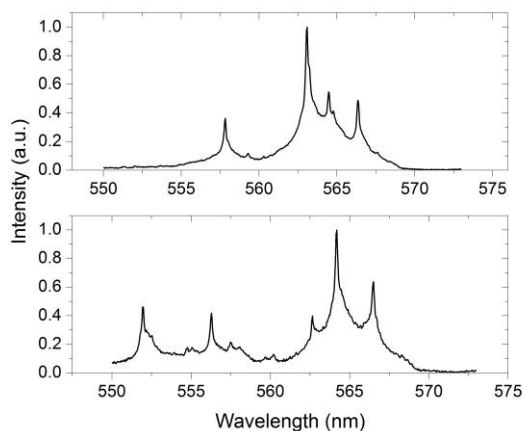


Fig. 3- Experimentally observed emission spectrum from longitudinal direction of the microdroplet array.

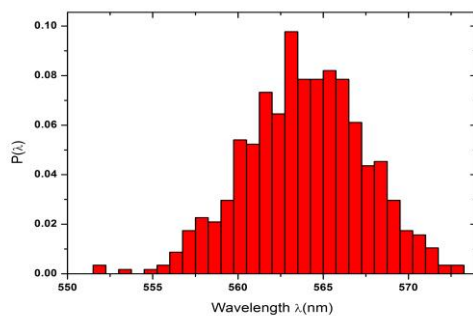


Fig. 4- Probability distribution of wavelength at which random lasing were observed.

200 spectra were taken to analyze the frequency fluctuation behavior of these lasing modes. The coherent peaks fluctuate in wavelength over a range of $\sim 15\text{nm}$ as shown in Fig (4). Most of the lasing peaks appear at the gain max of dye as expected.

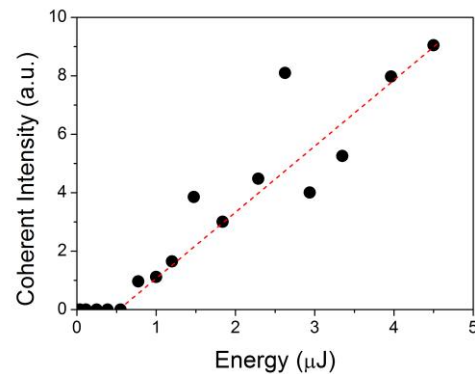


Fig. 5- Threshold behavior of peak intensity, circle indicate coherent intensity in the longitudinal direction.

The variation of coherent intensity in the longitudinal direction as a function of pump energy is shown in Fig. (5). A threshold behavior is observed at $E_p = 0.5$ μJ , after which the output emission grows steadily and shows fluctuations.

We explain the phenomenon in the following way. The fluorescence from the droplets is emitted in all directions. The photons that propagate along the droplet array undergo multiple scattering from the surfaces of droplets and thus the dwell time of photon increases along the droplet stream. This non-resonant feedback between the droplets helps the photons to repeatedly transit between the gain centers and helps in avalanche amplification.

We believe our system can be utilized as a microfluidic optical source [4]. It also adds an exciting dimension of random laser with uncorrelated disordered amplifying scatterers. Coherent emission from such an ultra-small system (~ 1 mm) is also a motivating factor for deeper study.

REFERENCES

- [1] D.S. Wiersma "The physics and application of random lasers" *Nature Physics*, 4, 359 (2008).
- [2] S.Mujumdar et.al. "Amplified extended modes in random laser" *Phys. Rev. Lett.*, 93, 5, 053903 (2004).
- [3] M. Noginov, *Solid state random lasers*, Springer series in Optical sciences, 76, 2005.
- [4] Zhenyu Li et.al. *Opt. Express* 14 (2006) 10494-10499.

W-Shaped resonator of a thin disk Yb:YAG laser

Zh. Osgoui,¹ M. Shayganmanesh,^{1,2} M.H. Daemi,¹ Sh. Kazemi¹

¹ Iranian National Center for Laser Science and Technology (INLC), PO Box: 14665-576

² Department of physics, Iran University of Science and Technology, Narmak, Tehran, Iran
osgoui@inlc.ir

Abstract: This paper describes a W-shaped thin disk laser resonator consisting of two thin disks. We have developed a computer code for designing of optical resonator for W-shaped thin disk lasers. The output power and beam quality factor M^2 is measured and results are compared with design predictions.

1. INTRODUCTION

Thin disk laser have particular features such as power scaling, minimal thermal lensing, high output power, high efficiency and good beam quality[1-2].

Scaling of the output power in thin disk laser is possible either by enlarging the pump spot radius using one disk or by increasing the number of discs at constant pump spot radius.

In this paper we scale the output power by using two disks in a single resonator. We have designed and setup a W-shaped resonator and measured output power and beam quality factor M^2 .

2. W-SHAPED RESONATOR

In the W-shaped disk laser resonator, the active mediums act as two folding mirrors, since the disks act as thermal variable lenses, we could replace a W-shaped resonator with a linear resonator with two internal variable lenses.

We have developed a computer code for designing of optical resonator for disk lasers. The code is written by visual fortran programming language. It is developed based on the Gaussian beam theory. The computer code scans all of the W-shape resonator parameters and chose the best resonator based on the optimization of beam quality factor.

3. EXPERIMENTAL SETUP

For experimental investigations a W-shaped resonator is set up. Fig. 1 shows the values of the output power P_{out} and the optical efficiency η in terms of the pump power P_p . Fig. 2, show the dependence of the beam quality factor M^2 on the dioptric power of the disk. The measured value of the beam quality factor for this resonator is: $M_x^2=70.99$, $M_y^2=54.17$.

REFERENCES

- [1] A. Giesen, J. Speiser, IEEE J. SEL TOP QUANT. Vol. 13, No. 3, May/June (2007)
- [2] J. Deile, R. Brockmann, D. Havrilla, J. Opt. Soc. Am. (2009)

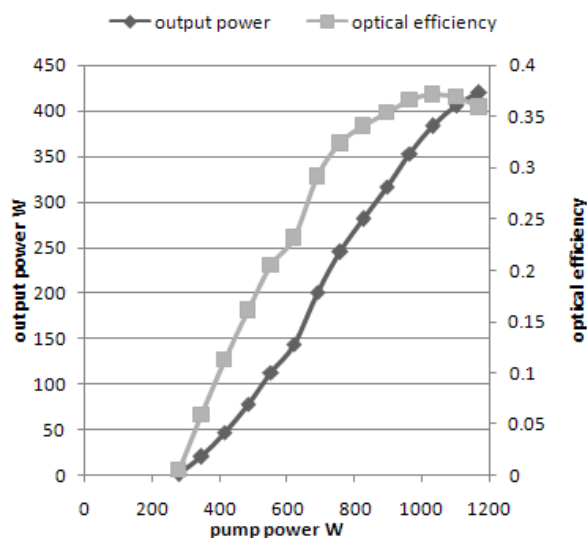


Fig. 1. output power and optical efficiency of a W-shaped resonator as a function of pump power. ($R_1=2$ m, $R_2=2$ m, $R_3=0.9$ m, $L_1=1.2$ m, $L_2=0.9$ m, $L_3=0.9$ m, $L_4=1.2$ m)

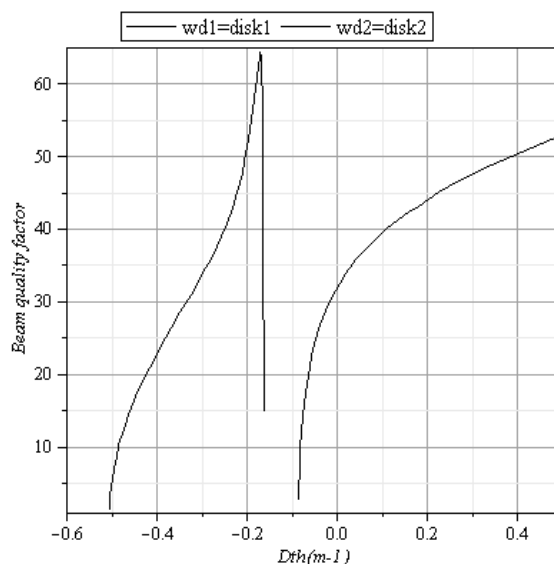


Fig. 2. Calculated dependence of beam quality factor to dioptric power of the disk for a W-shaped resonator. ($R_1=2$ m, $R_2=2$ m, $R_3=0.9$ m, $L_1=1.2$ m, $L_2=0.9$ m, $L_3=0.9$ m, $L_4=1.2$ m)

ANALYSIS OF YB:YAG THIN DISK LASER RESONATOR CONSIDERING THERMAL LENS EFFECTS: EXPERIMENTALLY AND BY LASCAD

M. Asl Dehghan, M. H. Daemi, S. S. Seyed Zamani, M. Shayganmanesh, ZH. Osgoui
Iranian National Center for Laser Science and Technology (INLC)
dehghan@inlc.ir

Abstract: Numerical calculations of thermal lensing in a face-pumped Yb:YAG thin disk is presented. The spatial profile of pump power on disk was recorded and the changes of refractive index and their effects on output power and beam quality were examined. Finally, the experimental results were compared with theoretical simulations.

1. INTRODUCTION

In Yb:YAG thin disk lasers, due to the special geometry of active medium, thermal effects are very weak in a first-order approximation so they have the potential for operation with high output power, high efficiency and very good beam quality [1]. In practice however, the fraction of absorbed power deposited as heat, generates a radial temperature gradient inside the crystal, which in turn causes thermal lensing to occur. Besides thermal lensing, stress behavior and the mounting design, limit the output power and beam quality, and should be considered in the development of high-power disk lasers. In this report the captured pump profiles were used for analysis of thermal lensing in a V-shaped resonator. Fig.1 shows the corresponding resonator.

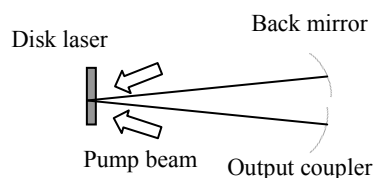


Fig. 1 Schematic of the face-pumped Yb:YAG disk laser with a folded resonator.

2. EXPERIMENTAL RESULTS

An 8% dopant Yb:YAG crystal with thickness of 200 micron and diameter of 14mm was pumped with a 940 nm diode laser. By using a relay-optics setup and imaging the fluorescence of the disk on a CCD camera, pump power profile was obtained. Some frames were taken and the corresponding data were recorded. Fig.2 shows disk's fluorescence distribution which is pumped at 1.1kW pump power. The laser output power and beam quality factor were also measured for some different pump power. Increasing the pump power, the M^2 parameter builds-up smoothly.

3. THEORETICAL RESULTS

In LASCAD software, the experimental pump data was loaded for each pump power. Finite Element Analysis (FEA) was then performed to analyze the change of refractive index of thin disk.

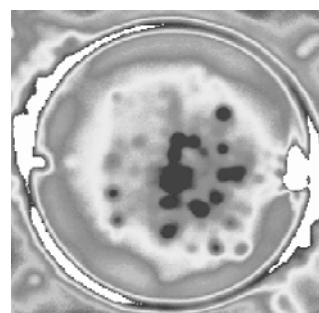


Fig. 2 The fluorescence image of the disk when is pumped at 1.1kW.

The distribution of the refractive index was fitted parabolically transverse to the optical axis [2,3] then output power and parameter M^2 of the related resonator computed. Figure 3, shows the refractive index of Yb:YAG disk and its parabolic fit in x and y axis.

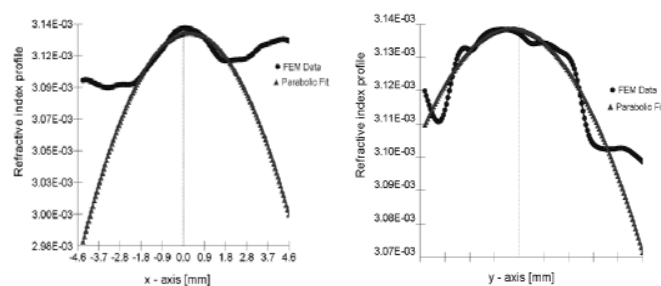


Fig3. Refractive index of Yb:YAG disk and its parabolic fit pumped at x and y axis

REFERENCES

- [1] J. Mende, et al, "Thin-disk laser – Power scaling to the kW regime in fundamental mode operation", *Proc. of SPIE* **7193**, 71931V, (2009).
- [2] E. Safari, A. Kachanov, "Estimation of thermal lensing effect in the high-power end-pumped direct-cut crystal lasers", *Optics & Laser Technology*, **38**, 534 (2006).
- [3] W. Lubeigt, D. Burns, "Adaptive optics control of solid-state lasers", *Proc. of SPIE* **6452**, 64520B, (2007)

STABILITY ANALYSIS OF ACTIVE MODE-LOCKED FIBER LASERS USING A DISTRIBUTED MODEL

Anish Bekal, Balaji Srinivasan

Department of Electrical Engineering, Indian Institute of Technology Madras, Chennai - 36
ee08d022@smail.iitm.ac.in

Abstract: A new distributed model approach for analyzing mode-locked lasers in terms of pulse width, pulse chirp and amplitude is described in this paper. This approach is used to understand the stability aspects of such lasers and a comparison with a conventional lumped model is made to ascertain the validity of the model.

Actively mode-locked lasers (MLL) are used in ultrashort pulse generation with high repetition rates mainly for optical communication. Theoretical understanding of the process done either by lumped or distributed model approaches. In the lumped model [1,2], the ring laser components are treated as lumped elements and the pulse is passed through all elements in every iteration until the pulse stabilizes. This approach is typically time-consuming and hence not amenable to stability analysis.

In contrast, pulse evolution in conventional distributed model is represented by Master mode-lock equation [3], which is solved numerically. We propose an alternative approach, that is to derive a system of differential equations for the pulse parameters such as width, chirp and peak power phenomenologically. The result of this approach is similar to variational analysis used on the master equation [4]. The system of differential equation is detailed in Eqn. 1. It is derived by considering the effect of each component on pulse parameters. For example, the second term in the second row gives the rate of pulse width reduction due to the modulator.

In order to compare lumped and distributed model, we have studied the effect of nonlinearity on pulse width as shown in Fig. 2 & 3. The two approaches are mostly similar in result. Divergence of the two

methods is observed mainly in the highly non-linear region because the pulse shape is no-longer Gaussian.

$$\frac{d}{dN} \begin{bmatrix} C \\ T_F \\ T_F \\ P \end{bmatrix} = \begin{bmatrix} (1+C^2) \frac{\beta L 1.665^2}{T_F^2} - \frac{CM}{2} (\omega T_F) + \gamma L P \\ T_F - \frac{\ln|2|}{\omega M N^2} \frac{1}{\sqrt{1 - \left(\frac{\ln|2|}{2MN}\right)^2}} \\ \frac{\beta L 1.665^2}{T_F} \frac{dC}{dN} - \frac{T_F}{T_F} \\ |g - \alpha| P \end{bmatrix} \quad (1)$$

where C – Chirp, T_F – FWHM of the pulse, M – mod index, N – Round trip number, P – Peak power, α – loop atten., g – loop gain, β – dispersion coefficient, γ – Non-linear coefficient, L – Loop length

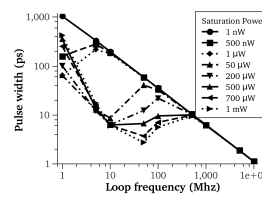


Fig.2 Lumped model

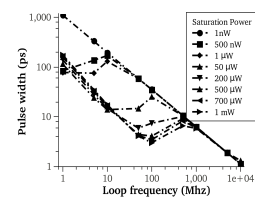


Fig. 3 Distributed model

REFERENCES

- [1] L.N. Binh and N.Q. Ngo, "Ultra-Fast Fiber Lasers," CRC press.
- [2] www.photonics.umd.edu/software/ssprop/
- [3] H. A. Haus, "A Theory of Forced Mode Locking," *Quantum Electronics*, vol. 10, no. 7, p. 8, 1975.
- [4] B. G. Bale and J. N. Kutz, "Variational method for mode-locked lasers," *Journal of the Optical Society of America B*, vol. 25, no. 7, p. 1193, Jun. 2008.

ASYMMETRIC DETUNING IN ACTIVE MODE LOCKED FIBRE LASERS

S. Thiruthakkathevan, D. Jayavel and A. Prabhakar

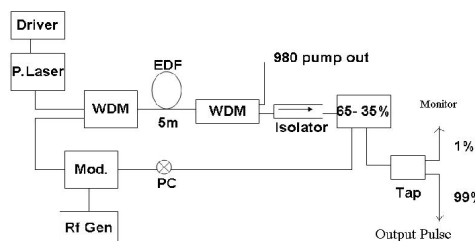
Dept. of Electrical Engineering, IIT - Madras

thevan@tenet.res.in, djayavel@ee.iitm.ac.in, anilpr@iitm.ac.in

Abstract: Active mode locking of a fibre laser was achieved by the introduction of an electro-optic modulator within the fibre ring cavity. The use of an automatic tuning system, using a microcontroller in a control loop was also demonstrated. The feedback to the control loop was possible by monitoring both the fundamental frequency component of the optical pulse train, and also only the power in the higher frequency components. In both cases, detuning of the cavity mode locking was observed to be asymmetric about the locking frequency.

1. INTRODUCTION

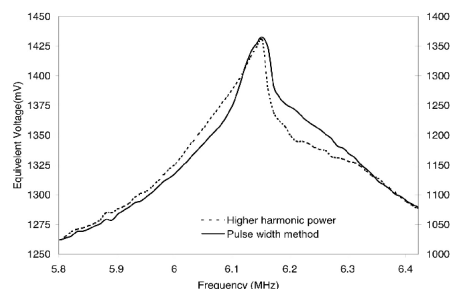
Active mode locking of cavity lasers is a commonly used technique to generate an optical pulse train [1]. We have demonstrated such active mode locking in a fibre ring laser, with Er-doped fibre as the gain medium, and using an electro-optic modulator (EOM). In addition to the optical circuit, the laser package contains the necessary control electronics to determine the mode locking frequency. Such a mode locked laser (MLL) typically suffers from detuning, caused by fluctuations in the gain and cavity round times, especially when one does not use polarization maintaining fibre (PMF).



For typical cavity lengths of around 10 m, the RF frequency, related to the cavity round trip time, is less than 20 MHz. Detection of the pulse amplitude requires simple electronics and we use a microcontroller to sweep the RF frequency, monitor the pulse width using a mean value extractor (MVE) and determine when the cavity has been mode locked. The

MVE method was further improved by monitoring the power in the higher harmonics of the pulse train.

2. DETUNING IN THE FIBRE CAVITY



To achieve mode locking, we sweep the frequency of the RF input signal, fed to the EOM, within a pre-determined range. We observe that mode-locking occurs when the pulse width is a minimum, and the power in the higher harmonics is a maximum. However, we also observe that the cavity comes out of mode-locking differently on either side of the peak. This suggests that the cavity is more sensitive to detuning at higher frequencies than at a lower frequency.

REFERENCES

- [1] J.S. Wey, J. Goldhar, G.L. Burdge, "Active harmonic modelocking of an erbium fibre laser with intra-cavity Fabry Perot filters", *J. Light. Tech.*, **15**, 1171 (1997).

SYNTHESIS AND CHARACTERIZATION OF TiO₂- SiO₂ COMPOSITES

S. Divya¹, Indu Sebastian^{1,2}, V. P. N. Nampoori¹, P. Radhakrishnan^{1,2} and A. Mujeeb^{1,2}

¹International School of Photonics, Cochin University of Science and Technology, Cochin, Kerala, India.

²Centre of Excellence in Lasers and Optoelectronic Sciences, Cochin University of Science and Technology, Cochin, Kerala, India.

Email: divyasasi7@gmail.com

Abstract: The study presents the synthesis of the TiO₂-SiO₂ composites by simple sol gel process. Here titanium isopropoxide and tetraethyl orthosilicate were used as the precursors for TiO₂ and SiO₂ respectively. The prepared sample was characterized using EDS, XRD, FTIR, UV-Vis-NIR spectrophotometer. This was followed by its nonlinear investigation.

1. INTRODUCTION

To explore novel physical properties related phenomenon of composites or materials and to successfully realize their application in various fields, generally one dimension of the material has to be confined to nanoscale regime. Different technologies have been explored to fabricate nanostructures and nanomaterials. One of the methods which is easy to realize at room temperature is sol gel processing. Composite materials prepared by sol gel process are potentially used for the fabrication of optical wave guide sensors, optical fibers and photonic crystal. Materials with different refractive indices are mixed together to get resultant composites having an intermediate value which in turn can be modified based on the requirement by varying the composition of the constituents. Here SiO₂ and TiO₂ have been used as the low and high refractive index materials respectively. With the composition variation it has been observed that the net refractive index of the material changes from 1.55 to 2.55 in the visible and near infra-red region [1-4]. As the amount of the SiO₂ content increases the crystallization property of TiO₂ gets retarded. It is noted that crystallization of TiO₂ in the composite films will lead the TiO₂ phase to

segregate from the SiO₂ phase. Accordingly, the resultant inhomogeneous structure can cause considerable scattering of light.

2. EXPERIMENTAL

2.1 Preparation

In this work we report the synthesis and characterization of TiO₂-SiO₂ composites. The synthesis is done by simple sol gel process, TEOS [Si(OC₂H₅)₄] and TTIP[Ti(O-i-C₃H₇)₄] were used as precursors for SiO₂ and TiO₂, respectively. TEOS and TTIP were dissolved in absolute ethanol separately to form two pre-solutions. TEOS was first mixed with absolute ethanol with a molar ratio of 1:4, hydrolyzed by adding 0.1 N HCl to adjust the water to alkoxy molar ratio to 2:1, and then stirred with a magnetic stirrer for 2h at room temperature. For pure TiO₂, TTIP (7 ml) was hydrolyzed in absolute ethanol (60 ml) by adding a few drops of concentrated HNO₃ and then stirred for 30 min. The two presolutions were mixed with various TEOS/TTIP molar ratios and stirred for 1 h [1]. TiO₂ is one of the novel materials that can be used for various applications. The physical and chemical properties of TiO₂ in the nanometer size range depend on phase composition, grain size, and

dispersity. Nano sized TiO_2 show significant differences with its bulk material in many aspects due to quantum size effect.

2.3 Characterization

The composition, crystal structure, and chemical bonding configuration of the prepared TiO_2 - SiO_2 composites were analyzed using Energy Dispersive X-ray spectroscopy (EDS), X-ray diffraction (XRD) and Fourier transform infrared spectroscopy (FTIR). Optical properties were characterized by UV-Vis-NIR spectrophotometer followed by the nonlinear investigation by Z Scan method using Q switched Nd-YAG laser .

3. RESULTS

Fig. 1 shows the X-ray diffraction (XRD) patterns of TiO_2 thin film annealed at 400°C for 30 minutes.

It is seen that TiO_2 thin layer has a crystalline structure after annealing under oxygen. The anatase phase has been observed with the preferential orientation of the crystallites along the (101) direction as indicated by the peak at angle $2\theta=25.342$. When crystallites are less than approximately $1,000\text{\AA}$ in size, appreciable broadening occurs in the X-ray diffraction lines. These regions correspond to the actual size of the particles. The extent of broadening is described by full width at half maximum intensity of the peak. An estimate of the grain size (G) from the broadening of the main (101) anatase peak can be done by using the Scherrer formula given below:

$$G = 0.9\lambda \ / \ \Delta (2\theta) \cos \theta \quad (1)$$

Where λ is the Cu $K\alpha$ radiation wavelength and $\Delta (2\theta)$ is peak width at half-height.

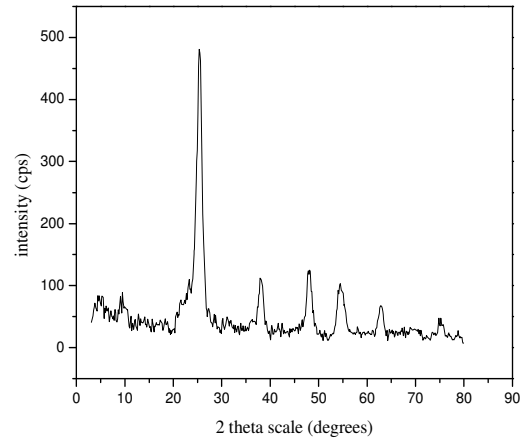


Fig: 1 X-ray diffraction pattern of nano TiO_2 - SiO_2 composite.

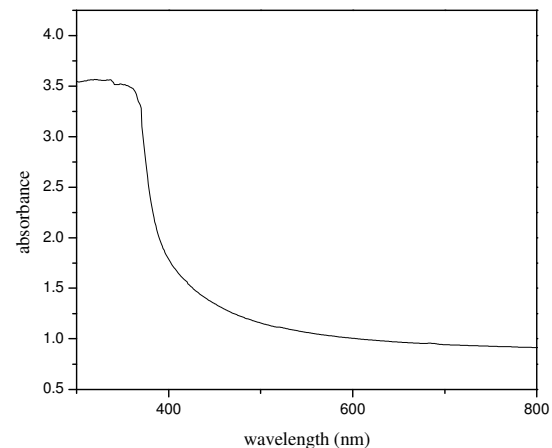


Fig: 2 Absorption spectra of nano TiO_2 - SiO_2 composite.

The optical absorbance of the films was measured using a JASCO V570 UV-visible-near IR spectrophotometer in the wavelength range 300- 800 nm. A typical optical absorption spectrum of the TiO_2 - SiO_2 thin film is given in figure 2. It showed a blue shift relative to that of bulk TiO_2 , which could be due to the quantum confinement effects. The direct bandgap of TiO_2 - SiO_2 film was estimated from the graph of $h\nu$ vs $(\alpha h\nu)^2$ for the absorption coefficient α which is related the bandgap E_g as

$$(\alpha h\nu)^2 = \text{const} (h\nu - E_g) \quad (3)$$

where $h\nu$ is the incident light energy.

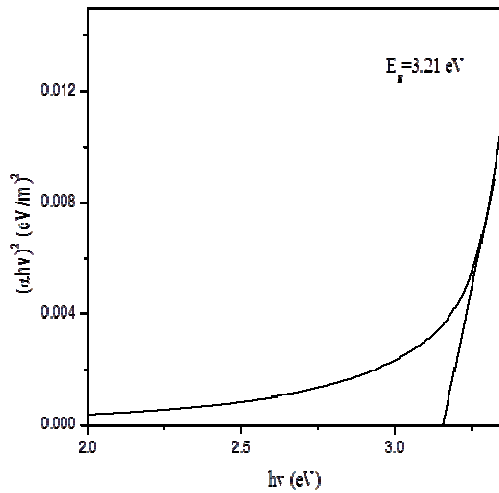


Fig: 3 Optical band gap of $\text{TiO}_2\text{-SiO}_2$ thin film

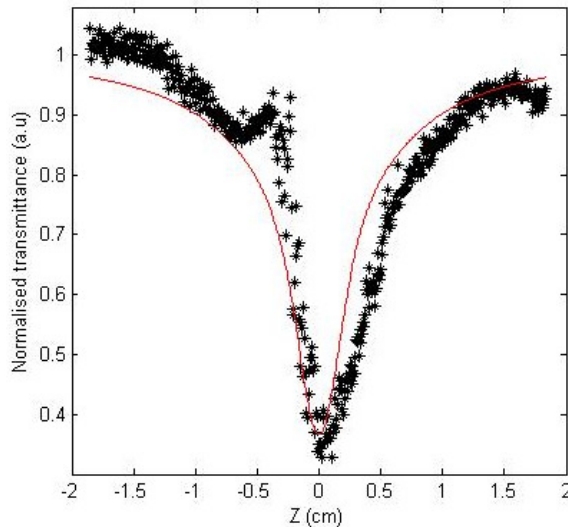


Fig: 4 Open-aperture Z-Scan trace. Solid line is the fitted curve using Eq (5).

In this work we also report the nonlinear investigation done on the sample using single beam Z-Scan technique with nanosecond laser pulses to measure nonlinear optical absorption. Z-scan technique which was developed by Sheik Bahae and his co-workers is a single beam method for measuring the sign and magnitude of nonlinear refractive index, n_2 and has sensitivity comparable to interferometric methods. The laser used is a frequency-doubled and Q-switched Continuum nanosecond, Nd:YAG laser, operating at the repetition rate of 10 Hz and producing 7ns laser pulses at 532nm wavelength. The laser

pulses are spatially and temporally Gaussian. The open aperture Z-scan experiments were conducted using a typical setup [8]. The sample was moved in the direction of light incidence near the focal spot of the lens with the focal length being 200 mm. The radius of the beam waist was calculated to be 35.4 μm . The Rayleigh length,

$$z_0 = \pi \omega_0^2 / \lambda \tag{4}$$

was estimated to be 7.4 mm, much greater than the thickness substrate, which is an essential prerequisite for z-scan experiments. The transmitted beam energy, reference beam energy and their ratio were measured simultaneously by an energy ratiometer (Rj7620, Laser Probe Corp.) having two identical pyroelectric detector heads (Rjp735). The open-aperture curve exhibited a normalized transmittance valley, indicating the presence of nonlinear absorption in the film. The glass substrate had negligible nonlinear optical response at 532 nm, which was measured by the same method and hence the high nonlinear response observed here resulted from the sample. Transmittance was a minimum at the focus and increased steadily on both sides of the focus. The data were analyzed by using the procedure described by Sheik Bahae et. al [7-9] and the nonlinear absorption coefficient β is obtained by fitting the experimental z-scan plot to equation (5).

$$T(z) = \frac{c}{q_0 \sqrt{\pi}} \int_{-\infty}^{\infty} \ln(1 + q_0 e^{-t^2}) dt \tag{5}$$

Where $q_0(z, r, t) = \beta I_0(t) L_{\text{eff}}$

Here,

$$L_{\text{eff}} = 1 - e^{-\alpha l} / \alpha \tag{6}$$

is the effective thickness of the film with linear absorption coefficient α and I_0 is the irradiance at focus. The open-aperture experiment revealed a reverse saturation curve. The obtained nonlinearity is found to be of the third order, and is probably due to a two photon absorption (TPA) process. The nonlinear absorption coefficient obtained was 7.326 m/MW.

3. CONCLUSIONS

TiO₂-SiO₂ thin films with good optical properties and good orientation were obtained by the sol-gel technique. The band gaps and linear absorption coefficients of the films were obtained through optical absorption measurements. The large nonlinear absorption effects were revealed using Z-Scan technique which confirmed its application as efficient optical limiter.

ACKNOWLEDGEMENT

The authors wish to acknowledge DST for research fellowship.

REFERENCES

- [1]. M.Hemissi, H. Amardjia-Adnani , “ Optical and structural properties of titanium oxide thin films prepared by sol-gel method”, Dig J Nanomater Bios 2, 299 (2007).
- [2].Li-Lan Yang, Yi-Sheng Lai, and J.S. Chen, P.H. Tsai, C.L. Chen, and C. Jason Chang, “Compositional tailored sol-gel SiO₂-TiO₂ thin films:Crystallization, chemical bonding configuration, and optical properties”, J. Mater. Res.20,3141 (2005).
- [3]. X. Wang, H. Masumoto, Y. Someno, and T. Hirai: “Microstructure and optical properties of amorphous TiO₂-SiO₂ composite films synthesized by helicon plasma sputtering”, Thin Solid Films 338,105 (1999).
- [5]R. Laird and A. Belkind,“Cosputtered films of mixed TiO₂/SiO₂”,J. Vac. Sci. Technol. A 10, 1908 (1992).
- [6] J.S. Chen, S. Chao, J.S. Kao, H. Niu, and C.H. “Chen Mixed films of TiO₂-SiO₂ deposited by double electron-beam coevaporation”.Appl. Opt. 35, 90 (1996).
- [7].K.Balachandaran,R.Venckatesh, Rajeshwari Sivaraj, “Synthesis of nano TiO₂-SiO₂ composite

using sol-gel method”, Int J Environ Sci Te 2, 3695 (2010) .

[7].M.S. Bahae, A.A. Said, E.W. Van Stryland, “ High-sensitivity, single-beam n₂ measurements” Opt. Lett.”, 14, 955 (1989).

[8].M.S. Bahae, A.A. Said, T.H. Wei, D.J. Hagan, E.W. Van Stryland, “Sensitive measurement of optical non linearities using single beam” , IEEE J. Quantum Electron., 14, 760 (1990).

[9] P. Chen, D. A. Oulianov, I. V. Tomov, and P. M. Rentzepis, “Two-dimensional Z scan for arbitrary beam shape and sample thickness”, J. Appl. Phys.,85, 7043 (1999).

NONLINEAR OPTICAL CHARACTERIZATION OF Ge-Ga-Se GLASS SOLUTIONS

Indu Sebastian^{1,2}, S. Divya¹, V. P. N. Nampoori¹, P Radhakrishnan^{1,2}, and Sheenu Thomas^{1,2}

¹International School of Photonics, Cochin University of Science and Technology, Cochin, Kerala.

²Centre of Excellence in Lasers and Optoelectronic Sciences, Cochin University of Science and Technology, Cochin, Kerala.

indusebastian@gmail.com

Abstract: We present the preparation and nonlinear optical characterization of nanocolloidal solutions of Ge₂₇Ga₉Se₆₄ glass with different concentrations. Their nonlinear absorption is studied using Z-scan technique. Nonlinearity increases with decrease in optical band gap which in turn depends on the concentrations of the nanocolloidal solutions. Studies reveals that the material is applicable as optical limiters due to its nonlinear absorption.

1. INTRODUCTION

Chalcogenide glasses belonging to the class of non oxide glasses where O atom is substituted by another chalcogen atom i.e S, Se, Te are known to possess the highest optical nonlinearity among nonlinear glass materials. Large nonlinear refraction and nonlinear absorption combined with an infrared transparency makes them a promising candidate for linear and nonlinear optical application. Nonlinear refractive indices and nonlinear absorption coefficients of chalcogenide bulk glasses of different composition and thin films prepared by thermal evaporation, sputtering or pulsed laser deposition were investigated elsewhere [1–4]. Chalcogenide glasses when dissolved in organic solvents allow new and simple deposition routes such as spin coating technique [5]. Dissolution of chalcogenides results in the formation of clusters with dimensions of several nanometers. Band gap of these nanoclusters varies with the size, which in turn depends upon the concentration of the solution. The nonlinear studies on these nanocolloidal solutions predicts their application as optical limiters for protecting sensitive devices from intense optical radiations. Optical limiting occurs when the absolute transmittance of a material decreases with an increase in input fluence. Different

non-linear optical phenomena such as non-linear refraction, nonlinear absorption and non-linear scattering can be used to obtain optical limiting properties, which can be observed in different materials. Chalcogenide glasses exhibit reverse saturable absorption (RSA), in which the excited state absorption cross section is higher than the ground state absorption cross section.

2. EXPERIMENTAL STUDIES

In this study we have undertaken studies on Ge₂₇Ga₉Se₆₄ glass which was prepared by conventional melt quenching method. High purity materials were used for the glass preparation. The sample were prepared by melting elemental form of Se, Ge, Ga in an evacuated fused quartz ampoule at 1000°C for 24 hours for thorough mixing and homogenization of the melt and then rapidly quenched in ice cold water. X-ray diffraction (XRD) studies confirmed its amorphous nature. Nanocolloidal chalcogenide glass solutions of three different concentrations, cc1=0.54mg/ml, cc2=0.72mg/ml, cc3=1.45mg/ml were prepared by dissolving it in n-butyl amine. Optical absorption measurements of both bulk and solutions were carried by using a UV-Vis-NIR spectrophotometer.

Nonlinear absorption coefficient (β) was calculated using open aperture Z-scan technique comprising of Nd-Yag Laser (532 nm, 7 ns, 10 Hz).

3. RESULTS AND DISCUSSION

The absorption spectra of the solutions of different concentrations are presented in Fig. 1. The absorption edge of the chalcogenide glass solutions is located in the visible range, whereas for bulk glass it is located in the near IR range. As the solute concentration in the nano colloids decreases, a blue shift in the band edge is found because of decreasing cluster size. The dependence of the bandgap with cluster size was reported T. Kohoutek et.al [6]. The dependence of band gap on the concentration is given in Fig.2.

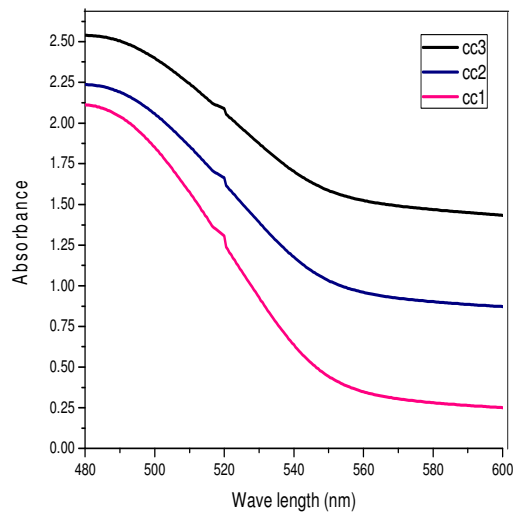


FIG. 1. Spectral dependence of absorption spectra on different concentrations. The concentration used are cc1=0.54mg/ml, cc2=0.72mg/ml, cc3=1.45 mg/ml.

The optical band gap (E_g) of bulk $\text{Ge}_{27}\text{Ga}_9\text{Se}_{64}$ glass is 1.47 eV and that of colloidal solutions cc1, cc2, cc3 are 2.31, 2.24, 2.18 respectively.

The nonlinear optical characterization of the samples was studied using the Z-scan technique. The samples to be investigated were taken in a 1mm

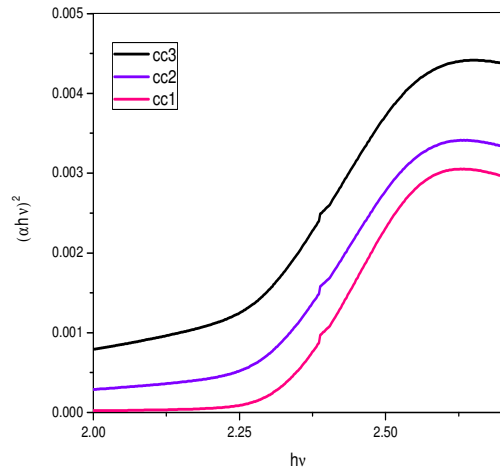


FIG. 2 Plot of $(ahv)^2$ against (hv) for $\text{Ge}_{27}\text{Ga}_9\text{Se}_{64}$ nano colloidal solutions, cc1, cc2, and cc3.

cuvette and were translated along the Z-axis through the focal point of a lens of focal length 20cm. The radius of the beam waist ω_0 was calculated to be $35.4\mu\text{m}$. The Rayleigh length $Z_0 = \pi\omega_0^2/\lambda$ was estimated to be 7.4mm.

The open-aperture curve exhibits a normalized transmittance valley, indicating the presence of reverse saturable absorption (RSA) in the nanocolloidal solutions.

The normalized transmittance for the open-aperture condition is given by[8].

$$T = q^{-1} \ln(1+q) \tag{1}$$

Where

$$q = \beta I_0 L_{\text{eff}} / (1+Z^2/Z_0^2) \tag{2}$$

Here I_0 is the laser intensity in the focal plane, β is the nonlinear absorption coefficient, L_{eff} is the effective thickness with linear absorption coefficient α .

L_{eff} is given by,

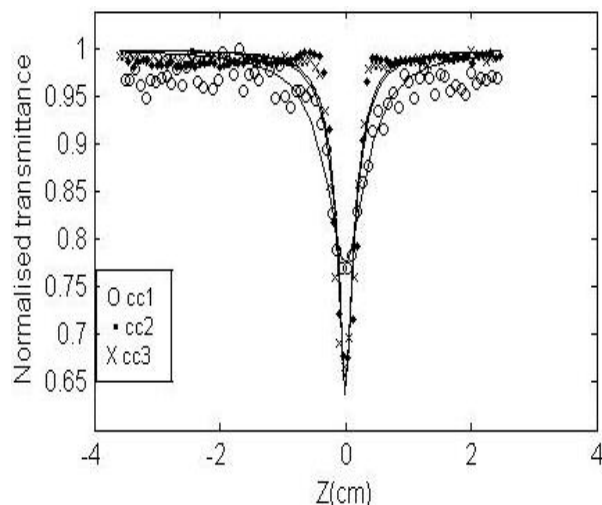
$$L_{\text{eff}} = (1-e^{-\alpha l}) / \alpha \tag{3}$$

The open aperture Z scan plot for different concentrations is depicted in figure.3. The fits of Eq.(1) to the experimental data are shown as solid

curves. The non linear absorption coefficient (β) calculated from these fits shows a dependence on cluster size.

Applying a semiconductor concept, it is observed that nonlinear properties become greater in the materials with smaller optical band gaps [8].

FIG.3 Normalized transmittance as a function of the



position for different concentrations in the open aperture scheme at 532 nm with a laser power of 473 MW/cm^2 . The solid line shows the theoretical fit.

The measured values of optical band gap for cc1, cc2, cc3 and nonlinear absorption coefficient at wavelength of 532 nm for input laser power density of 473 MW/cm^2 , are given in the table 1.

TABLE.1

Sample	Optical gap (E_g) eV	Band	Nonlinear absorption coefficient (β) cm/GW
cc1	2.31		0.209
cc2	2.24		0.274
cc3	2.18		0.283

The experimental data shows that β value increases with decreasing band gap. Generally photo induced nonlinear absorption can occur in nanoclusters due to

various reasons such as TPA, free carrier absorption, transient absorption, interband absorption, photoejection of electrons, and nonlinear scattering. We can confirm that the basic mechanism involved in the nonlinear absorption of nanocolloidal solutions of $\text{Ge}_{27}\text{Ga}_9\text{Se}_{64}$ glass is two-photon absorption (TPA) process because the photon energy of the 532 nm laser is within the range $E_g < 2h\nu < 2E_g$, where $h\nu = 2.33 \text{ eV}$ [9]. Optical nonlinear interaction between radiations and the sample increases with cluster size resulting from high concentration. Thus cluster size has a significant effect on limiting performance.

4. CONCLUSIONS

$\text{Ge}_{27}\text{Ga}_9\text{Se}_{64}$ glass and its nanocolloidal solutions of different concentrations were synthesized. Linear and non linear optical properties were studied using optical absorption spectroscopy and open aperture z-scan technique. The energy gap of the dispersed chalcogenide nanoclusters was found to be tunable with concentration. It increases with decrease in concentration.

Nonlinear optical response studies using nano second laser shows reverse saturable absorption (RSA) explained through two photon absorption (TPA). The measured β values are found to enhance with decrease in optical energy gap. The studies show that these materials are promising candidates for optoelectronic devices.

ACKNOWLEDGEMENT

The authors wish to acknowledge KSCSTE for Research funding.

REFERENCES

- [1] Fedus K, Boudeds G, Coulombier Q, Troles J and Zhang, "Nonlinear characterization of $\text{GeS}_2\text{-Sb}_2\text{S}_3\text{-CsI}$ glass system", J. Appl. Phys., 107, (2010) 023108
- [2] Kazuhiko Ogusu, Jun Yamasaki, and Shinpei

Maeda, "Linear and nonlinear optical properties of Ag-As-Se chalcogenide glasses for all-optical switching", *Optics letters*, 29, (2004) 265.

[3] J. Troles, F. Smektala, G. Boudebs, A. Monteil, B. Bureau, J. Lucas, "Chalcogenide glasses as solid state optical limiters at 1.064 μm ", *Optical Materials* 25, (2004) 231–237.

[4] A. Zakery and S. R. Elliott, "Optical Nonlinearities in Chalcogenide Glasses and Their Applications", Springer-Verlag, Berlin, (2007).

[5] G. C. Chern and I. Lauks, "Spin coated amorphous chalcogenide films: Structural characterization", *J. Appl. Phys.* 54 (5), (1983) 2701.

[6] T. Kohoutek, T. Wagner, M. Frumar, A. Chrissanthopoulos, O. Kostadinova, and S. N. Yannopoulos, *J. Appl. Phys.* 103, (2008) 063511.

[7] R. Tintu, V. P. N. Nampoori, P. Radhakrishnan, and Sheenu Thomas, "Nonlinear optical studies on nanocolloidal Ga-Sb-Ge-Se chalcogenide Glass", *J. Applied Physics* 108, (2010) 073525.

[8] L. Irimpan, B. Krishnan, A. Deepthy, V. P. N. Nampoori, and P. Radhakrishnan, *J. Appl. Phys.* 103, (2008) 033105.

[9] M. Sheik-Bahae, D.C. Hutching, D.J. Hagan, E.W. Van Stryland, "Dispersion of Bound Electronic Nonlinear Refraction in Solids", *IEEE J. Quantum Electron.* (1991) 27.

[10] R Tintu, V P N Nampoori, P Radhakrishnan and Sheenu Thomas. "Preparation and optical characterization of novel Ge-Se-Sb/PVA composite films for optical limiting application". *J. Phys. D: Appl. Phys.* 44 (2011) 025101.

[11] R Tintu, V P N Nampoori, P Radhakrishnan and Sheenu Thomas, "Nanocomposite thin films of $\text{Ga}_5\text{Sb}_{10}\text{Ge}_{25}\text{Se}_{60}$ chalcogenide glass for optical limiting applications". *Optical materials.* (2011).

DESIGN PARAMETERS FOR THE ANALYSIS OF ANNUAL PERFORMANCE OF DYE-SENSITIZED SOLAR CELLS

^aDivya Jyoti*, ^aDevendra Mohan, ^aRakesh Dhar, ^aPurnima and ^bS.K. Ghoshal

^aLaser Laboratory, Department of Applied Physics, Guru Jambheshwar University of Science and Technology, Hisar-125001, Haryana, India, Phone no. 01662-263386.

^bDepartment of Physics, AOMRG, Faculty of Science, Universiti Teknologi Malaysia, 81310 Skudai, Johor, Malaysia

*Corresponding author's E mail: divyabathla17@gmail.com

Abstract: The present simulation has emerged from the two different models combined together to predict the variation of annual performance of dye-sensitized solar cell as a function of the thickness of the TiO₂ layer, the porosity and the tilt angle. The day June 16 of 2010 and the place Hisar, India are chosen for the simulation and further analyses. It is found that a low porous material enhances the maximum power obtained from cell while increase in TiO₂ layer thickness increases the current density until a limiting value. The tilt angle governs the incident irradiation and shows a non- monotonic effect on energy density obtained.

1. INTRODUCTION

In the pursuit of environmentally benign and efficient means of producing energy has accelerated researches in the field of renewable energy sources. The focus of the present study is on dye sensitized solar cell (DSSC) [1, 2], also called the Grätzel cell which is an attractive candidate for a renewable energy source because of low-cost materials and the facile manufacturing used in its production [3, 4]. A physical model based on assumptions related to fundamental processes taking place in the cell that can adequately describe the solar cell performance is an essential tool in the optimization procedure. Electron transport is a key step in the overall cell performance and it is affected by properties of TiO₂ layer viz. thickness and porosity and the orientation of the cells too.

In an effort to determine the optimal design and operating conditions of a dye-sensitized solar cell (DSSC) installation with reference to solar radiation reception on earth, the simulation code SMARTS v2.9.5 developed by Guyemard et al. [5, 6] has been used which has a capability to simulate solar spectrum for various regions. The region selected for present simulation is Hisar, India (Latitude: 29°9'11" N, Longitude: 75°43'6" E, Northern Hemisphere). To begin with, the performance of dye-sensitized solar cell has been analyzed for a particular time of day namely, June 16, 2010 at 11:55 hrs.

Papageorgiou et al. [7] developed a mass transfer simulation model of a DSSC that describes the interfacial oxidation-reduction reaction at the cathode using the Butler-Volmer equation. Ferber et al. [8] developed a complete model of the DSSC considering the interfacial loss mechanism associated with the recombination of injected electrons in the TiO₂ network with the oxidized species (I_3^- ions) in the electrolyte. Penny et al. [9, 10] presented a mathematical model of the semiconductor dye-electrolyte interface that accounts for each interfacial

charge injection and recombination reaction within the DSSC. Ni et al. [11, 12] developed a relation for the effect of porosity on the diffusion coefficient of electron in the TiO₂ layer.

The present model combines the models given by Ferber et al. [8] and Penny et al. [10] to study the transport and diffusion of charged species in DSSC

2. MATHEMATICAL MODELLING

To illustrate the methodology for analysis and optimization of the selected cell design and operational parameters for maximum energy density, a one-dimensional model along the cell thickness presented by Ferber et al. [8] and Penny et al. [10] is employed.

The transport equation in DSSC is given by

$$D \frac{d^2 n}{dx^2} + \mu \frac{d}{dx} (nE) + G - R = 0 \quad (1)$$

Here E is electric field, D , μ , n are the diffusion coefficient, mobility and concentrations of the charged species respectively. G is rate of generation of charge carriers and R rate of loss of charge carriers.

The diffusion coefficient is calculated by means of equations deduced by Ni et al. [12] as a function of porosity, P

$$D = \begin{cases} 1.69 \times 10^{-4} (-17.48P^3 + 7.39P^2 - 2.89P + 2.15), & 0 < P < 0.41 \\ 4 \times 10^{-4} (0.76 - P)^{0.82}, & P \geq 0.41 \end{cases} \quad (2)$$

And the absorption coefficient is given by

$$\alpha = \begin{cases} 2.97 \times 10^4 P^2, & 0 < P < 0.41 \\ 2568(1 - P)(P + 2.89), & P \geq 0.41 \end{cases} \quad (3)$$

Using the daily variation of maximum power density, the maximum energy density, $E_{M,max}$ for each half month of a year is calculated from following equation

$$E_{M,max} = \begin{cases} \left(\int_{SR}^{SS} P_{M,max} dt \right)_{Day 1} \times 15 & \text{first 15 days} \\ \left(\int_{SR}^{SS} P_{M,max} dt \right)_{Day 15} \times (M - 15) & \text{remaining days} \end{cases} \quad (4)$$

Here M represents duration of the month, that can take values-28, 30, 31 depending upon the month, and the limits of integration SR and SS correspond to the time of sunrise and sunset, respectively for the year under consideration. The integration is carried out using the trapezoidal rule based on the respective daily variation profiles for Day 1 and Day 15 of each month, to obtain daily-total maximum power density. $E_{M,max}$ is assumed to be the daily-total maximum power density for Day 1 of a month ($P_{M,max}^{(1)}$) applies to the first 15 days and that for Day 15 ($P_{M,max}^{(15)}$) applies to remainder of that month.

3. RESULTS AND DISCUSSION

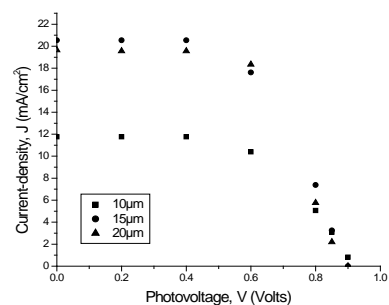
Along with material properties viz. thickness and porosity of photoelectrode amount of solar irradiation also influences cell performance. The major input parameters that govern the solar irradiation at a particular time of the day and at a particular region are the latitude, longitude, elevation, surface pressure, temperature, humidity, ozone amount and visibility, which are obtained from literature sources [13, 14]. The input parameters required to generate solar spectrum are documented in research articles of Gueymard et al. [5, 6]. The region selected for the present simulation is a sun dominating area named Hisar, India (Latitude: $29^{\circ}9'11''$ N, Longitude: $75^{\circ}43'6''$ E, Northern Hemisphere). The design parameters considered in this present study are the thickness of TiO_2 layer, d and porosity, P and tilt angle, θ . The default case pertains to $d = 15\mu m$, $P = 0.4$, and $\theta = 25^{\circ}$. The input parameters used in the present simulation are documented in Table 1.

Table 1. Parametric values used in the presented work

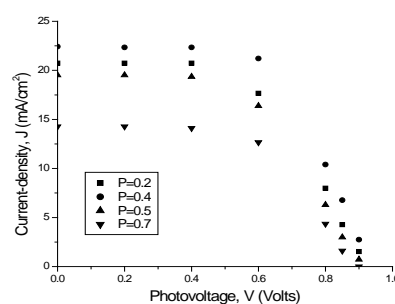
Parameter	Value
Electron relaxation rate constant, k_e (s^{-1})	10^4
Electron mobility, μ_e (cm^2/s)	0.3
Effective relative dielectric constant, ϵ	50
Incident spectral photon flux density, $\phi(\lambda)$	AM 1.5 global
Temperature, T (K)	300

Figure 1(a)-(c) respectively show the current-density, Voltage (J - V) curve as the thickness of TiO_2 layer, the porosity and the tilt angle are varied. It can be seen in Figure 1(a) that open-circuit voltage (V_{OC}) decreases as electrode thickness increases. The light intensity gradually decreases with penetration depth of the electrode, and with increase in electrode thickness excessive electron density decreases due to

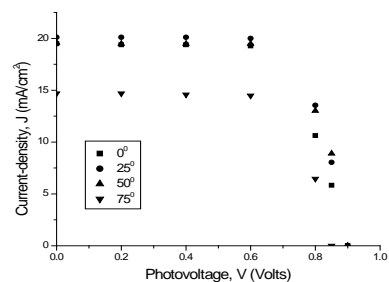
electron dilution effect, resulting in lower value of V_{OC} . It is clear from figure 1(b) that as porosity (P) decreases V_{OC} slightly decreases but short-circuit current density (J_{SC}) increases. It is because at low P , there are more TiO_2 particles in the porous thin film contributing in higher value of α and D thereby increasing J_{SC} . But after P becomes equal to 0.4 both J_{SC} and V_{OC} decrease as electrode porosity decreases. Combining the effects of both α and D , both J_{SC} and V_{OC} are reduced. Figure 1(C) represents the effect of tilt angle on J - V curve. The tilt angle decides the amount of photon flux incident on the DSSC which in turn influences the J - V curve of DSSC. Based on incident photon flux distribution for various tilt angles provided by SMARTS v 2.9.5, for the simulated time of the day, $\theta = 25^{\circ}$ is found to have the highest incident photon flux distribution, which in turn gives the maximum current density.



(a)



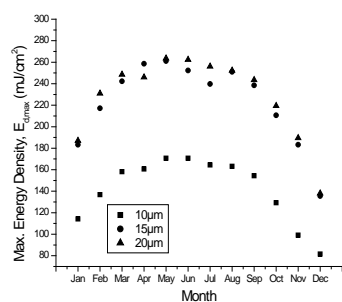
(b)



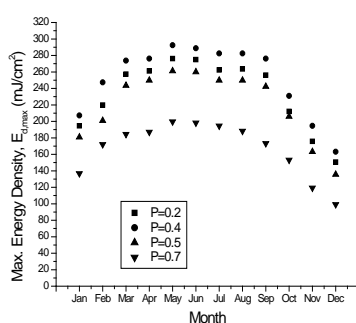
(c)

Figure 1. Variation of J - V characteristics with (a) electrode thickness, (b) porosity and (c) tilt angle

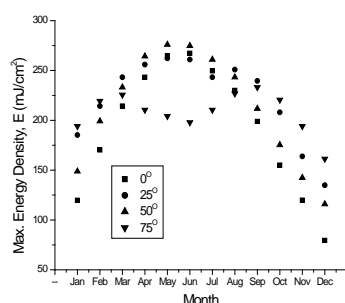
Figure 2 presents the parametric effects on the maximum energy density as a function of each half-month in the year considered. In general, it is seen that the maximum energy density increases from January (Winter) to the middle of the year (Summer) and decreases later in the year. The maximum energy density levels off with increasing thickness of TiO₂ layer and monotonically decreases as the porosity increases after 0.4. Figure 2 (c) shows that the variation of maximum energy density is non-monotonic with the tilt angle.



(a)



(b)



(c)

Figure 2. Parametric effects of (a) photoelectrode thickness, (b) porosity and (c) tilt angle on the maximum energy density simulated for the year 2010.

5. CONCLUSIONS

The simulation results presented in this paper illustrate a methodology to determine the annual variation of the performance of a DSSC. For the parametric studies adopted, it is found that optimum value of porosity is 0.40 and corresponding thickness is 15µm. the tilt angle showed non-monotonic effect on the performance of dye-sensitized solar cell.

ACKNOWLEDGEMENT

Financial support from IUAC (an autonomous Centre of UGC) and UGC-SAP is gratefully acknowledged.

REFERENCES

- [1]. M. Gratzel, *Nature*, **414**,338 (2001).
- [2]. M. Gratzel, *J. Photochem. Photobiol. A*, **164**,3 (2004).
- [3]. G. Smestad, C. Bignozzi, R. Argazzi, *Sol. Energy Mater. Sol. Cells*, **32**, 259 (1994).
- [4]. R.D. Rogers, *Ionic liquids as green solvents: Progress and Prospects*, American Chemical Society, Washington, 2003.
- [5]. C. Gueymard, "Parameterized Transmittance Model for Direct Beam and Circumsolar Spectral Irradiance," *Solar Energy*, **71**(5), 325 (2001).
- [6]. C. Gueymard, "SMARTS, A Simple Model of the Atmospheric Radiative Transfer of Sunshine: Algorithms and Performance Assessment," Professional Paper FSEC-PF-270-95, Florida Solar Energy Center, 1679 Clearlake Rd., Cocoa, FL 32922, 1995.
- [7]. N. Papageorgiou, P. Liska, A. Kay, M. Grätzel, "Mediator Transport in Multilayer Nanocrystalline Photoelectrochemical Cell Configurations," *J. Electrochem. Soc.*, **146**(3), 898 (1999).
- [8]. J. Ferber, J. Luther, R. Stangl, "An Electrical Model of Dye-Sensitized Solar Cell," *Sol. Energy Mater. And Sol. Cells*, **53**, 29 (1998).
- [9]. M. Penny, T. Farrell, C. Please, "A Mathematical Model for Interfacial Charge Transfer at the Semiconductor-Dye-Electrolyte Interface of a Dye-Sensitized Solar Cell," *Sol. Energy Mater. Sol. Cells*, **92**, 11 (2008).
- [10]. M. Penny, T. Farrell, G. Will, "A mathematical model for the anodic half cell of a dye-sensitized solar cell," *Sol. Energy Mater. Sol. Cells*, **92**, 24 (2008).
- [11]. M. Ni, M.K. H. Leung, D. Y. C. Leung, "Theoretical Modeling of the Electrode Thickness Effect on Maximum Power Point of Dye-Sensitized Solar Cell," *Canadian J. Chem. Eng.*, **86**(1), 35 (2008).
- [12]. M. Ni, M.K. H. Leung, D. Y. C. Leung,

K. Sumathy, , “An Analytical study of the Porosity Effect on Dye- Sensitized Solar Cell Performance,” *Sol. Energy Mater. Sol. Cells*, **90**(9), 1331 (2006).

[13]. Weather Underground, Inc.,

www.wunderground.com

viewed: September–October, 2009.

[14]. R. McPeters, 2009, Principal Investigator, Earth Probe TOMS,

http://jwocky.gsfc.nasa.gov/teacher/ozone_overhead_archive_v8.html viewed: September, 2009

EMISSION ANALYSIS OF Eu^{3+} AND Tb^{3+} : $\text{CdO} - \text{Bi}_2\text{O}_3 - \text{B}_2\text{O}_3$ GLASSES

C. Nageswara Raju, C. Adinarayana Reddy, S.Sailaja, B. Sudhakar Reddy*
 Department of Physics, Sri Venkateswara Degree College, Kadapa-516003, India
 *Email: drbsreddyphd@gmail.com

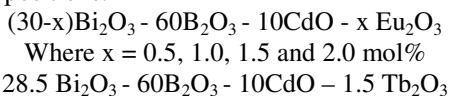
Abstract: This article reports on the emission properties of Eu^{3+} and Tb^{3+} ions doped cadmium bismuth borate (CdBiB) glasses. The functional groups present in the glass composition have been identified by using FTIR spectra. The emission spectra of Eu^{3+} and Tb^{3+} : CdBiB glasses have shown bright red and green emissions at 614 nm ($^5\text{D}_0 \rightarrow ^7\text{F}_2$) with $\lambda_{\text{exci}} = 392\text{nm}$ and at 543 nm ($^5\text{D}_4 \rightarrow ^7\text{F}_5$) with $\lambda_{\text{exci}} = 376\text{ nm}$ respectively.

1. INTRODUCTION

In recent years, there is an extensive work that has been devoted to inorganic luminescent compounds such as bismuth borate glasses because of their advantageous characteristics such as high physical and chemical stability, high refractive index, extensive glass formation range, low melting temperature, long infrared cutoff and high third order nonlinear optical susceptibility, high density and high infrared transparency [1]. Moreover, the preparation of rare earth ions doped glasses has also attracted the researchers, because of their applications in solid state lasers, channel waveguides and optical fiber amplifiers for optical communications. Earlier we have reported on the J-O theory, optical absorption and NIR emission spectral studies of Nd^{3+} : CdBiB glasses [2]. In this article, we have report on the emission properties of Eu^{3+} and Tb^{3+} : CdBiB glasses.

2. EXPERIMENTAL STUDIES

In the present work, the glasses were prepared by melt quenching method with the following chemical compositions:



3. RESULTS, DISCUSSION AND CONCLUSIONS

The emission spectra of Eu^{3+} : CdBiB glasses are shown in Fig.1. In the emission spectra, the most intense band was located at 614 nm and is the characteristic of red emission of Eu^{3+} : CdBiB glasses.

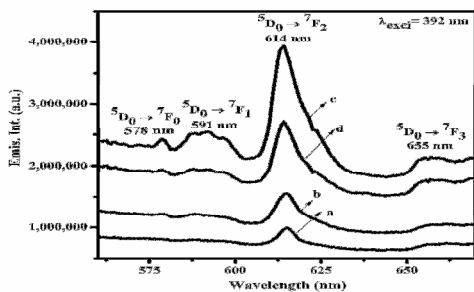


Fig.1. Emission spectra of Eu^{3+} : CdBiB glasses

From the emission spectra, it is observed that the emission intensity gradually increases from 0.5 to 1.5 mol % of Eu^{3+} and then it was decreased for 2.0 mol % indicating the concentration quenching phenomena. Thus, 1.5 mol % is the optimized concentration. The emission spectrum of 1.5 mol % of Tb^{3+} : CdBiB glass is shown in Fig.2. From the figure it is observed that, the transition at 543 nm has shown a bright green emission. Thus it could be concluded that, the emission spectra of 1.5 mol % of Eu^{3+} and Tb^{3+} : CdBiB glasses have shown intense red and green emissions and hence these glasses may be used as novel optical materials.

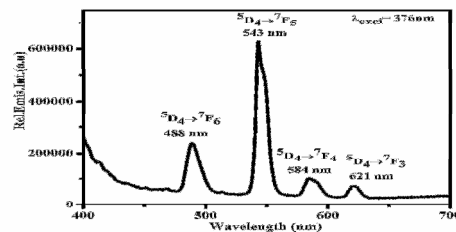


Fig.2. Emission spectrum of Tb^{3+} : CdBiB glasses

ACKNOWLEDGEMENT

This work was supported by the CSIR, New Delhi in the form of MRP No.03 (1172)/10/EMR-II sanctioned to the author (BSR), and also provided the financial assistance to one of the author (SS) in the form of SRF, who would like to thank the Head, CSIR, New Delhi, India.

REFERENCES

- [1] Ch.Rajyasre, D. Krishna Rao, "Spectroscopic investigations on alkali earth bismuth borate glasses doped with CuO ", J. Non-Cryst. Solids, **357**, 836 (2011).
- [2] C.Nageswara Raju, C. Adinarayana Reddy, S.Sailaja, Hyo Jin Seo, B. Sudhakar Reddy, "Judd-Ofelt theory-Optical absorption and NIR emission spectral studies of Nd^{3+} : $\text{CdO} - \text{Bi}_2\text{O}_3 - \text{B}_2\text{O}_3$ glasses for laser applications", J. Mater. Science, (2011) doi 10.1007/s10853-011-5853-5.

SPECTROSCOPIC ELLIPSOMETRY STUDY OF In_2O_3 THIN FILMS GROWN ON DIFFERENT SUBSTRATE

Chaman Singh, Shyama Rath*

Department of Physics and Astrophysics, University of Delhi, Delhi-110007, India

*srath@physics.du.ac.in

Abstract: The complex dielectric function $\epsilon(E) = \epsilon_1(E) + i\epsilon_2(E)$ of pulsed-laser-deposited In_2O_3 thin films on different substrate namely GaAs, Si, and quartz has been studied in the spectral range 190 to 900 nm using variable angle spectroscopic ellipsometer. An Urbach modified Tauc Lorentz model with three oscillators has been employed to fit the line shape of dielectric function. A strong correlation has been found between the substrate induced strain and the optical properties such as band gap and Urbach absorption tail.

1. INTRODUCTION

Transparent conductive oxides (TCO's), such as ZnO and In_2O_3 , have become increasingly important due to recent developments of optoelectronic devices including solar cells [1]. For these applications one needs a better understanding of the factors controlling the optical properties of the thin films.

The selection of substrate is very important for the growth of thin films because the strain induced by the lattice and thermal mismatch between the substrate and the films plays an important role in the structural and the optical properties of the films. In this paper, the effects of substrate-induced strain in In_2O_3 thin films were investigated by studying the structural and optical properties.

2. MODELLING AND PARAMETRIZATION

Spectroscopic ellipsometric measurements were performed in air at room temperature at various angles of incidence of 55, 60, 65 and 70° in the spectral range of 190 – 900 nm. The modified Tauc –Lorentz oscillator model with Urbach absorption tail [2] is used here to fit the line shape of dielectric function of In_2O_3 film. According to this model, the imaginary part of the complex dielectric function is given by

$$\epsilon_2(E) = \sum_{n=1}^N \frac{AE_0 C(E - E_g)^2}{(E^2 - E_0)^2 + C^2 E^2} \frac{1}{E} \quad E > E_g \quad (1)$$

$$= A_u \exp\left(-\frac{E - E_g}{E_u}\right) \quad E \leq E_g$$

The five fitting parameters are E_0 (the center of the oscillator), E_g (the onset value of absorption), A (the oscillator strength), E_u (Urbach energy) and C (the broadening term). The fitting is done using a three-layer model consisting of the Si substrate, the In_2O_3 layer (T-L oscillators), and an additional roughness layer BEMA (Bruggemann Effective Medium Approximation). Moreover, we added three oscillators in equation (1) so as to minimize the mean square error.

3. RESULTS AND DISCUSSION

Figure 1 show the spectral dependence of the real and imaginary part of the complex dielectric function. The strong spectral feature near 280 nm corresponds to the absorption due to the optical band gap of In_2O_3 [3].

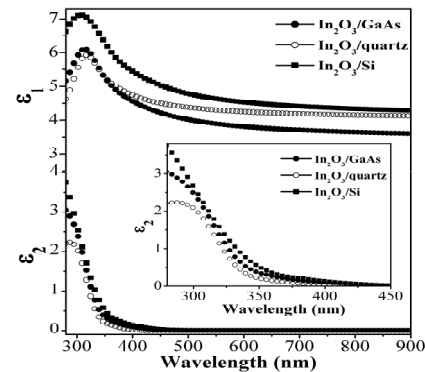


Fig. 1 The ϵ_1 and ϵ_2 spectra of In_2O_3 thin films on various substrate (the inset shows the extended spectra of ϵ_2)

The calculated band gap calculated by the Tauc plot and the strain values calculated by the x-ray diffraction for the different substrates are shown in Table 1. It is clear from the table that the thin films show a compressive strain. The substrate induced strain and disorder changes the Urbach absorption tail below the band gap hence the band gap. As the compressive strain decreases from -0.36 to -0.14 the band gap increases from 3.725 to 3.768 eV and matches well with reported values [3]

Table 1 Calculated values of strain and the band gap

Sample	Strain (%)	Band gap (eV)
$\text{In}_2\text{O}_3/\text{GaAs} \langle 111 \rangle$	-0.14	3.768
$\text{In}_2\text{O}_3/\text{Si} \langle 100 \rangle$	-0.25	3.752
$\text{In}_2\text{O}_3/\text{quartz}$	-0.36	3.725

3. REFERENCES

- [1] C. Y. Huang, G. C. Lin, Y. J. Wu, T. Y. Lin, Y. J. Yang, and Y. F. Chen, J. Phys. Chem. C, **115**, 13083 (2011)
- [2] M. Foldyna, K. Postava, J. Bouchala and J. Pistora Proc. SPIE 5445, 301 (2004)
- [3] L. Miao, S. Tanemura, Y. G. Cao, G. Xu, J. Mater Sci: Mater Electron **20**, S71 (2009)

OPTICAL LIMITING IN NICKEL-COMPLEX DYE DOPED SELF-PROTECTING GEOMETRY

^aDevendra Mohan, ^aPurnima*, ^aDivya Jyoti, ^bAmrik Singh

^aLaser laboratory, Department of Applied Physics, Guru Jambheshwar University of Science and Technology, Hisar Pin125001, Haryana, India, Phone no. 01662-263386

^bDepartment of Physics, Ch. Devi Lal University, Sirsa

*Corresponding author E-mail: arya.manu14@gmail.com, & manu.arya14@ymail.com

Abstract: In the present work, a self-protecting geometry is fabricated from bis (4-dimethylaminodithiobenzyl)-nickel) (BDN) dye doped polymeric material. Nanosecond pulses of Nd: YAG laser at 532nm wavelength with 10Hz repetition rate and 200mJ maximum energy per pulse is employed as source for experimental characterization of optical limiting action. In addition, continuous wave Ar⁺ laser beam at wavelength 514nm and 488nm is used for excitation to study optical limiting nature of media under reference. The designed 26mm long geometry with spherically polished ends behaves as thick media. The self-action effects (self-focusing and defocusing) occur within the medium ascribed to Kerr effect. This allows the collimated input beam to focus inside the medium and it is recollimated on leaving. The limiting threshold and dynamic range are reported. No laser induced damage is observed on surfaces of geometry that confirms its self-protecting behavior. Hence the considered geometry is efficient to be used to develop passive optical limiter for broad visible region.

1. INTRODUCTION

Optical limiting property need to be explored for human eye and sensor protection against optical damage due to potential use of lasers in diverse fields of life. An optical power limiter exhibits linear transmittance at low incident fluence and a clamped transmittance above a material dependent critical incident fluence known as limiting threshold [1-3]. An ideal limiter must have low limiting threshold, rapid response and large optical nonlinearity since material with large nonlinearity covers a broad bandwidth [4]. Also, high dynamic range defined as ratio of input energy at which device fails to the limiting threshold is preferable [5]. Due to intense laser signal, the limiter may itself get damaged that limits its performance. Thus self-protecting thick media are needed to be developed for passive limiter devices [6, 7].

2. EXPERIMENTAL

Monomer methylmethacrylate (MMA) is used for growing polymeric cage for encapsulating BDN dye molecules by polymerization method. BDN dye doped polymeric sample at concentration 1.00mM is grown by mixing monomer MMA with the dye dissolved methyl alcohol in the ratio 4:1. The mixture with the initiator is put in covered glass tubes and kept in a constant temperature bath maintained at 50°C for polymerization for 6-7 days. The obtained polymerized sample is tailored into 26mm long geometry with spherically polished ends with radius of curvature 12mm. Optical limiting experiment is carried out with experimental set-up as shown in Figure 1. A Q-switched, Nd: YAG laser at 532nm with pulse width of 5ns is used as source. The sample is placed in the path of focused beam with focusing lens (focal length =150mm). The expanded beam has been

focused to beam waist (ω_0) \cong 24.3 μ m calculated by $\omega_0 = 1.22\lambda f / d$ here, λ is the incident laser wavelength and d is the aperture diameter. The Rayleigh range ($z_0 = \pi\omega_0^2 / \lambda$) of used configuration is 3.48mm. Attenuator varies input intensity and corresponding output intensity via aperture is detected by detector (Thorlabs, DET-110) and recorded by oscilloscope (Tektronix, TDS-2024).

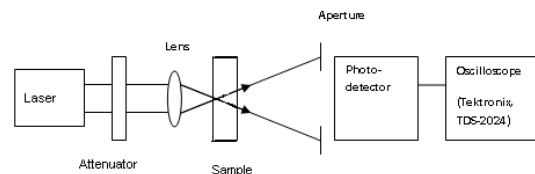


Figure 1. Experimental set-up for optical limiting of thick media

Furthermore, nonlinear transmission depending on position of focus (on front/rear surface of geometry) is investigated using cw Ar-ion laser at two wavelengths, 514nm and 488nm. The expanded beam has been focused to beam waist (ω_0) \cong 13.4 μ m and calculated Rayleigh range (z_0) is \cong 1.1mm.

3. RESULTS AND DISCUSSION

Figure 2(a) depicts the scheme of beam propagation through sample. The sample behaves as a thick media ($L/n_0z_0 \approx 5$ with linear refractive index $n_0 = 1.48$) for 532nm of ND:YAG laser pulses experiencing change in refractive index due to thermal lens effect with self-focusing and self-defocusing occurring within it [6]. This allows the collimated input beam to focus inside the medium and recollimate it on leaving [7]. The limiting profile of tailored geometry is shown in Figure 2(b). The observed limiting threshold is

nearly $2.25\text{kJ}/\text{cm}^2$. No damage is observed on surfaces of geometry that confirms its self-protecting behavior against laser induced damage. Whereas, damage at input fluence $>8\text{kJ}/\text{cm}^2$ particularly, at focal point within the sample has been observed which may be due to thermal self-focusing effect and needs to be eliminated.

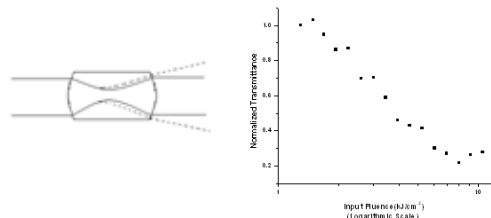


Figure 2. (a) Scheme of beam propagation (b) Optical limiting curve of self-protecting configuration at 532nm of Nd: YAG laser pulses.

Nonlinear transmission for the long geometry under reference is further characterized by using continuous Ar^+ laser beam at 514nm wavelength with maximum power of 130mW. In this case, the ratio $L/n_0z_0 \approx 16$ confirms the thick medium configuration. Absorption of photons in thick nonlinear absorbing sample produces a spatial variation of temperature within it that produces a spatial variation of refractive index, giving rise to thermal lens. The rise time of thermal lens ($\tau = \omega_0/v_s$) is $\approx 5\text{ns}$ with velocity of sound in PMMA given as $v_s \approx 2760\text{ms}^{-1}$ [8]. The normalized transmitted output power of thick polymeric media on positioning the focus at different points is depicted in Figure 3. The laser beam is focused at front surface (a) middle of geometry (b) and rear surface (c) and graph shows three different curves corresponding to each position. The obtained limiting thresholds are 0.72mW, 0.63mW and 0.55mW for a, b and c positions, respectively. It is found that the limiting threshold is minimum when focus is positioned at rear surface. Also, drastic change in transmittance is observed on focusing at front and rear surface. The calculated dynamic range is approx. 5.4×10^{10} , by taking damage threshold of $>30\text{MW}$ that is estimated with nanosecond Nd; YAG laser.

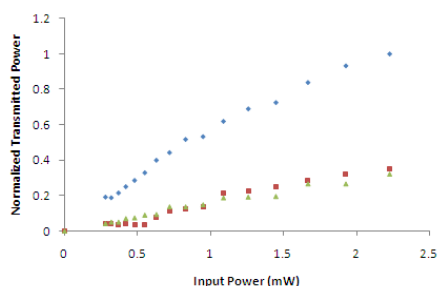


Figure 3. Limiting curves for 26mm long geometry at

514nm with focus at (a) front surface (b) middle and (c) rear surface.

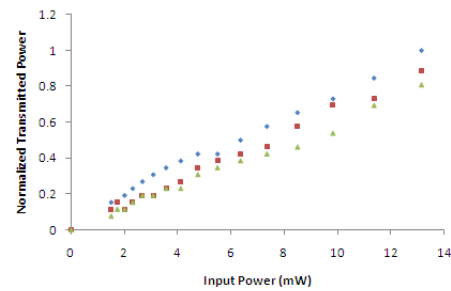


Figure 4. Limiting curves for 26mm long geometry at 488nm with focus at (a) front surface (b) middle and (c) rear surface.

Similar limiting trend of the long geometry with respect to position of focus at 488nm wavelength with maximum 125mW power is observed (Figure 4) because nonlinear refraction due to nonlinear absorption has less variation with wavelength than the band gap energy dependence for a fixed wavelength. The limiting thresholds at positions a, b and c are 3.56mW, 3.08mW and 2.67mW, respectively. The self-protecting geometry under reference exhibits no damage at both wavelengths and purpose of eliminating laser induced damage is served well. Hence the geometry has potential to be used as limiting device for broad visible region with quite high dynamic range.

4. CONCLUSION

A nickel-complex dye encapsulated thick self-protecting geometry is designed and its optical limiting tendency is characterized using nanosecond pulses of Nd: YAG laser at 532nm wavelength along with cw Ar^+ laser at 514nm and 488nm wavelengths. The self-action effects (self-focusing and defocusing) occur within the medium itself due to Kerr effect. The limiting threshold and dynamic range are reported. The demonstration of self-protecting optical limiting behavior by this geometry eliminates laser induced damage. Therefore, the considered geometry can be efficiently used for development of passive optical limiter with high dynamic range. However, thermal self-focusing effects may be a problem, but it is expected that for long wavelength of ultra-short pulses would enhance the limiting performance of the geometry.

ACKNOWLEDGEMENTS

Financial support from DST-FIST, UGC, UGC-SAP-DRS and DRDO is gratefully acknowledged. One of the authors Purnima is thankful to DTE, Panchkula for providing C.V. Raman fellowship.

REFERENCES

- [1] Y. Chen, L. Gao, M. Feng, L. Gu, N. He, J. Wang, Y. Araki, W. J. Blau, O. Ito, "Photophysical and optical limiting properties of axially modified phthalocyanines," *Mini-Rev. Org. Chem.*, **6**, 55 (2009).
- [2] B. Zhao, B. Cao, W. Zhou, D. Li and Wei Zhao, "Nonlinear optical transmission of nanographene and its composites", *J. Phys. Chem. C*, **114**, 12517 (2010).
- [3] Jun Wang and Werner J Blau, "Inorganic and hybrid nanostructures for optical limiting", *J. Opt. A: Pure Appl. Opt.*, **11**, 024001 (2009).
- [4] S. Kim and D. McLaughlin, "Propagation of electromagnetic field in optical limiting reverse-saturable absorbers," *Phys. Rev. A*, **61**, 025801 (2000).
- [5] F. E. Hernandez and S. Yang, "High-dynamic range cascaded-focus optical limiter," *Opt. Lett.*, **25**, 1180 (2000).
- [6] M. Sheik Bahae, A. A. Said, D.J. Hagan, M.J. Soileau and E.W. Van Stryland, "Nonlinear refraction and optical limiting in thick media", *Opt. Eng.*, **30**, 1228 (1991).
- [7] D. J. Hagan, E. W. Van Stryland, M. J. Soileau and Y. Y. Wu, "Self-protecting semiconductor optical limiters", *Opt. Lett.*, **13** 315 (1988).
- [8] M. Sheik-Bahae, A. A. Said, T. H. Wei, D. J. Hagan, E. W. V. Stryland, "Sensitive measurements of optical nonlinearities using a single beam", *IEEE J. Quantum Elect.*, **26**, 760 (1990) .

DOPED Na₂O.Bi₂O₃.B₂O₃ GLASS AS NEUTRAL DENSITY FILTER

MEENA RANI*, AJAY SHANKAR, ASHISH AGARWAL

Department of Applied Physics, Guru Jambheshwar University of Science and Technology,
Hisar-125001, India

Email: * meenaverma02@gmail.com

Abstract: Sodium Bismuth Borate(NBB) glass doped with transition metal (vanadium, iron, cobalt) with composition 20Na₂O.30Bi₂O₃.(50-x)B₂O₃.xV₂O₅ (x=0.2,0.3), 20Na₂O.30Bi₂O₃.(50-x)B₂O₃.xFe₂O₃ (0.2≤x≤0.5) , 20Na₂O.30Bi₂O₃.(50-x)B₂O₃.xCoO(x=5,7.5) were prepared using conventional melt quenching technique. Optical transmission spectra of doped sodium bismuth borate have been recorded in wavelength range 400-700nm. The results showed that the transmittance decrease with increase the content of transition metal in the glass .This transmission spectra showed that doped Na₂O.Bi₂O₃.B₂O₃ have the characteristics of neutral density filter.

1. INTRODUCTION

Glass play an important role as both passive and active materials in wave guides, lenses, lasing materials, optical switching materials. In conventional glasses, metal oxide, such as Na₂O, Li₂O etc are used as modifiers with network forming oxide like B₂O₃,SiO₂ ,P₂O₅ etc [1].Bismuth oxide cannot form glass by itself like other traditional glass former but it can form glass in the presence of conventional glass formers. Bismuthate glasses containing alkali oxide act as ionic conductor and possess high conductivity. Wide transmitting window in the optical region having sharp cutoff in both ultraviolet-visible and infrared region may make these glasses useful in spectral devices [2].Glasses with high Bi₂O₃ content are chemically very stable and wide transmission range with low OH content which is very important for high laser. Addition of alkali oxide may improve the the physical properties of these glasses as well as modify even their preparation condition. In addition transition metal oxides are used as colouring agents in glass industry and also to increase the refractive index of the glasses [1].Iron oxide (ferric and ferrous) impart different optical properties to the glass. Ferrous oxide absorbs infrared energy with a high ultra-violet transmission and a lower level of visible light transmission and shifting to blue colour [3].Glass having low visible transmission that include transition metal like iron, cobalt and titanium as colourant. These achieve desired spectral properties include low visible light transmission, low IR and low u-v transmission [4]. Glass containing transition metal ions exhibit interesting optical , magnetic and electrical properties due to the possible presence of such TM ions in two or more valence or coordinate states. Cobalt has the strongest coloration effect in glasses. In borate glasses with slight alkali content, an expansion to [Co^{II}O₄] takes place through the strong surrounding fields ,through which a pink color arises[5]. It is believed that much of cobalt in the oxide state of CO₃O₄.Other oxide states is termed as cobalt oxide CoO also observed. Ferromagnetic

materials such as cobalt are particularly interesting for future magneto-optical applications[6]. The study of vanadate glasses is of interest because of their relatively high electrical conductivity, stability and glass formation range compared with other transition metal oxide glasses. Electrical conductivity in these glasses, like other transition metal oxide glasses is due to transfer of charge carriers from lower valence state to higher valence states of vanadium ions. Vanadium is an element with many easily accessible valences, so that numerous color changes are observed. As increasing alkali content , the color changes from green to colorless, a change which is produced by oxidation [5].

Neutral Density Filter decrease the intensity of light without affecting the spectral response i.e. Neutral Density Filter have constant attenuation across the range of visible wavelength[7]. Neutral Density Filter reduces transmission either by reflection or absorption. Neutral density filter can be produced using a combination of transition metal ions or by use of optical coating. They are charecterised by their percent transmission range of wavelength where transmission is constant. A Neural density filters to be employed in the visible region of the spectrum are commonly constructed of absorbing filter glasses. Such materials are not useful in the ultraviolet spectral region between 200 and 300nm. Neutral density filter are specified by the optical density (OD) of the filter, which is the negative of the common logarithm of the transmission coefficient.

$$OD = -\log T$$

$$\text{Where } T = I_0/I_T$$

Wherein: I₀ = incident light intensity

I_T = transmitted light intensity

If 10% of light is transmitted (T=0.1), filter is said to be OD 1. At T=0.01, filter is OD 2.

Glass filter produced by putting an absorbing substance in a glass and changing the bulk property of glass [6] . Bulk absorber make use of the physical properties of a bulk material or impurities suspended in a bulk material [5].Bulk absorber typically can is

handle high optical powers since any power absorbed is distributed over a larger volume of material with typically larger thermal path so that optic stays cooler. Coloured glass absorber also have generally low reflectance. This is useful when working with laser since a direct reflection with high power can be very dangerous to a person or other piece of equipment[8].

2. EXPERIMENTAL

2.1 Glass Preparation

Glasses were prepared by using a conventional melt quench technique. In this technique glass is formed by the continuous hardening of melt. All the chemicals were in powder form. The starting material used for making glass were H_3BO_3 (99.5%), Bi_2O_3 (99.5%), Na_2CO_3 and transition metal oxides (V_2O_5 (99%), Fe_2O_3 (98%), CoO (98.5%)) mixed in appropriate proportions yield about 20g in a porcelain crucible. Then melted in the porcelain crucible in an electrical programmable furnace. To melt the mixture of chemicals, the temperature of the furnace is set at 1273K and melting time is half an hour with a constant stirring of the sample after every ten minutes to make the mixture homogeneous. The melted material was quickly poured onto a stainless steel plate and immediately pressed with another stainless steel plate, forming the coin shaped samples of about 1-2mm thickness. Glasses obtained were apparently homogeneous. After preparation, the samples were stored in desiccator to prevent further oxidation or degradation. Samples for recording transmission spectra polished with emery powder.

2.2 Optical Measurement

The optical transmission spectra of the glasses were recorded at room temperature using UV/VIS/NIR spectrophotometer in wavelength range 400-700 nm. Transmission spectra of all the samples were measured for well polished bulk sample. Measurement was carried out at room temperature.

3. RESULT AND DISCUSSION

Optical transmission spectra of $20Na_2O.30Bi_2O_3.49.8B_2O_3.0.2V_2O_5$ (NBBV.2) and $20Na_2O.30Bi_2O_3.49.5B_2O_3.0.5V_2O_5$ (NBBV.5) are shown in fig 1.

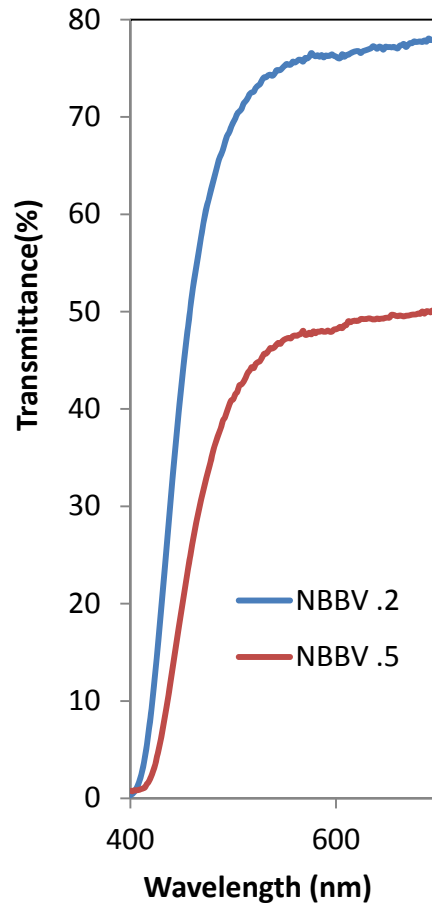


Fig 1. Optical transmission spectra for two optical glass : $20Na_2O.30Bi_2O_3.(50-x)B_2O_3.xV_2O_5$ ($x=0.2,0.5$).

Fig 1. shows that NBBV.2 have transmission approximate 70% and NBBV.5 have transmission is about 40%. This shows that, as increase the value of dopant (vanadium) transmission reduced gradually. Optical density of these sample is 0.15(NBBV.2) and 3(NBBV.5). These plots show that the prepared glass samples may act as neutral density filter in some portion of visible region.

Optical transmission spectra of $20Na_2O.30Bi_2O_3.49.8B_2O_3.2Fe_2O_3$ (NBBF.2), $20Na_2O.30Bi_2O_3.49.7B_2O_3.3Fe_2O_3$ (NBBF.3) and $20Na_2O.30Bi_2O_3.49.5B_2O_3.5Fe_2O_3$ (NBBF.5) are shown in fig. 2.

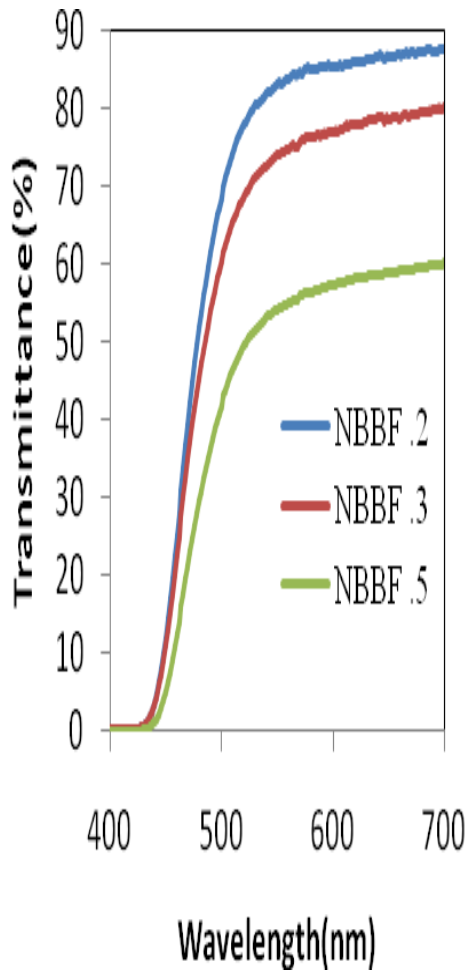


Fig 2. Optical transmission spectra for three optical glass : $20\text{Na}_2\text{O}.30\text{Bi}_2\text{O}_3.(50-x)\text{B}_2\text{O}_3.x\text{Fe}_2\text{O}_3$ ($x=0.2,0.3,0.5$).

Fig 2. shows that NBBF.2 have transmission approximate 80% , NBBF.3 have transmission is about 70% and NBBF.5 have transmission is about 50%. This shows that, as increase the value of dopant (iron oxide) transmission reduced gradually . Optical density of these sample is 0.15, 3 (NBBF0.3,0.5) . These plots show that the prepared glass samples may act as neutral density filter in 520-700nm .

Optical transmission spectra of $20\text{Na}_2\text{O}.30\text{Bi}_2\text{O}_3.45\text{B}_2\text{O}_3.5\text{CoO}$ (NBBC5) are shown in fig. 3.

Fig. 3. shows that NBBC5 have transmission approximate 0.6% .Its optical density is 2.3.This plots show that the prepared glass samples may act as

neutral density filter in visible region(400nm-675nm).It has good potential for high density neutral density filter.

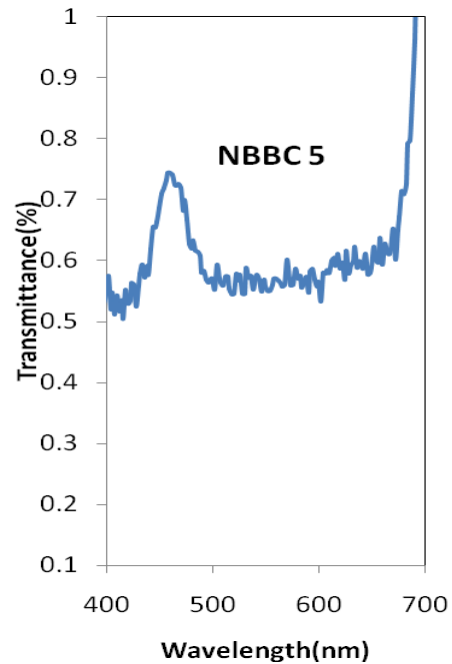


Fig. 3. Optical transmission spectra for optical glass: $20\text{Na}_2\text{O}.30\text{Bi}_2\text{O}_3.(50-x)\text{B}_2\text{O}_3.x\text{CoO}(x=5)$.

Optical transmission spectra of $20\text{Na}_2\text{O}.30\text{Bi}_2\text{O}_3.42.5\text{B}_2\text{O}_3.7.5\text{CoO}$ (NBBC7.5) are shown in fig. 4.

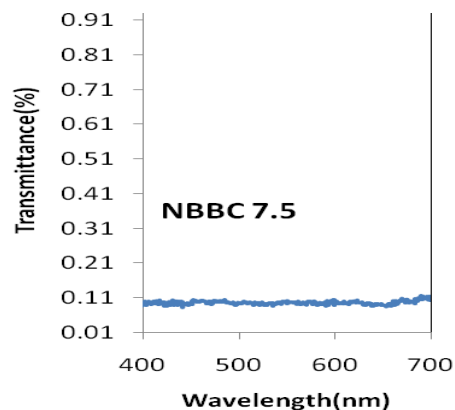


Fig . 4. Optical transmission spectra for optical glass: $20\text{Na}_2\text{O}.30\text{Bi}_2\text{O}_3.(50-x)\text{B}_2\text{O}_3.x\text{CoO}(x=7.5)$.

Fig. 4. shows that NBBC7.5 have transmission approximate 0.11% . Optical density of this sample is 2.95. This sample have constant transmittance in visible region. This plots show that the prepared glass samples may act as neutral density filter in visible region. It probably used for transmission controlling applications.

REFERENCES

- [1] N. S. Rao and M. Purnima, “Spectroscopic Investigations of Cu^{2+} in Li_2O - Na_2O - B_2O_3 - Bi_2O_3 Glasses” Bull Mater. Sci., Vol. 29, No. 4, p.no.365-370, Aug, 2006.
- [2] N. Ahlawat, S. Sanghi, A. Agarwal and Rajni Bala, “Influence of SiO_2 on the structure and optical properties of lithium bismuth silicate glasses” journal of molecular structure 963(2010) 82-86.
- [3] Y. Sakurai, Y. Hamakawa, T. Masumoto, K. Shiraie, K. Suzuki, “Current topics in Amorphous Materials: Physics and Technology”, Elsevier Science Ltd, Amsterdam, 1994.
- [4] A. Landa, Leonid landa, “Glass Composition With Low Visible and IR Transmission”, United States Patent, Patent no. 7325417 B2, Feb. 2008.
- [5] H. Scholze, “Glass: Nature, Structure and Properties”, Springer-Verlag, New York, p.no.3.1991.
- [6] T. Kloss, E. Watzke, “Coloured Borosilicate Glass”, Patent no.5612262, March 18, 1997.
- [7] K. E. Bennett, H. Beach, J. R. Staley, “Neutral Density Filter”, United States Patent 19, patent no.5018833(1991).
- [8] S. A. Kawasaki, Mitsuharu Sawamura and Yokohama, “Neutral Density (ND) Filter”, United States Patent 19, patent no. 5715103(1998).

STUDY OF THIRD ORDER NONLINEAR OPTICAL PARAMETERS OF CHALCOGENIDE As_2S_3 THIN FILM AND Ge IRRADIATED As_2S_3 THIN FILM AT 532nm

Sunita Rani*, Devendra Mohan, Nawal Kishore and Purnima.

Laser Laboratory, Department of Applied Physics, Guru Jambheshwar University of Science and Technology, Hisar, Pin-125001, Haryana, India, Phone no. 01662-263386

*Corresponding author's e.mail: sgarhwal48@gmail.com

Abstract: Nonlinear behavior of As_2S_3 thin film and Ge irradiated chalcogenide As_2S_3 thin film (Ge/As_2S_3) have been characterized and nonlinear optical parameters viz. nonlinear refractive index (n_2) and nonlinear absorption coefficient (β) have been calculated using single beam Z-scan technique with second harmonic of Nd: YAG laser. The larger nonlinearity of Ge irradiated chalcogenide As_2S_3 thin film due to electrorestriction effect leading to stimulated Brillouin scattering has been observed.

1. INTRODUCTION

The interest in chalcogenide semiconductor thin films have been due to their wide applications in optical devices [1]. These films have good transparency from visible to infra-red spectral range and exhibit strong nonlinearity [2]. Ion beams passing through materials have been widely used for modification of selective properties of chalcogenide materials [3, 4]. Ion beams of almost all the elements of periodic table with a wide range of energies are available. A specific element can be deposited within the specimen by ion implantation. keV energy Ni ion implanted in thin film of $a-As_2Se_3$ can induce doping effects [5]. In ion implantation, ions having low energy collide with nuclei, while higher energy ion beam interacts through inelastic collision with the electrons that normally have no effect on the lattice. Fast ions with energy greater than MeV/nucleon are called swift heavy ions.

Presently the changes in nonlinear optical behavior of As_2S_3 thin film and (Ge/As_2S_3) film have been observed. Among various methods to analyze nonlinear response, Z-scan technique based on change in transmission with spatial translation of sample that is an effective tool to determine nonlinear optical constants [6] has been utilized.

2. EXPERIMENTAL

Bulk sample of chalcogenide As_2S_3 has been prepared by the conventional melt quenched technique. Thermal evaporation method has been employed to synthesize chalcogenide As_2S_3 film of bulk sample on corning glass substrate and further irradiated by Ge ions of 75MeV energy with fluence of 1×10^{13} ions/cm². The film of thickness is $\sim 0.5\mu m$. The transmission spectra of films recorded by UV-Visible spectrophotometer have been shown in figure1. Transmission of sample decreases due to irradiation with Ge ion beam. The laser induced nonlinear response of prepared material has been measured by Z-scan technique. Z-scan is a technique with simple configuration and high sensitivity to measure both the sign and magnitude of nonlinear

refractive index.

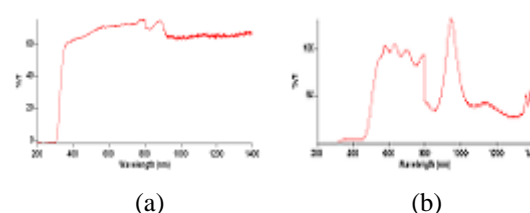


Figure 1. UV-Visible transmission spectra of (a) As_2S_3 thin film (b) Ge irradiated chalcogenide As_2S_3 thin film

The followed Z-scan experimental set-up has been shown in Figure 2 [6]. The source is an Nd: YAG laser (Quanta System, HYL-101) of 532nm wavelength with repetition rate of 10Hz and pulse width of 5ns. The laser beam has been focused with 15cm focal length lens. The film is moved in the focal plane with intensity of $2.1TW/cm^2$ at focus. An aperture of diameter 4mm is used to record on-axis fluence to study refractive changes. The transmitted intensity has been recorded by silicon photo detector (Thorlabs, DET-110). The calculated beam waist (w_0) is $24.3\mu m$ which gives Rayleigh range z_0 equal to 3.48mm by using the relation $z_0 = k\omega_0^2/2$, $k=2\pi/\lambda$ being the wave vector

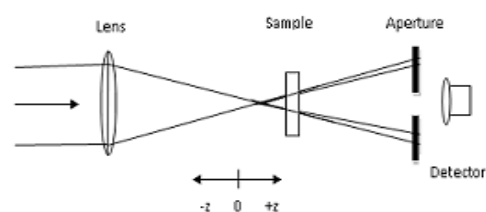


Figure 2. The experimental set-up.

3. RESULTS AND DISCUSSION

Absorption and refraction changes have been studied with Z-scan technique by using open-aperture

(OA) and close-aperture (CA) configurations. Peak and valley orientation in Figure 3(a) confirms the presence of negative nonlinearity ($n_2 < 0$) which shows self defocusing of laser radiation in Ge/As₂S₃ film and As₂S₃ thin film. The nonlinear refractive index of films has been calculated using the relation [7].

$$n_2 = \frac{|\Delta\Phi_0|}{kL_{eff}I_0}$$

k is the wave number, $L_{eff} = (\frac{1-e^{-\alpha L}}{\alpha})$ is the effective thickness, I_0 is the intensity at focus, α is the linear absorption coefficient, L is the sample thickness and $|\Delta\Phi_0|$ the on-axis nonlinear phase shift [8].

$$|\Delta\Phi_0| = \frac{\Delta T_{p-v}}{0.404(1-S)^{0.25}}$$

ΔT_{p-v} is transmittance difference between the peak and valley in the closed aperture configuration. The estimated magnitudes of n_2 are $7.2 \times 10^{-18} \text{ cm}^2/\text{W}$ and $2.1 \times 10^{-17} \text{ cm}^2/\text{W}$ for As₂S₃ thin film and Ge/As₂S₃ film respectively, that shows that Ge/As₂S₃ thin film has higher nonlinearity. Open aperture curves in Figure 3(b) shows the saturable absorption in both films. Nonlinear absorption coefficient has been calculated using

$$\beta = \frac{2\sqrt{2}\Delta T}{I_0 L_{eff}}$$

Here ΔT is transmittance difference between base line and peak in the open aperture scheme. For As₂S₃ thin film and Ge/As₂S₃ film, the calculated value of β is 3.0×10^{-9} and $7.8 \times 10^{-9} \text{ cm}^2/\text{W}$. The high value of nonlinearity is due to electrorestriction in which the sample tends to compress by the applied field inducing nonlinear coupling further resulting in stimulated brillouin scattering [9]. Hence, the irradiation of Ge ion supports nonlinearity.

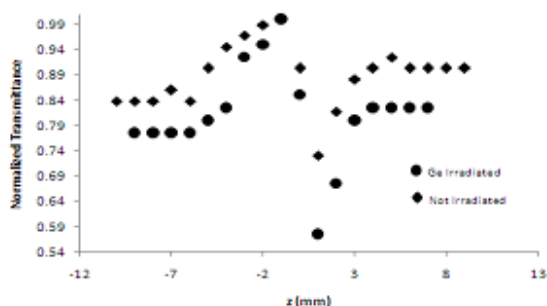


Figure 3. (a) closed aperture

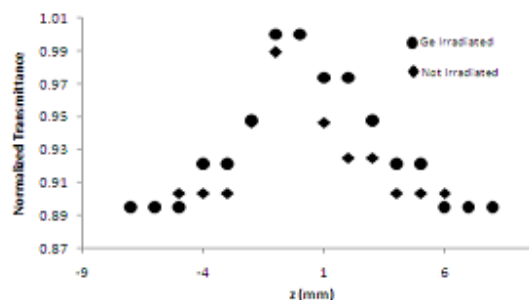


Figure 3. (b) open aperture

4. CONCLUSION

Irradiation of Ge ion induces structural changes in As₂S₃ film and thereby makes it more absorbing. The observed strong third order nonlinearity due to electrorestriction which further results in stimulated brillouin scattering ensures it as a promising nonlinear material for optical device applications.

ACKNOWLEDGEMENT

Financial support from DST-FIST, UGC and UGC-SAP is gratefully acknowledged.

REFERENCES

- [1] Keiji Tanaka, Koichi Shimakawa, "Amorphous chalcogenide semiconductors and related material", Springer Science, New York, USA, 2011.
- [2] R. A. Ganeev, A I Ryasnyansky, T Usmanov, "Effect of nonlinear refraction and two-photon absorption on the optical limiting in amorphous chalcogenide films" *Phys. Solid State+* **45**, 207 (2003).
- [3] Mahender Singh, K.L. Bhatia, Nawal Kishore, R.S. Kundu, D.Kanjilal, "High energy ion implantation induced electrical effects in bulk amorphous As₂Se₃", *Nuclear Instruments and Methods In Physics Research B* **140** 349 (1998).
- [4] P. Sharma, "Study of Transport properties of Ni Ion irradiated Ge₂₀Se₇₄Bi₆ for Different Ion fluences", *Journal of Optoelectronics and Advanced materials* **9** 1988 (2007).
- [5] T. Tsvetkoya, B. Amov, E. Vateva, V. Averyanov, "Ion Implantation Induced Modification of Vitreous Chalcogenides", *Phys. Status Solidi A* **119** 107 (1990).
- [6] Mansoor Sheik-Bahae, Ali A. Said, Tai-Huei Wei, David J. Hagan and E. W. Van Stryland, "Sensitive measurement of optical nonlinearity using a single beam", *IEEE J. Quantum Electron.* **26** 760 (1990).
- [7] R.K. Rekha, A. Ramalingam, "Optical Nonlinear Properties and Optical Limiting Effect of Metanil Yellow", *American Journal of Engineering and Applied Sciences* **2** 285 (2009).
- [8] Tadanori Hashimoto, Tsuyoshi Yamamoto,

Tomohiro Kato, Hiroyuki Nasu, and Kanichi Kamiya, "Z-Scan Analysis for Pbo-Containing Glass with Large Optical Nonlinearity" *Journal of Applied Physics* **90** 533 (2001).

- [9] A. Zakery, S.R. Elliott, "Optical Nonlinearity in Chalcogenide Glasses and Their Applications" Springer.

Spectroscopic Properties of Nd³⁺ in Novel Heavy Metal Based Zinc Silicate Glasses

Inder Pal^{a*}, Ashish Agarwal^a, Sujata Sanghi^a, Sanjay^a, Mahender Prasad Aggarwal^b, Sunil Bhardwaj^c

^aDepartment of Applied Physics, Guru Jambheshwar University of Science & Technology, Hisar-125001, Haryana, India

^bDepartment of Physics, Guru Nanak Khalsa College, Yamunanagar-135001, Haryana, India

^cDepartment of Physics, Deenbandhu Chhotu Ram University of Science & Technology, Murthal, Sonapat, Haryana, India

*Email: ip_gjust@yahoo.com

Abstract: The absorption and fluorescence properties of Nd³⁺ ions are investigated as a function of Bi₂O₃ content. The intensity parameters Ω_2 , Ω_4 and Ω_6 are determined from absorption spectra. The variations of Ω_2 with Bi₂O₃ content have been attributed to change in the asymmetry of the ligand field at the rare earth ions site and to the change in the rare earth-oxygen (RE-O) covalency, whereas the variation of Ω_6 is found to be strongly dependent on nephelauxetic effect. The spontaneous probability (A_{rad}) and branching ratio (β_r) are determined using intensity parameters. The emission cross-sections for ${}^4F_{3/2} \rightarrow {}^4I_{11/2}$ transition decrease from 15.19×10^{-20} to 9.27×10^{-20} cm² as Bi₂O₃ decrease from 69.5 to 49.5 mol%. Therefore, Nd³⁺ doped zinc bismuth silicate glass is good candidate for development of photonic devices.

1. INTRODUCTION

In last few years, optical and spectroscopic properties of various trivalent lanthanides have been investigated in various host materials for optical devices. Such as, up-conversion fluorescence, high density optical storage, amplifiers, optical fiber, electro-luminescent devices, memory devices and flat panel display, etc.. Among many trivalent lanthanides, researches on Nd³⁺-doped glasses have been performed because Nd³⁺-doped fiber has attracted much interest for optical amplifier at the region around 1325 nm with rapid development of telecommunication as well as at around 1050 nm for high power laser applications [1].

In, general the optical and spectroscopic properties are strongly dependent on host materials. Many potential host materials for rare earth ions have been developed. Among them, heavy metal doped glasses shows high refractive index, high transmission for infrared radiation, high chemical stability and low phonon energy as compared to borate, phosphate and silicate glasses [2]. It was also found that with a heavy metal the glass, a relatively higher degree of line broadening and smoother line shape can be obtained. Those advantages can represent one of the best potential host materials for several rare earth dopants for laser applications. Typically, heavy metal based glasses have been used for non-linear optics such as switching. The emission quantum efficiency strongly depends on the phonon energy of host glass. Thus non-radiative losses to the lattice will be small and fluorescence quantum efficiency will high in heavy metal glasses. The optical and spectroscopic properties based on zinc/cadmium bismuth borate glass doped with Pr³⁺, Sm³⁺ and Er³⁺ were successfully investigated and presented as laser host in our previous work [2-4]. The intensity of the transitions for the rare earth ion can be calculated by

using Judd-Ofelt theory [5-6]. This theory define a set of three intensity parameters Ω_λ ($\lambda = 2, 4, 6$) which are sensitive to the environment of the rare earth ion. These intensity parameters are used to calculate radiative transition probability for spontaneous emission, radiative lifetime of excited states, branching ratio and stimulated emission cross-section in order to optimize the best configuration of ion-host to improve the laser efficiency of specific electronic transitions. The absorption and emission properties of rare earth ions for different glass compositions have been investigated. These radiative spectroscopic parameters are essential for design and development of optical glass materials for devices applications.

2. EXPERIMENTAL

Glasses having composition $20ZnO \cdot xSiO_2 \cdot (79.5-x)Bi_2O_3 \cdot 0.5Nd_2O_3$ ($10 \leq x \leq 30$) (ZSBN) were prepared by using melt quench technique. The 15g batches of analar grade chemicals were melted at 1150°C for 40 min. The melt was stirred frequently for homogeneous mixing of all the constituents. The glass samples were obtained by pouring and quenching the melt in between two stainless steel plates held at room temperature (RT). The amorphous nature of the prepared samples was confirmed by X-ray diffraction spectra. The Brewster angle method using He-Ne laser (632 nm) measured the refractive index of the polished samples. The optical absorption spectra of all the polished samples were recorded at RT in wavelength range 300-3200 nm using a spectrophotometer (Varian-Carry 5000). Emission spectra were recorded using a spectrofluorometer (Jobin Yvon Fluorolog-3-II) at an excitation wavelength of 610 nm.

3. RESULTS AND DISCUSSION

Fig. 1 shows the absorption spectra of ZSBN1

($x = 10$) glass exhibits different transitions from the ground state: ${}^4I_{9/2} \rightarrow {}^4G_{9/2}$, ${}^4G_{7/2}$, ${}^4G_{5/2} + {}^2G_{7/2}$, ${}^4F_{9/2}$, ${}^4S_{3/2} + {}^4F_{7/2}$, ${}^4F_{5/2} + {}^2H_{9/2}$ and ${}^4F_{3/2}$. The experimental oscillator strength (f_{expt}) for absorption bands (Fig. 1) are determined with the known values of the Nd^{3+} ions concentration, sample thickness, peak position and peak area for all the samples under study. The Judd-Ofelt intensity parameters Ω_λ ($\lambda = 2, 4, 6$) have been determined by using the experimental oscillator strengths and least square fitting. The values of f_{expt} , f_{cal} , refractive index and intensity parameters are listed in Table 1.

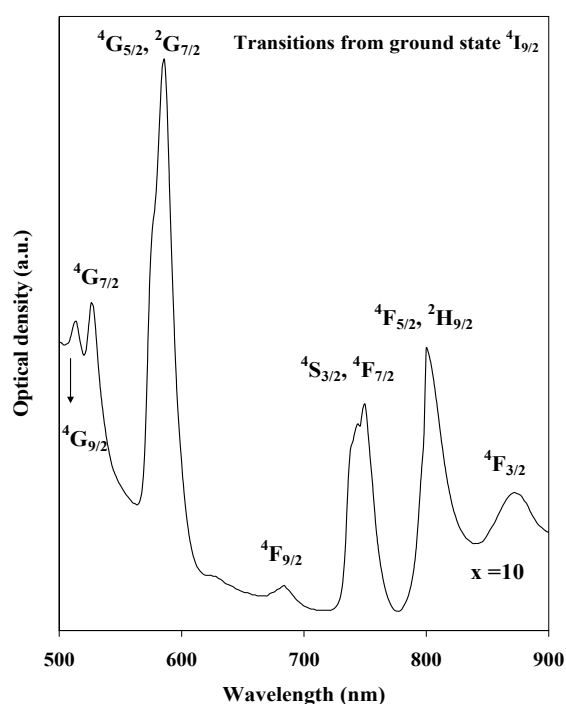


Fig. 1 Optical absorption spectra of ZSBN1 glass.

TABLE 1. Oscillator strength of some transition from the ground level ${}^4I_{9/2}$ to the indicated levels for Nd^{3+} doped zinc bismuth silicate glasses, refractive index and J-O intensity parameters.

Transition From ${}^4I_{9/2}$	λ (nm)	Oscillator strength (10^{-6})					
		X=10		X=20		X=30	
		f_{expt}	f_{cal}	f_{expt}	f_{cal}	f_{expt}	f_{cal}
${}^4F_{3/2}$	870	3.45	3.39	2.95	2.35	2.82	2.50
${}^4F_{5/2}, {}^2H_{9/2}$	800	2.62	2.51	2.37	2.43	2.27	2.35
${}^4S_{3/2}, {}^4F_{7/2}$	750	2.92	3.43	2.76	3.20	2.55	2.97
${}^4F_{9/2}$	682	0.77	0.72	----	----	----	----
${}^4G_{5/2}, {}^2G_{7/2}$	586	5.07	5.04	5.02	4.98	4.94	4.89
${}^4G_{7/2}$	526	2.47	2.95	1.94	2.92	1.48	2.25
${}^4G_{9/2}$	514	1.31	1.39	----	----	----	----
n		2.23		2.18		2.15	
Ω_2 (10^{-20}cm^2)		1.40		0.92		0.64	
Ω_4 (10^{-20}cm^2)		4.29		3.47		2.88	
Ω_6 (10^{-20}cm^2)		3.61		3.32		2.18	

The absorption spectra of all the samples were

observed in similar shape for all the glasses. This implies that the rare earth ions experiences similar environment in all the samples. The position and shape of the some of electric dipole transitions of rare earth (RE) ions are very sensitive to the environment. These transitions are called “hypersensitive transitions” and can be employed for finding out the covalency of the RE-O bond. The shift in the peak wavelength of a hypersensitive transition observed when rare earth ions is doped in the host glass because of the “nephelauxetic effect” [3]. This happens when the electronic orbitals within the $4f$ configuration are deformed in the presence of host ligand field. With the increase in the overlap of the oxygen orbitals and $4f$ orbitals, the energy level structure of the Nd^{3+} ion contracts, leading to the wavelength shift [7].

For Nd^{3+} ion the transition ${}^4I_{9/2} \rightarrow {}^4G_{5/2} + {}^2G_{7/2}$ is more intense than other transitions, and it also satisfies the selection rules of hypersensitive transition such as $J \leq 2$; $\Delta L \leq 2$ and $\Delta S \leq 0$. The peak wavelength of the hypersensitive transition of Nd^{3+} ion shift from 586 nm to 590 nm, with Bi_2O_3 content in the host glass and this red shift is indicative of the covalent nature of the Nd-O bond. The intensity (oscillator strength) of hypersensitive transitions shows a minimum value around 30 mol% of SiO_2 for ZSBN glasses indicating a low asymmetry of the crystal field at the rare earth ion site at this composition. In present glasses, it has been observed that $\Omega_4 > \Omega_6 > \Omega_2$. The monotonic decrease of Ω_2 with Bi_2O_3 content and hence the asymmetry of crystal field at the rare earth site with decrease in Bi_2O_3 content for Nd^{3+} ions indicate that the rare earth ion in zinc bismuth silicate glasses might be surrounded by bismuthate groups that effect the symmetry of ligand field at the rare earth ions site.

The parameter Ω_6 in glasses is inversely proportional to the covalence of the Nd-O bond whereas the Ω_4 is related to the rigidity of the host. To monitor the covalency of the Nd-O bond in the glass matrix, the variation of the spectral profiles of the transitions ${}^4I_{9/2} \rightarrow {}^4G_{5/2} + {}^2G_{7/2}$ (HST) of Nd^{3+} with a glass composition as also investigated. In this transition, two peaks are distinguished by Stark splitting and relative intensity ratio between the peaks varied with the glass composition. In the present glasses, the Stark splitting of the transition ${}^4I_{9/2} \rightarrow {}^4G_{5/2} + {}^2G_{7/2}$ is not well resolved.

The fluorescence spectra of Nd^{3+} ZSBN1 glass is shown in Fig. 2 at excitation wavelength of 610 nm. From the spectra two emission lines are found, which are due to radiative transition of ${}^4F_{3/2} \rightarrow {}^4I_{9/2}$ and ${}^4I_{11/2}$ of Nd^{3+} ions. The fluorescence spectrum has been used to derive radiative properties like radiative transition probability (A_{rad}), branching ratio (β_r), radiative lifetime (τ_r) and stimulated emission cross-section (σ), etc. and these parameters are presented in Table 2.

It is also noted that the intensity of fluorescent bands increase with decrease in Bi_2O_3 content in the host glass composition. A large value of stimulated emission cross-section is related with low threshold and high gain amplifier applications. The stimulated emission cross-section can be calculated from the fluorescence spectra and also listed in Table 2.

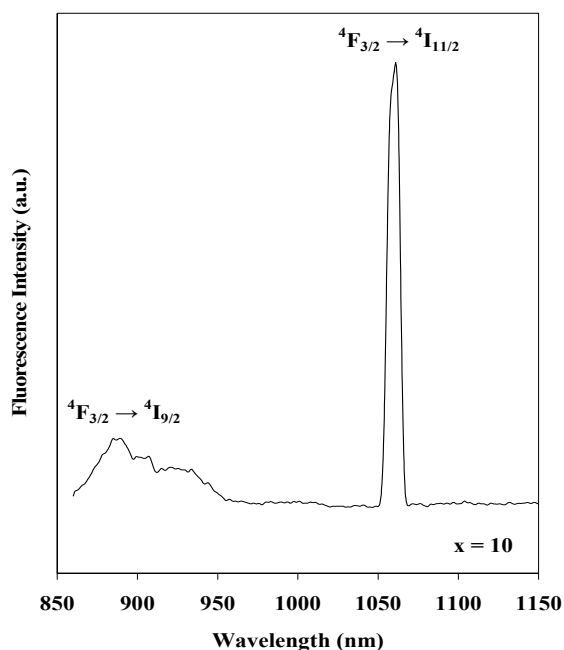


Fig. 2 Fluorescence spectra of ZSBN1 glass.

As shown in Table 2, the value of σ is dependent on composition of glasses. Taking into account the relation between the radiative lifetime τ_r and refractive index the σ increase with increase in refractive index of the host as $\sigma \sim (n^2 + 2)^2/n$ for electric dipole transition and as $\sigma \sim n$ for the magnetic dipole transition.

TABLE 2. Radiative transition probability (A_{rad}), radiative lifetime (τ_r), branching ratio (β_r), and stimulated emission cross-section (σ) of Nd^{3+} doped ZSBN glasses.

	$A_{\text{rad}} (\text{s}^{-1})$	$\tau_r (\text{ms})$	$\beta_r (\%)$	$\sigma (10^{-20} \text{ cm}^2)$
ZSBN1				
${}^4\text{F}_{3/2} \rightarrow {}^4\text{I}_{9/2}$	854	0.532	0.454	15.19
${}^4\text{F}_{3/2} \rightarrow {}^4\text{I}_{11/2}$	1127		0.546	9.01
ZSBN2				
${}^4\text{F}_{3/2} \rightarrow {}^4\text{I}_{9/2}$	722	0.662	0.478	14.19
${}^4\text{F}_{3/2} \rightarrow {}^4\text{I}_{11/2}$	789		0.522	7.64
ZSBN3				
${}^4\text{F}_{3/2} \rightarrow {}^4\text{I}_{9/2}$	482	0.928	0.447	9.27
${}^4\text{F}_{3/2} \rightarrow {}^4\text{I}_{11/2}$	595		0.552	6.27
$A_T \rightarrow$	ZSBN1	ZSBN2	ZSBN3	
	1981	1511	1077	

It is observed that σ is directly proportional to the total spontaneous emission probability and inversely proportional to the effective bandwidth of the

emission transition. It has been observed by Becker [8] that the refractive index increases with increase in Bi_2O_3 content. In the present study, the decrease in the value of 'n' (Table 1) and A_T (Table 2) provide us decreasing value of σ with decrease in Bi_2O_3 content in the host glass composition. The branching ratios β_r evaluated for each transitions of Nd^{3+} ions are shown in Fig. 3.

The radiative transition probabilities in the present ZSBN glasses are of the order of those reported for Er:Yb:GdCa₄O(BO₃)₃ [9] and ZBLAN [10] glasses and therefore these ZSBN glasses can be also be utilized as active laser host materials.

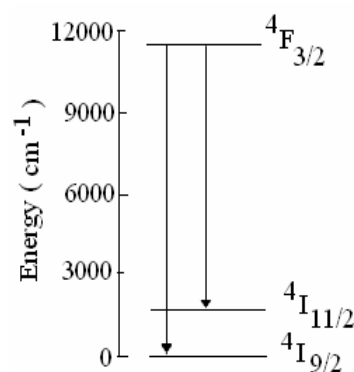


Fig. 3 Lasing transitions of Nd^{3+} in zinc bismuth silicate glasses

4. CONCLUSIONS

Optical properties, absorption and emission spectra of neodymium doped zinc bismuth silicate glasses have been investigated. The refractive index of the glasses decrease from 2.23 to 2.15 with decrease in Bi_2O_3 : SiO_2 ratio. The shift of the hypersensitive bands of the Nd^{3+} ions (${}^4\text{I}_{9/2} \rightarrow {}^4\text{G}_{5/2} + {}^2\text{G}_{7/2}$; 584 nm) shows that the covalency of the RE-O bond decrease with decreases in Bi_2O_3 content.

From absorption spectra by using Judd-Ofelt theory, the intensity parameters have been calculated. These parameters have been used to calculate transitions probabilities, radiative lifetime, branching ratio and stimulated emission cross-section by applying the usual formulas. The effect of composition in neodymium doped zinc silicate glasses on spectroscopic properties of the both the transitions ${}^4\text{F}_{3/2} \rightarrow {}^4\text{I}_{11/2}$ and ${}^4\text{I}_{9/2}$, including the stimulated emission cross-section were investigated. Stimulated emission cross-section is maximum for the investigated composition range when the Bi_2O_3 content is 69.5 mol%. The spectroscopic properties of neodymium doped zinc bismuth silicate glasses are better than other silicate glasses and some of the spectroscopic parameters are comparable to the frequently used laser glasses. This indicates that the zinc bismuth silicate glasses can be act as potential laser host materials.

5. REFERENCES

- [1] E. Pacoraro, J. A. Sampaio, L. A. O. Nunes, S. Gama and M. L. Baesso, "Spectroscopic Properties of Water free Nd₂O₃ Doped Low Silica Calcium Aluminosilicate Glass", *J. Non-Cryst. Solids*, **277**, 73 (2000).
- [2] I. Pal, A. Agarwal, S. Sanghi and M. P. Aggarwal, "Structural, Absorption and Fluorescence Spectral Analysis of Pr³⁺ ions Doped Zinc Bismuth Borate Glasses", *J. Alloys Compds.*, **509**, 7625 (2011).
- [3] A. Agarwal, I. Pal, S. Sanghi and M. P. Aggarwal, "Judd-Ofelt Parameters and Radiative Properties of Sm³⁺ ions Doped Zinc Bismuth Borate Glasses", *Opt. Mater.*, **32**, 399 (2009).
- [4] S. Sanghi, I. Pal, A. Agarwal, and M. P. Aggarwal, "Effect of Bi₂O₃ on Spectroscopic and Structural Properties of Er³⁺ Doped Cadmium Bismuth Borate Glasses", *Spectro. Chema. Acta A*, **83**, 94 (2011).
- [5] B. R. Judd, "Optical Absorption Intensities of Rare-Earth Ions" *Phy. Rev.*, **127**, 750 (1962).
- [6] J. S. Ofelt, "Intensities of Crystal Spectra of Rare-Earth Ions", *J. Chem. Phys.*, **37**, 511 (1962).
- [7] B. Karthikeyan, R. Philip and S. Mohan, "Optical and Non-linear Optical Properties of Nd³⁺-doped Heavy Metal Borate Glasses", *Optics Commun.*, **246**, 153 (2005).
- [8] P. Becker, "Thermal and Optical Properties of Glasses of the System Bi₂O₃-B₂O₃", *Cryst. Res. Technol.* **1**, 74 (2003).
- [9] H. R. Xia, P. Zhao, X. F. Cheng, W. L. Liu, S. J. Zhang, Z. X. Cheng, and Z. H. Yang, "Raman and absorption spectra and thermal conductance of Er:Yb:GdCa₄O(BO₃)₃ crystals", *J. Appl. Phys.* **95**, 5383 (2004).
- [10] X. Zou and T. Izumitani, "Spectroscopic properties and mechanisms of excited state absorption and energy transfer upconversion for Er³⁺-doped glasses", *J. Non-Cryst. Solids*, **162**, 68 (1993).

Optical Absorption and Fluorescence of Er³⁺ Doped Lead Bismuth Silicate Glasses

S. Bhardwaj^a, R. Shukla^a, S. Sanghi^b, A. Agarwal^b, Inder Pal^b

^aDepartment of Physics, Deenbandhu Chhotu Ram University of Science and Technology,
Murthal, Sonapat, Haryana, India

^bDepartment of Applied Physics, Guru Jambheshwar University of Science and Technology,
Hisar-125001, Haryana, India
Email sunilbhardwaj.phy@gmail.com

Abstract: Glasses with composition 20PbO.(79.5-x)Bi₂O₃.xSiO₂ (x = 10, 30, 50) containing 0.5mol% of Er³⁺ ions were prepared by melt-quench technique. Optical absorption and fluorescence spectra were recorded at room temperature for all glass samples. Based on the Judd-Ofelt theory, spectroscopic properties of Er³⁺ ions are discussed by changing the host glass compositions. The intensity parameters Ω_2 , Ω_4 , and Ω_6 are determined by applying least square analysis method. The variation of Ω_2 with Bi₂O₃ content has been attributed to changes in the rare earth oxygen covalency. Using these intensity parameters various radiative properties like spontaneous emission probability, branching ratio, radiative life time and stimulated emission cross-section of various emission lines have been evaluated. The amorphous nature of the glass was confirmed by X-ray diffraction studies, and the structural investigations of these glasses were carried out by recording the IR spectra.

1. INTRODUCTION

Over the past several decades, optical and spectroscopic properties of various trivalent lanthanides have been extensively investigated for various host materials to apply optical devices. After showing laser action of Er³⁺ by Snitzer and Woodcock in 1965 [1] considerable efforts are made on the research of Er³⁺ ions doped oxide glasses. Due to their rich energy level structure, the trivalent erbium doped glasses have been used as media of the up-conversion laser, wave-guide laser, and erbium-doped fiber amplifier (EDFA) which is one of the key elements used in the wavelength-division-multiplexing (WDM) network for optical communication. Recently, much attention has been given to the research of the Er³⁺ ions doped glasses [2-4] due to the 1.5 μ m emission from the ⁴I_{13/2}→⁴I_{15/2} transition is eye safe and located in the optical third communication window where the losses are minimum.

In general, the optical and spectroscopic properties are strongly dependent on host materials. Many potential host materials for rare earth ions have been developed. It was found that the oxide glasses have small absorption coefficient, high chemical and thermal durability, therefore they are suitable material for technology applications. Silicate glasses are chemically durable, thermally stable and optically transparent at the excitation and lasing wavelength. Bismuth oxide glasses are more suitable due to its high refractive index, low phonon energy and good chemical suitability. The efforts to improve quantum efficiency of the luminescence bands have paid attention to heavy metal host materials. Heavy metal lead (Pb) has been chosen as it has large glass forming

region, high refractive index, good physical and chemical stability and large window transmission. The Judd-Ofelt theory is usually adopted to calculate, by assuming certain approximation, transitions probability from the data of absorption cross-section of several f-f transitions. According to this theory, the strength of an f-f transitions may be expressed by the sum of the products of three intensities parameters Ω_λ ($\lambda = 2, 4, 6$) times the squared matrix elements $U^{(t)}$ between the initial J-states and the terminal J* state. Once the phenomenological parameters Ω_λ have been calculated, it is possible to derive the strength of any absorption or emission transmission, as well as the stimulated cross-section, the fluorescence branching ratio from level J to J*, and the radiative life time of an excited level. Such spectral studies give valuable information about the structure and bonding in glass and radiative and non radiative properties of rare earth ions doped in glass matrix. This information is essentially required while developing new optical devices.

The purpose of this paper is to introduce the upgraded lasing material glasses by including the heavy metal with bismuth and silicate glasses. In the present work, glasses with compositions 20PbO.(79.5-x)Bi₂O₃.xSiO₂ (x = 10, 30, 50) containing 0.5mol% of Er³⁺ ions by changing the host glass compositions have been systematically investigated on spectroscopic properties, intensity parameters, emission cross-section, radiative life time, and branching ratio are determined from the absorption and emission spectra using Judd-Ofelt parameter theory. We have also discussed the role of Bi₂O₃ on optical absorption and on the spectroscopic properties of the ⁴I_{13/2}→⁴I_{15/2} transition.

2. EXPERIMENT

Glasses with composition 20PbO.(79.5-x)Bi₂O₃.xSiO₂ (x = 10, 30, 50) containing 0.5mol% of Er³⁺ ions were prepared by melt-quench technique. The well mixed raw materials (batches of 15gm) were melted for 40 minutes in porcelain crucibles at 1100^oC. The crucibles were shaken frequently for homogeneous mixing of all the constituents. The molten was then poured between two stainless steel plates. The melt was annealed to minimize the strain and then allowed to cool slowly to room temperature. The sample was polished carefully to meet the optical requirements. The density of all the samples was measured by using Archimedes principle (using xylene as a reference liquid). The refractive index of the polished samples was measured by the Brewster angle polarization method using He-Ne laser (632nm). The formation of glass was confirmed by X-ray diffraction method. The optical absorption spectra were recorded at room temperature on a spectrophotometer in the range 300-3200nm. The emission spectra were recorded using a Spectrofluorometer (Jobin Yvon Fluorolog-3-11).

3. JUDD-OFELT THEORY

Judd-Ofelt [5-6] theory has been used to investigate radiative nature of trivalent rare earth ions in a variety of laser host materials. The intensity parameter, radiative life time, and branching ratio are calculated with refractive index using Judd-Ofelt analysis. The experimental oscillator strength was calculated from the absorption spectra by using the equation [7].

$$f_{meas.} = 4.32 \times 10^{-9} \int \epsilon(\nu) d\nu$$

where $\epsilon(\nu)$ is the molar absorptivity (cm²) of absorption band at energy ν (cm⁻¹).The experimental oscillator strengths were used to obtained values of the intensity parameters ($\lambda = 2, 4, 6$) following the standard least square fitting method. The validity of the fitting is examined by comparing the experimental and theoretical oscillator strengths. The Judd-Ofelt intensity parameters (Ω_λ) are phenomenological characteristics for the influence of surrounding environment of the rare earth ions as they contain implicitly the crystal field terms and the radial wave function. According to the Judd-Ofelt theory the oscillator strength for an electronic transition from the initial manifold (SL, J) to the final manifold (S'L', J') is given by the expression.

$$f_{cal} = \frac{8\pi^2 mc}{3h(2j+1)\lambda_p} \left(\frac{(n^2 + 2)^2 S_{ed}}{9n} \right)$$

Where c represents the velocity of light, n represent refractive index, λ_p represent the absorption peak wavelength, e and m the electron charge and mass, S_{ed}

represents the line strengths for the induced electric dipole transition, which is given by:

$$S_{ed} = \sum_{t=2,4,6} \Omega_t \left\langle \left\langle SLJ \left\| U^t \right\| S'L'J' \right\rangle \right\rangle^2$$

The spontaneous emission probability for the radiative decay, A_{rad} (sec-1), from the initial manifold (SLJ) to the final manifold (S'L'J') is given by the expression.

$$A_{rad} = \frac{64\pi^4 e^2 \bar{\nu}^3 n(n^2 + 2)^2}{3h(2j + 1)9} \times$$

$$\sum_{\lambda=2,4,6} \left\langle \left\langle (S, L)J \left\| U^{(\lambda)} \right\| (S', L')J' \right\rangle \right\rangle^2$$

Where $U^{(\lambda)}$ ($\lambda=2, 4, 6$) are the matrix elements of unit tensor operators and had been calculated by Carnall et al. [8]. The total probability, A_T , obtained by carrying out the summation of all the transitions to the final state bj' is given by

$$A_T = \sum A_{rad}$$

The fluorescence branching ratio is given by

$$\beta_r = \frac{A_{rad}}{A_T}$$

The radiative life time is represented by

$$\tau_r = \frac{1}{A_T}$$

The induced emission cross-section for each transition could be estimated from the emission spectra by [9].

$$\sigma = \frac{\lambda_p^4 A_{rad}}{8\pi c n^2 \Delta\lambda}$$

Where λ_p is peak wavelength and $\Delta\lambda$ is the full width at half maxima of the fluorescent peak for different transitions obtained from emission spectra.

4. RESULTS AND DISCUSSION

Fig. 1 shows the X-ray diffraction patterns of a glass sample (x=10) and the amorphous nature of the prepared samples is confirmed.

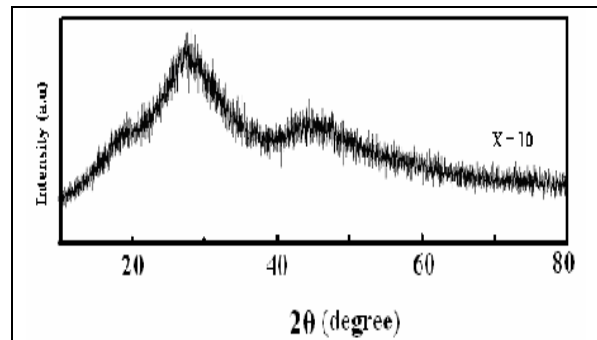


Fig. 1 X-ray diffraction patterns

Fig. 2 shows the optical absorption spectra of lead bismuth silicate glass ($x = 10$). From the figure, it is clear that there are seven peaks at 488, 520, 538, 650, 816, 976 and 1534nm in the spectrum corresponding to absorption from the ground state $^4I_{15/2}$ to the excited states $^4F_{7/2}$, $^2H_{11/2}$, $^4S_{3/2}$, $^4F_{9/2}$, $^4I_{9/2}$, $^4I_{11/2}$, and $^4I_{13/2}$ respectively. The experimental and calculated values of oscillator strength are presented in Table 1. According to the Judd-Ofelt theory [5-6], the effect of the crystal field can be described by three intensity parameters Ω_λ ($\lambda = 2, 4, 6$). These parameters are obtained from the experimental oscillator strengths and the calculated double reduced matrix elements by using least square analysis method.

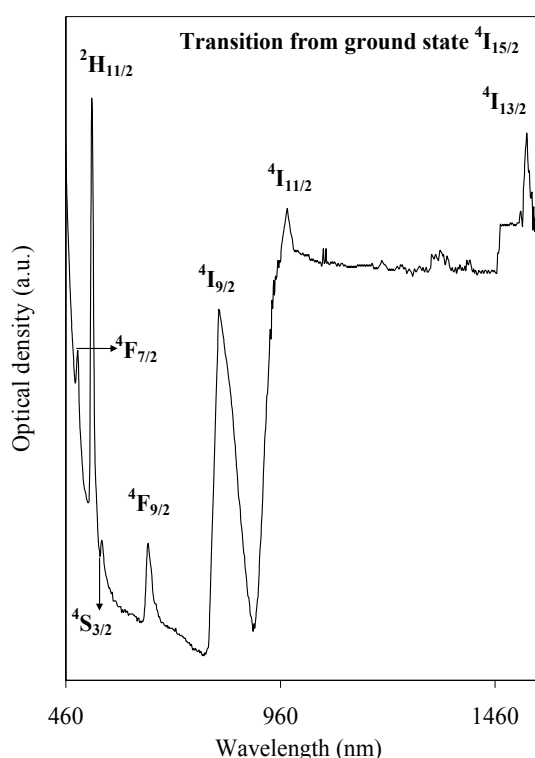


Fig: 2 Optical absorption of PBSE1 glass.

TABLE 1: Oscillator strength for some transition from the indicated levels to the ground level 3H_4 and their root mean square (δ_{RMS}) parameters for $20PbO(79.5-x)Bi_2O_3 \cdot xSiO_2 \cdot 0.5Pr_6O_{11}$ glasses.

Transitions	PBSE1 λ	PBSE1		PBSE2		PBSE3	
		f_{exp}	f_{cal}	f_{exp}	f_{cal}	f_{exp}	f_{cal}
$^4I_{15/2}$							
$^4F_{7/2}$	488	2.72	3.14	1.91	1.81	1.57	0.93
$^2H_{11/2}$	520	2.97	2.52	2.76	2.33	2.15	2.43
$^4S_{3/2}$	538	0.70	1.07	0.46	0.85	1.04	1.16
$^4F_{9/2}$	650	2.37	3.02	1.72	2.25	1.57	1.64
$^4I_{9/2}$	816	0.61	0.54	0.42	0.36	0.68	0.64
$^4I_{11/2}$	976	0.90	0.67	0.79	0.60	0.40	0.53
$^4I_{13/2}$	1534	-----		1.92	1.67	1.08	0.87
δ_{RMS}		0.251		0.182		0.132	

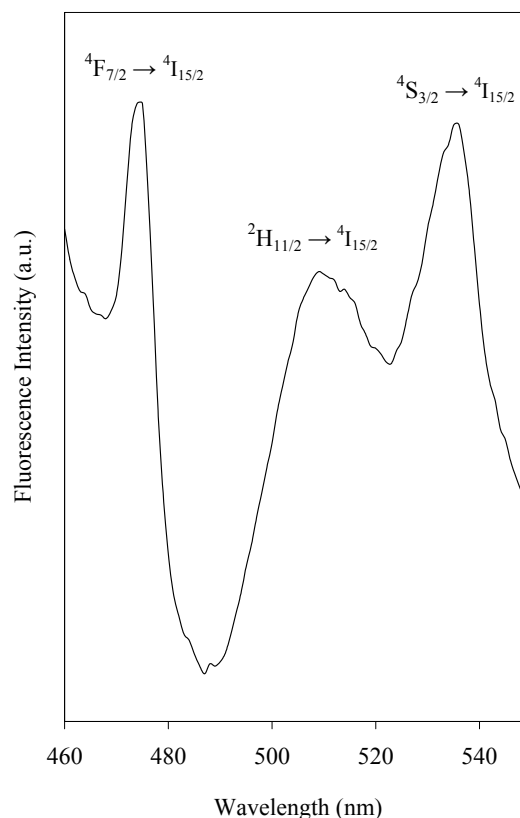


Fig: 3 Fluorescence spectra of PBSE1 glass.

The intensity parameters determined for Er^{3+} ions doped glasses for all the concentration of SiO_2 are listed in Table 2. These intensity parameters reflect the local structure and bonding in the vicinity of rare earth ion to some degree of covalency of the lanthanide-ligand bonds. The variation of Ω_2 with Bi_2O_3 content has been attributed to changes in the asymmetry of the ligand field at the rare earth ion site and to the changes in their rare earth oxygen (RE-O) covalency [10]. Where as the intensity parameters Ω_4 and Ω_6 are related to the rigidity of the host [11]. From the table 2, decrease in the value of Ω_4 and Ω_6 with Bi_2O_3 content in the host glass is observed.

The shift in the hypersensitive band shows that the covalency of the RE-O bond decreases with decrease of Bi_2O_3 content, and it is attributed to the increased interaction between the rare earth ions and the non-bridging oxygen's (NBO's). Therefore the covalency of the rare-earth oxygen decreases with the increase in SiO_2 content in the host glasses. A measure of the accuracy of the fitted values of the Ω_λ parameters are given by δ_{RMS} deviation which is also given in table 1. Fig. 3, shows the emission spectrum of lead bismuth silicate glass ($x = 10$). From the figure, it is clear that there are three peaks at 475, 516, 536 nm that assigned the following emission transitions $^4F_{7/2} \rightarrow ^4I_{15/2}$, $^2H_{11/2} \rightarrow ^4I_{15/2}$, $^4S_{3/2} \rightarrow ^4I_{15/2}$ respectively. It shows that the radiative transition probability decrease with decrease in Bi_2O_3 content in the host glass.

The trend observed in the present study follows the same pattern as reported by I Pal et al. [12] in Er³⁺ ion doped zinc bismuth borate glass. For laser applications, the values of the emission cross-section are of great interest. A large stimulated emission cross-section is benefit for a low threshold and a high gain in laser operation. Therefore, the large stimulated emission cross-section in the present glass is an attractive feature for low-threshold, high gain applications and can be utilized to obtain continuous wave laser action.

The effective bandwidth of the emission spectra is mainly caused by splitting of the levels of transitions and the site to site variation of the ligand field around Er³⁺ ions in the glass that is the inhomogeneous broadening. The slight decrease in effective bandwidth implies that the asymmetry of the ligand field becomes weaker. This result is again in accordance with decrease in the value of Ω_2 with Bi₂O₃ content in the host glass.

TABLE 2: Judd-Ofelt intensity parameters (Ω_2 , Ω_4 , Ω_6) of various Er³⁺ doped glasses.

Glass	$\Omega_2(\times 10^{-20})$	$\Omega_4(\times 10^{-20})$	$\Omega_6(\times 10^{-20})$	Ω_4/Ω_6 (SQF)
PBSE1	1.93	2.57	3.93	0.65
PBSE2	1.35	2.18	2.90	0.75
PBSE3	0.61	1.54	2.32	0.66

TABLE 3: The peak wavelength (λ_p), radiative transition probability (A_{rad}), branching ratio (β_r), stimulated emission cross-section (σ), radiative lifetime (τ_r) of PBSE glass for various transitions.

Transitions	PBSE1	PBSE2	PBSE3
475 nm	$^4F_{7/2} \rightarrow ^4I_{15/2}$	$^4F_{7/2} \rightarrow ^4I_{15/2}$	$^4F_{7/2} \rightarrow ^4I_{15/2}$
516 nm	$^2H_{11/2} \rightarrow ^4I_{15/2}$	$^2H_{11/2} \rightarrow ^4I_{15/2}$	$^2H_{11/2} \rightarrow ^4I_{15/2}$
536 nm	$^4S_{3/2} \rightarrow ^4I_{15/2}$	$^4S_{3/2} \rightarrow ^4I_{15/2}$	$^4S_{3/2} \rightarrow ^4I_{15/2}$
$A_{rad} (s^{-1})$	161, 2709, 5731	354, 2527, 4225	182, 2232, 3020
A_T	8601	7106	5434
β_r (%)	0.018, 0.11 0.66	0.049, 0.108 0.594	0.033, 0.410 0.556
σ ($10^{-20} cm^2$)	1.95 1.41, 0.14,	1.34 0.97, 0.11,	0.92 0.51, 0.08,
τ_r (μs)	116	141	184

From table 3, it is observed that the value of stimulated emission cross-section (σ) decreases with the decrease in Bi₂O₃ content in the host glass.

On comparing the emission intensity of various compositions it is found that on decreasing the concentration of bismuth ions, a decrease in the fluorescence intensity is observed. From the figure 3 two green luminescence bands with maximum around 516 nm and 536 nm are assigned to the $^2H_{11/2} \rightarrow ^4I_{15/2}$

and $^4S_{3/2} \rightarrow ^4I_{15/2}$ transitions respectively. Another emission band is identified as due to $^4F_{7/2} \rightarrow ^4I_{15/2}$ electronic transition. The most intense emission (easily seen by naked eyes) corresponds to the green emission from the $^4S_{3/2}$ level. The good agreement between the results indicates the glassy state of the fiber. Further-more, these emissions are in agreement with previous investigations on erbium-doped glasses [13-15]. From Table 3, it is concluded that the spectroscopic parameters shows variation with Bi₂O₃ content in the host glasses. The high value of stimulated emission cross-section tells about the prepared glass samples are potentials candidates for the lasing host materials.

CONCLUSIONS

The spectroscopic properties of Er³⁺ doped glass has been analyzed on the basis of Judd-Ofelt theory. The Ω_2 parameter shows the covalent nature of the prepared glass and it decreases with the decrease in Bi₂O₃ content in the host glass. The branching ratio for the transition $^4S_{3/2} \rightarrow ^4I_{15/2}$ is 66% therefore the radiative transition probability is high as 5731 s⁻¹ as shown in Table 3. From here it concluded that the prepared glasses are suitable host for the lasing materials. It shows lasing emission in the visible range.

REFERENCES

- [1] E. Snitzer, R. Woodcock, *Appl. Phys. Lett.* **6**, 45 (1965)
- [2] Y. D. Huang, M. Mortier, F. Auzel, *Opt. Mater.* **17**, 501 (2001).
- [3] Y. D. Huang, M. Mortier, F. Auzel, *Opt. Mater.* **15**, 243 (2001).
- [4] H. Lin, E. Y. B. Pun, X. R. Liu, *J. Non-Crystal. Solids.* **283**, 27 (2001).
- [5] B. R. Judd, *Phys. Rev.* **127**, 94 (1962).
- [6] G. S. Ofelt, *J. Chem. Phys.* **37**, 511 (1962)
- [7] W.J. Weber, B.H. Matsinger, V.L. Donan, G.T. Surratt, *J. Chem. Phys.* **57**, 562 (1972).
- [8] W.T. Carnall, P.R. Fields, K. Rajnak, *J. Chem. Phys.* **49**, 4424 (1968).
- [9] A.P. Thorne, Spectrophysics, second ed., Chapman and Hall, London, 1988.
- [10] S. Tanabe, T. Ohagi, N. Soga, T. Hanada, *Phys. Rev. B* **46**, 3305 (1992)
- [11] L.R.P. Kassab, A.de O. Preto, W. Lozano, F.X.de Sa, G.S. Maciel, *J. Non-Cryst. Solids* **43-45**, 3468 (2005)
- [12] S. Sanghi, I. Pal, A. Agarwal and M.P. Agarwal, *Spectra. Chemica. Acta Part A* **83**, 94, (2011).
- [13] R. Balda, A. J.G. Adeva, J. Fernandez and J. M. Fdez-Navarro, *J. Opt. Soc. Am.* **B 21**, 744 (2004)
- [14] Z. Pan, S. H. Morgan, A. Loper, V. King, B. H. Long and W. E. Collins, *J. Appl. Phys.*, **77** (9), 4688, (1995)
- [15] Z. Pan, S. H. Morgan, K. Dyer and A. Ueda, *J. Appl. Phys.*, **79** (12), 8906, (1996).

EFFECT OF OXYGEN FLOW RATE ON STRUCTURAL AND OPTICAL PROPERTIES OF Ta₂O₅ THIN FILMS PREPARED BY DC SPUTTERING METHOD

Kanta Rathee^{1,a}, Mukesh Kumar^{2,b}, B P Malik^{3,c}

¹Department of Applied Sciences, DCRUST, Murthal (Sonapat), India

²Electronic Science Department, Kurukshetra University, Kurukshetra, India.

³Department of Applied Sciences, DCRUST, Murthal (Sonapat), India

^arathee111@yahoo.co.in, ^bkumarmukesh@gmail.com, ^cdrbpmalik@rediffmail.com

ABSTRACT : We have studied and characterized the process of deposition of tantalum oxide thin film. For deposition of tantalum pentoxide thin film we have used the DC magnetron sputtering technique. Oxygen flow rate has been varied to observe the effect on crystallinity, deposition rate and refractive index of the deposited film. I-V characteristics have been reported using I-V set. The value of leakage current ranges from $I = (0 \text{ to } 2.33 \times 10^{-5} \text{ A})$ with corresponding values of electric field density $E = (0 \text{ to } 5 \text{ MV/cm}^2)$. A wide energy band gap has been obtained (4.4 eV) using the transmittance of the deposited film.

1. INTRODUCTION

MOS fabrication technology has been largely dominated by the scaling of the device feature size. However as the thickness of traditional dielectric SiO₂ is reduced, gate leakage current through the dielectric layer becomes a major problem. As a result high K materials, such as HfO₂, TaO₂ and ErO₃ etc are under consideration as a replacement for currently dominant SiO₂. In the present work Ta₂O₅ has been selected for detailed study due to its potential properties, such as a wide band spectral range.

Tantalum oxide thin film can be grown by a large variety of chemical vapour and physical vapour deposition technique as reported in literature. The various techniques are anodization [9], ion plating [1,10], magnetron sputtering [2,7], laser ablation [11,12], atomic layer deposition, plasma enhanced CVD [3,4,14], electron beam evaporation, metalorganic solution deposition technique [15]. Out of these DC magnetron sputtering has been employed in the present work, as it involves low deposition temperature and better adhesion [16,17]. In this paper the material properties of Tantalum oxide thin film deposited by DC magnetron sputtering has been investigated using I-V set model (Keithley, 595) and effect of O₂ flow rate on deposition rate has been studied using uv visible spectrophotometer.

2. EXPERIMENT

For depositing Tantalum oxide thin film DC sputtering technique has been used. Pure tantalum [99.99%] has been used as a sputtering target. Argon gas [99.99 pure] and oxygen [99.995 pure] were used as sputtering ambients. The composition of oxygen was kept in the range of [2-15% to 20%]. The silicon substrate with resistivity of 4-11 Ω-cm was p-type with [100] orientation. Firstly the silicon wafer was cleaned using standard RCA technique to remove the surface oxide layers. Then tantalum pentoxide thin film (50 nm) was deposited by sputtering with pressure of chamber maintained at 100 millitorr, and a target distance of 75 mm and sputtering power of 140 W. The flow rate of argon was maintained at 60 sccm and that of oxygen was at 10 sccm. The thickness of the deposited film was determined by stylus profiler (Ambios Technology USA). Crystallinities of the thin film were examined using X-Ray diffractometer. Transmittance of the thin film was measured by ultraviolet, visible spectro photometer at different flow rates of oxygen. For electrical measurements circular aluminum dots were deposited on the surface of Ta₂O₅ by thermal evaporation method. Surface morphology of the deposited film has been studied using Atomic Force microscopy. I-V measurements of the mos capacitor

(al/ Ta₂O₅/Si) were characterised using I-V set model(keithly,595).

3. RESULT AND DISCUSSION

3.1 Structural Analysis

Fig.-1 shows the XRD spectra of tantalum oxide thin film deposited on silicon wafer. The diffraction pattern of the film has been studied at various flow rates of oxygen keeping the argon flow rate constant. The XRD spectra of tantalum oxide thin film did not reveal from tantalum oxide lattice planes at oxygen flow rate of 5sccm indicating the amorphous nature of deposited film. With increase in oxygen flow rate [i.e at flow rates of 7sccm and 10sccm] the crystallinity of the film is improved as is evident from the observed peaks in XRD pattern, but the crystalline nature reduces with further increase in oxygen flow rate (i.e 12sccm). Thus maximum crystalline nature of the film is observed at moderate rate of flow of oxygen.

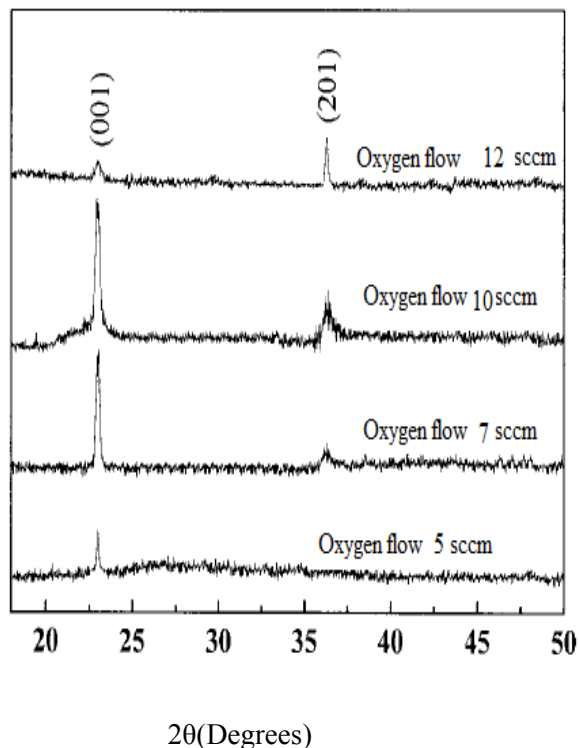


Fig.-1 : XRD patterns of Ta₂O₅ at different flow rate of oxygen.

3.2 Deposition Rate

The deposition rate per minute of the thin film as a function of oxygen flow rate has been studied. With the increase in oxygen flow rate, the probability of the reaction b/w tantalum and oxygen increases forming oxide and sputtering with tantalum oxide is difficult then with tantalum metal and hence the deposition rate decreases , which is clearly indicated in the graph.(Fig-2)

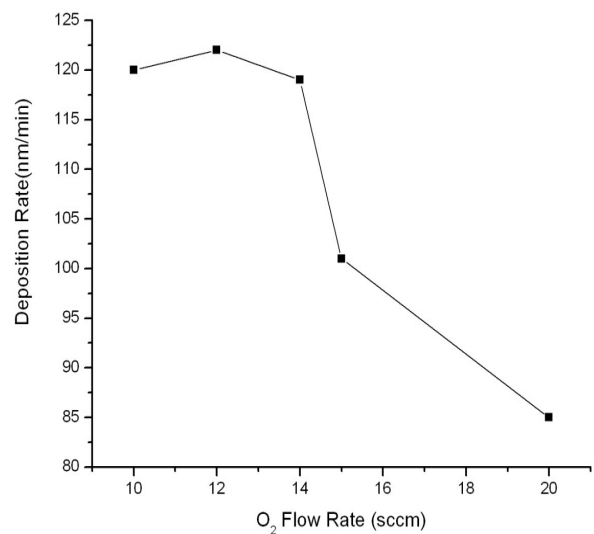


Fig.-2 : Graph between average deposition rate and O₂ Flow rate at constant Argon flow and pressure

3.4 AFM(Atomic Force Microscopy)

In order to study the surface properties of tantalum oxide thin films AFM was performed (fig.-3) .An AFM is an exceptional tool for measuring grain structure on surfaces. This is because AFM has great contrast on flat samples . The analysis of grains is advantageous because the images have three dimensional topography and the grain boundaries can be easily identified .

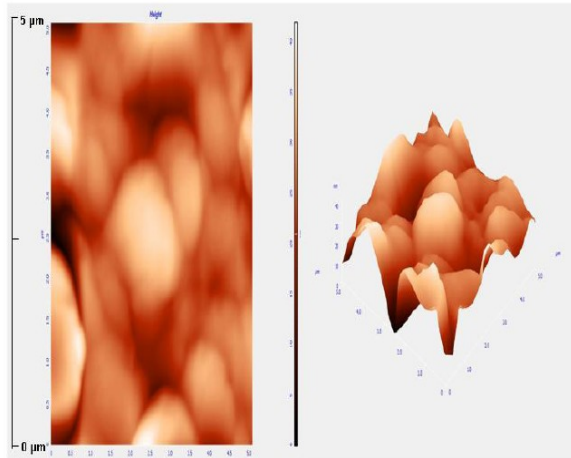


Fig.-3 : AFM Images of Ta₂O₅ film

3.4. Optical Characteristics (Transmittance)

The sample has been subjected to the ultra violet radiation using UV visible spectrophotometer to measure the transmittance of the deposited film at different wavelengths keeping the oxygen flow rate 5% and 10% . Transmittance is found to be almost independent of oxygen flow rate . The energy band gap of the deposited film has also been calculated from this graph using the relation $E = hc/\lambda$ and the value is found to be 4.4eV .

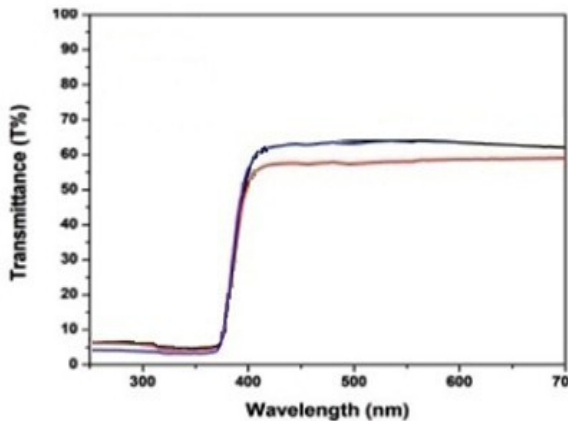


Fig.-4: Graph between Transmittance and wavelength at different flow rate of oxygen
 Note : Red curve for 5% oxygen, blue 10% oxygen

3.5 Refractive Index

The refractive Index of the deposited film has been measured at different flow rates of oxygen using ellipsometer. The refractive index is found to vary with oxygen flow rate. It first increases , reaches a maximum value and then starts decreasing , as listed below in Table 1

Table 1 : Refractive Index With different Flow Rates of Oxygen

% O ₂ Flow Rate	Refractive index
10	2.10
12	2.13
15	2.18
20	2.12

3.6 Leakage Current

The I-V measurements has been obtained using I-V set (keithly 595) The value of leakage current ranges from $I = (0 \text{ to } 2.33E-05 \text{ A})$ with crossponding values of electric field density $E = (0 \text{ to } 5\text{MV}/\text{Cm}^2)$

4. CONCLUSIONS

1. As the oxygen flow rate increases , the deposition rate first increases and then decreases.
2. It is observed that the as deposited film is amorphous ,but the crystallinity of the film increases as the oxygen flow rate is increased to a moderate value.
3. Transmittance is found to be almost independent of oxygen flow rate.
4. Refractive index increases with oxygen flow rate but decreases when oxygen flow rate is increased beyond 20%.

REFERENCES

- [1] A J.Waldorf, J.A.Dobrowolski,B T. Sullivan ,and L. M.Plante, Appl. Opt. 32,5583(1993).
- [2] S.W. Park and H. B. Im, Thin Solid Films 207, 258 (1992).
- [3] S. O. Kim, J. S. Byun, and H. J. Kim, Thin Solid Films 206, 102 (1991).
- [4] I.Kim , J.S. Kim , O.S.Kwon , S.T. Ahn , J.S.Chun, and W. J. Lee, J. Electron. Mater. 24, 1435(1995).
- [5] M. Cevro and G. Carter, Opt. Eng. 34, 603 (1995).
- [6] H. Demiryont , J. R. Sites , and K. Gelb , Appl. Opt. 24, 490 (1985).
- [7] W .B. Westwood , R. J . Boynton , and S.J.Ingrej, J.Vac. Sci. Technol.11,381(1972).
- [8] X. H. Pan, S. L. Qiu, M. I. Florit, M. L. Shek, and M. Strongin, Phys. Rev.B 35, 3740 (1987).
- [9] D.J. Werder and R R.Kola ,Thin Solid Films 323,6 (1998).
- [10] K.Gurtler, K.Bange, W.Wagner, F.Rauch, and H.Hantsche,Thin Solid Films 175, 185 (1989).
- [11] Y. Nishimura , A. Shinkawa , H . Ujita , M.Tsuji , and M.Nakamura, Appl. Surf. Sci. 136, 22 (1998)
- [12] Z.W.Fu, L.Y.Chen, and Q.Z.Qin, Thin Solid Films 340, 164 (1999).
- [13] K. Kukli, J. Aarik, A. Aidla, O.Kohan,T. Uustare , and V. Sammelselg, Thin Solid Films 260, 135 (1995).
- [14] D. Laviale , J. C. Oberlin , and R. A. B. Devine, Appl. Phys. Lett. 65, 2021 (1994).
- [15] P. C. Joshi and M. W. Cole, J. Appl. Phys. 86, 871 (1999).
- [16] Zhou J C, Chen H B, Li Y. Z. Diffusion barrier performance of nanoscale TaN_x[J]. Trans Nonferrous Me Soc China, 17(4) : 733-738.,(2007).
- [17] Chandra Jagadeesh SV and Uthanna, S and Rao, Mohan G(2008) Effect of Substrate Temperature on the Stuctural, Optical and Electrical Properties of dc magnetron sputtered tantalum oxide films .In:applied Surface Science , 254(7) .pp. (1953-1960).

DIGITAL PHOTONIC SWITCHING IN GOLD NANOPARTICLE DOPED SiO₂-TiO₂ SOL-GEL FILMS

Parag Sharma*

Quantum Optics & Photon Physics
CSIR-National Physical Laboratory
Dr. K.S. Krishnan Marg, New Delhi-110012
*Email: sharmap2@nplindia.org

Abstract: Digital photonic switching is theoretically analyzed in Au-nanoparticle doped SiO₂-TiO₂ sol-gel films. The effect of various control laser parameters on switching characteristics is analyzed. There exists an optimum value of peak modulating intensity for given pulse train frequency (f) at which maximum signal modulation can be achieved.

1. INTRODUCTION

Realization of all-optical information processing systems at nanoscale dimensions beyond diffraction limit, appears feasible by exploiting unique photonic properties of plasmonic nanostructures [1]-[2]. High polarizability and ultrafast nonlinear optical response of metal nanoparticles attract attention for their potential use in designing nanophotonic switching devices [2]-[3].

Among wide variety of metallic nanoparticles, gold (Au) and silver (Ag) are considered as potential candidates due low losses in visible and IR ranges [2]. Recently, nonlinear optical absorption and switching in gold nanoparticle (Au-NP) doped SiO₂-TiO₂ sol-gel films has been reported [3]. In the present study, we theoretically analyze and optimize the digital photonic switching properties in the same system using rate equation approach and demonstrate its applicability in designing all-optical information processing systems.

2. MATHEMATICAL MODEL

The rate equations for the population densities of the three most important states (ground state conduction band, 1st excited-state conduction band, and high lying continuum of states, respectively) [3], induced by a modulating laser pulse train $I_m(t)$ with pulse repetition rate f , are simulated numerically. The normalized transmitted signal intensity (T) is calculated by $T = \exp[-\mathbf{a}_s(I_m)L]$, where $\mathbf{a}_s(I_m)$ is the intensity-dependent nonlinear absorption coefficient at signal wavelength and L is the thickness of the sample.

3. RESULTS

T at 532 nm switched by a modulating laser pulse train at 532 nm is simulated, using rate equation approach. The effect of concentration of Au-NP (C_{Au}), peak modulating intensity (I_{m0}) on switching characteristics is analyzed in detail.

Figure 1 shows the variation of signal beam modulation (h) with I_{m0} at $f=4$ for various C_{Au} values. h initially increases and after reaching its maximum

value starts decreasing with increase in I_{m0} . Optimum value of I_{m0} decreases with increase in C_{Au} , and corresponding h value also decreases with increase in C_{Au} .

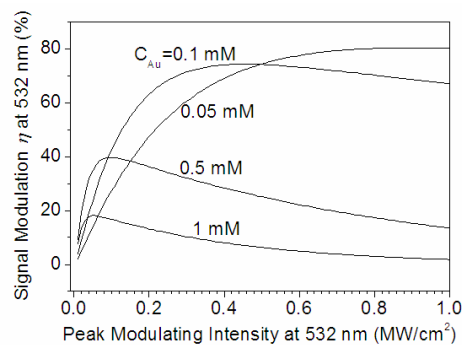


Fig.1 Variation of signal modulation (h) at 532 nm with peak modulating intensity (I_{m0}) at pulse repetition rate $f=4$ MHz, for various gold nanoparticle concentration (C_{Au}) values.

4. CONCLUSION

At given modulating laser pulse repetition rate, optimum value of peak intensity shifts towards lower values with increase in Au-NP concentration.

ACKNOWLEDGEMENT

The author wishes to acknowledge Dr. H.C. Kandpal and Director, NPL, for kind support.

REFERENCES

- [1] R. Zia, J. A. Schuller, A. Chandran and M. L. Brongersma, "Plasmonics: the next chip-scale technology," *Mat. Today*, **9**, 20 (2006).
- [2] A. L. Stepanov, "Nonlinear optical properties of implanted metal nanoparticles in various transparent matrixes: A review," *Rev. Adv. Mater. Sci.*, **27**, 115 (2011).
- [3] N. Vankatram, R. S. S. Kumar, D. N. Rao, S. K. Medda, S. De, and G. De, "Nonlinear optical absorption and switching properties of gold nanoparticle doped SiO₂-TiO₂ sol-gel films," *J. Nanosci. Nanotechnol.*, **6**, 1990 (2006).

OPTICAL NON-LINEARITY IN AMORPHOUS $\text{Ge}_{30}\text{Se}_{70-x}\text{As}_x$ THIN FILMS

R. Chauhan^{†*}, A. Tripathi[‡], and K. K. Srivastava*

[†]Department of Physics, DA-V College, Kanpur, India – 208001

[‡]Research Foundation for Education and Technology, Datia, India – 475661

*Department of Physics, DBS College, Kanpur, India - 208006

chauhanrasmi@gmail.com

Abstract: $\text{Ge}_{30}\text{Se}_{70-x}\text{As}_x$ ($x = 0, 12$) thin films were prepared using thermal evaporation technique. Linear optical constants of the film are calculated from transmission spectra (300-1100 nm) and non-linear optical constants are determined from linear optical parameters using semi-empirical relations. Changes in optical properties are understood on the basis of structural changes and proposed for various optical/photonics applications.

1. INTRODUCTION

Optical non-linearity of Ge-As-Se chalcogenide glassy system is many hundred times greater than silica based glasses, which allows fabrication of compact waveguides for all-optical signal processing at low powers [1]. Thus, these glasses are very useful for telecom applications. Moreover, this system provide wide range of glass formation region, hence, it is possible to tune optical properties easily according to desired application [2].

Experimental determination of non-linear optical properties requires complicated techniques such as Z-scan, two-photon absorption spectroscopy, optical Kerr-shutter, self-phase modulation etc. In present study, we are determining non-linear refractive index (n_2) from optical bandgap (E_g) using semi-empirical relations in long wavelength limit [3]. Non-linear optical constants of As_2Se_3 thin films using these methods were reported by us in the past [4], which are close (~ 99%) to the results in literature.

2. EXPERIMENTAL

Bulk glassy samples of $\text{Ge}_{30}\text{Se}_{70-x}\text{As}_x$ ($x = 0, 12$) were prepared by melt quenching technique and amorphous thin films were prepared by thermal evaporation technique onto a rotating cleaned glass substrates at room temperature. Thicknesses of films were measured by thickness profilometer. Amorphous nature verification and compositional analysis were done using XRD and EDX measurements. The optical transmissions of thin films were measured using a double beam UV/VIS spectrophotometer in wavelength range 300-1100 nm.

3. RESULTS

Optical band gap (E_g) is obtained using Tauc's plot [5] (Table 1):

$$(\alpha h\nu)^{1/2} = A^{1/2} (h\nu - E_g) \quad (1)$$

Where, A is a constant.

Non-linear refractive index (n_2) is determined using semi-empirical relation [3] (Table1):

$$n_2 \sim B / E_g^4 \quad (2)$$

Where, $B = 1.26 \times 10^{-9}$ [esu (eV)⁴].

From Table 1, it is clear that addition of As in Ge-

Se system cause reduction in optical bandgap and increase in non-linear refractive index, which is a consequence of increase in disorderness [6] due to transition of the system from rigid mode to floppy mode [7].

4. TABLES

Table 1: E_g and n_2 of $\text{Ge}_{30}\text{Se}_{70-x}\text{As}_x$ and As_2Se_3 thin films.

	E_g [eV]	n_2 [esu]	
		Theoretical	Experimental
$\text{Ge}_{30}\text{Se}_{70}$	1.90	9.66×10^{-11}	
$\text{Ge}_{30}\text{Se}_{58}\text{As}_{12}$	1.55	2.18×10^{-10}	
As_2Se_3	1.79 [4]	1.22×10^{-10} [4]	1.23×10^{-10} [3]

5. CONCLUSION

Addition of As in Ge-Se glassy system cause reduction in E_g and increase in n_2 .

REFERENCES

- [1] B. J. Eggleton, B. Luther-Davies and K. Richardson, "Chalcogenide photonics", *Nature Photon.*, 5, 141 (2011).
- [2] Z. U. Borisova, *Glassy Semiconductors*, Plenum Press, Newyork, U. S. A., 1981.
- [3] H. Tichá and L. Tichý, "Semiempirical relation between non-linear susceptibility (refractive index), linear refractive index and optical gap and its application to amorphous chalcogenides", *J. Optoelectron. Adv. M.*, 4[2], 381 (2002).
- [4] R. Chauhan, A. K. Srivastava, A. Tripathi and K. K. Srivastava, "Linear and nonlinear optical changes in amorphous As_2Se_3 thin film upon UV exposure", *Prog. Nat. Sci.: Materials International*, 20[1], 54 (2010).
- [5] J. Tauc, *Amorphous and Liquid Semiconductors*, Plenum Press, Newyork, U. S. A., 1979.
- [6] N. F. Mott and E. A. Davis, *Electronic processes in Non-Crystalline Materials*, 2nd ed., Clarendon Press, Oxford, 1979.
- [7] Y. Wang, P. Boolchand and M. Micoulaut, "Glass structure, rigidity transitions and the intermediate phase in the Ge-As-Se ternary", *Europhys. Lett.*, 52, 633 (2000).

Yb-DOPED OPTICAL FIBER THROUGH VAPOUR PHASE DOPING TECHNIQUE

Maitreyee Saha, Archi Bhattacharya, Atasi Pal and Ranjan Sen*

CSIR - Central Glass & Ceramic Research Institute, 196, Raja S.C. Mullick Road, Kolkata, India.

*rsen@cgcri.res.in

Abstract: Presenting well controlled fabrication procedure of Yb-doped Aluminosilicate optical fiber with core diameter of 36 μm and NA of 0.11 through vapour-phase chelate delivery technique, for fiber laser application.

1. INTRODUCTION

Rare earth doped optical fibers have gained immense importance in past few decades for producing fibers for amplifier and laser applications [1-3]. A number of methods have been followed to incorporate rare earth (RE) ions into the silica glass structure, most of which are modifications of the conventional MCVD process. Two of the most common techniques are solution doping method [1] and vapour-phase chelate delivery process [2-3]. Solution doping method was invented in the mid 1980's, optimized over the years and now providing the maximum part of the commercially available RE doped optical fibers. However, solution doping method suffers from poor repeatability and reached to the limit regarding large core size which is essential for laser fibers. So, new fabrication techniques are required to have larger core diameter and low background losses in fibers to accelerate the high power fiber laser technology forward.

On this background, vapour-phase chelate delivery process based on high temperature sublimation of RE chelate compounds reported by Tumminelli et al in 1990, is gaining much importance. The advantages of the technique are: a) the possibility of "in-situ" preform fabrication process which reduces impurities in the fiber, b) better control of the process parameters, c) ability of fabricating large mode area (LMA) fibers by increasing number of layers during RE doping and d) enhanced repeatability over solution doping method to fabricate a particular preform structure. However, till date, very few fibers have been made by this process due to many critical challenges of the process such as: condensations of precursor materials, decomposition of RE chelate compounds and variation in RE concentrations over the length of the preform etc. In addition, lack of availability of suitable external chelate delivery system also restricted proper utilization of the process to its full potential. Here we present successful fabrication procedure of high concentration Yb-doped aluminosilicate fibers through vapour-phase chelate delivery technique by optimizing the process parameters which can be used for fabricating different design of RE doped preforms and fibers.

2. EXPERIMENTS

Description of the modified MCVD system:

Fibers doped with Ytterbium Oxide (Yb_2O_3) and Aluminium Oxide (Al_2O_3) were fabricated by using OFC-12 MCVD system (Nextrom Technology, Finland), a schematic diagram of which is shown in Fig.1.

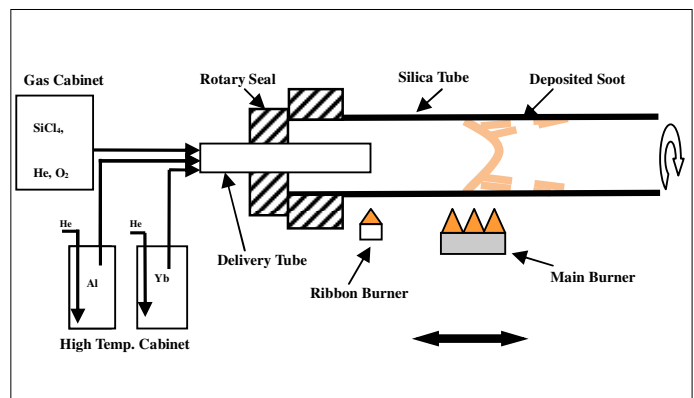


Fig. 1: Schematic diagram of MCVD system with vapour phase delivery unit

The MCVD system consists of one gas cabinet which delivers Silicon Tetrachloride (SiCl_4) and other refractive index modifying dopants and one high temperature vapour delivery unit for the sublimation and delivery of Aluminium Chloride (AlCl_3) and RE chelate compounds. Volatized precursors were transported and delivered to the hot reaction zone by a system of heated sublimators, high-temperature delivery lines with rotary seal and one ribbon burner at the input end of the delivery line to avoid condensation of precursor materials. Another ribbon burner was there at the output end of the substrate tube to avoid condensation of unreacted materials at the joining of substrate and collector tubes. All the vapour delivery lines are provided with heaters, insulators, flow regulators, temperature and pressure sensors to maintain high level of accuracy of the temperature and flow rate of the delivered vapour mixture to the reaction zone. There is an electronic pyrometer and a diameter controlling unit attached with the main burner which are used to monitor

temperature and pressure of the substrate tube respectively. Both are provided with feedback controlling loops to ensure auto control of temperature and pressure which are important for uniform deposition and sintering of the soot layers.

Preform fabrication process:

Preform fabrication consists of two parts:

1. Controlled deposition of core and clad layer
2. Collapsing of the silica tube

During deposition step, Silica (SiO_2) cladding layer deposition was followed by SiO_2 - Al_2O_3 - Yb_2O_3 core layer deposition using vapour-phase chelate delivery technique. Al_2O_3 was co-doped with Yb_2O_3 , primarily as the refractive index raising dopant as well as to prevent clustering of the RE ions and also for maintaining homogeneity of the glass matrix. We used a Yb chelate compound called Yb(thd)₃ [thd = 2,2,6,6-tetramethyl-3,5-heptanedionate] and anhydrous AlCl_3 as precursor materials, having relatively high vapour pressure at low temperature.

O_2 was used to carry SiCl_4 and other dopants from main gas cabinet while Helium (instead of O_2) was used as carrier gas for AlCl_3 and RE chelates from high temperature cabinet. The temperature and flow rate of Helium have been calibrated to supply the dopants in controlled amount and to maintain inert moisture free condition of the cabinet to prevent chemical reactions in between the constituents. The dopants were allowed to mix with O_2 and SiCl_4 vapours delivered from the main gas cabinet before the reaction zone. The temperature and pressure of vapour delivery lines, ribbon burner temperature, diluent inert gas flow rate and purging steps have been optimized for preventing decomposition of the rare earth compounds prior to the reaction zone.

We deposited up to 30 core layers over 500 mm length in substrate tubes of diameter 28/24 and 20/17 mm to obtain different core sizes needed for various fiber designs. The deposition temperature was adjusted judiciously according to the proportion of SiCl_4 and AlCl_3 for perfect sintering of the particulate deposited. For a particular experiment, all conditions including gas flow rate, bubbler temperature, ribbon burner temperature, main burner temperature and traverse speed were kept constant to maintain uniform deposition and sintering of the soot layers. For all experiments additional O_2 was used to maintain oxidizing atmosphere inside the substrate tube.

Subsequent to deposition of core layers, the substrate tube was collapsed into solid rod in oxidizing atmosphere following soft collapsing technique, which permits improved geometrical characteristics of

the preform and helps to avoid central dip due to Al_2O_3 evaporation.

3. RESULTS AND DISCUSSIONS

Preforms with length up to 400 mm and diameter of 10.5–14.6 mm were produced with numerical aperture (NA) in the range of 0.08–0.24. The maximum core diameter achieved in the preform is 4.2 mm. For the first time, the Al^{+3} could be increased beyond 22 mol% in the core. Fibers with diameter of $125 \pm 0.2 \mu\text{m}$ were drawn by Fiber Drawing Tower to characterize their properties. Maximum core diameter of $36 \mu\text{m}$ has been achieved with NA of 0.11 corresponding to 2.3 mol% of Al_2O_3 in the core. It has been observed that collapsing is the most critical step of preform fabrication for large core fibers as well as fibers having high RE concentrations in the core. For both the cases, the tendency of the core is to become non-circular or elliptical which can be avoided by proper optimization of collapsing steps.

Figures 2, 3 and 4 represent cross sectional view of an Yb-doped preform, refractive index profile (RIP) and absorption spectrum of the fabricated fiber respectively. The RIP of the fabricated preforms has been measured using Preform analyzer and the same has been determined for the fibers using Fiber analyzer. Both the results showed good agreement with each other. Yb concentration was estimated from the absorption peak at 915 nm determined by 'cut-back' method. The maximum Yb^{+3} concentration achieved in the fiber is 1.3 mol%.

From our experiments, we have observed that the temperature of the precursor material delivery lines and valves should be higher than the evaporator temperature; otherwise these materials condense and cause clogging of the delivery lines.

Front ribbon burner temperature is the most critical one to control the decomposition of the RE precursors as well as to maintain uniform concentration throughout the length of the preform. If the temperature of the front ribbon burner is very high, uncontrolled and unsintered deposition of RE compound takes place at the reaction zone. Besides, carbon deposition is also observed inside the tube prior to the front ribbon burner. On the other hand, if the temperature is very low, recrystallization of precursor materials on the substrate tube prior to the front ribbon burner can be observed.

If the temperature of the back ribbon burner is not adjusted properly, unreacted precursor materials will condense in the collector tube.

We have optimized the above said steps and parameters to fabricate good quality preforms. Fibers

have been drawn and characterized from the two ends of the preforms to estimate the variation in dopant concentrations over the length of the preforms. From the RIP of the fibers and absorption data, it has been observed that the variation of dopant concentrations at the two ends of the preform is negligible. The dopant concentrations were also evaluated by Electron Probe Micro Analysis (EPMA) which shows uniform radial as well as axial distribution of dopants and good agreement with the values measured in the fibers.

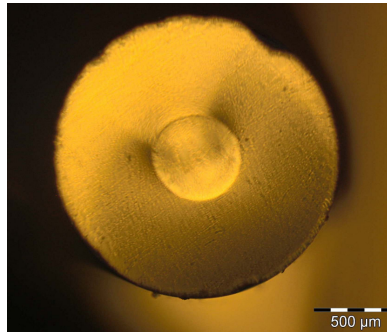


Fig. 2: Cross Sectional View of an Yb-doped preform

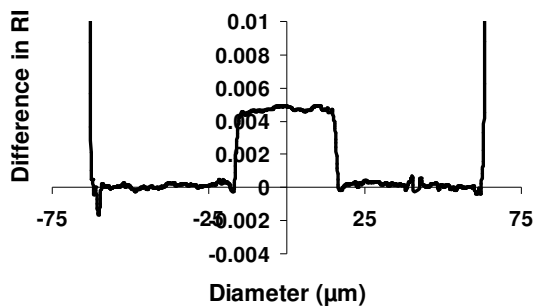


Fig. 3: Refractive Index Profile of an Yb-doped fiber

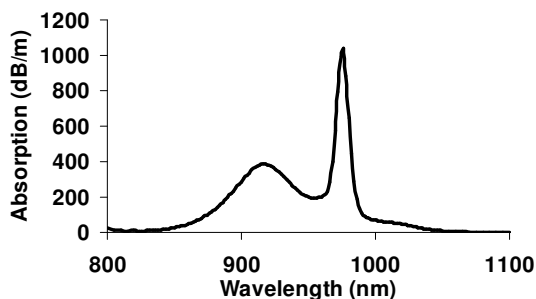


Fig. 4: Absorption spectrum of an Yb-doped fiber

4. CONCLUSION

We report fabrication of rare earth doped optical fibers following vapour-phase chelate delivery process. The fabrication parameters were optimized through a systematic investigation to achieve good control over the process and overcome several existing problems. A number of good quality preforms of different parameters and compositions were successfully fabricated with good repeatability. We so far investigated incorporation of Al and Yb ions but this will be extended to other rare earth chelate compounds like Erbium and Thulium.

ACKNOWLEDGEMENT

The authors wish to acknowledge the support of CSIR, India and DIT, India for providing financial assistance. One of the authors, Maitreyee Saha wishes to acknowledge DIT, India for providing Research Fellowship.

REFERENCES

- [1] Townsend, J.E., Poole, S.B., Payne, D.N., "Solution doping technique for fabrication of rare earth doped fiber lasers", *Electron. Lett.* **23** (1987) p 329.
- [2] Tumminelli, R.P., McCollum, B.C., Snitzer, E., "Fabrication of high-concentration rare-earth doped optical fibers using chelates", *Journal of Lightwave Technology*, **8**(11) (1990) p 1680.
- [3] Sekiya, E.H., Barua, P., Saito, K., Ikushima, A.J., "Fabrication of Yb-doped silica glass through the modification of MCVD process", *J. Non-Cryst. Solids* **354** (2008) p 4737.

MODELING OF ALL-OPTICAL FLIP-FLOP BASED ON COUPLED SEMICONDUCTOR OPTICAL AMPLIFIERS

Yogesh Kumar* and M R Shenoy

Indian Institute of Technology Delhi, New Delhi-110016

*yog_yogeshkumar@yahoo.com

Abstract: Modeling and simulation of an all-optical flip-flop is presented, which is based on coupled semiconductor optical amplifiers (SOAs) through separate cavities, resonating at different wavelengths. The flip-flop's set-reset state is determined by the SOA which is currently lasing. A carrier density and photon rate equations based modeling has been carried out, to determine steady state and transient characteristics of flip-flop.

1. INTRODUCTION

SOA based all-optical flip-flops are expected to play a central role in future optical bistable devices as storage elements, for potential application in optical computing and telecommunication [1]. Different configuration using SOA-MZI structures with feedback loops are extensively studied [2]. A flip-flop architecture using two coupled SOAs but not requiring any MZI structure is reported in Ref.[3]. Laser cavities are formed out of SOAs using Fiber Bragg Gratings (FBGs). The optical bistable system considered here is based upon the concept of gain quenching. Lasing at the natural lasing wavelength in a laser can be quenched when sufficient external light is injected into the laser cavity. The injected external light is not at the same wavelength as that of the lasing light. Lasing is stopped because the gain inside the laser drops below lasing threshold due to the amplified external light. An optical flip-flop based on gain quenching offers a number of advantages:

- 1) It can provide high contrast ratios between set-reset states.
- 2) There is no difference in the mechanisms that change from State 1 to State 2 and vice-versa, permitting symmetric set–reset operation.
- 3) The wavelength range of the input light, and the choice of output wavelengths, can be quite large.
- 4) The flip-flop does not rely on second-order nonlinear effects such as refractive index changes or nonlinear gain. Thus, the flip-flop can be implemented with a wide range of laser and interconnection types. This configuration also allows photonic integration capabilities as have been reported with other flip-flop configuration

Here, we use the rate equation model to explain the flip-flop operation. Based on this model, important properties and results about the flip-flop are derived. Simulation results are first presented to analyze the effect of external light injection on a SOA based laser, these result are then carried forward to study the steady state and transient response of the flip-flop.

2. FLIP-FLOP ACTION USING COUPLED SOAs

The schematic of a flip-flop using two coupled SOAs

is shown in Fig. 1. The arrangement forms two coupled lasers. The SOA cavities are coupled using a directional coupler which allows the output of either of the SOAs to be injected into the other. External pulses now act as set and reset pulses. To understand the flip-flop action, consider cavity 1 at λ_1 to be lasing. The lasing cavity is called 'master cavity' and the other 'slave'. The injection of photons from cavity 1 to cavity 2 prevents it from resonating at λ_2 . The output is at λ_1 . This forms one state of the flip-flop.

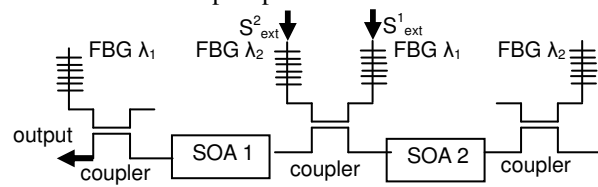


Fig.1: Schematic of coupled SOA based flip-flop

To switch the flip-flop state external photons S^l_{ext} are injected in to the master cavity with sufficient amplitude so that photons at λ_1 decrease. This in turn reduces the number of photons injected in to the slave. The slave thus starts recovering. So now, even if External pulse is removed from the master, the photon injection from the slave forces it to stop resonating. The Master and slave cavities hence exchange roles. Photons at λ_2 injected into cavity 1 travel through it and the output is now at λ_2 , the other state of the flip-flop.

3. RATE EQUATION MODEL

The flip flop is mathematically modeled using two coupled sets of rate equations (1) and (2), with $i=1,2$ and $j=3-i$ to describe SOA 1 and SOA 2 respectively, each set describing one of SOAs [3].

$$\frac{dS_i}{dt} = \left(V_g G_i - \frac{1}{\tau_p} \right) S_i + \beta \frac{N}{\tau_c} \quad (1)$$

$$\frac{dN_i}{dt} = \frac{I}{e} - \frac{N}{\tau_c} - V_g G_i S_i - V_g G_i \zeta_i \left(\eta S_j L n \left(\frac{1}{R} \right) + S^i_{ext} \right) \quad (2)$$

where

$$G_i = \frac{\Gamma a}{V} (N_i - N_0) \quad (3)$$

$$\zeta_i = \frac{(\exp(G_i - \alpha)L) - 1}{2L(G_i - \alpha)} \quad (4)$$

$$S_{ext}^i = \frac{2LP^i_{ext}}{V_g E} \quad (5)$$

S_{ext} is the number of external photons at λ_2 per cavity round trip time ($2L/V_g$). The photon life time τ_p is given by

$$\frac{1}{\tau_p} = V_g \left(\alpha + \frac{1}{L} \ln \left(\frac{1}{R} \right) \right) \quad (6)$$

A description of other parameters is given in Table 1 below.

Table 1 Symbols and their values used for flip-flop simulation [3]

Symbol	Description	Value
I	Injection current	75 mA
q	Electronic charge	1.6×10^{-19} C
V_g	Group velocity in active region	8×10^9 cm/s
a	Material gain factor	2.9×10^{-16} cm ²
Γ	Confinement factor	0.5
τ_c	Carrier lifetime	1 ns
N_o	Carrier number for transparency	2.25×10^8
β	Spontaneous emission factor	5×10^{-5}
V	Volume of active region	2.5×10^{-10} cm ³
L	Length of active region	0.05 cm
α	Internal losses	27 cm ⁻¹
R	Mirror reflectivity	0.04
η	Coupling parameter	0.3

In the rate equation model, we have made the following assumptions:

- 1) Carrier concentration is assumed to be constant over the length of the cavity.
- 2) The effects of amplified spontaneous emission and residual facet reflectivities are ignored.
- 3) The light injected into the laser experiences the same gain, guiding and internal loss as the light at the lasing wavelength inside the laser.
- 4) Light emitted from the master laser flows all the way through the active region of the slave laser, without any light being reflected back into the master laser.

These assumptions are valid for the SOA under lasing condition. Furthermore, generally the SOAs had residual facet reflectivities which are negligible as compare to the mirror reflectivities used to form the lasers. The wavelengths of operation are generally very close, so the gain and loss at these wavelengths can be assumed to be same.

The solution of these coupled differential equations have been obtained using fourth order Runge-Kutta method, under different condition to explain the

operation and important properties of flip-flop.

4. SIMULATION FOR SINGLE SOA BASED LASER

The steady state solution of the rate equations for a single laser can be found by taking $S_j=0$ in equation (2). A plot of steady state N_i and S_i versus S_{ext}^i is shown in Fig. 2

For a given value of S_{ext} , the time dependent differential equations (1) and (2) give the steady state solution for S_i and N_i . The initial value of N (N_{th}) with $S_{ext} = 0$ can be found by equating optical loss and gain i.e. $V_g G = I/\tau_p$. N_{th} is then from equ. (3)

$$N_{th} = \frac{V}{\tau_p \Gamma V_g a} + N_o \quad (7)$$

Using this in (2) gives the initial value of S as

$$S_{st} = \tau_p \left(\frac{I}{q} - \frac{N_{th}}{\tau_c} \right) \quad (8)$$

The equilibrium values can be found for different S_{ext} . The results are shown in Fig. 2.

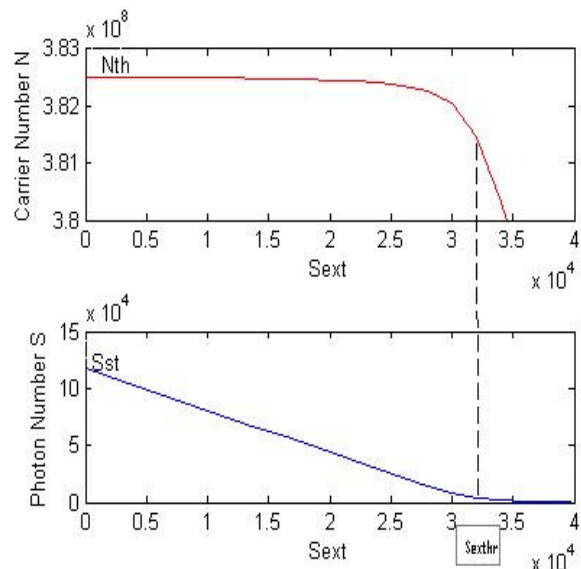


Fig. 2 : Steady-state solutions for carrier and photon number , at different values of S_{ext} for a SOA based laser

The carrier density initially maintains an almost constant level at N_{th} while S reduces linearly with increasing S_{ext} . The slope of the initial linear part of S curve (ζ_{th}) is given by ζ evaluated at N_{th} .

$$\zeta_{th} = \frac{1/R - 1}{2 \ln(1/R)} \quad (9)$$

This linear part of the curve extrapolated to S_{ext} axis gives $S_{ext_{thr}}$, the value of S_{ext} at which S reduces to zero.

$$S_{ext_{thr}} = S_{st}/\zeta_{th} \quad (10)$$

The value of N_{th} , S_{st} and $S_{ext_{thr}}$ estimated to be 3.8285×10^8 , 1.1792×10^5 and 3.163×10^4 for values of parameter used in the simulation. Thus it can be seen that for some values of $S_{ext} < S_{ext_{thr}}$, the laser is still

in action, lasing at λ_1 , although with a very low output at λ_1 . Beyond S_{ext} , the cavity is no more in lasing state due to gain quenching induced by external photons. it has been observed in simulation studies that with increase confinement factor more is the external photon required to stop the lasing.

5. SIMULATION FOR FLIP-FLOP

Considering the flip-flop system without any external influences that is S_{ext} set to zero in equ. (2), and the only light injected is $\eta S_j Ln\left(\frac{1}{R}\right)$ from the other laser. A curve similar to that of Fig. 2 can be plotted but now with S_j versus S_i .

N_i and S_i can be considered as state variables of the flip-flop because the set of four variables describe a unique operating point or state of the flip-flop. We are particularly interested in the N_i , S_i which satisfies the rate equations for the steady state. The steady-state solutions of the four rate equations can be found from the intersection points of the curves S_1 versus S_2 and S_2 versus S_1 as shown in Fig. 3

Since the flip-flop requires only one of the cavities to be lasing at a time, a condition on the minimum coupling coefficient η results [3]. The condition is

$$\eta > \frac{2R}{1-R} \tag{11}$$

.This condition also guarantees stability of the flip-flop states. For $R=0.04$ this value is estimated to be 0.083

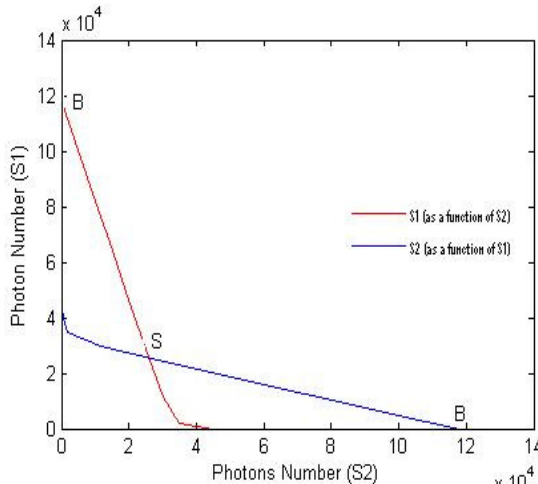


Fig.3: Steady state curves of two coupled SOAs for $\eta=0.3$

Two of the intersection points (labeled B in Fig. 3) represent states with only one of the lasers above threshold. The other point (labeled S in Fig. 3) represents a symmetric state with both lasers lasing and at the same power. If the coupling is weak e. g. $\eta=0.05$, that is does not satisfy (11), as shown in fig. 4 then the curves will only intersect at one point, leading to only one possible symmetric state, thus under this condition no bistable operation can be obtained. The maximum value of η (without amplification of photons travelling

between the lasers) is one. From Equ.(11), the

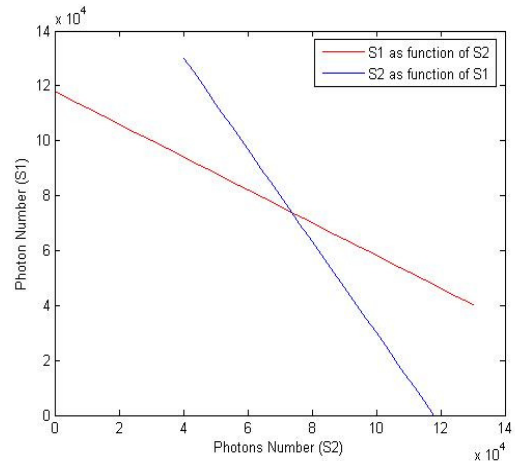


Fig.4: Steady state curves of two coupled SOAs for $\eta=0.05$

maximum value of R for intersection at three points and, hence, possible bistable operation is $R=1/3$. This medium value for indicates it may not be possible to use all types of semiconductor lasers. Specifically, devices with high such as VCSELs (vertical cavity surface emitting lasers), which benefit from low threshold currents and small cavity size, may not be suitable.

A regular toggle between the flip flop states is seen if two continuous pulse streams S_{ext}^1 and S_{ext}^2 with mutual delay of one bit are applied to respective cavities. The results are given in Fig. 5 for external pulse amplitude of 4×10^4 respectively. Ripples, observed since the laser takes some time to stabilize to new threshold. It has been observed in simulation that an increase in the external pulse amplitude reduces the switching time.

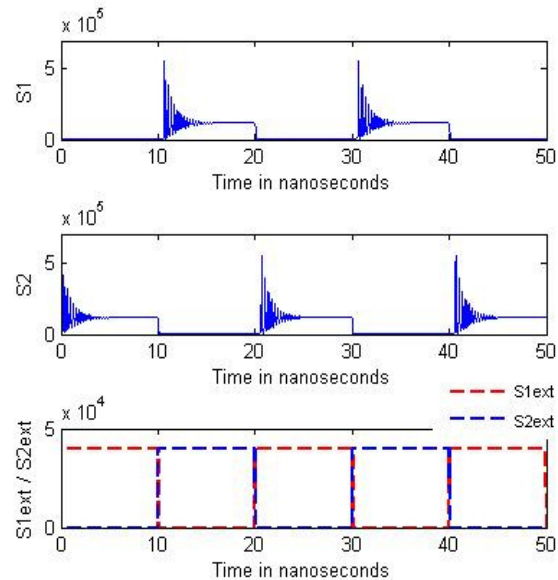


Fig. 5 : Regular switching between the flip-flop states with S_{ext}^1 and S_{ext}^2 pulses of amplitude 4×10^4 .

6. EFFECT OF PHOTON AND CARRIER LIFETIME

It seems quite obvious that a flip-flop with such relaxation oscillations can not be used for optical pulses with length less than about 5 ns. Since the cause for these oscillations is the photon and carrier lifetime, it is to be expected that a decrease in any of these could lead to a reduction in these relaxation oscillations. For a smaller photon lifetime, SOAs with shorter lengths can be used. The simulation results for a flip-flop using 250 μm length instead of 500 μm SOAs is shown in Fig. 6 (a). Indeed the oscillations have been eliminated so that the flip-flop can work even with pulses of duration less than 5 ns.

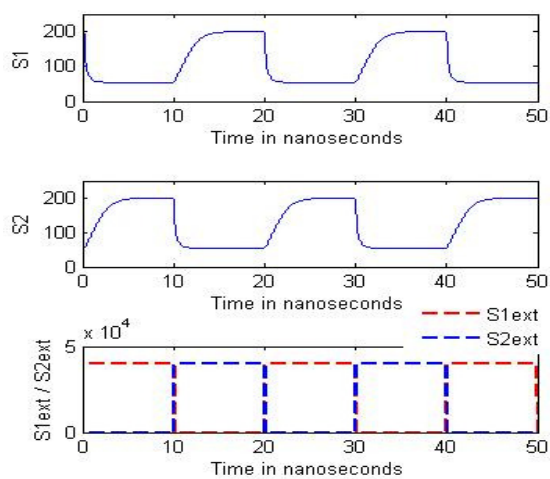


Fig. 6 (a) : Elimination of relaxation oscillations, for an SOA length of 250 μm , due to a reduction in photon lifetime

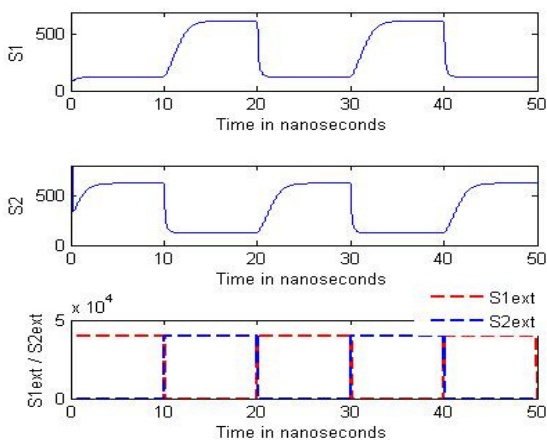


Fig. 6 (b) : Elimination of relaxation oscillations, for an SOA with carrier lifetime of 0.8 ns, due to a decrease in carrier lifetime

A similar effect is observed if the carrier lifetime is reduced from 1ns to 0.8 ns, as is given in Fig. 6 (b). Carrier life time reduction has been reported using

concept of carrier sweep with applied electric field [4]. However, reducing the length of the SOA or carrier lifetime also reduces the gain of the SOA and correspondingly the photon numbers (S_1 and S_2) at the output are reduced significantly.

7. CONCLUSION

Steady state and transient response of the flip-flop based on coupled SOAs are analyzed in this paper. First the operation of SOA based laser is simulated. Then these results were extended to explain the operation of flip flop. It is observed that for small amplitude of external set-reset pulses, relaxation oscillations are observed at all rising and falling edges of external pulses. With an increase in the amplitude, only the ripples at the falling edges can be reduced. A solution for the complete elimination of oscillations is to decrease the photon lifetime by using shorter length SOAs, or by reducing carrier lifetime. It has been observed in simulation that more the confinement factor of SOA more the power required to switch the state of flip-flop. So SOAs with less confinement factor and more coupling factor is ideal for flip flop action.

ACKNOWLEDGEMENT

The author wish to acknowledge Mr. Umesh Tiwari, Scientist CSIO Chandigarh and Ms. Shweta Sharma, Scientist LASTEC Delhi for helpful comments and support.

REFERENCES

- [1] M. J. Connelly, "Semiconductor Optical Amplifier" Kluwer Academic Press, 2002.
- [2] R. Clavero, F. Ramos and J. Marti, "All-Optical flip-flop based on a single SOA-MZI," IEEE Photonics Tech. Lett. Vol. 17, pp. 843-845, 2005.
- [3] M.T. Hilli, H. De Waardt and H.J.S. Dorren, "All-optical Flip-flop based on coupled laser diodes," IEEE J. Quant. Elect., Vol. 37, n0.3, pp. 405-413, 2001.
- [4] A. Cavilles, et al. "Simultaneous measurement of electron and hole sweep-out from quantum wells and modeling photoinduced field screening dynamics" IEEE J. Quant. Elect., Vol. 28, 2486-2497, 1992.

A SEMI-ANALYTICAL REFLECTANCE MODEL FOR OCEANIC WATERS

Surya Prakash Tiwari and Palanisamy Shanmugam^{*}
 Ocean optics and Imaging Group, Department of Ocean Engineering,
 Indian Institute of Technology Madras, Chennai – 600036, India
 E-mail: sptiwariitm@gmail.com, pshanmugam@iitm.ac.in

Abstract: A semi-analytical reflectance model has been developed for oceanic waters. The inherent optical properties (absorption by phytoplankton, absorption by dissolved organic matter and absorption by detrital particles, and absorption by pure seawater; backscattering by pure water and backscattering by particulates) of oceanic waters are modeled as a function of the seawater constituents such as phytoplankton pigments (as characterized by chlorophyll). Validation of this new model indicates that it has the potential for accurate modeling of remote sensing reflectance for a wide range of oceanic waters.

1. INTRODUCTION

In marine and aquatic environments, the solar spectrum is modified on its way through the atmosphere, water surface, wind speed and the water body. These environments are very heterogenic and show severe concentrations of Chlorophyll (Chl), Suspended Sediment Matter (SSM) and Coloured Dissolved Organic Matter (CDOM). Therefore, detection of ocean colour signals reflected by different marine water components, with optical remote sensing using generic spectral algorithms, are often not easily possible. Studies in coastal and extremely turbid waters are still very complex and rare; because for coastal waters, variable terrigenous CDOM, SSM, and bottom reflectance do not co-vary with the Chl concentration [1]. Further, advance research in optical remote sensing requires improvements in monitoring of signal from boundary layers of the subsurface marine waters. In each of these boundary layers sunlight is absorbed, scattered, and reflected in specific manner, depending on the wavelength. Consequently, the reflected light carries spectral information about the particular compositions of these matters.

2. DATA SETS

2.1 In Situ and Simulated Data Sets

In this study two separate datasets are used to parameterize and to test the model performance. The first data set was generated from in situ measurements in a wide range of waters for NOMAD database. The second set is a bio-optical database that includes inherent optical properties (IOPs) and apparent optical properties (AOPs) obtained from IOCCG scientific community. An updated version of NASA bio-optical marine algorithm data sets (NOMAD) obtained from SeaWiFS Bio-optical Archive and Storage System (SeaBASS, maintained by the NASA Ocean Biology Processing Group) was used. The NOMAD datasets are global high quality in situ bio-optical data acquired over 4459 stations and stored in the system for use in ocean colour algorithm development and validation activities with Chl $0.09 \sim 77.8 \text{ mg m}^{-3}$; $a_g 0.019 \sim 1.9 \text{ m}^{-1}$ (412); $b_{bp} 0.0004 \sim 0.09 \text{ m}^{-1}$ (412). After extensive analysis, 84

(NOMAD $R_{rs}(\lambda)$) and 16 (IOCCG simulated $R_{rs}(\lambda)$) valid retrievals were selected for the model validations for the five key wavelengths corresponding to SeaWiFS bands centered at 412, 443, 490, 555 and 670 nm.

3. FORMULATION OF THE MODEL

Remote sensing reflectance $R_{rs}(\lambda)$ is defined as the nadir direction ratio of the water-leaving radiance to the downwelling irradiance just above the surface [2].

$$R_{rs}(0^+ \lambda) = \frac{L_w(\lambda)}{E_d(0^+ \lambda)} \quad (1)$$

where the $R_{rs}(\lambda)$, referred in units of sr^{-1} , is an apparent optical property (AOP) that contains the spectral information of the water-leaving radiance, but which is largely free of its magnitude variability.

For this analysis, spectral $R_{rs}(\lambda)$ at any wavelength (λ) is related to the absorption, a , and backscattering, b_b , coefficient of seawater through the relation (e.g., [1-3]):

$$R_{rs}(\lambda) = \frac{t^2}{n^2} \times R(\lambda, 0^-) = \frac{f(\lambda)t^2}{Q(\lambda)n^2} \left[\frac{b_b(\lambda, Chl)}{a(\lambda, Chl) + b_b(\lambda, Chl)} \right] \quad (2)$$

where $b_b(\lambda)$ is total backscattering coefficient of seawater (i.e., $b_b(\lambda) = b_{bw}(\lambda) + b_{bp}(\lambda)$), and $a(\lambda)$ is total absorption coefficient,

$$(i.e., a(\lambda) = a_w(\lambda) + a_{ph}(\lambda) + a_g(\lambda) + a_d(\lambda))$$

All water constituents are treated as variables, and parameterized as function of Chl concentration. In theory, distribution function of optical field Q is ranges from 0.3 to 6.5, but is generally expected to be 3 to 4 [2], n is refractive index of seawater; Austin proposed the factor 0.544 for correlating radiance just above the surface to radiance just beneath the surface ($t^2/n^2 = 0.54$ is transmissibility of sea-atmosphere interface), f is a function of solar zenith angle. As reported by Gordon, f/Q ($f/Q = 0.095$) is independent of the solar angle changes [4, 5].

4. RESULTS

The resultant spectra of $R_{rs}(\lambda)$ in Fig. 1 reveal two types (e.g., clear and bloom) of the $R_{rs}(\lambda)$ spectra which show a great variability of water constituents of marine waters. This variability can be clearly seen

from the spectral slope and magnitude of the $R_{rs}(\lambda)$ data set. Two maximal reflectance peaks are very typical, which appeared in the vicinities of 570 and 700 nm, respectively. The former is due to an important role of backscattering by particles [7]; while the latter one noticeable at 685 to 715 nm is closely related to fluorescence by Chl pigments [8]. Then it was revealed that in productive turbid waters the position of peak shifts towards longer wavelength and magnitude increases as Chl concentration increases [9, 10]. Thus, the nature of the peak is minimum owing to the combined absorption by all particulate matter and water [8-11]. For these two peak sizes, however, some stations are bigger at the first peak, while others are bigger at last peak. The reflectance valley near 675 nm suggests an important role of absorption by Chl [8], whereas this trough corresponds to large pigment variations. This could be observed in the longer-wavelength domain, where the R_{rs} spectra increase rapidly from approximately 700 nm and then gradually decrease to near-infrared wavelength domain.

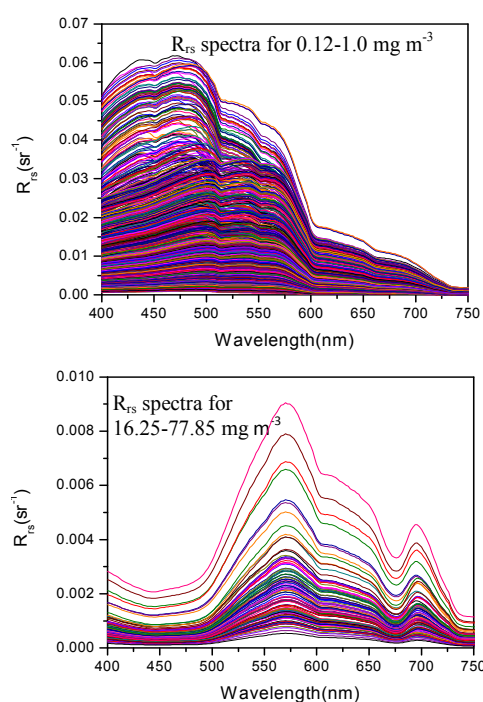


Fig. 1. Remote sensing reflectance (R_{rs}) spectra predicted by a SA approach for different ranges of Chlorophyll (Chl), 0.12-1.0 and 16.25-77.85 mg m^{-3} of NOMAD data set.

4.1 Comparison between Modeled and in situ R_{rs} from NOMAD Data

To illustrate our validation results, we first compare in situ $R_{rs}(\lambda)$ with in situ measurements which vary from 0.0001 to 0.008 sr^{-1} . Fig. 2 shows the model-derived $R_{rs}(\lambda)$ values versus in situ values. Table 1 presents statistical analysis results for the SA approach for all five selected wavelengths (412, 443,

490, 555, and 665 nm). Note that the $R_{rs}(\lambda)$ values from this model deviate with increasing $R_{rs}(\lambda)$ at 510 nm, which resulted in a large underestimation (at 510nm) and showed good agreement at 412, 443, 490, 555, and 665nm with errors (RMSE 0.0043 ~ 0.00068 with an average 0.0038, MRE 0.0021~ 0.045, slope 0.17 ~ 0.77, R^2 0.085 ~ 0.63 and positive intercept values). The statistical analysis performed on these data revealed the RMSE and MNB to be with in 0.068~0.471 % and 2.162~4.527 %, respectively. It is seen that the above-water $R_{rs}(\lambda)$ values are nearly close to the 1:1 line.

Table 1. Statistical comparison between the modeled and in situ data (NOMAD) of Remote sensing reflectance. RMSE and MNB and linear-regression results of the NOMAD data at 412, 443, 490, 555 and 665nm.

AOP's	RMSE	MNB	S	I	R^2
$R_{rs}(412)$	0.0044	0.0272	0.7137	0.0009	0.621
$R_{rs}(443)$	0.0043	0.0216	0.7758	0.0007	0.628
$R_{rs}(490)$	0.0045	0.0452	0.6188	0.0014	0.468
$R_{rs}(555)$	0.0047	0.0353	0.1753	0.0025	0.085
$R_{rs}(665)$	0.0006	0.0368	0.3689	0.0002	0.294
Average	0.0037	0.0333	0.5305	0.0010	0.419

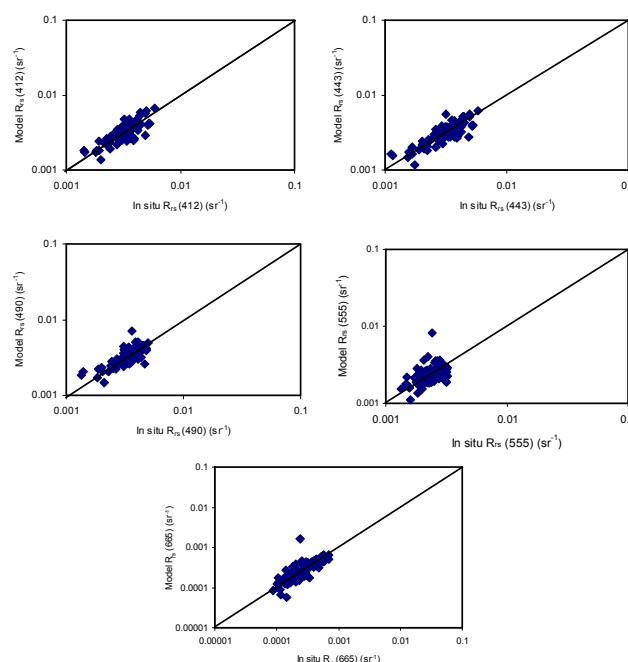


Fig. 2. Comparison between the derived values of the semi-analytical (SA) approach applied on NOMAD data set and in situ data set for remote sensing reflectance at $R_{rs}(412)$, $R_{rs}(443)$, $R_{rs}(490)$, $R_{rs}(555)$ and $R_{rs}(665)$.

4.2 Comparison between Modeled and R_{rs} from IOCCG Simulated Data Sets

We also validated our model on the simulated data set developed by the International Ocean Colour Coordinating Group (IOCCG) Ocean-Colour Algorithm Coordinating Group [12]. The data set includes spectral IOPs and $R_{rs}(\lambda)$ generated at 10 nm interval. For the simulated data set, the pigment concentration ranges from 0.03 to 30 mg/m³ for 500 data simulated from this model. Fig. 3 shows the comparison of model R_{rs} values with the known R_{rs} values (simulated data) considered at six SeaWiFS wavebands (412 to 670 nm). As shown in Fig. 3 and Table 2, it is found that the average R_{rs} from the new model is more closer to in-situ $R_{rs}(\lambda)$. The best overall retrievals, i.e. with lower statistical errors, are obtained with this model for all five wavelengths. The modeled values have shown reasonably good agreement for the wavelength ranges from 410 to 670 nm. Overall, these results indicate that $R_{rs}(\lambda)$ values are very close to the 1:1 line, which means that the performance of the model is reasonably good.

Table 2. Statistical comparison between the modeled and simulated data of reflectance model. RMSE and MNB results of the IOCCG_Simulated data at 410, 440, 490, 550 and 670nm.

AOP's	RMSE	MNB	S	I	R ²
$R_{rs}(410)$	0.0031	0.1771	1.0938	0.0003	0.981
$R_{rs}(440)$	0.0046	0.1303	1.3724	-0.0009	0.976
$R_{rs}(490)$	0.0031	-0.0737	1.6260	-0.0039	0.808
$R_{rs}(550)$	0.0039	-0.1833	0.7367	0.0031	0.938
$R_{rs}(670)$	0.0010	-0.2243	0.6410	0.00008	0.951
Average	0.0032	-0.3479	1.0940	-0.0002	0.931

4.3 Implications for the Optical Remote Sensing

The remote sensing reflectance is an essential parameter among the AOPs, used to derive all IOPs. Usefulness of remote sensing reflectance in coastal/oceanic waters is highlighted by many researchers on regional and global scales. Most of the recent reflectance modeling approaches generally follow three distinct methods: Analytical, semi-analytical and empirical [13]. In these approaches, parameterization is mainly dependent upon radiance. However, we developed a SA approach as a function of Chl, which is totally independent on the radiance (AOPs). The current model works fairly well in relatively clear and bloom waters. The new approach is more suitable and provides encouraging results for both bloom and clear waters. The values of remote sensing reflectance derived from this model can be effective for modeling the inherent optical properties and solving inversion problems in ocean optics. This model also has the potential to describe the variability of reflectance spectra in both clear and bloom waters. Further, this variability shows the

considerable scenario to understand and inspect the fluorescence phenomenon around the red wavelength regions.

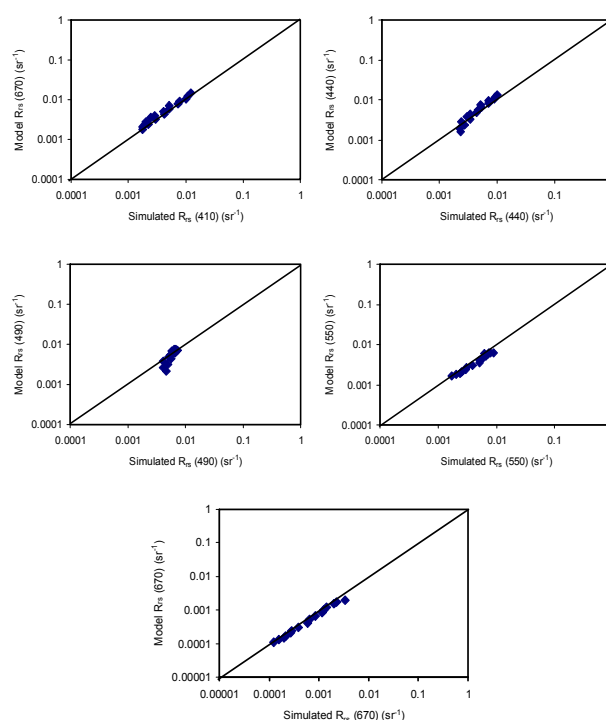


Fig. 3. Comparison between the derived values of the semi-analytical (SA) approach applied on IOCCG_Simulated data set and IOCCG_Simulated at $R_{rs}(410)$, $R_{rs}(440)$, $R_{rs}(490)$, $R_{rs}(550)$ and $R_{rs}(670)$.

5. CONCLUSION

The current research demonstrates a more realistic, accurate reflectance model to retrieve the remote sensing reflectance in oceanic waters. This model relies on the total absorption and backscattering coefficients which are calculated as a function of Chl concentrations. The main objective of this research was to examine the remote sensing reflectance attributed by water constituents in different oceanic regions, in terms of shape, magnitude, and variability across the visible domains. The variability in the reflected radiance gives an indication about concentrations of marine water constituents that vary from one region to another. The validation results showed that the simulated $R_{rs}(\lambda)$ at key wavelengths (normally used in most ocean colour sensors) are better consistent with in situ data. In principle, the model validation can be extended to any region of oceanic waters in which the concentrations of seawaters constituents will co-vary from one region to another.

ACKNOWLEDGEMENTS

This work was supported by grants from the Space Application Center (SAC), Ahmadabad to Indian Institute of Technology (IIT) Madras, Chennai, India.

The authors would like to thank the NASA Ocean Biology Processing Group for making available the global, high quality bio-optical (NOMAD) data set to this study. The authors would also like to thank many scientists who have shared their in situ data in NOMAD and IOCCG databases.

REFERENCES

- [1] Z. P. Lee, K. L. Carder, S. K. Hawes, R. G. Steward, T. G. Peacock, C. O. Davis, "Model for interpretation of hyperspectral remote sensing reflectance," *Appl. Opt.*, 33, 5721 (1994).
- [2] C. D. Mobley, *Light and Water: Radiative Transfer in Natural Waters*, Academic, San Diego, California, USA, 1994
- [3] R. W. Austin. *Inherent spectral radiance signatures of the ocean surface: Ocean Colour Analysis*. La Jolla, CA: Scripps Institute of Oceanography, (1974).
- [4] H. R. Gordon, O. B. Brown, M. M. Jacobs. *Computed Relationships between the Inherent and Apparent Optical Properties of a Flat Homogeneous Ocean*. *Appl. Opt.*, 14, 417 (1975).
- [5] A. Morel and B. Gentili, "Diffuse reflectance of ocean waters. II. Bidirectional aspects," *Appl. Opt.*, 32, 6864 (1993).
- [6] H.R. Gordon, O. B. Brown, R. H. Evans, J. W. Brown, R. C. Smith, K. S. Baker, D. K. Clark, "A semi-analytic model of ocean colour," *J. Geophys. Res.*, 9, 10909 (1988).
- [7] B. Lubac and H. Loisel, "Variability and classification of remote sensing reflectance spectra in the eastern English Channel and southern North Sea," *Remote Sens. Environ.*, 110, 58, (2007).
- [8] H. R. Gordon, "Dependence of the diffuse reflectance of natural waters on the sun angle," *Limnol. Oceanogr.*, 34, 1409, (1989).
- [9] A. Vasilkov and O. Kopelevich, "Reasons for the appearance of the maximum near 700 nm in the radiance spectrum emitted by the ocean layer," *Oceanology*, 22, 701, (1982).
- [10] A. A. Gitelson, "The peak near 700 nm on radiance spectra of algae and water: Relationships of its magnitude and position with chlorophyll concentration," *Int. J. Rem. Sen.*, 13, 3373, (1992).
- [11] H. M. Dierssen, J. P. Ryan, and R. C. Zimmerman, "Red and black tides: Quantitative analysis of water-leaving radiance and perceived colour for phytoplankton, coloured dissolved organic matter, and suspended sediments," *Limnol. Oceanogr.*, 51, 2659, (2006).
- [12] Z. P. Lee, "Models, parameters, and approaches that used to generate wide range of absorption and backscattering spectra. Retrieved from http://www.ioccg.org/groups/lee_data.pdf," IOCCG, 2003.
- [13] A. Morel, and H. R. Gordon, "Report of the working group on water color," *Boundary Layer Meteorology*, 18, 343 (1980).

COMPUTATION OF FRESNEL DIFFRACTION BY VHDL

Arindam Banerjee, Atin Mukherjee, Prabir K. Saha and Debesh Choudhury

Department of Electronics and Communication Engineering,

JIS College of Engineering, Kalyani, Pin-741235, West Bengal

Email: banerjee.arindam1@gmail.com

Abstract: Computation of Fresnel diffraction is indispensable in various areas of information optics and digital holography. We present a VHDL (Very High Speed Integrated Circuit Hardware Description Language) implementation for computation of Fresnel diffraction. Some implementation results have been presented here.

1. INTRODUCTION

The diffracted wave field behind an aperture can be obtained by using the well-known Fresnel-Kirchhoff diffraction integral [1]. Experimental diffraction patterns can be projected on a screen or can be recorded on a photographic film/plate. In optical holography, the reconstruction of the object wave is obtained by Fresnel propagation. Nowadays, holograms are also recorded on digital cameras. The digital holograms are reconstructed by computational Fresnel propagation. The time required for such computation sometimes may be very large depending upon the size of the hologram. Hence, efforts are being made to implement computation of diffraction wave fields by hardware programming. In what follows we present a VHDL implementation of the circuitry for computation of Fresnel diffraction.

II. Proposed algorithm for computation of discrete wave-amplitude distribution function

II.1. Mathematical Description of proposed algorithm

Suppose an aperture $A(x,y)$, where 'x' and 'y' are the rectangular Cartesian coordinates, is illuminated by a coherent plane wave of wave length λ , the complex wave-amplitude distribution at a distance z is

$$\psi(x, y, z) = A(x, y) \otimes f_z^\lambda(x, y) \quad (1)$$

where $f_z^\lambda(x, y) = i(\lambda z)^{-1} \exp[i\pi(\lambda z)^{-1}(x^2 + y^2)]$ (2)

is the well-known Fresnel function [2]. Here $i = \sqrt{-1}$ and the symbol ' \otimes ' signifies the convolution operation.

We have utilized the convolution property of Fourier transform to realize the convolution operation of equation (1).

The two dimensional discrete wave-amplitude distribution function corresponding to equation (1) may be expressed in terms of a linear convolution as,

$$a_{m,n}(k, l) = c \sum_{n=0}^{N-1} \sum_{m=0}^{N-1} A(m, n) \times \exp\left[\frac{i\pi(\lambda z)^{-1}(k-m)^2}{N}\right] \exp\left[\frac{i\pi(\lambda z)^{-1}(l-n)^2}{N}\right] \quad (3)$$

Where, $c = i(\lambda z)^{-1}$, N = number of discrete samples of the distribution function and $m, n, k \in \{0, 1, 2, \dots, N-1\}$. Equation (3) can be reformulated as,

$$a_{m,n}(k, l) = c \sum_{n=0}^{N-1} \sum_{m=0}^{N-1} A(m, n) \times \exp\left[\frac{i(\lambda z)^{-1}\pi(k^2+l^2+m^2+n^2-2(km+ln))}{N}\right] \quad (4)$$

$$= c \left\{ \sum_{n=0}^{N-1} \left(\sum_{m=0}^{N-1} A(m, n) \exp\left[\frac{i\pi(\lambda z)^{-1}}{N}(m^2 + n^2)\right] \right) \exp\left[-\frac{2i(\lambda z)^{-1}\pi(km+ln)}{N}\right] \right\} \exp\left[\frac{i(\lambda z)^{-1}\pi(k^2+l^2)}{N}\right] \quad (5)$$

$$= DFT(f(m, n)) \times h(k, l) \quad (6)$$

Where, $f(m, n) = c \sum_{n=0}^{N-1} \sum_{m=0}^{N-1} A(m, n) \times$

$$\exp\left[\frac{i(\lambda z)^{-1}\pi}{N}(m^2 + n^2)\right] = c \sum_{n=0}^{N-1} \sum_{m=0}^{N-1} A(m, n) \times D(m, n) \text{ and } h(k, l) = \exp\left[\frac{2i(\lambda z)^{-1}\pi(k^2+l^2)}{N}\right].$$

It follows from equations (6) that to obtain the discrete distribution coefficient, we need only one DFT and two complex multiplications depending upon the value of 'k'. Fig.-1 indicates the architecture for the proposed algorithm. VHDL implementation of the architecture has been reported in this paper and the functionality has been checked by ModelSim-Altera6.3g (QuartusII-8.1) and Xilinx ISE-8.2i. The ASIC implementation of the architecture has been left for future work.

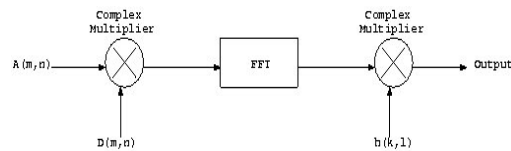


Fig.-1 Block Diagram of Proposed Architecture

II.2. Architecture of proposed algorithm

II.2.1. Radix-2 Two Dimensional FFT algorithm

We know that 2-D DFT of $f(m, n)$ can be expressed

$$\text{as, } DFT(f(m, n)) = c \sum_{n=0}^{N-1} \sum_{m=0}^{N-1} A(m, n) \times \exp\left[\frac{i(\lambda z)^{-1}\pi}{N}(m^2 + n^2)\right] \exp\left[-\frac{2i(\lambda z)^{-1}\pi(km+ln)}{N}\right] \quad (7)$$

Since the product ' λz ' is constant for a certain wavelength (λ) and a distance z , for simplicity we consider the product as a positive integer and call it B , i.e., $B = \lambda z$. In this paper Radix-2D FFT algorithm has been reported for the computation of DFT.

$$\text{Equation (7) can be reformulated as, } DFT(f(m, n)) = c \sum_{n=0}^{N-1} \sum_{m=0}^{N-1} A(m, n) \times \exp\left[\frac{i\pi}{BN}(m^2 + n^2)\right] \exp\left[-\frac{2i\pi(km+ln)}{BN}\right] \quad (8)$$

Considering $BN = M$. So equation (8) can be reformulated as, $F(k, l) = DFT(f(m, n)) =$

$$c \sum_{n=0}^{M-1} \sum_{m=0}^{M-1} A(m, n) \times \exp \left[\frac{j\pi}{M} (m^2 + n^2) \right] \exp \left[-\frac{2i\pi k (km + ln)}{M} \right] \quad (9)$$

Where, $k=0, 1, 2, \dots, (M/B) - 1$.

Now using Radix-2 FFT algorithm, we can partition ‘m’ and ‘n’ into even and odd component.

$$f(m, n) = [f(m, n)_{n \text{ even}} + f(m, n)_{n \text{ odd}}]_{m \text{ even}} + [f(m, n)_{n \text{ even}} + f(m, n)_{n \text{ odd}}]_{m \text{ odd}} \quad (10)$$

Where, $f(m, n) = A(m, n) \exp \left[\frac{j\pi}{M} (m^2 + n^2) \right]$.

Equation (9) can be reformulated as,

$$F(k, l) = c \sum_{n=0}^{M-1} \sum_{m=0}^{M-1} f(m, n) \exp \left[-\frac{2i\pi (km + ln)}{M} \right] \quad (11)$$

$$= F_1(k, l) + W_M^l F_2(k, l) + W_M^k F_3(k, l) + W_M^k W_M^l F_4(k, l) \quad (12)$$

Where, $W_M^k = \exp \left[-\frac{2i\pi k}{M} \right]$, $W_M^l = \exp \left[-\frac{2i\pi l}{M} \right]$

and $k, l=0, 1, 2, \dots, (M/2B) - 1$.

Using the properties of twiddle factor of Fast Fourier Transformation, Equation (12) can be rewritten as,

$$F(k, l) = F_1(k, l) + W_M^l F_2(k, l) + W_M^k F_3(k, l) + W_M^k W_M^l F_4(k, l) \quad (13)$$

$$= F_1(k, l) + W_M^l F_2(k, l) + W_M^k (F_3(k) + W_M^l F_4(k)) \quad (14)$$

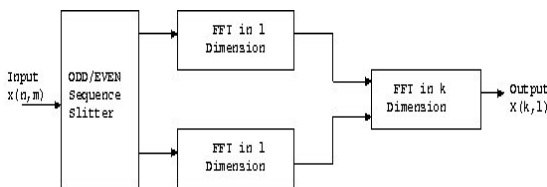
$$= H_1(k, l) + W_M^k H_2(k, l) \quad (15)$$

Where, $H_1(k, l) = F_1(k, l) + W_M^l F_2(k, l)$ and $H_2(k, l) = F_3(k, l) + W_M^k F_4(k, l)$.

Using the periodic property of twiddle factor and Fast Fourier Transformation, it can be written as,

$$F \left\{ \left(k + \frac{M}{2} \right), \left(l + \frac{M}{2} \right) \right\} = H_1 \left\{ \left(k + \frac{M}{2} \right), \left(l + \frac{M}{2} \right) \right\} + W_M^{(k+\frac{M}{2})} \times H_2 \left\{ \left(k + \frac{M}{2} \right), \left(l + \frac{M}{2} \right) \right\} = H_1(k, l) - W_M^k H_2(k, l) \quad (16)$$

Fig.-2 Block Diagram of 2D-FFT architecture



II.2.2. Radix-2 One Dimensional FFT Algorithm

From the above subsection, it is clear that we need exactly three one dimensional FFT computation to compute two dimensional FFT. That is why one

dimensional Radix-2 FFT algorithm has been described in this subsection. If $Y(k)$ is the Fast Fourier Transformation of $x(n)$ then it can be written as, $Y(k) = \sum_{n=0}^{N-1} x(n) W_N^{nk}$ (17)

Where, $W_N^{nk} = e^{-j\frac{2\pi nk}{N}}$ = Twiddle Factor.

$$Y(0) = \sum_{n=0}^{N-1} x(n) \quad (18)$$

Now consider, $nk = lN + p$. Then $W_N^{nk} = W_N^{lN+p} = e^{-j\frac{2\pi(lN+p)}{N}} = e^{-j2\pi l} \times e^{-j\frac{2\pi p}{N}} = e^{-j2\pi l} W_N^p$.

Therefore, $Y(k) = \sum_{n=0}^{N-1} x(n) W_N^{nk} =$

$e^{-j2\pi l} \sum_{n=0}^{N-1} x(n) W_N^p = e^{-j2\pi l} Y(p) = (\cos 2\pi l - j \sin 2\pi l) Y(p) = Y(p)$, Where, $n, p = 1, 2, 3, \dots, N-1$ and $k = 0, 1, 2, 3, \dots, N-1$ and N is the number of sequences.

$Y(k)$ can be written as,

$$\begin{bmatrix} Y(0) \\ Y(1) \\ Y(2) \\ Y(3) \\ Y(4) \\ Y(5) \\ Y(6) \\ Y(7) \end{bmatrix} = \begin{bmatrix} 1 & 1 & 1 & 1 & 1 & 1 & 1 & 1 \\ 1 & w^1 & w^2 & w^3 & w^4 & w^5 & w^6 & w^7 \\ 1 & w^2 & w^4 & w^6 & w^8 & w^{10} & w^{12} & w^{14} \\ 1 & w^3 & w^6 & w^9 & w^{12} & w^{15} & w^{18} & w^{21} \\ 1 & w^4 & w^8 & w^{12} & w^{16} & w^{20} & w^{24} & w^{28} \\ 1 & w^5 & w^{10} & w^{15} & w^{20} & w^{25} & w^{30} & w^{35} \\ 1 & w^6 & w^{12} & w^{18} & w^{24} & w^{30} & w^{36} & w^{42} \\ 1 & w^7 & w^{14} & w^{21} & w^{28} & w^{35} & w^{42} & w^{49} \end{bmatrix} \times \begin{bmatrix} x(0) \\ x(1) \\ x(2) \\ x(3) \\ x(4) \\ x(5) \\ x(6) \\ x(7) \end{bmatrix} \quad (19)$$

Equation (21) can be simplified by partitioning the values of k into even and odd set of numbers as,

If k is odd, then

$$\begin{bmatrix} y(1) \\ y(3) \\ y(5) \\ y(7) \end{bmatrix} = \begin{bmatrix} x(1) & x(2) & x(3) & x(4) & x(5) & x(6) & x(7) \\ x(3) & x(6) & x(1) & x(4) & x(7) & x(2) & x(5) \\ x(5) & x(2) & x(7) & x(4) & x(1) & x(6) & x(3) \\ x(7) & x(6) & x(5) & x(4) & x(3) & x(2) & x(1) \end{bmatrix} \times$$

$$\begin{bmatrix} \frac{1}{\sqrt{2}}(1-j) \\ -j \\ -\frac{1}{\sqrt{2}}(1+j) \\ -1 \\ -\frac{1}{\sqrt{2}}(1-j) \\ j \\ \frac{1}{\sqrt{2}}(1+j) \end{bmatrix} + \begin{bmatrix} x(0) \\ x(0) \\ x(0) \\ x(0) \end{bmatrix} \quad (20)$$

If k is even, then $\begin{bmatrix} y(2) \\ y(4) \\ y(6) \end{bmatrix} =$

$$\begin{bmatrix} x(1) & & x(2) & & x(3) \\ 0 & x(1) + x(3) + x(5) + x(7) & 0 & & \\ x(3) + x(7) & & x(2) + x(6) & & x(1) + x(5) \end{bmatrix} \times \begin{bmatrix} -j \\ -1 \\ j \end{bmatrix} + \begin{bmatrix} x(0) + x(4) \\ x(0) + x(2) + x(4) \\ x(0) + x(4) \end{bmatrix} \quad (21)$$

II.2.2.1 Formulation of rotating circuitry of Radix-2 One Dimensional FFT Algorithm

Since we are describing an 8 point Radix-2 one

dimensional architecture, we require only eight addresses which are composed of three bits only.

For odd value of 'k', consider that a_i ($i=0$ to 2) represents the positions of first row elements. If b_i ($i=0$ to 2) represents the positions of second row elements then b_i can be expressed as, $b_0 = a_0$, $b_1 = a_1 \oplus a_0$ and $b_2 = (a_2 \oplus a_1)\overline{a_0} + a_2a_0$. Similarly if c_i ($i=0$ to 2) be the positions of third row elements, then c_i can be expressed as, $c_0 = b_0$, $c_1 = b_1 \oplus b_0$ and $c_2 = (b_2 \oplus b_1)\overline{b_0} + \overline{b_2}b_0$. Similarly if d_i ($i=0$ to 2) be the positions of fourth row elements, then d_i can be expressed as, $d_0 = a_0$, $d_1 = a_1 \oplus a_0$ and $d_2 = (a_2 \oplus a_1)\overline{a_0} + \overline{a_2}a_0$. From equation (23), it is clear that the input matrix elements are not in a regular arrangement, so it is efficient to store them in some look up table and use them accordingly. So we have designed a look up table for the input matrix.

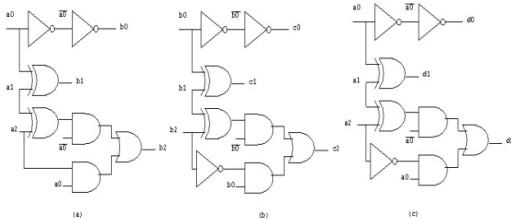


Fig.-3 Architecture of Rotating Circuitry for (a) first row to second row, (b) second row to third row and (c) first row to fourth row.

II.2.4. Formulation of squaring algorithm using Vedic Mathematics (Yavadunam Sutra)

Consider a number $X = x_{n-1}2^{n-1} + \sum_{i=0}^{n-2} x_i2^i$, where x_k ($k = 0$ to $n - 1$) $\in \{0,1\}$ and 2^{n-1} is the chosen radix. $X^2 = (x_{n-1}2^{n-1} + \sum_{i=0}^{n-2} x_i2^i)^2 = x_{n-1}^22^{2(n-1)} + 2x_{n-1}2^{n-1}\sum_{i=0}^{n-2} x_i2^i + (\sum_{i=0}^{n-2} x_i2^i)^2$ (22)

Equation (22) can be deduced as, $X^2 = x_{n-1}2^{n-1} \times (x_{n-1}2^{n-1} + 2\sum_{i=0}^{n-2} x_i2^i) + (\sum_{i=0}^{n-2} x_i2^i)^2$ (23)

$= x_{n-1}2^{n-1}(X + \sum_{i=0}^{n-2} x_i2^i) + (\sum_{i=0}^{n-2} x_i2^i)^2$ (24)

Equation (24) is the mathematical formulation of 'Yavadunam' Sutra used in Vedic manuscript for computation of square of a number. Now consider, $X_1 = (\sum_{i=0}^{n-2} x_i2^i) = x_{n-2}2^{n-2} + \sum_{i=0}^{n-3} x_i2^i$. Using this consideration, equation (24) can be reformulated as,

$$X^2 = x_{n-1}2^{n-1}(X + \sum_{i=0}^{n-2} x_i2^i) + x_{n-2}2^{n-2}(X_1 + \sum_{i=0}^{n-3} x_i2^i) + \dots + 1$$
 (25)

Finally it can be deduced as,

$$X^2 = x_{n-1}2^{n-1}(X + \sum_{i=0}^{n-2} x_i2^i) + x_{n-2}2^{n-2}(X_1 + \sum_{i=0}^{n-3} x_i2^i) + \dots + 1$$
 (26)

II.2.4.1. Architecture of Squaring Circuitry

Squaring circuitry is required to compute the square of m and n as shown in equation (6). The squaring operation has been taken from the ancient Indian Vedic mathematics. From equation (26), the squaring architecture consists of several components such as, (i) Radix Selection Unit (RSU), (ii) Adder, (iii) Shifter, (iv) Decrementer and (v) Zero Detector.

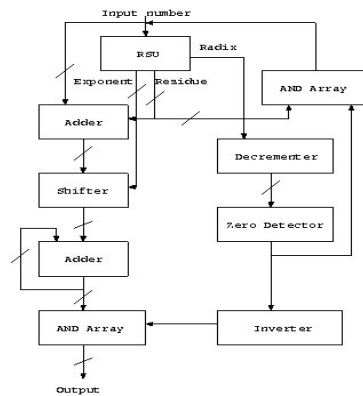


Fig.-4 Architecture of Squaring Circuitry

II.3. Design of complex multiplier

Two complex multiplications have been implemented in this architecture. For complex multiplications we have used the energy efficient high speed technique implemented by Saha & Banerjee [3].

II.4. Exponential function computation circuitry

From equation (10), the exponential part of the equation can be written as,

$$\exp\left[\frac{i\pi}{BN}(m^2 + n^2)\right] = \exp[i\theta] = \cos \theta + i \sin \theta \cong \left(1 - \frac{\theta^2}{2}\right) + i\left(\theta - \frac{\theta^3}{6}\right) = \left(1 - \frac{\theta^2}{2}\right) + i\theta\left(1 - \frac{\theta^2}{6}\right)$$
 (27)

Where, $\frac{\pi}{BN}(m^2 + n^2) = \theta$. Here we have used Taylor's Series expansion and calculated the exponential value approximately. The hardware implementation of equation (27) is depicted in Fig.-5. In this architecture division operation has been implemented by the methodology described by Saha

& Banerjee [4]. Also the multiplier that has been used here has been taken from the methodology implemented by Saha & Banerjee [3].

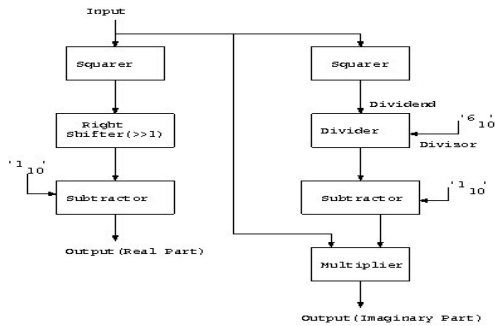


Fig.- 5 Architecture of exponential function computation circuitry

III. Result Analysis

In this architecture, the 1-D FFT computation has been decomposed into odd and even parts and both the subsections are computed in parallel. So the architecture performs much faster than the other architectures. Performance of the proposed architecture in terms of propagation delay has been measured in Xilinx ISE-8.2i Compiler and compared with the architecture designed by Guo [5] and Benhamid [6] and the result has been tabulated in Table-1 and Table-2.

Architecture used	Propagation Delay (ns)
Guo [5]	41.3
Benhamid [6]	39.6
Proposed	36.8

Table-1 Comparative study of Propagation delay of proposed architecture for 1-D FFT with other architectures

Name of architecture	Propagati on Delay (ns)	No. of Look Up Table required
Proposed Architecture for Computation of Fresnel Diffraction	41.8	3038

Table-2 Performance parameter analysis for the architecture of computation of Fresnel Diffraction

IV. CONCLUSION

In this paper an efficient architecture for the

computation of Fresnel Diffraction has been reported. Computation of Fresnel Diffraction has been implemented by ModelSim-Altera6.3g (QuartusII-8.1) and Xilinx ISE-8.2i VHDL compiler. The performance parameters of the architecture such as propagation delay, No. of look up tables etc. have been measured using the same VHDL platform.

REFERENCES

[1] M. Born and E. Wolf, Principles of Optics, 6th edition, Cambridge University Press, 1980) p.382.
 [2] L. Sevigny and M. De, “Fresnel-transform and holography”, Bull Opt Soc India 2, 52–63 (1968).
 [3] Prabir Kumar Saha, Arindam Banerjee, Anup Dandapat, “High Speed Low Power Complex Multiplier Design Using Parallel Adders and Subtractors”, International Journal on Electronic and Electrical Engineering, (IJEEE), Vol 07, No. 11, Page No. 38-46, 2009.
 [4] Prabir Saha, Arindam Banerjee, Partha Bhattacharyya, Anup Dandapat, “Vedic Divider: Novel Architecture (ASIC) for High Speed VLSI Applications”; accepted at ISED-2011 proceedings organized at Kochi.
 [5] J. I. Guo, C.-M. Liu, and C.-W. Jen, “The efficient memory-based VLSI array designs for DFT and DCT,” IEEE Trans. Circuits Syst. II., vol. 39, pp. 723–733, Oct. 1992.
 [6] Mahmud Benhamid and Masuri Bin Othman, “Hardware Implementation of a Genetic Algorithm Based Canonical Singed Digit Multiplier less Fast Fourier Transform Processor for Multiband Orthogonal Frequency Division Multiplexing Ultra Wideband Applications”, Journal of Mathematics and Statistics 5 (4): 241-250, 2009.

SUSCEPTIBILITY OF DOUBLE RANDOM PHASE AMPLITUDE ENCRYPTION TO THE POINT SPREAD FUNCTION ATTACK

Pramod Kumar*, Arvind Kumar, Joby Joseph, and Kehar Singh#

Physics Department, IIT Delhi, New Delhi

Gyandeeep, Mayur Vihar, Ph-1, Delhi

* Email : pramodkumar.24@gmail.com

Abstract: Various types of attacks have revealed weakness of the conventional double random phase encryption (DRPE) scheme due to the linearity of the scheme. It has been claimed earlier that the double random phase-amplitude encryption (DRPAE) scheme is able to resist the known-plaintext attack, due to breaking of the linearity of the double random phase encryption scheme. However, the known-plaintext attack free DRPAE scheme is found susceptible to a point spread function attack, as it has similarity with the 4-f imaging set-up. Existence of the linearity in the DRPAE scheme is also verified. Numerical simulation results are provided to show the efficacy of the proposed attack.

1. INTRODUCTION

Exploitation of various parameters of light like phase, wavelength, spatial frequency, polarization, and angular momentum has resulted in various methods to encode the information. A large number of optical encryption schemes [1] have been investigated based on different principles. One of the oldest and the most exhaustively investigated optical encryption schemes is the ‘double random phase encryption’ (DRPE) scheme [1]-[3]. Replacement of the Fourier transformation (FT) with a more generalized form of transformation e.g. fractional FT and Fresnel transform further enhances the security of the DRPE systems, with the inclusion of the fractional orders and free-space propagation distances respectively as the new encryption keys, in addition to the RPMs [2]-[4].

Recent studies on the DRPE have shown that the DRPE scheme is susceptible to different attacks [5]-[13] such as the impulse-, chosen-plaintext-, and known-plaintext attack etc. Viability of these attacks is based on the fact that the DRPE scheme follows the linearity principle.

Various new encryption schemes [14]-[17] have been developed to resist these attacks effectively, and with enhanced security. Recently, a new security enhanced scheme termed as the ‘double random phase-amplitude encryption’ (DRPAE) scheme [16] is able to endure the powerful known-plaintext attack, due to the introduction of the amplitude modulation. It has been claimed that the additional amplitude mask at the Fourier plane works as an additional encryption key and is able to break the linearity of the conventional DRPE scheme. We show that a point spread function attack is able to reveal the vulnerability of the DRPAE.

2. THEORY

The conventional DRPE scheme [Fig. 1] employs two statistically independent random phase masks

(RPMs) $R_1(x, y)$, and $R_2(u, v)$. The input RPM

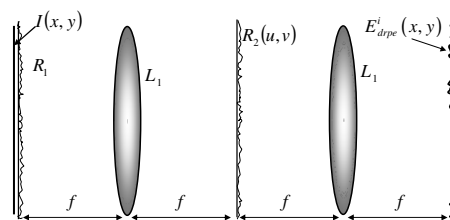


Fig. 1 Schematic diagram of the DRPE scheme

R_1 is bonded with the original input image $I(x, y)$ at the input plane. The Fourier transformed input function is multiplied with the second RPM R_2 at the Fourier plane. The subsequent inverse Fourier transformation provide the encrypted image $E(x, y)$ which is,

$$E^i_{drpe}(x, y) = \{I(x, y)R_1(x, y)\} \otimes FT\{R_2(u, v)\} \quad (1)$$

Here, the $FT\{\}$, and \otimes denote respectively, the Fourier transform operator and the convolution operation.

The security enhanced known-plaintext free DRPAE scheme [Fig. 2] employs an additional amplitude mask $A(u, v)$ at the Fourier plane in addition to the Fourier plane RPM.

$$E^i_{drpae}(x, y) = \{I(x, y)R_1(x, y)\} \otimes FT\{A(u, v)R_2(u, v)\} \quad (2)$$

Here the function $A(u, v)$ is the amplitude mask. The DRPAE is optically realized with a 4-f imaging set-

up. It has been stated [16] that the introduction of the amplitude mask at the Fourier plane in addition to the RPM $R_2(u, v)$, breaks the linearity of the conventional DRPE scheme.

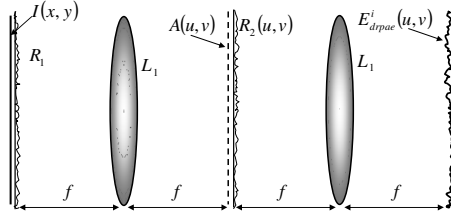


Fig. 2 Schematic diagram of the DRPAE scheme

Usually, the 4-f set-up is employed for coherent imaging, and is one of the traditionally employed systems in coherent information processing. It modifies the input image with the help of the Fourier plane mask $h_2(u, v)$ into the spatially filtered image, $O(x, y)$.

$$O(x, y) = \{I(x, y)\} \otimes FT\{H_2(u, v)\} \quad (3)$$

The point spread function (PSF) of the 4-f imaging system is the function $FT\{H_2(u, v)\}$. The image of the impulse function obtained from the 4-f imaging system is the PSF.

For the characterization of the optical imaging system, an impulse function is employed in place of the input image. Therefore, when the input function is assumed to be an impulse function, Eqn. (3) becomes,

$$O(x, y) = \{\delta(0, 0)\} \otimes FT\{H_2(u, v)\} \quad (4)$$

As Eqn (1) is analogous to Eqn (3), the 4-f imaging system is similar to the DRPE encryption system. Therefore the obtained PSF_{drpe} of the DRPE is as $FT\{R_2(u, v)\}$. All the information about the DRPE encryption system is contained in the PSF_{drpe} . The impulse function attack gives,

$$E_{drpe}^{\delta}(x, y) = \{\delta(0, 0)R_1(x, y)\} \otimes FT\{R_2(u, v)\} \quad (5)$$

With the retrieval of the PSF_{drpe} of the DRPE, an attacker is able to recover the complete information about the original image, which is encrypted through the system. The cracked information is,

$$\{I(x, y)R_1(x, y)\} = FT^{-1}\{E_{drpe}^i(x, y)\}/FT\{PSF_{drpe}\} \quad (6)$$

A similarity is observed between the Eqns (1) and (2), due to which the PSF of the DRPAE scheme becomes known to the attacker. The PSF_{drpae} of the system is

$$E_{drpae}^{\delta}(x, y) = \{\delta(0, 0)R_1(x, y)\} \otimes FT\{A(u, v)R_2(u, v)\} \quad (7)$$

From the retrieved PSF_{drpae} , the attacker is able to retrieve the original encoded information from the DRPAE scheme.

$$\{I(x, y)R_1(x, y)\} = FT^{-1}\{E_{drpae}^i(x, y)\}/FT\{PSF_{drpae}\} \quad (8)$$

The original image is obtained by recording the intensity of the output function of Eqn (8). Therefore, the known-plaintext attack-free DRPAE scheme is vulnerable to the simple PSF attack.

2.1 Proof for the Linearity of the DRPAE Scheme

It has been stated [16] that due to the introduction of the amplitude mask at the Fourier plane, the DRPAE scheme becomes nonlinear. We show below that this is not so.

The input images I^1 and I^2 are respectively encrypted as E_{drpae}^1 and E_{drpae}^2 .

$$E_{drpae}^1(x, y) = \{I^1(x, y)R_1(x, y)\} \otimes FT\{A(u, v)R_2(u, v)\} \quad (9)$$

and,

$$E_{drpae}^2(x, y) = \{I^2(x, y)R_1(x, y)\} \otimes FT\{A(u, v)R_2(u, v)\} \quad (10)$$

For the image I^3 which is formed with the summation of I^1 and I^2 , the encrypted image is

$$E_{drpae}^3(x, y) = \{I^3(x, y)R_1(x, y)\} \otimes FT\{A(u, v)R_2(u, v)\} \quad (11)$$

Replacing I^3 with $I^1 + I^2$,

$$E_{drpae}^3(x, y) = \left\{ \left[I^1 + I^2 \right] R_1(x, y) \right\} \otimes FT \left\{ A(u, v) R_2(u, v) \right\} \quad (12)$$

$$E_{drpae}^3(x, y) = E_{drpae}^1(x, y) + E_{drpae}^2(x, y) \quad (13)$$

Hence, Eqn (13) shows the existence of linearity in the DRPAE scheme.

3. RESULTS AND DISCUSSION

A number of numerical simulations have been performed for the verification of the vulnerability of the known-plaintext attack-free DRPAE scheme against a simple PSF attack. A gray-scale image of ‘baboon’ [Fig. 3(a)] having 256×256 pixels is considered as the input image for encryption. When an attacker is able to perform the PSF attack on the conventional DRPE scheme, the PSF_{drpe} cracks the encrypted image [Fig. 3(b)], as the decrypted image [Fig. 3(c)] completely resembles the original image.

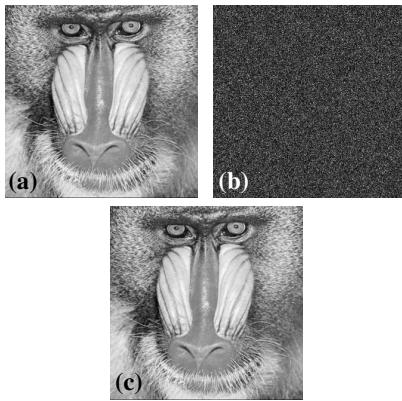


Fig.3 PSF attack on the DRPE, (a) Original image, (b) Encrypted image, and (c) Image cracked with the PSF attack.

Similarly in the case of the security enhanced DRPAE, when PSF_{drpae} [Fig 4 (a)] become available to the attacker, the encoded information [Fig. 4 (b)] from the encrypted image is divulged. The cracked image [Fig. 4(c)] completely resembles the original image. The binary amplitude mask consisting of ‘1’, and ‘0.01’ amplitude values, and the percentage of the number of pixels having transmittance ‘1’ with respect to the total pixel, is 50.

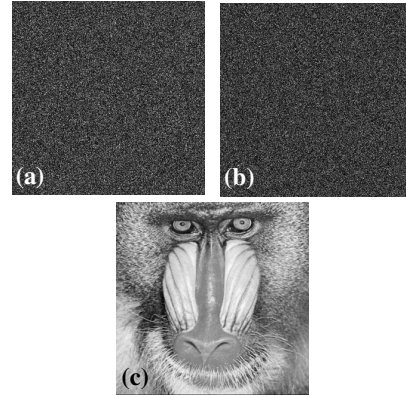


Fig.4 Resistance of the DRPAE scheme against the PSF attack, (a) amplitude of PSF_{drpae} , (b) Encrypted image, and (c) Image retrieved from the PSF attack.

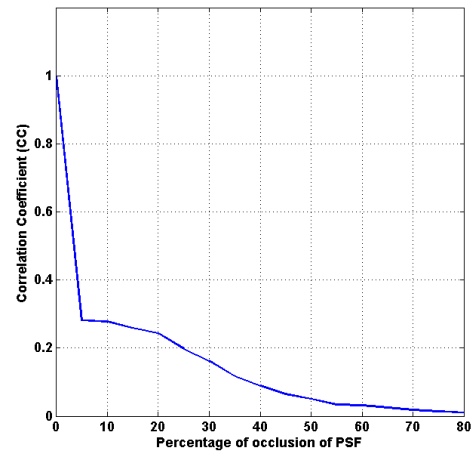


Fig. 5 Sensitivity of the PSF_{drpae} against the occlusion.

The similarity between the input, I and the decrypted image D is evaluated with the correlation coefficient (CC) [16].

$$CC = \frac{\text{cov}(I, D)}{(\sigma_i \sigma_D)} \quad (14)$$

Here, the $\text{cov}(I, D)$ denotes the cross-covariance of two images, and σ is the standard deviation. Fig. 5 illustrates the deterioration of CC with the occlusion of the retrieved PSF_{drpae} . The decrypted images [Figs. 5(a)-(d)] obtained from the occluded PSF_{drpae}

at different percentage values of respectively 0, 20, 40, and 80 show that the retrieved image becomes unrecognizable above a value of 20.

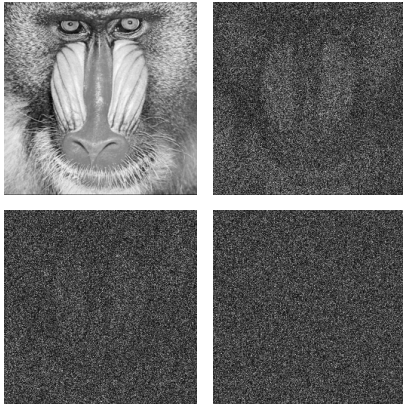


Fig. 5 Decryption of image from the occluded $PSF_{drpaе}$ by percentage, (a) 0, (b) 20, (c) 40, and (d) 80.

4. CONCLUSIONS

Recovery of the PSF of the DRPAE system exposes vulnerability of the system. Numerical results confirm the simplicity of the attack which demands only one-time access to the system.

REFERENCES

- [1] B. Javidi, Ed., *Optical and Digital Techniques for Information Security*, Springer, N.Y., 2005.
- [2] G. Unnikrishnan, J. Joseph, and K. Singh, "Optical encryption by double-random phase encoding in the fractional Fourier domain," *Opt. Lett.* **25**, 887 (2000).
- [3] N. K. Nishchal, J. Joseph, and K. Singh, "Securing information using fractional Fourier transform in digital holography" *Opt. Commun.* **235**, 253 (2004).
- [4] G. Situ and J. Zhang, "Double random-phase encoding in the Fresnel domain," *Opt. Lett.* **29**, 1584 (2004).
- [5] A. Carnicer, M. Montes-Usategui, S. Arcos, and I. Juvells, "Vulnerability to chosen-ciphertext attacks of optical encryption schemes based on double random phase keys," *Opt. Lett.* **30**, 1644 (2005).
- [6] X. Peng, P. Zhang, H. Wei, and B. Yu, "Known-plaintext attack on optical encryption based on double random phase keys," *Opt. Lett.* **31**, 1044 (2006).
- [7] X. Peng, H. Wei, and P. Zhang, "Chosen-plaintext attack on lensless double-random phase encoding in the Fresnel domain" *Opt. Lett.* **31**, 3261 (2006).
- [8] U. Gopinathan, D. S. Monaghan, T. J. Naughton, and J. T. Sheridan, "A known-plaintext heuristic attack on the Fourier plane encryption algorithm" *Opt. Express* **14**, 3181 (2006).
- [9] Y. Frauel, A. Castro, T. J. Naughton, and B. Javidi, "Resistance of the double random phase encryption against various attacks," *Opt. Express.* **15**, 10253 (2007).
- [10] G. Situ, U. Gopinathan, D. S. Monaghan, and J. T. Sheridan, "Cryptanalysis of optical security systems with significant output images" *Appl. Opt.* **46**, 5257 (2007).
- [11] W. Liu, G. Wang, and K. Xie, "A hybrid heuristic algorithm to improve known-plaintext attack on Fourier plane encryption" *Opt. Express* **17**, 13928 (2009).
- [12] W. Qin, and X. Peng, "Vulnerability to known-plaintext attack of optical encryption schemes based on two fractional Fourier transform order keys and double random phase keys" *J. Opt. A: Pure Appl. Opt.* **11**, 075402-1 (2009).
- [13] T. J. Naughton, B. M. Hennelly, and T. Dowling, "Introducing secure modes of operation for optical encryption" *J. Opt. Soc. Am. A* **25**, 2608 (2008).
- [14] P. Kumar, A. Kumar, J. Joseph, and K. Singh, "Impulse attack free double-random-phase encryption scheme with randomized lens-phase functions" *Opt. Lett.* **34**, 331 (2009).
- [15] P. Kumar, J. Joseph, and K. Singh, "Impulse attack-free four random phase mask encryption based on a 4-f optical system" *Appl. Opt.* **48**, 2356 (2009).
- [16] X. C. Cheng, L. Z. Cai, Y. R. Wang, X. F. Meng, H. Zhang, X. F. Xu, X.X. Shen, and G. Y. Dong, "Security enhancement of double-random phase encryption by amplitude modulation," *Opt. Lett.* **33**, 1575 (2008).
- [17] H. Tashima, M. Takeda, H. Suzuki, T. Obi, M. Yamaguchi, and N. Ohyama, "Known plaintext attack on double random phase encoding using fingerprint as key and a method for avoiding the attack" *Opt. Express.* **18**, 13722 (2010).

Optical MEMS pressure sensor - Designing and Analysis

Bhawna Dhingra¹, K.Thyagarajan², Sudhir Chandra³

IIT, Delhi, India

dhibha27@yahoo.com¹, ktarajan@physics.iitd.ac.in², sudhirchandra1950@gmail.com³

Abstract: This paper reports the theoretical analysis and designing of a completely passive optical MEMS pressure sensor based on Fabry-Perot (FP) interference. The mechanical analysis of the diaphragm and the optical response of the sensing head to the gaussian beam incident normally is shown here.

I. Introduction

Measurements of pressure based on optical techniques offer several advantages such as immunity from electromagnetic interference, small size, light weight, high measurement accuracy and resolution, resistance to harsh environments, and capability of high capacity multiplexing. In conjunction with well-established Micro-electromechanical systems (MEMS), the optical methods of sensing have given rise to a new class of devices called Optical-MEMS. This paper proposes the design (shown in Fig.1) and optical and mechanical analysis of optical MEMS pressure sensor.

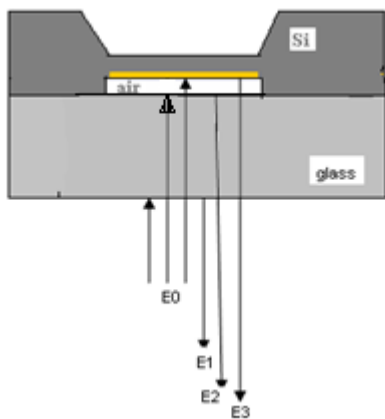


Fig. 1 shows the sketch of the optical MEMS pressure sensor.

II. Principle of operation

Figure.- 1 shows the transverse cross-section of the optical MEMS pressure sensor proposed for fabrication and testing. Silicon diaphragm made on the silicon wafer is used as a pressure sensing element. The FP cavity of depth 'd' is formed between the underside surface of the silicon diaphragm (coated with Al of thickness > skin depth to increase reflectivity) and glass. An air cavity was made between the silicon wafer and a glass wafer to make FP cavity. Light is introduced into the sensor through a single mode fiber (SMF) and reflected light beams from the glass-air and air-metal interfaces interfere to result an interference pattern. When pressure is applied on the silicon diaphragm, the diaphragm deflection results in the change in the air cavity depth which changes the optical path difference between the interfering beams and hence the reflectance from the sensor. This change in reflectivity with the applied pressure is used to calibrate the sensor. There are number of factors determining the desirable operation of the sensor. Size and thickness of the silicon

diaphragm affects the sensitivity and dynamic range of the sensor. However due to FP effect, sensitivity also depends on the depth of the air cavity. Selection of the wavelength and the optical fiber also determines the quality of the sensor. Although with MMF (multimode fiber), it is easier to collect back reflected light from the sensor due to its large numerical aperture (NA), but because of phase dispersion between the divergent rays emerging from the fiber's end, MMF gives poor fringe visibility. Therefore, SMF (single mode fiber) is preferred for a good interferometric signal.

III. Light Loss inside the sensor

Light loss inside the sensor depends upon the type of optical fiber used as well as on the thickness and the depth of the glass and air FP cavity respectively.

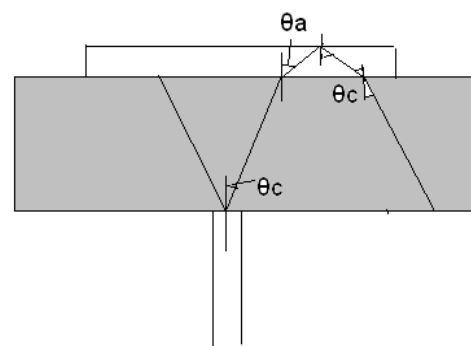


Fig. 2: Estimation of light loss inside the sensor.

Assuming that light is uniformly distributed in the core region of the optical fiber, maximum power that can be coupled back into the optical fiber is calculated as:

$$\frac{P_{out}}{P_{in}} = \frac{\pi a^2}{\pi(2w_g + 2w_{air} + a)^2} \quad (1)$$

where, light divergence in the glass = $w_g = t \tan(\theta_c)$.

Light divergence in the air cavity, $w_{air} = d \tan(\theta_a)$ where $\theta_a = \sin^{-1}(n_g \sin \theta_c)$ and d is the air cavity depth and t is the thickness of glass.

Thus,

$$\text{For SMF, } \frac{P_{out}}{P_{in}} = 0.086\% \quad (2)$$

$$\text{For MMF, } \frac{P_{out}}{P_{in}} = 0.52\% \quad (3)$$

where depth 'd' of the air cavity was taken as 5μm, and glass wafer thickness as 500μm (minimum thickness of the borosilicate glass required for fabrication available in our lab) for calculating (2) and (3). We can see from above calculations that the maximum optical power that can be coupled back into SMF is significantly lower than that for MMF and the loss inside the sensor can be greatly reduced if we decrease the thickness of glass in the sensing head.

IV. Reflectance from the sensor with Gaussian input

Assuming multiple beam interference, reflectance from the sensing head (Fig. 1) is calculated as:

$$R(\lambda) = \left| \frac{r_{12} + \left(\frac{r_{23} + r_{34} e^{i\theta}}{1 + r_{23} r_{34} e^{i\theta}} \right) e^{i\phi}}{1 + r_{12} \left(\frac{r_{23} + r_{34} e^{i\theta}}{1 + r_{23} r_{34} e^{i\theta}} \right) e^{i\phi}} \right|^2 \quad (4)$$

Above was derived for the sensor knowing the reflectance from the Fabry Perot etalon under the plane wave incidence [3] of the input light.

where, $\phi = \frac{4\pi n_{glass} t}{\lambda}$, n_{glass} and t are the refractive index and thickness of the glass respectively and λ is the operating wavelength, $\theta = \frac{4\pi n_{air} d}{\lambda}$,

n_{air} (=1) and d are the refractive index and depth of the air cavity respectively. r_{12} , r_{23} and r_{34} are the reflection coefficients for normal incidence at fiber-glass, glass-air, and air-aluminum interfaces respectively given by: $r_{ij} = \frac{n_i - n_j}{n_i + n_j}$.

The beam interacting with the sensor emanates from a single mode fiber (SMF) whose transverse distribution can be well approximated by a Gaussian function. Thus, taking into account the effect of beam divergence and beam radius of curvature for normal incidence of Gaussian beam, the reflected light from the sensing head was estimated. This was carried out by calculating the overlap integral of the reflected fields at each interface with the fundamental mode of SMF. Thus reflected power at the photo-detector is given by:

$$P = \left| \int_{-\infty}^{\infty} \int_{-\infty}^{\infty} E_1 E_0^* dx dy + \int_{-\infty}^{\infty} \int_{-\infty}^{\infty} E_2 E_0^* dx dy + \int_{-\infty}^{\infty} \int_{-\infty}^{\infty} E_3 E_0^* dx dy \right|^2 = |I_1 + I_2 + I_3|^2 \quad (5)$$

where,

$$E_0 = \sqrt{\frac{2}{\pi}} \frac{1}{w_0} \exp\left(-\frac{(x^2 + y^2)}{w_0^2}\right) \quad (6)$$

If the amplitude reflection coefficient at the fiber-glass interface is given by r_1 , then reflected field E_1 is given by

$$E_1 = r_1 E_0 = r_1 \left(\sqrt{\frac{2}{\pi}} \right) \frac{1}{w_0} \exp\left(-\frac{(x^2 + y^2)}{w_0^2}\right) \quad (7)$$

The remaining field traverses glass of thickness t . The part of which gets reflected at air-glass interface and part gets transmitted. The reflected field E_2 is given by

$$E_2 = t_1^2 r_2 \left(\frac{2}{\pi} \right) \frac{1}{w_0} \sqrt{\frac{\pi^2 w_0^4}{\pi^2 w_0^4 + \lambda^2 (2t)^2}} \exp\left(\frac{-ik(x^2 + y^2)}{2R(2t)}\right) \times \exp\left(\frac{-(x^2 + y^2)}{w^2(2t)}\right) \exp(-ik(2t)) \quad (8a)$$

$$E_3 = t_1^2 t_2^2 r_3 \sqrt{\frac{2}{\pi}} \frac{1}{w_0} \sqrt{\frac{\pi^2 w_0^4}{\pi^2 w_0^4 + \lambda^2 (2t + 2d)^2}} \times \exp\left(\frac{-ik(x^2 + y^2)}{2R(2t + 2d)}\right) \exp\left(\frac{-(x^2 + y^2)}{w^2(2t + 2d)}\right) \times \exp(-ik(2t + 2d)) \quad (8b)$$

where, $R(z) = z \left(1 + \frac{\pi^2 w_0^4}{\lambda^2 z^2} \right)$,

$$w(z) = w_0 \sqrt{\left(1 + \frac{\lambda^2 z^2}{\pi^2 w_0^4} \right)} \text{ and } t_1^2 = 1 - r_1^2 \quad (9)$$

$R(z)$ is the radius of curvature of the wavefront, $w(z)$ is the spot-size, which is equal to the distance in the transverse direction at which field amplitude decays to 1/e of its maximum value, and λ is the light wavelength in the medium.

Solving I_1 , I_2 and I_3 , we get

$$I_1 = r_1, I_2 = \left(\frac{2}{\pi w_0^2} \right) t_1^2 r_2 \sqrt{\frac{\pi^2 w_0^4}{\pi^2 w_0^4 + \lambda^2 (2t)^2}} \exp(-k(2t)) \frac{\pi}{p},$$

$$\text{and } I_3 = \left(\frac{2}{\pi w_0^2} \right) t_1^2 t_2^2 r_3 \sqrt{\frac{\pi^2 w_0^4}{\pi^2 w_0^4 + \lambda^2 (2t + 2d)^2}} \times \exp(-k(2t + 2d)) \frac{\pi}{q} \quad (10)$$

$$\text{where, } p = \frac{\pi w_0^4 (2 + \xi) + i\lambda(2t)}{\pi w_0^4 (1 + \xi)}, \xi = \frac{\lambda^2 (2t)^2}{\pi^2 w_0^4}$$

$$q = \frac{\pi w_0^4 (2 + \xi_1) + i\lambda(2t + 2d)}{\pi w_0^4 (1 + \xi_1)}$$

$$\text{and } \xi_1 = \frac{\lambda^2 (2t + 2d)^2}{\pi^2 w_0^4} \quad (11)$$

V. Simulation Results

Simulating the reflected power from the sensing head in Matlab following results were obtained. Reflection spectrum consists of high frequency component (frequency proportional to thickness of glass used) along with slowly varying sinusoidal component (whose frequency is proportional to the depth of air cavity). At longer wavelengths, beam divergence is more and hence the reflectance decreases. Figure.-7 shows that as the thickness of glass used increases, it is much more difficult to couple back reflected light into the SMF. However, for the Gaussian interaction of the sensor, dynamic range of the sensor for single wavelength interrogation is much less than $\lambda/4$ (as in plane wave normal incidence case).

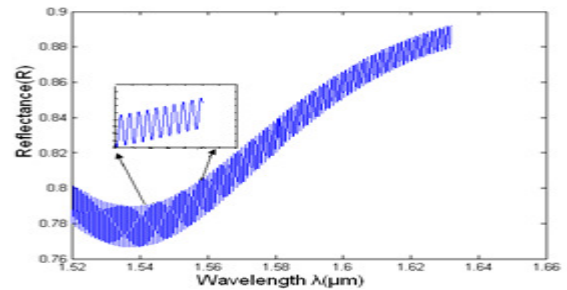


Fig. 3: Reflection spectrum at a wavelength resolution of 0.1 nm from the sensor under plane wave incidence.

Rapid oscillations are due to FP interference in glass (of thickness $800\mu\text{m}$).

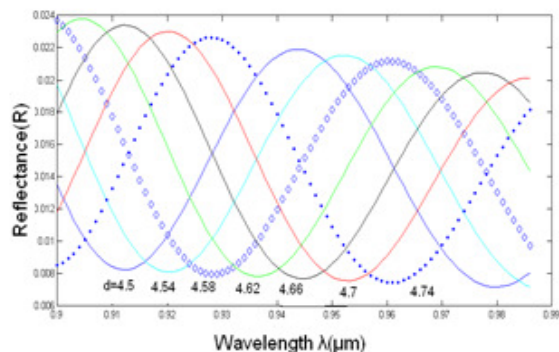


Fig. 4: Reflection spectrum of the sensor. As d (depth of air cavity) changes there is a shift in the spectrum which can be used to demodulate the pressure. Here, complete FSR is the dynamic range of the sensor.

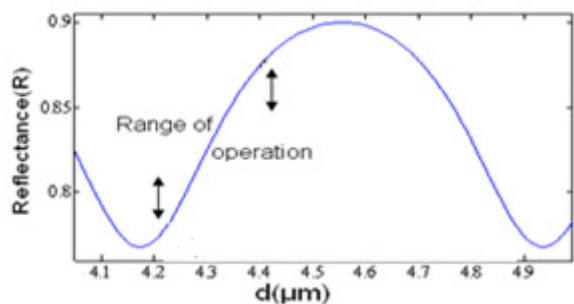


Fig. 5: Above figure shows the range of operation (single wavelength interrogation) of the sensor under plane wave assumption of the input light. Range of operation in this case is 80% of $\lambda/4$.

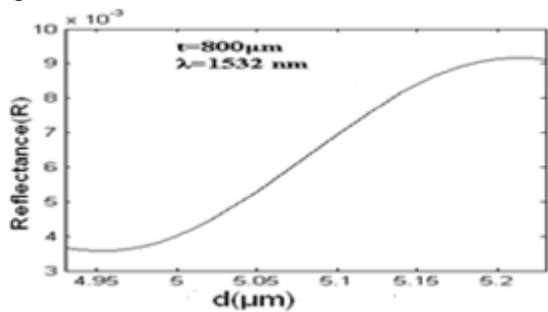


Fig. 6: Variation in the reflectance from the sensing head with the change in the depth of the FP cavity (applied pressure). Thickness of the glass is assumed as $800\mu\text{m}$. Above figure shows that the range of operation (single wavelength interrogation) of the sensor for Gaussian input is of the order of $\lambda/6$.

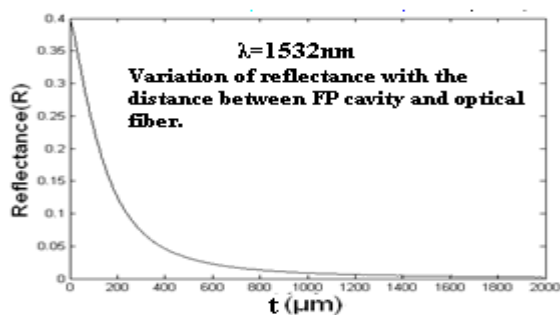


Fig.7: Reflectance from the sensing head decreases exponentially with the increase in thickness of glass.

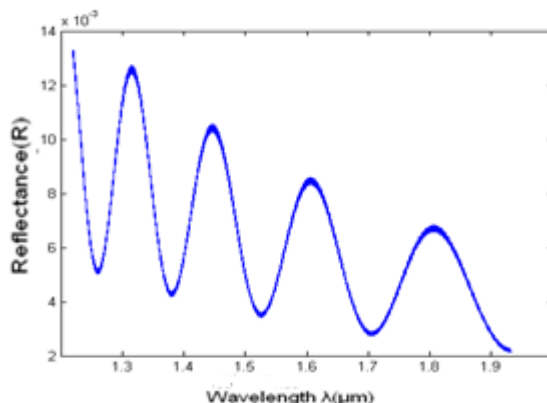


Fig. 8: Reflectance decreases as the wavelength increases due to greater beam divergence at longer wavelengths.

VI. Depth of the FPI cavity:

The depth of the etched cavity in the silicon wafer must be greater than $\lambda/6$ (to cover its dynamic range), but to avoid ambiguities, must be small enough to yield a cavity where free spectral range is somewhat greater than the source line width. That is, the spectral width of source imposes an upper bound for the cavity depth. For moderately large fringe order m , the free spectral range is

$\Delta\lambda_{FSR} \approx \lambda_m^2 / \Lambda_{OPD}$ which can be written as $\Delta\lambda_{Laser} \leq \lambda_m^2 / \Lambda_{OPD}$ (Λ_{OPD} =optical path difference). The line width of tunable laser source available in our setup is, $\Delta\lambda_{Laser}=0.4 \text{ nm}$, which corresponds to a cavity depth of $\approx 2888\mu\text{m}$. We have to choose a cavity depth to lie within these two limiting values.

VII. Sensitivity of the sensor

Sensitivity of the sensor is determined by a) dimensions of the silicon diaphragm i.e, size and thickness of the diaphragm. b) Depth of the FP cavity. Mechanical analysis of the silicon diaphragm was performed based on FEM using a software tool Coventorware MEMS. By applying the appropriate boundary conditions on the silicon diaphragm, the effect of variation in diaphragm size and thickness on the sensitivity and dynamic range of the sensor was studied (Fig. 10 and 11). Deflection map (Figure.-9) as well as the stress map were obtained to give the deflection 'd' of the diaphragm when the pressure 'P' was applied. Simulation results showed that as radius of the diaphragm increases and the thickness of the diaphragm decreases, sensitivity decreases at the cost of its dynamic range and vice-versa.

Apart from the mechanical analysis, sensitivity of the sensor also depends on the depth of the FP cavity as the period of oscillation is inversely proportional to the depth of FP cavity. As the depth increases, sensitivity increases, but again at the cost of dynamic range and decreased reflectance.

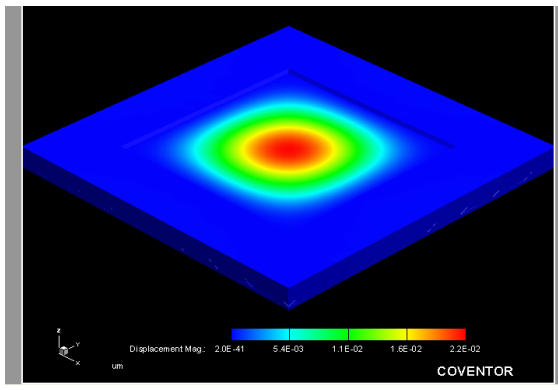


Fig. 9: Deflection map of the diaphragm when pressure $P= 0.1\text{MPa}=1\text{ atm}$ was applied on the square diaphragm of thickness $25\mu\text{m}$ and size of $300\times 300\mu\text{m}^2$, diaphragm bends with maximum deflection at the centre, which in this case is $d_{\text{max}}=0.022\mu\text{m}$.

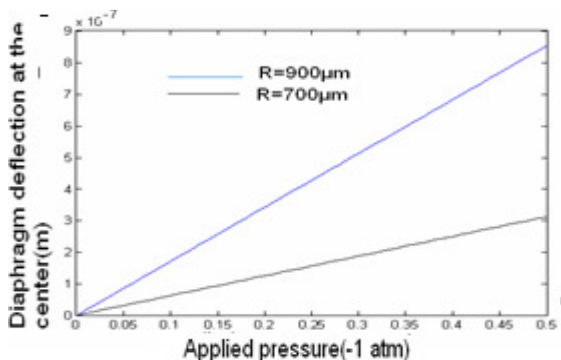


Fig. 10: At a given diaphragm thickness, increase in size of the diaphragm increases the sensitivity at the cost of dynamic range.

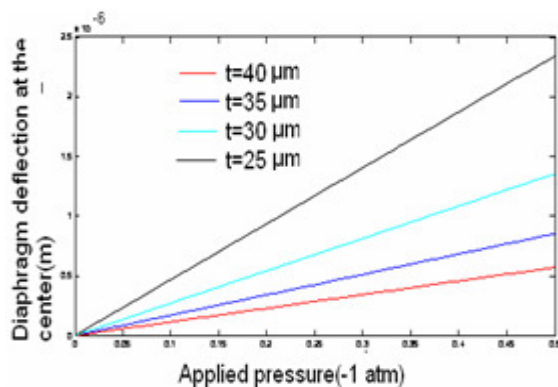


Fig. 11: For a given diaphragm size, decrease in the thickness of the diaphragm increases the sensitivity at the cost of dynamic range.

VIII. Optical Demodulation Scheme

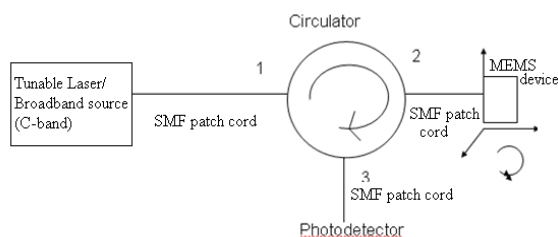


Fig.12: A schematic of experimental setup for optical demodulation of the sensor.

Figure.-12 shows the schematic of experimental set up required for detecting the reflected light from the sensing head. This system in general consists of a light source (tunable laser), single mode fiber FC/PC patch cords, circulator or a 3 dB directional coupler, a photo detector, and a power meter. Light emerging from the source is coupled into the port (port 1) of circulator. An input signal on port 1 is sent out on port 2, signal on port 2 is used to address the sensing element. Reflected signal from the sensing element is an input to port 2 and is sent out at port 3 of the circulator connected to the photo detector. However, with the use of optical spectrum analyzer instead of photo-detector, and a broadband source at the input, frequency shift with the application of pressure in the reflection spectrum can be used for demodulation. This has an added advantage of increase in dynamic range of the sensor at the expense of increase in cost of the sensor.

IX. Conclusion

We have provided a theoretical analysis and designing of a completely passive optical MEMS pressure sensor based on Fabry-Perot (FP) interference. The mechanical analysis of the diaphragm and the optical response of the sensing head to the Gaussian beam incident normally has also been presented. This should help in the design and realization of MEMS based pressure sensor.

REFERENCES

- [1] Wang, Li, Ruso, T.Roman, K.Chin, Kenneth R.Farmer," Diaphragm design guidelines and an optical pressure sensor based on MEMS technique", Microelectronics Journal 37(2006) 50-56,11 August 2005.
- [2] Ajoy Ghatak and K.Thyagarajan, Introduction to Fiber Optics, Cambridge University Press.
- [3] M Born and E Wolf, Principle of Optics, Cambridge University Press; 6 edition, 1997.
- [4] G.Keiser, Optical Fiber Communications, McGraw Hill Higher Education, 2000

DETERMINATION OF PHASE OF QUASI MONOCHROMATIC LIGHT IN TIME DOMAIN BY YOUNG'S DOUBLE SLIT EXPERIMENT

Manish Verma^{1,2}, S. Joshi¹, N. S. Bisht¹, P. Senthilkumaran², Joby Joseph², H. C. Kandpal¹

¹National Physical Laboratory (CSIR), New Delhi-110012.

²Indian Institute of Technology, New Delhi-110016.

Email: vermam@mail.nplindia.ernet.in

Abstract: It is shown that the phase and amplitude of the complex degree of coherence can be determined by performing intensity measurements in the diffracted field at various off-axis points in the observation plane in a Young's double slit setup. In this paper we have calculated experimentally the phase and amplitude of the complex degree of coherence in time domain, first with a spatially fully coherent quasi-monochromatic light and then with a spatially partially coherent quasi-monochromatic light. From this study the dependence of spatial coherence of the incident field on the experimental measurement of the phases is also investigated.

1. INTRODUCTION

Recently, Wolf has shown that in time domain the phase and amplitude of the complex degree of coherence of a quasi-monochromatic light can be calculated [1] by performing intensity measurements at various off-axis points at the observation plane in Young's interference experiment. This research was conducted to have the information of the relative phase of the x-rays for solving the reconstruction problem in the field of x-ray crystallography [1]-[2] as of now the reconstruction in x-ray crystallography is done only by intensity measurements.

In the same context [1] we have experimentally calculated the initial phase difference associated with the quasi-monochromatic field on two slits of a double slit system by measuring intensity of the diffracted field at various off axis points at the observation plane in the Young's double slit setup. For both spatially fully coherent and spatially partially coherent quasi-monochromatic light the experimentally determined phase difference is shown in Fig. 3 and Fig. 6 respectively. From this experimental study, we have shown that for accurate determination of the initial phase difference, the spatial coherence of the incident field should be high.

2. THEORY

Consider a Young's double slit experiment shown in Fig. 1. S was an incoherent low pressure mercury discharge lamp. From this source, a narrow band quasi-monochromatic green light with central wavelength $\approx 546.1\text{nm}$ was extracted by a monochromator M. Spatially fully coherent field was produced by passing the light through a very narrow slit S_1 (of slit width $20\mu\text{m}$) and then propagating [3] it to distance $z_1 = 199\text{cm}$, where a double slit DS having two narrow slits Q_1 and Q_2 (each slit with width $b=0.25\text{mm}$ and separated by a distance $d=0.5\text{mm}$) was kept. Similarly, spatially partially

coherent field was produced by passing the light through a slit (1000nm wide) and then propagating it to a distance of 190cm. The interference fringes were obtained on the observation screen O at a distance of $z_2=48.5\text{cm}$ from the double slit where its intensity pattern was recorded by a CCD camera. From the intensity interference law [4], we get

$$\frac{I_{12}(P) - I_1(P) - I_2(P)}{2\sqrt{I_1(P)I_2(P)}} = |\gamma(Q_1, Q_2, \tau)| \times \cos[\alpha(Q_1, Q_2, \tau) - \bar{\omega}\tau] \quad (1)$$

where, $\gamma(Q_1, Q_2, \tau)$, is the complex degree of coherence at the two slits Q_1 and Q_2 , $I_{12}(P)$ is the observed intensity at point P when both slits Q_1 and Q_2 were open, $I_1(P)$, $I_2(P)$, are respectively the intensities when only slit Q_1 was open or only slit Q_2 was open. $\alpha(Q_1, Q_2, \tau)$ is initial phase difference at the two slits and $\delta = \bar{\omega}\tau = 2\pi(R_2 - R_1)/\lambda$ is the phase difference associated with the paths Q_1P and Q_2P shown in Fig.1.

Let,

$$F(\tau) = |\gamma(Q_1, Q_2, \tau)| \times \cos[\alpha(Q_1, Q_2, \tau) - \bar{\omega}\tau] \quad (2)$$

On simplifying,

$$F(\tau) = C_{12} \times \cos[\bar{\omega}\tau] + S_{12} \times \sin[\bar{\omega}\tau] \quad (3)$$

where

$$C_{12} = \text{Re}\{\gamma(\tau)\} = |\gamma(\tau)| \times \cos[\alpha(Q_1, Q_2, \tau)] \quad (4)$$

and

$$S_{12} = \text{Im}\{\gamma(\tau)\} = |\gamma(\tau)| \times \sin[\alpha(Q_1, Q_2, \tau)] \quad (5)$$

so that

$$|\gamma(\tau)| = \sqrt{C_{12}^2 + S_{12}^2} \quad (6)$$

$$\text{Cos}[\alpha(Q_1, Q_2, \tau)] = \frac{C_{12}}{\sqrt{C_{12}^2 + S_{12}^2}}, \quad (7)$$

and,

$$\text{Sin}[\alpha(Q_1, Q_2, \tau)] = \frac{S_{12}}{\sqrt{C_{12}^2 + S_{12}^2}}. \quad (8)$$

For two different observation points P_1 and P_2 ; C_{12} and S_{12} can be evaluated using Eq. (3),

$$C_{12} = \frac{\text{Sin}[\bar{\omega}\tau_2]F(\tau_1) - \text{Sin}[\bar{\omega}\tau_1]F(\tau_1)}{\text{Sin}[\bar{\omega}(\tau_2 - \tau_1)]}, \quad (9)$$

and

$$S_{12} = -\frac{\text{Cos}[\bar{\omega}\tau_2]F(\tau_1) - \text{Cos}[\bar{\omega}\tau_1]F(\tau_1)}{\text{Sin}[\bar{\omega}(\tau_2 - \tau_1)]}, \quad (10)$$

where, τ_1 and τ_2 are the time delays associated with the paths Q_1P_1 , Q_2P_1 and Q_1P_2 , Q_2P_2 (provided that $\tau < 1/\Delta\bar{\omega}$) respectively.

By measuring intensities $I_{12}(P)$, $I_1(P)$ and $I_2(P)$ at various off axis points at the observation plane O as shown in Fig. 2 and Fig. 5 and with the help of Eq. (9) and Eq. (10) we calculated C_{12} and S_{12} for different pairs of points. Then from Eq. (6), Eq. (7) and Eq. (8) we have determined the amplitude and phase of the complex degree of coherence at the double slit for different off axis points at the observation plane O.

3. FIGURES:

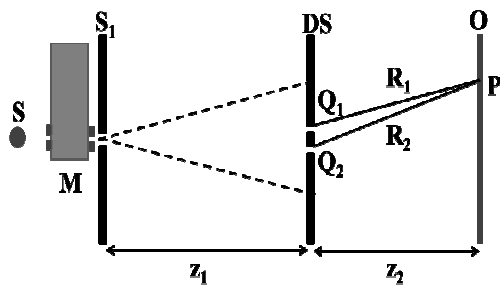


Figure 1: Schematics of the experimental setup. S is a mercury discharge lamp, M is a monochromator, S_1 is single slit, DS is a double slit and O is the observation plane.

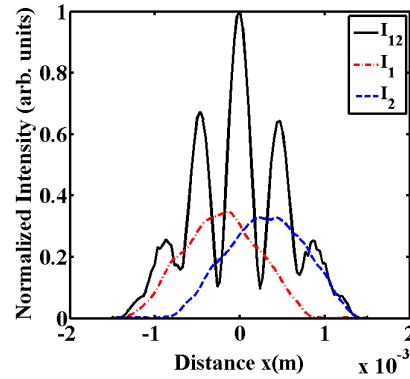


Figure 2: Double slit interference pattern at the observation plane for a spatially fully coherent light. Here I_{12} represents the intensity of the diffracted field when both slits were open, I_1 correspond to the intensity when only slit Q_1 was open and I_2 correspond to the intensity when only slit Q_2 was open.

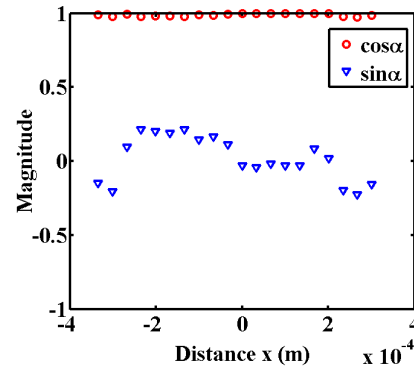


Figure 3: Initial phase difference $\alpha(Q_1, Q_2, \tau)$ in terms of cosine and sine for spatially fully coherent light.

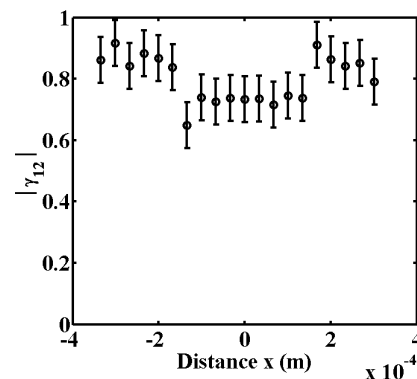


Figure 4: Magnitude of the complex degree of coherence for spatially fully coherent light. Dots represent experimentally calculated values and solid bars represent standard deviation in the measurements.

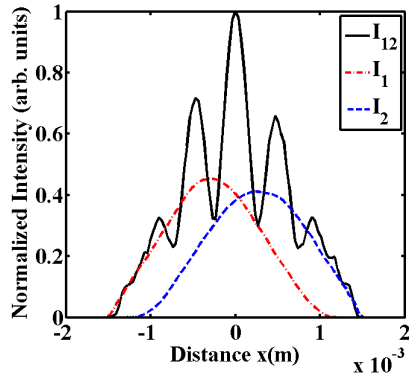


Figure 5: Double slit interference pattern at the observation plane for spatially partially coherent light. Here I_{12} represents the intensity of the diffracted field when both slits were open, I_1 correspond to the intensity when only slit Q_1 was open and I_2 correspond to the intensity when only slit Q_2 was open.

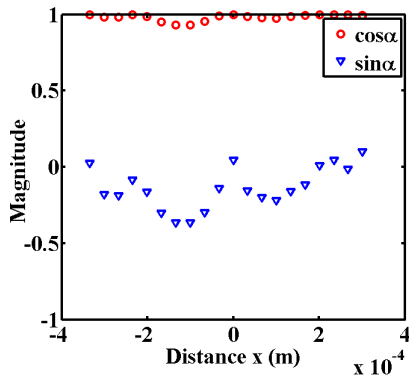


Figure 6: Initial phase difference $\alpha(Q_1, Q_2, \tau)$ in terms of cosine and sine for spatially partially coherent light.

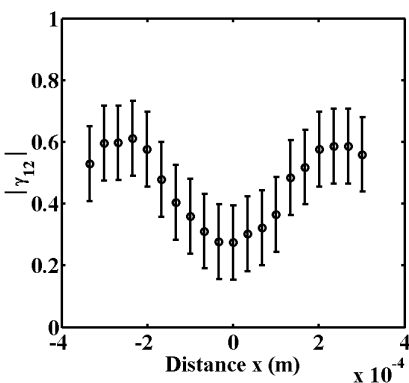


Figure 7: Magnitude of the complex degree of coherence for spatially partially coherent light. Dots represent experimentally calculated values and solid bars represent standard deviation.

4. CONCLUSION

In this paper, the initial phase difference on the two slits was determined by performing intensity measurements at various off axis points at the observation plane for both spatially fully coherent light (as shown in Fig. 3) and partially coherent light (as shown in Fig.6).

As we can see in Fig. 1 that the field is incident normally on the double slit therefore the phase difference associated with the two slits should be approximately zero. This is in agreement with our experimental study shown in Fig. 3 and Fig. 6 for both spatially fully coherent and partially coherent light. In the case of spatially fully coherent light the fluctuations are much smaller than the latter case. The calculated magnitude of the complex degree of coherence is also in agreement with our results as shown in Fig. 4 and Fig.7.

There are also some experimental limitations associated with the measurement, for example, we can see from Fig. (2) that even for spatially fully coherent light the minima do not go to a real minima i.e. zero. Some statistical fluctuations are always present in the measurement. Therefore, the fluctuations in the measurement of the magnitude of the complex degree of coherence, shown by error bars in Fig. (4) and Fig. (7), represent the experimental limitations.

This study might be used for reconstructing the sources where a prior knowledge of the intensity distribution of the source is known.

5. ACKNOWLEDGEMENT

The authors MV and SJ thank the Council of Scientific and Industrial Research (CSIR), New Delhi for providing financial support as Junior Research Fellowship. The Authors also thank the Director NPL and Director IIT-Delhi for giving permission to present this paper.

REFERENCES

- [1]. E. Wolf, "Solution of the Phase Problem in the Theory of Structure Determination of Crystals from X-Ray Diffraction Experiments", *Phy. Rev. Lett.* **103** 075501 (2009).
- [2]. E. Wolf, "History and Solution of the phase problem in the theory of Structure Determination of crystals from X-ray Diffraction Measurements", *Advances in imaging and electron physics*, Amsterdam, Elsevier, 2010.

- [3]. W. H. Knox et al., "Spatial coherence from ducks" *Physics Today* **63** 11 (2010).
- [4]. L. Mandel, E. Wolf, *Optical Coherence and Quantum Optics*, Cambridge University Press, Cambridge, U.K.

LIDAR STUDIES ON THE OPTICAL PROPERTIES OF AEROSOLS IN THE UPPER TROPOSPHERE AND LOWER STRATOSPHERE AT A LOW LATITUDE TROPICAL STATION GADANKI (13.5⁰ N, 79.2⁰ E), INDIA

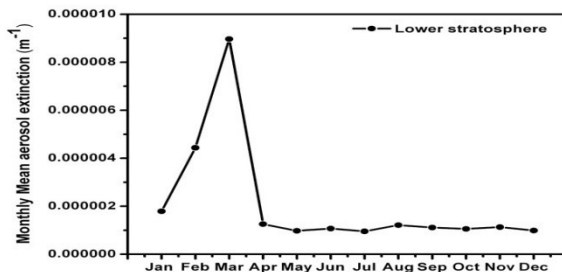
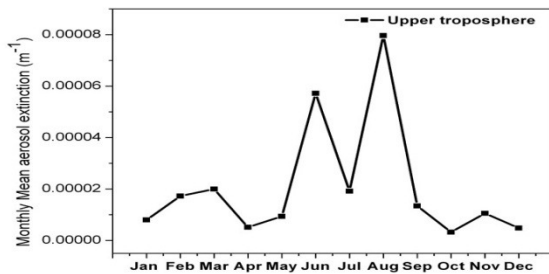
S.R Radhakrishnan¹, M.Satyanarayana¹, Leena Raj¹, V.Krishnakumar¹, Reji K Dhaman, G.S.Motty, V.P Mahadevan Pillai¹ & K Raghunath²

¹Department of Optoelectronics, University of Kerala, Kariavattom, Trivandrum-695 581, Kerala, India

²National Atmospheric Research Laboratory, Gadanki, Tirupati-517 502, India

*drsathyanarayana.malladi@gmail.com

Abstract: Knowledge of the vertical distribution of atmospheric aerosols and their optical properties are important for determining the direct and indirect radiative forcing of aerosols. Aerosols in the upper troposphere and lower stratosphere (UTLS) region are mainly due to particle formation through gas-to-particle conversion from precursor gases involving homogenous/heterogeneous nucleation, condensation and coagulation. Lidar is a useful instrument that can measure vertical distribution of extinction/ backscattering coefficient of aerosols. Vertical distribution of UTLS aerosols over the tropics and their optical and microphysical properties are not fully understood mainly because of the scarcity of observational data. As such, reliable and large data base are required on the vertical structure, optical properties, and dynamics of the aerosols to determine their radiative effects. In this chapter we present the details of the investigations carried out on the vertical structure of the aerosols in the altitude region of 10-30 km using the lidar installed at the tropical Indian station Gadanki (13.5⁰ N, 79.2⁰ E). The data obtained over a period of two years (2009 and 2010) are used in the study. Figure 1 shows the monthly mean of the UTLS aerosol extinction in the years 2009 and 2010 over the Gadanki station derived from the lidar data using Fernald's lidar inversion algorithm.



It is observed that in the upper tropospheric region the aerosol extinction coefficient values are higher during May to September period. In the lower stratospheric region the extinction values are higher in the month of January and February compared to the other months. From the above observations it is clear that there is strong monthly as well as seasonal variation in the UTLS aerosol loading.

Figure 1: Monthly mean aerosol extinction for the years 2009 and 2010 over Gadanki

INVESTIGATION OF EFFECTIVE INTERACTION AREA FOR SECOND HARMONIC GENERATION IN PHOTONIC CRYSTAL FIBER

Ritapa Bhattacharjee

Physics Division, School of Advanced Sciences, VIT University, Vellore, 632014, India

ritapabhattacharjee@vit.ac.in

Abstract: This paper presents some new designs of index guided photonic crystal fiber (PCF) for second harmonic generation (SHG) by varying the pitch and keeping air hole inclusion diameter constant for each design. We investigate the modal distribution, nonlinearity coefficient and variation of effective area of input fundamental wave and its second harmonic inside the fiber. We observe that the best result comes with fiber having pitch value as $1.6 \mu\text{m}$ where the effective areas of fundamental and its second harmonic are $2.88 \mu\text{m}^2$ and $2.52 \mu\text{m}^2$ respectively.

1. Introduction

Photonic crystal fiber (PCF) added a new flavour in recent trend of second harmonic generation (SHG). Here we investigate the effective area of fundamental and second harmonic in several designs of index guided PCF. As efficiency of SHG is inversely proportional to the effective area of interaction between fundamental and second harmonic [1], This study tries to achieve this by lowering the effective area of both the waves inside the fiber core as well as lowering the difference of effective area between them for better power transfer.

2. Modal Area and SHG

The modal area in PCF is generally calculated as follows [2]

$$A_{eff} = \frac{\left(\iint |E|^2 dx dy \right)^2}{\iint |E|^4 dx dy}$$

where E is the field distribution of the mode. Here we also investigated the mode field diameter which comes from twice the modal radius w as given $A_{eff} = \pi w^2$ and also nonlinearity coefficient as $\gamma = \frac{2\pi}{\lambda} \frac{n_{eff}}{A_{eff}}$

where γ is the nonlinearity coefficient and n_{eff} is the effective index of the mode passing through the core.

2.1 Fiber Design

Here eleven structures of index guided PCF are designed where the hole to hole distance that is pitch (Λ) varies from $1.6 \mu\text{m}$ to $6 \mu\text{m}$ and core diameter (d) is remains constant as $1 \mu\text{m}$ for all designs. Below $1.6 \mu\text{m}$ the design was not feasible and above $6 \mu\text{m}$ leakage of light occurs in cladding. Fig1. (a) gives the field distribution of fundamental and Fig.2(b) gives the field distribution of the second harmonic for $\Lambda=2\mu\text{m}$.

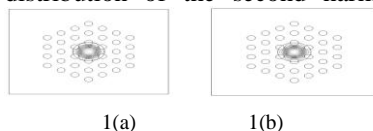


Fig 1. (a) fundamental mode distribution, (b) second harmonic mode distribution.

3. Result

Finite element method has been used for all the studies here. Also Nd:YAG range of fundamental wavelength at $1.06 \mu\text{m}$ used for all studies. The Fig. 2(a) gives the plot of modal distribution with respect to pitch variation, Fig.2(b) gives variation of nonlinear coefficient with respect to relative hole diameter ($D= d/\Lambda$) and Fig.2(c) gives variation of effective area of fundamental and second harmonic with respect to pitch.

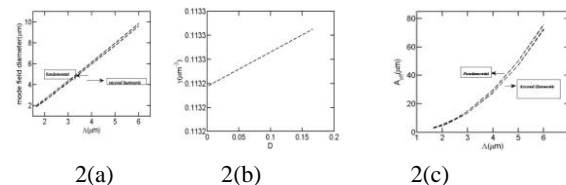


Fig2. (a) Modal diameter Vs pitch, (b) nonlinear coefficient of fundamental wave Vs relative hole diameter, (c) Effective area vs. of fundamental and second harmonic Vs fiber pitch.

From above graphs we see nonlinearity factor increases with relative hole diameter and modal distribution and effective area of interaction increases with fiber pitch. We achieved lowest area of fundamental and second harmonic as $2.88 \mu\text{m}^2$ and $2.52 \mu\text{m}^2$ which are pretty better than the designs of [2],[3] and [4]. Hence we conclude by lowering pitch we achieve reduced effective area of both fundamental and second harmonic and can expect better overlap between them for good power transfer and high efficiency of SHG.

References

- [1] Tanya M. Monro, "Broad-Band Second-Harmonic Generation in Holey Optical Fibers", IEEE Photo. Technol. Lett., **13**, 981 (2001).
- [2] Shuqin LOU et al, "Photonic crystal fiber with novel dispersion properties", Front. Optoelectron. China, **2**, 170(2009).
- [3] M. Koshiba and K. Satoh, "Structural dependence of effective area and mode field diameter for holey fibers", Optics Express, **15**, 1741(2003).
- [4] D. Chen et al, "Optical properties of photonic crystal fibers with a fiber core of arrays of sub-wavelength circular air holes: birefringence and

dispersion",Prog.inElec Mag.Res, **105**,193(2010)

A BIDIRECTIONAL DIRECTLY MODULATED RADIO OVER FIBER TRANSPORT SYSTEMS EMPLOYING SOA AND RSOA

A. S. Patra¹, A. Das¹, B. Bag¹, and Hai-Han Lu²

¹Haldia Institute of Technology, Haldia, India

²National Taipei University of Technology, Taiwan

Email: ardhendu4u@yahoo.com

Abstract: A novel directly modulated bidirectional radio over fiber transmission scheme based on Fabry-Perot Laser Diodes (FP-LD) is proposed and demonstrated to transmit baseband signal employing a semiconductor optical amplifier (SOA) and reflective semiconductor optical amplifier (RSOA) as wavelength reuse and remodulation. Good transmission performances estimated by bit error rate (BER) and eye diagram are obtained in our proposed systems. Since our proposed systems use only FP LDs as light source for down-link and reuse of wavelength by RSOA for up-link transmissions, it reveals a prominent alternative in simplicity and cost.

Keywords: *Reflective semiconductor optical amplifier, QoS, bit error rate.*

1. INTRODUCTION

In modern days communication system it is seen to be the most promising approach to build the next generation communication infrastructure with increasing the data rate remarkably than compared to currently available, particularly in optical communication systems using standard optical fiber with high Quality of Service (QoS), low Bit Error Rate (BER) and high Signal to Noise Ratio (SNR). Radio-over-fiber (ROF) transport systems, the integration of optical and wireless access networks, have potentially provided flexibility and large capacity [1, 2]. In ROF transport systems, light injection technique plays an important role to improve system performance, such as increasing the resonance frequency and side-mode suppression ratio (SMSR) of semiconductor laser diode, as well as reducing the threshold current and chirp of one [3 - 5]. In recent studies, RSOA has been used as wavelength reuse and remodulation schemes in bidirectional wavelength-division-multiplexing passive optical network and radio-over-fiber systems [6 - 8]. But, its application in analog lightwave transport systems has not been reported. RSOA, which has wavelength reuse and remodulation characteristics, is expected to have good performances in bidirectional directly modulated fiber optical transport systems. In this paper, an architecture based on FP-LD is proposed and demonstrated to transmit baseband signal with bidirectional directly modulated ROF transport system employing a semiconductor optical amplifier (SOA) and reflective semiconductor optical amplifier (RSOA) as wavelength reuse and remodulation. Transmission performances over a 40-km standard single-mode fiber (SMF) transport both for up-link and down-link were investigated. Good performances of bit error rate (BER) and clear eye diagram were

achieved in our proposed full-duplex ROF transport systems. The proposed directly modulated bidirectional simpler than the conventional externally modulated ones due to wavelength reuse and remodulation by a gain saturated RSOA. It is relatively simple to generate optical SSB signal.

2. EXPERIMENTAL SETUP

The Experimental setup of our proposed Bi-directional radio over fiber transmission scheme based on FP-LD employing a SOA and RSOA is shown in Fig.1. A free running FP LD passes through an OBPF and divided into two parts by an optical splitter. Both the parts are injected in the counter-propagation direction through two optical circulators (OCs) to two directly modulated FP LDs With 11Mbps and 20 mbps data signals. A maximum central wavelength shift of 0.003 nm/ C is needed to avoid the wavelength misalignment problem. It is important to delicately control the temperatures of FP LDs. If without temperature controller, performance results will be fluctuated in room temperature due to wavelength shift 0.003 nm/ C, resulting in large performance degradation. The wavelengths of the injected light must be accurately chosen to match two FP LD longitudinal modes and ensure that the optimal enhancement in side-mode suppression ratio (SMSR) is obtained. All 3-port OC is worth employing due to good optical characteristics including low insertion loss (~0.7 dB), high isolation (>40 dB), and environment stability. Outputs of the OCs are coupled by optical coupler and send through a SOA, a variable optical attenuator and OC for down-link Transmissions. The OC is used to separate the uplink signal. The downlink signal transmitted over 40 Km SMF and the received signal is separated by 1×2 optical splitter. One part of received signal is detected by a broadband photodiode (PD), and then

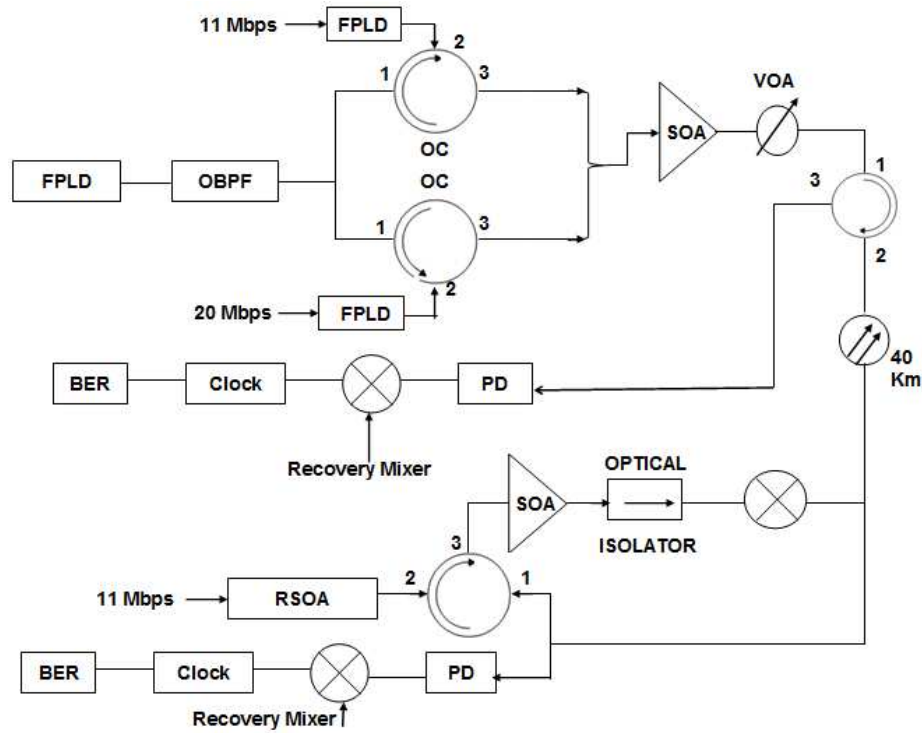


Fig.1. Experimental setup of our proposed Bi-directional transport system

applied to a demodulator and into a BER tester for BER analysis after demodulation. The other half was circulated and reused by OC and RSOA. As to up-link transmission, a RSOA with 11 Mbps data signal modulated. The uplink signal is transmitted through SOA and optical isolator. After 40 Km SMF transmissions the uplink signal is detected by a PD, and then passes through a demodulator and fed into a BER tester for BER analysis.

3. EXPERIMENTAL RESULTS

The optical spectra of the free-running FP LD before and after the OBPF are shown in Fig. 2(a) and (b), respectively. It can be seen that FP LD inherently possesses wider spectra envelope (1545-1560 nm), however, the multiple longitudinal modes have changed into two longitudinal modes characteristics after passed through the OBPF. Two wavelengths of λ_1 (1553 nm) and λ_2 (1554.1 nm) were selected for down-link and up-link light sources. In Fig. 2(b), the SMSR value is about 23 dB; when FP LD is injection-locked, the side modes of the FP LD are suppressed to be 41 dB (as shown in Fig. 2(c) & d). Injection locking was achieved effectively in an FP LD due to the fact that the SMSR value increases largely.

The gain model of SOA which explains the gain saturation phenomenon is given by [9]:

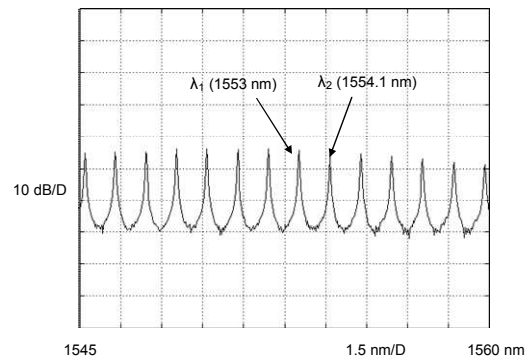


Fig. 2(a) The optical spectrum of the free-running FP LD before the OBPF.

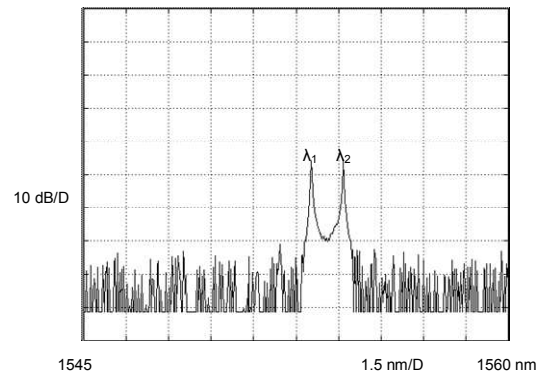


Fig. 2(b) The optical spectrum of the free-running FP LD after the OBPF.

$$G = \frac{P_{out}}{P_{in}} = \frac{G_0}{1 + P_{in} / P_{out}} \quad (1)$$

where, G_0 is the unsaturated gain, P_{in} is the input optical power, and P_{out} is the output optical power. To define the saturation optical power P_{sat} , at that power in which gain reducing to half of the G_0 . The output power ($P_{R, out}$) and optical gain (G_R) of RSOA can be expressed as:

$$P_{R,out} = RG_R^2 P_{in} \quad (2)$$

$$G_R = \frac{-(P_{sat} + P_{in}) + \sqrt{(P_{sat} + P_{in})^2 + 4RG_0 P_{sat} P_{in}}}{2RP_{in}} \quad (3)$$

where R is the reflectivity. It is obvious that, from equations (2) and (3), the $P_{R, out}$ and G_R depend on the P_{in} ; higher P_{in} leads to higher $P_{R, out}$ and lower G_R .

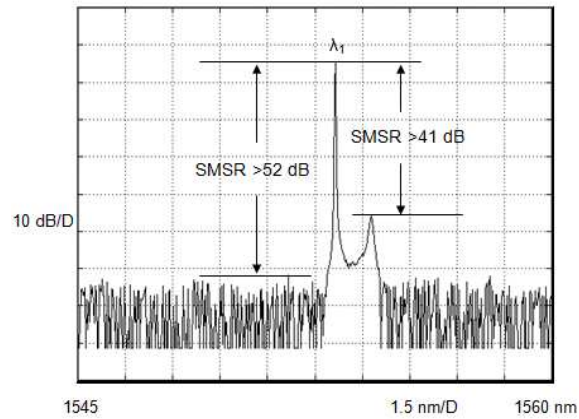


Fig. 2(c) The optical spectrum (λ_1) of the FP LD after injection-locking.

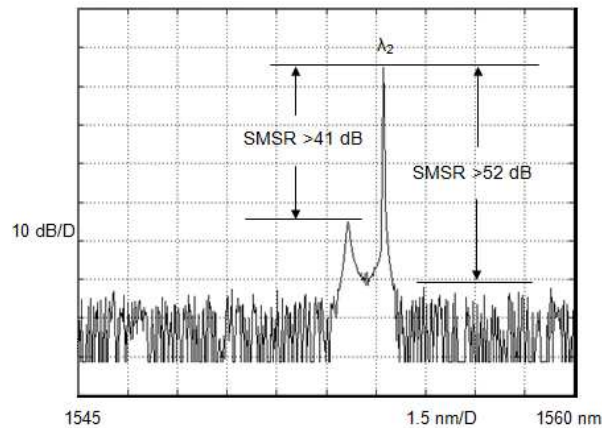


Fig. 2(d) The optical spectrum (λ_2) of the FP LD after injection-locking.

The measured down-link (λ_1) and up-link (λ_2) BER curves as a function of the received optical power level are plotted in the Fig. 3(a) and (b), respectively. For down-link transmission and at a BER of 10^{-9} , in

the free-running, the received optical power level is -23.5 dBm; with 0 dBm light injection, the received optical power level is -26.8 dBm. A 3.3-dB received optical power reduction is achieved as light injection technique is employed. For up-link transmission and at a BER of 10^{-9} , in the free-running, the received optical power level is -22.1 dBm; with 0 dBm light injection, the received optical power level is -25.2 dBm. A 3.1-dB received optical power reduction is achieved as light injection technique is employed. Injection-locked technique will reduce the threshold current of FP LD, leading to an increment of optical output power. Due to longer distance transmission, the up-link transmission exhibits power penalties of 1.4 (free-running) and 1.6 (0 dBm light injection) dB compared to down-link transmission. The clear Eye-diagram is observed in our proposed system in fig 4 (a) and (b) for free-running and light injection for down-link signal after 40 Km SMF transmission.

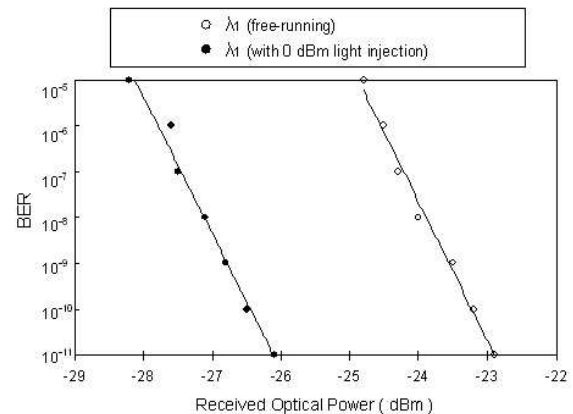


Fig. 3(a) The measured down-link (λ_1) BER curves as a function of the received optical power level.

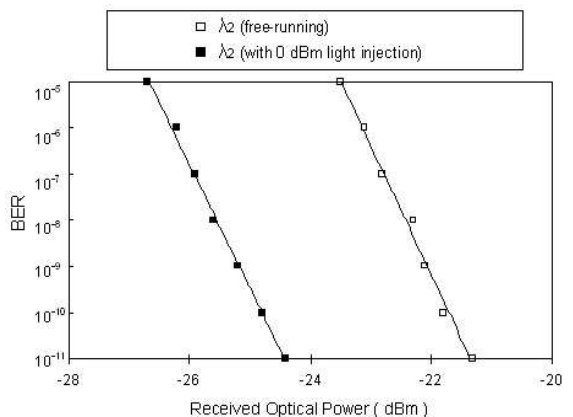


Fig. 3(b) The measured up-link (λ_2) BER curves as a function of the received optical power level.

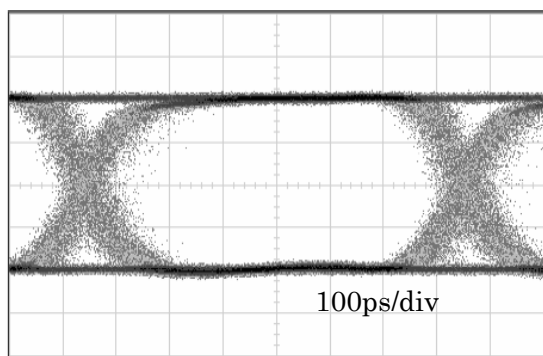


Fig. 4 (a) The eye-diagram for Free running FP LD for downlink signal after 40 Km SMF transmission.

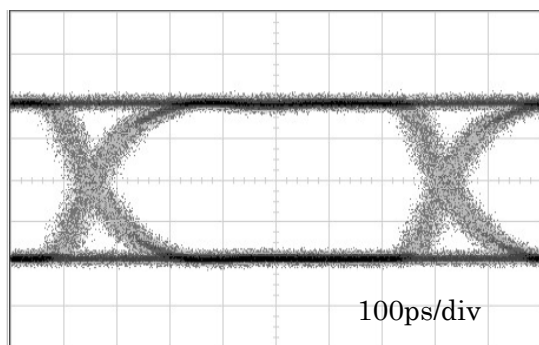


Fig. 4 (b) The eye-diagram for injection locked FP LD for downlink signal after 40 Km SMF transmission.

4. CONCLUSION

A bidirectional directly modulated fiber optical transport system based on injection locking laser diodes is proposed and demonstrated employing a SOA at transmitting site and RSOA at the receiving site. Our proposed scheme is suitable for long-haul bidirectional transmission over a 40 K.M. single-mode fiber (SMF). The low bit-error-rate (BER) and clear eye diagram is observed in our system.

5. ACKNOWLEDGEMENT

The authors would like to thank the support from the National Taipei University of Technology, Taiwan and Haldia Institute of Technology, Haldia, India.

6. REFERENCES

- [1] Stohr, K. Kitayama, and D. Jager, "Full-duplex fiber-optic RF subcarrier transmission using a dual-function modulator/ photodetector," *IEEE Trans. Microwave Theory Tech.*, vol.47, pp. 1338-1341, 1999.
- [2] H-C. Kwon, Y-Y. Won, and S-K. Han, "Bidirectional SCM transmission using a noise-

suppressed Fabry-Perot laser diode and areflective semiconductor optical amplifier in WDM/SCM-PON link," *IEEE Photonics Technology Letters*, vol. 19, pp. 858-860, 2007.

- [3] Olsson, N. A., Temkin, H., Logan, R. A., Johnson, L. F., Dolan, G. J., Van Der Ziel, J. P. and Campbell, J. C. Chirp-free transmission over 82.5 km of single mode fibers at 2 Gbit/s with injection locked DFB semiconductor lasers. *J. Lightwave Technol.* Vol. 3, pp. 63–66, 1985.
- [4] Lang, R. Injection locking properties of a semiconductor laser. *IEEE J. Quantum Electron.* Vol. 18, pp.976–983, 1982.
- [5] Mogensen, F., Olesen, H. and Jacobsen, G. Locking Conditions and Stability Properties for a Semiconductor Laser with External Light Injection. *IEEE J. Quantum Electron.* Vol. 21, pp. 784-793, 1985.
- [6] K. Y. Cho et. al, "Effects of reflection in RSOA-based WDM PON utilizing remodulation technique," *J. Lightw. Technol.*, Vol. 27, pp. 1286, 2009.
- [7] H. C. Kwon, Y. Y. Won and S. K. Han, "Bidirectional SCM transmission using a noise-suppressed Fabry-Perot laser diode and a reflective semiconductor optical amplifier in a WDM/SCM-PON link," *IEEE Photon. Technol. Lett.*, Vol. 19, pp. 858- 860, 2007.
- [8] J-M. Kang, and S-K. Han, "A novel hybrid WDM/SCM-PON sharing wavelength for up-and down-link using reflective semiconductor optical amplifier," *IEEE Photonics Technology Letters*, vol. 18, pp. 502-504, 2006.
- [9] S. I. Pegg, M. J. Fice, M. J. Adams, and A. Hadjifotiou, "Noise in wavelength conversion by cross-gain modulation in a semiconductor optical amplifier," *IEEE Photon. Technol. Lett.*, vol. 11, pp. 724 -726, 1999.

Topic code: OTH

presentation preference: poster

TUNNELING EFFECTS ON OPTICAL SOLITONS IN AN ERBIUM DOPED FIBER

M.S.MANI RAJAN¹, A.MAHALINGAM²

Anna university, chennai -600025.

¹senthilmanirajanofc@gmail.com, ²mahabs22@yahoo.com

Abstract: We consider optical pulse propagation in an Erbium doped inhomogeneous fiber which is governed by a system of Generalized Inhomogeneous Nonlinear Schrödinger Maxwell-Block (GINLS-MB) equation. Two soliton propagation is observed analytically by means of deriving associated Lax Pair and the soliton solutions are obtained using Darboux Transformation. We investigate the nonlinear tunneling effect by choose the dispersion and nonlinear parameter.

1. INTRODUCTION

Optical soliton is one of the most important innovations in the area of communication technology. The principle of solitons in an optical fiber is based on the perfect balance between the Group Velocity Dispersion (GVD) and the Kerr effect. The GVD causes the temporal broadening of the optical pulse, due to the frequency dependent refractive index and the Kerr effect is the change in refractive index due to pulse intensity [1].

To avoid the problems caused by the electronic amplifiers, all-optical communication systems involving Erbium-Doped Fiber Amplifiers (EDFA) are presently employed. When the core of the optical fiber is doped with erbium, the wave propagation has both effects due to silica and Er impurities.

2. GINLS-MB SYSTEM

Here, we propose GINLS-MB system which explains the optical pulse propagation in an inhomogeneous doped fiber with loss and time dependent modulation as given below:

2.1 Equation

$$i Q_z + \frac{D(z)}{2} Q_{tt} + R(z) |Q|^2 Q + F_1(z, t) Q + F_2(z, t) Q - 2i \langle p \rangle = 0 \quad (1)$$

where $Q(z, t)$ is the complex envelope of the field, $p(z, t)$ is the measure of the polarization of the resonant medium.

2.2 Solution

We solve the Eq.(1) to get Solution) by using Darboux transformation based on the Laxpair [2]

$$Q(z, t) = 2 \alpha_1 \sqrt{\frac{D}{R}} \operatorname{sech} h(2 A) \exp(i B) \quad (2)$$

$D(z)$ and $R(z)$ are dispersion, nonlinearity respectively.

3. PLOTS AND DISCUSSIONS

In the following plot and qualitative analysis, we can choose some special values for parameters in solution (2). For example we choose the dispersion and nonlinearity parameter as follows to describe the nonlinear tunneling effect on solitons.

3.1. Nonlinear tunneling

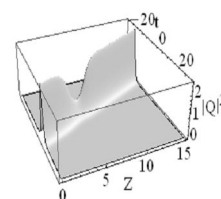
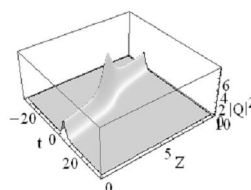
Research has shown that the soliton can pass lossless through the barrier under special conditions which depend on the ratio between the solitonic amplitude and the height of the barrier.

3.2. Dispersion and nonlinear barrier

For first case, we consider dispersion parameter $D(z)$, Nonlinear parameter $R(z)$ as follows.

$$D(z) = 1 + 2.0 \operatorname{Sech}(z - 5.0)^2 \quad \text{And} \quad R(z) = 1 \quad (3)$$

$$D(z) = 1 \quad \text{And} \quad R(z) = 1 + 2.0 \operatorname{Sech}(z - 5.0)^2 \quad (4)$$



1.(a) one soliton plot for dispersion barrier and (b) nonlinear barrier.

Eqs.(3) and (4) represents dispersion and nonlinear barrier for solution of Eq.(1). In Eq.(3) and (4) numbers 2.0 and 5.0 are denotes the amplitude and position of the barrier respectively. Solitonic tunneling may create a new field of applications of spatial solitons as the tunneling effect makes it possible to design new kinds of all-optical switches and logic circuits.

REFERENCES

- [1] G.P. Agrawal, *Nonlinear Fiber Optics*, fourth ed., (Academic Press, New York, 1995).
- [2] R. Hao, L. Li, Z. Li, W. Xue and G. Zhou, "A new approach to exact soliton solution and soliton interaction for the NLS equation with variable coefficient," *Opt. Commun.* **236**, 79 (2004).

Topic: OTH

Preference: Poster

RESPONSE OF A HUMAN EYE TO PERIODIC BAR TARGETS IN THE PRESENCE OF SCE-I

P K MONDAL and SUMIT GHOSH
School of Optics, C-31, Tirumala Towers, Hyderabad-500080.

Email: saisum@hotmail.com

Abstract: The cones and the rods of the retina on the human eye have directional sensitivity. We have analytically determined the optical transfer function values and hence studied the response to periodic bar patterns by a human eye for all transmitted spatial frequencies in the presence of SCE-I.

Keywords : Human visual optics, Fourier optics, Apodization etc.,

1. Introduction

One of the path-breaking discoveries of the 20th century in the field of visual optics is the discovery that highlights the active role of the retinal receptors in the acceptance of energy by the photo-transductive process. While trying to estimate the size of an observer's pupil indirectly by measuring the apparent brightness of a light target for various pupil diameter, Stiles and Crawford found that large pupils were not nearly as effective in raising the brightness of a constant-luminance target as might have been expected if there is passive summation of energy from all zones of the pupil. This sensitivity of a human eye to the angle of incidence of light on the retina is described as the Stiles–Crawford effect of the first kind [1] to be referred to as SCE-I in what follows in this paper. The responsible mechanism has been identified with the wave-guide nature of the photoreceptors [2]. This leads one to believe that the various effects arising out of the SCE-I phenomenon can be interpreted as some sort of apodizing [3] action of a human eye.

In the present paper we have analytically studied the incoherent response of a general periodic bar pattern and have also calculated the modulations in the images along with the equivalent sine wave response for each transmitted frequency.

2. Theory

Like any optical system, in our case, the human eye, behaves as a linear, passive, low-pass filter, the transmittance of spatial frequencies from the object to the image plane can be investigated by applying Fourier techniques.

Each harmonic component of the bar wave objects are attenuated by the response function corresponding to that frequency. The irradiance distribution in the image is given by

$$B'(u', v') = (a - b + 2b\alpha) + \frac{4b}{\pi} \sum_{n=1}^{\infty} \frac{\text{Sin}(n\pi\alpha)}{n} T_n(n\omega, 0) \text{Cos}(n\omega u') \quad \dots(1)$$

where $T_n(x, y)$ is the normalized incoherent transfer function of the optical system.

An important parameter for assessing the optical system image quality is the modulation. The contrast in the final images for the two types of targets is given by

$$M = \frac{B'_{\max} - B'_{\min}}{B'_{\max} + B'_{\min}} \quad \dots(2)$$

Here B'_{\max} and B'_{\min} being the maximum and minimum intensities respectively in the images.

Results and Discussions:

Eq (1) gives the intensity distribution in the images of a periodic bar targets, formed by a human eye in the presence of SCE-I. In order to use these expressions for determining the intensity distributions in the images, it is necessary to know $T_n(n\omega, 0)$, the normalized incoherent transfer function of the human eye in the presence of SCE-I. We [4] succeeded in evaluating the values of $T_n(n\omega, 0)$, for various values of the fundamental frequency ω in the transmitted band of allowable spatial frequencies $0 \leq \omega \leq 2$. We have utilized the values of $T_n(n\omega, 0)$ for our present study.

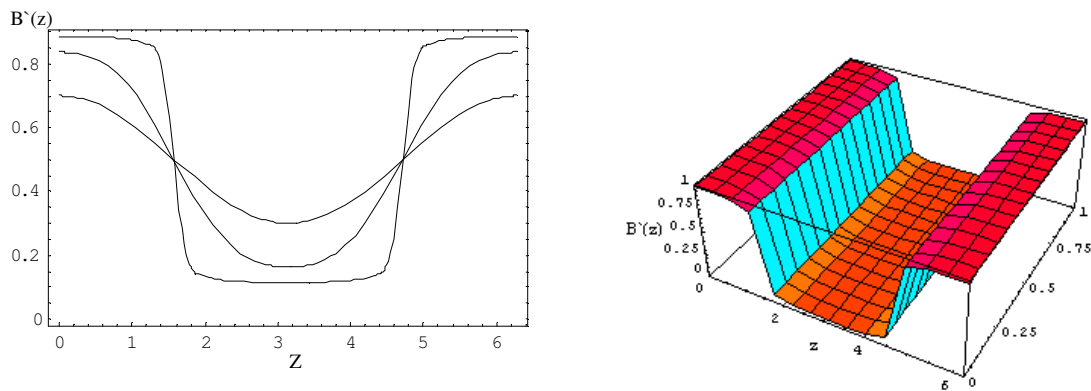


Figure 1 – 2D and 3D Intensity distributions in the images of periodic bar pattern

In Figure 1, we have shown that the intensity distributions in the images of periodic bar targets for $\alpha=0.1, 0.5, 1.0$ and for $\omega=0.1, 0.5, 1.0$. The intensity distributions have been shown over a complete cycle of 0 to 2π radians. It is not difficult to realize that the intensity distribution pattern very nearly follows a bar pattern for $\omega=0.1$. With higher values of ω , the situation will degrade further as the number of transmitted frequencies will be less and less.

The modulations in the images have been evaluated by using Eq (2). The results obtained have been shown in Figure 2 for various values of ω and α . The response of the eye to these targets is in accordance with the discussions made above. For lower values of both ω

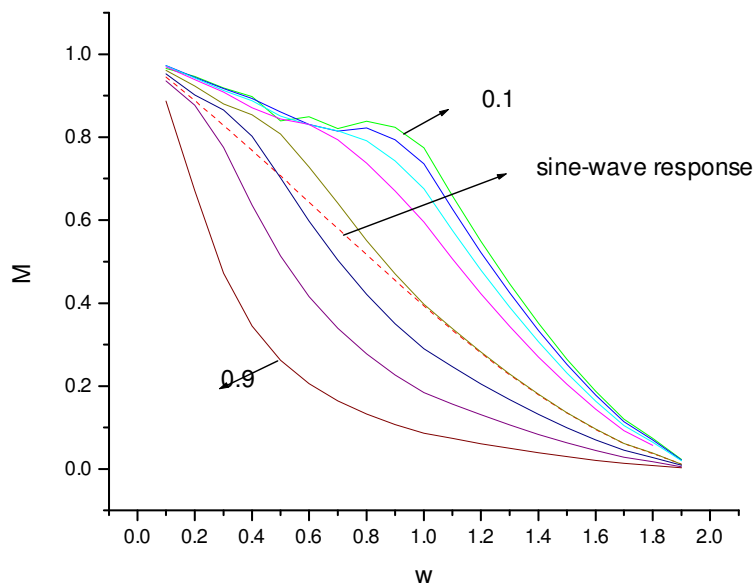


Figure 2 – General periodic bar response of a human eye in presence of SCE-I

and α , the response of the eye is better than that for higher values of ω and α . Also of interest is the value of α for which a periodic bar object responses are similar to the sine wave response. The equivalent sine-wave response values are found to be around 0.60. It is envisaged that our present study will lead to proper interpretation of numerous results obtained in the experimental side. Finally as the response of a human eye to various shapes of periodic targets is considered an important image-quality assessment parameter, it is hoped that this present study will contribute to the subject of the assessment of the performance of a human eye.

Acknowledgements:

The author expresses his deep sense of gratitude to Prof. P K Mondal for his guidance and interest in the present work.

4. References:

- [1] W.S. Stiles and B.H. Crawford, Proc. Roy. Soc., London, B112,1933, pp 428-450.
- [2] J.M.Enoch and F.L. Tobey Jr., "Vertebrate Photoreceptor Optics", Springer-verlag, Berlin, 1981.
- [3] D. A. Atchison, A. Joblin, G.J.Smith, J. Opt. Soc Am. A., 9 , 1998, pp 2545-2551.
- [4] S.Subramanyam, Sumit Ghosh, Pronab Mondal, J.P.A.P, 16, 3, 2004, pp 1-12.

UV-VIS UP-CONVERSION LUMINESCENCE OF Tm^{3+}/Yb^{3+} DOPED MODIFIED YTTRIUM-GERMANIUM-ALUMINIUM-PHOSPO-SILICATE GLASS BASED OPTICAL FIBERS UNDER EXCITATION AT 980 NM

Arindam Halder^{1*}, Mukul C. Paul¹, Mrinmay Pal¹, Shyamal Das¹ and Shyamal K. Bhadra¹
¹Fiber Optics and photonics Division, Central Glass and Ceramic Research Institute (CGCRI),
Council of Scientific & Industrial Research (CSIR), Jadavpur, Kolkata – 700 032, India.
Email: * arindam.cgcri@gmail.com

Abstract: Strong upconversion luminescence [UC] at 364nm, 474nm, 650nm and 790nm are reported for Tm+Yb codoped modified yttrium-germanium-aluminium-phospo-silicate (YGAPS) glass based optical fibers under excitation at 975nm. The theoretical study for spectral process was done based on photo-physical kinetic mechanisms to explain the originality of such fluorescence bands.

1. INTRODUCTION

480nm blue upconversion emission was reported earlier [1] in Tm^{3+} -doped $SiO_2-P_2O_5$ channel waveguides pumped by 1.064 μm infrared along with 650nm and 800nm emission. In this work 364nm, 474nm, 650nm, 790nm intense up-conversion luminescences are reported into thulium and ytterbium codoped, YGAPS glass based large core optical fiber. This modified glass host shows efficient energy transfer from Yb to Tm under 975nm core pumping excitation of Yb by conventional diode laser (L) with fiber pig tailed. Upconversion process is observed to occur in two ways, one in energy transfer upconversion (ETU) between Yb and Tm ions, other in cross relaxation (CR) mechanism between Tm ions [2]. It is observed that 790nm peak is mainly overlapping of two fluorescence lines of 790nm and 804nm wavelengths.

2. EXPERIMENTS

2.1 Material Analysis

Yb and Tm co-doped YGAPS core glass based multimode optical fibres have been fabricated by the modified chemical vapour deposition (MCVD) process, followed by solution doping (SD) techniques. The dopants' compositions of prepared optical preforms are given in Table-1. An alcoholic solution of $TmCl_3$, $YbCl_3$, YCl_3 , $AlCl_3$, P_2O_5 of Alfa standard was used for solution soaking process. The concentrations of dopant ions are changed into each solution during solution doping process to make variation of dopants concentration into preforms. In Fig-1, cross section of LCTP-2 fiber is shown. Preform profiles have been analyzed by preform analyzer (PKL 2600, Photon Kinetics, USA) to generate RI profiles for calculation of numerical aperture (NA) (calculated values given into Table-1).

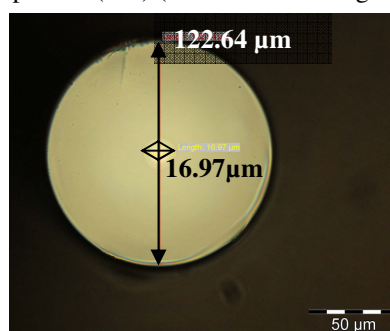


Fig-1:
Cross
sectional
view of
LCTP-2
fiber

Table1: The details of optical fiber samples.

Sample no.	Concentration of dopants with respect to solution	Yb and Tm ratio (Yb:Tm)	Core diameter	N.A.
LCTP-1	0.03(M) $YbCl_3$, 0.015(M) $TmCl_3$, 0.15(M) $AlCl_3$, 0.03(M) YCl_3 and 0.15(M) P_2O_5	2:1	12.83 μm	0.0766
LCTP-2	0.03(M) $YbCl_3$, 0.02(M) $TmCl_3$, 0.3(M) $AlCl_3$, 0.03(M) YCl_3 and 0.15(M) P_2O_5	1.5:1	16.97 μm	0.1327
LCTP-3	0.03(M) $YbCl_3$, 0.03(M) $TmCl_3$, 0.3(M) $AlCl_3$, 0.03(M) YCl_3 and 0.15(M) P_2O_5	1:1	14.684 μm	0.2102

To get a clear view about probable distribution of dopants at the core glass, surface mapping is done by scanning electron microscopic [SEM] analysis of those preforms. The mapping of elements at the core of LCTP-2 preform's surface signifies the probable distribution pattern of dopants along cross section (Fig.-2). The white spots are represented the probable dopant centers at the surface. It clearly indicates that the dopants are distributed almost homogeneously into core.

2.2 Spectral Analysis

Into Fig.-3 UC emission spectra of LCTP-1, 2, 3 fiber samples are displayed under excitation by 975nm 'L' at 140mW pump power applying core pumping techniques. At 975nm excitation, Yb^{3+} ions are

directly excited by applying energy. At the same time, Tm^{3+} ions are indirectly excited by resonance energy transfer [ET] process from excited Yb^{3+} ions [2, 3]. Maximum energy transfer from Yb^{3+} to Tm^{3+} ions are obtained at 975 nm. Strong blue and red UC luminescence has been seen through naked eye, scattering out from LCTP fibers surface. Emission spectra of UC luminescence of LCTP fiber samples have been analysed by splicing 42cm length of active fiber with fiber pig tail of diode laser for efficient core pumping activation. The emission spectra have been taken by FS920 model spectrometer of Edinburg instrument along transverse direction. Four UC luminescence peaks at 364 nm, 474 nm, 650 nm, 790 nm are obtained for Tm^{3+} (Fig-3) at room temperature.

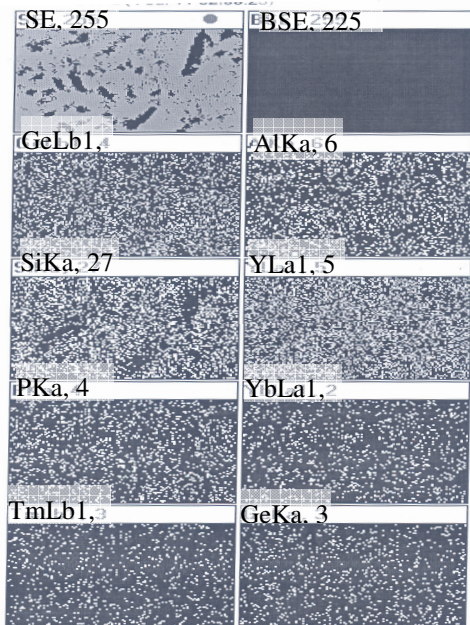


Fig-2: Surface mapping of doping elements within the core region of LCTP-2 preform.

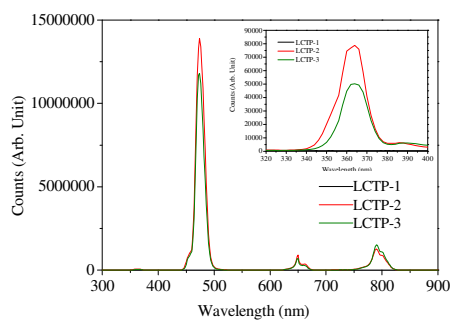


Fig-3: Emission spectra of all fibers pumped at 140 mW under 975 nm excitation. Inset 364 nm peak is displayed.

790 nm fluorescence band is found to be overlapping of two closely spaced fluorescence lines i.e. 790 nm and 804 nm. Using Gaussian multi peaks fitting techniques they are separated (Fig-4). 364 nm fluorescence band is generated from YGAPS glass host which seems to be an excellent prospect of using YGAPS glass for Tm laser system.

3. RESULTS AND DISCUSSION

Y_2O_3 was used to decrease the phonon energy of YAGPS glass than that of normal phosphate glass. GeO_2 , Al_2O_3 and Y_2O_3 also serve to distribute Yb and Tm homogeneously into the core glass matrix for modifying the glass structure. It is observed that up to a certain concentration of Y^{3+} i.e. 0.03(M) with respect to solution concentration this host is optically transparent. The probability of radiative emission and energy transfer efficiency are increased for low phonon energy host.

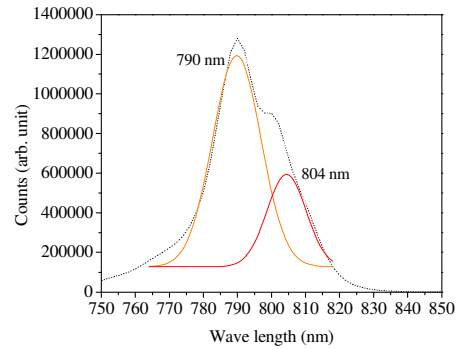


Fig-4: Gaussian multiple peaks fit for 790nm peak (in dotted line) of LCTP-2 fiber at 140 mW excitation power shows two overlapping peaks at 790nm (in orange line) and 804nm (in red line).

With Yb ions excitation at 975 nm by 'L', an electronic transition occurred from ground $^2F_{7/2}$ to excited $^2F_{5/2}$ energy level of Yb ions. At the time of deexcitation of Yb, a multisteps non radiative resonance energy transfer is occurred from Yb to Tm [4]. The excitation to upper energy state of Tm ions due to energy transfer by Yb is assigned as ETU process (Fig-5). Another energy transfer is found between excited Tm ions i.e. CR process (Fig-6) [1, 2].

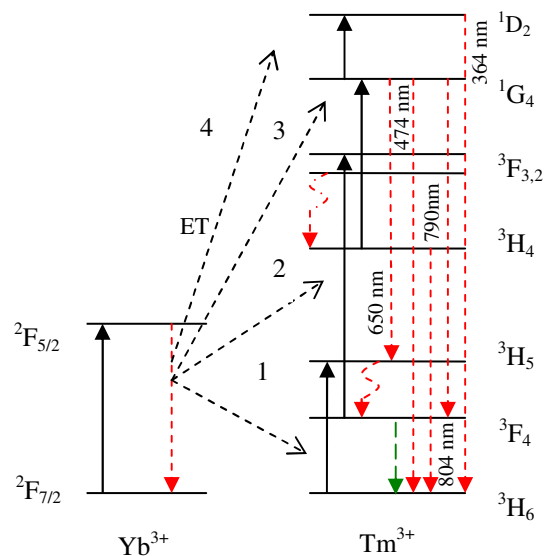


Fig-5: Energy diagram of Yb^{3+} and Tm^{3+} system for ETU mechanism, showing Yb^{3+} to Tm^{3+} energy transfer (black dotted arrow), absorption (black solid arrow), luminescence emission (red dotted arrow), nonradiative emission (waving dotted red arrow) and expected $2\mu m$ laser emission (green dotted arrow) [1, 2].

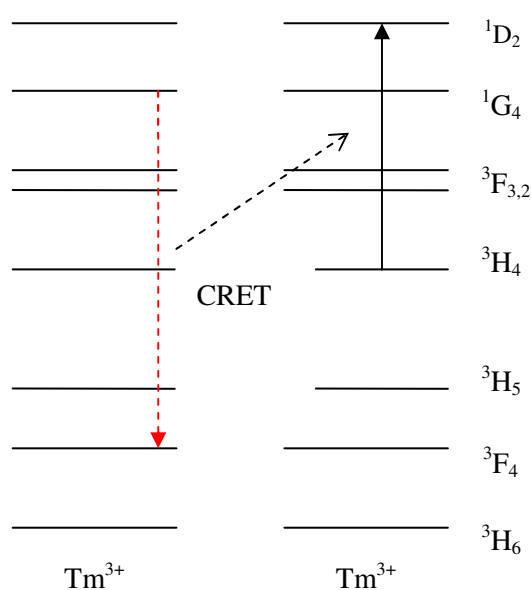


Fig-6: Energy diagram of Tm^{3+} - Tm^{3+} CRET process, showing emission (red dotted arrow), absorption (black solid arrow) and CRET (black dotted arrow) [1, 2].

Following photophysical kinetic mechanism the ETU is explained. The complete excitation of Tm ions is occurred through a four steps resonance energy transfer process. For each step, there is needed an Yb to Tm resonance energy transfer (ET). Due to first ET an electronic transition from $^3H_6 \rightarrow ^3H_5$ state of Tm ion is occurred. Then through a nonradiative multiphonon emission, excited Tm ions come at metastable 3F_4 energy state. At that state, Tm ion again accepts another ET from Yb and excited from $^3F_4 \rightarrow ^3F_{3,2}$ state. From $^3F_{3,2}$ state via another multiphonon emission excited Tm ions come to metastable 3H_4 state. The third ET from Yb, is caused an electronic transition of $^3H_4 \rightarrow ^1G_4$ state of Tm ion. Receiving fourth ET from Yb, the excitation of Tm occurred via $^1G_4 \rightarrow ^1D_2$ electronic transition. The four UC luminescence lines are observed due to following electronic transition process (Fig-3) [2].

Electronic transition	Luminescence peak
$^1D_2 \rightarrow ^3H_6$	364 nm
$^1G_4 \rightarrow ^3H_6$	474 nm
$^1G_4 \rightarrow ^3F_4$	650 nm
$^1G_4 \rightarrow ^3H_5, ^3H_4 \rightarrow ^3H_6$	790 nm (790 nm and 804 nm)

The 790 nm band is an overlap of 790nm and 804nm bands (Fig-5).

For ETU the following mechanism is proposed:

- $Yb(^2F_{7/2}) + h\nu_{975\text{ nm}} \rightarrow Yb(^2F_{5/2}) \rightarrow Yb(^2F_{7/2}) + ET$
- $Tm(^3H_6) + ET \rightarrow Tm(^3H_5) \rightarrow Tm(^3F_4) + \Delta$

- $Tm(^3F_4) + ET \rightarrow Tm(^3F_{3,2}) \rightarrow Tm(^3H_4) + \Delta$
- $Tm(^3H_4) + ET \rightarrow Tm(^1G_4) + h\nu_{804\text{ nm}}$
- $Tm(^1G_4) + ET \rightarrow Tm(^1D_2) + h\nu_{650\text{ nm}} + h\nu_{474\text{ nm}} + h\nu_{790\text{ nm}}$
- $Tm(^1D_2) \rightarrow h\nu_{364\text{ nm}}$

Through a detailed analysis according to photo physical kinetics, it is find that the following relationship holds between emission intensity of peaks (I) and absorbed pump power (P) i.e.

$$I \propto P^n \quad (1)$$

Where 'I' is calculated by integrated peak area for a particular emission peak at a particular absorb pump power 'P'. A double logarithm linear fit plot of I vs P gives slope value 'n'. This n represents the ET pulse count for excitation of Tm ion up to corresponding energy state from which the emission is occurred through ETU mechanism.

Now according to equations (1), double logarithmic plots of intensities of Tm luminescence at 364 nm (for 1D_2), 483 nm (for 1G_4) 790nm (for 1G_4) and 804 nm (for 3H_4) vs P are generated for samples LCTP-2 and LCTP-3, at which spectral intensities shows quite good (Fig-7). The slope values, slope error and statistical linear fitting accuracy factor 'R²' values are given at Table-2.

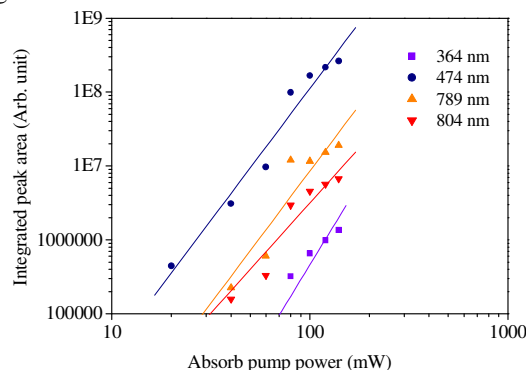


Fig-7: Double logarithm linear fit plot for all peaks for LCTP-2 fiber.

Table2 : Details data of double logarithmic linear plot.

Fiber name	Wave length of Tm luminescence (nm)	Slope value	Slope error	R ² value
LCTP-2	364	4.39	± 0.8505	0.9482
	474	3.57	± 0.2998	0.9828
	790	3.58	± 0.4142	0.9681
	804	2.98	± 0.2944	0.9765
LCTP-3	364	2.10	± 0.0974	0.9957
	474	1.68	± 0.0604	0.9968
	790	1.34	± 0.0318	0.9986
	804	1.15	± 0.0319	0.9981

From the linear fit plot (Fig-7) and data given in Table-2, for 42 cm long LCTP-2 fiber, excitation upto 140 mW input pump power, 364 nm and 483 nm luminescences' slope values are always found to be around four and three respectively. The calculated slopes correspond to 790 nm and 804 nm lines, three and two respectively. These results clearly demonstrated the role of ETU mechanism into the spectral process of Yb-Tm codoped system. Though from 1G_4 level, 650 nm is also possible, but it is not considered for this count. The reason to neglect 650nm is that, via this emission Tm ions do not come to ground state. So it is treated as a hot band.

In case of LCTP-3 fiber with 42 ± 20 cm length and excitation up to 140mW pump power, the slope value of those luminescence are come out in between 2.10 to 1.15. From literature [2] it is found that this decrease of count happened due to Tm-Tm CR effect. Tm-Tm cross relaxation energy transfer [CRET] occurred between two excited Tm ions (Fig-6). According to Tm-Tm CR mechanism, an ET occurred from $^1G_4, ^3F_4 \rightarrow ^3H_4, ^1D_2$ energy states between two nearby Tm ions in excited state ET. For samples with high Tm concentration, Tm-Tm distances are found in a range, where an excited Tm ion can easily transfer its energy to another nearby Tm ions. Not only for concentration, if the input pump power is high, the linearity of double log plot is destroyed. It is found that excitation of Tm, at high power, are occurred obeying both ETU and CR mechanism. For LCTP-3 fiber CR is found due to the concentration effect of Tm ions. Thus it can be assumed that, all the metastable states of excited Tm ions exist into a dynamic equilibrium. The CRET is always happened associated with ETU. Only the $^1G_4, ^3F_4, ^3H_4$ and 1D_2 energy states are directly involved into that process. The population of 3F_4 state is not affected by CRET and it is treated as ground state for this process. Applying photo physical kinetic path it is found that:

$$I \propto N_{T1} P^{n-1} \quad (2)$$

Where, N_{T1} is population of 3F_4 energy state of excited Tm ions at dynamic equilibrium condition. Here it is found that ET count is one less than that of ETU for UC emission. Not only so, this equation suggests a non linearity for CRET process. As ETU and CR are found to happen associatively, the exact slope value can't be obtained by double log linear fit plot. This effect clearly demonstrated into the slope values for LCTP-3 fiber (Table-2).

From the above expression it can also inferred that the population of upper excited states are depended on the population of 3F_4 i.e. N_{T1} at the moment of CRET. So equations can't be totally explained with the help of the double log plot. The less slope count only signifies the existence of CRET and ETU jointly into the spectral process.

4. CONCLUSION

Yb, Tm co-doped YGAPS glass based optical fibers are acted as a good wave guide as well as efficient fluorescence source in comparison with normal phosphate or silica glass hosts. The energy transfer from Yb to Tm is obtained appreciably high in this modified YGAPS host fibers at room temperature. Four distinct up-conversion luminescences are observed in UV-visible region from modified YGAPS glass based optical fibers. Detailed photophysical kinetic studies for up-conversion luminescence mechanism clearly explain the existence of ETU and CR throughout the spectral process. The 790 nm band is found to overlap of 790 nm and 804 nm bands. 364 nm emission band occurs from 1D_2 level of Tm ions. The LCTP-2 fiber can be used to make a 474nm tunable optical fiber blue light source, for various applications.

ACKNOWLEDGEMENT

The authors acknowledge the financial assistance from DST and CSIR, Govt. of India. AH is also thankful to CSIR, India for awarding CSIR-NET fellowship. They also thank Prof. Indranil Manna, Director, CGCRI for his support and encouragement. The authors also acknowledge to the staff members of the SEM Division, CGCRI for their help to get elemental mapping data of surface of core of preform. The authors are grateful to the other staff members of the Fiber Optics and Photonics Division, CGCRI for their help and co-operation.

REFERENCES

- [1] D. N. Messias, M. V. D. Vermelho, M. T. de Araujo, A. S. Gouveia-Neto, and J. S. Aitchison, , *IEEE J. Quant. Elec.*, **38(12)**, 1647-1650 (2002).
- [2] F. Pandozzi, F. Ventrone, J. C. Bayer, R. Naccache, J. A. Capobianco, A. Speghini and M. Bettinelli, *J. Phys. Chem. B*, A-F (2005).
- [3] B. Zhou, H. Lin, and E. Y. B. Pun, *Opt. Express*, **18**, 18805-18810 (2010).
- [4] A. S S de Camargo, I. A A Terra, L. A. de O Nunes and M S. Li, *J. Phys-Condens. Mat*, **20**, 255240(1-6) (2008).

DESIGN OF SEGMENTED CLADDING FIBER FOR FEMTOSECOND-PULSE LASER BEAM DELIVERY

Babita* and Vipul Rastogi

Department of Physics, Indian Institute of Technology Roorkee, Roorkee 247 667, India

*Email: babitaphy@gmail.com

Abstract: Fiber delivery of ultra-short femtosecond (fs) pulses is constrained by nonlinear distortions accumulated during pulse propagation. We circumvent this problem with a segmented cladding fiber (SCF) design. We numerically demonstrate the possibility of propagating 100-fs pulse with peak power 56 kW in the LP_{01} mode with $A_{\text{eff}} = 1943 \mu\text{m}^2$ and dispersion $= +21.6 \text{ ps/nm/km}$ at 1550-nm wavelength. Distortion free propagation of the secant-hyperbolic pulse is achieved by keeping ratio of dispersion length to nonlinear length very close to 1.

1. INTRODUCTION

Ultra-short pulse (USP) lasers find applications in micro-machining, laser ablation of solids [1], femtochemistry [2], multiphoton fluorescence microscopy, terahertz generation and detection [3], and frequency combs [4]. Advancements in high-power fiber amplifiers and lasers, and specialty optical fibers have opened new doors for generation of USPs [5,11]. Pulse energy and power from amplified fiber laser system now compete in performance with conventional bulk-optic based USP systems. The inherently flexible nature of such lasers make them attractive to fulfill the present laser source requirements, and to scale in performance, form factor, and cost in order to keep pace with industrial growth. Apart from generation of USPs through fiber-based lasers, transport of high energy USPs through optical fibers has also found importance in various applications. Fiber delivery of USPs gives much flexibility for laser integration and allows easy access to otherwise inaccessible regions. However, propagation of USP through small core standard silica fiber leads to significant nonlinear effects and results in distortion of the pulses. To circumvent this problem researchers have used specialty fibers such as photonic crystal fibers (PCFs) or photonic band gap fibers [5, 9], OmniGuide fibers [6], multi-mode high dispersion fibers [11], higher-order mode fibers [10], and rigid glass rod fibers [7]. Glass rod has drawn much attention because of large mode area with low susceptibility to mode coupling. However, these structures are not suitable for long length devices because of difficulty in compact packaging. PCFs can be designed with large differential leakage loss between fundamental mode (LP_{01}) and LP_{11} mode, and therefore, can give higher modal purity at the output. However, modal coupling remains an issue with the PCFs [8]. The largest mode area reported in PCFs is approximately $1400 \mu\text{m}^2$. Hollow core photonic band-gap fibers can be the promising choice because optical nonlinearities are reduced by a factor of 1000 compared with silica-core fibers. However, this technology is costly and is susceptible to

polarization mode dispersion. The guidance of laser beam through the hollow core fiber also negates the possibility of constructing a distributed amplifier by incorporating rare earth dopants. Recently, the higher-order-mode (HOM) fibers with very large mode area and low susceptibility to mode coupling emerged for USP delivery, however they require selective higher-order-mode excitation using a long-period grating [8]. In this paper we propose a design of segmented cladding fiber (SCF) for delivery of high energy fs-pulses through the fundamental mode of the fiber. The design has low susceptibility to mode coupling, leaky higher-order modes except LP_{11} . We numerically demonstrate the distortion-free propagation of 100-fs 56-kW peak power laser pulses over 3.3-m length of the fiber with mode area of about $1946 \mu\text{m}^2$.

single mode operation appears to be a viable option for USP delivery.

2. FIBER DESIGN AND ANALYSIS

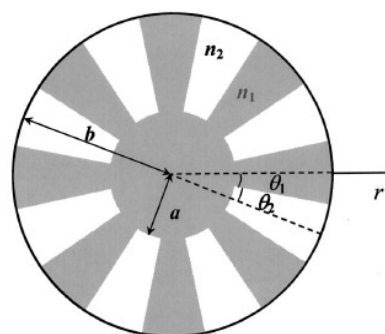


Fig.1 Transverse cross section of SCF

The schematic of the transverse cross section of the fiber is shown in Fig. 1. An SCF is characterized by uniform guiding core ($0 < r < a$) of refractive index n_1 and specially designed cladding having alternate high index medium (n_1) of angular width ($2\theta_1$) and low index medium (n_2) of angular width ($2\theta_2$). The period

and the duty cycle of segmentation are given by $\Lambda=2\theta_1+2\theta_2$ and $\gamma =2\theta_2/\Lambda$ respectively. We have analyzed the structure by using well established transfer-matrix method (TMM) in conjunction with the radial effective index method (REIM) [12, 13]. Pulse propagation in optical fiber can be analyzed by using the parameters dispersion length, L_D and

suppress parametric nonlinear processes such as four wave mixing. The large A_{eff} of the fiber can suppress other dispersion independent nonlinear effects.

.FEMTOSECOND PULSE PROPAGATION

Propagation of pulses through the fiber can be characterized by ratio of dispersion length, L_D and the nonlinear length L_{NL} given by $L_D / L_{NL} = \gamma P_0 T_0^2 / |\beta_2|$ where γ is the nonlinear coefficient of the fiber, P_0 is the peak power of the incident pulse, T_0 is the pulse width and β_2 is the group velocity dispersion. When $L_D / L_{NL} < 1$, pulse evolution along the fiber is dominated by dispersion and pulse will get broaden in absence of any chirp otherwise it stretches or compresses in time as it propagates through the fiber depending on the sign of initial chirp. However, if $L_D / L_{NL} > 1$ then nonlinearity dominates during the evolution of the pulse and pulses suffer spectral broadening or narrowing and the pulse duration changes. In order to avoid nonlinearities, one needs to limit peak power in order to make L_{NL} larger than L_D . It makes sure that linear stretching happens in shorter time so that the nonlinear interactions do not build up. One approach to do this is by increasing the A_{eff} . We have employed a segmented cladding large-mode area fiber design to achieve large mode with central core of 29- μm radius, duty cycle 50%, and 8 numbers of segments. It results in LP_{01} mode effective area of 1943 μm^2 with 275 dB/m leakage loss of LP_{02} mode at 1550-nm wavelength. LP_{02} mode will leak out within few centimeters length of the fiber therefore modal purity is good at the output of the fiber. To study pulse propagation through the fiber we have launched a secant-hyperbolic un-chirped pulse into the fiber and studied its propagation dynamics by solving the nonlinear Schrödinger equation by split step Fourier method [14]. In the simulation of pulse propagation through the fiber, we have considered

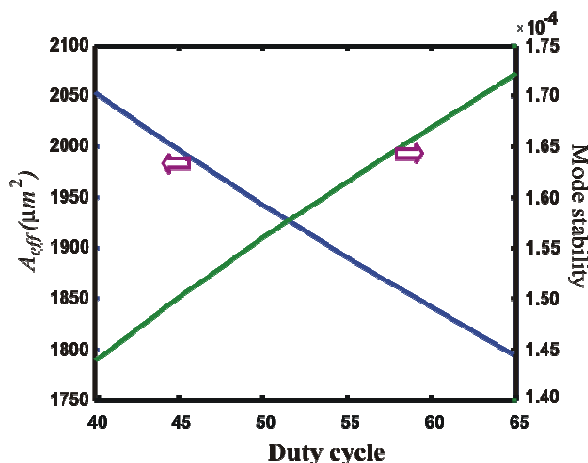


Fig. 2 Variation in A_{eff} of LP_{01} mode and mode stability with duty cycle of SCF

nonlinear length, L_{NL} . For distortion-free pulse propagation, the interplay between dispersion and A_{eff} plays an important role. For solitonic propagation, the ratio L_D/L_{NL} should be 1. In this study we have achieved $L_D/L_{NL} = 0.997$ using the SCF. Variation of mode stability and mode area (A_{eff}) of the fundamental mode with duty cycle of SCF is depicted in Fig. 2, which shows that as we go on increasing the duty cycle mode area of the fundamental mode goes on decreasing but mode stability increases. Therefore, we have optimized the duty cycle of the fiber by maintaining mode stability, to avoid modal coupling with sufficient large mode area. The dispersion of the fiber is 21.6 ps/nm/km, which is large enough to

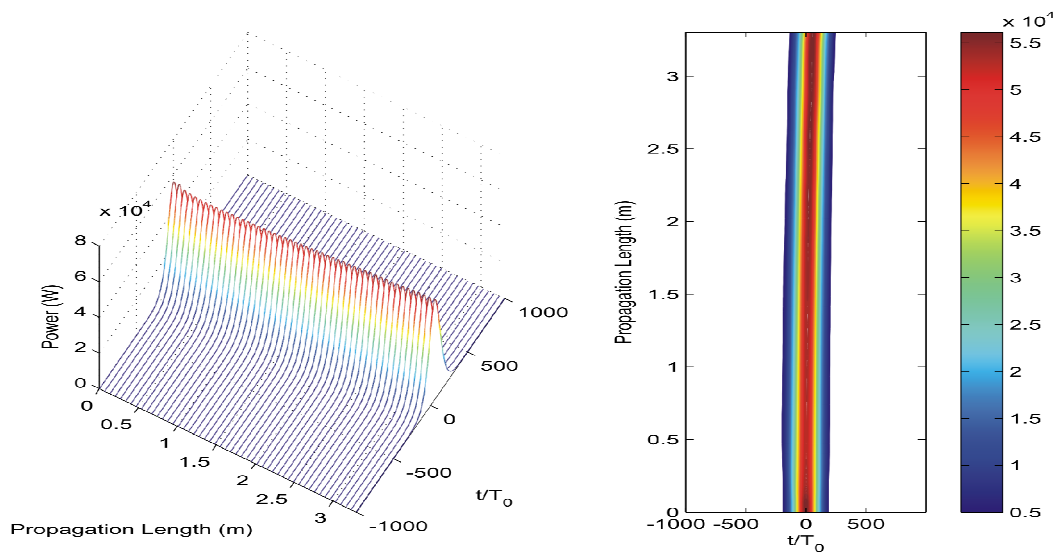


Fig. 3 Propagation of secant hyperbolic pulse through SCF

second order and third order dispersion, SPM, and Raman effect. Evolution of pulse through 3.3-m length of the fiber is shown in Fig. 3. We can see near distortion-free propagation of the pulse. We have also compared the temporal profiles of the input and output pulses as shown in Fig. 4. We can see that the temporal profiles match each other excellently. The small shifting of the pulse on time axis is due to the Raman effect.

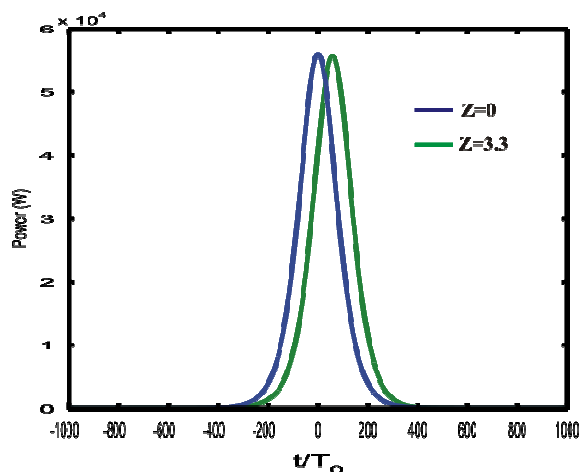


Fig. 4 Input and output temporal profiles of 100 fs pulse

CONCLUSION

In summary we have proposed a segmented cladding large-mode-area fiber for ultra-short pulse propagation and delivery. We have numerically shown the near distortion-less propagation of sech pulse of 100-fs duration and 56 kW peak power through 3.3-m length of the fiber with effective mode area as large as $1943 \mu\text{m}^2$. The pulse propagates in the LP_{01} mode of the fiber. A mode stability of 1.6×10^{-4} has been ensured while designing the fiber. However, any power coupled into the higher-order modes is stripped-off within few meters owing to 275 dB/m loss of LP_{02} mode. The fiber should find applications in delivery of ultrashort pulses.

ACKNOWLEDGEMENT

This work has been partially supported by a DST project on "Development of silica-based segmented cladding fiber."

REFERENCES

- [1] X. Liu, D. Du, and G. Mourou, "Laser ablation and micromachining with ultrashort laser pulses," *IEEE J. Quantum Electron.*, **33**, 1706 (1997).
- [2] A. H. Zewail, "Laser femtochemistry," *Science*, **242**, 1645 (1988).
- [3] J. Takayanagi, S. Kanamori, K. Suizu, M. Yamashita, T. Ouchi, S. Kasai, H. Ohtake, H. Uchida, N. Nishizawa, and K. Kawase, "Generation and detection of broadband coherent terahertz radiation using 17-fs ultrashort pulse fiber laser," *Opt. Express*, **16**, 12589 (2008).
- [4] B. R. Washburn, W. C. Swann, and N. R. Newbury, "Response dynamics of the frequency comb output from a femtosecond fiber laser," *Opt. Express*, **13**, 10633 (2005).
- [5] X. Peng, M. Mielke, and T. Booth, "High average power, high energy 1.55 μm ultra-short pulse laser beam delivery using large mode area hollow core photonic band-gap fiber," *Opt. Express.*, **19**, 923 (2011).
- [6] S. G. Johnson, M. Ibanescu, M. Skorobogatiy, O. Weisberg, T. D. Engeness, M. Soljačić, S. A. Jacobs, J. D. Joannopoulos, and Y. Fink, "Low-loss asymptotically single-mode propagation in large-core OmniGuide fibers," *Opt. Express*, **9**, 748 (2001).
- [7] Y. Zaouter, D. N. Papadopoulos, M. Hanna, J. Bouillet, L. Huang, C. Aguergeray, F. Druon, E. Mottay, P. Georges, and E. Cormier, "Stretcher-free high energy nonlinear amplification of femtosecond pulses in rod-type fibers," *Opt. Lett.*, **33**, 107 (2008).
- [8] S. Ramachandran, J. W. Nicholson, S. Ghalmi, M. F. Yan, P. Wisk, E. Monberg, and F. V. Dimarcello, "Light propagation with ultralarge modal areas in optical fibers," *Opt. Lett.*, **31**, 1797 (2006).
- [9] S. O. Konorov, A. B. Fedotov, O. A. Kolevatova, V. I. Beloglazov, N. B. Skibina, A. V. Shcherbakov, E. Wintner, and A. M. Zheltikov, "Laser breakdown with millijoule trains of picosecond pulses transmitted through a hollow-core photonic-crystal fibre," *J. Phys. D Appl. Phys.*, **36**, 1375 (2003).
- [10] J. W. Nicholson, S. Ramachandran, S. Ghalmi, M. F. Yan, P. Wisk, E. Monberg, F. V. Dimarcello, "Propagation of femtosecond pulses in large-mode-area, higher-order-mode fiber," *Opt. Lett.*, **31**, 3191 (2006).
- [11] S. Ramachandran, M. F. yan, J. Jasapara, P. Wisk, S. Ghalmi, E. Monberg, and F. V. Dimarcello, "High-energy (nanjoule) femtosecond pulse delivery with record dispersion higher-order mode fiber," *Opt. Lett.*, **30**, 3225 (2005).
- [12] V. Rastogi and K. S. Chiang, "Analysis of segmented-cladding fiber by the radial-effective-index method," *J. Opt. Soc. Am. B.*, **21**, 258 (2004).
- [13] K. Thyagarajan, S. Diggavi, A. Taneja, and A. K. Ghatak, "Simple numerical technique for the analysis of cylindrically symmetric refractive-index profile optical fibers," *Appl. Opt.*, **30**, 3877 (1991).
- [14] G. P. Agrawal, *Nonlinear Fiber Optics*, Academic, San Diego, 2001.

SIMULATION AND EXPERIMENTAL CHARACTERIZATION OF SOA-EDFA HYBRID AMPLIFIER

Umesh Tiwari^{1,2}, K Thyagarajan² and M R Shenoy²

¹Central Scientific Instruments Organization, Chandigarh – 160030 (CSIR, New Delhi)

²Department of Physics, Indian Institute of Technology Delhi-110016, INDIA

*Corresponding author's e-mail: umeshtiwari@csio.res.in

Abstract: We present design, simulation and experimental characterization of an Erbium doped fiber amplifier (EDFA) – Semiconductor Optical Amplifier (SOA) hybrid. The hybrid amplifier in the proposed configuration is experimentally characterized in terms of single channel gain, noise figure and multi-channel gain in two different configurations. It is shown that the multi-channel gain spectrum is quite different from the single-channel case. The measured results were validated through the simulations, which show a qualitative match.

1. INTRODUCTION

Broadband erbium-doped fiber amplifiers (EDFAs) have become key components in dense wavelength-division-multiplexed (DWDM) systems. In recent years, as the cost and performance of SOAs have improved, and their applications in new metro- and access optical networks are viable. With increased capacity requirements, wide gain bandwidth amplifiers have become important. Several methods have been proposed to enhance the gain bandwidth of the hybrid amplifiers [1-3]. Recently Yeh et. al. [4] experimentally demonstrated an EDFA/SOA hybrid amplifier in series for broadband amplification. They carried out measurements in terms of single channel gain and noise figure for two different lengths of erbium doped fiber with a 110 nm amplification bandwidth. In this paper an EDFA / SOA hybrid amplifier has been experimentally studied in terms of single channel gain, noise figure. We have also simulated the single channel gain and noise figure characteristics of this hybrid amplifier using OptiAmplifier 6.0; insertion losses and splice losses have been incorporated in the simulation.

Due to the increasing demand of bandwidth, DWDM systems need to accommodate more and more channels. Hence it is essential to study the performance of these amplifiers in terms of gain and noise figure when multiple channels are present. The characterization of EDFAs for WDM transmission is weighed down by the requirement of large numbers of optical sources necessary for noise and gain measurements [5]. To characterize the WDM performance of an EDFA, one requires as many as 50 DFB lasers with 100 GHz separation or 100 DFB lasers with 50 GHz separations. Procurement of this many lasers is expensive and in addition, the experimental setup becomes unmanageably large. There exist techniques of WDM characterization of EDFA in which requirement of DFB lasers is drastically reduced as in [6]. This method is based on an approximation of the largely homogeneous saturation characteristic of EDFA, which allows for a

reduced set of sources for WDM characterization. In this method, a group of WDM channels is replaced with a broadband probe and a smaller group of saturating sources set to the appropriate wavelengths and powers. In [6], the authors have evaluated the use of non-uniform WDM source spacing for EDFA gain characterization. Using the methods described therein, source configurations incorporating spacing as large as 800 GHz could be used to give fairly accurate results. The multi-channel gain characteristics of the two hybrid configurations (EDFA/SOA & SOA/EDFA) have also been presented in this paper, which was not presented in the reported literature.

2. EXPERIMENTAL SETUP AND RESULTS

Schematic of the experimental setup of the configuration studied is shown in Fig. 1. In the first configuration an EDFA section in the co-pump geometry is followed by an SOA. In the experiment, a Nufern-made EDF with a length of 10 m was used. In this scheme, signal amplification occurs first in the EDF segment, which is followed by the SOA. The second configuration studied is shown in Fig.2. In this configuration, the SOA is followed by the EDFA section in the co-pump geometry. The single channel gain and noise figure measurements were carried out using a tunable laser source for three different signal input powers of -25, -15 and -5 dBm with 60 mW of 980 nm pump power for the EDFA and 150 mA current for the SOA. In order to obtain the single channel gain and noise of the hybrid EDFA/SOA amplifier, the standard 'interpolation source subtraction technique' was employed. Figure 3 shows the measured gain and noise figure characteristics of the hybrid amplifier for three different signal input powers. The highest small signal gain observed was 35 dB and the lowest noise figure obtained was less than 4 dB. Due to limitations of the SOA, in terms of gain and noise figure, in optical communication system for amplification, the EDFA in the preamplifier configuration has been used in series with the SOA to get enhanced performance. The

experiments were carried out at three different input signal powers for the single channel and multi-channel configuration to investigate the performance and behavior of the hybrid amplifier in terms of gain saturation and tilt.

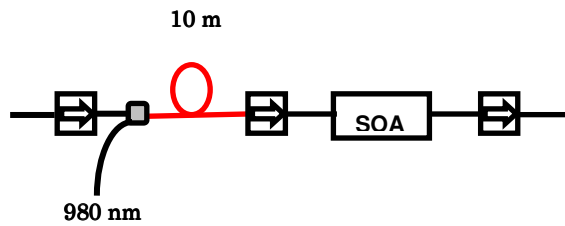


Fig.1: The EDFA/SOA hybrid amplifier configuration.

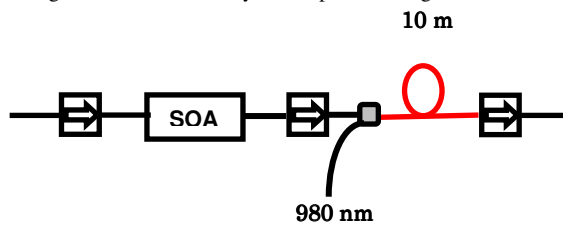


Fig.2: The SOA/EDFA hybrid amplifier configuration.

Multi-channel gain measurements were carried out using eight DFB lasers sources operating at ITU-T grid wavelengths and a low power broadband probe to measure the wavelength dependent gain. In the experiments performed, the saturating wavelengths were $k_1 = 1530.33$ nm, $k_2 = 1533.47$ nm, $k_3 = 1536.61$ nm, $k_4 = 1539.77$ nm, $k_5 = 1542.94$ nm, $k_6 = 1547.72$ nm, $k_7 = 1552.52$ nm and $k_8 = 1557.36$ nm. For the three different sets of measurements, the total powers in all the channels were -5, -15 and -25 dBm, distributed equally among the eight non-uniformly spaced channels. In the eight channel measurements, five sources were operated in the lower wavelength band of the EFDA spectrum (1527 to 1546 nm) with 400 GHz spacing, and three sources in the higher wavelength region (1546–1565 nm) with 800 GHz spacing. As expected there is a significant difference in the gain spectra between the single channel and the multi-channel cases. A small gain tilt was observed in the multi channel case, as EDFA section is operated in the unsaturated pump regime. We have also carried out the multi-channel gain characterization of SOA/EDFA hybrid configuration for the comparison and we found similar behavior in the L- band whereas in C-band EDFA/SOA configuration exhibit slightly different gain characteristics. There is a 2dB enhancement in the gain measurement in the case of SOA/EDFA. Multichannel measured Gain spectrum of EDFA/SOA and SOA/EDFA hybrid amplifier are shown in Fig.5 (a) & (b).

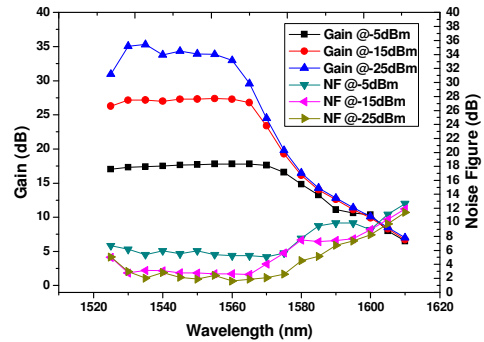


Fig.3: Measured Gain and Noise spectrum of EDFA/SOA hybrid amplifier for single channel

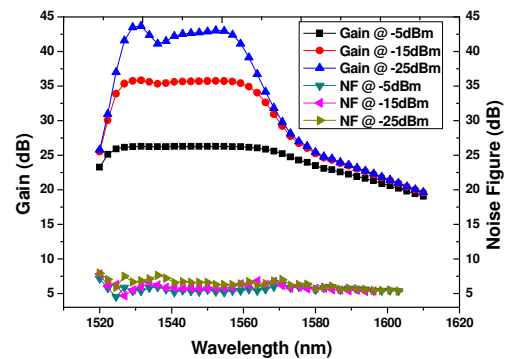


Fig.4: Simulated Gain and Noise spectrum of EDFA/SOA hybrid amplifier for single channel

Simulations were carried out to calculate single channel gain and noise figure at three different input signal powers of -25, -15 and -5 dBm with 60 mW of 980 nm pump power for the EDFA and 150 mA current for the SOA using OptiAmplifier 6.0. The simulated results for single channel gain and noise figure are shown in Fig.4. Experimental results and simulated results found to have a qualitative match.

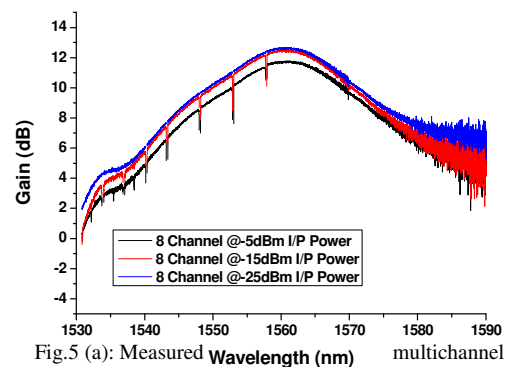


Fig.5 (a): Measured multichannel Gain spectrum of EDFA/SOA

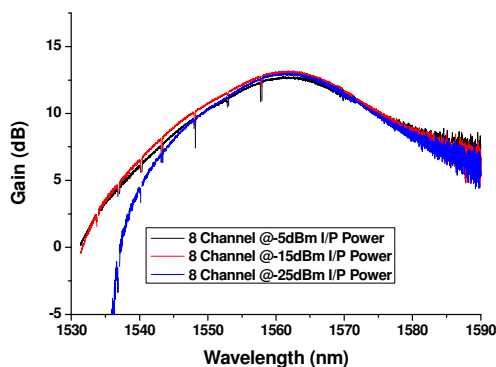


Fig.5 (b): Measured multichannel Gain spectrum of SOA/EDFA hybrid amplifier

3. CONCLUSION

We have reported experimental characterization and simulation of single channel gain and noise figure characteristics of a EDFA /SOA hybrid amplifier. The obtained results reveal that experimental and simulated results show similar behavior of the hybrid amplifier. It has been shown that the multi-channel gain spectrum of the hybrid amplifier is different from the single channel case and a small tilt in the gain spectrum was observed.

REFERENCES

- [1] H. Ahmad, N.K. Saat, and S.W. Harun, "Effect of doped-fiber's spooling on performance of S-band EDFA" *Laser Phys. Lett.*, 2, no. 8, 412–414, 2007.
- [2] A.W. Naji, M.S.Z. Abidin, M.H. Al-Mansoori, A.R. Faidz, and M.A. Mahdi "Experimental investigation of noise in double-passerbium-doped fiber amplifiers", *Laser Phys. Lett.*, 4, no. 2, 145–148, 2007.
- [3] D.-M. Liang, Y. Li, J.-H. Pei, Y. Jiang, Z.-H. Kang, and J.-Y. Gao, "Multi-wavelength fiber laser based on a highbirefringence fiber loop mirror," *Laser Phys. Lett.*, 4, no. 1, 57–60, 2007.
- [4] C. H. Yeh and S. Chi "Utilization of EDFA and SOA in series for broadband gain amplification", *Laser Phys. Lett.* 4, no. 6, 433-436 (2007).
- [5] D. M. Baney and J. Stimple, "WDM EDFA Gain Characterization with a Reduced Set of Saturating Channels", *IEEE Photon. Technol. Lett.* 8 1615-1617. 1996.
- [6] Shamal Kulkarni, John Medberry, and Kevin L. Lear, "Evaluation of Nonuniform WDM Source Spacing for EDFA Gain Characterization", *IEEE Photon. Technol. Lett.* 14, no.6, 783-785, 2002.

Study of Fundamental Noise Limits in Distributed Anti-Stokes Raman Thermometry Systems

Amitabha Datta*, Deepa Venkitesh, Balaji Srinivasan
Department of Electrical Engineering, IIT Madras, Chennai 600036, India
*amitabha.datta12@gmail.com

Abstract: In this paper we carry out an analysis of noise sources in our distributed anti-Stokes Raman thermometry (DART) system, including Raman scattering and receiver noise. Our analysis shows that the system performance is primarily limited by thermal noise and provides clues to further enhance the performance.

1. Introduction

Distributed Temperature Sensing (DTS) based on spontaneous Raman scattering is an attractive choice for several applications such as oil and gas pipe line monitoring, transmission line and power cable monitoring, fire detection in tunnel, temperature monitoring in power plant [1, 2]. The fundamental limitation in Distributed Anti-Stokes Raman Thermometry Systems (DART) is the temperature uncertainty (ΔT)/RMS temperature resolution is inversely proportional to signal to noise ratio (SNR) of the system. Every scattering detection and amplification process is the addition of noise to the original signal by which it degrades SNR of the system. A model is constructed for quantifying noise contribution from various source of the DART which is validated by experiment.

2. Noise Model

The experimental set-up used for implementing the ROTDR is illustrated in Fig.1 [3]. The electrical pulse is generated through a FPGA-based digital board are converted into optical pulses by a single mode fiber-pigtailed semiconductor laser diode directly modulated using a high speed current driver.

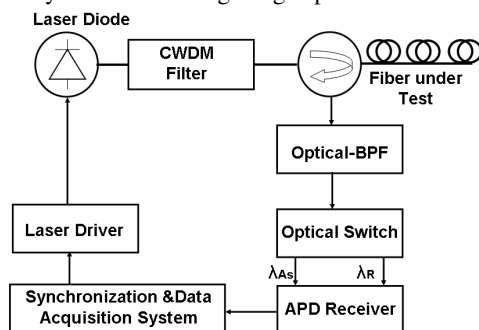


Fig.1: Schematic diagram DART sensor with 12km sensing range using SMF-28

The laser pulses are injected into the sensing fiber through a CWDM filter and optical circulator. The circulator also directs the back-scattered power band-pass filter which is capable of separating the anti-Stokes spectrum from the Rayleigh spectrum. The Rayleigh and anti-Stokes signals are subsequently sending to the receiver using optical switch where the signal is detected using InGaAs photodiode.

Noise sources effectively degrade the performance of R-OTDR because it limits the SNR of the system. We have studied the various noise sources and its effect on the experimental setup. In this model we are dealing with two types of noise, Raman scattering noise and receiver noise.

2. Raman Scattering Noise

The spontaneous scattering of a photon by an optical phonon mode is an inherently random process that is governed by Bose-Einstein statistics, although it is traditionally modeled as a Markovian stochastic process with Gaussian statistics [4]. Such randomness in the scattering phenomena gives rise to noise in the Raman scattered signal, whose noise spectrum is similar to the Raman gain spectrum [5] and is shown in Fig. 2.

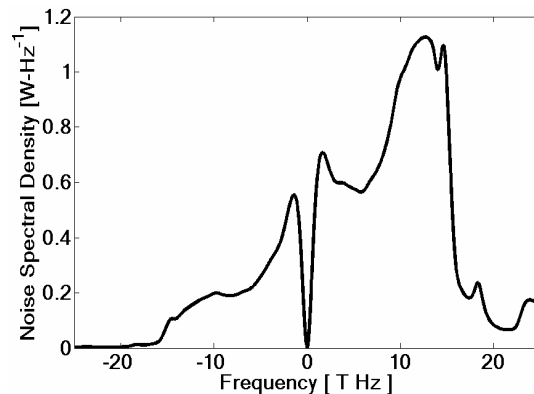


Fig.2: Raman scattering noise power spectral density of SMF-28 fiber at room temperature

A key aspect to be considered while quantifying this noise source is the effective bandwidth of this interaction. Even though the spontaneously scattered photons are present over a bandwidth in excess of 10 THz, the number of such photons reaching the optical receiver within the response time of the receiver is rather small (mean number of photons <100) since the Raman scattering gain is quite low (10^{-13} m/W). The Bose-Einstein distribution of photon for mean number of 70 is shown in Fig. 3.

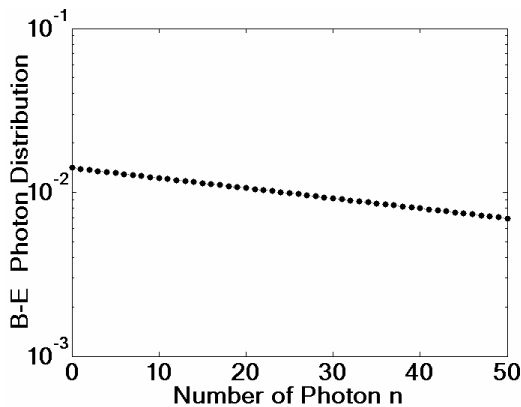


Fig.3: Bose-Einstein distribution $p(n)$ for a photon number of 70.

This implies that the probability of photons arriving at the receiver at the same time is quite low (~ 0.01 according to Fig.3) and hence the effective bandwidth of the noise spectrum corresponds to the receiver bandwidth itself. In our case, an effective bandwidth of 10 MHz results in the rms Raman scattering noise of 3.1623×10^{-10} A.

3. Receiver Noise

The schematic of the APD based receiver is illustrated in Fig.4. We have used a three stage receiver design so that the overall gain is high ($2.3 \text{ M}\Omega$) without compromising the bandwidth.

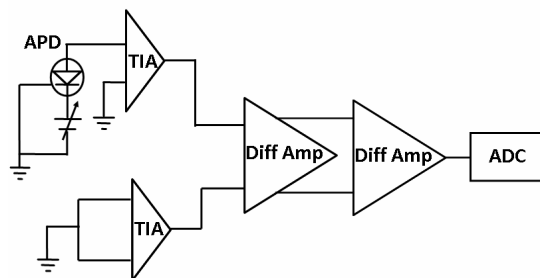


Fig.4: Schematic diagram of our APD based receiver consisting of a trans-impedance amplifier stage followed by two differential amplifiers

The photocurrent generated by the APD is converted to a voltage using the transimpedance amplifier (TIA), which is paired with a dummy unit to reject any common mode noise. The TIA stage is followed by two differential amplifier stages where signal is amplified before entering the ADC. In our receiver, we have used InGaAs APD-20 diode, which is having a breakdown voltage of 50 V. The diode is operated at 48 V bias voltage so that the amplified dark current noise does not significantly alter the noise floor. At this operating voltage, one can achieve maximum Signal to Noise Ratio (SNR). If one operates the diode beyond optimal operating voltage, the noise contributed by APD dominates the signal amplification. In the receiving section we are mainly dealing with shot noise due to photo detection, thermal noise due to random thermal motion of electrons in resistor and quantization noise due to analog to digital conversion in data acquisition system.

3.1 Shot Noise

Shot noise arises from statistical nature of the production of photo-generated electrons upon optical illumination incident on the photodiode. It can be mathematically modeled as stationary random process with Poisson statistics. For an APD based receiver, there exist an extra noise due to the process of generation of secondary electron (e) and hole (h) pairs by impact ionization. The Root Mean Square (RMS) value of shot noise current density is given by

$$\sigma_s^2 = \langle i_s^2(t) \rangle = 2q(I_p + I_d)BM^2F(M) \dots(1)$$

where q is the charge of electron, B is effective bandwidth of the receiver, M is multiplication factor, I_p is the photocurrent, $F(M)$ is the excess noise factor. There are two contributions to the shot noise: the dark current in the APD and the photocurrent noise. Since our APD bias voltage is experimentally optimized such that the noise floor does not change significantly, the latter noise contribution may be assumed to be negligible. For our receiver, we calculate the rms value to be 9.9×10^{-10} A at the noise floor based solely on a dark current of 0.1 nA provided in our APD datasheet (APD-20 from oemart).

3.2 Thermal Noise

At finite temperature, electrons move randomly in any conductor. Random thermal motion of electrons in a resistor manifests as a fluctuating current even in the absence of applied voltage.

Thermal noise in TIA stage is due to the feedback resistance of the operational amplifier, which arises due to thermal agitation of the charge carriers. The input thermal noise variance contributed by feedback resistance is given by:

$$\sigma_T^2 = \langle i_t^2(t) \rangle = \frac{4k_B T}{R_L} B \quad \dots(2)$$

where k_B is Boltzmann constant, R_L is feedback resistance and T is temperature in K. The contribution to this noise is due to feedback resistance (47 kΩ) of the trans-impedance amplifier and is calculated to have a rms value of 1.8775×10^{-9} A.

2.3 Quantization Noise (ADC)

The fact that the input signal is quantized means that noise is added to it. Quantization does not affect distortion, but does affect SNR. This Quantization Noise is less with higher resolution converters because the input range is divided into a greater number of smaller ranges, so the error is lower than with lower resolution converters. The quantization noise for n bit ADC is given by [6]

$$\Delta_q^2 = \left(\frac{\delta^{-2n}}{12} \right) \ln(1 + \mu) \left[\frac{1}{\mu^2} + \langle x^2 \rangle + 2 \frac{\langle x^2 \rangle}{\mu} \right] \dots(3)$$

where x is pre-averaged signal and μ is companding parameter. The fact that the input signal is quantized means that noise is added to it. For a 10 bit ADC used in our receiver, the quantization noise is given by 4.2×10^{-12} A.

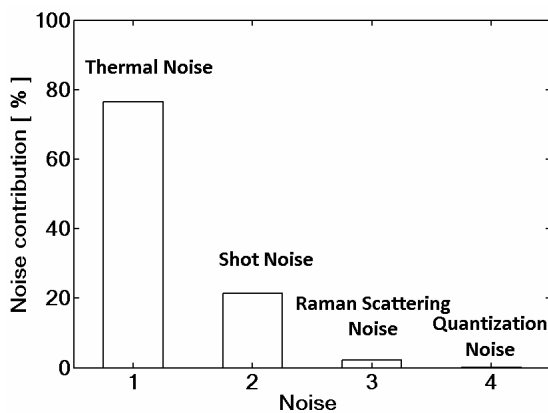


Fig.5: Noise contribution of the model which shows thermal noise dominates over other noise

A Raman-OTDR sensor capable of measuring temperature over 12km range using SMF is considered in our case and each of the four contributions is compared. The noise contributions are

shown in Fig.5. One can see that the most dominant noise term is the unavoidable thermal noise from the trans-impedance and amplifying section. It is at least five times higher than any other noise term. The Raman scattering and shot noise constitutes only a small fraction of the total noise. The total noise calculated above is found to be 8 mV of single average for a receiver gain of $2.4 \text{ M}\Omega$.

4. Results

We used the experimental setup shown in Fig. 1. We have set optimum APD bias voltage (48 V) without using laser diode and capture noise voltage trace for different level of averages which is shown in Fig.6.

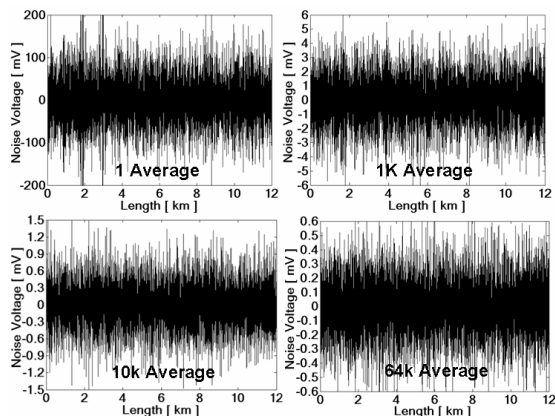


Fig.6: Total noise voltage for different label of averaging at optimum APD bias voltage

Standard deviation /rms noise voltage for single average is 66.14 mV which is roughly consistent with our estimation. The rms noise voltage deduced for different number of averages is shown in the Fig.7.

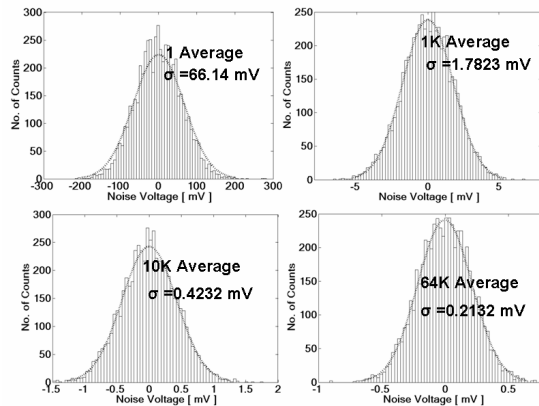


Fig.7: Histogram of measured noise voltages which is well fitted with Gaussian distribution

Based on the above results for one average (raw data), we can conclude that the noise distribution

follows Gaussian statistics. As such, further improvement can be achieved through averaging. Fig. 8 shows the noise improvement as function of digital average number. The noise floor reduction is expected to be according to square root of N , where N is the number of averages.

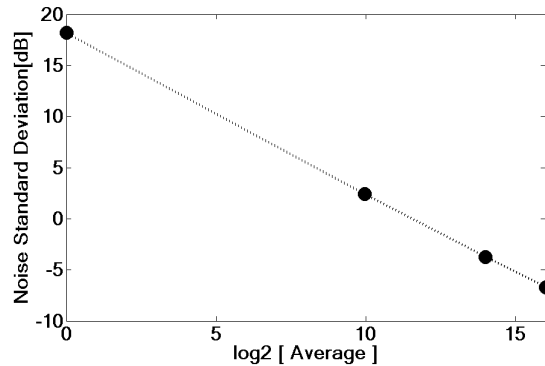


Fig.8: Noise voltage standard deviation for different label of averages

5. Conclusion

In summary, we have developed a theoretical noise model that represents the performance of our Raman scattering-based distributed temperature sensing system. We find that the present system is primarily limited by the thermal noise in our receiver. Based on such analysis, we conclude that the noise performance may be improved by obtaining more optical gain through either cooling or gating the APD used in our receiver. Such work is currently being pursued.

The authors acknowledge research funding from the Department of Information Technology (DIT).

REFERENCES

- [1] Alan Rogers, "Distributed optical-fiber sensing", Meas. Sci. Technol. 10 R75-R99 (1999)
- [2] Hartog A H, Leach A P and Gold M P "Distributed temperature sensing in solid-core fibres" Electron. Lett. 21 1061-63(1985)
- [3] Amitabha Datta, B. K. Lagishetty, B. Srinivasan, "Performance Evaluation of Temperature Sensing System Based on DART", Paper # JThA4, Proceedings of the Optical Sensors Conference, Karlsruhe (2010)

[4] Clifford Headley and G.P. Agarwal "Raman Amplification in Fiber Optical Communication Systems", Elsevier Academic Press (2005)

[5] F. X. Kartner, D. J. Dougherty, H. A. Haus, and E. P. Ippen, "Raman noise and soliton squeezing", J. Opt. Soc. Am. B 11, 1267 (1994)

[6] R. Maciejko, L. Hadellis, "Two Signal Processing Enhancements for optical Time Domain Reflectometry", J. of Lightwave Technol LT-4, 5, (1986).

FIBER BRAGG GRATING AS AN OPTICAL LIMITER

Santosh Pawar^a, S. Kumbhaj^{b*}, P. Sen^c and P. K. Sen^b

^aDepartment of Electronics & Communication, Malwa Institute of Technology, Indore, 452016, India

^bDepartment of Applied Physics, S G S Institute Technology & Science, Indore, 452003, India

^cSchool of physics, Devi Ahilya Vishvavidyalaya, Khandwa Road, Indore, 452017, India

(*corresponding author: s_kumbhaj@rediffmail.com)

Abstract: A simple analytical model has been developed using nonlinear coupled mode theory to analyze the optical limiting phenomena in Kerr fiber Bragg grating (FBG). The result shows that after certain threshold intensity transmittance become constant and FBG works as a perfect optical limiting device.

1. INTRODUCTION

The ever-increasing demand for faster and more reliable devices to process the optical signals through periodic structure offers new opportunities in developing all-optical signal processing systems. All-optical switches, all-optical memories, all-optical limiters, all-optical discriminators and all-optical transistors [1-8] are only a few of the many devices proposed during the last two decades. In particular the development of modern optical technology demands the ability to control the intensity of light in a pre-determined and predictable manner. In this aspect optical limiters have received significant attention. Nowadays, optical fiber network technology demands the all-optical fiber based nonlinear devices to control the intensity of light in an efficient manner. In this aspect optical fiber based optical limiters have received significant attention.

Optical limiting (OL) is a nonlinear phenomenon in which the transmittance of the device decreases with increased incident light intensity. An ideal optical limiter has a linear transmittance at low input intensities, but above the threshold intensity its transmittance becomes constant. Optical limiting results from irradiance-dependent nonlinear optical properties of materials. The incoming intense light alters the refractive and absorptive properties of the materials resulting in a greatly reduced transmitted intensity and therefore it is important to determine the magnitude of the nonlinearity of materials to select suitable materials as optical limiting media. After the pioneer work of Siegman in 1962 [9], OL is extensively investigated both theoretically and experimentally in a wide range of materials via different nonlinear optical mechanisms such as: (1) Reverse Saturable Absorption; (2) Nonlinear Refraction (due to molecular reorientation, Kerr effect); (3) Induced Scattering (optically induced heating or plasma generation in the medium); (4) Thermal Blooming; and (5) Multiphoton Absorption [10-14].

Recently, optical signal processing using nonlinear periodic structures is the interest of the researchers

for current photonic network technology. Nonlinear periodic structures works on the phenomena of nonlinear index change and distributed Bragg reflection. These structures also offer many structural and material degrees of freedom for achieving desired optical signal processing functionality. Herbert et al [8] for the first time experimentally observed optical power limiting in nonlinear periodic structures using a thermal nonlinearity in a dye-doped colloidal crystal. Brzozowski and Sargent [15-16] have analyzed broad-band optical limiting behavior in disordered nonlinear structures that are periodic on average. They have shown that highly disordered structures exhibit true optical limiting over a spectral range much greater than the limiting bandwidth of perfectly periodic nonlinear media. The same authors provided the solutions of coupled-mode equations for one-dimensional (1-D) periodic medium composed of layers with an identical linear refractive index and alternating opposite Kerr coefficients [17]. Pelinovsky et al analyzed both theoretically and numerically the all-optical limiting in nonlinear periodic structure when the Kerr nonlinearity is compensated exactly across the alternating layers [18-20].

In the present work, we have investigated analytically the optical limiting phenomena in Kerr fiber Bragg grating (FBG) using nonlinear coupled mode theory. The investigation is based on the nonlinear refraction mechanism which describes an intensity dependent refractive index modulation. The expression for transmittivity is obtained for a quasi CW beam. The results demonstrate that after the threshold intensity transmittance become constant for higher excitation intensities and FBG works as a perfect optical limiter.

2. THEORETICAL MODEL

At sufficiently high input intensity the intensity dependent refractive index of FBG can be written as

$$n(\omega, z) = n_{eff}(\omega) + n_2 |E(z)|^2 + n_g(z) \quad (1)$$

The wave propagation in nonlinear FBG is governed by following NLCMEs [21]

$$i \frac{\partial A_f}{\partial z} + \delta A_f + \kappa A_b + \gamma (|A_f|^2 + 2|A_b|^2) A_f = 0, \quad (2)$$

$$-i \frac{\partial A_b}{\partial z} + \delta A_b + \kappa A_f + \gamma (|A_b|^2 + 2|A_f|^2) A_b = 0. \quad (3)$$

Here, A_f and A_b are the amplitudes of the forward and backward propagating waves, δ , κ and γ are detuning parameter, linear coupling coefficient and nonlinear parameter, respectively, and are defined as

$$\delta = 2\pi n_{eff} \left(\frac{1}{\lambda} - \frac{1}{\lambda_B} \right), \quad \kappa = \frac{2\pi n_g}{\lambda_B} \quad \text{and}$$

$$\gamma = \frac{2\pi n_2}{\lambda_B}.$$

In the following analysis we have solved the above NLCMEs analytically by neglecting higher order terms of backward propagating mode and solutions are obtained as [13]

$$A_f(z) = A_1 \exp(iSz) + A_2 \exp(iTz), \quad (5)$$

and

$$A_b(z) = B_1 \exp(iSz) + B_2 \exp(iTz). \quad (6)$$

$$\text{with } S = \frac{-\mathcal{H}_0 + \sqrt{\gamma^2 I_0^2 + 4q_{nl}^2}}{2} \quad \text{and} \quad T = \frac{-\mathcal{H}_0 - \sqrt{\gamma^2 I_0^2 + 4q_{nl}^2}}{2}.$$

Here, $I_0 = |A_f|^2 + |A_b|^2$ is the input intensity at Bragg wavelength λ_B , q_{nl} is the nonlinear dispersion parameter in cubic medium and is given by

$$q_{nl}^2 = q^2 + \delta X + Y, \quad (7)$$

where $q (= (\delta^2 - \kappa^2)^{1/2})$ being the linear dispersion parameter for the Bragg grating and the parameter X and Y are defined as

$$X = \gamma (I_0 + 2|A_f|^2) \quad \& \quad Y = \gamma^2 |A_f|^2 (I_0 + |A_f|^2).$$

On substituting parameter q_{nl} in equations (5) and (6), the fields of forward and backward propagating modes take the form [22]

$$A_f(z) = A_1 \exp(iSz) + r_{nl} B_2 \exp(iTz) \quad (9)$$

and

$$A_b(z) = B_2 \exp(iTz) + r_{nl} A_1 \exp(iSz). \quad (10)$$

The corresponding expression for the effective transmission coefficient (t_{nl}) in nonlinear regime is found to be

$$t_{nl} = - \frac{\kappa}{S + \delta + \gamma (I_0 + |A_f|^2)} \quad (11)$$

Applying the proper boundary conditions, the nonlinear transmission coefficient (t_{ng}) for a grating

of length L has been obtained by using equations (9) to (11) as

$$t_{ng} = \frac{A_f(z=L)}{A_f(z=0)} = \frac{(\psi^2 - \kappa^2) \exp(iSL)}{\psi^2 - \kappa^2 \exp(ikL)} \quad (12)$$

with $\Psi = \left(\frac{k}{2} + \tau \right)$, $\tau = \delta + \gamma |A_f|^2$ and

$$k = \sqrt{\gamma^2 I_0^2 + 4q_{nl}^2}.$$

The corresponding expression for the transmittivity $T_{ng} (= |t_{ng}|^2)$ in the nonlinear regime is

$$T_{ng} = \frac{(\psi^2 - \kappa^2)^2}{\psi^4 + \kappa^4 - 2\psi^2 \kappa^2 \cos(\phi)} \quad (13)$$

With $\Phi = kL$.

RESULTS AND DISCUSSION

On the basis of the theoretical formulations developed in the preceding sections (Equation 13), we have demonstrated optical limiting behaviour of fiber Bragg grating in nonlinear Kerr regime by plotting the transmitted intensity as a function of input intensity in Figure 1. The response of the FBG limiter was investigated for four different incident wavelengths such as 1550.5 nm (dotted curve), 1551 nm (dashed curve), 1551.5 nm (dashed-dotted curve) and 1552 nm (solid curve) considering the reflectivity of the grating as 99% corresponding to value of $\kappa L = 3.65$. The incident wavelength illuminated here are slightly greater than the Bragg wavelength of the Bragg grating. The tunable quasi-CW laser source in C-band (1535 – 1565 nm) is assumed as the light source. It may be noted here that a similar order of magnitude of the pump intensity was considered by Lee and Agrawal [6] to be obtained from a quasi CW-laser of 1 ns pulse duration. Also, Taverner et al [23] used a quasi-CW Diode-seeded LA-EDFA chain radiation source at 1536 nm in their experimental work to demonstrate all-optical AND gate in an apodized FBG. All the results presented here are for chalcogenide FBG because of their attractive nonlinear optical properties such as high refractive index, low absorption losses over a wide range of wavelength and high value of nonlinear Kerr coefficient n_2 [24]. We have used following physical parameters of chalcogenide glass FBG such as effective index $n_{eff} = 2.45$, change in grating index $n_g = 6 \times 10^{-4}$, nonlinear Kerr coefficient $n_2 = 2.7 \times 10^{-17} \text{ m}^2/\text{W}$, length of the grating $L = 3 \text{ mm}$ and Bragg wavelength $\lambda_B = 1550 \text{ nm}$ [28].

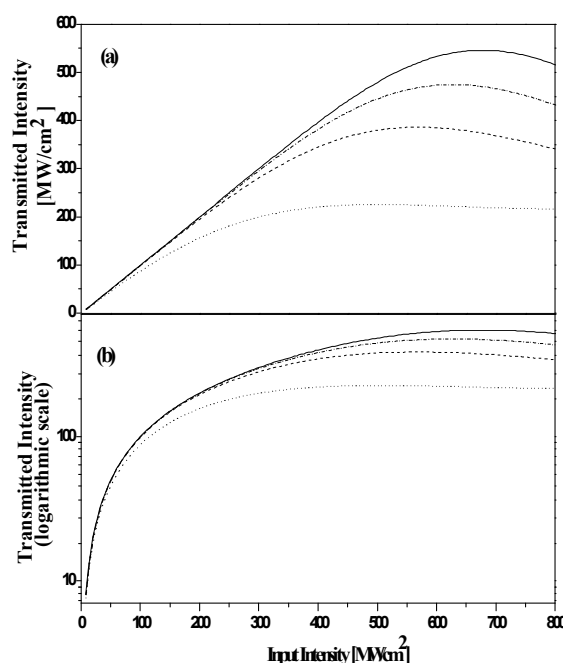


Figure 1: Optical limiting behavior of chalcogenide FBG with four detuning wavelengths 1550.5 nm (dotted curve), 1551 nm (dashed curve), 1551.5 nm (dashed-dotted curve) and 1552 nm (solid curve). Curve (a) corresponds to the transmitted intensity with incident intensity whereas curve (b) show transmitted intensity is plotted on a logarithmic scale as a function of incident intensity

We show linear and logarithmic plots of transmitted intensity as function of incident intensity in Figure 1 (a & b). The optical limiting actions of fiber Bragg grating is studied in the range of incident intensity increased from 0 to 800 MW/cm². It is clear from the Figure that for very low excitation intensity the transmitted intensity increases with incident intensity as a ramp function. The physical mechanism behind this can be explained as follows: It is well established that at low excitation intensity the FBG is highly reflective for wavelengths falling in the range $-\kappa < \delta < \kappa$ and transmissive for $-\kappa > \delta > \kappa$. The detuning parameter δ represents the difference between the frequency of the applied signal and the Bragg frequency of the grating. At high excitation intensity detuning parameter δ becomes intensity dependent and lies in the range $-\kappa < \delta(1 + X/\delta + Y/\delta^2)^{1/2} < \kappa$ [24], as a result the nonlinear dispersion parameter q_{nl} becomes purely imaginary and most of the incident field will be reflected due to the fact that the grating will not support the propagating wave. If the frequencies of the illuminated beam are chosen outside of the stopband the incident field will be transmitted and increases equal to the incident one in linear case. As the input intensity is increased further the photonic band gap shows red shift due to increase in the

average index of the grating. Such dynamic movement in photonic bandgap decreases the coupling between the forward and backward propagating waves, as a result transmission at detuning wavelength decrease causing an increase in the reflection. It is also observed from Figure 1 that after a threshold input intensity, the transmitted intensity begins to roll off and become constant over a wide range of input intensity. Such nonlinear characteristic of the grating look like as an optical limiter and can be interpreted as follows; It is known that the stable optical limiting can be achieved when the frequency of the incoming beam completely lies within the stopband, it means that the photonic band gap should widen with increasing excitation intensity rather than shifting of the stopband.

In the recent analysis we have chosen the strong grating with $\kappa L \approx 3.65$. The important fact is that the width of photonic band gap of such grating increases with incident intensity so that the more frequencies can be accommodated in the stopband. Moreover, the grating maintains their central frequency position at particular range with other frequencies which is generating due to the self phase modulation. At large value of κL , strong periodic sidelobes are observed when incident light is tuned slightly lower the Bragg wavelength whereas for higher wavelength the optical limiting function is developed to clamp the transmitted intensity at a level which is independent of the incident intensity. However, when input intensity reaches a threshold limiting intensity (I_T), the sidelobes tends to infinity. Very large increase of input intensity above I_T results in very small changes in transmitted intensity and the intensity being mainly reflected satisfying the energy conservation principle. Therefore the transmitted intensity remains nearly clamped and device acts as a limiter in transmission as shown in Fig. 1.

CONCLUSIONS

We have analyzed optical limiting phenomena in nonlinear fiber Bragg grating by incorporating optical Kerr effect in the coupled mode analysis. The expression for the intensity dependent transmittivity of fiber Bragg grating is obtained analytically. We have found that the transmittance of grating become constant after certain threshold intensity. The present model indicates that the FBG is potential candidate for all-optical limiting applications for future of all-optical computing and communication applications.

ACKNOWLEDGEMENTS

The work is financially supported by University Grant Commission (UGC), New Delhi.

REFERENCES

- [1] Winful, H. G., Marburger, J. H., Garmire, E.: Theory of bistability in nonlinear distributed feed back structure. *Appl. Phys. Lett.* 35, 379-381 (1979).
- [2] N. D. Sankey, D. F. Prelewitz and T. G. Brown, All - optical switching in a nonlinear periodic waveguide structure *Appl. Phys. Lett.*, 60, 1427-1429 (1992).
- [3] C. J. Herbert and M. S. Malcuit, Optical bistability in nonlinear periodic structures, *Opt. Lett.*, 18, 1783-1785 (1993).
- [4] H. Kawaguchi, K. Inoue, T. Matsuoka and K. Otsuka, Bistable output characteristics in semiconductor laser injection locking, *IEEE J. Quantum Electron.*, 21, 1314-1317 (1985).
- [5] N. G. R. Broderick, "Bistable Switching in Nonlinear Bragg Gratings," *Optics Comm.* 148, 90-94 (1998)
- [6] H. Lee, G. P. Agrawal, "Nonlinear switching of optical pulses in fiber Bragg grating," *IEEE J. Quantum Electron.* 39, 508-515 (2003)
- [7] C. X. Shi, "Optical bistability in reflective fiber grating," *IEEE J. Quantum Electron.* 31, 2037-2043 (1995).
- [8] C. J. Herbert, W. S. Capinsky, and M. S. Malcuit, "Optical power limiting with nonlinear periodic structures," *Opt. Lett.* 17, 1037-1039 (1992).
- [9] A. E. Siegman, "Nonlinear Optical Effects: An Optical Power Limiter," *Appl. Opt.* 1, 739-744 (1962).
- [10] R. C. Hollins, "Materials for optical limiters," *Curr. Opin. SolidState Mater. Sci.* 4, 189-196 (1999).
- [11] Y.-P. Sun and J. E. Riggs, "Organic and inorganic optical limiting materials. From fullerenes to nanoparticles," *Int. Rev. Phys. Chem.* 18, 43-90 (1999).
- [12] T. F. Boggess, A. L. Smirl, S. C. Moss, I. W. Boyd and E. W. V. Stryland, "Optical limiting in GaAs," *IEEE J. Quantum Electronics*, 21, 488-494 (1985).
- [13] S. K. Han, Z. G. Huo, R. Srivastava, and R. V. Ramaswamy, "Thermal Nonlinear Absorption and Power Limiting in Waveguides," *J. Opt. Soc. Am. B*, 6, 663-667 (1989).
- [14] L. W. Tutt and T. F. Boggess, "A review of optical limiting mechanisms and devices using organics, fullerenes, semiconductors and other materials," *Prog. Quantum. Electron.*, 17, 299-338 (1993).
- [15] L. Brzozowski and E. H. Sargent, "Nonlinear disordered media for broad-band optical limiting," *IEEE J. Quantum Electron.* 36, 1237-1242 (2000).
- [16] L. Brzozowski and E. H. Sargent, "Nonlinear distributed-feedback structures as passive optical limiters," *J. Opt. Soc. Am. B*, 17, 1360-1365 (2000).
- [17] L. Brzozowski and E. H. Sargent, "Optical signal processing using nonlinear distributed feedback structures," *IEEE J. Quantum Electron.* 36, 550-555 (2000).
- [18] D. Pelinovsky, L. Brzozowski, J. Sears, and E. H. Sargent "Stable all-optical limiting in nonlinear periodic structures. I. Analysis," *J. Opt. Soc. Am. B*, 19, 43-53 (2002).
- [19] D. Pelinovsky and E. H. Sargent, "Stable all-optical limiting in nonlinear periodic structures. II. Computations," *J. Opt. Soc. Am. B* 19, 1873-1889 (2002).
- [20] D. Pelinovsky and E. H. Sargent, "Stable all-optical limiting in nonlinear periodic structures. III. Nonsolitonic pulse propagation," *J. Opt. Soc. Am. B* 120, 695-705 (2002).
- [21] G. P. Agrawal, *Nonlinear Fiber optics*. San Diego: Academic Press, (2001).
- [22] S. Pawar, S. Kumbhaj, P. Sen and P. K. Sen, "Fiber Bragg grating based intensity dependent optical notch filter," *Nonlinear Optics Quantum Optics*, 41, 253-264 (2010).
- [23] D. Taverner, N. G. R. Broderick, D. J. Richardson, M. Ibsen and R. I. Laming, "All optical AND gate based on coupled gap-soliton formation in a fiber Bragg grating," *Optics Letter*, 23, 259-261 (1998).
- [24] M. Popescu, "Modelling of the structure and structural transformations in amorphous chalcogenides," *J. Optoelectron. Adv. Mater.* 3, 279 (2001).
- [28] Y. Yosia and Shum Ping, "Double optical bistability and its application in nonlinear chalcogenide-fiber Bragg grating," *Physica B*, 394, 293-296 (2007).

FLUORESCENCE CHEMO SENSOR FOR THE MEASUREMENT OF FLUORIDE ION CONCENTRATION IN POTABLE WATER

Lokesh Jain, Shubhada Kumbhaj* and P. K. Sen

Department of applied physics, S G S Institute of Technology & Science, Indore

(*Corresponding author: skumbhaj@gmail.com)

Abstract: A simple, low cost fiber optic chemofluorescence sensor has been developed for measurement of the fluoride ion concentration in drinking water. The present technique is based on the change in fluorescence intensity of fluoride sensitive turn on fluorophore in presence of fluoride ion in water.

1. INTRODUCTION

Nowadays, the investigation of fluoride ion concentration in drinking water, minerals, foods, plants and animal tissues is an area of research because of its toxic effects at higher concentrations. At present, the fluorimeters are common tool of measuring the concentration of fluoride ion in water. Although, spectroscopic techniques may give higher precision in measurement but it is observed that measurement of fluoride concentration is affected by presence of other impurities. So it is very necessary to develop a new technique to be a cost-efficient and give high resolution. Integration of fiber optics with spectroscopy may give better results. Recently, fluorescence chemo sensors with high specificity and sensitivity and safety handling have received considerable attention, and a number of fluorescence sensors have been reported that are capable of detecting fluoride ions. The recognition proceed mostly through hydrogen bonding or lewis acid coordination, and the sensor could only be operate in organic solvents to detect tetrabutylammoniumfluoride (tbaF) rather than inorganic fluoride salts. This incompatibility with aqueous environments is one of the main drawbacks of this type of method. In present work we have developed a simple measurement technique to measure the fluoride concentration in the water using UV excitation. The method relies on certain dyes that give fluorescence in the presence of fluoride. This technique is cheaper as compared to the existing ones.

2. EXPERIMENTAL SETUP & RESULTS

In the Present work we have chosen N-(3-(benzo[d]thiazol-2-yl)-4-(tert-butyl-diphenylsilyloxy) phenyl) benzamide (BTTPB) as Fluorophores. BTTPB is blue-violet fluorescent dye and when excited by 380nm gives fluorescence emission at 418 nm wavelength. But upon addition of fluoride ion, the Si-O bond of BTTPB is immediately cleaved and 3-BTHBP is formed which exhibit's a bright yellow emission at 560 nm. The intensity of emitted wave increases gradually with increasing concentration of Fluoride Ion. The schematic diagram of experimental set up used to perform the experiment is show in figure 1.

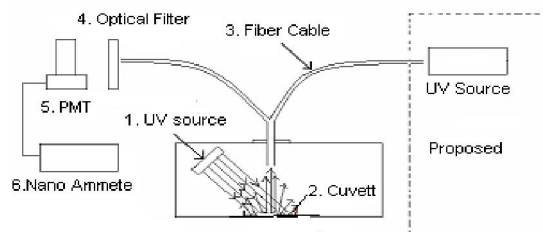


Figure 1: Schematic Experimental Setup.

The experimental setup is calibrated using a dummy sample RH6G fluorophore and fluorescence intensity is measured as a function of fluorophore concentration as shown in figure 2.

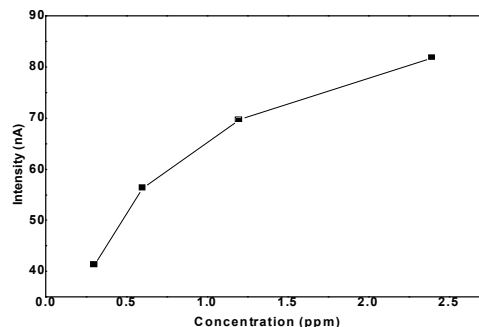


Figure 2: Fluorescence output as a function of concentration of RH6G.

It is clear that the relation between fluorophore concentration and out put intensity is almost linear. Hence we can easily calculate concentration of unknown sample with the help of above calibration curve of fluorescence output as a function of concentration. Using above setup measurement of concentration of fluoride ion in water is under progress and final result will be presented during the conference.

REFERENCES

- [1] N. Vijayaraghavan and V. Sathyamurthy, "Journal of IWWA **31**, 249 (1999).
- [2] Rui Hu, Jiao Feng, Dehui Hu, Shuangqing Wang, Shayu Li, Yi Li, and Guoqian Tang, *Angewandte Chemie*, **49**, pp. 4915-4918 (2010).

TEMPERATURE INSENSITIVE FIBER OPTIC DEVICES USING MULTIMODE INTERFERENCE EFFECT

Arun Kumar¹, Saurabh Mani Tripathi² and Manoj Kumar¹

¹Department of Physics, Indian Institute of Technology Delhi, New Delhi – 110016, India.

²Photonics Research Centre, University of Quebec, Outaouais, Quebec, Canada.

Email: akumar@physics.iitd.as.in, tripathi.sm1@gmail.com, ep.manoj888@gmail.com

Abstract: We show that the fiber optic devices using multimode interference effects can be made temperature insensitive by adjusting the concentrations of P₂O₅ and GeO₂ in the core region of the multimode fiber. Using parabolic index multimode fiber, as an example, we report the temperature insensitive transmission spectrum for a core composition of 1.57 mol% P₂O₅ and 13.5 mol% GeO₂ in the SiO₂ host.

1. INTRODUCTION

Fiber optic devices based on the modal interference among guided modes of optical waveguides have been an active area of research due to their low cost, ease of fabrication, and the freedom they offer in tailoring the output spectrum. A number of devices such as sensors [1]-[3], modulators, power splitters [4], optical switches and directional couplers [5], band pass/stop filters [6], [7] and fiber lenses [8] etc. have been recently reported using multimode interference in optical fibers. Except the temperature sensors, the performance of such devices, however, is highly susceptible to temperature fluctuations and, therefore, the thermal insulation is a prerequisite for the satisfactory operation of these devices.

Recently, while analyzing the transmission characteristics of modal interference effect based devices [2], we observed that the nature and concentration of dopants in the Multimode fiber (MMF) core region plays an important role in the output spectral response of the device. We found that the presence of P₂O₅ (typically co-doped with GeO₂ to reduce the softening temperature) can alter the nature of spectral shift: blue shift for no P₂O₅ presence (Corning multimode fiber) and a red spectral shift for P₂O₅ co-doped fiber (Sterlite multimode fiber) with respect to increasing temperature [2]. Thus, it seems possible that a temperature insensitive transmission spectrum can be realized by employing a suitable combination of GeO₂ and P₂O₅ concentrations in the MMF core region.

In this paper we obtain the transmission spectrum of a single-multi-single (SMS) mode fiber structure for various combinations of P₂O₅ and GeO₂ concentrations in the MMF core region and show that by properly selecting the concentrations of P₂O₅ and GeO₂, one can realize temperature insensitive fiber optic devices using modal interference effect.

2. THEORETICAL ANALYSIS

The SMS structure considered in this paper consists of a parabolic profile MMF of length L axially spliced at both the ends to identical step index single mode fibers (SMFs) as shown in Fig.1. At the first splice

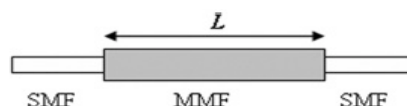


Fig.1. Schematic diagram of a SMS structure.

light is launched into the MMF section through the lead-in SMF. Generally, the spot size of the fundamental mode of the MMF is different than that of the SMF. This leads to the excitation of a number of guided modes in the MMF, at the input splice, which propagate with their respective propagation constants along the length of the MMF developing a certain phase difference among them. At the second splice these modes along with their respective phases are coupled back to the fundamental mode of the SMF leading to a periodic transmission pattern, with the period governed by the accumulated phase difference among the MMF modes. If at the first splice the MMF is axially aligned with the SMF, only the axially symmetric modes (LP_{0m}) of the MMF will be excited, whereas a transverse misalignment will lead to the excitation of modes other than axially symmetric modes also.

Considering $\Psi_s \equiv \Psi_s(r)$ as the normalized fundamental mode field of the SMF, the field within the MMF can be expressed as $\Psi = \sum_i a_i \Psi_i$, where a_i and Ψ_i are the field amplitude at the lead-in splice and the normalized axially symmetric field of the i^{th} mode of the MMF, respectively. The field amplitude a_i are basically determined by the modal overlap between the fundamental mode of the SMF and the concerned i^{th} mode of the MMF, i.e.,

$$a_i = 2\pi \int_0^\infty \Psi_s \Psi_i^* r dr \quad (1)$$

Now, as different guided modes have different propagation constants, they will develop a certain phase difference as they propagate along the MMF length. At the lead-out splice these fields are then coupled back to fundamental mode of the SMF, and the power in the lead-out fiber can be written as [2]

$$P_{SM} = \left| a_1^2 + a_2^2 e^{i(\beta_1 - \beta_2)L} + a_3^2 e^{i(\beta_1 - \beta_3)L} + \dots \right|^2 \quad (2)$$

where, β_i is the propagation constant of i^{th} mode. The normalized fundamental modal field of the SMF can be approximated as [9]

$$\Psi_s(r) = \sqrt{\frac{2}{\pi}} \frac{1}{w_s} e^{-\frac{r^2}{w_s^2}} \quad (3)$$

here, w_s is the Gaussian spot size of the mode, which can be approximated as

$$\frac{w_s}{a_s} = \left[0.65 + \frac{1.619}{V_s^{3/2}} + \frac{2.879}{V_s^6} \right]; \quad 0.8 \leq V_s \leq 2.5, \quad (4)$$

here, a_s and V_s represent the core radius and the V -number of the SMF, respectively.

Now since the spot size of the SMF is very small as compared to the MMF core diameter, only the first few modes of the MMF will be excited at the input splice. These modes are typically tightly confined within the MMF core region and hence the MMF core can be approximated as an infinitely extended parabolic refractive index distribution. This enables us to use the WKB approximation to obtain the propagation constant and the field distribution of the MMF modes, using this the propagation constant for m^{th} symmetric mode can be obtained as [2, 10],

$$\beta_m = k_0 n_0 \left[1 - \frac{2(2m+1)\alpha_m}{k_0^2 n_0^2} \right]^{1/2} \quad (5)$$

here, $m = 0, 1, 2, 3, \dots$ and $\alpha_m = (k_0 n_0 / a_M) \sqrt{2\Delta_M} V_M / a_M^2$, with V_M being the V -number of the MMF defined through, $V_M = k_0 a_M \sqrt{n_0^2 - n_{cl}^2}$. The normalized field distribution can be expressed as, [2, 10]

$$\Psi_m(r) = \sqrt{\frac{2}{\pi}} \frac{1}{w_M} L_m \left(\frac{2r^2}{w_M^2} \right) e^{-\frac{r^2}{w_M^2}} \quad (6)$$

here, $L_m(r)$ is the Laguerre polynomial of degree m , and w_M is the Gaussian spot size of the fundamental mode given by

$$w_M = \left[\frac{2a_M}{k_0 n_0 \sqrt{2\Delta_M}} \right]^{1/2} = a_M \sqrt{\frac{2}{V_M}} \quad (7)$$

Using these expressions for propagation constant and the modal field distribution in Eq.(1) and Eq.(2), the power in the lead-out SMF can be calculated.

3. RESULTS AND DISCUSSION

In our calculations the SMF core region is considered to be made of 3.1 mole% GeO₂ in SiO₂

host. The MMF core region is considered to be co-doped with p mole% of GeO₂ and q mole% of P₂O₅ in SiO₂. The cladding region for both the SMF and MMF is considered to be made of fused SiO₂. The MMF length has been taken as 42 cm. Further, the SMF core diameter has been taken as 8.2 μm and that of the MMF is taken as 62.5 μm . The wavelength dependent refractive indices of various regions are obtained by using the Sellmeier relation [11], with the peak refractive index of the MMF core region at the fiber axis being obtained as,

$$n_c^2 = n_{\text{SiO}_2}^2 + \delta n_{\text{GeO}_2}^2 + \delta n_{\text{P}_2\text{O}_5}^2 \quad (8)$$

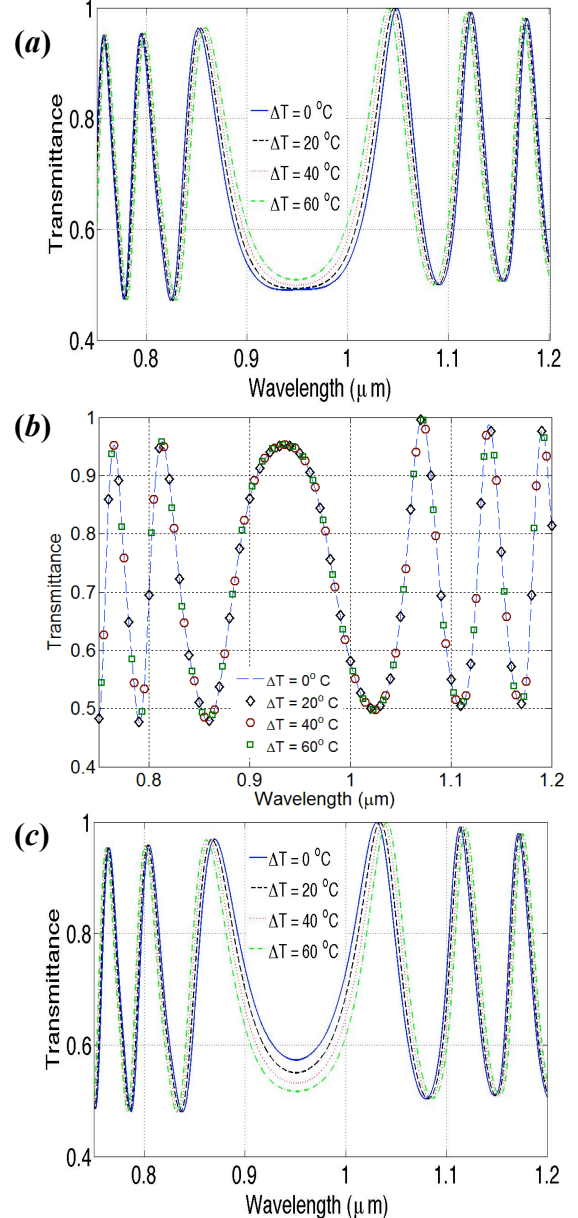


Fig.2. Transmission spectrum of the SMS structure with MMF core co-doped with (a) 1.47 mole% P₂O₅ (b) 1.57 mole% P₂O₅ and (c) 1.67 mole% P₂O₅. The core host material is considered to be 13.5 mole% GeO₂ in the SiO₂. Opposite spectral shifts with varying temperatures can be clearly observed for 1.47 mole% P₂O₅ doped core and 1.67 mole% P₂O₅ doped core.

In Eq.(8) the δn_m^2 is the incremental dielectric constant introduced by the dopant m ; which according to the *Clausius-Mossotti* equation, is proportional to the doping concentration of dopant m [12].

The temperature dependence of the refractive index of i^{th} region has been obtained by using the relation $n_i = n_{0i} + (dn_{0i}/dT)(T - T_0)$, where n_{0i} represents the refractive indices at room temperature T_0 . The thermo-optic coefficient dn/dT for fused SiO₂, 15 mole% GeO₂ doped SiO₂ and P₂O₅ are known to be $1.06 \times 10^{-5}/^\circ\text{C}$, $1.24 \times 10^{-5}/^\circ\text{C}$, and $-9.22 \times 10^{-5}/^\circ\text{C}$, respectively [2].

Assuming a linear dependence of the thermo optic coefficient on the dopant concentration [2], its value for different dopants has been obtained. The changes in length and core radius with temperature are taken as $\Delta l = \alpha l T$ and $\Delta a_M = \alpha a_M T$, respectively. Here α is the thermal expansion coefficient whose value is taken as $\alpha = 5.0 \times 10^{-7}/^\circ\text{C}$ for fused silica [2].

In Fig.2, we have plotted the transmission spectrum of the SMS structures with the MMF core co-doped with three different concentrations of P₂O₅ namely 1.47 mole%, 1.57 mole% and 1.67 mole% P₂O₅. The core host material has been considered to be 13.5 mole% GeO₂ in the SiO₂. The transmission spectrums have been intentionally shown near the critical wavelength [2] where the modal interference based devices are maximum sensitive [2], [3], [6]. It can be observed from Fig.2(a) and Fig.2(c) that the nature of spectral shifts are exactly opposite for the SMS structures employing MMF core co-doped with 1.47 mole% P₂O₅ and 1.67 mole% P₂O₅. On the other hand, from Fig.2(b) we can clearly see that the transmission spectrum corresponding to 1.57 mole% P₂O₅ doped core is temperature independent.

4. CONCLUSIONS

In this paper we have analyzed the effect of P₂O₅ and GeO₂ co-doped MMF core on the transmission spectrum of an SMS structure. We have shown that a temperature independent transmission spectrum can be obtained employing a MMF core composition of 1.57 mol% P₂O₅ and 13.5 mol% GeO₂ in SiO₂ host.

REFERENCES

- [1] E. Li, X. Wang, and C. Zhang, "Fiber-optic temperature sensor based on interference of selective higher-order modes," *Appl. Phys. Lett.*, **89**, 091119 (2006).
- [2] S. M. Tripathi, A. Kumar, E. Marin and J.P. Meunier, "Strain and Temperature Sensing Characteristics of Single mode-Multimode-Single mode Structures," *J. Lightw. Technol.*, **27**, 2348 (2009).
- [3] S. M. Tripathi, A. Kumar, E. Marin and J.P. Meunier, "Critical Wavelength in the

- Transmission Spectrum of SMS Fiber Structure Employing GeO₂-Doped Multimode Fiber," *IEEE Photon. Technol. Lett.*, **22**, 799 (2010).
- [4] Y. O. Yılmaz, A. Mehta, W. S. Mohammed, and E. G. Johnson, "Fiber optic beam shaper based on multimode interference," *Opt. Lett.*, **32**, 3170 (2007).
- [5] D. M. Mackie and A. W. Lee, "Slotted multimode-interference devices," *Appl. Opt.*, **43**, 6609 (2004).
- [6] S. M. Tripathi, A. Kumar, E. Marin and J-P Meunier, "Single-Multi-Single Mode Structure Based Band Pass/Stop Fiber Optic Filter With Tunable Bandwidth," *J. Lightw. Technol.*, **28**, 3535 (2010).
- [7] J. Lopez, A. Guzman, D. Arrijoja, R. Aguilar, and P. Wa, "Tunable multimode-interference bandpass fiber filter," *Opt. Lett.*, **35**, 324 (2010).
- [8] W. S. Mohammed, A. Mehta, and E. G. Johnson, "Wavelength tunable fiber lens based on multimode interference," *J. Lightw. Technol.*, **22**, 469 (2004).
- [9] D. Marcuse, "Gaussian approximation of the fundamental modes of graded-index fibers", *J. Opt. Soc. Am.*, **68**, 103 (1978).
- [10] A.K. Ghatak, and K. Thyagarajan, *Introduction to Fiber Optics*, Cam. Univ. Press, Cambridge, 1998.
- [11] M.J. Adams, *An Introduction to Optical Waveguides*, John Wiley & Sons, New York, 1981.
- [12] J. D. Jackson, *Classical Electrodynamics*, John Wiley & Sons, New York, 1998.

DESIGN AND ANALYSIS OF DUAL-CORE LEKY WAVEGUIDE GAIN FLATTENING FILTERS FOR ERBIUM DOPED WAVEGUIDE AMPLIFIER

N. Ashok* and Vipul Rastogi

Department of Physics, Indian Institute of Technology Roorkee, Roorkee 247 667, India

*Email: nandam.ashok@gmail.com

Abstract: We present a dual-core resonant leaky waveguide design for flattening the gain spectrum of erbium-doped waveguide amplifier (EDWA). The waveguide works on the principle of resonant coupling phenomenon. The waveguide has a multilayer leaky cladding and supports leaky modes. The waveguide is analyzed by transfer matrix method. The leakage loss spectrum resulting from the resonance between the two cores, namely, core-1 and core-2, has been utilized to achieve the gain flattening of EDWA. The loss spectrum can be tuned by varying the outer-clad refractive index, outer clad width, and inner clad width. We show 17.5-dB gain with gain excursion of ± 1.45 dB in the C-band (1526 nm -1566 nm). The proposed waveguide should find applications in integrated optic gain flattening filters.

1. INTRODUCTION

Erbium doped waveguide amplifiers [1-3] (EDWA) have attracted great attention in present optical communication systems, because of their compactness, low cost, and possibility of integration with the other optical components such as filters, switches, couplers, and wavelength division multiplexers (WDM). WDM is an effective way to increase the capacity of an optical communication link. EDWA is an attractive option for the amplification of WDM signals as it can be integrated with other components. However, an EDWA has a non uniform gain spectrum. EDWA in a WDM network requires flat gain in the entire C-band in order to achieve the uniform output power and similar signal-to-noise ratios (SNR). Several designs have been explored earlier to achieve flat gain in EDWA. Planar optical waveguide amplifiers can be used to have gain flattening in broad wavelength range [4,5]. Chen et al have proposed a gain flattening design employing the multilayer thin film filter at the output end of erbium-ytterbium co-doped waveguide amplifier (EYCDWA) [6]. The transmission spectrum of the multilayer thin film filter suppresses the gain peak of the waveguide amplifier and results in a flattened gain spectrum from 1531 nm to 1550 nm with a gain difference of < 3 dB. There have also been reports on cascaded multilayer medium thin film filters [7]. Use of long period waveguide gratings (LPWG) is another way of achieving flat gain spectrum in EDWA. Chen et al have studied gain flattening of EYCDWA employing LPWG [8]. Over the last few years we have designed leaky optical waveguides for potential applications in high power amplifiers and lasers [9-11]. In this article, implement our leaky optical waveguide design in single-mode guiding film to design gain flattening filters for EDWA. The structure is essentially a dual-core leaky planar

waveguide such as the one proposed in Ref. [10]. We have analyzed the proposed structure by calculating the leakage loss of mode using the transfer matrix method (TMM) [12, 13]. The spectral leakage loss of the mode has been utilized to suppress the gain peak of the EDWA. We show that proposed waveguide exhibits a gain of 17.5 dB with a gain ripple of ± 1.45 dB, over entire C-band. We have also carried out the effect of various waveguide parameters on the leakage loss of mode and on the gain flattening of the EDWA.

2. DESIGN AND ANALYSIS

The proposed dual-core leaky planar waveguide (DCLW) is shown in Fig. 1. The structure consists of two cores, core-1 of refractive index n_1 and width a_1 formed on a substrate of refractive index n_2 , and core-2 of refractive index n_1 and width a_2 . The two cores are separated by a layer of refractive index n_2

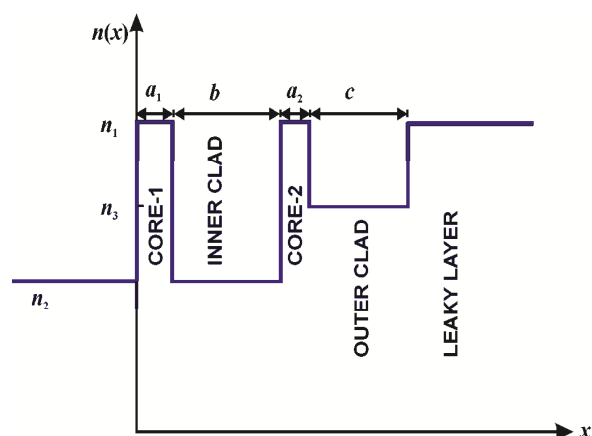


Fig. 1 Refractive index profile of a dual-core leaky waveguide

and width b . The structure is made leaky by having the outermost high-index leaky layer of the refractive index n_1 , which is separated from core-2 by an outer clad of refractive index n_3 and width c . All the modes supported by the waveguide are leaky in nature and have the complex propagation constants. The complex propagation constants of the modes in the desired wavelength range have been calculated by using the transfer matrix method, which is an established method for multilayer structure analysis. The leakage loss spectrum of the structure has been utilized to suppress the gain peak of EDWA.

3. NUMERICAL RESULTS

To design the gain flattening filter based on the proposed structure, we have considered the typical EDWA gain spectrum as given in Ref. [14]. The wavelength corresponding to the gain peak has been chosen as the resonance wavelength of the proposed dual-core waveguide. The tuning of resonance wavelength can be achieved by varying the outer clad index n_3 for a given core-1. The effect of n_3 on the loss spectrum of the dual-core structure is shown in Fig. 2. Where we have used the following waveguide parameters:

$$\begin{aligned} n_1 &= 1.64, n_2 = 1.51, \\ a_1 &= 1.1 \mu\text{m}, a_2 = 0.9 \mu\text{m}, \\ b &= 3.5 \mu\text{m}, c = 3.3 \mu\text{m} \end{aligned} \quad (1)$$

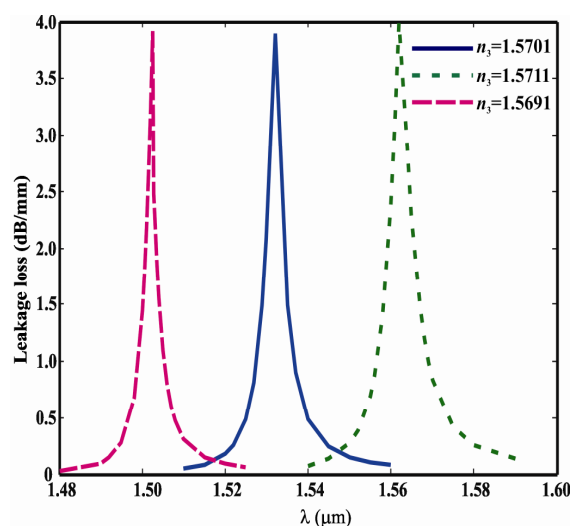


Fig. 2 Leakage loss of mode as a function of wavelength for different values of n_3

For a particular value of n_3 leakage loss of fundamental mode increases with wavelength and peaks up at a particular wavelength, which is signature of the resonant coupling. From Fig. 2 it is clear that n_3 plays an important role in achieving the resonant coupling condition at desired wavelength. An increase in the value of n_3 shifts the resonance

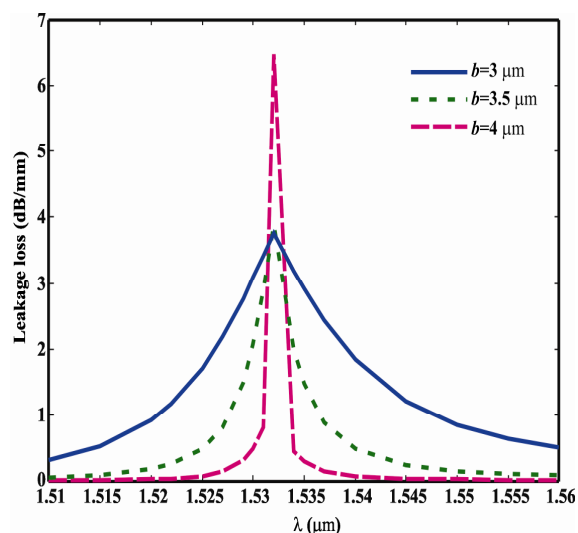


Fig. 3 Effect of inner-clad width b on leakage loss of mode

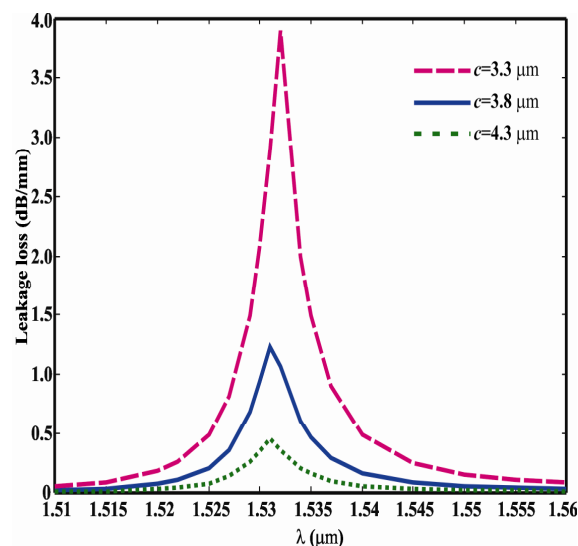


Fig. 4 Effect of outer-clad width c on leakage loss of mode

wavelength towards longer wavelength side. We see that a change in n_3 by 0.001 shifts the resonance wavelength by about $0.03 \mu\text{m}$ and the magnitude of the loss remains almost unaltered. Fig. 2 helps us to choose a suitable value of n_3 , for flattening the gain spectrum of a given EDWA. For $1.532\text{-}\mu\text{m}$ resonance wavelength the optimized value of n_3 is 1.5701 .

The peak value and the width of the loss spectrum can be tuned by inner and outer clad widths. The effect of inner-clad width b on the loss spectrum is shown in Fig. 3 and that of outer clad width c is shown in Fig. 4 for $n_3 = 1.5701$. One can see from Fig. 3 that the full width at half maximum (FWHM) of the loss curve decreases with increasing inner-clad width b . This is because the leakage loss of the mode

decreases on increasing the core separation b . From the figure we observed that changing the inner-clad width from $b = 3 \mu\text{m}$ to $b = 4 \mu\text{m}$ changes the magnitude of loss from 3.8 dB/mm to 6.4 dB/mm and the corresponding bandwidth decreases from 15 nm to 4 nm loss.

By changing the outer-clad width c the magnitude of loss can be fine tuned. This can be seen from the loss spectrum plotted in Fig.4 for three different values of c . On decreasing the outer clad width c the leaky layer comes closer to the outer core and the leakage loss increases. On decreasing the value of c from $4.3 \mu\text{m}$ to $3.3 \mu\text{m}$ the magnitude of the loss increases from 0.45 dB/mm to 3.8 dB/mm. At around $c = 3.3 \mu\text{m}$ the leakage loss spectrum of the proposed design closely matches with the gain spectrum of the EDWA.

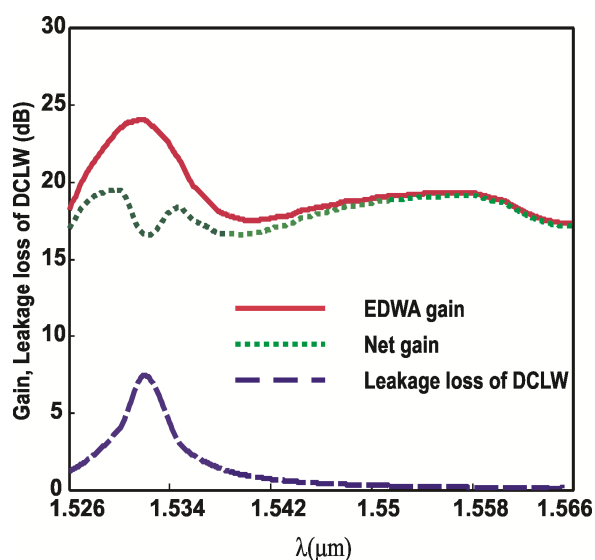


Fig. 5 Flattening of EDWA gain spectrum in the C-band using DCLW filter

Thus, by choosing the suitable design parameters leakage loss spectrum of the mode can be matched with the gain spectrum of EDWA and one can flatten the EDWA gain spectrum. The loss spectrum of the waveguide for $n_3 = 1.5701$, $b = 3.5 \mu\text{m}$, and $c = 3.3 \mu\text{m}$ and all the other parameters given by Eq. (1) is shown in Fig. 5 along with the EDWA gain spectrum and the net gain. Leakage loss spectrum of the dual-core leaky waveguide matches closely with the gain spectrum of EDWA. Such a leakage loss spectrum suppresses the gain peak of EDWA and flattens the gain spectrum. We can see the flattened gain of 17.5 dB with a gain ripple of ± 1.45 dB in the wavelength range $1.526 - 1.566 \mu\text{m}$. From the figure one can also see that the design shows a ripple of ± 1.1 dB in the wavelength range $1.532 \mu\text{m}$ to $1.566 \mu\text{m}$. Such a design should be useful as gain flattening filter in integrated optical erbium doped waveguide amplifier.

4. CONCLUSION

We have presented an integrated optic gain flattening filter based on dual-core leaky structure. The structure has been analyzed by using the transfer matrix method. We show the flat gain of 17.5 dB with the gain excursion of ± 1.45 dB in the entire C-band. The design parameter n_3 has been used to maintain the resonance wavelength at $1.532 \mu\text{m}$ wavelength and the parameters b and c help to achieve the low ripple gain. Such a gain flattening technique should be useful in erbium-doped waveguide amplifier systems to prevent the accumulation of relative gain differences among the channels in WDM network.

ACKNOWLEDGEMENT

Nandam Ashok acknowledges the financial support provided by Indian Institute of Technology, Roorkee, Ministry of Human Resources and Development (MHRD), Government of India. This work has been partially supported by the UKIERI major award.

REFERENCES

- [1] M. V. D. Vermelho, U. Peschel and J. Stewart Aitchison, "Simple and accurate procedure for modeling erbium-doped waveguide amplifiers with high concentration," *J. Lightwave Technol.* **18**, 401 (2000).
- [2] A. Polman and F. C. J. M. V. Veggel, "Broadband sensitizers for erbium-doped planar optical amplifiers: review," *J. Opt. Soc. Am. B.* **21**, 871 (2004).
- [3] R. Selvaraj, H. T. Lin and McDonald J F 1988 integrated optical waveguides in polyimide for wafer scale integration *J. Lightwave Technol.* **6** 1034 (1988)
- [4] J.-M.P. Delavaux, C. McIntosh, J. Shmulovich, A.J. Bruce, R.K. Pattnaik and B.R. Wirstiuk, "Gain flatness of a planar optical waveguide amplifier," Technical Digest, OFC 2000, Baltimore, 2000, WA2.
- [5] C. M. McIntosh, J. -M. P. Delavaux, J. Shmulovich, S. Chandrasekhar and H.K. Kim, "Gain flatness of a 980nm pumped planar optical waveguide amplifier," *11th Optical amplifiers and their applications, OSA Technical Digest, OAA 2000*, Washington, D.C. 2000, pp. 154-156.
- [6] C. Haiyan, D. Jizhi and L. Yongzhi, "Thin film filter for broadband IR integrated waveguide amplifier," *Int. J. Infrared Milli. Waves.* **26(2)**, 297 (2005).
- [7] C. Haiyan, "Optimal design of thin film filters for IR integrated photonic amplifier," *Int. J. Infrared Milli. Waves.* **26(8)**, 1141 (2005).
- [8] C. Haiyan, "Design and simulation f broad band IR integrated waveguide amplifiers with long

- period waveguide grating filter,” *J. Infrared Milli. Terahz Waves.* **31**, 24 (2010).
- [9] A. Kumar, V. Rastogi and K. S. Chiang, “Leaky optical waveguide for high power applications,” *Appl. Phys. B*, **85**, 11 (2006).
- [10] A. Kumar and V. Rastogi, “Multilayer-cladding leaky planar waveguide for high-power applications,” *Appl. Phys. B*, **92**, 577 (2008).
- [11] A. Kumar, V. Rastogi and K. S. Chiang, “Large-core single-mode channel waveguide based on geometrically shaped leaky cladding,” *Appl. Phys. B*, **90**, 507 (2008).
- [12] M. R. Ramadas, E. Garmire, A. K. Ghatak, K. Thyagarajan and M. R. Shenoy, “Analysis of absorbing and leaky planar waveguides: a novel method,” *Opt. Lett.*, **14**, 376 (1989).
- [13] M. R. Ramadas, R. K. Varshney, K. Thyagarajan and A. K. Ghatak, “A matrix approach to study the propagation characteristics of a general nonlinear planar waveguide,” *J. Lightwave Technol.*, **7**, 1901 (1989).
- [14] J. L. Philipsen, C. L. Thomsen, L. Leick, Y. Shen, P. C. Nielsen, C. Laurent-Laud, M. G. Dyndgaard and T. Feuchter, “Erbium doped waveguide amplifier technology and components,” *Proc., ECOC-2003*, Italy, 21 Sep - 25 Sep 2003.

CHARACTERIZATION OF BURIED CHANNEL WAVEGUIDES FROM THE DIFFRACTION PATTERN UNDER TRANSVERSE ILLUMINATION

Ruchi Garg, M. R. Shenoy and K. Thyagarajan

Physics Department, Indian Institute of Technology Delhi, New Delhi 110016, India
ruchigarg19@gmail.com, mrshenoy@physics.iitd.ac.in, ktrajan@physics.iitd.ac.in

Abstract: We propose a novel method using Fraunhofer diffraction to characterize buried channel waveguides, formed in a transparent substrate. The waveguide is illuminated transversely by a laser beam incident normally on the surface, and the diffraction pattern is analyzed to estimate the waveguide parameters.

1. INTRODUCTION

There exists various fabrication techniques for waveguide devices that include deposition, ion exchange, thermal diffusion, ion implantation, epitaxial technique, electron-beam direct writing etc.[1]. Most of these techniques fabricate waveguides at the surface of the substrate. Femtosecond laser writing is an upcoming fabrication method, where it is possible to create a permanent refractive index modification by tightly focusing femtosecond infrared laser pulses inside bulk glass material [2]. Femtosecond laser inscription of waveguiding structures is fundamentally different from conventional lithographic techniques, since waveguide inscription is possible in the bulk of the material, without affecting any of the surfaces. Thus one can realize direct-write fabrication of optical devices, active and passive, in a variety of dielectric optical materials including amorphous glasses, crystalline materials like LiNbO_3 , and optical polymers, simply by moving the sample through the focus of a femtosecond laser beam [3-6]. By using computer controlled substrate displacements, it is possible to fabricate complex geometries of waveguide-based devices using this technique [7]. Different devices could be fabricated in the same substrate by focusing the writing beam at different depths. The ability to write waveguiding regions within the bulk of the substrate gives an additional degree of freedom in the design of waveguide based devices.

Since these waveguides are written in depth, they cannot be characterized using conventional techniques such as the prism coupling method [8]. Interferometric techniques can be employed in the case of channel waveguides for determining the refractive index profiles [9]. Characterization of femtosecond laser written waveguides has also been carried out by excitation of waveguide modes [10]. Different microscopic techniques e.g. phase contrast microscopy, optical transmission microscopy may be employed to characterize the laser written features, greatly depending over the availability of the facility

[11]. In this paper, we propose a simple characterization technique for such waveguides using transverse illumination by a laser beam, and analyzing the resulting diffraction pattern. The technique is applicable for buried as well as surface channel waveguides and even for channels whose refractive index is lower than the surrounding. In the latter case the channels do not guide light and this technique should be very interesting for characterization.

2. ANALYSIS AND RESULTS

A waveguide is a higher refractive index channel inside the bulk sample [12]. A straight channel of a different refractive index in a bulk sample acts as a 'phase slit' for a plane wave incident perpendicular to the channel; the wave develops a transverse phase distribution as it emerges from the substrate, depending on the parameters of the phase slit. This wave then undergoes diffraction generating a far field pattern. Since the far field pattern of the output wave is the Fourier transform of the 'phase-slit aperture', a measurement of the Fraunhofer diffraction pattern of the phase slit can give us information on the refractive index changes and width of the channel. Figure 1 shows the schematic of the experimental set-up used

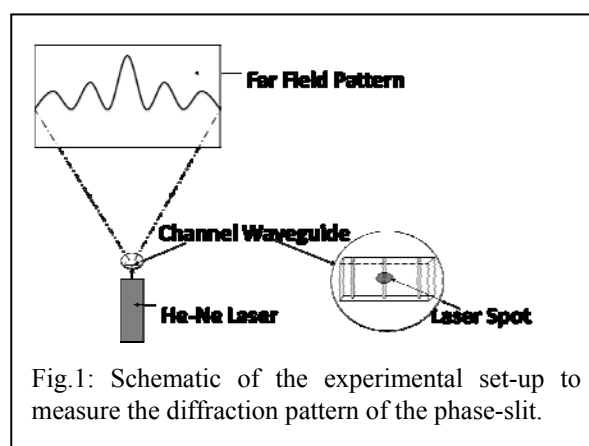


Fig.1: Schematic of the experimental set-up to measure the diffraction pattern of the phase-slit.

to observe the Fraunhofer diffraction pattern. Experiments were conducted on femtosecond laser written channel waveguides in BK7 glass.

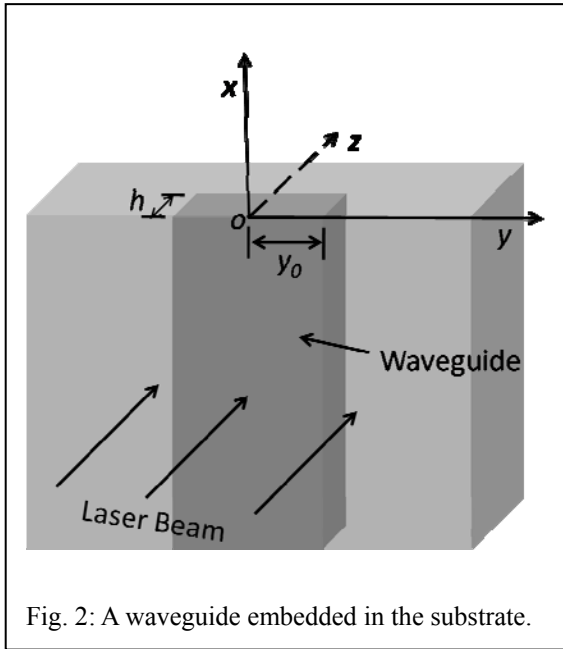


Fig. 2: A waveguide embedded in the substrate.

Using FFT package in MATLAB[®], diffraction patterns corresponding to various (channel waveguide) phase-slits were generated to match with the measured diffraction pattern. Assuming unit amplitude, the transmission function $\tau(y)$ of the channel waveguide can be written as:

$$\tau(y) = \begin{cases} e^{-i\varphi(y)} & |y| \leq y_0 \\ 1 & |y| > y_0 \end{cases} \quad (1)$$

where $2y_0$ is the waveguide width and $\varphi(y)$ is the phase change introduced by the waveguide aperture with $\varphi_0 = \varphi(y=0)$.

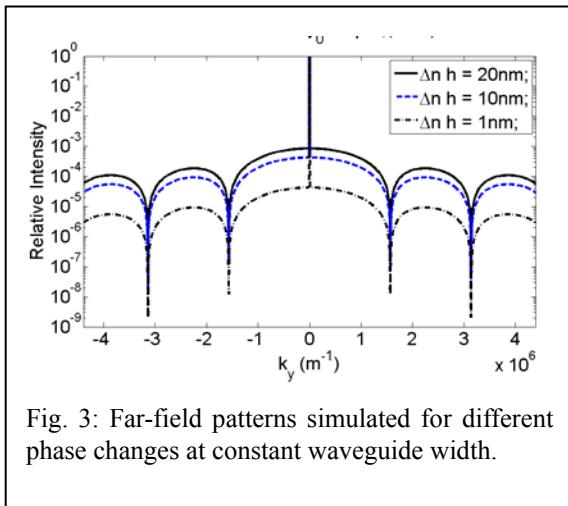


Fig. 3: Far-field patterns simulated for different phase changes at constant waveguide width.

For the incident laser beam of characteristic width W_0 , the far-field pattern is given by the following integral:

$$F(k_y) = \left| \int_{-\infty}^{\infty} \tau(y) \exp(-y^2/W_0^2) \exp(ik_y y) dy \right|$$

(2)

We first carried out simulations for uniform phase

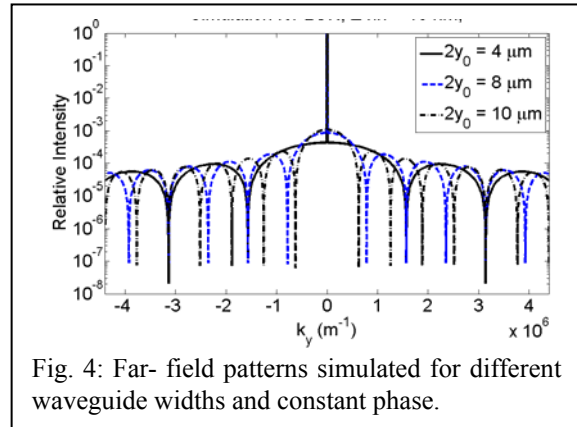


Fig. 4: Far-field patterns simulated for different waveguide widths and constant phase.

change which corresponds to the case of a rectangular waveguide phase-slit. Here,

$$\varphi(y) = \varphi_0 = (2\pi/\lambda_0)\Delta n h \quad (3)$$

λ_0 is the wavelength of the incident beam, Δn is the refractive index change and h is the waveguide depth (see Fig. 2). Figure 3 shows simulation results for different values of $\Delta n h$ at a wavelength of 543 nm.

From Fig. 3, we observe that the spread of the diffraction pattern remains the same whereas the ratios of intensity (at chosen value of k_y) vary with magnitude of the phase changes introduced. Higher the phase change, higher is the ratio. Figure 4 shows the simulated far field patterns corresponding to fixed value of phase, $\varphi_0 = 0.04\pi$, with variations in width of the phase slit. From Fig. 4, we observe that a narrower phase slit will have a broader diffraction pattern, as expected. Also, for a constant phase change, there occurs no change in the intensity ratios of the patterns.

As the actual refractive index profile created due to femtosecond laser is not known, we include a product of two y -dependent functions in the phase profile; the first one is assumed to be a q -profile which gives flexibility for analyzing different gradation profiles. Also, as these waveguides are created through a tight focus in the substrate, we choose the waveguide depth to be a linear function of y . This yields the following profile:

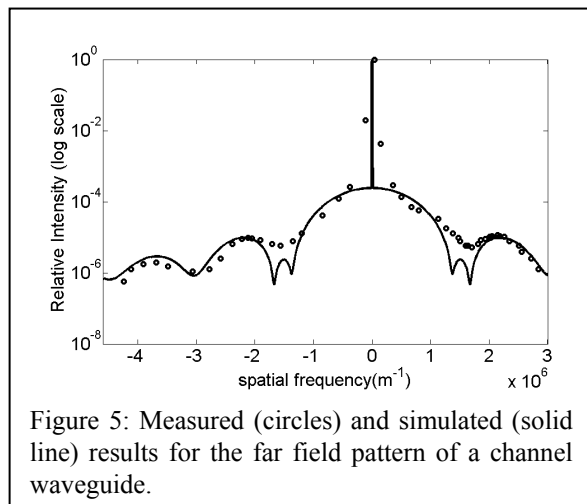
$$\varphi(y) = \Delta n k_0 h(y) \left(1 - |y/y_0|^q\right) \quad (4)$$

with

$$h(y) = h_0 (1 - |y/y_0|)$$

Diffraction patterns were generated for different profiles to obtain the best fit with the experimental results. Figure 5 shows a comparison between the

experimentally measured Fraunhofer diffraction pattern and the simulation results. We observe a good match between the two; the estimated width of the waveguide is $\sim 9 \mu\text{m}$ with $\varphi_0 = 0.02\pi$ and $q = 5$. Thus, if we know the refractive index change Δn , then the waveguide depth profile can be determined.



3. CONCLUSIONS

An easy application of diffraction to decipher the waveguide parameters and complex refractive index profiles has been proposed. The idea has been established by obtaining a good agreement between simulation and experiment carried out on a channel waveguide written using a femtosecond laser. The method can be applied to characterize a modified refractive index channel within homogeneous substrates and thus should find applications in waveguide characterization.

ACKNOWLEDGEMENTS

Author Ruchi Garg thanks the Council of Scientific and Industrial Research (CSIR) for grant of Senior Research Fellowship. This work was partially supported by a research grant from the Office of Principal Scientific Advisor to the Government of India through a project titled “*Fabrication and submicron tailoring of materials for photonic applications with ultrafast lasers*”. The authors thank Center for Atomic and Molecular Physics, Manipal University for providing with the femtosecond laser written samples.

REFERENCES

- [1] See, e. g., R. G. Hunsperger, *Integrated Optics Theory and Technology*, Springer, 2005.
- [2] K. M. Davis, K. Miura, N. Sugimoto and K. Hirao, “Writing waveguides in glass with a femtosecond laser”, *Opt.Lett.*, **21**, 1729 (1996).
- [3] A. M. Streltsov and N. F. Borrelli, “Fabrication and analysis of a directional coupler written in glass by nanojoule femtosecond laser pulses,”

Opt. Lett., **26**, 42 (2001).

- [4] R. Osellame, V. Maselli, N. Chiodo, D. Polli, R. M. Vazquez, R. Ramponi and G. Cerullo, “Fabrication of 3D photonic devices at 1.55 μm wavelength by femtosecond Ti:Sapphire oscillator,” *Electron Lett.*, **41**, 315 (2005).
- [5] S. Nolte, M. Will, J. Burghoff and A. Tuennermann, “Femtosecond waveguide writing: A new avenue to three dimensional integrated optics,” *Appl. Phys. A*, **77**, 109 (2003).
- [6] A. H. Nejadmalayeri and P. R. Herman, “Ultrafast laser waveguide writing: lithium niobate and the role of circular polarization and picoseconds pulse width,” *Opt. Lett.*, **31**, 2987 (2006).
- [7] R.R. Thompson, H. T. Bookey, N. D. Psaila, A. Fender, S. Campbell, W. N. MacPherson, J. S. Barton, D. T. Reid and A. K. Kar, “Ultrafast-laser inscription of a three dimensional fan-out device for multicore fiber coupling applications,” *Opt. Express*, **15**, 11691 (2007).
- [8] P. K. Tien, R. Ulrich and R. J. Martin, “Modes of propagating light waves in thin deposited semiconductor films”, *App. Phys. Lett.*, **14**, 291(1969).
- [9] R. Oven, “Measurement of two dimensional refractive index profiles of channel waveguides using an interferometric technique,” *App. Opt.*, **48**, 5704 (2009).
- [10] R. Graf, A. Fernandez, M. Dubov, H. J. Brueckner, B. N. Chichkov and A. Apolonski, “Pearl-chain waveguides written at megahertz repetition rate,” *Appl. Phys. B*, **87**, 21 (2007).
- [11] S. M. Eaton, M. L. Ng, J. Bonse, A. M. Blondin, H. Zhang, A. Rosenfeld and P. R. Herman, “Low-loss waveguides fabricated in BK7 glass by high repetition rate femtosecond fiber laser,” *App. Opt.*, **47**, 2098 (2008).
- [12] A. Ghatak and K. Thyagarajan, *Optical Electronics*, Cambridge University Press, Cambridge, UK, 1989.

OPTIMAL DESIGN OF LPWG FOR FLATTENING ASE SPECTRUM OF EDFA USING ADAPTIVE PARTICLE SWARM OPTIMIZATION

Girish Semwal^{1*} and Vipul Rastogi²

¹Instrument Research and Development Establishment Dehradun, 248008, India

²Indian Institute of Technology Roorkee, Roorkee, 247667, India

*girishsemwal@rediffmail.com

Abstract: Long Period Waveguide Grating (LPWG) parameters have been optimized for flattening the ASE spectrum of EDFA by Adaptive Particle Swarm Optimization (APSO). Grating length, period, corrugation height, chirp and the cladding thickness have been optimized to achieve flattened ASE spectrum with a ripple of ± 1.0 dB in 30 nm band.

1. INTRODUCTION

Application of Long Period Fiber Grating (LPFG) has been demonstrated in optical communication and sensor technologies [1-6]. LPWG on planar waveguide was proposed to enhance the functionality LPFG [7]. The attractive feature of LPWG is elimination the material and cladding thickness constraints. The LPWG design proposed in Ref [7] is based on the four-layer waveguide structure with grating embedded in the film in sinusoidal form, known as the sinusoidal or phase grating. LPWG has two variants 1) phase grating and 2) corrugated grating. Corrugated grating is easier to fabricate as compare to phase grating. The phase matching curve and the coupling coefficients of corrugated grating can be tuned by the cladding thickness and corrugation height respectively [8]. Apart from this, the transmission spectrum of LPWG depends on number of parameters such as length, period, corrugation height, cladding thickness and chirp of grating. As the number of controllable parameters increases, the design becomes more complex and requires optimizing the parameters to achieve the desired output from transmission grating. Hence, implementation of suitable optimization technique is required to achieve the best optimized set of parameters for generating pre-defined application specific target spectrum.

In the present study, we propose the use of APSO to optimize the parameters of the 4-layer planar waveguide and the LPG inscribed in the guiding film of the waveguide. The device is proposed for the application of flattening the ASE of Erbium doped fiber amplifier.

2. PARTICLE SWARM OPTIMIZATION

PSO was originated with the understanding of socio-cognitive behavior of the graceful motion of swarm of birds or schooling of fishes in their social environment. The PSO algorithms consists three basic steps. These basic steps are random generation of velocity and position of particles, velocity update and finally position update. Velocity update is governed by three basic socio-cognitive factors. The

convergences of PSO algorithms are completely govern by appropriate selection of these three factors. Mathematical relations governing basic steps of these algorithms are given as [9]

$$x_0^i = x_{\min} + \text{rand}(x_{\max} - x_{\min}) \quad (1)$$

$$v_0^i = \frac{(x_{\min} + \text{rand}(x_{\max} - x_{\min}))}{\Delta t} \quad (2)$$

$$v_{k+1}^i = w v_k^i + c_1 \text{rand} \frac{(p_i - x_k^i)}{\Delta t} + c_2 \text{rand} \frac{(p_k^g - x_k^i)}{\Delta t} \quad (3)$$

$$x_{k+1}^i = x_k^i + v_{k+1}^i \Delta t \quad (4)$$

Relation (3) is the velocity update for next iteration and related to the position and velocity of previous value as well as the socio-cognitive factors. These factors are inertia factor (w), self confidence (c_1) and swarm confidence (c_2). x_{\min} and x_{\max} are the minimum and maximum values of assigned variable in the domain. Considerable research has been carried out to assign the suitable value of these three socio-cognitive variables. Special care should be taken during the selection of these variables otherwise the optimization is trapped in local minimum instead of global minimum. Fixed values of inertia weight and acceleration coefficient were suggested however these fixed values change with different optimization problems [10]. Recently, the Adaptive Particle Swarm Optimization (APSO) based on k -mean clustering method [11] and fuzzy logic based method [12] was suggested. The fuzzy logic based APSO is the fusion of PSO and fuzzy logic algorithms. The membership function is based on the dimensionless parameter which is computed with the distance of globally best particle, minimum distance and maximum distance of populations. Here we adopted the procedure followed in Ref. [12] for APSO. The parameters c_1 , c_2 and w change on the basis of fuzzification of membership function. The procedure ensures the definite convergence to its optimum value without trapping into its local minimum. During the update process of

velocity, new velocity may be out of bound and suitable boundary conditions are required to keep the value within domain [13]. Here we used damped boundary condition to bring these parameters within the domain.

3. ANALYSIS

Four layered waveguide structures used in this analysis is shown in Fig.1. the structure consists of thick substrate layer of refractive index n_s , guiding film of refractive index n_f and thickness d_f , cladding layer of refractive index n_{cl} and thickness d_{cl} and infinitely extended external layer of refractive index n_{ex} . The refractive index of all layers are taken in such a way that they should satisfy the condition $n_f > n_{cl} > n_s \geq n_{ex}$. The modes of the structure have been obtained by the solving the waveguide structure analytically. Thickness of film is selected in such a way that it supports only the fundamental mode and higher order modes are supported by cladding layer. Variations in the thickness of cladding layer primarily affect the properties of the cladding modes without significantly affecting the fundamental mode. This feature of the structure has been utilized in the design of application specific waveguide grating devices.

The coupling between the fundamental and the desired cladding mode has been analyzed by the coupled mode theory, which follows the coupling of guided mode with co-propagating cladding mode in the presence of perturbation. The perturbing agent is the long period grating embedded in the film region. The coupled mode equations corresponding to the amplitude of guided mode and cladding modes are given as

$$\frac{dA_0}{dz} = j\kappa A_m e^{j\delta z} \quad (5)$$

$$\frac{dA_m}{dz} = -j\kappa A_0 e^{-j\delta z} \quad (6)$$

$$\delta = (\beta_0 - \beta_m) - \frac{2\pi}{\Lambda} \quad (7)$$

$$\kappa = \frac{k_0 \Delta n^2}{2\pi c \mu_0} \int_{d_f-h}^{d_f} E_0 E_m dx \quad (8)$$

Where δ is detuning parameter, $A_0(z)$, $A_m(z)$ are the amplitudes of core mode and m^{th} cladding mode, respectively, and κ is the coupling coefficient which determines the overlap integral between two modes.

Here we have considered the chirped grating and therefore, the grating period is not constant. The period is function of Z and defined as

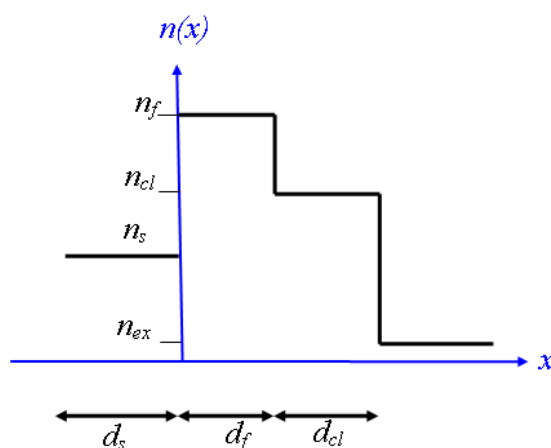


Fig.1. Schematic of the refractive-index profile of the 4-layer waveguide for LPWG.

$$\Lambda(z) = \Lambda_0 + \xi \cdot (z/L) \quad (9)$$

where ξ is the chirp parameter of the grating. We have used transfer matrix approach for solving the coupled mode equations [14].

4. DESIGN PROCEDURE

The transmission spectrum S_c has been computed for some initial values ascribed to various corrugated LPG parameters such as pitch Λ , corrugation depth h , grating length L , cladding thickness d_{cl} and chirp parameter ξ . The fitness function has been evaluated using following relation.

$$Fitness = \sqrt{\sum (S_t - S_c)^2} \quad (10)$$

Where, S_t is the pre-defined target spectrum. Following steps have been used for design and optimization of the grating parameters with APSO.

Steps for PSO optimization

1. Randomly generate an initial population for velocity and position by using Eqs. (1) and (2).
2. Evaluate the suitability or fitness of each member of population by using Eq. (10).
3. Compute new velocity from Eq. (3).
4. Use suitable boundary condition to keep the particle within domain.
5. Update the position with respect to new velocity as per Eq. (4).
6. Continue from step 2 until the desired solution is obtained.

5. NUMERICAL RESULTS

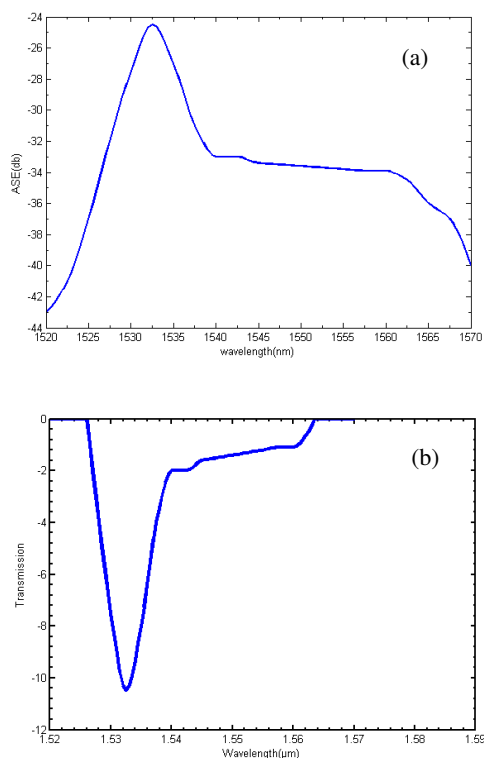


Fig.2. (a) ASE spectrum of an EDWA (Ref. [14]). (b) Corresponding rejection band required for flatten the spectrum.

With above theoretical background, we designed long period waveguide grating for ASE flattening of erbium doped fiber amplifier. The typical ASE spectrum of EDWA is obtained from literature and is shown in Fig. 2(a) [15]. The required rejection band for flattening the ASE curve is shown in Fig. 2(b) and serves as the target spectrum S_t . We have considered the following waveguide parameters to design the LPWG device to flatten the gain.

$$n_s = 1.5, n_f = 1.52, n_{cl} = 1.51, n_{ex} = 1 \text{ and } d_f = 2$$

The film thickness is selected in such a way that it supports only one guided mode. Unlike the fiber grating, in waveguide, we have flexibility to change the cladding thickness, which controls the coupling coefficient. Apart from this, nature of rejection band also depends on other factors such as grating length, grating period, corrugation height and chirp of the grating. The rejection bands in such types of applications are asymmetric in nature. Hence, chirp is an important parameter for designing the asymmetric rejection band.

In the simulation process, first the swarms are initialized with minimum and maximum limits of parameters. After that, search process to obtain the suitable value of corresponding parameter in the defined domain is implemented. The minimum and maximum limits of the swarms are defined on the

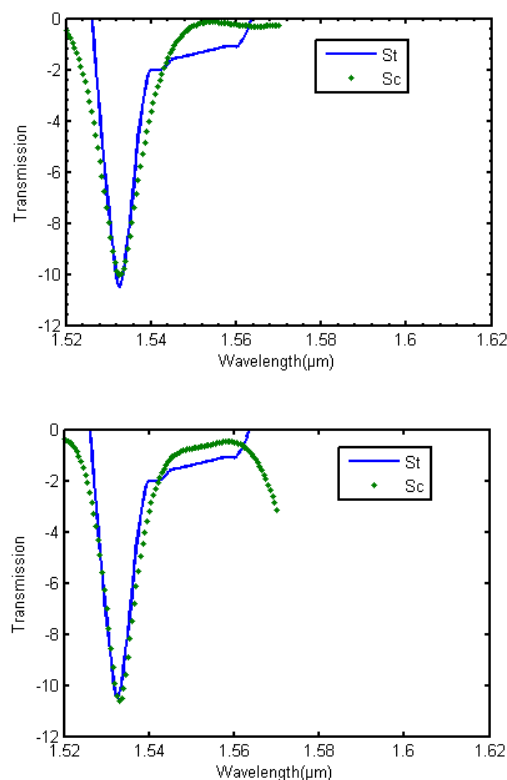


Fig.4. Target spectrum, S_t , and computed spectra S_c , corresponding to $N=10$, (a), and $N=40$, (b).

basis of fabrication limit, application and physical significance of parameters' properties. In this simulation the grating period domain's minimum and maximum values are $50 \mu\text{m}$ and $800 \mu\text{m}$ respectively. This range covers the complete domain of long period grating. Hence, the search algorithms search the value of period in this domain only. Similarly the length of grating was taken between 10 mm and 50 mm . Other parameters' domains are selected with similar constrains. The initial population of swarm was taken as 20. Total numbers of iterations were taken 150. With these values of initial population size and number of iterations, almost 90% of swarms converge to its global value.

The nature of transmission spectrum depends on the number of sections of grating taken for simulating the chirp grating. The grating and waveguide parameters are highly dependent on the number of sections used for designing chirp grating. Table-1 shows that the parameters of grating changes with changing the number of sections, N from 10 to 40.

Table-1

Λ (μm)	L (mm)	h (nm)	d_{cl} (μm)	ξ (μm)	N
364.6	27.8	160.9	11.7	36.4	10
242.6	45.9	220.8	9.7	51.2	40

Figure 4 shows the computed spectrum S_c for $N =$

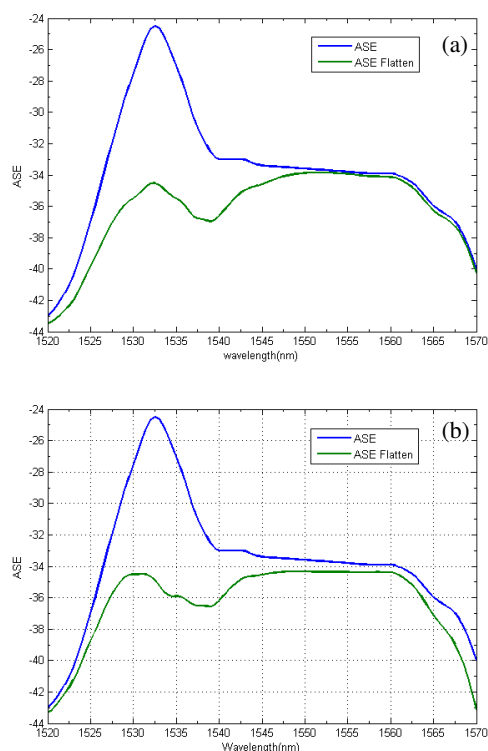


Fig.5. ASE spectrum along with the flattened spectra corresponding to $N = 10$, (a), and $N = 40$, (b).

10 and $N = 40$ along with the target spectrum S_t . These rejection bands were implemented for flattening the ASE spectrum. The flattened ASE spectra corresponding to the optimized values of various parameters are shown in Fig. 5. We can see that the ripple in the flattened spectrum decreases with the increase in the value of grating sections, N . Hence, the judicious selection of number of section to design of chirp grating reduces the ripple and makes the flattening better. In our simulation, the flattening has been achieved with ± 1.0 dB ripple in the wavelength range 1530 - 1560 nm.

6. CONCLUSION

Our simulations show that the APSO is a quicker way to optimize the waveguide and grating parameters for flattening the ASE spectrum of EDFA. The APSO is immune to trapping in local minimum and is independent of number of parameters to be optimized. The method is powerful for designing the waveguide structure and grating parameters when the numbers of optimization parameters are large. With APSO optimization, we have designed the chirped long period waveguide grating to achieve flattening ASE spectrum with a ripple of ± 1.0 dB in the C-band.

7. REFERENCES

[1] A D Kersey, M A Davis, H J Patrick, M LeBlanc, K P Koo, C G Askins, M A Putnam and E Joseph,

- “Fiber Grating Sensor”, *J. Lightwave Technol.*, **15**, 1442 (1997).
- [2] B Lee, “Review of the present status of optical fiber sensor”, *Opt. Fiber Technol.* **9**,57 (2003).
- [3] S A Vasiliev and OI Medvedkov, “Long Period refractive index fiber grating: properties, application and fabrication techniques”, *Proc. SPIE*, **4083**, (2000).
- [4] A M Vengsarkar, P J Lemaire, J B Judkins, V Bhatia, T Erdogan and J E Sope, “Long Period Fiber Grating as Band Rejection Filter”, *J. Lightwave Technol.*, **14**, 58 (1996).
- [5] V Bhatia, “Application of Long period grating to single and multi-parameter sensing”, *Opt. Express.* **4**, 457(1999).
- [6] H Hochriener, “Modeling of Long period fiber grating in chemical sensing application”, *PhD Thesis* (2008).
- [7] V. Rastogi and K. S. Chiang, “Long-period gratings in planar optical waveguides,” *Appl. Opt.*, **41**, 6351 (2002).
- [8] Q Liu, K S Chiang V Rastogi, “ Analysis of corrugated long period grating in slab waveguide and their polarization dependence”, *J. Lightwave Technol.* **21**,3399 (2003).
- [9] R Hassan, B Cohanin and O Weck, “A comparison of Particle Swarm Optimization and The Genetic Algorithm”, *AIAA*, **1** (2004).
- [10] S Das, A Abraham and A Konar, “ Particle Swarm Optimization and Differential Evolution Algorithms: Technical Analysis, Applications and Hybridization Perspectives” www.springerlink.com, Springer-Verlag Berlin Heidelberg, **1** (2008)
- [11] Z H Zhan, J Xiao, J Zhang and W N Chen, “Adaptive Control of Acceleration Coefficients for Particle Swarm Optimization Based on Clustering Analysis”, *IEEE Congr. Evol. Comput.*, 3276(2007).
- [12] Z. H. Zhan, J. Zhang, Y. Li and H. S. Chung, “Adaptive particle swarm optimization,” *IEEE Trans. Syst., Man, Cybern. B, Cybern.* **39**, 1 (2009).
- [13] T Huang and A S Mohan, “ A Hybrid Boundary Condition for Robust Particle Swarm Optimization” *IEEE Antennas and Wireless Propag. Lett.*, **4**,112(2005).
- [14] Q. Liu and K S Chang, “design of Long Period Waveguide Grating Filter by Controlling of Waveguide Cladding Profile”, *J. Lightwave Technol.*, **24**,3540(2006).
- [15] M S Kwon and S Y Shin, “Spectral tailoring of uniform long period waveguide grating by the cladding thickness control”, *Opt. Commun.*, **417**(2005).

Performance limitations in 10 Gb/s ITU-T G.653 fiber based all optical WDM system in presence of combined nonlinearities and ASE noise

Sridhar Iyer*, Shree Prakash Singh* and Subrat Kar⁺

*Division of ECE, Netaji Subhas Institute of Technology,
Sector-3, Dwarka, New Delhi-110078
Email: sridhar@nmsu.edu and sps_nsit@yahoo.co.uk

⁺Department of Electrical Engineering,
IIT Delhi, Hauz Khas, New Delhi-110016
Email: subrat@ee.iitd.ac.in

Abstract— In this paper we study the impact of combined nonlinear effects (i.e. stimulated Raman scattering (SRS) and four wave mixing (FWM)) and their interplay with amplified spontaneous emission (ASE) noise on the performance of all optical WDM network in terms of Quality factor (Q-factor) for various system parameters based on ITU-T Recommendation G.692 for applications on G.653 fibers. The worst affected channels due to SRS has been considered for performance evaluation. The accuracy of the proposed model is confirmed by the match found between the results obtained theoretically and those using OptSim™ software. In both the cases it is observed that performance of the network is severely limited by the combined nonlinear effects and ASE noise generated by the amplifier.

1. Introduction

Wavelength-Division multiplexing (WDM) systems dominate long-haul and ultra-long-haul networks due to performance and cost advantages [1]. The accumulation of amplified spontaneous emission (ASE) noise due to Erbium Doped Fiber Amplifiers (EDFAs) and the dominant nonlinear effects of stimulated Raman scattering (SRS) and four wave mixing (FWM) [2] hinders the attempts made to utilize the large bandwidth provided by the optical fiber along the links, thus limiting the throughput of WDM networks [3].

Most investigations primarily focus on individual effects of nonlinearities and ASE noise on various WDM system parameters [4-6]. The transmission engineering of WDM networks though, requires an in-depth understanding of the collective nonlinear effects and their interplay with ASE noise in order to reliably identify their impact on the Q-factor.

Few works consider the combined effects of nonlinearities in presence of ASE noise on WDM system performance. Djordjevic [7] studied the limitations imposed by SRS, FWM and ASE noise in WDM system with dispersion compensated links using inline optical amplifiers. Maximum possible transmission distance in terms of various system parameters is discussed for data rates of 2.5 and 10 Gbps ignoring the beating of ASE noise with other nonlinearities.

Yu and Mahony [8] have studied the transmission limitations imposed by the combined effect of SRS, FWM, ASE noise and fiber dispersion. The authors concluded that a compromise is needed between conflicting requirements imposed by FWM and SRS effects on channel spacing to maximize the transmission distance. Analysis is performed at the data rate of 2.5 Gbps ignoring the beating between ASE noise and the nonlinearities.

Singh et al. [9] investigated the effect of FWM, ASE noise and wavelength converter noise on the performance of WDM all-optical networks and concluded that in presence of FWM, after a certain power level, performance of the network starts degrading. The probability of error evaluation is carried out in the absence of SRS effect.

Singh and Iyer [10] analyzed the performance of an optical star network considering the combined effect of FWM and SRS. It was observed that the network performance depends on FWM noise and power received at the receiver due to SRS. The

analysis takes into account the beating between SRS and FWM but does not consider their interplay with ASE noise.

We extend the work in [10] and develop a mathematical model considering an intensity-modulated/direct-detection (IM/DD) system with N equally spaced channels to evaluate the performance considering the combined effect of FWM, SRS and ASE noise. The novelty of the model is that it accounts for beating between nonlinearities and beating between ASE noise and nonlinearities. Since the number of channels is large, effect of SRS is assumed to be deterministic and the Raman gain profile is assumed to be triangular [2].

The paper is organized as follows. Section 2 describes the system model. In section 3, we present the performance evaluation of the network when FWM, SRS and ASE noise are present. Finally, Section 4 discusses the numerical results and conclusion.

2. System Model

The network shown in Fig. 1 consists of two passive star couplers that distribute the input power equally among all N output ports. The amplifier is used as an inline amplifier and is considered to have a uniform gain G over the optical bandwidth B_0 . Each receiver receives signal on all the wavelengths and the optical filter is used to filter out the required wavelength. The received signal is then detected with the help of a photo detector. Maximum power will be depleted from the 1st channel due to SRS. The combined effect of FWM and ASE noise on this channel will further degrade the signal quality. Hence, 1st channel is considered for performance evaluation. Let the signal power at the 1st receiver be $P_{(s,1)}^{(r)}$ at frequency f_l and let P_t be the transmitted power. Data bits '1' and '0' are transmitted as a "mark" and "space" respectively and the signal power for bit '0' has been assumed to be zero.

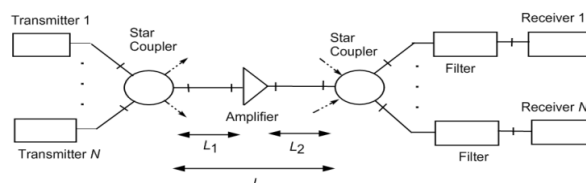


Fig.1. Optical star network with amplifier.

3. Performance Evaluation Considering the Combined Effect of FWM, SRS and ASE noise

For the network shown in Fig. 1, the total electric field at the receiver is given by

$$E(t) = B_s \sqrt{2P_{SRS(s,1)}^{(r)}} \cos(\omega_1 t) + \sqrt{2P_{FWM}^{(r)}} \cos(\omega_1 t - \theta_{FWM}) + \sum_{k=-M}^M \sqrt{2P_{sp} \delta\nu} \cos((\omega_1 + 2\pi k \delta\nu)t + \phi_k) \quad (1)$$

where ϕ_k is a random phase for each component of spontaneous emission. The first term is the electric field due to signal component while the second and third terms represent electrical field due to FWM and ASE noise respectively.

The mean value of currents $i_1(t)$ and $i_0(t)$ represented as $\langle i(1) \rangle$ and $\langle i(0) \rangle$ is given by [11]

$$\langle i(1) \rangle = R_0 P_{SRS(s,1)}^{(r)} + R_0 S_{sp} \delta\nu \cdot 2M \quad (2)$$

and

$$\langle i(0) \rangle = R_0 \langle P_{FWM}^{(r)}(0) \rangle + R_0 S_{sp} B_0 \quad (3)$$

respectively, where

$$\langle P_{FWM}^{(r)}(0) \rangle = 2 \left[\frac{1}{8} \sum_{k \neq l \neq m} P_{klm}^{(r)} + \frac{1}{4} \sum_{k=l \neq m} P_{kkm}^{(r)} \right] \quad (4)$$

The noise variance for bit '1' is [11]

$$\sigma^2(1) = \sigma_{Signal}^2 + \sigma_{ASE-Shot}^2 + \sigma_{ASE-Signal}^2 + \sigma_{ASE-ASE}^2 + \sigma_{FWM-signal}^2(1) + \sigma_{FWM-ASE}^2(1) + \sigma_{Thermal}^2 \quad (5)$$

The different noise variances in the above equation are given by [12]

$$\sigma_{ASE-ASE}^2 = R_0^2 S_{sp}^2 [2B_e B_0 - B_e^2] \quad (6)$$

$$\sigma_{ASE-signal}^2 = 4R_0^2 P_{SRS(s,1)}^{(r)} S_{sp} B_e \quad (7)$$

$$\sigma_{ASE-shot}^2 = 2eR_0 S_{sp} B_e B_0 \quad (8)$$

$$\sigma_{Thermal}^2 = 4K_B T B_e / R_L \quad (9)$$

$$\sigma_{FWM-ASE}^2(1) = 4R_0^2 \langle P_{FWM}^{(r)}(1) \rangle \cdot S_{sp} B_e \quad (10)$$

where

$$\langle P_{FWM}^{(r)}(1) \rangle = 2 \left[\frac{1}{8} \sum_{k \neq l \neq m} P_{klm}^{(r)} + \frac{1}{4} \sum_{k \neq l \neq m=1} P_{kll}^{(r)} + \frac{1}{4} \sum_{k=l \neq m} P_{kkm}^{(r)} \right] \quad (11)$$

and B_e is the ideal electrical filter bandwidth in the receiver.

The noise variance for bit '0' is [11]

$$\sigma^2(0) = 2eR_0 S_{sp} B_0 B_e + R_0^2 S_{sp}^2 [2B_e B_0 - B_e^2] + \sigma_{FWM-ASE}^2(0) + 4K_B T B_e / R_L \quad (12)$$

where

$$\sigma_{FWM-ASE}^2(0) = 4R_0^2 \langle P_{FWM}^{(r)}(0) \rangle \cdot S_{sp} B_e \quad (13)$$

The Q-factor specifies the performance as it is related to signal to noise ratio to achieve a specific probability of bit error. The Q-factor is given as

$$Q = \frac{\langle i(1) \rangle - \langle i(0) \rangle}{[\sigma(1) - \sigma(0)]} \quad (14)$$

For probability of error of 10^{-9} , value of Q is 6. Substituting $\langle i(1) \rangle$, $\langle i(0) \rangle$ from equations (2), (3) into equation (14), we obtain

$$Q = \frac{R_0 P_{SRS(s,1)}^{(r)} - 2R_0 P_{FWM}^{(r)} \left[\frac{1}{8} \sum_{k \neq l \neq m} \frac{P_{klm}^{(r)}}{P_{SRS(s,1)}^{(r)}} + \frac{1}{4} \sum_{k=l \neq m} \frac{P_{kkm}^{(r)}}{P_{SRS(s,1)}^{(r)}} \right]}{\sigma(1) + \sigma(0)} \quad (15)$$

4. Numerical Results and Conclusion

In order to evaluate the exactness of the theoretical results, we conducted extensive computer simulations of an 8 and 16 channel WDM transmission system based on ITU-T G.692 recommendation [13] for applications on G.653 fibers [14]. We used the commercial package Rsoft OptSimTM simulation software version 4.0 to simulate the 8 channel WDM system shown in Fig. 2. The same system was extended by adding 8 more channels in order to simulate a 16 channel WDM system. The channels are modulated at 10 Gbps data rate using NRZ format and the analysis concerns the 'worst case', i.e. the case of the 1st channel with the simultaneous presence of '1' bits in all the other channels. For details of the simulation system shown in Fig.2 which consists of three major sections viz., Transmitter section, Fiber section and Receiver section, we point the reader to [11].

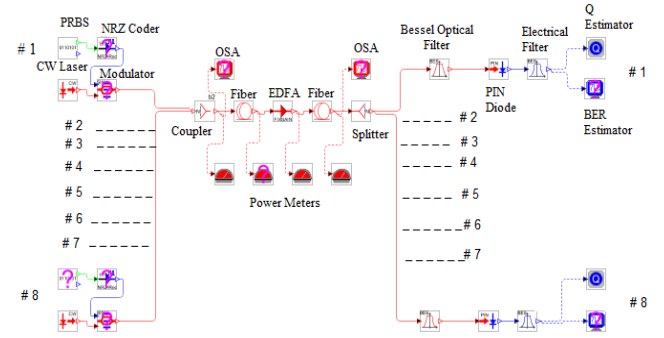


Fig.2. Architecture of the analyzed 8 channel WDM system.

With the parameters mentioned in Table 1, Q for different values of transmitted power has been computed for the worst affected channel when (a) thermal, shot and SRS (b) thermal, shot, FWM and SRS and (c) thermal, shot, FWM, SRS and ASE noise are present.

Table 1: Typical values of different parameters.

Parameters	Symbol	Values
Quantum efficiency of photo detector	η	0.95
Length of the fiber between star coupler	L	120 km
Attenuation coefficient of Fiber	α	0.2 db/km
Raman gain profile	γ_p	$7 \times 10^{-12} \text{ cm/W}^2$
Unsaturated amplifier gain	G	10 dB
Optical filter bandwidth	B_o	10 GHz
Insertion loss of each 2x2 Coupler	L_i	0.5 dB
Splice loss	L_{sp}	0.5 dB
Receiver temperature	T	300K
Electrical bandwidth of receiver	B_e	1 GHz
Load Resistance	R_L	100
Output power variability of NxN coupler	L_{cv}	0.5 dB
Frequency separation between channels	Δf	75 & 125 GHz
Spontaneous emission factor	n_{sp}	3
Nonlinear refractive index of fiber	n_2	$2.7 \times 10^{-20} \text{ m}^2/\text{W}$
Dispersion coefficient	D_c	17 ps/nm.km

The theoretical results are presented in Fig. 3, 4 and 5. Fig. 3 and 4 show the variation of Q with transmitted power for a WDM system with frequency separation of 125 GHz and 75 GHz between the channels for 8 and 16 channel WDM systems respectively. Fig. 5 shows the variation of Q with transmitted power for the worst affected channel when there are 8 and 16 channels with frequency separation of 75 GHz.

It can be observed from these figures that when the number of users is 8 or 16:

- i. In presence of SRS, thermal and shot noises, Q increases linearly with the transmitted power irrespective of the channel separation.
- ii. In presence of FWM, SRS, shot and thermal noises, Q increases to a certain power level after which it starts decreasing as FWM noise is dominant at high power level.
- iii. In presence of ASE noise along with FWM, SRS, thermal and shot noises, the maximum value of Q further decreases for a given transmitted power.
- iv. Performance of the network when the frequency separation is 75 GHz is worst compared to when the separation is 125 GHz. The maximum Q value obtained is observed to decrease as the channel separation decreases since the effect of FWM increases with decrease in channel separation and the signal power degrades due to SRS.
- v. Performance of a 16 channel network is worst compared to the performance when the number of channels is 8. This is due to the following reasons:
 - a) With the increase in number of channels, power loss in the splitter increases as a result of which higher transmitted power is required to obtain a given value of Q, and
 - b) With the increase in the number of channels, the number of FWM components generated increase leading to degraded network performance.

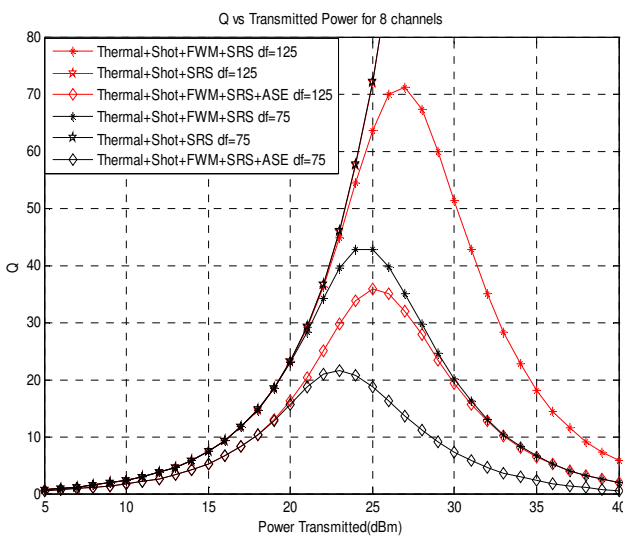


Fig.3. Variation of Q-factor with transmitted power for the worst affected channel for 8 channels with channel separation of 125 GHz and 75 GHz.

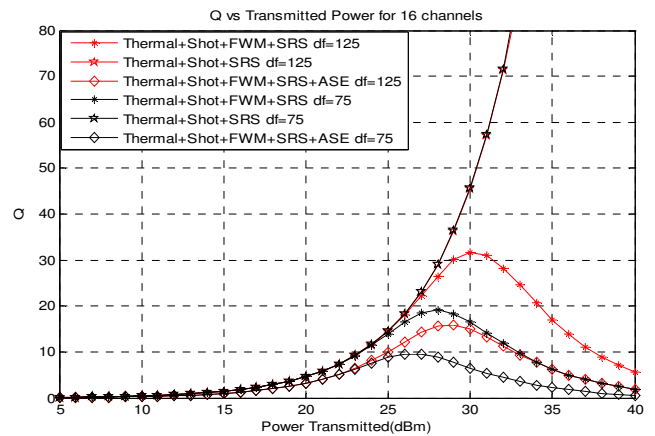


Fig.4. Variation of Q-factor with transmitted power for the worst affected channel for 16 channels with channel separation of 125 GHz and 75 GHz.

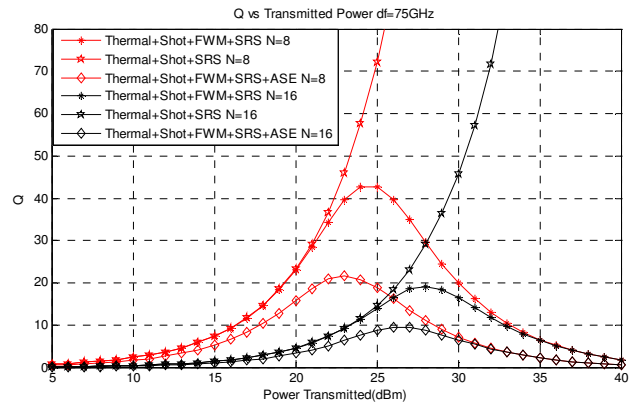


Fig.5. Variation of Q-factor with transmitted power for the worst affected channel when there are 8 and 16 channels.

The comparison of theoretical results with OptSim simulation results considering the presence of all the noises (i.e. shot, thermal, SRS, FWM and ASE noise) is presented in figure 6 which shows the variation of Q with transmitted power for an 8 channel WDM system with frequency separation of 125 GHz and 75 GHz respectively.

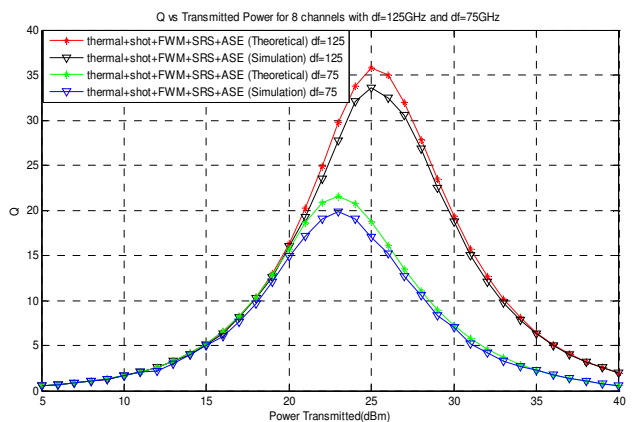


Fig.6. Variation of Q-factor with transmitted power for the worst affected channel for 8 channels with channel separation of 125 GHz and 75 GHz respectively.

It can be observed from the plot that the simulated results give a lower value of Q compared to the theoretical results. Also, the comparison of theoretical results with OptSim simulation results is found to match which shows that our model calculates the network performance accurately. Similar observations and conclusions were drawn when a 16 channel WDM system with frequency separation of 125 GHz and 75 GHz respectively was simulated.

To conclude, performance of the network depends on the collective effect of SRS, FWM, and ASE noise. Results of this study indicate that the optimum value of power per channel depends on the number of channels and channel separation.

Acknowledgment

The authors would like to thank the AICTE for funding this work under research promotion scheme (RPS-11/2008-09). Authors are also thankful to Ms Sujata Sengar for giving valuable comments.

References

- [1] B. Mukherjee, "WDM-based local lightwave networks part-1: Single-hop systems," *IEEE Network*, vol. 6, no. 3, pp. 12–27, May 1992.
- [2] F. Forghieri, R. W. Tkach and A. R. Chraplyvy, "Fiber nonlinearities and their impact on transmission systems", *Optical Fiber Telecommunications*, I. P. Kaminov and T. L. Koch, Eds. San Diego, CA: Academic, 1997, vol. IIIA, ch. 8, pp. 196-264, 1997.
- [3] G. P. Agrawal, *Fiber optics communication systems*, 3rd edition, John Wiley & Sons, 2002.
- [4] J. Villarroel, A. G. Grandpierre, "On statistical effects on stimulated Raman cross-talk", *J. Phys. B: At. Mol. Opt. Phys.* 38, pp. 2601–261, 2005.
- [5] K. P. Ho, "Statistical properties of stimulated Raman crosstalk in WDM systems," *J. Lightwave Technol.*, Vol. 18, pp. 915-921, 2000.
- [6] Michael Eiselt, "Limits on WDM Systems Due to Four-Wave Mixing: A Statistical Approach", *Journal of Lightwave Technology*, vol. 17, no. 11, November 1999.
- [7] I. B. Djordjevic, "Transmission limitations of WDM transmission systems with dispersion compensated links in the presence of fiber nonlinearities", In: *Proc. TELSIS, IEEE*, Nis, Yugoslavia, pp. 496–499, 2001.
- [8] A. Yu, M. J. O'Mahony, "Optimization of wavelength spacing in a WDM transmission system in the presence of fibre nonlinearities", *IEE Proc. Optoelectron*, vol. 142, no. 4, pp. 190–196, 1995.
- [9] S. P. Singh, S. Kar, V. K. Jain, "Performance of All-Optical WDM Network in Presence of Four-Wave Mixing, Optical Amplifier Noise, and Wavelength Converter Noise", *Fiber and Integrated Optics*, vol. 26, no. 2, pp. 79-97, 2007.
- [10] S. P. Singh and Sridhar Iyer, "Impact of SRS and FWM on Performance of Optical Star WDM Networks", In *Proc. Of International Symposium on Photonics and Optoelectronics (SOPO 2011)*, pp. 1-4, May 2011.
- [11] Sridhar Iyer and Shree Prakash Singh, "Impact of combined nonlinearities and ASE noise on Performance of 10 Gbps all Optical Star WDM Networks", accepted for publication in *Communications and Networks, Scientific Research*, vol. 3, no. 4, Nov. 2011.
- [12] S. P. Singh, S. Kar, V. K. Jain, "Effect of four-wave mixing on optimal placement of optical amplifier in WDM star networks", *Fiber Integrated Opt.*, vol. 25, pp. 111–140, 2006.
- [13] ITU-T Rec. G.692, "Optical interfaces for multichannel systems with optical amplifiers", 1997.
- [14] ITU-T Rec. G.653, "Characteristics of a non-zero dispersion shifted single-node optical fiber cable", 1996.
- [15] G. P. Agrawal, "Nonlinear Fiber Optics", 3rd edition, Academic Press, New York, 2001.

NUMERICAL ANALYSIS OF SNR PERFORMANCE OF 1.55μm INLINE TWSOA UNDER WDM SIGNAL TRANSMISSION

P.Manimaran¹, M.Ganesh Madhan²

Department of Electronics Engineering, MIT Campus, Anna University, Chennai and 600044, India.

¹maran_pm@yahoo.co.in, ²mganesh@annauniv.edu

Abstract: A detailed analysis of noise performance of 1.55μm traveling wave semiconductor optical amplifier (TWSOA) under DWDM signal transmission is performed. The device parameters such as gain, ASE power, spectrum, SNR for 8 ITU band DWDM wavelengths are analyzed.

1. INTRODUCTION

WDM networks are the main core of optical signal communication systems. TWSOA being a multifunctional device [1] it is employed for signal amplification in WDM networks, since it can handle high bandwidth with an appreciable gain [3][4]. The SNR of an amplifier is always limited by the noise factor associated with the device and signal being amplified [5]. It is due to the fact that the amplifier not only amplifies the signal, it also generates the noise along with it [6]. The SNR being the figure of merit of any communication system, the main idea of this work is to analyze and compute the carrier density variations, signal gain, output signal power, SNR of the TWSOA for different ITU band DWDM wavelengths for a particular bias current of 100mA for an input signal power of -30dBm.

2. MODELLING

We adopt the steady state numerical model proposed by Connelly [2], since it is more suited for wideband TW-SOA analysis. This model also provides spatial variations of photon and carrier densities. The carrier density rate equation of SOA, is given by

$$\begin{aligned} \frac{dn(z)}{dt} = & \frac{I}{edLW} - R(n(z)) \\ & - \frac{\Gamma}{dw} \left\{ \sum_{k=1}^{N_s} g_m(\nu_k, n(z)) (N_{sk}^+(z) + N_{sk}^-(z)) \right\} \\ & - \frac{2\Gamma}{dw} \left\{ \sum_{k=1}^{N_m-1} g_m(\nu_k, n(z)) K_j ((N_j^+(z) + N_j^-(z))) \right\} \end{aligned} \quad (1)$$

The rate equation incorporates the carrier injection to the active region due to the bias, spontaneous radiative and non-radiative recombination mechanisms and radiative recombination of carriers by the amplified signal and ASE. The confinement factor 'Γ' is also incorporated in the model.

The material gain coefficient of the semiconductor medium is given as

$$g_m = g_m' - g_m'' \quad (2)$$

Where, g_m' is gain coefficient and g_m'' is absorption coefficient.

$$\begin{aligned} g_m' = & c^2 / (4\sqrt{2}\pi^{3/2} n_1^2 \tau \nu^2) \times \\ & (2m_e m_{hh} / ((h/2\pi)m_e + m_{hh}))^{3/2} \\ & \times \sqrt{[\nu - (E_g(n))]/h} [f_c(\nu)(1-f_v(\nu))] \end{aligned} \quad (3)$$

$$\begin{aligned} g_m'' = & c^2 / (4\sqrt{2}\pi^{3/2} n_1^2 \tau \nu^2) \\ & \times [2m_e m_{hh} / ((h/2\pi)m_e + m_{hh}))^{3/2}] \\ & \times \sqrt{[(\nu - (E_g(n)))/h] (f_v(\nu)(1-f_c(\nu)))} \end{aligned} \quad (4)$$

The Fermi-Dirac distributions of conduction band and valance band of the active region material are given by the usual relations. The parameters used in the above equations are as follows.

c = speed of light in vacuum

ν = optical frequency

τ = carrier radiative recombination lifetime

n = CB carrier density

The values of various parameters used in the simulation are given in Table I. By solving the rate equation (1) by steady state numerical algorithm [2], the carrier density, gain, output signal power, ASE power, are obtained at -30 dBm input power levels and 100 mA bias currents. Further, the variation of gain and signal power along the different positions of the cavity length is also determined under WDM condition.

TABLE I
SOA PARAMETERS [2]

Symbol	Parameter	Value
L_c	Central active region length	450 μm
L_t	Tapered active region length	50 μm
d	Active region Thickness	0.4 μm
W	central active region width	0.4 μm
Γ	Confinement factor	0.45
K_g	Band gap shrinkage coefficient	0.9×10^{-10} eVm
n_1	InGaAsP active region Refractive Index	3.22

Symbol	Parameter	Value
n_2	Refractive index of InP region	3.167
dn_1/dn	Active region RI change with n	$-1.8 \times 10^{-26} \text{ m}^{-3}$
n_{eq0}	Equivalent RI at $n = 0$	3.22
dn_{eq}/dn	Equivalent RI of active region change	$-1.34 \times 10^{-26} \text{ m}^{-3}$
$\eta_{in}\eta_{out}$	input and output coupling loss	3 dB
R_1, R_2	Input, output Reflectivity	5×10^{-5}
K_0	independent loss coefficient	6200 m^{-1}
K_1	dependent loss coefficient	7500 m^2
A_{rad}	linear radiative recombination coefficient	$1 \times 10^7 \text{ s}^{-1}$
B_{rad}	bimolecular radiative recombination coefficient	$5.6 \times 10^{-16} \text{ m}^3 \text{ s}^{-1}$
C_{aug}	auger recombination coefficient	$3 \times 10^{-41} \text{ m}^6 \text{ s}^{-1}$
D_{leak}	leakage recombination coefficient	$0.0 \times 10^{-48} \text{ m}^{13.5} \text{ s}^{-1}$
A_{nrad}	linear non radiative recombination coefficient	$3.5 \times 10^8 \text{ s}^{-1}$
N_T	carrier density at threshold	$4.5 \times 10^{22} / \text{m}^3$

3. SIMULATION RESULTS AND ANALYSIS

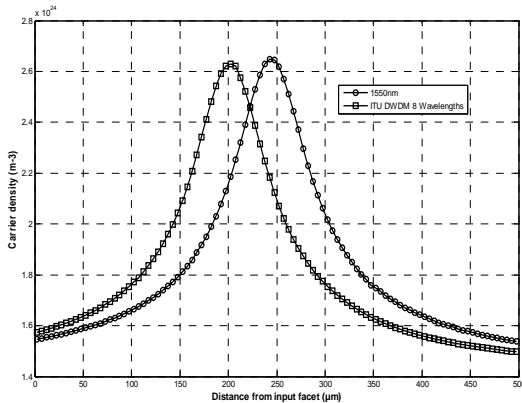


Fig 1. Spatial variation of carrier density for single (1550nm) and ITU band DWDM signals.

To evaluate the TWSOA gain under dc current, the rate equation (1) is solved for various dc currents ranging from 0 to 150 mA, using Matlab. It is found that for 100mA current, a gain of 30 dB is achieved. Further, the spatial variation of the carrier density and consequent gain is evaluated.

The carrier density shows a peak, whose position shifts towards the left for 8 channel WDM transmission. Fig 1 shows this behavior and a 50μm shift towards the input facet is observed. Fig 2 prominently shows the gain variation for different wavelengths of the WDM signals, at a constant bias of 100 mA.

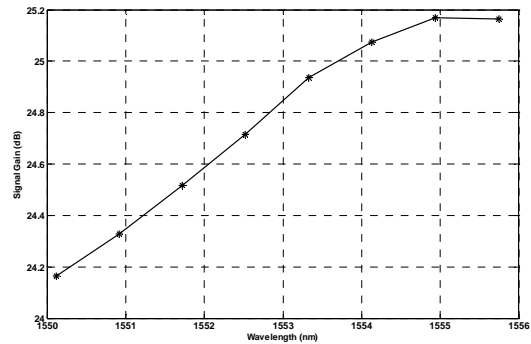


Fig.2 Signal gain for various ITU band DWDM wavelengths

The input optical spectrum of eight WDM ITU band signal ranging from 1550.12nm to 1555.75nm with a constant signal power of -30dBm and 100mA bias current.

The output amplified spectrum of the TWSOA shows non uniform signal level due to the influence gain and ASE noise floor which is clearly seen fig 3.

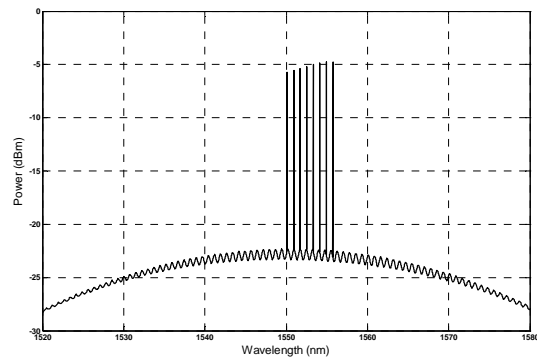


Fig.3. Optical output spectrum for various ITU band DWDM wavelengths

Fig.4 shows the SNR plotted against the various DWDM ITU band wavelengths, which reveals that the SNR degradation is high for lower wavelengths compared to higher wavelengths and follows the gain profile.

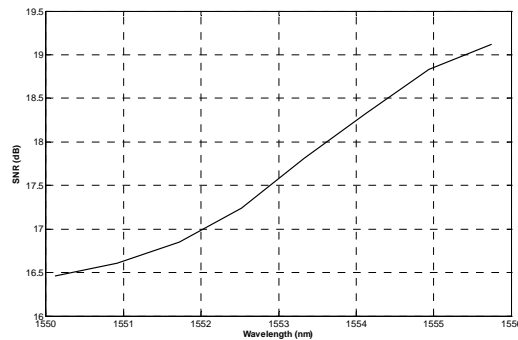


Fig.4. Optical output spectrum for various ITU band DWDM wavelengths

4. CONCLUSION

A detailed SNR analysis of TWSOA under 8 channels WDM (ITU band) is carried out for 100 mA bias and – 30 dBm signal level. The carrier density shift, non uniform gain characteristics and the SNR at TWSOA output is evaluated.

ACKNOWLEDGEMENT

The authors gratefully acknowledge Department of Science and Technology (DST), Govt of India, New Delhi for providing financial support to carry out this research work under PURSE scheme. One of the authors, Mr.P.Manimaran is thankful to Department of Science and Technology (DST), Govt of India, New Delhi for the award of DST-PURSE fellowship.

REFERENCES

- [1] K. T. Koai and R. Olshansky, "Simultaneous Optical amplification, Detection, and Transmission Using InLine semiconductor Laser Amplifiers", IEEE Photonics Tech. Lett., Vol. 4, No. 5, pp 441 - 443, 1992.
- [2] Michael J. Connelly, "Wideband Semiconductor Optical Amplifier Steady-State Numerical Model" IEEE, JQE, Vol. 37, No. 3, March 2001.
- [3] H.H.Lee et al "A gain-clamped-semiconductor optical amplifier combined with a distributed Raman-fiber amplifier a good candidate as an inline amplifier fo WDM networks", Optics Communications 229, (2004) 249–252.
- [4] Walid Mathlouthi et al "Fast and Efficient Dynamic WDM semiconductor optical amplifier model" Journal of lightwave technology, vol. 24, no. 11, November 2006
- [5] Ernesto Ciaramella et al "Using semiconductor-optical amplifiers with constant envelope WDM signals" journal of quantum electronics, vol. 44, no. 5, May 2008
- [6] T. Rogowski, et al "SOA-based WDM metro ring networks with link control technologies" Photonics technology letters, vol. 19, no. 20, october 15, 2007

EXPERIMENTAL ANALYSIS OF 900MHz RF SIGNAL TRANSMISSION THROUGH COMMERCIAL CATV FIBER OPTIC LINK

S.Piramasubramanian¹, M.Ganesh Madhan² and J.Sankar³

Department of Electronics Engineering, MIT Campus, Anna University, Chennai, India.^{1,2}
Amptronix Ltd, Chennai, India.³

Email: spirama@annauniv.edu¹, mganesh@annauniv.edu²

Abstract: We have evaluated the performance of 900MHz RF signal transmission through commercial CATV fiber optic link. RF link efficiency is measured for (48 – 750) MHz band and 900 MHz in 1.54km single mode fiber link. The performances of above links are evaluated for various values of RF and optical power levels.

1. INTRODUCTION

The Radio over Fiber (RoF) technology is used to transmit CATV, mobile and other wireless signals in order to overcome RF signal loss, EMI and to improve coverage in wireless and other transmission mediums[1]-[3]. In RoF scheme, RF signal directly modulates the optical carrier in a laser diode then transmitted through fiber link. In a significant advantage, it reduces the number of equipments used in mobile base station, in the case of cellular signal transmission. In CATV distribution systems, television signals are received from satellites at one point and retransmitted to subscriber nodes through optical fibers. Television channels are transmitted in the band of (48-750) MHz. In GSM-900 Cellular standard, (890-915) MHz frequency band and (935-960) MHz band are used for uplink and downlink respectively. In this paper, We evaluate the performance of 900MHz RF signal (GSM) transmission through single mode CATV fiber optic links. We determined the link efficiency under different RF and optical power conditions.

2. RADIO OVER FIBER LINK

Radio over Fiber (ROF) transmission is an attractive means of delivering radio service signals to remote antenna locations. The block diagram of basic radio over fiber system is shown in Figure.1. Optical transmitter, fiber and receiver are main parts of this system. RF signal from the antenna is given to the circulator. In the uplink, RF signal is amplified by low noise amplifier (LNA) and given to the laser diode. Direct or external modulation can be used at this stage. Mach-Zehnder modulator or electro absorption modulator are used as external modulator. After the modulation, the light is transmitted through either single mode or multi mode fiber. Single mode fiber is used for long distance optical communication links. The RF signal is detected at the central station. In the down link, RF signal is modulated with light at central site and transmitted through fiber. This signal again detected at base station and transmitted through antenna. The distance between base station and central site is depends on the type of application. Circulator is used to isolate the transmitter and receiver, whenever single antenna is used. This RoF

architecture shown in Figure 1, is slightly modified so as to accommodate broad cast of broadband CATV signals from antenna site to a large number of consumers. We investigate the performance of such a link, when a 900 MHz GSM signal channel is transmitted in 1310 nm CATV link.

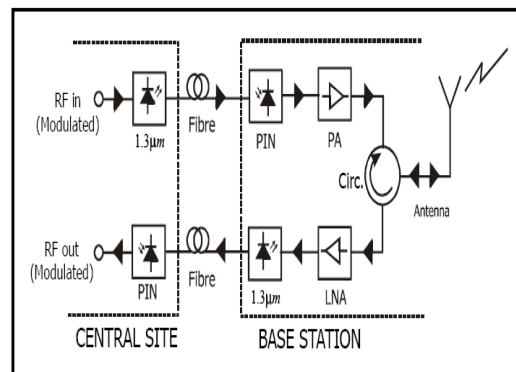


Fig.1. Block diagram of basic Radio over fiber system.

3. EXPERIMENT AND RESULTS

In this work, 1.54km single mode fiber is used, since single mode fibers are conventionally used for long distance optical communication links. Further, single mode fiber also supports higher bit rate than multi mode fiber. The laser transmitter used in this work is a conventional CATV laser transmitter, which uses a DFB laser with 1 GHz modulation bandwidth operating at 1310nm. The specifications of laser diode module in the transmitter are given in the table 1.

Table 1 Laser Diode Module specifications

Parameters	Specifications
Centre wavelength	1310nm
Spectral width (-20dB)	0.1nm
Optical Output power	20mW
Threshold Current	12mA

Forward Voltage	1.2V
Monitor dark current	200nA
Thermistor resistance	10kΩ
TEC current	2A

In this experimental setup, commercial CATV optical transmitter comprising of a 1310nm DFB Laser (Mitsubishi – FU-436SDF), optical receiver, 1.5GHz spectrum analyzer (Agilent E4411B), optical splitters, optical attenuator, 1.54 Km single mode fibers are used. The experimental blocks are shown in Figure.2. The RF signal can be generated from a vector signal generator or the tracking generator of the Spectrum analyzer. This signal directly modulates the laser diode in the optical transmitter. Optical coupler (80/20) is used after laser transmitter. Optical attenuator is used to reduce the optical power. This signal is transmitted through fiber link and received. The received RF signal is measured by using spectrum analyzer.

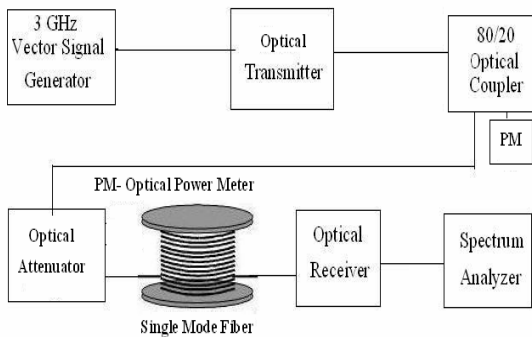


Figure2.Experimental setup for 900MHz RF signals transmission through fiber.



Figure 3. Photograph of the experimental setup for 900MHz RF signals transmission through fiber.

3.1 Performance of 900 MHz signal at various input RF power levels.

In this experimental setup, single mode fiber with length of 1.54km is used. The RF sweep signal is generated in the tracking generator of spectrum analyzer and transmitted through the fiber link. The photograph of this setup is given in figure 3.

The optical power is measured at every stage in the link. Optical attenuators are used to reduce the optical power in the link. The input optical power at front end of the fiber link is measured as 6.92dBm. The optical transmitter and receiver used in this experiment are similar to that used in CATV applications. Patch chords are used to connect the optical components in the link. This experimental block diagram is shown in figure 2. The optical attenuator is used to vary the optical power in the experiment. The 900 MHz RF signal is transmitted through the fiber link and the response is shown in the figure 4. The received signal is compared with CATV signal (48MHz – 750MHz).

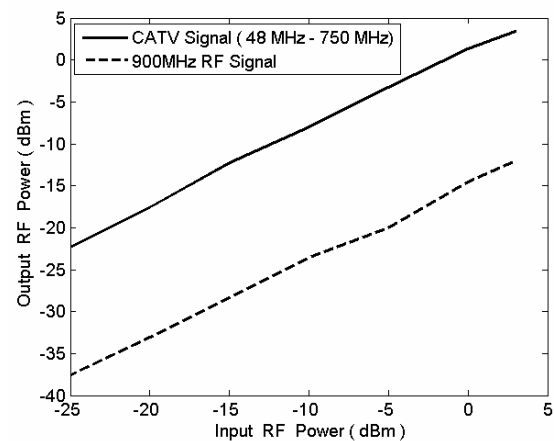


Figure 4. RF output power variation with transmitted CATV signal and 900MHz in 1.54km single mode analog fiber link.

The received RF signal power at 900 MHz is found to be less than that of CATV input signal. The output RF power increases when the input RF power is increased. The RF power received after the link is -15.59 dBm at 900 MHz. The received RF power is -24.62 dBm at the same frequency, when the RF input signal source amplitude is kept at -10 dBm. The screen shot of the spectrum analyzer for the above measured signal is shown in figure 5.

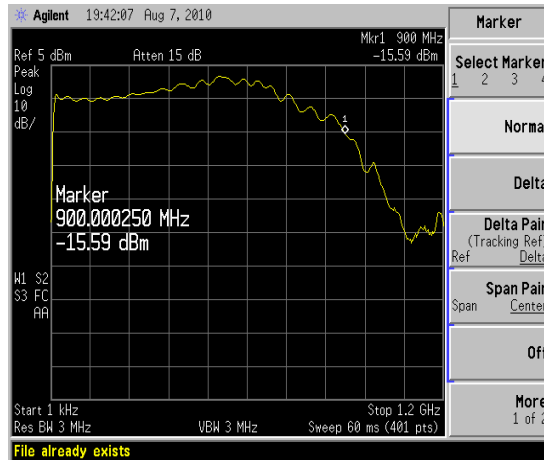


Figure 5. RF output power variation with transmitted optical power

3.2. Performance of 900MHz RF signal under different levels of optical power

In this experiment, RF signal is swept between 10 MHz to 1 GHz from the spectrum analyzer and given to CATV optical transmitter. Optical power from the transmitter is measured as 6.92 dBm. This optical power is varied by an optical attenuator and (50/50) optical coupler. Single mode optical fiber (1.54km) is connected between coupler and receiver for the experiments. Output RF signal power is measured in the spectrum analyzer for various optical power levels. Received RF power for different values of optical powers in a 1.54km single mode fiber link is shown in Figure 6.

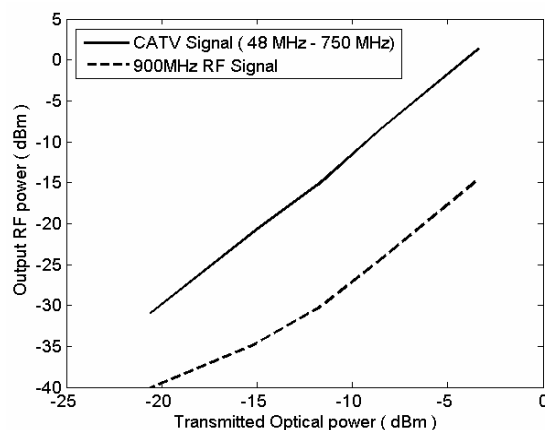


Figure 6. RF output power variation with transmitted optical power for CATV signal and 900MHz in 1.54km single mode analog fiber link.

The CATV signal in the band of (48-750) MHz produces a larger RF power at the receiver when compared to the 900MHz signal. The GSM band signal provides RF power of 15dB less than CATV signal. However considering narrow band nature of GSM signal, it is possible to successfully retrieve the signal from the CATV fiber link for wireless transmission. The link efficiency is lower for 900MHz due to bandwidth restrictions in the commercial CATV transmitter, but still provides reasonable RF output which can be used effectively.

4. CONCLUSION

Radio over Fiber (RoF) technology is used to transmit CATV, mobile and other wireless signals in order to overcome signal loss, EMI and to improve coverage in wireless and other transmission mediums. Large bandwidth and modulation independent transmission capacity of optical fiber is major attraction for this approach. In this work, Single mode analog fiber optic link is constructed with 1.54km length. Laser transmitter with modulation bandwidth of 1.0 GHz is used in this experiment. CATV signal and 900MHz RF signal are transmitted through 1.54km single mode fiber link and performance are evaluated. The GSM band signal provides RF power of 15dB less than CATV signal. However considering narrow band nature of GSM signal, it is possible to successfully retrieve the signal from the CATV fiber link for wireless transmission.

ACKNOWLEDGEMENT

We thank the Centre for Technology Development and Transfer (CTDT), Anna University-Chennai for providing financial support under Young Faculty Research Support Scheme (YFRSS- 2009 - 10).

REFERENCES

- [1] C.H.Cox, G.E.Betts and L.M.Jhonson, "An analytic and experimental comparison of direct and external modulation in analog fiber optic links", *IEEE Microwave Theory and Techniques*, **38**, 501 (1990).
- [2] Hamed Al-Rawesshidy, Shozo Komaki, "Radio over Fiber Technologies for Mobile Communication Networks", Artech House Inc. 2002.
- [3] William S.C. Chang, "RF photonic technology in optical fiber links", Cambridge University press, 2002.

- [4] Yuen, Roland, Fernando, Xavier. N, Krishnan, Sridhar, "Radio over multimode fiber for wireless access", *Canadian Conference Electrical and Computer Engineering*, **3**,1715 (2004).
- [5] A.Takemoto, H.Watanabe, Y.Nakajima, Y.Sakakibara, S.Kakimoto, J.Yamashita, T.Hatta and Y.Miyake, "Distributed feedback laser diode and module for CATV systems", *IEEE journal of selected areas in communication*", **8** ,1359 (1990)

AN EFFICIENT FAST (PARALLEL) CONNECTION RECOVERY STRATEGY FOR SURVIVABLE WDM OPTICAL NETWORK

Dharmendra Singh Yadav, Santosh Rana, Shashi Prakash*

Photonics Laboratory, Department of Electronics and Instrumentation Engineering, Institute of Engineering & Technology, Devi Ahilya University, Indore-452001, INDIA

*Email: sprakash_davv@rediffmail.com

Abstract: A parallel switching strategy for surviving the connection failures in WDM networks is proposed. The simulation experiments were conducted for the determination of average recovery time and resource utilization on practical topology of NATIONAL and ARPANET network. The results of the investigation conclusively establish that the proposed strategy (PS) performs better than the existing strategies.

1. INTRODUCTION

In WDM networks when a failure occurs, a huge amount of data is lost in a fraction of second. Therefore, the failed connection request should be re-routed through backup route as soon as possible. In the WDM network Shared Path Protection (SPP) and Shared Link Protection (SLP) connection recovery strategies are used to reroute the failed backup lightpath. In the protection strategy the alternate backup lightpath is reserved in advance at the time of connection setups. Whenever, connection failure occur the reserved backup lightpath is used to reroute the primary lightpath. In SPP approach [1], the failed lightpath is replaced by a new alternate backup lightpath, while in SLP [1] only failed link of the lightpath is replaced by the alternate route.

In order to achieve fast switching of primary lightpath many connections recovery strategies have been presented in the literature [1-7]. These fast switching techniques are based on the two mechanisms. In the first mechanism, efforts are put to minimize the length of the backup lightpath [2-4], and in the second mechanism efficient signaling procedure is developed for the backup lightpath establishment [5-7]. In [2-3], primary lightpath is segmented into several un-overlapped sub-primary paths until the segment's backup lightpaths satisfy the recovery time constraints. In [4], hops constraint has been used to compute the primary and back-up sub-paths for achieving the fast switching of the primary lightpaths. In [5], Disjoint Path Restoration (DPR) algorithm based on the one way signaling protocol has been presented for the fast switching of the primary lightpath. In [6, 7], the strategy proposed calculates the approximate upper bound value for the switching time of the failed primary lightpath.

The fast switching in SLP or Shared Segment Protection (SSP) is achieved at the cost of the

inefficient resources utilization [2, 3, 4]. Similarly, one way signaling or the offset based signaling is fast, but in these procedures source node does not receives acknowledgement of the connection setup message, which may result in the loss of data. In this paper, we present a connection recovery strategy which not only undertakes efficient resources allocation but also recovers connections in minimum time. The rest of the paper is organized as follows. Section II, deals with the system model; Section III presents the explanation of various strategies used in this work and the recovery for the strategies is also estimated. In section IV, the results of the investigation are discussed and in section V, the conclusions of research are presented.

2. SYSTEM MODEL

In this section, we will define the notations, which are used in the system model. We assume that the network topology and the randomly generated different sets of requests are given as input parameters. Our objective is to minimize the network capacity requirement for a given traffic demand, and to minimize the average recovery time to protect the network against single connection failure assumption. The notations are defined as follows:

- n Number of nodes in the network
- ℓ Number of links in the network.
- w Maximum number of wavelengths available per link.
- s Source node.
- d Destination node.
- R Number of demands i.e. $\{(s_1, d_1), (s_2, d_2), (s_3, d_3) \dots (s_i, d_i)\}$, where $\forall (s, d) \in n, \forall s \neq d, \forall i \in N$.
- $L_{ij}^p \in \{0,1\}$ which takes the value '1', if the primary route of i^{th} connection request

- uses j^{th} link of the network; otherwise '0', where $\forall i \in R, \forall j \in \ell$
- PR_i Primary route of the i^{th} connection request where $\forall i \in R$.
- BR_i Backup route of the i^{th} connection request, where $\forall i \in R$
- $W_{x,y}^p \in \{0,1\}$ which takes value '1', if x^{th} wavelength of y^{th} link is assigned to the primary lightpath of the request; otherwise '0', $\forall x \in w, \forall y \in \ell$.
- $W_{x,y}^b \in \{0,1\}$ which takes value '1', if x^{th} wavelength of y^{th} link is assigned to the backup lightpath of the request; otherwise '0', $\forall x \in w, \forall y \in \ell$
- $T_{n,k}$ Recovery time of connection request when the n^{th} link of the primary route of the k^{th} connection request fails $\forall n \in L_{i,j}^p, \forall k \in R$.

Objectives

- Minimize the network capacity used by the s-d pair requests in the network i.e.

$$\text{minimize } \sum (W_{x,y}^p + W_{x,y}^b)$$

- Minimize the average recovery time per request of the network. Average recovery time represents the average time taken to recover the primary lightpath failure. It is calculated by taking average of the recovery times of all the connection requests.

$$\text{minimize } \frac{\sum_{\forall i \in L_{j,k}^p, \forall k \in R} T_{i,k}}{\sum_{\forall i \in L_{j,k}^p, \forall k \in R} BR_{i,k}}$$

3. EXISTING AND PROPOSED STRATEGY (PS)

In this section, the connection recovery time of the existing strategies (SPP and SLP) is calculated. Before discussing the strategies, the recovery time parameter is defined as follows:

- Failure detection time i.e. time taken by the end nodes of the failed link to detect fault. We assume the failure detection time (T_f) to be 10 μ s.

- Message processing time (T_m) at a node is 10 μ s.
- Propagation delay (T_p) of the signal on each link is 400 μ s per 85 km.
- Cross connect time (T_c) to configure, test and setup an OXC the backup connection is setup, it is assumed to 2 ms.
- Number of hops (links) between the source node of the failed link to the source node of the connection request is H_{fs} .
- Number of hops between the destination node of the failed link to destination node of request is H_{fd} .
- Number of hops in the backup lightpath in the network is H_b .

3.1 SHARED PATH PROTECTION (SPP)

In SPP, a pre-computed backup lightpath (i.e. A-E-F-G-D in Fig. (1)) is reserved for the primary lightpath (A-B-C-D). Whenever the failure occurs, the source node of the failed link sends the failure notification message to the connection request source node. After receiving the failure notification, the source node sends the connection setup message via backup lightpath and waits for the acknowledgement. When source node receives the acknowledgement, it starts the data transmission through the backup lightpath. The connection recovery time is given as:

$$[T_f + (H_{fs} \times T_p) + \{ (H_{fs} + 1) \times T_m \}] + [\{ (H_b + 1) \times T_c \} + (H_b \times T_p) + \{ (H_b + 1) \times T_m \}] + [(H_b \times T_p) + \{ (H_b + 1) \times T_m \}] \text{--- (i)}$$

3.2 SHARED LINK PROTECTION (SLP)

In SLP, when the failure is detected by the failed link source node, it generates the connection setup message to the failed link destination node via reserved backup lightpath (i.e. B-F-C in Fig. (1)), and waits for the acknowledgement. After receiving the acknowledgement, the connection setup process is completed and data transmission begins. The connection recovery time is given as:

$$T_f + [\{ (H_b + 1) \times T_c \} + (H_b \times T_p) + \{ (H_b + 1) \times T_m \}] + [(H_b \times T_p) + \{ (H_b + 1) \times T_m \}] \text{--- (ii)}$$

3.3 PROPOSED STRATEGY (PS)

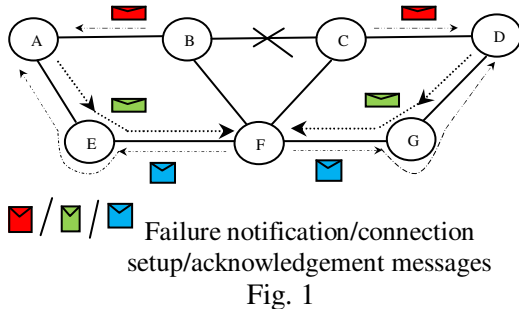
In the PS, the pre-computed backup lightpath is the same as in SPP (i.e. A-E-F-G-D in Fig. (1));

only the signaling procedure is different from the SPP. When the connection failure is detected at the end nodes of the failed link, the end nodes generate the failure notification messages to their respective end nodes of the connection request (i.e. A and D) as shown in Fig. (1). After receiving failure notification, both the end nodes (i.e. A & D) of the connection request send the connection setup messages along the backup lightpath to the pre-decided intermediate node 'F'. This intermediate node, generates the acknowledgements to the respective nodes after receiving the information of both the setup messages. Thus, the signaling delay due to propagation and switching cross connection becomes approximately half compared to the SPP and lower than the SLP as well. The recovery time is calculated as follows:

Let T_1 (T_2) be the time between the instant the connection setup message is send from source (destination) node to the intermediate node, and the acknowledgement is received. The T_1 and T_2 can be calculated as:

$$T_1 = (m_{si} + 1) \times C + 2 \times m_{si} \times P + 2 \times (m_{si} + 1) \times D \text{ -(iii)}$$

$$T_2 = (m_{di} + 1) \times C + 2 \times m_{di} \times P + 2 \times (m_{di} + 1) \times D \text{ -(iv)}$$



m_{si} (m_{di}) represents the number of hops between source (destination) node & the intermediate node. For the proposed strategy the intermediate node is selected such that $T_1 \geq T_2$. The total recovery time is given as:

$$T = F + n \times P + (n+1) \times D + T_1 \text{ --- (v)}$$

In the PS use of the parallel signaling by both the end nodes of the connection request reduces the connection setup time without sacrificing the resource utilization of the network.

4. RESULTS AND ANALYSIS

In order to evaluate the performance of the proposed strategy, the simulation program has been developed in the MATLAB environment. The network topology (i.e. number of nodes, links, wavelengths) is given as the input parameter. The different sets of connection requests which are to be survived are generated randomly. If a wavelength is not available for a particular connection request, it will be rejected immediately i.e. there is no waiting queue in the network. The network is wavelength continuous i.e. there is no availability of wavelength conversion at the node. The maximum wavelength availability at the fiber is fixed and is equal to $w=40$. Fig. 2 & 3 are the simulation results performed on the NATIONAL and ARPANET network topologies given in [8] respectively.

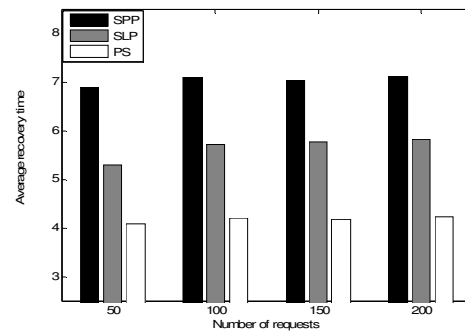


Fig. 2(a) Average recovery time per request required for the establishment of connection request in case of NATIONAL topology ($w=40$)

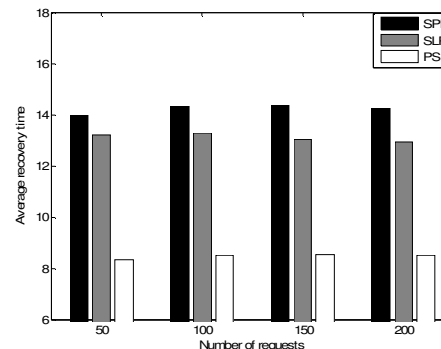


Fig. 2(b) Average recovery time per request required for the establishment of connection request in case of ARPANET topology ($w=40$)

Fig. 2(a)-(b), show that the comparisons of the average recovery time in case of SLP, SPP & PS for NATIONAL and ARPANET topology respectively. The average recovery time for SPP, SLP, PS for NATIONAL topology is 7.04 ms.,

5.65 ms., 4.17ms respectively. The average recovery time of the PS is 59.2% and 73.8% of the SPP and SLP strategies respectively. Similarly, average recovery time for ARPANET topology is 14.24 ms. 13.10 ms, 8.46 ms for SPP, SLP, PS respectively. The recovery time of PS is 59.4% and 64.5% of the SPP and SLP respectively.

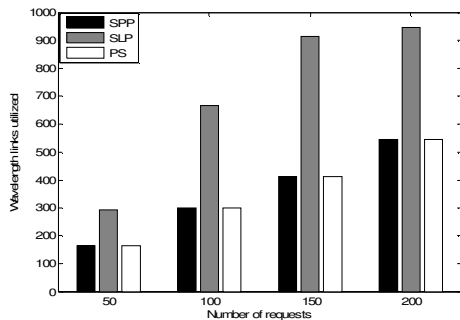


Fig. 3(a) Graph showing comparison of the total wavelength links required in case of the SPP, SLP & PS, strategies for NATIONAL network (w=40)

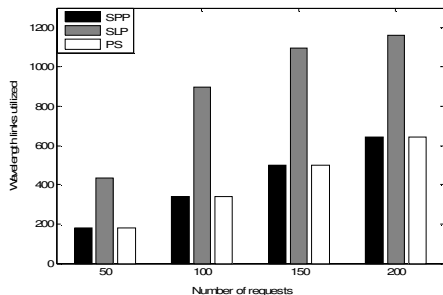


Fig. 3(b) Graph showing comparison of the total wavelength links required in case of the SPP, SLP & PS, strategies for ARPANET network (w=40).

Fig. 3(a)-(b), shows the total wavelength links utilized by all the three strategies for different sets of connection requests. It is evident from the figures that PS utilizes lesser number of wavelength links than SLP, and it is equally resource efficient as the SPP strategy. Hence, the proposed strategy performs better than the two existing strategies on the metric of recovery time and network capacity utilization.

5. CONCLUSION

In this paper, we presented the parallel connection recovery mechanism for achieving fast switching mechanisms whenever the failure occurs. In the proposed strategy, both the end

nodes of the connection requests generate the connection setup messages to the intermediate node simultaneously, which results in reduction in the signaling delay compared with the traditional SPP connection setup mechanism. The simulation results show that proposed strategy not only recovers the failed connections fast, but also efficiently utilizes network capacity (i.e. equal to SPP).

REFERENCE

1. S. Ramamurthy, L. Sahasrabudde, B. Mukherjee, "Survivable WDM Mesh Network", IEEE J. Lightwave Tech., 21(4), 870 (2003).
2. L. Guo, "Recovery time guaranteed heuristic routing for improving computation complexity in survivable WDM networks," Computer Commun., vol. 30pp. 1331-1336, 2007.
3. Y. Ouyang, and Q. Zeng, "Connection provisioning with guaranteed recovery time in survivable WDM optical network," Photon Netw. Comm., pp. 309-319, 2006.
4. J. Cao, L. Guo, and H. Yu, Lemin Li, "A novel hop constrained sub-path protection routing algorithm in WDM networks," Optics Commun., vol. 260, pp. 155-163, 2006.
5. M. Lee, J. Yu, Y. Kim, and J. Park, "A restoration method independent of failure location in all optical networks," Computer Commun., vol. 25, pp. 915-921, 2002.
6. C. Assi, Y. Ye, S. Dixit, and M. Ali, "Control and management protocol for survivable optical mesh networks," J. Lightwave Technol., vol. 21, no. 11, pp. 2638-2651, 2003.
7. C. Assi, W.Huo, A. Shami, and N. Ghani, "Improving signaling recovery in shared optical networks," Comp. Commun., vol. 29, pp. 59-68, 2005.
8. Dharmendra Singh Yadav, Santosh Rana, Shashi Prakash, "Hybrid connection algorithm: A strategy for efficient restoration in WDM optical network", Optical Fiber Technology.

MPR CODE Vs OOC THROUGHPUT COMPARISON IN O-CDMA NETWORKS

Shrikant S. Tangade and Shivaleela E. S.

Dept. of Electrical Communication Engineering, Indian Institute of Science, India
stangade@gmail.com and lila@ece.iisc.ernet.in

Abstract: In this paper optical code-division multiple-access (O-CDMA) packet network is considered, which offers inherent security in the access networks. Two types of random access protocols, in protocol-1 all distinct codes and in protocol-2 distinct codes as well as shifted versions of codes, are proposed for packet transmission. O-CDMA network performance using Optical Orthogonal Codes (OOCs) 1-D and two-dimensional (2-D) Wavelength/Time Multiple-Pulses-per-Row (W/T MPR) codes are analyzed with correlation receiver. Using analytical model, we compare the OOC and MPR code performance in O-CDMA networks using packet-success probability (P_s) and throughput (β). The analysis shows improved performance with MPR codes as compared to OOC codes, due to reduced multiple access interference (MAI).

1. INTRODUCTION

In broadcast optical code-division multiple-access (O-CDMA) networks multiple users transmit information over the same physical channel concurrently using unique orthogonal sequences and the performance of CDMA systems is limited by MAI [1]. In broadcast networks like O-CDMA, multiple access interference (MAI) is dominant compared to receiver noises. Besides OTDM and WDM, O-CDMA is another multiplexing technology and a potentially promising technique for optical networks in the future, and especially, due to its easy access and flexible network structure, for the access networks. A typical network architecture for O-CDMA [2] is shown in Fig. 1. The O-CDMA technique has several advantages over other multiple access techniques, e.g., asynchronous scheme, simple communication protocols, better utilization of the time-frequency domain by each subscriber, flexibility in network design, and inherent security against interception [3].

In this paper, we propose two random access protocols, Protocol-1 and Protocol-2, for slotted O-CDMA packet networks, which use OOCs or W/T MPR codes [4]. In [3] and [5] 1-D codes are used in the O-CDMA packet networks. Among several 1-D codes OOCs have the lowest out-of-phase autocorrelation and cross-correlation values, equal to 1. But the disadvantage of OOCs is that as the number of users or the weight of the code is increased, the length of the sequence increases rapidly. As a result of this, for a given chip width the bit rate reduces which is not desirable. Hence, aimed at the shortcoming of 1-D codes, 2-D O-CDMA codes are used.

With the aid of cyclic redundancy check (CRC) codes, a receiver can determine whether a received packet is correctly detected or not. If not it will ask for retransmission. This would increase the channel traffic and interference. A transmitter asked for data retransmission is not allowed to generate new packets; rather it keeps retransmitting the same packet (after random delay time slots) until it receives a successful acknowledgment from destination [5].

First, two types of performance measures are examined in this paper. Packet success probability, P_s , is calculated by knowing the probability of one-

chip, P_l and W -chip, P_w , interference and throughput, β . The main objective of this paper is to compare the throughput of the optical CDMA networks using 1-D codes with that of the 2-D codes. In our analysis, we have considered the correlation receiver model. The organization of the paper is as follows: In section II, the O-CDMA system architecture and the two MAC protocols are explained. Analytical modeling of the two protocols with correlation receiver for OOCs and W/T MPR codes is derived, in section III. Further, in section IV, the results obtained from the analytical models are discussed for the two protocols.

2. SYSTEM ARCHITECTURE

The notations used in this section are:

- N # of nodes or users in network
- C Cardinality
- W Weight of 1-D and 2-D code
- R # of rows
- $Wp = W/R$ Weight per row
- L temporal length of code
- λ_a out-of-phase autocorrelation peak
- λ_c cross-correlation peak

The cardinality $|C|$ of 1-D codes depends on L , W , λ_a and λ_c . In the case of OOCs, $\lambda_a = \lambda_c = 1$, we have

$$|C| = \left\lfloor \frac{L-1}{W(W-1)} \right\rfloor \quad (1)$$

The cardinality $|C|$ of 2-D codes depends on L , R , λ_a and λ_c . For the case of W/T MPR codes, $\lambda_a = 1$, $\lambda_c = 1$, we have

$$|C| = \left\lfloor \frac{L}{Wp^2} \right\rfloor \quad (2)$$

Assumptions made in this section are:

- N is allowed to be greater than $|C|$
- Codes are assigned to users depending on Protocol-1 or Protocol-2

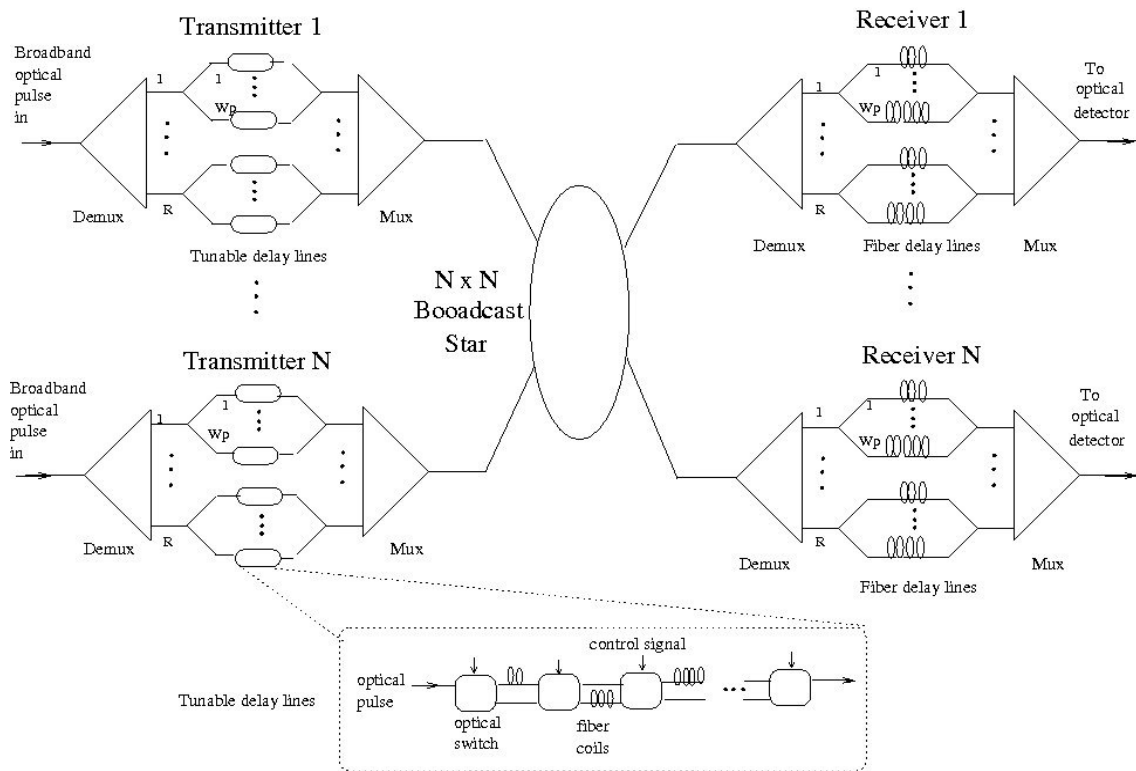


Figure 1. Architecture of 2-D O-CDMA network in star configuration

3. ANALITICAL MODELING OF THE SYSTEM

The definitions used in this section are:

- *thinking mode*: the mode where users transmit newly generated packets
- *backlogged mode*: the mode where users retransmit same (faulty) packet
- *active user*: one that is about to transmit a packet
- *thinking user*: the user who is in thinking mode
- *backlogged user*: the user who is in backlogged mode

The notations used in this section are:

- K = the length of a packet in bits
- n = number of backlogged users out of total N users in network
- r = number of active users in a given slot
- $r-1$ = number of interfering users to the desired user
- s = number of users (out of $r-1$ users) interfere with desired user at 1-chip
- a = number of users (out of $r-1$ users) interfere with desired user at w -chips
- Z = total received pulses from all weighted chips
- $P_{bl}(in)$ = the probability of i backlogged users (given n)
- $P_{th}(j|N-n)$ = the probability of j thinking users (given $N-n$)

- $P_{bc}(a,s)$ = the conditional bit-correct probability (given a & s)
- $P_s(r|a, s)$ = the conditional probability of a packet-success (given a & s)
- $P_s(r)$ = the probability of a packet success given ' r ' active users.
- P_I = the probability of 1-chip interference between two users
- P_w = the probability of W -chip interference between two users
- $r = i + j$

Let the system consist of N users having same average activity A . The packets are transmitted in slotted manner. The length of a packet is K bits and corresponds to slot duration. An active user is assigned a code before packet transmission depending on the protocol used (Protocol-1 or Protocol-2). On the other hand, the intended node transmits an acknowledgment to the sender as soon as packet is received successfully. If packet is not received successfully, the sending user enters a backlog mode and retransmits the packet after a random delay time with average d time slots. Assuming that at a given slot the number of backlogged users are ' n ', then system throughput in case of protocol-1 $\beta_1(n)$ and protocol-2 $\beta_2(n)$ for correlation receiver is shown in (3) and (4) respectively at the end of this paper, where the symbol ' $x \wedge y$ ' denotes the minimum of two numbers x and y . The two probabilities denotes the probabilities of i backlogged ($P_{bl}(in)$) and j thinking (transmitting new packets) users ($P_{th}(j|N-n)$), respectively, being active at a given time slot with n backlogged users, and $P_s(r)$

denotes the probability of a packet success given r active users. In the next section we calculate a packet-success probability $P_s(r)$ for the correlation receiver model [5].

$$p_{bl}(i|n) = \binom{n}{i} \left(\frac{1}{d}\right)^i \left(1 - \frac{1}{d}\right)^{n-i}$$

$$p_{th}(j|N-n) = \binom{N-n}{j} A^j (1-A)^{N-n-j} \quad (5)$$

A. Packet Success Probability with Correlation Receiver

Correlation receiver decides a data bit 1 was transmitted if the total received pulses Z from all weighted chips is greater than or equal to a threshold $\theta = W$. A data bit 0 is decided otherwise [6]. Since we are using codes with correlation constraints equal to 1, that is users who are assigned distinct codes interfere with each other at one chip at most. On the other hand, users who are assigned shifted version of the same code interfere with each other by zero, one, or W chips.

Assuming chip-synchronous interference model among users, we derived the probabilities of 1-chip interference (P_i) and probabilities of W -chip interference (P_w), for OOCs and W/T MPR codes are [6]:

$$p_i(ooc) = \begin{cases} \frac{W^2}{L}; & \text{protocol-1} \\ \frac{W^2}{L} \cdot \frac{|C|-1}{|C|}; & \text{protocol-2} \end{cases} \quad (6a)$$

$$p_i(mpr) = \begin{cases} \frac{R \cdot Wp^2}{L}; & \text{protocol-1} \\ \frac{R \cdot Wp^2}{L} + R \cdot \frac{Wp \cdot (Wp-1)}{L} \cdot \frac{1}{|C|}; & \text{protocol-2} \end{cases} \quad (6b)$$

$$p_w = \begin{cases} 0, & \text{protocol-1} \\ \frac{1}{L} \cdot \frac{1}{|C|}; & \text{protocol-2} \end{cases} \quad (7)$$

Assuming there are r active users and $r-1$ interfering users with the desired user. Out of these $r-1$ users, let s users interfere, with the desired user, at 1-chip and a users interfere at W -chip. Also by assuming equally likely binary data bits ($\Pr\{0\} = \Pr\{1\} = 1/2$), the conditional bit-correct probability $P_{bc}(a,s)$ is calculated as

$$P_{bc}(a,s) = \Pr\{\text{bit success} | a, s\}$$

$$= \frac{1}{2} \Pr\{\text{bit success} | a, s, 1 \text{ was sent}\}$$

$$+ \frac{1}{2} \Pr\{\text{bit success} | a, s, 0 \text{ was sent}\}$$

$$= \frac{1}{2} \Pr\{Z \geq W | a, s, 1 \text{ was sent}\} + \frac{1}{2} \Pr\{Z < W | a, s, 0 \text{ was sent}\}$$

$$= \frac{1}{2} + \frac{1}{2} \Pr\{\text{all 'a' users send 0 and } Z < W | a, s, 0 \text{ was sent}\}$$

$$= \frac{1}{2} + \frac{1}{2} \cdot \frac{1}{2^a} \cdot \frac{1}{2^s} \sum_{i=0}^{W-1} \binom{s}{i} \quad (8)$$

Thus the conditional success probability for the correlation receiver is

$$P_s(r|a,s) = \left[P_{bc}(a,s) \right]^K = \left[\frac{1}{2} + \frac{1}{2} \cdot \frac{1}{2^{s+a+1}} \sum_{i=0}^{W-1} \binom{s}{i} \right]^K \quad (9)$$

Finally, the packet success probability given r active users for protocol-1 and protocol-2 are as shown in (10) and (11) respectively at the end of this paper.

4. RESULTS AND DISCUSSION

Performance comparison of OOC and MPR codes in an O-CDMA network is analyzed in this section for the two protocols earlier. The O-CDMA network performance is analyzed by using OOC and MPR codes with variation in the spread sequence length.

In Figures 2 and 3, β is plotted for different spread sequence lengths, $L=50$ and $L=100$, for correlation receiver using OOCs and MPR codes respectively. The parameters $C=5$, $W=4$, $R=2$, $N=30$, $n=10$, $K=127$ and $d=1/A$ are kept constant. In Protocol-1, network using OOCs or MPR codes achieve β equal to maximum of C . In Protocol-2, MPR codes offer higher β compared to that of OOCs. The results also show that, in case of protocol-2, there is increase in β as L increases.

5. CONCLUSIONS

Optical CDMA has attracted considerable attention in the recent years for high speed access network applications due to the salient features it has such as inherent security, asynchronous transmission, concurrent access to the channel etc. Two MAC protocols for O-CDMA access networks have been proposed and analyzed, with correlation receiver, for 1-D OOCs and 2-D W/T MPR codes.

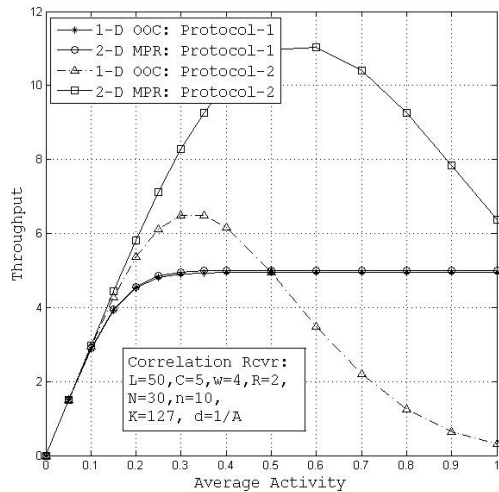


Figure 2. Throughput comparison between OOCs and MPR codes in case of protocol-1 and 2 for $L=50$.

From our analysis, we find that MPR codes with correlation receiver performs better over OOC codes, due to decreased interference between codes, for a given weight of the code, as a result have higher packet success probability, this leads to higher

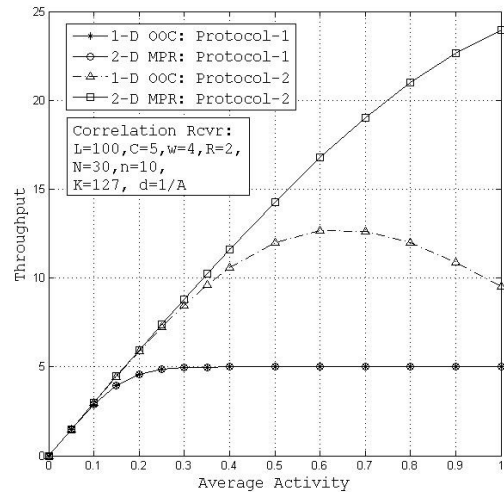


Figure 3. Throughput comparison between OOCs and MPR codes in case of protocol-1 and 2 for $L=100$.

throughput. We have observed from the analysis, the throughput of OCDMA networks using MPR code is higher than that of the OOCs due to reduced MAI. Hence MPR codes are better suited for O-CDMA access networks.

System throughputs for protocol-1 and protocol-2 are:

$$\beta_1(n) = \sum_{j=0}^{N-n} \sum_{i=0}^n ((i+j) \wedge C) P_S((i+j) \wedge C) P_{bl}(i|n) P_{th}(j|N-n) \quad (3)$$

$$\beta_2(n) = \sum_{j=0}^{N-n} \sum_{i=0}^n (i+j) P_S(i+j) P_{bl}(i|n) P_{th}(j|N-n) \quad (4)$$

For protocol-1 and protocol-2 the packet success probabilities are:

$$P_S(r) = \sum_{s=0}^{r-1} \frac{(r-1)!}{s!(r-1-s)!} p_1^s (1-p_1)^{r-1-s} \left[\frac{1}{2} + \frac{1}{2^{s+1}} \sum_{i=0}^{W-1} \binom{s}{i} \right]^K \quad (10)$$

$$P_S(r) = \sum_{s=0}^{r-1} \sum_{a=0}^{r-1-s} \frac{(r-1)!}{s!a!(r-1-a-s)!} p_1^s p_w^a (1-p_1-p_w)^{r-1-s-a} \left[\frac{1}{2} + \frac{1}{2^{a+s+1}} \sum_{i=0}^{W-1} \binom{s}{i} \right]^K \quad (11)$$

REFERENCES

- [1]. T. Eltaif, H. M. H. Shalaby, S. Shaari, and M. M. N. Hamarsheh, "Analytical comparison of optical code-division multiple-access systems with and without a successive interference cancellation scheme using modified prime-sequence codes," *SPIE Opt. Eng.*, vol. 47(9), pp. 095001(1-6), Sept. 2008.
- [2]. Hongxi Yin, David J. Richardson, "Optical Code Division Multiple Access Communication Networks, Theory and Applications", Springer, 2007
- [3]. H. M. H. Shalaby, "Performance analysis of an optical CDMA random access protocol," *IEEE/OSA J. Lightwave Technol.*, vol. 22, pp. 1233- 1241, May. 2004
- [4]. E. S. Shivaleela and T. Srinivas, "Construction of wavelength/time codes for fiber-optic CDMA networks", *IEEE Journal of Selected Topics in Quantum Electronics*, vol. 13, No. 5, Sept/Oct. 2007
- [5]. Hossam M. H. Shalaby, "Optical CDMA Random Access Protocols With and Without Pretransmission Coordination", *Journal of Lightwave Technology*, vol. 21, No. 11, pp. 2455-2462, Nov-2003.
- [6]. Shivaleela E. S. and Shrikant S. Tangade, "Analysis of MAC Protocols with Correlation Receiver for OCDMA Networks", *ICCNS-2011*, Paris, June 23-25, 2011.

DESIGN OF AN EDFA BASED WDM DISTRIBUTION NETWORK WITH 1:64 SPLIT FOR RADAR APPLICATIONS

Abdul Hameed P P, Shivaleela E S, Dept. of ECE, IISc, Bangalore-560012
Meena D, LRDE, C V Raman Nagar, Bangalore-560093
ppahameed@gmail.com

Abstract: We present the design and analysis of 1:64 ways split EDFA based hybrid wavelength division multiplexing (WDM) network for the simultaneous transmission of eight channels consisting of analog S-band RADAR signals and digital control signals through a standard single mode fiber to distribute each signal among 64 receiver array panel in an active phased array antenna (PAA). Optical transmitters are realized from distributed feedback (DFB) lasers modulated with either analog S-band RADAR signals or digital signals of about 700 Mbps. Selection criteria of the wavelengths based on the flat band characteristics of EDFA and the power budget of the proposed network are analyzed.

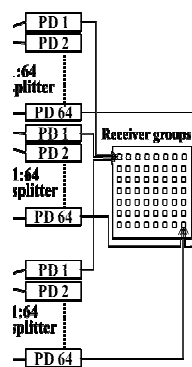
1. INTRODUCTION

Large bandwidth offered by the optical fiber and WDM technology have enabled the upgradation from conventional electronic transmission path to optical path with higher speed, system compactness and light weight. Besides this, analog fiber optic transmission has the potential to reduce the weight footprint of the system especially when co-axial RF cables are replaced with optical fibers having diameter of micrometer dimension. In this paper we have proposed and analyzed a novel hybrid fiber optic link that is capable reducing the hardware footprint of phased array radar antenna and it can be further upgraded to antenna remoting applications.

about 700 Mb/s. The channels are multiplexed by WDM multiplexer and transmitted through standard single mode fiber of length 10 to 15 meters and demultiplexed at the other end with a demultiplexer device having filter bandwidth < 1 nm. Each of the eight demultiplexed output is split into 64 branches using 1:64 splitter and distributed to each of the 64 receiver groups in a PAA. Optical receiver with InGaAs APD is used for optical to electrical conversion at the splitter output and the demodulated electrical signals are then fed to the respective receiver groups of the PAA.

3. TRANSMITTER AND RECEIVER SELECTION

The set up mainly consists of eight transmitter receiver pairs. The transmitters consist of directly modulated DFB lasers that will produce 8 different wavelengths in C-band region in the ITU grid, viz. 1548.51, 1549.32, 1550.12, 1550.92, 1551.72, 1552.52, 1553.33 and 1554.13 nm. The spectral width of each channel is about 0.3 nm and has central wavelength spacing of 100 GHz (0.8 nm) corresponding to ITU grid [2]. The receiver part consists of InGaAs APDs which are characterized with large spectral response that typically range from 950 nm to 1650 nm and with a high sensitivity of -28 dBm to -34 dBm [3].



W network for the transmission and its distribution using 1:64 splitters.

2. THE PROPOSED CONFIGURATION

Design of an optically amplified hybrid WDM fiber optic distribution network for simultaneous transmission of analog and digital signals through a standard single mode optical fiber is proposed here. Figure 1 shows the schematic diagram of the proposed network configuration. The set up consists of 8 directly modulated DFB lasers out of which two are modulated using analog signals having bandwidth in the S-band region of RADAR [1] and remaining 6 are modulated with digital signals with data rate of

4. MULTIPLEXER AND DEMULTIPLEXER

Filter bandwidth is an important parameter in deciding multiplexer/demultiplexer devices. In the case of optically amplified networks additional noise sources like amplified spontaneous emission (ASE) noise and signal-ASE beat noise come into the role and wide filter bandwidth will degrade the system performance. So a narrow bandwidth filter is necessary to maintain the required bit error rate 10^{-10} and also to retrieve the analog signal without distortion.

The influence of an optical filter on the receiver performance is shown in Figure 2. The analysis shows

the effect of filter bandwidth on receiver sensitivity and also on the extinction ratio at the receiver [4]. For APD receiver, it is found that as the filter bandwidth is decreased from 20 nm to 2.5 nm the value of receiver sensitivity improves from -32.5 dBm to about -39 dBm. The extinction ratio at the receiver, i.e. the ratio of the powers of a 1 bit to a 0 bit, increases from 3 to 5.5 dB and 4 to 7.5 dB for APD and PIN receiver respectively when the bandwidth is reduced from 20 nm to 2.5 nm.

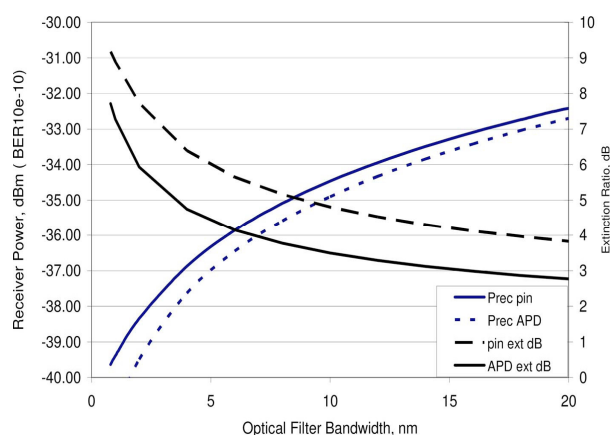


Figure 2: Influence of optical filtering on PIN and APD receiver performance [4].

An 8 channel multiplexer/demultiplexer device is used to multiplex the eight channels with a channel spacing of 0.8 nm. The demultiplexer has a filter bandwidth of ± 0.1 nm and offers a maximum insertion loss of 3 dBm [5].

5. EDFA FLAT GAIN AND λ SELECTION

EDFAs exhibit large gain bandwidth and a single EDFA can amplify multiple channels simultaneously. However, the non-uniform gain spectrum of EDFA causes signal power and SNR differential among WDM channels while adding and dropping channels [6] and gain-tilt also imposes a critical problem in multi-channel amplification. A theoretical investigation has been carried out on various configurations of hybrid WDM EDFAs for amplitude modulated, CATV signals and multiple digital baseband signals and the single staged forward-and-backward pumping scheme is found to be the best design for hybrid WDM lightwave systems [7]. A five channel hybrid WDM system with one vestigial-sideband channel and four 2.5 Gb/s channels for a fiber span of 100 km using two EDFAs were demonstrated for analog and digital trunking and distribution applications [8].

It was observed that the gain and NF values primarily depended on the pumping configurations and gain-spectra and noise characteristics depend mainly on the population inversion level which, in turn, can be controlled by choice of appropriate fiber length and injected pump power to EDFA with

minimum gain-tilt at C-band regime [9].

Many studies have been conducted to stabilize EDFA gain to obtain flat gain over multiple channels. A two stage EDFA that accurately controls output power per channel has been demonstrated in [10]. A new type of EDFA that is capable of providing flat gain at C-band and having core glass compositions of zirconia-yttria-alumino-phospho-silicate with high erbium concentration is reported in [11].

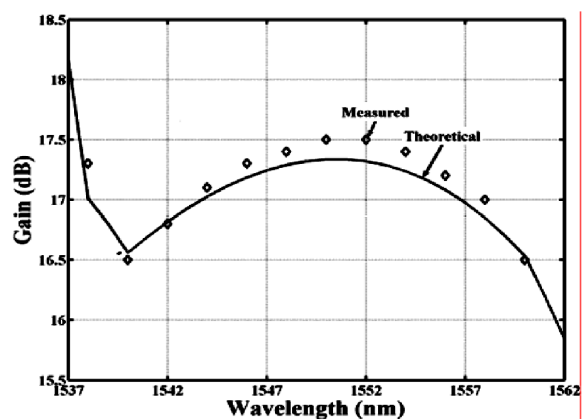


Figure 3: Comparison of the gain spectrum characteristics of the synthesized and real EDFA [12].

Investigation based on multiwavelength signal amplification shows that maximum gain flatness within 1 dB is in the range of 1538 nm to 1560 nm. Figure 3 shows a comparison of simulated model with experimentally obtained gain values of 21 wavelengths with 1 nm separation and each of them with equal powers of -13 dBm adding up to 0 dBm [12]. The simulation experiment also shows that the gain flatness remains approximately ± 0.5 dB for a change in the total input power to EDFA from -6 to +6 dBm by changing the individual channel power from -19 to -7 dBm respectively as shown in Figure 4 [13].

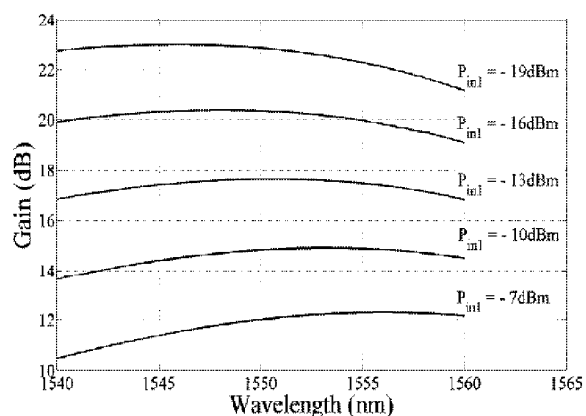


Figure 4: Gain spectrum for 100 mW pump power at 980 nm for input power from -19 to -7 dBm [13].

In our design eight channel wavelengths with a channel spacing of 0.8 nm are selected such that all the channels are to be packed in the flat gain

bandwidth of EDFA. The pump power, input signal power and EDFA lengths are all optimized to obtain a relatively flat gain for all the eight channels. Variable optical attenuator is used before EDFA to adjust the input signal power level to EDFA.

6. POWER BUDGET CONSIDERATIONS

The power budget analysis for each of the eight channels between 1548.51 nm to 1554.13 nm has been carried out neglecting the transmission loss due to the short length of the fiber and it is illustrated in Table 1.

The link design in this paper is based on the following parameters.

- 8 DWDM wavelengths are used: 1548.51, 1549.32, 1550.12, 1550.92, 1551.72, 1552.52, 1553.33 and 1554.13 nm.

- Transmitter launch power: 0 dBm
- Extinction ratio: 8 dB
- Receiver sensitivity: -28 dBm
- BER: 10^{-10}
- Fibre type SMF
- Connector pairs: 2
- Splitter insertion loss: -21 dB [14]
- Modulation type: NRZ and analog S-band
- Mux/Demux insertion loss: 6 dB
- EDFA (BW): C-band, G: 17, PDG: 0.5, NF: 4 dB

To estimate the power penalty, the following impairments in the subsystem is considered for each channel in the link [15].

Transmitter power margin (dB): 2.65

- chirp margin: 0.5
- extinction ratio margin: 1.4
- ageing margin: 0.25
- electrical response: 0.5

Multiplexer/demultiplexer power margin (dB): 6.6

- polarization dependency: 0.1
- cross talk: 0.3
- insertion loss: 6
- ageing: 0.2

Fiber power margin (dB): 0

- dispersion: 0
- self-phase modulation: 0
- cross phase modulation: 0
- polarization mode dispersion: 0
- Raman effects: 0

Amplifier power margin (dB): 4.1

- gain tilt: 3
- polarization dependency gain: 0.5
- input loss: 0.1
- ageing margin: 0.5

Receiver power margin (dB): 2.1

- input loss: 0.1

- electrical response: 1
- sensitivity tilt: 0.5
- ageing: 0.5

Table 1: Power budget calculation for each of the 8 channels between 1548.51 nm to 1554.13 nm.

Parameters	Values
Launched input power (dBm)	0
Receiver sensitivity (dBm)	-28
Margin (dB)	15.45
Fiber loss (dB)	0
Connector loss (dB)	4
Splitter loss (dB) (1 × 64 splitter)	21
Minimum EDFA gain required to satisfy receiver sensitivity (dB)	12.45

7. RESULTS AND DISCUSSIONS

An 8 channel optically amplified WDM distribution network has been designed for hybrid signal transmission including analog S-band RADAR and digital signals. Flat gain bandwidth of EDFA is used for the simultaneous, optical amplification of 8 channels in a cost effective way by avoiding expensive and complicated methods for gain stabilization such as gain flattening filter and gain clamped EDFA.

8. CONCLUSIONS

The report mainly deals with the application of WDM technology in phased array RADAR for transmission of S-band RADAR signals and digital control signals. Power budget analysis has been carried out with direct modulated DFB lasers as optical sources which are time tested and reliable optical sources. The study can be further extended by comparing the effect of less expensive Fabry-Perot laser and suitable multiplexer/demultiplexer devices on the system performance.

REFERENCES

- [1] P. A Morton *et al.*, "Packaged 1.55 μ m DFB laser with 25 GHz modulation bandwidth" *Electron. Lett.*, 2044 (1994).
- [2] http://www.jdsu.com/ProductLiterature/sfp-daxxc_s00c_ds_cms_ae.pdf
- [3] Application notes, <http://www.osioptoelectronics.no/application-notes/AN%20optical%20communication%20photodiodes%20and%20receivers.pdf>
- [4] C. Michie *et al.*, "Optically amplified passive optical networks: a power budget analysis" *J. Optical Networking*, **8**, 370 (2009).
- [5] <http://www.santec.com/jp/wp-content/uploads/M>

[DM_8ch-C-E-v440710.pdf](#)

- [6] M. Karasek and J. A. Valles, "Analysis of channel addition/removal response in all-optical gain-controlled cascaded erbium-doped fiber amplifiers." *J. Lightwave Tech.*, **16**, 1795 (1998).
- [7] T.-C. Liang *et al.*, "Optimum configuration and characteristic comparisons of multiwavelength erbium-doped fiber amplifier for hybrid digital/analog WDM systems" *Optics Communications*, **177**, 259 (2000).
- [8] K.-Po. Ho *et al.*, "Hybrid Wavelength-Division-Multiplexing Systems for High-Capacity Digital and Analog Video Trunking Applications", *IEEE Photon. Technol. Lett.*, **10**, 297 (1998).
- [9] M. Pal *et al.*, "Investigation of the optical gain and noise figure for multi-channel amplification in EDFA under optimized pump condition" *Optics Communications*, **273**, 407 (2007).
- [10] S. Y. Park *et al.*, "A gain-flattened two-stage EDFA for WDM optical networks with a fast link control channel" *Optics Communications*, **153**, 23 (1998).
- [11] M. Pal *et al.*, "Study of Multichannel Amplification in Erbium-Doped Zirconia-Yttria-Alumino-Silicate Fiber" *J. Lightwave Tech.*, **29**, 2109 (2011).
- [12] L. Jordanova and V Topchiev, "Amplification of the Multi-Wavelength Signal by Using EDFA with Constant Gain" *IJCSNS*, **9**, 38 (2009).
- [13] L. Jordanova and V Topchiev, "EDFA Application in WDM CATV Systems", *ICEST 2009, Conference Proceedings*, Veliko Tarnovo, Bulgaria, June 2009.
- [14] <http://archive.ericsson.net/service/internet/picovget?DocNo=28701-RDJ901200&Lang=EN&HighestFree=Y>
- [15] R. Radziwilowicz *et al.*, "Power budget considerations in CWDM/TDM based Passive Optical Networks" 173, 978-1-4244-2921-9/08 ©2008IEEE.

GREENING THE IP OVER OPTICAL WDM NETWORK

T. Srinivas, R. Krishnamurthy
 Dept. of Electrical Communication Engineering
 Indian Institute of Science (IISc), Bangalore-560012
 Email: {tsrinu, krishna}@ece.iisc.ernet.in

Abstract—As the number of Internet users increases, the Internet expands in reach and capacity. This results in increased energy consumption of the network. Minimizing the power consumption, termed as “Greening the Internet”, is desirable to help service providers (SP) operate their networks and provide services more efficiently in terms of power consumption. Minimizing the operational power typically depends on the strategy (e.g., lightpath bypass, lightpath non-bypass and traffic grooming) and operations (e.g., electronic domain versus optical domain). We consider a typical optical backbone network model and develop a model which minimizes the power consumption. Performance calculation shows that our method consumes less power compared to traffic grooming approach.

Index Terms—IP over Optical WDM networks, Energy consumption, Green Internet, Lightpath bypass, MILP, WDM.

I. INTRODUCTION

Internet Protocol (IP) traffic (in the electronic layer) is carried over the optical WDM networks (optical layer). Such layered network architecture can exploit the logical processing capability offered by the legacy electronics as well as the enormous bandwidth offered by WDM [1]. So the energy consumption of the network also increases. The growth of the Internet is favorable to the customers only by the availability of inexpensive high capacity optical transmission equipment and the IP routers. Today the energy consumption and the cost of optical transmission and switching equipment is considered one of the major barriers to the growth of the Internet. The total energy consumption of the Internet is a small fraction of the national electricity supply in most countries, e.g., about 1% – 2% of the total electricity consumption in the US in 2001 [2]. However as the Internet expands, these percentage will rise.

Research has been initiated in recent years for energy saving of the Internet. This effort was called the “Greening the Internet” [2]. An IEEE 802.3 Energy Efficient Ethernet Study Group was established in November 2006 [3]. The study group is currently exploring standardization of ideas to Adaptive Link Rate (ALR). Now ALR is renamed as Rapid (PHY) Selection (RPS). A consortium called Green Grid was also formed recently to improve energy efficiency in data centers around the globe [4].

Now the researchers concentrated on minimizing the energy

(or power) consumption of the backbone IP over Optical WDM networks. But the backbone network consumes a small fraction of the total energy consumption of the IP over Optical WDM networks. So the energy consumption of the IP over Optical WDM networks can be reduced by bypassing the lightpath in the optical layer. This method is widely used because it reduce the number of required IP router ports. The IP router Consumes maximum amount of energy.

The design of an energy efficient IP over optical WDM network is important because electricity power consumption is the major operational cost for an Internet Service Providers (ISP) and electricity power is a more and more a scarce resource. The *energy-oriented* IP over Optical WDM networks and the *energy-minimized* MILP optimization model are novel, in which the physical layer issues such as power consumption of each component and the layout of the optical amplifiers etc., are considered. In contrast, these issues are not considered in the traditional IP over Optical WDM network designs [5], [6]. The recent research in the optical communication networks concentrates on technologies, design methodologies and network techniques. There is a little amount of importance is given to the cost and energy consumption of the optical networks. We concentrate on minimizing the energy consumption of the backbone IP over WDM network. To reduce the energy consumption in the IP over WDM network, lightpath bypass in the optical layer is applied. It requires less number of IP ports [6].

This paper is organized as follows. Section II explains the structure of IP over Optical WDM networks. It also explains the lightpath bypass and lightpath non-bypass. In section III we examine the energy minimized design of IP over Optical WDM networks. Section IV presents the simulation results. Finally we conclude in section V.

II. IP OVER OPTICAL WDM NETWORKS

The simplified picture of IP over Optical WDM networks is shown in Fig 1. The user will send the Internet Protocol (IP) packets to the access networks. Then this packet will enter into the core networks via the edge router. The edge routers are present around the periphery of the core networks. The packets are routed to their destination via the core networks. Each packets will travel from source to destination through

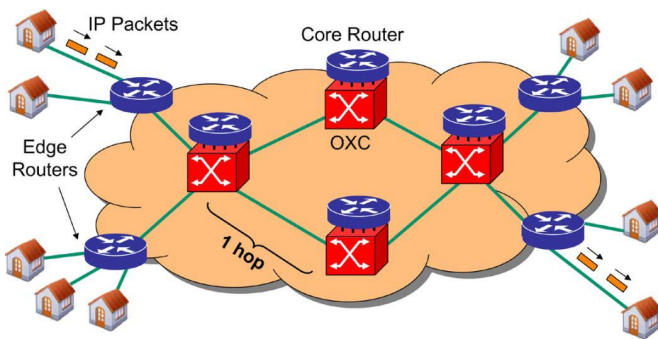


Fig. 1. An IP over Optical WDM Network

various core routers and large number of hops. Wavelength Division Multiplexing (WDM) is technique is used between the routers. WDM system contains multiple wavelengths and the links contain more than one fibers. There is no constraints on the number of fibers between the routers.

The IP over Optical WDM networks consists of two layers: (i) IP layer and (ii) Optical layer. In the IP layer the edge router aggregates the data traffic from the low end access routers. The optical layer provides lightpaths for communications between the routers. Optical fibers are interconnected by the physical fibers. For each fiber, a pair of multiplexers/demultiplexers are deployed to multiplex and demultiplex the wavelengths.

There are two ways to implement the IP over Optical WDM networks: Lightpath non-bypass and (ii) Lightpath bypass. In lightpath non-bypass method all the lightpaths incident to a node must be terminated, i.e., all the data carried by lightpaths is processed and forwarded by IP routers. In contrast, the lightpath bypass approach allows IP traffic, whose destination is not the intermediate node, to the destination via the cut through lightpath. This method requires that the optical should have intelligence to enable lightpath bypass. So this method can reduce the total number of IP router ports. The lightpaths are used to establish the communication between the core routers and interconnects a pair of router ports in the core networks. Lightpaths are considered as a virtual link for the IP layer data traffic.

III. ENERGY CONSUMPTION MINIMIZATION MODEL FOR IP OVER WDM NETWORK

In a typical IP/multiprotocol label switching over reconfigurable optical backbone architecture, IP router [or digital crossconnect (DXC)] interfaces are connected to the ports of WDM optical crossconnects (OXCs), and OXCs are interconnected in a mesh configuration with multiwavelength fiber links. Typically, traffic in the electronic domain enters an IP router attached to an OXC is converted to an optical signal, and then is transmitted via fiber links. Within the reach of

a lightpath, traffic optically bypasses the intermediate OXCs through express channel, without the need of being processed. An optical signal needs to be converted to an electronic signal at the end of each lightpath.

$$P = P_O + P_T \times t \quad (1)$$

where P_O and P_T are two operation-dependent parameters on one-wavelength basis, t is the actually carried traffic amount and $t \in [0, 1]$. According to (1), the smaller is the portion of a wavelength used, the larger is the portion of overhead.

Considering the overhead, power efficiency can be improved by traffic grooming, i.e., multiple subwavelength traffic flows can be multiplexed on a single wavelength. This strategy addresses the problem of bandwidth fragmentation so that fewer lightpaths are needed. In addition, when new traffic is groomed to an existing lightpath, the overhead can be avoided, since it has already been paid by an existing traffic flow. Though traffic grooming can reduce overhead, it requires cumbersome O/E/O conversions and electronic processing, which consume significantly more power than optical switching (bypass). Tucker [8] gave some typical values of power consumption for several operations. Also, traffic grooming typically takes longer routes to exploit existing lightpaths, which requires more transmission power. As the power saved by reducing overhead and number of lightpaths may be exceeded by extra operations and transmission, traffic grooming is not always optimum. It is likely that a direct lightpath between a source and a destination node consumes less power, or a connection may partly use a newly set up lightpath and partly be groomed to an existing lightpath, so that overall power can be minimized. We analyze the power efficiency of both multi-hop bypass and direct bypass.

The following inputs are given to the problem. A physical topology $G_p = (N, E)$. It consists of set of nodes N and edges E . The node set corresponds to IP routers and optical switch nodes. The link set represents the physical fibers in the network. The traffic demand matrix $[\lambda]$ which indicates the traffic demand λ^{sd} between the every source and destination. The number of wavelength carried by each fiber is W and the capacity of each wavelength B Gb/s. All the given inputs are parameters of the minimization model.

Indices: The following indices are used in our optimization model:

- m and n denote an *end points of a physical link that might occur in a lightpath*. A physical link connects two such end nodes.
- i and j denote *originating and terminating nodes*, respectively, in a virtual lightpath topology (IP) layer. A lightpath virtual link connects two such end nodes. Physically the nodes can be a pair of IP routers connected by the virtual link.
- s and d denote *source and destination nodes of an end-to-traffic demand*. This demand is aggregated from low-end IP routers and is routed over virtual lightpath topology.

Parameters

- N_m denotes a set neighboring nodes of node m in the physical topology G_P
 L_{mn} denotes a physical distance of a physical link between nodes m and n
 A denotes the number of EDFAs that should be deployed on each fiber of a physical link (i, j)
 Δ^i number of ports that are used to aggregate the data traffic from the low end routers at node i
 λ_{ij}^{sd} denote the traffic (interms of lightpaths) demand from source s to destination d on a link ij

Variables

- λ_{ij}^{sd} denote the traffic (interms of lightpaths) demand from source s to destination d on a link ij
 C_{ij} denote number of wavelength channels on the virtual between node pairs (i, j) (integer)
 w_{mn}^{ij} denote number of wavelength channels between node pair (i, j) that traverses physical link (m, n) (integer)
 w_{mn} number of used wavelength channels on physical link (m, n) (integer)
 f_{mn} number of fibers on physical link (m, n) (integer)

Mathematically, the energy minimized model is as follows:

Objective: Minimize

$$\sum_{i \in N} E_r \cdot (\Delta_i + \sum_{j \in N: i \neq j} C_{ij}) + \sum_{m \in N} \sum_{n \in N_m} E_t \cdot w_{mn} + \sum_{m \in N} \sum_{n \in N_m} E_e \cdot A_{mn} \cdot f_{mn} \quad (2)$$

Subject to:

$$\sum_{i \in N: i \neq j} \lambda_{ij}^{sd} - \sum_{j \in N: i \neq j} \lambda_{ji}^{sd} = \begin{cases} \lambda^{sd} & i = s, \\ -\lambda^{sd} & i = d, \\ 0 & \text{otherwise} . \end{cases} \quad (3)$$

Explanation of equations

Equation (2) minimizes the total energy consumption in both IP and optical layers. The term $\sum_{i \in N} E_r \cdot (\Delta_i + \sum_{j \in N: i \neq j} C_{ij})$ computes the total energy consumption of routers in the IP layer. The term $\sum_{j \in N: i \neq j} C_{ij}$ gives the total virtual link capacity. The term $\sum_{m \in N} \sum_{n \in N_m} E_t \cdot w_{mn}$ calculates the energy consumption of all the transponders in the optical layer, and the term $\sum_{m \in N} \sum_{n \in N_m} E_e \cdot A_{mn} \cdot f_{mn}$ evaluates the total energy consumption of the EDFA in the optical layer. Constraints (3) ensures the flow conservation constraint in the IP layer, in which IP traffic between a pair of routers is allowed to be split and transmitted over multiple flow paths.

IV. SIMULATION RESULTS

We simulate a WDM-enabled IP over optical backbone network to evaluate the performance. The network we consider is a 6-node with 8 fiber link (Fig.2) and maximally

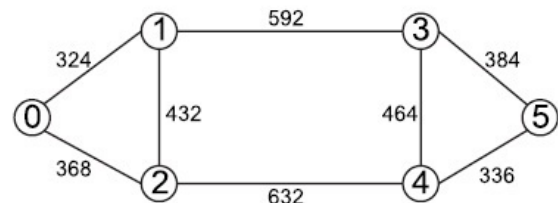


Fig. 2. 6 node 8 link network with distance in kilometers

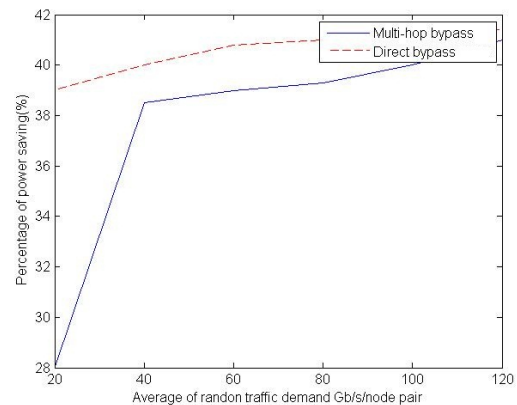


Fig. 3. Power consumption saving by multihop bypass and direct bypass

16 wavelengths are multiplexed in each fiber, and there is no limit on the total number fibers on each physical link. The transmission capacity of each wavelength is OC-768 (40 Gbits/s). The bandwidth granularity is OC-1 (51.84 Mb/s), and bandwidth requests are uniformly distributed among OC-1, OC-3, OC-12, OC-48, and OC-192. The traffic demand between each node pair is generated with a uniform distribution within a certain range. The range is centered at an identical average. That is, given an average demand intensity $X \in \{20, 40, 60, 80, 100, 120\}$ Gb/s, the actual demand between a node pair is generated by a random function uniformly distributed within the range $[10, 2X - 10]$.

For comparison, we use a multihop bypass and direct bypass approach as described in [6]. The aggregate network load (the total requested bandwidth) varies from 0 Tbits/s to 12.8 Tbits/s. We see in Fig 3 that direct bypass scheme needs less power than multihop bypass scheme. As the network load increases, the gap between the two curves also becomes larger.

Fig 3 shows the result of a total power consumption of the n6s8 network (Fig 2). The curve multihop bypass provides an upper bound on the total power consumption. By applying the strategy of lightpath bypass, we can maximally save power consumption from 12.5 kW (i.e., 23.5%) to 58.2 kW (i.e., 25.5%) under the optimized design, when the average traffic demand per node pair is increased from 10 Gbits/s to 40 Gbits/s. An important observation is that with the increase

of network size, the power saving by the lightpath strategy increases because with the increase of the network size, there are more chances to establish longer lightpaths, which bypasses more intermediate switch nodes and hence requires relatively fewer IP router ports. IP router ports consumes highest percentage (more than 90%) of the total power. The remaining energy is shared by transponders and EDFAs, among which transponders occupy about 5% and EDFAs consume $\leq 3\%$.

V. CONCLUSION

Energy consumption of network equipment may eventually become a barrier for the Internet to further grow. It is important to explore energy-efficient networking techniques for future communication networks. This paper looks into the power saving of the IP over WDM network. To reduce power consumption, we developed an optimization model which is based on the lightpath bypass strategy for the IP over WDM network. It was found that the strategy of lightpath bypass can significantly save power consumption over the non-bypass design, ranging from 23% to 45%. Such saving increases with the increase of network size. It was also found that the energy consumption of the IP over WDM network follows an approximately linear relationship with the network traffic demand.

REFERENCES

- [1] B. Mukherjee, *Optical WDM Networks*. New York: Springer-Verlag, Feb. 2006.
- [2] M. Gupta and S. sing, "Greening of the Internet," in *Proc. ACM SIGCOMM*, Aug. 2003.
- [3] IEEE 802.3 Energy Efficient Ethernet Study Group, <http://grouper.ieee.org/groups/802/3/eee-study/index.html>.
- [4] The Green Grid, <http://www.thegreengrid.org/pages/overview.html>.
- [5] B. Mukherjee, *Optical Communication Networks*, New York: McGraw-Hill, 1997.
- [6] K. Zhu and B. Mukherjee, "Traffic grooming in an optical WDM mesh networks" *IEEE Journal of Selected Areas in Communications*, vol. 20, no. 1, pp.122-133, January 2002.
- [7] J. Baliga, K. Hinton, and R. S. Tucker, "Energy consumption of the internet," *COIN-ACOFT'07*, Melbourne, Australia, June 2007.
- [8] R. Tucker, "The role of optics and electronics in high-capacity routers," *IEEE/OSA J. Lightw. Technol.*, vol. 24, no. 12, pp. 4655-4673, Dec. 2006.
- [9] J. Baliga, R. Ayer, K. Hinton, W. V. Sorin, and R. S. Tucker, "Energy consumption in optical IP networks," *Journal of Lightwave Technology*, vol.27, no.13, pp. 2391-2403, July 2009.
- [10] L. Shi, S. S. Lee, and B. Mukherjee, "Energy-efficient long reach passive optical network: A dynamic wavelength allocation scheme," *Photonics in Switching'10*, Monterey, CA, July 2010.
- [11] M. Xia, S. S. Lee, and B. Mukherjee, "Greening the Optical Backbone Network: a Traffic Engineering Approach," *Proc. IEEE ICC 2010*.

Performance Evaluation of Optical OFDM Communication System

Varun Srivastava and Gireesh G. Soni

Dept. of Applied Physics, S.G.S.I.T.S., Indore, India

Email: gireeshsoni@gmail.com

Abstract: This paper gives an implementation of orthogonal frequency-division multiplexing (OFDM) technique for optical fiber communication. Optical OFDM system using FFT is simulated using OPTISYSTEM ver-5.0 and MATLAB. It is shown that transmission of 2.5Gb/s over 40km of standard single-mode fiber is possible without any dispersion compensation. The system performance parameters like bit error rate (BER) and signal to noise ratio (SNR) are evaluated. BER of 10^{-9} is achieved for the link range up to 60 km.

Key-words—Bit Error Rate (BER), Signal to noise ratio (SNR), Orthogonal frequency division multiplexing (OFDM), Quadrature Amplitude Modulation (QAM).

I. INTRODUCTION

Optical fiber communications provided a challenging environment for communications and systems engineers to meet the ever-growing demand for transmission capacity. Classical digital communications techniques entered the field of optical communications, such as forward error correction codes, multicarrier modulation, and maximum likelihood sequence estimation to support this growth. Orthogonal frequency division multiplexing (OFDM) is a multicarrier modulation technique which is now being used in the emerging broadband wired and wireless communication systems because it provides an effective solution to intersymbol interference caused by a dispersive channel [1].

In order to efficiently exploit the optical bandwidth, OFDM as a special case of single carrier modulation was introduced in the optical domain [2]. One of the main reasons for suitability of OFDM in optical communications is its ability to deal with large pulse spreads due to chromatic dispersion by dividing the broad optical channel spectrum into a number of sub-channels each with a narrow spectrum and thereby decreasing the dispersion effect [4]. Optical OFDM is based on electronic signal processing before the optical modulation and after the optical detection. The optical components are used just for converting the electrical OFDM signal into an optical band pass signal at the transmitter for transmission through an optical fiber and for converting the received optical signal back into the electrical domain at the receiver. This has a big advantage because the microwave technology is more developed than its optical counterparts and because of the availability of frequency selective microwave filters and the frequency stable oscillators [3][5].

II. IMPLEMENTATION

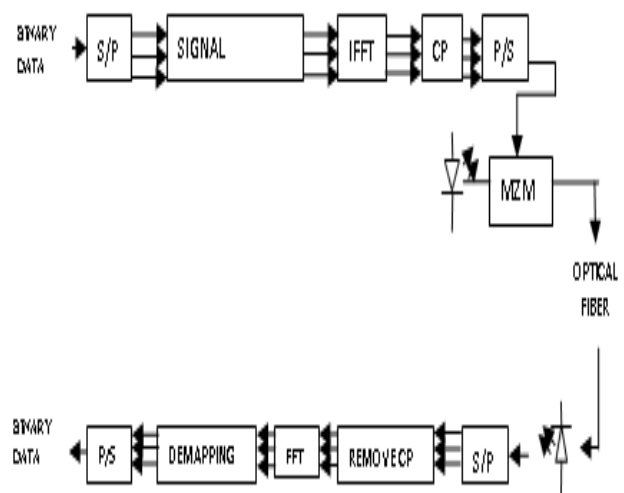


Fig:1- Block diagram of the optical OFDM system

An optical OFDM transmission system is shown in fig.1. The input binary signal is processed electronically to form OFDM symbols. These OFDM symbols then modulates a laser radiation. The input binary data is feeded in parallel to a set of quadrature amplitude modulation (4-QAM). This input signal is 1024-bit user defined sequence, 128-sample-per-bit, and the total data rate is 2.5 Gbit/s. The modulated data undergoes a 512 input inverse Fast Fourier-transform (IFFT). Then, the IFFT input is transformed from parallel to serial (P/S). The Mach-Zehnder (MZI) modulator is used to modulate electrical OFDM signal to optical OFDM signal.

We have used a standard 40-km single-mode fiber (SMF) with attenuation of 0.2 dB/km and dispersion of 16ps/nm/km at 1550 nm along with an EDFA for OFDM signal transmission. The entire model is implemented in Optisystem version 5.0 and MATLAB. The electronic processing of the data is carried out using MATLAB. The amplifiers have a 16-dBm gain and a 4.5- dBm noise figure. The PIN photodiode used for detection of the optical radiation has a responsivity of 1 A/W. The photocurrent is converted to in-phase (I) and quadrature (Q) component using a QAM demodulator. The best received sensitivity is obtained when the power in optical carrier equals to the power in OFDM sidebands. Then, the received signal is formed serially and transformed to parallel data. The demodulated QAM signal is converted to its frequency domain by using the fast Fourier transform (FFT). Once in frequency domain, each sub-channel is equalized to compensate for phase and amplitude distortion due to the optical and electrical paths. This is achieved by using a separate complex multiplication for each sub-channel. The output of the equalizer is then digitally demodulated and converted into a single data channel by parallel to serial conversion.

III. SIMULATION RESULTS

To verify the validity of the results, a user defined bit sequence is given at the input which undergoes the entire system process and finally extracted from the OFDM symbols at the receiver. Fig-1 shows the input bit sequence (0101101110) and the corresponding output received at the receiver for the link range of 40km. This section discusses the performance metrics i.e. BER and SNR of the proposed Optical OFDM system. The electrical SNR is evaluated for varying link ranges. Fig-3 indicates a linear decrease in SNR as the length of the SMF is increased. A similar analysis is carried out for BER as shown in fig-4. The BER of 10^{-9} is achieved up to the fiber length of 60 km and it starts decreasing as the range is increased further. Finally fig-5 relates the standard performance measure i.e. BER and the SNR. According to it, a minimum 35 dB SNR is required to achieve the BER of 10^{-9} .

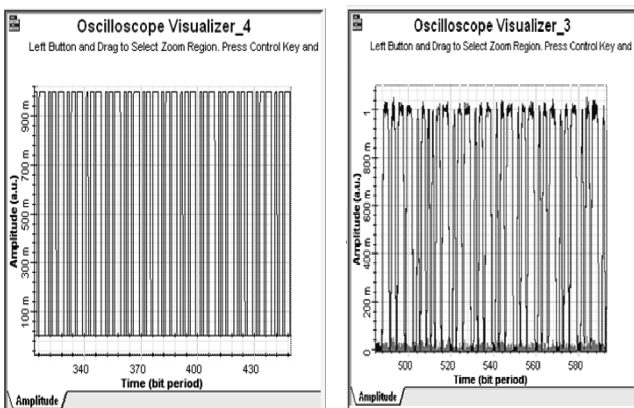


FIG:2- USER DEFINED I/P AND THE RECEIVED O/P (BIT SEQUENCE-0101101110)

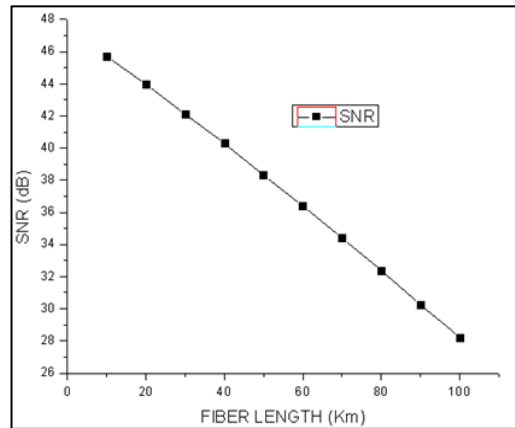


FIG:3- SNR VS LINK LENGTH

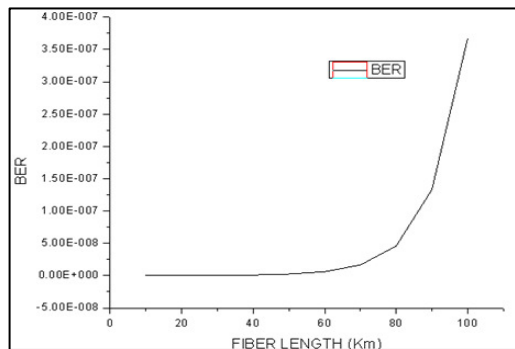


FIG:4- BER VS LINK LENGTH

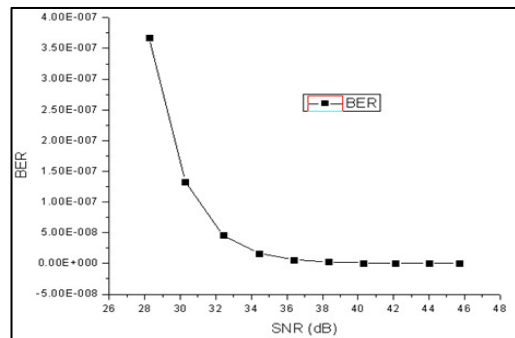


FIG:5- BER VS SNR

IV. CONCLUSION

An OFDM based Optical communication system is successfully realized. On the basis of the results obtained, we conclude that the optical OFDM will be the feasible option for the next generation technology like 4G and other high data rate standards. Though the simulated system is FFT based implementation of Optical OFDM, the rapid progressive research in this field will surely make it in to all optical OFDM. It is an efficient modulation format for long-haul systems, being quite robust towards the specific nonlinear impairments.

Nevertheless, OFDM is still an emerging research field for optical transmission engineering. Well known digital communication techniques like channel estimation and peak power reduction may be implemented for optical channel.

REFERENCES

- [1] B. Djordjevic and B. Vasic, "Orthogonal frequency division multiplexing for high-speed optical transmission," *Optic Express*, vol.14, pp.3767–3775, May 2006.
- [2] S. L. Jansen, I Morita, K. Forozesh, R. Sebastian, "Optical OFDM, a hype or is it for real?" *ECOC Brussels*, 21-25 Sept. 2008.
- [3] Itsuro Morita, "Optical OFDM for High-Speed Transmission", *IEEE proceedings*, 2009.
- [4] J. Armstrong, "OFDM for Optical Communications", *Journal of Lightwave Technology*, vol. 27, pp. 189-204, Feb. 2009.
- [5] D. Wake, A. N. kansah and Nathan J. Gomes, "IEEE Radio over Fiber Link Design for Next Generation Wireless Systems", *IEEE Proceedings*, 2010.

Performance characterization of high Speed point to point dual broadcast service PON system without using any source at ONUs

Ambrish kumar*, Jiten Boruah and R. K. Sinha

TIFAC-Centre of Relevance and Excellence in Fiber Optics and Optical Communication, Department of Applied Physics, Delhi Technological University (Formerly Delhi College of Engineering, Faculty of Technology, University of Delhi), Bawana Road, Delhi-110042, India

Telephone No. - +91-11-27871017, Fax No.-+91-11-27871023

(Email: ambrish.juit@gmail.com, jitenboruah1@rediffmail.com, dr_rk_sinha@yahoo.com)

Abstract: We propose the simulation model for typical high speed point to point dual broadcast service PON system layout which does not require any source in Optical network units (ONUs). The PON layout supports the analysis of important characteristics of various parameters Viz. BER, SNR, Q-Factor, Threshold power. The analysis outcomes may be used to optimize the performance of the existing PON Architecture available till date [1, 2 and 3] with the possible use of Photonic crystal fiber in the same. The proposed scheme verifies the feasibility of high quality factor, low bit error rate etc., obtained after 25 Km transmission with 1.25 Gbps data rate.

Keywords: PON, ONU, BER, SNR, OLT

1. INTRODUCTION

We are communicating dual broadcast service PON system that can enhance the existing systems performance by using high quality parameters Viz. BER, SNR, Q-Factor, Threshold power. To verify the feasibility of parameters we demonstrate the Passive Optical Network (PON) structure using Optiwave's Optisystem 10, 0, 0, 677 version simulation software tool.

2. PON ARCHITECTURE

A PON is a point-to-multipoint optical network consisting of an Optical Line Terminator (OLT) located at the Central Office (CO) and a group of Optical Network Units (ONUs) at remote nodes located at the user end. The connection between the OLT and ONUs is formed by using a single fiber and

one or more optical splitters, called the optical distribution network (ODN).

3. POINT TO POINT DUAL BROADCAST SERVICE PON SYSTEM

The simulation model for typical high speed point to point dual broadcast service PON system layout without using any source in Optical network units (ONUs) is designed as shown in Fig1. In this design the optical line terminal (OLT), DPSK signal is given as input to a dual port dual drive Mach-Zehnder modulator and driven by the electrical sub carrier multiplexing (SCM) signal format [3,4]. The orthogonal DPSK/IRZ format is used at sub-MZMA input terminal [5]. This PON layout supports the analysis of important characteristics of various parameters Viz. BER, SNR, Q-Factor, Threshold power.

4. EXPERIMENTAL SETUP AND RESULTS

The proposed scheme verifies the feasibility of it by using an experimental setup shown in the fig. 1. The DPSK signal obtained by using the Phase modulator with an input laser light at 1550nm is driven through

a 1.25 Gb/s pseudorandom bit sequence (PRBS) data word length of 2^7-1 , the generated data is fed into the dual port DDMZM. The sub carrier multiplexing (SCM) signal for one input of the DDMZM achieved after multiplexing the 20 GHz sinusoidal signal with 1.25 Gb/s pseudorandom bit sequence (PRBS) data of word length of 2^7-1 .

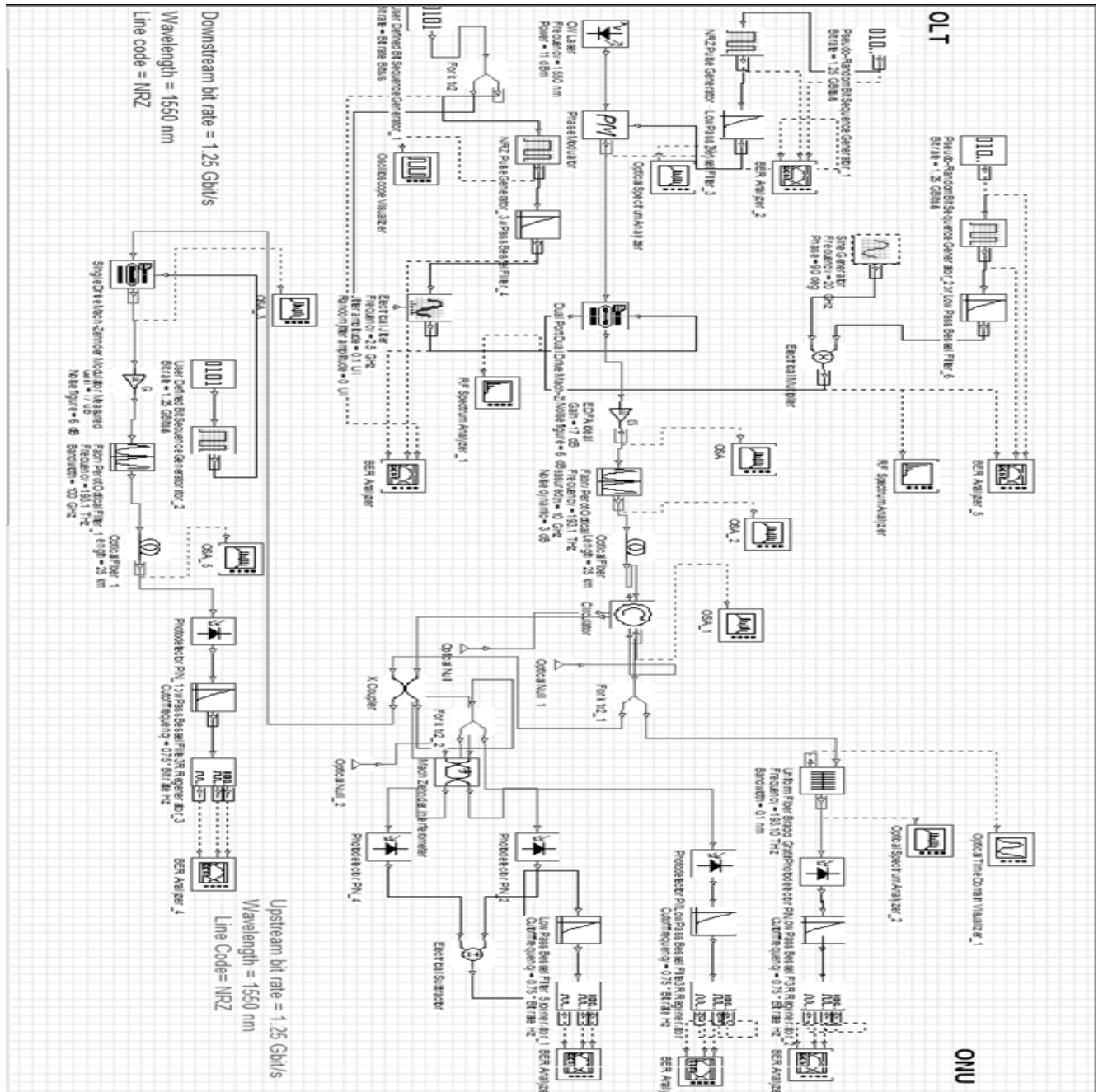


Fig.1 Schematic diagram of Proposed PON architecture.

The DPSK/RZ signal is obtained by ANDing of the PRBS signal and clock frequency of 2.5 GHz. This DPSK/RZ signal is fed to one input of the DDMZM. The generated output from the DDMZM is amplified through an EDFA (GAIN 17 dB, Noise Figure 6dB) amplifier. A tunable Fabry- Perot optical filter (frequency 193.1 THz) is connected to suppress the amplified spontaneous emission noise. After transmission over 25-km single mode optical filter, a circulator is used which reflects the DPSK/IRZ signal and passes the optical SCM signal. This SCM signal will pass through a Fiber Bragg grating (0.1 nm, 3dB bandwidth & 90% reflection ratio) filter. The SCM signal is detected through a photodetector. The SCM signal outputs are shown in the eye diagram of figure 2. The eye diagrams of each signal output shows the parameters Viz. quality factor, min BER, threshold power, eye height and BER pattern. The reflected DPSK signal after circulator is divided into three parts. The downstream IRZ signal directly detected from photo detector. Different outputs for IRZ signal are shown in the eye diagram of figure 3. A 1-bit Mach-Zehnder delay interferometer and two parallel photo detectors are used to detect the downstream DPSK signal. The DPSK signal outputs are shown in the eye diagram of figure 4. The upstream ASK signal is detected through a photo detector after transmission from 25-km single mode fiber followed by a signal drive MZM modulator, an EDFA amplifier (GAIN 17 dB, Noise Figure 6dB) and a tunable Fabry- Perot optical filter (frequency 193.1 THz). This upstream ASK signal is used for re-modulation. The outputs for ASK signal are shown in the eye diagram of figure 5.

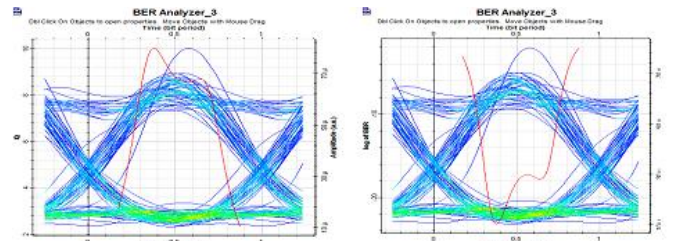


Fig.3a Quality Factor (Q=10.0148) for IRZ signal

Fig.3b Min BER (BER=5.21481e-024) for IRZ signal

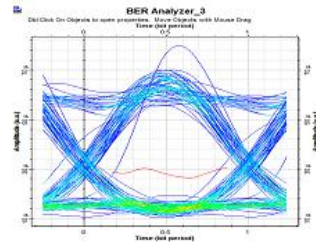


Fig.3c Threshold power (Th=8.01301e-005) for IRZ signal

Fig.3d Eye height (H=8.33025e-002) for IRZ signal

Fig 3. Eye diagram for downstream IRZ signal

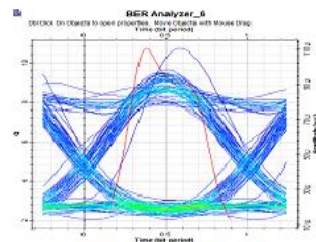


Fig.4a Quality Factor (Q=10.707) for DPSK signal

Fig.4b Min BER (BER=4.20448e-027) for DPSK signal

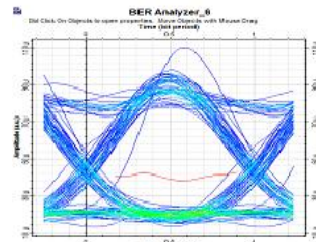


Fig.4c Threshold power (Th=4.19771e-003) for DPSK signal

Fig.4d Eye height (H=4.33884e-003) for DPSK signal

Fig 4. Eye diagram for downstream DPSK signal

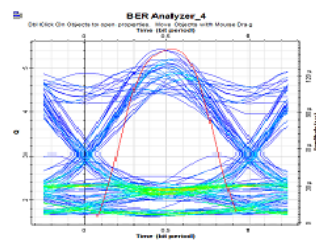


Fig.5a Quality Factor (Q=5.43036) for ASK signal

Fig.5b Min BER (BER=2.32625e-028) for ASK signal

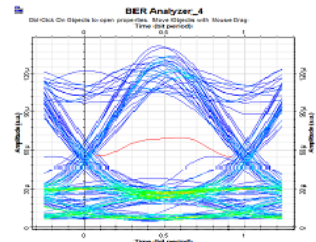


Fig.5c Threshold (Th=6.93383e-005) for ASK signal

Fig.5d Eye Height (H=4.30272e-003) for ASK signal

Fig 5. Eye diagram for upstream ASK signal

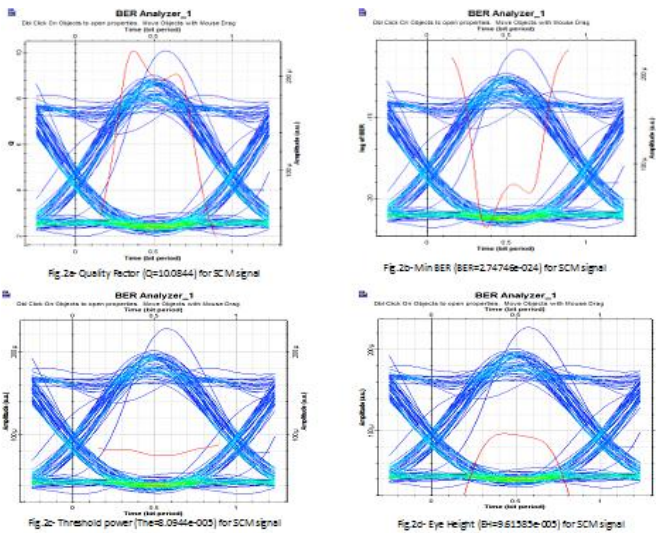


Fig 2. Eye diagram for downstream SCM signal

5. CONCLUSIONS

The simulation model for typical high speed point to point dual broadcast service PON system layout which does not require any source in Optical network units (ONUs) is designed. The PON layout supports the analysis of important characteristics of various parameters Viz. BER, SNR, Q-Factor and Threshold Power. The analysis outcomes may be used to optimize the performance of the existing PON Architecture available till date with the possible use of photonic crystal fiber in the same. The proposed scheme verifies the feasibility of high quality factor, low bit error rate, low threshold power and low dispersion rate obtained after 25 Km transmission with 1.25 Gbps data rate as detailed in the results shown in the eye diagrams of fig. 2,3,4,5.

REFERENCES

- [1] Qingjiang Changa, Mingfang Huangb, and Yikai Sua*, “Simultaneous transmission of high-speed point-to-point data and double broadcast services in a WDM-PON system with source-free ONUs” Proc. of SPIE Vol. 7136 71360S-4, 2008.
- [2] S. Park, C-H. Lee, K-T. Jeong, H-J. Park, J-G. Ahn, and K-H. Song, “Fiber-to-the-Home Services Based on Wavelength-Division- Multiplexing Passive Optical Network,” J. Lightw. Technol., vol. 20, no. 11, pp. 2582-2591, Nov. 2004.
- [3] Qingjiang Chang, Junming Gao, Qiang Li, Yikai Su, “Simultaneous Transmission of Point-to-Point Data and Selective Delivery of Video Services in a WDM-PON Using ASK/SCM Modulation Format,” in Proc. OFC, paper OWH2, 2008.
- [4] P. P. Iannone, K. C. Reichmann, and N. J. Frigo, “High-speed point-to-point and multiple broadcast services delivered over a WDM passive optical network,” *IEEE Photon. Technol. Lett.*, 10, pp. 1328-1330, Sep. 1998.
- [5] S-S. Pun, C-K. Chan and L-K. Chen, “Demonstration of a Novel Optical Transmitter for High-Speed Differential Phase-Shift-Keying /Inverse-Return-to-Zero (DPSK/Inv-RZ) Orthogonally Modulated Signals,” *IEEE Photon. Technol. Lett.*, vol. 17, no. 12, pp. 2763-2765, Dec. 2005.

Tunable mid-infrared radiation with mercury thiogallate crystal

S Das

Physics Department, Laser Laboratory, Burdwan University, Burdwan 713104, India
(e-mail:buphysd@gmail.com)

Abstract: Optical properties of orange phased HgGa_2S_4 crystal is investigated. Generation of tunable mid-infrared radiation by second harmonic of tunable CO_2 laser radiation has been demonstrated. Second harmonic conversion efficiency in this crystal with respect to ZnGeP_2 crystal has been compared.

1. Introduction

Nonlinear crystal is the heart in frequency conversion techniques for generation of tunable coherent radiation. Numerous crystals have been invented and research is still continuing to find suitable material having broad spectral transmission from ultraviolet to infrared. Mercury thiogallate [HgGa_2S_4 (HGS)] is considered one of the most promising nonlinear crystals for mid-infrared laser device applications. It has enough IR ($13.3\mu\text{m}$) transmission coupled with visible ($0.5\mu\text{m}$) transmission and so it could be a potential candidates for infrared generation due its attractive properties like high laser damaged threshold and sufficient figure of merit. It is a negative uniaxial crystal having tetragonal S_2^4 space group and $\bar{4}$ point group symmetry, melting temperature is 880°C , mohr hardness is 3–3.5 and density is 4.95 g/cm^3 . Its energy band gap is 2.84 eV [1,2]. Though this crystal is known since 1955 [3], but its detailed optical properties were first reported in 1979 [4]. But laser device application using this crystal was restricted due to its poor optical quality. Now with the development in growth technology, large size (20 to 50 mm) and good optical quality ($\alpha=0.5\text{ cm}^{-1}$ and down to 0.1 cm^{-1}) [5-7] HgGa_2S_4 single crystals have been reported. Various devices like CO_2 laser second harmonic generators (SHG) [1,5,8,9] optical parametric oscillator (OPO) [10], difference frequency and optical parametric generator in femtosecond pumped by $1.25\mu\text{m}$ in this crystal [6,7] have been reported. Detection of CO_2 laser radiation by up-conversion technique has also been reported [11]. But there are some discrepancies observed in theoretical calculation and available experimental data on HgGa_2S_4 crystal in various device applications. In particular, Takaoka et al [5] found significant differences in SHG phase-matching angle from the theoretical prediction obtained with Sellmeier coefficients reported by Badikov et al [4]. Again thermal conductivity is an important parameter for high average power application. The thermal conductivity of the crystal is measured by thermal calorimetric technique [12] and the measured value was 0.39 W/cm.K . In this paper, characterisation of HgGa_2S_4 crystal for laser device application is reported, generating second harmonic of tunable CO_2 laser radiation.

2. Optical properties of HgGa_2S_4 single crystal

A HGS crystal having size $10 \times 5 \times 3.4\text{ mm}^3$ was available for investigation. The crystal was 75° type-I cut. The transmission characteristic of 3.4 mm thick crystal is shown in figure 1. Short-wavelength transmission is measured with a UV–VIS–NIR spectrophotometer of M/S Shimadzu (model UV 1601 PC) while the long wavelength transmission is measured with infrared spectrophotometer of M/S Shimadzu (model IR 470). From this figure it is seen that short wavelength cut-off of this crystal is 506 nm (at 0% level) while the long-wavelength cut-off is down to $13.3\mu\text{m}$.

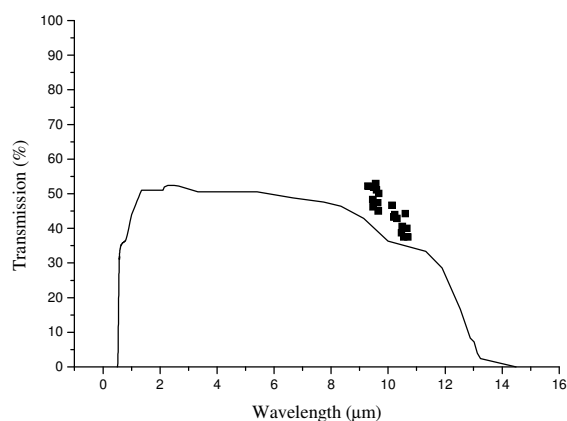


Figure 1: Transmission characteristics of 3.4 mm thick HgGa_2S_4 crystal. The solid curve represents the spectrophotometric measurement while dots (■) represent the experimental value.

3. Experimental

The schematic experimental arrangement for second harmonic generation (SHG) of the CO₂ laser radiation is shown in fig. 2. The crystal was placed on a precision rotation stage having resolution of 20 seconds allowing the crystal to rotate in the horizontal plane. The CO₂ laser beam was focused onto the crystal by a 50 cm focal length ZnSe lens. The polarization of the laser radiation was vertical to satisfy the type-I (oo → e) interaction condition. By rotating the crystal in the horizontal plane the phase-matched situation was attained and by rotating the crystal clockwise and anticlockwise the phase-matched peak was ascertained. The external phase-matching angles are then measured. Liquid nitrogen cooled Mercury Cadmium Telluride (MCT) detector operated without preamplifier senses the generated second harmonic radiation. It was found that a 3mm thick sapphire plate was sufficient to block the unconverted fundamental beam. The output signal of the detector was displayed on a 500 MHz storage oscilloscope.

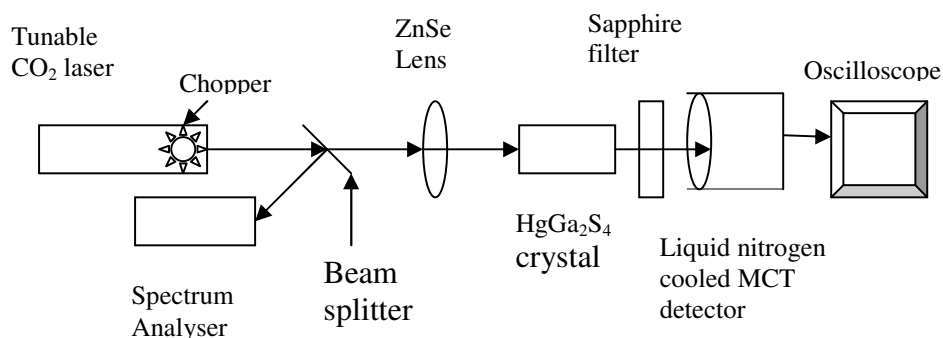


Figure. 2: Schematic experimental arrangement for SHG of CO₂ laser radiation

4. Results and Discussion

The angular phase-matched tuning characteristic for SHG in HGS crystal is shown in fig. 3. Here smooth curves are the theoretical prediction obtained with Sellmeier coefficients reported earlier [4,5] as well as the Sellmeier coefficients derived by G C Bhar given in table-I, while different dots represent the experimental points. This is also represented in an expanded graph shown in figure 4. It is seen from these figures that the present measured phase matching angles agree well with that of the theoretical prediction obtained from the Sellmeier coefficients developed by Bhar given in table-I. From these figures, it is also seen that there is a significant difference about 10–11° between the present measured phase matching angles and the theoretical prediction obtained from Badikov's Sellmeier coefficients [4]. It is also seen that the present measurement differ slightly about 4–5° from the theoretical prediction obtained from the Takaoka *et al* [5] Sellmeier coefficients.

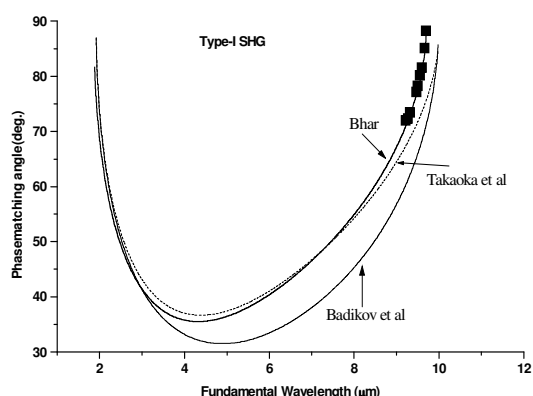


Figure 3: Angular tuning characteristics for second harmonic generation in HgGa₂S₄ crystal for type-I interaction. Different dots (■) represents the present measure

The measurement was restricted to 9 μm band because the noncriticality in phase matching was attained at 9.7 μm, which follows the theoretical prediction from Sellmeier coefficients developed by Bhar given in table I. It was also observed that there were no differences in phase matching angles obtained from Andreev's Sellmeier coefficients [13] and that obtained from

Badikov's Sellmeier coefficients [4]. Both overlapped. The theoretical prediction of phase matching angles obtained from Andreev's Sellmeier coefficients did not plotted here to avoid the clumsiness.

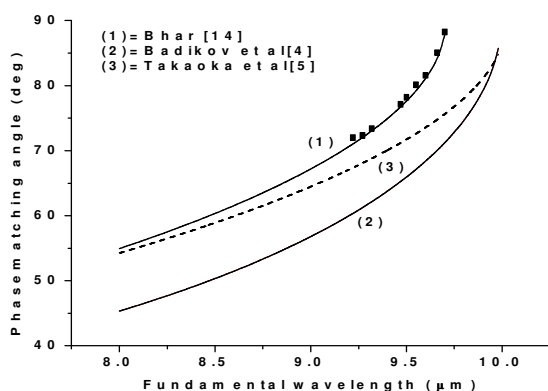


Figure 4: Angular tuning characteristics in 9-11 μm spectral range. The (■) represents the present measurement.

The angular acceptance in this crystal has also been measured. Both theoretical and experimental measured values are plotted in figure 5. Measured $\Delta\theta$ (at full-width half maxima) was 3.07° while the theoretical value is 2.82° using Sellmeier coefficients given in table-I. This value is 1.96° and 2.5° , respectively; obtain from Badikov's Sellmeier coefficients [4] and Takaoka et al. [5] Sellmeier coefficients.

5. Conclusion

Though it is less efficient than ZnGeP_2 [14] the HGS could be a potential candidate for tunable infrared sources using Nd:YAG and visible lasers in comparison with other infrared crystal like GaSe, AgGaSe_2 , AgGaS_2 , CdSe due to its better figure of merit and damage threshold.

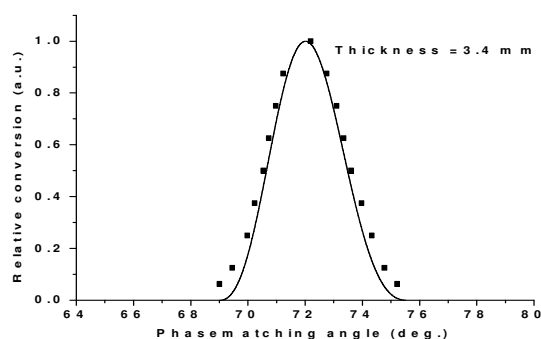


Figure 5: Angular acceptance HgGa_2S_4 crystals. The smooth curve is theoretical prediction obtained from Sellmeier coefficients of derived by G C Bhar given in table-I, while different square (■) represent the experimental value.

6. Acknowledgement

The author gratefully acknowledges Prof Yu M Andreev of Russia for providing the crystal and DRDO, Govt. of India for partial financial support.

Table-I
Sellmeier coefficients for HgGa₂S₄ crystal derived by G C Bhar

$$n_{o,e}^2 = A + \frac{B\lambda^2}{\lambda^2 - C} - \frac{D\lambda^2}{\lambda^2 - E}, \lambda \text{ is in } \mu\text{m}$$

	A	B	C	D	E
'O'-ray	3.96254	1.987528	0.109476	2.269709	950
'E'-ray	3.97091	1.780497	0.109245	2.249414	950

7. References

- [1] Yu.M. Andreev, V.V. Badikov, V.G. Voevodin, L.G. Geiko, P.P. Geiko, M.V. Ivaschenko, A.I. Karapuzikov, I.V. Sherstov, "Radiation resistance of nonlinear crystals at a wavelength of 9.55 μm " Quant. Electron, **31** (2001)1075..
- [2] R. Deming, H. Jinzhe, Q. Yanchen, H. Xiaoyong, Z. Lili, Yu. Andreev, P. Geiko, V. Badikov, G. Lanskii, A. Tikhomirov, Optical properties and CO₂ laser SHG with HgGa₂S₄ Chin. Opt. Lett., **1** (2003) 613..
- [3] R. Nitsche, H.U. Bolsterli, M. Lichtenshteiger, "Crystal growth by chemical transport reactions—I: Binary, ternary, and mixed-crystal chalcogenides" J. Phys. Chem. Solids, **21** (1961) 199..
- [4] V.V. Badikov, I.N. Matveev, V.L. Panyutin, S.M. Pshenichikov, T.M. Ropyakhova, O.V. Rychik, A.E. Rozenson, N.K. Trosenko, N.D. Ustinov, "Growth and optical properties of mercury thiogallate" Sov. J. Quant. Electron. **9** (1979) 1068.
- [5] E. Takaoka, K. Kato, "Tunable IR generation in HgGa₂S₄" Tech. Digest. CLEO 98 (1998) 253.
- [6] F. Rotermund, V. Petrov, F. Noack, "Difference-frequency generation of intense femtosecond pulses in the mid-IR (4–12 μm) using HgGa₂S₄ and AgGaS₂" Opt. Commun. **185** (2000) 177.
- [7] F. Rotermund, V. Petrov, "Mercury thiogallate mid-infrared femtosecond optical parametric generator pumped at 1.25 μm by a Cr:forsterite regenerative amplifier" Opt. Lett. **25** (2000) 746.
- [8] Yu.M. Andreev, P.P. Geiko, V.V. Badikov, V.L. Panyutin, G.S. Shevyrdyaeva, M.V. Ivashenko, A.I. Karapuzikov, I.V. Sherstov, Proc. "Parametric frequency converters with LiInSe₂, AgGaGeS₄, HgGa₂S₄ and Hg_{0.65}Cd_{0.35}Ga₂S₄ crystals" SPIE. **5027** (2003) 120.
- [9] M. V. Kabanov, Yu. M. Andreev, V. V. Badikov, and P. P. Geiko, "Parametric frequency converters based on new nonlinear crystals" Russian Phys. Journal **46** (2003) 835.
- [10] V.V. Badikov, A.K. Don, K.V. Mitin, A.M. Seregin, V.V. Sinaiskii, N.I. Shchebetova, "A HgGa₂S₄ optical parametric oscillator, Quan. Electron. **33** (2003) 831.
- [11] S.A. Andreev, N.P. Andreeva, V.V. Badikov, I.N. Matveev, S.M. Pshenichnikov, "Frequency up-conversion in a mercury thiogallate crystal" Sov. J. Quant. Electron. **10** (1980) 1157.
- [12] J.D. Beasley, "Thermal conductivities of some novel nonlinear optical materials" Appl. Opt. **33** (1994) 1000.
- [13] Yu.M. Andreev, P.P. Geiko, V.V. Badikov, G.C. Bhar, S. Das, A.K. Chaudhury, "Nonlinear optical properties of defect tetrahedral crystals HgGa₂S₄ & AgGaGeS₄ and mixed chalcopyrite crystal Cd_(0.4)Hg_(0.6)Ga₂S₄" Nonlinear Opt.Quan. Opt. **29** (2002) 19.
- [14] S Das, U Chatterjee, C Ghosh, S Gangopadhyay, Yu M Andreev, G Lanskii and V V Badikov, "Tunable middle infrared radiation with HgGa₂S₄ crystal" Opt. Commun. **259** (2006) 868.

SPECTRAL AND OPTICAL LIMITING APPLICATIONS OF SOL-GEL DERIVED LEAD CHLORIDE CRYSTALS

Rejeena.I, Lillibai,V.P.N.Nampoore and P.Radhakrishnan.
International School of Photonics, Cochin University of Science and Technology, Cochin
rejeenanaufal@gmail.com

Abstract: Here we report the nonlinear optical behaviour of pure Lead Chloride crystals by single beam z-scan experiment. Linear absorption and fluorescence studies were also done on the same crystal samples in solution phase. Reverse saturable absorption nature of the material makes it suitable for optical limiting applications.

1. INTRODUCTION

Lead chloride is a highly luminescent crystal which exhibits excitonic and recombinational luminescence [1]. Lead chloride has structures of mainly ionic character based on close packing of the halide ions. $PbCl_2$ exists in nature in crystalline form as large needles. Lead halide based materials have recently emerged as laser hosts with low phonon energy. In the present work we have performed linear and non linear optical absorption studies on pure lead chloride samples .

2. EXPERIMENTAL

Lead chloride crystals were prepared by sol-gel technique using lead nitrate, tartaric acid and HCl as reagents. X ray diffraction studies (XPERT PRO using k-alpha 1.54 \AA) confirmed the orthorhombic dipyramidal structure of $PbCl_2$. The crystal samples were powdered and dissolved in single distilled water to make a clear solution. Optical absorption spectra was recorded using Jasco V-570 UV/VIS/IR Spectrophotometer. The fluorescence emission from the sample was taken using a Cary Eclipse fluorescence spectrophotometer (Varian). Open aperture z scan experiment was carried out by a Q switched Nd:YAG laser (Spectra physics lab-1760,532 nm, 7 ns, 10 Hz).

3. RESULTS AND DISCUSSION

Absorption edge of $PbCl_2$ is located in the UV region. The direct band gap of the sample was estimated from the graph of $h\nu$ verses $(\alpha h\nu)^2$ where α is linear absorption coefficient and that is related to the band gap E_g as $(\alpha h\nu)^2 = k(h\nu - E_g)$, where $h\nu$ is the incident light energy, k is a constant and E_g is the optical band gap of lead chloride. The fluorescence spectroscopy reveals that the emission is in the visible region for an excitation of 250-300 nm.

Nonlinear absorption coefficient β can be obtained from open aperture z scan data by fitting the normalized transmittance data to the open aperture formula given as

$$T(Z, S = 1) = \sum_{m=0}^{\infty} \sum_{m=0}^{\infty} \frac{[-q_o(z)]^m}{[m+1]^{3/2}} |q_o(z)| < 1$$

where:

$$q_o(z) = \frac{[I_0 \beta L_{eff}]}{1 + (Z^2 / Z_0^2)}$$

$Z_0 = kw_0^2/2$ is the diffraction length of the beam

$k = 2\pi/\lambda$ is the wave vector, w_0 = the beam waist radius at the focal point, $L_{eff} = (1 - \exp(-\alpha L))/\alpha$ is the effective thickness of the sample, I_0 is the laser intensity at the focal plane. Figure.1 shows the open aperture z-scan plot of $PbCl_2$ at a concentration of $2.8 \times 10^{-5} M$. For our samples, there is no depletion of ground state population because the transmission curves exhibit RSA. The optical limiting studies were carried out at the same concentration of $2.8 \times 10^{-5} M$. $PbCl_2$ is a good optical limiter that transmits light at low input intensity while becomes opaque at high input fluences

Fig.1. Open aperture z-scan plot of $PbCl_2$ at a laser power of 100 MW/cm^2

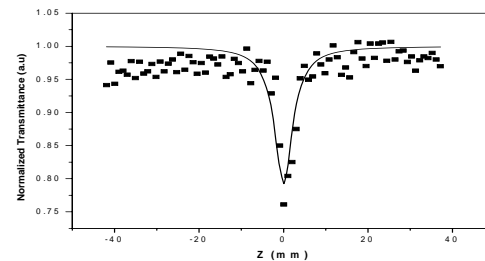


Table.1. Measured values of nonlinear absorption coefficient and optical limiting threshold for $PbCl_2$.

Input laser power density (I_0) (MW/cm^2)	Nonlinear absorption coefficient, β (cm/GW)	Optical limiting threshold (MW/cm^2)
100	122	68
125	65	83

ACKNOWLEDGEMENT

The author Rejeena thanks UGC for the financial assistance through Moulana Azad National Fellowship. KSCSTE is also acknowledged.

REFERENCE

[1] M.Fujita, H.Nakagawa, D.L.Alov "Optical spectra and electronic structures of lead halides" *Phys.Rev.b* **61**,23(2000)

Second order nonlinear optical and laser damage threshold studies on gamma glycine single crystals for photonic applications

G. Peramaiyan^a, P. Pandi^{a, b}, R. Mohan Kumar^{a,*}

^a Department of Physics, Presidency College, Chennai- 5

^b Department of Physics, Panimalar Engineering College, Chennai-123

Email: kutty.peram@gmail.com

Abstract: The γ -glycine single crystal was grown by solution growth technique. Structural studies XRD and FTIR have been carried out. The plasma energy, Penn gap energy, Fermi energy and polarizability have been calculated and these values are compared with theoretical data using Clausius-Mossotti equation. The SHG and Laser damage threshold properties were studied.

1. INTRODUCTION

In the recent years, nonlinear optical materials play a vital role in the emerging photonic and optoelectronic technologies. The most popular nonlinear optical materials used to generate the SHG signal have been inorganic bulk crystals with rather small second order nonlinear optical susceptibilities, such as KDP, Lithium triborate (LBO), β -Barium borate(BBO), lithium niobate (LiNbO₃) etc.,[1,2]. Due its lower SHG efficiency and laser damage threshold, scientists focused their attention on organic materials because the advantage of organic materials over their inorganic counterparts is that they have high electronic susceptibility ($\chi^{(2)}$) through high molecular hyperpolarizability (β), facile modification through standard synthetic methods and relative ease of device processing. Among the amino acids, glycine has three polymorphic crystallites in nature such as α , β and γ . For the past two decades, many authors have reported of about γ -glycine with various additives such as sodium chloride, potassium chloride, potassium fluoride, lithium sulphate, lithium nitrate etc,

2. EXPERIMENT

2.1 Synthesis and Crystal growth

A stoichiometric mixture of glycine (AR grade) and lithium nitrate was dissolved in millipore water (resistivity 18.2 M Ω cm). The resulting filtered solution was slowly evaporated at a temperature of approximately 30 °C with an initial pH value 5.5. After 10 days good quality of gamma glycine single crystals were harvested from the mother solution. The size of the crystal obtained with the effect of Lithium nitrate is 9 mm \times 9 mm \times 8 mm which is shown in Fig. 1

2.2 Theoretical Studies

The result of single XRD reveals that γ -glycine single crystal crystallizes into hexagonal crystal system with the space group P3₁. From the

empirical formula, the molecular weight of the grown crystal measured as M = 75.07 g/mol, and

total number of valance electron in the structural unit is Z = 20. The density of the grown crystal was determined as $\rho = 1.598$ g/m³. From these data, the valance electron plasma energy calculated by,(1), $\hbar\omega_p = 28.8 \left(\frac{Z\rho}{M}\right)^{1/2}$ (1), $E_p = \frac{\hbar\omega_p}{(\epsilon_\infty - 1)^{1/2}}$ (2)

where Z = (2 \times Z_C) + (5 \times Z_H) + (1 \times Z_N) + (2 \times Z_O) = 20 is the total number of valance electrons, ρ is the density and M is the molecular weight of the γ -glycine single crystal. In terms of Plasma energy, the Penn gap and Fermi energy are derived from the following relation

In terms of Plasma energy, the Penn gap and Fermi energy are derived from the following relation (3) where ϵ_∞ is the value of dielectric constant of the material at higher frequency. Fermi energy (E_F) is calculated from the plasma energy relation as $E_F = 0.2948 (\hbar\omega_p)^{4/3}$ (3)

The molecular Polarizability, ' α ' is obtained using the relation (4),

$$\alpha = \left[\frac{(\hbar\omega_p)^2 S_0}{(\hbar\omega_p)^2 S_0 + 2E_p^2} \right] \times \frac{M}{\rho} \times 0.396 \times 10^{-24} \text{cm}^{-1} \quad (4)$$

where S₀ is a constant for a particular material, and is given by,

$$S_0 = 1 - \left[\frac{E_F}{4E_p} \right] + \frac{1}{2} \left[\frac{E_F}{4E_p} \right]^2 \quad (5), \alpha = \frac{3M}{4\pi N_a \rho} \frac{\epsilon_\infty - 1}{\epsilon_\infty + 2}$$

value of ' α ' obtained in the present study agrees well with Clausius-Mossotti equation, which is given by,

The theoretical parameters are calculated for γ -glycine crystal is presented in Table 1[1,2]

3. CHARACTERIZATION

3.1 Single and X-Ray Diffraction Analyses

The cell parameters of the gamma glycine crystal were estimated by single crystal X-ray diffraction analysis. It is observed that lattice parameter values and unit cell volume of gamma glycine are in good agreement with the reported values. The grown crystal belongs to hexagonal crystal system with space group P3₁. In the powder X-ray diffraction pattern, the presence of prominent Bragg peaks at specific 2θ angles confirm the perfect crystalline nature of the picolinium tartrate monohydrate crystal.

3.2 NLO and Laser damage Threshold studies

The operation of nonlinear devices obviously involves the exposure of material to high power laser source. For harmonic generation, the efficiency of conversion is strongly dependent on the incident power level. The utility of NLO crystal depends not only on the linear and nonlinear optical properties but also greatly on its ability to withstand high power lasers. The bulk materials appear more damage resistant than the surfaces. Therefore, the performance of the crystal mainly depends on surface quality. In fact, the polishing process used in the finishing of optical elements leaves residual scratches and imperfections on the surface. At these points, the electric field in the light wave is greatly intensified so that the effective field value just inside the surface is much greater than the average field. When breakdown or failure of the surface occurs, it occurs near one of these imperfections. Furthermore, damage also occurs due to minute inclusions of polishing materials, airborne particles, fingerprints, etc., providing a nucleus around which damage may occur. Thus, the surface damage is caused either by absorption of submicron inclusions or by formation of a plasma at the surface because of electron avalanche breakdown in the dielectric. However, the local heating caused by macroscopic inclusion is a more severe problem in high intensity short-pulse system than in low-intensity long-pulse or CW system of equal average intensity. Moreover, the occurrence of damage is probabilistic in its nature, and the laser pulse whose power is lower than the single-shot damage threshold still has a non-zero probability to cause damage. However, damage threshold depends on a great number of laser parameters such as wavelength, energy, pulse duration, transverse and longitudinal mode structure, beam size, location of beam, etc. The surface damage threshold of the crystal was calculated using the expression:

$$Power\ density\ (P_d) = E / \tau \pi r^2$$

where E is the energy (mJ), τ the pulse width (ns) and r the radius of the spot (mm). The measured

multiple shot (150 pulses) laser damage threshold value is 4.7 GW/cm² for 1064 nm wavelength of Nd:YAG laser radiation for gamma glycine crystal.

where E is the energy (mJ), τ is the pulse width (ns) and r is the radius of the spot (mm). The measured multiple shot (150 pulses) laser damage threshold value is 4.7 GW/cm² for 1064 nm wavelength of Nd:YAG laser radiation.

4. TABLES

Table 1 Theoretical values of γ-glycine crystal

Parameters	Values
Plasma energy	30.10 eV
Penn gap	5.160 eV
Fermi energy	27.62 eV
Polarizability Penn analysis	1.65×10 ⁻²³ cm ³
Clausius-Mossotti Equation	1.71×10 ⁻²³ cm ³

5. FIGURES

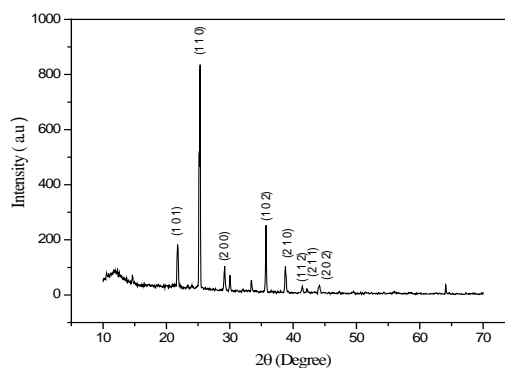


Figure 1 Powder X-rd pattern of gamma glycine crystal

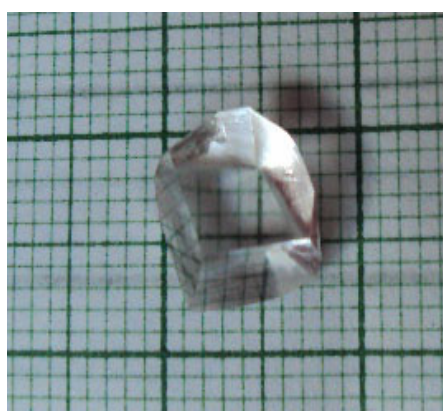


Figure 2 Photograph of γ-glycine single crystal

ACKNOWLEDGEMENT

One of the author (G.P) is grateful to University Grants Commission, India for the financial support under the UGC-Major Research Project (F.NO:38-162/2009(SR))

REFERENCES

- [1] N.M. Ravindra, R.P. Bhardwaj, K.Sunil Kumar, V.K. Srivastava, *Infrared Phys.* 21 (1981) 369.
- [2] N.M. Ravindra, V.K. Srivastava, *Infrared Phys.* 20 (1980) 67.
- [3] S.K. Kurtz and T.T. Perry, *J. Appl. Phys.* 39 (1968) 3798.

Ultrafast Degenerate Pump-Probe Studies of SI-GaAs

P.T. Anusha, Debasis Swain, Surya P. Tewari, S. Venugopal Rao*

Advanced Centre of Research in High Energy Materials (ACRHEM)
University of Hyderabad, Hyderabad -500046
e-mail: *svrsp@uohyd.ernet.in, soma_venu@yahoo.com

Abstract We present time-resolved pump probe measurements of the change in reflectivity of semi-insulating Gallium Arsenide (SI-GaAs) under optical pumping using picosecond (ps) and femtosecond (fs) laser pulses. The excitation wavelength of 800 (1.55eV) nm was used in the ps case, which is above the band gap. An ultrafast increase in the reflectivity followed by decay was observed. The carrier relaxation life time obtained from the data was ~95 ps. The intensity dependence of the relaxation time was performed using 40 fs pulses at a wavelength of 600 nm. The data shows the change in reflectivity ΔR to be positive. The relaxation was found to be faster when compared with ps excitation.

1. INTRODUCTION

The continuing miniaturization of semiconductor devices into the nano-scale regime has emphasized the importance of understanding carrier dynamics on increasingly shorter timescales. For example, in a nano-scale transistor electron transit times can be as short as a few picoseconds. This time scale is the domain of electron and phonon scattering, and in some cases bulk and surface recombination processes. Thus femtosecond/picosecond relaxation times of such non-equilibrium carrier dynamics in semiconductors are important to perceive their application potential and can be measured using ultrafast pump-probe spectroscopy. [1-3] Recently, there has been a growing interest in switching cavities on ultrafast timescales. Switching cavities are important for dynamic control of light, such as optical wavelength modulation, band width conversion, density of states switching and trapping and releasing photon.[4,5] Four techniques have been particularly useful in probing the carrier dynamics of semiconductors: transient reflectivity (and/or transmission), transient grating diffraction (including two beam self-diffraction), photo-thermal deflection, and time resolved photo emission.[8,9] In all of these techniques a relatively strong laser pulse (or two crossed pulses in the case of transient grating diffraction) excites the valence band electrons into the conduction band. The relaxation of these electrons and/or the redistribution of the excess energy initially contained in these excited carriers is then monitored with a time resolved probe. From these studies the picture of carrier dynamics in the semiconductors can be emerged.

When a semiconductor is excited with photons of energy greater than its band gap E_g , electron-hole pairs are created with excess kinetic energy $h\nu - E_g$. This excess energy will then redistribute among the electronic and lattice degrees of freedom until

equilibrium are reached with the surroundings. A switchable mirror with high initial reflectivity requires materials that have low absorption at the desired operation wavelength, and a large index contrast is desirable in order to keep the mirrors as thin as possible. Thus one material must possess a large nonlinear index of refraction to allow effective all-optical switching. GaAs meet these criteria and mirrors with, 30 layer pairs can be grown with reflectivity of 99.99%. GaAs has a Kerr nonlinearity and in addition, the nonlinearity in index of refraction related to free carriers in GaAs has previously been studied [6,7]. SI-GaAs is extensively used in terahertz generation and detection. Therefore the knowledge of carrier lifetime in this material is important. Pump-probe studies of SI-GaAs using ps pulses at 800 nm and 600 nm are reported here. In our experiments pump and probe signals were created from the same source at 800 nm/600 nm. The experiments are performed in non resonant condition with photon energy (~1.55 eV) higher than band gap of SI-GaAs. The intensity dependent studies performed using femtosecond pulses are also analyzed and discussed.

2. EXPERIMENT

Degenerate pump probe measurements were performed using ~2 ps (FWHM), 800 nm pulses with a repetition rate of 1 kHz with an energy ~13 μ J and 40 fs, 600 nm pulses with an energy of ~22 μ J. Figure 1 shows the schematic diagram of the experimental set up for picosecond pump probe reflectivity measurements. The main beam is split into pump and probe beams. The pump and probe beams are sent along different optical paths and focused into the sample with a time delay between them (provided by a delay stage), whereas in femtosecond pump-probe reflectivity measurements both the beams were not focused.

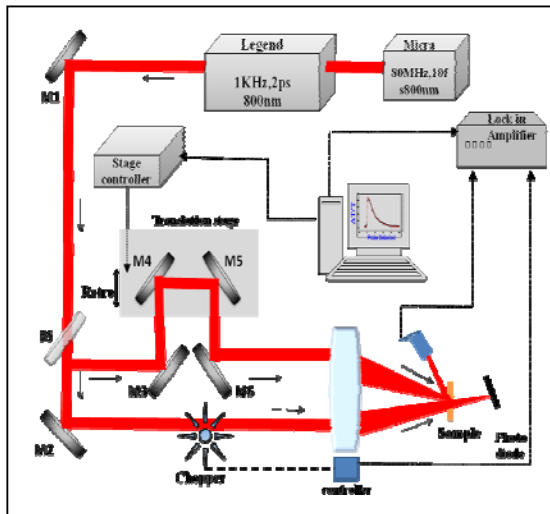


Figure 1 Typical picosecond degenerate pump probe experimental set up at 800 nm.

The amplifier was seeded with pulses of duration ~ 15 fs (FWHM, spectral bandwidth of ~ 50 - 60 nm) from the oscillator (Mira, Coherent). The chopper frequency was kept at 100 Hz. The pump-probe scan was performed by a high-resolution linear translation stage (Newport ILS250PP) by recording the sample transient reflectivity using a photodiode (Thor Labs SMR05/M) and lock-in amplifier (Signal Recovery 7265) combination. A LabVIEW program was designed and used for automating the data acquisition. Ratio of the pump and the probe power is controlled at 10:1 with the help of the neutral density filters in the probe arm of the set up. For good overlap of pump and the probe we have ensured very low angle ($\sim 5^\circ$) between pump and probe beams along with different diameters for the beams (large for pump and small for probe beams). Pump and probe spot size at the overlapping region is 4:1. The sample was a 1 mm thick GaAs wafer. Polarization of pump and probe were perpendicular to each other. Figure 2 depicts a typical pump-probe data for SI-GaAs recorded at 800 nm. The change in reflectivity was measured as a function of the delay of probe pulses using a fast photodiode.

3. RESULTS & DISCUSSION

Three different independent measurements with ps pulses resulted in a carrier recovery time of 90 ± 5 ps from the fits to the experimental data (data presented in figure 2). At negative delay, the transmission was constant. The initial fast response, peaking at maximal pump probe overlap, is attributed to the Kerr nonlinearity in GaAs, which changes the index of refraction, and led to an increase in transmission of 62%.

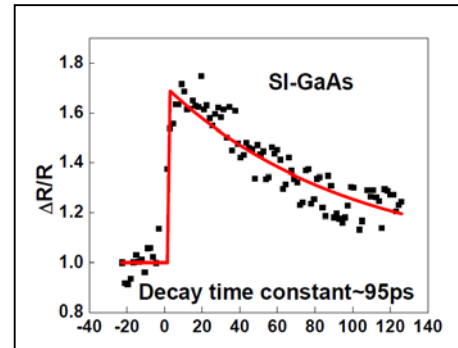


Figure 2 Typical pump probe data obtained for SI GaAs with ps pulses at 800 nm. Open circles are experimental data while solid line is the fit.

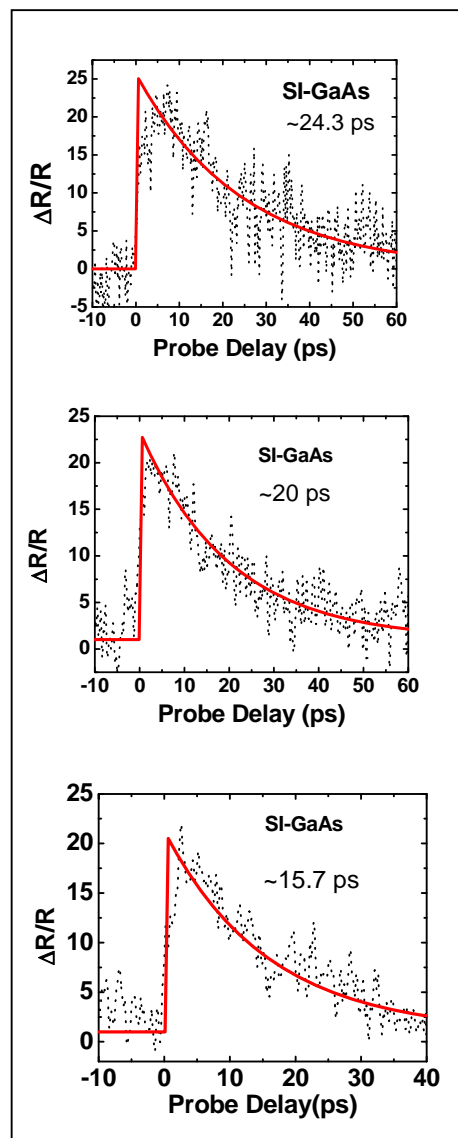


Figure 3 Femtosecond pump probe data obtained at 600 nm.

Topic Code:

Presentation Preference: **Poster**

Intensity dependent pump-probe study has been done using fs pulses of pulse duration 40 fs and at 600 nm wavelength and the data is presented in figure 3. The lifetimes observed were in the 15-24 ps range. The difference in the lifetimes observed with ps and fs pulses are being investigated in detail.

In summary, the carrier relaxation times have been extracted using both ps and fs pump probe techniques. Under femtosecond excitation the recovery was observed to be faster compared to that of ps excitation.

ACKNOWLEDGEMENTS

The authors wish to acknowledge DRDO, India for financial support.

REFERENCES

- [1] J.S. Yahng, D.S. Kim, N. Del Fatti, F. Vallee, "Femtosecond Degenerate and Non Degenerate Pump-probe experiments in Bulk GaAs below band gap", *J. Opt. Soc. Korea.* **2**, 100 (1997).
- [2] S. S. Prabhu and A. S. Vengurlekar, "Dynamics of the pump-probe reflectivity spectra in GaAs and GaN" *J. Appl. Phys.* **95**, 7803 (2004).
- [3] K. Ushida, K.G. Nakamura and H. Shibata, "Subpicosecond carrier dynamics in GaAs studied with optical heterodyne detection," *Solid State Commun.* **103**, 525 (1997).
- [4] V.R. Almeida, C.A. Barrios, R.R. Panepucci and M. Lipson, "All-optical control of light on a silicon chip," *Nature.* **431**, 1081 (2004).
- [5] Q. Xu, P. Dong, and M. Lipson, "Breaking the delay-bandwidth limit in a photonic structure", *Nature Phys.* **31**, 406 (2007).
- [6] S. R. Hastings, M. J. A. de Dood, H. Kim, W. Marshall, H. S. Eisenberg, D. Bouwmeester "Ultrafast optical response of a high-reflectivity GaAs/AlAs Bragg mirror", *Appl. Phys. Lett.*, **86**, 031109(2005).
- [7] L. Huang, J. P. Callan, E. N. Glezer, and E. Mazur, "GaAs under Intense Ultrafast Excitation: Response of the Dielectric Function", *Phys. Rev. Lett.*, **80**, 185 (1998).
- [8] F. E. Doany, D. Grischkowsky, G. G. Ghi, "Carrier lifetime versus ion- implantation dose in silicon on sapphire", *Appl. Phys. Lett.*, **52**, 36 (1988).
- [9] A. J. Sabbah, D. M. Riffe, "Femtosecond pump-probe reflectivity study of silicon carrier dynamics", *Phys. Rev. B*, **66**, 165217 (2002).
- [10] K. Ma, R. Urata, D. A. B. Miller, J. S. Harris, "Low Temperature growth of Gas on Si used for Ultrafast photoconductive switches", *IEEE J. of Quant. Elect.*, **40**, 6 (2004)

MODULATIONAL INSTABILITY IN OPTICAL FIBERS NEAR THE ZERO DISPERSION POINT FOR A RELAXATIONAL KERR MEDIUM

K.Nithyanandan^a, Vasantha Jayakantha Raja^b, T. Uthayakumar^a, and K.Porsezian^a

^aDepartment of Physics, Pondicherry University, Puducherry.

^bDepartment of Physics, Central University of Tamil Nadu, Thiruvarur.

nithi.physics@gmail.com, rvjraja@yahoo.com, uthayapu@gmail.com and ponzsol@yahoo.com

Abstract: A theoretical analysis of modulational instability of optical pulses propagating near the zero dispersion wavelength of a optical fiber in a lossless fiber with the effect of delayed nonlinear response is presented. We also investigate the combined interplay between the higher order dispersion and the non-instantaneous nature of the nonlinear response. We calculate the exact dispersion relation with the effect of higher dispersion for the harmonic perturbation.

1. INTRODUCTION

Modulation instability (MI) is a universal good old phenomenon, which is an inherent feature of most nonlinear wave systems in nature [1-3]. MI is known to be the process where weak perturbations, typically the noise imposed on a CW state grow exponentially, as a result of the interplay between nonlinear and dispersive effects. The weak perturbation can be either the quantum noise or the frequency shifted signal. As a consequence the corresponding MI can be called as spontaneous MI or the Induced MI [2]. In the time domain, MI leads to the breakup of a cw or quasi-cw beam into a periodic pulse train. Modulational instability (MI) is a general phenomenon that exists for a wide class of nonlinear wave processes in plasma, optical waveguides, etc. In the optics community, MI is relevant in many topics, including Bragg gratings, cross-phase modulations, four-wave mixing, novel materials, parametric oscillators, polarization and birefringence, saturable nonlinearity, spatial instability, supercontinuum generation, and temporal solitons in fibers [1-5]

Following the detailed introduction, we are moving on to the objective of the paper by providing a glimpse of the research activities on the MI in fibers and the motivation of us to go for this problem. Although MI is a good old phenomenon known for more than a few decades but still remains as the subject of intensive research activities due to its applicability and versatility. The possibility of MI in optical fiber was introduced theoretically by Hasegawa et al., [3] and later experimentally proved by Mollaneur et al., Soon then MI picks momentum and evolves as the most dramatic effects of the nonlinear optics. Initially MI was predicted in the anomalous dispersion regime but later by the virtue of fourth order dispersion it is also extended to the normal dispersion regime. Moreover, coupling between the two co-propagating pulses was of interest due to their ability to achieve MI in the normal dispersion regime. Then the perception of analyzing MI takes different dimension depending upon the nonlinear contribution of the refractive index. All the

above way of using MI is governed by the generalized nonlinear Schrodinger equation (GNLSE). Recently, much attention is devoted to the influence of the relaxation of the nonlinear response [4]. For the case of ultrashort pulses the usual assumption of instantaneous nonlinear response fails and thus delayed contributions of the nonlinear responses has to be taken into account. The non-instantaneous nature of the nonlinear response plays crucial role in the MI dynamics, like the possibility of MI in the normal dispersion regime and the evolution of additional bands of sideband in the anomalous dispersion regime and so on. It is also observed that the characteristic delay time suppress the MI gain and extend the range of unstable frequency. In the case of pulse propagation near the zero dispersion wavelength higher order dispersion effects will inevitably enter into the picture thus requires the contribution of the HOD in the NLSE [6,7]. Thus in this context, we would like to answer the question, what would happen to the MI spectrum for the combined action delayed nonlinear response and the higher order dispersion for the first time to the best of our knowledge.

2. THEORETICAL MODEL

In the regime of ultrashort pulses, the pulse propagation in nonlinear waveguide also needs to include the finite response time of the nonlinearity. The delay in the nonlinear response is given by the simple relaxation model as follows

$$i \frac{\partial E}{\partial z} = \frac{\beta_2}{2} \frac{\partial^2 E}{\partial t^2} + i \frac{\beta_3}{6} \frac{\partial^3 E}{\partial t^3} - \frac{\beta_4}{24} \frac{\partial^4 E}{\partial t^4} + \gamma N E \quad (1a)$$

$$\frac{\partial N}{\partial t} = \frac{1}{\tau} (-N + |E|^2) \quad (1b)$$

Where β_n is the nth order dispersion coefficient, N represents the nonlinear index of the medium and τ is the medium's response time.

3. LINEAR STABILITY ANALYSIS

The stability of the steady-state solution of the above dynamical equations against the presence of small harmonic perturbations can be studied using linear stability analysis. The steady-state solution, i.e., the CW solution is given by

$$E_s = E_0 \exp[-i |E_0|^2], \quad (2)$$

The harmonic perturbation is of the form

$$E_p = (E_0 + a(z, t)) \exp[-i |E_0|^2], \quad (3a)$$

$$N_p = N_0 + n(z, t) \quad (3b)$$

where, $a(z, t)$ and $n(z, t)$ are small deviations from the stationary solutions of the electric field and nonlinear index, respectively. After some mathematical manipulation, the dynamical equation for the perturbation can be written as

$$i \frac{\partial a}{\partial z} = \frac{\beta_2}{2} \frac{\partial^2 a}{\partial t^2} + i \frac{\beta_3}{6} \frac{\partial^3 a}{\partial t^3} - \frac{\beta_4}{24} \frac{\partial^4 a}{\partial t^4} + \gamma n E_0 \quad (4)$$

$$i \frac{\partial n}{\partial t} = \frac{1}{\tau} (-n + (a + a^*) E_0) \quad (5)$$

Solving the above equation in the Fourier domain, one will arrive into the dispersion relation given by

$$K = \sqrt{(\tilde{\gamma}^2 P_0^2 + \beta_2 \frac{\Omega^2}{2} + \beta_4 \frac{\Omega^4}{24}) - \tilde{\gamma}^2 P_0^2}, \quad (6)$$

$$\tilde{\gamma} = \frac{1}{(1+i\Omega)}$$

4. MODULATIONAL INSTABILITY ANALYSIS

The above dispersion relation Eq. (6) is a more general case for the ultrashort pulse propagation near the zero dispersion wavelength. In principle, one can analyze MI in two distinct way depending upon the wavelength of the propagation. Former is the pulse propagation at anomalous GVD regime, where the wavelength of the pump source is greater than the ZDW and the latter is the pumping at or near to the ZDW wavelength.

The dispersion relation for the pulse propagation at anomalous GVD regime is given by

$$K_{AD} = \frac{1}{2} |\beta_2| \Omega \sqrt{[\Omega^2 + \text{sgn}(\beta_4) \Omega_{AD}^2]}, \quad (7)$$

The dispersion relation for the pulse propagation at ZDW is given by

$$K_{ZDW} = \frac{\beta_3}{6} \pm \frac{|\beta_4| \Omega^2}{24} \sqrt{[\Omega^4 + \text{sgn}(\beta_4) \Omega_{ZD}^4]}, \quad (8)$$

where, Ω_{AD} and Ω_{ZD} are the critical modulation frequency (CMF) of SNL for the pulse centered at anomalous GVD and ZDW, respectively. The CMF take its functional form respectively as

$$\Omega_{AD} = \frac{4 \gamma |E_0|^2}{|\beta_2| (1+i\Omega)} \quad \text{and} \quad \Omega_{ZD} = \frac{48 \gamma |E_0|^2}{|\beta_4| (1+i\Omega)}$$

The above dispersion relation leads to an exponential growth of the weak perturbation only for imaginary value of K . This can be achieved only when the frequency Ω registers value lower than the CMF, where Ω being the frequency shift from the central frequency ω_0 .

4.1 MI in Anomalous dispersion regime

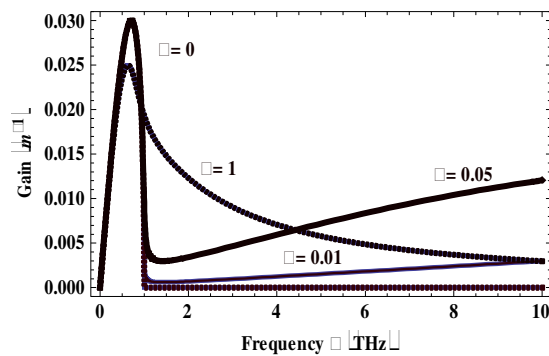


Fig. 1(a) MI spectrum in the anomalous dispersion regime for $(\beta_2 = \pm 0.06, \beta_4 = \pm 0.0007, P = 1W, \gamma = 0.015W^{-1}m)$

For instance, we consider the anomalous dispersion regime whose dispersion relation is given by the Eq. (7). To have a quantitative picture of the MI in the presence of relaxation, we plot in Fig. 1(a) the gain spectrum for some representative cases. Interestingly, due to the delay in the nonlinear response a second band of unstable frequencies emerges, this is attributed to the retarded raman contribution to the nonlinear response of the medium.

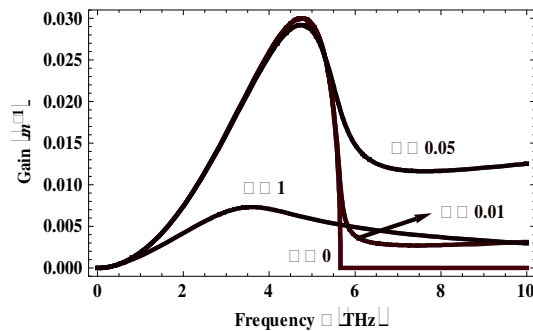


Fig.1 (a) MI spectrum at ZDW dispersion regime for $\beta_4 = -0.0007$ other parameters take the same value.

For short response time the delay in the nonlinear response is not having appreciable effect on the MI gain but extends the unstable regime. But for slow responses both the MI gain and the MI instability is strongly reduced. It is evident from the Fig. 1(a) that two instability band are resolved only at short response time of the medium.

4.2 MI in Normal dispersion regime

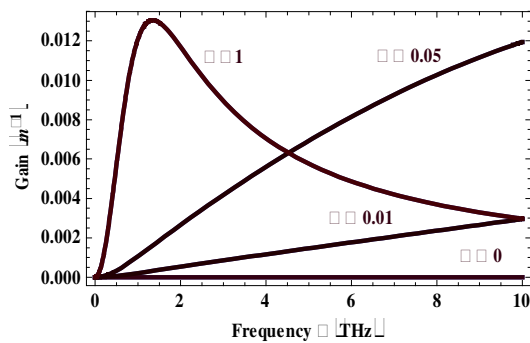


Fig.2 (a) MI spectrum in the normal dispersion regime for $(\beta_2 = \pm 0.06, \beta_4 = \pm 0.0007, P = 1W, \gamma = 0.015W^{-1}m)$

Now we move on to the case of normal dispersion regime ($\beta_2 > 0$). It is a proven fact that MI is not possible in the single pump case for normal dispersion regime due to lack of phase matching between the linear and nonlinear effects. Quite interestingly, the delay in the nonlinear response induces the emergence of an instability band even in this normal GVD. The emergence of instability in the normal dispersion regime is attributed to the fact that any finite relaxation time produces an imaginary part to the wave vector at any frequency irrespective of the nature of the dispersion regime. The gain spectrum for for some representative cases of delay response is show in the Fig. 2 (a). Unlike the case of anomalous dispersion regime, here in the normal regime only single band is obtained which is the characteristic of the delayed Raman response.

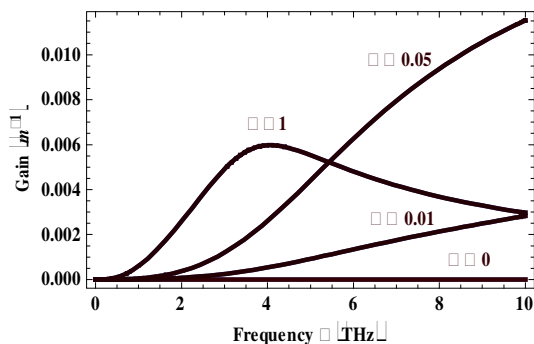


Fig.2 (b) MI spectrum at ZDW dispersion regime for $\beta_4 = + 0.0007$ other parameters take the same value

4.3 MI at Zero dispersion wavelength

We now extend the same for the case of pulse centered at or near ZDW, for this case β_2 is very small or takes zero. In this context, the dispersion effects will be taken care of by the HOD, especially the fourth order dispersion (FOD). It is obvious that HOD more than four order is literally insignificant. From the dispersion relation Eq. (8), we can directly infer that the third order dispersion is practically of no use in the MI dynamics and thus the entire dispersion effects are contributed by the FOD. Fig. 1(b) and 2(b) shows the MI gain spectra by virtue of FOD for the parameters quoted below.

5. RESULTS AND DISCUSSION

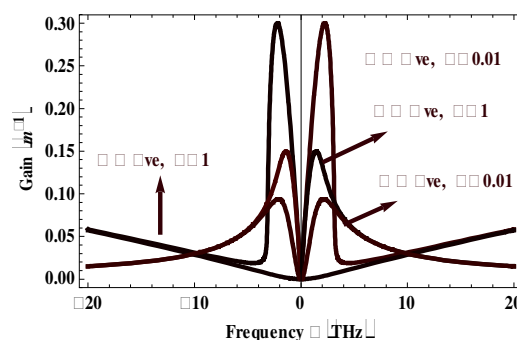


Fig.3 (a) MI spectrum at anomalous GVD dispersion regime for $(\beta_2 = \pm 0.06, \beta_4 = \pm 0.0007, P = 1W, \gamma = 0.015W^{-1}m)$

The section features a comparative analysis about the influence of FOD in the delayed nonlinear system. For the case of pulse propagating at ZDW wavelength, with $\beta_2 = 0$, FOD will be the dominant contender of the dispersion effects. From the Fig. 1(a) and Fig. 1(b), corresponding to the anomalous dispersion regime, MI can be achieved even when the GVD effects are ignored. It can also be observed like in the case of anomalous GVD, FOD also results in two bands in the MI spectrum, i.e., MI instability band and the raman band. Although MI gain is not of any appreciable change, FOD shifts the MI peak gain to the higher frequency side and also increases the instability region Fig 1(b).

To give a quantitative picture, we plot Fig. 3(a) and 3(b) to illustrates the role of FOD in minimum GVD regime. Now we move on to the normal dispersion region, it is obvious in our context that MI occurs even in the normal dispersion regime, which is purely attributed to the fact that any finite relaxation time produces an imaginary part to the wave vector at any frequency irrespective of the nature of the dispersion regime. Fig. 2(a) and Fig. 2(b) shows the MI spectrum for the normal dispersion regime, like our earlier argument, here too FOD serve the necessary contribution to the phase matching

condition. One can observe that both the cases are identical except a slight shift of the MI peak gain towards higher frequency side is observed for the case of FOD system Fig. 2(b).

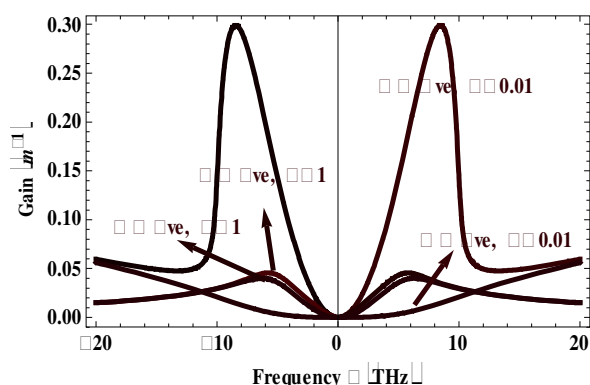


Fig.3(b) MI spectrum at anomalous GVD dispersion regime for $(\beta_2 = \pm 0.06, \beta_4 = \pm 0.0007, P = 1W, \gamma = 0.015W^{-1}m)$

6. CONCLUSION

We have presented the impact of higher order dispersion in the MI spectrum of the delayed nonlinear system. Using Linear stability analysis, we have theoretically shown the role of FOD in the minimum GVD regime with the realistic fiber parameters. We have shown the possibility of MI in both the normal and anomalous dispersion regime even in the absence of GVD.

ACKNOWLEDGEMENT

KP thanks DST, DAE-BRNS, and UGC, Government of India, for the financial support through major projects. K. Nithyanandan express his gratitude to the speakers and the resource of the DST-SERC school on “Guided wave optics and devices”, Centre for Glass and Ceramic Research Institute (CGCRI), Council of Scientific and Industrial Research (CSIR), Kolkata- 700 032.

REFERENCES

- [1] Ajoy Ghatak and Thyagarajan “An Introduction to Fiber Optics” cambride University Press(2000)
- [2] G. P. Agrawal, “Nonlinear Fiber Optics” third Edition, Academic Press, San Diego(2001).
- [3] A. Hasegawa and F. Tappert, , “Transmission of stationary nonlinear optical pulses in dispersive dielectric fibers I Anomalous dispersion” Appl. Phys. Lett **23** (1973).
- [4] X. Liu, J. W. Haus, S.M. Shahriar, “Modulational Instability for a relaxational Kerr medium, opt.comm.,281,2907(2008)
- [5]. G. L. da Silva, Iram Gleria, M. L. Lyra, and A. S. B. Sombra, “Modulational instability in

lossless fibers with saturable delayed nonlinear

- [6] B. Kalithasan, K. Porsezian, and Tochofo Dina “Modulational Instability in resonant optical fiber with higher order dispersion effects, J. Opt. **12**, 035210 (2010)
- [7] Tchofo Dinda and K. Porsezian, “Impact of fourth order dispersion in the modulational instability spectra of wave propagation in glass fiber with saturable nonlinearity,” J. Opt. Soc. Am. B **27** 143 (2010).

PLASMONIC CAVITY MADE OF DEFECT IN AN ARRAY OF ASYMMETRIC T-SHAPED STRUCTURES

Mohammed Nadhim Abbas^{1,2}, Yia-Chung Chang¹, and M. H. Shih¹

¹Research Centre for Applied Sciences, Academia Sinica, Taipei, 115 Taiwan

²Nano Science and Technology Program, Taiwan International Graduate Program, Academia Sinica, Taipei 115, Taiwan

Abstract: We study plasmonic cavity in a 1D array of asymmetric T-shaped plasmonic gratings. The asymmetric T-shaped plasmonic grating contains a silver bigrating structure. The first metallic grating contains the post of the T-shaped structure embedded in SiO₂ and the second metallic grating is the cap of the T-shaped structure embedded in air. The bigrating can open a large plasmonic band gap ($\sim 0.15\text{eV}$). We introduce a defect in a 1D array of asymmetric T-shaped structure by reducing the width of the cap in one line or in multiple lines. We have studied two kinds of defects. The first defect is a missing line from the T-shaped grating and it has a relatively low quality factor of 64 and a very small effective mode area [$0.026(\lambda/n)^2$]. The second one is done by removing or shifting more than one line from the T-shaped grating to make a gentler confinement and it leads to an enhancement of the quality factor (~ 200) and a slight increase in the effective mode area to [$0.0375(\lambda/n)^2$].

1. INTRODUCTION

Recently, SPP cavities are attracting more interest in the area of photonic circuits, because of their ability to confine light in a small volume below the diffraction limit. Plasmonic cavities generate localized SPP modes in the band gap region. This is similar to the cavity formation in photonic crystals where perfect periodicity of the dielectric system is broken by a local defect, leading to localized electromagnetic modes within the forbidden band gap [1]. Recently, several groups have demonstrated plasmonic cavities using various schemes such as metallic distributed Bragg reflectors [2], metallic Moire surfaces [3], biharmonic metallic gratings [4],

2. DEVICE DESCRIPTIONS

A uniform grating of asymmetric T-shaped structure [5]. We made a defect in Asymmetric T-shaped structure either by modifying only one line (abrupt defect) or gradually through several lines (smooth defect). In the case of abrupt defect, we modify only one column by removing the cap of the T-shaped structure. In the case of smooth defect, we modify several columns by reducing W gradually from both edges to the centre of the defect. Fig. 1(a) and (b) show the schematic diagram of the abrupt and smooth defects, respectively. The characteristics of the defect mode are calculated by using finite element method based on COMSOL software.

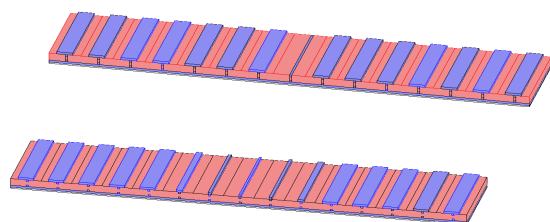


Figure 1. Schematic representation of the asymmetric T-shaped structure with (a) abrupt defect and (b) smooth defect.

3. CAVITY MODE CHARACTERISTICS

The quality factor (Q) of abrupt defect is about 64 and the low quality factor is due to abrupt change at the cavity edges which leads to weak vertical confinement [6]. One way to improve vertical confinement is to use a gentle defect. Though the defect region is increased for the gentle defect, the mode profile is only slightly increased in comparison with the abrupt defect. Furthermore, the quality factor is increased to 190. In general, radiative loss due to leaky modes is caused by scattering of the surface plasmon from higher-order grating harmonics due to the abrupt change of the localized mode profile in the cavity region. A_{eff} is about two orders of magnitude smaller than diffraction limit.

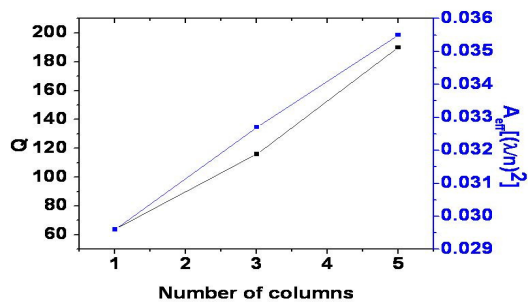


Figure 2. Quality factor and effective mode area A_{eff} versus the number of modified columns

ACKNOWLEDGEMENT

The author M. N. Abbas wishes to acknowledge, with thanks, the Taiwan International Graduate Program (TIGP) of Academia Sinica for financial support towards attending this conference. This work was supported by Academia Sinica and National Science Council, Taiwan, Republic of China under the grant number NSC 98-2112-M-001-022-MY3.

REFERENCES

- [1] Yablonovitch, et al., Phys Rev Lett **67**, 3380 (1991).
- [2] Gong et al., App Phys Lett **90**, 033113 (2007).
- [3] Kocabas et al., Phys Rev Lett **102**, 063901 (2009).
- [4] Kocabas et al., Phys Rev B **77**, 195130 (2009).
- [5] Abbas et al., Opt. Exp. **18**, 2509 (2010).
- [6] Akahane et al., Nature, **425** (London) (2003).

LONG RANGE PLASMONIC BRAGG GRATING BASED REFRACTIVE INDEX SENSOR

Prabhat Behere, M. R. Shenoy, K. Thyagarajan

Department of Physics, Indian Institute of Technology Delhi, Hauz Khas, New Delhi-16
prabhatbehere2811@gmail.com, mrshenoy@physics.iitd.ac.in, ktrajan@physics.iitd.ac.in

Abstract

Long Range Surface Plasmon Polaritons (LRSP), supported by thin metal stripes, depend strongly on the refractive index of the surrounding dielectric medium. Here, we analyze the width modulated Bragg grating structure based on the LRSP waveguide for its reflection characteristics and the effect of asymmetry in the refractive index on the shift in Bragg wavelength. We report the sensitivity defined as the change in refractive index required for one angstrom shift in Bragg wavelength as 0.0002.

1. INTRODUCTION

Surface Plasmon Polaritons are electromagnetic waves coupled to the electron oscillations on the metal-dielectric interface [1]. These waves have been used to design and develop many waveguides [2-5] and photonic devices [6-8]. Long range surface plasmon polaritons are formed on a thin metal stripes due to coupling between surface plasmon modes on metal-dielectric interface on either side of the stripe. These coupled modes have long propagation length of the order of few cm.

The long range surface plasmon polariton (LRSP) mode is strongly dependent on the symmetry in refractive index of the dielectric medium on either of the metal-dielectric interfaces. The index mismatch between the substrate and cover can result in cut-off of the long range mode. It has been found that thick metal slabs can support larger asymmetry in refractive index as compared to thinner slabs [9]. The cut-off condition results when the effective index of the LRSP mode becomes smaller than the refractive index of one of the dielectric media. Beyond cut-off, the mode travels as plane wave in the high index dielectric medium. The propagation length reduces drastically as the asymmetry in refractive index is increased.

In this paper, the Bragg grating geometry based on the LRSP waveguide as shown in Fig.1 has been used to study the effect of the asymmetry on its reflection characteristics. The Bragg grating structure and its results were verified from [10] for the symmetric case. It has been extended to include asymmetry in refractive index. The paper has been divided into four sections. Section 2 describes the Bragg grating architecture. Section 3 discusses results of the symmetric and asymmetric structure and finally, Section 4 concludes with a discussion on the application of this geometry to refractive index sensor.

2. GEOMETRY

Width modulated PPBG based on LRSP waveguide consists of constant period variation of effective

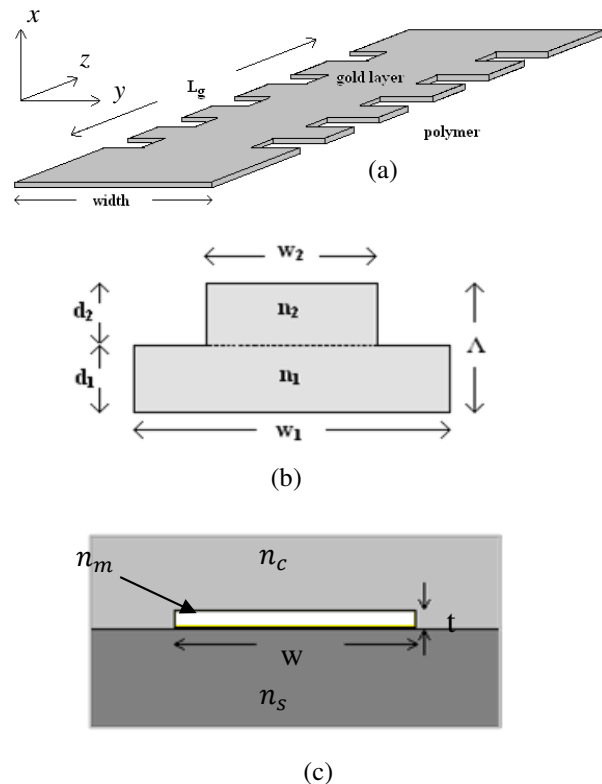


Fig.1 Schematic representation of (a) the Bragg grating based on LRSP waveguide where L_g represents the grating length. (b) a fundamental cell of the grating. d_1 and d_2 represent the lengths of waveguide sections of width w_1 and w_2 respectively. n_1 and n_2 represent the effective index of the LRSP mode corresponding to the waveguide dimensions (c) the cross-section of the grating structure. n_c , n_s and n_m are the refractive indices of the cover, substrate and metal layer respectively.

refractive index along the direction of propagation. The grating is designed for operation in 1550nm wavelength region with gold strips embedded in a polymer. The thickness of gold strips is chosen to be 10nm. The

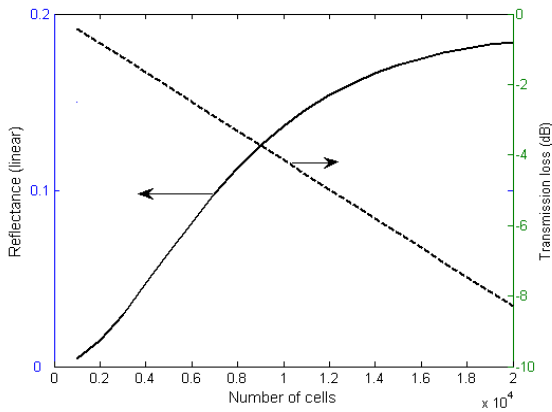


Fig.2 Reflectance and transmission loss with number of fundamental cells. Both the reflectance and transmission loss increase with the number of cells.

refractive indices of gold and polymer at 1550nm are $n_{Au} = 0.55 + 11.5i$ and $n_{polymer} = 1.45$ respectively. The grating can be formed by concatenating fundamental cell of the grating. The fundamental cell [Fig.1(b)] consists of two waveguide sections with widths w_1 and w_2 and lengths d_1 and d_2 respectively. The physical parameters decide the wavelength and the bandwidth over which the reflected waves can constructively interfere for an optical signal propagating along the grating axis i.e., in the z -direction. We define the period of the grating as

$$\Lambda = d_1 + d_2 \quad (1)$$

The free space wavelength called the Bragg centre wavelength is given by

$$\lambda_B = 2n_{avg}\Lambda \quad (2)$$

where the n_{avg} is the weighted average of the effective indices of the two waveguide sections forming the fundamental cell and is given by

$$n_{avg} = \frac{Re\{n_1\}d_1 + Re\{n_2\}d_2}{\Lambda} \quad (3)$$

where n_1 and n_2 are complex refractive indices of the waveguide sections. Thus, the dimensions of the waveguide sections forming the fundamental cell, the pitch of the grating and thickness of the metal stripe decide the Bragg centre wavelength. Only the real part of the indices have been considered to calculate the n_{avg} as the imaginary part is much smaller compared to the real part. But the imaginary part plays a significant

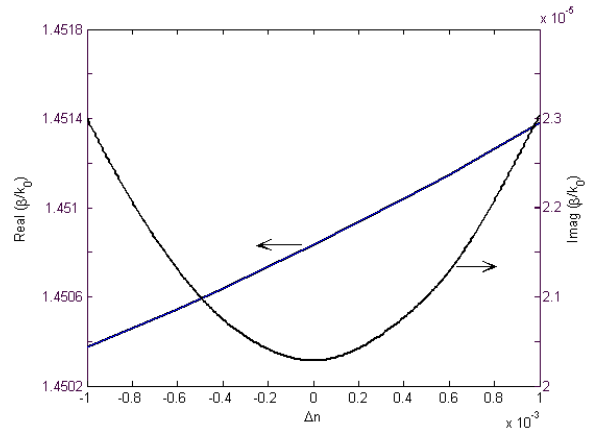


Fig.3 Effective index and propagation loss variation with asymmetry for the waveguide

role in determining the reflection characteristics and transmission loss. The length of the grating decides the FWHM of the reflection curve and the transmission loss for the off-resonance wavelengths. It is seen from Fig.2 that the peak reflection increases with number of cells but the transmission loss for off-resonance wavelengths also increases. The peak reflection increases with the number of cells but the transmission loss for off-resonance wavelengths increases. Here the length of the grating is chosen to be 5.36mm which corresponds to 10000 fundamental cells with a period of $0.536\mu\text{m}$. The widths of the waveguide sections are chosen to be $8\mu\text{m}$ and $7\mu\text{m}$. The Bragg grating formed with above dimensions can be modeled as dielectric stack with index of each layer taken as the effective index of the waveguide section obtained from FEM and the wavelength response of the Bragg grating is derived from the Transfer matrix method (TMM) [12]. This method of analysis is adopted from [10].

Asymmetry in refractive index is introduced by varying the refractive index of the cover with respect to the refractive index of the substrate dielectric medium. The index difference is defined as $\Delta n = n_c - n_s$, where n_c and n_s are the refractive indices of the cover and the substrate dielectric medium.

3. RESULT

Figure 3 shows the effective index and propagation loss variation with asymmetry for waveguide thickness of 10nm and width of $6\mu\text{m}$. The effective index increases as the index of the cover is increased. On the other hand, the loss increases with asymmetry as the field penetrates more into the metal.

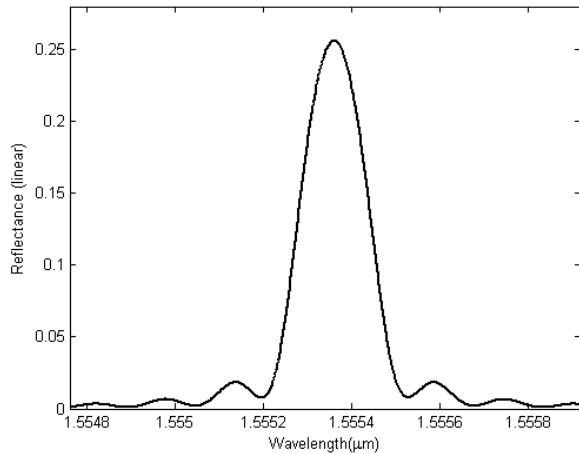


Fig.4 Reflection spectrum for grating structure with waveguide sections of width $7\mu\text{m}$ and $6\mu\text{m}$ and thickness 10nm .

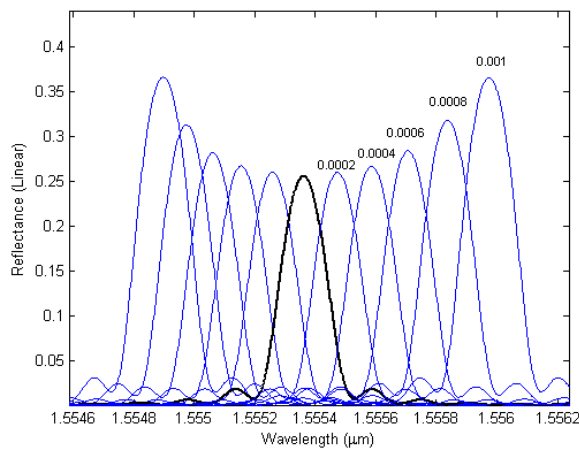


Fig.5 Shift in grating response with increase in index contrast between the cover and substrate dielectric medium.

Figure 4 shows the reflection spectra for the Bragg grating with symmetric refractive index medium. The peak reflection is around 26%, and the FWHM of the peak 1.7\AA . The transmission loss has been found to be around 0.76dB/mm for the grating geometry. The low value of peak reflectance is due to the propagation loss inherent in the LRSP propagation as well as the small depth of modulation of the grating. The grating depth is kept small for two reasons. First, the LRSP mode approaches cut-off with asymmetry as the width of the waveguide is reduced for a given thickness of the waveguide. For larger depth of modulation, thicker waveguides are suitable but they would introduce larger losses. Moreover, small grating depth also provides a

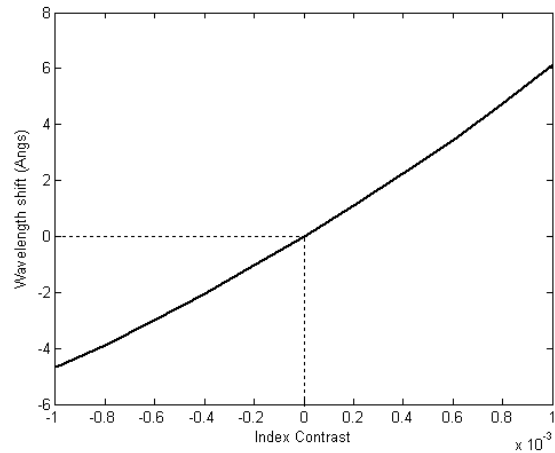


Fig.6 Shift in Bragg wavelength with index contrast. The slope of the curve around zero is 5.23×10^3 which gives a sensitivity of $0.0002/\text{\AA}$.

narrow peak in the reflection spectrum which is suitable for sensor applications.

Figure 5 shows the shift in reflection spectrum as the asymmetry is introduced. The effective index of the LRSP mode reduces for negative index contrast while it increases for positive index contrast. This results in corresponding shift in the Bragg wavelength to the left and right of the peak corresponding to the symmetric case. With increase in asymmetry, the difference in the effective indices of the two waveguide sections increases as seen in Fig.3. This increases the index contrast with asymmetry which results in increase in the peak reflection. This also results in slight increase in FWHM from 1.7\AA at zero asymmetry to 1.88\AA at asymmetry of 0.001. The shift in Bragg wavelength is larger for positive index contrast as the increase in effective index for positive index difference is larger as compared to negative index difference. Fig.6 shows the shift in Bragg wavelength with index contrast. The slope of the curve near zero index contrast gives sensitivity of Bragg wavelength to change in refractive index. The sensitivity defined as inverse of the slope is found to be about $0.0002/\text{\AA}$. As discussed earlier, slope is not constant but it increases towards positive index contrast.

4. CONCLUSION

The long range surface plasmon polariton waveguide based Bragg grating geometry has been theoretically studied using FEM and Transfer matrix method. The emphasis is on the study of asymmetry in refractive index on the response of the grating. The shift in Bragg wavelength with asymmetry can be used to develop a refractive index based sensor. This compact Bragg

grating geometry with high sensitivity to refractive index change has many potential applications such as a refractive index sensor, temperature sensor and pressure sensor. Its narrow peak and response to asymmetry can be used to form a simple temperature sensor based on an interrogator wavelength. The shift in reflected wavelength for minute changes in the dielectric medium can be applied to real time applications and analysis techniques in chemistry and medicine.

REFERENCES

1. A. D. William, L. Barnes and T. W. Ebbesen, "Surface plasmon subwavelength optics", *Nature*, vol. 424, pp. 824-830, 2003.
2. D.F.P. Pile, "Two-dimensionally localized modes of a nanoscale gap plasmon waveguide", *Appl. Phys.Lett.*, vol.87, pp. 2611-14, 2005.
3. T.Holmgaard and S.I. Bozhevolnyi, "Efficient excitation of dielectric-loaded surface plasmon-polariton waveguide modes at the telecommunication wavelengths", *Phys. Rev. B*, vol. 78, pp.165431, 2008.
4. E. Moreno, "Channel plasmon-polaritons: modal shape,dispersion, and losses", *Opt. Lett.*, vol. 31, pp. 23-27, 2006.
5. J.C.Quail, J.G.Rako and H.J.Simon, "Long-range surface-plasmon modes in silver and aluminum films", *Opt. Lett.*, vol. 8, pp. 377-379, 1983.
6. A.V. Krasavin and A.V. Zayats, "All-optical active components for dielectric-loaded plasmonic waveguides", *Opt. Comm.*, vol. 283, pp. 1581-1584, 2010.
7. T. Nikolajsen, K. Leosson and S.I. Bozhevolnyi, "Surface plasmon polariton based modulators and switches operating at telecom wavelengths", *Appl. Phys. Lett.*, vol. 85, pp. 24, 2004.
8. Jian-Wei Mu and W. Huang, "A Low-Loss Surface Plasmonic Bragg Grating", *J. Lightwave Tech.*, vol. 27, pp. 436-439, 2009.
9. L. Wendler and R. Haupt "Long-range surface plasmon-polaritons in asymmetric layer structures", *J. Appl. Phys.*, vol. 59, pp. 3289-3291, 1986.
10. S. J. Charbonneau and P. Berini, "Theoretical performance of Bragg gratings based on long-range surface plasmon-polariton waveguides", *J. Opt. Soc. Am. A*, vol. 23, pp. 1757-1767, 2006.
11. P. Berini, "Plasmon-polariton waves guided by thin lossy metal films of finite width: Bound modes of asymmetric structures", *Phys. Rev. B*, vol. 63, pp. 125417, 2001.
12. P.Yeh, *Optical waves in layered media*, John Wiley, 2005.

IMAGING SURFACE PLASMON RESONANCE POLARIMETER

Shankar Pidishety[†] and Nirmal K. Viswanathan*

Beam Optics and Applications Group

School of Physics, University of Hyderabad, Hyderabad-500046, India

Email: [†]pd.shankara@gmail.com / ^{*}nirmalisp@uohyd.ernet.in

Abstract: We demonstrate an imaging surface plasmon resonance (SPR) polarimeter to investigate and quantify the state of polarization changes in the SPR signal due to photo-thermal effect via spatially-resolved Stokes polarization parameter measurement. Spatial polarization changes in the SPR signal beam is attributed to changes in the refractive index of the thin gold film induced by an external laser.

1. INTRODUCTION

Surface Plasmon Resonance (SPR) is an optical phenomenon which involves resonance absorption of p-polarized light by the surface electron density oscillation of a metal film under specific wave vector matching conditions, determined by the dispersion relations of the surface plasmons at dielectric-metal interface [1, 2]. Ever since the technique of the optical excitation of surface plasmon polaritons (SPPs) was established [3], the SPR has been extensively studied and developed into a useful technique to study the optical properties of thin films and probe the refractive index changes in the surrounding medium which enabled the construction a variety of optical sensors for measuring the concentration of chemicals, humidity, pressure, bio-molecular interactions etc [2].

The sensitivity and accuracy of an SPR sensor critically depends on the mode of operation such as angular interrogation at fixed wavelength, spectral interrogation at fixed incident angle or phase and state of polarization (SOP) monitoring [2]. Among all these schemes, the phase change monitoring provides the highest refractive index sensitivity of 10^{-8} RIU [4]. However, it is highly desirable to simplify the technique and to improve the capability of this technique further via including spatially resolved method [4]. Stokes polarimetry is one of the powerful techniques to track the electric field vector orientation of the SPR signal through a series of simple measurements [5, 6]. To further improve the capability of the SPR sensor system using stokes polarimetry we use a CCD camera to obtain spatially resolved measurement suitable to use and characterize independent reaction rates in the micro array cells, for example, wherein independent reaction rates in the micro cells can be monitored simultaneously and independently.

Here we demonstrate an imaging SPR polarimeter similar to the technique proposed in Ref. [7] with improved capability. The technique measures changes in the phase and the state of polarization of the SPR signal beam from spatially-resolved Stokes parameter measurements. This technique also enables

visualization of the phase and polarization changes corresponding to spatial variations in refractive index. Surface plasmons are optically excited in ~37nm thick gold film through the Kretschmann geometry by using a CW He-Ne (632.8nm) laser. A CW Ar⁺ laser of fixed power and of beam size ~4 times smaller than that of the He-Ne laser beam at the sample is used for localized photo-thermal induced changes in the refractive index of the metal film. We measure the Stokes parameters of the SPR signal beam using a CCD image, using which we characterize polarization changes across the beam cross section, which is attributed to spatial variation of the refractive index of the thin gold film. From the measured phase and state of polarization changes in the exposed area with respect to the rest of the SPR beam, we estimate the localized thermally induced changes in the refractive index of the gold film, which is believed to be a highly sensitive, simplistic and more reliable method for sensor applications.

2. THEORY

Ellipsometry is a powerful optical technique for characterizing the optical parameters (n and t for example) of materials [9], and for sensing applications [10]. The technique is based on the measurement of two essential parameters, the ellipsometric angles ψ and Δ , which determine the state of polarization and the phase of the optical field. The ellipsometric parameters are related to the complex Fresnel reflection coefficients as,

$$\rho = \frac{R_p}{R_s} = \tan \psi \exp(i\Delta) \quad (1)$$

Where R_p and R_s are the complex reflection coefficients for light polarized linear horizontal and linear vertical respectively. The ellipsometry parameters ψ and Δ can also be obtained from the Stokes polarization parameter measurements. The phenomenon of surface plasmon resonance changes only the horizontal (R_p) component of the reflected light due to the optical excitation of the electrons at the dielectric-metal boundary. This results in Change in the orientation of the polarization state in the

reflected beam. The SPR reflectance signal is sensitive to the dielectric constant ϵ_m of the metal as follows [11, 12]:

$$R = \left| \frac{\sqrt{\epsilon_m} - 1}{\sqrt{\epsilon_m} + 1} \right|^2 \quad (2)$$

In 1852 G. G. Stokes proved that any orientation state of polarization of light can be characterized in terms of four intensity parameters and those can be measured with simple experiments [8]. The two orthogonal electric field components along the x, y coordinates of an EM wave, E_x , E_y , propagating in the z direction is given as

$$E_x(z, t) = E_{0x} \cos(\omega t - kz + \delta x) \quad (3)$$

$$E_y(z, t) = E_{0y} \cos(\omega t - kz + \delta y) \quad (4)$$

Where $\omega = 2\pi c/\lambda$, $k = 2\pi/\lambda$ are the angular frequency, wave number and δx δy are the phase constants along the x, y directions respectively. And the polarization ellipse with resultant phase δ can be described as

$$\frac{E_x^2(z, t)}{E_{0x}^2} + \frac{E_y^2(z, t)}{E_{0y}^2} - \frac{2E_x(z, t)E_y(z, t)}{E_{0x}E_{0y}} \cos(\delta) = \sin^2(\delta) \quad (5)$$

The time average of the polarization ellipse leads to the Stokes parameters related as

$$S_0^2 = S_1^2 + S_2^2 + S_3^2 \quad (6)$$

Where,

$$S_0 = E_{0x}^2 + E_{0y}^2 = I(0,0) + I(90,0) \quad (7)$$

$$S_1 = E_{0x}^2 - E_{0y}^2 = I(0,0) - I(90,0) \quad (8)$$

$$S_2 = 2E_{0x}E_{0y} \cos(\delta) = I(45,0) - I(135,0) \quad (9)$$

$$S_3 = 2E_{0x}E_{0y} \sin(\delta) = I(45, \pi/2) - I(135, \pi/2) \quad (10)$$

S_0 describes the total intensity of the optical field, S_1 , S_2 and S_3 are respectively the polarization of the linear horizontal polarization over linear vertical polarization, linear $+45^\circ$ polarization over linear -45° polarization, and right circularly polarized light over the left circularly polarized light, respectively.

From the Stokes parameters the polarization ellipse parameters are ellipticity (ϵ) and ellipsometric angle (ψ) between semi-major axis and horizontal axis ($'x'$) are calculated using.

$$\epsilon = \frac{1}{2} \sin^{-1} \left(\frac{S_3}{S_0} \right) \quad (11)$$

$$\psi = \frac{1}{2} \tan^{-1} \left(\frac{S_2}{S_1} \right) \quad (12)$$

Thus by measuring the Stokes polarization parameters we can obtain information about the refractive index and thickness of the Au film

3. EXPERIMENTAL DETAILS

Schematic of the experimental setup used in imaging SPR polarimeter is shown in Fig. 1:

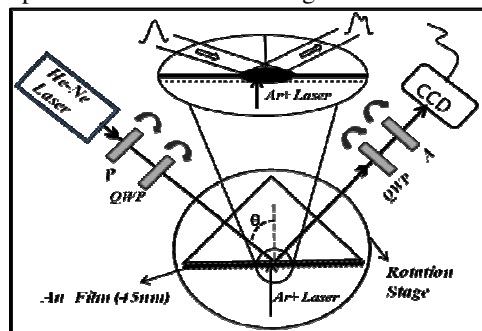


Fig. 1 Schematic of the experimental setup

The He-Ne laser ($\lambda=632.8\text{nm}$) is first polarized and then passed through a quarter-wave plate (QWP) to generate circularly polarized Gaussian beam which resonantly excites the surface plasmons at the metal-air interface in the $\sim 37\text{nm}$ thick Au film. The Au film was deposited on the base of a BK7 right angle prism by thermal evaporation method and its thickness was measured using a profilometer (Ambios XP-1, USA) with 1nm resolution. The Au coated prism is placed on a computer controlled rotation stage (Thorlabs, USA) with an angular resolution ~ 1 arc-sec. The reflected light beam profile is imaged using a CCD (Thorlabs, USA) camera after passing it through a QWP and analyzer to obtain the Stokes polarization parameters as a function of the incident angle. A CW Ar+ laser (Melles-Griot, USA) operating at $\lambda=514\text{nm}$ and at fixed optical power of $\sim 50\text{mW}$ is used to thermally induce changes in the dielectric constant of the gold thin film via photo-thermal effect by illuminating it from the metal-air interface side as shown in the Fig.1. The illuminated position on the metal film is scanned by the laterally movable mirror mounted on a micrometer translation stage (not shown in Fig.1).

3. RESULTS AND DISCUSSION

As the incident angle of the circularly polarized light on the Au film is changed by rotating the stage, at a certain angle of incidence the evanescent field of parallel component couples resonantly with the free electrons in the metal-air interface and excites the plasmons, which results in a sharp dip in the reflected light intensity, designated as the resonance angle

(θ_{\min}). The exact resonance angle is obtained from the theoretical fit to the experimentally measured SPR curve (Fig 2) to be 43.912deg. As the magnitude of the parallel and perpendicular components are equal in the in-input circularly polarized light beam, only ~50% of SP's excitation efficiency is achieved due to absorption of parallel component by the surface electrons as compared with the reflection of the perpendicular component of the input beam as shown in the Fig 2. An interesting point to note here is that as the incident angle approaches the resonance angle θ_{\min} , due the magnitude of the parallel component of the incident light reduction, the ellipticity of the reflected light also reduces, eventually becoming linear vertical at θ_{\min} as shown in Fig 2 (a, b inset). Beyond θ_{\min} , the parallel component starts adding up to the reflected light which again increases the ellipticity. Additionally, the orientation angle of the polarization ellipse (S_2) increases as the prism table is rotated further as shown in Fig 3. From the Figure3 we see that the ellipticity of the reflected light changes rapidly as a function of incident angle around θ_{\min} . These observations indicate clearly sensitivity improvement of the present method of monitoring the ellipticity and polarization orientation of the SPR signal as compared to the conventional measurement methods of R- θ or R- λ for SPR sensors. In our spatially polarization resolved measurements, we have preferred the ellipticity as a sensitive parameter to sense photo-thermally induced changes in the dielectric constant of the thin gold film.

Now, the rotation stage is rotated to the resonance angle θ_{\min} , and locked at this position.

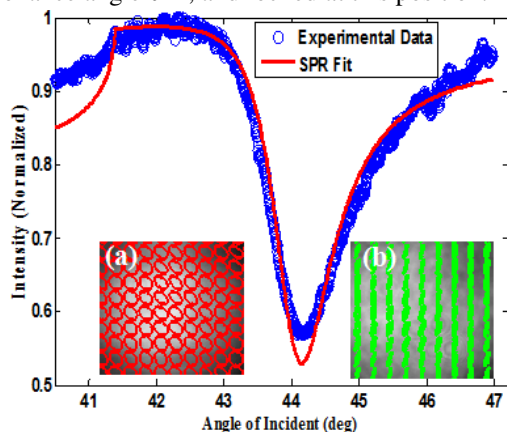


Fig. 2 SPR curve for circularly polarized input light. Inset: (a) Polarization map of input beam and (b) reflected beam at θ_{\min} .

Next, a small area in the elliptical foot print of the He-Ne laser on the gold film, where the SPR is excited is exposed to the Ar⁺ ion laser operating at 514 nm, with fixed optical power of 50mW. The Ar⁺ laser spot size is ~4 times smaller than the beam size of the He-Ne laser. At this wavelength of Ar⁺ laser due to the absorption of the laser, the metal film heats

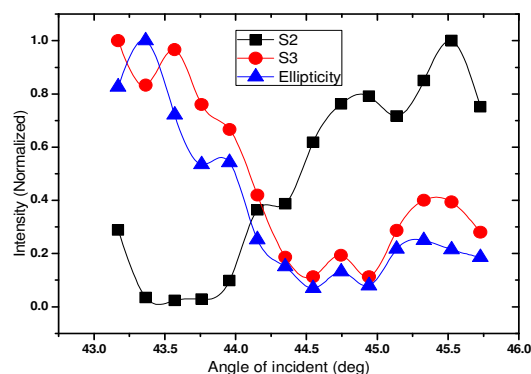


Fig. 3 Angle dependence of Stokes paramtrs S_2 , S_3 and the ellipticity.

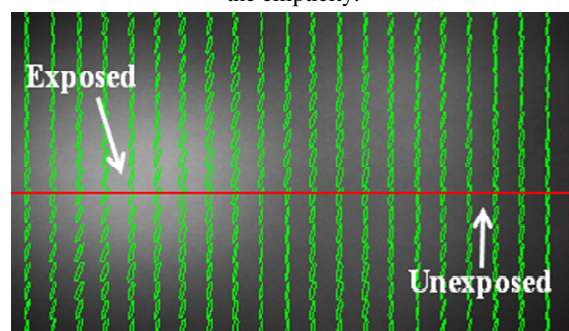


Fig. 4 Spatial variation of the ellipticity of reflected SPR signal beam with superposed spatially resolved Stokes polarization map image at θ_{\min} obtained while gold film is illuminated by the Ar⁺ laser.

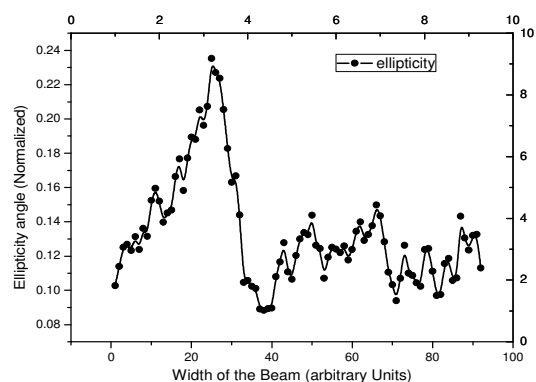


Fig. 5 Ellipticity variation along the horizontal line across beam, shown in Fig. 4. Peak in the curve indicates the Ar⁺ laser exposed region of the beam.

-up which changes the refractive index/dielectric constant (ϵ_m) of the metal which in turn changes the resonance condition for the SPR. The photo-thermal effect on the real part of dielectric constant ϵ_r , shifts the resonance curve and broadens the resonance curve due its effect on the imaginary part ϵ_i [12]. The changes in the SPR signal due to the photo-thermal effect results in changing in the ellipticity of the SPR signal beam within the irradiated region with respect to the rest of the signal beam (Fig. 5).

The spatial polarization variation of the reflected beam is imaged using the CCD from which at each

pixel the Stokes parameters are calculated using equations (7) - (10). From the analysis of these Stokes parameters, we calculate the ellipticity changes at each pixel of the image using eqn. (11) as shown in Fig 4. As we see in Fig 4, from left to right, the elliptical polarization becomes linear in the exposed and unexposed region of the metal film, which is in reasonable agreement with previously reported results [12]. Where, complete SPR curve shifts to the lower angles, when film is illuminated with the Ar+ laser. In our case as the SPR curve shifts to the lower angles the ellipticity increases ~2 times which is shown in the Fig 5. From this measured changes in the ellipticity of Ar+ laser exposed region, it is possible to calculate the changes in the dielectric constant of the metal film due to photo-thermal effect.

4. SUMMARY

Imaging SPR polarimeter technique is proposed and demonstrated for high-sensitivity sensor applications via spatially-resolved Stokes polarization parameter measurements. Preliminary measurements on photo-thermal effect are also presented.

ACKNOWLEDGEMENT

The authors wish to acknowledge financial support from ACRHEM, UH and Dr. Abhilash's help in film coating.

REFERENCES

- [1] Heinz Reather, "Surface Plasmons on smooth and rough surfaces and on gratings", Springer-Verlag, 1986
- [2] J. Homola, Sinclai S, Yee, Gunter "Surface plasmon resonance sensors review", *Sens. and Actuators B* **54** (1999) 3-15
- [3] J. R. Sambles, G. W. Bradber and Fuzi Yang "Optical excitation of surface plasmons: an introduction", *Cont. Phys.* **32** (1991) 173-183
- [4] Y.H. Huang, H.P.Ho, S.Y. Wu, and S.K. Kong "Detecting phase shifts in surface plasmon resonance: A Review", *Adv. Opt. Techn.* **2012** (2011) 471957
- [5] A K Nikitin "Polarimetric detection of the photon excitation of surface plasmons", *Quant. Electron.* **30** (2000) 73-77
- [6] L. S. Maksimenko, I.E. Matyash, I.A. Minailova, O. N. Mishchuk, S. P. Rudenko, and B. K. Serdega "Polarization Stokes polarimetry of the amplitude and phase characteristics of surface plasmon polariton resonance", *Opt. and Spectrosc.* **109** (2010) 5
- [7] Marat S. Soskin, Vladimir G. Denisenko, Roman I. Egorov "Singular Stokes-polarimetry as a new technique for metrology and inspection of polarized speckle fields", *Proc. of SPIE* (2004) 5458
- [8] Beth Schaefer, Edward Collett, Robert Smyth, Daniel Barrett, and Beth Frahe "Measuring the Stokes polarization parameters", *Am. J. Phy* **75** (2007) 2
- [9] R. M. A. Azzam, N. M. Bashara "Ellipsometry and polarized light", North-Holland, Amsterdam,

1977

- [10] H. Arwin "Is ellipsometry suitable for sensor application?", *Sens. and Actuators A* **92** (2001) 43-51
- [11] Kikuo Ujihara "Reflection of the metals at high temperature," *J. Appl. Phys.* **43** (1972) 5
- [12] Shankar Pidishety and Nirmal K Viswanathan "All optical thermo-plasmonic device", *Appl. Opt.* **50** (2011) 5966

TIGHT FOCUSING OF HYPERGEOMETRIC-GAUSSIAN TYPE-II OPTICAL MODE BEAM WITH HIGH NA LENS AXICON

K. Prabakaran^a, P.Suresh^a, Mohamed Musthafa.A^b, Z.Jaroszewicz^c, K. B. Rajesh^{d*}

^aAnna University of Technology Tirunelveli, Tamilnadu-627007, India.

^bDepartment of Physics, KSR college of technology, Tiruchengode, Tamilnadu, India.

^cInstitute of Applied Optics, Department of Physical Optics, Warsaw.

^dDepartment of Physics, Government Arts College, Dharmapuri, Tamilnadu, India.

***e-mail: rajeskb@gmail.com**

Abstract: we propose to use pure phase filter in combination with high NA lens axicon to achieve high efficient longitudinally polarized beam with a sub wavelength spot size and large depth of focus. Using this system, the spot size is reduced to 0.394λ and the depth of focus is increased to 12λ . The efficiency of such system is found to be 88.05%. This high efficient longitudinally polarized beam generated by hyper geometric Gaussian beam is useful for most of the near-field optics applications.

Key Words: - Axicon, Aberration, Optical engineering, Polarization.

1. INTRODUCTION

The Hypergeometric Gaussian beam is having a confluent hyper geometric transverse profile, in which these modes are eigen modes of the photon orbital angular momentum and they have the lowest beam divergence at waist among all known finite power families of paraxial modes. This beam presents a new family of solutions to the paraxial wave equation carrying finite power. Actually, these modes can be also regarded as a limit subfamily of circular beam (CiB) introduced in [1], where however, their special features under focusing were not analyzed or discussed. Over the past decade great success has been achieved in the creation of radially polarized light. However, the creation of longitudinally polarized light has been a big challenge until now. In this article, we present a new family of solutions to the paraxial wave equation carrying finite power and having better features than the BG beams under strong focusing. This high efficient longitudinally polarized beam generated by hyper geometric Gaussian beam is

useful for most of the near-field optics applications.

2. THEORY

The analysis was performed on the basis of Richards and Wolf's vectorial diffraction method widely used for high-NA focusing systems at arbitrary incident polarization [1]. In recent years, an increasing research effort has been put into creating paraxial light beams having uncommon properties tailored for particular uses. Notable examples include non-diffracting beams [2], beams with large longitudinal non-propagating component of the field [3], and beams possessing an integer value of the photon orbital angular momentum [4]. Such special beams have found a wide range of applications, such as optical lithography, data storage, microscopy, material processing, optical trapping, optical tweezers and metrology [4,5,6,7,8]. In the case of the radial incident polarization, adopting the cylindrical coordinates r, z , radial and longitudinal

components of the electric field $E_r(r,z)$ and $E_z(r,z)$ in the vicinity of the focal spot can be written as

$$E(r, z) = (E_r e_r + E_z e_z) \quad (1)$$

Where e_z and e_r are unity factor. E_r and E_z can be given as

$$E_r(r, z) = \int_0^\alpha \sqrt{\cos \theta} \sin(2\theta) l(\theta) J_1(kr \sin \theta) \exp(ikz \cos \theta) d\theta$$

$$E_z(r, z) = 2iA \int_0^\alpha \sqrt{\cos \theta} \sin^2 \theta l(\theta) J_0(kr \sin \theta) \exp(ikz \cos \theta) d\theta$$

We perform the integration of Eq.(1) numerically using parameters $\lambda=1$, and $NA=0.95$ as in [9]. Here, for simplicity, we assume that the refractive index $n = 1$ and $A = 1$.

For illumination by a Hyper Geometric beam with its waist in the pupil, this function is given by

$$l(\theta) = \exp\left(-\beta^2 \left(\frac{\sin \theta}{\sin \alpha}\right)^2\right) \left(\beta \left(\frac{\sin \theta}{\sin \alpha}\right)\right) F_1\left(\frac{1}{2}, 2; \beta^2 \left(\frac{\sin \theta}{\sin \alpha}\right)^2\right)$$

Here $k = 2\pi/\lambda$, f is the focal length and β is the aberration coefficient. In our calculations we have taken $f = 18.4\text{mm}$, $\beta = 6.667 \times 10^{-5} \text{mm}^{-3}$, this results in an equiconcave diverging lens that is simple to manufacture.

The efficiency (η) of the beam is calculated using

$$\eta = \frac{\phi_z}{\phi_z + \phi_r} \quad \text{Where} \quad \phi_z = 2\pi \int_0^{r_0} |E_z(r, 0)|^2 r dr$$

$$\phi_r = 2\pi \int_0^{r_0} |E_r(r, 0)|^2 r dr$$

3. RESULTS

The Intensity profile of the the total field ($E_r^2 + E_z^2$) of the focal plane of the high NA lens axicon for radial polarized Hypergeometric Gaussian beam.(b) On axial intensity of lens with phase filter and high NA lens axicon with a phase filter.

From fig.1 (a) it is observed that the FWHM of focal generated by the high NA lens is 0.6λ . However the FWHM of focal spot generated by lens in combination with a phase filter is 0.426λ . In the case of proposed high NA lens axicon in combination with a dedicated phase filter ,the focal spot further reduced 0.394λ which is 12.31% smaller then the high NA lens. Fig.1(b) shows the DOF of the proposed high NA lens axicon and a dedicated phase filter drastically increased 12λ .we have also calculated efficiency of the generated longitudinally beam for our proposed system and is observed to be 88.05% .

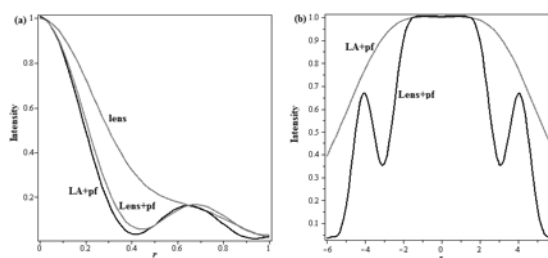


Fig.1(a) Intensity profile of the the total field ($E_r^2 + E_z^2$) of the focal plane of the high NA lens axicon for radial polarized Hypergeometric Gaussian beam.(b) On axial intensity of lens with phase filter and high NA lens axicon with a phase filter.

This high efficiency longitudinally polarized beam is found to be useful optical lithography, data storage, microscopy, material processing, optical trapping, optical tweezers and metrology.

4. CONCLUSION

In conclusion, we studied a tight focusing of Hypergeometric – Gaussian type – II optical mode beam with high NA Lens Axicon. This type of high efficiency longitudinally polarized beam is found to be useful optical lithography, data storage, microscopy, material processing, optical trapping, optical tweezers and metrology. This analysis shows that the DOF of the proposed high NA lens Axicon and a dedicated phase filter drastically increased 12λ . We have also calculated efficiency of the generated longitudinally beam for our proposed system and is observed to be 88.05%.

REFERENCES

1. Karimi, B. Piccirillo, L. Marrucci, and E. Santamato, "Improved focusing with Hypergeometric-Gaussian type-II optical modes" *Optics Express*, 16, 25 (2008).
2. K. Dholakia, "Optics: Against the spread of the light," *Nature* 45, 413 (2008).
3. H. Wang, L. Shi, B. Lu, Y. Kyanchuk, C. Sheppard and C. T. Chong, "Creation of a needle of longitudinally polarized light in vacuum using binary optics," *Nat. Photon.* 2, 501-505 (2008).
4. G. Molina-Terriza, J. P. Torres, and L. Torner, "Twisted photons," *Nat. Phys.* 3, 305-310 (2007).
5. G. D. M. Jeffries, J. S. Edgar, Y. Zhao, J. P. Shelby, C. Fong, and D. T. Chiu, "Using polarization-shaped optical vortex traps for single-cell nanosurgery," *Nano. Lett. Proc. R. Soc. London Ser. A* 7, 415-420 (2007).
6. J. Durnin, J. J. M. Jr., and J. H. Eberly, "Diffraction-free beams," *Phys. Rev. Lett.* 58, 1499-1501 (1987).
7. J. Durnin, "Exact solutions for nondiffracting beams. I. The scalar theory," *J. Opt. Soc. Am. A* 4, 651-654 (1987).
8. Y. Zhao, J. S. Edgar, G. D. M. Jeffries, D. McGloin, and D. T. Chiu, "Spin-to-orbital angular momentum conversion in a strongly focused optical beam," *Phys. Rev. Lett.* 99, 073901 (2007).
9. J. A. Davis, D. E. McNamara, D. M. Cottrell, and J. Campos, "Image processing with the radial Hilbert transform theory and experiments," *Opt. Lett.* 25, 99-101 (2000).
10. J. Salo, J. Fagerholm, A. T. Friberg, and M. M. Salomaa, "Nondiffracting bulk-acoustic X wave s i n crystals," *Phys. Rev. Lett.* 83, 1171 (1999).
11. K.B.Rajesh, Z. Jaroszewicz and P. M. Anbarasan, "Improvement of lens axicon's performance for longitudinally polarized beam transmittance" *Optics Express*, 18, 26 (2010).

SURFACE PLASMON PROPAGATION IN METAL STRIP WAVEGUIDE WITH ANISOTROPIC SUBSTRATES

Anju Babu¹, C Bhagyaraj¹, Jesly Jacob^{1,2} and Vincent Mathew¹

¹Postgraduate and Research Department of Physics, St. Thomas College, Palai, Kerala - 686574, India.

²Research and Development Centre, Bharathiar University, Coimbatore-641 045, India.

Email: anjubabu05@gmail.com

Abstract: In this paper we study the properties of surface plasmon waves in an asymmetric strip waveguide with anisotropic substrate. The variation in propagation properties of the modes propagating through the strip waveguide is analyzed by changing the dielectric material used as the substrate. We consider an isotropic material, a uniaxial material and a biaxial material as the substrates. The variation of propagation length as a function of metal thickness, for different substrate materials, has been studied for various modes in the waveguide.

1. INTRODUCTION

Surface plasmon polaritons (SPPs) are electromagnetic waves that propagate at a metal–dielectric interface. Plasmonic devices have now become an integral part of nanophotonics and by suitably manipulating the waveguide geometries and surrounding materials, plasmonic waveguides with sufficient propagation range are fabricated [1].

SPPs supported by a thin metal film of finite width (metal strip) have been considered as the simplest structure for waveguiding applications. Changing the substrate materials can modify the propagation properties of the fundamental modes in the strip waveguide. The modes supported by metal strip-waveguides with similar and dissimilar dielectric substrate and cladding materials have been subjected to detailed analysis by P. Berini [2, 3].

In this paper, we consider the propagation properties of the fundamental modes in a metal strip waveguide surrounded by dissimilar dielectric materials (asymmetric structure), with an isotropic cladding and an anisotropic substrate. The waveguide structure is studied numerically using the semi-analytical technique, the method of lines (MoL) [4, 5], which is discussed in Section 2. Numerical results and discussion are presented in Section 3.

2. THEORY

Figure 1 shows the geometry of the waveguide structure under consideration. It consists of a metal strip of thickness t , width $w=1\mu\text{m}$, an isotropic cladding of permittivity $\epsilon_2=3.61$ [3] and an anisotropic substrate with permittivity given by,

$$\epsilon_1 = \begin{pmatrix} \epsilon_x & 0 & 0 \\ 0 & \epsilon_y & 0 \\ 0 & 0 & \epsilon_z \end{pmatrix}$$

with principal dielectric constants $\{\epsilon_x, \epsilon_y, \epsilon_z\}$. Propagating fields are assumed to have a common dependence $\exp-j(\gamma z - \omega t)$, where γ is the complex propagation constant with propagation along z direction.

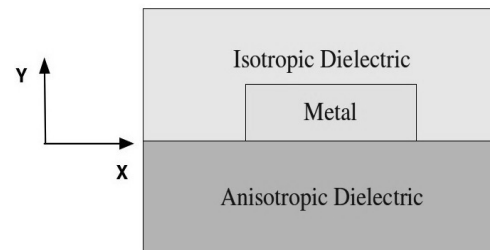


Figure 1: Geometry of the waveguide structure.

The electric and magnetic vector field components supported by this structure are obtained by solving the time harmonic vectorial wave equations:

$$\nabla \times \nabla \times E - \omega^2 \mu \epsilon(x, y) E = 0$$

$$\nabla \times [\epsilon(x, y)]^{-1} \nabla \times H - \omega^2 \mu H = 0$$

where the permittivity $\epsilon(x, y)$ is a complex function of cross-sectional space. For the structure under study permeability μ is homogeneous and taken as the permeability of free space μ_0 . The wave equations are solved in each layer for E_y^{TE} and H_y^{TM} field components corresponding to TE and TM modes

respectively. The modes are not purely TM or TE in nature, but are a superposition of both TE and TM fields due to the inhomogeneity along the horizontal x direction [4]. The wave equations for E_y^{TE} and H_y^{TM} are obtained as,

$$\frac{\partial^2 E_y^{TE}}{\partial y^2} + \frac{\epsilon_z}{\epsilon_y} \frac{\partial^2 E_y^{TE}}{\partial x^2} + \frac{\omega^2 \epsilon_0 \mu_0 \epsilon_z + \gamma^2 \epsilon_z}{\epsilon_y} E_y^{TE} = 0$$

$$\frac{\partial^2 H_y^{TM}}{\partial y^2} + \frac{\epsilon_x}{\epsilon_z} \frac{\partial^2 H_y^{TM}}{\partial x^2} + (\omega^2 \epsilon_0 \mu_0 \epsilon_x + \gamma^2) H_y^{TM} = 0$$

As it is difficult to solve the two dimensional differential equation, we adopt the Method of Lines, where the wave equations are discretised using two shifted line systems along x direction. Alternate electric wall or magnetic wall lateral boundary conditions are incorporated [6] in the discretization scheme in order to separate different modes supported by the structure. These wave equations are solved analytically and a dispersion relation for the guided modes as explained in ref 4 and 5 [4, 5]. Propagation constant is extracted numerically from the dispersion relation. Numerical root search in complex domain is carried out using both Nelder-Mead minimization approach [6] as well as the direct root search based on Muller's method [7].

3. RESULTS AND DISCUSSIONS

In this work we consider the propagation properties of the fundamental modes propagating in the waveguide structure shown in Figure 1. The modes propagating in the structure are determined by the symmetry or asymmetry of the field distribution with respect to the horizontal and vertical axes of the waveguide. The fundamental modes supported by a nano metal strip waveguide are as_b , sa_b , aa_b and ss_b [8]. The metal used for the study is silver (Ag), with an equivalent permittivity $\epsilon_m = -19-j0.53$, at a wavelength of 633nm [9]. The anisotropic materials under consideration are a highly anisotropic uniaxial material with principal dielectric components $\{2, 2, 7.5\}$ [10] and a biaxial material with dielectric constants $\{2, 7, 5\}$ [11]. The propagation length of the modes is studied as a function of the metal film thickness. The results obtained for each mode is then compared with the propagation length of the modes when an isotropic material ($\epsilon_1=4$) [3] is used as the substrate.

Figure 2 shows the variation of propagation

length as a function of metal film thickness for sa_b mode in the asymmetric strip waveguide with different substrate materials. From the figure, it is observed that for the sa_b mode there is an increase in propagation length when a biaxial material is used as the substrate. The value of propagation length is very small when uniaxial substrate is used. On the contrary, propagation length is highest in aa_b mode when the uniaxial material is used as the substrate as observed from Figure 4.

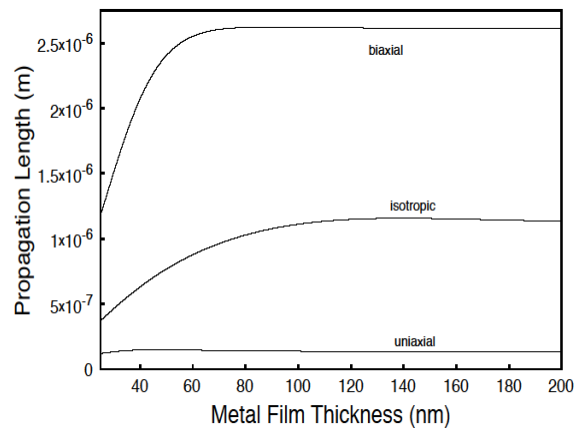


Figure 2: Variation of propagation length as a function of metal thickness for sa_b mode, using different substrate materials.

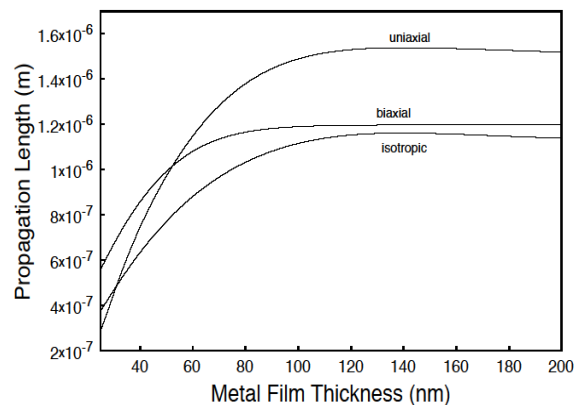


Figure 3: Variation of propagation length as a function of metal thickness for aa_b mode, using different substrate materials.

A similar characteristics is observed for propagation length of the ss_b and as_b respectively, for different substrate materials as observed from figures 4 and 5. From figure 4 it is observed that propagation length is highest when biaxial material is used as the substrate, as in the case of sa_b mode, whereas it is highest for a uniaxial substrate for as_b which is similar to results of aa_b

mode.

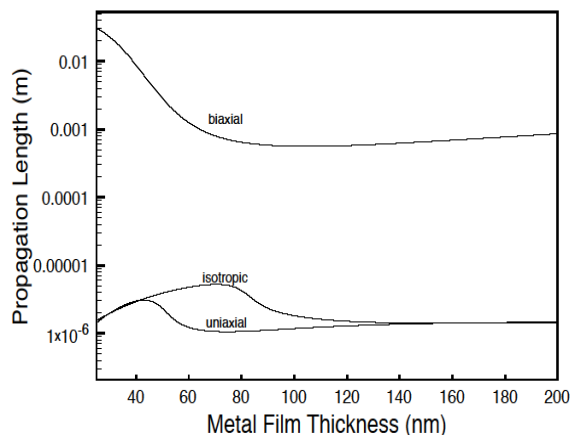


Figure 4: Variation of propagation length as a function of metal thickness for ss_b mode, using different substrate materials.

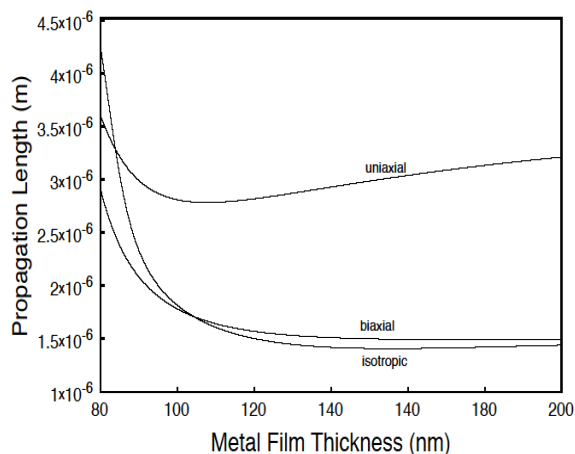


Figure 5: Variation of propagation length as a function of metal thickness for as_b mode, using different substrate materials.

Thus it is observed that the propagation properties of the fundamental modes depend on the nature of the substrate material used. The propagation length is highest when a biaxial substrate is used, for sa_b and ss_b modes whereas for aa_b and as_b modes it is highest when a uniaxial substrate is used. High propagation range is obtained for ss_b modes when a biaxial material is used as the substrate.

3. CONCLUSIONS

The propagation properties of the various modes in an asymmetric strip waveguide are studied using different substrate materials. High propagation range is obtained for ss_b modes when a biaxial material is used as the substrate. It is observed that by properly choosing the substrate material we can modify the propagation length of the modes propagating in the waveguide.

ACKNOWLEDGEMENT

The authors are grateful for the financial support to the Department of Science and Technology, Government of India, through a research grant (No SR/S2/CMP-0012/2009)

REFERENCES

- [1] A. Derigon and D. R. Smith, "Numerical simulation of long range plasmon", *Opt.Express*, **14**, 1611, (2006).
- [2] P. Berini, "Plasmon-Polariton Waves Guided by Thin Lossy Metal Films of Finite Width: Bound Modes of Symmetric Structures," *Phy. Rev. B*, **61**, 10484 (2000).
- [3] P. Berini, "Plasmon polariton waves guided by thin lossy metal films of finite width: Bound modes of asymmetric structures", *Phy. Rev. B*, **63**, 125417, (2001).
- [4] R. Pregla, *Analysis of Electromagnetic Fields and Waves The method of Lines*, Wiley, London, (2008).
- [5] P. Berini, "Modeling lossy anisotropic dielectric waveguides with the method of lines", *IEEE Trans. Microwave Theory Tech*, **44**, 749, (1996).
- [6] W. H. Press, S. A. Teukolsky, W. T. Vetterling, and B. P. Flannery, "Numerical recipes recipes in Fortran", Cambridge University Press, (1996).
- [7] J. H. Mathews and K. D. Fink, "Numerical Methods using MATLAB", Prentice Hall (2004).
- [8] A. Babu, C Bhagyaraj, G. Mathew and V. Mathew "Dispersion of plasmon polaritons guided by a metal film of finite width deposited on a uniaxial substrate," *J. Phys. D: Appl. Phys.* **44**, 335301 (2011).
- [9] P. B. Johnson and R. W. Christy, "Optical Constants of the Noble Metals", *Phy. Rev. B*, **6**, 4370, (1972).
- [10] A. A. Krokhin, A. Neogi, and D. Mcneil,

Phy. Rev. B, “*Long-range propagation of surface plasmons in a thin metallic film deposited on an anisotropic photonic crystal*”, 75, 235420, (2007).

- [11] M.Liscidini and J. E. Sipe, “*Quasiguidded surface plasmon excitations in anisotropic materials*”, Phys. Rev. B, 81, 115335, (2010).

PLASMON POLARITON MODES OF A METAL STRIP EMBEDDED IN UNIAXIAL DIELECTRIC MATERIALS

Ajith R¹, Anju Babu¹, Jesly Jacob^{1,2} and Vincent Mathew¹

¹Postgraduate and Research Department of Physics, St. Thomas College, Palai, Kerala - 686574, India

²Research and Development Centre, Bharathiar University, Coimbatore-641 045, India

Email: vmresearchgp@gmail.com

Abstract: The numerical analysis of surface plasmon polariton modes guided by a metal film of finite width embedded in a homogenous anisotropic medium is studied using the method of lines (MoL), a finite difference based semi-analytical scheme, and Finite Element Method. The mode profiles of the fundamental modes are studied for a symmetric strip waveguide in a uniaxial medium and compared with the mode profile of the corresponding waveguide structure in isotropic medium. The dispersion characteristics of the sa_b mode are also studied.

1. INTRODUCTION

Surface plasmon polaritons (SPPs) are electromagnetic surface waves propagating along the interface between a dielectric and a metal, with fields exponentially decaying in both media [1]. They are quasi-particles resulting from the coupling of electromagnetic waves with oscillations of conduction electrons in a metal. The surface plasmon polariton based photonic devices have been attracting researchers due to their ability to confine light in subwavelength scale, where the diffraction limit opposes the operation of dielectric waveguides or fibers for visible and infrared light. SPPs can be excited by an optical input so that light can be converted to surface plasmon polaritons of much smaller wavelengths, which can be used to transmit data over short distance and finally converted back to light [2]. The other advantages of SPP waveguides over conventional dielectric waveguides include ease of fabrication and ability to carry both electrical and optical signals.

Over the past few years, the metal film with finite width has been a subject of intensive study, both experimentally and theoretically, since it is the prime candidate for nanophotonic integrated circuits, combining the bandwidth of photonics along with nanoscale dimensions. The two-dimensional nature of SPPs provides significant flexibility in constructing SPP-based all optical integrated circuits needed for optical computing and optical communications. The SPP at a single-interface between a metal and a dielectric exhibits interesting properties such as an energy asymptote in its dispersion curve and very high surface and bulk sensitivities. But it is also characterized by a high attenuation limiting the scope for applications. For a metal bounded by a dielectric, free-electron scattering in the metal

and interband transitions causes the attenuation.

One method of reducing the attenuation in SPP is to use a stripe bounded on all sides by a dielectric material. Metal film of finite width offers two-dimensional confinement. The plasmon polariton modes supported by a metal stripe waveguide have been studied by Berni [3, 4]. The behavior of the four fundamental modes as_b , sa_b , aa_b and ss_b are investigated in detail [3]. In addition to purely bound modes, leaky modes are also reported to exist in such structures [3, 4].

In this paper, we consider a waveguide comprising of a metal stripe embedded in uniaxial medium. Because of the inhomogeneous nature of the waveguide geometry at the metal/dielectric interfaces, a dispersion relation cannot be formulated in analytical form. We employ the method of lines (MoL), a finite difference based semi-analytical scheme for constructing dispersion relation numerically. In addition, Finite Element Method (FEM) is used to obtain the profile of the modes supported by the structure.



Figure 1: Geometry of the waveguide structure: a metal strip embedded in a uniaxial material.

Purely bound modes supported by a stripe waveguide are classified into as_b , sa_b , aa_b and ss_b as in the case of a metal stripe embedded in an isotropic medium, based on the dominant

superposition of symmetric and asymmetric fields supported by the corresponding slab structure. A brief description of the method of analysis is presented in the next section and numerical results in the third section.

2. METHOD OF ANALYSIS

The stripe waveguide geometry considered in this paper is shown in Fig. 1. The structure consists of a metal film of width w , thickness t and equivalent permittivity ϵ_m embedded in a uniaxial material of permittivity given by $[\epsilon_i] \equiv \text{diag}\{\epsilon_x, \epsilon_y, \epsilon_z\}$. In this study, we considered the photonic material with the principal dielectric constants given by $\{2, 2, 7.5\}$ and $\{2, 7.5, 2\}$ [5], referred to as parallel and perpendicular orientation according to the direction of optical axis of the anisotropic substrate with respect to the metal strip plane, respectively. Computations were carried out at a wavelength of 633 nm with silver having an equivalent permittivity $(-19-0.53i)$ which is close to the data of Johnson and Christy [6].

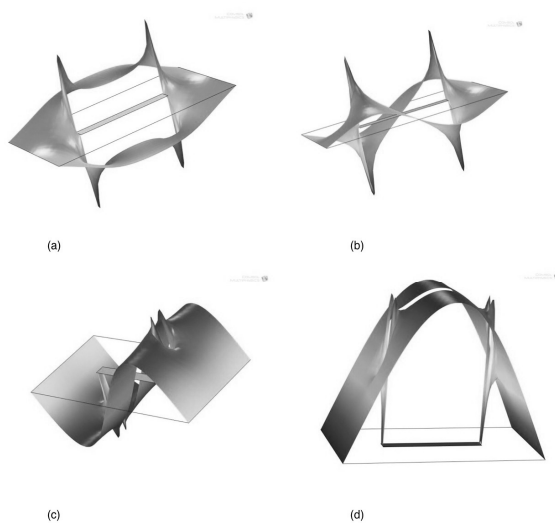


Figure 2: Spatial distribution of the field components (E_y) related to the sa_b , aa_b , as_b , and ss_b mode supported by a metal film of thickness 100 nm and width 1 μm embedded in an isotropic medium.

Propagating fields are assumed to have a common dependence $e^{-j(\gamma z - \omega t)}$ where γ is the complex propagation constant with propagation along the z direction. The permeability of the dielectric is taken as that of free space. Dependence of the permittivity on the vertical (y) direction is removed by dividing the structure into a number of homogeneous layers along that

direction. The wave equations are solved in each layer for E_y^{TE} and H_y^{TM} field components corresponding to TE and TM modes, respectively. Owing to the inhomogeneity along the horizontal (x) direction the modes are neither purely TM, nor TE in nature, but are superposition of both TE and TM fields.

As it is difficult to solve the two-dimensional differential equation, we adopt the Method of Lines (MoL) [7], where the wave equations are discretized using two shifted line systems along the x direction. Alternatively, electric wall or magnetic wall lateral boundary conditions are incorporated into the discretization scheme in order to separate different modes supported by the structure.

Discretized coupled wave equations are diagonalized using a suitable transformation matrix to obtain the one-dimensional wave equation, separately for TE and TM modes in the transformed domain. These wave equations are solved analytically and from these solutions we determine the other field components. The homogenous matrix equation is obtained by applying the tangential boundary matching conditions at the layer interfaces. Condition for obtaining the non-trivial solution for this matrix equation ($\det [G(k)] = 0$) leads to the dispersion relation for the guided modes [8]. Propagation constant is extracted numerically from the dispersion relation [8, 9].

The mode profile is studied using Finite Element Method (FEM) with the commercial software COMSOL [10]. The data inputted to the FEM is the same as those used in MoL. The structure is illuminated in such a way as to excite hybrid modes in the structure.

3. RESULTS AND DISCUSSION

The study begins with the reproduction of the fundamental modes in a stripe waveguide in an isotropic medium having permittivity $\epsilon_1=4$. In order to remain consistent with the results in [3], the free-space wavelength of excitation is set to 633 nm. The width of the metal is given as 1 μm . The mode profile of the four fundamental bound modes as_b , sa_b , aa_b and ss_b are shown in Fig. 2.

Next, the behavior of the fundamental mode sa_b is investigated for the geometry consisting of metal stripe embedded in a uniaxial medium. In this study, for the uniaxial medium, the parallel and perpendicular orientation with equivalent

permittivity $\{2, 2, 7.5\}$ and $\{2, 7.5, 2\}$ are considered. Figure 3 shows the variation of propagation constant with metal film thickness for the sa_b mode. The figure compares the behavior of the mode in the geometry with uniaxial material with that of a stripe embedded in an equivalent isotropic medium. The effect of anisotropy is enhanced in a thin metal film, giving the possibility of controlling the propagation range by orientation of the optical axis of the medium.

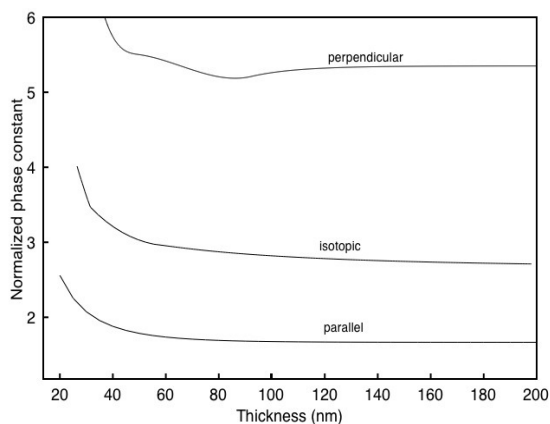


Figure 3: Variation of normalized phase constant for sa_b mode supported by a stripe embedded in a uniaxial medium (parallel and perpendicular orientation) and an equivalent isotropic medium.

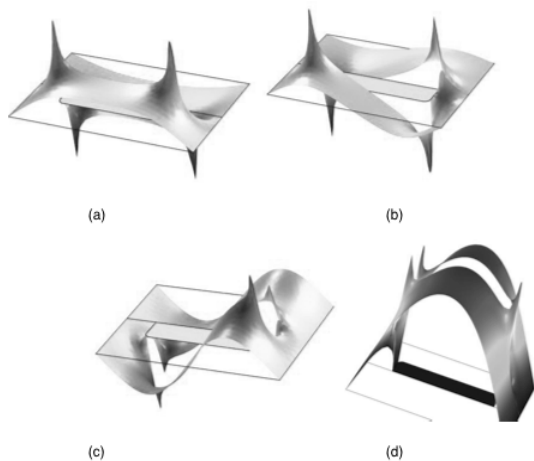


Figure 4: Spatial distribution of the field components (E_y) related to the sa_b , aa_b , as_b , and ss_b mode supported by a metal film of thickness 100 nm and width 1 μm embedded in an anisotropic medium.

Figure 4 shows the profile of the fundamental modes supported by the metal stripe embedded in an anisotropic medium. The profile of these modes is similar to those obtained in the case of a metal

stripe embedded in an isotropic medium. The main transverse electric field component is the E_y component and the symmetries in the spatial distribution of this component can be observed from these figures. It can be seen that very little field couples at parallel edges, though coupling does occur along all edges between adjacent corners and also between perpendicular edges through the corner.

4. CONCLUSION

The propagation properties of the various modes in a symmetric strip waveguide are studied using FEM. The dispersion characteristics of sa_b mode for a symmetric strip waveguide with different surrounding medium are numerically analyzed using MoL. Metal strip waveguide is the simplest practical geometry and has the ability to easily couple with other photonic components. They also offer two-dimensional confinement of plasmon wave and are useful in designing various components in integrated plasmonic devices.

ACKNOWLEDGEMENT

The authors thank the Department of Science and Technology, Government of India for the financial support through a research grant (No. SR/S2/CMP-0012/2009).

REFERENCES

- [1] S. A. Maier and H. A. Atwater, "Plasmonic: Localization and guiding of electromagnetic energy in metal/dielectric structures," *J. Appl. Phys.* 98, 011101 (2005).
- [2] A. Sellai and M. Elzain, "Characteristics of a dielectric-metal-dielectric plasmonic waveguide", *Physica E* 41, 106-109 (2008).
- [3] P. Berini, "Plasmon-polariton waves guided by thin lossy metal films of finite width: Bound modes of symmetric structures", *Phys. Rev. B* 61, 10484-10503 (2000).
- [4] P. Berini, "Plasmon-polariton waves guided by thin lossy metal films of finite width: Bound modes of asymmetric structures", *Phys. Rev. B* 63, 125417 (2001).
- [5] A. A. Krokhin, A. Neogi, and D. McNeil, "Long-range propagation of surface plasmons in a thin metallic film deposited on an anisotropic photonic crystal", *Phys. Rev. B* 75, 235420 (2007).
- [6] P. B. Johnson and R. W. Christy, "Optical Constants of the Noble Metals", *Phys. Rev. B* 6, 4370-4379 (1972).

- [7] Pregla R 2008 “Analysis of Electromagnetic Field and Waves, The Method of Lines” (London: Wiley)
- [8] A. Babu, C Bhagyaraj, G. Mathew and V. Mathew “Dispersion of plasmon polaritons guided by a metal film of finite width deposited on a uniaxial substrate,” J. Phys. D: Appl. Phys. 44 335301 (2011).
- [9] Mathews J H and Fink K D 2004 “Numerical Methods using MATLAB” (Englewood Cliffs, NJ: Prentice-Hall)
- [10] COMSOL multiphysics,
<http://www.comsol.com>

QUANTUM CONFINEMENT EFFECT IN THE SILICON NANOSTRUCTURES

Vivek Kumar and A.K. Shukla

Laser Assisted Materials Processing and Raman Spectroscopy Laboratory,
Department of Physics, Indian Institute of Technology, New Delhi, 110016, India
Email: vivekphys@gmail.com

Abstract: Photoluminescence and Raman scattering from silicon nanostructures are reported here. Room temperature PL is observed in the visible region, which reveals the formation of quantum structures. Quantum confinement model has been used here to explain the acoustic mode observed in the Raman scattering. Raman and PL studies reveal the presence of quantum confinement effect in the silicon nanostructures.

1. INTRODUCTION

In recent years, the silicon nanostructures (SiNS) have been investigated due to its novel physical properties and immense use in the electronic and optoelectronic devices [1]. Vibrational properties of these nanostructures are fascinating areas of research for their technological importance since mobility of the electrons is affected primarily due to scattering by acoustic vibrations of long wavelength [2]. Furthermore, the quantum confinement of phonons modifies the phonon related properties such as thermal conductivity [3], Raman active phonons [4] and electron - phonon interactions [5] etc. in the semiconductor nanostructures. First-order Raman scattering usually exhibits an acoustic mode ($< 100 \text{ cm}^{-1}$) and an optic mode (around 520 cm^{-1}) in the SiNS. Over the last two decades, Raman scattering due to optical phonons has been studied extensively for the SiNS [5,6]. It is well known that the acoustic mode is absent in the low-frequency Raman scattering ($< 100 \text{ cm}^{-1}$) of the crystalline silicon (c-Si). As nanostructures (size $\leq 10 \text{ nm}$) are formed, the acoustic mode is found in the region of $0 - 100 \text{ cm}^{-1}$ [7-9]. Lamb [10] has proposed torsional and spherical modes characterized by radial index (n) and angular indices (l, m). Duval [11] has predicted that polarized and depolarized Raman scattering are observed for symmetric ($l = 0$) spheroidal mode and quadrupole ($l = 2$) spheroidal mode respectively. Here Low-frequency Raman scattering has been extensively studied for SiNS.

Since the discovery of porous silicon photoluminescence in visible range at room temperature, materials of nanometer sized silicon crystallites have become the subject of great interest because they exhibit new quantum phenomena and have favorable applications in optoelectronic devices. In this article, the photoluminescence and low-frequency Raman scattering has been investigated here. Low-frequency Raman scattering can be used to determine the size distribution of silicon nanostructures.

2. EXPERIMENTAL DETAILS

Three samples (sample S1, sample S2 and sample S3) of the silicon nanostructures (SiNS) were

fabricated by the laser induced etching (LIE) method [6]. The LIE was done by immersing n-Si wafer into HF acid (concentration 48%) and then focusing the argon-ion laser beam (COHERENT, INNOVA 90, $\lambda = 514.5 \text{ nm}$) on it. The n-Si wafers were etched to fabricate the SiNS of different sizes using laser power density of 1.76 kW/cm^2 . Etching time was 25 minutes, 45 minutes and 60 minutes for sample S1, sample S2 and sample S3 respectively. Raman and photoluminescence (PL) spectra were recorded by using micro-Raman setup of the triple monochromator (T64000 Jobin Horiba).

3. RESULTS AND DISCUSSION

3.1 Raman Scattering

Figures 1(a) - 1(c) show the low-frequency Raman spectra of samples S1 - S3 respectively. Low-frequency Raman spectra of these samples (S1 - S3) are also shown in Fig. 1. Acoustic mode is observed at 22.9 cm^{-1} , 27.6 cm^{-1} and 29.8 cm^{-1} in Fig. 1 for sample S1, sample S2 and sample S3 respectively. Acoustic mode is hardened with decreasing size of the SiNS. Phonon hardening, FWHM and asymmetry toward higher wavenumber of the acoustic mode are increased from Fig. 1(a) to 1(c) with decreasing size of the SiNS. As average size of the SiNS is decreased from sample S1 to sample S3, oscillator strength of the Raman scattering due to acoustic mode is increased in Fig. 1.

Generally, Raman spectrum of the Stokes [12,13] component is expressed as

$$I_{ij} \propto C_{ij}(\omega)[n(\omega) + 1] \frac{g(\omega)}{\omega} \quad (1)$$

where $C_{ij}(\omega)$ is the square of a matrix element of light interaction with the vibrational excitations. The $C_{ij}(\omega)$ in Eq. (1) is proportional to ω^2 for low-frequency range of phonons [14]. Temperature dependence of the Raman scattering is described by $n(\omega)$, Bose - Einstein distribution factor. The $g(\omega)$, which is the density of vibrational states, is also proportional to ω^2 in the low-frequency region [15]. The ω^2 dependence of $g(\omega)$ is in agreement with Debye's theory of the lattice vibrations for molar heat capacity of solids.

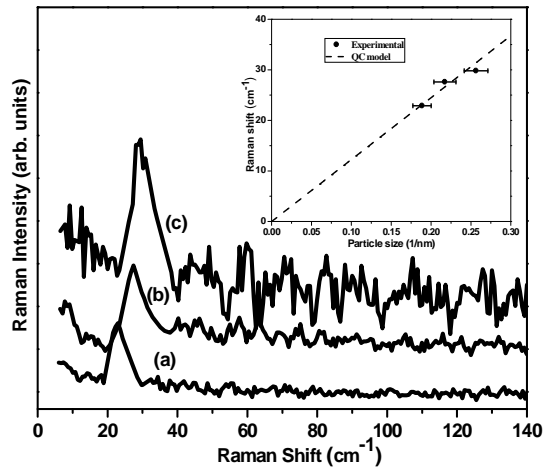


Figure 1: Raman Spectra from samples S1, S2 and S3 are shown in (a), (b) and (c) respectively. Raman shift has been plotted with the inverse of the diameter of the SiNS in the inset.

In a perfect crystal, the first-order Raman scattering takes place due to participation of the phonons at the Γ point ($q = 0$) of the Brillouin zone. Since there is no acoustic phonon at the Γ point in the phonon dispersion curve, first-order Raman scattering due to acoustic phonons is not observed for the c-Si. Spatial confinement of phonons leads to the relaxation of the momentum conservation rule (i.e. $q = 0$). It allows the first-order Raman scattering due to acoustic phonons of nonzero wavevector ($q \geq 0$) in the SiNS. Therefore, hardening of the acoustic mode is observed with decreasing size of the SiNS. This can be explained by dispersion curve where the acoustic phonons have increasing frequency with increasing wavevector ' q ' from the Γ point. Furthermore, localization of phonons in the nanostructures is described by a Gaussian weighting function [16,17]. It is expressed as $W(r, L) = \exp(-c r^2/L_0^2)$. Fourier coefficient of this weighing function is given by $|F(q)|^2 = \exp(-c q^2 L_0^2/a^2)$ where L_0 is the average size of the SiNS and ' c ' is a constant. The ' a ' is lattice parameter of the silicon.

As a result of the quantum confinement (QC) of acoustic phonons, Raman intensity for two dimensionally confined SiNS can be described by [18]

$$I(\omega) \propto \int_0^1 \frac{\omega^3}{[\omega - \omega(q)]^2 + (\frac{\Gamma_0}{2})^2} [n(\omega) + 1] |F(q)|^2 2\pi q dq \quad (2)$$

where Γ_0 is inversely proportional to the life time. Life time of the acoustic phonons in the Si is 30 ps at room temperature [19]. Since short range order (ie. diamond structure as well as identical nearest neighbor distances) is preserved in the nanostructures as well as amorphous material [20], dispersion curve of the c-Si is good enough to map the acoustic phonons in the SiNS. Quantum confinement of

phonons is generally seen in the Raman scattering when size ' L_0 ' is less than exciton Bohr radius. Acoustic phonons can contribute appreciably in the integration of Eq. (2) for range $0 \leq q \leq 2\pi/L_0$. Therefore, anisotropic phonon dispersion may not be important in Eq. (2) due to participation of phonons near to zone-center (ie. $q_{max} \approx 2\pi/L_0$). Weighing function, $F(q)$ also localizes the acoustic phonons within the nanostructures. Phonon dispersion relation of the Si for TA phonons, which is used here to explain our experimental Raman data with Eq. (2), is written as

$$\omega(q) = A \left[-\left(q \cos^{5/3}(\pi q/4) - 1 \right)^2 + 1 \right] \quad (3)$$

where $A = 182 \text{ cm}^{-1}$ is a constant. Raman shifts calculated by the Eq. (2) are shown by dashed line for various sizes of the SiNS as shown in the inset of Fig. 1. Experimental Raman shifts observed in Fig. 1 is shown by dark circles in inset of Fig. 1 where sizes are calculated by a phenomenological quantum confinement model for the Raman active optical phonons [16]. Experimental Raman shifts fit well with Raman shifts calculated by Eq. (2). Frequency of the acoustic mode is inversely proportional to size of the SiNS in Fig. 1. Frequency of the acoustic mode approaches zero in Fig. 1 for the case of crystalline limit ($L_0 \rightarrow \infty$), i.e. first-order Raman scattering due to acoustic phonons is absent in the c-Si. It is emphasized here that the TA like phonons participate in the low-frequency Raman scattering. Asymmetry towards higher wavenumber of the acoustic mode in Fig. 1 reveals the participation of acoustic phonons having increasing frequencies with increasing ' q ' in agreement with the Eq. (3).

In conclusion, first-order Raman scattering due to acoustic phonons is absent in the c-Si. Agreement between our calculations and experimental data indicates that low-frequency Raman scattering is due to participation of the TA acoustic phonons in the SiNS. As size of the SiNS is decreased, the acoustic mode is hardened. Frequency of the acoustic mode is found to be inversely proportional to size of the SiNS. Furthermore, oscillator strength of the Raman scattering due to acoustic mode increases with decreasing size of the SiNS. Phonon hardening and phonon softening are observed in the first-order Raman scattering due to acoustic phonons and optical phonons respectively. More lineshape asymmetry of the first-order Raman scattering are found towards higher wavenumber and lower wavenumber for acoustic mode and optical mode respectively.

3.2 Photoluminescence:

Photoluminescence (PL) spectra were studied as a function of etching time. The PL results are also utilized to reveal the nature of electronic states present in the SiNS samples. Figure 2 shows PL spectra of the Si samples etched for different etching times in the

range 25 - 60 minutes. The PL is recorded with excitation energy of 2.41 eV. No PL is observed for crystalline Si. The PL spectra from samples S1 - S3 are shown in Figs. 2(a) - 2(c) respectively. Visible PL at room temperature in the Fig. 2 is attributed to the quantum confinement effect of electrons in the Si NS.

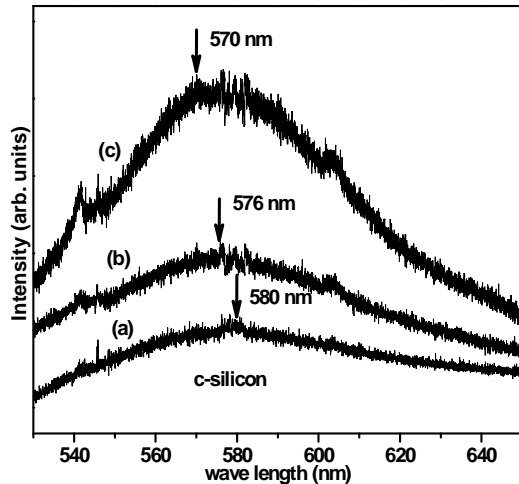


Figure 2: Photoluminescence spectra from samples S1, S2 and S3 are shown in (a), (b) and (c) respectively.

The PL spectrum in Fig. 2 shows broad PL. Size calculation of the SiNS by Raman scattering shows the formation of smaller Si NS for 60 minutes as compared to the etching time of 25 minutes. It is consistent with the blue-shift in PL spectrum. This is the typical characteristics of the quantum confinement effect with decreasing size of the SiNS.

ACKNOWLEDGEMENT

One of the authors (V.K.) acknowledges the financial support from University Grants Commission (UGC), India.

REFERENCES

- [1] C. Delacour, S. Blaize, P. Grosse, J. M. Fedeli, A. Bruyant, R. Salas-Montiel, G. Lerondel, and A. Chelnokov, *Nano Lett.* **10**, 2922 (2010).
- [2] E. B. Ramayya, D. Vasileska, S. M. Goodnick, and I. Knezevic, *J. Appl. Phys.* **104**, 063711 (2008).
- [3] A. A. Balandin, S. Ghosh, W. Z. Bao, I. Calizo, D. Teweldebrhan, F. Miao, and C. N. Lau, *Nano Lett.* **8**, 902 (2008).
- [4] K. H. Khoo, A. T. Zayak, H. Kwak, and J. R. Chelikowsky, *Phys. Rev. Lett.* **105**, 115504 (2010).
- [5] R. Kumar, H.S. Mavi, A.K. Shukla, and V.D. Vankar, *J. Appl. Phys.* **101**, 064315 (2007).
- [6] H. S. Mavi, A. K. Shukla, R. Kumar, and S. S. Islam, *Semicond. Sci. Technol.* **21**, 1627 (2006).
- [7] K. Yadav, V. Gupta, K. Sreenivas, S. P. Singh, B. Sundarakannan, and R. S. Katiyar, *Phys. Rev. Lett.* **97**, 085502 (2006).
- [8] L. Saviot, D. B. Murray, and M. C. Marco de Lucas, *Phys. Rev. B* **69**, 113402 (2004).
- [9] X. L. Wu, S. J. Xiong, Y. M. Yang, J. F. Gong, H. T. Chen, J. Zhu, J. C. Shen, and P. K. Chu, *Phys. Rev. B* **78**, 165319 (2008).
- [10] H. Lamb, *Proc. London Math. Soc.* **13**, 187 (1882).
- [11] E. Duval, *Phys. Rev. B* **46**, 5795 (1992).
- [12] Y. M. Yang, L. W. Yang, and P. K. Chu, *Appl. Phys. Lett.* **90**, 081909 (2007).
- [13] R. Shuker, and R. W. Gammon, *Phys. Rev. Lett.* **25**, 222 (1970).
- [14] G. Winterling, *Phys. Rev. B* **12**, 2432 (1975).
- [15] K. R. Patton, and M. R. Geller, *Phys. Rev. B* **67**, 155418 (2003).
- [16] H. S. Mavi, A. K. Shukla, R. Kumar, S. Rath, B. Joshi, and S. S. Islam, *Semicond. Sci. Technol.* **21**, 1627, (2006)
- [17] H. Richter, Z. P. Wang, and L. Ley, *Solid State Commun.* **39**, 625 (1981).
- [18] A.K. Shukla, and Vivek Kumar, *J. Appl. Phys.* **110**, 064317 (2011).
- [19] B. C. Daly, K. Kang, Y. Wang, and D. G. Cahill, *Phys. Rev. B* **80**, 174112 (2009).
- [20] K. P. Jain , A. K. Shukla, R. Ashokan , S. C. Abbi, and M. Balkanski, *Phys. Rev. B* **32**, 6688(1985).

Raman Study of disorder in the polycrystalline graphite

Kapil Saxena, B L Sueeval and A K Shukla*

*Laser Assisted Materials Processing and Raman Spectroscopy Laboratory,
Department of Physics, Indian Institute of Technology,
Hauz Khas, New Delhi 110016, India.*

*Corresponding author: akshukla@physics.iitd.ernet.in

Abstract: A comprehensive analysis of Raman scattering is discussed here as a function of disorder in the polycrystalline graphite. Disorder is characterized here by oscillator strength and phonon softening of Raman activated D mode and G' mode for a given wavelength of probing light. Increasing disorder allows the D mode in polycrystalline graphite. Enhancement of the $C_{ij}(\omega)$, coupling light to vibrational band of amorphous carbon is observed at 1363 cm^{-1} , 1480 cm^{-1} and 1557 cm^{-1} . Low frequency Raman scattering is observed here for amorphous carbon.

1. INTRODUCTION

Soon after their discovery of carbon nanotubes, amorphous carbon became widely used materials in different fields of modern technology which turned Raman spectroscopy into a routinely used method for quality assurance of these materials [1 - 3]. This method has proved to be a well suitable tool for structural characterization of different carbon containing materials including amorphous carbons [4–12]. Raman scattering is very widely used spectroscopy technique to characterize the vibrational properties of materials. It can be employed to monitor various disorders such as compositional disorder, topological disorder and phase transition. Raman spectroscopy is highly sensitive to changes in the bonding configuration of carbon atoms, especially of sp^2 hybridized ones, since the scattering is resonant in the sp^2 clusters of these structures. Light scattering is one of the most important methods for studying the structural disorder in the solids. Quantitative distinction between a crystalline lattice and a disordered lattice can be made by Raman spectroscopy. Identification of disorder in the sp^2 network of different carbon structure related systems such as graphite intercalated compounds [13 - 15], nano-structured carbon [16] is a major problem for the applications of such materials. Raman spectroscopy has been found to be the most suitable technique to differentiate the many types of sp^2 carbon structures & probe disorder in carbon structures. Defects modify the electronic and optical properties of the carbon system. There is considerable interest in understanding the bonding of various carbon materials.

Physical properties of carbon materials depend on the ratio of sp^2 (graphite like) to sp^3 (diamond like) bonds. In fact, the amorphous carbon is totally disordered state containing mixture of sp^2 and sp^3 hybridization. Carbon based materials can exist in a wide range of disordered forms. As a result of breakdown

Raman selection rule, an asymmetrically broad and disorder activated modes are observed. Disorder activated Raman scattering needs very careful analysis for fundamental physics involved during phase transition from polycrystalline graphite to amorphous carbon (a-C). Raman spectroscopy of graphite can provide fundamental frequency of the optical phonons in the first-order Raman scattering. Selection rule ($\mathbf{q} = 0$) of the first-order Raman scattering allows the participation of optical phonons.

In this article, we report in-depth analysis of the structural transition from polycrystalline graphite to a-C using Raman spectroscopy. The G mode, which is a common characteristic of all graphitic materials, appears at 1582 cm^{-1} . Since, the G band corresponds to first-order scattering at $\mathbf{q} = 0$, we do not need defects for the G mode scattering processes [9-12]. Phonon softening of the G mode is not observed with increasing disorder but broadening of the G mode also takes place from Fig. 1(a) to Fig. 1(c). Furthermore, a broadband near 1355 cm^{-1} , which is referred to as the D mode (disorder activated mode). The D mode which corresponds to two scattering processes is phonon-related scattering as well as elastic scattering by a defect [10 - 12]. It is due to localization of sp^2 contents in graphite planes coupled by weak van der Waal bonds. The D mode is absent in Fig. 1(a) for HOPG. The a-C has mixture of sp^2 and sp^3 hybridizations in total disordered states. Structural transformation from graphite (sp^2 hybridization) to amorphous state is observed when G mode and D mode disappear in the broad Raman band of all optical phonons. Low frequency ($200 - 800\text{ cm}^{-1}$) of Raman scattering is attributed here to acoustic mode here for the a-C. It is reasonable to believe that this low frequency feature is also disorder induced.

2. EXPERIMENTAL DETAILS

Ar-ion laser (COHERENT INNOVA 90, $\lambda=514.5$

nm) was used to excite Raman scattering from commercially available HOPG (highly oriented pyrolytic graphite), graphite powder and a-C material. Horiba Jobin-Yvon (T64000) triple monochromator Raman spectrometer was used to collect Raman scattering using integration time of 120 seconds. Laser power density for exciting Raman scattering was less than 10^7 mW/cm² at room temperature. The laser intensity was set to levels that had been not to produce photo degradation effect. Sample A is commercially available HOPG which is expected to have no spatial disorder. Samples B & C are polycrystalline graphite powder which is made by ball-milling method for milling times 15 and 30 hours respectively. Sample D is amorphous carbon which is expected to have totally disordered state of carbon.

3. RESULTS AND DISCUSSION

Figure 1 displays the first-order Raman spectra of carbon samples where (a) – (d) are for the samples A – D respectively. Raman spectra of sample A (HOPG) are shown in Fig. 1(a). It is well known that the defect-activated D mode (~ 1350 cm⁻¹) is absent in Fig. 1(a) for the HOPG sample. As disorder (i.e. localization of sp² hybridization) is increased in graphite, the D

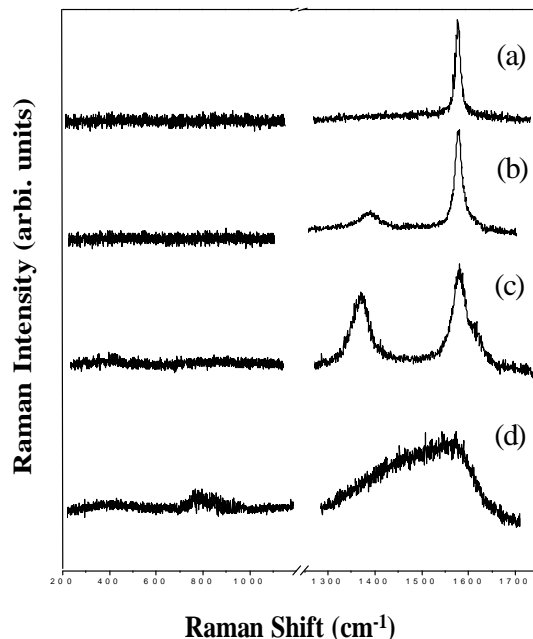


Figure 1: Raman spectra for (a) HOPG, (b) & (c) disordered graphite having I_D/I_G ratio 0.49 and 0.86 respectively, and (d) amorphous carbon.

mode appears at 1355 cm⁻¹. Furthermore, softening and enhanced oscillator strength of the D mode are observed from Fig. 1(b) to Fig. 1(c) revealing enhancement of spatial disorder. The D mode which has been explained by double-resonance Raman scattering, is due to disorder, TO phonons and electrons at the K point of BZ []. Furthermore, increase of I_D/I_G ratio from Fig. 1(b) to Fig. 1(c) also indicates the enhancement of spatial disorder. Raman spectra of amorphous carbon where distinct D mode and G mode of graphite just merges in the asymmetric broadband from 1250 cm⁻¹ to 1750 cm⁻¹ in Fig. 1(d). This can be seen as enhanced oscillator strength of Raman scattering in the region between D mode and G mode. A broad band in Fig. 1(d) is more reminiscent of Raman scattering from a-C where disorder containing mixture of sp² and sp³ hybridizations is present. It reflects basically one phonon density of states of optical phonons.

Low frequency Raman scattering (200 cm⁻¹ - 800 cm⁻¹), which is absent for HOPG and graphite in Figs. 1(a) – 1(c), is observed for a-C in Fig. 1(d). It is due to participation of acoustic phonons. Selection rule of the first-order Raman scattering allow participation of phonons with $\mathbf{q} = 0$. Since acoustic phonons do not exist at the Γ point of the BZ of graphite, the first-order Raman scattering due to acoustic phonons is absent in Figs. 1(a) – 1(c). Graphite structure is thermodynamically unstable due to increase of free energy, i.e. it tend to transform into amorphous phase. As the phase transition takes place from graphite to amorphous carbon, low frequency Raman scattering appears in the a-C material due to relaxation of above mentioned selection rule. It is reasonable to believe that this low frequency feature is also disorder induced. It is measure of degree of disorder.

Generally, Raman spectrum of amorphous solid, which is represented by one phonon density of states and is expressed as [18]:

$$I_{ij} \propto C_{ij}(\omega)[n(\omega) + 1] \frac{g(\omega)}{\omega} \dots (1)$$

where C_{ij} is the square of matrix element of light excitation with the vibrational excitation, i.e. coupling of light to vibrational band of solids. Temperature dependence of the Raman scattering is described by $n(\omega)$, the Bose-Einstein distribution factors. The $g(\omega)$ is the density of vibrational states for graphite. It belongs to optical phonons which can easily be excited by visible photons. The C_{ij} , which is calculated by Eq. (1) using Raman data of Fig. 1(d) and $g(\omega)$ [18]. Then it is found that deconvoluted C_{ij} is enhanced at 1363 , 1480 and 1557 cm⁻¹. These

peaks indicate the possibility of their overtones due to enhanced coupling light to vibration band. Overtones are observed due to anharmonic effect in the restoring force exerted on the electrons i.e. maximum change of the polarizability (α) with respect to displacement co-ordinate ξ of the atom. Usually second-order Raman scattering is much weak scattering in comparison with that of first-order Raman scattering. Nevertheless, second-order Raman scattering is enhanced in graphite due to double-resonance phenomenon [9]. As the structural transition takes place from graphite to amorphous, double-resonance phenomenon is suppressed. Therefore, residual second-order Raman scattering is observed.

4. CONCLUSION

In this paper, we have presented the light scattering study of HOPG, graphite powder and a-C. Phonon softening of the G mode is almost insensitive and more asymmetric on lower energy side with increasing disorder. Disorder can also be studied by phonon softening of the D and G' modes by double-resonant Raman scattering. Increasing disorder localizes the sp^2 content in polycrystalline graphite.

In addition to this, disorder is manifested in the D mode of polycrystalline graphite and a broad band of a-C. Structural transformation from graphite to a-C is observed when the D mode merges in the broad band of the a-C. There is enhancement of C_{ij} , coupling of light to vibrational band of a-C. Low-frequency Raman scattering is attributed to acoustic mode in the total disordered state. The I_D/I_G can be used as a measure of disorder in polycrystalline graphite.

ACKNOWLEDGEMENT

One of the authors (K. Saxena) acknowledges the financial support from Council of Scientific and Industrial Research (CSIR), India.

REFERENCES

- [1] S. Iijima, Nature 354, (1991) 56-58.
- [2] D. Camino, A.H.S. Jones, D. Merces, D.G. Teer, Vacuum 52, (1999) 125.
- [3] R.G. Lacerda, P. Hammer, F. Alvarez, F.C. Marques, F.L. Freire, Diamond Relat. Mater. 9, (2000) 796.
- [4] R. Nemanich, J. Glass, G. Lucovsky, R. Shroder, J. Vac. Sci. Technol. 6, (1988) 1783.
- [5] M.A. Tamor, J.A. Haire, C.H. Wu, K.C. Hass, Appl. Phys. Lett. 54, (1989) 123.
- [6] S. Xu, M. Hundhausen, J. Ristein, B. Yan, L. Ley, J. Non-Cryst. Solids 1127, (1993) 164-166.
- [7] M.A. Tamor, W.C. Vassel, J. Appl. Phys. 76, (1994) 3823.
- [8] J. Schwan, S. Ulrich, V. Bathori, H. Erhardt, S.R.P. Silva, J. Appl. Phys. 80, (1996) 440.
- [9] A.C. Ferrari, J. Robertson, Phys. Rev. B 61, (2000) 14095.
- [10] A.C. Ferrari, J. Robertson, Phys. Rev. B 64, (2001) 075414.
- [11] C. Casiraghi, A.C. Ferrari, J. Robertson, Phys. Rev. B 72, (2005) 085401.
- [12] E. H. Martins Ferreira et.al., Phys. Rev. B 82, (2010) 125429.
- [13] A.C. Ferrari, Solid State Commun. 143, (2007) 47.
- [14] M. S. Dresselhaus et al., Nano Lett. 10, (2010) 751.
- [15] S. Reich and C. Thomson, Phil. Trans. R. Soc. London. A 362, (2004) 1824.
- [16] Martin Hulman et. al., J. Appl. Phys. 98, (2005) 024311.
- [17] M. A. Pimenta et. al., Phys. Chem. Chem. Phys. 9, (2007) 1276.
- [18] R. Suker, R. W. Gammon, Phys. Rev. Lett. 25, (1970) 222.

SURFACE PLASMON RESONANCE BASED SUGAR CONCENTRATION SENSOR USING A CD-R

Neha Gupta^{1*}, Babita², and Vipul Rastogi²

¹Department of Applied Sciences, T. M. University, Moradabad, India

²Department of Physics, Indian Institute of Technology Roorkee, Roorkee, India

* Email: nehag0211@gmail.com

Abstract: We present the feasibility of CD-R structure for sensing concentration of sugar solution through surface plasmon resonance. CD-R is a pre-grooved structure and serves as grating coupler for surface plasmon resonance. By simulating silver coated CD-R structure we found that SPR dip angle in the reflectance curves shifted continuously with increase in sugar concentrations. The sensitivity of the concentration sensor, thus obtained is in the range $\sim 3.7^\circ/(\text{gm/ml})$ upto $11.3^\circ/(\text{gm/ml})$ with our structure parameter.

1. INTRODUCTION

Over the last two decades, Surface Plasmon Resonance (SPR) sensing has attracted attention for biological and chemical sensing due to low cost, portability and high sensitivity. Principle of SPR sensing involves excitation of surface plasmon at the interface between a metal film and a dielectric medium by electro-magnetic (EM) wave [1]. Any change in the Refractive Index (RI) of the dielectric medium produces a corresponding change in propagation constant of the surface plasmon which in turn alters the condition for coupling of EM wave to the surface Plasmon. Measurement of this change in the coupling condition can lead to the estimation of RI of the dielectric medium. Based on different schemes for coupling of light into Surface Plasmon mode, SPR sensors can be classified as angular, wavelength, intensity, phase or polarization modulation sensors.

Generally, the configuration of SPR sensors is based on either attenuated total reflection (ATR) prism coupling [2] or grating coupling. The use of commercially available Gold coated Recordable Compact Disk (CD-R) as a means for grating coupling has been reported [3]. The angular sensitivity of the SPR sensor based on prism is has been reported to lie in the range 94.46 deg/RIU to 204.41 deg/RIU [4], and for grating based methods it is 103 deg/RIU in a short range method, 97 deg/RIU in a typical single-mode method [5], and 70 deg/RIU in a metallic method [6]. Grating-based optical SPR sensors have been demonstrated which use the measurement of the light intensity variations at SPR [7, 8], and the wavelength interrogation [9, 10]. A high-sensitivity SPR grating based gas sensor using silver as an SPR active metal has shown a sensitivity of 1000 nm RIU^{-1} in wavelength interrogation mode [10], and about 100 deg RIU^{-1} in angular

interrogation mode.

Here, we investigate the measurement of sugar solution concentration in the range $0-0.18 \text{ gm/ml}$ using a CD-R without a lacquer coating. The structure has been simulated by the finite difference time domain (FDTD) method. The effect of pitch and wavelength of light on the sensitivity offered by the structure have been investigated.

2. DESIGN AND ANALYSIS

The schematic of the transverse cross section of the

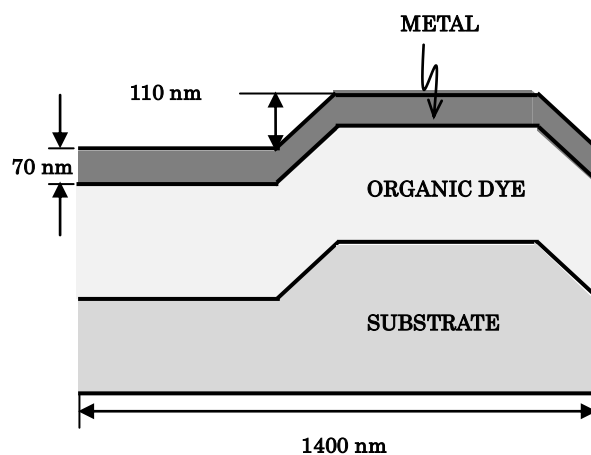


Fig. 1: Schematic of transverse cross section of a CD-R

CD-R is shown in Fig.1. The disk is built upon a polycarbonate substrate. An organic dye layer is sandwiched between Ag-metal layer and substrate. Pitch and depth of the grooves are 1400 nm and 110 nm respectively. Here we investigate the feasibility of the structure for sensing the concentration of sugar solution. The concentration of sugar solution has been varied in the range $0 - 0.18 \text{ gm/ml}$ and the

reflection from the structure as a function of incidence angle has been calculated by FDTD method. The position of dip in the reflectance curve indicates the excitation of SPP and is highly sensitive to the concentration of sugar solution used as the superstrate. The essential condition for the excitation of surface plasmon waves by grating coupling is

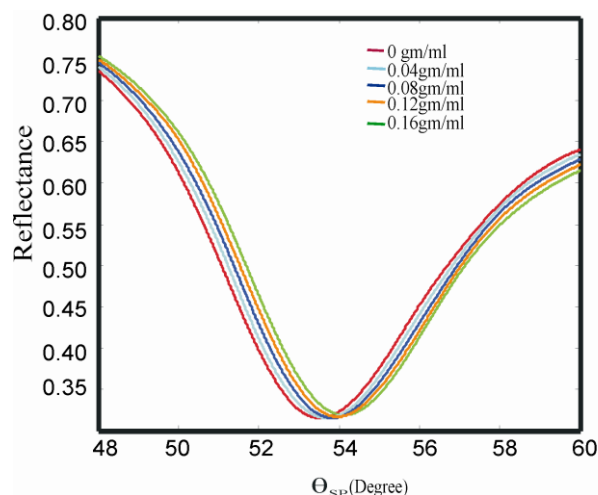


Fig. 2 Reflectance curves for $\Lambda = 1.6 \mu\text{m}$

$$\theta_{SP} = \text{Sin}^{-1} \left(\pm \left(\frac{\epsilon'}{\epsilon' + n_a^2} \right)^2 - m \frac{\lambda}{\Lambda} \right)$$

Where θ_{SP} is the angle of incidence, ϵ is the real part of the dielectric constant of metal, ϵ' is the imaginary part of the dielectric constant of metal, n_a is the refractive index of the analyt, λ is the wavelength of light, Λ is the grating pitch, and m is the order of diffraction. We analyzed sensitivity of sensor structure by varying the pitch and the wavelength of incident light. For simulation purpose, we used FDTD method, first introduced by Yee in 1966 and used for solving Maxwell's equations in complex geometries. This technique is discrete in both space and time.

3. NUMERICAL RESULTS

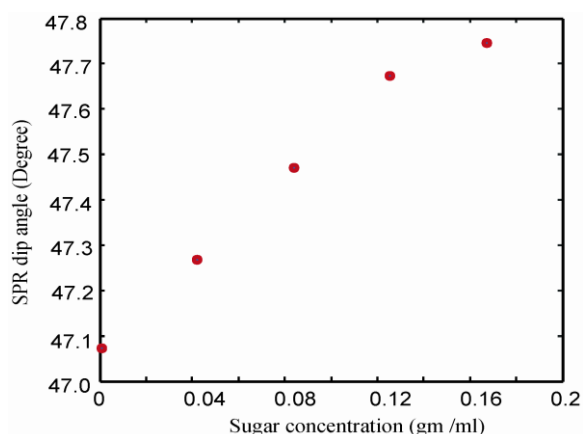


Fig. 3 SPR dip angle /sugar concentration for $\Lambda = 1.6 \mu\text{m}$

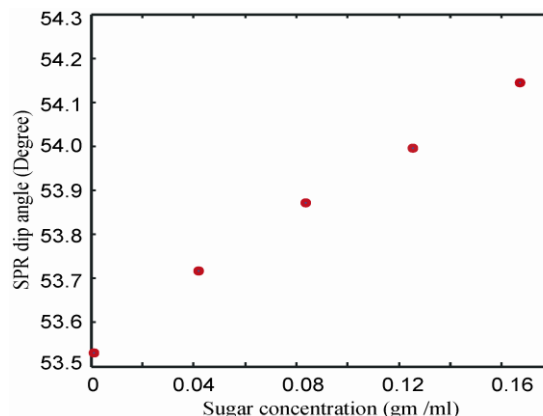


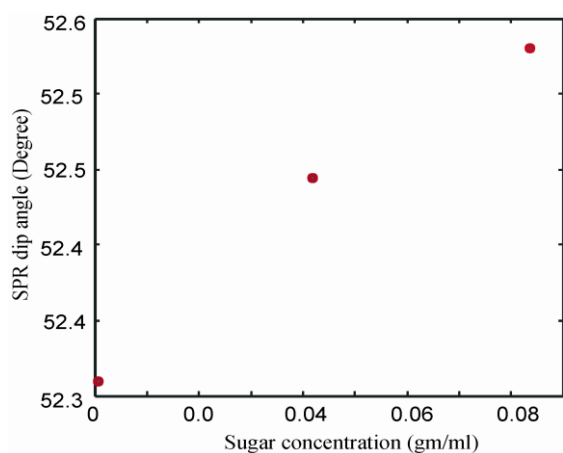
Fig. 4 SPR dip angle / sugar concentration for $\Lambda = 1.4 \mu\text{m}$

We considered the CD-R structure and the parameters as shown in Fig. 1. We calculated the reflectance as a function of angle of incidence for different concentrations of sugar solution. The reflectance curves for $\Lambda = 1.6 \mu\text{m}$ are shown in Fig. 2. The curves shift towards higher values of θ as the concentration increases and the SPR dip angle increases with concentration. The variation of SPR dip angle with concentration for $\Lambda = 1.6 \mu\text{m}$ is plotted in Fig. 3. The sensitivity of the structure defined as $\Delta\theta/\Delta c$ is $3.7 \text{ }^\circ/(\text{gm/ml})$. We have also investigated the sensitivity of the structure for $\Lambda = 1.4 \mu\text{m}$, the results are shown in Fig. 4. The sensitivity slightly increases to $4 \text{ }^\circ/(\text{gm/ml})$.

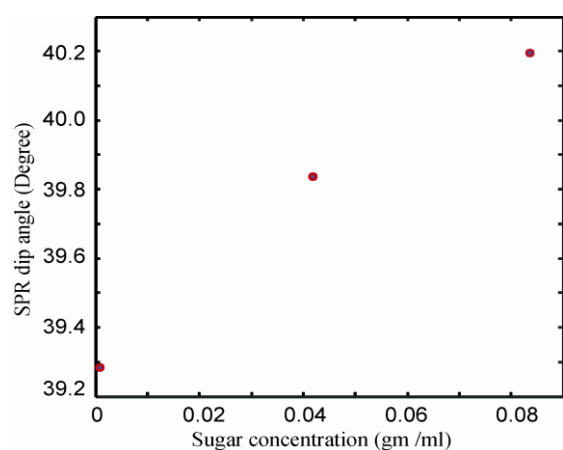
We have also investigated the effect of wavelength light on sensitivity. As can be seen from Eq. (1) the SPR dip angle also changes with wavelength of light and therefore, the sensitivity can be affected by varying the wavelength of interrogating light. To illustrate this we have plotted the variation of SPR dip angles with concentration at two more wavelengths $0.531 \mu\text{m}$ and $0.831 \mu\text{m}$ in Fig. 5 for $\Lambda = 1.4 \mu\text{m}$. The sensitivities at $0.531\text{-}\mu\text{m}$ and $0.831\text{-}\mu\text{m}$ wavelengths were found to be 2.7 and $11.3 \text{ }^\circ/(\text{gm/ml})$, respectively as compared to $4 \text{ }^\circ/(\text{gm/ml})$ at $0.633\text{-}\mu\text{m}$ wavelength.

4. CONCLUSION

We have numerically calculated the change in SPR dip angle with concentration of sugar solution. The sensitivity of the structure for sugar concentration measurements have been calculated. The effect of pitch and the wavelength of light on the sensitivity has been investigated. Our analysis shows that in the concentration range $0\text{-}0.18 \text{ gm/ml}$, the sensitivity can vary from 3.7 upto $11.3 \text{ }^\circ/(\text{gm/ml})$ with our structure parameters.



(a)



(b)

Fig.5 (a) SPR dip angle / sugar concentration for $\lambda = 0.531 \mu\text{m}$ and $\Lambda = 1.4 \mu\text{m}$, (b) SPR dip angle / sugar concentration for $\lambda = 0.831 \mu\text{m}$ and $\Lambda = 1.4 \mu\text{m}$

REFERENCES

- [1] S. A. Maier, "Plasmonics fundamental and application", *Springer Sc.*, 15 (2007).
- [2] N. Mehan, V. Gupta, K. Sreenivas and A. Mansingh, "Surface Plasmon Resonance Based Refractive Index Sensor for Liquids," *Ind. J. Pure & Appl. Phys.*, **43** 854 (2005).
- [3] E. Fontana, "Theoretical and Experimental Study of the Surface Plasmon Resonance Effect on a Recordable Compact Disk," *Appl. Opt.*, **43** 79 (2004).
- [4] G. Gupta and J. Kondon, "Tunning and Sensitivity Enhancement of Surface Plasmon Resonance Sensor," *Sens. Actuators B*, **122**, 381 (2007).
- [5] J. Guo, P.D. Keathley, and J. T. Hastings, "Dual-Mode Surface Plasmon -Resonance Sensors

using Angular Interrogation," *Opt. Lett.*, **33**, 512 (2008).

- [6] K. M. Byun, S. J. Kim, "Grating-Coupled Transmission-Type Surface Plasmon Resonance Sensors based on Dielectric and Metallic Gratings," *Appl. Opt.*, **46**, 5703 (2007).
- [7] D. C. Cullen, R. G. Brown, C. R. Lowe, "Detection of Immune-Complex Formation via Surface Plasmon Resonance on Gold- Coated Diffraction Gratings," *Biosensors*, **3**, 211 (1987).
- [8] D. C. Cullen, R. G. Brown, C. R. Lowe, "A Direct Surface Plasmon-Polariton Immunosensor: Preliminary Investigation of the Non Specific Adsorption of Serum Components to the Sensor Interface," *Sensors and Actuators B*, **1**, 576 (1987).
- [9] P. S. Vukusic, G. P. Bryan, J.R. Sambles, "Surface Plasmon Resonance on Grating as Novel means for Gas Sensing," *Sensors and Actuators B*, **8**, 155 (1992).
- [10] M. J. Jory, P. S. Vokusic, J. R. Sambles, "Development of a Prototype Gas Sensor using Surface Plasmon Resonance on Gratings," *Sensors and Actuators B* **17**, 1203 (1994).
- [11] I. P. Kaminow, W. L. Mammel, and H. P. Weber, "Metal-Clad Optical Waveguides Analytical and Experimental Study", *Appl. opt.*, **13**, 396 (1974).

Synthesis and optical characterization of strong red light emitting $\text{KLaF}_4:\text{Eu}^{3+}$ nanophosphors

Shahzad Ahmad^a, Subrata Das^b, A. Amarnath Reddy^b, R. Nagarajan^a and G. Vijaya Prakash^{b*}

^aMaterials Chemistry Group, Department of Chemistry, University of Delhi, New Delhi-110007 India

E-mail: rnagarajan@chemistry.du.ac.in, Fax: +91-11-2766 6605

^bNanophotonics Laboratory, Department of Physics, Indian Institute of Technology Delhi, New Delhi 110016, India, E-mail: prakash@physics.iitd.ac.in, Fax: +91-11-2658 1114

Abstract: Cubic $\text{KLaF}_4:\text{Eu}^{3+}$ nanophosphors with 5 nm crystallite size are synthesized for the first time by an environmentally benign approach, which show strong red emission at 612 nm ($^3\text{D}_0 \rightarrow ^7\text{F}_2$ of Eu^{3+}) with high lifetime under UV/blue/green excitation. These results suggest a potential red phosphor for white LEDs, mercury-free lamps and plasma display panels (PDPs).

1. Introduction: In recent years, fluoride nanophosphors such as YF_3 [1], NaYF_4 [2], GdF_3 [3], and LaF_3 [4] are gaining intense interest owing to due to their many interlinked facts that could reveal the maximum emissive nature of trivalent rare earth ions (Re^{3+}) without the interference of the lattice phonons. The special class of fluorides, Re^{3+} doped ALnF_4 (A = Alkali ion, Ln = rare earth ion) phosphors (for ex: Re^{3+} -doped NaYF_4) are attractive due to its optical transparency over a wide wavelength range and site-selective doping capability apart from its low phonon energies [5]. In this work, we report monophasic red emitting Eu^{3+} doped KLaF_4 nanophosphor, which can be effectively excited by UV/blue/green lights and suitable for use in white LEDs.

2. Results and discussions: In the present work, monophasic KLaF_4 possessing cubic symmetry with varied Eu^{3+} concentrations were synthesized by wet-chemical reaction, which can be effectively excited by UV/blue/green lights and suitable for use in white LEDs. The prepared nanocrystals exhibit average crystallite size of 5 nm as determined by the Scherer analysis of the powder X-ray diffraction patterns. Uniform doping in the host lattice with Eu^{3+} for La^{3+} was indicated by the change in color from dirty white to light pink and from powder X-ray diffraction patterns. The various laser excited (NUV/Blue/Green) $\text{KLaF}_4:\text{Eu}^{3+}$ nanophosphors showed dominant red color emission at 612 nm from the hypersensitive ($^5\text{D}_0 \rightarrow ^7\text{F}_2$) transition of Eu^{3+} indicates the inversion antisymmetry crystal field around Eu^{3+} ion, which is favorable to improve the red color purity. The emission intensity decay profiles for the 612 nm emission of the $\text{KLaF}_4:\text{Eu}^{3+}$ nanophosphors were recorded and the decay curves fits into a single-exponential function,

which is due to homogeneous distribution of doping ions inside the host matrix without any cluster formation [6] and the observed life time values are also consistent with the analogous phosphor $\text{NaYF}_4:\text{Eu}^{3+}$ [7]. Furthermore, the emission life times are high enough and our results broadly suggest the potential application for white LEDs, mercury-free lamps and display panels.

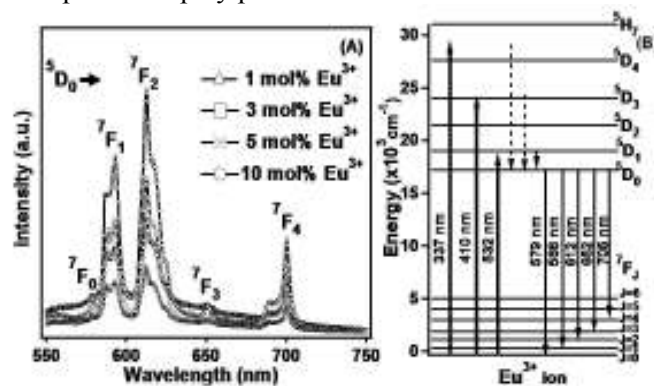


Fig: (A) Room temperature emission spectra of x mol% (x = 1, 3, 5, 10) Eu^{3+} doped in KLaF_4 nanophosphor. (B) Energy level diagram of Eu^{3+} ions ($\lambda_{\text{ex}} = 532$ nm).

References:

- [1] D. Chen, Y. Wang, Y. Yu and P. Huang. *Appl. Phys. Lett.*, **91** (2007) 051920.
- [2] G. Wang and Q. Peng. *J. Solid State Chem.*, **184** (2011) 59.
- [3] X. Zhang, T. Hayakawa, M. Nogami and Y. Ishikawa. *J. Alloys Compd.*, **509** (2011) 2076.
- [4] S.N. Achary, A.K. Tyagi, T.K. Seshagiri and V.N. Natarajan. *Mater. Sci. Eng. B*, **129** (2006) 256.
- [5] N. Tyagi, A. Amarnath Reddy and R. Nagarajan. *Opt. Mater.*, **33** (2010) 42.
- [6] N.S. Singh, R.S. Ningthoujam, M.N. Luwang, S.D. Singh and R.K. Vatsa. *Chem. Phys. Lett.*, **480** (2009) 237.
- [7] G. Jia and P.A. Tanner. *J. Alloys Compd.*, **471** (2009).557.

DESIGN AND ANALYSIS OF PLASMONIC BEND WAVEGUIDE

Venus Dillu, Shruti, Triranjita Srivastava and R.K Sinha

Department of Applied Physics, Delhi Technological University (Formerly: Delhi College of Engineering), Delhi-110042, INDIA
venusdillu@gtu.ac.in

Abstract: We propose a plasmonic bend waveguide composed of silver nanorods embedded in silicon over silica substrate exhibiting narrow transmission bandwidth of ~ 10 nm, which can be utilized as a narrow bandwidth filter. Ag nanorods are structured at nano dimensions to control and manipulate surface plasmon polariton propagation in the bend design.

1. INTRODUCTION

An explicit property of surface plasmons is that they couple with photons via corrugated surfaces and vice-versa. Metallic nanorods have recently drawn attention due to its remarkable optical and electronic properties like extinction spectra, optical near fields, non-linear optical properties and particle interactions [1]. These nanorods array hold tremendous promise for the development of new applications such as nanoparticle-based plasmonic waveguides, bends, splitters, band pass filter, etc. which are very canonical optical interconnects and therefore are essential components of the integrated optical circuitry. Various designs for plasmonic components have been proposed [3-6] and their practical applications demands for new designs. Different geometries are employed to filter frequencies of particular electromagnetic regime [7, 8]. In this paper we propose a design of plasmonic bend waveguide incorporating silver (Ag) nanorods into silicon on insulator (SOI) as substrate. This structure is optimized for the transmission of 633 nm wavelength, with ultra narrow bandwidth of 10nm. Transmission spectra (including the resonance wavelengths and bandwidths) of the filter can be easily controlled by modulating the geometrical parameters of the nanorods based waveguides.

2. STRUCTURE

The bend waveguide comprises of silver nanorods and SOI substrate. Complete structure as shown in Fig 1(a), consists of periodically arranged square lattice (lattice constant, $a=100\text{nm}$) of silver nanorods (radii, $r=45\text{nm}$, height= 150nm) with dielectric constant as, $\epsilon = -13.6089 + i0.995$, on silicon slab ($n = 3.5$, thickness = 100nm) over insulator with refractive index of 1.5. These rods were embedded into silicon to an optimized depth of 50nm .

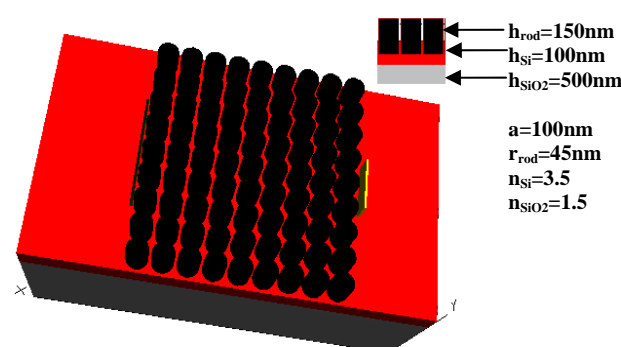


Fig. 1 Design of the proposed structure with silver rods arranged as square lattice over silicon on insulator.

3. RESULTS AND DISCUSSION

The simulations for the bend waveguide were performed by employing Finite difference time domain method. 3D simulation is done over an array of 5×9 nanorods placed in square lattice in X-Z plane including total height (Y-X plane) of the device. The grid size was chosen as $0.00625\mu\text{m}$ along X, Z - axis and $0.1\mu\text{m}$ along Y - axis. Also, the PML boundary conditions were applied with PML width = $0.5\mu\text{m}$ along X, Y and Z directions.

We first examined the transmission spectra for the complete structure with no defect as a function of wavelength and obtained a bandgap in the wavelength range of $200\text{nm} - 1200\text{nm}$ for the y-polarized modes. We have observed that by introducing a line defect in the square lattice array and by optimizing the structure, the wavelength in the Bandgap range could be propagated through the waveguide structure.

The L-shaped smooth bend was designed by removing row of silver nanorods and optimizing the radii of rods (radii $\sim 35\text{nm}$) adjacent to the defect and placing extra rods of radii $\sim 25\text{nm}$, at

the corner of the bend (as shown in the Fig. 2). These extra rods act as a reflector due to which the light is allowed to propagate in the bend region.

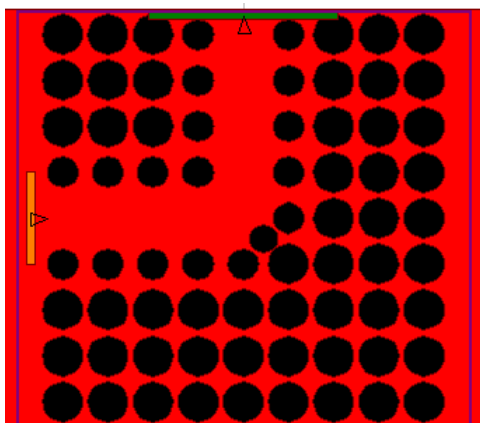


Fig. 2. Schematic of the bend waveguide with extra rods placed at the corner region

In order to achieve a transmission in the visible regime, we obtained the variation of the transmission with respect to the wavelength, as shown in Fig. 3. A transmission peak at $0.633 \mu\text{m}$ is observed with a narrow bandwidth of 10 nm . Thus the proposed waveguide can be utilized as a narrow bandwidth filter.

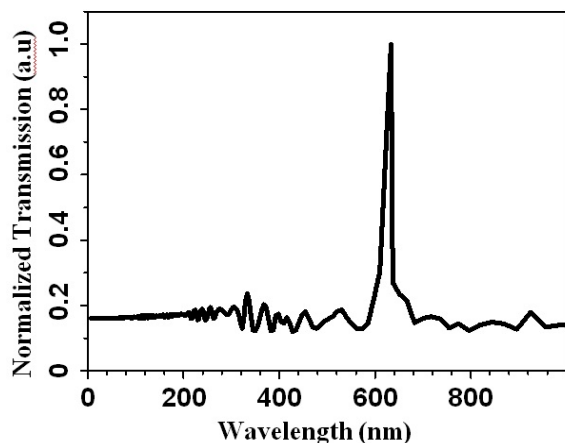


Fig 3 Transmission spectrum of the proposed bend plasmonic waveguide

We also obtained the Electric field profile E_y of the y-polarized mode along the direction of propagation (as shown in Fig 4), which reveals that light stays propagates through the bend waveguide. The confinement factor is also calculated, which is about of 92 at 633 nm wavelength.

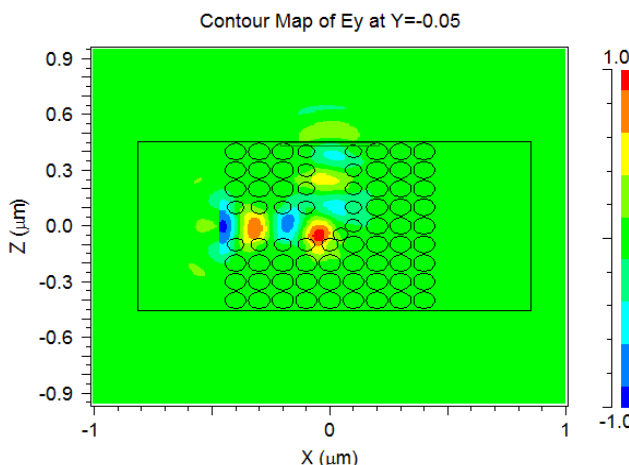


Fig. 4 Electric field profile for the bend waveguide along the direction of propagation.

4. CONCLUSION

In conclusion, a compact subwavelength plasmonic L-shaped bend waveguide has been proposed and numerically analyzed using FDTD method. It can be further modified for desired wavelengths and can filter selectively to serve specific requirements by modulating various parameters.

ACKNOWLEDGEMENT

The authors wish to acknowledge the support of "TIFAC Centre of Relevance and Excellence in Fiber Optics and Optical communication at Delhi Technological University" through Mission Reach program of Technology Vision 2020, by Government of India.

REFERENCES

- [1] G A Wurtz, W Dickson, D O'Connor, R Atkinson, W Hendren, P Evans, R Pollard Atkinson, W. Hendren, P. Evans, R. Pollard, and A. V. Zayats "Guided plasmonic modes in nanorod assemblies : strong electromagnetic coupling regime" *Opt. Exp.* **16**, 7460 (2008).
- [2] Feifei Hu, Huaxiang Yi, and Zhiping Zhou, "Band-pass plasmonic slot filter with band selection and spectrally splitting capabilities", *Opt. Exp.* **19**, 4848 (2011).
- [3] Georgios Veronis and Shanhui Fan, "Bends and splitters in metal-dielectric-metal subwavelength plasmonic waveguides," *Appl Phys Lett*, **87**, 131102 (2005).
- [4] YanWang, Rubaiyat Islam and George V. Eleftheriades, "An ultra-short contra-directional coupler utilizing surface plasmon-polaritons at optical frequencies" *Opt. Exp.* **14**, 16, 7279 (2006).
- [5] Nobuhiko P. Kobayashi, "Nanometer-scale photonic passive and active components for

- future communications,” *J of Nanophot.*, **2**, 021765 (2008).
- [6] Jun Shbayama, Akifumi Nomura, Ryoji Ando, Junji Yamauchi and Hisamatsu Nakano, “ A frequency dependent LOD- FDTD method and its application to the analyses of plasmonic devices,” *IEEE J of Quant Elect*, **46**, 1, 40 (2010).
- [7] Amir Hosseini, Hamid Nejati, and Yehia Massoud, “Design of a maximally flat optical low pass filter using plasmonic nanostrip waveguide,” *Opt. Exp.* **15**, 23, 15280 (2007).
- [8] Jin Tao, Xu Guang Huang*, Xianshi Lin, Qin Zhang, Xiaopin Jin, “A narrow-band subwavelength plasmonic waveguide filter with asymmetrical multipleteeth-shaped structure,” *Opt. Exp.* **17**, 16, 13989 (2009).

Simple Experiment for Studying Correlation in the Field Assisted by Surface Plasmons

Stuti Joshi, Manish Verma, H. C. Kandpal

CSIR-National Physical Laboratory

Email: joshis@mail.nplindia.ernet.in

Abstract: We report a simple experiment to study second-order correlation of the field assisted by surface plasmons. It has been shown that second-order correlation of the field emerging from the metallic double slit due to surface plasmons as a function of the displacement of the detectors changes with slit separation in the double slit. The interference pattern changes with slit separation and for a particular value of slit separation interference pattern changes into Hanbury-Brown and Twiss (HBT) effect. It is also shown that coincidence counts modulate with the slit separation.

1. INTRODUCTION

When a TM polarized electromagnetic field is incident on a metal-dielectric interface, surface plasmon polaritons (SPPs) are generated and enhance the optical transmission significantly [1-2]. Surface plasmons (SPs) can be used to minimize the size of the photonic circuit [3]. Recently it has been shown that the position of Young's interference fringes could be controlled by changing the film thickness and slit width differences [4].

Two photon interference has received a lot of attention in quantum optics and imaging [5-7]. In ref [8] sub-wavelength interference with two independent pseudo thermal sources has been and the second-order correlations have been explained by quantum theory with no classical analogy.

In this paper we have theoretically investigated the second-order correlation function of the field assisted by surface plasmons (SPs). SPs are generated at one slit and propagate to the other slit where it reappears as a freely propagating field. Field emerging from the double slit modulates the second-order correlation as a function of displacement of the detectors for different values of slit separation in Young's double slit.

3. ANALYSIS

The proposed setup for studying second-order correlation is shown in Fig. 1. We assumed that a TM polarized light of wavelength 600nm is incident on a metallic double slit (say Au double slit). The SPs generated at one slit propagates to the other slit where they reappear as a freely propagating field. Field that emerges from the double slit falls on a HBT type setup as shown in the Fig.1. The second-order correlation can be determined by using the experimental setup shown in Fig.1.

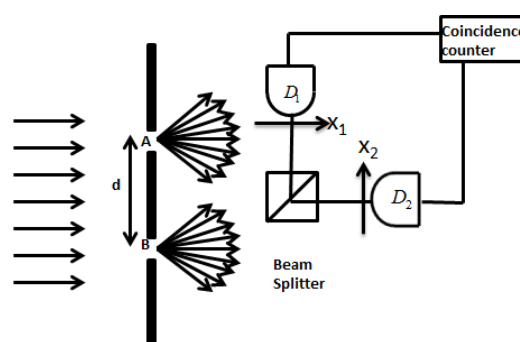


Fig.1. Principle setup for second-order correlation measurement of the field assisted by SPs. Abbreviations are defined in the text

We have assumed that the field incident on the two slits (each of width s and separated by d) is the same. Let a fraction α of the incident field is directly transmitted and a fraction $\alpha\beta$ is converted into SPs which travel to the other slit where it reappears as a freely propagating field. Therefore, the field in the two slits A and B is given as [8]

$$U_A = \alpha U_A^{inc} + \alpha\beta U_B^{inc} \exp(ik_{sp}d), \quad (1)$$

$$U_B = \alpha U_B^{inc} + \alpha\beta U_A^{inc} \exp(ik_{sp}d), \quad (2)$$

where k_{sp} is the wave number associated with SPs.

k_{sp} is given by

$$k_{sp} = \frac{2\pi}{\lambda_{sp}} = \sqrt{\frac{\epsilon_m \epsilon_d}{\epsilon_m + \epsilon_d}},$$

where ϵ_m and ϵ_d are the permittivity of the metal and the dielectric.

The transmission function of the slit A can be written as

$$T_A(x_0) = \begin{cases} \alpha(1 + \beta \exp(ik_{sp}d), & (d-s)/2 \leq x_0 \leq (d+s)/2 \\ 0, & \text{otherwise} \end{cases} \quad (3)$$

Similarly for slit B

$$T_B(x_0) = \begin{cases} \alpha(1 + \beta \exp(ik_{sp}d), & -(d-s)/2 \leq x_0 \leq -(d+s)/2 \\ 0, & \text{otherwise} \end{cases} \quad (4)$$

where x_0 is the distance from the center point between the slits. The relation between second-order correlation function and the first order correlation function for Gaussian thermal light is given by [9]

$$\begin{aligned} G^{(2)}(x_1, x_2) &= \langle a^\dagger(x_1) a^\dagger(x_2) a(x_2) a(x_1) \rangle \\ &= \left| \langle a^\dagger(x_1) a(x_2) \rangle \right|^2 + \\ &\quad \langle a^\dagger(x_1) a(x_1) \rangle \langle a^\dagger(x_2) a(x_2) \rangle \\ &= \left| G^{(1)}(x_1, x_2) \right| + G^{(1)}(x_1, x_1) G^{(1)}(x_2, x_2), \end{aligned} \quad (5)$$

where $a^\dagger(x_i)$ and $a(x_i)$ are the creation and annihilation operators at the detectors D_i respectively.

The first-order correlation function for the fields contributed by the fraction of the incident field transmitted directly and that contributed by the SPs emerging from the slit A is given as [8]

$$\begin{aligned} G_A^{(1)}(x_1, x_2) &= \frac{k}{2\pi z} \frac{1}{2\pi} \left[\iiint T_A^*(x'_0) T_A(x_0) \delta(x' - x'_0) \times \right. \\ &\quad \left. \delta(x' - x_0) \right] \times \\ &\quad \exp \left[i \left(\frac{kx_1}{z} - q_1 \right) - i \left(\frac{kx_2}{z} - q_2 \right) \right] dq_1 dx_0 dx'_0 \end{aligned} \quad (6)$$

Substituting the value of the transmission function from Eq. (2) into Eq.(6) we get

$$\begin{aligned} G_A^{(1)}(x_1, x_2) &= \frac{1}{\pi(x_1 - x_2)} |\alpha|^2 |1 + \beta \exp(ik_{sp}d)|^2 \times \\ &\quad \left\{ \cos \left[\frac{k(x_1 - x_2)d}{2z} \right] \sin \left[\frac{k(x_1 - x_2)s}{2z} \right] \times \right. \\ &\quad \left. + i \sin \left[\frac{k(x_1 - x_2)d}{2z} \right] \sin \left[\frac{k(x_1 - x_2)s}{2z} \right] \right\} \end{aligned} \quad (7)$$

where λ is the wavelength of the incident light field and z is the distance to the detector.

Similarly for the slit B the first-order correlation function is given by

$$\begin{aligned} G_B^{(1)}(x_1, x_2) &= \frac{1}{\pi(x_1 - x_2)} |\alpha|^2 |1 + \beta \exp(ik_{sp}d)|^2 \times \\ &\quad \left\{ \cos \left[\frac{k(x_1 - x_2)d}{2z} \right] \sin \left[\frac{k(x_1 - x_2)s}{2z} \right] \right. \\ &\quad \left. - i \sin \left[\frac{k(x_1 - x_2)d}{2z} \right] \sin \left[\frac{k(x_1 - x_2)s}{2z} \right] \right\} \end{aligned} \quad (8)$$

Here we are considering that the fields emerging from the two slits have the same polarization. For the same polarization the second-order correlation function in terms of first-order correlation function can be expressed as

$$\begin{aligned} G^{(2)}(x_1, x_2) &= \left| G_A^{(1)}(x_1, x_2) + G_B^{(1)}(x_1, x_2) \right|^2 + \\ &\quad G_A^{(1)}(x_1, x_1) G_A^{(1)}(x_2, x_2) + G_A^{(1)}(x_1, x_1) G_B^{(1)}(x_2, x_2) + \\ &\quad G_B^{(1)}(x_1, x_1) G_A^{(1)}(x_2, x_2) + G_B^{(1)}(x_1, x_1) G_B^{(1)}(x_2, x_2) \end{aligned} \quad (9)$$

Substituting Eqs.(7) and (8) into Eq.(9), the correlation function when the detectors are moved in opposite direction is given by

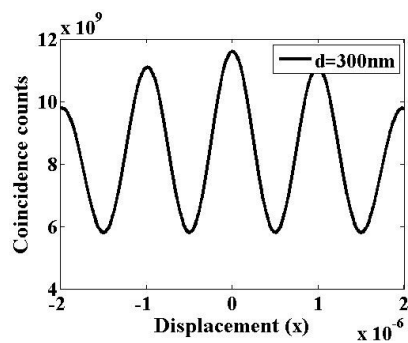
$$\begin{aligned} G^{(2)}(x, -x) &= \left(\frac{ks}{\pi z} \right)^2 |\alpha|^4 |1 + \beta \exp(ik_{sp}d)|^4 \times \\ &\quad \left[1 + \sin^2 c^2 \left(\frac{sx}{(\lambda/2)z} \right) \cos^2 \left(\frac{\pi dx}{(\lambda/2)z} \right) \right] \end{aligned} \quad (10)$$

Eq.[10] represents the second-order correlation function for the field emerging from the metallic double slit. It is the modified version of equation (11) of ref. (8). Eq.(10) shows that Second-order correlation function depends on the transmission function of the field emerging from the metallic double slit which varies with the slit separation.

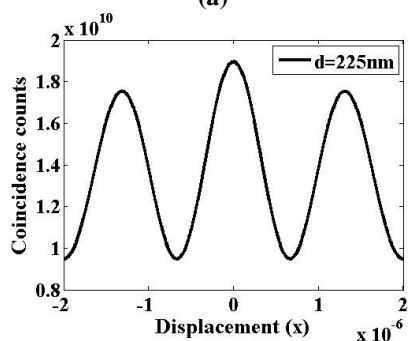
3. RESULT

We have theoretically investigated the second-order correlation function of the field emerging from the metallic double slit. Eq.(10) shows the relation between second-order correlation function and slit separation. It shows how the second-order correlation function depends on the transmission function which is due to the generation of SPs. It is plotted as a function of displacement for different values of slit separation and is shown in Fig. (2). From Fig. (2) we interpret that the modulation in the

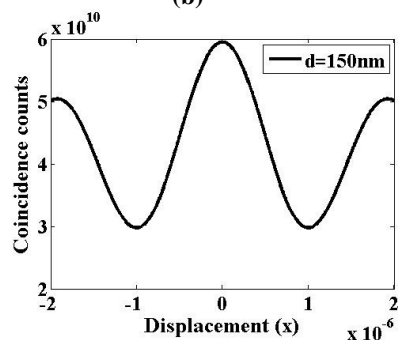
coincidence counts is due to the wave nature of the field emerging from metallic double slit (interference fringes) for $d=450\text{nm}$, $d=300\text{nm}$ and $d=150\text{nm}$ while for $d=75\text{nm}$ a single peak distribution indicates the particle nature (HBT effect). Thus we have investigated that in the same experiment we can study both the wave nature as well as the particle nature of the field that is assisted by SPs.



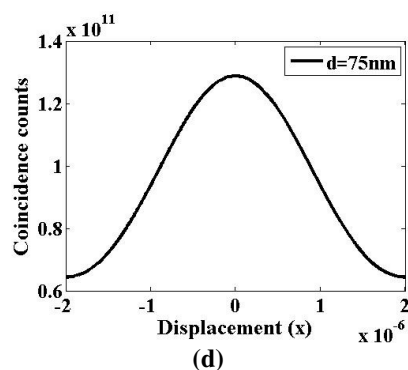
(a)



(b)



(c)



(d)

Fig. 2. Plots of second- order correlation verses displacement when detectors are moved in opposite direction. Slit width $s=50\text{nm}$ and $z=1\mu\text{m}$ in each case. (a) for slit separation $d=300\text{nm}$, (b) for slit separation $d=225\text{nm}$, (c) for slit separation $d=150\text{nm}$, (d) for slit separation $d=75\text{nm}$.

4. ACKNOWLEDGEMENT

The authors S.J. and M.V. thank the CSIR, India for financial support as Junior Research Fellowship. The Authors are also thankful to the Director CSIR-NPL for giving permission to present the paper.

4. REFERENCES

- [1]. T. W. Ebbesen, H. J. Lezec, H.F. Ghaemi, T. Thio and P. A. Wolff, Extraordinary optical transmission through sub-wavelength hole arrays, *Nature*, 391, 667, (1998).
- [2]. T.Thio, K. M.Pellerin, R.A. Linke, H. J.Lezec, T.W.Ebbesen, Enhanced light transmission through a single subwavelength aperture, *Opt. Lett.* 26, 1972, (2001).
- [3]. W. L. Barnes, A. Dereux and T. W. Ebbesen, Surface plasmon sub-wavelength optics, *Nature*, 424, 824-830, (2003).
- [4]. H. Shi, X. Luo and C. Du, Young's interference of double metallic nanoslit with different widths, *Optics Express* 15, 11321-11327, (2007).

- [5]. L. Mandel, Quantum theory of interference effect produced by independent light beams, *Phys. Rev.* 134, A10-A15 (1964).
- [6]. R. L. Pfleegor and L. Mandel, Interference of independent photon beams, *Phys. Rev.* 159, 1084-1088, (1967).
- [7]. R. L. Pfleegor and L. Mandel, Interference of independent photon beams, *Phys. Rev.* 159, 1084-1088, (1967).
- [8]. Y. H. Zhai., X. H. Chen and L. A. Wu, Two photon interference with two independent pseudo-thermal sources, *Phys. Rev. A* 74,053807 (2006).
- [9]. C. H. Gan, G. Gbur, and T. D. Visser, Surface plasmons modulate the spatial coherence of light in Young's interference experiment, *Phys. Rev. Lett.* 98, 043908 (2007).
- [10]. J. W. Goodman, *Statistical Optics* (Wiley, New York, 1985).

SPR BASED OPTICAL WAVEGUIDE REFRACTIVE INDEX SENSORS

Saurabh Mani Tripathi¹, Arun Kumar², Manoj Kumar² and Wojtek J. Bock¹

¹Photonics Research Centre, Université du Québec en Outaouais, Québec, QC J8X 3X7, Canada

²Physics Department, Indian Institute of Technology Delhi, New Delhi-110016, India
tripathi.iit@gmail.com, akumar@physics.iitd.ac.in, ep.manoj888@gmail.com, wojtek.bock@uqo.ca

Abstract: We examine the role of the longitudinal dimension of the metallic layer on the performance of the surface Plasmon resonance (SPR) based optical waveguide refractive index sensors. It is found that such sensors work efficiently only for certain values of the interaction length between the waveguide and the metallic layer making the interaction length a critical design parameter.

1. INTRODUCTION

The SPR based sensors have attracted great interest in the past decade and a number of refractive index sensors using metal coated integrated optical waveguides [1], [2], side polished fibers [3]-[6] and optical waveguide gratings [7]-[10] etc. have been reported in literature. All these sensors rely on the resonant power coupling between the core mode and the Surface Plasmon wave, supported at the metal/dielectric interface. To maximize the sensitivity of these devices, the studies so far have been focused primarily on increasing the modal field in the ambient region by optimizing the transverse dimensions of the waveguide structure [2], [11]. The effect of the longitudinal dimension of the metallic layer, on the other hand, has not been looked into.

Employing the super-mode analysis, in this paper we examine the effect of the longitudinal dimension of the metallic layer on the sensitivity of the SPR based sensors. We found that such sensors work only for certain values of the interaction length between the waveguide and the metallic layer making the interaction length a critical design parameter.

2. THEORETICAL ANALYSIS

We consider a SPR based waveguide sensor consisting of a metal coated planar optical waveguide, as shown in Fig.1. The liquid, whose refractive index is to be sensed, is placed over metallic layer which interacts with the waveguide over a distance 'L' only. Light is launched from the left and the output on the right end is detected. The structure is basically a directional coupler such that the waveguide mode excites the supermodes supported in the metal-coated region which propagates with different propagation constants and losses deciding the output power detected.

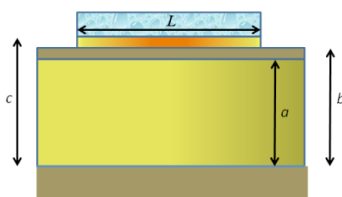


Fig.1 Schematic of the sensor structure

It may be noted that only TM modes interact with the SP waves which are obtained by solving the following wave equation [12, 13]:

$$\frac{d}{dx} \left(\frac{1}{n^2} \frac{dH_y}{dx} \right) + \left(k_0^2 - \frac{\beta^2}{n^2} \right) H_y = 0 \quad (1)$$

where, k_0 , n , and β are the free space propagation constant, the refractive index distribution and the propagation constant, respectively. The direction of propagation is taken to be along z -axis and the (z, t) dependence of the fields is taken of the form $\exp\{i(\omega t - \beta z)\}$. The propagation constants and the field distributions of the symmetric and anti-symmetric supermodes are obtained by solving Eq.(1) employing the continuity of H_y and $(1/n^2)dH_y/dx$ field components at every dielectric discontinuity. The continuity conditions can be written, in the Matrix form, as:

$$\begin{bmatrix} H_y \\ \frac{1}{n^2} \frac{dH_y}{dx} \end{bmatrix} = M_m \begin{bmatrix} A_m \\ B_m \end{bmatrix} \quad (2)$$

with the matrix M_m given by,

$$M_m = \begin{bmatrix} \exp(\gamma_m x) & \exp(-\gamma_m x) \\ \frac{\gamma_m}{n_m^2} \exp(\gamma_m x) & -\frac{\gamma_m}{n_m^2} \exp(-\gamma_m x) \end{bmatrix} \quad (3)$$

here, the index $m = su, co, cl, me, se$ represents the substrate, core, cladding, metal and sensing region, respectively; A_m and B_m are field coefficients in the m th region, and the variable $\gamma_m = \sqrt{\beta^2 - k_0^2 n_m^2}$. At the junction of the two neighbouring regions m and n , therefore, the field amplitudes are connected as:

$$M_n \begin{bmatrix} A_n \\ B_n \end{bmatrix} = M_m \begin{bmatrix} A_m \\ B_m \end{bmatrix} \quad (4)$$

thus, the amplitudes in the substrate and sensing regions will be connected as:

$$\begin{bmatrix} A_{su} \\ B_{su} \end{bmatrix} = M \begin{bmatrix} A_{se} \\ B_{se} \end{bmatrix} \quad (5)$$

where, M is given by

$$M = (M_{su}^{-1} M_{co})_{x=0} (M_{co}^{-1} M_{cl})_{x=a} (M_{cl}^{-1} M_{me})_{x=b} (M_{me}^{-1} M_{se})_{x=c} \quad (6)$$

The

Now, since for physically acceptable solutions the fields must be finite in all the regions: the field coefficients B_{su} and A_{sc} of the exponentially growing components in substrate region and the sensing region must be zero. Using this condition in Eq.(6) gives us the eigen-value equation as:

$$M_{22} = 0 \quad (7)$$

To solve this equation for the complex roots, we use the *Lorentzian* fitting method proposed by Ramdas et al. [14]. In this method, the parameter $P = |1/M_{22}|^2$ is plotted as a function of the real valued trial propagation constant. The position of minima for P yields the real part of the propagation constant and the HWHM gives the imaginary part of the propagation constant. Having obtained the complex propagation constants, the field coefficients in various regions are calculated by using Eq.(5) and Eq.(6). Similarly, the propagation constants and the field distributions in non-metallic regions are also calculated. The fields are then normalized to carry unit power per unit length (along infinitely extended y direction) along the z direction [13]. Finally, the power at the output of the sensor is obtained as:

$$P_o = \left| \begin{array}{l} a_0^2 \exp\{-im(\beta_s L)\} \\ + a_1^2 \exp\{-im(\beta_a L)\} \exp\{re(\beta_s - \beta_a)L\} \end{array} \right|^2 \quad (8)$$

here, a_0 , a_1 are the modal overlap integrals of the core mode of the non-metallic region with that of the symmetric and anti-symmetric supermodes supported within the metal-coted waveguide region. Further, β_s and β_a are the complex valued propagation constants of the symmetric and anti-symmetric super modes, respectively.

3. RESULTS AND DISCUSSION

In our analysis we consider the following waveguide parameters: core and cladding regions are made of 3.1 mol% GeO₂ doped silica and fused silica, respectively, with their refractive indices obtained from the Sellmeier relation [15]. The metal is considered to be Gold with its refractive index obtained by Drude relation [16]. The thickness of core, upper cladding and metallic regions are taken as $a = 6 \mu\text{m}$, $(b-a) = 1.3 \mu\text{m}$, and $(c-b) = 35 \text{ nm}$, respectively. The overlay refractive index (n_{sc}) has been taken as 1.437, at which the supermodes are formed due to coupling between the core mode and the symmetric surface Plasmon polariton (SPP) mode supported by the metal film.

Figs. 2(a, b) show the variation of the real part of the normalized field distributions for the symmetric (solid) and antisymmetric (dashed) supermodes. The coupling of the core mode with the symmetric SPP mode of the metal film (between $8.2 - 8.235 \mu\text{m}$)

Presentation Preference: Oral

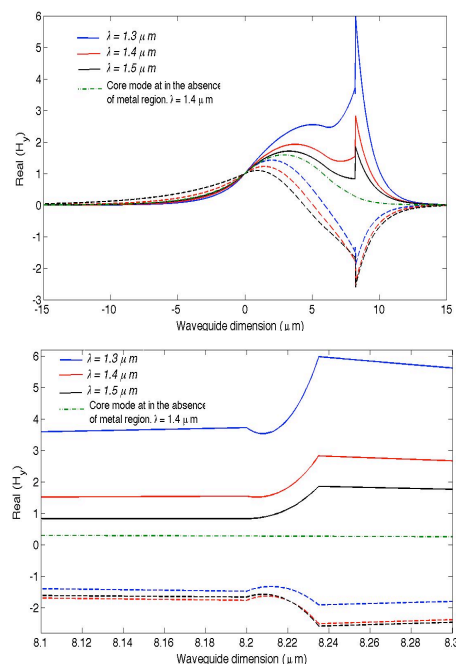


Fig. 2 Variation of the real part of the normalized field distributions for the symmetric (solid) and antisymmetric (dashed) supermodes (a) across the whole structure (b) zoomed near cladding-metal-sensing region.

from the origin, taken at the lower cladding-core boundary) can be easily noticed from Fig.2(b). The transmission characteristics of the present directional coupler are quite different as compared to the normal lossless waveguide directional couplers. We would like to point out that both the super modes are lossy and that the real and imaginary parts of their propagation constants are highly wavelength dependent. As a result, the interaction length plays a very critical role in the functioning of these sensors.

In order to show the above, in Fig.(3) we have plotted the transmitted power as a function of interaction length for three different wavelengths and two different upper cladding thicknesses, taking metal thickness as 35 nm.

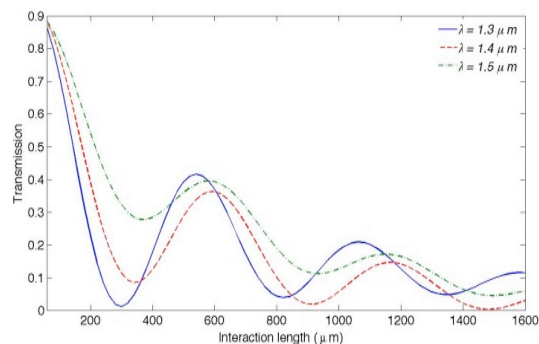


Fig. 3 Transmission as a function of interaction length for three different wavelengths.

The following points can be easily deduced from the above figure:

- (1) Coupling length is highly dependent on wavelength (λ) as well as on interaction length.
- (2) Both the super-modes are lossy & their losses depend on λ . This is clear from the fact that after two coupling lengths power coupled back is not 100% and is different for different λ .
- (3) As a result it is not possible to achieve a dip for every value of interaction length. For example, a dip between 1.3 μm to 1.5 μm is possible only for L between 365 - 600 μm , and 850 - 1180 μm .

In order to show the last point more clearly, in Fig.4 we have plotted the transmission spectrum for three different interaction lengths, two lying inside and one outside the range 365 μm - 600 μm .

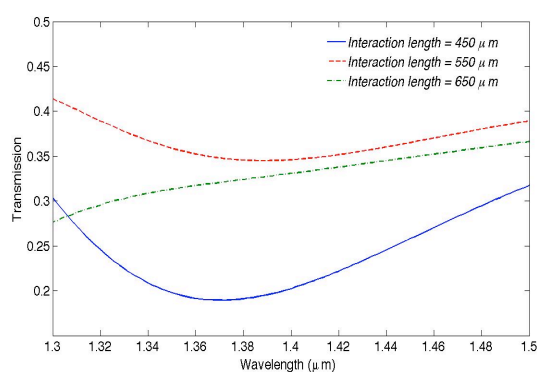


Fig.4 Transmission spectrum for three different interaction lengths.

As expected for interaction length 650 μm there is no wavelength dip. It may be noted that even if we select the interaction length such that a dip exists, the position of the dip will depend on the value of the interaction length selected, which can be clearly observed from the position of minima for interaction length = 450 μm and 550 μm .

In view of the above the refractive index sensitivity of such sensors is highly dependent on the interaction length. Defining the sensitivity as spectral shift in the position of dip per unit change in overlay index, in Fig. 5 we have plotted the sensitivity as a function of interaction length (L).

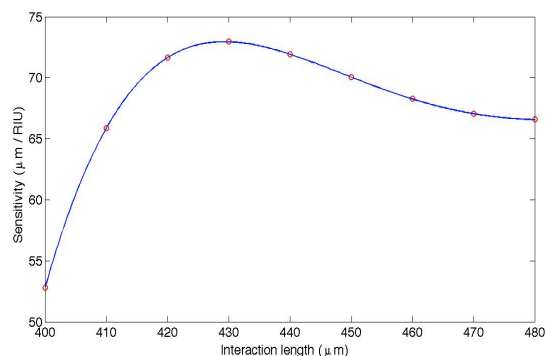


Fig.5 Sensitivity as a function of interaction length

Thus, we see that the selection of the interaction length is extremely important in realizing a wavelength encoded SPR sensor.

Finally to study the effect of various metal thicknesses, in Figs. 6(a,b) we have plotted the transmission spectrum as a function of interaction length for two different metal thicknesses, namely 35 nm and 39 nm, respectively.

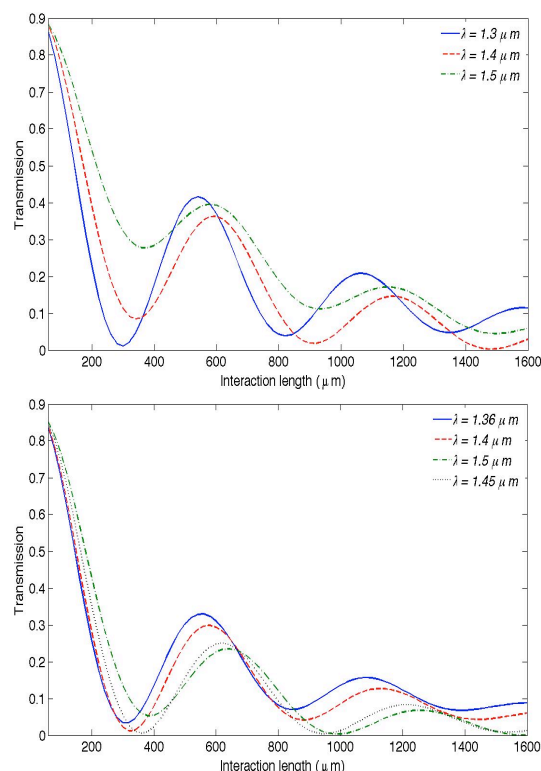


Fig.6 Transmission as a function of interaction length for a metal thickness of (a) 35 nm and (b) 39 nm.

From these figures, we follow that the transmission strongly depends upon the metal thickness, and hence the designing parameters have to be adjusted accordingly.

4. CONCLUSIONS

In this paper we have shown that the interaction length between waveguide and the metal film plays a very crucial role in the functioning of the SPP based optical waveguide sensors. Since both the super-modes are lossy and both the real and imaginary parts of their propagation constants are highly wavelength dependent, the wavelength dips can be obtained only over a certain regions of interaction length. Further, the position of the dip and its sensitivity with respect to the overlay index depends critically on the value of the interaction length selected.

REFERENCES

- [1] A. A. Oliner and S. T. Peng, "Effects of metal overlays on 3-D optical waveguides", *Appl. Opt.* **17**, 2866 (1978).
- [2] J. Homola, *Surface Plasmon Resonance Based Sensors* (Springer, 2006).
- [3] J. Homola, "Optical fiber sensor based on surface plasmon excitation", *Sens. & Act. B*, **29**, 401 (1995).
- [4] R. Slavik, J. homola, and J. Ctyroki, "Miniaturization of fiber optic surface plasmon resonance sensor" *Sens. & Act. B*, **51**, 311 (1998).
- [5] R. Slavik, J. homola, and J. Ctyroki, "Single-mode optical fiber surface plasmon resonance sensor", *Sens. & Act. B*, **54**, 74 (1999).
- [6] R. Slavik, J. homola, J. Ctyroki and E. Brynda, "Novel spectral fiber optic sensor based on surface plasmon resonance", *Sens. & Act. B*, **74**, 106 (2001).
- [7] Y.-J. He, Y.-L. Lo, and J.-F. Huang, "Optical-fiber surface-plasmon resonance sensor employing long-period fiber gratings in multiplexing," *JOSA B.*, **23**, 801 (2006).
- [8] G. Nemova and R. Kashyap, "Fiber-bragg-grating-assisted surface plasmon-polariton sensor," *Opt. Lett.*, **31**, 2118 (2006).
- [9] Y. Y. Shevchenko and J. Albert, "Plasmon resonances in gold-coated tilted fiber bragg gratings," *Opt. Lett.*, **32**, 211 (2007).
- [10] S. M. Tripathi, A. Kumar, E. Marin, and J.-P. Meunier, "Side-polished optical fiber grating-based refractive index sensors utilizing the pure surface plasmonpolariton," *J. Lightw. Technol.*, **26**, 1980 (2008).
- [11] D. Sarida, *Modern Introduction to Surface Plasmons*(Cambridge, 2010).
- [12] A. K. ghatak and K. Thayagarajan, *Optical Electronics* (Cambridge, 1989).
- [13] K. Okamoto, *Fundamentals of Optical Waveguides* (Academic, 2000), Chap. 2.
- [14] M. R. Ramadas, E. Garmire, A. K. Ghatak, K. Thyagarajan, and M. R. Shenoy, "Analysis of absorbing and leaky planar waveguides: A novel method," *Opt. Lett.*, **14**, 376, 1989.
- [15] M. J. Adams, *An Introduction to Optical Waveguides*. New York: Wiley, 1981
- [16] D. W. Lynch and W. R. Hunter, "Comments on the optical constants of metals and an introduction to the data for several metals," in *Handbook of Optical Constants of Solids*, E. D. Palik, Ed. (Academic, 1985).

Effects of Arbitrary Phase Shift on the Higher- Order Self-Diffraction in Absorptive Optically Active Photorefractive Crystal

Neha Katyala^a, Natasha^a, Amitava Roy^b, Avinashi Kapoor^a

^a Department of Electronic Science, Delhi University, South Campus, New Delhi-110021
neha.k.14@gmail.com; natasha2du@yahoo.co.in; avinashi_kapoor@yahoo.com

^b SERC Division, Deptt. of Science & Technology, New Mehrauli Road, New Delhi – 110016
amitava@nic.in

Abstract: The effect of arbitrary phase shift between intensity grating and refractive index grating have been analyzed on the generation of higher order beams in two-wave mixing in transmission geometry in optically active photorefractive BSO crystal. It has been observed that when this phase shift is other than $\pi/2$, the energy is transferred on both sides of the input beams. It has been observed that by the variation of various input parameters, the intensity and polarization of higher orders beams can be controlled. This feature can be applicable for optical interconnects and beam splitters with specific polarization.

1. INTRODUCTION: We have considered two-waves A (pump) and B (signal) incident on a photorefractive crystal (fig. 1), which create a phase grating inside the medium. Due to high coupling between the beams and also considering the interbeam angle between the input beams to be small enough, two-wave mixing will generate higher diffraction orders [1-3]. Higher diffraction orders are finding various applications [4] in the field of optical signal processing. Here we have considered generation of only two higher orders C and D as shown in fig.1.

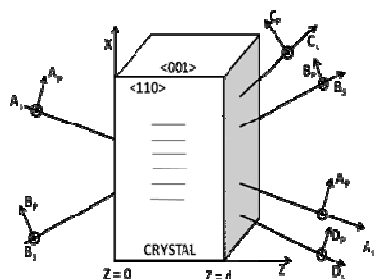


Fig.1 Crystal orientation and input and output beams with their respective polarizations

Each beam considered to be consists of two orthogonally polarized components, designated as “s” and “p” components.

2. RESULTS AND DISCUSSION:

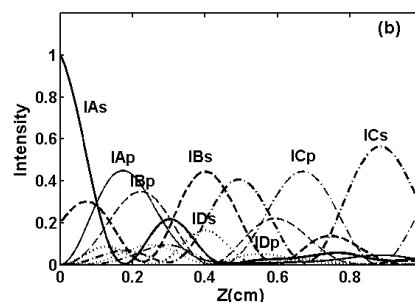
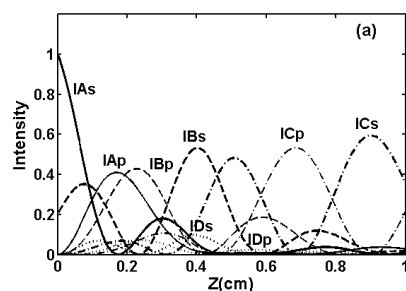


Fig 2. Intensities of output beams plotted as a function of thickness of crystal. Intensities of input beams considered as $IA_s=1$, $IB_s=0.2$, $IA_p=IB_p=0$. The parameters of BSO crystal is considered as absorption coefficient (α) = 0.65 cm^{-1} , optical rotatory power = $386^\circ/\text{cm}$, off -Bragg parameter (ϕ) = 1cm^{-1} . The phase shift of gratings taken as (a) $\theta=\pi/2$, (b) $\theta=\pi/4$

The graphical results are represented by solving set of eight coupled wave equations by fourth-order Runge-Kutta method. The effect of off- Bragg parameter, phase shift, crystal thickness and Input beam polarization is being analyzed on the intensities and polarization of the output beams. For the case of $\pi/2$ phase shift there is unidirectional transfer of energy. We have analyzed that when phase shift is other than $\pi/2$, the energy transfer is significant for higher order on both sides of input beams. At a particular thickness we are getting output beams of a particular polarization which can be utilized for routing to different systems.

REFERENCES:

- [1] A. Roy, K. Singh, Opt. Commun. 87 (1992) 351
- [2] A. Roy, K. Singh, J. Mod. Opt. 39 (1992) 2149
- [3] A. Roy, K. Singh, J. Appl. Phys. 71 (1992) 5332
- [4] D. Gong, Z. Zhou, H. Tian, J. Zhang, Q. Meng, Opt. L. Tech. 40 (2008) 481-486

POLARIZATION SHIFT KEYING SYSTEMS

Ram Soorat, Balaji Yendeti and *Ashok Vudayagiri
School of Physics, University of Hyderabad, Hyderabad
E.mail: avsp@uohyd.ernet.in

Abstract: We build a system that can be used either as a homodyne communication system which filters out the noise in a PSK scheme or can be used to study correlation of fluctuations of noise in time domain. These studies will ensure us to give a good signal to noise ratio and also the study of correlation between fluctuation in noise in time will give information about the behaviour of noise. In a typical PSK transmission system, polarized optical signals are used as information. Due to noise during transmission, the degree of polarization is degraded. Compared to the polarized signal, optical noise is depolarized, thus, by measuring the intensity of polarized signal and unpolarized noise background, we can obtain the degree of polarization (DOP) of the signal and the relative OSNR information by the relationship. optical signal-to-noise ratio (OSNR) = $DOP/(1-DOP)$ [1, 2]. We show how signal can be obtained from the degraded signal.

1 Introduction:

In telecommunications, modulation is the process of varying a carrier signal to transmit information. In optics this carrier signal is a light beam. The physical characteristics of the signal, on which the information is modulated, can be the amplitude, the phase, the frequency, or the polarization. It is also distinguished between analog and digital transmission. Optical free space laser communications with its ability to transmit information via a collimated laser beam at high data rates using compact, low-mass terminals. Laser communications from ground suffers from cloud coverage, harsh weather conditions, and atmospheric turbulence. Most of the previous work on optical free space laser communications through the atmosphere was concentrated on intensity modulated systems. However, polarization modulated systems may be more appropriate for such communication links, because the polarization seems to be the most stable characteristic of a laser beam while propagating through the atmosphere. polarization modulated direct detection optical transmission system was researched by Betti [3], suitable for binary and multilevel transmission. The aim of my work is to build physical system for secure communication based on state of polarization. The polarization based system is composed of a transmitter which is Mach-Zehnder Interferometer. The transmitter imprints standard digital modulation techniques in optical communications polarization shift keying (PolSK) is proposed [4], where

the digital information is encoded in the state of polarization (SOP) of the launched light. The study of the vectorial nature of light has shown that a planar electro-magnetic wave is a solution to Maxwell's equations in free space. The motion of the electric field in this plane governs the polarization of the wave [5]. Starting from a linear polarized laser field, the PM (Liquid Crystal Variable Retarder) generates two orthogonal polarization states, which correspond to '1' and '0' bits.

2 Why we Need to Understand Noise

- Noise is often a limiting factor for the performance of a device or system. Examples: transmission rate of telecommunication system limited by the need to keep the bit error rate low enough. sensitivity of measurements is limited by noise.
- Efficient product development often requires
 - quantification of noise from components
 - calculation of noise effects on system performance
- Noise issues can have an important impact on system cost. Example: by choosing the right measurement scheme, which is less

sensitive to noise, one might do the job with a less costly laser system.

3 Theory

let carrier modulated signal $E_s = \epsilon_s(x\cos(\Omega t) + y\sin(\Omega t))\cos(\omega_s t + \phi)$ after liquid crystal $f(t)$ add as a noise then total signal $S = (E_s + f(t))\cos(\omega_s t + \phi)$ local oscillator signal $L = E_l \cos(\omega_l t)$ where $E_l = \epsilon_l(x + y)$

$$\begin{aligned}
 I &= |S + L|^2 \\
 I &= S^2 + L^2 + 2SL \\
 I &= (E_s + f(t))\cos(\omega_s t + \phi)^2 + E_l^2 \cos^2(\omega_l t) \\
 &+ 2(E_l \cos(\omega_l t))(E_s + f(t))\cos(\omega_s t + \phi) \\
 I &= \frac{(E_s + E_l)^2}{2} + f^2(t)(1 + \cos 2(\omega_s t + \phi))/2 \\
 &+ f(t)[E_s \cos(\omega_s t + \phi) + E_l \cos((\omega_s + \omega_l)t + \phi) + E_l \cos((\omega_s - \omega_l)t + \phi)] + E_s^2 \cos(\omega_s t + \phi)/2 + E_l^2 \cos(\omega_l t)/2 + E_l E_s \cos((\omega_s + \omega_l)t + \phi) + E_l E_s \cos((\omega_s - \omega_l)t + \phi)
 \end{aligned}$$

If we pass total Intensity I through low pass filter, $I = \frac{(E_s + E_l)^2}{2} + f^2(t) + (E_l f(t)) \cos((\omega_s - \omega_l)t + \phi) + E_l E_s \cos((\omega_s - \omega_l)t + \phi)$. when $\omega_s = \omega_l$ and $\phi = 0$, and sending the light through a polarizer we get I_x by keeping $y=0$ and I_y by keeping $x=0$.

$$I_x = \epsilon_s^2 \cos^2(\Omega t)/2 + \epsilon_l^2/2 + f^2(t) + \epsilon_l f(t) + \epsilon_s \epsilon_l \cos(\Omega t)$$

$$I_y = \epsilon_s^2 \sin^2(\Omega t)/2 + \epsilon_l^2/2 + f^2(t) + \epsilon_l f(t) + \epsilon_s \epsilon_l \sin(\Omega t)$$

$$\begin{aligned}
 I_x - I_y &= \epsilon_s^2 (\cos^2(\Omega t) - \sin^2(\Omega t))/2 + \epsilon_s \epsilon_l (\cos(\Omega t) \\
 &\quad - \sin(\Omega t))
 \end{aligned}$$

If we can use $I_x(t) + I_y(t + \tau)$, then $f^2(t)$ in above equation becomes noise correlation $\langle f(t)f(t + \tau) \rangle$

4 Experimental Setup

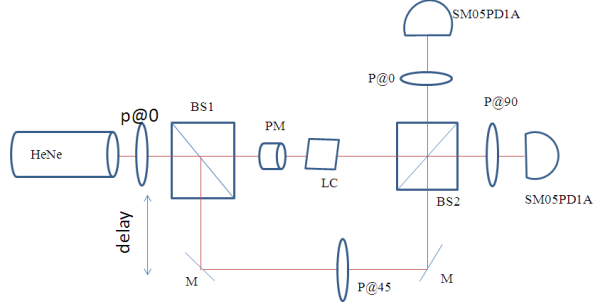


Figure. Experimental setup

4.1 Description of the experimental setup:

From He-Ne laser(632nm,5mW,Edmund optics), an un polarized laser beam would become horizontally polarized after passing through a polarizer and is sent into a beam splitter1(50:50). The transmitting beam(S-polarized) is passed through a Liquid crystal variable retarder (LCVR). A square wave of amplitude with 2 V signal at 1Hz frequency is given to LCVR to modulate the S-polarized light beam and so the polarization of the transmitting beam flips between S and P polarizations. This modulated signal is coupled at beam splitter 2 with an optical signal which got reflected from the beamsplitter1 and is made to pass through a polarizer at 45 0 to have equal amounts of S and P polarizations. This coupled optical signal will again split into two paths. The optical signal on the transmission side from the beam splitter 2 is passed through a polarizer at 00 and the signal on the reflection side from the beam splitter 2 is passed through a polarizer at 900 and the corresponding voltages are as shown in figure below. Then a liquid crystal medium(5CB) is introduced in between LCVR and beam splitter 2. This 5CB liquid crystal is in nematic phase. Because of the inhomogeneity of the domains in the liquid crystal, the state of polarization of the incoming beam should get reoriented into different state of polarization randomly

4.2 Liquid Crystal Retarder(PM):

Liquid crystal variable retarder is used to modulate the polarization of a beam, the linearly polarized input beam should be aligned so that its polarization axis is oriented at a 45 angle with respect to the optical axis of the LCVR in order to maximize the dynamic range of the optic.

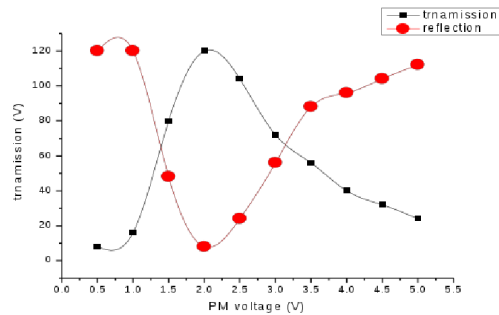


Figure2. PM applying voltage 0-2V, f=2kHz

4.3 Liquid Crystal:

A liquid crystal(5CB) in nematic phase can be used in randomly orienting the state of polarization of the optical signal. Because of the inhomogeneity of the nematic phase of the liquid crystal, it is expected to reorient the state of polarizations of the optical signal randomly and independently. So, this can be used in generating random states of polarizations in the optical signal and it becomes noise added to the optical signal .

5 Result



Figure3. Signal without LC

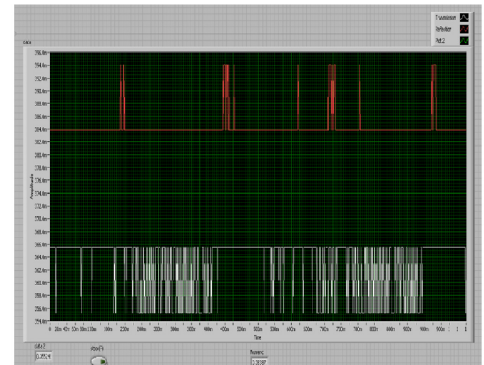


Figure4. Signal with LC

The modulated signal from the LCVR gets completely depolarized by the liquid crystal and there is no change in the intensity levels of the laser beam after passing through the liquid crystal. The state of polarization of the signal is verified by rotating the polarizers in front of the photo diodes to all angles and observed that there is no change in intensity levels. Because of the random orientations of the domains in the liquid crystal, all the states of polarizations of the optical signals gets modified and they would get depolarized.

6 conclusion

In this experimental setup, the s-Polarization of the optical signal gets modulated by the LCVR at 1HZ frequency and with an amplitude of 2V and there is a dynamic range of polarization change in both photodiodes. i.e., the modulated signal has all components of optical polarizations in the signal. But, with the introduction of 5CB liquid crystal(LC) there is clear depolarization of the modulated signal and there is no change in intensity levels of the signals on both photo diodes.

7 Future Work:

- Analyze the observed depolarization in the optical signal.
- Use these result to do polarizing shift keying.
- To find the noise correlation in the liquid crystal.
- dynamic of the LC can be understand.

Y.B thanks ACRHEM, university of Hyderabad and R S thanks RGNF for financial assistance.

References

- [1] Noise in homodyne and heterodyne detection, Horace P. Yuen , Vincent W. S. Chan , March 1983 / Vol. 8, No. 3 / OPTICS LETTERS 177
- [2] "Simultaneous Monitoring of Both Optical Signal-to-Noise Ratio and Polarization-Mode Dispersion Using Polarization Scrambling and Polarization Beam Splitting" L.-S. Yan, , X. Steve Yao, Y. Shi, Alan E. Willner, J. light wave Tech., **23** (2005)
- [3] , Polarization modulated direct detection optical transmission systems,"S. Betti, G. D. Marchis, and E. Iannone Journal of Light-wave Technology, Vol. 10, no. 12, pp. 1985-1997(1992).
- [4] " Investigation of Polarization Modulation in Optical Free Space Communications through the Atmosphere "Jasmin Grosinger Matrikelnummer 9925521 Hohe Gasse 9 7441 Pilgersdorf,
- [5] Polarization Optics in Telecommunications,J. N. Damask, ser. Springer series in optical sciences. New York: Springer Science and Business Media, Inc., Vol. 101 (2005).

High Power Mid-IR Generation using PPLN Based OPO

Rouchin Mahendra, O. P. Naraniya, Nimish Dixit, A. N. Kaul and A. K. Gupta

Photonics Division, IRDE, Raipur Road, Dehradun -248008

Email: rmahendra@irde.drdo.in

Abstract: An optical parametric oscillator (OPO) based on MgO doped periodically poled lithium niobate (MgO: PPLN) crystal was demonstrated and the results are presented in this paper. A Q-switched Nd:YVO₄ laser was used as a pump source with a wavelength of 1.064 μ m. Pump pulse duration of \approx 10 ns at a PRF of 25 kHz being used. An average idler power of \approx 1W was achieved with an idler generation efficiency of \approx 12%.

1. INTRODUCTION

Optical parametric oscillators (OPO) are a class of nonlinear optical devices that permit wavelength shifting and are particularly useful because they split the photons of an existing laser, called the pump, into two other photons at longer wavelengths. In addition, the output of an OPO is usually tunable across a much wider spectrum than traditional lasers. However, like traditional laser devices, nonlinear optical devices are limited by the properties of available materials.

In the past few years, periodically poled lithium niobate (PPLN) has drawn enormous interest as a unique material for highly efficient quasi-phase-matched (QPM) frequency conversion because of its much higher non-linearity, long interaction length, and the convenience of collinear non-critical phase-matching at arbitrary wavelengths. Indeed, the development of PPLN and the successful implementation of this material in various optical parametric oscillation (OPO) configurations, has demonstrated the potential of QPM PPLN in the realization of infrared solid-state lasers, which can be demonstrated for many applications, such as direct infrared counter measure (DIRCM), molecular analysis, material spectroscopy, remote sensing, and air pollution detection.

This nonlinear parametric generation essentially relies on phase matching i.e. photon momentum conservation. The phase matching can either be achieved by exploiting inherent birefringence of the material in which case it is termed as Birefringent Phase Matching (BPM) or by Quasi Phase Matching (QPM) [1-2] which is based on periodically reversing the nonlinear coefficient of the material. In QPM the accumulated phase mismatch is offset by modulating the second order nonlinear coefficient (d_{33}) with a period twice the coherence length [1-2]. The distinct advantages of QPM over BPM has encouraged researchers world over to develop technologies to produce periodically poled ferroelectric materials for implementation of QPM [2-4]. One of the most efficient and commonly used technique to realize QPM based devices is Electric Field poling (popularly known as E-field poling) in which a high

voltage greater than material coercive field is applied across the thickness of the crystal to periodically reverse the sign of nonlinear coefficient.

Among the commercially available ferroelectric nonlinear materials, congruent Lithium Niobate (LN) has been found to be one of the most suitable material for employing QPM owing to its high figure of merit, high value of nonlinear coefficient ($d_{33} = 27.2\text{pm/V}$), wide transparency range (0.35 to 5 μ m), large degree of homogeneity, good optical quality and mechanical robustness. Due to these advantages, researchers world wide have exploited the use of QPM based periodically poled Lithium Niobate (PPLN) for optical parametric generation experimentally [3-9]. Numerical models for optical parametric generation have also been developed. However, the performance of PPLN is limited due to the photorefractive damage that occurs at the room temperature, which therefore necessitates the heating of PPLN chip at elevated temperatures. In addition, since the coercive field of Lithium Niobate is 21.0 kV/mm, it limits poling thickness of the wafer to around 0.5 mm and also requires the application of very high voltages. However, the so far limited aperture sizes in PPLN together with its sensitivity to photorefractive damage and thermal effects, suggest that for certain applications, especially for those directed towards high power, another choice of material would be preferred. MgO: LiNbO₃ (MgLN) crystal has attractive material properties for QPM devices, due to its higher resistance against photorefractive damage, and shorter wavelength transparency compared with LN. Moreover, because of its low switching field, PPMgLN has been expected to be fairly easily fabricated by means of electric field poling. It has been experimentally established that with MgO doping in Lithium Niobate, its coercive field goes down drastically to about 4.8 KV/mm [11-12] and also there is an increase in its conductivity thereby making it less susceptible to photorefractive damage and consequently it can be used at low temperatures [11,13]. This substantial reduction in the coercive has led to the fabrication of MgO:PPLN with 3 mm and 5 mm thickness. These inherent advantages have led to immense research activity on MgO:PPLN based

OPO in recent years [14-16] and it still continues to be an area of active research.

In the present work we have demonstrated the realization of a broad tunable mid-IR OPO using MgO:PPLN chip based multi-grating with DPSS Nd:YVO₄ laser as the pump source. We have studied output signal and idler powers as a function of pump power and repetition rate for different grating periods. It was observed that with the increase in grating period there was increase in idler and signal power. Apart from this for idler wavelength above 4 μm there was significant absorption loss in the LiNbO₃. A maximum Idler power of nearly ≈1W was successfully achieved at an idler wavelength of 3.5 μm. Based on the bench top model of OPO we have fabricated the OPO-prototype with same output powers.

2. Theoretical Consideration

2.1 QPM based Optical Parametric Oscillator

For the nonlinear conversion to be efficient it is required that the relative phase of the interacting beams remains constant as they propagate through the nonlinear medium. This is generally referred to as the *phase-matching requirement*. Due to dispersion (the refractive index of the medium changes with frequency), this requirement cannot generally be satisfied in isotropic media. Therefore, nonlinear conversion devices are normally based on anisotropic materials, where phase-matching can be achieved by choosing different polarizations for the interacting waves; so-called *birefringent phase-matching*. This method of phase-matching not only restricts the number of available nonlinear materials. It also restricts the allowed propagation directions and polarizations in such a way that the resulting effective nonlinear susceptibility is generally far below the maximum value for a given material. In addition, unless phase-matching can be achieved for propagation along one of the crystal axes (so-called noncritical phase-matching), there will also be a spatial walk-off between the beam, which limit the interaction distances and tends to distort the beam profiles. Finally, even for birefringent materials, it is not always possible to achieve phase matching for a given set of pump and signal frequencies, even if these frequencies are all within the crystal's transparency range.

A solution to these problems is to employ so-called quasi-phase-matching (QPM). In QPM-devices it is common to choose a beam propagation direction in the crystal, as well as polarizations, which lead to maximum nonlinear susceptibility and zero walk-off. In a normal nonlinear material, this would mean that the phase-matching condition could not be satisfied, and the energy would be transferred periodically forth and back between the pump and the signals

through the crystal, with a resulting negligible energy conversion. The trick played in QPM-devices is to invert the crystal orientation for every half-period of these oscillations. This is equivalent to changing the sign of the nonlinear susceptibility for every half-period, or, equivalently, to change the phase in the driving term in the coupled wave equations by π . The net effect is that the energy transfer oscillations are rectified, such that energy is always transferred from the pump to the signals in all half-periods.

For efficient quasi-phase matched OPO operation, the output wavelengths were decided by the energy conservation and phase matching conditions.

$$\frac{1}{\lambda_p} = \frac{1}{\lambda_s} + \frac{1}{\lambda_i} \quad (1)$$

$$\Delta k = 2\pi \left(\frac{n_p}{\lambda_p} - \frac{n_s}{\lambda_s} - \frac{n_i}{\lambda_i} - \frac{1}{\Lambda} \right) = 0 \quad (2)$$

where Δk is the phase mismatching and must be zero for efficient OPO operation; λ_p , λ_s and λ_i are the pump, signal and idler wavelengths, n_p , n_s and n_i are extraordinary refractive indices at pump, signal and idler wavelengths respectively and Λ is the QPM period or domain grating period. It can be seen from Eqn (2) that any wavelength within the transparency range of the material can be generated by suitably tailoring the grating period for a particular pump wavelength. These two equations can easily be solved by using temperature dependent Sellmeier equations [16] and the grating period required for a particular wavelength generation can be estimated. The appearance of the red light (SFG) during the parametric generation can be explained with the help of following equation:

$$\frac{1}{\lambda_{SFG}} = \frac{1}{\lambda_p} + \frac{1}{\lambda_s} \quad (3)$$

As mentioned this is basically due to the sum frequency generation (SFG) between the pump and the signal beams.

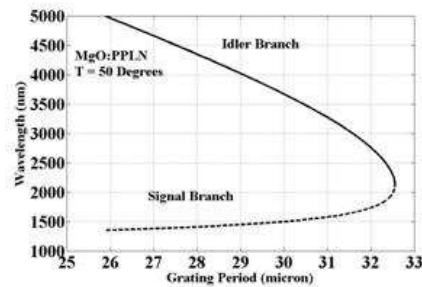


Fig.1. Tuning curve for Multigrating MgO:PPLN

As depicted Fig.1, the wavelength tuning curve of this multi-grating PPLN chip can be obtained by

solving Eqns (1) and (2) in tandem with temperature dependent Sellmeier equations. Further, it can be seen that by varying periods from 26 to 31.5 μm , the signal wavelength can be tuned from 1.37 to 1.64 μm with corresponding idler from 3.0 to 4.8 μm .

2.2 Experimental Set-up

The pump beam from a Q-switched 1064nm Diode pumped solid state (DPSS) Nd: YVO₄ laser was focused into MgO: PPLN with a pulse width of $\approx 10\text{ns}$ and PRF of 25KHz.

As shown in Fig.2, We have used a 5cm long MgO: PPLN crystal for parametric generation. The crystal was placed at the center of a resonant cavity with a cavity length of 9cm. A pair of dichoric plano-concave mirrors is used as input and output couplers. A singly resonant linear cavity configuration has been chosen for our OPO set-up. The input cavity mirror M₁ with a 200mm radius of curvature has been used for obtaining high transmission ($> 90\%$) for 1.064 μm pump and high reflection ($>97\%$) for the signal beam in the spectral range of 1.37-1.64 μm . The output cavity mirror M₂ also having a 200mm radius of curvature offers a partial transmission (50-75%) for the signal and a very high transmission for both pump ($>90\%$) & idler ($>90\%$) beams respectively. It is evident that the signal is resonating in the OPO and the idler is automatically generated due to the energy conservation requirements. In principle, there are two reasons behind resonating signal; first it is easier to make sure a good overlap of pump and signal as compared to that with idler; second the wavelength variation in signal is 0.6 μm (1.3–1.9 μm) in contrast to that nearly 3.0 μm (2–5 μm) for idler leading to easier mirror coatings. We have designed and used input optics to achieve optimized pump beam waist for the maximum conversion efficiency. The Ge filter with suitable AR coating was used to filter out undesired signal and pump. The tunable output wavelength of the OPO has been generated by precisely scanning the edge of the multi-grating MgO:PPLN chip with respect to the input pump beam. An average idler power of $\approx 1\text{W}$ was achieved with an idler efficiency of $\approx 12\%$.

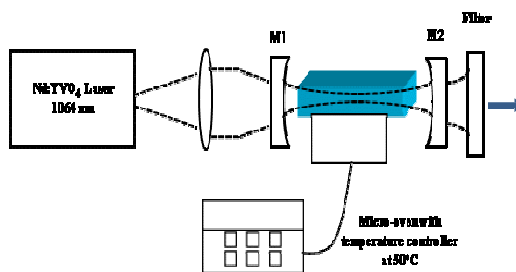


Fig.2. Experimental setup for tunable MgO:PPLN-OPO

3. RESULTS AND DISCUSSION

In the present work we have demonstrated the realization of a broad tunable mid-IR OPO using MgO:PPLN chip based multi-grating with DPSS Nd:YVO₄ laser as the pump source. Based on the bench top model of OPO we have fabricated the OPO-prototype with same output powers. Our objective here was to generate an Idler power of $\approx 1\text{W}$. We have studied output signal and idler powers as a function of pump power & repetition rate for different grating periods. It was observed that with the increase in grating period there was increase in idler and signal power. There was also a decrease in output power beyond 30.5 μm grating period as shown in Fig.3. Theoretically there should be increase in the output power with increase in grating period which is inconsistent with the result, which may be because of difference of coating at different wavelengths and the incompleteness of the domain structure at the corresponding periods. A maximum Idler power of nearly $\approx 1\text{W}$ was successfully achieved at an idler wavelength of 3.5 μm .

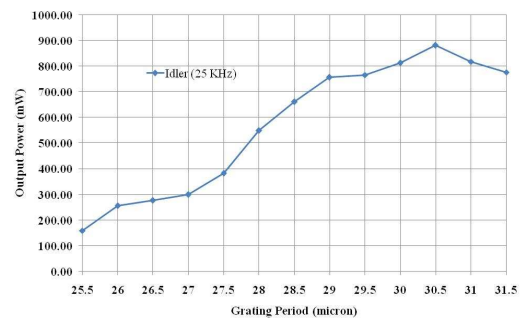


Fig.3. Idler power with variation in grating period

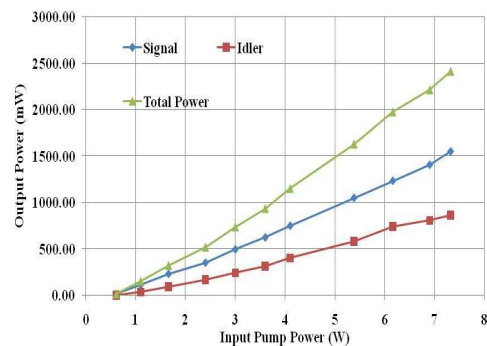


Fig.4. Output power at a grating period of 30.5 μm

Fig. 4 shows the output power dependence of the developed parametric oscillator on the input power for 30.5 μm grating period. A maximum output power of $\approx 2.5\text{W}$ (including the signal and the idler light) was obtained when the input pumping power was 7.32 W. Fig.5. shows that an idler efficiency of

Topic: NQO

12% was achieved with an optic-optic conversion efficiency of 35%.

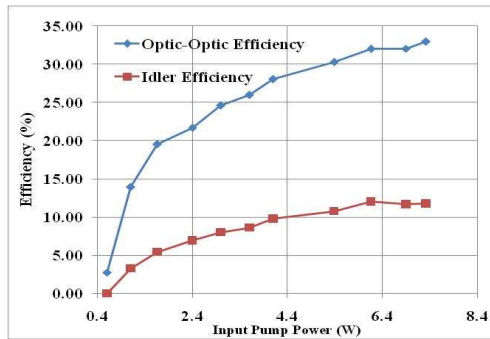


Fig.5. Conversion efficiency variation as a function of input pump power for grating period of 30.5 μ m

An average idler power of ≈ 1 W was achieved on the OPO-prototype with an idler efficiency of $\approx 12\%$.

ACKNOWLEDGEMENT

The authors wish to acknowledge Director, IRDE for granting his permission to publish this paper.

REFERENCES

- [1] J. A. Armstrong, N. Bloembergen, J. Ducuing, P. S. Pershan, "Interactions between light waves in a nonlinear dielectric." *Phys. Rev.* **127**, 1918-1939, (1962).
- [2] M. M. Fejer, G. A. Magel, D. H. Jundt, R. L. Byer, "Quasiphasematched second harmonic generation: Tuning and tolerances." *IEEE J. Quantum. Electron.* **28**, 2631-2654, (1992).
- [3] L. E. Myers, R. C. Eckardt, M. M. Fejer, R. L. Byer, W. R. Bosenberg, Progress in quasi-phase matched optical parametric oscillators using periodically poled LiNbO₃, *SPIE Proc.*, **2700**, 216-224, (1996).
- [4] L. E. Myers, R. C. Eckardt, M. M. Fejer, R. L. Byer, W. R. Bosenberg, J. W. Pierce, "Quasi-phase-matched optical parametric oscillators in bulk periodically poled LiNbO₃." *J. Opt. Soc. Am. B*, **12**, 2102-16, (1995).
- [5] S. Sanders, R. J. Lang, L. E. Myers, M. M. Fejer, R. L. Byer, "Broadly tunable mid-IR radiation source based on difference frequency mixing of high power wavelength-tunable laser diodes in bulk periodically poled LiNbO₃." *Electron Lett.*, **32**, 218-219, (1996).
- [6] L. E. Myers, R. C. Eckardt, M. M. Fejer, R. L. Byer, W. R. Bosenberg, Multigrating quasi-phase-matched optical parametric oscillator in periodically poled LiNbO₃, *Opt. Lett.*, **21**, 591-593, (1996).
- [7] Chih-Wei Hsu, C. C. Yang, "Broadband infrared generation with noncollinear optical parametric processes on periodically poled LiNbO₃." *Opt. Lett.*, **26**, 1412-14, (2001).
- [8] U. Bader, T. Mattern, T. Bauer, J. Bartschke, M. Rahm, A. Borsutzky, R. Wallenstein, "Pulsed nanosecond optical parametric generator based on periodically poled lithium niobate." *Opt. Commun.*, **217**, 375-380, (2003).
- [9] Pu Zhao, B. Zhang, Enbang Li, Rui Zhou, Degang Xu, Yang Lu, Tieli Zhang, Feng Ji, Xueyu Zhu, Peng Wang, Jianquan Yao, "Experimental study on a high conversion efficiency, low threshold, high-repetition-rate periodically poled lithium niobate optical parametric generator." *Opt. Exp.*, **14**, 7224-29, (2006).
- [10] A. V. Smith, Russel J. Gehr, Mark S. Bowers, "Numerical models of broadband nanosecond optical parametric oscillators." *J. Opt. Soc. Am. B*, **16**, 609-619, (1999).
- [11] A. Kuroda, S. Kurimura, "Domain inversion in ferroelectric MgO:LiNbO₃ by applying electric fields." *Appl. Phys. Lett.*, **69**, 1565-67, (1996).
- [12] H. Ishizuki, I. Shoji, T. Taira, "Periodical poling characteristics of congruent MgO:LiNbO₃ crystals at elevated temperature." *Appl. Phys. Lett.*, **82**, 4062-4064, (2003).
- [13] D. A. Bryan, R. Gerson, H. E. Tomaschke, "Increased optical damage resistance in lithium niobate." *Appl. Phys. Lett.*, **44**, 847-49, (1984).
- [14] H. Ishizuki, I. Shoji, T. Taira, "High-energy quasi-phase-matched optical parametric oscillation in a 3-mm-thick periodically poled MgO:LiNbO₃ device." *Opt. Lett.*, **29**, 2527-29, (2004).
- [15] Markku Vainio, Jari Peltola, Stefan Persijn, Frans J. M. Harren, Lauri Halonen, "Singly resonant cw OPO with simple wavelength tuning." *Opt. Exp.*, **16**, 11141-46, (2008).
- [16] D. H. Jundt, "Infrared corrected Sellmeier coefficients for congruently grown lithium niobate and 5 mol % magnesium oxide-doped lithium niobate." *J. Opt. Soc. Am. B.*, **14**, 3319-22, (1997).

MODULATIONAL INSTABILITY IN AN OPTICAL FIBER WITH VARYING DISPERSION AND NONLINEARITY DRIVEN BY AN EXTERNAL POTENTIAL

A.Uthayakumar, A.Mahalingam* and Rajapriya*.

Department of Physics, Presidency College, Chennai – 600 005,

*Department of Physics, Anna University, Chennai – 600 025.

uthayk@yahoo.com.

Abstract : We consider the nonlinear pulse propagation through inhomogeneous optical fiber, which is described by a system of generalized inhomogeneous nonlinear Schrodinger equation. We obtained modulational instability gain through linear stability analysis. The gain spectrum is analysed for the various choices of variable group velocity dispersion and nonlinearity parameters.

1. INTRODUCTON

When a nonlinear optical pulse propagates in a nonlinear optical fiber, there is an interplay between linear effects (group velocity dispersion) and nonlinear effects (self phase modulation) leading to many interesting phenomena like modulational instability (MI), optical soliton, pulse compression, etc. The MI in optical fibers was predicted by Hasegawa and Brinkman [1] and experimentally demonstrated by Tai *et al* [2]. Of particular interest in optical communication is the case of dispersion and nonlinearity managed systems, wherein both dispersion as well as the nonlinearity is assumed to be inhomogeneous, because of its role which could be either beneficial leading to solitons or detrimental causing the breakup of the pulse [3]. Either way, MI is an important phenomenon that should be analysed because it would give the conditions under which a weak perturbation would be amplified as there will be an enhancement in gain in certain frequency range. From a practical standpoint, modulation instability is useful for generating a train of short pulses whose repetition rate can be externally controlled. This technique has been used to create optical sources capable of producing periodic trains of ultrashort pulses at repetition rates higher than those attainable from mode locked lasers.

2. THEORETICAL MODEL

In this present work, we consider phenomena of MI in an inhomogeneous fiber with varying dispersion and nonlinearity driven by external potential which is governed by inhomogeneous NLS equation of the following form [4]

$$i \frac{\partial q}{\partial z} + \frac{\partial^2 q}{\partial t^2} + R(z) |q|^2 q + F_1(z, t) q + F_2(z) q = 0 \tag{1}$$

where $F_1(z, t) = -(2t\alpha + \frac{t^2}{2} \frac{\partial \theta}{\partial z} + \frac{D(z)}{2} (i\theta^2 - t^2 \theta^2))$

$$F_2(z) = \frac{1}{2} \left(\frac{1}{R(z)} \frac{\partial R(z)}{\partial z} - \frac{1}{D(z)} \frac{\partial D(z)}{\partial z} \right)$$

$$\theta(z) = \frac{W[R(z), D(z)]}{D(z)R(z)^2}$$

with $W[R(z)D(z)] = R(z)D_2 - D(z)R_2$

where, $q(z, t)$ is the complex envelope of the field, $D(z)$ represents GVD function, $R(z)$ is the nonlinearity management function, $F_1(z, t)$ is related to time-dependent phase modulation, $F_2(z)$ is loss or gain.

3. LINEAR STABILITY ANALYSIS

To examine the onset of MI, we consider the steady state solutions of Eq. (1) in the following form [5]

$$q(z, t) = \sqrt{P_0} e^{i\phi(z)}$$

where P_0 is the initial input power and $\phi(z)$ is the nonlinear phase shift induced by self phase modulation $\phi(z) = P_0 R(z) z$. To analyse whether the steady state solution is stable against small perturbations, we perturb the steady state slightly such that

$$q(z, t) = (\sqrt{P_0} + a_1(z, t)) e^{i\phi(z)} \tag{2}$$

where the complex field $|a_1(z, t)| \ll 1$. Thus, if the perturbed field grows exponentially, the steady state becomes unstable. The evolution of the perturbation $a_1(z, t)$ is examined using a linear stability analysis. Substituting Eq. (2) in Eq. (1) and linearizing in a_1 , we obtain

$$\frac{\partial a_1}{\partial z} = - \frac{D(z)}{2} \frac{\partial^2 a_1}{\partial t^2} + a_1 p_0 z \frac{\partial R(z)}{\partial z} \tag{3}$$

$$- R(z) p_0 (a_1 + a_1^*) - F_1(z, t) a_1 - F_2(z) a_1$$

Eq.(3) can be solved easily in the frequency domain. However, because of the a^* term, the Fourier components at frequencies Ω and $-\Omega$ are coupled. Thus, its solution is considered in the form

$$a_1(z, t) = u_1 \cos(Kz - \Omega t) + i v_1 \sin(Kz - \Omega t) \tag{4}$$

and u_1, v_1 are real amplitudes of infinitesimal perturbation, Ω is an arbitrary real frequency of the perturbation and K the respective wave number. Inserting Eq. (4) in Eq.(3), we obtain the dispersion relation as

$$\begin{aligned}
 K = & \pm \left(\frac{1}{4} \Omega^4 D(z)^2 - \Omega^2 D(z) F_1(z, t) + F_1(z, t)^2 \right. \\
 & - \Omega^2 D(z) F_2(z) + F_2(z)^2 + 2 F_1(z, t) F_2(z) \\
 & - P_0 \Omega^2 D(z) R(z) + 2 P_0 F_1(z, t) R(z) + 2 P_0 F_2(z) R(z) \\
 & + P_0 \Omega^2 D(z) \frac{\partial R(z)}{\partial z} - 2 P_0 z F_1(z, t) \frac{\partial R(z)}{\partial z} \\
 & - 2 P_0 z F_2(z) \frac{\partial R(z)}{\partial z} - 2 P_0^2 z R(z) \frac{\partial R(z)}{\partial z} \\
 & \left. + P_0^2 z^2 \left(\frac{\partial R(z)}{\partial z} \right)^2 \right)^{\frac{1}{2}} \quad (5)
 \end{aligned}$$

The steady state solution becomes unstable whenever K has an imaginary part since the perturbation then grows exponentially with intensity given by the growth rate or the MI gain spectrum is given by

$$G(\Omega) = 2|\text{Im}(K)| \quad (6)$$

Investigation of MI in a fiber with periodically modulated dispersion and nonlinearity is of great interest in recent years [6,7]. Therefore, using Eq. (5), we have analysed the MI gain spectrum for the various choices of dispersion and nonlinear functions.

4. RESULTS AND DISCUSSION

From Eq. (5), the parameters that govern the growth of the instability are $D(z)$, $R(z)$, gain or loss and initial power. Therefore, we study the MI spectra for two choices of dispersion and nonlinearity parameters.

4.1. Case(i)

The GVD and the nonlinearity functions are distributed in the form given as follows

$$D(z) = d_1 \exp(-g_1 z), R(z) = r_1 \exp(-k_1 z) \quad (7)$$

where d_1 and g_1 related to GVD and r_1 and k_1 are the nonlinear parameters. The above case is used to show pulse compression in Ref.[8]. The MI gain spectrum for Eq. (7) is shown in Fig. 1 (a-d)

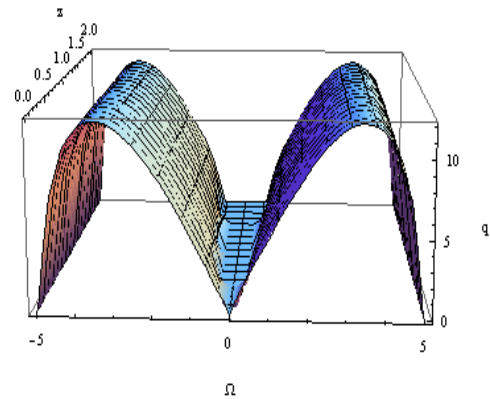


Fig 1.(a) MI gain for the frequency Ω and the propagation distance z for normalized values of $p_0=6, \alpha=0.35, t=0.05, d_1=r_1=1, g_1=0.35, k_1=0.025$ (b) for $F1 = F2 = 0$

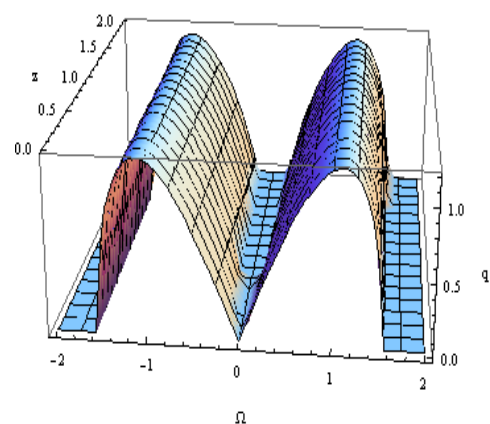
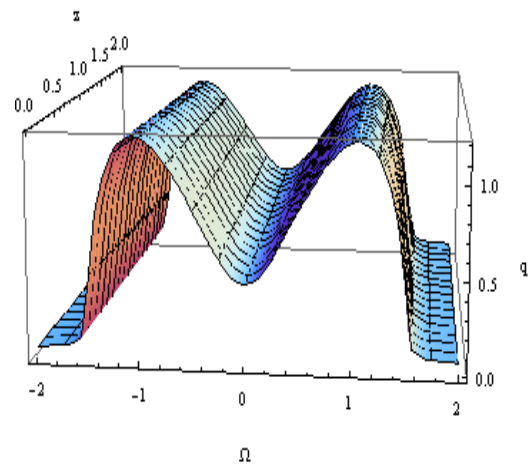


Fig 1.(c) MI gain for the frequency Ω and the propagation distance z for normalized values of $p_0 = 0.6, \alpha=0.35, t=0.05, d_1=r_1=1, g_1=0.35, k_1=0.025$, (d) for $F1=F2=0$.

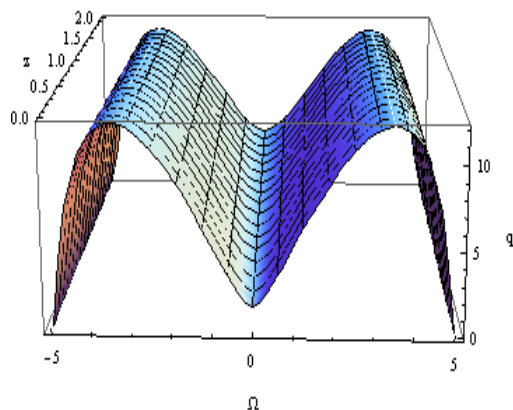


Fig1.(a) shows the evolution of the MI gain spectra for propagation distance with constant

power $P_0=6$. We obtain the gain spectrum which consists of two symmetric side bands corresponding to Stokes and anti-Stokes lines. It is seen that there is an appreciable MI gain for even $\Omega=0$ due to the presence of gain term in Eq. (1). From the figure 1 (b) it is clearly seen that in the absence of the gain term MI gain becomes zero at $\Omega=0$ and it is also observed that the space between the side bands increases as z increases. Further we analysed the influence of initial input power on MI gain spectrum. It is seen that the MI gain decreases as the initial power decreases and also there is a shrink in the MI gain spectrum as shown in figure 1(c). Similar result is obtained for $F_1=F_2=0$ which is shown in Fig. 1 (d).

4.2 Case(ii)

Recently in Ref. [9], a particular type of soliton namely boomerang soliton propagation in an inhomogeneous optical fiber has been discussed for the choice of GVD and nonlinearity parameters as

$$D(z) = R(z)=a+bz \tag{8}$$

where a and b are constants. We plotted the MI gain spectrum with choice Eq.(8) as shown in Fig. 2 (a-d)

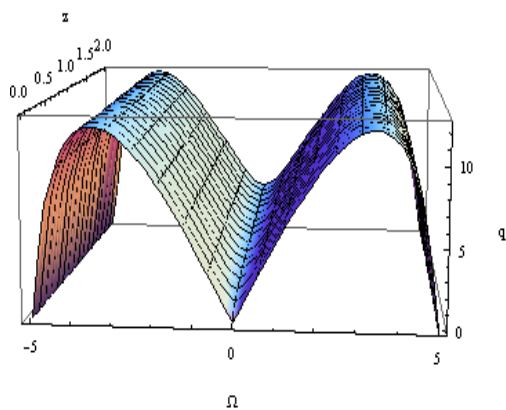
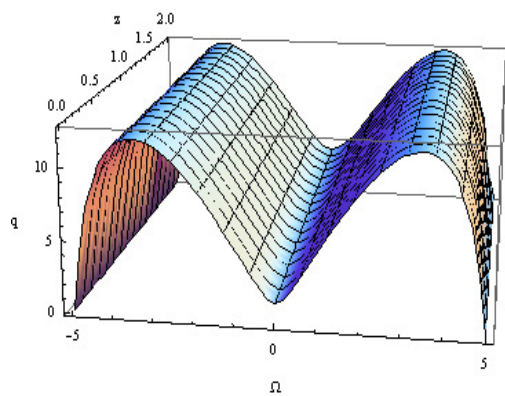
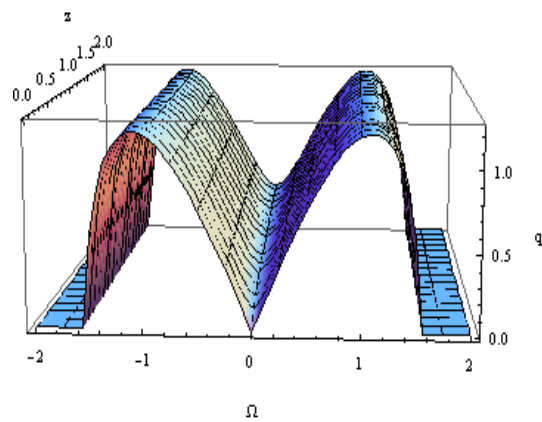
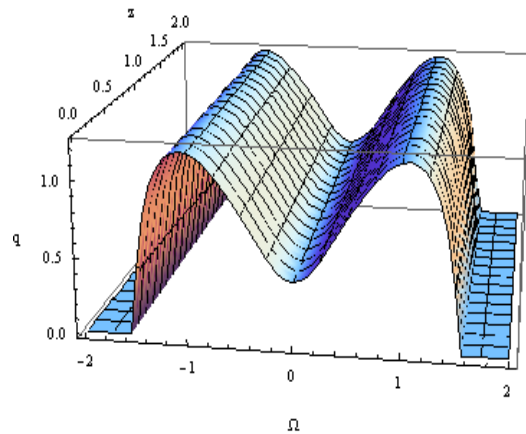


Fig.2.MI spectrum for the parameters (a) $p_0=6, a=1, b=0.02, \alpha=0.35, t=0.05$, (b) for $F_1 = F_2 = 0$.



(c) $p_0 = 0.6, \alpha=0.35, t=0.05, a=1, b=0.02$. (d) for $F_1 = F_2 = 0$.

From the Fig. 2 (a) and (c) it is clear that the gain spectrum strongly depends on the input power P_0 . Further we have analysed the role of gain term on MI by plotting MI gain spectrum without loss/gain and phase terms as shown in Fig. 2 (b) and (d). Here also we found that like case (i), the MI gain vanishes at $\Omega=0$.

It is noteworthy to mention that if we choose $D(z) = R(z)= \text{constant}$ and $F_1=F_2=0$, then the dispersion relation (5) reduces to dispersion relation for homogeneous NLS equation given by Agarwal [6] which validates our analysis.

5. CONCLUSION

We have investigated the properties of MI of a pulse propagating in an inhomogeneous fiber which is modeled by GINLS equation. The associated MI gain is obtained through linear stability analysis. We studied the influence of variable GVD, nonlinearity and gain parameters on MI gain for two particular choices. We found that like homogeneous fibers, the MI gain spectrum strongly depends on GVD, nonlinearity and gain parameters.

Our analysis will be helpful for generation of solitons and controlling instabilities with the magnitude of the variable parameters.

ACKNOWLEDGEMENT

The authors A.U and A.M would like to thank Department of Science and Technology for their financial assistance through major research projects.

REFERENCES

- [1] A. Hasegawa and W. F.Brinkman, IEEE, J. Quan. Elect. **16**, 694, 1980.
- [2] K .Tai, A .Hasegawa and A .Tomita, Phys. Rev. Lett. **56**, 135, 1986.
- [3] M. Nakazawa, K. Suzuki, E. Yamada, Y. Kimura, Electron. Lett. 34, 103 (1998).
- [4] Serkin V.N. and Hasegawa A., J. Sel. Topics Quantum Electron. **8**, 418 (2002).
- [5] G.P.Agarwal, Nonlinear Fiber Optics, Academic Press, Boston, 1989.
- [6] Ajit Kumar, A. Labruyere, P. Tchofo Dinda, Optics Comm., 219, 221–232 (2003).
- [7] F.Kh. Abdullaev, S.A. Darmany, S. Bischoff, M.P. Sorensen, J. Opt. Soc. Am. B **14**, 27 (1997).
- [8] T. Soloman Raju, Prasanta K. Panigrahi and K.Porsezian, Phys. Rev. E, 71, 026608, 2005.
- [9] A.Mahalngam, K.Porsezian, M.S.Manirajan. A.Uthayakumar, J. Phys. A, **42**,165101, 2009.

PROPAGATION OF TWO SOLITON IN AN ERBIUM DOPED INHOMOGENEOUS LOSSY FIBER WITH PHASE MODULATION

A.Mahalingam, M.S.Manirajan⁺ and A.Uthayakummar*.

Department of Physics, Anna University, Chennai – 600 025.

⁺Department of Physics, Anna university of Technology, Madurai.

Department of Physics, Presidency College, Chennai – 600 005.

mahabs22@yahoo.com

Abstract : In this work we investigate a system of Generalized Inhomogeneous Nonlinear Schrödinger Maxwell-Block (GINLS-MB) equation which explains the optical pulse propagation in an Erbium doped inhomogeneous lossy optical fiber with time dependent phase modulation. We obtain two-soliton solution by means of Darboux transformation through Lax pair. We analyse periodic distributed amplification in fiber and explain the soliton control by suitable choices of the various inhomogeneous parameters.

1. INTRODUCTON

Fiber optic communication has revolutionized the long distance communication by enormously increasing bit rate and band width. The problems of optical fiber communications like dispersion and fiber loss require use of repeaters increasing the noise content and cost. Optical solitons are the promising candidature to address above problems. In a fiber, optical solitons are formed by exact balance between the Group Velocity Dispersion (GVD) and the Self Phase Modulation (SPM). Optical soliton propagation in an ideal fiber governed by Nonlinear Schrodinger (NLS) equation has been investigated by many authors [1-3]. In a real fiber, due to various reasons such as impurities, fiber geometry deviation, density fluctuations soliton propagation will be affected. Therefore it is essential to consider such inhomogeneties which are governed by inhomogenous NLS (INLS) equations. There is another kind of lossless propagation which is known as Self Induced Transparency (SIT) which is described by Maxwell-Bloch (MB) equations which occurs in two level resonant media such as Erbium (Er). Now a days, Er is doped in optical fibers to provide amplification of signals as the electronic amplifiers in repeaters create noises degrading the signal quality. When the core of the optical fiber is doped with erbium, the wave propagation has both effects due to silica and Er impurities. Er impurities are responsible for the Self-Induced Transparency (SIT) effect to the optical pulse whereas the silica waveguide gives the NLS soliton effect and the corresponding governing equations are called as NLS-MB equations [4].

2. THEORETICAL MODEL

Here, optical pulse propagation in an inhomogenous lossy fiber doped with Er atoms affected by a time dependent phase modulation

which is governed by Generalised inhomogeneous nonlinear Schrodinger – Maxwell Bloch (GINLS-MB) system is considered [5]:

$$iQ_z + \frac{D(z)}{2}Q_z + R(z)|Q|^2Q + F_1(z,t)Q + F_2(z,t)Q - 2i < p > = 0$$

$$p_t = ip[2\omega - t\theta] + 2Q\eta$$

$$\eta_t = -\frac{R(z)}{D(z)}(p^*Q + pQ^*)$$

(1)

where $Q(z, t)$ is the complex envelope of the field, $p(z, t)$ is the measure of the polarization of the resonant medium and $\eta(z, t)$ denotes the extent of the population inversion. $D(z)$ represents the GVD function and $R(z)$ is the nonlinearity function.

3. LAX PAIR

To obtain Lax pair of Eq. (1), we construct the linear eigen value problem of Eq. (1) is given by [6]

$$\psi_t = U\psi, \quad \psi_z = V\psi \quad (2)$$

where U and V are given by

$$U = -i\lambda J + P$$

$$V = \lambda^2 D(z)J + \lambda(z)D(z)P + iR + iT$$

where

$$J = -i \begin{pmatrix} 1 & 0 \\ 0 & -1 \end{pmatrix}, \quad P = \begin{pmatrix} 0 & q \\ q^* & 0 \end{pmatrix}$$

$$R = i \begin{pmatrix} \frac{1}{2} D q q^* - \alpha(z)t & D \left(\frac{1}{2} q_t - i\theta t q \right) \\ D \left(\frac{1}{2} q_t^* + i\theta t q^* \right) & -\frac{1}{2} D q q^* + \alpha(z)t \end{pmatrix}$$

$$T = \frac{i}{(\lambda + \omega)} \begin{pmatrix} \eta & -p' \\ -p^* & -\eta \end{pmatrix}$$

with the transformation

$$q(z, t) = \sqrt{\frac{R}{D}} Q(z, t) \exp\left(\frac{1}{2}(it^2 \theta)\right)$$

$$p'(z, t) = \sqrt{\frac{R}{D}} p(z, t) \exp\left(\frac{1}{2}(it^2 \theta)\right) \quad (3)$$

Eq. (1) can be obtained from the compatibility condition $U_z + V_t - [U, V] = 0$ and this condition is satisfied by considering the flow to be non-isospectral as given below:

$$\lambda = e^{\int_0^z D(z') \theta(z') dz'} (\lambda(0) + \int_0^z e^{-\int_0^{z'} D(z'') \theta(z'') dz''} \alpha(z') dz') \quad (4)$$

4. DARBOUX TRANSFORMATION AND TWO SOLITON SOLUTION

The two soliton solution of Eq.(1) is obtained by using Darboux transformation [7]

$$\psi [1] = (\lambda I - S) \psi$$

$$S = H \Lambda H^{-1} \quad (5)$$

$$\Lambda = \text{diag} (\Lambda_1, \Lambda_2) \quad (6)$$

where H is the non singular matrix, requiring

$$H = \begin{pmatrix} \phi_1 & -\phi_2^* \\ \phi_2 & \phi_1^* \end{pmatrix}, \Lambda = \begin{pmatrix} \lambda_1 & 0 \\ 0 & -\lambda_1^* \end{pmatrix}$$

$$\Psi_1[1] = U_1 \Psi_1[1] \quad (11)$$

where $U_1 = \lambda J + P_1$ with

$$P_1 = \begin{pmatrix} 0 & q_1 \\ q_1^* & 0 \end{pmatrix} \quad (7)$$

We can get the Darboux Transformation for Eq. (1) in the following form,

$$P_1 = P + JS - SJ \quad (8)$$

It is easy to verify that if $(\phi_1, \phi_2)^T$ is a solution of Eq. (2) which is corresponding to the eigenvalue λ_1 , then $(-\phi_2^*, \phi_1^*)^T$ is also a solution of Eq. (2) which is corresponding to the eigenvalue $-\lambda_1^*$. Now we take

$$J = \begin{pmatrix} 1 & 0 \\ 0 & -1 \end{pmatrix}$$

Hence the basic format of S_{ij} is represented through Eq.(9) as

$$S_{ij} = -i \lambda_1^* \delta_{ij} - \frac{i(\lambda_1 + \lambda_1^*) \phi_i \phi_j^*}{\Delta} \quad (9)$$

$$\Delta = |\phi_1|^2 + |\phi_2|^2$$

Comparing Eq. (7) and (8), we can get the relation between q_1 and q_1^* as

$$q_1 = q - 2\sqrt{\frac{D}{R}} S_{12}$$

$$q_1^* = q^* - 2\sqrt{\frac{D}{R}} S_{21} \quad (10)$$

Hence the basic form of Darboux transformation for N -soliton solution is,

$$q_n = q + 2\sqrt{\frac{D}{R}} \sum \frac{(\lambda_m + \lambda_m^*) \phi_{1,m}(\lambda_m) \phi_{2,m}^*(\lambda_m)}{A_m}$$

where (11)

$$\phi_{k,m+1}(\lambda_{m+1}) = (\lambda_{m+1} + \lambda_m^*) \phi_{k,m}(\lambda_{m+1}) - \frac{B_m}{A_m} (\lambda_m + \lambda_m^*) \phi_{k,m}(\lambda_m)$$

$$A_m = |\phi_{1,m}(\lambda_m)|^2 + |\phi_{2,m}(\lambda_m)|^2$$

$$B_m = \phi_{1,m}(\lambda_{m+1}) \phi_{1,m}^*(\lambda_m) + \phi_{2,m}(\lambda_{m+1}) \phi_{2,m}^*(\lambda_m)$$

where $k=1, 2 \dots n$, $m=1, 2 \dots n$ and $((\phi_{1,1}(\lambda_1), \phi_{2,1}(\lambda_1))^T$ is the eigen function of Eq. (4)

corresponding to λ_1 . Substituting $q = 0$ in Eq. (11), one can get one-soliton solution for Eq. (1). Using the one-soliton solution as the seed solution in Eq. (11), we can derive the two-soliton solution. Thus in recursion, one can generate up to N -soliton solution. Here we present the one and two-soliton solutions in explicit forms.

$$Q(z, t) = Q_1 + 2\sqrt{\frac{D}{R}} (\alpha_1 \exp(i \beta_1) \text{sech}(2A_1) + 2\alpha_2 \frac{G}{F}) \quad (12)$$

$$G = -e^{-2(iB_2 + A_1 + A_2)} ((e^{2iB_2 + 2A_1} - e^{2iB_2} + e^{2(iB_1 + A_1 + A_2)}) \text{sech}(2A_1) \alpha_1 + e^{2iB_2 + 2A_1} (\alpha_2 + i(\beta_1 - \beta_2)) (e^{2iB_1} \text{sech}(2A_1) \alpha_1 + e^{2iB_2 + 2A_2} (-\alpha_2 + i(\beta_1 - \beta_2) + \alpha_1 \tanh(2A_1)))$$

$$F = 2(\cosh(2A_2) \alpha_1^2 + (-2 \cos(2(\beta_1 - \beta_2)) + \cosh(2(A_1 - A_2)) - \cosh(2(A_1 + A_2))) \text{sech}(2A_1) \alpha_1 \alpha_2 + \cosh(2A_2) (\alpha_2^2 + (\beta_1 - \beta_2)^2))$$

$$A_2 = \int \beta_2 D(z) \theta(z) t dz - \int 2\alpha_2 \beta_2 D(z) dz - \int \frac{\beta_2}{\beta_2^2 + (\alpha_2 + \omega_2)^2} dz - \beta_2 t$$

$$B_2 = (\int \alpha_2^2 D(z) dz - \int \beta_2^2 D(z) dz - \int \alpha_2 D(z) \theta(z) t dz + \int \frac{\alpha_2}{\beta_2^2 + (\alpha_2 + \omega_2)^2} dz + \int \frac{\omega_2}{\beta_2^2 + (\alpha_2 + \omega_2)^2} dz - \alpha_2 t) + \frac{1}{2} \theta(z) t^2$$

5. RESULTS AND DISCUSSIONS

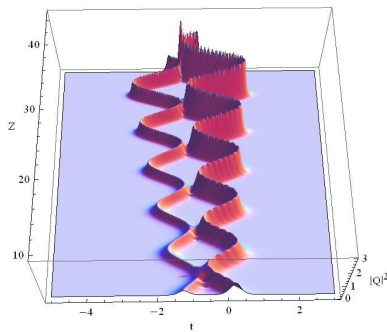
The distributed amplification is considered to be superior than the lumped amplification as the former provides amplification locally at each point along the length of the fiber. We have analysed two-soliton solution for a periodic distributed amplification system by choosing dispersion and nonlinearity parameters as [7]

$$D(z) = \frac{1}{d_0} \exp(kz) R(z)$$

$$R(z) = R_0 + R_1 \sin(gz) \tag{13}$$

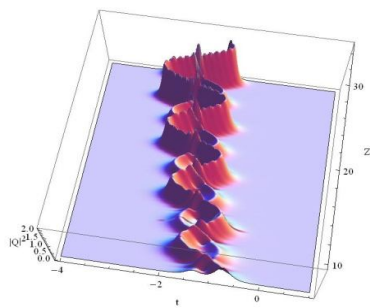
Case I : $k > 0$

When $k > 0$, the dispersion of the fiber increases as it is clearly evident from Eq. (13), which results in broadening of the pulse. When $k > 0$ the pulse intensity will increase while the pulse width will broaden and compress periodically along the propagating distance. It can be clearly seen in the below Fig. 1(a) and 1(b). Also, we can see from the Figures that the pulse positions change due to the combined effects of the varying group velocity dispersion and the varying nonlinearity coefficients.



1(a)

Fig. 1(a) Two soliton solution with $\omega_1=6.7$, $\omega_2=0.5$, $\alpha_1 = -0.12$, $\alpha_2 = 0.18$, $\beta_1=0.5$ and $\beta_2=-1$



1(c)

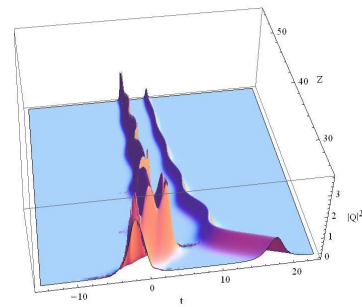
Fig. 1(c) Two soliton solution with $\omega_1=6.7$, $\omega_2=0.5$, $\alpha_1 = -0.12$, $\alpha_2 = 0.18$, $\beta_1=0.5$ and $\beta_2=-1$.

For this case, the gain/loss coefficient will become positive which corresponds to gain in the fibre and the pulse intensity will increase along the propagating distance, which is evident from the

above figures 1(a) and 1(b). Here also in the absence of the MB term there is no phase shift.

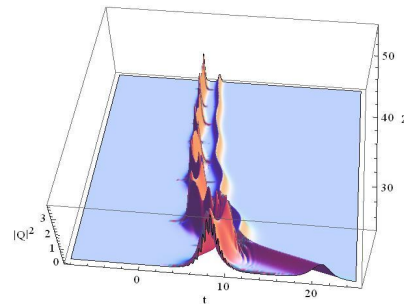
Case 3: $k < 0$

For this case, the gain/loss coefficient will become negative which corresponds to loss and the pulse intensity will decrease along the propagating distance, which is evident from the above figures 1(c) and 1(d). Once again it can be seen that the presence of the resonant atoms leads to a phase shift.



1(b)

Fig. 1(b) Corresponding two soliton solution with $\omega_1=0$, $\omega_2=0$ (without MB).



1(d)

Fig. 1(d) Corresponding two soliton solution with $\omega_1=0$, $\omega_2=0$ (without MB).

Fig 1(c) and 1(d) corresponds to dispersion decreasing fiber ($k < 0$) for with and without MB part respectively. Because of dispersion decreasing case, the pulse get compressed during the propagation along the fiber as can be clearly seen in

the above figures. In real applications, it may be useful in relay stations to deform and amplify the optical pulse every suitable distance. We can see from the above figures which correspond to $k = -0.05$ that the pulse positions change due to the combined effects of the varying group velocity dispersion and the varying nonlinearity coefficients. In the absence of SIT effect in the fibre, a phase shift occurs.

6. CONCLUSION

We have carried out an investigation about optical pulse propagation in an inhomogeneous fiber doped with erbium atoms. We have proposed a generalized NLS-MB system with variable coefficients to explain the various dynamics of wave propagation in the doped fiber. The Lax Pair of INLS-MB equation is derived considering the eigenvalue parameter as non-isospectral. The Darboux Transformation is obtained straightforwardly from Lax pair in a systematic way. Through Darboux Transformation, one- and two-soliton solutions in explicit forms are presented and their properties are analyzed for the case of distributed amplification. The results have revealed that the combined effect of GVD distribution and nonlinearity distribution can enhance the stability between the neighboring soliton. We believe that our solutions may provide more information to further study the inhomogeneous nonlinear fibre optical systems and their properties are might be important to improve the quality of soliton based optical communication.

ACKNOWLEDGMENT

The authors A.M. and A.U. would like to thank Department of Science and Technology, India for financial assistance through major research projects.

REFERENCES :

1. G.P. Agrawal, *Nonlinear Fiber Optics*, fourth ed., (Academic Press, New York, 1995).
2. A. Hasegawa, and Y. Kodama, *Solitons in Optical communications* (Oxford U. Press, Oxford, 1995).
3. V.N. Serkin and A. Hasegawa, "Novel soliton solution of the nonlinear Schrodinger equation model," *Phys. Rev. Lett.* **85**, 4502 (2000).
4. K. Porsezian and K. Nakkeeran, "Optical soliton propagation in an Erbium doped nonlinear light guide with higher order dispersion," *Phys. Rev. Lett.* **74**, 2941 (1995).
5. V. N. Serkin and A. Hasegawa, "Exactly integrable nonlinear Schrödinger equation models with varying dispersion, Nonlinearity and Gain: Application for soliton dispersion management," *J. Sel. Topics Quantum Electron.* **8**, 418-431 (2002).
6. M. J. Ablowitz, D. J. Kaup, A. C. Newell and H. Segur, "Novel evolution equations of physical significance," *Phys. Rev. Lett.* **31**, 125 (1973).
7. R. Hao, L. Li, Z. Li, W. Xue and G. Zhou, "A new approach to exact soliton solution and soliton interaction for the NLS equation with variable coefficient," *Opt. Commun.* **236**, 79 (2004).

SUPERCONTINUUM EMISSION FROM WATER SOLUBLE DYES

S. Sreeja,^{1,2} S. Venugopal Rao,^{1,*} P. Radhakrishnan,² Surya P. Tewari,¹ P. Prem Kiran^{1,*}

¹ Advanced Centre of Research in High Energy Materials (ACRHEM), University of Hyderabad, Hyderabad 500046, India.

² International School of Photonics, Cochin University of Science and Technology, Cochin 682022, India.

Authors for correspondence: svrsp@uohyd.ernet.in and premsp@uohyd.ernet.in

Abstract: We present our results on the Supercontinuum emission (SCE) from different water soluble dye solutions and compare with that from the solvent. A suppression of SCE from solutions compared to that of solvent is observed due to either by absorption or the scattering losses from the dye molecules.

1. INTRODUCTION

Femtosecond filamentation and associated supercontinuum emission (SCE) has gained much attention for its wide application in long range propagation, remote sensing and lightning control [1]. The propagation of powerful ultrashort pulses in transparent media results in the strong modification of spatial and temporal profile due to self focusing of laser pulse and self phase modulation [2-4]. To date, attention has mainly been focused on filamentation and SCE from transparent materials [5] such as air, water, quartz, noble metal nanoparticles [6], polystyrene microsphere in water [7], CuSO₄ solution [8] to name a few. Herein, we present our results of SCE from different kinds of dyes and compare the data with SCE from that of the pure solvent.

2. EXPERIMENT

Transform limited laser pulses of duration ~ 40 fs, 800 nm, 1 kHz repetition rate pulses are focused with a lens in $f/6$ focusing geometry into a 8 cm long cuvette containing the liquid media. The input diameter before the focusing lens is 10 ± 0.1 cm. The SCE spot was scattered using a Teflon sheet kept at a constant distance from end face of the cuvette. The scattered light was collected using a fiber optic coupled spectrometer (USB 4000, Ocean Optics). The pulse energy used in this experiment is 0.8 mJ and was monitored by a power meter (Coherent, PM30).

3. RESULTS AND DISCUSSIONS

We performed the experiments in different water soluble dyes Phthalocyanines (ZnPC, NiPC), blue ink and black tea. All these dyes result in the strong scattering and absorption which leads to the distortions of the filament energy [7]. In all the cases the whole spectral intensity decreases with increasing concentration of dye. This decrease in SCE may be attributed due to the pump energy loss from the absorption of dye molecule during filamentation and/or from the scattering loss of conical emission due to dye molecule but it does not greatly alter the propagation dynamics of ultrashort pulse [7, 8]. Figure 1 depicts the SCE intensity from blue ink with increasing concentration. Details of the SCE emission, bandwidth, and efficiency as a function of dye concentration will be presented.

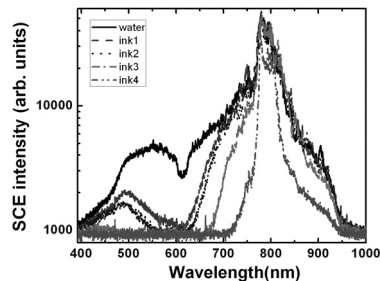


Figure 1: SCE from water and solutions of ink with different concentrations (ink1, ink2, ink3, ink4 denote the increasing concentrations of ink)

ACKNOWLEDGEMENTS

The authors acknowledge DRDO for financial support. SS acknowledges UGC for JRF.

REFERENCES

- [1] J. Kasparian and J. P. Wolf, "Physics and Applications of Atmospheric Nonlinear Optics and Filamentation." *Opt. Express* **16**, 466 (2008)
- [2] R.W. Boyd, S.G. Lukishova, and Y.R. Shen, Eds. *Self-focusing: Past and Present: Fundamentals and Prospects Chapter 1*, Springer Science+Business Media, Inc., New York, USA, (2009).
- [3] S.L. Chin, *Femtosecond laser filamentation*, Springer Science+Business Media, Inc., New York, USA, (2009).
- [4] R.R. Alfano (Ed.): *The Supercontinuum Laser Source*, Springer, Berlin, 1989.
- [5] A. Couairon, A. Mysyrowicz, "Femtosecond filamentation in Transparent Media" *Phys. Rep.* **441**, 47 (2007).
- [6] C. Wang, Y. X. Fu, Z. H. Zhou, Y. Cheng, and Z. Z. Xu, "Femtosecond filamentation and supercontinuum generation in silver-nanoparticle-doped water." *Appl. Phys. Lett.* **90**, 181119 (2007).
- [7] V. Jukna, G. Tamosauskas, G. Valiulis, M. Aputis, M. Puida, F. Ivanauskas, and A. Dubietis, "Filamentation of ultrashort light pulses in a liquid scattering medium" *Appl. Phys. B* **94**, 175 (2009)
- [8] L. Wang, Y.-X. Fan, Z.-D. Yan, H.-T. Wang, Z.-L. Wang, "Flat-plateau supercontinuum generation in liquid absorptive medium by femtosecond filamentation," *Opt. Lett.*, **35**, 17, (2010)

WIGNER DISTRIBUTION FUNCTION FOR OPTICALLY-POLARIZED SCHRODINGER-CAT STATES

Ravi S. Singh^{1#}, Sunil P. Singh², Lallan Yadava¹ and Gyaneshwar K. Gupta^{1*}

¹Department of Physics, D.D.U. Gorakhpur University, Gorakhpur-273009 (U.P.) India

²Department of Physics, K.N.I.P.S.S., Sultanpur (U.P.) India

E-mail: #yesora27@gmail.com, nislay06@rediffmail.com, *gyankg@gmail.com

Abstract: Polarization of mono-modal rectilinearly propagating optical field is characterized by characteristic parameters: 'ratio of real amplitudes' and 'difference in phases' of two transverse complex amplitudes along orthogonal bases of description. Probability Distribution Function of optical-polarization state in phase space may be derived by employing Cahill-Glauber C(s)-correspondence. Wigner distribution function of optically-polarized Schrodinger-cat state is evaluated by this procedure.

The characteristic optical-polarization-parameters for mono-modal rectilinearly travelling field are 'ratio of real amplitudes' and 'difference in phases' of two complex amplitudes along transverse orthogonal bases of description [1], which can be deciphered by Index of Polarization (IOP) introduced by Prakash and Singh [2]. The generalization in theory of optical-polarization has recently been carried out where the concept of higher-order optical-polarization [3] and generation of hidden optical-polarization is performed in degenerate parametric amplification [4].

In 1932 Wigner put forth the first Quasi Probability Distribution Function (QPDF) now bears his name. Wigner Function is viewed as an alternative formulation of Quantum Mechanics as QPDF furnishes pseudo-classical analogue of a dynamic state of a quantum system, specified by density operator in Hilbert space. Variant QPDFs have been extensively used in many Quantum Optical Applications. A great deal of interest is seen in the s-parameterized QPDF because of their indirect roles in setting modern algorithm for measuring the quantum state of optical field. s-parameterized generalized correspondence rule is introduced by Cahill and Glauber [5] which governs the correspondence between density-operatoric (Hilbert space) to QPDF description (Quantum Phase space) of system.

Accordingly, the dynamic state of a single harmonic oscillator of classical complex amplitude, α is described in quantum theory by its density operator, $\hat{\rho}$ in Hilbert space of which description in phase space is governed by QPDF $W(\alpha, s)$ such that

$$W(\alpha, s) = \text{Tr} [\hat{\rho} \hat{t}(\alpha, s)] \quad (1a)$$

where $\hat{t}(\alpha, s)$ are Kernel-operators, defined as complex Fourier transform of the s.ordered displacement operators $D(\alpha, s)$. Simple algebraic manipulation provides expression for, $\hat{t}(\alpha, s)$ as

$$\hat{t}(\alpha, s) = \left(\frac{2}{1-s}\right) \hat{D}\left(\alpha\right) \left(\frac{s+1}{s-1}\right) \hat{D}^\dagger(\alpha), \quad (1b)$$

The phase space description of the two independent transverse harmonic oscillators may, correspondingly, be projected by operator $\hat{T}(\alpha_x, \alpha_y, s)$ defined to be

$$\hat{T}(\alpha_x, \alpha_y, s) = \hat{t}(\alpha_x, s) \hat{t}(\alpha_y, s), \quad (2)$$

using Eq.(1b) for each orthogonal oscillators one

obtains the transiting operator (TO) which helps in transition of density operator ρ for two independent transverse oscillators from Hilbert space to Quantum Phase space [6]. Notably, since usual optical polarization of radiation field is characterized by IOP, p in Classical Optics ($\alpha_y = p\alpha_x$), the transiting operator may be derived. The higher-order optical-polarization in classical optics is introduced by the relation $\alpha_y^n = p^{(n)}_{(\hat{e}_x \hat{e}_y)} \alpha_x^n$, between classical amplitudes $\alpha_{x,y}$. The transiting operator for two independent orthogonal oscillators in this scenario may be set up as

$$\hat{T}^{(n)} \quad \propto \quad \exp\left(\frac{2\alpha_x^n (\hat{a}_x^{\dagger n} + p_{ps}^{(n)} \hat{a}_y^{\dagger n})}{1-s}\right) \\ \cdot \exp\left(\frac{-2(\hat{n}_x^n + \hat{n}_y^n)}{1-s}\right) \cdot \exp\left(\frac{2\alpha_x^{*n} (\hat{a}_x^n + p_{ps}^{*(n)} \hat{a}_y^n)}{1-s}\right) \quad (3)$$

where n represents higher-order optical-polarization and proportionality constant taken care as intensity dependent. The Schrödinger-cat states ($\hat{\rho}$) possess higher-order optical-polarization. Substituting $\hat{\rho}$ and transiting operator (Eq.(3)) into (Eq.1a) one may obtain Wigner distribution function for optically-polarized Schrödinger-cat states, on taking $s = 0$.

References

- [1] A. Peres, *Quantum Theory: Concept and Methods*, Kluwer Academic Publishers, London, U. K., 2002, pp. 9-11.
- [2] H.Prakash and Ravi S. Singh, *Operator for Optical Polarization*, *J. Phys. Soc. Japan*, **69**, 284 (2000).
- [3] Ravi S Singh and H. Prakash, *Higher-order optical-polarization*, arXiv.1103.4243.
- [4] Gyaneshwar K Gupta, Akhilesh kumar and Ravi S Singh, *Generation of hidden optical-polarization: squeezing and nonclassicality*, *opt. commun.*, **284**, 4951 (2011).
- [5] K. E. Cahill and R. J. Glauber, *Density Operators and Quasiprobability Distribution*, *Phys. Rev.*, **177**, 1882 (1969).
- [6] Ravi S Singh, Sunil P Singh and Gyaneshwar K Gupta, *Quasiprobability Distribution functions for optical-polarization*, *Proc. SPIE 8173*, 81731O (2010).

ANALYSIS OF TUNABLE TERAHERTZ GENERATION IN DAST USING DIFFERENCE FREQUENCY MIXING

Maria Farooqui¹, Kuldeep Meena², Nimish Dixit^{1*}, A. N. Kaul¹ and A. K. Gupta¹

¹Photonics Research Center, Instruments Research & Development Establishment, Dehradun

²Physics Department, IIT Delhi, New Delhi

Email- ndixit@irde.drdo.in

Abstract: In this paper numerical analysis has been carried out to study the tunable terahertz (THz) generation in DAST using difference frequency generation (DFG) between the outputs, which can be generated from a periodically poled lithium niobate (PPLN) based optical parametric oscillator (OPO). By varying the input wavelengths in the range 1300- 1450 nm we obtained 0-23 THz tunable THz frequency. The output THz power at the 1.67 THz, 2.14 THz and 3 THz were 6.1 W, 12.5 W and 3 W respectively.

1. INTRODUCTION

Electromagnetic radiations whose frequency ranges from 0.1 THz to 10 THz are generally known as terahertz (THz) radiations or T-rays. Owing to the unique properties, T-rays have made its place in several areas of applications, in particular, imaging and spectroscopy [1-2].

Though there are several techniques to generate THz [3-4], the nonlinear optical techniques which include short pulse rectification commonly known as optical rectification (OR) and difference frequency generation (DFG), have become quite popular. Both of these techniques involve the mixing of the two closely spaced wavelengths such that their difference lies in the THz regime. In fact OR of a femtosecond pulse is difference frequency generation between the particular spectral components within the ultra-short laser pulse. However, for laser pulses of long duration, the frequency spectrum is narrow and therefore two different wavelengths are needed to be mixed in order to achieve the DFG. Thus we can say that for OR to take place an ultra-short pulse, or a femtosecond laser is must, while DFG can be achieved from a nanosecond or even with a continuous wave (CW) laser. Among the two above mentioned nonlinear optical processes, the DFG has come out to be an attractive option for THz generation. The advantages of DFG include narrow line-widths, high peak powers, widely tunable THz wavelength range and compactness.

Tunable THz waves from DFG in the frequency range 0.3 THz – 4 THz has been reported in inorganic crystals like LiNbO₃ [5], GaP [6], GaAs [7] and ZnTe [8]. Among these inorganic materials like LiNbO₃, velocity matching cannot be easily achieved because the refractive index at THz frequency ($n_{\text{THz}} \approx 5.2$) is significantly higher than the optical group index ($n_{\text{opt}} \approx 2.15$). However, phase matching has been observed in the materials like ZnTe [8] and GaSe [9], where the nonlinear susceptibility is relatively low leading to poor conversion efficiency.

On the contrary, an organic crystal namely DAST (4N, N-dimethylamino-4'-N'-methyl-stilbazoliumtosylate) has very large second order susceptibility (≈ 230 pm/V), which is nearly ten times higher than that of LiNbO₃ (27.2 pm/V) resulting into higher conversion efficiency [10]. DAST also provides excellent velocity matching as the refractive index of the DAST in optical and THz region are nearly the same ($n_{\text{opt}} \approx n_{\text{THz}} \approx 2.2$) [11]. Thus difference frequency mixing of properly selected wavelengths in DAST crystal can provide a wide range of tunable THz radiation.

In this work, a collinear difference frequency mixing between two wavelengths (say λ_1 and λ_2) which can be provided by the PPLN based OPO, has been treated theoretically. An appropriate range of wavelength has been estimated which would be suitable for the generation of THz tunable from 0.1 – 23 THz. The refractive index of DAST has been calculated by making use of Sellmeier equation in IR as well as THz region. With the help of these values of indices, the coherence length (which is a measure of momentum mismatch) corresponding to the input infrared wavelengths has been estimated. The absorption coefficient of DAST has also been calculated. We have also studied the dependence of THz power on the thickness of the DAST crystal. We have incorporated the effect of momentum mismatch and the absorption within the DAST while studying the tuning characteristics of the THz power.

2. THEORY

For the efficient THz generation through nonlinear parametric process, it is important to have an adequate phase matching between the participating wavelengths. The phase matching condition for collinear DFG is given by energy conservation and momentum conservation which can be expressed as below

$$\left| \frac{1}{\lambda_1} - \frac{1}{\lambda_2} \right| = \frac{1}{\lambda_3} \quad \text{and} \quad \left| \frac{n_1}{\lambda_1} - \frac{n_2}{\lambda_2} \right| = \frac{n_3}{\lambda_3} \quad 1$$

where n_1 , n_2 and n_3 are the refractive indices corresponding to the wavelengths λ_1 , λ_2 and λ_3 respectively. The phase matching condition gives an estimation of the wavelength range and the thickness of the DAST crystal to be used.

Consider, E_1 , E_2 and E_3 to be the three participating wavelengths propagating collinearly in the y - axis direction such that their electric fields are given as

$$E_m = E_{m0} \exp\{i(k_m y - \omega_m t)\} \quad m = 1, 2 \text{ and } 3$$

where E_{m0} , k_m and ω_m are the field amplitudes, propagation constants and the angular frequencies respectively corresponding to these fields.

The nonlinear coupled wave equation for collinear DFG, taking into account the absorption coefficient of the material, can be derived from the Maxwell's equation and is given as [12]

$$\frac{\partial E_{10}(y)}{\partial y} = \frac{-i\omega_1 d_{ij} E_{20} E_{30}}{n_1 c} e^{i\Delta k y} - \frac{\alpha_1}{2} E_{10}(y) \quad (1.1)$$

$$\frac{\partial E_{20}(y)}{\partial y} = \frac{-i\omega_2 d_{ij} E_{10}^* E_{30}}{n_2 c} e^{-i\Delta k y} - \frac{\alpha_2}{2} E_{20}(y) \quad (1.2)$$

$$\frac{\partial E_{30}(y)}{\partial y} = \frac{-i\omega_3 d_{ij} E_{10}^* E_{20}}{n_3 c} e^{-i\Delta k y} - \frac{\alpha_3}{2} E_{30}(y) \quad (1.3)$$

The growth of THz power after propagating the thickness ' L ' is obtained by solving equation (1.3) and it is given as

$$P_3 = \frac{2\omega_3^2 d^2 L^2}{\epsilon_0 n_1 n_2 n_3 c^3} \left(\frac{P_1 P_2}{\pi r^2} \right) \times S \quad (2)$$

where

$$S = \frac{\left\{ 1 + e^{-\alpha_3 L} - 2 \cos(\Delta k L) e^{-\frac{\alpha_3 L}{2}} \right\}}{(\Delta k L)^2 + \left(\frac{\alpha_3 L}{2} \right)^2}, \text{ and } \Delta k = |k_1 - k_2 - k_3|$$

where d is the nonlinear coefficient and L is the thickness of the DAST crystal. P_1 , P_2 are the power of two input beams at λ_1 and λ_2 respectively; T_1 , T_2 and T_3 are the Fresnel transmission coefficients; r is the focal spot radius and has been assumed equal for both the input beams and Δk is the momentum mismatch between optical beams and THz wavelength. n_1 , n_2 and n_3 are the refractive indices whereas α_1 , α_2 and α_3 are the absorption coefficients at wavelengths λ_1 , λ_2 and λ_3 respectively. ω_3 is the angular frequency corresponding to λ_3 .

The refractive indices of DAST crystal at optical

frequencies are calculated by using Sellmeier equations [13]. Fig. 1 shows the refractive indices of the DAST as a function of infrared wavelength.

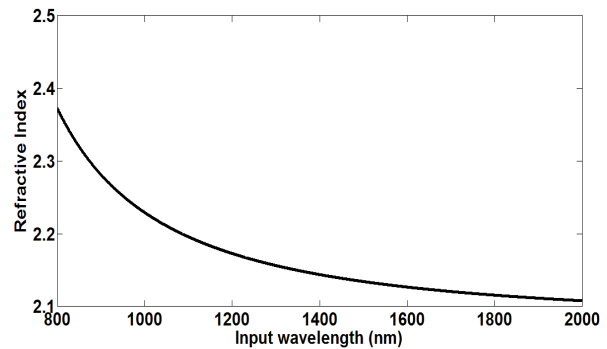


Fig. 1 Refractive index of DAST at infrared wavelengths

We have summed up two Lorentzian line shape functions obtained on the basis of harmonic oscillator model for the evaluation of refractive index and absorption for DAST in THz wavelength regime [14]. According to this model, THz refractive index and absorption coefficient can be given as:

$$n(\omega) = n_\infty + \sum_{i=1,2} \frac{\alpha_i (\omega_i^2 - \omega^2)}{(\omega_i^2 - \omega^2)^2 + 4\gamma_i^2 \omega^2} \quad (3)$$

$$\alpha(\omega) = 2K\omega^2 \sum_{i=1,2} \frac{2\gamma_i \alpha_i}{(\omega_i^2 - \omega^2)^2 + 4\gamma_i^2 \omega^2} \quad (4)$$

where $K=17.9 \times 10^{12} \text{s}^{-1} \text{mm}^{-1}$ and the values of other parameters are given in the table below [14]:

Oscillator	Amplitude α_i	Frequency $\nu_i = \omega_i / 2\pi$	Damping parameter $\gamma_i (\text{s}^{-1})$
1	6.9	1.10	0.40×10^{12}
2	3.4	3.05	3.1×10^{12}

Fig. 2 and Fig. 3 show the variation of refractive index and absorption coefficient of DAST as a function of THz frequencies. We have used these values in calculation given hereinafter.

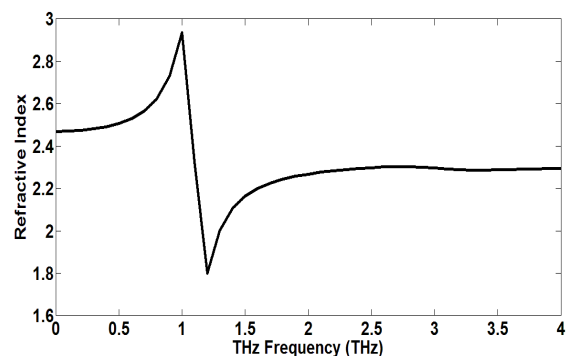


Fig. 2 Refractive index of DAST at THz frequency

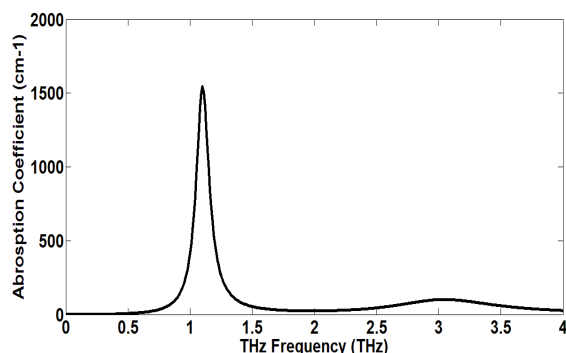


Fig. 3 Absorption coefficient of DAST at THz frequency

3. RESULTS AND DISCUSSION

Fig.4 depicts the variation of the coherence length as a function of input wavelength. We found that for 100 μm (3 THz), 140 μm (2.14 THz) and 180 μm (1.67 THz) coherence length was maximum (or momentum mismatch was minimum) at input wavelengths of 1409 nm, 1452 nm and 1685 nm respectively. The estimated THz power as function of input wavelength is shown in Fig. 5, where it is evident that the THz power attains the maximum value at the points where phase matching is satisfied.

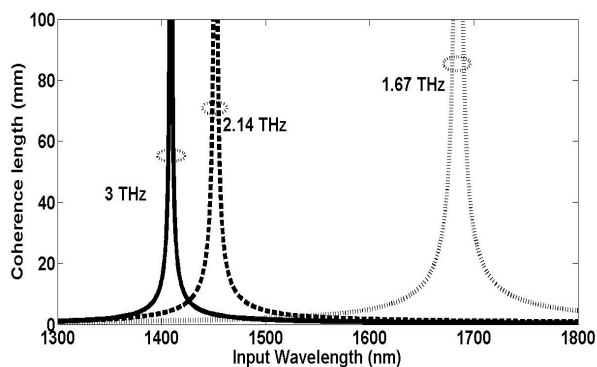


Fig. 4 Coherence length as a function of input wavelengths

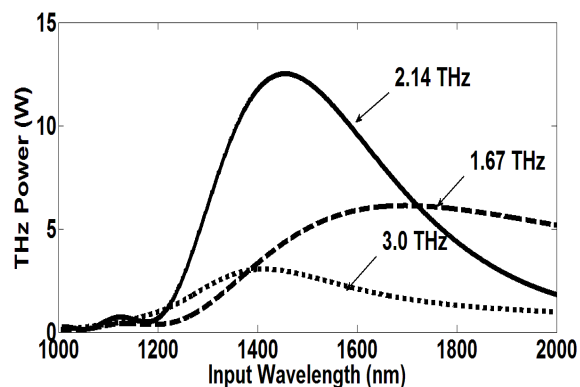


Fig. 5 THz power as a function of input wavelengths

The theoretical values of peak power corresponding to 1.67 THz, 2.14 THz and 3 THz were 6.12 W, 12.5 W and 3 W respectively. It should be noted from Fig. 3 that the absorption coefficients of DAST at these three frequencies were 33.41 cm^{-1} , 26.38 cm^{-1} and 101.4 cm^{-1} respectively, i. e. output power is minimum at that THz frequency for which the absorption coefficient is maximum which also shows the role of absorption coefficient in the expression of THz DFG power apart from the fulfillment of phase matching condition (eq. 2).

Fig. 5 also shows that phase matching is not very much specific and hence the wavelength ranging from 1300-1700 nm can be used for efficient generation above 1 THz. Thus we fixed one of the input wavelengths to be 1450 nm and varied the other input in its vicinity i. e. from 1300-1450 nm which theoretically corresponds to the frequency tuning from 0.1 - 23 THz.

We have also studied the dependence of THz power on thickness of the nonlinear medium for a frequency of 3 THz. We have used the following data for the theoretical calculations; $L=1 \text{ mm}$, $d_{11}=210 \text{ pm/V}$, $P_1=P_2=30 \text{ kW}$, $r=170 \mu\text{m}$, $\alpha_1=\alpha_2=0.5 \text{ cm}^{-1}$ while α_3 was calculated with the help of eq. 4.

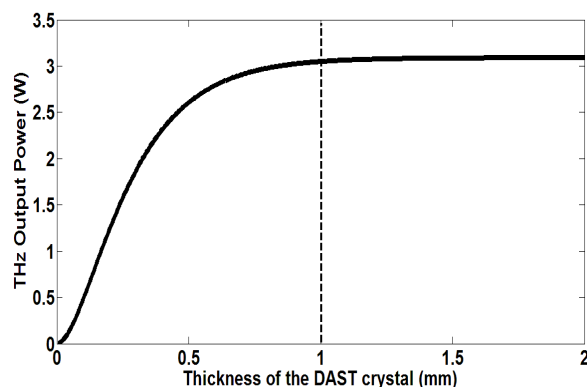


Fig. 6 THz output power as a function of thickness of DAST crystal

From eq. 2, it is clear that THz power increases as the square of the crystal thickness. However, even for the completely phase-matched condition it does not grow indefinitely (see Fig. 6). Rather, the power saturates beyond a certain value ($\approx 1 \text{ mm}$) of thickness due to the absorption of THz waves in DAST.

Fig.7 shows the continuous tunability of THz frequency over the range 1- 3 THz. However, the actual tunability extends from 0.1 - 23 THz as the input wavelengths are tuned from 1300 - 1450 nm.

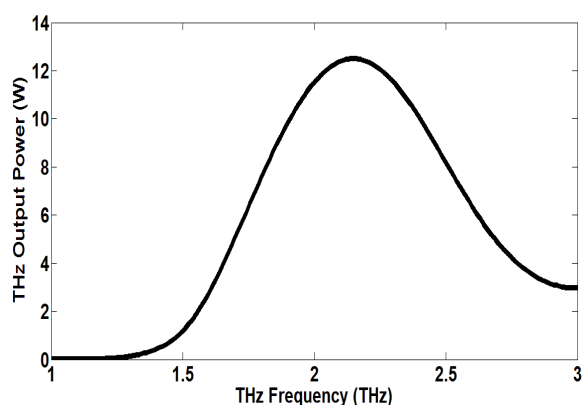


Fig. 7 THz power as a function of the THz frequency

4. CONCLUSION

It was concluded that phase matching in the DAST crystal is not very particular. With a fixed wavelength (say λ_1) of 1450 nm and a variable input wavelength (say λ_2) from 1300-1450 nm, a wide range of THz wavelength (0-23 THz) can be obtained. The refractive index of DAST crystal both in IR and THz region was calculated by using Sellmeier equation. The absorption coefficient of DAST crystal in THz region was also taken into account. In this study it was found that the absorption coefficients of DAST at the frequencies 1.67 THz, 2.14 THz and 3THz were 33.41 cm^{-1} , 26.38 cm^{-1} and 101.4 cm^{-1} respectively while peak power corresponding to these frequencies were 6.12 W, 12.5 W and 3 W respectively. It was also found that for the 3 THz frequency the output power saturated beyond 1 mm of thickness of the DAST crystal.

ACKNOWLEDGEMENT

The authors wish to acknowledge Director, IRDE for giving permission to publish this work.

REFERENCES

- [1] J. Hebling, K. L. Yeh, M. C. Hoffmann and K. A. Nelson, "High power THz generation, THz nonlinear optics, and THz nonlinear spectroscopy" *IEEE J. Sel. Top. in Quantum Electron.*, **14**, 345-353 (2008).
- [2] Eric. R. Muler, "Terahertz radiation sources for imaging and sensing applications" *Photonics Spectra* November issue (2006).
- [3] M. Tonouchi, "Cutting-edge terahertz technology," *Nat. Photon.*, **1**, 97-105 (2007).
- [4] Francois Blanchard et. al. "Generation of intense THz radiation via optical methods" *IEEE Transactions on Geosciences and Remote Sensing*, **1**, No. 1 (2002).
- [5] J. A. Huillier, G. Torosyan, M. Theuer, C. Rau, Y. Avetisyan, R. Beigang "Generation of THz radiation using bulk, periodically and

aperiodically poled lithium niobate – Part 1: Theory", *Appl. Phys. B* **86**, 197- (2007).

- [6] R. T. Taniuchia and H. Nakanishi, "Collinear phase-matched terahertz-wave generation in GaP crystal using a dual-wavelength optical parametric oscillator" *J. Appl. Phys.*, **95**, 7588-7591 (2004)
- [7] Konstantin L. Vodopyanov, "Optical THz-wave generation with periodically-inverted GaAs", *Laser & Photon. Rev.*, **2**, 11-25 (2008)
- [8] Q. Wu and X. C. Zhang, "Design and characterization of travelling wave electro-optic terahertz sensors", *IEEE J. Sel. Top. Quantum Electron.* **2**, 693-700 (1996).
- [9] Y. Geng, X. Tang, X. Li and J. Yao, "Compact and widely tunable terahertz source based on a dual-wavelength intracavity optical parametric oscillation", *Appl. Phys. B Lasers and Optics*, **99**, 181-185 (2010).
- [10] H. Ito, K. Suizu, T. Yamashita, A. Nawahara and T. Sato, "Random frequency accessible broad tunable terahertz wave source using phase matched 4-dimethylamino-4'-N'-methylstilbazoliumtosylate crystal", *Jpn. J. Appl. Phys.*, **46**, 7321-7324 (2007)
- [11] T. Taniuchi, S. Okada and H. Nakanishi, "Widely tunable THz wave generation in an organic crystal and its spectroscopic application", *J. Appl. Phys.*, **95**, 5984 (2004).
- [12] Rosita Sowade, "Continuous-wave terahertz light from optical parametric oscillators" Dissertation (2010).
- [13] M. Jazbinsek, L. Mutter and P. Gunter "Photonics Application with the Organic Nonlinear Optical Crystal DAST" *IEEE J. Sel. Top. Quantum Electron.* **14**, 1298-1311 (2008).
- [14] A. Schneider, M. Neis, M. Stillhart, B. Ruiz, R. U. A. Khan and P. Gunter, "Generation of Terahertz pulses through optical rectification in organic DAST crystal: theory and experiment," *J. Opt. Soc. Am. B*, **23**, 1822 (2006).

COHERENT INTERACTION OF OFF-AXIS VORTEX SOLITONS IN STRONGLY NONLOCAL NONLINEAR MEDIA

Pravin Vaity, R. P. Singh, Ashok Kumar, A. Aadhi and S. G. Reddy
Physical Research Laboratory, Ahmedabad

pravinvaity@prl.res.in, rpsingh@prl.res.in, ashokk@prl.res.in, aadhi@prl.res.in, sgreddy@prl.res.in

Abstract: We study the interaction of two separate coherent off-axis vortex solitons in a strongly nonlocal nonlinear medium. The two solitons combine to form an optical vortex soliton and separate again. The combination and separation of solitons shows a periodic behavior.

1. INTRODUCTION

The soliton is a localized beam which maintains its shape during its journey in a nonlinear medium [1]. It is a universal phenomena observed in plasma, solids, fluids and BEC. To explain these phenomena various complex models have been proposed; however, the present work uses accessible soliton model developed by Snyder and Mitchell [2].

The soliton interaction is the most interesting feature of solitons. In this paper we have studied the interaction of two off-axis vortex solitons in the strongly nonlocal nonlinear medium (SNNM).

2. THEORY

The field amplitude for the off-axis vortex embedded in a Gaussian beam can be written as

$$u(x, y) = (x + x_o \pm iy)^m \exp\left[-\frac{(x^2 + y^2)}{w^2}\right]$$

where w is the beam radius, m is the charge of vortex, x_o is the distance between beam axis and position of vortex. The propagation dynamics of any field inside the SNNM can be calculated by solving 2D nonlocal nonlinear Schrödinger equation [2, 3],

$$iu_z + \frac{1}{2}(u_{xx} + u_{yy}) - P(x^2 + y^2)u = 0$$

where P is the total power of field.

3. RESULTS

Figure 1 shows the propagation dynamics of the off-axis vortex shifted by $x_o = w/2$ from the beam axis. The first row of Fig. 1 shows the dynamics in free space, which is just a rotation of the intensity distribution by 90° . However, the dynamics is different in the case of SNNM as shown in the second row of Fig. 1. It is observed that along with the rotational dynamics, the off-axis vortex beam forms a soliton inside the media for a particular value of power P . This rotation sustains up to the full length of medium.

Next we study the coherent interaction of two off axis vortex solitons separated by the distance d . The results are shown in Fig. 2. At $z=0$, they are separated by the distance $d=4w$. But after the propagation, they come closer to each other and form a single vortex

soliton. This can be confirmed by the interference pattern shown in the second row of Fig. 2. However, this vortex soliton breaks into two off axis vortex solitons on further propagation. This kind of construction and destruction of vortex soliton occurs throughout the length of SNNM.

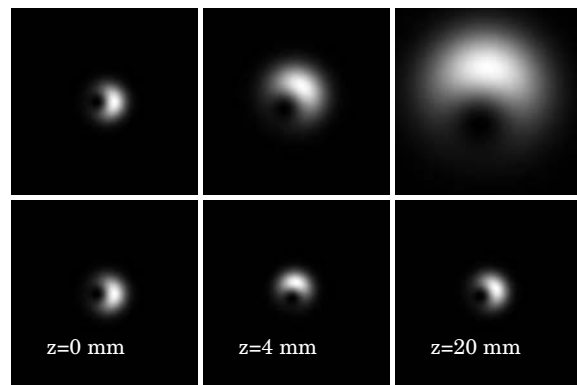


Fig. 1. Intensity profile of off-axis vortex (first row) and formation of soliton (second row).

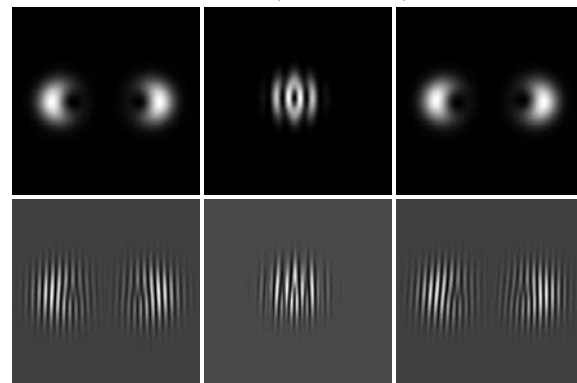


Fig. 2. Interaction of solitons (first row) and interference pattern (second row).

REFERENCES

- [1] G. Stegeman and M. Segev, "Optical spatial solitons and their interactions: universality and diversity," *Science*, **286**, 1518 (1999).
- [2] A. Snyder and D. Mitchell, "Accessible solitons," *Science*, **276**, 1538 (1997).
- [3] Y. He, B. Malomed, D. Mihalache, and H. Wang, "Crescent vortex soliton in strongly nonlocal nonlinear media," *Phys. Rev. A*, **78**, 023824 (2008).

PROBING COLD ATOMS IN OPTICAL LATTICE USING ATOM-PHOTON INTERACTION

Jasleen Lugani, Sankalpa Ghosh, K. Thyagarajan
 Department of Physics, IIT Delhi, India-110 016
jaslphy@gmail.com, sankalpa@physics.iitd.ac.in, ktrajan@physics.iitd.ac.in

Abstract: We present a study of an all optical method to probe the atomic quantum properties of ultracold atoms in an optical lattice using atom photon interaction of the cavity mode with the cold atoms. The method can be further extended to map other response functions of the atoms onto the cavity photons.

1. INTRODUCTION

Ultracold atoms in optical lattices provide a means to study strongly correlated many body systems useful in condensed matter, quantum optics as well as in quantum information processing. The standard methods to observe quantum properties of Bose Einstein Condensates (BEC) are based on matter wave interference of ultracold atoms and their absorption image is taken with a laser. For this, atoms have to be released from the traps [1-4] which ultimately, destroys the coherent superposition of various many body states of these atoms that form the macroscopic quantum mechanical state. A new method was proposed recently for probing atomic quantum properties of such systems without actually destroying the coherent superposition [5-7]. This involves the interaction of the BEC with the cavity modes of a high Q cavity and performing optical measurements on the cavity photons. It was shown in Ref [5-6] that the transmitted photons of the cavity carry signatures of the atomic statistics of the corresponding quantum phase of the BEC. Thus, this method proves to be very useful in studying phase transitions (from Mott insulator (MI) to superfluid (SF)) and quantum statistical properties of BEC and finds application in the field of quantum optics and quantum information.

In the subsequent sections, we describe the above method by taking a simplified model of the system. The authors in ref [5-6] use a statistical approach and concentrate on deep inside MI or SF phases and study their respective cavity transmission spectra. In contrast, we adopt an exact diagonalization method to obtain the ground state wavefunction of the system at any point in the phase diagram. This method provides us with the flexibility such that in addition to deep MI and deep SF, we can study the transmission spectra as the system makes a transition from MI to SF, as the lattice depth is varied. We show through numerical simulations, that each point in the phase diagram has a characteristic transmission spectra. Thus, using this method, one can qualitatively scan the whole phase boundary and study the quantum phase transition from SF to MI.

2. THE MODEL

The BEC is modeled as N two level atoms of a BEC in a deep periodic one-dimensional optical lattice with M sites, (formed by external far off resonant laser beams) as shown in Fig 1.

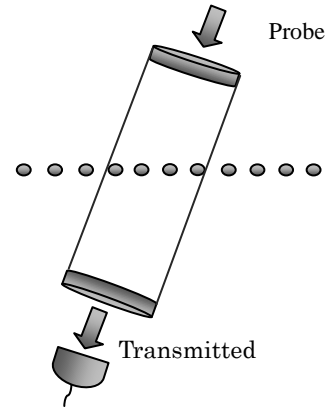


Fig 1: Schematic representation of BEC in the optical lattice being illuminated by a probe laser. The transmitted spectrum of the cavity photons is measured using a detector.

A region of $K < M$ sites is coupled to a cavity mode, which is pumped through a probe laser. The Hamiltonian of the system can be written as follows.

$$\hat{H} = \hat{H}_0 + \hat{H}_I \quad (1)$$

where H_0 is the self energy of the system (cavity and BEC) and H_I is the term arising from the atom-photon interaction in the cavity. Substituting the corresponding expressions, the Hamiltonian of the system in second quantization formalism, after adiabatic approximation and rotating wave approximation (RWA) is given as [5]

$$\hat{H} = \hbar\omega\hat{a}^+\hat{a} + \hbar g^2 \frac{\hat{a}^+\hat{a}}{\Delta} \left(\sum_{i=1}^K J_{i,i} \hat{n}_i \right) + (\eta(t)\hat{a}^+ + \eta^*(t)\hat{a}) - \kappa\hat{a}^+\hat{a} \quad (2)$$

The first term in Eq (2) represents the self energy of the cavity photons (H_0), where, ω is the frequency corresponding to the cavity mode,

represented by the annihilation operator \hat{a} ; In the present problem, the self energy of the atoms of the BEC has been neglected, as it does not play any dynamics in the photon mode operator, to the first order approximation. The second term in Eq (2) represents the atom-photon interaction (H_I), g is the atom-photon coupling strength, Δ is the cavity atom detuning, $J_{i,i}$ is given by the expression : $J_{i,i} = u^*(r_i) u(r_i)$, $u(r_i)$ being spatial mode function of the cavity photons at i^{th} lattice. Mode functions can have travelling wave solutions or standing waves. \hat{n}_i is the atom number operator at i^{th} lattice point. \hat{n}_i when operated on a lattice point gives the number of BEC atoms occupied at that point, $(\eta(t)\hat{a}^+ + \eta^*(t)\hat{a})$ describes the interaction between the external probe and the cavity mode, where $\eta(t) = \eta e^{-i\omega_p t}$ is the probe strength and ω_p is the probe frequency. The last term in Eq (2) represents the cavity decay and determines the number of photons going out of the cavity due to the finite cavity decay constant κ . In deriving the Hamiltonian (Eq (2)), as a simplification, we have neglected the term arising due to finite tunneling of atoms from one lattice site to another. Tunneling has been taken into consideration later, when we derive the exact wavefunction of the atoms at a particular point in the phase diagram, using the Bose Hubbard Hamiltonian discussed in the next section.

Using Eq (2), we derive the Heisenberg equation of motion for the cavity mode operator as

$$\dot{\hat{a}} = -i(\omega + \delta_0 \bar{D})\hat{a} - \kappa \hat{a} + \eta(t) \quad (3)$$

where $\delta_0 = \frac{g^2}{\Delta}$ is the term arising due to the presence of atoms inside the cavity and their interaction with the cavity photons. This term signifies the shift in the cavity spectra due to the presence of the atoms of the BEC. $\bar{D} = \sum_i^K u^*(r_i) u(r_i) \hat{n}_i$; for a 1D optical lattice with period d , atoms are trapped at $x_i = id, (i = 1, 2, \dots, M)$ and the mode functions are travelling modes: $u_i = \exp(ik_0 x)$ or standing wave modes at particular angles: $u_i = \cos(k_0 x)$, where $k_0 = |k_0| \cos \theta$, θ being the angle between the mode and the lattice axis. In this paper, we present the calculations for the angles for which $u^*(r_i) u(r_i) = 1$; hence $\bar{D} = \sum_i^K \hat{n}_i$, which determines the total number of atoms at the illuminated (K) sites (total number of illuminated atoms).

From the stationary solution of the above equation, the transmitted photon number operator is derived as

$$\hat{a}^+ \hat{a} = \frac{|\eta|^2}{(\Delta_p - \delta_0 \bar{D})^2 + \kappa^2} \quad (4)$$

where Δ_p is the probe-cavity detuning. The

transmission spectrum is measured by determining the expectation value of the above photon number operator in the ground state wavefunction of the BEC. It can be seen from Eq (4) that the transmission spectra of the cavity photons admits a Lorentzian behavior. The transmission spectra of an otherwise empty (classical) cavity is also a Lorentzian. Under classical limit, Eq (4) corresponds to Maxwell's equations, with the dispersion induced frequency shifts in the cavity transmission; the amount of shift being determined by an amount $\delta_0 \bar{D}$ (or $\delta_0 \sum_i^K \hat{n}_i$, total number of atoms at the illuminated sites). Thus an information about atom number fluctuations at different sites will get automatically reflected in the transmission spectra.

In the next section, we present some simulation results illustrating how the transmission spectra as computed from Eq (4) carry these signatures characteristic of a particular phase of the BEC.

3. NUMERICAL SIMULATIONS

In this section, we present the methodology to compute the transmission spectra of the cavity photons in the presence of the BEC. We adopt an exact diagonalisation method (EDM) to obtain the ground state wavefunction of the system. EDM is a standard and well established method to diagonalize the Hamiltonian matrix describing a given system and obtaining its energy eigenvalues and eigenvectors exactly [8,9]. This method gives us the flexibility as it helps to scan through the phase transition but is computationally very expensive if carried out for a large number of particles and sites. This limitation, though, can be overcome after some finite size scaling, i.e. if the overall behavior of the results get saturated as we increase the number of particles and sites.

As an illustration of the above method, we consider $N (=8)$ particles, $M (=8)$ lattice sites, out of which $K (=4)$ sites are illuminated by the cavity. For the calculation of the ground state wave function, as a simplification, we consider the standard Bose Hubbard model as given by Eq (5).

$$\hat{H} = -J \sum_{\langle ij \rangle} (\hat{b}_i^+ \hat{b}_j + \hat{b}_j^+ \hat{b}_i) + \frac{U}{2} \sum_i^M \hat{n}_i (\hat{n}_i - 1) \quad (5)$$

where the first term arises due to the finite tunneling, J being the hopping element (and is considered to be site independent in this case), \hat{b}_i (\hat{b}_j^+) annihilates (creates) a particle at site i (j), i.e. it describes the effect that a particle tunnels from site i to site j with an amplitude J . In the above, we are considering hopping to the nearest neighbor only. Second term in Eq (5) arises due to particle-particle interaction at site i , \hat{n}_i being the atom number operator and gives the number of atoms at lattice site i .

We must mention here, that we could have

considered the overall effect of atom-photon interaction on the tunneling of atoms from one site to another, but as a simplification, we used the Hamiltonian given by Eq (2), to calculate the transmitted photon number operator; and the Bose Hubbard Hamiltonian (Eq (5)) to calculate the ground state wave function, as it scans the phase diagram of the ultracold atoms completely. Our goal in the present paper is to capture the characteristics of the transmission spectra of the cavity across the whole phase boundary and at the phase transition.

For the given system of particles and sites, we first compute all possible Fock state basis vectors and calculate the corresponding Hamiltonian matrix using Eq (5). The Hamiltonian matrix is then exactly diagonalised and ground state wavefunction is computed as a function of the onsite particle interaction (U), and the tunneling/hopping parameter (J).

It is the relative magnitudes of U and J or b ($=U/J$), which determine whether the BEC is in the Mott phase, or in SF phase or at some other point in the phase diagram. Using this method (EDM), we can compute the wavefunction exactly at any point in the phase diagram.

Once we obtain the ground state wavefunction, the transmission spectra of the cavity is then evaluated by calculating the expectation value of the photon number operator given by Eq (4), in the ground state. As an illustration, we present the results for transmission spectra as shown in fig 2. Fig 2a shows the transmission spectra at MI and SF phase plotted using the method proposed by the authors of Ref [5-6]. As a comparison, we plot the transmission spectra as calculated by our method (EDM) for six different points in the phase diagram, characterized by $U/J = 0$ (deep SF), $U/J=2.5, 5, 10$, (transition from SF to MI), and $U/J=15,25$ (deep MI), as shown in fig 2b.

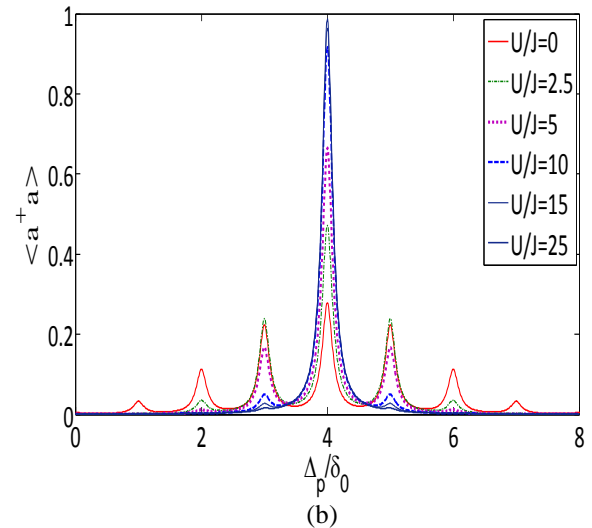
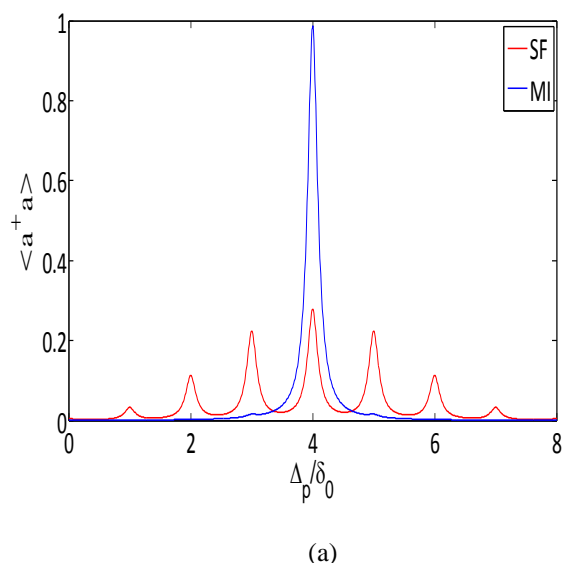


Fig 2: Transmission spectra of the cavity photons as a function of detuning. (a) calculated for MI and SF phase using the statistical approach used in ref [5-6] (b) calculated for $U/J=0, 2.5, 5, 10, 15, 25$, using our Exact diagonalization method (EDM).

It can be easily seen from the figure that the transmission spectra changes as the system makes a transition from the SF to Mott phase. This can be inferred from the reduction of the number of peaks in the transmission spectra. For instance, for a MI ($U/J=25$), which has a fixed number of particles at each lattice site, there are no atom number fluctuations i.e. the atoms do not hop from one lattice site to another, the transmission spectra of the cavity photons consists of a single peak (single Lorentzian). On the contrary, in a superfluid, the atoms are highly delocalized, and keep on hopping between the sites, due to which the number of atoms at each lattice is not fixed and keep changing from time to time, resulting in large fluctuations in the atom number. Thus the total number of atoms at the illuminated sites (K) also fluctuates. This results in large number of peaks in the transmission spectra for a SF. As the system makes a transition from SF to MI, the fluctuations in the atom number get suppressed, the atoms get more and more localized, giving rise suppression of the side peaks and resulting in only one peak as in MI. Thus the cavity transmission spectra characterizes the quantum phase of the BEC and using the EDM method one can characterize the whole phase boundary completely. It can also be seen in fig 2a, that our result matches exactly with the one given in Ref [5] for the case of deep MI and deep SF case.

The above results were plotted without taking into account atom-photon interaction on the tunneling of atoms from one site to another. Considering this further, we believe that it would give further insight in the many body system of the BEC. This method would also be helpful in

studying other response functions of the BEC such as susceptibility as a function of onsite interaction and hopping.

diagonalization: the Bose Hubbard model as an example”, [arXiv:1102.4006v1](https://arxiv.org/abs/1102.4006v1).

4. CONCLUSION

In this paper, we have studied the transmission spectra of the cavity and used it as a tool to study and investigate the quantum properties and quantum phases of ultracold atoms non-destructively. We have illustrated the above idea using an exact diagonalisation method which is very useful to obtain the ground state wavefunction of the system at any point in the phase diagram, in contrast to the statistical approach as mentioned in ref [5-6] which enables to calculate the wavefunction for two particular phases only. This enables us to scan the phase boundary completely and map its characteristics onto the transmission spectra of the cavity photons. Within this framework, we plan to study other response functions of the BEC useful in the field of quantum optics.

ACKNOWLEDGEMENT

JL wishes to acknowledge the financial support from the University Grants Commission (UGC), New Delhi under SRF scheme.

REFERENCES

- [1] D. Jaksch, C. Bruder, J. I. Cirac, C.W. Gardiner, and P. Zoller, “Cold bosonic atoms in optical lattices”, *Phys. Rev. Lett.* **81**, 3108 (1998).
- [2] I. Bloch, J. Dalibard, W. Zwerger, “Many body physics with ultracold gases”, *Rev. Mod. Phys.* **80**, 885 (2008).
- [3] E. Altman, E. Demler, and D. M. Ludkin, “Probing many body states of ultracold atoms via noise correlations”, *Phys. Rev. A* **70**, 013603 (2005).
- [4] S. Fölling, F. Gerbier, A. Widera, O. Mandel, T. Gericke, and I. Bloch, “Spatial quantum noise interferometry in expanding ultracold atom clouds”, *Nature* **434**, 481- 484 (2005).
- [5] I. B. Mekhov, C. Maschler, and H. Ritsch, “Probing quantum phases of ultracold atoms in optical lattices by transmission spectra in cavity quantum electrodynamics”, *Nature Physics* **3**, 319-323 (2007).
- [6] H. Zoubi, and H. Ritsch, “Quantum phases of bosonic atoms with two levels coupled by a cavity field in an optical lattice”, *Phys. Rev. A* **80**, 053608 (2009).
- [7] I. B. Mekhov, C. Maschler, H. Ritsch, “Cavity enhanced light scattering in optical lattices to probe atomic quantum statistics”, *Phys Rev Lett* **98**, 100402 (2007).
- [8] R. Roth, and K. Burnett, “Phase diagram of bosonic atoms in two-color superlattices”, *Phys. Rev A* **68**, 023604 (2003).
- [9] J. M. Zhang, and R. X. Dong, “Exact

Supercontinuum Generation in All-Solid Photonic Crystal Fiber

Manish Tiwari

Department of Electronics & Communication Engineering
Jaipur Engineering College & Research Centre
Jaipur, India
Email: manishtiwari.ece@jecrc.ac.in

Vijay Janyani

Department of Electronics & Communication Engineering
Malaviya National Institute of Technology
Jaipur, India
Email: vijay.janyani@ieee.org

Abstract—In this paper, we demonstrate supercontinuum generation in an all-solid photonic crystal fiber and compare the results of the same with a more conventional, silica based photonic crystal fiber with air holes arranged in a hexagonal lattice structure. The proposed design for the all-solid fiber is shown to exhibit improved performance in terms of nonlinearity and dispersion characteristics leading to generation of a broader supercontinuum at lower powers and shorter distances, and hence a more potential candidate for a variety of telecommunication applications utilizing supercontinuum generation. We have used SF6 glass along with silica glass in the all-solid fiber design.

Keywords- all-solid; nonlinearity; photonic crystal fiber; silica; supercontinuum.

I. INTRODUCTION

Supercontinuum is extreme spectral broadening of optical pulses due to interplay between various nonlinear processes like self phase modulation, cross phase modulation, self steepening, four wave mixing, stimulated Raman scattering, stimulated Brillouin scattering etc with third order dispersion [1]. It was first observed in bulk glass by Alfano and Shapiro in 1970 [2] and then in optical fiber by Lin and Stolen in 1976 [3]. In recent years, photonic crystal fibers (PCFs) have become a popular choice for supercontinuum generation, after it was discovered by Ranka et al. in 2000 [4], due to the design flexibility which enables the optimization of various parameters like zero dispersion wavelength, nonlinearity and dispersion flattening.

Supercontinuum generation has a variety of telecom and non-telecom applications. The telecom applications of the supercontinuum include ultrashort pulse generation, wavelength division multiplexing, all optical analog-to-digital conversion, TDM-to-WDM-to-TDM conversion [5]. Supercontinuum has also been found very useful in applications like optical coherence tomography, frequency metrology, fiber characterization etc [6].

In this paper, we have presented a relatively new configuration, i.e. an all-solid photonic crystal fiber (AS-PCF) design and numerically investigated its optical properties and compared them with that of more conventional PCF, i.e. silica based PCF with air holes [7–9]. We have also demonstrated the generation of supercontinuum in these PCFs and shown that the supercontinuum generated in AS-PCF is much broader than

that generated in conventional silica based PCF due to enhanced nonlinearity of the AS-PCF. The proposed AS-PCF can be made using conventional stack – and – draw process.

The silica based PCF with air holes that we have modeled and simulated is SC – 5.0 – 1040TM, a highly nonlinear PCF by NKT Photonics [10]. We have found dispersion relations for both fibers using an iterative mode solver and material dispersion of the SF6 and silica have been included using their respective Sellmeier coefficients. Then, we have solved generalized nonlinear Schrödinger equation using split-step Fourier method to model the propagation of ultrashort optical pulses in nonlinear fiber.

II. FIBER PARAMETERS

A. Physical properties

We have analyzed two fibers in this paper. Fiber 1 is a hexagonal lattice structured PCF with SF6 used as the core material and the silica rods in place of air holes as a low index material. Fiber 2 is a conventional PCF with silica as core material and air holes in hexagonal lattice structure. Table 1 shows other geometrical properties of both the fibers.

TABLE I. PHYSICAL PROPERTIES OF THE PCFS ANALYSED

Fiber	Pitch	Hole diameter	No. of rings
Fiber 1	3.25	1.7	6
Fiber 2	3.25	1.7	6

SF6 glass offers special properties like high nonlinear refractive index (almost 10 times than that of silica), low melting temperature, high rare-earth solubility and low phonon energy. The cross-sectional layout of the structure of the fibers is as shown in figure 1.

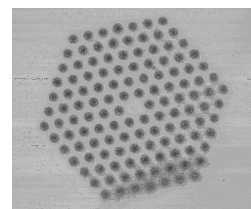


Figure 1. Electron Micrograph of SC – 5.0 – 1040TM (Courtesy: NKT Photonics)

B. Optical Properties

The dispersion relations of the both the fibers were computed using beam propagation method. The fundamental mode has zero dispersion wavelength at 1650 nm for Fiber 1 and 1040 nm for Fiber 2. The dispersion characteristics of both the fibers have been shown in figure 2 (a) and 2 (b) respectively.

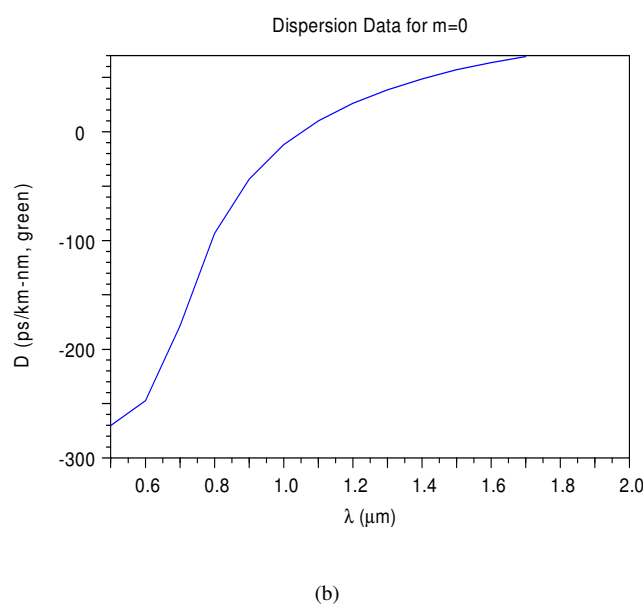
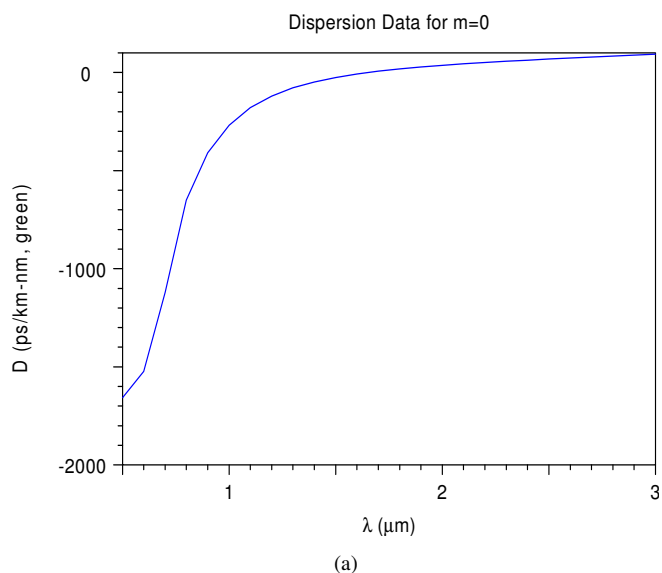


Figure 2. Dispersion curves for (a) Fiber 1 (b) Fiber 2

Some other typical optical properties of Fiber 1 and Fiber 2 have been calculated and are presented below in table 2. We have estimated nonlinearity γ [11], based on a nonlinear refractive index n_2 of $2.2 \times 10^{-19} \text{ m}^2/\text{W}$ for SF6 [12].

TABLE II. ZDW, EFFECTIVE AREA AND NONLINEARITY

	Zero Dispersion Wavelength	Effective Area (m^2) @ ZDW	Nonlinearity ($\text{W} - \text{km}$) ⁻¹ @ ZDW
Fiber 1	1650 nm	1.81868×10^{-11}	46
Fiber 2	1040 nm	1.6715×10^{-11}	9

III. PULSE PARAMETERS

The input pulse shape is taken as hyperbolic secant with $t_0 = 28$ fs and peak power of 1.5 kW. Mathematically, the input pulse can be expressed as:

$$A(z=0, t) = \sqrt{P_0} \operatorname{sech}\left(\frac{t}{t_0}\right) \exp\left(-i \frac{C}{2} \frac{t^2}{t_0^2}\right)$$

$$t_0 = t_{FWHM} / 1.7627 \quad (1)$$

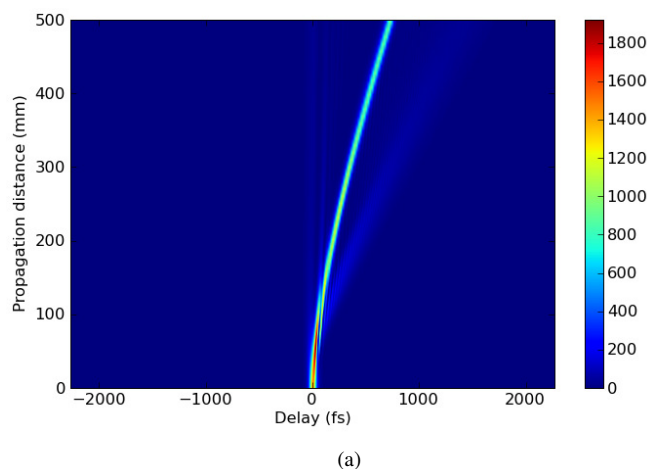
where P_0 : Peak pulse power, t_0 : Pulse period and C: chirp parameter.

TABLE III. PULSE PARAMETERS

Pulse Shape:	Hyperbolic Secant
Peak Power:	1.5 kW
T_{FWHM} :	50 fs
Center wavelength:	Fiber 1: 1680 nm Fiber 2: 1065 nm

IV. SUPERCONTINUUM GENERATION

We launched the optical pulse into both the fibers and solved the nonlinear Schrödinger equation using split-step Fourier method. Figure 3 (a) and 3 (b) show the temporal evolution and figure 4 (a) and 4 (b) show the spectral evolution of the optical pulse in both the fibers. The length of the fiber is 0.5 m in case of Fiber 1 and 1 m in case of Fiber 2.



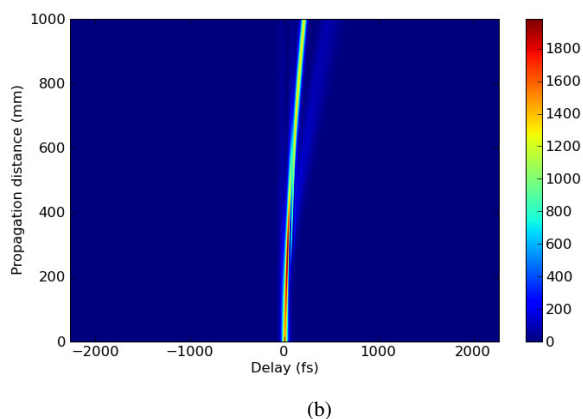


Figure 3. Temporal evolution of optical pulse in (a) Fiber 1 (b) Fiber 2

It can be seen in figure 3 (a) and 3 (b) that the red shifted peaks are delayed more in Fiber 1 at a shorter length than in Fiber 2 due to higher nonlinearity of the Fiber 1.

In figure 4(a) and (b), it can be seen that the supercontinuum generated in Fiber 1 is much broader than what is generated in Fiber 2. The span of the spectrum is about 450 nm in Fiber 1 in comparison to 150 nm in Fiber 2, that too in a smaller propagation distance as compared to that in Fiber 2.

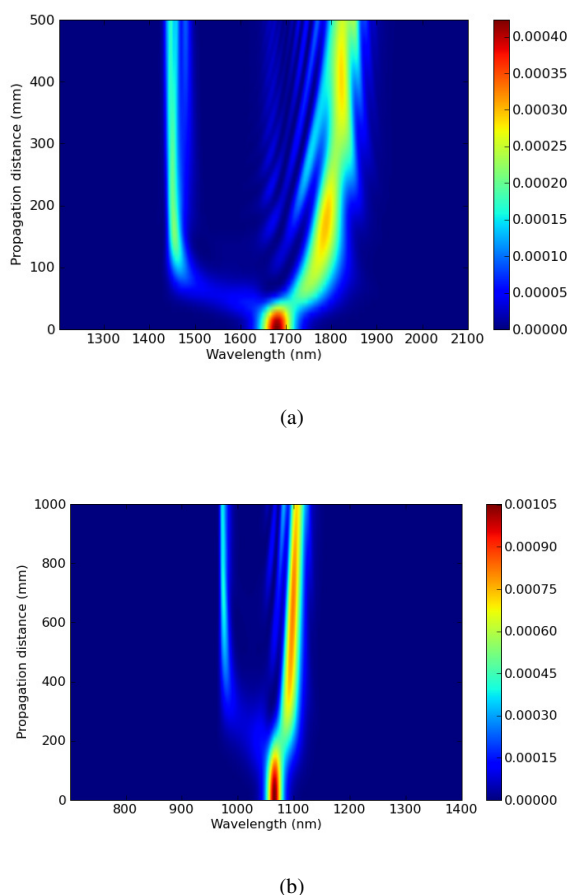


Figure 4. Spectral evolution of the optical pulse in (a) Fiber 1 (b) Fiber 2

In Fiber 1, the broadening begins to start at a very short length i.e. 50 mm and gives a broad, flat and coherent supercontinuum in comparison to Fiber 2.

V. CONCLUSION

Photonic crystal fiber with SF6 glass as the core and silica in place of air holes enhances the optical characteristics which are favorable of generating reasonably broad, flat and coherent supercontinuum and shifts the ZDW of the fiber to higher wavelength. A supercontinuum source with such properties can be used in a variety of telecom applications such as designing multi wavelength optical sources [13], all-optical analog-to-digital conversion based on splicing nonlinearly broadened spectrum using an arrayed waveguide grating [14], TDM-to-WDM conversion and vice versa [15, 16].

ACKNOWLEDGEMENT

The authors wish to acknowledge the UKIERI Major Grant on Microstructured Optical Fibres for support. The authors also acknowledge NKTPhotonics for providing physical properties of SC – 5.0 – 1040TM PCF.

REFERENCES

- [1] G.P. Agarwal, "Nonlinear fiber optics-4e", Academic Press, 2007
- [2] R. R. Alfano and S. L. Shapiro, "Observation of self-phase modulation and small-scale filaments in crystal and glasses," *Physical Review Letters*, vol. 24, pp. 592–594, Mar. 1970.
- [3] Lin and R. H. Stolen, "New nanosecond continuum for excited-state spectroscopy," *Applied Physics. Letters*, 28, pp. 216–218, 1976.
- [4] J. K. Ranka, R. S. Windeler, and A. J. Stentz, "Visible continuum generation in air-silica microstructure optical fibers with anomalous dispersion at 800 nm," *Optics Letters*, vol. 25, pp. 25–27, Jan. 2000.
- [5] S. V. Smirnov, J. D. Ania-Castanon, T. J. Ellingham, S. Kobtsev, and S. K. Turitsyn, "Optical spectral broadening and supercontinuum generation in telecom applications." *Opt. Fiber Technol.*, 12, 122-147 (2006).
- [6] F. Poli, A. Cucinotta and S. Selleri, "Photonic Crystal Fibers: Properties and Applications", Springer, 2007.
- [7] M. Tiwari and V. Janyani, "Spectral broadening of ultrashort optical pulses in nonlinear photonic crystal fiber", in *Proc. International Conference on Optics and Photonics*, Chandigarh, 2009, pp: 252
- [8] M. Tiwari and V. Janyani, "Supercontinuum Generation and Optimisation in Nonlinear Photonic Crystal Fibres", in *Proc. International Conference on Computer and Network Technology - ICCNT 2010*, Bangkok, Thailand, pp: 606 – 607.
- [9] M. Tiwari and V. Janyani, "Effect of Peak Pulse Power on the Supercontinuum Generation in Highly Nonlinear Photonic Crystal Fiber", *Asia-Pacific Microwave Photonics Conference - APMP2010*, Hongkong, paper 519.
- [10] "NKTPhotonics® SC-5.0-1040TM nonlinear PCF"- Specification sheet. <http://www.nktphotonics.com/files/files/SC-5.0-1040.pdf>.
- [11] N. A. Mortensen, "Effective area of photonic crystal fiber", *Opt. Express*, 10., 341–348. (2002),
- [12] V. V. R. K. Kumar, A. K. George, W. H. Reeves, J. C. Knight, P. St.J. Russell, F. G. Omenetto and A. J. Taylor, "Extruded soft glass photonic crystal fiber for ultrabroad supercontinuum generation," *Opt. Express* 10, 1520- 1525 (2002).
- [13] T. Morioka, K. Mori, M. Saruwatari, "More than 100-wavelength-channel picosecond optical pulse generation from single laser source

using supercontinuum in optical fibers”, *Electron. Lett.* 29 (1993) 862–864.

- [14] S. Oda, S. Okamoto, A. Maruta, “A novel quantization scheme by slicing supercontinuum spectrum for all optical analog-to-digital conversion”, in *Proceedings of NLGW 2004*, Toronto, Canada, 2004, paper TuB3.
- [15] H. Sotobayashi, W. Chujo, K. Kitayama, “Photonic gateway: TDM-to-WDM-to-TDM conversion and reconversion at 40 Gbit/s (4 channels \times 10 Gbits/s)”, *J. Opt. Soc. Amer. B* 19 (11) (2002) 2810.
- [16] H. Sotobayashi, W. Chujo, T. Ozeki, Bi-directional photonic conversion between 4×10 Gbit/s OTDM and WDM by optical time-gating wavelength interchange, in: *Proceedings of OFC 2001*, Anaheim, 2001, paper WM5.

GENERATION OF OPTICAL PHASE CONJUGATION PROPERTIES IN DYE SENSITISED SILVER HALIDES USING DFWM

K. Kochunarayanan, Krishnakumar V. and V.P. Mahadevan Pillai*

**Department of Optoelectronics, University of Kerala, Kariavattom, Thiruvananthapuram,
Kerala, India**

***Email:vpmpillai9@gmail.com**

Abstract: Optical phase-conjugate beam is generated in organic dyes embedded in silver halide films and phase conjugation properties have been investigated.

1. INTRODUCTION

Over the last three decades, optical phase-conjugation (OPC) has been one of the major research subjects in the field of nonlinear optics and quantum electronics. Optical phase-conjugation defines usually a special relationship between two coherent optical beams propagating in opposite directions with reversed wave front and identical transverse amplitude distributions. Several technical approaches are there to efficiently produce the backward phase-conjugate beam. Organic dye-doped solid matrices are very attractive materials in recent years for the generation of phase-conjugate waves [1,2]. Dyes having strong absorption at the wavelength of He-Ne laser and a long life time of their triplet state can generate the phase-conjugate wave at a low laser powers. In the present investigation, backward DFWM method is used to generate phase-conjugate beam in organic dye (Lissamine Green B) coated on silver halide holographic plates and its phase conjugation properties have been studied [3]. Lissamine Green B dye belongs to the triphenyl methane groups. The chemical structure of Lissamine Green B dye is shown in Figure 1.

Nonlinear optical phase conjugation by degenerate four wave mixing (DFWM) in organic materials has several real time applications in holography, phase conjugation and spectroscopy. Due to the excited π -bond electrons, organic molecules

exhibit large polarisabilities. These electrons are delocalized and can be easily polarizable. Saturable absorption plays a very important role when dyes are

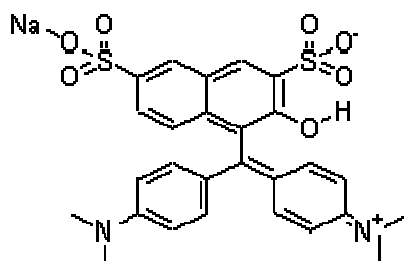


Fig. 1. Chemical structure of triphenylmethane group

used for the production of phase conjugation light. [1]. Organic molecules exhibit third order susceptibilities, which can be explained by a three level system [2]. When light energy is incident on these dyes, electrons excite from the ground level S_0 to the excited state S_1 and the dye switches to a triplet state. The energy absorbed by the S_0 level is a function of the intensity of the incident light energy. As intensity increases, absorption increases at first, reaches a maximum value and then decreases. The absorption of energy gives rise to the formation of thermal gratings and are formed due to the change in refractive index of the material when energy is incident on the dye. These thermal gratings formed are temporary in nature and vanishes when the incident beams are removed. The grating period can be determined using the relation

$$\Lambda = \frac{\lambda}{2n \sin(\theta/2)} \quad (1)$$

where λ is the incident wavelength and θ is the angle between the pump beam and the probe beam. The grating frequency is determined by the angle θ , for wider angle a transmission grating is formed and for a smaller angle reflection gratings are formed. The theory of DFWM was formulated for a Two-level saturable absorber by Abrams and Lind [3] which was subsequently modified by Silberberg and Bar-Joseph [4] for a three level absorber. The phase conjugated reflectivity is given by the following Equation,

$$R = \frac{|k|^2}{|\alpha + w \cot(wL)|^2} \quad (2)$$

where $w = (|k|^2 - \alpha^2)^{1/2}$ and α is the absorption coefficient[7]. The absorption coefficient α is obtained from the intensity of pump beam as given below in Eq.3. The beam coupling constant is given by Eq.4.

$$\alpha = \alpha_0 \frac{1 + I_1 + I_2}{[1 + 2(I_1 + I_2) + (I_1 - I_2)^2]^{3/2}} \quad (3)$$

$$k = 2\alpha_0 i \frac{I_1 I_2}{[1 + 2(I_1 + I_2) + (I_1 - I_2)^2]^{3/2}} \quad (4)$$

The interference produced by the beams in the experiment creates a spatial variation of refractive index. The refractive index of the illuminated region is less compared to the non exposed region. So the interference pattern of refractive index change is created in the process which can lead to large non-linear optical effects [5, 6]. The creation of thermal refractive index can be explained by the following steady-state heat transport equation,

$$\frac{\Delta(nL)}{nL} = \frac{1}{n} \frac{\partial n}{\partial T} \Delta T + \frac{1}{L} \frac{\partial L}{\partial T} \Delta T \quad (5)$$

where n is refractive index, L is sample thickness and T is the temperature.

2. Experimental Details.

The holographic plates supplied by Slavich Inc are used for the study. The silver halide deposition on the Slavich PFG02 plate is removed by immersing it in sodium thiosulphate solution for few minutes. The dye (Lissamine Green B) film is coated on the gelatin base that is already present in the holographic plate. For this dip-coating technique is used. The solution for the dip coating is prepared by dissolving Lissamine Green B dye (concentration 5% and 10%) in polyvinyl alcohol. The silver halide removed Slavich PFG02 plates are dipped in Lissamine Green B dye solution. A homogeneous film obtained is dried in an oven for six hours at a temperature 40°C.

Figure 2 shows the schematic diagram of the experimental setup for the generation of optical phase conjugated wave.

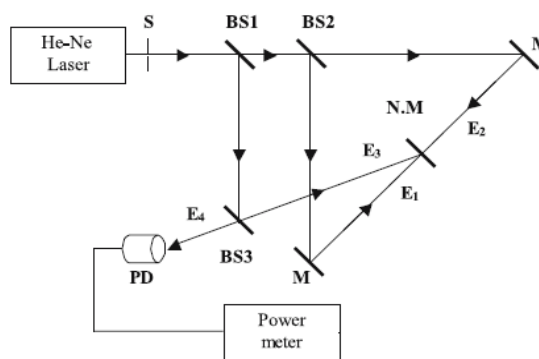


Fig.2: Schematic diagram of the experimental set-up setup for generating PC wave. BS1–BS3, Beam splitters; M, Mirror; NM, Sample; PD, Photo-detector. S, Shutter.

The output beam from the He-Ne laser is first split by a beam-splitter BS1 whose splitting ratio can be adjusted. The beam reflected from BS1 is used as the probe beam. The transmitted beam from BS1 is further divided by another beam-splitter BS2 of

splitting ratio 50:50 to provide the counter-propagating pump beams, called forward-pump wave E_1 and backward-pump wave E_2 respectively. Beam-splitter BS3 is used to direct the probe beam to the dye-doped sample and to transmit the PC (Phase conjugated) signal, which is opposite to the direction of the probe beam. The intensity of PC wave is measured by a photo detector fed to the digital power meter. The constant intensity ratio of the probe beam (E_3), forward-pump beam (E_1), and backward-pump beam (E_2) used in this study is $\sim 1: 10: 10$. The incident angle (θ) between the probe beam and forward-pump beam is fixed at ~ 10 . The optical path lengths of all the three beams are made equal, so that they are coherent at the sample. The absorption and transmission of the sample is studied by a V550 double beam spectrophotometer. The peak absorbance of the material is around 630 nm which is same as the wavelength of laser source used for the study.

3. Results and Discussion

Figure 3a and 3b show the PC signal versus the time for two different dye concentrations of the films. The measurements are taken by varying the parameters which influence the PC signal during the DFWM processes. PC signal intensity rises linearly to a maximum and then decreasing. The temporal interference decays with time. As the dye is exposed to more energy the interference pattern decays. This decay reduces the transmission of phase conjugated signal.

Figure 4 shows the PC transmission as a function of change in wavelength. The material has peak transmission at 630 nm. When the same sample is illuminated with different intensities, the transmittance is found to be increasing with increasing intensity. This confirms the existence of a light-induced bleaching process associated with this dye-doped system. For lower intensities the bleaching

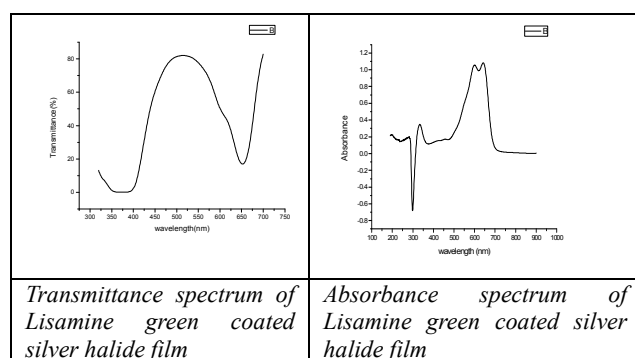
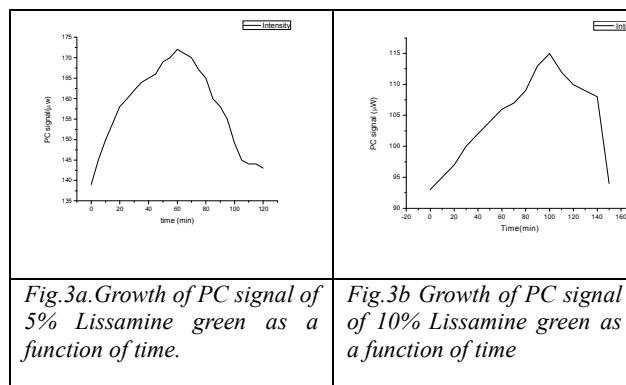


Fig.4. PC transmission as a function of change in wavelength.

may be reversible. But higher intensities may result in complete decomposition of dye molecules. Such observations have already been reported [4,5,6]. The initial increase to the peak within a few minutes is due to degenerate four wave mixing and the drop in the intensities of the PC signal after reaching a maximum is due to the photo bleaching process.

4. Conclusion.

It is found that Lissamine green exhibits a third order optical nonlinearity thereby generating a phase conjugate wave by degenerate four wave mixing. The transmittance, absorbance are studied. It is found that the materials have a good nonlinear response to a laser radiation of wavelength 630 nm even for low intensities. The UV-VIS absorption spectrum of dye exhibits the absorbance peak at 630 nm.

- [1] M. A. Kramer, W. R. Tompkin, and R. W. Boyd, "Nonlinear optical interactions in fluorescein-doped boric acid glass," *Physical Review A*, **34**, 3, 2026(1986).
- [2] Y. Silberberg and I. Bar-Joseph, "Transient effects in degenerate four-wave mixing in saturable absorbers," *IEEE Journal of Quantum Electronics*, **17**, 9, 1967(1981).
- [3] R. L. Abrams and R. C. Lind, "Degenerate four-wave mixing in absorbing media," *Optics Letters*, **2**, 4, 94(1978).
- [4] Y. Silberberg and I. Bar-Joseph, "Low power phase conjugation in thin films of saturable absorbers," *Optics Communications*, **39**, 4, 265, (1981).
- [5] R. W. Boyd, *Nonlinear Optics*, Academic Press, New York, NY, USA, 1992
- [6] R. Y. Choie, T. H. Barnes, W. J. Sandle, A. D. Woolhouse, and I. T. McKinnie, "Observation of a thermal phase-grating contribution to diffraction in erythrosin-doped gelatin films" *Optics Communications*, **186**, 1-3, 43, (2000).
- [7]. M. H.Majles Ara, S.Mehrabani, and R.Malekfar "Phase Conjugation Using Four-WaveMixing in Fast Green FCF Dye-Doped Gelatin Film" *Advances in Nonlinear Optics* Volume 2009,(2009)

COMPETITION BETWEEN FIELD STRENGTH AND D-D INTERACTION IN TWO TWO-LEVEL ATOMS

Shaik Ahmed, V.S. Ashoka and P. Anantha Lakshmi
School of Physics, University of Hyderabad
Hyderabad – 500 046, India

Abstract: A study of two identical two level atoms interacting with a single mode radiation field, wherein the atoms themselves are coupled through dipole-dipole interaction is presented. In this study, comparison between direct two photon excitation and stepwise excitation of two single photons is carried out. It is found that there is an optimal value of the dipole coupling parameter for a given Rabi field strength for which the direct two photon transition dominates. Steady state and transient solutions of different populations and coherences are presented as a function of different system parameters.

1. INTRODUCTION

The interaction of a laser field with a collection of atoms has been the subject of intense interest due to several reasons, one of them being that it can serve as a prototype model for investigating the dynamics of dense atomic systems such as Bose Condensates. The simplest possible system one can study is a pair of two level atoms interacting with a single mode radiation field, where both the atoms not only interact with the radiation field but also interact with each other through dipole-dipole coupling. Recent advances have enabled trapping and studying as few as one atom by optical/magnetic means, in light of which the above study gains relevance.

Studies on pairs of two level atoms have been carried out by several research groups [1-5]. Several earlier studies reported that correlation between two identical atoms can give rise to new resonances in the resultant fluorescence spectrum [6]. In a collection of atoms, the first excited atom prevents the excitation of neighboring atoms due to the dipole-dipole interaction, which is referred to as dipole blockade effect. This dipole blockade can give rise to the production of single atom excited collective states. In an earlier work, Varada and Agarwal [7] have worked in the dressed state space of dipole-dipole interaction between two two-level atoms and derived the conditions under which enhancement of the two photon resonance can be achieved. In another work [8] the entanglement characteristics of such a system were explored via a study of two photon correlations. In a more recent work [9] the effect of dipole blockade on the dynamical evolution of two two-level atom system in the presence of a driving field was studied to gain insight into the entanglement characteristics of the system.

In this work, we examine in detail, the behavior of the two two-level atom system for the case of identical as well as non-identical atoms. We work in the product space of the single atom states. We model the two two-level atom system as an equivalent four level atom system. We take into

account the spontaneous decays in the master equation formalism and the same are solved both in steady state as well as in transient regimes. We explore the competing behavior between the Rabi field strength and the dipole interaction on the level populations, the atomic coherences and the total one photon as well as two photon absorption from the system.

The model and the equations of motion and the method of solution are described in section 2. In Section 3, some of the numerical results with discussion are presented.

2. THE MODEL

Consider two non-identical isolated two-level atoms fixed in position with a distance r such that ($r \ll \lambda$), driven by a single mode laser field, which is nearly resonant with transition frequency of one of the atoms. The atomic system is treated quantum mechanically while the laser field interaction as well as the dipole-dipole interaction are incorporated phenomenologically.

The two two-level atom systems can be represented as an effective four level system as shown below.

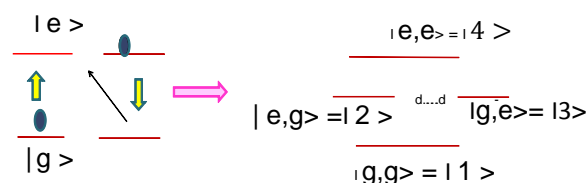


FIG. 1. Schematic energy level diagram of two two-level atoms and the equivalent four-level system. Here label g (e) indicates ground (excited) state.

The level $|g,g\rangle$ ($|e,e\rangle$) corresponds to both the atoms being in their ground (excited) state. The intermediate state $|e,g\rangle$ ($|g,e\rangle$) represents the case when first (second) atom is in excited state and second (first) atom is in the ground state. We

simplify our notation of the energy levels by introducing the following: $|g,g\rangle \equiv |1\rangle$, $|e,g\rangle \equiv |2\rangle$, $|g,e\rangle \equiv |3\rangle$ and $|e,e\rangle \equiv |4\rangle$. We use the master equation formalism to study the dynamical evolution of the density operator of the atomic system.

The Hamiltonian for the system is given by

$$H = \begin{bmatrix} \omega_1 & -\alpha_{21}^* & -\alpha_{31}^* & 0 \\ -\alpha_{21} & \omega_2 & -g & -\alpha_{42}^* \\ -\alpha_{31} & -g & \omega_3 & -\alpha_{43}^* \\ 0 & -\alpha_{42} & -\alpha_{43} & \omega_4 \end{bmatrix} \quad (1)$$

where ω_i ($i=1,2,3,4$) is the frequency of level i , α_{ij} are the different Rabi frequencies in the problem which stand for the coupling constant of the atoms with the electric field and g is the strength of the dipole interaction.

The equation of motion for the density matrix is given by

$$i\hbar \partial \rho / \partial t = [H, \rho] - \mathcal{L}\rho \quad (2)$$

where the first term on the RHS represents the interaction with the radiation field and the dipole interaction and the second term represents the decay mechanisms. In this study, we have only taken into account the spontaneous emission decays. The resulting equations of motion for the sixteen density matrix elements in the rotating wave approximation are obtained as follows:

$$\begin{aligned} \partial_t \rho_{11} &= i\alpha_{21}^* \rho_{21} - i\alpha_{31} \rho_{12} + i\alpha_{31}^* \rho_{31} - i\alpha_{31} \rho_{13} + 2\gamma_{21} \rho_{22} + 2\gamma_{31} \rho_{33} \\ \partial_t \rho_{12} &= (i\Delta_2 - \gamma_{21}) \rho_{12} + i\alpha_{21}^* \rho_{22} + i\alpha_{31}^* \rho_{32} - i\alpha_{21}^* \rho_{11} - ig \rho_{13} - i\alpha_{42} \rho_{14} \\ \partial_t \rho_{13} &= (i\Delta_3 - \gamma_{31}) \rho_{13} + i\alpha_{21}^* \rho_{23} + i\alpha_{31}^* \rho_{33} - i\alpha_{31}^* \rho_{11} - ig \rho_{12} - i\alpha_{43} \rho_{14} \\ \partial_t \rho_{14} &= (i\Delta_2 + i\Delta_3 - \gamma_{43} - \gamma_{42}) \rho_{14} + i\alpha_{21}^* \rho_{24} + i\alpha_{31}^* \rho_{34} - i\alpha_{42}^* \rho_{12} - i\alpha_{43}^* \rho_{13} \\ \partial_t \rho_{21} &= (-i\Delta_2 - \gamma_{21}) \rho_{21} - i\alpha_{21} \rho_{22} - i\alpha_{31} \rho_{23} + i\alpha_{21} \rho_{11} + ig \rho_{31} + i\alpha_{42}^* \rho_{41} \\ \partial_t \rho_{22} &= -i\alpha_{21}^* \rho_{21} + i\alpha_{21} \rho_{12} + ig(\rho_{32} - \rho_{23}) + i\alpha_{42}^* \rho_{42} - i\alpha_{42} \rho_{24} + 2\gamma_{42} \rho_{44} - 2\gamma_{21} \rho_{22} \\ \partial_t \rho_{23} &= (i\Delta_3 - i\Delta_2 - \gamma_{21} - \gamma_{31}) \rho_{23} + i\alpha_{21} \rho_{13} + i\alpha_{42}^* \rho_{43} - i\alpha_{31}^* \rho_{21} - i\alpha_{43} \rho_{24} + ig(\rho_{33} - \rho_{22}) \\ \partial_t \rho_{24} &= (i\Delta_3 - \gamma_{21} - \gamma_{42} - \gamma_{43}) \rho_{24} + i\alpha_{21} \rho_{14} + i\alpha_{42}^* \rho_{44} - i\alpha_{42}^* \rho_{22} + ig \rho_{34} - i\alpha_{43} \rho_{23} \\ \partial_t \rho_{31} &= (-i\Delta_3 - \gamma_{31}) \rho_{31} - i\alpha_{21} \rho_{32} - i\alpha_{31} \rho_{33} + i\alpha_{31} \rho_{11} + ig \rho_{21} + i\alpha_{43}^* \rho_{41} \\ \partial_t \rho_{32} &= (-i\Delta_3 + i\Delta_2 - \gamma_{21} - \gamma_{31}) \rho_{32} - i\alpha_{21}^* \rho_{31} - i\alpha_{42} \rho_{34} + i\alpha_{31} \rho_{12} + i\alpha_{43}^* \rho_{42} - ig(\rho_{33} - \rho_{22}) \\ \partial_t \rho_{33} &= -i\alpha_{31}^* \rho_{31} + i\alpha_{31} \rho_{13} - ig(\rho_{32} - \rho_{23}) + i\alpha_{43}^* \rho_{43} - i\alpha_{43} \rho_{34} + 2\gamma_{43} \rho_{44} - 2\gamma_{31} \rho_{33} \\ \partial_t \rho_{34} &= (i\Delta_2 - \gamma_{31} - \gamma_{42} - \gamma_{43}) \rho_{34} + i\alpha_{31} \rho_{14} + i\alpha_{43}^* \rho_{44} - i\alpha_{43}^* \rho_{33} + ig \rho_{24} - i\alpha_{42}^* \rho_{32} \\ \partial_t \rho_{41} &= (-i\Delta_2 - i\Delta_3 - \gamma_{43} - \gamma_{42}) \rho_{41} - i\alpha_{21} \rho_{42} - i\alpha_{31} \rho_{43} + i\alpha_{42} \rho_{21} + i\alpha_{43} \rho_{31} \\ \partial_t \rho_{42} &= (-i\Delta_3 - \gamma_{21} - \gamma_{42} - \gamma_{43}) \rho_{42} - i\alpha_{21}^* \rho_{41} - i\alpha_{42} \rho_{44} + i\alpha_{42} \rho_{22} - ig \rho_{43} + i\alpha_{43} \rho_{32} \\ \partial_t \rho_{43} &= (-i\Delta_2 - \gamma_{31} - \gamma_{42} - \gamma_{43}) \rho_{43} - i\alpha_{31}^* \rho_{41} - i\alpha_{43} \rho_{44} + i\alpha_{43} \rho_{33} - ig \rho_{42} + i\alpha_{42} \rho_{23} \\ \partial_t \rho_{44} &= i\alpha_{42} \rho_{24} - i\alpha_{42}^* \rho_{42} + i\alpha_{43} \rho_{43} - i\alpha_{43}^* \rho_{43} + 2(\gamma_{42} + \gamma_{43})(1 - \rho_{11} - \rho_{22} - \rho_{33}) \end{aligned} \quad (3)$$

where $\Delta_2 = \omega_{atom1} - \omega_{field}$

$\Delta_3 = \omega_{atom2} - \omega_{field}$ and the total detuning $\Delta = \Delta_2 + \Delta_3$.

By using the completeness relation among the level populations, these equations can be reduced to 15 inhomogeneous equations which can be written as

$$\partial \Psi / \partial t = M \Psi + \Phi \quad (4)$$

The steady state solution of the density matrix elements is obtained as

$$\Psi(t \rightarrow \infty) = -M^{-1} \Phi \quad (5)$$

The time dependent solutions can be obtained by solving the set of 15 differential equations. In the next section we present some of our numerical results for both the steady state as well as the transient case for both identical as well as non identical atoms. We have studied the case where the coupling between the atom and the field is assumed to be same which corresponds to all α_{ij} being equal which we designated as α all the decay parameters also are taken to be equal ($\gamma_{ij} = \gamma$).

3. RESULTS AND DISCUSSION

In this section, some of the numerical results both for identical as well as non-identical atoms are presented. It should be mentioned that we have studied the identical as well as non-identical atoms for a wide choice of parameters but are presenting results for only one representative set of values of the parameters.

In Figure 2, the steady state populations of all the four levels are plotted for the case of identical atoms for a typical value of Rabi frequency $\alpha = 2$ and for different values of the dipole interaction parameter $g = 0, 1, 5$ and 10 . All parameters are taken in units of γ .

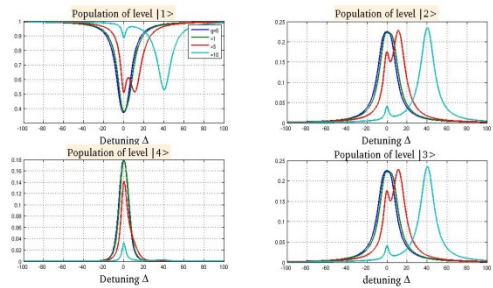


FIG 2. Level populations for the case of identical two-level atoms for Rabi frequency $\alpha = 2$ and for different values of dipole coupling g as shown in the center box.

From the plots of the populations, it is observed that for the case when there is no dipole interaction (which corresponds to both atoms acting independently of each other), the population of levels 2 and 3 both show a single peak. With the

inclusion of dipole coupling g , a second peak appears in both ρ_{22} and ρ_{33} , in addition to the central peak. The population of the two photon excited state ρ_{44} exhibits only a central peak both for $g=0$ as well as for moderate values of g and it starts to develop a shoulder as g is further increased ($g=10$). Further, it is observed that as g is increased from 0 to 10, the population ρ_{44} decreases monotonically. This is because the dipole-dipole coupling inhibits the simultaneous excitation of two atoms which is nothing but dipole-blockade.

We next present the results for the populations for the case of non-identical atoms. The two atoms are rendered non identical by considering different level spacings.

In figure 3, the populations for the case of non-identical atoms are presented, where the choice of parameters is chosen to be the same as in figure 2 except for the level spacings, which are taken as $\omega_{atom2} = \omega_{atom1} + 10$. It is to be noted that all quantities are considered in units of γ . In this case, as opposed to the case of identical atoms, there is a non-monotonic increase in the population of two-photon excited state ($|4\rangle$).

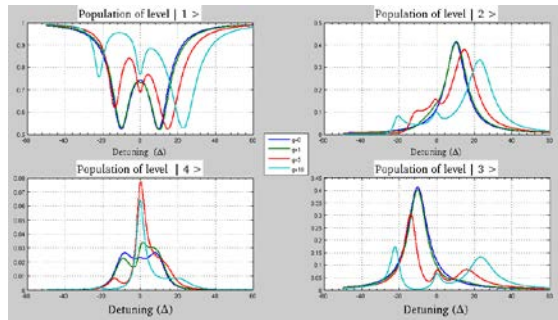


FIG 3. Level populations for the case of non- identical two-level atoms for Rabi frequency $\alpha = 2$ and for different values of dipole coupling g as shown in the center box.

The central peak in ρ_{44} is increasing in height as g is increased from 0 to 5 and it starts to decrease with further increase in g ($=10$ in the figure). Similar to ρ_{44} , the populations of the intermediate one-photon excited levels are also exhibiting a three peaked structure. The redistribution of population in the two-photon excited state *vis a vis* the populations of the one-photon excited states needs to be further explored.

Next, imaginary part of the atomic coherence ρ_{14} is plotted for both identical as well as non-identical atoms in two adjacent frames in figure 4. The non monotonic nature of this quantity with respect to increase in g is observed for both the cases. The height of the central peak is found to increase up to

a value of $g = 10$ and a further increase in g ($g=20$) results in a decrease of the same. This suggests an optimal combination of α and g which maximizes this function which is shown in Fig. 5 for different values of α .

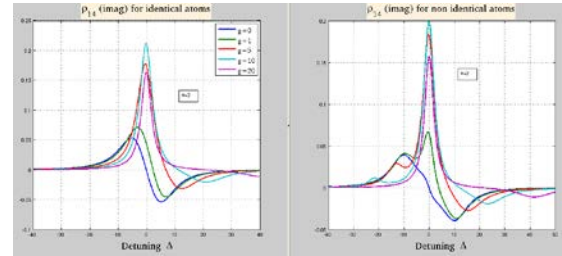


FIG. 4 Imaginary part of atomic coherence ρ_{14} for the case of both identical and non- identical two-level atoms for Rabi frequency $\alpha = 2$ and for different values of dipole coupling g as shown in the center box.

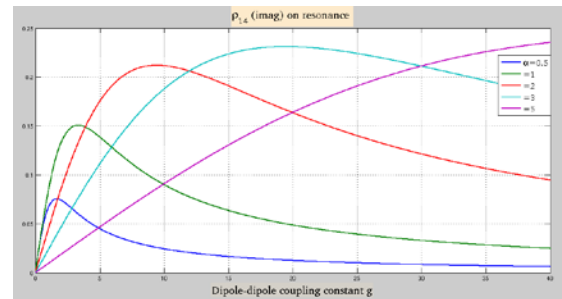


FIG. 5 Imaginary ρ_{14} at resonance as a function of dipole coupling parameter g for different values of α

A numerical study of the atomic coherence ρ_{23} is also carried out. For identical atoms, it remains positive throughout the range of Δ whereas for non identical atoms, as g is increased, one observes two peaks of opposite signs on either side of $\Delta = 0$.

It is expected that atomic coherences ρ_{14} and ρ_{23} are measure of the entanglement between the pairs $|ee\rangle - |gg\rangle$ and $|eg\rangle - |ge\rangle$ respectively. Further investigation of their behavior needs to be carried out to gain clearer insight into the entanglement characteristics of this system.

The four independent channels of single photon absorption give rise to the atomic coherences ρ_{21} , ρ_{31} , ρ_{42} and ρ_{43} . Imaginary part of each of these, which signify absorption, are plotted in figures 6 and 7. For identical atoms, $\text{Im}(\rho_{21}) = \text{Im}(\rho_{31})$; and $\text{Im}(\rho_{42}) = \text{Im}(\rho_{43})$.

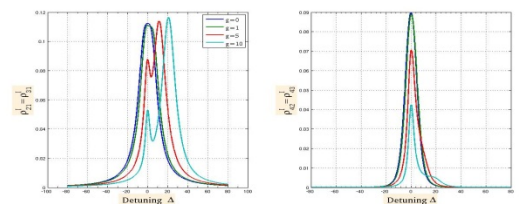


FIG. 6 One-photon absorption cross sections for identical atoms

The profile of $\text{Im}(\rho_{21}=\rho_{31})$ plotted in Fig. 6 is consistent with that of ρ_{22} in Fig. 2 and $\text{Im}(\rho_{42})$ with ρ_{44} , showing cause and effect relation. Fig. 7 shows that, for non identical atoms the four channels of excitation are different as expected.

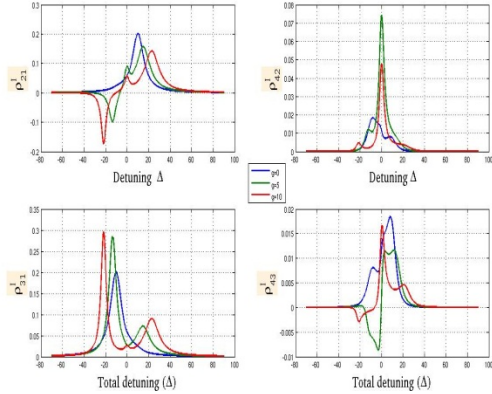


FIG 7: One-photon absorption for the case of non-identical atoms

$\text{Im}(\rho_{21})$ shows signature of gain at a point $\Delta < 0$. The specific value of this Δ is a function of g . However $\text{Im}(\rho_{31})$ shows a large absorption for the same Δ , nullifying the effect of this gain. Similarly gain in $\text{imag}(\rho_{43})$ channel is nullified by $\text{imag}(\rho_{42})$. The total response of the two atom system being the sum of all four channels, is showing absorption for all values of Δ [Fig. 8].

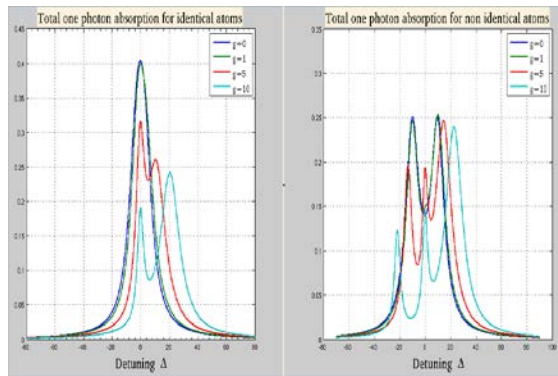


FIG 8: The total one photon absorption for the case of both identical and non- identical two-level atoms for Rabi frequency $\alpha = 2$ and for different values of dipole coupling g as shown in the center box.

In figure 9, the time evolution of the level populations are plotted for $\alpha=2$ and for different values of $g = 0.5, 10$. As the dipole coupling strength is increased, the number of oscillations (before steady state is attained) is increasing in all of the populations. Increase in dipole coupling is resulting in a decrease in the steady state value of

all the excited state populations. Correspondingly there is an increase in the ground state population.

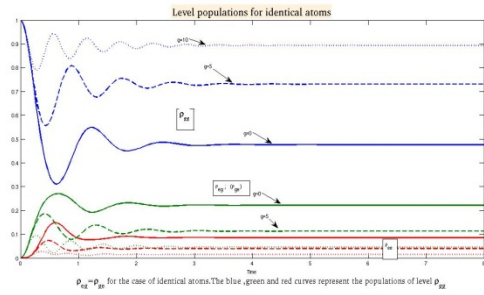


FIG. 9: Level populations as a function of time taken in units of γ .

This shows that d-d coupling is inducing both the atoms to be trapped in the ground state.

4. CONCLUSION

We have studied the effect of dipole-dipole interaction on a pair of two-level atoms interacting with a laser field. The strength of dipole interaction is incorporated phenomenologically by the parameter g . Populations as well as coherences were computed for different values of g . Results are presented for both identical and non identical atoms and they are in qualitative agreement with the experimental results [10]. These initial results indicate areas in which more detailed calculations need to be performed to understand the full dynamics of the various interactions which are under investigation currently.

5. ACKNOWLEDGEMENTS

Shaik Ahmed gratefully acknowledges the financial support from University Grants Commission, Govt. of India.

6. REFERENCES

1. U. Fano, Rev. Mod. Phys. **55**, 855(1983)
2. G. S. Agarwal, A. C. Brown, L. M. Narducci, and G. Vetri, Phys. Rev. A **15**, 1613(1977)
3. I. R. Senitsky, Phys. Rev. Lett. **40**, 1334(1978)
4. H. S. Freedhoff, Phys. Rev. A **19**, 1132(1979)
5. Z. Ficek, R. Tanas and S. Kielich, Opt. Acta **33**, 1149(1983)
6. G. S. Agarwal, L. M. Narducci and E. Apostolidis, Opt. commun. **36**, 285 (1981).
7. G. V. Varada and G. S. Agarwal, Phys. Rev. **A**, **45**, 1992.
8. J. Von Zanthier, T Bastin and G.S. Agarwal, Phys. Rev. A Rapid Communication **74**, 061802 (2006)
9. J. Gillet, G. S. Agarwal and T. Bastin, Phys. Rev. **A**, **81**, 2010.
10. C. Hettich, C. Schmitt, J. Zitzmann, S. Kuhn, I. Gerhardt and V. Sandogdar, Science **298**, 2002.

STUDIES ON SOL-GEL COATED POLYCARBONATE BI-ASPHERIC LENSES FOR INDIRECT OPHTHALMOSCOPY

Neeraj Kumar, Vinod Mishra, Keshvanand, G S Singh, S V Ramagopal, Pawan Kapur
CSIR-Central Scientific Instruments Organisation (CSIR-CSIO), Sector-30C, Chandigarh 160030
neerajkumar2009@gmail.com

Aspheric optics offer more degrees of freedom to control optical aberrations, while adhering to the system budgets of weight, volume and footprint. Additionally, optical grade plastics provide cost effective large volume production of aspheric-optic modules and systems. Development of precision aspheric fabrication equipment and technological advances in profilometry facilitate aspheric-based optics deliver desired image quality while meeting system weight & geometry constraints.

However, aspheric surface generation comes at notable cost and image penalties. To maintain commercial viability of aspheric-based optics, one must address the sources of form errors and find the means to reduce these errors. Also, the optical grade plastics are scratch-prone and hygroscopic. To maintain profile integrity (to deliver desired aberration-free performance) and nanometric surface finish (to reduce scattering), the precision aspheric surfaces need to be protective-coated. Thermal features of plastic optics are not amenable for conventional vacuum coating techniques. Hence, one needs to explore novel coating techniques viz: cold plasma, sol-gel for plastic optics. Protected surface is essential benchmark of precision aspheric optics for various applications. Hence, CSIR-CSIO in its PolyCarbonate (PC) Aspheric Optic Development for Indirect Ophthalmoscopy, is collaborating with ARCI (Hyderabad), for sol-gel coating of PC aspheric lenses.

To explore sol-gel coating and to resolve the relevant issues for its application for plastic aspheric

lenses, a series of studies are conducted with PC lenses (of plane, spherical and aspheric profiles with different diameters) developed by single point diamond turning (SPDT). The surface quality is assessed by surface profilometry in terms of form error (maximum amplitude of peak-to-valley) and average roughness (Ra). In first part, a series of plane profiles are developed and after profilometry are sol-gel coated. The coated lenses are once again profiled. Based on the metrology results, the composition of coating constituents is optimized to obtain acceptable uniform coating thickness. In second stage, four spherical PC profiles of 20D and 28D are generated (by SPDT). The lenses are also profiled, sol-gel coated and re-characterized to assess the uniformity of sol-gel coating.

Finally, four plano-aspheric 20D & 28D profiles (in varying gradients) are fabricated (by point-to-point interpolation during SPDT). In each set, three samples are developed and sol-gel coated to assess repeatability in terms of machining and coating. Similarly, each of these four profiles are repeatedly scanned (pre and post coating). The surface quality (pre and post coating) of these four profiles is analyzed with each sample. It is noted that, waviness error increases with curvature of surface, due to oblique machining of deep profiles and the resultant tool deflection therein. Additionally, the PC lenses exhibit larger non-uniformity coating errors with increasing curvatures. The reasons thereof are analyzed. Suitable compensation methods to reduce the profile error during sol-gel coating are explored.

ERROR COMPENSATION IN SOL-GEL COATED POLYCARBONATE BI-ASPHERIC LENSES

Vinod Mishra, Neeraj Kumar, Keshvanand, G S Singh, S V Ramagopal, Pawan Kapur
CSIR-Central Scientific Instruments Organisation (CSIR-CSIO), Sector-30C, Chandigarh 160030
er_vmishra_1234@yahoo.co.in

CSIR-CSIO is currently working towards the development of Production Technology of Plastic Bi-Aspheric Lens Development for Indirect Ophthalmoscopy under DST funding. This effort involves several simultaneous and sequential tasks with synergy of: aspheric optics development, ophthalmic optic development, precision aspheric die design and fabrication, injection molding, sol-gel coating and quality assurance as per WHO / ISO standards. Accordingly, CSIR-CSIO is collaborating with the Sol Gel Centre at the International Advanced Research Centre for Powder Metallurgy and New Materials (ARCI), Hyderabad and with Central Institute of Plastic Engineering & Technology (CIPET), Chennai.

In the run-up of this project tasks, the sol-gel coating technique for protective coating of PolyCarbonate (PC) lens substrates is explored by spin and dip coating methods. However, both the processes need to resolve the issue of non-uniform coating on aspheric surfaces. This coating uniformity is affected by: sol-gel material properties, sol-gel preparation, coating process, substrate geometry etc. The non-uniform coating will alter functional surface profile of substrate leading to distorted image.

In this project, CSIR-CSIO has developed a profile error compensation process to minimize the aspheric profile mismatch of coated lenses w.r.t the design values of aspheric surface aperture and corresponding sag. This compensation process has two pronged approach.

In the first part, we start from a best fit spherical profile. Then this surface is aspherized by Single Point Diamond Turning (SPDT). The aspheric surface profile suffers with form / figure errors and roughness due to material non-homogeneity, tool-job misalignment, tool wear, tool path errors, machine vibrations, unbalanced machining parameters, metrology errors or combination of all these. Study of error sources can be helpful to reduce large errors. But, residual waviness error and resident roughness need to be addressed. The gross residual errors can be contained by compensation of either tool nose radius or work piece inputs. The small recalcitrant residual errors can be corrected by mapping the figure error vs. aperture and adjusting the tool path profile by incorporating the error profile into the same.

While the lenses are protective coated by the sol-gel technique, the coating will bring a new set of coating non-uniformities into play. In case, the coating errors are non-consistent and seen in few lenses, each lens needs to be corrected individually. At CSIR-CSIO, an algorithm is developed to generate a new sample-specific compensated aspheric profile and the lenses are individually processed to reduce the non-uniformity within acceptable limits. On the contrary, if the coating process results in a consistent non-uniformity over a large number of samples, one needs to look at holistic optimization of sol-gel process. This study is helpful to control the effects of non uniform coating on performance of aspheric surface.

THERMAL ISSUES IN PRECISION MACHINING OF POLYCARBONATE OPTICS

Keshvanand, Vinod Mishra, Neeraj Kumar, G S Singh, S V Ramagopal, Pawan Kapur
CSIR-Central Scientific Instruments Organisation (CSIR-CSIO), Sector-30C, Chandigarh 160030
keshvannd96@gmail.com

Optical Grade Plastic lenses are fast replacing glass lenses in numerous applications of optical instrumentation, due to their light weight, machinability, injection moldability, low rejection rates, economies of production and other associated advantages. Out of the commonly considered optical grade plastics, PMMA and PolyCarbonate (PC) are the leading candidates for development of precision optical modules and components in a multitude of systems. Due to its higher refractive index, PC scores over PMMA.

CSIR-CSIO, as part of its Aspheric Optics program, is pursuing various aspects of optical grade plastic processing. In precision machining of PC-based optics, it is seen that, the chip flow is often influenced by heat generated at tool-job interface, leading to unacceptable surface quality (in terms of profile error and surface finish). To study this effect in detail, series of precision machining and metrology experiments are conducted under similar conditions, using PC discs (50mm & 40mm diameter) with plane and curved surfaces (spherical and aspherics of different conic constants).

In this study, the machining process is optimized in two stages. The first step optimizes the surface finish (to obtain minimum roughness Ra). For this purpose, a detailed machining parametric study (for different ranges of tool nose radii, tool feed rates, spindle speeds and depths of cut) of PC substrates is conducted to explore and establish optimum combinations of machining parameters offering best possible surface finish (Ra). The second stage

involves the minimization of form / figure error, while accounting for the thermal effects of the substrates. Generally, the single point diamond turning (SPDT) process uses an alcoholic based coolant. However, the coolant used in SPDT affects adversely the surface profile. To contain this damage, dry SPDT is performed (without coolant). It is seen observed that during SPDT, due to low thermal diffusivity of PC, the heat generated at tool-job interface is trapped within the substrate. This heat causes "swelling" of the PC profile and the 'swelling' becomes part of SPDT machined profile. However, after gradual cooling, the 'swelling' component of the surface profile disappears. And the remaining profile (post-cooling) is quite different than the machined one and hence from the desired one.

In SPDT, the profile (form / figure) error has its origins in: job-tool misalignment, tool wear and faulty tool path. However, in the present study, material swelling dominates over other effects. This profile error differential is studied for PC samples of various profiles and diameters. In order to compensate for this 'swelling', the range of spindle speeds is explored and suitable spindle speed is deployed during SPDT, to reduce the heat generated (at tool-job interface) below a certain threshold. The SPDT tool path is modified with error profile (due to 'swelling' and machining) incorporated within. Accordingly, the residual surface error can be reduced by an iterative compensation SPDT process. This study gives optimum machining conditions for SPDT of PC work-pieces for effective machining and good surface quality.

USE OF HOLOGRAPHIC OPTICAL ELEMENT IN LASER DOPPLER ANEMOMETRY

Abhijit Ghosh¹ Kingshuk Bose¹ H.L.Yadav²

¹Department of Applied Physics, Birla Institute of Technology - Mesra, Ranchi, Jharkhand, India ²Photonics Lab, Department of Physics, National Institute of Technology, Jamshedpur-831014, India

Email : hly_physics@rediffmail.com

Abstract In present work a detailed investigation on design and analysis of a novel holographic technique used for Laser Doppler Anemometry (LDA) is presented. Inaccuracy in LDA measurement due to distortion and nonuniformity of fringe pattern in the measurement volume arising out of two coherent converging beams in present LDA system can be avoided using holographic lenses. Holographic lenses give diffraction limited performance almost free from all monochromatic aberrations thereby leading to formation of good quality interference fringes. In this paper two collimated beams which interfere to form interference fringes in measurement volume are obtained from two holographic lenses.

1. Introduction

Dual beam interference fringe method of Laser Doppler Anemometry (LDA) used for the measurement of average flow velocity of a fluid, requires a good quality optical system to form evenly spaced undistorted interference fringes in the measurement volume. In this method two beams are generated from a single laser source using a beam splitter and are then focused using a converging lens as shown in fig.1. The region of intersection of the two beams where interference fringes are formed is utilized for measurement of velocity of fluid and is called measurement volume[1,2].

Obviously measurement volume where plane wave fronts of both the converging beams exist is a singularity covering very small volume. Due to interference of two converging beams in measurement volume the resulting fringe pattern are neither evenly spaced nor parallel to each other (fig.2). Particles with the same velocity but crossing different parts of the probe volume will therefore produce different Doppler frequencies [3-4]. For a fluid flowing through a tube of large cross sectional area having large velocity gradient in radial direction, evenly spaced undistorted fringe pattern spreading over the entire cross sectional area is required (fig.3). For this configuration two undistorted plane waves should interfere over the entire measurement volume.

Further the imaging lens should give diffraction limited performance over the two small areas encompassed by the two apertures through which the two light beams pass. Monochromatic aberrations (spherical aberration, coma, astigmatism, field curvature and distortion) of the optical system may lead to formation of unevenly spaced and distorted fringe pattern in LDA measurement volume which causes inaccuracy in measurement of fluid velocity [5]. To get better averaging in measurement of fluid velocity fringe spacing should be moderately optimized for different particle concentration and size. This optimization of fringe spacing in measurement volume may be achieved by optimizing beam angle. For closely spaced fringes, beam angle should be large which requires a lens of large aperture and small focal length. Refractive lenses of large aperture and short focal length generally suffers from several monochromatic aberrations. Such lenses are costly and require tedious processing for their production. Subsequently Christo G.Stojanoff et.al used holographic beam splitter and holographic lenses [6-7] in LDA which get credit of replacing costly and bulky conventional optical system by light weight compact holographic optical system. Holographic optical system is not only light weight compact low cost but also it give diffraction limited performance almost free from all monochromatic aberration under proper recording and play back geometry. Elimination of monochromatic errors ensures formation of good quality fringes in measurement volume. In present work we are presenting the aberration analysis of the holographic optical system and it is shown that under proper recording and play back geometry we can get undistorted plane wave fronts from two holographic lenses which is required for formation of evenly spaced undistorted fringes.

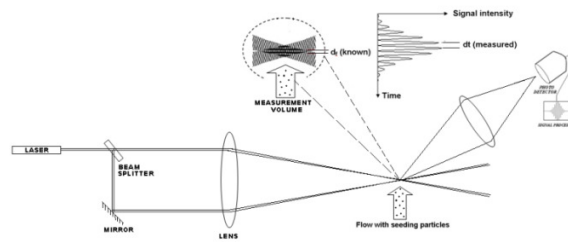


Figure 1. Experimental set up for dual beam LDA system

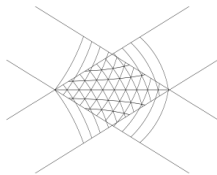


Figure 2. Distorted fringe pattern formation at measurement volume due to interference of spherical wavefronts

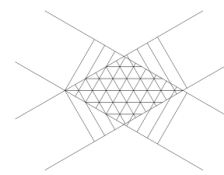


Figure 3. Uniform fringe pattern formation at measurement volume due to interference of plane wavefronts

2. Lens recording and playback geometry of optical system for LDA

Two identical holographic lenses to be used as optical system to form interference fringes in measurement volume can be recorded on high resolution holographic plate using suitable coherent laser source. The angle between the two beams may be optimized at the time of recording to achieve high efficiency operation at all points of lens aperture. The schematic of the recording geometry for recording holographic lenses is shown in Fig.4. To prevent formation of spurious grating, lenses may be recorded in the index-matched conditions and films should be processed using reversal bleach process to enhance diffraction efficiency and to minimize scattering noise [8,9].

Fig. 5 shows the schematic of a novel holographic technique applied to LDA system to form distortion free evenly spaced fringe pattern in measurement volume. The holographic lenses are recorded and played back at suitable angle so that plane wavefronts emerging out from holographic lenses meet obliquely to generate good quality interference fringes in measurement volume. For desired fringe spacing and length of measurement volume recording and play back geometry may be optimized suitably.

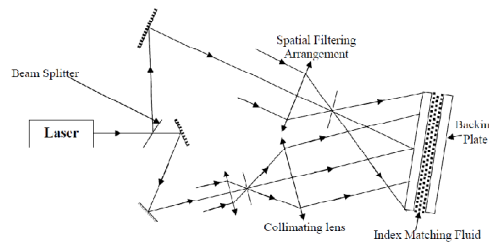


Figure 4. Experimental setup for recording holographic lenses.

3. Analysis

The radius of curvature of the wave propagated from HL₁ is given by

$$\frac{1}{R_{I_1}} = \frac{1}{R_{C_1}} \pm \mu \left(\frac{1}{R_{O_1}} - \frac{1}{R_{r_1}} \right) \dots\dots\dots(1)$$

Where the subscripts I₁, C₁, O₁ and r₁ stand for image, reconstruction, object and reference beams respectively. For the hololens, μ is the ratio of the wavelengths of light used for reconstructing and recording the holograms. For He-Ne laser which is source for recording and reconstructing μ = λ_c / λ_r = 1

The ‘+’ sign normally denotes a virtual image and ‘-’ a real image. As the hololens HL₁ is used in the imaging system after being rotate through 180 degrees with respect to the axis perpendicular to the plane of the fig.1 and played back by a diverging beam so as to achieve a real point focus, we take negative sign in equation (1) , i.e.

$$\frac{1}{R_{I_1}} = \frac{1}{R_{C_1}} - \left(\frac{1}{R_{O_1}} - \frac{1}{R_{r_1}} \right) \dots\dots\dots(2)$$

For HL₁ under recording and play back geometry as discussed above

$$R_{C_1} = - R_{r_1}$$

Therefore, $R_{I_1} = R_{O_1} = \infty \dots\dots\dots(3)$

This shows that under the playback geometry considered , the wave coming out of the hololens HL₁ will be a plane wave. Based on same arrangement we can show that under recording and play back geometry considered plane wave front emerges out of lens HL₂ .

To assess the aberrations introduced by HL₁ and HL₂ for the conditions under which they are fabricated and used in the system, we use expressions given by Meier [10] and Champagne [11]. The coefficients of spherical aberration (S), coma (C_X , C_Y) , astigmatism (A_X , A_Y , A_{XY}), curvature of field (F) and distortion (D_X, D_Y) can be written as :

$$\begin{aligned}
 S &= \frac{1}{R_C^3} - \left(\frac{1}{R_O^3} - \frac{1}{R_r^3} \right) - \frac{1}{R_I^3} \\
 C_X &= \frac{X_C}{R_C^3} - \left(\frac{X_O}{R_O^3} - \frac{X_r}{R_r^3} \right) - \frac{X_I}{R_I^3} \\
 C_Y &= \frac{Y_C}{R_C^3} - \left(\frac{Y_O}{R_O^3} - \frac{Y_r}{R_r^3} \right) - \frac{Y_I}{R_I^3} \\
 A_X &= \frac{X_C^2}{R_C^3} - \left(\frac{X_O^2}{R_O^3} - \frac{X_r^2}{R_r^3} \right) - \frac{X_I^2}{R_I^3} \\
 A_Y &= \frac{Y_C^2}{R_C^3} - \left(\frac{Y_O^2}{R_O^3} - \frac{Y_r^2}{R_r^3} \right) - \frac{Y_I^2}{R_I^3} \\
 A_{XY} &= \frac{X_C Y_C}{R_C^3} - \left(\frac{X_O Y_O}{R_O^3} - \frac{X_r Y_r}{R_r^3} \right) - \frac{X_I Y_I}{R_I^3} \\
 F &= \frac{X_C^2 + Y_C^2}{R_C^3} - \frac{X_O^2 + Y_O^2}{R_O^3} + \frac{X_r^2 + Y_r^2}{R_r^3} - \frac{X_I^2 + Y_I^2}{R_I^3} \\
 D_X &= \frac{X_C^3 + X_C Y_C^2}{R_C^3} - \frac{X_O^3 + X_O Y_O^2}{R_O^3} + \frac{X_r^3 + X_r Y_r^2}{R_r^3} - \frac{X_I^3 + X_I Y_I^2}{R_I^3} \\
 D_Y &= \frac{Y_C^3 + Y_C X_C^2}{R_C^3} - \frac{Y_O^3 + Y_O X_O^2}{R_O^3} + \frac{Y_r^3 + Y_r X_r^2}{R_r^3} - \frac{Y_I^3 + Y_I X_I^2}{R_I^3}
 \end{aligned}$$

Where (X_C , Y_C) , (X_O , Y_O) , (X_r , Y_r) and (X_I , Y_I) are coordinates of the constructing , object , reference and reconstructed beams .

We see that a plane wave emerges out of lens HL₁, i.e R_I=∞ for the first lens .

Lens HL₁ is constructed under the condition ‘R_O = ∞’ and played back after being rotated through 180 degrees . under the condition X_{C₁} = X_{r₁} , Y_{C₁} = Y_{r₁} and (C_X , C_Y) , astigmatism (A_X , A_Y , A_{XY}) field curvature (F) and distortion (D_X, D_Y) become zero. Same arrangement holds good for second lens HL₂

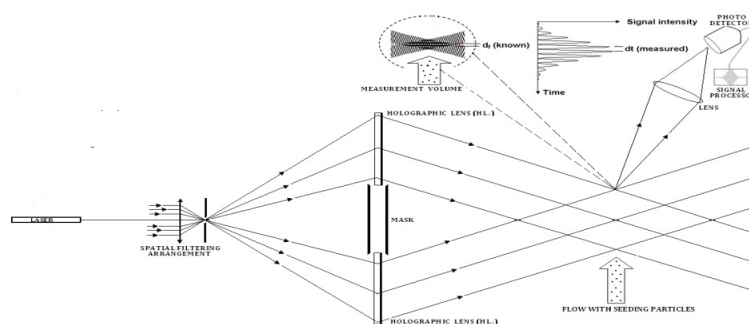


Figure 5. Holographic optical setup for dual beam interference fringe method of LDA system to form evenly spaced undistorted fringe pattern in measurement volume.

4. Discussion / Conclusion

To have uniformly spaced undistorted interference fringes at measurement volume required for accurate measurement of fluid velocity both the interfering beams should be well collimated. The present design consideration ensures formation of good quality evenly spaced fringes in measurement volume. Also we can have diffraction limited performance over the two apertures using holographic lenses which are cheap and light weight. Measurement volume can be increased considerably using such configuration.

5. Acknowledgements

Moral support rendered by Director, N.I.T Jamshedpur, Head, Department of Physics, N.I.T. Jamshedpur, Head, Department of Applied Physics, B.I.T. Mesra, Ranchi and Professor P.K.Barhai for the present work is highly acknowledged.

References :

1. Zh. Zhang, "*LDA APPLICATION METHOD Laser Doppler Anemometry for fluid Dynamics*", Springer Verlag Berlin Heidelberg, (2010).
2. F. Durst, A. Melling and J.H. Whitelaw, "*Principles and Practice of Laser Doppler Anemometry*", Second Edition, Academic Press, London, (1981).
3. Abhijit, Ghosh, H.L. Yadav and P.K. Barhai, "*DESIGN AND ANALYSIS OF OPTICAL SYSTEM CONSISTING OF HOLOGRAPHIC LENSES FOR LASER DOPPLER ANEMOMETRY*", Proceedings of 10th International Conference on Fiber Optics and Photonics (PHOTONICS 2010), IIT Guwahati, INDIA, pp 462, (2010).
4. S. Hanson "Broadening of the measured frequency spectrum in a differential Laser Anemometer due to interference plane gradients", *J. Physics D Applied Physics* **6** 164-171 (1973)
5. Z. Zhang, K. Eisele, "On the overestimation of the flow turbulence due to fringe distortion in LDA measurement volume" *J. Experimental fluids* **25** 371-374 (1998c).
6. Christo G. Stojanoff, Hans D. Tholl, Hubertus A. Luebbers and Wilbert Windeln "*Development, manufacturing, and integration of holographic optical elements for laser Doppler velocimetry applications*", Proceedings of SPIE, Holographic Optics III: Principles and Applications, Vol. 1507, pp 426-434, (1991).
7. F. Schneider, W. Windein, "*Three-dimensional Doppler anemometer using a holographic optical element*" *Appl. Opt.*, Vol. 27, pp 4481-4486, (1988).
8. Graham, Saxby, "*Practical Holography*" Printice hall international U.K, (1985).
9. C. Shakher, H.L. Yadav, A.K. Nirala, "*Design and analysis of low f-number imaging system using Hololenses*" *J.opt.(Peris)*, Vol. 20, pp 259, (1989).
10. R.W. Meier, "*Magnification and third order aberrations in holography*", *J.Opt. Soc. Am.* Vol. 55, pp 987, (1965).
11. E.B. Champagne, "*Non paraxial imaging, magnification and aberration properties in Holography*", *J.Opt. Soc. Am.*, Vol. 57, pp 51, (1967).

APPLICATION OF THICK PHASE TRANSMISSION HOLOGRAM RECORDED IN DICHROMATED GELATIN FILM FOR MAXIMUM DATA STORAGE

Abhijit Ghosh¹ R.Ranjan² H.L.Yadav²

¹Department of Applied Physics, Birla Institute of Technology - Mesra, Ranchi, Jharkhand, India

²Photonics Lab, Department of Physics, National Institute of Technology, Jamshedpur-831014, India

Email : hly_physics@rediffmail.com

Abstract Based on theoretical investigation for variation of diffraction efficiency on film thickness and depth of refractive index modulation it is shown that large film thickness and high depth of refractive index modulation are quite promising for page-oriented Bragg-selective holographic optical memory recorded in dichromated gelatin film.

1. Introduction

A volume holographic storage device is a page-oriented device that writes and read data in an optical form. Holographic memory uses a photosensitive material to record interference pattern of an object beam and a coherent reference beam. For a volume holographic memory with maximum data storage, diffraction efficiency of recorded hologram should fall sharply with small change in angle of reconstruction. The next data appears with maximum efficiency after disappearance of first data.

Volume phase hologram recorded in dichromated gelatin have several advantages over the holograms recorded in other recording materials; these includes high diffraction efficiency, low noise, high resolution, long life time and high refractive index modulation capacity [1-3]. In present work dependence of angular selectivity on processing parameters of thick phase transmission holograms recorded in dichromated gelatin film has been studied in detail in the light of coupled wave theory[4]. Higher angular selectivity can be advantageously exploited for restoring multiple data pages where different reference beam angle can be used for each input page . The minimum difference between adjacent reference beam angle is determined by the Bragg angular selectivity which depends on thickness of the recording medium. To read out a single page of data selectively, the hologram is illuminated with a read beam, which propagates in the same direction as the reference beam that was originally used to write the same page.

2. Analysis of Design Parameters

The complete formula for diffraction efficiency (η) of thick phase transmission holograms, which takes into account the angular deviation from Bragg's angle in the reconstruction, is given by coupled wave theory assuming refractive index variation to be sinusoidal as:

$$\eta = \frac{\sin^2 \left\{ \left(\xi^2 + \nu^2 \right)^{\frac{1}{2}} \right\}}{\left(1 + \frac{\xi^2}{\nu^2} \right)} \quad \text{Where} \quad \xi = \delta \frac{2\pi n_1}{\lambda} d \sin \theta \quad \& \quad \nu = \frac{\pi n_1 d}{\lambda \cos \theta}$$

Where n_1 is the depth of refractive index modulation, d is the film thickness, n is the average refractive index of the medium, λ is the free space wave-length of the reconstruction light beam and δ is the angular deviation in radians with respect to Bragg's angle θ .

Bragg angle θ is related to the fringe spacing Λ recorded in the hologram through the relation:

$$\sin \theta = \frac{\lambda}{2n\Lambda} \quad \& \quad \cos \theta = \left\{ 1 - \left(\frac{\lambda}{2n\Lambda} \right)^2 \right\}^{\frac{1}{2}}$$

When the illumination is made at Bragg's angle (i.e. $\delta = 0$) we have from (1)

$$\eta = \sin^2 v$$

To have maximum efficiency at Bragg's angle v should be equal to $\pi/2$ or odd multiple of $\pi/2$ i.e.

$$v = m \frac{\pi}{2} \quad \text{where } (m = 1, 3, 5, \dots)$$

$$\text{On substituting value of } v, \quad \frac{\pi n_1 d}{\lambda \cos \theta} = m \frac{\pi}{2} \quad \text{or,} \quad d = \frac{m \lambda \cos \theta}{2 n_1}$$

Curves drawn using equation (1) for Variation in diffraction efficiency (η) with angular deviation (δ) with respect to Bragg's angle θ for different value of 'm' ($m=1,3,5$) and fixed value of depth of refractive index modulation $n_1 = 0.06$ at reconstruction wavelength $\lambda = 0.514 \mu\text{m}$ have been presented in figure 1.

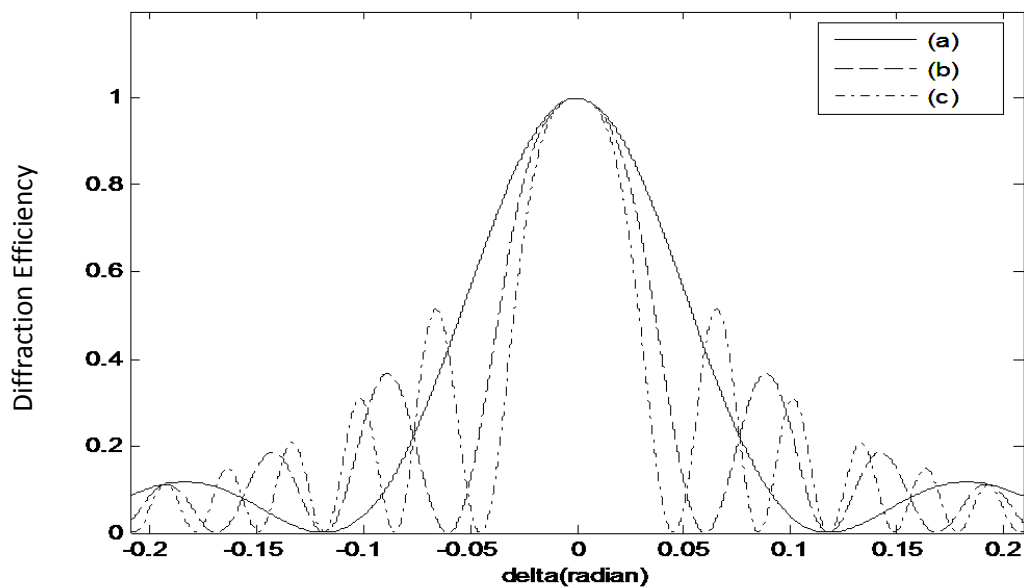


Figure 1. Variation in diffraction efficiency with angular deviation with respect to Bragg's angle θ for different value of 'm' at reconstruction wavelength $\lambda = 0.514 \mu\text{m}$ and depth of refractive index modulation $n_1 = 0.06$ where for curve (a) $m = 1$, (b) $m = 3$, (c) $m = 5$.

From the curves drawn in fig.1 it is clear that diffraction efficiency falls sharply for higher odd multiple of $d (= m \frac{\lambda \cos \theta}{2 n_1})$. i.e. higher is the thickness higher will be the angular selectivity [5]. While drawing

the curves care has been taken to ensure that criteria for thick phase holograms i.e. $Q = \frac{2\pi\lambda d}{n\Lambda^2} > 10$ is fulfilled [6]. Further curves for variation of diffraction efficiency with angular deviation from Bragg's angle for different values of depth of refractive index modulation and film thickness at reconstruction wavelength $0.514\mu\text{m}$ are drawn as shown in figures 2, 3 and 4. Curves drawn in figure 2, 3 and 4 show that for high angular selectivity which is necessary for maximum data restoration, film of large thickness and high depth of refractive index modulation are quite promising.

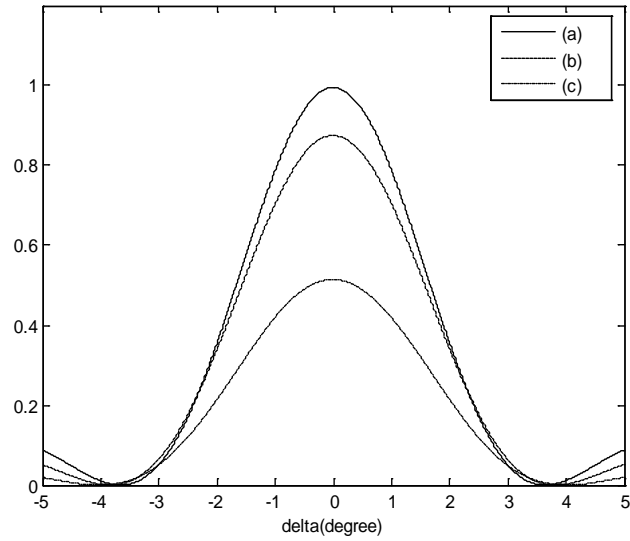


Figure 2. Variation of diffraction efficiency with angular deviation with respect to Bragg's angle θ for different values of n_1 (a) $n_1 = 0.0304$ (b) $n_1 = 0.0245$, (c) $n_1 = 0.0162$ For a given film thickness $d = 12 \mu\text{m}$ and given fringe width $\Lambda = 0.8696$.

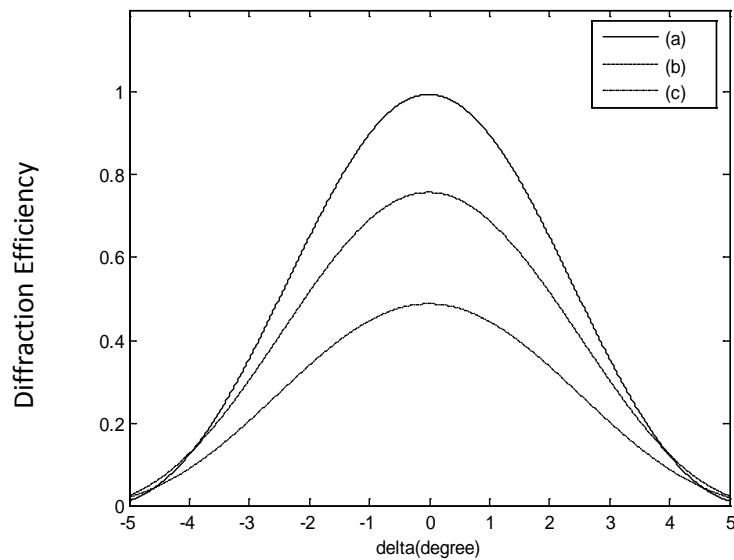


Figure 3. Variation of diffraction efficiency with angular deviation with respect to Bragg's angle θ for different values of n_1 (a) $n_1 = 0.0457$, (b) $n_1 = 0.0321$, (c) $n_1 = 0.0245$ for a given film thickness $d = 8 \mu\text{m}$ and given fringe width $\Lambda = 0.8696$.

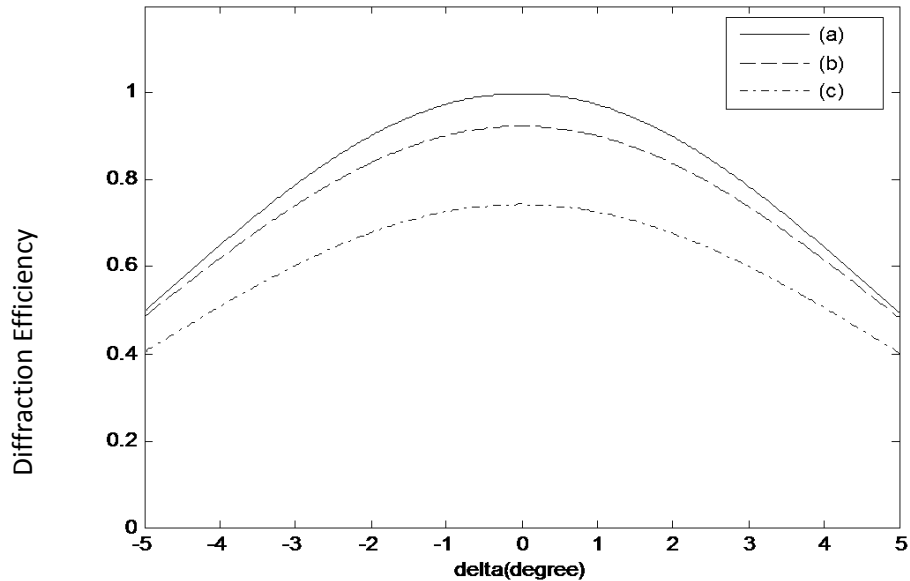


Figure 4. Variation of diffraction efficiency with angular deviation with respect to Bragg's angle θ for different values of n_1 (a) $n_1 = 0.0954$, (b) $n_1 = 0.0785$, (c) $n_1 = 0.0632$ for a given film thickness $d = 4 \mu\text{m}$ and given fringe width $\Lambda = 0.8696$.

4. Discussion / Conclusion

Present investigation reveals that a large data storage capacity can be achieved in case of holographic recording in dichromated gelatin film by suitably optimizing the processing parameters. Large film thickness and high depth of refractive index modulation are quite promising for high angular selectivity which is desirable for maximum data storage.

5. Acknowledgements

Moral support rendered by Director, N.I.T. Jamshedpur, Head, Department of Physics, N.I.T. Jamshedpur and Head, Department of Applied Physics, B.I.T. Mesra, Ranchi for the present work is highly acknowledged.

References :

1. T. A. Shankoff, "Phase hologram in dichromated gelatin", *Appl. opt.*, **7** 2101 (1968).
2. L. H. Lin, "Hologram formation in hardened dichromated gelatin film", *Appl. opt.*, **8** 963 (1969).
3. B. J. Chang and C. D. Leonard, "Dichromated gelatin for the fabrication of holographic optical elements", *Appl. Opt.*, **18** 2407 (1979).
4. H. Kogelnik, "Coupled wave theory for thick hologram grating", *Bell Syst. Tech. J.*, **48** 2909 (1969).
5. T. Todorov et al, "Spectral characteristic of thick phase holographic grating", *Optica Acta*, **28** 379 (1981).
6. T. K. Gaylord, and M. C. Moharm, "Thin and thick gratings: Terminology Clarification", *Appl. opt.*, **20** 3271 (1981).

HOLOGRAPHIC MULTIPLEXING OF DIGITAL HOLOGRAMS USING ORTHOGONAL PHASE ENCODING METHOD

Samsheerali PT* and Joby Joseph
Photonics Group, Physics Department, IIT Delhi
*samsheerali@gmail.com

Abstract: We propose a method to carry out holographic multiplexing of digital holograms using the orthogonal phase encoding method. Digital holograms are recorded using orthogonal phase encoded reference beams and are multiplexed numerically, which can be reconstructed by the corresponding orthogonal phase codes with very less cross talk.

1. INTRODUCTION

Encoding two or more holograms in a single one either numerically or optically is called multiplexing. Various methods have been proposed so far for the multiplexing of optical holograms such as wavelength, angular, shift, phase encoding and speckle multiplexing techniques [1-3,7]. Orthogonal phase encoding technique has been proposed as an alternative to carry out volume holographic multiplexing of optical hologram for high capacity optical data storage [8]. The hologram of each object is obtained with deterministic orthogonal phase coded reference beams with the possibility of retrieval of each image without any crosstalk. If the orthogonal phase encoding technique is introduced in digital holography it would provide a light efficient method to carry out multiplexing in digital holography with reduced crosstalk. This would enable us to transmit a single hologram which can be used to reconstruct multiple object information.

2. EXPERIMENTAL SET UP

The holograms are recorded in Mach-Zehnder configuration, where the orthogonal phase codes are displayed on Phase SLM kept in the reference arm. The orthogonal phase codes are generated by Walsh Hadamard matrices containing -1 and 1 corresponding to 0 and π phase modulation respectively [7, 8]. Thus N digital holograms are recorded with N phase encoded reference beams. And each of them is added numerically to get the multiplexed hologram,

$$I_{\text{mux}} = I_1 + I_2 + I_3 + \dots + I_N \quad (1)$$

Then, the Fresnel propagation pattern of each orthogonal phase map is recorded by acquiring an interference pattern with a plane beam after removing the object. Let ψ_i be the Fresnel propagated amplitude of i^{th} phase code, and thus addressing the multiplexed hologram with ψ_i will give the i^{th} reconstructed image with very less cross talk. Suppose the hologram of p^{th} image is recorded by the reference beam with phase address $\Psi_p = (\varphi_{p1}, \varphi_{p2}, \dots$

$\varphi_{pN})$ then the reconstruction of the hologram with the orthogonal phase code Ψ_q should fulfill the condition

$$\sum_{k=1}^N \exp[i(\varphi_{pk} - \varphi_{qk})] = 0 \quad \text{for } p \neq q \quad \dots 2(a)$$

$$\sum_{k=1}^N \exp[i(\varphi_{pk} - \varphi_{qk})] = N \quad \text{for } p = q \quad \dots 2(b)$$

Thus when orthogonal phase encoding is used there is no cross talk because the reconstructions of undesired images interfere destructively

Numerical simulation has been carried out for recording of a multiplexed hologram with 8 holograms of size 512x512 pixels. The Hadamard matrix of order 512 x 512 is generated using the matlab code. Each row or column of a hadamard matrix is orthogonal to each other and can be used to generate orthogonal phase codes.

Holograms of different amplitude objects (letters) have been simulated and each of them is added together to get the multiplexed hologram as shown in figure 1(a). Three of the reconstructed images from the multiplexed holograms are also shown (fig.1b-d).

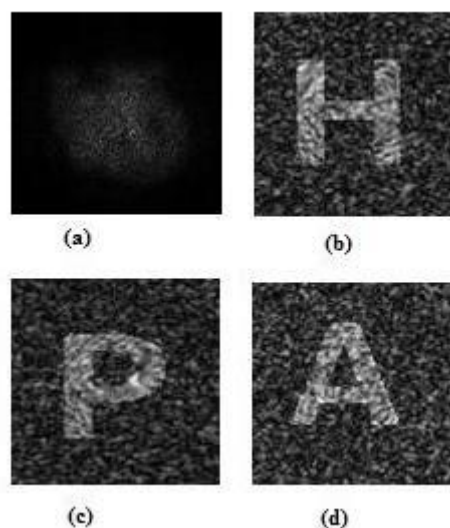


Figure 1. (a) Multiplexed Hologram and (b)-(d) Reconstructed images from Multiplexed Hologram

3. CONCLUSION

A method to carryout holographic multiplexing of digital holograms with orthogonal phase coded reference beam has been proposed. Since only the phase of the reference beam is changed the method is very light efficient and the orthogonality between the phase codes ensures very less cross talk during demultiplexing.

It would be possible by this method to store different frames of holographic video sequence as a single hologram which would facilitate the transmission and reconstruction of the same.

REFERENCES

- [1] G. A. Rakuljic, V. Leyva, and A. Yariv, "Optical data storage by using orthogonal wavelength multiplexed volume holograms," *Opt. Lett.* **17**, 1471 (1992)
- [2] F. H. Mok, "Angle-multiplexed storage of 5000 holograms in lithium niobate," *Opt. Lett.* **18**, 915(1993)
- [3] D. Psaltis, M. Levene, A. Pu and G. Barbastathis, "Holographic stroagfe using shift multiplexing," *Opt. Lett.* **20**, 782 (1995)
- [4] T. Colomb, F. Dürr, E. Cuche, P. Marquet, H. G. Limberger, R. -P. Salathé, and C. Depeursinge, "Polarization microscopy by use of digital holography: application to optical-fiber birefringence measurements," *Appl. Opt.* **44**, 4461 (2005),
- [5] P. Picart, E. Moisson, and D. Mounier, "Twin-Sensitivity Measurement by Spatial Multiplexing of Digitally Recorded Holograms," *Appl. Opt.* **42**, 1947 (2003),
- [6]. Z. Liu, M. Centurion, G. Panotopoulos, J. Hong, and D. Psaltis, "Holographic recording of fast events on a CCD camera," *Opt. Lett.* **27**, 22 (2002),
- [7]. M. Paturzo, P. Memmolo, A. Tulino², A. Finizio and P. Ferraro, "Investigation of angular multiplexing and de-multiplexing of digital holograms recorded in microscope configuration", *Opt.Exp* 17,8709(2009)
- [7] C.Denz, G. Pauliat, G. Roosen, "Volume hologram multiplexing using a deterministic phase encoding method", *Opt.Comm.* **85**, 171(1991).
- [8]. M.Ezura, S.baba and N. Kihara, "Holographic Memories using 2-Dimensional Phase-Code Multiplexing Method", *Jpn. J. of Appl. Phys.* **43**, 4954(2004).

HOLOGRAPHIC LIVE MEASUREMENT OF STRESS IN PHOTOPOLYMER FILM DURING HOLOGRAM RECORDING

Shaji Sam TL¹, Abhishek Pathak², Abhay Jith³, Sreebha AB⁴, Ajith Kumar PT⁵

¹Optical Image Processing Division and Holography Studio, Centre for Development of Imaging Technology (C-DIT), Trivandrum- 27, Kerala, India

²UM-DAE Centre for Excellence in Basic Sciences, University of Mumbai, Kalina, Santacruz (E), Mumbai 400 098.

³Department of Physics, Hyderabad Central University, Gachibowli, Hyderabad-500046

^{4,5}Light Logics Holography and Optics, Kuttanad, Technopark, Trivandrum, Kerala, India.

E-mail – ajithpt@gmail.com, shajisam@gmail.com

Abstract: Photopolymers are attracting great importance in photonic device development, integrated optics, data storage (1) etc. and the material is generally considered as the ‘silicon of photonics’. However, suitability of the material for a set of advanced applications such as display holography, data storage, development of holographic solar concentrators, optical interconnects and multi function elements depend not only on its high diffraction efficiency and better transmittance, but on the mechanical stability also. Thus stress development during exposure and the study of stress in photopolymers are of critical importance in device development. Several methods can be applied for the measurement of stress in thin films (2,3). Holographic measurement of stress in thin films has various advantages over other methods. We have mapped stress in photopolymer thin films during hologram recording by using live fringe holographic interferometry. A two level holographic recording setup and *Holomer 6A*, a red sensitive photopolymer plate were used for the study. Silver-halide green sensitive recording plate, in conjunction with a green diode laser, was applied to record the real-time hologram of the photopolymer film. The photopolymer film was exposed for hologram formation by using a He-Ne laser (633 nm). Excellent high contrast fringes were formed (Figure1, 2) in both the object and reference beam directions (2,4). The paper describes the experiment in detail and the preliminary results obtained.

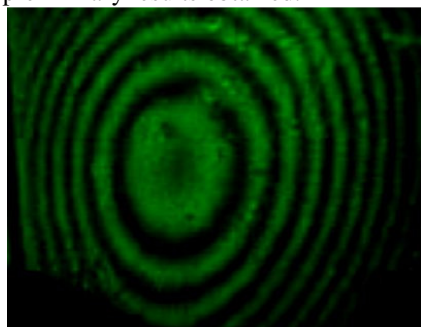


Figure 1

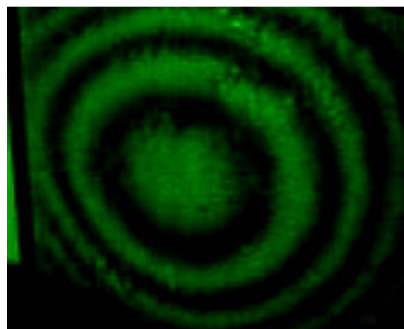


Figure 2

ACKNOWLEDGEMENT

Financial and equipment support from Light Logics Holography and Optics is gratefully acknowledged.

REFERENCES

- [1] P.T. Ajith Kumar, “A photopolymer based machine readable holographic security system for variable data storage and encryption”, HOLO EXPO International conference, Moscow, Nov (2005).
- [2] P.T. Ajith Kumar and C.Purushothaman, Optics and Laser Technology, 22, 47-49 (1990)
- [3] Ramprasad BS and Radha TS, “Thermal stress in thin films using real time Holographic Interferometry” Proceeding Second International Conference on Holographic systems, Components and Applications ,29-32 (1989)
- [4] Shaji Sam TL, Vadivelan V, Ajith Kumar PT, “A Real-Time Holographic Sensor for Remote surface Temperature Monitoring and Measurement” Proceedings of National seminar and Exhibition on Non-Destructive Evaluation (NDE 2009), p 137-139, 2009, India.

CHARACTERIZATION OF A PHASE SLM FOR ENHANCEMENT OF RESOLUTION IN MICROSCOPIC IMAGERY

S. Mukhopadhyay, S Sarkar, K Bhattacharya and L N Hazra
Department of Applied Optics and Photonics, University of Calcutta,
92, Acharya Prafulla Chandra Road, Kolkata 700009
E-mail: somparna@gmail.com,

Abstract: Resolution enhancement in microscopic imagery is associated with tailoring of the point spread function of the imaging system. The latter can be accomplished by using phase filters on the exit pupil of the microscope objective. Programmable spatial light modulators (SLM) facilitate the practical realization of the desired phase filters. This paper reports a new technique for characterization of the SLM.

1. INTRODUCTION

The resolving power of a light microscope is limited by several factors. Residual aberrations of a microscope objective affect its resolving power significantly. Even for an aberration free objective, the finite size of the microscope aperture gives rise to diffraction effects, which pose a fundamental limit for least resolvable distance in the transverse as well as the axial direction within the object. Several scanning microscopy [1-4] techniques have been exploited to circumvent this problem. A different paradigm in addressing this problem arises from the domain of pupil plane filtering. Here one aims to modify the shape of the point spread function by using phase filters at the exit pupil of the microscope objective. Tailorable phase filters can be synthesized by using a programmable Spatial Light Modulator (SLM). We have used a programmable reflective liquid crystal SLM from Holoeye Photonics (HOLOEYE-PLUTO) for the purpose.

In practice, the SLM needs to be calibrated for determination of its amplitude and/or phase response. The optimized complex modulation curves need to be verified by either interferometric or diffractive techniques. The interferometric techniques utilize the use of various interferometers like Mach-Zender interferometer [5-6], Twyman-Green interferometer [6-8], digital phase shifting interferometer [9], double split interferometer [10], dual imaging interferometer [11], radial [12] and lateral shear interferometer [13], etc. For all interferometer based techniques a measurement of the fringe shift determines the phase modulation. These methods are quite reliable and well established, producing almost unambiguous results; but the drawback is that, these set ups are highly sensitive and susceptible to presence of disturbances from air turbulence, mechanical vibration, etc.

The diffractive techniques on the other hand [14-16] are insensitive to such environmental

disturbances. For diffractive techniques, in contrast with fringe shift measurements of interferometric techniques, dedicated patterns are coded onto the SLM and the diffractive far field intensity is measured with the setup either in a few positions or over a large area. The fitting of measured data with simulated far field pattern yields the phase modulation of the SLM. These simulations are known as phase retrieval algorithms. They are, however, not fully reliable due to their ambiguity in the retrieved phase and so one usually writes simple patterns with less number of unknown parameters onto the SLM which still yield sufficiently different phase response values.

However, interferometric methods are much preferable for the characterization of the device since for every combination of the gray level an exact phase shift can be determined whereas the curves from the diffraction measurements must be accompanied with a sophisticated numerical fitting.

In this report the polarization phase shifting interferometric technique is presented for evaluation of the addressed grayscale vs. phase relationship of the SLM, taking into account phase introduced due to surface quality of the SLM. The theory and preliminary experimental results are presented.

2. EXPERIMENTAL ARRANGEMENT

The interferometric setup employed for calibration of the Liquid Crystal on Silicon (LCOS) SLM as shown in the figure 1, consists of a Twyman-Green interferometer adapted for polarization phase shifting. To obtain the interference pattern on the image of the SLM a typical 4-f setup is used. The mathematical details are discussed in the following section.

2.1 Mathematical Analysis

Assuming a unit amplitude input beam, the propagating wavefront reflected from the SLM after the final polarizer $P(\theta)$ is expressed as

Topic Code (HOL)

Presentation Preference: Oral/Poster

$$\varepsilon_{SLM} = \frac{1}{\sqrt{2}} P(\theta) W(\pi, 45^\circ) P(90^\circ) \cdot P(90^\circ) \cdot \begin{pmatrix} 1 \\ 1 \end{pmatrix} e^{i\delta(x,y)} \quad (1)$$

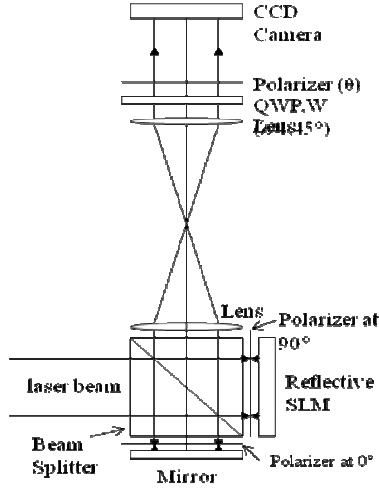


Fig.1. experimental arrangements

where in general, $P(\theta)$ is Jones' matrix for the arbitrarily oriented linear polarizer with transmission axis at an angle θ to the reference X axis, and is given by,

$$P(\theta) = \begin{pmatrix} \cos^2 \theta & \cos \theta \sin \theta \\ \cos \theta \sin \theta & \sin^2 \theta \end{pmatrix} \quad (2)$$

$W(\gamma, \phi)$ is the Jones' matrix of a retarder of retardation γ , oriented with its first axis at an angle ϕ to the reference x axis and is given by,

$$W(\gamma, \phi) = \begin{pmatrix} \cos \frac{\gamma}{2} + i \sin \frac{\gamma}{2} \cos 2\phi & i \sin \frac{\gamma}{2} \sin 2\phi \\ i \sin \frac{\gamma}{2} \sin 2\phi & \cos \frac{\gamma}{2} - i \sin \frac{\gamma}{2} \cos 2\phi \end{pmatrix} \quad (3)$$

$\delta(x,y)$ is the spatial phase over the SLM. Using the specific values of $P(\theta)$ and $W(\gamma, \phi)$ employed eq. 1 reduces to,

$$\begin{aligned} \varepsilon_{SLM} &= \frac{-i}{2} P(\theta) \begin{pmatrix} 1 \\ -i \end{pmatrix} e^{i\delta(x,y)} \\ \varepsilon_{SLM} &= -\frac{i}{2} (\cos \theta - i \sin \theta) e^{i\delta(x,y)} \begin{pmatrix} \cos \theta \\ \sin \theta \end{pmatrix} \\ \varepsilon_{SLM} &= \frac{1}{2} e^{i(3\pi/2 - \theta + \delta(x,y))} \begin{pmatrix} \cos \theta \\ \sin \theta \end{pmatrix} \end{aligned} \quad (4)$$

Similarly the reference wavefront may be expressed as,

$$\begin{aligned} \varepsilon_R &= \frac{1}{\sqrt{2}} P(\theta) W(\pi, 45^\circ) P(90^\circ) \cdot P(90^\circ) \cdot \begin{pmatrix} 1 \\ 1 \end{pmatrix} \\ \varepsilon_R &= \frac{1}{2} P(\theta) \begin{pmatrix} 1 \\ i \end{pmatrix} \end{aligned}$$

$$\varepsilon_R = \frac{1}{2} e^{i\theta} \begin{pmatrix} \cos \theta \\ \sin \theta \end{pmatrix} \quad (5)$$

The intensity distribution of the interference pattern may be written as

$$I_T = |\varepsilon_{SLM} + \varepsilon_R|^2$$

$$I_T = \frac{1}{2} \left| e^{i(3\pi/2 - \theta + \delta(x,y))} + e^{i\theta} \right|^2$$

$$I_T = \frac{1}{2} \{1 + \cos(3\pi/2 - 2\theta + \delta(x,y))\} \quad (6)$$

$$I_{T1} = \frac{1}{2} \{1 + \cos \delta(x,y)\} \quad (7)$$

$$I_{T2} = \frac{1}{2} \{1 + \cos(\pi/2 + \delta(x,y))\} \quad (8)$$

$$I_{T3} = \frac{1}{2} \{1 + \cos(\pi + \delta(x,y))\} \quad (9)$$

$$I_{T4} = \frac{1}{2} \{1 + \cos(3\pi/2 + \delta(x,y))\} \quad (10)$$

The four transmission expression are generating by putting 135° , 90° , 45° and 0° for θ in equation (6), respectively. The phase profile in the two lateral halves are evaluated by employing the standard four phase-step algorithm,

$$[\delta(x,y)] = \tan^{-1} \left[\frac{I_{T4} - I_{T2}}{I_{T1} - I_{T3}} \right] \quad (11)$$

4. PRILIMINARY RESULTS

The SLM is initially calibrated for surface errors by addressing it with a uniform grayscale. The four phase-shifted interferograms are shown in fig 2.

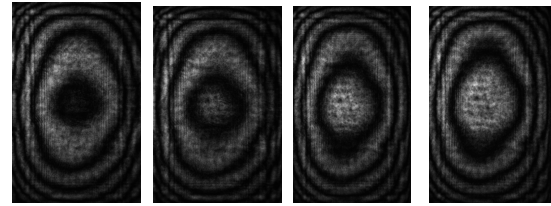


Fig 2. Set of four phase-shifted interferograms of the SLM surface

The surface quality of the SLM evaluated from these four interferograms is shown in fig 3.

Topic Code (HOL)

Presentation Preference: Oral/Poster

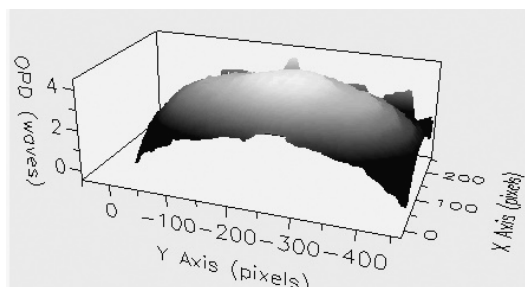


Fig 3. The surface quality of the SLM evaluated from the above four interferograms

The two halves of the SLM are now addressed with two different grayscale values so that a phase difference between the two halves is introduced. The set of interferograms thus obtained is shown in fig 4.

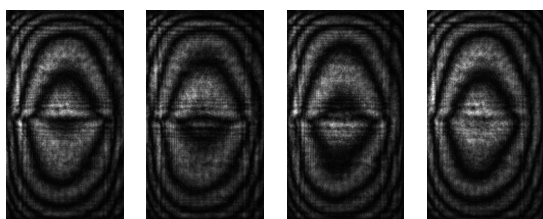


Fig 4. Set of four interferograms obtained with two symmetrical halves of the SLM addressed with uniform grayscale values of 0 and 250

The resulting surface profile generated is shown in fig 5.

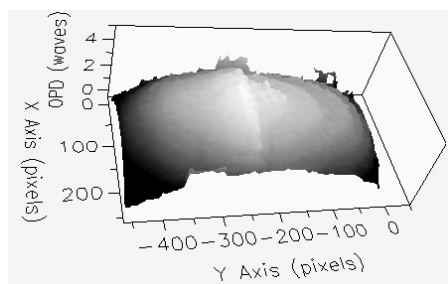


Fig 5. Phase profile generated from the above interferograms

Finally the phase profile due to the grayscale addressing is obtained by simple subtraction of the two generated profiles.

CONCLUSION

A full-field method for calibration of an LCOS reflective SLM in terms of its surface quality and addressed grayscale, which is eventually manifested as phase, is presented. The methodology, as explained in the text, is carried out with one half of the SLM retaining a constant gray level, while the

other half is addressed for all possible values of grayscale from 0 to 255.

REFERENCES

- [1] M. A. Paesler and P. J. Moyer, *Near-Field optics: Theory, introduction, and applications* (John Wiley, New York, 1996)
- [2] T. Wilson and C J R Sheppard, *Theory and practice of scanning optical microscopy.*(Academic, London, 1984)
- [3] <http://www.leica-microsystems.com>.
- [4] M. G. L. Gustafsson, "Nonlinear structured-illumination microscopy: wide field fluorescence imaging with theoretically unlimited resolution," *PNAS* 102(37), 13081-13086 (2005).
- [5] E. Martin – Badosa et. Al., "Complex modulation characterization of liquid crystal devices by interferometric data correlation," *Meas. Sci. Technol.* 8, 764-772, 1997
- [6] M. B. Roopashree et. Al., "Phase characteristics of reflecting and transmitting type twisted nematic spatial light modulators," *Proc. ICOP*, CSIO, Chandigarh, India, 30th Oct.- 1 Nov. 2009
- [7] F. Bai et. al., "Experimental validation of closed-loop adaptive optics based on a self-referencing interferometer wave front sensor and a liquid-crystal spatial light modulator," *Opt. Commun.* 283, 2782-2786, (2010).
- [8] H. Zhang et. Al., "Evaluation of phase only liquid-crystal spatial light modulator for phase modulation performance using a Twyman-Green interferometer," *Meas. Sci. Technol.* 18, 1724-1728, (2007).
- [9] Z. H. Wang et. Al., "Measuring of the phase modulation of liquid crystal spatial light modulator and correcting of the wave front," *Opt. Tech.* 31, 196-201, (2005).
- [10] H. X. Chen et. al., "Optical modulation characteristics of liquid-crystal television (LCTV) and its application in optics information processing," *Chin. J. Lasers* 27, 741-745, (2000).
- [11] H. Zhang et. al., "Measurement of phase and intensity by Dual-imaging Interferometry for performance evaluation of liquid crystal spatial light modulator," *Optik*, 122, 1249-1253, (2011)
- [12] X. F. Zhao et. Al., "Measuring phase modulation characteristics of liquid crystal spatial light modulators by using cyclic radial shearing interference," *J. Sichuan University* 39, 675-679, (2002).
- [13] F.P. Ferreira et. al., "Direct calibration of a spatial light modulator by lateral shearing interferometry," *Opt. Exp.* 18(8), 7899-7904, (2010).

Topic Code (HOL)

Presentation Preference: Oral/Poster

- [14]Z. Zhang et. al., "Simple method for measuring phase modulation in liquid crystal televisions." Opt Eng. 33(9), 3018-3022,(1994)
- [15]J. L. McClain et. al., "Spatial light modulator phase depth determination from optical diffraction information," Opt. Eng. 35(4), 951-954, (1996).
- [16]D. Engstrom et. al., "Diffraction based determination of the phase modulation for general spatial light modulators," Appl. Opt. 45(28), 7195-7204, (2006)

Electromagnetically induced transparency in a Doppler broadened Y-type system

Azeem Baig Mirza and Suneel Singh*

School of Physics, University of Hyderabad, Hyderabad 500 046, India.

*Email: suneelsp@uohyd.ernet.in

Abstract: We study the electromagnetically induced transparency (EIT) of a probe field in a Doppler broadened four level Y-configuration atomic system driven by two additional coherent laser (coupling) fields. We examine the effects of various wave-vector mismatch occurring when the coupling field wavelength is higher ($\lambda_c > \lambda_p$), equal ($\lambda_c = \lambda_p$) or lesser ($\lambda_c < \lambda_p$) than that of the probe field. We show that under the influence of the coherent coupling fields, the steady-state linear susceptibility of the probe laser shows almost perfect and very wide EIT window for the case when $\lambda_c < \lambda_p$. Analytical results are also obtained to explain this unusual behavior.

1. INTRODUCTION

Electromagnetically induced transparency (EIT) is an unusual phenomenon [1] produced by atomic coherence and interference effects that enable propagation of light through an otherwise opaque medium without significant attenuation. EIT is of tremendous interest due to possibility of wide applications in optical switching via light velocity control [2, 3] quantum information [4] and nonlinear optics [5]. Early works on EIT primarily focused on one-photon transitions between states of opposite parity in simple three level Λ , V and cascade (ladder) systems. However currently there is considerable interest in study of EIT and its effect on nonlinear optical interactions in four level systems of various configurations. Pertinent to the present work is four level Y type system interacting with two strong laser fields and a low-intensity probe field. Earlier theoretical work of Agarwal and Harshwardhan [6] predicted that a Y-type atomic system under one strong-field and two-weak-field excitation can give rise to interesting effects such as, inhibition and enhancement of the two-photon absorption. This effect was first experimentally observed by Gao et. al. in sodium atoms [7] and

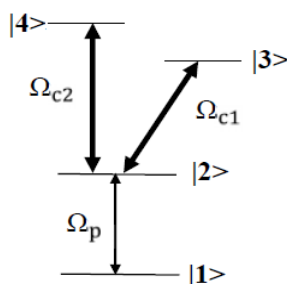


Fig. 1: EIT scheme in Four-level Y-type atomic system with dual ladder-type EIT. Here Ω_p is Rabi frequency of the probe and Ω_{c1} , Ω_{c2} are strong pump fields Rabi frequencies.

subsequently electromagnetically induced one-photon and two-photon transparency were experimentally observed in both ^{85}Rb and ^{87}Rb atomic vapors [8]. In a similar model, the resonance fluorescence [9] and vacuum-induced interference effects [10] were also investigated theoretically.

In this work we present a few interesting results of our study of EIT in a Doppler broadened four level Y system interacting with two strong laser fields of Rabi frequencies (Ω_{c1} , Ω_{c2}) and a low-intensity probe field (Ω_p) coupled to the lower levels ($|1\rangle$ - $|2\rangle$) as shown in Fig.1. In particular we show that by changing the relative wavelength (frequency) between the coupling and probe fields, complete transparency over a much wider range of frequencies can be achieved for the probe field in an inhomogeneously broadened medium. The absorption profile of a weak probe field shows one or more EIT windows whose location, width, and depth can be controlled by manipulating the parameters of the coupling fields. For example, we show that the system can have single or double EIT windows depending on the amplitude and the detuning of the coupling lasers. Analytical results are derived to explain this unusual behavior and are found to be in good agreement with the numerical results as well as earlier EIT experiments in simple three level ladder systems conducted under similar conditions.

2. GENERAL THEORY FOR THE Y- SYSTEM

2.1. Formulation

The interaction Hamiltonian in the interaction picture under resonant interaction condition and rotating wave approximation is obtained as

$$\begin{aligned}
 V^{\text{int}} = & -\hbar [\Omega_p e^{i(\vec{k}_p \cdot \vec{r} + \Delta_{21}t)} |2\rangle\langle 1| \\
 & + \Omega_{c1} e^{i(\vec{k}_{c1} \cdot \vec{r} + \Delta_{32}t)} |3\rangle\langle 2| \\
 & + \Omega_{c2} e^{i(\vec{k}_{c2} \cdot \vec{r} + \Delta_{42}t)} |4\rangle\langle 2| + \text{H. c.}] . \quad (1)
 \end{aligned}$$

Topic: Quantum Optics

Here $\Delta_{21} = \omega_{21} - \omega_p$, $\Delta_{32} = \omega_{32} - \omega_{c1}$ and $\Delta_{42} = \omega_{42} - \omega_{c2}$ denote the detuning of probe and coupling (or ‘control’) fields frequencies from the atomic resonance frequencies ω_{21} , ω_{32} and ω_{42} respectively, and $|i\rangle < j\rangle$ ($i, j = 1, 2, 3, 4$) are the atomic raising or lowering operators. Eq.(1) is used for obtaining the density matrix equations of motion in which the various relaxation processes such as spontaneous emissions from upper levels $2\gamma_{ij}$ ($i, j = 1 - 4$) are included phenomenologically. Doppler broadening of the vapor is also taken into account. As usual for the EIT problems, we make an expansion of the density matrix to all orders in the strong (pump) field amplitudes and to first order in the probe amplitude to obtain the density matrix equations as,

$$\dot{\rho}_{21}^{(1)} = -i(\Delta_{21} + \vec{k}_p \cdot \vec{v}) + \gamma_{21} \rho_{21} + i\Omega_p \rho_{11}^{(0)} + i\Omega_{c1} \tilde{\rho}_{31}^{(1)} + i\Omega_{c2} \tilde{\rho}_{41}^{(1)}, \quad (2a)$$

$$\dot{\rho}_{31}^{(1)} = -i(\Delta_{21} + \Delta_{32} + (\vec{k}_p + \vec{k}_{c1}) \cdot \vec{v}) + \gamma_{32} \rho_{31} + i\Omega_{c1} \tilde{\rho}_{21}^{(1)}, \quad (2b)$$

$$\dot{\rho}_{41}^{(1)} = -i(\Delta_{21} + \Delta_{42}) + (\vec{k}_p + \vec{k}_{c2}) \cdot \vec{v} + \gamma_{42} \rho_{41} + i\Omega_{c2} \tilde{\rho}_{21}^{(1)}, \quad (2c)$$

The steady-state solutions obtained by setting the time derivatives zero on the left-hand side of Eqs. (2), yield the velocity averaged one-photon coherence as

$$I_{21}^{(1)} = \int \tilde{\rho}_{21}^{(1)}(\vec{v}) d\vec{v}^3, \\ = i\Omega_p \int \frac{A_{31}(\vec{v})A_{41}(\vec{v})M(\vec{v})d\vec{v}^3}{A_{21}(\vec{v})A_{31}(\vec{v})A_{41}(\vec{v}) + A_{31}(\vec{v})|\Omega_{c2}|^2 + A_{41}(\vec{v})|\Omega_{c1}|^2}, \quad (3a)$$

where

$$A_{21}(\vec{v}) = i(\Delta_{21} + \vec{k}_p \cdot \vec{v}) + \gamma_{21}, \quad (3b)$$

$$A_{31}(\vec{v}) = i\{(\Delta_{21} + \Delta_{32} + (\vec{k}_p + \vec{k}_{c1}) \cdot \vec{v})\} + \gamma_{32}, \quad (3c)$$

$$A_{41}(\vec{v}) = i\{(\Delta_{21} + \Delta_{42}) + (\vec{k}_p + \vec{k}_{c2}) \cdot \vec{v}\} + \gamma_{42}, \quad (3d)$$

2.2. Linear Susceptibility:

The susceptibility of the medium is related to the velocity averaged one-photon coherence as follows:

$$\chi = N \frac{|\mu_{21}|^2}{\hbar} (I_{21}^{(1)} / \Omega_p), \quad (4)$$

where N is the atomic density of the vapor. It is well known that the imaginary part of the susceptibility gives the absorption and real part gives the dispersion of the probe field.

3. Numerical results and discussions:

We now present numerical results for EIT applying theory to an atomic vapor contained in a cell. Nature of EIT in a three level systems depends on critically on the sign of the residual Doppler width $\delta k = k_p - k_c$ which,

depending on the probe and control field wave-vector mismatch, is either positive ($k_p > k_c$) (or) negative ($k_p < k_c$) and is markedly dissimilar in this two cases. If the wave-vectors k_p and k_c are the same in magnitude the residual Doppler width $\delta k = 0$ ($k_p = k_c$), and the medium can be considered as Doppler free. The positive and negative residual broadening cases, the associated asymmetric features of EIT resonance and their origin have been discussed earlier by various authors [11].

We consider the case in which $k_p < k_c$ (or $\lambda_p < \lambda_c$ where $c=1,2$) so the sign of the residual Doppler width is negative. This situation can be realized, for example, in the four-level Y-type (dual ladder type) $3S_{1/2} \rightarrow 3P_{3/2} \rightarrow 4D_{3/2}$ ($3S_{1/2} \rightarrow 3P_{3/2} \rightarrow 4D_{5/2}$) transitions in sodium atom. The four-level Y-type atomic system with dual ladder-type EIT configuration has one stable ground state $3S_{1/2}$, an intermediate level $3P_{3/2}$ and two nearly degenerate upper states $4D_{3/2}$, $4D_{5/2}$ respectively. The level separation wavelength of the lower and upper transition respectively, $\lambda_p = 5890\text{\AA}$ and $\lambda_{c1} = \lambda_{c2} = 5688\text{\AA}$. The large wavelength mismatch between the counter propagating coupling fields (Ω_{c1}, Ω_{c2}) and probe field (Ω_p) in dual ladder EIT system introduces residual Doppler width $\delta k \bar{v} / \gamma_D \approx -0.04$ where $\gamma_D = \bar{k} \bar{v}$ and $\bar{k} = (k_p + k_{c1})/2$ since $k_{c1} \approx k_{c2}$. For comparison purpose we also consider the other two possible cases: one of positive wave-vector mismatch i.e., $\delta k \bar{v} / \gamma_D \approx +0.04$ ($k_p > k_c$) and the other of matched wave-vector i.e., $\delta k \bar{v} / \gamma_D \approx 0$ ($k_p = k_c$) hypothetically for this four-level Y-type atomic system. It may be possible to realize the above two cases in other atomic systems. In our numerical calculation all parameters are expressed in units of Doppler width $\gamma_D / 2\pi = 1$ GHz, i.e., $\gamma_{21} / \gamma_D = 0.005$, $\gamma_{32} / \gamma_D = 0.001$, $\gamma_{42} / \gamma_D = 0.001$.

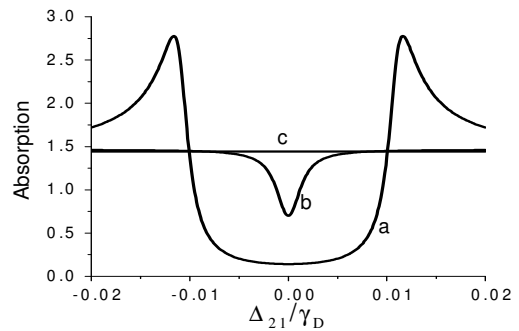


Fig. 2: EIT of probe field as a function of the probe field detuning (Δ_{21}/γ_D) for various wave-vector mismatch cases, $\delta k = -0.04\gamma_D$ (curve a), $\delta k = 0$ (curve b) and $\delta k = +0.04\gamma_D$ (curve c). Here both the coupling fields are on resonance i.e., $\Delta_{32} = \Delta_{42} = 0$ and $\Omega_{c1} = \Omega_{c2} = 0.02\gamma_D$.

Topic: Quantum Optics

In Fig. 2 probe absorption profile (proportional to the imaginary part of $I_{21}^{(1)}$) is shown as a function of the probe detuning for various cases of pump and probe field wavelength (frequency) mismatches. Here $\Omega_{c1}/2\pi = \Omega_{c2}/2\pi = 0.02\gamma_D$ ($= 20$ MHz) are amplitudes of the strong pump and both the coupling fields are on resonance i.e., $\Delta_{32} = \Delta_{42} = 0$. Clearly there is no transparency (see curve c) when the pump field frequency is smaller than that of the probe field, i.e., residual broadening given by $\delta k = +0.04\gamma_D$ is positive.

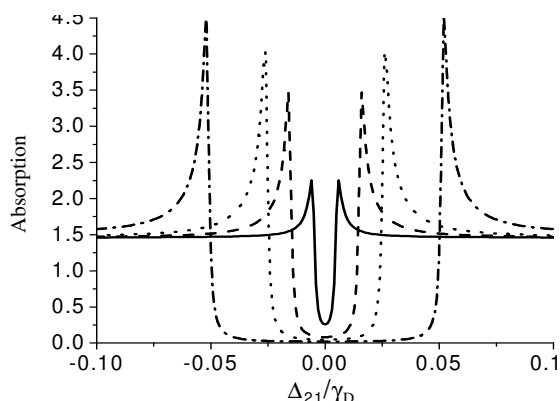


Fig.3: EIT of probe field as a function of the probe field detuning (Δ_{21}/γ_D) for various values of the coupling field Rabi frequencies $\Omega_{c1} (= \Omega_{c2}) = 0.01\gamma_D, 0.03\gamma_D, 0.05\gamma_D,$ and $0.1\gamma_D$ depicted respectively, by solid, dashed, dotted and dash-dotted curves. Both the coupling fields are on resonance i.e., $\Delta_{32} = \Delta_{42} = 0$ and the wave-vector mismatch is $\delta k = -0.04\gamma_D$.

Contrary to usual expectation, even in the case of exact wave vector matching $\delta k = 0$, there is no perfect EIT (see curve b). Surprisingly however, almost perfect EIT occurs (see curve a) when pump wavelength is smaller than that of the probe field. Moreover the EIT window is observed to be very wide. Thus it is possible to attain complete transparency over a broad range of frequencies which is essential for the propagation of a probe pulse through the system. We henceforth focus only on the negative mismatch case. Furthermore, the effect of larger coupling field Rabi frequencies on probe absorption for the same on-resonance case as in Fig. 2 is shown in Fig. 3. We observe that as the equal Rabi frequencies of the two coupling fields ($\Omega_{c1} = \Omega_{c2}$) increase in value from $0.01\gamma_D$ (solid line) to $0.1\gamma_D$ (dash-dotted line) through $0.03\gamma_D$ (dashed) and $0.05\gamma_D$ (dotted lines), the depth and width of the EIT window increases with the increasing values of Rabi frequencies.

This unusual feature of EIT can be attributed to non availability of velocity subclasses which would shift the absorbing Autler-Townes doublet to overlap with transparency at the line center. To elaborate, we consider explicitly the following resonances predicted by the denominator of the expression (3a) for $I_{21}^{(1)}$

$$\Delta_{21} = \left(\frac{k_c}{2} - k_p \right) v - \frac{\Delta_{42}}{2} + \frac{i}{4} (\tilde{\gamma}_{42} + \tilde{\gamma}_{21}) \pm \sqrt{|\Omega_{c1}|^2 + |\Omega_{c2}|^2 + \left[\frac{k_c v}{2} - \frac{\Delta_{42}}{2} \right]^2} \quad (5)$$

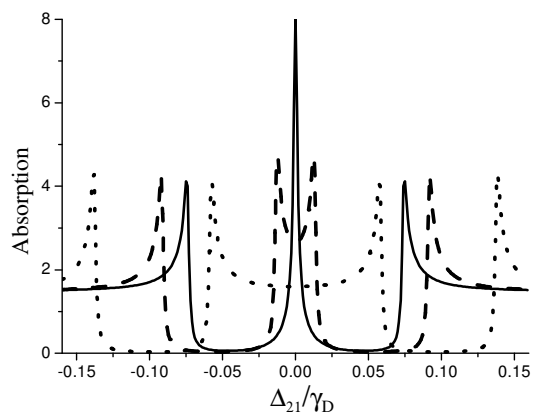


Fig. 4: EIT of probe field as a function of the probe field detuning (Δ_{21}/γ_D) for various detunings of strong coupling fields ($\Delta_{32} = -\Delta_{42} = 0.03\gamma_D$ (solid line), $0.05\gamma_D$ (dashed line) and $0.1\gamma_D$ (dotted line). The value of strong coupling field Rabi frequencies is fixed at $\Omega_{c1} = \Omega_{c2} = 0.1\gamma_D$ for all the curves and the wave-vector mismatch $\delta k = -0.04\gamma_D$.

Eq.(5) reveals the existence of Autler Townes (AT) doublet arising due to splitting of levels by the strong coupling fields. More importantly we find that these are Doppler shifted away by $k_c v$ from the line center $\Delta_{21} = 0$. It is thus clear that for larger coupling field wavevector values $k_c > k_p$, the absorbing AT doublet will shift farther away from line center where EIT occurs. Especially in the case when $k_c = 2k_p$ we observe that there is no velocity term to shift the probe detuning. Hence there will be no overlapping of velocity shifted absorption associated with AT doublet with EIT at line center and we observe a wide and deep EIT window whose width is governed by separation between the AT doublet.

We now consider the situation when both the coupling fields are detuned from resonance i.e., $\Delta_{32} = \Delta_{42} \neq 0$. For this case, plots of the probe absorption as a function of probe detuning are shown in Fig. 4. The

Topic: Quantum Optics

applied strong coupling field Rabi frequencies are equal. The absorption profile of probe field as a function of the probe field detuning (Δ_{21}/γ_D) varies with the detunings of the strong coupling fields Δ_{32} and Δ_{42} . When $\Delta_{32}=-\Delta_{42}=0.03\gamma_D$ (solid line), we get two transparency windows and a middle absorption peak situated at the line center. When $\Delta_{32}=-\Delta_{42}=0.05\gamma_D$ (dashed line), we see three transparency windows, the middle absorption peak (solid line) of the previous case, becomes a much weaker transparency window than the other two. When $\Delta_{32}=-\Delta_{42}=0.1\gamma_D$ (dotted line), we observe that the two transparency windows are well separated by a wider and weaker middle transparency window. Thus we find that with increasing values of detunings of both strong coupling fields the condition for shift of the two transparency windows is $\Delta_{21}=-\Delta_{32}=-\Delta_{42}$.

4. Conclusion:

In conclusion, we have studied the electromagnetically induced transparency (EIT) effect of a probe field in a Doppler broadened four level Y-type (dual ladder EIT-type) atomic system that can be considered to be composed of two three-level ladder sub-systems that share common ground and intermediate levels. Yet we find that the EIT response of the composite system can be dramatically distinct and more complicated than single three-level ladder system. For large field frequency detunings of two strong coupling fields we get the two well separated usual EIT profiles of the two three-level ladder systems. The absorption profile of a weak probe field shows two EIT windows whose location, width, and depth can be controlled by manipulating the parameters of the coupling fields. Analytical results are derived to explain this unusual behavior and are found to be in good agreement with the numerical results as well as earlier EIT experiments in simple three level ladder systems under similar conditions.

References:

- [1] K. J. Boller, A. Imamoglu, and S. E. Harris, *Physical Review Letters* **66**, 2593 (1991).
- [2] L. V. Hau, S. E. Harris, Z. Dutton and C. H. Behroozi, *Nature* **397**, 594 (1999).
- [3] A. M. Akulshin, S. Barreiro and A. Lezama, *Physical Review A* **57**, 2996 (1998).
- [4] M. Fleischhauer and M. D. Lukin, *Physical Review Letters* **84**, 5094 (2000).
- [5] P. R. Hemmer, D. P. Katz, J. Donoghue, M. Cronin-Golomb, M. S. Shahriar and P. Kumar, *Optics Letters* **20**, 982 (1995).
- [6] G. S. Agarwal and W. Harshawardhan, *Physical Review Letters* **77**, 1039 (1996).
- [7] J. Y. Gao, S. H. Yang, D. Wang, X. Z. Guo, K. X. Chen, Y. Jiang and B. Zhao, *Physical Review A* **61**, 23401 (2000).
- [8] D. Wang, J. Y. Gao, J. H. Xu, G. La Rocca, F. Bassani, *Europhysics Letters* **54**, 456 (2001);
J. H. Xu, G. C. La Rocca, F. Bassani, D. Wang, J. Y. Gao. *Optics Communications* **216**, 157 (2003).
- [9] R. Arun, *Physical Review A* **77**, 033820 (2008).
- [10] B. K. Dutta and P. K. Mahapatra, *Journal of Physics B: Atomic Molecular and Optical Physics* **41**, 055501(2008).
- [11] J. Gea-Banacloche, Y. Q. Li, S. Z. Jin, and M. Xiao, *Physical Review A* **51**, 576 (1995);
S. Shepherd, D. J. Fulton, and M. H. Dunn, *Physical Review A* **54**, 5394 (1996).

FDTD MODELING OF PHOTONIC CRYSTALS FOR OLED LIGHT EXTRACTION

Manish Kumar, Rajeev Jindal* and Joby Joseph
 Indian Institute of Technology, New Delhi.
 *MoserBaer India Ltd., Greater NOIDA.
 manishk.iitd@gmail.com

Abstract: We do FDTD modeling and simulations to show that Photonic Crystals are very promising to improve the light extraction from OLED devices. 2D FDTD simulation using Lumerical software are carried out for TE polarizations. We further investigate and compare two different Photonic crystals embedded OLED methods, and make an attempt to conclude which is better option for mass manufacturing.

1. INTRODUCTION

The internal efficiency of OLED devices has already been increased to close to 100% [1] but actual external extraction efficiency is very small (~20-30%) due to trapped waveguide modes in high index organic layer and ITO anode layer, and total internal reflection occurring at the glass-air interface.

There are many methods to improve the overall extraction efficiency. We focus on the photonic crystal approach for light extraction [2] where a photonic crystal inserted between ITO and glass substrate helps to improve extraction efficiency. Through 2D FDTD simulations, we compare two different Photonic crystal embedded OLED methods, both having mass manufacturing capabilities, and make an attempt to conclude which is better option to try for industrial manufacturing. To save simulation volume we do a 2D FDTD simulation for TE polarizations which can easily be extended to 3D FDTD simulations.

2. FDTD MODELING OF PHOTONIC CRYSTALS EMBEDDED OLED

The present paper aims at the optimization of 2D photonic crystal structures embedded in an OLED device for improved light extraction. FDTD simulations are done on two different methods of forming the Photonic Crystal layer in OLED device between the substrate and ITO layers. The first method [3] makes use of reactive ion etching in SiN_x layer and fills the holes of an optimized 2D photonic structure with Silicon on Glass (SOG) material for planarization. Second method makes use of nano-imprinting or rather stamp printing in polycarbonate and filling of holes by sol gel process with ZnO [4]. Both the methods can be used in mass scale fabrications but in the best knowledge of authors there is no comparative FDTD study of these two methods to know the effectiveness of one method over the other. So, in present work we carry out the OLED device modeling of the above two methods using Lumerical FDTD software and come up with an optimized design of photonic crystal embedded OLED design for improved extraction efficiency and having mass scale fabrication capabilities.

The above two methods differ in the material used

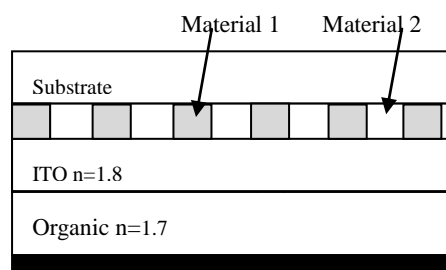


Figure1: The schematic of OLED with Photonic Crystal layer in between the substrate and ITO layers.

for substrate, material 1 and material 2, and in their fabrication procedures (Fig.1). The cases studied involve, use of glass or polycarbonate as substrate and combinations of SOG, SiN_x, ZnO & Polycarbonate for photonic crystal layer.

3. CONCLUSION

FDTD simulation results of OLED device embedded with the Photonic Crystals are presented showing extraction improvements, and the far-field illumination profiles.

ACKNOWLEDGEMENT

The authors wish to acknowledge CSIR and Min. of Inf. Techn. for financial support.

REFERENCES

- [1] S R Forrest, "The road to high efficiency organic light-emitting devices," *Org. Elect.*, **4**, 45 (2003).
- [2] Y. J. Lee, S. H. Kim, J. Huh, G. H. Kim, Y. H. Lee, "A high extraction efficiency nanopatterned OLEDs" *Appl. Phys. Lett.*, **82**, 3779 (2003).
- [3] A. M. Adawi, R. Kullock, J. L. Turner, C. Vasilev, D. G. Lidgey, A. Tahraouri, P. W. Fry, D. Gibson, E. Smith, C. Foden, M. Roberts, F. Quereshi, N. Athanassopoulou, "Improvement of light extraction efficiency of polymeric LEDs using 2D photonic crystals" *Org. Elect.* **7**, 222 (2006)
- [4] H. H. Cho, B. Park, H. J. Kim, S. Jeon, J. H. Jeong, J. J. Kim, "Solution processed photonic crystal to enhance the light coupling efficiency of organic light-emitting diodes" *Appl. Opt.* **49**, 4024, (2010)

SLOW LIGHT SYMMETRIC DIRECTIONAL COUPLER WITH ELLIPTICAL CELL

Nagesh Janrao¹, Vijay Janyani²

Department of Electronics & Communication Engineering,
Malaviya National Institute of Technology, Jaipur, India
¹janraonl@yahoo.com, ²vijay.janyani@ieee.org

Abstract: Output power of waveguide in a photonic crystal symmetric directional coupler (consisting of circular holes with hexagonal lattice geometry) is weak. To improve coupled waveguide power, the present paper proposes a new, slow light based, design for symmetric directional coupler using elliptical rods arranged in a square lattice with refractive index of rods equal to 3.41. Proposed photonic crystal waveguide has applications such as optical and electro-optic switches at optical frequency.

1. INTRODUCTION

Photonic crystals have attracted much attention of today's optical engineers, due to their unique properties and advantages. By using photonic crystals, the conventional optical devices can be miniaturized. Waveguides, sharp bends of waveguides, optical power splitters, interferometers, resonators, couplers and many other optical devices can be made in much smaller dimensions using the unique properties of photonic crystals [1]. A directional coupler is important component for optical communication system and used in wavelength demultiplexing, optical switches etc [2, 3]. However, it is observed that the output power in conventional photonic crystal based directional coupler (consisting of circular holes in a hexagonal lattice structure) is quite low, resulting in lower efficiency. If directional couplers are designed to operate in slow light region, it enhances light matter interaction and can increase the coupling efficiency also.

Hai-Feng Zhou et al. investigated a tuneable photonic crystal switch based on two-mode interference directional coupler [4]. They modulate the central row of the rod of coupler to change refractive index, and finite difference time domain method (FDTD) is employed to predict the characteristic of the switch [4]. Structure of 2x2 directional coupler with small coupling length and decoupling input-output channel was proposed by Yang Qu et.al. [1]. This was based on 2D photonic crystal with hexagonal lattice of air holes. A total length of coupling component of 24a is achieved, where 'a' is lattice constant. Sangwoo Hal et. al. analyzed dispersion less tunnelling of slow light in anti symmetric photonic couplers in slow light region [5]. We have also performed finite-difference time-domain (FDTD) simulations to investigate pulse propagation through the symmetric coupler having circular shaped holes in hexagonal lattice, and observed weak pulse propagation. To overcome this limitation, we propose this new structure design., with higher power transfer and significantly lower device length as reported in [1].

A directional coupler consists of two parallel identical waveguides running together over some distance. When placed closely together, the modes in each guide interact to produce two super modes, one at a lower frequency and one at a higher frequency. Therefore, the input power will couple to the other waveguide and exchange between them periodically [6, 7].

Photonic crystals do not have continuous symmetry rather; they have discrete translational symmetry. There are two symmetries seen in case of such waveguide [8]. First one is due to periodicity of photonic crystals, according to Bloch's theorem,

$$\omega(k) = \omega(k + \frac{2\pi}{a}) \quad (1)$$

where 'a' is the period along the waveguide direction. Moreover, electric field is given by

$$E(x, z; \omega, k) = E(x, z; \omega, k + \frac{2\pi}{a}) \quad (2)$$

where E is electric field. The point $k, k \pm 2\pi/a, k \pm 4\pi/a, \dots$ all have, exactly the same distributions of electric and magnetic fields. The second symmetry appears in case of waveguides were

$$\omega(k) = \omega(-k) \text{ \& } E(x, z; \omega, k) = E^*(x, z; \omega, -k) \quad (3)$$

The photonic crystal based couplers are usually classified as anti-symmetric or symmetric coupler, with respect to reflection about a central line, as shown in Fig.1.

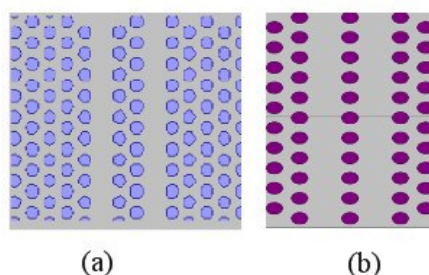


Figure 1. (a) anti symmetric coupler, (b) symmetric coupler

Due to the hexagonal lattice geometry, the coupler symmetry depends on the number of rows present between created defect. When odd number of rows are present, the coupler is symmetric with respect to reflection about central line between the waveguides. When even number of rows are present, then the coupler becomes anti-symmetric [8].

For a photonic crystal coupled waveguide, to act as directional couplers the following conditions must be satisfied.

1. The two modes propagating in coupler must have different symmetry, i.e. one odd and other even.
2. These two modes, i.e. odd and even, which are propagating in coupled waveguide must have same sign of group velocities.

In general, at the band-edge of Brillouin zone, above-mentioned first condition is not satisfied in case of symmetric couplers with circular holes and hexagonal lattice geometry [8]. So that when we have performed finite-difference time-domain (FDTD) simulations to investigate pulse propagation through the symmetric coupler having circular shaped holes in hexagonal lattice, we observed weak pulse propagation. It is possible to couple pulses much strongly between waveguides as in the design proposed here, by making the rods elliptical in shape and also, shifting first row of elliptical rods adjacent to waveguide as shown in Fig. 2 (a) that is analyzed in next section.

2. DESIGN AND SIMULATION RESULTS

When line defect is introduced into the 2D photonic crystal lattice by changing the center radius or entire centerline removing completely, some defect states are created. For a convenient design of the defect, some of these states should be located within the band gap of the photonic crystal. As light cannot pass in the photonic crystal, it is localized in the surrounding of the defect thus line defect acts as a waveguide [9]. We obtained two waveguides by removing two neighbor rows of the center row from a square lattice of elliptical shaped dielectric rods in air. The bulk structure have minor radius of the rods $r_1 = 0.25a$ and major radius of the rods $r_2 = 0.33a$. Central row has minor radius $dr_2 = 0.3528\mu\text{m}$ and major radius $dr_1 = 0.5\mu\text{m}$. The refractive index of all the rods equal to 3.41. The elliptical photonic crystal waveguide has the lower propagation losses in comparison with other shaped structures. It has been observed that orientation of the ellipse also affects the transmission through waveguide. This however will be discussed in detail in an other paper. We designed symmetric directional coupler using elliptical cells, and modified the symmetry by making the central row rods slightly bigger and by shifting the adjacent rows as detailed earlier and as shown in Fig. 2 (a).

The plane wave expansion method is used to calculate the model dispersion curves. With above

parameters, the basic 2D square lattice with elliptical rods of radii r_1 and r_2 (but no defect or shifting) has a band gap for TE modes in the spectral range $0.23 \leq a/\lambda \leq 0.33$, and the corresponding dispersion diagrams for defect free photonic crystal structure is as shown in Fig.2(b), corresponding band surfaces are shown in Fig.3.

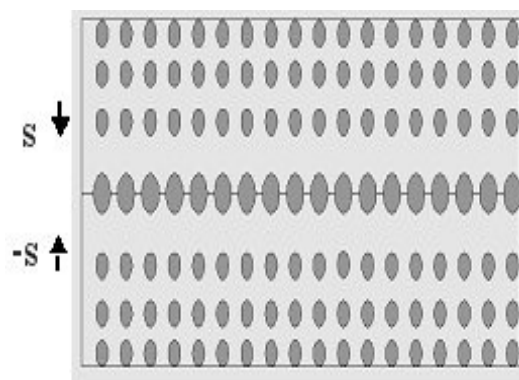


Figure 2 (a) Layout for symmetric directional coupler using elliptical cells

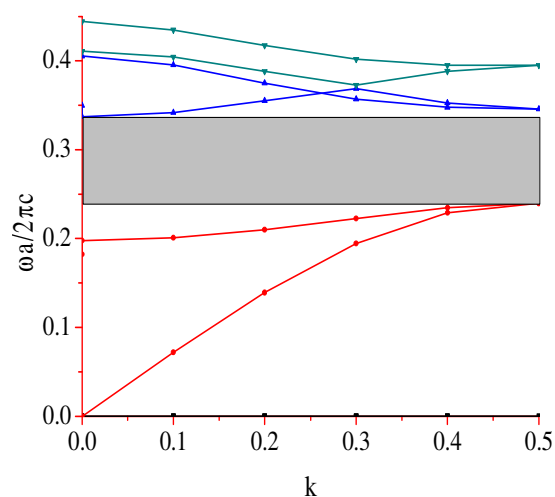


Figure 2 (b). Dispersion diagrams for defect free photonic crystal structure. Refractive index equal to 3.41, bulk structure with minor radius of the rods $r_1 = 0.25a$ and major radius of the rods $r_2 = 0.33a$.

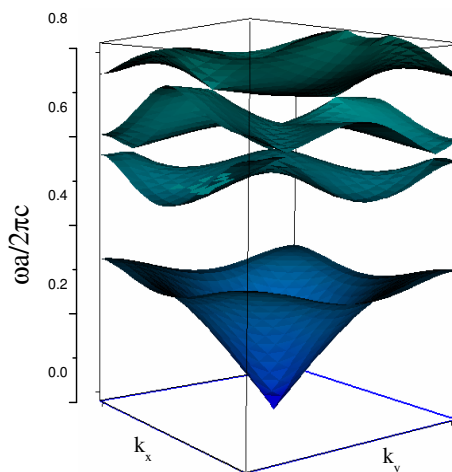


Figure 3. Band surfaces for defect free photonic crystal structure.

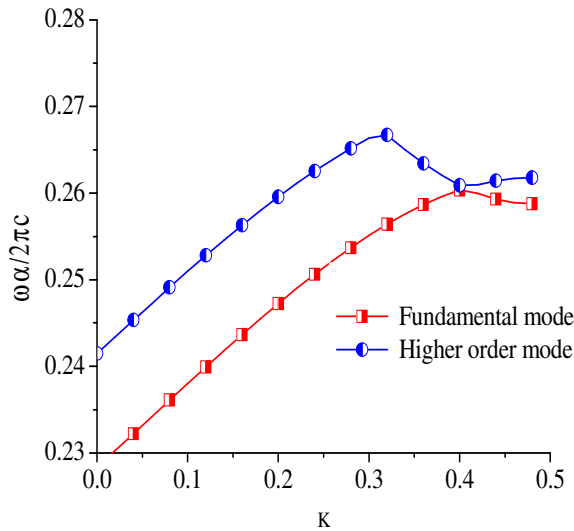


Figure 4. Dispersion relation for guided modes in spectral range $0.23 \leq a/\lambda \leq 0.33$ with vertical shift $s=0.2\mu\text{m}$

First we investigate, pulse propagation through newly designed symmetric coupler. The width of waveguide is varied by shifting the position of first two rows (one on each side of the defect) with $s=0.1\mu\text{m}$, $s=0.2\mu\text{m}$, $s=0.3\mu\text{m}$ and $s=0.4\mu\text{m}$, in steps. Minus ‘s’ is the shift, corresponding in opposite direction as seen in Fig.2 (a). Fig. 4 shows guided modes in spectral range $0.23 \leq a/\lambda \leq 0.33$ with vertical shift $s=0.2\mu\text{m}$. In next stage we perform FDTD analysis for band-edge, where $\Delta k=0.1$ is excited. Propagation of pulse through the symmetric directional coupler then observed, which is shown in Fig. 5. Altering minor axis dr_2 , refractive index material near waveguide gets modified in ΓK direction. So, effect of variation of minor radius dr_2 ; on output, power of waveguide has been analyzed. Simultaneous effect of variation of minor radius dr_2 and variation of width of waveguide on normalized output waveguide power is as shown in Fig. 6. For vertical shift $s=0.20\mu\text{m}$, maximum normalized output waveguide power obtained which is equal to $0.66\mu\text{w}$, where as without shifting ($s=0$), very low power be coupled to other waveguide.

3. SLOW LIGHT PERFORMANCE

Slow light has group velocity larger than zero but smaller than that of phase velocity. Slow light is defined as [10],

$$v_g = \begin{cases} \frac{d\omega}{dk} > 0 \\ \frac{d\omega}{dk} < v_p \end{cases}$$

where v_p is phase velocity, ω is the angular frequency and k the wave vector.

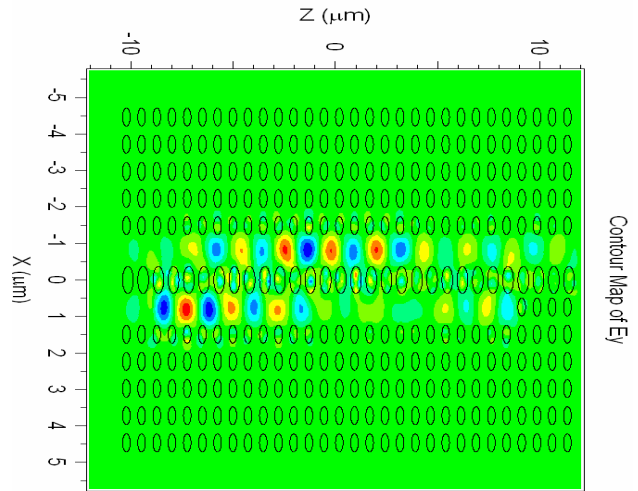


Figure 5. Propagation of pulse through the symmetric directional coupler for $s=0.20\mu\text{m}$ shift.

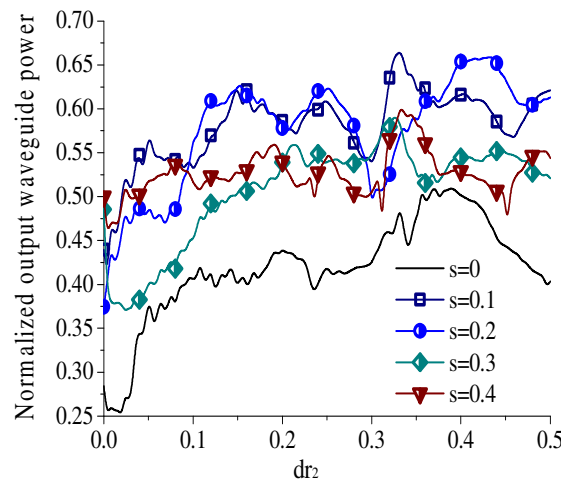


Figure 6. Normalized output waveguide power

Group index, is a quantifying parameter that measures the performance of slow light devices that how much the light is slow. Group index is defined as $n_g=c/v_g$ [11], where v_g is group velocity $= d\omega/dk$ [11-14]. Different values of group velocity v_g versus normalized frequency is plotted for fundamental and higher guided modes in Fig. 7. It seen from Fig. 7, for wide range of frequency, constant value of group velocity is obtained. Value of v_g is very close to zero, which means speed of light is low.

Normalized delay bandwidth product *NDBP* is other quantifying parameter that measures the capacity of device. It is calculated as the product of average group index n_g [14], and frequency range (bandwidth) over which n_g remains constant.

NDBP is defined as [14]

$$NDBP = n_g \times \left[\frac{\Delta\omega}{\omega_0} \right] \tag{4}$$

Calculated value of $NDBP=0.20$ as average group index n_g for higher order mode is equal to 110.8 and ratio $\Delta\omega/\omega_0 = 0.017$.

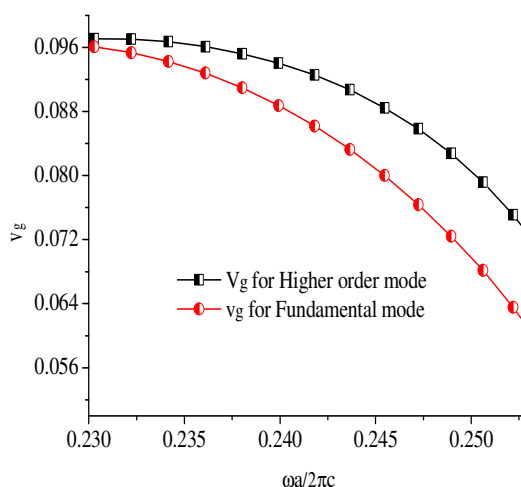


Figure 7. Group velocity v_g versus normalized frequency.

Simulations of pulse propagation through the symmetric coupler is analyzed for frequency of the pulse $\omega = 0.235$. It is tuned close to the gap-edge where $\Delta k=0.1$. Estimated pulse velocity at that point is $v_g \approx 0.096$, it is approximately same for fundamental and higher guided modes.

CONCLUSIONS

In this paper, we proposed and simulated the slow light device consisting of the symmetric couplers waveguide, which exhibits approximately zero group velocity near band edge. By varying the width of waveguide, which is obtained by changing vertical shift 's' of first rows of structure, normalized output power is changed. This is due to improvement in slow light. Maximum normalized output waveguide power has been obtained equal to $0.66\mu\text{w}$ at $s=0.20\mu\text{m}$.

REFERENCES

- [1] Yang Qu, Hongliang Ren, and Chun Jiang, "A novel design of 2-D photonic crystal directional coupler with high extinction ratio and short coupling length," *IEEE Journal of Quantum Electronics*, Vol. 43, No. 11, Nov. 2007.
- [2] Chun Jiang, "Flat band slow light in asymmetric line defect photonic crystal waveguide featuring low group velocity and dispersion," *IEEE Journal of Quantum Electronics*, Vol. 44, No. 8, 2008.
- [3] J. Hou, D. Gao, H. Wu, R. Hao, "Flat band slow light in symmetric line defect photonic crystals waveguide," *IEEE Photon. Tech. Lett.* 21, 1571-1573, Oct 2009.
- [4] Hai-Feng Zhou, Xiao-qing Jiang, Tian-bao Yu, Jian-yi Yang, Ming-hua Wang, "Two-mode-interference switching in photonic crystal waveguides," 0-7803-9774-6/06, IEEE, 2006.
- [5] Sangwoo Ha1, Andrey A. Sukhorukov, Kokou B. Dossou, "Dispersion less tunnelling of slow light in anti symmetric photonic crystal couplers," Vol. 16, No. 2, *Optics Express* 1104, 2008.
- [6] Azadeh Taher Rahmati, Nosrat Granpayeh, "Kerr nonlinear switch based on ultra-compact photonic crystal directional coupler," *Optik* 122 -502-505, Elsevier, 2011.
- [7] M. L. Povinellia, S. G. Johnson, and J. D. Joannopoulos, "Tunable time delays in photonic-crystal waveguides," *SPIE Vol. 6128*, 61280R. 2006.
- [8] Andrey A, Sangwoo Ha, Kokou B. Dossou, "Photonic crystal couplers for slow light," *SPIE Vol. 6904*, 69040S, 2008.
- [9] John D. Joannopoulos, Steven G. Johnson., "Photonic Crystals Molding the Flow of Light," Princeton University Press, 2008.
- [10] T.F. Krauss, "Slow light in photonic crystal waveguides," *App. Phy*, Vol. 40, pp 2666-2670, USA, 2007
- [11] J. Hou, D. Gao, H. Wu, R. Hao, "Flat band slow light in symmetric line defect photonic crystals waveguide," *IEEE Photon. Tech. Lett.*, vol. 21, pp 1571-1573, Oct 2009.
- [12] J. Li, T. P. White, L. O Faolain, A. Gomez-Iglesias, and T. F. Krauss, "Systematic design of flat band slow light in photonic crystal waveguides," *Opt. Express* 16 (9), 6227-6232 2008.
- [13] Feng Chun, WenYao Liang, "Wideband slow light and dispersion control in oblique lattice PhcWG," *Optics Express* Vol.18, No 6, 5707, 2010.
- [14] Ran Hao, Eric Cassan, Hamza Kurt, Xavier Le Roux, Delphine Marris-Morini, Laurent Vivien, Huaming Wu, Zhiping Zhou, and Xinliang Zhang, "Novel slow light waveguide with controllable delay-bandwidth product and ultra-low Dispersion," *Opt. Express*, Vol. 18, pp 5942-5950, 2010.

Modulational Instability induced by cubic–quintic nonlinearity and higher order dispersive effect in nonlinear metamaterials

Manirupa Saha* and Amarendra K. Sarma

Indian Institute of Technology Guwahati, Guwahati-781039

*Email: manirupa@iitg.ac.in

Abstract: We investigate the modulation instability (MI) of a nonlinear metamaterial (MM) in a medium with cubic-quintic electric nonlinearity. The role of higher order nonlinear effect and higher order dispersive effect on the evolution of modulational instability has been studied.

1. INTRODUCTION

Metamaterials are artificial structures that exhibit negative refractive index due to its simultaneous negative permittivity and negative permeability[1-5]. Recently, a number of linear and nonlinear MMs have been studied in theory and experimentally over a range of frequencies from microwave to optical region[6-10]. On the basis of dispersion relation for Drude medium, the dynamical models for propagation of ultrashort pulses in nonlinear MMs have been developed. It is discussed that the main difference between MMs and ordinary materials is the dispersive magnetic permeability $\mu(\omega)$, which influences the propagation of short pulses. The first significant attempt in deriving a proper model equation to describe pulse propagation equation was made by Scalora et al.[10-11]. Wen et al. have derived a coupled NLSE for few cycle pulse propagation in a MM with both nonlinear electric and magnetic polarization[12-13]. Modulation instability (MI) is closely related to the formation of solitons in a nonlinear medium occurs as a result of the interaction between the linear dispersive effect and the nonlinear effect [14]. Xian et al. have studied MI with higher order nonlinear effect in Kerr medium [15-16]. In this work, we present modulation instability analysis of a MM with cubic-quintic nonlinearity. In our analysis, we have included higher order linear and nonlinear dispersion effects which arise due to the dispersive nature of magnetic permeability. Our study shows that higher order nonlinear dispersion effect tends to suppress the MI gain but higher order nonlinear effect due to quintic nonlinearity increases the gain.

2. THEORETICAL MODEL

The most fundamental differences between an ordinary material and an MM is may be due to the fact that MM exhibits strong dispersive behavior in both electric permittivity and magnetic permeability while in ordinary materials any one of them become dominant in one time. We consider a nonlinear negative index material with nonlinear electric polarization (\mathbf{P}_{NL}) as $\mathbf{P}_{NL} = \epsilon_{NL} \mathbf{E} = \epsilon_0 \chi_P^{(3)} |E|^2 \mathbf{E} + \epsilon_0 \chi_P^{(5)} |E|^4 \mathbf{E}$; where ϵ_{NL} is nonlinear electric permittivity and $\chi_P^{(n)}$ is the n-

order electric susceptibility and in our model we have included the cubic and quintic nonlinearity. \mathbf{E} and \mathbf{H} are the electric and magnetic fields respectively. The nonlinear pulse propagation through metamaterials, being a dispersive medium, is characterized by electric flux density (\mathbf{D}) and magnetic induction (\mathbf{B}) which depends on electric (\mathbf{E}) and magnetic (\mathbf{H}) field intensities as $\mathbf{D} = \epsilon \mathbf{E} + \mathbf{P}_{NL}$. The dielectric permittivity (ϵ) and magnetic permeability (μ) are dispersive in MMs otherwise the energy density could be negative and their frequency dispersion is given by lossy Drude model [8]. In MM loss can not be neglected but the imaginary parts of permittivity and permeability are very small at some frequency and so we neglect the loss. We assume that the electric field is propagating in a uniform, bulk MM containing no free charge and no free current. It is straightforward to get the following nonlinear pulse propagation equations from the Maxwell equations in this frame is

$$\frac{\partial A}{\partial \xi} = \frac{i\beta_2 \partial^2 A}{2 \partial \tau^2} - \frac{1}{2k_0} \frac{\partial^2 A}{\partial \xi^2} + \frac{1}{k_0 V} \frac{\partial^2 A}{\partial \xi \partial \tau} + \sum_{m=3}^{\infty} \frac{i^{m+1} \delta_m \partial^m A}{m! \partial \tau^m} + (1 + \frac{i}{\omega_0}) \sum_{m=3}^{\infty} \frac{i^{m+1} v_m \partial^m}{m! \partial \tau^m} (|A|^2 A) + (1 + \frac{i}{\omega_0}) \sum_{m=3}^{\infty} \frac{i^{m+1} \sigma_m \partial^m}{m! \partial \tau^m} (|A|^2 A) \tag{1}$$

Where $\beta_2 = \delta_2 - \frac{1}{k_0 V^2}$; $v_m = \frac{\omega_0 \epsilon_0 \chi^{(3)}}{2k_0} \frac{\partial^m(\omega\mu)}{\partial \omega^m} \Big|_{\omega=\omega_0}$

$\sigma_m = \frac{\omega_0 \epsilon_0 \chi^{(5)}}{2k_0} \frac{\partial^m(\omega\mu)}{\partial \omega^m} \Big|_{\omega=\omega_0}$

We now calculate the Non-SVEA correction terms

by using the above equation to evaluate $\frac{\partial^2 A}{\partial \xi^2}$ and $\frac{\partial^2 A}{\partial \xi \partial \tau}$

of the following form:

$$\frac{\partial^2 A}{\partial \xi^2} \approx \frac{\beta_2 \partial^2 A}{4 \partial \tau^2} - v_0 |A|^2 A + \frac{v_0 \beta_2}{2} \frac{\partial^2}{\partial \tau^2} (|A|^2 A); \frac{\partial^2 A}{\partial \xi \partial \tau} \approx -\frac{i\beta_2 \partial^2 A}{2 \partial \tau^3} + i v_0 \frac{\partial}{\partial \tau} (|A|^2 A) \tag{2}$$

Using equation (2) in Eq.(1) and keeping the dispersion terms to third order and the nonlinear terms to second-order derivatives of time, we finally obtain the propagation equation as follows

$$\frac{\partial A}{\partial \xi} = -\frac{i\beta_2}{2} \frac{\partial^2 A}{\partial \tau^2} + \frac{\beta_3}{6} \frac{\partial^3 A}{\partial \tau^3} + iP_{nl} \left(|A|^2 A + iS_1 \frac{\partial}{\partial \tau} (|A|^2 A) - S_2 \frac{\partial^2}{\partial \tau^2} (|A|^2 A) \right) + iP_{nl}' |A|^4 A \quad (3)$$

Where

$$P_{nl} = v_0 = \frac{\omega_0^2 \mu(\omega_0) \epsilon_0 \chi_E^{(3)}}{2k_0}; \quad P_{nl}' = \sigma_0 - \frac{v_0^2}{2k_0} = \frac{\omega_0^2 \mu(\omega_0) \epsilon_0 \chi_E^{(5)}}{2k_0} - \frac{1}{2k_0} \left(\frac{\omega_0^2 \mu(\omega_0) \epsilon_0 \chi_E^{(3)}}{2k_0} \right)^2$$

$$S_1 = \left[\frac{1}{\epsilon_0} \frac{v_1}{v_0} \frac{1}{k_0 V} \right]; S_2 = \left(\frac{v_1}{v_0 \epsilon_0} + \frac{v_2}{2v_0} \frac{\beta_2}{4k_0} \right)$$

$$\beta_2 = \delta_2 - \frac{1}{k_0 V^2} = \frac{1}{c \omega_{pe}^2} \left[\frac{1}{n \omega_0} \left(1 + \frac{3 \left(\frac{\omega_{pm}}{\omega_{pe}} \right)^2}{\omega_0^4} \right) - \frac{1}{n^3 \omega_0} \left(1 + \frac{\left(\frac{\omega_{pm}}{\omega_{pe}} \right)^2}{\omega_0^4} \right) \right]$$

$$\beta_3 = \delta_3 - \frac{3\beta_2}{k_0 V} = -\frac{1}{c \omega_{pe}^2} \left[\frac{12 \left(\frac{\omega_{pm}}{\omega_{pe}} \right)^2}{n \omega_0^6} + \frac{3\beta_2}{n^2 \omega_0} \left(1 - \frac{\left(\frac{\omega_{pm}}{\omega_{pe}} \right)^2}{\omega_0^4} \right) \right];$$

With $V = 2k_0 / [\omega_0 \epsilon(\omega_0) \gamma + \omega_0 \mu(\omega_0) \alpha]$; $\gamma = \partial[\omega \mu(\omega)] / \partial \omega|_{\omega=\omega_0}$;

$\alpha = \partial[\omega \epsilon(\omega)] / \partial \omega|_{\omega=\omega_0}$ where β_2 and β_3 are the second and third order nonlinear parameter respectively. P_{nl} and P_{nl}' are the first order and second order nonlinear coefficients and S_1 and S_2 are first and second order self-steepening coefficients due to third order polarization for the electric field. Eq. (3) is the generalized NLSE for pulse propagation for a negative index material having cubic and quintic nonlinearity. In Fig. 1 we plot the variation of refractive index n, β_2 and β_3 with the normalized frequency ω_0/ω_{pe} for $\omega_{pm}/\omega_{pe}=0.8$. In Fig.2 we have plotted the nonlinear parameter and higher order nonlinear dispersion parameter with the normalized frequency ω_0/ω_{pe} for $\omega_{pm}/\omega_{pe}=0.8$. Here ω_{pe} and ω_{pm} are the respective electric and magnetic plasma frequency and the parameters are plotted at $\omega=\omega_0$. In the plot P_{nl} is calculated in units of $\omega_{pe} \chi_E^{(3)} / c$ and P_{nl}' is calculated in units of $\omega_{pe} \chi_E^{(5)} / c$ while S_1 and S_2 are calculated in the units of $1/\omega_{pe}$ and $1/\omega_{pe}^2$ respectively. We have studied the parameters both in negative and positive index regime.

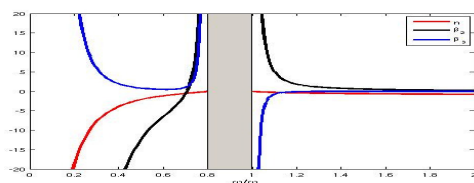


Fig1: Fig.1 Variation of n, β_2 and β_3 with ω_0/ω_{pe} with $\omega_{pm}/\omega_{pe}=0.8$.

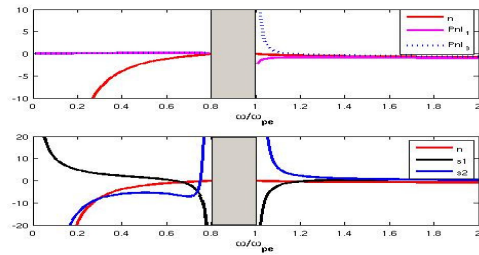


Fig2: Variation of n, P_{nl} and P_{nl}' with ω_0/ω_{pe} and variation of n, S_1 and S_2 with ω_0/ω_{pe} having $\omega_{pm}/\omega_{pe}=0.8$

For the purpose of simplification it is convenient to write the NLSE in normalized form. First we assume the normalized variables as $Z = \xi/L_D, T = \tau/T_0, A = \sqrt{P_0} U, u = NU$, where T_0 is the pulse width, $L_D = T_0^2 / |\beta_2|, L_D' = T_0^3 / |\beta_3|$ are the second and third order dispersion length respectively and N is termed as the order of soliton, defined as $N^2 = L_D / L_{Pnl}$. Here we are also define the nonlinear polarization length as $s_1 = |S_1|/T_0$ and $s_2 = S_2/T_0$ are the first and second order electric self-steepening parameter due to cubic nonlinearity and $\sigma = \frac{P_{nl}'}{P_{nl}^2 L_D} \frac{1}{2k_0 L_D}$ is the normalized parameter and the normalized form of NLSE is

$$\frac{\partial u}{\partial Z} = -\frac{i\delta}{2} \frac{\partial^2 u}{\partial T^2} + \frac{k_3}{6} \frac{\partial^3 u}{\partial T^3} + i|u|^2 u + i\sigma |u|^4 u - s_1 \frac{\partial}{\partial T} (|u|^2 u) - is_2 \frac{\partial^2}{\partial T^2} (|u|^2 u) \quad (4)$$

Now, we would carry out a modulational instability (MI) analysis of the generalized coupled field equations (2) mainly due to its close relation with the existence of solitary waves or solitons. Modulation instability is a fundamental process that appears in most nonlinear systems in nature. It occurs as a result of interplay between the nonlinear effect and nonlinear dispersive effect in time domain or diffraction in spatial domain. Now we would carry out a modulation instability (MI) analysis of the above generalized NLSE mainly due to its close relation with the existence of solitary waves or solitons. We are going to study the effect of higher order nonlinearity on MI gain.

$$\frac{\partial u}{\partial Z} = -\frac{i\delta}{2} \frac{\partial^2 u}{\partial T^2} + i|u|^2 u + i\sigma |u|^4 u - s_1 \frac{\partial}{\partial T} (|u|^2 u) - is_2 \frac{\partial^2}{\partial T^2} (|u|^2 u) \quad (5)$$

We assume that above equation(4.6) have two steady state continuous wave solution as $u = \sqrt{P} \exp[i(P + P^2 \sigma)Z]$, where P is the normalized optical power and $\delta = \text{sign}(\beta_2)$. Now we assume that cw

solution is slightly perturbed from the steady state such that $u(Z,T) = [\sqrt{P} + a(Z,T)] \exp[i(P + P^2\sigma)Z]$ where the complex field $a(Z,T) \ll \sqrt{P}$. Substituting these in Eq.(1.7) we obtain the evolution equations for the perturbations as

$$\frac{\partial a}{\partial Z} = \left(\frac{\delta}{2} + 2s_2P \right) \frac{\partial^2 a}{\partial T^2} + iP(a + a^*) + 2i\sigma P^2(a + a^*) - s_1P \left(2\frac{\partial a}{\partial T} + \frac{\partial a^*}{\partial T} \right) - is_2P \frac{\partial^2 a^*}{\partial T^2} \tag{6}$$

Now $a = a_1 e^{i(KZ - \Omega T)} + a_2 e^{-i(KZ - \Omega T)}$ where K and Ω are wavenumber and frequency of perturbation in normalized units respectively. From Eq.(1.8) we get the following dispersion relation

$$K = \frac{1}{2} \left[4s_1P\Omega \pm \left((4P\Omega^2 + 8P^2\Omega^2\sigma + 8Ps_2\Omega^4)\delta_2^2 + (4P^2s_1^2 + 8P^2s_2 + 16P^3s_2\sigma)\Omega^2 + (\delta^2 + 12P^2s_2^2) \right)^{1/2} \right] \tag{7}$$

The steady-state solution becomes unstable whenever K has an imaginary part since the perturbation then grows exponentially with the power and the growth rate or MI gain is

$$g(\Omega) = 2\text{Im}(K) = \frac{1}{2} \left[\left(-(4P\Omega^2 + 8P^2\Omega^2\sigma + 8Ps_2\Omega^4)\delta - (4P^2s_1^2 + 8P^2s_2 + 16P^3s_2\sigma)\Omega^2 - (\delta^2 + 12P^2s_2^2) \right)^{1/2} \right] \tag{8}$$

With the condition

$$\left((4P\Omega^2 + 8P^2\Omega^2\sigma + 8Ps_2\Omega^4)\delta + (4P^2s_1^2 + 8P^2s_2 + 16P^3s_2\sigma)\Omega^2 + (\delta^2 + 12P^2s_2^2) \right) < 0 \tag{9}$$

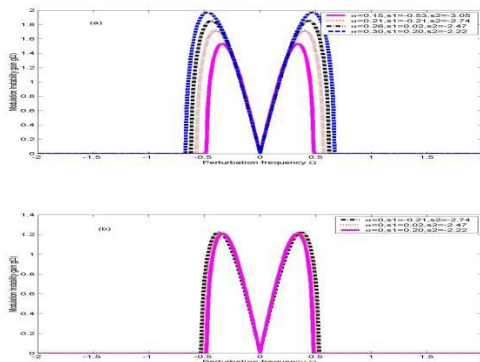


Fig.3 MI gain with normalized perturbation frequency with $\omega/\omega_{pe} = 0.8$ and $T_0 = 10\text{fs}$ with $P = 1$ (a) Joint effect of σ , s_1 and s_2 .(b)effect of s_1 and s_2 with $\sigma = 0$.

It can be seen clearly seen that MI gain spectrum depends on σ , s_1 and s_2 and the perturbation frequency (Ω). It can be seen that the nonlinear parameter σ increases the MI gain and also enlarge the MI gain band in the negative index regime when we are considering focusing cubic-quintic nonlinear

medium. Our analysis shows that though higher order nonlinear dispersion effect try to suppress the gain but the higher order polarization effect increase the MI gain of electromagnetic pulses in a metamaterial and thereby it suggests new way of generating solitons with the unusual nonlinear effects of MMs.

4. CONCLUSIONS

We have derived pulse propagation equation in a nonlinear medium with cubic-quintic nonlinearity in negative index metamaterial. We have also investigated the modulation instability in this media. We have found that the higher order nonlinear parameter increases the MI gain and we have also noticed that the higher order linear and nonlinear effect providing us various ways to control MI gain..

ACKNOWLEDGEMENT

Manirupa Saha would like to thank MHRD, Government of India for a research fellowship.

REFERENCES

[1]. J. B. Pendry, Phys. Rev. Lett. **85**, 3966 (2000).
 [2]. D. R. Smith, W. J. Padilla, D. C. Vier, S. C. Nemat-Nasser, S. Schultz S, Phys. Rev. Lett. **84**, 4184 (2000).
 [3].C. Caloz and T. Itoh, *Electromagnetic Metamaterials: Transmission line theory and Microwave applications* (Wiley Interscience, New Jersey, 2006).
 [4]. V. G. Veselago, Sov. Phys. Usp. **10**, 509 (1968).
 [5]. S. A. Ramakrishna and T. M. Grzegorzczuk, *Physics and Applications of Negative refractive index materials* (CRC Press, Boca Raton, 2009).
 [6]. A. Berrier, M. Mulot, M. Swillo, M. Qiu, L. Thyl'en, A. Talneau and S. Anand, Phys. Rev. Lett. **93**, 073902 (2004).
 [7]. E. Schonbrun, M. Tinker, W. Park and J. B. Lee, IEEE Photon. Technol. Lett. **17**, 1196, (2005).
 [8]. S. A. Ramakrishna and T. M. Grzegorzczuk, *Physics and Applications of Negative refractive index materials* (CRC Press, Boca Raton, 2009).
 [9]. D'Aguzzo, G., N. Mattiucci, M. Scalora, and M. J. Bloemer, Phys. Rev. Lett. **93**, 213902 (2004).
 [10]. M. Scalora, D. D'Ceglia, G. D'Aguzzo, N. Mattiucci, N. Akozbek, M. Centini, and M. J. Bloemer, Phys. Rev. E **75**, 066606 (2007).
 [11]. M. Scalora, M. S. Sychin, N. Akozbek, E. Y. Poliakov, G. D'Aguzzo, N. Mattiucci, M. J. Bloemer, and A. M. Zheltikov, Phys. Rev. Lett. **95**, 013902 (2005).
 [12]. S. Wen, Y. Wang, W. Su, Y. Xiang, and X. Fu, Phys. Rev. E **73**, 036617 (2005).
 [13]. S. Wen, Y. Xiang, X. Dai, Z. Tang, W. Su, and D. Fan, Phys. Rev. A **75**, 033815 (2007).
 [14]. G. P. Agrawal, *Nonlinear Fiber Optics*, 4th ed. Academic, New York (2007).
 [15]. S. Wen, Y. Xiang, W. Su, Y. Hu, X. Fu, and D. Fan, Opt. Express **14**, 1568 (2006).

[16]. S. Wen, Y. Xiang, X. Dai, Z. Tang, W. Su, and D.Fan, *J.Opt.Am.B* **24**, 3058(2007)

DESIGN OF 2D SILICON CARBIDE BASED PHOTONIC CRYSTAL WAVEGUIDES

Yogita Kalra, Jiten Boruah and R.K. Sinha
Delhi Technological University, Bawana Road, Delhi

dryogitakalra@gmail.com, jitenboruah1@rediffmail.com, dr_rk_sinha@yahoo.com

Abstract: The design of two dimensional photonic crystal based on silicon carbide is proposed, which is one of the hardest well as most commonly used materials in power electronics, which can lead to the advancement towards stable photonics at high power and temperature.

Photonic Crystals exhibit photonic band gaps in which electromagnetic fields cannot propagate in given directions, if the geometrical parameters and dielectric contrast of the photonic lattices are chosen, is a well known fact [1]. Because of the strong photon confinement shown by these crystals they can be used in variety of applications. However the most widely used materials to design photonic crystal devices are silicon and gallium arsenide because of the available and mature technology of fabrication. Moreover the refractive index contrast offered by these materials is optimum for the existence of the photonic band gaps.

We here propose to design photonic crystals using silicon carbide which is one of the hardest materials known and further the creation of photonic crystal waveguides in SiC photonic crystals. The reason for using silicon carbide is its high mechanical strength, large thermal conductivity and small thermo optic coefficient [2]-[3].

DESIGN OF SiC PHOTONIC CRYSTALS

In this paper we explore the possibility of designing SiC based photonic crystals and further the variation of photonic band gaps in Si photonic crystals and SiC photonic crystals with change in temperature.

To design the SiC photonic crystals, we first explore

the possibility of existence of photonic band gaps in these crystals as the refractive index of SiC is 2.6 which is much less as compared to silicon or gallium arsenide.

For that we report the design of two types of photonic crystals :

- (i) PhC composed of hexagonal arrangement of SiC rods in air
- (ii) PhC composed of hexagonal arrangement of holes in SiC.

The gap maps for both the reported structures have been obtained using the plane wave expansion method as shown in figure1 and 2. The gap maps indicate that the band gaps do open up in the designed photonic crystal structures.

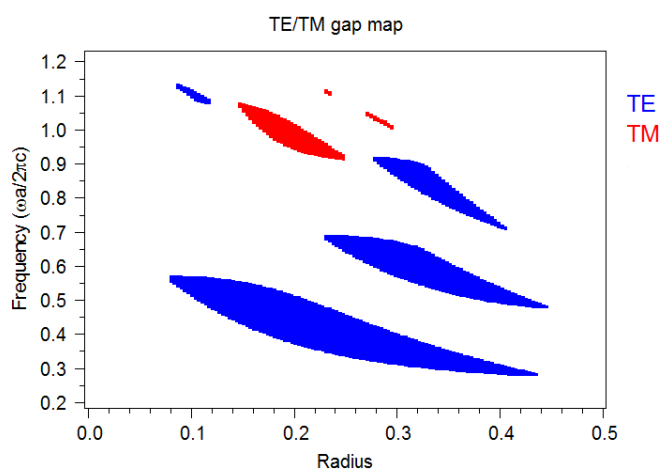


Fig1. Gap map of hexagonal arrangement of SiC rods in air

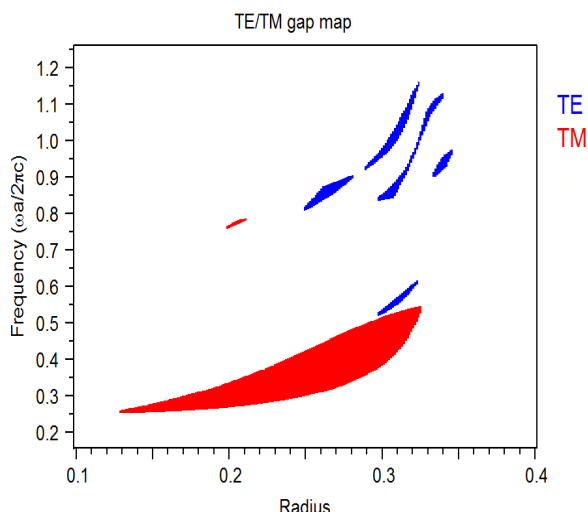


Fig2. Gap map of hexagonal arrangement of air holes in SiC

The figures indicate the band gaps exhibited by these crystals are smaller as compared with those exhibited by Si photonic crystals because the SiC photonic crystals have lower refractive index contrast. Further, line defects can be created in the designed silicon carbide photonic crystals to form SiC PhC waveguides as shown in figure 3(a) and 3(b).

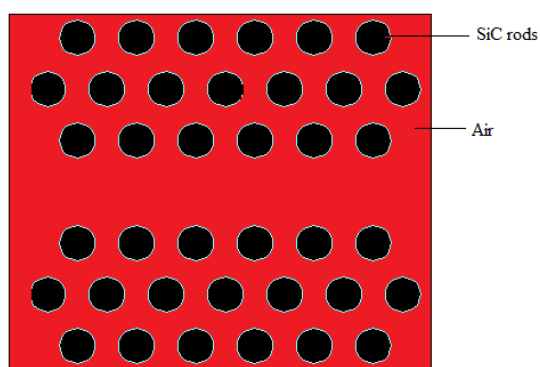


Fig 3(a) Schematic view of the SiC PhC wave guide in PhC composed of SiC rods in air

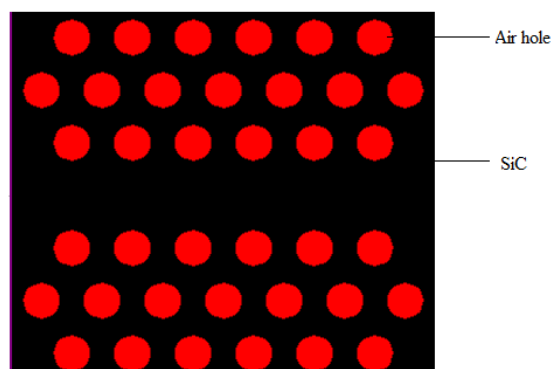


Fig 3(b) Schematic view of the SiC PhC wave guide in PhC composed of air holes in SiC

VARIATION OF BAND GAPS WITH TEMPERATURE IN Si PhCs AND SiC PhCs AND WAVEGUIDES.

To study the effect of temperature on the proposed photonic crystal structures, the temperature of the four samples of photonic crystals was raised from 25⁰C to 200⁰C

- (i) PhC composed of hexagonal arrangement of SiC rods in air
- (ii) PhC composed of hexagonal arrangement of holes in SiC.
- (iii) PhC composed of hexagonal arrangement of Si rods in air
- (iv) PhC composed of hexagonal arrangement of holes in Si.

Band gap calculations have performed for the above samples at different temperatures ranging from 25⁰C to 200⁰C using the plane wave expansion method.

Similar analysis was done for the photonic crystal waveguides for all the samples which were designed by creating linear defects in the respective photonic

crystal structures. It was observed that Si based photonic crystals exhibited stronger variation with temperature whereas the SiC based photonic crystals exhibited a very small variation with change in temperature. Moreover if photonic crystal waveguides are designed for the operational wavelength of 1550nm, the SiC based photonic crystal waveguides exhibited a shift of 5nm in the operational range while the temperature is varied from 25⁰C to 200⁰C. On the other hand the Si based photonic crystal waveguides exhibited a shift of 16nm in the operational range which is three times the variation observed with respect to the SiC based photonic crystals.

The results indicate that the silicon carbide based photonic crystals and waveguides are nearly three times more resilient than silicon based photonic crystals and waveguides over a given ambient temperature region. This variation in the operational range of the SiC and Si PhC waveguides indicate the difference in the thermo optic effect of SiC and Si photonic crystal waveguides. Thus the SiC waveguides are less susceptible to the temperature fluctuations that lead to the instability of the optical properties of the opto electronic systems.

CONCLUSION

The SiC PhC waveguides can be used for the high power transmission which is difficult to achieve with Si or GaAs based photonic crystal based waveguides. Various other SiC based devices can be designed which are stable at high power and high temperature, at which the silicon photonics fails. This can lead to the era of silicon carbide power photonics analogous to silicon carbide power electronics.

ACKNOWLEDGEMENT

The authors gratefully acknowledge the initiatives and support towards establishment of the “ TIFAC-center of Relevance of Excellence in Fiber Optics and Optical Communication at Delhi College of Engineering now DTU-Delhi, through the “Mission REACH” program of Technology Vision-2020 of the Government of India.

REFERENCES

- [1] J.D. Joannapolous , R. D. Meade and J.N. Winn, *Photonic Crystals : Molding the flow of light*, Princeton University Press,New Jersey,1995
- [2] J.Zhou. H.Li. L.Ye,J.Liu,J.Wang , T.Zhao,L.Jiang and Y.Song“ Facile fabrication of Tough SiC inverse opal photonic crystals,”*J. Phys. Chem.C* , **114**, 22303,2010
- [3] G.L. Harris, *Properties of Silicon Carbide*, INSPEC, Institution of Electrical Engineers, London, 1995

ALL-OPTICAL PULSE SWITCHING IN TWIN CORE PHOTONIC CRYSTAL FIBER

T. Uthayakumar^a, R. Vasantha Jayakantha Raja^b, K. Nithyanandan^a, and K. Porsezian^a

^aDepartment of Physics, Pondicherry University, Puducherry – 605 014, India.

^bDepartment of Physics, Central University of Tamil Nadu, Thiruvarur - 610 001, India.

uthayapu@gmail.com, rvjraja@yahoo.com, nithi.physics@gmail.com and ponzsol@yahoo.com

Abstract: We investigate the consequence of different diameter to pitch ratio on transmission features of the twin core silica photonic crystal fiber (SPCF) structure at 850 nm. The necessary fiber parameters required to study the switching characteristics are calculated using the finite element method (FEM). From the obtained physical parameters the switching mechanism of different structures are studied and qualitative comparison is achieved numerically using the split step Fourier method (SSFM).

1. INTRODUCTION

Nonlinear optical fiber with multiple cores which provides the platform to light control governs the optical signal processing, optical switching and optical computing [1]. The wide range of flexibility provided by photonic crystal fibers (PCF) such as tailorable zero dispersion, enhanced nonlinearity, endless single mode operation and large effective mode area makes it best suitable for multiple core fibers [2, 3]. The nonlinear fiber couplers made from the PCF provides with above mentioned numerous advantages over that from the conventional fiber couplers. Hence, we showed much attention towards the dynamics and switching characteristics study of the twin core silica photonic crystal fiber (SPCF). Although there are lots of research findings that existing as well as blooming in PCF but with our best awareness, there is no significant study of optical switching at visible region. Also, at this regime, the SPCF finds many applications in coherence tomography, optical sensors and frequency metrology. Hence, we aimed at the study of switching properties of twin core PCF for different design parameters at 850 nm.

2. MODELING OF SPCF

To study the performance and steering characteristics of SPCF at 850 nm, we proposed three designs of symmetric SPCFs with the different air hole diameter d to the pitch constant Λ ratios d/Λ 0.5, 0.6 and 0.7 respectively with inter core separation ($C = 2\Lambda$) at $\Lambda = 1\ \mu\text{m}$. Fig.1 shows the schematic of the one of the designs. By employing finite element method (FEM), the optical properties such as nonlinearity, group velocity dispersion, effective index and the coupling length of the proposed design is calculated at 850 nm. The coupling length calculated for the SPCF designs with symmetric even and odd polarization modes of different d/Λ values 0.5, 0.6 and 0.7 at optical wavelength 850 nm are 0.23 mm, 0.46 mm and 1 mm respectively.

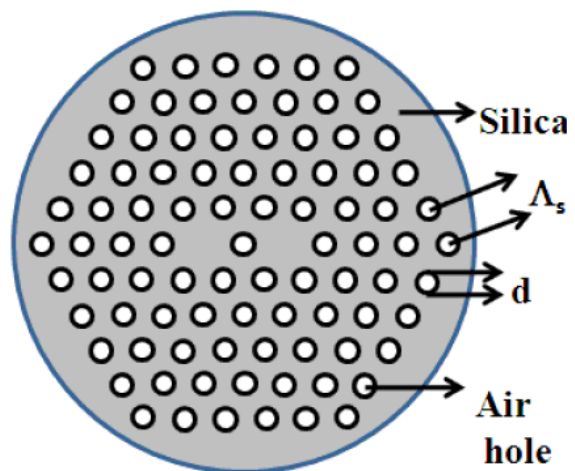


Fig. 1 Schematic of one of the proposed PCFC with the inter core separation ($C = 2\Lambda$) at $\Lambda = 1\ \mu\text{m}$

3. SPLIT STEP FOURIER METHOD

The dynamics and switching characteristics study of the optical pulse propagation through the nonlinear couplers are governed by a set of coupled nonlinear Schrödinger equations (CNLSE) [3]. For the study of our proposed PCF coupler designs, we assume the following CNLSE

$$i \frac{\partial E_j}{\partial z} - \frac{\beta_2}{2} \frac{\partial^2 E_j}{\partial t^2} + \gamma |E_j|^2 E_j + \kappa E_{2-j} - \frac{i}{2} \alpha E_j = 0$$

Where E_j is the input pulse through the coupler with $j=1, 2$ for core1 and core2 respectively. β_2 is the group velocity dispersion parameter and γ is the nonlinear coefficient. The coupling coefficient κ is defined as $\pi/(2L_c)$ where L_c is the coupling length and α extinction coefficient. The pulse propagation is along the longitudinal z axis.

To study the pulse dynamics and steering through the SPCF numerically, we employ the split step Fourier method (SSFM). Initial Gaussian pulse at $z = 0$, for core1 is given by $E(0, t) = E_0 \exp(-t^2/W_0)$.

where E_0 is the amplitude, W_0 is the pulse width and 0.01% of the input field of core1 is assumed to be the initial profile of core2. With the following sets of initial conditions: $L_c = 0.23$ mm, 0.46 mm and 1 mm for design 0.5, 0.6 and 0.7 d/Λ 's respectively, $\beta_2 = -0.0423$ ps²/km, $\gamma = 0.1518$ W⁻¹m⁻¹, $\lambda = 850$ nm and $\alpha = 0.01917$ dB/m the system dynamics is investigated.

4. RESULTS AND DISCUSSIONS

4.1 Coupling characteristics of SPCF

The dynamics of the input Gaussian pulse through the proposed designs of SPCF for 0.5, 0.6 and 0.7 d/Λ 's is illustrated by Fig. (2, 3 & 4) respectively. For the SPCF design of $d/\Lambda = 0.5$ with $L_c = 0.23$ mm, at $z = 0$ the pulse propagates through the input core until it reaches the coupling length $L_c = 0.23$ mm shown by maximum amplitude in Fig. 2 (a) and minimum amplitude in Fig. 2 (b). When it reaches the L_c the pulse transfer to the neighboring port occurs shown by raise in the amplitude of the pulse in the core2 illustrated by Fig. (b). This pulse exhibits continuous oscillation between the cores for the arrival of the every coupling length. Also, it can be seen clearly that there is no pulse breakup during the propagation and coupling which is primarily due L_c very much less than that of the dispersion length L_D . The Fig. 2 (c & d) are the contour plots representing the 2-dimensional picture of same pulse propagation. This clearly depicts the absence of pulse breakup during

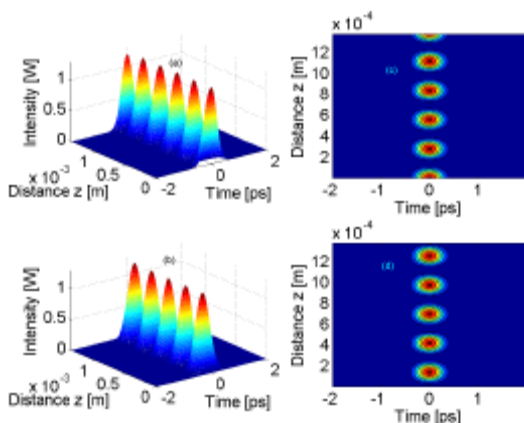


Fig. 2 Numerical evolution of the pulse propagation through PCFC design with $d/\Lambda = 0.5$. every pulse coupling.

Fig. 3 demonstrates the coupling characteristics of the input pulse through SPCF for $d/\Lambda = 0.6$. The proposed coupler exhibits the same coupling characteristics as discussed above for SPCF model for $d/\Lambda = 0.5$. But the number of times of coupling between the cores which is primarily due to the higher coupling length

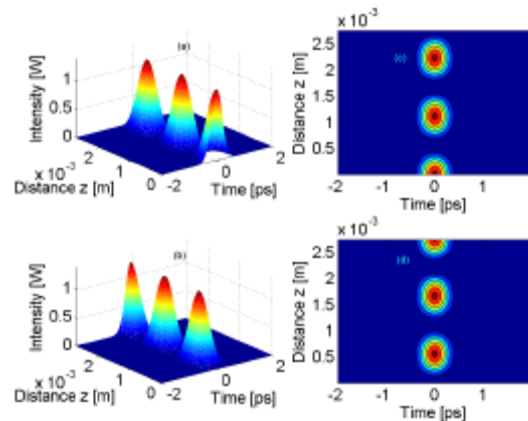


Fig. 3 Numerical evolution of the pulse propagation through PCFC design with $d/\Lambda = 0.6$.

value of this model with $L_c = 0.46$ mm, which is considerably greater than that of the above discussed model. Here also one can view clearly that there is no pulse breakup during the propagation and coupling.

In the case of SPCF model of $d/\Lambda = 0.7$, the coupling length is very high and which is equal to $L_c = 1$ mm. This SPCF has only few number of pulse oscillation when compared to the other two models. But it exhibits the similar coupling behavior as that of other two models with less pulse exchanging behavior with the absence of the pulse breakup which can be viewed clearly through the Fig. 3. When comparing all the three couplers of d/Λ s 0.5, 0.6 and 0.7, the coupler with $d/\Lambda = 0.5$ exhibits good coupling characteristics with short coupling and behaves as tuned coupler.

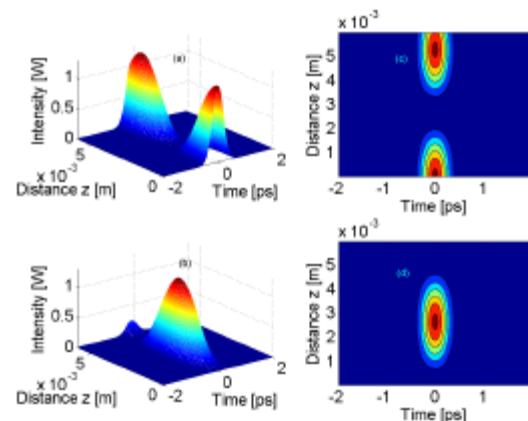


Fig. 4 Numerical evolution of the pulse propagation through PCFC design with $d/\Lambda = 0.7$.

4.2 Transmission characteristics of SPCF

The pulse transmission characteristics of the input Gaussian pulse through the proposed SPCFs are

displayed by the Fig. 5. When an optical pulse is introduced through the any one of the port of the coupler, it undergoes coupling when it reaches the coupling length. And this coupling occurs for the arrival of the every coupling length. For $d/\Lambda = 0.5$ with $L_c = 0.23$ mm, the transmission curve illustrates that at low power, there is an equal energy exchange between the cores shown by minimum value of solid plus line and maximum of dashed plus line for the core1 and core2 respectively. This energy exchange takes place up to the input peak power reaches the threshold peak power. For the threshold peak power greater than 2.2 W, the energy transmission through the core1 increase with decrease in the energy sharing to the core2, which is depicted clearly in Fig. 5.

For the SPCF with $d/\Lambda = 0.6$ the coupler behaves linearly and exhibit tuned coupler behavior with equal energy exchange between the cores, up to the threshold peak power. For the threshold peak power 1.2W portrayed in the Fig. 5 by line with circle, the transmission through the launched core increases with decrease in the energy sharing the neighboring core2. And at this peak power switching efficiency of around 60% is achieved. For further increase in the threshold peak power the efficiency of switching is increased greater than 80% at the threshold peak power of 1.46 W. Also, from the figure it can be viewed that this coupler system exhibits multiple switching behavior for the further raise in the threshold peak power. Also, this design provides the greater switching efficiency than that of the above discussed model of $d/\Lambda = 0.5$ where the switching efficiency is around 60% for the threshold peak power greater than 2.4 W.

In the case of SPCF design $d/\Lambda = 0.7$, coupler system exhibits excellent switching characteristics compared to that of other designs. Initially there is an equal sharing of the energy between cores. As input peak power is increase a part of the energy transmitted to the neighboring port increases until the arrival of threshold peak power.

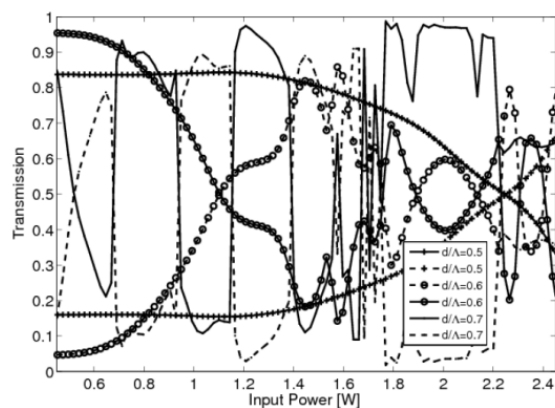


Fig.5 Transmission characteristics as a function of input power, where solid and dashed curve represents the pulse

propagation through core1 & 2 respectively.

For the threshold peak power of 0.7 W the energy transferred to the neighboring core drastically reduced with the maximum energy concentrated through the launched core. At this peak power, the coupler exhibits the switching efficiency greater than 90%. This system also exhibits the multiple switching behaviors and when compared with other two systems this system exhibits the very low switching threshold peak power. But from the FEM calculations, it is found that for the d/Λ above 0.6 can no longer maintain single mode property. Hence, when compare to the $d/\Lambda = 0.7$, the 0.6 is optimum for the polarization splitting less application.

5. CONCLUSION

We have studied the pulse coupling and switching through the proposed three types of SPCF designs. Using the FEM, the necessary the optical properties of the proposed desings are calculated. The dynamics and switching characteristics are studied numerically using the SSFM. From the results obtained for the coupler dynamics, it is evident that the SPCF design of $d/\Lambda = 0.5$ exhibits good coupling characteristics when compared to that of the other designs. Transmission characteristics curve shows that the SPCF model with $d/\Lambda = 0.7$ exhibits the low switching threshold peak power as well the coupler model of $d/\Lambda = 0.6$ also exhibits the very good switching characteristics. It is also found both these models exhibit multiple switching characteristics.

ACKNOWLEDGEMENT

KP thanks DST-DFG, DST, DAE-BRNS, and UGC, Government of India, for the financial support through major projects. TU express thankfulness to UGC Fellowship in sciences for meritorious students.

REFERENCES

- [1] G. P. Agrawal, "Applications of Nonlinear Fiber Optics" Academic Press, New York (2001).
- [2] J. M. Dudley and J. Roy Taylor, "Ten years of nonlinear optics in photonic crystal fibre", Nat. Photon, vol. 3, 85 (2009).
- [3] K. P. Hansen, "Introduction to nonlinear photonic crystal fibers", J. Opt. Fiber Commun. Rep. vol. 226, (2005).
- [4] K. R. Khan, T. X. Wu, D. N. Christodoulides, and G. I. Stegeman, "Soliton switching and multi-frequency generation in a nonlinear photonic crystal fiber coupler", Opt. Exp., vol. 16, 9417 (2008).

ITO COATED LONG PERIOD FIBER GRATING SENSOR WITH ENHANCED RI SENSITIVITY

Nidhi^{1,2}, Umesh Tiwari^{1*}, Vandana Mishra¹, RS Kaler², Subhash C.Jain¹, Nahar Singh¹, and Pawan Kapur¹

¹Central Scientific Instruments Organization, Chandigarh, 160030, India

(Council of Scientific and Industrial Research, New Delhi)

²Thapar University, Patiala 147004

*Email: umeshtiwari@csio.res.in

Abstract: In this paper, we have proposed and experimentally demonstrated the enhancement in the refractive index sensitivity by coating Indium Tin Oxide (ITO) on long period fiber grating (LPG). The characterization of coated and uncoated LPG was carried out with solutions of standard RI and glycerol with different concentrations. The coating of ITO on the surface of LPG was observed by FE-SEM Imaging and Fourier Transform Infrared Spectroscopy (FTIR). The ITO coating enhances RI sensitivity of LPG 2-3 times.

1. INTRODUCTION

A optical fiber based sensor are very compact in size and can be made suitable for various sensing applications in the areas like medicines, food industry and biosensing. The advantages of these sensors include their lightweight, small size, passive, low power loss, resistant to electromagnetic interference and high sensitivity. Refractive index is a fundamental physical property of any substance and its measurement has promising potential in the field of chemistry, biochemistry, process control, pharmaceuticals and biology [1,2] and the above said advantages of fiber has drawn the attention to develop fiber based RI sensors. Recent development in the field is fiber grating based sensors. Gratings are basically the periodic variation of refractive index written in the core of the fiber and sensors based upon grating are divided into two types: fiber Bragg grating (FBG) also called short period grating and Long Period Grating (LPG) sensors. The potential of FBG and LPG based refractometers have already been explored. A non-uniformly thinned FBG with self temperature compensating features and FBG in etched fiber have been reported as RI sensor [3,4]. These reported sensor has theoretical sensitivity of higher than 10^5 refractive index unit in a refractive index region close to the cladding index of the fiber. The changes in the transmission spectrum of LPG and tilted short-period FBG versus the refractive index of the surrounding medium has also been reported. Sensitivity analysis of weakly tilted FBG with different coating thickness have been reported

The modification in RI response of LPG occurs when a thin film overlay is deposited on it and the concept of cladding mode reorganization was explained in earlier reports. Enhancement in the tuning range of a single resonant band LPG by using an optimized high index indium tin oxide overlay

have been reported by Lee. The concept that an overlay of higher refractive index than the cladding starts to guide a mode if a certain thickness value is exceeded, causing large shifts in the resonance wavelength with change in external RI was proposed by Del Villar. A high-performance index/thickness-sensing LPG-based fiber sensor had been analysed with optical property variations of thin film coating by Wang [14]. The work related to the analysis of RI sensitivity of LPG with SiO₂ nanoparticle mesoporous thin have been reported recently. Recent studies have also shown that thin films ITO could be deposited onto non-conductive optical fiber tips, which were then used as working electrodes for the electrochemical deposition of polymers with reactive groups (biotin), so as to create a biosensor. More recently theoretical modeling of a Surface Plasmon Resonance (SPR) based fiber optic sensor with a conducting metal oxide (ITO) as the SPR active material is being demonstrated. Conducting films of ITO films have shown better sensitivity as compared to silver and gold on simple fiber as the SPR active material. Silver is a chemically active material and gets oxidized very quickly and layers of gold and silver are not continuous but agglomerate as islands. The other disadvantage can be the presence of roughness on the surface of the film that may occur due to the conditions of thermal evaporation. It is a transparent material in the visible and IR range of the spectral region. It does not involve band-to-band transition, and also there are no islands on even a very thin layer of it deposited on the dielectric surface [4]. In the present investigation we have made first attempt to find out the effect of ITO layer on RI sensitivity of LPG to the best of our knowledge.

2. WORKING PRINCIPLE

Long-period gratings considered as a special class of fibre Bragg gratings in which the period of the index modulation is such that it satisfies a phase matching condition between the fundamental core mode and a forward propagating cladding mode of an optical fibre [18]. The shift in the resonance bands are actually strong function of grating periods, order of the corresponding cladding mode and writing conditions. The effective indices of the cladding modes are strongly influence by refraction of the medium surrounding. When the value of surrounding refractive index become much higher than that of cladding the propagation constant of the cladding mode become complex and the mode become leaky. The spectral sensitivity of LPG is given by [19]

$$(d\lambda/dn_s) = (d\lambda/dn_{cl,m}^{eff}) (dn_{cl,m}^{eff}/dn_s)$$

The spectral sensitivity depends upon the effective refractive index of cladding mode, which is further dependent on the refractive index of surrounding material n_s . The sensor response also depend upon the order of the coupled cladding mode .

. ITO is essentially formed by sub situational doping of In_2O_3 with Sn which replaces the In^{3+} atoms from the cubic bix byte structure of indium oxide. Sn thus forms an interstitial bond with oxygen and exists either as SnO or SnO₂ - accordingly it has a valency of +2 or +4 respectively. This valency state has a direct bearing on the ultimate conductivity of ITO.

The presence of ITO coating introduced strong changes in the cladding mode distribution. When the surrounding RI is less than the cladding, total internal reflection condition satisfied. But when it becomes higher then bounded cladding modes are not supported. The presence of attenuation band in this case is due to Fresnel reflections forming leaky modes.

Due to presence of coating, the transition from cladding to overlay modes occurs, the lowest order cladding modes becomes guided into overlay. The higher modes move to recover the original field configuration leading to improvement in SRI sensitivity.

3. EXPERIMENTAL SETUP AND RESULTS

In our investigation a LPG of length 20 mm, with 575 μ m period and resonance wavelength was recorded as 1591 nm in a single mode boron co-doped fiber. Glycerol solution of different concentrations varying from (20% ,40%,60%,100%) was used in our experiment. The effect of thin film on the refractive index sensitivity is reported. We found that coating has enhanced the sensitivity by 2-3 times. To coat the

LPG, solution was prepared by Indium chloride and tin chloride is dissolved in ethanol. 0.01% of surfactant is added to the prepared solution. The LPG is kept absolutely bend free ,then glass slide with few drops of solution is given up and down moment by the mechanical stage shown in the setup (Fig 1.1). The ITO solution was kept on properly cleaned glass slide on a vertically moving stage. LPG was held straight between micro positioners. The stage was moved up till the LPG part was completely immersed. After 2-3 seconds the stage was moved down and LPG was kept undisturbed for drying. The LPG was dipped into the solution for few seconds .Then kept it undisturbed for air drying and afterwards heat treatment was applied. This process is repeated three times. For the thickness analysis of coated sampl, a standard optical fiber without sensing element was hosted together with LPG for coating deposition. In this way thickness and quality of coating was done by SEM analysis using the standard fiber.

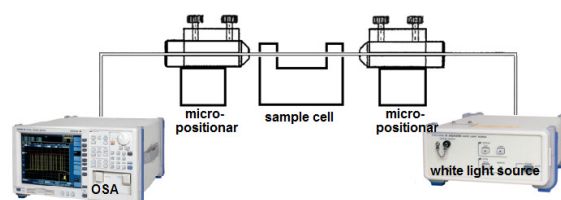


Fig.1: Schematic of the experimental setup

The fig.2 shows the SEM results of ITO deposited LPG of nm order. It can be observed that the crystallite size of the film deposited is uniform.



Fig. 2: SEM of ITO coated LPG

The Characterization for different standard refractive index solutions (1, 1.45, 1.454, 1.458) has been done for same simple LPG and coated LPG. The wavelength is recorded on OSA (Optical Spectrum Analyzer) for each solution. The simple LPG and coated LPG show the sensitivity of 0.145 μ m/RIU and 0.225 μ m/RIU respectively

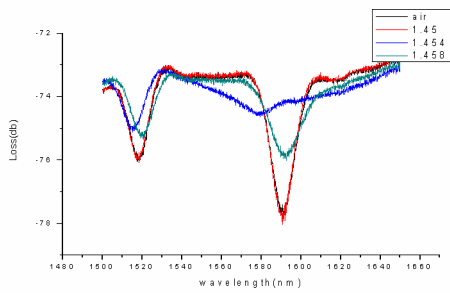
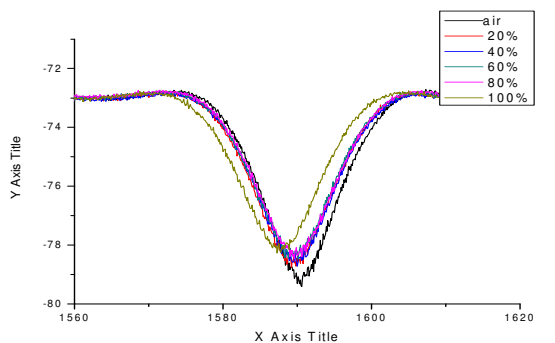
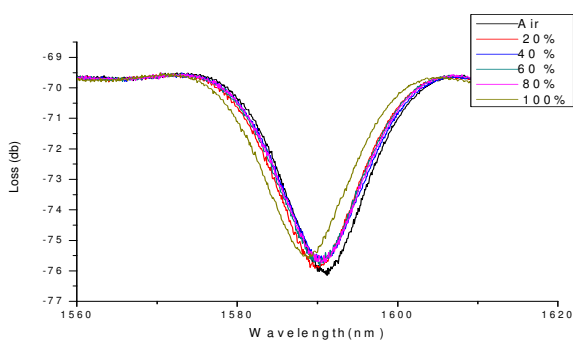


Fig.3 The shift in resonance wavelength for different RI

For better estimate of RI sensitivity different concentrations of glycerol was used and corresponding wavelength shifts were monitored. The RI value of different concentrations of glycerol solution is monitored by using BS-RFM840 Refractometer. This gives rise to the sensing region refractive indices (1.3490 to 1.4198). The analysis was done with simple LPG and coated LPG and shift in resonance wavelength was recorded on OSA. We found that the coated LPG is 2-3 times more sensitive than uncoated LPG. The Response of coated LPG with different concentrations of glycerol was shown in the fig 4.



(a)



(b)

Fig.3: (a) Response of CLPG for different concentrations of glycerol solution (b) Response of uncoated LPG for different concentrations of glycerol solution

FTIR transmission spectrum was acquired from 680 cm^{-1} to 410 cm^{-1} . The optical transmittance closely related to the free electrons in ITO film. we can see from the result shown in fig 5, the optical transmission of ITO film is maximum in the visible range (660 cm^{-1}). The relative intensity change of the FTIR vibrational peaks shows that there may be some predominant structure orientation change. Summitt and Borrelly, reported that the bands of SnO_2 at 690,630,310 cm^{-1} in the infrared spectrum same as found in our results.

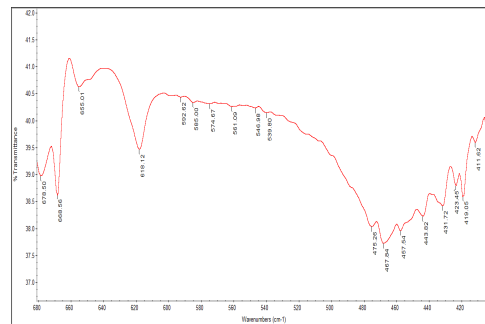


Fig.5 FTIR transmission spectrum of ITO film on optical fiber

4. Conclusion

This research illustrates the enhancement in the refractive index sensitivity of long period grating. A very simple, easy approach has been used for this enhancement. The properties of conducting metal oxides been found that they can support and perform better for the surface plasmon wave. The process like SEM, FTIR and Raman spectroscopy has given us a better understanding of coating structure and thickness. We demonstrated that the sensitivity has been enhanced by 2-3 times. This factor can be improved by further optimizing the coating methods

REFERENCES

- [1] Chin Chang and Rahul Mehta, Fiber Optic Sensors for Transportation Infrastructural Health Monitoring, American J. of Engineering and Applied Sciences, vol 3 pp. 214-221, 2010.
- [2] A Iadicicco, S Campopiano, A Cutolo, Mand Giordano, A Cusano, Self temperature referenced refractive index sensor by non-uniform thinned fiber Bragg gratings, Sensors and Actuators B, vol 120, pp.231-237, 2006.
- [3] Rajneesh K. Verma and Banshi D. Gupta, Surface plasmon resonance based fiber optic sensor for the IR region using a conducting metal oxide film, J. Opt. Soc. Am. A, Vol. 27, No. 4, pp. 846-851, 2010.

RADIATION RESPONSE BEHAVIOR OF CARBON DOPED ALUMINOSILICATE GLASS BASED OPTICAL FIBRE FOR USE AS RADIATION SENSOR

S. Ghosh¹, M. C. Paul^{1*}, S.Das¹, K.Dasgupta¹, D. Bohra², H. S. Chaudhary², L. Panwar² and P. K. Bhatnagar², S. G. Vaijapurkar²

¹Fibre Optics and Photonics Division, Central Glass & Ceramic Research Institute-CSIR
196, Raja S.C.Mullick Road, Kolkata-700 032, INDIA.

²Defence Laboratory, Jodhpur, INDIA.

*Corresponding author: mcpal@cgcri.res.in

Abstract: C+Al₂O₃ co-doped silica glass (CAS) based step index multimode (SIMM) fibre shows an excellent linear radiation response behavior with sensitivities around 0.01dB/m/Gy and 0.80 dB/m/Gy at 1300 nm and 850 nm wavelengths respectively as well as very low recovery at room temperature which enable its practical application as radiation sensor.

1. INTRODUCTION

A few work on carbon co-doped glass based material for its application in the field of dosimetry has been reported earlier[1]. We have fabricated first time C+Al₂O₃ codoped SIMM fibre and observed its radiation response behavior. We have examined the radiation response behavior at medium dose rates within 2.5- 10Gy/h using ⁶⁰Co emitting gamma rays with average photon energy 1.25 MeV at 1300nm and 850nm wavelengths. The fibre shows a good linear response behavior without any saturation. The radiation induced loss of the fibre is almost dose rate independent with low recovery in nature. Such radiation response behavior shows its potential to use as radiation sensor in radiation field.

2. EXPERIMENTS

2.1 Fibre sample fabrication

The C+ Al₂O₃ SIMM fibres were fabricated by modified chemical vapor deposition (MCVD) process [2] followed by double solution doping technique using CCl₄ as a source of C and aluminium chloride as a source of Al₂O₃. In double solution doping technique first, we doped aluminium oxide with aluminium chloride solution into unsintered porous silica layer and then oxidized the whole composition in presence of oxygen to produced aluminium oxide. In the next step we soaked porous layer with CCl₄ solution and then heated the whole composition in absence of oxygen to prevent the formation of CO₂ and CO. The sintering and collapsing at inert atmosphere were done in the next phase to prepare the final preform samples. The fibre was drawn from the preform sample using the fibre drawing tower. The fibre details were shown in the following table.

Table:1 Details of fibre parameters

Fibre name	Core composition	Core diameter(μm)	Numerical aperture
AC-3	SiO ₂ +Al ₂ O ₃ +C	22.0-23.0	0.21-0.23
AL-3	SiO ₂ +Al ₂ O ₃	22.0-23.0	0.21-0.23

EPMA and SEM experiments have been done to

understand the dopant concentration along with nature of glass. The distribution of doping levels of C and Al₂O₃ along the core diameter of fibre preforms (AC-3) was shown in Fig.1(a) and distribution of Al₂O₃ of preform sample (AL-3) shown in Fig. 1(b) measured from electron probe microanalyses (EPMA).

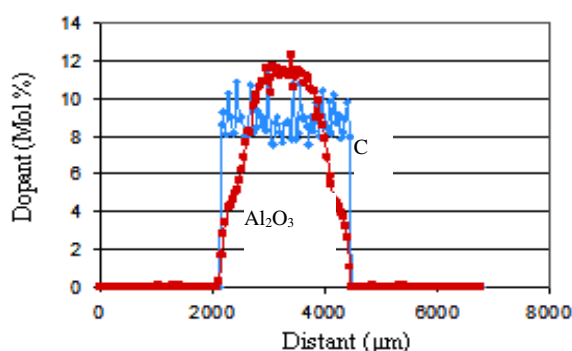


Fig.1a: Distribution of C and Al₂O₃ along preform diameter (AC-3)

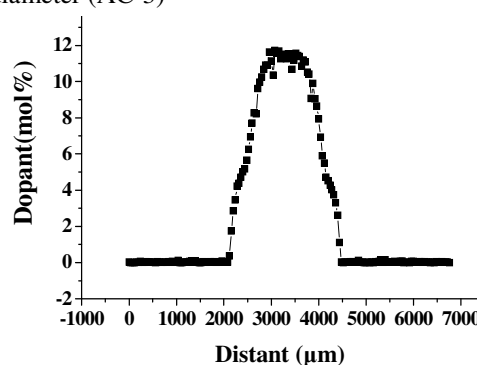


Fig.1b: Distribution of Al₂O₃ along diameter of preform (AL-3)

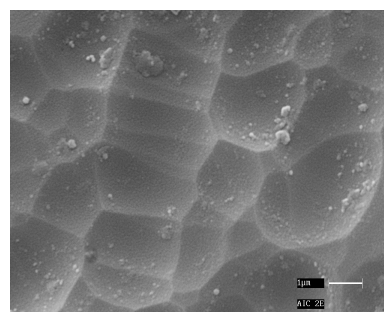


Fig. 2 : SEM image of carbon codoped aluminosilica glass based optical preform.(AC-3)

The SEM images of the sample AC-3 was shown in the above Fig.2. The image shows a clear grain boundary all over the region of the core portion of the preform. Grain boundary is the evidence of the formation of crystals in the core region. From the thermodynamics study it is shown that the formation of the two types of crystals aluminum carbide (Al_4C_3) and silicon carbide (SiC) becomes possible at high temperature range as the samples were made at high temperature. The high melting point of such kind of crystals ($Al_4C_{3m,p} = 2300^\circ C$, $SiC_{m,p} = 2730^\circ C$) be an evidence for formation of aluminum carbide and silicon carbide in the core region of the samples.

2.2 Induced loss measurement.

The experimental setup used for measurement of the radiation response behavior of the Al_2O_3 doped optical fibres with and without C was shown in Fig. 3. The ^{60}Co -gamma radiation source of constant energy 1.25MeV was used to measure the radiation induced loss along with its sensitivity and recovery nature with different dose rates at 850nm and 1300nm wavelengths.

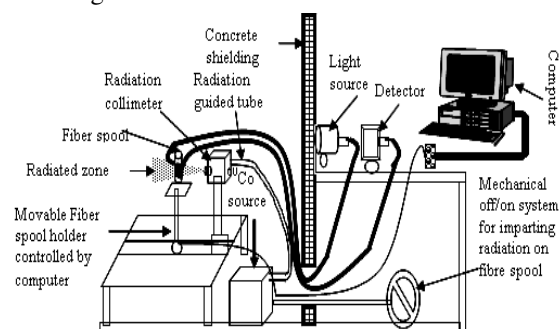


Fig.3 Experimental set up for study of radiation response behaviour of optical fibres using ^{60}Co -gamma radiation source projector

Four meter length of each radiation sensitive fibre was wrapped around a test reel of 2.5 cm diameter and placed at the center of the radiation field. To study the effect of dose rates on the fibre the dose rate was varied by changing the distance between the source and the fibre reel. Total dose was controlled by varying the exposure times for different dose rates. Quartz (100 W) halogen source with aspheric lens controlled by constant current supply at 8.5 A was used. Stability of the light output power is $\pm 0.1\%$ over 8 h. Modulated white light is passed through a monochromator for controlling the selection of wavelength before being launched into one end of the fibre under test. One end of each fibre was cut with a fibre cleaver and placed into the bare fibre holder with a connector along the light source of the Bentham Spectral Attenuation set-up. Other end was inserted into the detector assembly. This spectral attenuation set-up is computer controlled. The experimental data were recorded for further processing. The dose rates of

^{60}Co -gamma radiation source performed on each fibre are 0.1, 0.25, 0.5, 0.75, 1.0, 2.5, 5.0, 7.5, and 10 Gy/h with the total accumulated dose of 1.0Gy. The recovery nature of the fibre irradiated at different dose rates was recorded at 1300nm wavelength for one hour duration of the fibre samples AC-3 & AL-3.

3. RESULT AND DISCUSSION

The radiation induced absorption spectra of two different C+ Al_2O_3 codoped SIMM fibres (AC-3 and AC-2) irradiated at dose rates of 10 Gy/h is described in Fig.4 for evaluation of the suitable

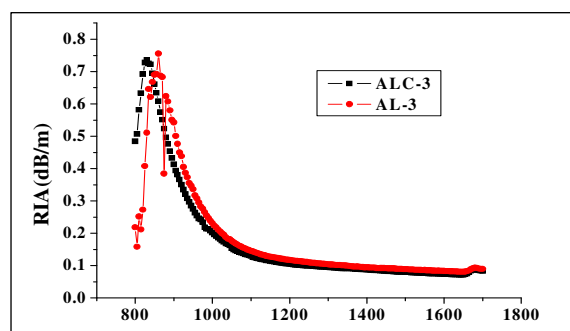


Fig. 4 Radiation induced attenuation of ALC-3 & AL-3

transmission wavelength at which the fibre shows the maximum radiation sensitivity. From the induced absorption curve we have selected first the transmission wavelength of 850nm for study of radiation response behaviour. After that we have selected 1300nm wavelength where the induced loss is found to be minimum. Both the fibres with (AC-3) and without C (AL-3) shows linear radiation response behavior with increasing the total accumulated dose under different dose rates as shown in Fig.5.

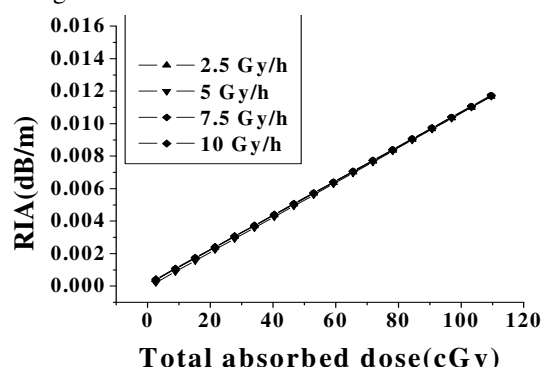


Fig.5. Radiation response behavior of AC-3fibre at 1300 nm wavelength

The fibre AC-3 shows dose rate dependency at lower dose rates region (not shown in Fig) but completely dose rate independent at higher dose rates shown in Fig.5. On the other hand, fibre (AL-3) without doping of C shows dose rate dependency behavior as shown in Fig. 6. The sensitivity of carbon doped fibre increases initially and then becomes constant with increasing carbon concentration shown

in Fig.7.

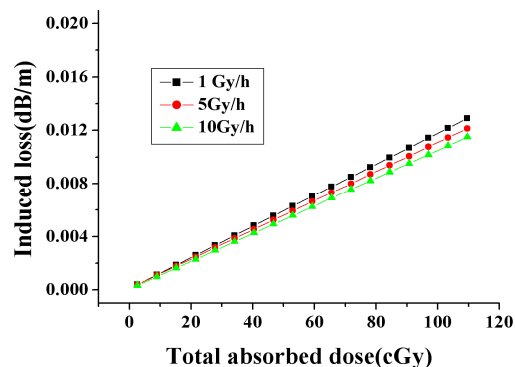


Fig.6. Radiation response behavior of AL-3 fibre at 1300 nm wavelength

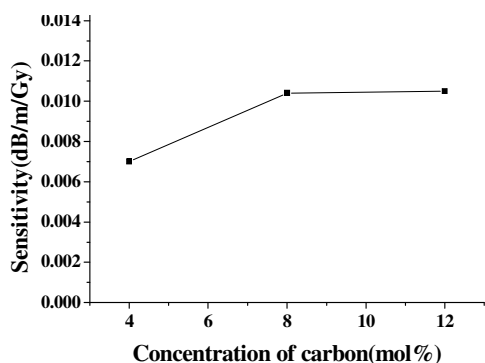


Fig.7 Sensitivity of fibres with different carbon concentration at 1300nm wavelength.

In this case carbon may play an important role for enhancing the sensitivity of the fibres through modification of the surrounding structure of Si and Al. The effect of dose rates on sensitivity of the fibre AC-3 was shown in the fig 8. It was observed that at higher dose rates the sensitivity is independent of dose rates.

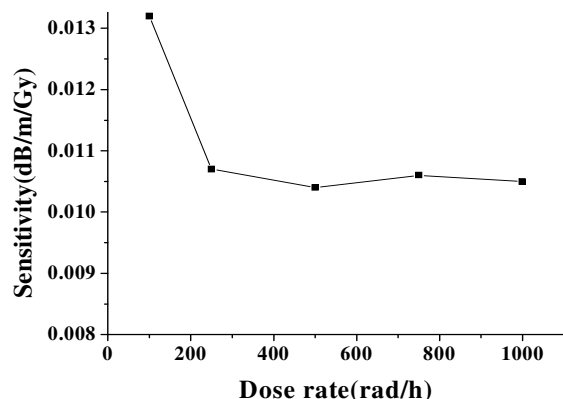


Fig.8 Effect of dose rates on sensitivity at 1300nm

The radiation sensitivity of two different kind of fibres with (AC-3) and without (AL-3) carbon shown in the Fig. 9. The recovery nature of C-doped SIMM fibre was evaluated at room temperature. The recovery nature of one C-Al₂O₃ co-doped fibre (AC-3) containing 12 mol% C was described after

irradiation at different dose rates of 10-1000 rad/hr under 1300 nm transmission wavelength which shown in Fig.10.

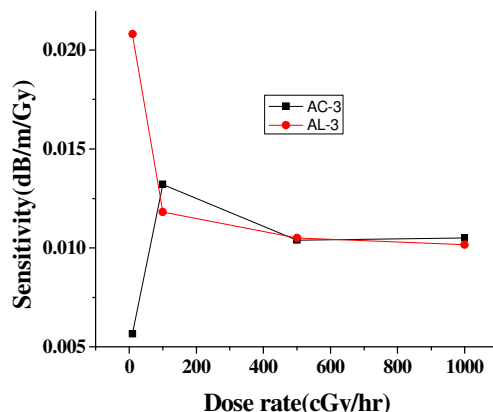


Fig. 9: Plot of sensitivity vs. dose rate of AC-3 & AL-3 at 1300nm

Recovery was taken for 1 hour after irradiation and shows very low fading behavior.

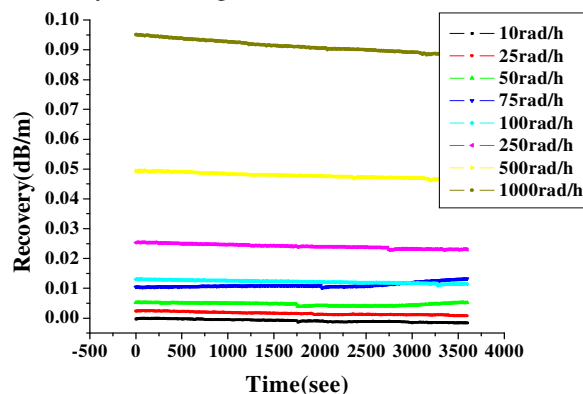
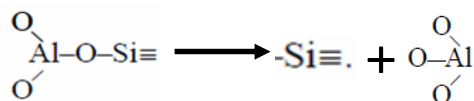


Fig. 10 Recovery nature of AC-3 at 1300nm wavelength

The formation of radiation induced defect is responsible for the radiation induced attenuation of different dopant fibres as studied earlier work [3]. In this case Si, Al and C related defect centers can be formed during gamma irradiation. The optical absorption curves of both the fibre preform samples with and without carbon before and after irradiation (total accumulated dose of 10 Gy) was shown in Fig.11. Both the samples before irradiation shows an absorption peak at 215nm which arises due to Si(E') centers[4]. A slight broad absorption peak at 290nm arises due to Al(E') center[5]. However after irradiation the intensity of the peak at 215 nm almost remains constant but the intensity of the peak at 290 increases. The absorption band in the range 280–300 nm is associated with the E'(Al) centers, which are formed on threefold-coordinated aluminum atoms according to the following reaction:-



On the other hand a slight broad absorption around

550nm appear after irradiation which may be due to formation of Al-hole center[6].

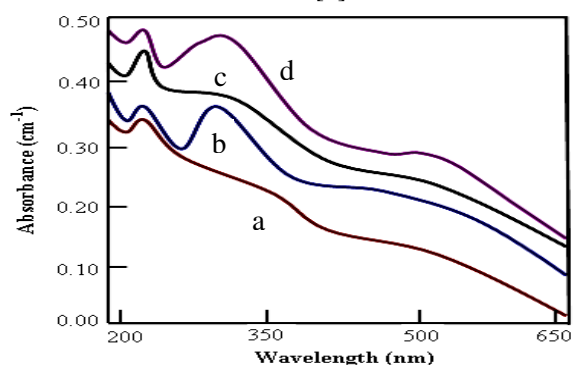


Fig.11: Optical absorption spectra fibre preform samples before gamma irradiation (a) AL-3 & (c) AC-3 and after gamma irradiation of 10Gy (b)AL-3 & (d) AC-3

No other characteristics signature of the presence of carbon related defect centers arises in this case. ESR spectra of both preform samples before and after irradiation was shown in Fig. 12 .

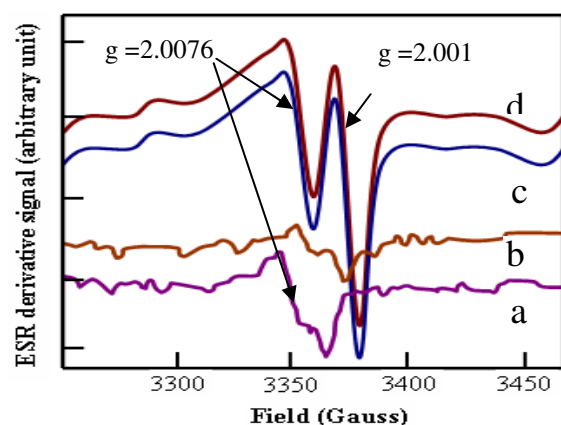


Fig.12: ESR spectra fibre preform samples before gamma irradiation (a) AL-3 & (b) AC-3 and after [gamma irradiation of 10Gy (c)AL-3 & (d) AC-3

From ESR study a resonance signal corresponding to g value of 2.001 arises for both preform samples with and without carbon after gamma irradiation due to formation of Si(E') or Al(E') centers. Both the preform samples before and after irradiation shows a resonance signal corresponding to g value of 2.0076 which may be generate due to formation of aluminum oxygen hole centers. The radiation induced attenuation of the C+Al₂O₃ doped fibre arises due to the formation of radiation induced defect centers which may be mainly responsible for Al-related defect centers. A broad peak of radiation induced loss observed shown in Fig.3 4 signifies that the induced defect population at this wavelength range is higher than other wavelengths. It also give an idea about the defect centers energy. The growth of defect centers with increasing accumulation dose follows the power law[7]. The recovery nature reveals that the induced defect centres of the C+Al₂O₃ fibre are stable at room

temperature and their thermal recombination or induced recombination is less at the experimental condition.

4. CONCLUSION

We are able to make Al with C codoped silica glass based optical fibre containing 10-12 mol % of Al₂O₃ and 8-10 mol% of C for use as radiation sensor at medium dose rate region within 1.5 – 10 Gy/hr. A detailed study about the radiation response behavior of such kind of optical fibre was done at room temperature. The radiation sensitivity of CAS fibre was found to be 0.80 dB/m/Gy at 850 nm transmission wavelengths which becomes 80 times higher than that of the radiation sensitivity at 1300nm transmission wavelength. The fibre shows very low recovery at room temperature using ⁶⁰Co gamma radiation source. The sensitivity of carbon-alumino-silica (CAS) fibre not only depends on carbon content but also depends on the transmission wavelength. Such type of CAS fibre shows good linearity in radiation response behavior as well as dose rate independency followed by low recovery in nature with moderate sensitivity which enables its practical application in fibre optic personal dosimeter for measurement of high dose gamma radiation specially in the space application.

ACKNOWLEDGEMENT

Authors wish to acknowledge DRDO-New Delhi for financial support. The authors are thankful to the Prof. Indranil Manna, Director (CGCRI) and Director , Defence Laboratory, Jodhpur for their continuous encouragement, guidance and support in this work.

REFERENCES

- [1] B. L. Justus, S. Rychnovsky, M. A. Miller, K. J. Pawlovich, and A. L. Huston, *Radiation Protection Dosimetry*, **74**, 151-154 (1997).
- [2] S.R. Nagel, J.B. Macchesney, K.L. Walker, "Review on MCVD process chemistry" T. Li (Ed.), Academic Press, New York, **1**, 1 (1985),
- [3] E. J. Friebele, K. J. Long, C. G. Askins, M. E. Gingerich, M. J. Marrone, D. L. Griscom, SPIE 541 - Radiation effects in optical glasses, P.W. Levy, Ed. (SPIE, Bellingham, WA, 1985), pp. 70-80 Critical reviews of technology: Optical materials in radiation environments SPIE, **541** 70-88 (1985)
- [4] Ryabov, A.I., Kritskaya, V.E., and Pirogova, G.N., *Neorg.Mater.*, **29**, 298-299(1993).
- [5] Amosov, A.V. and Malyskin, S.F., *Fiz. Khim. Stekla.*, **8**, 88-92(1982).
- [6] Amosov, A.V., Kornev, V.V., and Malyskin, S.F., *A, Fiz. Khim. Stekla*, **7**, 209-214(1981).
- [7] W. Schneider, U. Babst, H. Henschel, O. Kohn, and H. U.Schmidt, Proc. SPIE **721**, ~1986.

FIBER OPTIC ALCOMETER USING PVA/CHITOSAN POLYMER BLEND

J Linesh, M C Bobby, T M Libish, P Radhakrishnan and V P N Nampoori
International School of Photonics, Cochin University of Science and Technology, Cochin-22
lineshnair@yahoo.com

Abstract: A fiber optic gas sensor for the detection of alcohol vapour is presented in the present work. The cladding of a silica fiber is replaced by PVA/chitosan polymer blend whose refractive index changes upon the adsorption of –OH group. The sensor has a fast response and can be used as an alcohol breathalyzer.

1. INTRODUCTION

Gas sensors play vital role in detecting, monitoring and controlling the presence of gases in the environment and alcohol vapour sensors have found great demand in the biomedical, chemical, and food industries, especially in wine-quality monitoring and breath analysis. Fiber-optic sensors have been reported as powerful sensors for many physical, chemical and biological measurands and the potential of multi parameter sensing combined with distributed measurement give fiber optic sensors a clear edge over conventional sensing schemes [1].

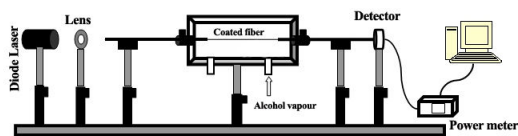
Polymers like PVA and chitosan attracts –OH group and swells causing a reduction in its refractive index [2]. Chitosan/PVA blend has been found to be miscible in all composition and El-Hefian et.al [3] has shown that the blend with 50% PVA has maximum degree of swelling compared with the pure polymers.

In this work we have tried to find out the alcohol sensing behavior of chitosan/PVA blend by coating the polymer over an exposed core region of a plastic clad silica fiber. The response of the fabricated sensor to ethanol and methanol vapour is presented.

2. EXPERIMENTAL

A 20 g/L solution of chitosan and PVA was prepared and mixed under continuous stirring at around 60°C.

A 5 cm length of the cladding of a multimode, step index, plastic clad silica fiber was removed from the central portion of the fiber. The unclad fiber was then dipped in the polymer solution prepared and pulled out at a constant speed and then dried at room temperature for more than 24 h. This probe was then fixed in a chamber as shown in Figure. 1.



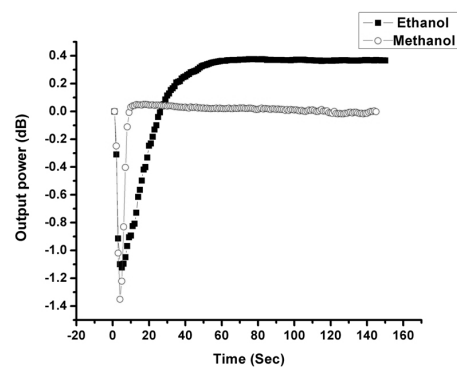
1. Experimental setup

One end of the fiber was coupled to a diode laser operating at 632.8 nm while the other end was coupled to a low power silicon photo detector (Newport 818-IR). Outputs of the power meter

(Newport, Model 1815C) were monitored in a real time using a computer based data acquisition system developed using Lab View.

3. RESULTS

The sensor is based on the phenomenon of intensity modulation through the change in refractive index of the modified cladding upon its hydration. By fixing the humidity level of the chamber to 30% RH we have passed alcohol vapour to the chamber and recorded the output power as a function of time. The output power variation thus obtained by passing methanol and ethanol is shown in figure 2.



2. Sensor response to alcohol vapour

ACKNOWLEDGEMENT

Author J Linesh acknowledges UGC, Govt. of India for financial support through RFSMS scheme and CELOS.

REFERENCES

- [1] B.D.Gupta, *Fiber Optic Sensors, Principles and Applications*, New India Publishing Agency, New Delhi, India, 2006.
- [2] Toshio Watanabe, Naoki Ooba, Yasuhiro Hida, and Makoto Hikita, "Influence of humidity on refractive index of polymers for optical waveguide and its temperature dependence", *Appl.Phys.Lett.*, **72**, 1533 (1998).
- [3] Esam A. El-Hefian, Mohamed Mahmoud Nasef and Abdul Hamid Yahaya, "The Preparation and Characterization of Chitosan / Poly (Vinyl Alcohol) Blended Films", *E-J. Chem.*, **7**, 1212 (2010).

MODELING OF SILICA TAPERED FIBERS IMMERSED IN ACETONITRILE FOR OPTICAL SENSING

Mohammad Mohebbi, Rasul Rezaei, Hadi Khormaei

Department of Electrical Engineering, Islamic Azad University, Qazvin Branch, Qazvin, IRAN
Email: mohebbi@qiau.ac.ir

Abstract: We model an optical sensor using two silica fibers immersed in acetonitrile for detection of nanoparticles in the infrared spectral range. Acetonitrile is used as the detecting solution because, in contrast to water, it has negligible losses in the infrared. The propagation constant difference at the output of the optical sensor becomes a maximum for a fiber diameter of 1.23 μm .

1. INTRODUCTION

Dielectric optical waveguides have been successfully used in many applications such as optical communication, optical power delivery systems, and nonlinear optics. Photonic device applications benefit from minimizing the width of waveguides, but fabricating low-loss optical waveguides with sub-micrometer diameters remains challenging because of their delicate structure, small dimensions, and high precision requirement. Several types of dielectric wires with diameters smaller than a micrometer have been obtained [1-3]. These wires can be used as air-clad wire-waveguides and building blocks in micro- and nano- photonic devices [4-6]. An area of application for these waveguides is as optical sensors in fields such as biology and chemistry [5]. Guiding light in subwavelength-diameter silica nanowires within the visible and near infrared spectral ranges has been demonstrated [7-9]. Because of circular uniformity and sidewall smoothness, these nanowires can guide light with low optical losses. In recent years, evanescent-field-based photonic nanowire sensors have been used in many sensing applications and extensive research and development activities have been devoted to this area [10]. These nanowire sensors are able to measure small changes in optical phase or intensity of light with high sensitivity. In addition they have immunity to electromagnetic fields and fast response and can be used in high risk applications involving combustible and explosive materials.

Single-mode subwavelength diameter nanowires immersed in a liquid can be used for optical sensing in the visible and infrared spectral ranges. In these nanowires, a large fraction of the guided field travels outside the wire as evanescent waves [10]. Therefore, immersing such a wire in a liquid makes it highly sensitive to an index change caused by the presence of a specimen in the liquid. In this paper, we numerically investigate an optical sensor by calculating the change in the propagation constant at the output of a Mach-Zehnder interferometer [11] assembled with two wires immersed in acetonitrile [12], as shown in Fig. 1. We have chosen to use acetonitrile, because it has negligible losses in the infrared compared to water

which has very high losses [13, 14].

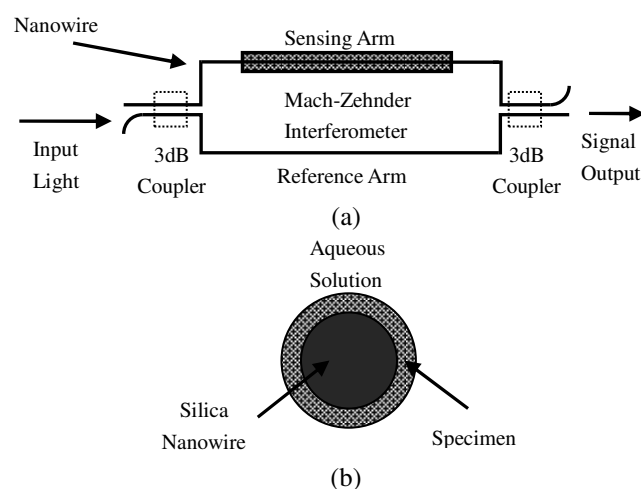


Figure 1 (a) Mach-Zehnder interferometer based nanowire optical sensor and (b) the cross section of the nanowire in aqueous solution. A layer of nanoparticles is formed around the fiber which has been immersed in acetonitrile.

Guiding properties of air-clad silica nanowires has been investigated for different applications. For optical sensing in chemical and biological surroundings, we must immerse the sensing nanowire in a liquid. In the Mach-Zehnder based optical sensor, one of the wires is immersed in an aqueous solution and used as the reference arm. The other wire is immersed in the same aqueous solution and used as the sensing arm in order to detect the presence of a specimen. The specimen under detection changes the composition and, thus, the index of refraction of the aqueous solution in the sensing arm of the optical sensor, as shown in the cross section of the nanowire in Fig. 1(b). A probe light is launched through the Mach-Zehnder interferometer using a 3 dB coupler, which splits it between the reference arm and the sensing arm. The lights from the two arms are then recombined via the second 3 dB coupler, as shown in Fig. 1(a). The phase shift caused by the index change due to the presence of the specimen in the aqueous

solution of the sensing arm is numerically calculated and evaluated from the output light.

Recently, a Mach-Zehnder optical sensor assembled with two silica nanowires, where the sensitive element is immersed in water, has been investigated at wavelengths of 325 nm (He-Cd laser) and 650 nm (laser diode) [10]. At these wavelengths, water does not have high losses and can be used as the detecting solution. However, in the near infrared region of the spectrum and at the important wavelengths of 1300 nm and 1550 nm, water has high losses [15] and cannot be used as the detecting solution, which is due to the O-H bond vibration overtones. Therefore, we propose to use single-mode wires immersed in acetonitrile for sensing in the infrared spectral range. Acetonitrile does not have O-H vibrational overtone absorption lines in the near infrared and is almost transparent in this spectral range. Acetonitrile can transmit about %99 of the light traveling through it at wavelengths of 1300 nm and 1550 nm [15]. In addition, under single mode condition, a large amount of the guided field travels outside the nanowire core and in the aqueous solution, which results in high sensitivity of the optical sensor. The measured data in the infrared from 1.2 μm to 2 μm [12] combined with measured data in the visible has been used to obtain the fitted Sellmeier equation for acetonitrile [15].

Using the propagation constant of the fundamental mode of a wire [16], we calculate the power distribution of silica nanowires immersed in acetonitrile at wavelengths of 1300 nm and 1550 nm. The fractional power in the wire cladding, which in this case is acetonitrile, is shown in Fig. 2. For a silica wire, the cutoff core diameter for single-mode operation at a wavelength of 1550 nm is 2 μm . At a wavelength of 1300 nm, the cutoff core diameter for single-mode operation is 1.7 μm . We can see that thinner fibers provide much higher fraction of evanescent waves in acetonitrile than fibers with thicker diameters, indicating that a thinner silica fiber is much more sensitive to the presence of a specimen in the solution. As seen in Fig. 2, for a diameter of 500 nm, more than %80 of power travels in the cladding (acetonitrile). This is not possible to achieve in a fiber with diameters larger than the wavelength and drops to below %20, as seen from Fig. 2.

We have plotted the variation in the propagation constant between the sensing and reference arm as a function of wavelength for different wire diameters in Fig. 3. The propagation constant difference peaks at a different wavelength for each fiber diameter and moves to the infrared wavelengths as the wire diameter increases. The peak value increases as the wire diameter is decreased indicating that thinner wires result in higher sensitivity. It is also seen that as the operating wavelength moves toward the infrared, the propagation constant curves approach the same value for different wire diameters.

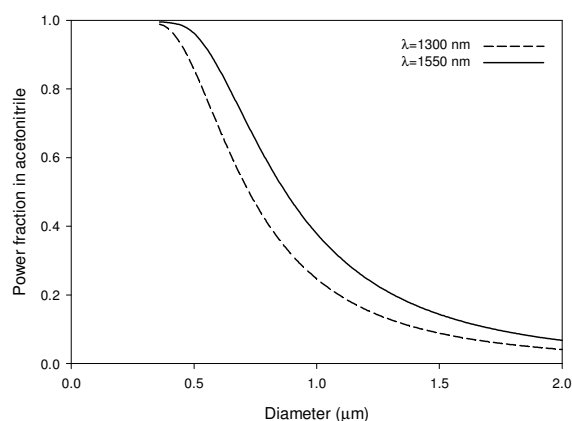


Figure 2 Power fraction in acetonitrile as a function of the nanowire diameter

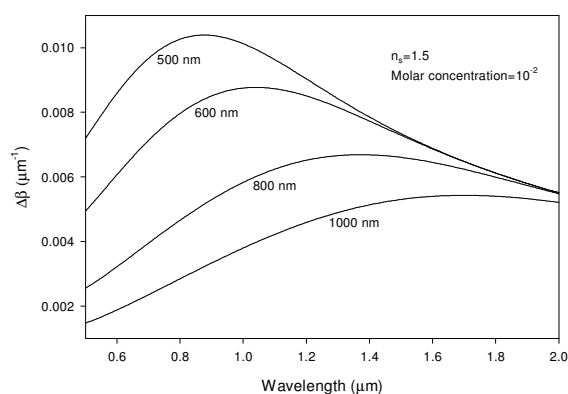


Figure 3 The propagation constant difference as a function of wavelength for different wire diameters. The specimen has a molar concentration of 10^{-2} and index of 1.5.

By modifying the surface of the nanowire, it is possible to selectively collect the specimen under detection forming a thin layer around the nanowire. We can then calculate $\Delta\beta$ by solving the Maxwell equations and applying the boundary conditions for a three layer cylindrical waveguide. We assume the specimen to be nanoparticles of 12 nm thickness and with refractive index of 1.4 (polystreptavidin) [17]. At an operating wavelength of 1550 nm, we solve the Maxwell equations for this three layer fiber and plot the variation of the propagation constant between the reference and sensing arms as a function of the silica fiber diameter in Fig. 4. The propagation constant difference initially increases with the increase of the wire diameter, reaches a maximum, and slowly reduces as the core diameter further increases. The propagation constant difference becomes a maximum at a fiber diameter of 1.23 μm , which is less than the nanowire diameter of 2 μm required for single mode

operation. At this fiber diameter, the fiber length must be about 955 μm in order to achieve a phase shift of π radians at the output of the optical sensor. When water is used as the detecting solution at an operating wavelength of 325 nm, the maximum of $\Delta\beta$ occurs at a fiber diameter of 240 nm and the fiber length must be 68 μm for a phase shift of π radians. The propagation constant difference for the two cases has been plotted in Fig. 5 for a specimen thickness of 12 nm and index of refraction of 1.4. If water is used as the detecting solution, it would be much more difficult to implement the optical sensor due to the small diameter and length of the fiber.

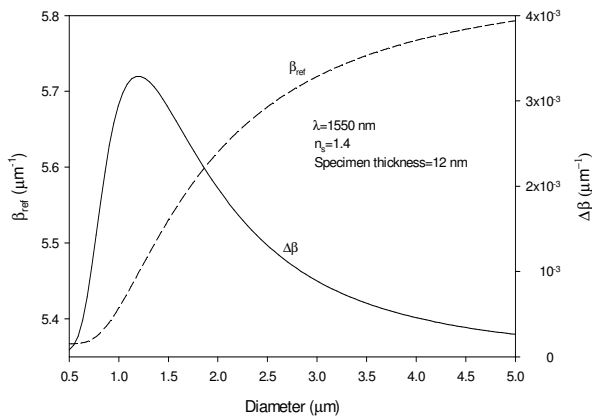


Figure 4 Propagation constant of the reference arm and propagation constant difference between the sensing and reference arms as a function of the fiber diameter. The detecting solution is acetonitrile.

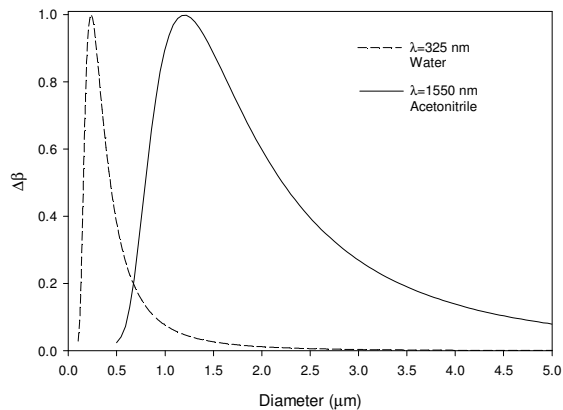


Figure 5 A comparison of the propagation constant difference for water as the detecting solution at an operating wavelength of 325 nm and acetonitrile as the detecting solution at an operating wavelength of 1550 nm. The specimen is assumed to have a thickness of 12 nm and index of refraction of 1.4.

In Fig. 6, the change in the propagation constant is

plotted as a function of wavelength in the infrared for a fiber diameter of 1.25 μm . As the operating wavelength is increased, the propagation constant difference decreases slowly yielding a slightly higher value at 1300 nm compared to 1550 nm. The variation of the propagation constant between the sensing and reference arms as a function of the specimen thickness has been shown in Fig. 7 at a wavelength of 1550 nm for different fiber diameters. The propagation constant difference is higher for a core diameter of 1 μm compared to smaller and larger core diameters of 800 nm and 1.25 μm , since as shown in Fig. 4 the propagation constant peaks at a wavelength of 1.23 μm . It is also seen that with an increase in the specimen thickness the propagation constant difference increases. This is because as the specimen thickness increases the index of refraction of the fiber cladding nears that of the silica core, resulting in a higher propagation constant for the sensing arm and higher propagation constant difference between the sensing and reference arms.

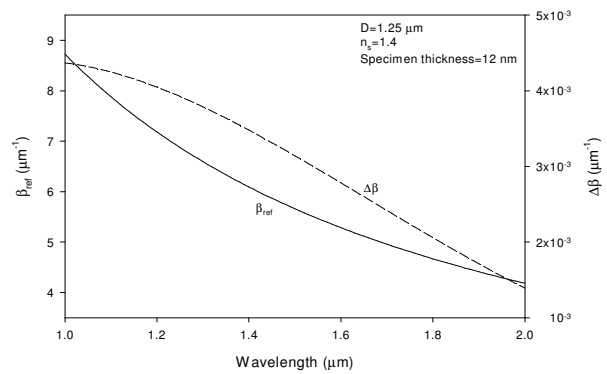


Figure 6 Propagation constant change as a function of wavelength in the infrared region of the spectrum.

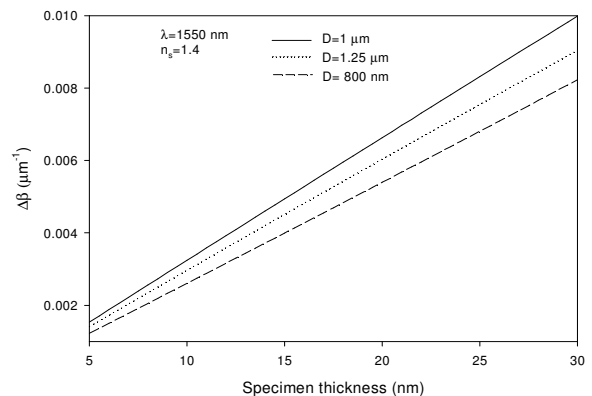


Figure 7 Change in the propagation constant as a function of the specimen thickness for different fiber diameters.

3. CONCLUSION

We showed that it is possible to use single-mode silica wires immersed in acetonitrile for optical sensing in the infrared spectral range. Because of high losses of water in this range, we proposed to use acetonitrile as the detecting solution. We showed that, by modifying the surface of the wire, it is possible to selectively collect and detect nanoparticles forming a layer around the sensing nanowire. At an operating wavelength of 1550 nm with acetonitrile as the detecting solution, wires with diameters of approximately 1.23 μm and length of 1 mm can be used for optical sensing. When water is used as the detecting solution at a wavelength of 325 nm, the wire must have a diameter of 240 nm and length of 68 μm , which is much more difficult to implement. The variation of the propagation constant with wavelength, nanowire diameter, specimen refractive index, and thickness of the specimen molecules coating the sensing wire were also studied.

REFERENCES

- [1] C. G. Poulton, M. A. Schmidt, G. J. Pearce, G. Kakarantzas, and P. St. J. Russell, "Numerical study of guided modes in arrays of metallic nanowires," *Opt. Lett.*, **32**, 1647 (2007).
- [2] L. Tong, L. Hu, J. Zhang, J. Qiu, Q. Yang, J. Lou, Y. Shen, J. He, and Z. Ye, "Photonic nanowires directly drawn from bulk glasses," *Opt. Express*, **12**, 82 (2006).
- [3] M. Law, D. J. Sirbuly, J. C. Johnson, J. Goldberger, R. J. Saykally, and P. D. Yang, "Nanoribbon waveguides for subwavelength photonics integration," *Science*, **305**, 1269 (2004).
- [4] C. J. Barrelet, A. B. Greytak, and C. M. Lieber, "Nanowire photonic circuit elements," *Nano Lett.*, **4**, 1981 (2004).
- [5] P. Debackere, S. Scheerlinck, P. Bienstman, and R. Baets, "Surface plasmon interferometer in silicon-on-insulator: Novel concept for an integrated biosensor," *Opt. Express*, **14**, 7063 (2006).
- [6] M. A. Foster, A. C. Turner, M. Lipson, and A. L. Gaeta, "Nonlinear optics in photonic nanowires," *Opt. Express*, **16**, 1300 (2008).
- [7] L. Tong, R. R. Gattass, J. B. Ashcom, S. He, J. Lou, M. Shen, I. Maxwell, and E. Mazur, "Subwavelength diameter silica wires for low-loss optical wave guiding," *Nature*, **426**, 816 (2003).
- [8] G. Brambilla, V. Finazzi, and D. J. Richardson, "Ultra-low-loss optical fiber nanotapers," *Opt. Express*, **12**, 2258 (2004).
- [9] S. G. Leon-Saval, T. A. Birks, W. J. Wadsworth, P. St. J. Russell, and M. W. Mason, "Supercontinuum generation in submicron fiber waveguides," *Opt. Express*, **12**, 2864 (2004).
- [10] J. Lou, L. Tong, and Z. Ye, "Modeling of silica nanowires for optical sensing," *Opt. Express*, **13**, 2135 (2005).
- [11] B. J. Luff, J. S. Wilkinson, J. Piehler, U. Hollenbach, J. Ingenhoff, and N. Fabricius, "Integrated optical Mach-Zehnder biosensor," *J. Lightw. Technol.*, **16**, 583 (1998).
- [12] J. Bertie, "Acetonitrile-water mixtures," *J. Phys. Chemistry*, **101**, 4111 (1997).
- [13] P. Klocek, *Handbook of Infrared Optical Materials*, Marcel Dekker, New York, 1991.
- [14] P. Schiebener, J. Straub, J. M. H. Levelt Sengers, and J. S. Gallagher, "Refractive index of water and steam as function of wavelength, temperature and density," *J. Phys. Chem. Ref. Data*, **19**, 677 (1990).
- [15] Rui Zhang, Jörn Teipel, Xinpeng Zhang, Dietmar Nau, and Harald Giessen, "Group velocity dispersion of tapered fibers immersed in different liquids," *Opt. Express*, **12**, 1700 (2004).
- [16] A. W. Snyder and J. D. Love, *Optical Waveguide Theory*, Chapman and Hall, New York, 1983.
- [17] C. Themistos, M. Rajarajan, B. M. Azizur Rahman, and Kenneth T. V. Grattan, "Characterization of silica nanowires for optical sensing," *J. Lightw. Technol.*, **27**, 5537 (2009).

SINGLE MODE ETCHED FIBER COUPLER FOR TEMPERATURE SENSING

Geeta Gupta, Ajay Kumar, Arun Mallik, Anuj Bhatnagar

Optoelectronics Division, Society for Applied Microwave Electronics Engineering and Research

(SAMEER), Hill Side, IIT Campus, Powai, Mumbai-400076

*E-mail: anuj@sameer.gov.in

Abstract: A pair of single mode optical fibers is twisted and their cladding is chemically etched to make fiber coupler. The fabricated etched fiber coupler tested at 1310 nm shows temperature dependent optical power splitting characteristics. A shift from 50:50 splitting at 50 °C to 80:20 at 135 °C is observed and reported for temperature sensing applications.

1. INTRODUCTION

Commercially available fiber optic couplers are fabricated using fiber fusion technique. The fused biconical tapered couplers are manufactured by twisting, fusing and elongating optical fibers at elevated temperatures [1]. The coupler specifications depend upon the type of fibers used, wavelength of operation, interaction length and gap between the cores of closely placed fibers. The nature of fiber mode field in the interaction region determines how strong or weak the evanescent field coupling is between the fibers. The fiber couplers used in telecommunication equipments are desired to be temperature insensitive over a wide temperature range.

We report the fabrication of single mode etched fiber coupler using wet etching technique and test results of our measurements.

2. COUPLER FABRICATION AND RESULTS

Two single mode optical fibers measuring 2 m each are taken and twisted in the 3 cm long central portion, as shown in fig. 1. The twisted fiber portion is without jacket. The four ends of fibers are fixed on a glass slide with uniform tension in each fiber.

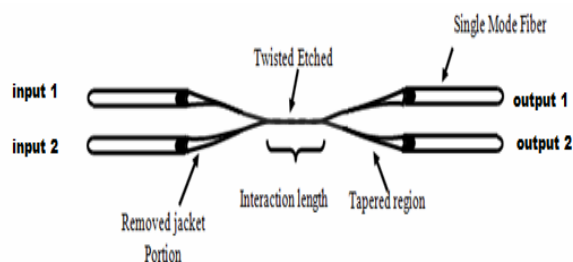


Fig 1: Twisted pair of single mode optical fibers

Twisted fibers over 1 cm region in the middle are exposed to 40% hydrofluoric acid to etch cladding, and bring their cores in close proximity to enable light coupling from one fiber to another. The diameter of etched fiber region is controlled by monitoring light transmitted through first fiber, which is connected to a source [2]. The etching process is stopped by gently pouring DI water and diluting the HF concentration,

followed by drying the region. The two output fiber ends are connected to optical power meter for coupling ratio measurement. The diameter of etched fiber varies between 10 to 12 μm in a working coupler device, measured using optical microscope as shown in fig. 2. Measured splitting ratio as a function of operating temperature is shown in fig. 3.



Fig 2: Fabricated etched fiber optic coupler

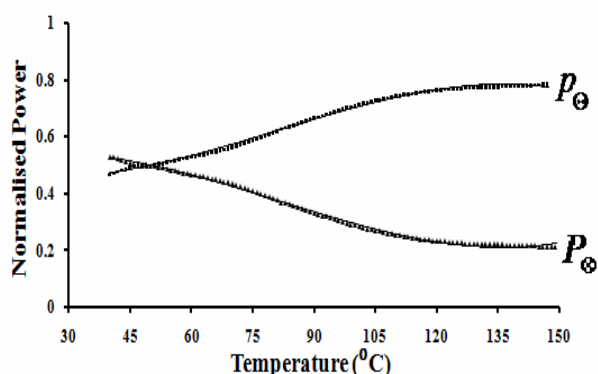


Fig 3: Measured normalised power distribution in output ports of coupler at varying temperatures

3. CONCLUSION

Optical measurements are performed on a coupler with $10.4 \pm 0.5 \mu\text{m}$ etched fiber diameter at 1310 nm. The splitting ratio is observed to vary from 50:50 at 50 °C to 80:20 at 135 °C, making the device temperature sensitive.

REFERENCES

- [1] B. P. Pal, "Fabrication and Modelling of Fused Biconical Tapered Fiber Couplers," *Fiber and integrated optics*, vol. 22, pp.97-117, 2003.
- [2] Ajay Kumar, Geeta Gupta, Arun Mallik, Anuj Bhatnagar, "Single mode optical fiber based refractive index sensor using etched cladding", *Journal of Instrument Society of India*, vol. 41, no. 2, pp. 80-83, 2011.

SELF-SENSING FIBRE REINFORCED COMPOSITES

L. Wang, D. Harris, ¹V.R. Machavaram, ¹A Tomlin, ²B.D. Gupta and ¹G.F. Fernando

¹School of Metallurgy and Materials, University of Birmingham, Edgbaston, Birmingham. UK.

²Department of Physics, IIT Delhi. India.

g.fernando@bham.ac.uk

Abstract: The focus of this paper is to demonstrate that conventional reinforcing glass fibres can be used as waveguides for sensing application. The first part of this paper will discuss the use of conventional E-glass fibres for monitoring cross-linking reactions. The second part of this paper describes the development of a technique to monitor the fracture of individual reinforcing fibres in real-time during mechanical loading.

1. INTRODUCTION

A wide range of optical fibre-based sensor systems are available to enable real-time chemical process monitoring and structural integrity assessment of advanced fibre reinforced composites [1-4]. However, the diameter of a conventional telecommunications optical fibre is 125 μm whereas that of the reinforcing glass fibre is 14 μm . In situations where the conventional optical fibre sensor is embedded in a composite, it can cause significant waviness in the reinforcing fibres. This in turn can have an adverse effect on specified properties of the composite. Therefore, the deployment of the reinforcing fibres as sensors has significant advantages.

2. MATERIALS

The resin system used was EpoTek 310M (Promatech, UK). The reinforcing fibres used were conventional E-glass (PPG Industries, UK) and custom-made small diameter (17 μm) optical fibres (SDOF).

3. EXPERIMENTAL

SMA connectors were attached to 8 cm length of a bundle of the E-glass fibres. In the case of the SDOF bundle, the length of the specimen was 20 cm. An external white-light source was used to illuminate the fibre bundle. With reference to the experiments where the cross-linking was monitored using the fibre bundles, the interrogation was carried out using a fibre-coupled FTIR spectrometer. Damage detection using the reinforcing fibres was demonstrated by end-tapping the fibre bundle and mechanically loading it in tension. One end of the SMA connector was illuminated with a white-light source and the other end was connected to a high-speed camera. This enabled the fracture of individual E-glass and SDOF to be monitored in real-time.

4. RESULTS AND DISCUSSION

Figure 1 clearly shows that evanescent wave spectroscopy can be used to study cross-linking kinetics on the surface of E-glass fibres. Figure 2 shows a series of images that were obtained during

the tensile loading of SDOF composite where the fracture of the individual fibres can be seen. Thus, it is now possible to study the influence of surface treatments and processing conditions on the cross-linking kinetics, and mechanical properties of advanced fibre reinforced composites.

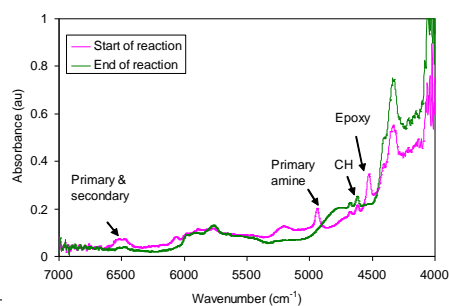


Figure 1. Typical FTIR spectra of EpoTek 310M obtained using evanescent wave spectroscopy during cross-linking at 65 °C for 200 minutes.

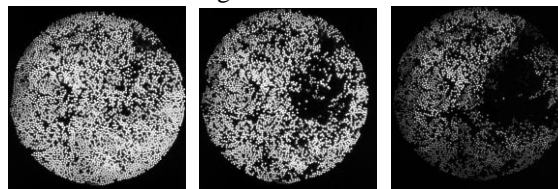


Figure 2 Images showing the fracture of the individual glass fibres during tensile testing of SDOF composite. A high-speed CCD camera was used to capture the images.

ACKNOWLEDGEMENT

The authors wish to acknowledge the financial support provided by EPSRC and TSB (TS/G000387/1, BD072K, AB135A) and the Royal Society.

REFERENCES

- [1] G. Kister *et al.* *Engineering Structures* 29 (3): 440-448, (2007).
- [2] C. Chen *et al.* *J Measurement Science and Technology*, 17 (8): 2313-2318, (2006).
- [3] G. F. Fernando *et al.* *J of Measurement Science and Technology*, 8, 1065-1079, (1997).
- [4] B. Degamber and G. F. Fernando, *IEEE Sensors Journal*, Vol 4, No 6, pp 713-721, (2004).

REAL TIME INTERACTION ANALYSIS OF IMMOBILIZED BIOMOLECULES OVER SU8 POLYMER WAVEGUIDE

Indrajit Boiragi, Roshan Makkar, Alok Verma, K. Chalapathi

Optoelectronics Division, Society for Applied Microwave Electronics Engineering and Research (SAMEER), Mumbai, India-400076. Email:indrajitboiragi@gmail.com

ABSTRACT: This work reports the real time analysis antibody/antigen interaction that immobilized over the surface of Mach-Zehnder Interferometer (MZI) sensor chip. The SU8, a photo conducting polymer is used as a core and cladding material for fabricating the single mode Mach-Zehnder Interferometer sensor chip. Figure-1 shows the basic layout configuration of the Mach-Zehnder Interferometer, the input light energy that propagates due to total internal reflection splits in two parts, one part through so called reference arm (R) and the other with a sensing window called the sensing arm (S). The intensity of the produced output light using a combiner, is highly sensitive to the phase difference of the light propagating through the interferometric arms. The phase difference can be very easily manipulated by applying an external constrain, usually an analyte for biosensor and it should selectively interact with the immobilized biomolecules, at the sensing arm of the chip.

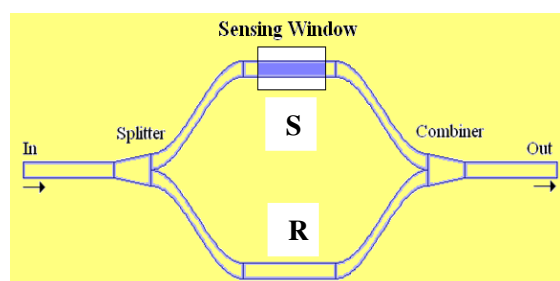


Figure 1 Basic layout structure of Mach-Zehnder Interferometer sensor chip.

The SU8 waveguide surface is modified through a chemical process. The schematic diagram of the bio-immobilized surface of the SU8 waveguide is shown in Figure-2. To ensure the specific recognition of the analyte, corresponding bioreceptors (or ligands) are covalently immobilized over the sensor surface.

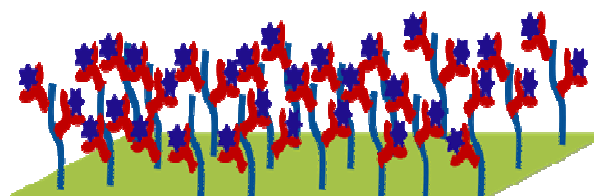


Figure 2 The schematic diagram of the bio-immobilized surface of the SU8 waveguide.

The symbol similar to “S” represents the population of the generated functional groups on SU8 surface on which the receptor antibodies, represented by “Y” symbol, are immobilized. As we allow to flow the analyte sample (represented by “star” symbol in fig-2) to the sensing window, due to the specific interaction between the receptor/analyte there is a change in output power of the waveguide. The absorption spectrum at 490nm of wavelength is shown in fig-3, the part-A is representing the stable baseline before interaction and part-B shows the continuous absorption of light due to the binding of the biomolecules over the sensor surface. The whole process is observed in real time using a spectrometer (Ocean optics), the total absorption ΔA gives the corresponding concentration of the measurands after adding buffer solution that removes the unspecifically bonded biomolecules.

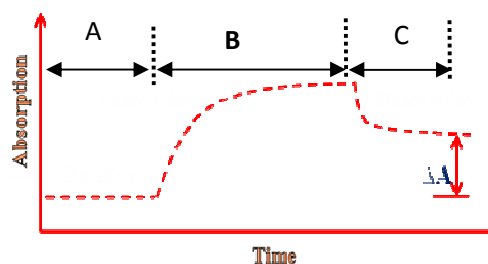


Figure 3 Optical response of SU8 MZI sensor chip with time when one branch comes to the contact of anti-IgG solution.

LONG RANGE SURFACE PLASMON RESONANCE SENSOR USING SILICON AND GRAPHENE: SENSITIVITY ENHANCEMENT

Roli Verma and B.D.Gupta*

Physics Department, Indian Institute of Technology Delhi, New Delhi – 110016, India

*bdgupta@physics.iitd.ernet.in

Abstract: Long range surface plasmon resonance (LRSPR) based prism sensor using magnesium fluoride, silicon and graphene have been numerically analyzed. It is shown the sensor based on LRSPR has better sensitivity than surface plasmon resonance (SPR) sensor.

1. INTRODUCTION

Surface plasmons (SPs) are the charge density oscillations, excite by p-polarized light at metal dielectric interface at resonance condition when the wave vector of incident light matches with that of SPs, this is called SPR. To excite Sps, Kretschmann configuration along with attenuated total reflection (ATR) spectroscopy is used. Apart from conventional SPR, there is another scheme in which thin metallic film embedded between two identical dielectrics, known as LRSPR [1]. LRSPR has many advantages over conventional SPR as long surface propagation length, high electric field strength and high sensitivity. In this study, we are giving high sensitivity LRSPR sensor, having an approach of biosensor.

2. THEORY

For simulations we have taken a high index SF10 prism whose base is coated with magnesium fluoride (MgF_2), gold (Au), silicon (Si) and graphene (GRP) for LRSPR sensing. MgF_2 film is absent for SPR sensing and sensing media are kept around GRP in both the sensing. The dispersion relations of all the films have been considered. Polychromatic light is launched at an angle at one face of prism and reflected light from the other face is collected by a spectrometer. We consider planer waveguide approach with N-layer modal for simulations, which have been discussed in previous studies [2]. Thicknesses of MgF_2 -300 nm, Au-50 nm and Si-5 nm were taken for simulations. The sensitivity have been calculated with the formula given as

$$S = \left(\frac{\Delta\lambda_{res}}{\Delta n} \right)$$

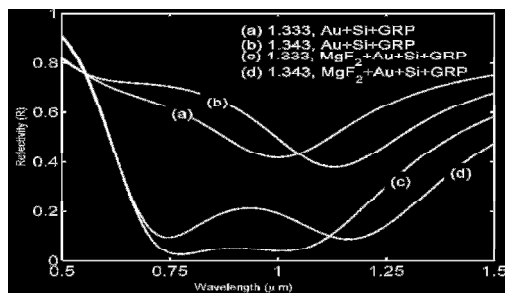


Figure 1. SPR and LRSPR spectra

3. RESULTS AND DISCUSSIONS

Figure 1 shows SPR and LRSPR spectra for earlier described sensing schemes with 7 number of GRP layer, for two refractive indices profile 1.333 RIU and 1.343 RIU. We have found larger shift in resonance wavelength (λ_{res}) in LRSPR than SPR. Moreover, the complete transfer of energy to SPs does not take place for conventional SPR. We plotted for 7 GRP layers because it gives the maximum sensitivity. We do not find narrow SPR curves for higher number of GRP layers. Figure 2 shows the shift in (λ_{res}) with number of GRP layers. It is observed that the higher shift in (λ_{res}) takes place for LRSPR curve than SPR curve with increasing number of graphene layer. The sensitivity has been calculated 2.73 μm /RIU and 6.13 μm /RIU for SPR and LRSPR respectively. We find the sensitivity more than twice for LRSPR than SPR.

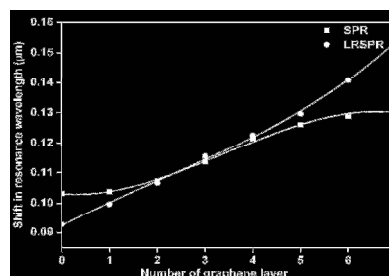


Figure2. Shift in (λ_{res}) for SPR and LRSPR

4. CONCLUSIONS

We have numerically simulated LRSPR based prism sensors and find enhanced sensitivity than SPR based prism sensor.

ACKNOWLEDGEMENT

Roli Verma is thankful to the CSIR for research fellowships. The present work was partially supported by the DST, India.

REFERENCES

- [1] A. W. Wark, H. J. Lee, R. M. Corn, Long Range Surface Plasmon Resonance Imaging for Bioaffinity Sensor, *Anal. Chem.*, **77**, 3904-3907 (2005).
- [2] R. K. Verma, B. D. Gupta, Surface Plasmon Resonance Based Fiber Optic Sensor for the IR Region Using a Conducting Metal Oxide Film, *J. Opt. Soc. Am. A.*, **27**, 846-851 (2010).

COMPARISON OF SENSITIVITIES OF SPR BASED FIBER OPTIC SENSOR USING DIFFERENT HIGH INDEX DIELECTRIC LAYERS

Priya Bhatia and B.D. Gupta

Department of Physics, Indian Institute of Technology Delhi, New Delhi-110016 (India)

priya.iitons@gmail.com, bdgupta@physics.iitd.ernet.in

Abstract: Theoretical analysis of surface plasmon resonance (SPR) based fiber optic sensor using different high index dielectric layers is proposed. The simulation predicts increase in the sensitivity of the sensor with the increase in the refractive index and the thickness of the dielectric layer. Further, comparison of collimated and diffused source for launching of light in the fiber has also been done and it shows that the use of collimated source-microscope objective combination is better than diffuse source for the performance of the sensor. However the use of diffuse source which launches mostly skew rays can be advantageous if the miniaturization and cost are the requirements. Apart from sensitivity enhancement, the additional dielectric layer also protects the metal layer from oxidation.

1. INTRODUCTION

In recent years, surface plasmon resonance technique has been popularly used in optical fiber sensors. Surface plasmons are TM polarized electromagnetic waves created as a result of coherent oscillations of charges at metal/dielectric interface. Light causes the excitation of charge density oscillations along the metal-dielectric interface [1]. In general, Kretschmann configuration is used to excite surface plasmons using evanescent field of p-polarized light [2]. In Kretschmann configuration, a thin metallic layer of either of silver or gold is deposited on the base of a coupling prism. The dielectric whose properties are to be determined is kept in contact with the metal layer. The p-polarized light with varying angle of incidence is incident on the interface of the prism base and the metal film. To know the resonance angle, the intensity of the reflected light through the prism is measured for different angles of incidence. The resonance angle depends on the refractive index of the dielectric. The prism based SPR sensing device has a number of shortcomings. First and foremost is that it cannot be used for remote sensing. It is bulky in size and since it utilizes angular interrogation method for sensing, the apparatus contains various optical and mechanical (moving) parts. These shortcomings can be removed by replacing the prism by an optical fiber [3, 4]. The additional advantage of optical fiber is that it requires minute sample for sensing because of small surface area of the probe.

In this study we have analyzed the design of a fiber optic SPR sensor in conjunction with a high index dielectric layer over the metal layer using Kretschmann configuration and wavelength interrogation method. Silver is used for metal layer while three different dielectric materials have been

considered for this additional layer. The dielectrics are silicon (Si), cuprite (Cu_2O) and zirconia (ZrO_2). The performance of the sensor is evaluated in terms of sensitivity and is compared for all the three dielectrics. The simulation is carried out for two kinds of sources. One launches only meridional rays in the fiber while the other (diffuse source) generates both meridional and skew rays. Maximum sensitivity has been obtained in the case of Si and the minimum in the case of ZrO_2 for both kinds of sources. Further, the sensor utilizing diffuse source possesses smaller sensitivity.

2. THEORETICAL ANALYSIS

The schematic diagram of the optical fiber SPR probe to be analyzed is shown in Figure 1. The probe is a four layer system consisting of fiber core, silver layer, high index dielectric layer and the sensing medium. Light from a polychromatic source is launched in the fiber.

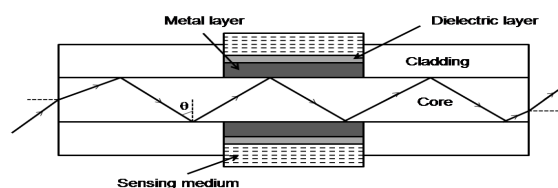


Fig.1. Proposed fiber optic SPR probe

To know the resonance wavelength corresponding to the refractive index of the sensing medium the spectrum of the transmitted light is determined at the other end of the fiber. Since the wavelength interrogation method is used for the analysis we require wavelength dependence of the refractive indices of various layers. For the silica core of the plastic clad silica fiber, the wavelength dependence

of the refractive index is given by the following Sellmeier relation

$$n_1(\lambda) = \sqrt{1 + \frac{a_1 \lambda^2}{\lambda^2 - b_1^2} + \frac{a_2 \lambda^2}{\lambda^2 - b_2^2} + \frac{a_3 \lambda^2}{\lambda^2 - b_3^2}} \quad (1)$$

where λ is the wavelength in μm and a_1, a_2, a_3, b_1, b_2 and b_3 are Sellmeier coefficients. The values of these coefficients are $a_1 = 0.6961663, a_2 = 0.4079426, a_3 = 0.8974794, b_1 = 0.0684043, b_2 = 0.1162414$ and $b_3 = 9.896161$ [5]. Drude formula is used for the wavelength dependence of the dielectric constant of the metal and can be written as

$$\varepsilon_m(\lambda) = \varepsilon_{mr} + i\varepsilon_{mi} = 1 - \frac{\lambda^2 \lambda_c}{\lambda_p^2 (\lambda_c + i\lambda)} \quad (2)$$

In this expression, λ_p and λ_c are the plasma and collision wavelengths of the metal respectively while ε_{mr} and ε_{mi} are the real and imaginary parts of the dielectric constant of metal layer ε_m . In this study we have used silver for the metal layer. For silver, the values of plasma and collision wavelength are: $\lambda_p = 1.4541 \times 10^{-7}$ m and $\lambda_c = 1.7614 \times 10^{-5}$ m [6]. The wavelength dependence of the refractive index of ZrO_2 was taken from reference [7] while for Cu_2O and Si these values were from references [8].

Collimated source – microscope objective combination:

In this case the collimated beam is focused on the face of the fiber at the axial point of the fiber axis. Assuming the propagation of only meridional rays inside the fiber, the power dP arriving at the axial point of the fiber between angles θ and $\theta+d\theta$ is given by

$$dP \propto \frac{n_1^2 \sin \theta \cos \theta}{(1 - n_1^2 \cos^2 \theta)^2} d\theta$$

where θ is the angle of the ray with normal to the core-cladding interface and n_1 is refractive index of the fiber core as given by Eq. (1). For SPR based fiber optic sensors utilizing this kind of light launching, the power transmitted through the fiber is given by

$$P_{trans} = \frac{\int_{\theta_{cr}}^{\pi/2} R_p^{N_{ref}} \frac{n_1^2 \sin \theta \cos \theta}{(1 - n_1^2 \cos^2 \theta)^2} d\theta}{\int_{\theta_{cr}}^{\pi/2} \frac{n_1^2 \sin \theta \cos \theta}{(1 - n_1^2 \cos^2 \theta)^2} d\theta} \quad (3)$$

where R_p is the net reflection coefficient of the ray incident at the core-metal interface, $\theta_{cr} = \sin^{-1}(n_2/n_1)$ is the critical angle of the fiber, n_2 is the refractive index of fiber cladding, and $N_{ref}(\theta)$ is the number of reflections the ray of angle θ undergoes inside the fiber and is given by

$$N_{ref}(\theta) = \frac{L}{D \tan \theta}$$

where L is the length of the sensing region and D is the diameter of fiber core.

Diffuse source:

In the case of diffuse source the power distribution inside the fiber is given as

$$dP \propto n_1^2 \sin \theta \cos \theta d\theta$$

when light is launched using diffuse source both meridional and skew rays exist inside the fiber. The power transmitted through the fiber is given by

$$P_{trans} = \frac{\int_0^{\pi/2} d\alpha \int_{\theta_{cr}}^{\pi/2} R_p^{N_{ref}(\theta, \alpha)} n_1^2 \sin \theta \cos \theta d\theta}{\int_0^{\pi/2} d\alpha \int_{\theta_{cr}}^{\pi/2} n_1^2 \sin \theta \cos \theta d\theta} \quad (4)$$

where α is the skewness angle of the ray and $N_{ref}(\theta, \alpha)$ is the number of reflections for the guided ray with angles (θ, α) and is given by

$$N_{ref}(\theta, \alpha) = \frac{L}{D \tan \theta \cos \alpha}$$

The reflection coefficient for p-polarized light in Eqs. (3) and (4) is determined as given in our previous studies [9]. A curve between the transmitted output power and the wavelength is plotted. The resonance wavelength corresponding to a given refractive index of the sensing medium is determined from this plot. If the refractive index of the sensing medium is altered by δn_s and the corresponding shift in resonance wavelength is $\delta \lambda_{res}$ then the sensitivity of the sensor is $S_n = \delta \lambda_{res} / \delta n_s$. Sensitivity is determined from the slope of the plot of resonance wavelength with refractive index of the sensing medium.

3. RESULTS AND DISCUSSION

To study the effect of additional dielectric layer on the sensitivity of the SPR based fiber optic sensor following values of the parameters have been used for the analysis: NA of the fiber = 0.24, $D = 600 \mu\text{m}$, silver layer thickness = $0.04 \mu\text{m}$ and $L = 1\text{cm}$. The spectrum of the transmitted power is determined for a given value of the refractive index of the sensing medium and thickness of the dielectric layer using Eq. (3). The spectrum determined shows a dip at a particular value of the wavelength called resonance wavelength. The resonance wavelength so obtained depends on the refractive index of the sensing medium in contact of the dielectric layer and on the thickness of the dielectric layer. Figure 2 shows the variation of sensitivity of the sensor with the

thickness of the three dielectric layers for $n_s = 1.333$ and $\delta n_s = 0.01$ in case of collimated source-microscope objective combination. Also in figure 3

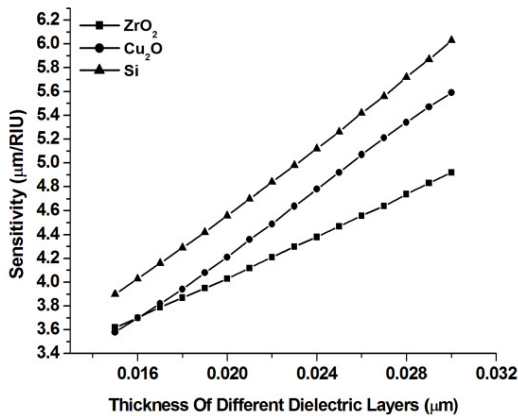


Fig.2. Variation of sensitivity with the thickness of three dielectrics for collimated source

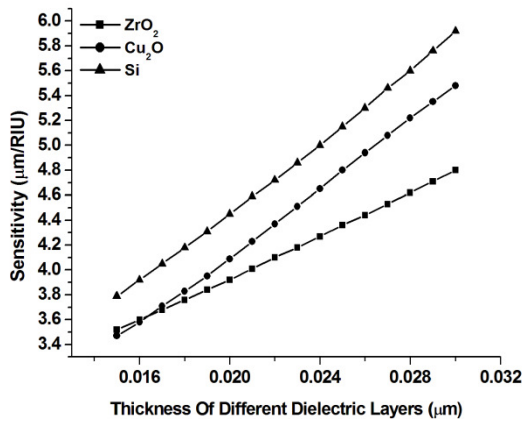


Fig.3. Variation of sensitivity with the thickness of three dielectrics for diffuse source

we have plotted the same curve for diffuse source illumination using Eq. (4). In both the cases, as the thickness of the dielectric layer increases the sensitivity increases. The sensitivity of the SPR sensor is more in the case of collimated source-microscope objective combination than in the case of diffuse source. The difference in the sensitivity in the two kinds of light launching will decrease if we also consider skew rays in the analysis of collimated source-microscope objective combination instead of all meridional rays which corresponds to an ideal case. Since the skew rays follow helical path inside the fiber core the difference in sensitivity appears to be mainly due to large number of reflections of skew rays at the core-cladding interface. The increase in sensitivity for dielectric layer of thickness $0.025 \mu\text{m}$ is about 2.0 times of the probe without dielectric layer (or silver only). The sensitivity, for a given thickness of the dielectric, is highest in the case of Si while it is lowest in the case of ZrO_2 . It appears that the sensitivity increases as the refractive index of the

dielectric layer increases. Out of all the three dielectrics chosen, silicon (Si) has the maximum refractive index. Increase in the refractive index of the dielectric increases the electric field at the dielectric-sensing medium interface and hence increases the sensitivity [10]. However, it has been found that increasing the refractive index of the additional dielectric layer increases the broadening of the SPR curve which is a disadvantage. Thus one cannot go on increasing the refractive index of the dielectric layer.

Figure 4 shows the variation of the sensitivity with the refractive index of the sensing medium for the three dielectrics in case of collimated source while figure 5 shows the variation of sensitivity with the refractive index of the sensing layer in the case of diffuse source illumination. The values of the parameters are the same except that the thickness of the dielectric layer is $0.025 \mu\text{m}$.

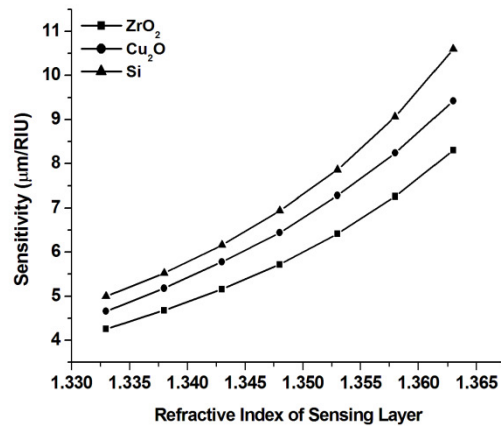


Fig.4. Variation of sensitivity with the R I of the sensing medium for the three dielectrics in case of collimated source

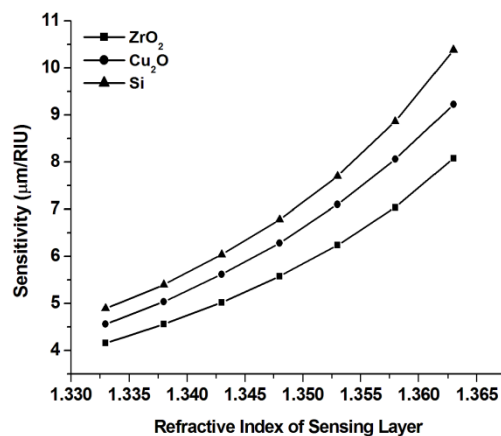


Fig.5. Variation of sensitivity with the R I of the sensing medium for the three dielectrics in case of diffuse source

It may be noted that the sensitivity increases as the refractive index increases for all the three dielectrics irrespective of the kind of source used. For a fixed refractive index of the sensing medium sensitivity is

highest for silicon and lowest for ZrO_2 in case of both the sources. Although the sensitivity is low with diffuse source, its advantage is that if one uses white LED as a source then the device can be miniaturised and will be cost effective.

plasmon resonance sensors”, *Optics Letters* 33, 2539 (2008).

4. CONCLUSION

We have analysed a SPR based fiber optic sensor by incorporating an additional dielectric layer between metal and sensing medium using wavelength interrogation method. The simulation predicts an increase in sensitivity of the sensor with the increase in the refractive index of the dielectric layer. The additional advantages of dielectric layer, in addition to the increase in sensitivity, are the protection of metal layer from oxidation and the tuning of wavelength range of operation of the sensor.

ACKNOWLEDGEMENTS

The present work is partially supported by the Department of Science and Technology (India). Priya Bhatia would like to thank CSIR (India) for providing Research Fellowships.

REFERENCES

- [1]. J. Homola, S. S. Yee, and G. Gauglitz, “Surface plasmon resonance sensors review”, *Sens. Actuators B* 54, 3 (1999).
- [2]. E. Kretschmann, “Radioactive decay of non-radiative surface plasmons excited by light”, *Z. Naturforsch. A* 23, 2135 (1968).
- [3]. R.C. Jorgenson and S.S. Yee, “A fiber-optic chemical sensor based on surface plasmon resonance”, *Sens Actuators B* 12, 213 (1993).
- [4]. Rajan, S. Chand, and B.D. Gupta, “Fabrication and characterization of a surface plasmon resonance based fiber-optic sensor for bittering component – naringin”, *Sens Actuators B* 115, 344 (2006).
- [5]. A.K. Ghatak and K. Thyagarajan, “Introduction to fiber optics”, *Cambridge University Press*, 1999.
- [6]. J. Homola, “On the sensitivity of surface plasmon resonance sensor with spectral interrogation”. *Sens Actuators B* 41, 207 (1997).
- [7]. D.L. Wood and K. Nassau, “Refractive index of cubic zirconia stabilized with yttria”, *Applied Optics* 21, 2978 (1982).
- [8]. SOPRA N&K Database, www.refractiveindex.info.
- [9]. A.K. Sharma, Rajan and B.D. Gupta, “Influence of dopants on the performance of a fiber optic surface plasmon resonance sensor”, *Optic Communications* 274, 320 (2007).
- [10]. A. Lahav, M. Auslender, and I. Abdulhalim, “Sensitivity enhancement of guided wave surface

Surface Plasmon Resonance based Fiber Optic Refractive Index Sensor utilizing Cu / TiO₂ layer

Sarika Singh, Satyendra K.Mishra and B.D. Gupta*

Physics Department, Indian Institute of Technology Delhi, New Delhi – 110016, India

*bdgupta@physics.iitd.ernet.in

Abstract: Modeling of a miniaturized fiber optic sensor based on surface plasmon resonance (SPR) utilizing a Cu/TiO₂ layer is presented. Attenuated total internal reflection with Kretschmann configuration is the basis of the theoretical model. The performance of the sensor is evaluated in terms of sensitivity and detection accuracy.

1. INTRODUCTION

For the last few decades the utilization of surface plasmons which are the collective oscillations of free electrons at metal-dielectric interface for sensing has been a topic of intense research. Several experimental and theoretical studies have been carried out for improving the performance of the SPR based fiber optic sensors. In this paper we have theoretically analyzed the performance of the SPR based fiber optic sensor in terms of sensitivity and detection accuracy for the Cu/TiO₂ multilayer. The results have been compared with the optimized thickness of gold and copper layer results.

2. THEORETICAL MODELING

In a SPR based fiber optic sensor, cladding is removed from a small portion of the fiber and the unclad core is coated with a thin layer of Cu metal in addition to a small thickness of dielectric layer because Cu can be easily oxidized on the surface. Here, TiO₂ act as a capping layer for reducing the oxidation of metal [1]. The sensing sample is placed in contact with the TiO₂ layer. The transmitted power through the fiber is given by

$$P_{trans} = \frac{\int_{\theta_{cr}}^{\pi/2} R_p^{N_{ref}} \frac{n_1^2 \sin \theta \cos \theta d\theta}{(1 - n_1^2 \cos^2 \theta)^2} d\theta}{\int_{\theta_{cr}}^{\pi/2} \frac{n_1^2 \sin \theta \cos \theta d\theta}{(1 - n_1^2 \cos^2 \theta)^2} d\theta} \quad (1)$$

R_p is the reflection coefficient, N_{ref} is the number of reflections a ray undergoes with the core-cladding interface in the sensing region, θ_{cr} is the critical angle of the fiber and n_1 and is the refractive index of the fiber core [2].

3. RESULTS AND DISCUSSION

Figures 1(a) and (b) show the variation of sensitivity and detection accuracy with the refractive index of the sensing medium for Cu/TiO₂ multilayer and gold layer. It may be noted that the sensitivity of Cu/TiO₂ layer is larger than the Cu and Au layer for optimized thicknesses. For a given refractive index, the detection accuracy is also higher for Cu/TiO₂ layer. Generally gold or silver are used and hence use of

copper in place of these reduces the cost of the probe.

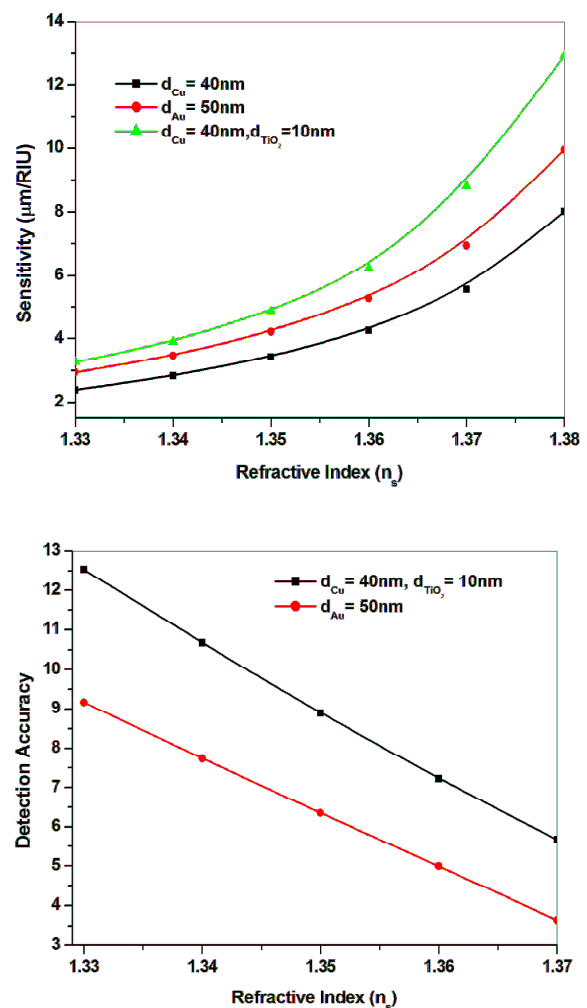


Figure 1: (a) Sensitivity and (b) detection accuracy.

REFERENCES

- [1] D. Vore "Refractive indices of rutile and sphalerite" *Journal of Optical Society of America*, 41, 416-417 (1951).
- [2] A.K. Sharma and B.D. Gupta, "On the performance of different bimetallic combinations in surface plasmon resonance based fiber optic sensors," *Journal of Applied Physics*, 101, 093111 (2007)

POLARIZATION STRUCTURING OF NON-DIFFRACTING VORTEX BEAMS

Geo M. Philip[†] and Nirmal K. Viswanathan^{*}

Beam Optics and Applications Group

School of Physics, University of Hyderabad, Hyderabad – 500046, India

Email: geo.m.philip@gmail.com[†], nirmalsp@uohyd.ernet.in^{*}

Abstract: By focusing elliptically polarized vortex beam, generated using a two-mode optical fiber using an axicon lens we demonstrate polarization structuring of the transverse intensity pattern to realize J_0 , J_1 and spiral intensity types of non-diffracting beams. We also obtain co-axial 0th- and 1st- order Bessel beams by selecting the right or left elliptic part using a quarter-wave plate and polarizer combination.

1. INTRODUCTION

Diffraction affects all finite electromagnetic fields and leads to changes in spatial intensity and phase profiles of the beam during free-space propagation. However, if the field is infinite in extent, ideal plane wave for example, it may not be the case and the beam can be propagation invariant or non-diffracting. Propagation invariant scalar fields have been studied extensively, both theoretically and experimentally since they were proposed by Durnin *et al* [1]. Although there were considerable theoretical studies on propagation invariant vector fields [2, 3] the experimental studies were limited. Different experimental techniques were developed for the generation of propagation invariant vector beams which include interferometric method [4] and computer generated sub-wavelength gratings [5]. These propagation invariant vector beams find wide application in super-resolution microscopy [6] laser focusing and acceleration of electrons [7] and optical tweezers [8]. Polarization structuring of vectorial optical beams was reported recently [9] and the conversion from bright to dark center for non-diffracting beams was also studied [10].

It is known that higher order Bessel beams can be generated by focusing Laguerre-Gaussian (LG) beam using an axicon [11]. Focusing vectorial LG beam using an axicon even in the paraxial limit can result in the generation and inter-convertibility of the different types of Bessel beams. We generate elliptically-polarized LG_{01} beam using a two-mode optical fiber (TMF) and focus this beam using an axicon for the generation of vectorial non-diffracting beams. In our case the input beam to the axicon has polarization singularities [12]: a C -point surrounded by circular s -line (where the polarization is linear) which allows the switchability between J_0 , J_1 Bessel

beams and a spiral intensity pattern by properly orienting the output polarizer. It is also possible to generate co-axial J_0 and J_1 Bessel beams by selecting the right circular part and left circular part using a quarter-wave plate and polarizer combination. These hollow and bright Bessel and spiral non-diffracting beams may find extensive application in STED microscopy [6] and next generation optical tweezers.

2. EXPERIMENTAL DETAILS

Figure 1 shows the schematic of the experimental setup used for polarization structuring of non-diffracting vortex beams. Partially polarized He-Ne laser beam ($\lambda=632.8\text{nm}$) is passed through a polarizer P1 and quarter-wave plate QWP1 to get circularly polarized beam for the fiber input. The circularly polarized Gaussian beam is launched at an angle into the horizontally held 42.8 cm long two mode optical fiber using microscope objective lens L1

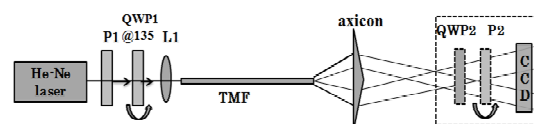


Fig. 1 Schematic of the experimental setup (40x, 0.65NA). The skew launching is adjusted such that the output from the fiber is an elliptically polarized vortex beam. The null intensity in the beam rotates with the analyzer rotation due to simultaneous propagation of left circular polarized fundamental mode and right circular polarized vortex mode [12]. The output from the fiber is then collimated and imaged using a CCD camera connected to a computer through IEEE-1394 interface card. A two beam interferometer is constructed in parallel (not shown in Fig. 1) to identify the presence of phase dislocation at the core region of the beam via the appearance of forklet interference pattern. The Stokes parameter of the beam is measured using a quarter-wave plate

QWP2 and polarizer P2 combination at each pixel of the image. After characterizing the output elliptically polarized vortex beam is allowed to pass through an axicon of open angle $\gamma=5^\circ$. The apex angle position of the axicon is adjusted with respect to the core of the vortex beam to generate different types of non-diffracting beams (J_0 , J_1 and spiral). The vortex and polarization structure of these propagation invariant beams is studied using Stokes parameter measurements. Rotating the analyzer kept at the output in any one of the beams (J_0 , J_1 or spiral) generated by the fiber-axicon combination gives the other two beams for specific analyzer positions. The output from the fiber which is a superposition of left circularly polarized fundamental mode also and right circularly polarized vortex mode allows the switching between the J_0 and J_1 Bessel beams using QWP2 and P2 combination.

3. RESULTS AND DISCUSSION

Partially polarized light from the He-Ne laser ($\lambda=632.8\text{nm}$) after passing through oriented polarizer (at 0°) and QWP (at 45°) is launched at an angle into the TMF of length 42.8cm. The launching is adjusted so that the output is a elliptically polarized vortex beam. The output from the fiber is then collimated using a microscope objective lens (20x, 0.40NA) and imaged using a CCD camera. The polarization state of the output beam is characterized by the four Stokes parameters (S_0 , S_1 , S_2 , and S_3) defined as follows [11].

$$\begin{aligned} S_0 &= E_{0x}^2 + E_{0y}^2 = I(0, 0) + I(90, 0) \\ S_1 &= E_{0x}^2 - E_{0y}^2 = I(0, 0) - I(90, 0) \\ S_2 &= 2E_{0x}E_{0y} \cos(\delta) = I(45, 0) - I(135, 0) \\ S_3 &= 2E_{0x}E_{0y} \sin(\delta) = I(45, \pi/2) - I(135, \pi/2) \end{aligned} \quad (1)$$

These parameters can easily be calculated from six intensity measurements as given in (1), where $I(\theta, \phi)$ is the intensity passed by polarizer aligned at an angle θ to the positive x axis and ϕ is the phase introduced to the y component before passing through the polarizer using a QWP [13]. The polarization ellipse parameters at each pixel point of the beam is calculated from the Stokes parameters and plotted overlapping the beam. When two orthogonally polarized optical fields superimpose two types of

polarization singularities are formed: C-point where the field is circular and the orientation of the polarization ellipse major axis is undefined and s-line where the field is linear and the handedness of the polarization ellipse is undefined [12,14]. Figure 2 gives the direct output beam from the fiber, the polarization map of the beam and the c-point s-line contour generated from Stokes parameters [14]. In the polarization map red colour indicates left circular rotation and green colour corresponds to right circular rotation.

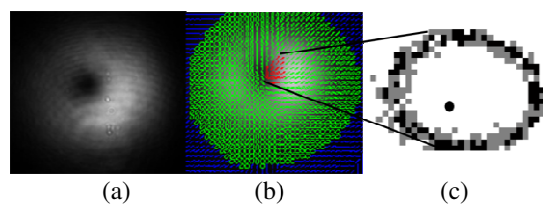


Figure.2 (a) Direct fiber output; (b) polarization map; (c) C-point and s contour (dot denotes C-point and the closed curve around it is s-contour)

This beam (without collimation) is the input to the axicon. Since the intensity of the fundamental mode is very less, the mathematical treatment can be approximated to that of a Laguerre-Gaussian (LG_{01}) beam. The electric field amplitude of an LG_{pl} beam can be represented by

$$\begin{aligned} E(r, \phi, 0) &= A(2r^2/\omega_0^2)^{\frac{|l|}{2}} L_p^{|l|}(2r^2/\omega_0^2) \\ &\times \exp(-r^2/\omega_0^2) \exp(il\phi) \end{aligned} \quad (2)$$

Where, L_{lp} is generalized Laguerre polynomial and ω_0 is the waist size of the beam. The modes are characterized by two indices. The radial mode index p is related to the number of concentric rings, in the intensity cross-section and the azimuthal mode index l describes the charge of the phase singularity. If a single ringed LG mode with azimuthal mode index l is used to illuminate the axicon an approximation to the Bessel beam of order l is generated [11]. In our case the axicon with open angle $\gamma=5^\circ$ is illuminated by the elliptically polarized LG_{01} beam output from the fiber then, the intensity in the transverse plane behind the axicon can be written as

$$I(r, z) \propto z^{2+1} \exp(2z^2/z_{max}^2) J_1^2(k_r r) \quad (3)$$

Where, $k_r \approx k(n-1)\gamma$ is the radial wave vector, γ small angle of the axicon and $z_{max} = \omega_0 k/k_r$ is the diffraction free propagation distance [15].

For obtaining J_1 Bessel beam the apex of the axicon is adjusted to be coincident with the vortex core of the LG_{01} beam. The J_1 Bessel beam generated is also characterized using two-beam interferometer and Stokes parameter, and the polarization maps are plotted. Figure 3 gives the CCD image of the J_1 beam, two beam interference pattern and the polarization map of the J_1 beam obtained using the axicon and the line intensity profile with the theoretical J_1 Bessel fit.

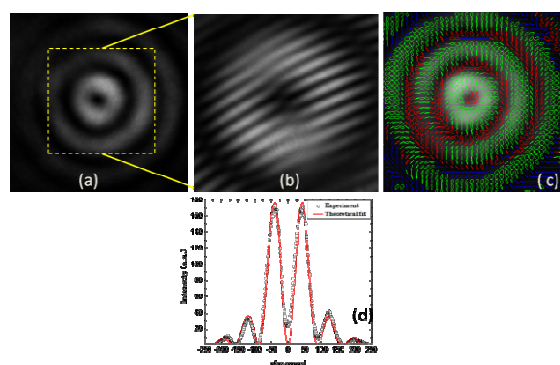


Fig.3 (a) CCD image of the J_1 Bessel beam; (b) two beam interference pattern; (c) Polarization map for the J_1 Bessel beam; (d) Intensity profile for the J_1 Bessel beam obtained with theoretical fit.

The special polarization structure of the output beam from the fiber consisting of polarization singularities, (C -point and s -line) and the phase singularity (vortex) which moves with polarizer rotation [12] in the J_1 beam help one to obtain both J_0 and spiral beams by selecting a particular polarization orientation using a polarizer in the output. We obtained both J_0 and spiral intensity distributions for particular polarizer orientations: output polarizer (P) at 136° gives J_0 intensity and P at 170° gives spiral intensity. These polarizer angles depend strongly on the polarization structure of the input beam to the axicon. When the polarizer after the axicon is rotated the null intensity in the beam moves through the closed curve defined by the s -contour where the superimposing orthogonal field (RCP and LCP) amplitudes are same and the state of polarization is linear. This null intensity rotation causes the shifting of the intensity pattern from J_1 to J_0 and spiral intensity distributions. In the interference pattern it can also be observed that the forklet moves with the polarizer rotation through s -contour. Figure 4 shows the CCD corresponding

polarization maps of the J_0 and spiral intensity pattern.

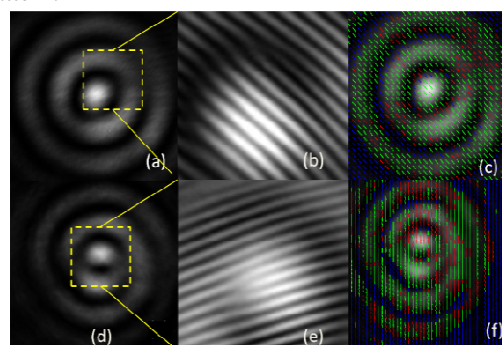


Fig.4 (a) J_0 when P is at 136° ; (b) interference pattern; (c) polarization map of (a); (d) Spiral pattern when P is at 170° ; (e) interference pattern of (d); polarization map of (d)

It is also possible to get co-axial J_0 and J_1 Bessel beams by using a polarizer and quarter-wave plate combination. We kept the QWP at 90° and P at 45° which selects only the right circular polarization (RCP) part of the beam and then rotating P to 135° selects only the left circular polarization (LCP) part. In our case as the LCP part is the fundamental fiber mode which is a Gaussian and a Gaussian input to the axicon generated J_0 Bessel beam [16]. And the annular LG_{01} RCP part generates J_1 Bessel beam [11]. By selecting RCP or LCP one can select the appropriate Bessel output from the axicon. Fig.5 shows the intensity profiles the QWP90 and for P at 45 and 135 .

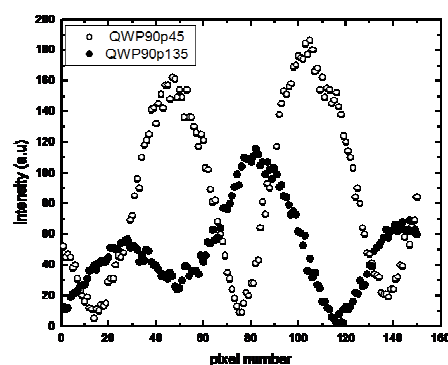


Fig. 5 Intensity profiles corresponding to QWP at 90 and P at 45° and 90° .

4. SUMMARY

We have presented polarization structuring of non-diffracting beams by focusing circularly polarized vortex beam using an axicon. We also demonstrated

the switching between J_0 and J_1 beams by suitable polarization selection.

ACKNOWLEDGEMENT

The authors acknowledge DST, India for the financial support for the project. GMP acknowledges CSIR India for SRF fellowship.

REFERENCES

- [1] J. Durnin, J. Miceli, Jr., and J. H. Eberly, "Diffraction-free Beams" *Phys. Rev. Lett.* **58** 1499 (1987).
- [2] S. R. Mishra, "A vector wave analysis of Bessel beams" *Opt. Commun.* **85** 159 (1991).
- [3] Z. Bouchal and M. Olšovík, "Non-diffractive Vector Bessel Beams" *J. Mod. Opt.* **42** 1555 (1995).
- [4] S. C. Tidwell, D. H. Ford, and W. D. Kimura, "Generating radially polarized beams interferometrically" *Appl. Opt.* **29** 2234 (1990).
- [5] A. Niv, G. Biener, V. Kleiner and E. Hasman, "Propagation-invariant vectorial Bessel beams obtained by use of quantized Pancharatnam–Berry phase optical elements" *Opt. Lett.* **29** 238 (2004).
- [6] K. I. Willing, S. O. Rizzoli, V. Westphal, R. Jahn and S. W. Hell, "STED microscopy reveals that synaptotagmin remains clustered after synaptic vesicle exocytosis" *Nature* **440** 935 (2006).
- [7] B. M. Rodríguez-Lara and R. Jáuregui, "Dynamical constants for electromagnetic fields with elliptic-cylindrical symmetry" *Phys. Rev. A* **78**, 033813 (2008).
- [8] R. D. Romea and W. D. Kimura, "Modeling of inverse Čerenkov laser acceleration with axicon laser-beam focusing" *Phys. Rev. D* **42** 1807 (1990)
- [9] H. Chen, Z. Zheng, BF. Zhang, J. Ding and HT. Wang, "Polarization structuring of focused field through polarization-only modulation of incident beam" *Opt. Lett.* **35**, 2825 (2010)
- [10] E M. Frins, J A. Ferrai, A Dubra and D Perciante, "Conversion of bright nondiffracting beams into dark nondiffracting beams by use of the topological properties of polarized light" *Opt. Lett.* **25**, 284 (2000)
- [11] J. Arlt, K. Dholakia, "Generation of high-order Bessel beams by use of an axicon" *Opt. Commun.* **177** 297 (2000)
- [12] V.V.G. Krishna Inavalli and N.K. Viswanathan, "Rotational Doppler-effect due to selective excitation of vector-vortex field in optical fiber" *Opt. Expr.* **19**, 448, (2011)
- [13] Dennis H. Goldstein and Edward Collett, "Polarized Light" 2nd ed. (Marcel Dekker, 2003).
- [14] Y. V. Jayasurya, V. V. G. Krishna Inavalli and N. K. Viswanathan, "Polarization singularities in the two-mode optical fiber output" *Appl. Opt.* **50**, 131 (2011)
- [15] V. Jarutis, R. Paskauskas, A. Stabinis, "Focusing of Laguerre-Gaussian beams by axicon" *Opt. Commun.* **184** 105 (2000)
- [16] G. Scott, N. McArdle, "Efficient generation of nearly diffraction-free beams using axicon" *Opt. Eng.* **31**, 2640 (1992)

SELECTIVE EDGE ENHANCEMENT USING SHIFTED ANISOTROPIC VORTEX FILTER

Manoj Kumar Sharma, Joby Joseph and P. Senthilkumaran

Indian institute of technology Delhi, Hauz khas New Delhi-110016

Email-imaging.mks@gmail.com

Abstract- We propose a new method for selective edge enhancement using shifted anisotropic vortex phase mask. The shifted anisotropic phase mask is generated by introducing anisotropy in conventional vortex mask $[\exp(i\theta)]$ with the help of sine function and shifting the singularity away from the centre

1. INTRODUCTION

Edge detection/enhancement has always been one of the most important operations in image processing and recognition. In image processing, to understand the images, it is always preferred to enhance the edges. For edge enhancement, the spatial filtering operation is employed by Fourier transforming the object and this Fourier transform is manipulated with the help of a filter function before taking the inverse Fourier transform. These Fourier transform techniques to filter out appropriate spatial frequency components are usually optimized by using spatial light modulators or mechanical spatial filters [1, 2]. An optical phase singularity with topological charge m can be used to perform m^{th} order Hankel transform [2]. Davis et al [3] has used a vortex phase mask, $\exp(i\theta); 0 < \theta < 2\pi$ as a spatial filter in the $4f$ geometry. To achieve radially symmetric edge enhancement the charge of the vortex m is unity and for selective edge enhancement m is non integer. If the phase profile of the vortex mask is analyzed, it is obvious that there is a phase difference of $m\pi$ at a symmetric position in any radial line with respect to the vortex core. Similar characteristics can be seen in the 1D-Hilbert transform [4-6]. The spiral phase filtering using an spiral phase plate (SPP), which is characterized by function $\exp(im\theta)$ performs symmetric Hilbert transform and is regarded as radial Hilbert phase mask with m as order of the radial Hilbert transform. Generally the edge enhancing effect is isotropic, particularly when spiral phase plate (SPP) of topological charge 1 is used as a radial Hilbert phase mask. In many image processing applications, it is preferred to have some edges to be emphasized more than others. The radial Hilbert transform which is effectively the vortex spatial filtering, does the edge enhancement by redistributing the intensity in a symmetric manner because the radial Hilbert mask is symmetric. Therefore, to enhance the selective edges in a particular desired direction, one has to break this symmetry of Hilbert mask.

The methods reported for selective edge enhancement, uses fractional vortex mask [7]. The fractional Hilbert transform [3, 8] method uses

modified Hilbert transform in which the phase difference between two radial points on either side of the origin is a fractional multiple of π . In another study, Guohai et al [9] have proposed selective edge enhancement using fractional spiral phase filter with additional offset angle and by shifting the singularity. Very recently we have proposed anisotropic vortex phase mask [10] for selective edge enhancement which can control the selectivity. In this paper we demonstrate a new method for the selective edge enhancement in any desired direction using shifted anisotropic vortex phase mask. The method performs the edge enhancement only in one direction unlike the previous method which provides selective but radially symmetric edge enhancement. Both of the methods are capable of controlling the selectivity.

2. ANISOTROPIC VORTEX FILTER

Isolated optical vortices are phase singularities characterized by helical wavefronts winding about amplitude zeros where the phase is indeterminate. Around the singularity, the phase variation shows helical structure keeping the singularity at the centre. The phase singularity in an optical beam is also known as optical vortex. Eventhough, the phase singularity exists at the centre; it affects the phase distribution over the entire beam. Analytically an optical vortex can be defined by a complex field

$$V_i(x, y) = x + iy = r \exp(i\theta)$$

where r is the distance from the vortex center and $\theta = \arctan(y/x)$ is the azimuthal angle. The phase distribution $\psi(r, \theta) = \theta$ and the rate of change of the phase around the vortex is given by

In an anisotropic optical vortex [11] this is not a constant. Consider an anisotropic vortex given by

$$\tilde{V}_a(x, y) = x + i\sigma y = r \exp(i\psi(x, y)) \quad (2)$$

where, the phase is given as

$$\psi(x, y) = \tan^{-1}\left(\sigma \frac{y}{x}\right) = \tan^{-1}\left(\sigma \frac{\sin \theta}{\cos \theta}\right) \quad (3)$$

Here σ is anisotropy parameter which determines the internal structure of the optical vortex.

3. SHIFTED ANISOTROPIC VORTEX FILTER FOR SELECTIVE EDGE ENHANCEMENT

The anisotropic vortex phase mask [10] is given by

$$S(r, \theta) = \exp[i\theta \{ \sin^n(\theta/2) \}] \quad (4)$$

In an anisotropic vortex filter the phase varies in such a manner that it enhances the edges selectively but in radially symmetric manner.

The shifted anisotropic vortex phase mask can be represented as

$$S_{sh}(r, \theta) = \exp(i\psi_{sh}) \quad (5),$$

where the shifted phase is given by the function

$$\psi_{sh} = \theta \{ \sin^n(\theta/2) \} * \delta(r_0 + R) \quad (6),$$

where, the convolution with delta function determines the shift R of the filter with respect to the central position r_0 . The filter function specified by equation (5) yields radially non symmetric selective edge enhancement after spatial filtering operation. The selectivity is controlled by parameter n , which is a measure of anisotropy in the filter function and the shift in the phase of the anisotropic vortex filter function provides the enhancement in one side of the centre of the object.

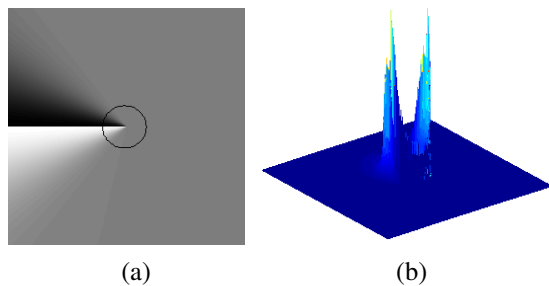


Fig.1 Simulation results for a circular aperture using anisotropic vortex filter with $n=30$ and no spatial shift is provided to the phase of the filter (a) phase mask (b) 3D plot of output intensity

4. SIMULATION RESULTS

Edge enhancement in a smaller region can be achieved by increasing the power n of sine function. The orientation selection is done by adding θ_0 to θ and the spatial shift in phase of the filter provides the enhancement in one side of the centre. More over after adding θ_0 to θ the function $\theta + \theta_0$ is made to lie between $-\pi$ and π by modulo 2π operation.

This is done to preserve the helical shape of the wavefront. **Fig.1** shows the simulation results of edge enhancement for a circular aperture, using anisotropic vortex function S and it can be seen that the edge enhancement is selective but the same region of the edges is enhanced on either side of the centre.

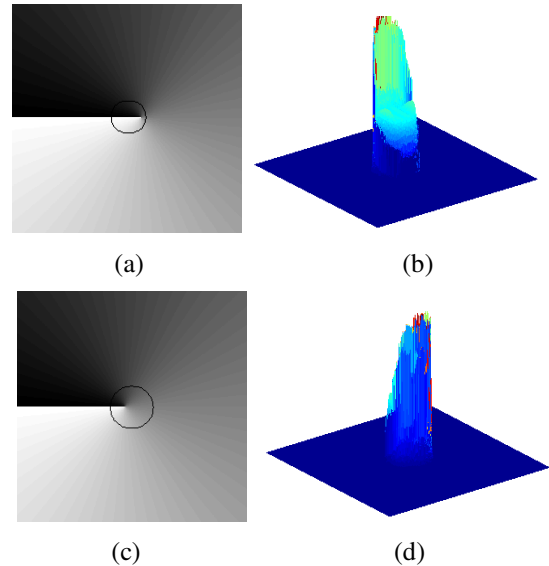


Fig.2 Simulation results for a circular aperture using shifted isotropic vortex mask (a) and (c) are right and left shifted masks each by 20 pixels, (b) and (d) are corresponding edge enhanced 3D plots of output intensity corresponding to (b) and (e) respectively.

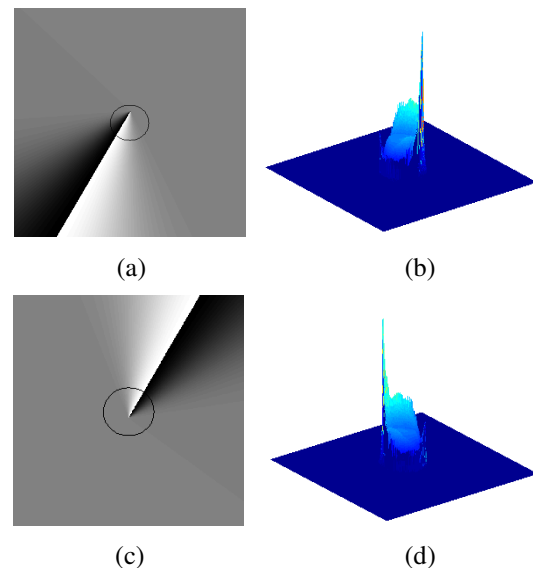


Fig.3 Simulation results for edge enhancement of a circular aperture when a shifted anisotropic filter with $n=30$ is used. (a), (c) are shifted anisotropic masks with different shifts, (b), and (d) are 3D plots of edge enhanced output intensity.

In our simulation the grid size is taken equal to 600×600 pixels and the size of circular aperture is kept equal to 150 pixels. **Fig.2** shows that as the power n in function S_{sh} is increased selective edge

enhancement is pronounced. The 3D plots of the intensity versus azimuthal angle, in Fig.3, show the angular selectivity of edge enhancement. Increased enhancement selectivity at different orientations is clearly visible.

5. EXPERIMENTAL RESULTS

We have implemented the phase masks corresponding to the function S with the help of reflective Spatial Light Modulator (SLM), Holoeye LC-R 2500 with resolution 1024×768 , pixel pitch $19 \mu\text{m}$. The objects used are a circular aperture of size $200 \mu\text{m}$. The experimental setup is shown in Fig.4.

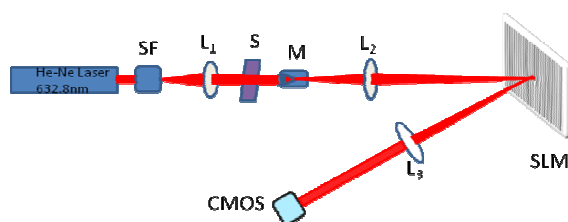


Fig.4 Experimental set L1: collimating lens, S: sample/object, M: microscopic object, L2: Fourier transforming lens, SLM: spatial light modulator in amplitude mode, L3: imaging lens and CMOS: infinity1 camera used to record the output images.

The object is illuminated by collimated beam from He-Ne laser (632.8nm) and Fourier transformed with the help of Newport 10X microscopic objective and the Fourier transform is imaged on the SLM with 4X magnification by a lens of focal length 135mm. The SLM is operated in phase mode keeping the polarizer at angle 170° to get the phase shift up to 2π .

The computer generated holograms (CGH) corresponding to function S is formed and displayed on the SLM. This CGH is a fork grating formed by interference of anisotropic vortex beam and a tilted plane wave. The CGH corresponding to the proposed function S and $S_{g,h}$ are formed in MATLAB keeping the resolution same as that of the SLM and the grating period has been kept equal to the six pixels of the SLM. The incident light wave is then diffracted by the fork grating displayed on the SLM, and only the light diffracted at the first diffraction order is used. The undesired diffraction orders are blocked. Imaging is done with help of a lens of focal length 200mm, kept in between SLM and infinity-1 CMOS camera. The experimental results recorded for different values of anisotropy and for a given shift, are shown in Fig.5 for circular aperture and the experimental results a given shift and for different values of angle of rotation are shown in Fig.6. The experimental results are in well support of simulated results.

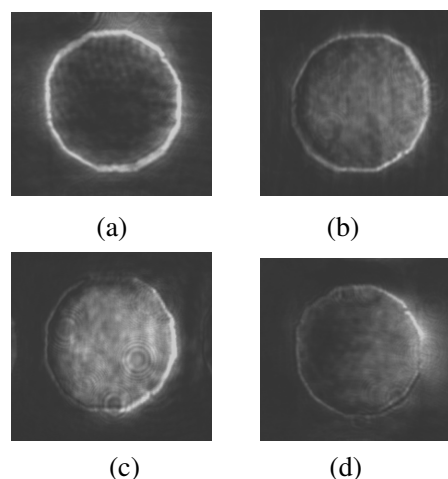


Fig.5 Experimental results for selective edge enhancement with (a) Vortex filter (b) Shifted vortex filter, (c) anisotropic ($n=5$) and shifted (20 pixels) vortex filter, (d) Anisotropic ($n=30$) and shifted (20 pixels) vortex filter

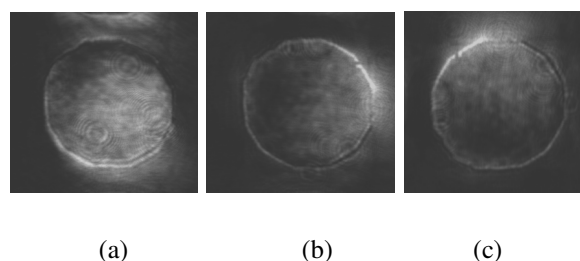


Fig. (6) Experimental results for selective edge enhancement with anisotropy ($n=30$) and the shift(20 pixels) is provided towards (a) right (b) left (c) down

ACKNOWLEDGEMENT

Manoj Kumar Sharma would like to thankfully acknowledge council of scientific and industrial research of India (CSIR) for senior research fellowship.

REFERENCES

1. Joseph W. Goodman; Introduction to Fourier optics; Roberts and Co.; Colorado; 2007
2. S.N.Khonina, V.V.Kotlyar, M.V.Shinkaryev, V.A.Soifer and G.V.Uspleniev; The phase rotor filter; J. Mod.Optics; 39, 1147 (1992).
3. Jeffrey A. Davis, Dylan E. Mcnamara, and Don M. Cottrel, Juan Campos; Image processing with the radial Hilbert transform: theory and experiments, Optics letters; 25, 99, (2000).
4. R.B.Bracewell, The Fourier transform and its application (McGraw-Hill, New York, 1965).
5. Jeffrey A. Davis, Dylan E. McNamara, and Don M. Cottrel, Analysis of the fractional Hilbert transform, Applied optics, 37, 6911, (1998).

6. Jeffrey A. Davis, David A. Smith, Dylan E. McNamara, Don M. Cottrell, and Juan Campos, Fractional derivatives—analysis and experimental implementation, *Applied optics*, 40, 5943, (2001).
7. Adolf W. Lohmann, David Mendlovic and Zeev Zalevsky; Fractional Hilbert transform; *Optics letters*, 21, 281, (1996).
8. A. W. Lohmann, E. Tepichín, and J. G. Ramírez, Optical implementation of the fractional Hilbert transform for two-dimensional objects; *Applied Optics* 36, 6620, (1997).
9. Guohai Situ; Giancarlo Pedrini; Wolfgang Osten; Spiral phase filtering and orientation-selective edge detection/enhancement; *J. Opt. Soc. Am. A*, 26,1788-1797 (2009).
10. Manoj Kumar Sharma, Joby Joseph and P.Senthilkumaran, Selective edge enhancement using anisotropic vortex filter, *Applied optics*, 50 , 5279, 2011
11. Guang-Hoon Kim, Hae June Lee, Jong-Uk Kim and Hyyong Suk; Propagation dynamics of optical vortices with anisotropic phase profiles; *J. Opt. Soc. Am. B*; 20,351-359 (2003).

GENERATION OF RESHAPED HOLLOW GAUSSIAN BEAM

Brijesh Kumar Singh, Manoj Kumar Sharma, Joby Joseph, D. S. Mehta and P. Senthilkumaran
Department of physics, Indian Institute of Technology, Delhi, Hauz khas, New Delhi-110016
brijeshsingh831@gmail.com

Abstract: A method to generate hollow Gaussian beam (HGB) with different profiles is presented. Computer generated holograms (CGHs) with phase dislocations are used for beam shaping. We tried to introduce phase defects in the diffractive optical element to change the shape of the beam. When we pass the Gaussian beam through this encoded diffractive optical element different shapes of the beam are generated with the dislocation at the centre of the beam. Some simulated results are presented in this paper.

1. INTRODUCTION

Reshaping of the Gaussian beam using different methods [1,2] have been reported earlier. The diffractive optical elements (DOEs) can be used to convert a coherent beam of light into different desired intensity profile at different plane by encoding a phase distribution on the incident field [3]. In this paper conversion of Gaussian beam into different shapes of hollow beam is presented. The conversion is done by using computer generated hologram (CGH) [4] in which phase singularities are embedded at desired locations. An important feature of a phase defect is that its centre, i.e. zero amplitude point belongs to a continuous line in space where the amplitude vanishes and the phase circulates around this line [5]. At the phase singular point amplitude is zero and phase is undefined. The singular beam is defined by the phase function $\exp(im\theta)$, where θ is the phase of the singular beam and m is the topological charge, which may be positive or negative, that defines the circulation of the helical wavefronts of singular beam. Due to the property of having the helical wavefront, singular beams have the orbital angular momentum [6] whose magnitude is given by $\pm m\hbar$. The singular beam finds applications in trapping of micro-particle [7] in optical tweezers due to orbital angular momentum.

The hollow Gaussian beam (HGB) can be generated by passing the Gaussian beam through the phase mask which is encoded with the phase dislocation. Beam shaping opens the new possibilities for improving the performance of the laser technologies where laser with different intensity profile is most desirable. This is one of the reasons for growing interest in various beam shaping techniques [8-14] in recent years.

Experimentally the hollow Gaussian beam (HGB) can be generated by displaying the encoded phase mask on the spatial light modulator (SLM) [15]. SLM is an electronic device which can display, amplitude only or phase only element with high resolution. Dynamically we can change the displayed phase mask on the SLM according to the beam profile requirement. Hollow Gaussian beam which has the phase dislocation at the centre of the beam finds the application in micro-particle manipulation [16],

metrology [17], astronomy [18], quantum computing [19] and microscopy [20].

2. METHOD

We tried to generate different shapes of hollow Gaussian beam profiles by passing the Gaussian beam through a phase mask which has the dislocations at desired locations. The output field profile is the diffraction pattern of the Gaussian beam through the phase mask.

The input Gaussian amplitude of the parallel laser beam is given by

$$t(x, y) = \begin{cases} \exp[-(x^2 + y^2)/r_g^2] & x^2 + y^2 < r_a^2 \\ 0 & x^2 + y^2 \geq r_a^2 \end{cases} \quad (1)$$

where (x, y) are the Cartesian coordinates on the CGH surface, r_g is the beam radius at e^{-2} intensity level and r_a is the radius of the output aperture.

The phase function of CGH used has equally spaced dislocations situated on a circle of radius r_d and can be written as

$$T(r, \theta) = \exp\left[(-1)^n i \left[\sum_{n=1}^N (\theta_n + \theta)m\right] - i\pi r^2 / \lambda f\right] \quad (2)$$

where θ_n are the phase of the n^{th} dislocations which are situated on a circle of radius r_d where $r_d < r_a$ and θ is the dislocation at the centre of the circle, m is the topological charge of each dislocation, f is the focal length of lens phase function and λ is the wavelength of the laser beam.

With the help of eq. (1) & (2) we can calculate the output field profile by taking the Fourier transform $\mathcal{F}[t(x, y)T(r, \theta)]$ which is the complex amplitude in the far -field after diffraction at the hologram.

The dislocations in the used CGH which is given by Eq.(2) are symmetrically arranged around the centre of the input beam where another dislocation is placed. The dislocations which are placed at the circumference of the input beam are arranged in such a manner so that their total charge, at the circumference, becomes equal to zero. Therefore, the generated hollow Gaussian beam has single charge vortex which comes because of the dislocation, placed at the centre of the circle of radius

r_d . The simulation results are given in the next section.

3. SIMULATION RESULTS

The different shapes of HGB profiles are generated by using Eq.(1) & (2) are shown in Fig.1. In fig.1 (a) & (b) the intensity & contour plot of used input Gaussian beam in the transverse plane before passing the phase mask are shown.

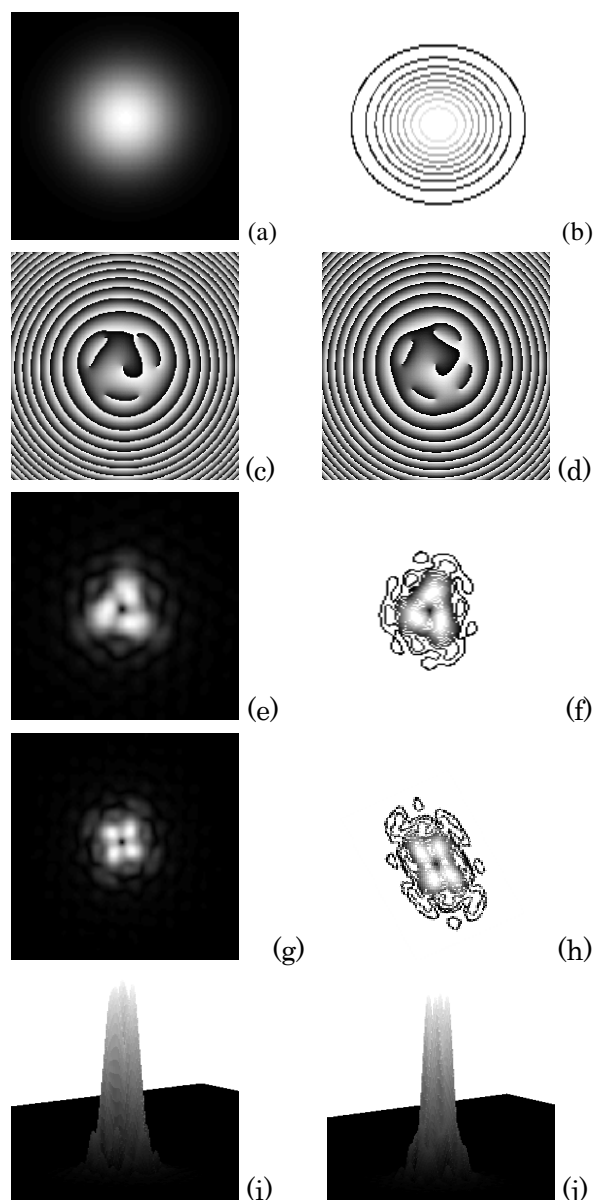


Fig.1 (a) Input Gaussian field & (b) its contour plot, (c) & (d) phase function of CGH in which 6 & 8 dislocations are at equal distances from central dislocation, (e) & (g) diffraction pattern of the Gaussian field through the CGH for 6 & 8 dislocations on the circle of CGH, (f),(h) & (i),(j) are the contour and mesh plot of field (e) & (g) respectively.

The phase masks for shaping the Gaussian beam which have 6 & 8 dislocations situated symmetrically

around the central dislocation are shown in fig.1 (c) & (d) respectively. Fig.1 (e) & (f) show the generated reshaped HGB field profile and contour plot which have one dislocation at the centre of the beam, when the input Gaussian beam (a) passes through the phase mask (c). Similarly when the input Gaussian beam (a) passes through the phase mask (d) we got the another reshaped HGB which field profile and contour plot in the Fourier Transform plane shown in the fig.1 (g) & (h) respectively. The mesh plot of the reshaped HGB field profile generated by passing the Gaussian beam through the phase mask (c) & (d) are shown in fig.1 (i) & (j) respectively.

4. DISCUSSION

The hollow Gaussian beams are generated by passing the Gaussian beam through the phase mask, shown in fig.1. The Gaussian beam becomes a hollow reshaped beam at the following conditions: $r_a = 2.1r_g$ and $r_d = 1.23r_g$. The resultant field has only one singularity which is at the centre of the beam. We have taken only even number of singular points at the circumference of the circle of radius r_d . We can change the shape of the HGB by changing the position and number of these dislocations in the CGH as shown in fig. (c) & (d). Here we present only two different shapes of HGB and similarly we can generate different shapes of HGB by using the higher topological charge vortices in the phase mask. From the mesh plot of the reshaped HGB field profile as shown in fig.1 (i) & (j) it is clear that at the centre of the HGB the intensity is zero and the reshaped beam is hollow. Also it is clear from the field profiles (e) & (g) and contour plots (f) & (h) that there is a dark point at the centre of the HGB which shows the location of the vortex.

The proposed experimental set-up for above simulation results is shown in fig.2. The transmissive type SLM in phase mode can be used to display the simulated phase masks which are shown in fig. 1 (c) & (d). A Gaussian beam is spatially filtered by spatial filtering set up and then is collimated with the help of a lens. This collimated Gaussian then illuminates the phase mask displayed on the SLM. The resultant field after passing through the SLM is Fourier transformed by the lens after the SLM. Finally we get the resultant reshaped HGB at the focal plane of the Fourier transforming lens as shown in fig. 2. We can get the different reshaped HGBs in real time by changing the different phase masks of different number of dislocations on the SLM.

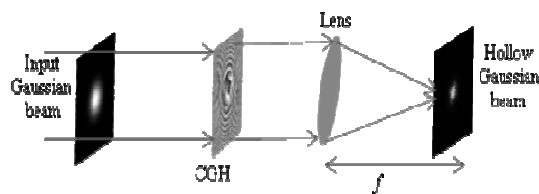


Fig.2 Proposed experimental set-up for above simulation results

5. CONCLUSION

An efficient method to generate reshaped hollow Gaussian beams has been proposed. One can easily generate hollow beams of different shapes just by rearrangement of dislocations in the phase mask.

ACKNOWLEDGEMENT

Brijesh Kumar Singh acknowledge to UGC for JRF.

REFERENCE

- [1] C.-Y. Han, Y. Ishii and K. Murata, "Reshaping collimated laser beams with Gaussian profile to uniform profiles" *Appl. Opt.*, **22**,3644 (1983).
- [2] E. G. Churin, "Diffraction-limited laser beam shaping by use of computer-generated holograms with dislocations", *Opt. Lett.*, **24**,620 (1999).
- [3] V. Soifer, *Methods for Computer Design of Diffractive Optical Elements* (Wiley 2002).
- [4] N. R. Heckenberg, R.McDuff, C.P.Smith, and A.G.White, "Generation of optical phase singularities by computer generated hologram," *Opt. lett.*, **17**, 221-223 (1992).
- [5] J.F.Nye, M.V.Berry "Dislocations in wavefronts,"(Proc.R.Soc.Lond.A **336**,165-190 (1974)
- [6] L. Allen, M.J. Padgett, M. Babiker, "The Orbital Angular Momentum of Light" , *Progress in Optics*, **39**, 291-372 (1999).
- [7] K. T. Gahagan, and G. A. Swartzlander Jr, "Optical vortex trapping of particles," *Opt. Lett.*, **21**, 827-829 (1996).
- [8] Fred M. Dickey, Louis S. Weichman, and Richard N. Shagam, "Laser beam shaping techniques", *Proc. SPIE* 4065, 338 (2000).
- [9] C.-Y. Han, Y. Ishii, and K. Murata, "Reshaping collimated laser beams with Gaussian profile to uniform profiles", *Appl. Opt.* **22**, 3644 – 3647(1983).
- [10] Y. Belvaux and S. P. S. Viridi, "A method for obtaining a uniform non-Gaussian laser illumination," *Opt. Commun.*,**15**,193–195 (1975).
- [11] C. Wang and D. L. Shealy, "Design of gradient-index lens systems for laser beam reshaping," *Appl. Opt.* **32**, 4763– 4769(1993).
- [12] Zalevsky, Z.; Mendlovic, D.; Shabtay, G.; Marom, E.," Beam shaping using diffractive optical elements and its use for array illumination and clock distribution", *IEEE*, 371-374 (1996).
- [13] C. S. Ih, "Absorption lens for producing uniform laser beams", *Appl. Opt.*, **11**, 694 – 695 (1972).
- [14] Fred M. Dickey, Scott C. Holswade, "Laser beam shaping: theory and techniques" (2000).
- [15] Joseph W. Goodman, "Introduction to Fourier optics" (2004).
- [16] Juan P. Torres, Lluís Torner, " Twisted Photons: Applications of Light with Orbital Angular Momentum" (2011).
- [17] W. Wang, T. Yokozeki, R. Ishijima, A. Wada, Y. Miyamoto, M. Takeda, and S. G. Hanson, "Optical vortex metrology for nanometric speckle displacement measurement," *Optics Express* **14**, 120-127 (2006).
- [18] G. D. Foo, D.M. Palacios, G.A. Swartzlander, "Optical vortex coronagraph," *Opt. Lett.* **30**, 3308-3310 (2005).
- [19] K.T.Kapale,J.P.Dowling, Vortex phase qubit:generating arbitrary, counterrotating, coherent superpositions in Bose-Einstein condensates via optical angular momentum beams, *Phy.Rev.Lett.* **95**,173-178 (2005).
- [20] S. Furchapter, A. Jesacher, S. Bernet, and M. Ritsch-Marte, "Phase contrast imaging in microscopy," *Opt. Express* **13**, 689–694 (2005).

COHERENCY MATRIX OF POLARIZED OPTICAL VORTEX BEAMS

V.K. Jaiswal^{*,a}, H.C. Kandpal^a, R.K. Sinha^b, R.P. Singh^c

^aNational Physical Laboratory, New Delhi, 110 012

^bDelhi Technological University, Delhi 110 042

^cPhysical Research Laboratory, Ahmedabad, 380 009

*jaiswalvk@nplindia.org

Abstract: We have produced optical vortex beams of different charges and constructed coherency matrix for different states of polarization of the generating beam and the vortex beams. Stokes vector formalism is used to quantify the polarization of each beam to calculate elements of coherency matrix.

1. INTRODUCTION

In general, light beams emitted by most lasers are described by Hermite-Gaussian beams, however, several other beams have been found as solution to Maxwell equations for electromagnetic waves. One of the very important beams is an optical vortex, a manifestation of phase singularity in the optical field [1]. It should be noted that phase singularities are found throughout optical physics. However, to produce them in a controlled manner one requires devices like computer generated holograms [2] (CGH) and spiral phase plates [3]. Because of their specific spatial structure, recently, they have found applications in quantum computation and quantum information. However, little attention has been paid to study the coherence properties of such phase singular beams. It is not very clear, what are the changes that take place in degree of coherence and in the effective phase difference after the transformation. It is interesting to note and quantify degree of polarization and degree of coherence during the transformation process.

2. EXPERIMENT

In laboratory we produce optical vortices with the help of a Computer Generated Hologram (CGH), and an intensity stabilized laser oscillating in HG₀₀ mode. A set of polarizer and Quarter Wave Plate (QWP) between laser and CGH is used to prepare certain known states of polarization. In order to quantify the polarization of the vortex beams, appearing in diffracted orders of CGH, polarization components are measured with an assembly of polarizer, QWP and optical multimeter [4]. These polarization components are used to construct the elements of coherency matrix from the Stokes vectors formulation.

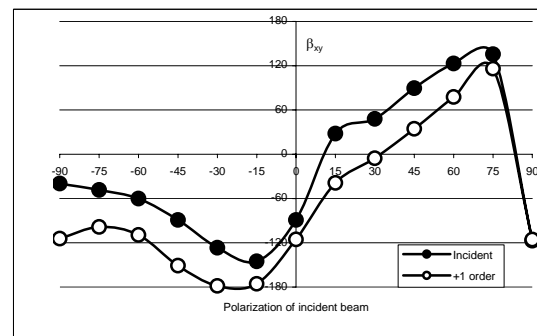
3. RESULTS AND DISCUSSION

To observe the effect of state of polarization of incident beam on the degree of coherence of vortex beams and the central non-diffracted beam we analyze optical vortex beams for their degree of coherence and its phase correlation with the incident beam. The coherency matrix for vertically linearly polarized incident beam and the corresponding vortex beam of

charge +1 are evaluated and given by:

$$\begin{bmatrix} 588.8 & -2.05 - 4i \\ -2.05 + 4i & 0.045 \end{bmatrix} \text{ and } \begin{bmatrix} 28.4 & -2.55 - 5.15i \\ -2.55 + 5.15i & 1.5 \end{bmatrix}$$

The effective phase β_{xy} of the incident beam and vortex of charge +1 is plotted for all states of polarization of the incident beam in the figure below. The upper curve is for incident beam. All diffracted orders are found to follow same trend for β_{xy} .



4. CONCLUSIONS

The study shows that effective phase β_{xy} of incident and the vortex beams are well correlated with each other. It is also unveiled that spin angular momentum and orbital angular momentum of photons are not coupled during the transformation.

ACKNOWLEDGEMENT

The authors wish to thank Director, NPL, New Delhi for his encouragement.

REFERENCES

- [1] M.S. Soskin, M.V. Vasnetsov, "Singular Optics," North-Holland, Amsterdam, E. Wolf (Ed.), *Progress in Optics*, **42**, 219 (2001).
- [2] J. Arlt, K. Dholakia, L. Allen, and J. Padgett, "The production of multiringed Laguerre-Gaussian modes by computer-generated holograms," *J. Mod. Opt.*, **45**, 1231 (1998).
- [3] M.W. Beijersbergen, R.P.C. Coerwinkel, M. Kristensen, and J.P. Woerdman, "Helical-wavefront laser-beams produced with a spiral phaseplate," *Opt. Commun.*, **112**, 321 (1994).
- [4] Max Born and E. Wolf, *Principles of Optics*, Cambridge University Press, New York, 1980.

NEAR/FAR FIELD PROPAGATION OF CUSTOM DESIGNED WAVEFRONTS

Awakash Dixit¹, Nilesh Goyal², Akshay Singh², and *Sanjay K. Mishra¹

¹Instruments Research and Development Establishment (DRDO), Dehradun-248008, India

²Indian Institute of Technology Guwahati, Guwahati-781039, India

*skmishra@irde.drdo.in

Abstract: In this paper we report free-space propagation of a customized wavefront and demonstrate the variation of vorticity under diffraction. Experimentally the wavefronts have been generated using phase only spatial light modulator (SLM) and its far-field pattern were recorded. Simulations reveal that exchange of the nature of topological charge occurs at a distance of 0.63 m.

1. INTRODUCTION

Laser beam propagation through strong turbulence encounters phase and amplitude fluctuations. In these conditions the amplitude fluctuations induces singular phase in the wavefront [1]. Phase singularities is a point phase defect, at which the phase is undefined, but in its neighbor the phase values circulates in between 0 to $2\pi m$ (where m being an integer representing topological charge of the vortex). The phase distribution of the wavefront is continuous and differentiable at every point except at the vortex core. Though vortex is a point defect, it influences the phase distribution on whole wavefront [2]. Propagation study of singular wavefronts is theoretically a complex problem and generally it is solved under near or far field approximations of diffraction. Several studies on the dynamic inversion of the topological charge of a superposition of Laguerre-Gauss (LG) modes carrying different charges was observed under free-space propagation [3]. It was demonstrated that in the near field the superposition of two coaxial Bessel-Gauss (BG) singular beams creates light pattern with complicated vortical structure which under diffraction dynamically evolves into rather simple structure [4]. The propagation of a combined beam consisting of two coaxial BG and LG vortex beams is investigated and it was demonstrated that the vortical properties of light field under diffraction depend on propagation length and amplitude ratio of individual beams [5].

In the reported work two types of customized wavefront have been designed and their propagation characteristics have been studied by simulation. Here we solved the Huygen-Fresnel diffraction equation directly using Gauss-Legendre quadrature method to estimate diffraction patterns at some arbitrary plane. Normally the Fraunhofer and Fresnel diffraction approximations are used to solve the Huygen-Fresnel diffraction equation for the estimation of the far field and near field diffraction patterns respectively.

New kinds of customized wavefront that is equivalent to an optical wedge were generated. Two different types of customized wavefronts were

considered for the simulation. Diffraction patterns after propagation to finite distance were simulated and verified experimentally. Evolution of phase singularities in wavefront as the wave propagates was also predicted for various near field distances.

2. WAVEFRONT CUSTOMIZATION

We solved the Huygen-Fresnel diffraction equation [6] by directly solving the double integral (Gauss-Legendre quadrature method) to estimate diffraction patterns at some arbitrary plane. Geometry illustrating the coordinate system for diffraction is shown in Fig. 1. The diffraction integral is given as below

$$U(P) = \frac{z}{i\lambda} \iint_S U(x_0, y_0, 0) \frac{e^{ik\sqrt{(x-x_0)^2 + (y-y_0)^2 + z^2}}}{[(x-x_0)^2 + (y-y_0)^2 + z^2]} dx_0 dy_0$$

where; $a \leq x_0 \leq b$ and $c \leq y_0 \leq d$, where λ is the wavelength of the light source and k is wave number i.e. equal to $2\pi/\lambda$.

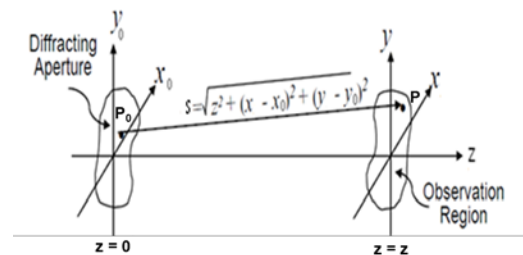


Figure.1 Geometry illustrating the coordinate system for diffraction

Sunil, et.al., have demonstrated a method of vortex generation using wavefront tilt only [7]. It was shown that if two different regions in a wavefront are given different tilts, at discrete points on the line of phase discontinuity, phase singularities may evolve upon propagation.

Here we define two types of customized wavefront that is equivalent to an optical wedge. These wavefronts can be generated using segmented adaptive mirror or SLM. The expressions for such waves, say Case-I and Case -II from now wards, are as follows,

Case - I

$$E = e^{-\frac{i4\pi\alpha(x+\frac{NT}{2})}{NT}} e^{i\pi} \quad y \geq 0;$$

$$E = e^{\frac{i4\pi\alpha(x+\frac{NT}{2})}{NT}} \quad y < 0 \quad (1)$$

Case - II

$$E = e^{\frac{i4\pi\alpha x}{NT}} \quad x \geq 0, y \geq 0$$

$$E = e^{-\frac{i4\pi\alpha x}{NT}} e^{i\pi} \quad x \geq 0, y < 0;$$

$$E = e^{\frac{i4\pi\alpha x}{NT}} \quad x < 0, y \geq 0$$

$$E = e^{-\frac{i4\pi\alpha x}{NT}} e^{i\pi} \quad x < 0, y < 0 \quad (2)$$

where N is number of pixels, T is pixel size, and α is 0.5 (for both cases).

Generation and propagation of custom designed wavefront

For the generation of these two customized wavefronts, we have taken the aperture of the input field as 4mm and divided into 512 pixels. The wavefronts were generated using the Eqns. 1 and 2 at MATLAB platform. Generated wavefronts are shown in the Fig. 2(a) and 2(b).

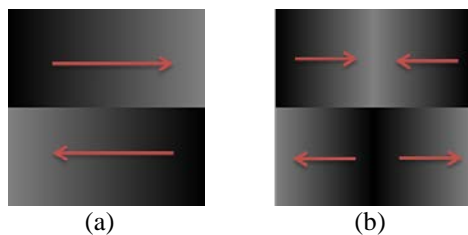


Figure 2. Defined customized wavefronts (a) for case I (b) for case II

In the first type of wavefront (for case I), phase varies 0 to π in the upper first half (in the direction of arrow head, tail is at zero and head is at π) and π to 0 in the lower half of the wavefront as shown in Fig. 2. (a). Besides that, in the second type of wavefront (for case II), phase varies 0 to π in the upper first quadrant, π to 0 in the upper second quadrant, similarly π to 0 in the lower first quadrant and 0 to π in the lower second quadrant as shown in Fig. 2. (b).

The propagating wavefront at some arbitrary plane was calculated by solving the Huygen-Fresnel diffraction equation directly. We computed the diffraction pattern of input field defined by eqns. (1) and (2) at a known distance z . The simulation timing for the computation of wavefront at any distance was long enough for the normal computer (nearly 35minutes). So, we used HP Z800 workstation (Intel Xeon processor E5630, 2.53GHz (2 processor), 16GB RAM) for the computation of wavefronts.

Now the computational time reduced to 400sec approximately for a known distance.

3. EXPERIMENTAL SETUP

The experimental setup which we used for recording the diffraction pattern of custom designed wavefronts is given in Fig. 3. Here we used phase only SLM (HOLOEYE PLUTO HES 6010-0225). SLM was illuminated using a collimated He-Ne laser beam (MELLES GARIOT 25-LHR-151-249) (wavelength 632.8nm, power 15mW). The SLM, which works in reflection mode, produces the same diffracting effect as that produced by a grating element with higher accuracy. We displayed the custom designed wavefronts to the SLM via a computer monitor interface. The resolution of the SLM is 1920×1080 , which matches with the interfacing computer monitor. Different phase patterns were provided to the SLM with a computer, and diffraction pattern were observed on a CMOS sensor. Because of 0th order intensity, it was difficult to observe the diffraction pattern of different phase modulated waves. To overcome this problem, the grating of the phase modulated waves was created, and the diffraction pattern was then observed in the first order. The designed gratings for wavefronts defined by equations (1) and (2) were displayed at the SLM. We recorded the far-field diffraction pattern of phase-modulated plane wave using a CMOS sensor (DALSA DS-21-001M0150) and a Fourier transform lens ($f=380\text{mm}$).

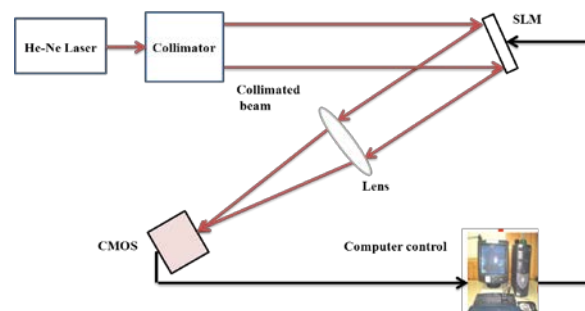


Figure 3. Experimental Schematic

4. RESULTS AND DISCUSSION

Results are discussed in two parts, viz., simulation part (in which we generated the custom wavefronts and studied their propagation properties) and experimental part (in which we recorded the fall field diffraction pattern of the custom wavefronts).

4.1. Simulation results

The propagating wavefront at some arbitrary plane was calculated by solving the Huygen-Fresnel diffraction equation at MATLAB platform. For

estimating the quadrature points for Gauss-Legendre quadrature method a routine is written in C language. An appreciable phase pattern starts appearing after 0.5m distance of propagation, before that some speckle type pattern were observed. Here we generate the phase pattern from a distance 2m with the interval 0.1m upto 2.8m. The phase patterns while propagation are given below in Fig. 4 (For case I) and Fig. 5 (For case II).

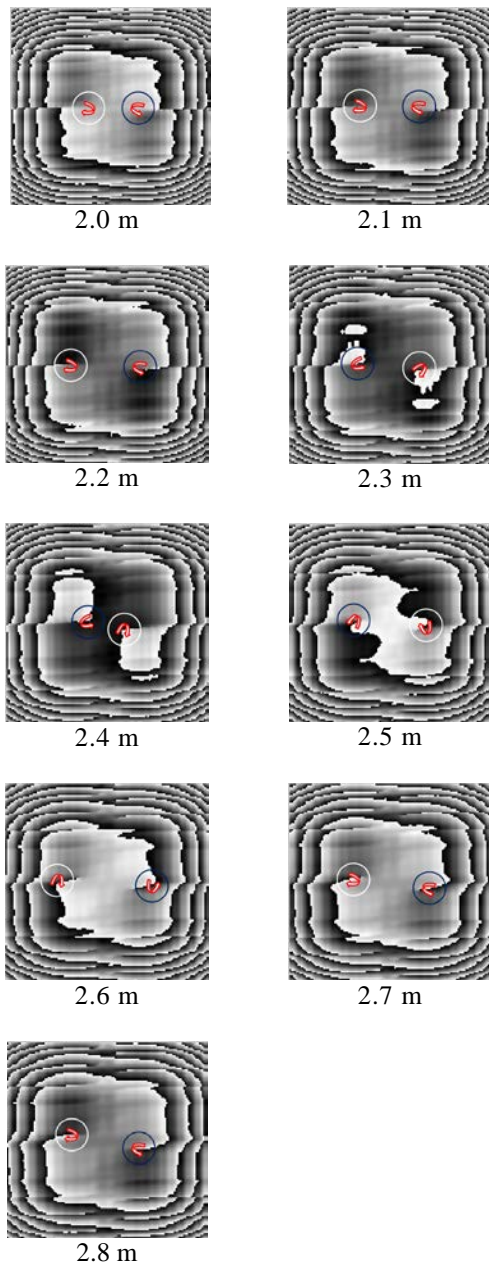


Figure 4. Wavefront evolution for different propagation distances: case I

The circulation of phase in the wavefronts were also visualised by observing the rotation of the arrows in

the below wavefronts. For the case I, the circulation of phase has been shown by the two arrows; one is in a clockwise direction (arrow with white circle) and another in an anticlockwise direction (arrow with blue circle) as shown in Fig. 4.

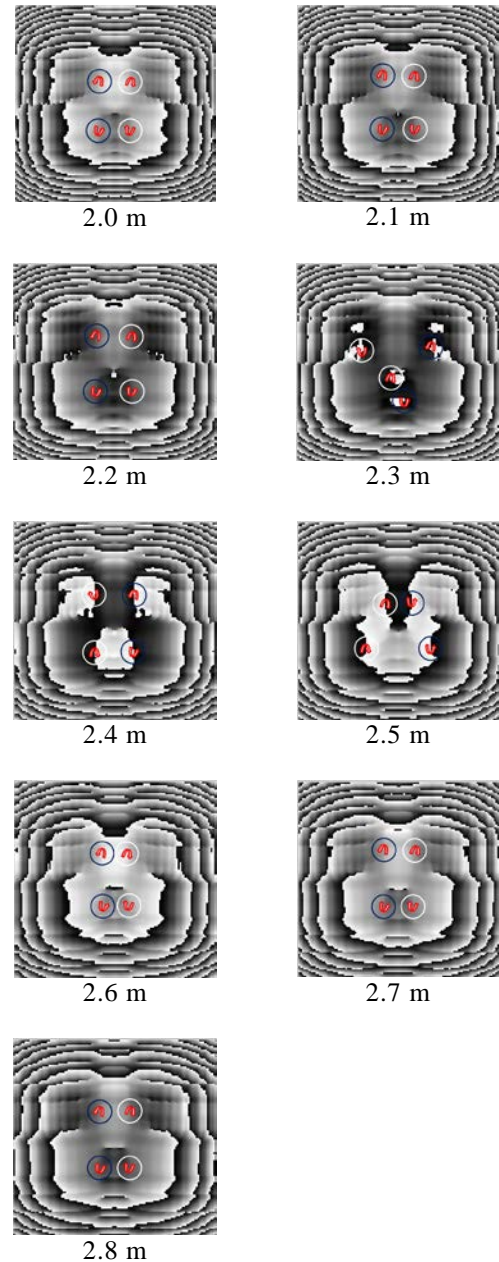


Figure 5. Wavefront evolution for different propagation distances: case II

Similarly, for the case II, the circulation of phase around the point of dislocation was shown by four arrows as shown in the Fig. 5, one is in an anticlockwise direction (arrow with blue circle) and another in a clockwise direction (arrow with white

circle). It has been observed that for the upper first and second quadrant the phase was circulated in anticlockwise and in clockwise direction respectively. Similarly for the lower first and second quadrant same circulation was reported.

Thus we presented the evolution of phase singularities while the propagation of wavefront for near field distances. After analysis it was found that the singularities repeated it self after propagating 0.63 m distances approximately for both the cases.

4. 2. Experimental results

The far-field diffraction patterns were simulated and verified with the experimental results for the customised wavefronts as shown in Fig. 6 (For case I) and Fig. 7 (For case II).

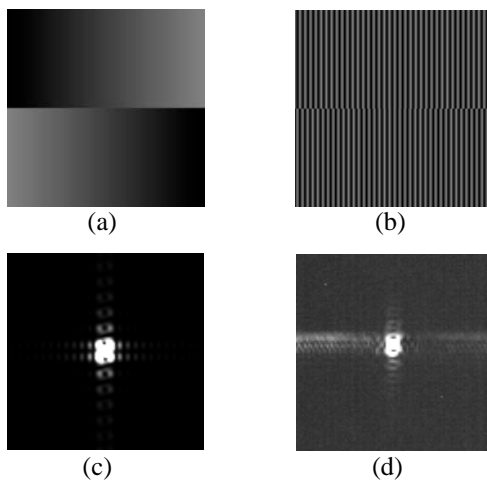


Figure 6. Results for wavefront as in case I
(a) Wavefront (b) Grating pattern (c) Simulated
(d) Experimental

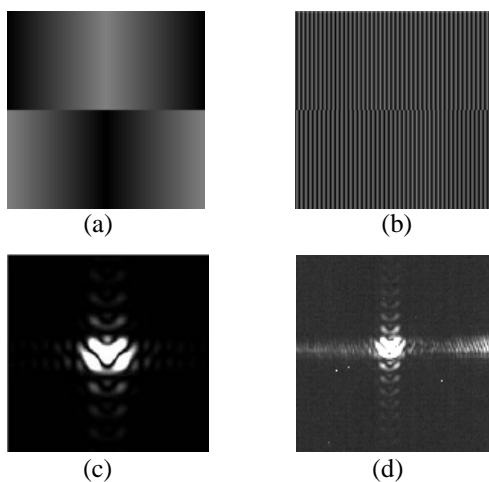


Figure 7. Results for wavefront as in case I
(a) Wavefront (b) Grating pattern (c) Simulated
(d) Experimental

Experimental validation of these custom designed wavefronts for near field propagation will be studied in future.

ACKNOWLEDGEMENT

The authors wish to acknowledge Sh. S. S. Sundaram Director IRDE for permitting to publish the work and Dr. A. K. Gupta and Mr. D. Mohan for their inspiration and overall support. First author is thankful to the IRDE, Dehradun-India for the award of Research Fellowship. Last author wish to thanks Prof. Anurag Sharma and Dr. Debjani Bhattacharya for stimulating discussions.

REFERENCES

- [1] M. C. Roggemann and A. C. Koivunen, "Branch point reconstruction in laser beam projection through turbulence with finite degree of freedom phase only wavefront correction," *J. Opt. Soc. Am. A*, **17**, 53-62, (2000).
- [2] J. F. Nye and M.V. Berry, "Dislocations in wave trains", *Proc. R. Soc. London A*, **336**, 165-190, (1974).
- [3] G. Molina, J. Rekolons, J.P. Torres and L. Torner, "Observation of the dynamical inversion of the topological charge of an optical vortex," *Phys. Rev. Lett.* **87**, 023902, (2001).
- [4] S. Orlov, K. Regelskis, V. Smilgevicius and A. Stabinis, "Propagation of Bessel beam carrying optical vortices," *Opt. Comm.*, **209**, 155-165, (2002).
- [5] S. Orlov and A. Stabinis, "Free-space propagation of light field created by Bessel-Gauss and Laguerre-Gauss singular beams," *Opt. Comm.*, **226**, 97-105, (2003).
- [6] M. Born and E. Wolf, *Principles of Optics*, 6th ed., Pergamon Press, Oxford, 1987.
- [7] S. Vyas and P. Senthilkumaran, "Vortices from wavefront tilts," *Opt. Las. Eng.* **48**, 834-840, (2010).

GENERATION OF LONGITUDINAL MAGNETIC PROBE WITH EXTENDED DOF FOR NEAR FIELD MAGNETO OPTICAL RECORDING

G.Threse Anita^a, C.Amala Prathiba Janet^a, S.Sumathi^a,K.Gokulakrishnan^a, Z.Jaroszewicz^b, K.B.Rajesh^{c*}.T.V.S.Pillai^a

^a Anna University Of Technology, Tirunelveli, Tamilnadu, India.

^bInstitute of Applied Optics, Department of Physical Optics, Warsaw,

^cDepartment of Physics, Government Arts College, Dharmapuri, Tamilnadu, India

*e-mail: rajesk@gmail.com

ABSTRACT

We propose to use pure-phase filter in combination with high NA lens axicon to achieve a sub wavelength uniform magnetization depth when illuminated by a circularly polarized Bessel Gaussian beam. The magnetization distributions are derived and evaluated based on the vector diffraction theory and the inverse Faraday Effect of the isotropic and non magnetically ordered material. With this kind of system, the longitudinal magnetization depth is increased to 12.2λ and the magnetic spot size has been reduced to 0.36λ . However, in the conventional lens with same NA, the FWHM of the magnetic spot is found to be 0.512λ and its corresponding magnetization depth is only 1.2λ . We expect such a sub wavelength longitudinal magnetic field can be widely used in high density magneto optic recording and the scanning near-field magnetic microscope for studies of magnetic responses of sub wavelength elementary cells of metamaterials.

Keywords: phase filter, lens axicon; circularly polarized beam; ultrafast magneto-optic recording.

1. INTRODUCTION

It is observed that the circularly polarized light should have the ability to act upon a magnetic system in a way similar to a magnetic field directed parallel to the wave vector of the light via the inverse Faraday Effect [1-2]. Recently, Stanciu et.al., demonstrated the all-optical magnetic recording by a single 40fs circularly polarized laser pulse [3]. In their experiment the beam was focused on a 100 μm spot and the laser-induced magnetic changes were studied by recording magneto-optical images of the domain patterns before, during and after the laser excitation. More recently, it was proposed that focused circularly polarized laser by high NA

lenses can induce small magnetization domains in the focal region with the magnetization direction almost completely perpendicular to the surface of the optical magneto film [3-6]. For all-optical magnetic storage, higher recording density is possible only by achieving a small magnetic spot. It was shown that all-optical magnetic super resolution can be achieved by using binary amplitude and phase filters [7]. However it is observed that use of those techniques can reduce the magnetic focal point, but it cannot increase the depth of focus (DOF) of the field simultaneously. In this paper, a new technique is demonstrated which uses a five belt phase plate in combination with a high NA lens axicon to achieve a

uniform magnetization depth while maintaining the super resolution. Thus the focusing of the circularly polarized Bessel–Gaussian beam with a diffractive optical elements and a high NA lens axicon and is very worth investigating because there may occur some interesting phenomena, and may also be useful in information processing applications.

2. NUMERICAL ANALYSIS

Suppose the field on the aperture of the focusing lens is left circularly polarized, then the field in the focal region is given as

$$E_{circ}^L(\rho_c, \phi_c, Z_c) = \begin{bmatrix} A(I_0 + I_2 e^{-i2\phi_c}) \\ -iA(I_0 - I_2 e^{-i2\phi_c}) \\ -2iA I_1 e^{-i\phi_c} \end{bmatrix} \quad (1)$$

Where

$$\begin{aligned} I_0 &= \int_0^\alpha (1 + \cos\theta) P(\theta) \sqrt{\cos\theta} \sin\theta J_0(k\rho_c \sin\theta) \exp(ikz_c \cos\theta) d\theta \\ I_1 &= \int_0^\alpha \sin^2\theta P(\theta) \sqrt{\cos\theta} J_1(k\rho_c \sin\theta) \exp(ikz_c \cos\theta) d\theta \\ I_2 &= \int_0^\alpha (1 - \cos\theta) P(\theta) \sqrt{\cos\theta} \sin\theta J_2(k\rho_c \sin\theta) \exp(ikz_c \cos\theta) d\theta \end{aligned} \quad (2)$$

Here α is the convergence semi angle of the lens such that $\alpha = \arcsin(NA)$ where NA is the numerical aperture, $k_0 = 2\pi/\lambda$ is the wave number, $J_0(x)$, $J_1(x)$ and $J_2(x)$ denotes the Bessel functions of zero, first and second order and A is a constant. $P(\theta)$ is the apodization function of the pupil filter. For illumination by a Bessel-Gaussian beam with its waist in the pupil, the function $P(\theta)$ is given by,

$$P(\theta) = \exp\left[-\xi^2 \left(\frac{\sin\theta}{\sin\alpha}\right)^2\right] J_1\left[2\xi \frac{\sin\theta}{\sin\alpha}\right],$$

Where, ξ is the parameter that denoted the ratio of pupil diameter to the beam diameter and in our calculation, we take them as unity. The recording medium we considered is an anisotropic optical magneto film magnetized along the optical axis. Magnetization of the film induced by the inverse Faraday effect can be expressed as

$$M(\rho_c, \phi_c, Z_c) \equiv i\gamma E \times E^* \quad (4)$$

Where γ is a magneto-optic constant. Substituting Eq(1) into (4) we obtain the magnetization $|M_n|$ normalized to γA .

$$M_n^L(\rho_c, \phi_c, 0) \equiv \frac{M^L(\rho_c, \phi_c, 0)}{\gamma A} \equiv \begin{bmatrix} -4I_1(I_0 + I_2) \sin\phi_c \\ 4I_1(I_0 + I_2) \cos\phi_c \\ -2(I_0^2 - I_2^2) \end{bmatrix}$$

To enhance the magnetic super resolution in the focal plane and to improve the magnetization depth we proposed to use high NA lens axicon in this paper. The high NA lens axicon is a doublet of aberrated diverging lens and a high NA converging lens [8-9]. A schematic diagram of the suggested method is shown in Fig.1.

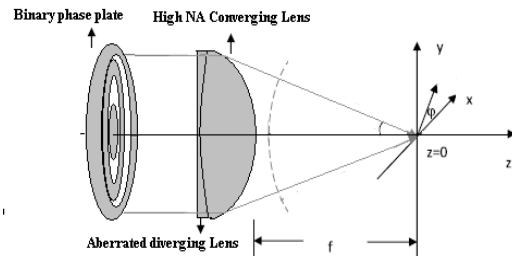


Fig 1. Schematic diagram of lens axicon with binary phase plate illuminated by circularly polarized Bessel Gaussian beam

The intensity distribution of the high NA lens axicon is evaluated by replacing the function $P(\theta)$ by the function $P(\theta)A(\theta)$ where $A(\theta)$ is the non paraxial transmittance function of the thin aberrated diverging lens [11].

$$A(\theta) = \exp \left(I.k \left(\beta \left(\frac{\sin(\theta)}{\sin(\alpha)} \right)^4 + \frac{1}{2f} \left(\frac{\sin(\theta)}{\sin(\alpha)} \right)^2 \right) \right),$$

Where $k=2\pi/\lambda$, f is the focal length and β is the aberration coefficient. In our calculation we take $f = 18.4\text{mm}$, $\beta = 6.667 \times 10^{-5}$ results in an equiconcave diverging lens which is simple to manufacture [10]. We solve equation (5) numerically by assuming a plane wave ($P(\theta) = 1$) and Bessel Gauss illumination for the case of aberration free lens and the proposed high NA lens axicon.

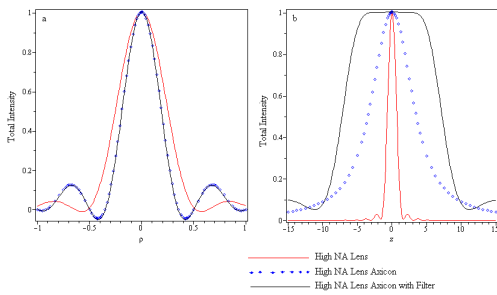


Figure 2. Magnetization distributions in the focal plane illuminated by circularly polarized Bessel Gaussian beam (a) and along the optical axis (b) Axial and transverse coordinates are expressed in units of λ .

The dotted lines in Figs 2(a) and 2(b) show the magnetization distribution of circularly polarized Bessel Gaussian beam in the focal plane and along the optic axis respectively. From the figure we measured that the FWHM of the magnetic spot is 0.512λ and its corresponding magnetization depth is only 1.2λ .

Thus to enhance the magnetization depth we proposed to use high NA lens axicon. The high NA lens axicon is a doublet of aberrated diverging lens and a high NA converging lens [8-9]. A schematic diagram of the suggested method is shown in Fig. 1.

The intensity distribution of the high NA lens axicon is evaluated by replacing the function $P(\theta)$ by the

function $P(\theta)A(\theta)$ where $A(\theta)$ is the non paraxial transmittance function of the thin aberrated diverging lens [10].

$$A(\theta) = \exp \left(I.k \left(\beta \left(\frac{\sin(\theta)}{\sin(\alpha)} \right)^4 + \frac{1}{2f} \left(\frac{\sin(\theta)}{\sin(\alpha)} \right)^2 \right) \right),$$

Where $k=2\pi/\lambda$, f is the focal length and β is the aberration coefficient. In our calculation we take $f = 18.4\text{mm}$, $\beta = 6.667 \times 10^{-5}$ results in an equiconcave diverging lens which is simple to manufacture.

The dashed lines in Figures 2.1 (a) and (b) show the normalized magnetization distribution of high NA lens axicon in the focal plane and along the optic axis respectively. From the figure 2.1(a) we measured that the FWHM of the magnetic spot is reduced to 0.36λ and its corresponding magnetization depth is increased to 7λ . Thus by using high NA lens axicon, it is possible to reduce the magnetization spot size by 30% of the original high NA lens system and can improve the magnetization depth up to five times of the original high NA lens system. However in order to achieve a large uniform magnetization depth we apply additional phase modulation to the incident circularly polarized Bessel Gaussian beam using five belt binary optical phase element.

The effect of phase modulation on the input circularly polarized Bessel gaussian beam tightly focused by high NA lens axicon is evaluated by replacing the function $P(\theta)$ by $A(\theta)T(\theta)$ where $T(\theta)$ is given by

$$T(\theta) = \begin{cases} 1 & \text{for } 0 \leq \theta < \theta_1, \theta_2 \leq \theta < \theta_3, \theta_4 \leq \theta < \alpha \\ -1 & \text{for } \theta_1 \leq \theta < \theta_2, \theta_3 \leq \theta < \theta_4 \end{cases} \quad (4)$$

We choose one structure with random values for θ_1 to θ_4 from all possibilities and simulate their

focusing properties by vector diffraction theory and the inverse Faraday Effect of the isotropic and non magnetically ordered materia . If the structure generates a sub wavelength longitudinal magnetic field with magnetization depth greater than 7λ and satisfies the limiting conditions of side lobe intensity less than 15%, it is chosen as the initial structure during the optimization procedures. The value of the newly chosen zone thickness is used in the next step. Then, we randomly choose the other zone and repeat these procedures to improve the uniformity of the on axial magnetization profile without affecting the limiting condition. We repeat these procedures and as an example The set of four angles optimized for uniform axial magnetization field in the focal segment of the lens axicon are $\theta_1 = 22^\circ$, $\theta_2 = 56.5^\circ$, $\theta_3 = 62.2^\circ$ and $\theta_4 = 66.5^\circ$.

The solid lines in Figures 2.1 (a) and (b) show the normalized magnetization distribution of circularly polarized Bessel Gaussian beam in the focal plane and along the optic axis respectively. From the figure we measured that the FWHM of the magnetic spot is 0.36λ and its corresponding magnetization depth drastically increased to 12λ .

Moreover it is observed that the axial magnetization depth remains uniform up to 10λ and gives an on axial flat top profile. It is observed from Figure 2.1 (a) the side lobe intensity of high NA lens axicon with and without phase modulation is little higher than that of the original system and it is measured as 13% of the main lobe intensity. This small raise in side lobe intensity will not produce any noise effect in recording process and it is expected the proposed system of five belt phase plate in combination with high NA lens

axicon is more suitable for high density all-optical magnetic storage.

CONCLUSION:

In conclusion, a new technique that uses use pure-phase filter in combination with high NA lens axicon to achieve a smaller magnetic focal spot with a larger uniform magnetization depth is demonstrated and analyzed numerically. It is believed that the observations reported here will lead to a design of better lens system for magneto optical recording on ultrashort time scales.

REFERENCES

1. L. P. Pitaevskii, Sov. Phys. JETP. 12 (1961) 1008.
2. J. P. van der Ziel, P. S. Pershan, and L. D. Malmstrom, Phys. Rev. Lett. 15 (1965) 190.
3. C. D. Stanciu, F. Hansteen, A. V. Kimel, A.Kirilyuk, A. Tsukamoto, A. Itoh, and Th.Rasing, Phys. Rev. Lett. 99 (2007) 47601.
4. Y. Zhang and J. Bai, Phys. Lett. A. 372 (2008) 6294.
5. L. E. Helseth, Opt. Commun. 281 (2008) 5671.
6. Y. Zhang and J. Bai, J. Opt. Soc. Am B. 26 (2009) 176.
7. Yaoju Zhang, Yoichi Okuno and Xun Xu, J.Opt. Soc. Am B. 26 (2009) 1379.
8. K. B. Rajesh and P. M. Anbarasan, Chin.Optic Lett. 6 (2008) 785.
9. K.B Rajesh, Z.Jaroszewicz , P.M.Anbarasan, Opt.Exp.18, 26 (2010) 26799
10. Z. Jaroszewicz and J. Morales, J. Opt. Soc.Am. A. 15 (1998) 2383.

NON-CONVENTIONAL JOINT TRANSFORM CORRELATOR FOR SECURITY APPLICATIONS

Sudheesh Kumar Rajput and Naveen K. Nishchal*

Department of Physics, Indian Institute of Technology Patna

Patliputra Colony, Patna-800 013, INDIA

Tel.: + 91-612-2552027; Fax: + 91-612-2277383; *E-mail: nkn@iitp.ac.in

Abstract: A non-conventional joint transform correlator for image encryption and verification is proposed. For image encryption, an input image bonded with a random phase mask and a separate key phase mask, are Fourier transformed independently. The obtained spectra are multiplexed together what is called as the encrypted joint power spectrum (EJPS). For decryption, the key phase mask is Fourier transformed and is multiplied with the EJPS, whose inverse Fourier transform results the original image. For security verification, the EJPS is inverse Fourier transformed. If image bonded phase mask matches with the key phase mask then an autocorrelation peak results in the output, which verifies the authenticity of the information. Parameters, such as signal-to-noise ratio and peak-to-side-lobe ratio have been calculated to check the effectiveness of the proposed method. Simulation results support the proposed idea.

1. INTRODUCTION

After the pioneering work proposed by Javidi and Horner [1] for security verification a large number of research papers have appeared in literature. The scheme has been modified by several researchers [2-5]. In double random phase encryption (DRPE) technique [2] the primary image is encrypted using two random phase masks (RPMs), one bonded with primary image placed in spatial domain and other placed in the Fourier domain. The DRPE technique has also been implemented using joint transform correlator (JTC) architecture, which has undergone several modifications for security verification applications [6-8]. Nomura and Javidi [6] proposed optical image encryption scheme using JTC in which input image bonded with phase mask is placed side by side with the key phase mask. The joint power spectrum (JPS) is recorded as the encrypted data. For other JTC based image verification scheme [8-10] there is no input image and both the functions at the input plane are phase-only. For given specific target image at the output plane, both the phase-only functions in the input plane can be determined by the use of a phase retrieval algorithm. The second phase function is fixed and refers to as a *lock* and the other phase function refers to as a *key*. Recently, Lu and Jin [11] proposed Fully phase color image encryption based on joint fractional Fourier transform (FRT) correlator and phase retrieval algorithm.

Based on the configuration of non-conventional JTC [12], the joint fractional correlator with FRT [13,14] and joint extended fractional correlators [15] have also been proposed. The easy implementation and its advantages over the conventional JTC scheme in terms of signal-to-noise ratio (SNR) and the accuracy of signal detection motivated us to use it for information security applications. In this paper, we propose an

image encryption and verification method employing the non-conventional JTC architecture. Intensity image and fully phase image have been used for study because complex phase patterns can be utilized for verification of authenticity of items because these patterns cannot be seen and also cannot be copied by an intensity sensitive detector. Simulation results demonstrate the successful operation of the proposed method.

2. IMAGE ENCRYPTION AND VERIFICATION SCHEME

2.1 Image encryption

The image encryption and image verification based on non-conventional JTC is shown in Figure 1. In the encryption scheme, the image bonded with an RPM and key phase mask are Fourier transformed independently. The encrypted joint power spectrum can be recorded by an intensity sensing device, which is called as the encrypted image. Fig. 1(a) shows the optical scheme for encryption. Let $f(x,y)$ represent the input image to be encrypted. The image $f(x,y)$ bonded with a phase mask $\exp[j2\pi r_1(x,y)]$ is Fourier transformed. Let $G(\xi,\eta)$ represent the Fourier transform of function $\{f(x,y) \times \exp[j2\pi r_1(x,y)]\}$.

$$G(\xi,\eta) = FT\{f(x,y) \times \exp[j2\pi r_1(x,y)]\} \quad (1)$$

where FT represents the Fourier transform. Now a key phase mask $\exp[j2\pi r_2(x,y)]$ is separately Fourier transformed. Let $R(\xi,\eta)$ represent the FT of this key phase mask.

$$R(\xi,\eta) = FT\{\exp[j2\pi r_2(x,y)]\} \quad (2)$$

Functions $r_1(x,y)$ and $r_2(x,y)$ are independent random distributions with values between 0 and 1. The coordinates (x,y) and (ξ,η) represent the coordinates of

spatial and Fourier domains, respectively. The obtained spectra from Eq. (1) and Eq. (2) are combined together what is called as the encrypted joint power spectrum (EJPS), given by

$$E(\xi, \eta) = G(\xi, \eta) \times R^*(\xi, \eta) \quad (3)$$

Here * represents the complex conjugate. Fig. 1(b) shows the optical scheme for decryption. For decryption, the encrypted image, $E(\xi, \eta)$, is multiplied with the Fourier spectrum of the key phase mask and the combined function is inverse Fourier transformed. The output can be recorded by a CCD camera as a decrypted image, $d(x, y)$.

$$d(x, y) = IFT[E(\xi, \eta) \times R(\xi, \eta)] \quad (4)$$

Here IFT represents the inverse FT operation. For optical implementation of this scheme, the EJPS can be displayed over a suitable spatial light modulator.

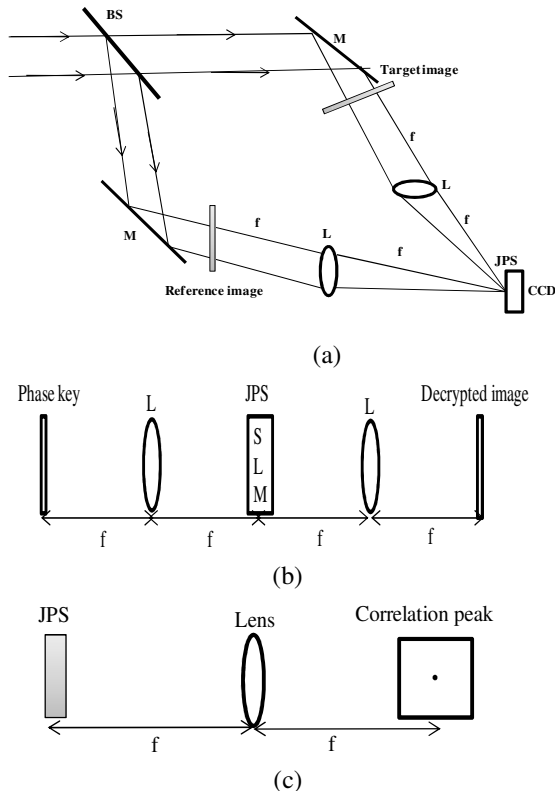


Fig. 1(a) for recording the encrypted joint power spectrum and (b) for image decryption, and (c) for image verification. BS: beam splitter, SLM: spatial light modulator, JPS: Joint power spectrum, L: lens, f: focal length of lens.

2.2. Image verification

For image authentication verification, we use the same optical scheme that was used for image

encryption as shown in Fig. 1(a). In this case, we calculate FT for both, the input image bonded with RPM and the key. Also both the RPMs used during encryption with input image and as the key phase mask must be identical. The FT of the primary image bonded with phase mask is given by Eq. (1). The FT of the key phase mask (identical to the phase mask bonded with input image) is given as

$$R_1(\xi, \eta) = FT\{\exp[j2\pi r_1(x, y)]\} \quad (5)$$

The EJPS is given as,

$$E'(\xi, \eta) = G(\xi, \eta) \times R_1^*(\xi, \eta) \quad (6)$$

Inverse FT of the EJPS, $E'(\xi, \eta)$ gives a sharp autocorrelation peak, if identical RPMs are used during encryption. Thus we find that to achieve a sharp autocorrelation peak, knowledge of the exact RPM is mandatory.

3. SIMULATION RESULTS

Numerical simulation experiment was carried out on MATLAB platform to verify the proposed idea. For simulation study, a binary text image of size 512×512 pixels has been used, as shown in Fig. 2(a). This input image is multiplied with an RPM and its Fourier transform is calculated. Another RPM used as a key is separately Fourier transformed. Thus obtained transformed spectrum gives the EJPS, as shown in Fig. 2(b). We used randomly generated two RPMs independent of each other for encrypting the input image. The decrypted image obtained after using correct keys is shown in Fig. 2(c). The decrypted image obtained after using wrong phase mask (key) is shown in Fig. 2(d). With simulation results we infer that without the knowledge of the correct keys it is not possible to retrieve the original information.

Robustness of the proposed method has been verified against occlusion/cropping attack. Figs. 3(a) and (b) show the occluded EJPS with 50% and 75% content losses, respectively. Figs. 3(c) and (d) show the corresponding decrypted images obtained respectively after using all correct keys. We find that the original information is retrieved even after 75% loss of the encrypted data. Therefore, we can infer that the proposed encryption scheme is tolerant to the data loss up to 75%.

Figs. 4(a,b) show the simulation results for image verification for intensity image of a binary text, as shown in Fig. 2(a). Fig. 4(a) shows the autocorrelation peak when the identical phase masks are used. Fig. 4(b) shows cross-correlation peak with wrong phase mask is used. Fig. 4(c) shows the phase-encoded image of binary text. Fig. 4(d) shows the autocorrelation peak

when the identical phase masks is used. Fig. 4(f) shows cross-correlation peak with wrong phase mask.

We have calculated the performance measure parameters for the proposed image verification system. Sensitivity of the autocorrelation peak to the additive noise at the input plane is measured by *SNR*. Mathematically it is defined by [16],

$$SNR = \frac{[E|C_{I,I+n}(0,0)|]^2}{VAR|C_{I,I+n}(0,0)|} \quad (7)$$

where *I* is the input image, *n* is an additive noise, and *C* is the correlation between input and output signal. Here *E{.}* denotes the expected value and *VAR* denotes the variance. The variance arises strictly as a result of noise.

Sharpness of the autocorrelation peak is measured in terms of peak-to-sidelobe ratio (*PSR*). The *PSR* characterizes how well the key phase mask matches with the phase mask bonded with the input image. The maximum output correlation value is defined by [16]

$$R_0^2 = \max[|C(u,v)|^2] \quad (8)$$

where R_0^2 is the output correlation-peak value and $C(u,v)$ is the correlation output value at (u,v) . The maximum sidelobe intensity in the correlation output plane based on R_0^2 , outside annular region is given as

$$SL = \max_{\substack{u,v > \text{circular} \\ \text{region with} \\ \text{diameter } R_0^2 / 2}} [|C(u,v)|^2] \quad (9)$$

The *PSR* is defined as [16]

$$PSR = \frac{R_0^2}{SL} \quad (10)$$

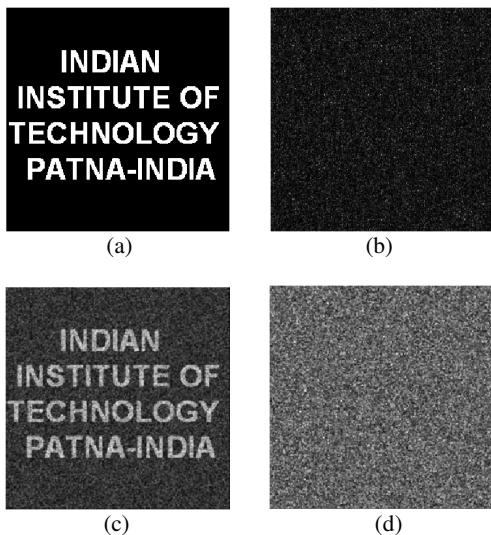


Fig. 2(a) input image, (b) encrypted image, (c) decrypted image obtained with the use of all correct keys, and (d) decrypted image with wrong key.

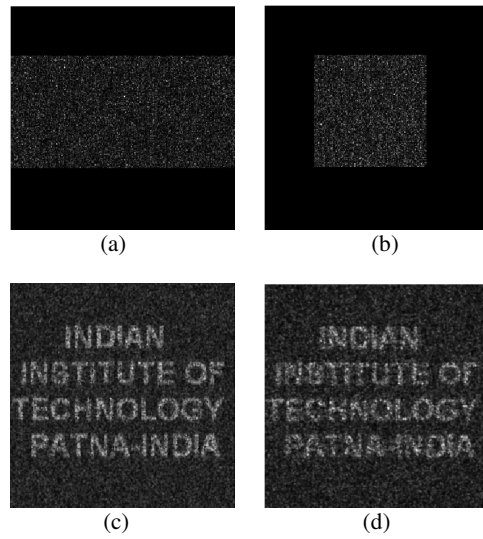


Fig. 3(a) 50% EJPS, (b) decrypted image, (c) decrypted 75% EJPS and (d) decrypted image.

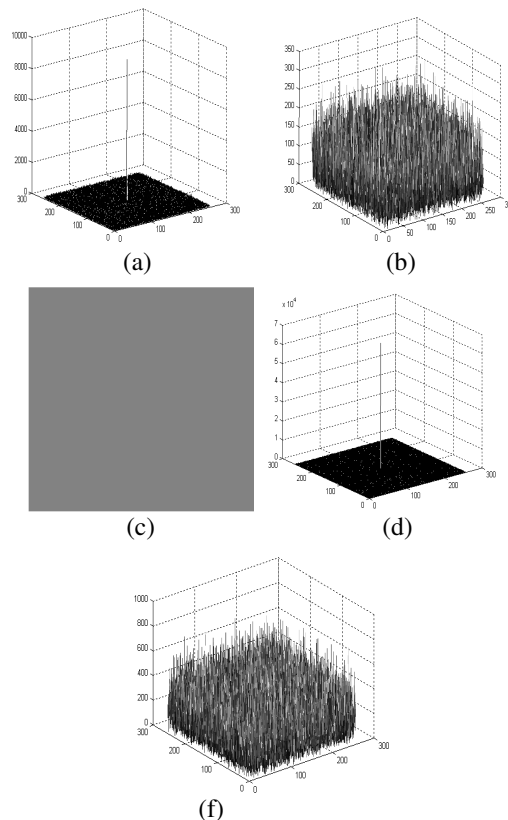


Fig. 4(a) correlation output for intensity image obtained after using correct keys, (b) correlation output for intensity image with wrong phase mask, (c) phase encoded image, (d) output for phase encoded image obtained after using correct keys, and (f) correlation output for phase encoded image with wrong phase mask.

The values of Peak intensity (PI), SNR, and PSR are calculated for the input image. The values for PI, SNR, and PSR for intensity image were 9.19×10^3 , 4.16, and 35.86, respectively. The corresponding values for phase-encoded image were 65.53×10^3 , 102.64, and 85.58, respectively. From these data we infer that values for PI, SNR, and PSR for phase-encoded image are much larger as compared to the intensity image.

3. CONCLUSION

An image encryption and verification scheme based on non-conventional JTC architecture has been proposed. The architecture offers easy optical implementation with better discrimination capability for authentication verification. For verification a fully phase image has also been used and the simulation results are encouraging. Performance measure parameters PI, SNR, and PSR have been calculated to evaluate the proposed scheme.

ACKNOWLEDGEMENT

The authors acknowledge the funding from the Council of Scientific and Industrial Research (CSIR), Government of India, under Grant No. 03/(1183)/10/EMR-II.

REFERENCES

- [1] B. Javidi, and J. L. Horner, "Optical pattern recognition for validation and security verification," *Opt. Eng.* **33**, 1752 (1994).
- [2] P. Refregier and B. Javidi, "Optical image encryption based on input plane encoding and Fourier plane encoding," *Opt. Lett.* **20**, 767 (1995).
- [3] B. Javidi, G. Zhang, and J. Li, "Experimental demonstration of random phase encoding technique for image encryption and image verification," *Opt. Eng.* **35**, 2506 (1996).
- [4] Y. Li, K. Kreske, and J. Rosen, "Security and encryption optical system based on a correlator with significant output image," *Appl. Opt.* **39**, 5295 (2000).
- [5] B. Javidi and E. Ahouzi, "Optical security system with Fourier plane encoding," *Appl. Opt.* **37**, 6248 (1998).
- [6] T. Nomura and B. Javidi, "Optical encryption using a joint transform correlator architecture," *Opt. Eng.* **39**, 2031 (2000).
- [7] T. Nomura, S. Mikan, Y. Morimoto, and B. Javidi, "Secure optical data storage with random phase key codes by use of a configuration of joint transform correlator," *Appl. Opt.* **42**, 1508 (2003).
- [8] D. Abookasis, O. Arazi, J. Rosen, and B. Javidi, "Security optical systems based on joint transform correlator with significant output images," *Opt. Eng.* **40**, 1584 (2001).
- [9] H. T. Chang and C. T. Chen, "Enhanced optical image verification based on joint transform correlator adopting Fourier hologram," *Opt. Rev.* **11**, 165 (2004).
- [10] H. T. Chang and C. C. Chen, "Fully phase asymmetric image verification system based on joint transform correlator," *Opt. Express* **14**, 1458 (2006).
- [11] D. Lu, and W. Jin, "Fully phase color image encryption based on joint fractional Fourier transform correlator and phase retrieval algorithm," *Chin. Opt. Lett.* **9**, 021002 (2011).
- [12] F. T. S. Yu, C. Zhang, Y. Jin, and D. A. Gregory, "Non-conventional joint transform correlator," *Opt. Lett.* **14**, 922 (1989).
- [13] S. Jin and S. Y. Lee, "Joint transform correlator with fractional Fourier transform," *Opt. Commun.* **207**, 161 (2002).
- [14] J. E. Rueda, M. Tebaldi, S. Granieri, and N. Bolognini, "Implementation of a photorefractive correlator based on a fake zoom lens," *Optik* **113**, 309 (2002).
- [15] W. Jin, C. Yan, L. Ma, H. Ye, and H. Wang, "Joint extended fractional Fourier transform correlator," *Opt. Commun.* **268**, 34 (2006).
- [16] B. V. K. Vijaya Kumar and L. Hasebrook, "Performance measures for correlation filters," *Appl. Opt.*, **29**, 2997 (1990).

STUDY OF BIREFRINGENCE IN POLYMERIC FLEXIBLE SUBSTRATE USED FOR DISPLAY APPLICATION BY MACH-ZEHNDER INTERFEROMETRY AND FOURIER TRANSFORM FRINGE ANALYSIS

Gyanendra Singh and D. S. Mehta^{a)}

Laser Applications and Holography Laboratory, IDDC, IIT Delhi, Hauz Khas, New Delhi -110 016, India

dsmehta@iddc.iitd.ac.in

Abstract: Polyethylene terephthalate (PET) substrates are being used for the fabrication of flexible display devices. Residual stresses are trapped in polymeric substrates due to their manufacturing process and this leads to the birefringence in flexible displays. Here, we report full field birefringence measurement of these polymeric substrates by using the Mach-Zehnder interferometry (MZI) and Fourier transform fringe (FTF) analysis technique.

1. INTRODUCTION

Nowadays, glass substrates are being replaced by the flexible plastic substrate for the flat panel display devices because of their light weight, easily scalable sizes, robustness and low cost [1]. These polymeric sheets are typically produced using the stretching process for the desired shape and thickness. During production process the mechanical stress causes the molecular re-orientation of polymeric material which leads to the structural anisotropy and to birefringence optical properties [2]. Different methods have been used by the various researchers to determine the optical birefringence of these polymeric substrates due to the mechanical stress in the fabrication process.

2. EXPERIMENTAL DETAILS

Schematic diagram of MZI set-up for the interferometric study of PET film is shown in Fig 1.

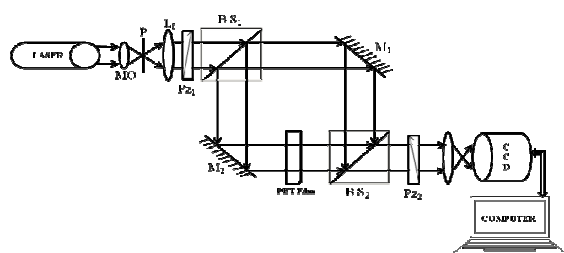


Figure 1. Schematic diagram of Mach-Zehnder interferometer.

Laser light was spatially filtered by using microscope objective (MO) and pinhole (P). The spatially filtered

collimated polarized beam was divided into two beams by beam-splitter (BS_1). The two beams were then redirected by mirror M_1 and mirror M_2 and are re-combined at the beam-splitter BS_2 . Interference fringes were passed through analyzer relayed by relay lens and recorded by the CCD camera.

3. RESULTS AND DISCUSSIONS

Recorded interferogram for two different wavelengths of light (632.8 and 532.6nm) by bending the PET sheet at various angle have been shown below in Fig. 2.

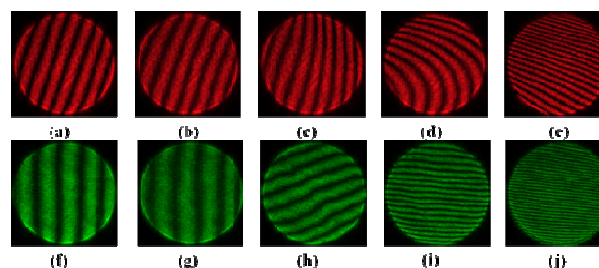


Figure 2. Optical interferogram recorded by set up shown in fig. 1 for different bending of the PET sheet by using two wavelengths.

The detailed experimental results for the measurement of birefringence are presented.

REFERENCES

- [1] D. R. Cairns and G. P. Crawford, *Proc. of the IEEE*, **93**, 1451 (2005).
- [2] M. Stchakovsky, C. Caillaud, M. Foldyna, R. Ossikovski, and E. Garcia-Caurel, *Thin Solid Films* **516**, 1414 (2008).

GENERATION OF FOCAL SHIFT WITH LARGE DEPTH OF FOCUS USING HIGH NUMERICAL APERTURE LENS AXICON

P.Suresh^a, C.Mariyal^b, C.KanchanaDevi^d, K.B. Rajesh^{*c}, Z. Jaroszewicz^f, T.V.S.Pillai^e

^{a,b} Dept. of ECE, National College of Engineering, Tirunelveli-627151, India.

^c Department of Physics, Government Arts College, Dharmapuri, India

^d Department of EEE, Anna University of Technology Tirunelveli, Tirunelveli-627007, India

^e Department of Physics, Anna University of Technology Tirunelveli, Tirunelveli-627007, India

^f Institute of Applied Optics, Department of Physical Optics and National Institute of Telecommunications, Warsaw, Poland.

* rajeskb@gmail.com

Abstract

The focusing properties of the radially polarized hollow gaussian beam (HGB) with radial phase wave front and high numerical aperture lens axicon system is investigated theoretically by vector diffraction theory. Simulation results show that the high Numerical Aperture (NA) lens axicon system generates smaller focal spot with larger depth of focus (DOF). It is observed that the radial cosine parameter C can alter the axial intensity distribution considerably and can generate tunable focal shift with large DOF along the axial direction. This kind of focal shifting with large focal depth can be used to trap elongated particles and to manipulate staked multiple spheres in optical manipulation technology.

Key Words: - Axicon, Aberration, Optical engineering, Polarization.

1. INTRODUCTION

The optical tweezers have found wide spread application for manipulation of biological or more generally, dielectric samples. Recently there has been considerable interest in the guiding of trapped particles. In order to trap long rod like samples, staking and manipulation of multiple spheres and guiding of micron sized spheres, we need a beam with smaller focal spot and extended depth of focus. Such a beam is also needed for single beam line tweezers, which is of a particular interest for studying of micromechanics with dipolar chains [1]. The focal line generated by the axicon can be approximated by a zero-order Bessel-type beam that preserves its transverse distribution along the axis. Recently we have introduced the possible design of high NA lens axicon to generate sub wavelength beam with large depth of focus [2, 3, 4]. The focal properties of tightly focused radially polarized HGB

with cosine phase wavefront were analysed using the vector diffraction theory [7]. The present paper is aimed to investigation of the tight focussing properties of radially polarized HGB with cosine phase wavefront through a high NA lens axicon system. Here we consider only systems that comprise a diverging lens that has third-order spherical aberration and a perfect high NA converging lens. The results are demonstrated numerically using vector diffraction theory.

2. THEORY OF TIGHT FOCUSING OF RADIALLY POLARIZED HGB.

In the focusing system we investigated, the radially polarized HGB is focused through an objective lens. The analysis was performed on the basis of Richards and Wolf's vectorial diffraction method [8] widely used for high-NA focusing systems at arbitrary incident polarization [9, 10]. In the case of the radial

incident polarization, adopting the cylindrical coordinates r , z and the notations of Ref. [11], the electric field of in the focal region is given by

$$\vec{E}(r, \varphi, z) = E_r \vec{e}_r + E_z \vec{e}_z \quad (1)$$

Where \vec{e}_r and \vec{e}_z are the unit vector in the radial and propagation direction respectively. E_r and E_z are the radial and longitudinal components of the electric field in the vicinity of the focal spot and can be written as

$$E_r(r, z) = A \int_{\alpha_1}^{\alpha_2} \cos^{\frac{1}{2}}(\theta) P(\theta) \sin(2\theta) J_1(kr \sin(\theta)) \exp(ikz \cos(\theta)) d\theta$$

$$E_z(r, z) = 2iA \int_{\alpha_1}^{\alpha_2} \cos^{\frac{1}{2}}(\theta) P(\theta) \sin^2(\theta) J_0(kr \sin(\theta)) \exp(ikz \cos(\theta)) d\theta$$

Here $k = 2\pi/\lambda$ is the wave number, and A denotes the amplitude of the electric field. The α_1 distinguishes the presence or absence of annulus and $\alpha_2 = \arcsin(NA/n)$, where NA is the numerical aperture and n is the index of refraction between the lens and the sample. $J_0(x)$ and $J_1(x)$ denote the Bessel functions of zero and first order, respectively. $P(\theta)$ describes the amplitude modulation. In order to describe the HGB beam with its waist in the pupil modulated by the radial cosine phase, the distribution of the electric field should be equal to [7]

$$E_0(r, \varphi, z=0) = D \cdot \left[\frac{\sin^2(\theta)}{w^2 \cdot NA^2} \right]^n \cdot \exp\left[-\frac{\sin^2(\theta)}{w^2 \cdot NA^2} \right] \cdot \exp(i\phi) \quad (2)$$

where $\omega = \omega_0/r_0$ denotes the relative waist width. Here the wavefront phase distribution is cosine function of radial coordinate and is written in the form of

$$\phi = \pi \cos\left(C \cdot \frac{\theta}{\alpha} \cdot \pi \right) \quad (3)$$

Hence the amplitude modulation of radially polarised HGB with radial cosine phase modulation is given by

$$E_0(r, \varphi, z=0) = D \cdot \left[\frac{\sin^2(\theta)}{w^2 \cdot NA^2} \right]^n \cdot \exp\left[-\frac{\sin^2(\theta)}{w^2 \cdot NA^2} \right] \cdot \exp\left[i\pi \cos\left(C \cdot \frac{\theta}{\alpha} \cdot \pi \right) \right] \quad (4)$$

3. RESULTS

We perform the integration of Eq. (1) numerically using parameters $\lambda = 1$, $NA=0.95$ and $AD=1$. Here it should be noted that the unit of coordinates in all figures in this article is k^{-1} , where k is wave number. Focus refers to the maximum optical intensity peak, and focal shift denotes the movement of this focus.

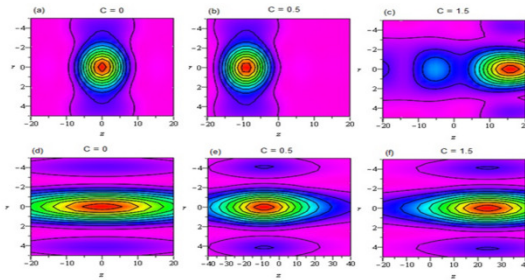


Fig. 1. Focal intensity distributions of high NA lens for $n = 1$ (a) $C = 0.0$, (b) $C = 0.5$, (c) $C = 1.5$. (d-f) Focal intensity distributions of high NA lens axicon for the same frequency parameter C

The intensity distributions in focal region of this kind of HGB for $n = 1$ are calculated by taking the square modulus of equation (1) and are illustrated in Fig. 1. It can be seen from Fig. 1 (a) that for small frequency C there is a single focal spot, and with increasing frequency parameter C , the focal spot shifts along in the axial direction towards the optical aperture, as shown in Fig.1(b). With further increase of the frequency parameter C , the focal intensity peak continues to shift along the optical axis, with its shape distorted and is shown in Fig.1(c). It is observed that this tunable focal shift is useful for optical manipulation of smaller particles but is not useful for trapping and manipulating long rod like samples and a system of stacked spheres. This is because for such a manipulation we need a system to produce smaller focal spot with large DOF capable of producing focal shifting along the optical axis without degrading the focal depth. We show that this is possible with the lens axicon by making a doublet

of aberrated diverging lens and a high NA converging lens. The intensity distribution of the lens axicon is evaluated by replacing the function $P(\theta)$ by the function $P(\theta)T(\theta)$, where $T(\theta)$ is the non-paraxial transmittance function of the thin aberrated diverging lens [2,3,4].

$$T(\theta) = \exp \left(ik \left(\beta \left(\frac{\sin(\theta)}{\sin(\alpha_2)} \right) \right)^4 + \left(\frac{1}{2f} \left(\frac{\sin(\theta)}{\sin(\alpha_2)} \right)^2 \right) \right) \quad (5)$$

Here $k = 2\pi/\lambda$, f is the focal length and β is the aberration coefficient. In our calculations we have taken $f = 18.4\text{mm}$, $\beta = 6.667 \times 10^{-5} \text{mm}^{-3}$, this results in an equiconcave diverging lens that is simple to manufacture. The intensity profile of high NA lens axicon is calculated by including the transmission function of the aberrated diverging lens on the aperture of the high NA focusing lens and is shown in Fig. 1(d-f). From the Fig.1(d) it is observed that the lens axicon generates a smaller focal spot with extended DOF when compared to the lens of same NA. It is also observed that for small frequency parameter C , this focal spot with large DOF starts to shift along in the axial direction towards the optical aperture, as shown in Fig. 1(e). However, further increasing of C makes this focal spot with large DOF to continue the shift along the optical axis without any distortion in shape and is shown in Fig.1 (f).

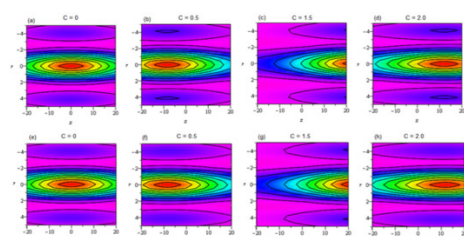


Fig 2. Focal intensity distributions of high NA lens axicon for $n = 1$ (a) $C = 0.0$, (b) $C = 0.5$, (c) $C = 1.5$ and (d) $C = 2.0$. (e-h) Focal intensity distributions of high NA lens axicon for the same frequency parameter C and $n = 3$

We have also investigated the intensity distribution in the focal region of the high NA lens axicon for the radially polarized HGB with cosine wavefront under the condition of different beam order n . Fig. 2(a-d) illustrates the focal intensity distributions of the high NA lens axicon for $n = 1$ and range of C from 0 to 2. Fig.2 (e-h) illustrates the focal intensity distributions of the high NA lens axicon for $n = 3$ for the same frequency parameter mentioned above. It can be observed from the Fig.2 (a-h) that the focal shift pattern is almost the same for different beam order.

CONCLUSION

Concluding, a tight focusing of a radially polarized cosine phase modulated HGB beam with high NA lens axicon was studied basing on the vector diffraction theory. Simulation results show that the radial cosine parameter C can alter the axial intensity distribution considerably and can generate tunable focal shift with large DOF along the axial direction. It is also observed that focal shift pattern generated by the high NA lens axicon remains the same for different beam order n . The authors expect that the proposed system which generates tunable focal shift with large DOF will turn out more useful to trap and manipulate rod like structures and to manipulate systems of stacked sphere.

References

- [1] E.M. Furst, A.P. Gast, "Micromechanics of dipolar chains using optical tweezers", Phys.Rev. Lett. **82** (1999) 4130-4133.
- [2] K.B.Rajesh, Z.Jaroszewicz, P.M. Anbarasan, "Improvement of lens axicon's performance for longitudinally polarized beam generation by adding a dedicated phase transmittance," Opt. Express **18**, (2010), 26799-26805
- [3] K.B. Rajesh, N. Veerabagu Suresh, P.M. Anbarasan, K. Gokulakrishnan, G. Mahadevan, "Tight focusing of double ring shaped radially polarized beam with high NA lens axicon" Opt. and Laser Tech., **43**, (2010), 1037-1040.

- [4] K.B. Rajesh, Zbigniew Jaroszewicz, P.M. Anbarasan, T.V.S. Pillai and N. Veerabagu Suresh. "Extending the depth of focus with high NA lens axicon", *Optik* **122**, (2011), 1619-1621.
- [5] G. Wu, Q. Lou, J. Zhou, Analytical vectorial structure of hollow Gaussian beams in the far field, *Opt. Express* **16** (2008) 6417–6424.
- [6] D. Deng, H. Yu, S. Xu, G. Tian, Z. Fan, "Nonparaxial propagation of vectorial hollow Gaussian beams", *J. Opt. Soc. Am. B* **25** (2008) 83–87.
- [7] X.Gao, M.Gao, Q. Zhan, J.Li, H.Guo, J. Wang, S.Zhuang. "Focal shift in radially polarized hollow Gaussian beam". *Optik*, **22**, (2011), 671-76.
- [8] Richards B, Wolf E. "Electromagnetic diffraction in optical systems. II. Structure of the image field in an aplanatic system". *Proc R Soc London Ser A* **253** (1959) 358–79.
- [9] C.C Sun, C.K Liu. "Ultra small focusing spot with a long depth of focus based on polarization and phase modulation". *Opt. Lett.* **28**, (2003), 99–101.
- [10] TG Jabbour, SM Kuebler. "Vector diffraction analysis of high numerical aperture focused beams modified by two- and three-zone annular multi-phase plates." *Opt Express*, **14**, (2006), 1033–43.
- [11] K Youngworth, T Brown. "Focusing of high numerical aperture cylindrical vector beams". *Opt Express*, **7**, (2000), 77–87.

ELASTIC SCATTERING NORMALIZED SYNCHRONOUS FLUORESCENCE SPECTROSCOPY FOR MULTICOMPONENTS EXTRACTION FROM HUMAN CERVICAL TISSUES

Seema Devi^a, Meghdoot Mozumder^a, Asima Pradhan^{a,c}

^aDepartment of Physics Indian Institute of Technology, Kanpur, India – 208016;

^cCenter for Laser Technology, Indian Institute of Technology, Kanpur, India – 208016
seemad@iitk.ac.in

Abstract: Fluorescence spectroscopy is an efficient technique to detect biochemical activities that occur during early stage of cervical cancer. However, the emission bands of multiple fluorophores generally overlap and individual fluorophore activities are difficult to isolate. Synchronous fluorescence spectroscopy has been demonstrated to decouple the overlapping spectra by choosing appropriate offsets during signal acquisition. Even here, there is still an effect of absorption by chromophores which distorts the information regarding individual fluorophores. We report the effect of normalizing the measured spectrum by the elastic scattering spectrum where the absorption effects due to chromophores and other fluorophores are diminished and several less dominant peaks are highlighted.

1. INTRODUCTION

Cervical cancer ranks as the 3rd most frequent cancer in women in the world and the World Health Organization (WHO) has estimated that there are 2 billion women in the world of ages 15 years and older who are at risk of developing cervical cancer. Statistics released by WHO indicates that every year about 500,000 women are diagnosed with cervical cancer and nearly 300,000 die from the disease¹.

Pre-cancerous cells can take 10-15 years to develop into cancer and more than 90% of the cancer are curable if the disease is detected and treated early enough². This highlights the importance of developing techniques that can detect cervical cancers in their nascent stage.

Optical techniques for cancer detection have come into prominence as it promises efficient objective tests for cancers. A cheap early detection technique such as fluorescence spectroscopy can be utilized for extraction of biochemical changes that lead to cancer growth. Several endogenous fluorophores are present in the tissue whose fluorescence properties are highly correlated to the pathological changes taking place during the progression of the diseases³. However, absorption and scattering effects by the chromophores, fluorophores and scatterers present in turbid tissue modify the intrinsic fluorescence spectra native to the tissue. Moreover, due to a large number of fluorophores present within a narrow wavelength regime, the fluorophore activities due to individual fluorophores are difficult to quantify. The information content of the individual fluorophore is vital in distinguishing the normal tissue from the diseased ones and so is a challenge that researchers have pursued by developing various algorithms for extracting the intrinsic fluorescence.

A simple way to decouple the activity of individual fluorophore in a single acquisition with the selection of an appropriate offset wavelength between excitation and emission wavelength is offered by

synchronous fluorescence spectroscopy. Such a spectrum is recorded by scanning of the excitation and emission wavelengths simultaneously, while maintaining a constant wavelength offset between them throughout recording of the spectrum. As a result, the synchronous fluorescence intensity can be written as the product of two functions⁴-

$$I_s(\lambda_{exc}, \lambda_{em}) = KcdE_x(\lambda_{exc})E_m(\lambda_{em}) \quad (1)$$

where **K** is a constant factor that depends upon the variation in the molar extinction coefficient with respect to the intensity distribution; **c** is concentration of the fluorophores; **d** is the path length of photons; and **E_x** and **E_m** are intensity distribution patterns of the excitation and emission wavelengths, respectively.

It has been demonstrated that synchronous fluorescence spectroscopy may be a viable tool for extraction of individual fluorophore activities using appropriate offset during signal acquisition.⁵⁻⁶ However, the effect of absorption by chromophores or other fluorophores masks few characteristic peaks. In this report, we demonstrate that by operating upon the measured synchronous fluorescence spectrum by the elastic scattering spectrum enhances the spectral features by diminishing absorption effects. Twenty nine cervical tissues were studied using different offsets and an optimum offset of 55nm was baselined.

2. MATERIALS AND METHODS

The synchronous fluorescence spectra with different wavelength offsets of 29 fresh cervical tissue specimens were recorded using a commercial spectrofluorometer (SPEX, Fluorolog 3, Model FL3-22) which has a 450 W xenon lamp as the source. Quartz cuvette containing cervical tissue samples was placed in sample holder and the spectra were recorded in backscattering mode at an angle of 22.5° with respect

to the incident unpolarized light. The epithelium layer of the tissue was exposed to the incident unpolarized light with 20nm, 40nm, 55nm, 90nm and 120nm offset wavelengths and spectra were recorded for the wavelength range 250-650nm with integration time of 0.1s and with wavelength interval of 1nm. In addition, corresponding elastic scattering spectra were also recorded with zero offset wavelengths between excitation and emission monochromator.

Fresh cervical tissue samples used in experiment were provided by the G.S.V.M. Medical College in two separate vials labeled as normal and abnormal. The samples were rinsed with saline water to remove superficial blood before performing the experiment. After completing the signal acquisition, these tissue samples were sent back to medical college for histopathology analysis.

The formula used to get information of hidden peaks from the tissue samples, using the above recorded data, is given below:

$$F_{SYN}^{EXTRACTED}(\lambda) = \frac{F_{SYN}^{MEASURED}(\lambda)}{\{R(\lambda) \times R^M(\lambda + \Delta\lambda)\}^{0.5}} \quad (2)$$

Here $R(\lambda)$ represents the elastic scattering of excitation photons before their interaction with fluorophores and $R(\lambda + \Delta\lambda)$ is the elastic scattering of isotropically scattered fluorescence photons. On an average both these processes contribute equally to the entire path of the measurements. M ($=N_{AVERAGE}^{FLUORESCENCE} / N_{AVERAGE}^{ESS}$) is used to account the discrepancies between the contribution of average number of scattering events suffered by fluorescence photons at any emission wavelength λ_{EM} to that of the elastically scattered photons at the same wavelength⁷. In this case M is calculated to be 0.87.

3. RESULT AND DISCUSSION

Figure 1 shows the typical measured synchronous fluorescence spectrum, the elastic scattering spectrum and the extracted synchronous fluorescence spectrum for a 55nm offset. It can be seen that several hidden peaks in the bulk synchronous fluorescence spectrum are now extracted in the intrinsic synchronous fluorescence spectrum after dividing by the elastic scattering spectrum according to the formula (2)⁸.

Among the different offsets as shown in figure 2, it was observed that 55nm offset show distinct narrow peaks that can be further used for monitoring biochemical activities among different tissue types. The peaks obtained using this technique are narrower and sharper and hence can be used efficiently for extraction of individual fluorophore activities for different tissue grades.

It can be observed from figure 2 that due the presence of different native fluorophores, the intensity of emission peaks vary with offset wavelengths⁷.

Figure 3 shows the extracted synchronous fluorescence curves for normal and dysplastic cervical tissue with a 55nm offset. As shown in the figure 4 (a & b), the difference between histopathologically certified normal and dysplastic tissues can be found from the scatter plot of collagen peak intensity of measured and extracted synchronous spectra.

Further, it is observed that sensitivity and specificity of measured synchronous spectra is 83% and 50% respectively for the intensity of the collagen peak. However, the extracted synchronous spectra show sensitivity as 88% and specificity as 50%. We can therefore conclude that the technique presented discriminates the normal and dysplastic tissue better than measured synchronous scan.

Covariance maps shown in figure 5 highlight these differences in collagen for all samples.

Conclusion

The extracted synchronous fluorescence spectra patterns clearly expose most of the biomolecules present in tissue. The extracted synchronous fluorescence technique described in the paper demonstrates high sensitivity in comparison to the measured synchronous fluorescence. In view of these results, it appears that the technique presented in this paper holds promise as an improved diagnostic tool for cervical precancer.

4. FIGURES

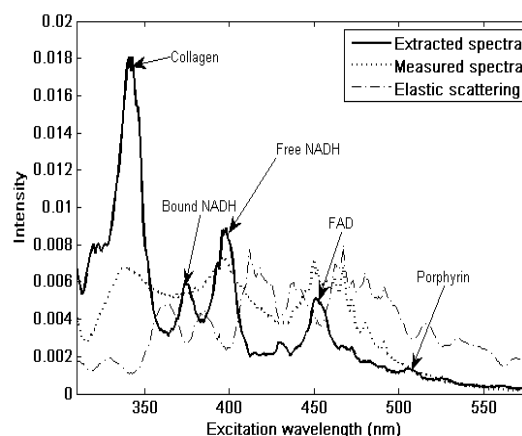


Figure 1: Typical measured synchronous fluorescence spectrum of a human cervical tissue with its elastic scattering and extracted synchronous fluorescence spectrum for 55nm offset.

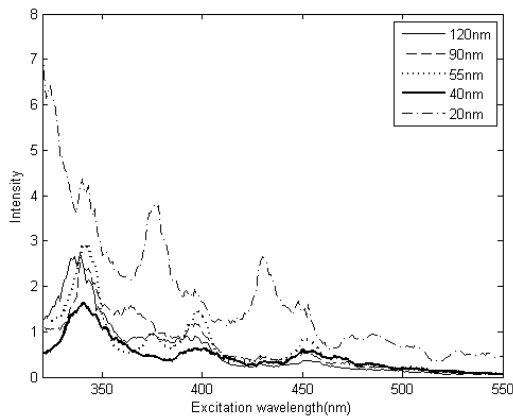


Figure 2 Extracted synchronous fluorescence spectra for different offset wavelengths respectively.

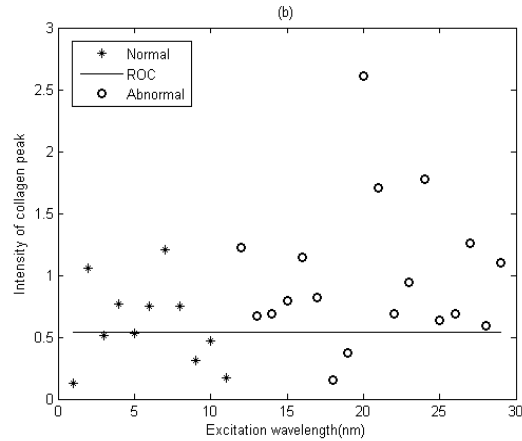


Figure 4: (a) & (b) Scatter plot of collagen peak intensity at 55nm offset for measured and extracted synchronous fluorescence spectra respectively of histopathologically certified normal and dysplastic cervical tissue samples.

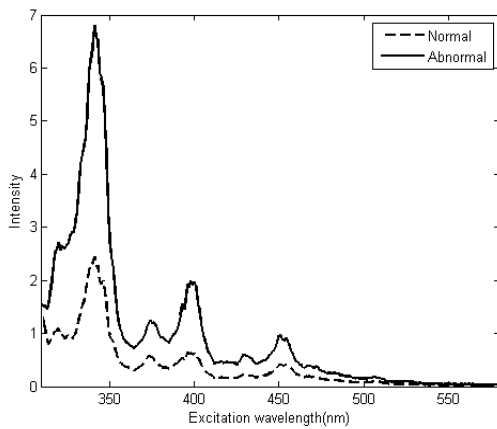


Figure 3: Typical extracted synchronous fluorescence spectra of normal and dysplastic cervical tissue with 55nm offset.

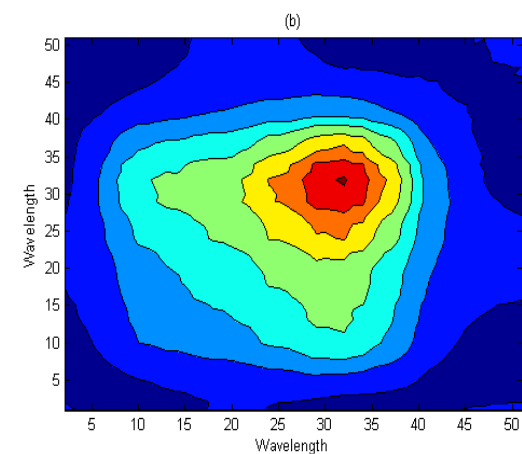
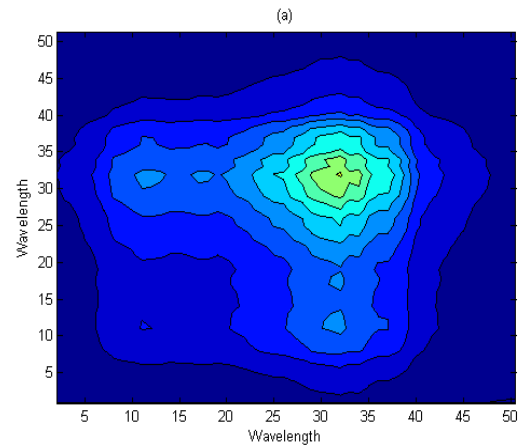
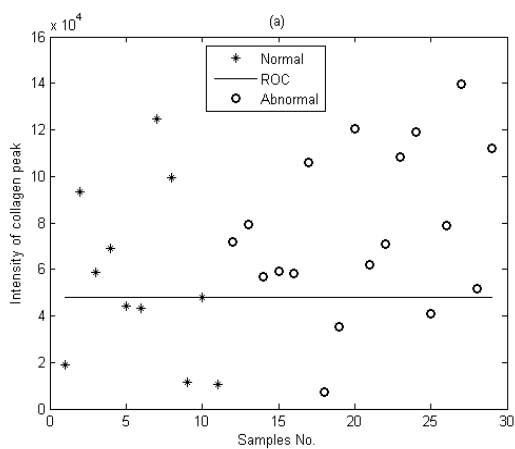


Figure 5: (a) & (b) Covariance matrix plots of histopathologically certified normal and dysplastic human cervical tissues show a high correlation among patients respectively for 55nm offset.



ACKNOWLEDGEMENT

The authors wish to acknowledge Dr. Kiran Pandey and Dr. Asha Agarwal of GSVM medical college, Kanpur for providing tissues and for fruitful discussions.

REFERENCES

- [1] <http://www.who.int/hpvcentre/statistics/en/>.
- [2] <http://www.cervicalcancer.org/statistics.html>
- [3] N. Ramanujam, *Neoplasia*, “Fluorescence spectroscopy of neoplastic and non-neoplastic tissues” vol. 2, pp. 89–117,(2000).
- [4] T. Vo-Dinh, *Appl. Spectrosc.*, “Synchronous luminescence spectroscopy: methodology and applicability”, vol.36, pp. 576–581(1982).
- [5] R R Alfano and Yuanlong Yang, “Stokes shift emission spectroscopy of human tissue and key biomolecules”, *IEEE JSTQE* 9(2), 2003.
- [6] Q Liu, G Grant and T Vo-Dinh, “Investigation of synchronous fluorescence method in multicomponent analysis in tissue”, *IEEE JSTQE* 16(4), 2010.
- [7] R. R. Alfano, Y. Yang, “Stokes shift emission spectroscopy of key biomolecules in human tissues” *Proceedings of SPIE* vol. 5326, 1605-742 2 (2004).
- [8] R Drezek, K Sokolov, U Utzinger and I Boiko, A Malpica, M Follen, R,R Kortum, “Understanding the contributions of NADH and collagen to cervical tissue fluorescence spectra: Modeling, measurements, and implications”, *Journal of Biomedical Optics* 6(4), page 385–396, 2001.

TESTING OF HANDHELD PROBE FOR EARLY DETECTION OF CERVICAL CANCER THROUGH POLARIZED FLUORESCENCE SPECTROSCOPY

Ravi Kumar^a, Srinivasa BS^a, Jaidip Japtap^b, Dr. Asha Agarwal^c, Dr. Kiran Pandey^c, Dr. Asima Pradhan^{a,b}

^aCenter for Laser Technology, Indian Institute of Technology, Kanpur, India – 208016

^bDepartment of Physics, Indian Institute of Technology, Kanpur, India – 208016

^cGSVM Medical College, Kanpur, India – 208016;

asima@iitk.ac.in

Abstract: Fluorescence spectroscopy can be an effective tool to discriminate dysplastic human cervical tissue from normal. However, vital information is masked due to scatterers and absorbers in turbid media like tissue. Hence a method of polarized fluorescence is developed and implemented in a handheld probe that may enable non-invasive clinical detection of cancers. This probe was tested in-vitro for detection of cervical pre-cancers.

1. INTRODUCTION

The *cervix* is the lower third portion of the uterus (womb). It serves as a neck to connect the uterus to the vagina. Cervical cancer occurs when cells in the cervix grow erratically and multiply out of control [1]. Pre-cancerous cells can take 10-15 years to develop into cancer so early detection is very important in treating cervical cancer. Fortunately, more than 90% of this type of cancer is curable if the disease is detected and treated early enough [2]. In spite of this, a woman dies of cervical cancer approximately every 2 minutes due to limitations in the current screening techniques.

The popular screening techniques for cervical cancers in vogue presently are the Papanicolaou test (Pap smear) and colposcopy. These are generally followed by biopsy for better accuracy in diagnosis and grading. Pap smear has significant false negative results as the accuracy is limited by sampling and reading errors [3,4]. Colposcopy can identify the location of the lesion but is not reliable in diagnosing the severity of the lesion. Colposcopy has average sensitivity of 96% and a very low specificity of 48% [5]. This indicates that many samples are overcalled or missed during the conventional screening.

The shortcomings of the screening techniques underline the importance of developing efficient diagnostic methods and instruments through novel means. Investigation of optical spectroscopy and imaging techniques are gaining prominence as they are minimally invasive and can provide qualitative results. Spectroscopic techniques have the advantage of being able to detect and to quantitatively assess changes in the cellular chemistry and tissue architecture associated with the progression of the disease. Fluorescence spectroscopy is an extremely sensitive tool for sensing subtle biochemical changes and has been extensively used both in vitro and in vivo studies of various organ systems [6]. Such studies have demonstrated the potential of

fluorescence spectroscopy to differentiate normal and abnormal tissue [6-8]. Differences in cellular chemistry associated with tissue pathology are reflected on the fluorescence spectral profiles providing quantitative diagnostic information. For example, studies have shown that abnormal tissues have a larger concentration of NADH at the epithelium layer due to higher metabolic activity in abnormal areas [9]. NADH is a natural fluorophore whose fluorescence peak is at 470nm under UV light irradiation. This indicates that abnormal tissues can be differentiated from normal ones based on their fluorescence intensity. However, the biochemical information is generally masked by scatterers and absorbers and lead to inconsistent results [10]. Such problems may be mitigated by extracting the intrinsic fluorescence using polarized light [10-13]. Polarized Fluorescence spectroscopy is a new diagnostic modality with the potential to bridge the gap between clinical examination and invasive biopsy [14]. To facilitate the clinical in-vivo use, a handheld probe was conceptualized to access the cervix directly and conduct fluorescence measurements. Such a probe was designed and tested in-vitro on fresh human cervical tissues provided by GSVM medical college and found to have promising results.

2. MATERIALS AND METHODS

The handheld probe is designed for in vivo clinical probing of the cervical cavity. However, all the tests described in this paper were conducted with the handheld probe on cervical tissue samples in vitro to investigate the efficiency of the design of the set up.

We received cervical tissue samples of 16 patients from the GSVM Medical College, Kanpur. For every patient we were provided two chunks of biopsy samples, normal and abnormal for fluorescence studies. The samples were washed in saline solution to remove excess blood and to keep the tissue moist during the measurements. The tissue chunk was

mounted on a slide and kept below the probe. Signals were recorded in co-polarized and cross-polarized modes.

We used a laser diode (375nm, Shanghai Dream Lasers, SDL-375-LM-010T) as the source and a CCD (Andor, DV 420 BV) as detector.

A laser diode was chosen to be the source as this ensured that the handheld probe was made compact by mounting the diode on the handheld probe itself. The low divergence and high output power of the laser diode at the sample site in comparison with other sources (eg. Xenon lamp) enables sufficient and easy focusing of the light on the tissue sample.

The CCD detector unit has a Spectrograph (Andor, Shamrock 303i) attached in front of it for spectral resolution.

The handheld probe consists of a source arm, a probe arm and a detector arm joined in a T configuration with a beam splitter at the junction and as shown by the schematic representation in figure 1. The probe arm is meant to be inserted into the cervix for probing the cervical area, while the source and detector arms remain outside the body. The dimensions of the probe arm were fine-tuned for minimal pain during insertion into the cervical cavity.

Figure 1 describes the design of the handheld probe. The source arm has the laser source mounted at one end and contains a converging lens and a polarizer. The light from the laser source is incident onto the beam splitter through the converging lens and is linearly polarized in either the parallel or perpendicular axis by the polarizer. The reflected part of the beam from the beam splitter enters the probe arm and is focused on to the tissue sample by means of two convex lenses. The incident light excites the cervical tissue fluorophores and causes fluorescence. A part of the emitted fluorescence is transmitted back through the beam splitter into the detector arm. The detector arm has the analyzer and a linear fiber array placed at the end of the detector arm. This makes possible the detection of a particular mode of polarized light emanating from the cervical tissue. The fiber jig focuses the collected light on to a spectrograph CCD arrangement.

The entire system is placed within a T-shaped modular tube to make it sturdy, portable and to minimize stray light. Data is measured in both the co and cross polarized states with this handheld probe after testing the configuration in the open setup.

3. RESULTS AND DISCUSSIONS

The typical fluorescence spectra recorded from normal and abnormal cervical tissues in the co-polarized state is as shown in figure 2, and the spectra recorded with cross-polarized state is as shown in figure 3. It is seen that the fluorescence intensity of abnormal cervical tissue is significantly higher than

that of the normal cervical tissues which could be due to the fact that the abnormal tissues have a higher concentration of the fluorophore, NADH. This observation means that fluorescence intensity may be used as a discrimination feature for classifying tissues as normal or diseased.

In our study, the cut-off line discriminating the abnormal and normal cervical tissues was obtained through ROC analysis is used on the relative area of the fluorescence band to the total area. As the NADH fluorescence spectrum peaks at around 470 nm, we chose a band 460-480 nm in the spectrum and calculated the area of this band. This NADH band area is normalized by the total. The samples were sent for histopathology and the histopathological report was accepted to be the gold standard while standardizing the handheld probe setup. Figure 4 and 5 shows the scatter plot of the patients against this normalized area for each patient in co and cross polarized modes respectively.

For 16 patients, we have obtained the values of sensitivity and specificity as 81% and 62% respectively for co-polarized mode. Similarly cross-polarized spectra were recorded for 10 patients and sensitivity of 60% and specificity of 70% were observed.

The sensitivity and specificity are not high for cross polarized data, which is expected since absorption and scattering mask intrinsic information. Co-polarization, on the other hand, displays a good sensitivity due to the retention of intrinsic information of the fluorophores.

The obtained values of sensitivity and specificity demonstrate that the technique presented is viable for cancer diagnosis. Intrinsic fluorescence is currently being pursued to improve the efficiency.

4. FIGURES

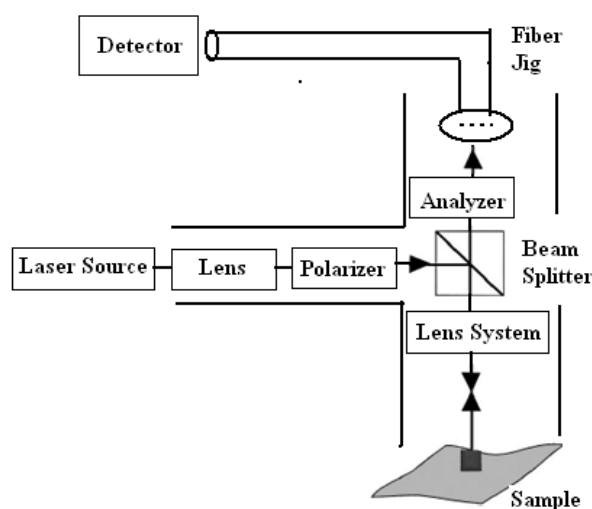


Figure 1: Block diagram of the handheld probe.

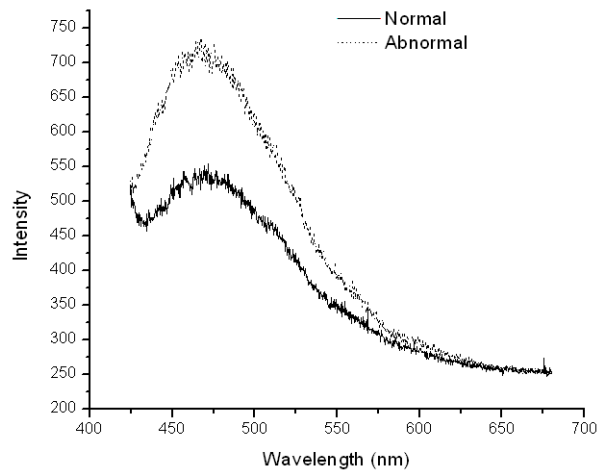


Figure 2: Typical fluorescence spectra of normal and abnormal cervical tissues (co-polarized).

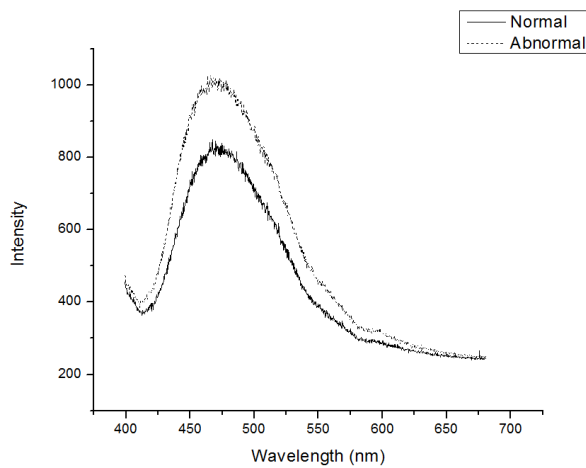


Figure 3: Typical fluorescence spectra of normal and abnormal cervical tissues (cross-polarized).

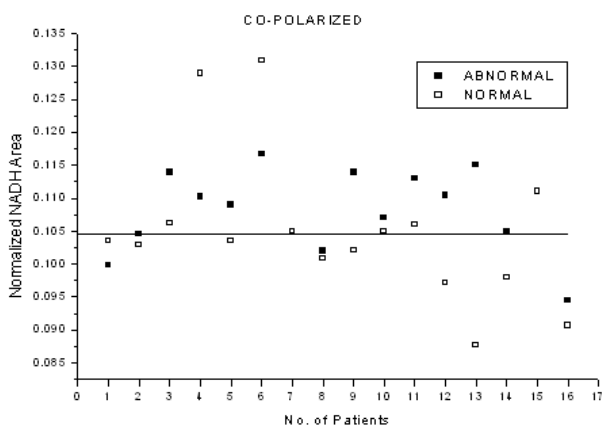


Figure 4: Scatter plot NADH component of 16 patients in co-polarized mode showing sensitivity of 81% and specificity of 62%

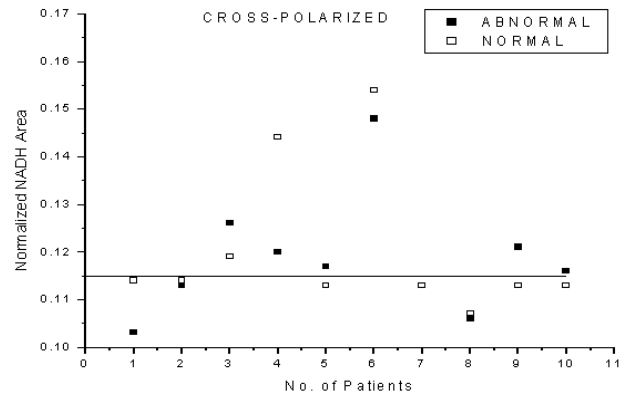


Figure 5: Scatter plot NADH component of 10 patients in cross-polarized mode showing sensitivity of 60% and specificity of 70%

ACKNOWLEDGEMENT

The authors wish to acknowledge the Department of Information Technology, MCIT, Govt. of India for funding the research.

REFERENCES

1. <http://www.imaginis.com/cervical-cancer/cervical-cancer-introduction>
2. <http://www.cervicalcancer.org/statistics.html>
3. S. Pairwuti, "False-negative papanicolaou smears from women with cancerous and precancerous lesions of the uterine cervix", *Acta Cytol.*, vol. 35, p. 40, 1991.
4. Nanda K, McCrory DC, Myers ER et al., "Accuracy of the papanicolaou test in screening for and follow up of cervical cytologic abnormalities: a systematic review." *Ann Intern Med.* 2000; 132:810-819
5. M. F. Mitchell, "Accuracy of Colposcopy", *Consult. Obstet Gynecol.*, vol. 6, p. 70, 1994.
6. R. R. Richards-Kortum, M. F. Mitchell, N. Ramanujam, A. Mahadevan and S. Thomsen, "In Vivo fluorescence spectroscopy: Potential for noninvasive, automated diagnosis of CIN and use as a surrogate endpoint biomarker", *J. Cell. Biochem.*, vol 19, pp. 111-119, 1994. (Suppl.)

7. Mahadevan Jasen A, Mitchell ME, Silva E, Thomsen S, Kortum KR., "Study of the fluorescence properties of normal and neoplastic human cervical tissues", *Laser Surg Med*, 1993; 13:647-55
8. R.R.Alfano, G.C.Tang, A.Pradhan, W.Lam, D.S.J. Choy, E.Opher, "Fluorescence spectra from cancerous and normal human breast and lung tissues," *IEEE J. Quantum Electron.* 23 (10), 1806-1811 (1987).
9. Drezek R et al. "Understanding the contributions of NaDH and collagen to cervical tissue fluorescence spectra: Modelling, measurements and implications", *J Biomed Opt* 20°1:6:385-96.
10. M. Keijzer, R.R. Kortum, S.L. Jacques, M.S. Feld, "Fluorescence spectroscopy of turbid media: Autofluorescence of the human aorta," *Appl. Opt.* 28, 4286 – 4292 (1989).
11. A.J. Durkin, S. Jaikumar, N. Ramanujam, R.R. Kortum, "Relation between fluorescence spectra of dilute and turbid samples," *Appl. Opt.* 33, 414 – 423 (1994).
12. Dharitri Rath; Md. Ejaz A. Lodhi; Prashant Shukla; Nidhi Agarwal; Kiran Pandey and Asima Pradhan, "Comparative study of intrinsic versus bulk polarized fluorescence in cervical tissues", *Proc. of SPIE* Vol 6853 685319, 2008
13. NC Biswal, S. Gupta, Nirmalya Ghosh and Asima Pradhan, "Recovery of turbidity free fluorescence from measured fluorescence: an experimental approach", *Optic Express*, Vol 11, No. 24 (2003).
14. Asima Pradhan et. al, Polarized fluorescence study in human cervical tissue: change in autofluorescence through different excitation wavelengths, *Proc. of SPIE*, 6853 (2010).

OPTICAL COHERENCE TOMOGRAPHY FOR NON-INVASIVE ASSESSMENT OF WOUND HEALING RESPONSE IN *PAERUGINOSA* INFECTED EXCISIONAL WOUNDS SUBJECTED TO PHOTODYNAMIC TREATMENT

K. Sahu, Y. Verma, M. Sharma, K. Divakar Rao, A. Dube and P. K. Gupta
Laser Biomedical Applications and Instrumentation Division
Raja Ramanna Centre for Advanced Technology, Indore 452 013 (India)
Email: kdivakar@rrcat.gov.in

Abstract: We report the use of optical coherence tomography (OCT) for non invasive monitoring of the healing of excisional mice skin wounds infected with a virulent strain of *P.aeruginosa*. Results of our study show that antimicrobial photodynamic treatment improves wound healing.

1. INTRODUCTION

Optical coherence tomography (OCT) is a non contact imaging modality for two-dimensional cross sectional imaging of biological tissues in real time with micrometer scale resolution [1]. As OCT can penetrate 2-3 mm in biological tissues, it is an attractive tool for monitoring the healing of cutaneous wounds. Polarization sensitive OCT (PS-OCT) can provide functional information such as collagen denaturation in terms of the changes in birefringence of the tissue. Anti-microbial photodynamic treatment (PDT) is very promising for treatment of localized wound infections [2]. Here we report studies carried out on the use of OCT imaging for monitoring the healing dynamics of excisional mice skin wounds infected with virulent strain of *Pseudomonas aeruginosa* and of the infected wounds subjected to PDT with polylysine chlorine p6 conjugate (pl-Cp₆).

2. MATERIALS AND METHODS

An excisional wound of ~1.2 x 1cm was created on the back of female Swiss albino mice and infected with 25µl (~ 10⁷ cells/ml) of stationary phase *P.aeruginosa* (MTCC 3541, Chandigarh, India) grown aerobically in tryptone soya agar broth. All the mice with excisional wounds were divided into four groups as: (1) uninfected, (2) infected control (infected but neither treated with conjugate nor light), (3) dark control (wounds infected with bacteria and treated with conjugate in the dark), (4) PDT group (wounds infected with bacteria, conjugate, and red light). The conjugate pl-Cp₆ (200 µM in 20 µl) was applied to the wounds 18h post bacteria application and following 30 minutes incubation, the wounds in the PDT group were illuminated with red light (660 ± 25 nm) at a power density ~100 mW/cm² to achieve irradiation doses of 60 and 120 J/cm². A PS-OCT setup was used for carrying out both intensity and retardance imaging of the wounds at different post wounding time points. Details of the setup are described in our earlier report [3]. Histology of excised wounds was carried out at the end of imaging experiments on day 21 to compare

the morphological changes in the wound tissue.

3. RESULTS & DISCUSSION

Figure 1 shows OCT images of uninfected (a), infected (b) and photodynamically treated infected (c) wounds acquired on day 21 post wounding. Compared to the uninfected wounds, the infected wound shows delayed healing as indicated by the presence of OCT signal free edematous region (arrow) and a high signal intensity crust (*) region. On the other hand, the photodynamically treated wound shows absence of any edema as evidenced by uniform scattering intensity. These changes indicate a faster healing of photodynamically treated wounds and were also validated by histology. In addition changes in collagen matrix of infected and treated wounds were also investigated by polarization sensitive OCT. Details of this study will be presented.

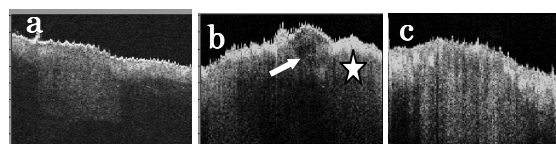


Fig 1: OCT images of mice skin wounds on day 21. a: Uninfected; b: Infected and dark control; c: Infected and subjected to PDT (60 J/cm²).

REFERENCES

- [1] A. F. Fercher, "Optical coherence tomography—development, principles, applications", *Z. Med. Phys.* **20**, 251 (2010).
- [2] T. Daia, Ying-Ying Huang, M. R. Hamblin, "Photodynamic therapy for localized infections – state of the art", *Photodiagnosis Photodynamic Ther* **6**, 170 (2009).
- [3] K. Sahu, Y. Verma, M. Sharma, K. D. Rao and P. K. Gupta, Noninvasive assessment of healing of bacteria infected and uninfected wounds using optical coherence tomography, *Skin Res. and Technol.* **16**, 428 (2010).

DEPTH-SENSITIVE RAMAN SPECTROSCOPY COMBINED WITH OPTICAL COHERENCE TOMOGRAPHY FOR ANALYSIS OF LAYERED TISSUE

K. M. Khan, H. Krishna, K. Divakar Rao, *S. K. Majumder and P. K. Gupta
Laser Biomedical Applications and Instrumentation Division, Raja Ramanna Centre for Advanced Technology, Indore - 452013, India
*shkm@rrcat.gov.in

Abstract: We report development of a combined depth-sensitive Raman spectroscopy and time-domain optical coherence tomography set-up and its validation using non-biological and biological layered phantoms.

1. INTRODUCTION

There is an increasing current interest in the development of dual-modal instruments combining the molecular specificity of Raman Spectroscopy (RS) with the sensitivity and rapid screening capabilities of high resolution microscopic optical imaging like Optical Coherence Tomography (OCT) [1]. However, a major limitation of systems developed thus far is that there is no direct correlation between the OCT information at a given depth to the Raman signal of that particular depth. We report development of a combined RS-OCT system capable of obtaining Raman signal corresponding to OCT locations at different depths of interrogation of a tissue sample.

2. EXPERIMENTAL METHODS

A real-time, time-domain (TD) OCT system was used as the platform for the development of the combined RS-OCT set-up. A schematic of the system is shown in Fig.-1.

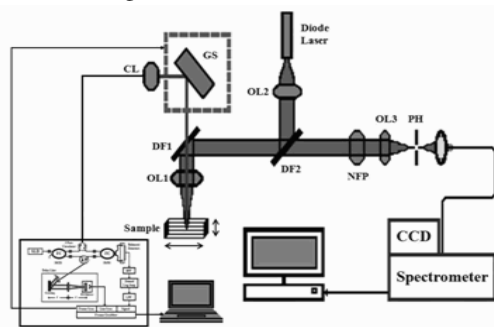


Fig. 1:- Experimental setup for combined depth-sensitive Raman spectroscopy and optical coherence tomography

The TD-OCT system was a fiber based Mach Zehnder interferometer that utilized a broadband superluminescent diode, with a center wavelength of 1310nm. The Raman system utilized a single mode 785nm diode laser as the excitation source. The co-aligned beams with the help of dichroic filter (DF1) were focused through the microscope objective (NA-0.40) onto the sample kept on a micrometer-controlled stage. For depth-sensitive Raman measurements, the stage was moved in steps of 10 μ m and the Raman beam backscattered from the sample was focused (after filtering) onto a 100 μ m pinhole coupled with an

optical fiber to finally image it on to an imaging spectrograph equipped with a thermoelectrically cooled CCD camera. The pinhole rejected out-of-focus light, allowing for depth resolution.

3. RESULTS AND DISCUSSIONS

The combined depth-sensitive RS-TDOCT device was validated using two samples, one prepared by depositing a thin layer of paraffin over acetaminophen and the other was a chicken rib bone. Figs.2a and b show the OCT images and the corresponding Raman spectra for the samples. For the non-biological sample, clear distinction between the layers is seen in the OCT image and the Raman spectra corresponding to the OCT images. In particular, the prominent tall peak at $\sim 1447\text{cm}^{-1}$ characteristic of paraffin was found to increase as the focus of the Raman probe beam was moved from the lower layer (i.e. acetaminophen) to the upper layer (i.e. paraffin) in the OCT image. For the chicken bone, the heights of the different Raman peaks for the bone and underlying bone marrow were also seen to be changing with the change in probing depth. The details of these results will be presented.

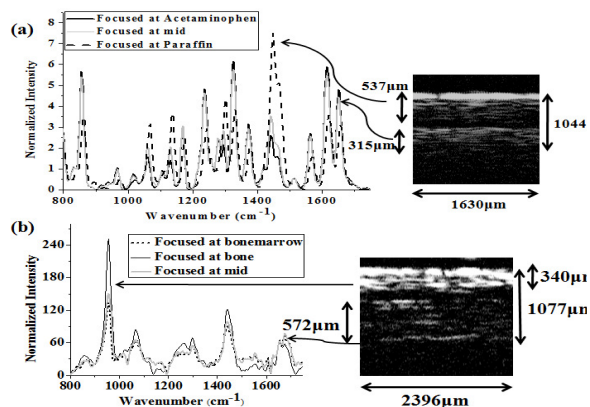


Fig.2: Raman spectra and OCT images of (a) paraffin-acetaminophen phantom and (b) chicken bone phantom

REFERENCES

- [1]. Patil C. A., Kalkman J. and Mahadevan-Jansen A., "Integrated system for combined Raman spectroscopy-spectral domain optical coherence tomography" *J. Biomed. Opt.* **16**(1), 011007, 1 (2011).

STUDIES ON THE INFLUENCE OF TOBACCO HABIT ON THE FLUORESCENCE SPECTRA OF HEALTHY ORAL MUCOSA

H. Krishna¹, * S. K. Majumder¹, M. Sidramesh², P. Chaturvedi² and P. K. Gupta¹

¹Laser Biomedical Applications and Instrumentation Division, Raja Ramanna Centre for Advanced Technology, Indore - 452013, INDIA

²Department of Surgical Oncology (Head & Neck), Tata Memorial Hospital, Mumbai - 400012, *email: shkm@rrcat.gov.in

Abstract: We report the results of statistical analysis of the *in vivo* spectral data of the oral cavity of healthy volunteers to investigate the influence of tobacco use on the autofluorescence signatures of the oral mucosa.

1. INTRODUCTION

There is enough epidemiological evidence that exposure to tobacco is one of the significant etiological factors for the development of oral cancers and pre-cancers. It is therefore expected that use of tobacco may cause changes in the spectral signatures of the oral cavity mucosa. Recently, we carried out detailed *in-vivo* optical spectroscopic studies at Tata Memorial Hospital (TMH), Mumbai to discriminate various oral tissue pathologies *in vivo* in a clinical setting. Probability based multi-class classification algorithms were used to delineate the investigated oral tissue sites belonging to either of the four histopathologic categories: 1) squamous cell carcinoma (SCC), 2) oral sub-mucosal fibrosis (OSMF), 3) leukoplakia (LP), or 4) normal squamous tissue. The results showed that when the set of spectra treated as normal included only the spectra from healthy volunteers with no history of tobacco habits the discrimination results were substantially better compared to when the normal data base included all spectra from clinically normal oral mucosa from healthy volunteers irrespective of their tobacco consumption habits. In order to understand the reason behind this, we carried out detailed analyses of the spectral data of healthy volunteers to investigate the influence of tobacco use on the autofluorescence signatures of healthy oral mucosa and also its role on the performance of the diagnostic algorithm. The results of these analyses are reported here.

2. EXPERIMENTAL METHODS

The study involved 26 healthy volunteers of which 18 had habits of either smoking and/or chewing tobacco, and the rest were tobacco non-users. *In-vivo* fluorescence spectra were measured using a N₂ laser based portable spectroscopic system developed in our group. The spectra from 11 different anatomical positions of the oral cavity were recorded in the 375-700 nm spectral range from each volunteer. In order to ascertain whether there are statistically significant differences in the set of spectra of tobacco users and non-users, an unsupervised discrimination analysis was performed on the whole set of spectral data using an expectation-maximization algorithm. Further, a supervised discrimination analysis of the data set was

conducted using a nonlinear binary classification algorithm.

3. RESULTS AND DISCUSSIONS

Fig.1a shows the mean fluorescence spectra of healthy volunteers with (n=197) and without (n=86) tobacco habits. Significant differences are observed in the intensity as well as the spectral distribution between the two groups. The spectra of tobacco users, in general, showed reduced total fluorescence intensity as compared to the non-users in the wavelength region below ~520nm. However, beyond 520nm the trend is reversed where the fluorescence intensity is seen to be higher for the tobacco users. Fig.1b shows the plot of Fisher measure as a function of wavelengths. It is clear that though there are differences in the 390nm (collagen) and 460nm (NADH) spectral bands, the most prominent differences are seen around 620nm region believed to be due to porphyrins.

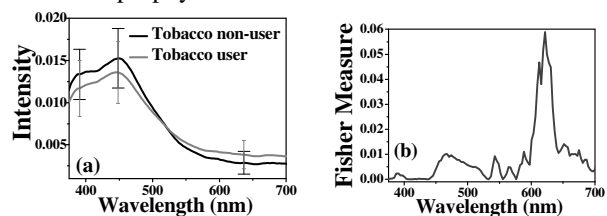


Fig.1: (a) Mean N₂ laser induced autofluorescence spectra of healthy oral mucosa of tobacco users and nonusers, and (b) Fisher measure as a function of wavelength.

The results of the unsupervised discrimination analysis over the limited data confirmed the presence of two categories. The results of supervised classification using the binary classification algorithm showed that normal volunteers with and without tobacco habits could be discriminated with an accuracy of better than 90%. The details of these results will be presented.

REFERENCES

- [1]. P. Chaturvedi, S. K. Majumder, H. Krishna, M. Sidramesh, and P. K. Gupta, "Fluorescence Spectroscopy for Non-Invasive Early Diagnosis of Oral Mucosal Malignant and Potentially Malignant Lesions", *J. Cancer Research Therapeutics*: 6, 497-502, (2010).

NUMERICAL APERTURE OF INDEX-GUIDING MICROSTRUCTURED OPTICAL FIBERS: AN ANALYTICAL STUDY

Dinesh Kumar Sharma and Anurag Sharma

Physics Department, Indian Institute of Technology Delhi, New Delhi - 110016, India

E-mail: dk81.dineskumar@gmail.com

Abstract: An analytical model for the modal field of an index-guiding microstructured optical fiber (MOF) has developed using the variational principle. Using the model, we calculate the numerical aperture (NA) of a single mode photonic crystal fiber (PCF) from half-divergence angle and compare with experimental results.

1. INTRODUCTION

Photonic crystal fibers (PCFs) are dielectric waveguides having complex air-silica cross-section. PCFs are also known as microstructured optical fibers (MOFs) and have received considerable attention because of their unique optical properties, based on the fact, that the properties of an optical media get modified by the periodic variation in refractive index [1, 2]. By varying the size of air-holes, their number and position, one can design an MOF with desirable dispersion and modal properties. The most common type of PCF, which was first fabricated in 1996 [3], consists of pure silica fiber with an array of air-holes running along the longitudinal direction. The one of the most important MOFs configuration is shown in Fig. 1, where Λ is the pitch (natural length of separation between two nearest air-holes) and d is the air-hole diameter. It consists of silica fiber with a solid core (the absence of an air-hole at lattice site) surrounded by microstructured cladding, that are typically hexagonally packed. These longitudinal air-hole patterns in cladding reduce the effective index, below that of pure silica [2, 3].

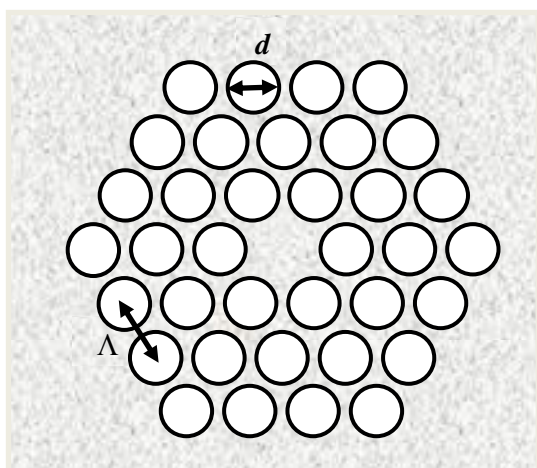


Fig. 1. Schematic transverse cross-section of an index-guiding microstructured fiber with six-fold rotational symmetry. The microstructured cladding consists of air-holes of diameter d arranged in a triangular lattice with pitch Λ .

The light guidance mechanism in such type of MOFs is essentially similar to total internal reflection as in the case of conventional optical fibers [1]. This analogy holds good in MOFs at longer wavelengths $\lambda \rightarrow \infty$, where the field spreads more in cladding as a consequence it cannot resolve the individual air-holes. In this case, the effective cladding index is taken as the average of air-silica refractive indices [4]. The complex dielectric structure of PCF, makes its electromagnetic analysis challenging. In absence of an analytical analysis, a weak guidance approximation based Effective Index Method (EIM) [1, 2] was proposed which is a simple technique that qualitatively provides the same modal properties of PCFs as obtained from any other numerical technique. We have developed a model based on variational principle which has given results for the effective index, near and far-fields and dispersion coefficient for the fundamental mode, which compare well with experimental and theoretical results available in the literature [5]. Our model has also given results for the evolution of fundamental mode from near-field to far-field, where it radiates out from the end facet of an MOF in free space [6] and splice losses between an MOF and a SMF-28 [7], which are in good agreement with those experimental and simulations results available in the literature.

PCFs have many remarkable optical properties compared to conventional optical fibers as they have number of parameters to be tailored. PCFs are believed to have a potential for high numerical aperture (NA) applications. The high index contrast between silica and air makes it possible to fabricate PCFs with large multimoded cores having very large NA values. Such types of fibers are useful for collection and transmission of high powers. The NA of a fiber is a very important property and essentially determines the efficiency of coupling from a source to the fiber as well as across a misaligned joint in a splice [8, 9]. NA is a measure of the light gathering power of the fiber. Here, we present the results on NA of index-guiding microstructured optical fibers (MOFs) calculated from the half-divergence angle [9] (a textbook result) $\theta \approx \tan^{-1}(\lambda/\pi w)$ which compare well with experimental results [8].

2. THE MODEL

Variational method is presented to obtain the transverse field distribution and the propagation constant of the fundamental mode using weakly guiding approximation. In this method, we construct a stationary expression for the propagation constant in term of the cross-sectional integrals involving the field and the refractive index distribution of the structure [10]. The integral form of the scalar wave equation can be written as [5];

$$\beta^2 = \frac{\int_0^{2\pi} \int_0^\infty \left[k_0^2 n^2(r, \phi) |\Psi(r, \phi)|^2 \right] - \left[\left| \frac{\partial \Psi}{\partial r} \right|^2 + \frac{1}{r^2} \left| \frac{\partial \Psi}{\partial \phi} \right|^2 \right] r dr d\phi}{\int_0^{2\pi} \int_0^\infty |\Psi(r, \phi)|^2 r dr d\phi}$$

where β denotes the propagation constant for the scalar mode and $\Psi(r, \phi)$ is an approximation for the modal field. The accuracy of the variational method depends mainly on the proper choice of the trial field. According to the variational principle, a trial field which maximizes β^2 could be a close approximation of the actual field. The closeness would depend on the proper choice of the form of the trial field and the number of parameters [5, 10].

In our model (as shown in Fig. 2, where $r_1 = \Lambda$, $r_2 = \sqrt{3}\Lambda$, and $r_3 = 2\Lambda$) we have considered the three rings of air-holes around the central missing air-hole (core) and the medium beyond the third ring, which is in fact an arrangement of rings, is modeled as uniform medium having index equal to the effective index of the fundamental space-filling mode [2]. The proposed model exhibits essential 6-fold angular symmetry of the field unlike the EIM which averages out such variation [5].

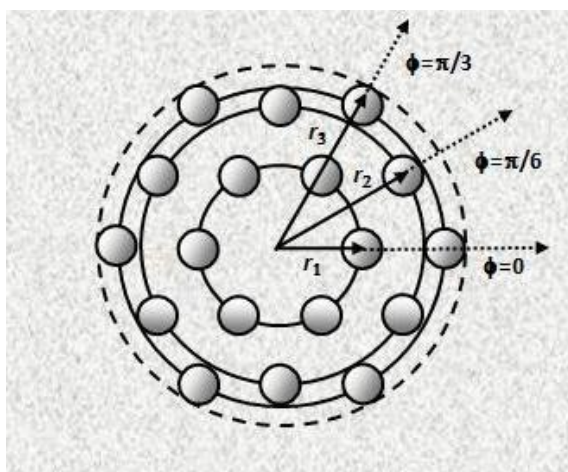


Fig. 2. Schematic diagram of an MOF structure with three rings of air-holes.

We consider a trial field which mainly consists of two parts, one is a simple Gaussian term and the

other is a shifted Gaussian term. The trial field is given by [5];

$$\Psi(r, \phi) = e^{-\alpha r^2} - A e^{-\alpha_1 (r - \sigma \Lambda)^2} (1 + \cos 6\phi) \quad (1)$$

where A, α, α_1 and σ are the variational parameters.

3. THE NUMERICAL APERTURE

The NA is used to describe how light is collected by an optical fiber and how it spreads out on leaving the fiber end. The measurement of acceptance angle is the NA, which is the Sine of the half acceptance angle, as shown in Fig. 3. In standard fibers, the numerical aperture is defined as [9];

$$\text{NA} = \sin \theta = \sqrt{n_1^2 - n_2^2} \quad (2)$$

where n_1 and n_2 are core and cladding refractive indices respectively. In conventional single mode step-index fiber the refractive index contrast Δ between core and cladding practically remains constant with wavelength, as core and cladding materials have similar dispersion coefficients. Consequently, the NA, which is a measure of the light gathering power of the optical fiber, is almost independent of operating wavelengths.

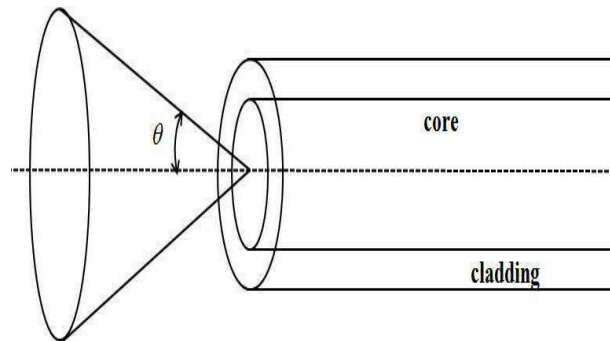


Fig. 3. Schematic diagram for measuring half-acceptance angle in conventional optical fiber.

In case of PCFs, the presence of air-holes in the cladding modifies the refractive index of cladding and dispersion coefficient. In short wavelengths regime ($\lambda \rightarrow 0$) field avoids air-holes as a result very amount little of the field penetrates into air-holes; consequently the cladding index is close to that of pure silica. At longer wavelengths ($\lambda \rightarrow \infty$) field penetrates deeply into the air-holes resulting reduction in the effective index of fundamental mode propagation in the cladding as a result Δ and NA both increases with wavelength [11]; consequently, in PCFs, it is impractical to calculate NA from measurements of the core and cladding refractive indices.

For PCFs, NA can be calculated directly by measuring the far-field intensity distribution (as shown in Fig. 4) of the fiber where the edge of beam

is defined as the angle at which intensity falls to 13.5% of its maximum value [8]. The light guiding properties of optical fibers are symmetrical, so the light emerging from end face of fiber over an angle is equal to its acceptance angle (as shown in Fig. 4).

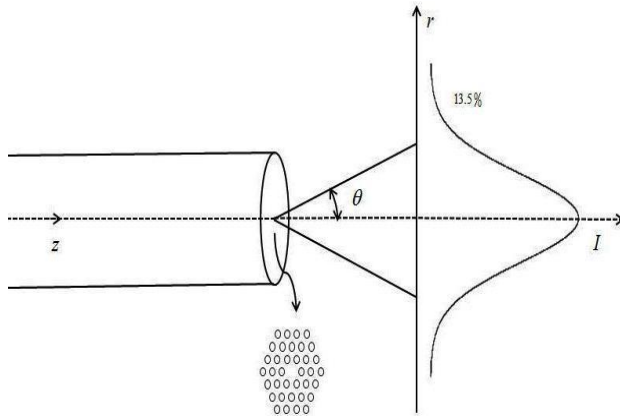


Fig. 4. Schematic diagram for measuring half-divergence angle of a PCF. The inset shows the transverse cross-section of a PCF.

The fundamental mode of conventional optical fiber is circularly symmetry, so divergence measurements are based on the radius of $1/e^2$ intensity contour. In case of PCFs, the far-field intensity profile of the fundamental mode has feature of circular symmetry close to its center, but it becomes more hexagonal in the wings of the beam (as shown in Fig. 5) in which the intensity contours are no longer circular.

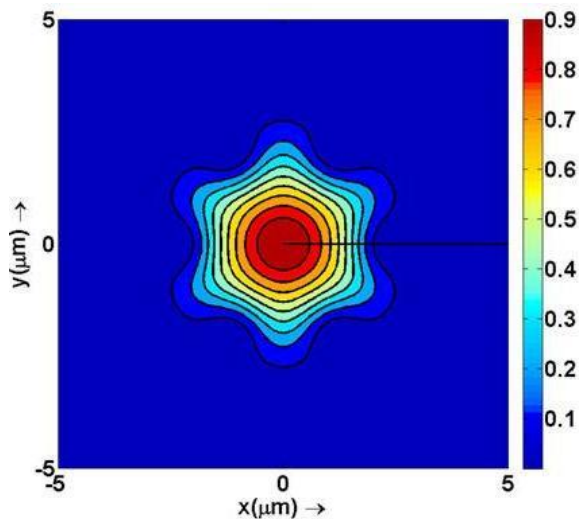


Fig. 5. Contour plot for a typical MOF structure having hexagonal features in the tail of the beam.

Therefore, we need a definition of beam divergence that does not assume circular symmetry of field but provide a link with the Gaussian approximation of the field [11].

For a Gaussian field of width w we have the standard approximate expression for intensity $I = 1/e^2 \approx 13.5\%$ [9];

$$\tan \theta \approx \lambda / (\pi w) \quad (3)$$

with πw^2 being the effective area of the mode and for $I = 5\%$ we have,

$$\tan \theta_{5\%} = \sqrt{\frac{\ln 20}{2}} \times \tan \theta_{13.5\%} \quad (4)$$

which is usually used in experimental measurements of beam divergence [8]. To apply Eq. (3) for PCFs [8], we have calculated effective area of fundamental mode as given by [9];

$$A_{\text{eff}} = \frac{\left[\int_0^{2\pi} \int_0^{\infty} |\Psi(r, \varphi)|^2 r dr d\varphi \right]^2}{\int_0^{2\pi} \int_0^{\infty} |\Psi(r, \varphi)|^4 r dr d\varphi} \quad (5)$$

where $\Psi(r, \varphi)$ is the modal field of the fundamental mode which is approximated by a trial field as given in Eq. (1). We have also calculated the beam divergence from Eq. (3) using the definition of Petermann-II spot size [9];

$$w = \left[\frac{2 \int_0^{2\pi} \int_0^{\infty} |\Psi(r, \varphi)|^2 r dr d\varphi}{\int_0^{2\pi} \int_0^{\infty} \left[\frac{d\Psi}{dr} \right]^2 r dr d\varphi} \right]^{0.5} \quad (6)$$

4. RESULTS AND DISCUSSION

In Fig. 6, we compare our calculations to a measurement of the NA [8]. The PCF taken for the calculations has $d/\Lambda = 0.53$ and $\Lambda = 7.2 \mu\text{m}$. As seen that the calculations are in good agreement with the measured values of numerical aperture.

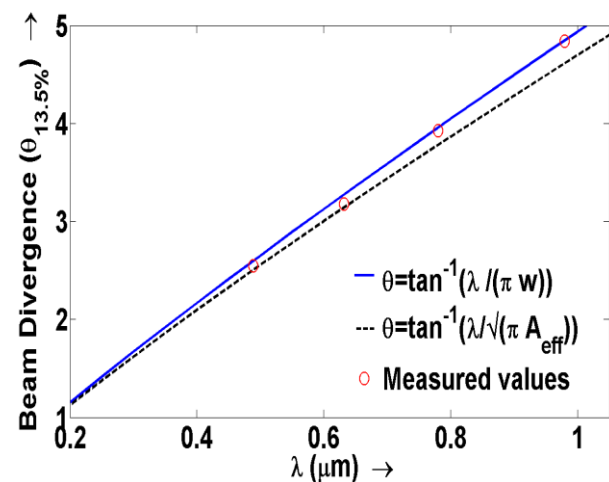


Fig. 6. Half-divergence angle of a PCF as a function of wavelength. The dotted line and the solid line are the results of calculation based on our model and the

data points are the results of measurements at $\lambda = 488\text{nm}$, 632nm , 780nm , and 980nm of the fiber.

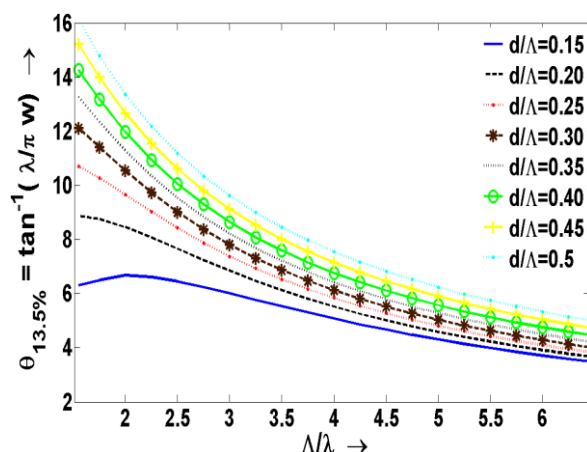


Fig. 7. Half-divergence angle of a PCF at different cladding parameters.

As the NA, is related to refractive index of material. As the material index is varying with the wavelength, the NA we measured must be the value at a particular wavelength. In Fig. 7, we have shown the variation of half-divergence angle for different values of cladding parameters d/Λ . The fiber taken for the calculations is endlessly single mode [1]. For small d/Λ (air-hole diameter to pitch ratio) values in long wavelengths regime (effective area increases) the operation is limited by the confinement losses [4]. In general, the NA increases for increasing air-hole diameter d at a given pitch and wavelength. By adjusting the pitch Λ and the air-hole diameter d it demonstrates a high degree of freedom in tailoring a fiber with certain NA at a given wavelength [11]. We have also calculated the NA for the fiber first fabricated by Knight *et al.*, [3] we find a $\text{NA} \sim 0.07$ [8] which compares well to standard fiber technology.

5. CONCLUSION

We have developed a semi-analytical method which approximates the field and the propagation constant of the fundamental mode. In this paper, we have studied the numerical aperture of PCF using standard textbook relation and have checked the validity, with those results available in the literature. We have studied the effect of different air-hole sizes to control NA for a given pitch and wavelength and have shown that PCF technology has a potential for large NA applications.

ACKNOWLEDGEMENT

This work was supported by grant from the Council of Scientific and Industrial Research (CSIR), India.

REFERENCES

- [1] T.A. Birks, J.C. Knight, and P.St.J. Russell, "Endlessly single-mode photonic crystal fiber," *Opt. Lett.*, **22**, 961-963 (1997).
- [2] J.C. Knight, T.A. Birks, P.St.J. Russell, and J.P. Sandro, "Properties of photonic crystal fiber and the effective index model," *J. Opt. Soc. Am. A* **15**, 748-752 (1998).
- [3] J.C. Knight, T.A. Birks, P.St.J. Russell, and D.M. Atkin, "All-silica single-mode optical fiber with photonic crystal cladding," *Opt. Lett.*, **21**, 1547-1549 (1996).
- [4] T.P. White, R.C. McPhedran, C.M. de Sterke, L.C. Botton, and M.J. Steel, "Confinement losses in microstructured optical fibers", *Opt. Lett.* **26**, 1660-1662 (2001).
- [5] Anurag Sharma and Hansa Chauhan, "A new analytical model for the field of microstructured optical fibers," *Opt. Quant. Electron.* **41**, 235-242 (2009).
- [6] Dinesh Kumar Sharma and Anurag Sharma, "Far-field of index-guiding microstructured fibers: an analytical field model," *SPIE Proc.*, **8173**, 81731F (2010).
- [7] Dinesh Kumar Sharma and Anurag Sharma, "Splice Losses in Microstructured Optical Fibers: An Analytical Approach," *AIP Conf. Proc.*, **1391**, 420-422 (2011).
- [8] N.A. Mortensen, J.R. Folken, Peter M.W. Skovgaard and J. Broeng, "Numerical aperture of single-mode photonic crystal fibers", *IEEE Photonics Technol. Lett.*, **14**, 1094-1096 (2002).
- [9] A.K. Ghatak and K. Thyagrajan, *Introduction to Fiber Optics*, Cambridge University Press, Cambridge, (1998).
- [10] Anurag Sharma, "Optimal variational method for rectangular and channel waveguides", *Guided Wave Optics; Selected Topics*, (Ed. A. Sharma), Viva Books, New Delhi (2005).
- [11] M.J. Gander, R. McBride, J.D.C. Jones, T.A. Birks, J.C. Knight, and P.St.J. Russell, P.M. Blanchard, J.G. Burnett, and A.H. Greenway, "Measurement of the wavelength dependence of beam divergence for photonic crystal fiber," *Opt. Lett.*, **24**, 1017-1019 (1999).

FDTD SIMULATION OF TWO PHOTON ABSORPTION IN SILICON WAVEGUIDE AND REALISATION OF ALL OPTICAL LOGIC GATES

Anirban Roy Chowdhury¹, Ivy Dutta¹, Kousik Mukherjee², Dharmadas Kumbhakar³

¹Department of Physics, Kanksa Academy of Technology & Management, Kanksa, Panagarh-713148, West Bengal, India, research_phy@rediffmail.com

²Department of Physics, B. B. College, Asansol-713303, West Bengal, India, lipton007@indiatimes.com

³Department of Electronics & Communication Engineering, Asansol Engineering College, Asansol-713305, West Bengal, India, dkbbcasn@gmail.com

ABSTRACT: Non-linear two photon absorption in silicon waveguide is incorporated in FDTD update equations. It is observed that the influence of a high intensity pump beam on a different frequency continuous probe beam can be utilized to form a NAND gate.

1. INTRODUCTION

Silicon-on-insulator waveguide is very attractive for designing all optical signal processing devices and switches due to the mature fabrication technology of silicon and the fact that it has comparatively higher non-linear parameters like third order non-linear Kerr coefficient, Raman susceptibility etc. than conventional silica fibers [1]. Silicon waveguides can be formed in the nano-scale size, requiring very small energy pulses in the range of pico-joules although high intensity optical beams are necessary to tap non-linear effects.

In silicon, electrons in the valence band can rise to the conduction band with the absorption of two photons in the spectral range around 1.55 μm , producing free carriers. The optical intensity decreases as light beam passes along the wave guide due to this two photon absorption (TPA). The free carriers generated by TPA also absorb light which is known as free carrier absorption (FCA).

Earlier all optical logic gates were produced [2] with silicon micro-ring resonators using free carrier dispersion. T. K. Liang et.al. [3, 4] proposed all optical NOR gates using two photon absorption only.

Earlier, we have shown that TPA can be utilized to form several all optical logic gates [5]. In this paper, we have observed that in principle, NAND gate also can be formed using two photon absorption effect in silicon waveguide. Some possible ways to enhance the extinction ratio are also discussed.

2. THEORY

In the range of 1 GW/cm² power, Kerr effect in silicon is not prominent. The modal field distribution practically does not change with power. In that case, one can use one-dimensional FDTD [6, 7] to simulate

the attenuation and change in pulse shape due to TPA as light propagates along the guide. The change in intensity due to a TPA when a single optical beam, the pump beam is present, is given by [3]

$$\frac{dI_p}{dz} = -\beta_{TPA} I_p^2 \quad (1)$$

β_{TPA} is the TPA coefficient. If this loss term is included, one can write Ampere's law in Maxwell's equation as

$$\frac{\partial \vec{E}_p}{\partial t} = -a_{TPA} \vec{E}_p^3 + \frac{1}{\epsilon_r} \vec{\nabla} \times \vec{H}_p \quad (2)$$

ϵ_r is the relative permittivity of the medium. In our 1D FDTD, we take $\epsilon_r = n_0^2$, where n_0 is the effective index of the waveguide. Then following [8]

$$a_{TPA} = \frac{1}{2} \epsilon_0 c_0^2 \beta_{TPA}$$

This leads to the following finite difference equation

$$E_{yp}^{n+1}(i) - E_{yp}^n(i) = -a_{TPA} \Delta t \{E_{yp}^{n+\frac{1}{2}}(i)\}^3 + \frac{F_c}{n_0^2} [H_{xp}^{n+\frac{1}{2}}(i-1) - H_{xp}^{n+\frac{1}{2}}(i)] \quad (3)$$

where $F_c = c_0 \Delta t / \Delta z$ is the Courant number. It is taken as unity.

To get FDTD update equations, one can make use of Taylor series expansion [9]

$$\begin{aligned} (E^{n+\frac{1}{2}})^3 &= (E^n)^3 + \frac{\partial (E^n)^3}{\partial t} \cdot \frac{\Delta t}{2} \\ &= (E^n)^3 + 3(E^n)^2 \cdot \frac{1}{2} [E^{n+1} - E^n] \\ &= \frac{3}{2} (E^n)^2 E^{n+1} - \frac{1}{2} (E^n)^3 \end{aligned}$$

Then equation (3) takes the form

$$E_{yp}^{n+1}(i) = F_{1p}(i)E_{yp}^n(i) + F_{2p}(i) \left[H_{xp}^{n+\frac{1}{2}}(i-1) - H_{xp}^{n+\frac{1}{2}}(i) \right] \quad (4)$$

$$\text{where } F_{1p}(i) = \frac{1 - (1/2)a_{TPA}\Delta t\{E_{yp}^n(i)\}^2}{1 + (3/2)a_{TPA}\Delta t\{E_{yp}^n(i)\}^2}$$

$$F_{2p}(i) = \frac{F_C}{n_0^2} \cdot \frac{1}{1 + (3/2)a_{TPA}\Delta t\{E_{yp}^n(i)\}^2}$$

When one pump beam and a probe beam are present, equation (1), for the change in intensity of the probe beam, becomes

$$\frac{dI_s}{dz} = -2\beta_{TPA}I_pI_s$$

In the update equation (4), E_{yp} and H_{xp} are replaced by E_{ys} and H_{xs} and the factors are

$$F_{1s}(i) = \frac{1 - a_{TPA}\Delta t\{E_{yp}^n(i)\}^2}{1 + a_{TPA}\Delta t\{E_{yp}^n(i)\}^2}$$

$$F_{2s}(i) = \frac{1}{1 + \alpha_{TPA}\Delta t\{E_{yp}^n(i)\}^2}$$

3. RESULTS AND DISCUSSIONS

We have used Gaussian pulses of 0.1 ps width for the pump beam and continuous oscillatory field of wavelength 1.55 μm for the probe beam. The peak strength of the pump beam is 1 GW/cm^2 and the power of the probe beam is 10^{-3} GW/cm^2 .

The parameters are taken as $n_0 = 3.17$ [8] and $\beta_{TPA} = 0.5$ cm/GW [10].

We have coded our FDTD program in MATLAB. The probe beam develops an inverted Gaussian pulse at the point of the pump beam. We have set up a program to get the envelope of the probe beam which shows the form of the dark pulse clearly. We have taken $\Delta z = 0.3 \times 10^{-8}$ μm ; numerical window size = $10000 \times \Delta z$ and a PML layer of 10 cell width. After 31700 time steps, as the fields reach the right edge, they are partially shifted to the left and the probe field is put at the right phase. In this way, same numerical window can be used taking time update as long as one wants saving computational time enormously.

The evolution of the pump pulse and dark probe pulse are shown in Fig.1. One pump pulse and its corresponding probe pulse are shown near the input end; the shape of those pulses is also shown at the output end – after propagation through 1 cm length of the waveguide.

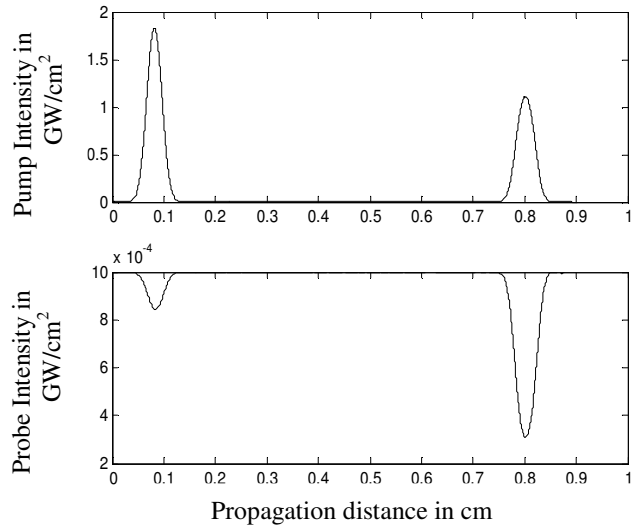


Fig. 1: Pump pulse and dark pulse formation in the probe beam

The minimum of the dark pulse after 1 cm propagation for a range of optical powers is shown in Fig.2. It shows that for 1 GW/cm^2 probe input power, the output power is down by about 50% and when the input power is 2 GW/cm^2 , the output is down by about 30%. If 40% power level is used as threshold, the switching of the output from high level to low as the input is changed from 1 to 2 GW/cm^2 can be used to form a NAND gate.

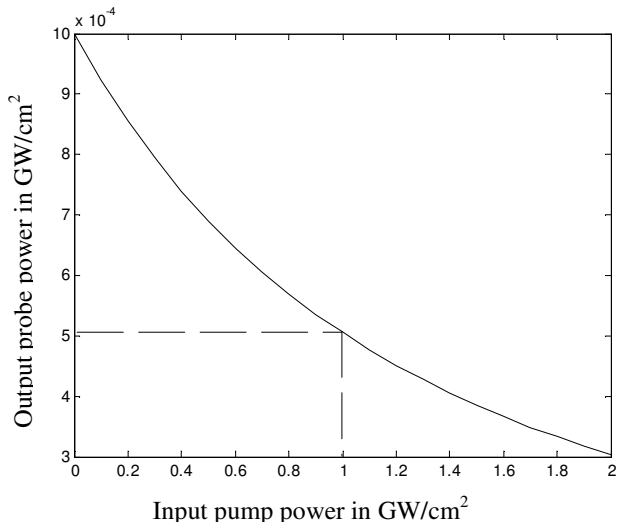


Fig. 2: Output probe power after 0.8 cm propagation with variation in input pump power

The NAND gate device that acts on this principle is shown in Fig.3. Two pump beams are fed into the waveguide through S-bends and the probe beam is injected straight at the center.

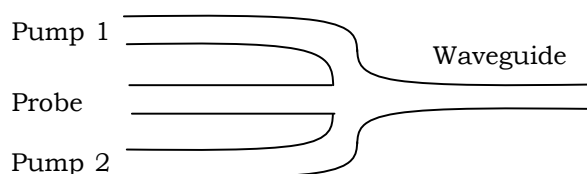


Fig. 3: Structure of the NAND gate device

When pump pulses 1 and 2 are both absent or any one is present, the output probe power remains above 50%, it is taken as logic 1. When both the pump pulses are present, the output falls to 30%; that is taken as logic 0.

The low difference of output power levels (50% and 30%) is the main problem of this proposed design. We have the following ideas to reduce this problem and aim to realize these ideas in our future works.

1. In the above simulation, we have used pump and probe frequency different but both close to 1.55 μm , as in [3]. Shifting pump frequency to around 2.2 μm cuts off two photon absorption in the pump beam. The undepleted pump beam lowers the probe intensity at the same propagation distance.
2. Kerr-nonlinearity sharpens the power at the centre of the transverse modal profile. Inclusion of this Kerr-nonlinearity may lower the output probe power when both pump beams are present.
3. Kerr-nonlinearity in silicon is not so high. Other materials or quantum-well structures which exhibit high Kerr-type nonlinearity may be more suitable.
4. We have neglected the effect of FCA. Inclusion of FCA may lower the absorption at higher power.
5. Comparable multi-photon absorption using longer probe wavelength can give rise to sharp fall in the intensity when power is doubled because of the law

$$\frac{dI}{dz} = -\alpha_N I^N$$

that describes N-photon absorption. α_N is the N-photon absorption co-efficient [11,12].

REFERENCES

- [1] Q. Lin, O. J. Painter, G.P.Agrawal: Nonlinear optical phenomena in silicon waveguides: Modeling and applications, *Opt. Express*, **15** (2007) 16604-44.
- [2] Q. Xu and M. Lipson, All-optical logic based on silicon micro-ring resonators, *Opt Express* **15** (2007) 924-29
- [3] T. K. Liang, L. R. Nunes, M. Tsuchiya, K .S. Abedin, T. Miyazaki, D. Van Thourhout, W. Bogaerts, P. Dumon, R. Baets, H.K. Tsang: High speed logic gate using two-photon absorption in silicon waveguides, *Opt. Commun.*, **265**, (2006) 171-176.
- [4] T. K. Liang, L. R. Nunes, T. Sakamoto, K. Sasagawa, T. Kawanishi, M. Tsuchiya, G. R. A. Priem, D. Van Thourhout, P. Dumon, R. Baets and H.K. Tsang: Ultrafast all-optical switching by cross-absorption modulation in silicon wire waveguides, *Opt. Express*, **13**, (2005) 7298-7303.
- [5] K. Mukherjee, D. Kumbhakar: Simulation and method of implementation of all optical logic gates based on two photon absorption in silicon wire wave guide, *Optik*, in press.
- [6] A. Taflove, S. C. Hagness: *Computational Electrodynamics: The Finite Difference Time Domain Method*, Artech House, 2000.
- [7] C. M. Dissanayake, M Premaratne, I. D. Rukhlenko and G. P. Agrawal: FDTD modeling of anisotropic nonlinear optical phenomena in silicon waveguides, *Opt. Express* **18** (2010) 21427-48.
- [8] N. Suzuki, FDTD analysis of two-photon absorption and free-carrier absorption in Si high-index-contrast waveguides, *IEEE J. Lightw. Technol.* **25**, (2007) 2495-2501
- [9] E. P. Kosmidou, T. D. Tsiboukis, *Opt. Quantum Electron*, **35**, (2003) 931.
- [10] A. D. Bristow, N. Rotenberg and H. M. van Driel: Two-photon absorption and Kerr coefficients of silicon for 850–2200 nm, *Appl. Phys. Lett.* **90** (2007), 191104.
- [11] W. C. Hurlbut, Yun-Shik Lee, K. L. Vodopyanov, P. S. Kuo and M. M. Fejer: Multiphoton absorption and nonlinear refraction of GaAs in the mid-infrared, *Opt. Lett.* **32**, (2007) 668-70.
- [12] B. Gu, K. Lou, H. T. Wang, and W. Ji: Dynamics of two-photon-induced three-photon absorption in nanosecond picosecond and femtosecond regimes, *Opt. Lett.* **35** (2010) 417

PHASE RETRIEVAL FROM FOURIER MODULUS- A NUMERICAL SIMULATION

Senthil Kumar.M*, A.S.Kiran Kumar* and C.S. Naryanamurthy#

*Space Applications Center (ISRO), Ahmedabad, India

Indian Institute of Space Sciences and Technology (IIST), DOS, Trivandrum

email:* senthil@sac.isro.gov.in, senthiliist@gmail.com

Abstract: Phase retrieval attempts to obtain the unknown phase from the observed focal plane intensity. The phase retrieval algorithms use information at input aperture and at observation plane(s). This work is inspired by Gerschberg-Saxton (GS) phase retrieval method and also its utility for space borne imaging systems. This paper brings out the numerical phase retrieval approach and their convergence with one or more observation planes and with and without quadratic phase function of focal plane. Ease of comprehending the convergence with block shifting cross correlation as merit function instead of mean sum squared difference error is also addressed.

1.0 INTRODUCTION

Phase retrieval is a subject of interest for researchers and engineers in the field of astronomy, adaptive optics, optical imaging system, laser beam characterization etc.

Two popular phase retrieval approaches, iterative [1] and non-iterative [2] are developed. Iterative methods based on GS algorithms found wide interest in the field of phase retrieval due to its ease and flexibility. In this paper, a phase retrieval method based on GS approach with phase diversity has been attempted with simulated noise free data sets.

2.0 PRINCIPLE & PROCEDURE

A narrow far-field object enters the imaging system records its image on the detector kept at the image plane in the form of intensity (I). I is the square of complex amplitude distribution of field $U_f(u, v)$ at focal plane propagated from input plane field U_1 given under Fresnel scalar approximation by [3]

$$U_f(u, v) = \exp\{i\pi \cdot [(u.s_m)^2 + (v.s_n)^2] / \lambda f\} \cdot \mathfrak{Z}(U_1) \quad \text{----- (1)}$$

f- focal length, D- pupil dia, $s_m = \lambda f / D$, $s_n = \lambda f / D$

The angular spectrum method [3], sampling invariant, is applied for propagation between nearby observation planes.

The intensity data are simulated with lower order zernike coeffs at focal plane and focus shifted plane that are inputs to phase retrieval.

The iterative optimization approach is,

$$U_1 = A \cdot e^{i\phi} \text{ where } A=1 \text{ \& } \phi - \text{guess or zero}$$

$$U_1 \rightarrow \mathfrak{Z}(U_1) \rightarrow U_f \text{ replace } |U_f| = I_f$$

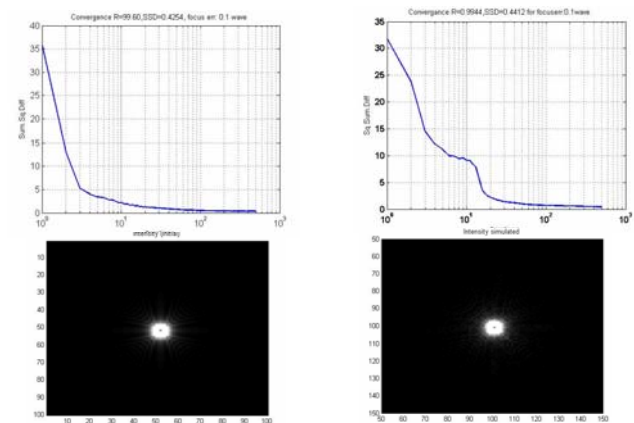
$$U_f \rightarrow \mathfrak{Z}(U_f) \rightarrow U_1 \text{ replace } |U_1| = A$$

Continued for k_1 times,

Iterations also carried out by propagating and back propagating the complex field between two observation planes k_2 times and in addition between focal plane and input plane k_3 times with known data constraints at respective planes.

3.0 RESULTS

Plot (1) and (2) shows convergence of with and without phase function defining 'f' in eq.(1)



4.0 CONCLUSION

Convergence sensitivities are brought out in this paper.

5.0 REFERENCES

- [1] R. Gerschberg and W.Saxton, Optik 34 237-246 1972
- [2] R.A.Gonsalves, Optics Letters 26 684-685 2001
- [3] Joseph W Goodman Introduction to Fourier Optics, Chapter: 3 & 5 McGraw Hill 1996

Design and modeling of diffractive sub-wavelength structures using Rigorous Coupled Wave Analysis

Raj Bahadur Yadav, Unnikrishnan G. and A. K. Gupta
 Photonics Division, Instruments Research and Development Establishment
 Raipur Road, Dehradun, India, Pin code 248 008
 Email: yadavraj12@gmail.com

Abstract: We have used Rigorous Coupled Wave Analysis for the design of diffractive sub-wavelength structures on *RSoft* platform. We have reported the design of an antireflection surface device made by fused silica with a period of $0.12\mu\text{m}$ that uses its zeroth order of diffraction to reduce the reflection at optical boundaries. We have also modeled a resonant grating filter useful for filtering applications where a very narrow band is required.

1. INTRODUCTION

Diffractive sub-wavelength structures design is an important problem for many applications i.e. optical communications, optical interconnection, integrated optics and optical sensing¹⁻⁸. Sub-wavelength structure (SWS) surfaces that contain diffraction grating with a period significantly smaller than the wavelength of light do not show a diffraction effect. Only zeroth transmitted and reflected orders propagate i.e. all diffraction orders other than the zeroth order are evanescent: they are also called zeroth order grating¹. SWS surfaces behave like thin film whose refractive index profile depends on their surface structure. Antireflection SWS grating have been studied by numerous researchers¹. These applications are usually achieved by the Gerchberg-Saxton and Yang-Gu algorithm and which are based on monochromatic wave propagation and far field assumption, because Fourier transform is used to model the wave propagation³.

Among theories which can predict the characteristics of Diffractive Sub-Wavelength Structures (DSWS) accurately; Rigorous Coupled Wave Analysis (RCWA) has been most popular owing to its advantages^{1,3-4}. RCWA has been reported for planer dielectric gratings and metallic surface relief gratings. A state - variables representation of coupled wave amplitudes permits the space harmonic amplitudes of the field inside the grating region to be obtained in terms of the eigenfunctions and eigen vectors of the coefficients matrix defined by Rigorous coupled wave equations⁵.

There are two main types of filters which exist either conventional spectral ones based on Perot-Fabry principle or resonant grating filters⁶. The performances of such filters are limited by their mechanical constraints due to a thick multilayer stack, and resonant filters have been considered as promising for narrow band free space filtering⁷⁻⁸. We have used RCWA algorithm for design of antireflection devices made by silica in Infra-red

applications and resonant grating filter narrow band filtering applications.

2. DESIGN AND MODEL

We have used *Rsoft* platform which has different modes based on different techniques. We have utilized *Diffractmod*, which is based on the RCWA method and implements several advanced algorithms including a fast converging formulation of Maxwell equations and a numerical stabilization scheme. We have designed antireflection surface devices, which is made by fused silica with a period (Λ) of $0.12\mu\text{m}$ as shown in Fig. 1. We have used $0.248\mu\text{m}$ wavelength of light to get antireflection properties of fused silica materials.

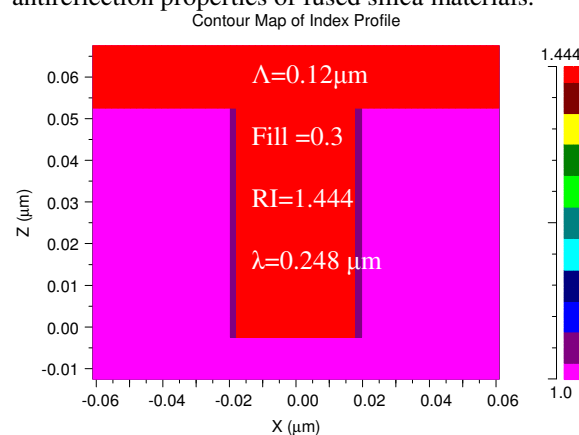


Fig. 1: Antireflection sub-wavelength structure

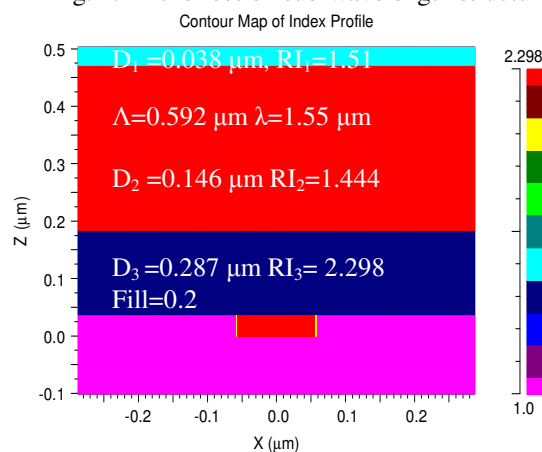


Fig. 2: Resonant grating filter stack

We have also designed resonant grating filter for grating filter applications, where we need a narrow band of wavelength as shown in Fig. 2. The filter consists of three layers on glass substrate. The first layer is made by titanium dioxide (TiO₂) upon the glass substrate and act as a waveguide. The second layer is made by SiO₂, which forms a separation layer between waveguide and the grating with a fill factor of 0.2. The third grating is made by same material as waveguide and act as grating itself. The thicknesses of three layers are d₁=38 nm, d₂=146 nm, and d₃=287 nm respectively. The refractive indices of two materials viz. TiO₂ and SiO₂ are 2.298 and 1.44 respectively. For wavelengths other than the design wavelength, the layer should fulfil antireflection conditions. The advantage of a no corrugated waveguide is that the dispersion relation is close to linear, with a nearly constant resonance line width that is important for tuning applications.

All the calculation for the design of the resonant filters is made by RCWA methods. The design procedure consists of several steps which are given as follows:

1. Choose the structure (layers, materials, angle of incidence, wavelength),
2. Fix a reasonable grating height, such as an equivalent homogenous layer,
3. Solve for the thickness to fulfil antireflection conditions,
4. Determine the grating period to achieve resonance at the desired wavelength,
5. Change the grating height to get desired FWHM
6. Implement numerical optimization

3. RESULTS AND DISCUSSION

The performance of antireflection surface are shown in Fig. 3(a). It shows the diffraction efficiencies versus various wavelengths. It is inferred that reflection reduces and get minimum for all infra red (IR) wavelengths and becomes almost zero for 0.24 ~ 0.26 μm wavelengths. Fig. 3(b) shows that the reflection becomes very less for

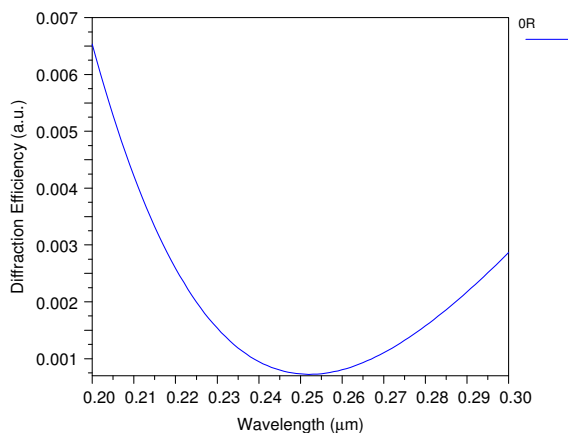


Fig. 3(a)

30° ~ 40° launch angles and increases against rise of angles. Hence we could get optimum launch angle and wavelength for a specific antireflection surface device design.

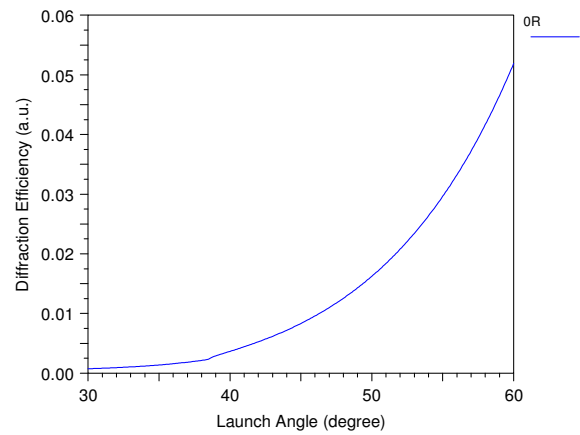


Fig. 3(b)

Fig.3 Antireflection Surface: a) diffraction efficiency versus wavelength and b) launch angle

A resonant grating filter is basically a sub-wavelength periodically structured planar waveguide that reflects and transmit light specularly. The principle is based on the excitations of modes in waveguide through a diffraction grating. The latter will couple the incident beam, for a given wavelength and incident angle, and thus excite a mode in the structure. By reciprocity this grating will uncouple the mode's field to emit the light. When the mode is excited, one observes a very thin peak in the reflectivity spectrum as shown in Fig 4(a-c) at different wavelengths. The potential of resonant grating filters for free-space filtering have been rapidly put forward and many studies, especially in 1-D case under classical mounting, have been conducted to understand and control the resonance phenomenon.

Performances of DSWS as grating filter for three wavelengths 1.5, 1.3 and 0.8 μm has been shown in Fig. 4(a - c) respectively. The structure

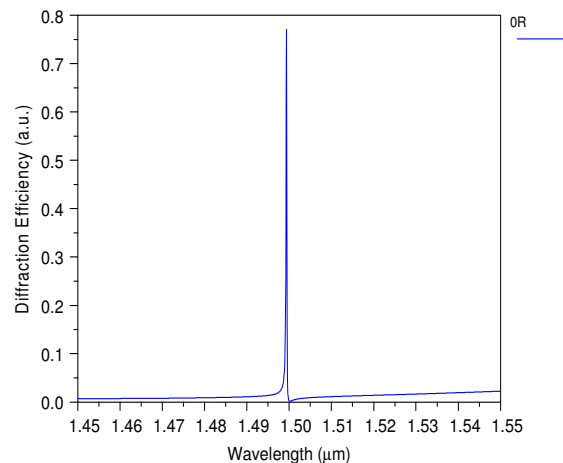


Fig. 4(a)

was designed to have a resonance peak with full width at half maximum (FWHM) of 0.5nm for the p polarization and 0.8nm for s polarization with respect to all considered communicated wavelengths.

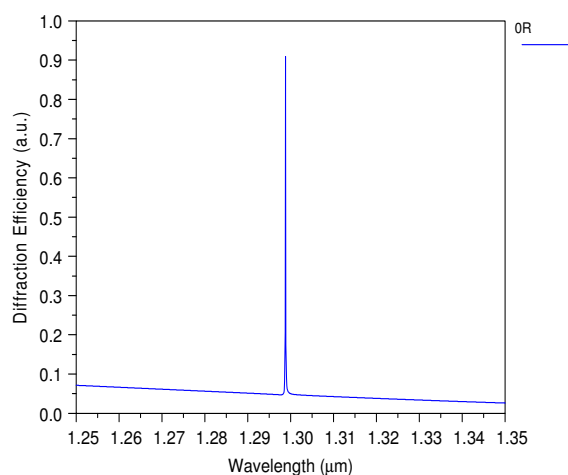


Fig. 4(b)

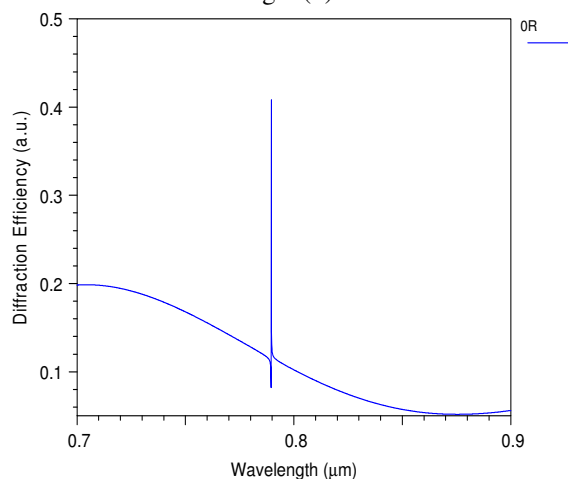


Fig. 4(c)

Fig.4 grating filter: a) diffraction efficiency @ 1.5 μm wavelength b) diffraction efficiency @ 1.3 μm wavelength c) diffraction efficiency @ 0.8 μm wavelength

CONCLUSION

We have used RCWA technique for the design of DSWS on *RSoft* platform. We have modeled an antireflection surface device made by fused silica with a period of 0.12 μm . It uses its zeroth order of diffraction to reduce the reflection at optical boundaries. We have also modeled a resonant grating filter which is promising alternatives to convenient spectral filters for very narrow band free space filtering. High performances have been achieved in simulation using 2-D grating in IR for telecommunication applications. The need for new spatial applications in IR has lead to the study of narrow band filters in the spectral range.

Acknowledgement: Authors are thankful to Director, IRDE, Dehradun to give permission to present this work.

References

1. Moharam M. G. and T. K. Gaylord, "Rigorous coupled-wave analysis of metallic surface-relief gratings," *J. Opt. Soc. Am. A.* 3 (1986) 1780.
2. Pfeffer M., "Nanotechnology in optics advances subwavelength-structures surfaces," *Europhotonics* (2003) 34.
3. Zhou Z. and T. J. Drabik, "Optimized binary, phase only, Diffractive optical element with subwavelength features for 1.55 μm ," *J. Opt. Soc. Am. A.* 12 (1995) 1104.
4. Chang Ni. Y. and C. J. Kuo, "Algorithm based on rigorous coupled wave analysis for diffractive optical design," *J. Opt. Soc. Am. A.* 18 (2001) 2491.
5. Sondergaard T., J. Gadegaard, P. K. Kristensen, T. K. Jensen, T. G. Pedersen and K. Pedersen, *Opt. Exp.* 18 (2010) 26245.
6. Hernandez S., O. Gauthier-Lafaye, A. -L. Fehrembach, S. Bonnefont, P. Arguel, F. Lozes-Dupuy and A. Sentenac, "High performance bi-dimensional resonant grating filter at 850 nm under oblique incidence of $\sim 60^\circ$," *Appl. Phys. Lett.* 92 (2008) 131112.
7. Niederer G, H. P. Herzig, J. Shamir, H. Thiele, M. Schnienper and C. Zschokke, "Tunable oblique incidence resonant grating filter for telecommunications," *Appl. Opt.* 43 (2004) 1683.
8. Niederer G, M. Salt H. P. Herzig, T. Overstolz, W. Noell and N. F. de Rooij, "Resonant grating filter for MEMS based add-drop device at oblique incidence," *Opt. MEMS conf. Lugano 22* (2002) 99.

LOW VELOCITY SOLITON PROPAGATION IN PHOTONIC CRYSTALS

Swati Rawal and R.K.Sinha

TIFAC- Centre of Relevance and Excellence in Fiber Optics and Optical Communication, Department of Applied Physics, Delhi Technological University (Formerly Delhi College of Engineering, University of Delhi), Bawana Road, Delhi-110042, India.

Email: swati.rawal@yahoo.com

Abstract: The proposed paper present, the possibility of soliton-like propagation of 111 fs pulses at 1.55 μm inside silicon-on-insulator photonic crystal waveguides.

Keyword : Photonic crystals, slow light, soliton

1. INTRODUCTION

Slow light refers to reduced group velocity and it offers major opportunities for controlled enhancement of light-matter interaction. High refractive index contrast structures such as photonic crystal (PhCs) waveguides have been demonstrated to be a promising approach to the achievement of slow light behaviour [1-5]. Linear effects such as gain, the thermo-optic effect - and some types of electro-optic interaction - scale linearly with the slow-down factor, while non-linear effects such as two photon absorption (TPA) and Kerr nonlinearity scale with the square of the slow-down factor [6,7]. The spatial compression experienced by light when it goes from a fast light situation to a slow light situation - and the greater time that light spends in the waveguide, because of the slow group velocity, increase the strength of the light-matter interaction and together imply the enhancement of nonlinear effects. Thus slow light behaviour causes a reduction in the input power level and the physical length of waveguide needed to produce given magnitudes of linear and nonlinear effects in the fast light regime [6,8,9]. By carefully engineering the photonic dispersion relationship, one may obtain unique opportunities for the realization of devices that exploit slow light effects [10, 11]. Recently, nonlinear effects such as the Raman Effect, soliton propagation, two-photon absorption (TPA), etc. have been observed by different authors [12-16]. Self phase-modulation (SPM), which leads to chirping and spectral broadening of ultra-short pulses, has also been reported earlier [14]. However TPA limits the extent of SPM through nonlinear absorption [17]. TPA typically involves transitions from the ground state of a system to a higher state by absorption of two photons from an incident radiation field having identical or, more generally, two different frequencies. TPA further creates free carriers that lead to additional losses through free-carrier absorption (FCA) and refractive index changes through free-

carrier dispersion (FCD) [18-20]. Thus TPA, FCA, FCD and SPM are important effects that influence the behaviour of short laser pulses in silicon waveguides. However soliton dynamics will dominate the propagation of femtosecond pulses in PhC waveguides when the group velocity dispersion (GVD) is strongly anomalous because of large waveguide dispersion [15]. It is important to mention here that, as optical pulses propagate through photonic crystal waveguides; their evolution in both the time and frequency domains is governed by the interplay of linear dispersion and nonlinearity. These effects are characterized by the characteristic lengths, namely the GVD length, L_D , and the nonlinear length L_{NL} [21]. Depending on the relative magnitudes of L_D , L_{NL} and the waveguide length, L , pulses evolve in various different ways. Here: $L_D = \frac{T_0^2}{|\beta_2|}$, $L_{NL} = \frac{1}{\gamma P_{in}}$

where T_0 is the initial width, in time, of the pulse, P_{in} is the incident power, β_2 is the GVD parameter and γ is the nonlinear parameter defined in subsequent sections. Monat and co-workers [22] have described how slow light with a group velocity on the order of $c/50$ can be obtained in silicon based PhC waveguides having an air-bridge, or membrane, structure. Such structures are inherently mechanically vulnerable. Monat *et al* have also shown that dispersion engineered slow-light PhC waveguides provide a suitable platform for enhancing nonlinear effects, making it possible to realize compact, low power, all-optical signal processing devices. For Gaussian pulses, an important criterion for comparing the relative magnitudes of the effects labeled as FCA, FCD and TPA comes from the dimensionless

parameter [23]: $r_a = \frac{S\sigma P_{in} T_0 \sqrt{\pi}}{2\sqrt{2}h\nu_o A_{eff}}$. The free carrier

density near the input end of the waveguide is negligible when $r_a \ll 1$ - i.e. the pulse peak power level is relatively low (e.g. a value of 100 mW in the context of the present paper). In this situation, only

TPA comes into play to a significant extent - and the observed reduction in output power is almost solely due to TPA. In the present paper, we have investigated the propagation of light in a nonlinear slow light medium formed by a channel waveguide in a silicon-on-insulator (SOI) photonic crystal structure having elliptical holes in a silicon core - and mechanically supported by the silica cladding, which remains in place. Our SOI PhC structure also uses a substantially thicker core layer that is compatible with the smaller index contrast implied by retaining the silica lower cladding layer. The supported PhC channel guide configuration is inherently more robust and practically suitable. Our choice of device architecture is demonstrably an effective and flexible way of controlling the speed of light (down to the order of $c/99$) and its associated group velocity dispersion (GVD), as described in reference [5].

We have further carried out a detailed study of the effect of the input peak power level and the impact of varying the slow-down factor on the nonlinear effects achievable in our proposed configuration for a photonic crystal channel waveguide - and have also shown the effect of the slow-down factor on the induced phase-shift at the optical frequency of the photonic bandgap. The transmitted spectrum becomes broader with increasing P_{in} - and develops multiple peaks when P_{in} is further increased - which is due to the magnitude of the induced nonlinear refractive index - and leads to a marked evolution of the optical frequency spectrum as the peak power level, P_{in} , is increased. The impact of the slow-down factor and the corresponding increase in nonlinear effects also defines the amount of input power required to achieve a particular level of spectral broadening in such waveguides. The present paper provides a comprehensive study of the effect of the slow-down factor and peak input power level on TPA, FCA and the SPM produced in PhC channel waveguides. The large SPM response achieved in the structure is vital for applications such as optical switching, as shown in the present paper. It has been reported [15] that femtosecond pulse propagation in SOI photonic wire waveguides can give rise to solitonic behaviour. With appropriate re-scaling, it becomes clear that the length of the PhC channel waveguide required to produce solitonic behaviour will be greatly reduced by comparison with such fast photonic wire waveguides.

2. SLOW LIGHT GENERATION

We have used an SOI based photonic crystal having a hexagonal arrangement of elliptical air holes in a silicon core layer as the basic structure for analysis. The thickness of the underlying silica layer was chosen to be $3\ \mu\text{m}$, on top of which the silicon core layer was chosen to have a thickness equal to $0.443\ \mu\text{m}$. The refractive index of silicon and silica are taken to be 3.49 and 1.45, respectively. A W0.7 waveguide was then created conceptually by omitting

a row of air holes along the ΓK direction - and shifting the two photonic crystal regions closer to each other so that the channel waveguide width becomes 0.7 times that of a W1 channel. The minimum values for the losses and defect mode dispersion below the silica light-line are found for a W0.7 waveguide. For this reason, one typical structure employed in experiments has been a W0.7 PhC waveguide [24]. The two neighbouring rows of holes on either side of the waveguide are filled with silica rods. This partially in-filled configuration may require one or two additional stages in its fabrication, but the benefits of enabling better control of dispersion justify the modest increase in fabrication complexity that is implied.

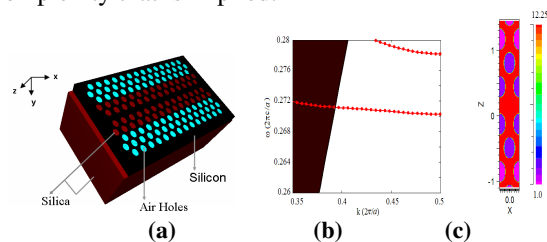


Fig. 1. (a) Schematic of the proposed structure with elliptical holes in a hexagonal arrangement. The two neighbouring holes on either side of the waveguide are filled with silica rods. (b) The calculated dispersion curve for transverse electric polarization in the defect mode. The black solid line is the silica light line and the lower pointed red dispersion curve is used for calculating the group velocity. (c) Super-cell used in computation of the band structure.

The lattice constant a , semi-major radius r_1 and semi-minor radius r_2 of the elliptical air holes were $0.42\ \mu\text{m}$, $0.16\ \mu\text{m}$ and $0.118\ \mu\text{m}$, respectively. These parameters were obtained by properly optimizing the proposed structure to obtain a flat section of dispersion curve below the silica light-line - because modes that lie above the light line are lossy in the vertical direction - i.e. into the substrate.

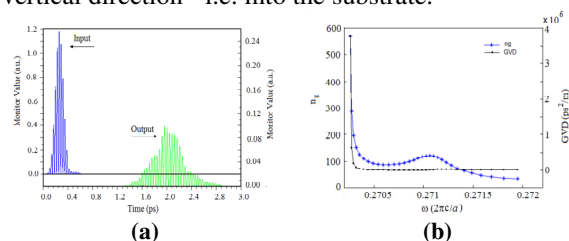


Fig. 2. (a) Field amplitude of Gaussian pulse at the input and output ends of the waveguide, at $\lambda_0=1.55\ \mu\text{m}$. (b) Variation of group index and group velocity dispersion with frequency.

Figure 1(a) shows a schematic of the proposed structure and fig. 1(b) shows the calculated dispersion curves for transverse electric (TE) polarization waves propagating in the defect mode. The flat section of the dispersion curve displays a slow group velocity over a substantial bandwidth. If we now define the low velocity range to be those values that give a $\pm 10\%$ variation in the group index n_g [25], we obtain $n_g = 99$ over a frequency range of 344 GHz. Therefore the normalized value of the Delay-Bandwidth Product

(DBP), which is defined as $n_g^*(\Delta\omega/\omega)$, is calculated to be 0.20. We have further investigated the delay for pulses propagating through the waveguide using FDTD simulations. Figure 2 shows the field amplitude of the Gaussian pulse recorded at the input and output ends of the waveguide, as a function of time, for $\lambda_0=1.55\mu\text{m}$. The length of the waveguide is $15a$. The group velocity dispersion (GVD) parameter β_2 is related to the second order derivative of the dispersion curve by the following expression:

$$\beta_2 = \frac{d^2k}{d\omega^2} = \frac{d}{d\omega} \left(\frac{1}{d\omega/dk} \right) \Rightarrow \beta_2 = -\frac{1}{v_g^3} \frac{d^2\omega}{dk^2} \quad (1)$$

The group velocity n_g and the GVD parameter, in the flat regime below the silica light line, are shown in Figure 3 - as a function of frequency. The figure shows that the GVD parameter is on the order of $10^4 \text{ ps}^2/\text{m}$ and that the average group index is 99. We further define the slow-down factor (S) as the ratio of the group index n_g to the refractive index, n_{si} , of bulk silicon. It is calculated to be 28.28 at $\lambda_0 = 1.55 \mu\text{m}$ for the designed elliptical hole PhC waveguide.

3. NONLINEAR PROPAGATION

Next we evaluate the nonlinearity of an SOI-based photonic crystal waveguide. The propagation of the optical pulse having amplitude $A(z,t)$ is given, for sufficiently strong confinement, by the following nonlinear Schrödinger Equation [18, 26, 27] in one space dimension and time:

$$\frac{\partial A}{\partial z} + \frac{\alpha}{2}A + \frac{i\beta_2}{2} \frac{\partial^2 A}{\partial t^2} - \frac{\beta_3}{6} \frac{\partial^3 A}{\partial t^3} = i\kappa|A|^2 A - N_c \left(\frac{\sigma}{2} + ik_c k_0 \right) A \quad (2)$$

where α accounts for the linear component of the propagation losses, β_2 is the dispersion parameter at wavelength λ_0 , n_2 is the Kerr coefficient of silicon, κ defines the nonlinearity in the waveguide and is given by $\kappa = \gamma + i\frac{\zeta}{2}$, where $\gamma = \frac{2\pi n_2}{\lambda_0 A_{eff}}$ is the nonlinear

parameter and ζ is related to the two photon absorption (TPA) coefficient, β_{TPA} , defined as $\zeta = \frac{\beta_{TPA}}{2A_{eff}} \cdot A_{eff}$ is the cross-sectional area of the PhC

channel waveguide mode and is found to be $0.12 \mu\text{m}^2$ for slow modes ($S=28.28$) whereas it is calculated to be $0.05 \mu\text{m}^2$ ($S=2$) for fast modes [26]. The second term on the right-hand side of equation (2) gives the free carrier absorption (FCA), defined by the parameter σ , and the free carrier dispersion (FCD), accounted for by k_c - and N_c is the carrier density produced by TPA. In silicon, the free carriers generated by TPA are governed by the following rate equation:

$$\frac{\partial N_c(t)}{\partial t} = \frac{\beta_{TPA}}{2h\nu_0} |A|^4 - \frac{N_c}{\tau_c} \quad (3)$$

where τ_c is the carrier lifetime in silicon and is taken to be approximately equal to 1 ns [18]. At $\lambda_0 = 1.55 \mu\text{m}$, the parameters identified in equations (2) and (3) have the values given in [18,26].

$A_{eff} = 0.12 \mu\text{m}^2$, the GVD and TOD are found to be $-8291 \text{ ps}^2/\text{m}$ and $-78 \text{ ps}^3/\text{m}$, respectively at $\lambda_0 = 1.55 \mu\text{m}$. The reduction in the group velocity of the waveguide mode causes optical localization and field enhancement in the waveguide. The slow-down factor, S , may therefore be introduced into equation (2) by replacing α , γ and β_{TPA} - by $\alpha \times S$, $\gamma \times S^2$ and $\beta_{TPA} \times S^2$, respectively. Equation (2) therefore becomes:

$$\frac{\partial A}{\partial z} + \frac{S\alpha}{2} A + \frac{i\beta_2}{2} \frac{\partial^2 A}{\partial t^2} - \frac{\beta_3}{6} \frac{\partial^3 A}{\partial t^3} = iS^2\gamma|A|^2 A - \frac{S^2\beta_{TPA}}{2A_{eff}} |A|^2 A - SN_c \left(\frac{\sigma}{2} + ik_c k_0 \right) A \quad (4)$$

When $T_0 \ll \tau_c$ - and the pulse repetition rate is very low, the second term on the right-hand side of Eq. (3) - corresponding to carrier recombination - can be ignored, because the recombination time, τ_c , is much larger than the pulse duration.

4. THE PHOTONIC CRYSTAL CHANNEL WAVEGUIDE AS A SOLITON PROPAGATOR

A soliton can be formed in a waveguide when the input pulse width is in the femtosecond regime, i.e. short compared with the width of the resulting soliton - and also $\beta_2 < 0$. According to standard soliton propagation theory [21], a fundamental soliton can be excited if the condition $\gamma P_0 L_D = 1$ is satisfied. Furthermore, the time-domain expansion is simultaneously accompanied by spectral narrowing. This criterion has been used previously as a test for soliton formation in silicon photonic waveguides [15]. The values obtained for the second and third order dispersion coefficients at a wavelength of $1.55 \mu\text{m}$ are $\beta_2 = -8291 \text{ ps}^2/\text{m}$ and $\beta_3 = -78 \text{ ps}^3/\text{m}$. We now consider $T_0 = 0.111 \text{ ps}$, $L_D = 1.5 \mu\text{m}$ and $L_{NL} = 1.5 \mu\text{m}$, with $\gamma = 202 \text{ mW}^{-1}$ and $P_{in} = 4 \text{ W}$ at $\lambda_0 = 1.55 \mu\text{m}$.

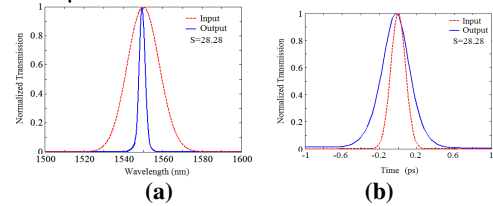


Fig. 8. Propagation of a 111 fs pulse through the SOI PhC waveguide; (a) Spectrum and (b) temporal pulse shape.

Hence the conditions for the propagation of a fundamental soliton are satisfied. Figure 8(a) and Figure 8(b) show the input and output pulse profiles and corresponding spectra. The presence of β_{TPA} and α deforms the shape of the output pulse and leads to spectral contraction - and time-domain expansion - of the output pulse with respect to the spectrum and length of the input pulse.

5. CONCLUSIONS

In this paper, we have reported the design of an SOI-based PhC channel waveguide with elliptical holes. Two neighbouring rows on either side of the channel waveguide are filled with silica rods to obtain an

average group index of 99 at a wavelength of 1550 nm. We have further carried out the nonlinear modelling of the wave propagation in such a waveguide and a detailed study of the effect of input peak power and different slow down factors on the nonlinear effects achieved in proposed photonic crystal channel waveguide is presented. If the input pulse width is in the hundred femtosecond regime, the waveguide can generate soliton-like propagation at moderate pulse energies.

ACKNOWLEDGEMENT

The authors gratefully acknowledge the initiatives and support towards establishment of the “TIFAC Centre of Relevance and Excellence in Fiber Optics and Optical Communication at the Delhi College of Engineering, Delhi” through the “Mission REACH” program of Technology Vision-2020 of the Government of India.

REFERENCES:

- H. Gersen, T.J. Karle, R.J.P. Engelen, W. Bogaerts, J.P. Korterik, N.F. Van Hulst, T.F. Krauss and L. Kuipers, “Real space observation of ultra slow light in photonic crystal waveguides”, *Phys. Rev. Letts.* **94**, 073903 (2005).
- Y.A. Vlasov, M.O’Boyle, H.F. Hamann and S.J. McNab, “Active control of slow light on a chip with photonic crystal waveguides”, *Nature* **438**, 65-69 (2005).
- R.M. De La Rue, “Slower for longer”, *2*, 715-716 (2008).
- T.F. Krauss, “Why do we need slow light?”, *Nature Photonics* **2**, 448-450 (2008).
- S. Rawal, R. K. Sinha and R. M. De La Rue, “Slow Light Miniature Devices with Ultra-Flattened Dispersion in Silicon-on-Insulator Photonic Crystal”, *Opt. Exp.* **17**, 13315-13325 (2009).
- T.F. Krauss, “Slow light in photonic crystal waveguides”, *J. Phys. D: Appl. Phys.* **40**, 2666-2670 (2007).
- M. Soljacic and J.D. Joannopoulos, “Enhancement of nonlinear effects using photonic crystals”, *Nature Material* **3**, 211-219 (2004).
- M. Soljacic, S.G. Johnson, S.H. Fan, M. Ibanescu, E. Ippen and J.D. Joannopoulos, “Photonic crystal slow light enhancement of non linear phase sensitivity”, *J. Opt. Soc. Am. B-Opt. Phys.* **19**, 2052-2059 (2002).
- M.D. Settle, R.J.P. Engelen, M. Salib, A. Michaeli, L. Kuipers and T.F. Krauss, “Flat band slow light in photonic crystals featuring spatial pulse compression and terahertz bandwidth”, *Opt. Exp.* **15**, 219-226 (2007).
- T. Baba and D. Mori, “Slow light engineering in photonic crystals”, *J. Phys. D: Appl. Phys.* **40**, 2659-2665 (2007).
- L.H. Frandsen, A.V. Lavrinenko, J. Fage-Pedersen and P. I. Borel, “Photonic crystal waveguides with semi slow light and tailored dispersion properties”, *Opt. Exp.* **14**, 9444-9450 (2006).
- H. Oda, K. Inoue, A. Yamanaka, N. Ikeda, Y. Sugimoto and K. Asakawa, “Light amplification by stimulated Raman scattering in AlGaAs based photonic crystal line defect waveguides”, *Appl. Phys. Letts.* **93**, 051114 (2008).
- V.N. Astratov, R.M. Stevenson, I.S. Culshaw, D.M. Whittaker, M.S. Skolnick, T.F. Krauss and R.M. De La Rue, “Heavy photon dispersions in photonic crystal waveguides”, *Appl. Phys. Letts.* **77**, 178-180 (2000).
- H. Tsang, H.K. Tsang, C.S. Wong, T.K. Liang, I.E. Day, S.W. Roberts, A. Harpin, J. Drake, and M. Asghari, “Optical dispersion, two photon absorption and self phase modulation in silicon waveguides at 1.5 μm wavelength”, *Appl. Phys. Letts.* **80**, 416, 2002.
- W. Ding, C. Benton, A.V. Gorbach, W.J. Wadsworth, J.C. Knight, D.V. Skryabin, M. Gnan, M. Sorel and R.M. De La Rue, “Solitons and spectral broadening in long silicon-on-insulator photonic wires”, *Opt. Exp.* **16**, 3310-3319 (2008).
- P. Millar, R. M. De La Rue, T. F. Krauss, J. S. Aitchison, N. G. R. Broderick and D. J. Richardson, “Nonlinear propagation effects in an AlGaAs Bragg grating filter”, *Opt. Letts.* **24**, 685-687 (1999).
- X. Chen Nicolae, C. Panoui, I. Hsieh, J.I. Dadap and R. M. Osgood, “Third order dispersion and ultrafast pulse propagation in silicon wire waveguides”, *IEEE Phot. Tech. Letts.* **18**, 2617-2619 (2006).
- L. Yin and G.P. Agrawal, “Impact of two photon absorption on self phase modulation in silicon waveguides”, *Opt. Letts.* **32**, 2031-2033 (2007).
- H. Oda, K. Inoue, Y. Tanaka, N. Ikeda, Y. Sugimoto, H. Ishikawa and K. Asakawa, “Self phase modulation in photonic crystal slab line defect waveguides”, *App. Phys. Letts.* **90**, 231102, 2007.
- K. Inoue, H. Oda, N. Ikeda and K. Asakawa, “Enhanced third order nonlinear effects in slow light photonic crystal slab waveguides of line defect”, *Opt. Exp.* **17**, 7206-7216 (2009).
- G.P. Agrawal, *Nonlinear Fiber Optics III*, Academic Press, San Diego, 2001.
- Christelle Monat, Bill Corcoran, Dominik Pudo, Majid Ebnali-Heidari, Christian Grillet, Mark D. Pelusi, David J. Moss, Benjamin J. Eggleton, Thomas P. White, Liam O’Faolain, and Thomas F. Krauss, “Slow Light Enhanced Nonlinear Optics in Silicon Photonic Crystal Waveguides”, *IEEE J. Selected Topics in Quant. Elect.*, **16**, 344-357, 2010.
- Q. Lin, O.J. Painter, and G.P. Agrawal, “Nonlinear optical phenomena in silicon waveguides: Modeling and applications”, *Opt. Exp.* **15**, 16604-16644 (2007).
- M. Notomi, A. Shinya, K. Yamada, J. Takahashi, C. Takahashi and I. Yokohama, “Single mode transmission within photonic bandgap of width varied single line defect photonic crystal waveguide on SOI substrates”, *Elect. Lett.* **37**, 293-295 (2001).
- Y. Hamachi, S. Kubo and T. Baba, “Slow light with low dispersion and nonlinear enhancement in a lattice shifted photonic crystal waveguide”, *Opt. Letts.* **34**, 1072-1074 (2009).
- C. Monat, B. Lorcoran, M. E. Heidari, C. Grillet, B.J. Eggleton, T.P. White, L. O’Faolain and T.F. Krauss, “Slow light enhancement of nonlinear effects in silicon engineered photonic crystal waveguides”, *Opt. Exp.* **17**, 2944-2953 (2009).
- I.D. Rukhlenko, M. Premaratne, C. Dissanayake, and G. P. Agrawal, “Nonlinear Pulse Evolution in Silicon Waveguides: An Approximate Analytic Approach” *IEEE J. Lightwave Technology* **27**, 3241-3248 (2009).

Imaging Exoplanet Transits with Hypertelescopes

A.Surya^{1*}, S.K.Saha¹ and A.Labeyrie²

¹Indian Institute of Astrophysics, Bangalore

²Colle`ge de France, 11, place Marcelin Berthelot, 75231 Paris Cedex 05, France

Email: arun@iia.res.in

Abstract: Optical stellar interferometers have demonstrated milli-arcsecond resolution with few apertures spaced hundreds of meters apart. To obtain rich direct images, many apertures will be needed, for a better sampling of the incoming wavefront. The coherent imaging thus achievable improves the sensitivity with respect to the incoherent combination of successive fringed exposures, heretofore achieved in the form of optical aperture synthesis. For efficient use of highly diluted apertures, this can be done with pupil densification, a technique also called "Hypertelescope imaging". One of the major applications of Hypertelescopes will be in imaging of exoplanet transits across a resolved star. Our simulations show the capabilities of Hypertelescopes to image exoplanets crossing the disk of the well resolved parent star.

1.1. INTRODUCTION

In the way of high-resolution optical astronomy with interferometric arrays, producing better images will require more apertures for a denser sampling of the optical wave. As few as three apertures can suffice in principle to reconstruct images through "optical aperture synthesis", using earth rotation or baseline changes to sample the needed Fourier components of the object. But a better sensitivity can be reached with systems using more apertures simultaneously, even if these are smaller for a conserved collecting area. The gain arises from the coherent combination of light vibrations achievable with many apertures working simultaneously, as opposed to the "optical aperture synthesis" approach where interference fringes are recorded with fewer apertures, repeatedly with different baseline settings, and then combined in the computer, i.e. incoherently. N number of phased beams combined coherently with a simple Fizeau arrangement indeed produces a highly constructive interference, in the form of a peak which is N times more intense than the average sidelobes.

Instead, successive exposures with subsets of the sub-apertures, even if they are enlarged to conserve the photon flux and moved to improve the u,v coverage, reduce the peak intensity and thus the dynamic range in the convolved image of a complex source (Labeyrie 1996). Fizeau combination however becomes inefficient with highly diluted apertures, since the narrow interference peak appearing in the image of a point source, at the center of the much broader envelope diffracted by the subapertures, contains a small proportion of the energy. A way of retrieving most energy in the peak, for efficiently observing faint sources with many-aperture interferometers capable of rich direct imaging, has appeared in the form of the Hypertelescope or "densified aperture" scheme (Labeyrie 1996, Lardi`re 2007). Practical designs for large Hypertelescopes, with a spherical geometry inspired from the Arecibo radio telescope, are under testing for terrestrial versions (Le Coroller 2011, Rondi A. 2011, Ower-Petersen et al., 2011) and also studied for space versions.

2. EXOPLANET TRANSITS

Periodic Eclipses of Exoplanets over the resolved star disk will be observable with Hypertelescopes. This is an easier way of imaging exoplanets without the use of coronagraphic techniques. Jupiter like planets which may eclipse its parent star may be 10 times smaller, thus covering 1 resel if star was resolved over 10 resels. The planet's darkness will be filled by the side lobes of the spread function, but sufficient contrast still remains to properly resolve it. Observations at several wavelengths will also give information about planets extended atmosphere.

3. SIMULATIONS

The Point Spread Function for a general Hypertelescope is given by the formulae, where A is the Diffraction function and I the Interference function given by

$$I_{PSF}(x, y) = A(x, y) \times I_0(x, y), \quad (1)$$

The interference function depends only on the array

$$I_0(x, y) = \left| \sum_{k=i}^{n_T} e^{-\frac{2\pi i}{\lambda}(xu_k + yv_k)} \right|^2. \quad (2)$$

configuration while the diffraction function $A(x, y)$ depends on the beam combination scheme used (Lardiere et al. 2004). For our analysis we have considered $A(x, y)$ to be an Airy function. In our simulation we are considering highly diluted arrays in which pupil densification is so strong that the shift of the airy envelope is negligible. In such a case the Pseudo Convolution Equation determining the image formation of the Hypertelescope is given by

$$I(x, y) = A(x, y) \times (I_0(x, y) \otimes O(x, y)), \quad (3)$$

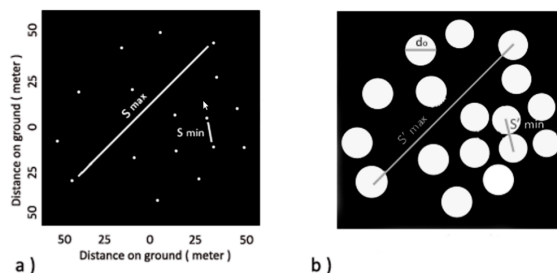
where $O(x, y)$ is the object configuration.

4. APERTURE CONFIGURATION

The aperture configuration used for the simulations are shown in the fig 1. We have used a non-redundant array of sub-apertures arranged inside a disc with maximum baseline of 100m.

Aperture configurations used in the simulations.

a) The input pupil of the a random 20 mirror array. b) The exit pupil after densification



5. EARTH ROTATION APERTURE SYNTHESIS

The sparse filling of the entrance aperture, although enhanced in the densified exit pupil, affects the performance of the speckle imaging reconstruction. But part of it is retrieved if the entrance aperture, as seen from the observed star, can be modified or rotated during an observation. Earth Rotation Aperture Synthesis is a common technique exploited in interferometry to increase the coverage of the frequency plane by an interferometric array. With the help of simulations we have tried to study the possible techniques of using aperture rotation through night with diluted aperture hypertelescope systems.

6. RESULTS

A simulation image of exoplanet transit is given below.

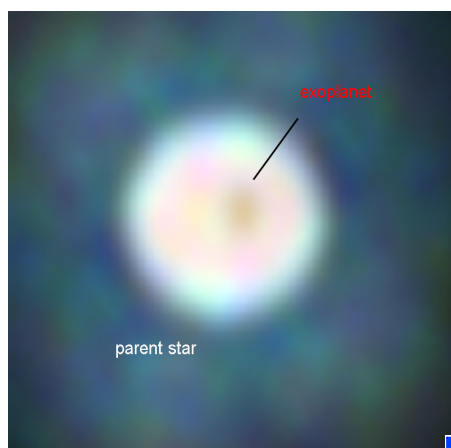
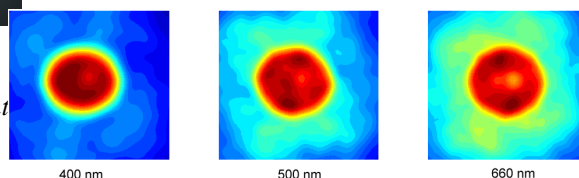


Fig 2.

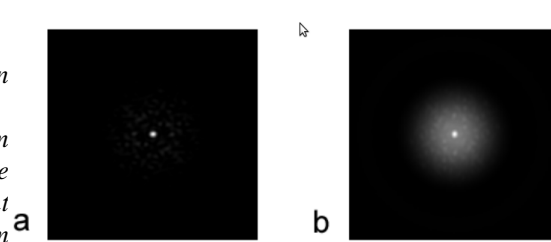
Simulated Hypertelescope Image of the Exoplanet Transit in different wavelengths.

Fig 1. Exoplanet transit across a resolved star, as imaged by a 20 mirror cophased diluted Hypertelescope with maximum baseline of 100m. The star disk is 27 resels while the exoplanet is 3 resels in the image. The simulated image is a combination of 3 separate images at different wavelengths.



Our results clearly shows that Hypertelescopes could be used in a new way of detecting exoplanets. Because of the limited resolution and smaller dynamic range of pairwise combination system used in the current interferometers, it is very difficult for this technique to succeed with the current optical interferometric telescopes of large baselines. But Hypertelescopes with their coherent combination of light beams from different sub-apertures allow for the use of above mentioned technique to image exoplanets.

3. *The Point Spread Function from 20 subapertures.*
 a) *PSF from hypertelescope all-in-one imaging mode with coherent combination of beams from the subapertures.*



- b) *The PSF from co-adding the fringe systems from all the possible pairs among the 20 sub apertures.*

The better contrast in the Point Spread Function of Hypertelescope mode is seen from the two images. This high dynamic range achievable in imaging will enable hypertelescopes to detect the transits of exoplanets over the resolved star disk.

7. REFERENCES

- [1] Labeyrie A., "[Resolved imaging of extra-solar planets with future 10-100 km optical interferometric arrays](#)", 1996, A&A, 118, 517
- [2] Le Coroller H. et al., ""2011 in preparation
- [3] Rondi A., 2011, proc. Kiruna Symp. "Integrated Modeling of Complex Optomechanical Systems "
- [4] Owner-Petersen et al., 2011, proc. Kiruna Symp. "Integrated Modeling of Complex Optomechanical Systems "
- [5] Lardière O. et al., "Direct imaging with highly diluted apertures. I. Field of view limitations ", 2007, MNRAS, 375, 977-988

VISUALIZING VECTOR FIELD STRUCTURES USING THE HELMHOLTZ HODGE DECOMPOSITION

Monika Bahl, S.Chopra, and P.Senthilkumaran

Department of Physics

Indian Institute of Technology, Delhi, Hauz khas, New Delhi-110016

Email: monikaiitd1@gmail.com

Abstract: The Helmholtz Hodge Decomposition separates the vector fields into parts that represent the directionality of data explicitly. It can be applied to identify vector field structures including sources, sinks and singularities. We have used the generalized differential operators to establish critical points in a field and segment it into regions of uniform behavior. We have implemented the extraction on a synthetic field and demonstrated the same on a single charged vortex phase field.

1. INTRODUCTION

Any random vector field would, in entirety, represent a non-homogeneous structure. They are ubiquitous in computational sciences. Vector fields are used in a large number of applications including fluid and smoke simulations, gaming, and in the analysis of MRI data in medical sciences, to name a few. In order to extract the information about the various elements present in it, it is required to segregate the field into sets which are uniform in behavior. Thus, partitioning the original field into intuitive and useful components render more information about the features contained in it.

There are many topological approaches to visualize vector fields. Many of them represent the field using streamlines and curves, which exhibit the field concisely [1-3]. There are also some techniques which extract the features by decomposing the original field. One such technique is the Helmholtz Hodge Decomposition (HHD) which allows a field to be separated into divergence-free (solenoidal) and curl-free (irrotational) parts [2, 3]. It has been used in the solution of many problems in fluid mechanics and electromagnetism. Poltheier et al [2] used a discrete Hodge decomposition to locate singularities in vector fields. In our approach, we use the Finite Difference Approximation to differential operators, and apply it to separate the optical phase field of a single charged vortex.

2. HELMHOLTZ HODGE DECOMPOSITION

The Helmholtz Hodge Decomposition is based on the Helmholtz theorem [4, 5], which allows a vector field F , entirely contained within a finite region of space, to be uniquely determined by two components, the irrotational component and the solenoidal component.

2.1 Helmholtz theorem

If a vector field F whose divergence $\nabla \cdot F = b(r)$ and curl $\nabla \times F = c(r)$ are known and entirely contained within a finite region of space, [5] then F is uniquely determined and has the value

$$F = -\nabla\phi + \nabla \times A$$

where,

$$\phi(r) = \frac{1}{4\pi} \int_V \frac{b(r')}{r} dv'$$

is the curl-free or the irrotational component, called the scalar potential, and

$$A(r) = \frac{1}{4\pi} \int_V \frac{c(r')}{r} dv'$$

is the divergence-free or the solenoidal component, called the vector potential.

The former contains only the sources and sinks, while the latter term contains only vortices.

2.2 Helmholtz Hodge decomposition

The Hodge-Helmholtz decomposition (HHD) is a technique used to decompose a vector field into a curl-free component, a divergence-free component and a harmonic remainder.

Thus, a field F is decomposed as

$$F = f_{CF} + f_{DF} + f_{HR}$$

where f_{CF} is the curl-free or the irrotational component, f_{DF} is the divergence-free or the solenoidal component, and f_{HR} is the harmonic remainder, which is the curl-free and divergence-free component.

It can be seen that $f_{CF} = \nabla\phi$, where ϕ is a scalar potential and $f_{DF} = \nabla \times A$, where A is a vector potential. As can be seen, $\nabla \times f_{CF} = 0$

Once the curl-free and the divergence-free parts are defined, the harmonic remainder is easily found by subtracting the former two components from the

initial original field.

The harmonic remainder satisfies

$$\nabla \cdot f_{HR} = 0 \text{ and } \nabla \times f_{HR} = 0$$

$\nabla, \nabla \cdot, \nabla \times$ represent the gradient, the divergence and the curl operators respectively. This decomposition is particularly interesting for extraction of the features and singularities of a flow. For instance, in 2D fields, the curl-free term $\nabla\phi$ contains only sources and sinks, while the divergence free term $\nabla \times A$ contains only vortices.

Fig. 1 is an example of how HHD works. A synthetic field is decomposed into its curl-free and divergence-free components. The corresponding harmonic remainder is also shown.

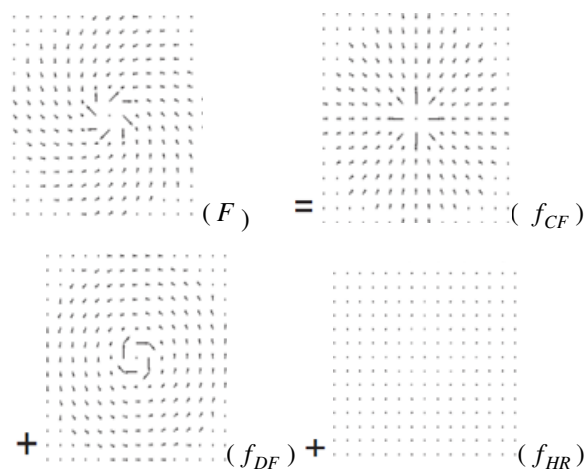


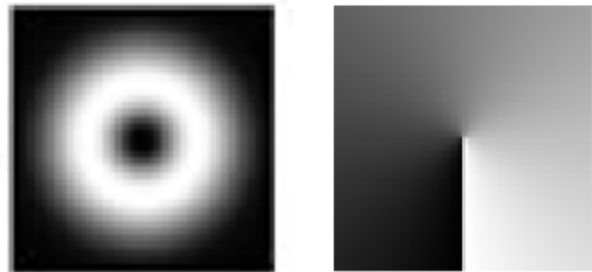
Fig 1. Helmholtz Hodge Decomposition. A field F is partitioned into a curl-free component (f_{CF}), a divergence-free component (f_{DF}), and a harmonic remainder (f_{HR}).

We present numerical simulation results of HHD applied on a synthetic vector field generated from the gradient of a scalar field.

2.3 Optical Vortex

A single charge vortex is an optical phase singularity and is characterized by an azimuthal phase dependence of the form $\exp(il\theta)$, where l is the topological charge of the phase singular beam [6-13]. The value of the topological charge of the vortex field determines the total phase, which the wavefront accumulates for one complete rotation around the vortex point. The sign of the charge determines the helicity of the phase singular beam. The phase gradient of the wavefield having phase singularity is non-conservative in nature, and curls around a critical point. The line integral of the phase gradient over any closed path surrounding the point of singularity is non-zero i.e. $\oint \nabla \zeta \cdot dl = 2\pi l$ where $\nabla \zeta$ is the phase gradient and is a line element [4 - 11]. At isolated point, where phase singularity occurs, the phase is

uncertain and the amplitude is zero, thereby creating an intensity null at the point of singularity. The intensity and the phase profile of a phase singular beam with topological charge 1 are shown in Fig 2.



(a) (b)

Fig 2. (a) Intensity and (b) Phase profile of a phase singular beam ($l = 1$) [12]

Optical Vortices are present in scintillated laser beams as speckles and many processed images, simulated representations and the like. Adaptive Optics (AO) technology is usually concerned about the correction of this scintillation to render improved quality at the other end. We introduce the removal of a vortex from a vector field using the Helmholtz Hodge Decomposition by minimizing the least square errors of various terms, as described in the next section.

2.4 The HHD method: Minimization of Least Squares

Defining ϕ as the curl-free component, A as the divergence-free component and h as the harmonic component of F , we need to find a solution that minimizes the sum of the following three terms,

$$\|\nabla \times \phi\|^2, \quad \|\nabla \cdot A\|^2, \quad \|h\|^2 = \|\phi + A - F\|^2$$

We apply the finite difference approximation to the operators for curl and divergence. We then apply the Helmholtz Hodge decomposition to the truncated domain. All simulations have been done in Matlab R2010.

3. RESULTS AND DISCUSSION

Using the Finite Difference Approximation to Differential operators, we have applied HHD to a synthetic field which has been derived from the scalar field $3x * \exp-(3x^2 + 3y^2)$ by taking its gradient. We have also applied it to the phase gradient of a complex field of an optical vortex of charge 1, i.e. $\exp(i\theta)$. All simulations have been done in Matlab. In Fig 3, (a) to (d) show the simulation results of HHD applied on the

synthetic vector field, and, (e) to (h) show the simulation results of the Hodge decomposed charge 1 vortex field. The vortex is an optical phase singularity whose phase gradient curls around a critical point. It can thus be removed from the field using HHD, as is evident from fig. (f).

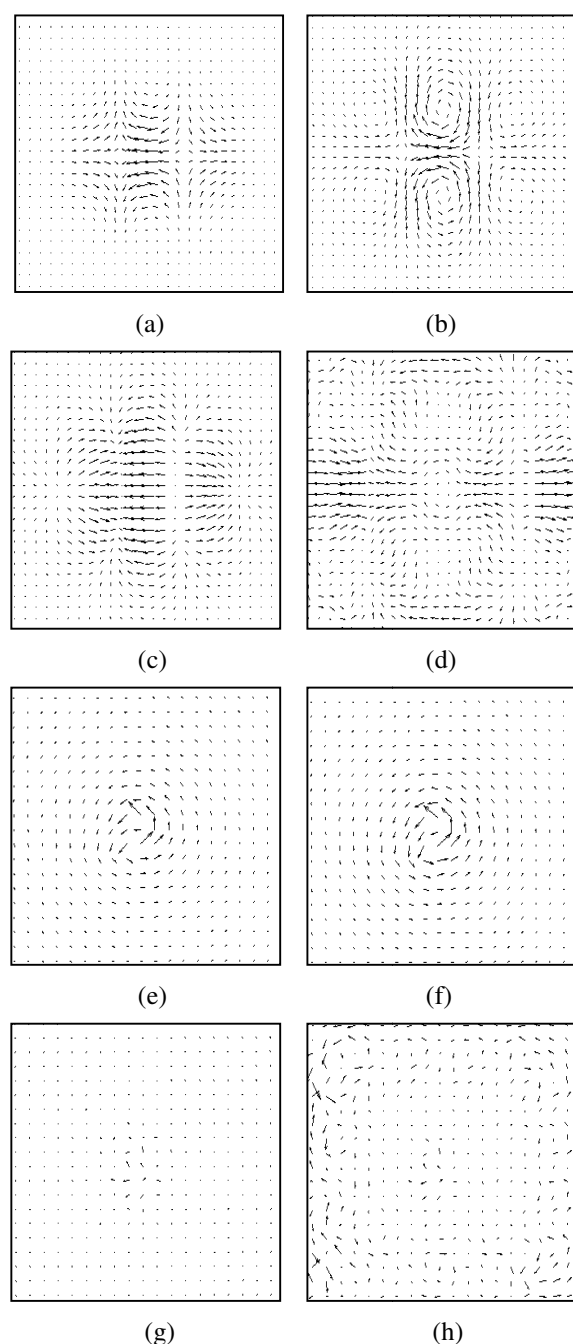


Fig 3. (a) to (d) show the Simulation results for the first field while (e) to (h) show the Hodge decomposed vortex field. (a), (b), (c) and (d), and correspondingly, (e), (f), (g) and (h) show the original field, the solenoidal, the irrotational and the harmonic fields respectively.

The results can, thus, be applied to manipulate fields which need to be partitioned for various applications.

REFERENCES

- [1] Globus A, Levit C, and Lasinki T, "A Tool for Visualizing the topology of Three-Dimensional Vector Fields". *In Proceedings of IEEE- Visualization 91*, 33–40, (1991)
- [2] K. Polthier and E. Preuss. "Identifying vector field singularities using a discrete hodge decomposition", H. C. Hege and K. Polthier, Springer Verlag, 2002
- [3] Y. Tong, S. Lombeyda, A. N. Hirani, and M. Desbrun, "Discrete multiscale vector field decomposition", *In SIGGRAPH 2003 Proceedings.*, ACM.,<http://www-grail.usc.edu/pubs/TLHD03.pdf>, 2003
- [4] K. E. Oughstu, "Helmholtz' Theorem", Lecture Notes, [http://www.cems.uvm.edu/~oughstun/LectureNotes141/Topic_03_\(Helmholtz Theorem\).pdf](http://www.cems.uvm.edu/~oughstun/LectureNotes141/Topic_03_(Helmholtz%20Theorem).pdf)
- [5] Arfken, G. B. and Weber, H. J., "Mathematical Methods for Physicists" Elsevier, 6th edition., 2005
- [6] M.S. Soskin, M.V. Vasnetsov, "Singular Optics", *Progress in Optics*, **42**, 219-276, 2001
- [7] M. R. Dennis, K. O. Holleran, M. J. Padgett, Singular Optics: Optical Vortices and Polarization Singularities, *Progress in Optics*, **53**, 293-363, (2009)
- [8] Enrique.J.Galvez, "Structured Light and Its Applications", 63-77, Academic Press, 2008
- [9] A. M. Yao and M. J. Padgett, "Orbital angular momentum: origins, behavior and applications", *Advances in Optics and Photonics*, **3**, 161–204, (2011)
- [10] G. Molina-Terriza, J. P. Torres & L. Torner, "Twisted Photons", *Nature Physics*, **3**, 305-310, 2007
- [11] J.F. Nye and M.V. Berry, "Dislocations in Wave Trains", *Proc. Royal Soc. London Ser. A*, **336**, 165-190, (1974)
- [12] I.V Basistiy, M.S Soskin and M.V Vasnetsov, "Optical wavefront dislocations and their properties", *Opt. Commun.*, **119**, 604, (1995)
- [13] I. V. Basistiy, V. Yu. Bazhenov, M. S. Soskin, M. V. Vasnetsov, "Optics of light beams with screw dislocations", *Optics Communications*, **103**, 422-428, (1993)

High Performance SiGe Metal Semiconductor Field Effect Transistor (MESFET) Based IR Photodetector

Rajni Gautam¹, Manoj Saxena², R.S.Gupta³, and Mridula Gupta¹

¹Deptt. of Elect. Sci., Univ. of Delhi, South Campus, Benito Juarez Road, New Delhi, India

²Deptt. of Elect., Deen Dayal Upadhyaya college, Univ. of Delhi, New Delhi, India

³Deptt. of ECE, Maharaja Agrasen Institute Of Technology, Delhi, India

Email: rajni7986@gmail.com, mridula@south.du.ac.in, saxena_manoj77@yahoo.co.in, rsgu@bol.net.in

Abstract: The paper demonstrates that SiGe metal-semiconductor field-effect transistors (MESFETs) can be used as high-performance IR photodetector under suitable gate bias and Ge composition. When a reverse gate bias is applied to Si_{1-x}Ge_x MESFET under illumination condition, it exhibits high photosensitivity, ($I_{\text{illumination}}/I_{\text{dark}} \approx 7.2 \times 10^5$), high current responsivity (32.8 mA/W) for $x=0.6$ i.e. Si_{0.4}Ge_{0.6}, $V_{\text{gs}}=-0.4\text{V}$ and wavelength=1.15 μm . Subthreshold slope variation (under illumination) can be used to detect the intensity of incident radiation.

1. INTRODUCTION

The Si_{1-x}Ge_x is an important compound semiconductor with a wide bandgap of 0.67-1.08 eV for x ranging from 1-0 at room temperature, has been considered as a prospective material for IR photodetector [1]-[5]. There is considerable interest in detectors for IR radiation wavelength in use for fiber optic transmission (1.3 and 1.55 μm). MESFET has been widely used for photodetection applications as it provides high speed photodetection along with good photosensitivity. MESFET and High Electron Mobility Transistor (HEMT) have been studied theoretically as well as experimentally by several researchers for various optically-controlled applications [6]-[8]. There are different ways by which incident radiation may be allowed to enter the active region. In the theoretical models discussed in [6]-[8] the radiation has been assumed to be incident to a semitransparent metal gate. The thickness of the gate is such that most of the incident radiation is transmitted to the underlying semiconductor region. Another method is the back illumination which also enhances the photo-response as suggested by [9]. The photosensitivity and IC compatibility of FETs have extended the potential of these devices justifies their usage as photo-detector. Further, MESFET has another advantage for photo-detection purpose as it provides various parameters in addition to $I_{\text{illumination}}/I_{\text{dark}}$ such as change in threshold voltage and subthreshold slope which changes significantly in presence of light. In this paper photo-response of a SiGe MESFET has been studied using ATLAS device simulator [10] at different biasing conditions and Ge compositions. $I_{\text{illumination}}/I_{\text{dark}}$ ratio and change in subthreshold slope are used to detect the presence of light and its intensity.

2. DEVICE STRUCTURE

Fig.1 shows the schematic structure of SiGe MESFET with semi-insulating Sapphire as a

substrate. The various models included in the simulation are: concentration dependent mobility model, field dependent mobility model to incorporate parallel electric field dependence of mobility and Shockley read hall recombination model for minority recombination.

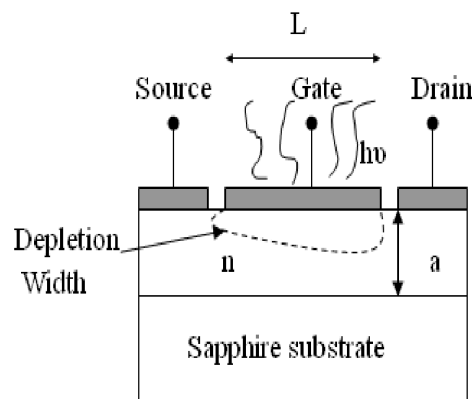


FIG. 1 Schematic structure of a SiGe MESFET. Channel length(L)=1 μm , channel width(Z)=10 μm , Active layer thickness(a)=0.3 μm , Active layer doping(N_d)=1 $\times 10^{22}\text{m}^{-3}$, Substrate doping(N_a)=10 $^{21}\text{m}^{-3}$, Metal workfunction=5.0 eV.

Gate metal is assumed to be transparent and thin so that most of the incident radiation is transmitted to the underlying semiconductor region. Silvaco's advanced Luminous 3D optical device simulator has been used to extract the device characteristics under illumination. Here radiation is incident on the gate region only. Location, intensity and wavelength of the radiation has been set using BEAM statement of the luminous module. Ray trace method has been used in simulator to solve for photogeneration rate at each grid point. Fig.2 shows the simulated figure of device under illumination.

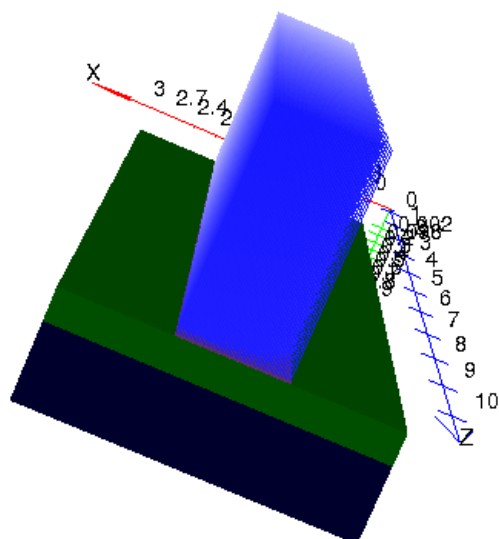


Fig.2 Simulated structure of a SiGe MESFET. Under illuminated. Wavelength=1.15 μm, optical power (P_{op})=4μW, Channel length(L)=1μm, channel width(Z)=10μm, Active layer thickness(a)=0.3μm, Active layer doping (N_d)=1x10²²m⁻³, Substrate doping (N_a)=10²¹m⁻³, Metal workfunction=5.0 eV.

3. RESULT AND DISCUSSION

When light (of energy greater than bandgap energy of the semiconductor) is incident on the gate of the MESFET reach to the semiconductor, it gets absorbed and additional EHPs are generated in the depletion region and undepleted neutral region of the active layer. These photogenerated carriers directly modulate current conduction (i.e. photoconductive effect). In illumination condition, due to photovoltaic effect a photovoltage will be developed across the Schottky barrier in the forward direction. This photovoltage developed across the gate depletion region is greatly influenced by the external resistance presented to it. For example, when the external resistance is small the photovoltage developed is negligible. As a result, no significant change is observed under illumination due to photovoltaic effect in such cases. In our analysis, the photoconductive effect is the dominating mechanism for enhanced drain current under illumination. Fig.3 shows the effect of illumination on transfer characteristics of Si_{1-x}Ge_x MESFET for x=0.6. As can be seen, the effect of illumination is more visible in subthreshold region than linear and saturation region as subthreshold current is 3-4 order less than the generated photocurrent whereas current in inversion region has same order as of photocurrent. So when device is to be used as a photodetector the bias point should be chosen so that device operates in the subthreshold region.

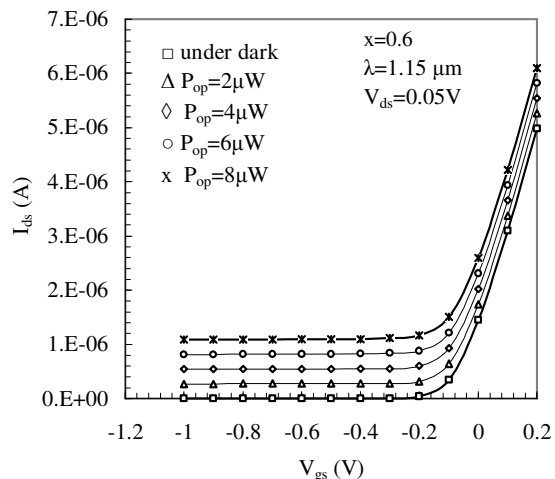


Fig.3 I_{dark}/I_{illumination} Vs wavelength at V_{gs}=-0.4V, V_{ds}=0.05V, P_{op}=4μW.

For SiGe as the content of Ge is changes the amount of absorption in the active layer changes because of the change in the absorption coefficient which depends on energy bandgap (E_g) of the active layer material as :

$$\alpha = \alpha_0 \sqrt{\frac{\frac{hc}{q\lambda} - E_g}{\frac{hc}{q\lambda}}} \quad (1)$$

Here h is the Planck's constant, c is the velocity of light in air and λ is the wavelength of the incident radiation. α₀ is the constant which is material dependent. Since E_g depends upon the Ge content thus absorption coefficient is also a function of Ge content (x) for SiGe. The absorption coefficient increases when both the wavelength and Ge content are increased. Fig. 4 shows the available photocurrent as a function of wavelength for different x values. As can be seen from the fig, the available photocurrent increases as the wavelength is increased because of enhanced absorption. Also the wavelength at which the peak photocurrent is obtained also shifts towards higher wavelength (towards IR region) as the Ge content increases. Similarly the I_{illumination}/I_{dark} ratio also increases as the value of Ge mole fraction increases peak response shifts towards higher wavelength as shown in fig.5. In case of MESFET, the I_{illumination}/I_{dark} ratio also depends upon the applied reverse gate bias since I_{dark} changes very significantly with gate-to-source bias (V_{gs}). At V_{gs}=-0.4V and drain-to-source bias (V_{ds})=0.05V higher I_{illumination}/I_{dark} is obtained at x=0.5 for all wavelengths (λ=0.05μm -1.55μm) except 1.15 μm and 1.35 μm at which I_{illumination}/I_{dark} is higher for x=0.6. Thus MESFET-based photodetectors have the unique advantage of an additional dimensionality to

control the channel conduction. By increasing the applied reverse gate bias enhanced $I_{illumination}/I_{dark}$ ratio can be obtained as much lower dark current is obtained at more negative gate voltages and the peak wavelength can also be tuned. Thus maximum value of $I_{illumination}/I_{dark}$ at a given wavelength depends on applied V_{gs} and Ge content. For example At $V_{gs}=-1V$, maximum $I_{illumination}/I_{dark}$ ($=1.03 \times 10^7$) is obtained at $\lambda = 0.35\mu m$ and $x=0.1$. On the other hand, at $V_{gs}=-0.4V$ maximum $I_{illumination}/I_{dark}$ ($=7.2 \times 10^5$) is obtained at $\lambda = 1.15 \mu m$ for $x=0.6$. At $V_{gs}=-0.2V$, maximum $I_{illumination}/I_{dark}$ ($=5 \times 10^1$) is obtained at $\lambda = 1.35\mu m$, $x=0.9$.

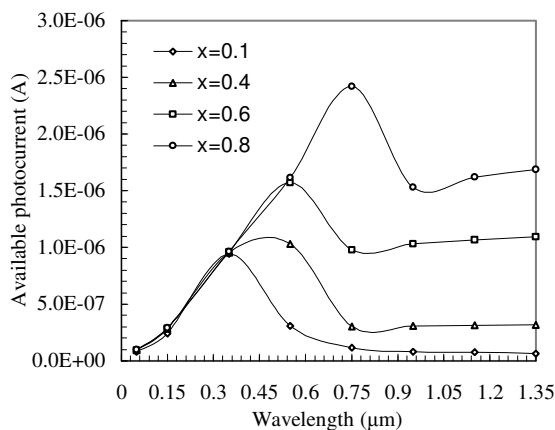


Fig.4 Available photocurrent Vs wavelength at $V_{gs}=-0.4V$, $V_{ds}=0.05V$, $P_{op}=4\mu W$.

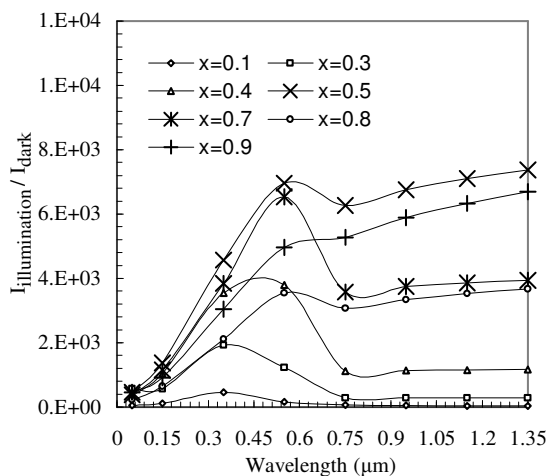


Fig.5 $I_{dark}/I_{illumination}$ Vs wavelength at $V_{gs}=-0.4V$, $V_{ds}=0.05V$, $P_{op}=4\mu W$.

When MESFET/MOSFET devices are used as photodetector, there are other parameters which can also be used for detection of intensity of incident light. One such parameter is subthreshold slope which changes very significantly with light. Table 1 illustrates the impact of illumination on subthreshold slope as a function of x and λ . Using change in subthreshold slope (ΔS) for photodetection has an

advantage of freedom from choosing the optimum bias point as to find subthreshold slope, V_{gs} is varied from $-1V$ to $0.2V$. At $x=0.6$, $\lambda=1.15\mu m$, optical power (P_{op}) of $4\mu W$ produces a change in subthreshold slope (ΔS) = 208.4 mV/Dec.

Table.1 Effect of illumination on subthreshold slope as a function of wavelength for different x for $P_{op}=4\mu W$.

Wavelength (μm)	Subthreshold slope (mV/Dec)			
	at $x=0.1$	at $x=0.4$	at $x=0.6$	at $x=0.8$
0 (under dark)	88.06	85.5	85.6	84
0.05	195.4	170.8	150.32	144.9
0.15	232.6	203.8	198.77	195
0.35	250	316.55	282	271
0.55	246.9	328	355	343
0.75	204.7	207	284	319
0.95	195.9	208.6	290	333
1.15	193	209	294	342
1.35	191	210	297	349

5. CONCLUSION

MESFET-based SiGe photodetector has an additional dimensionality for control of channel conduction, which has the advantages of greatly reducing the dark current and increasing the photoresponse. Also the spectral response can be tailored by varying the applied bias and Ge mole fraction. Thus SiGe MESFET is a suitable candidate for IR photodetection with high sensitivity.

ACKNOWLEDGMENT

Author (Rajni Gautam) is thankful to University Grants Commission (UGC), Government of India for necessary financial assistance to carry out this research work.

REFERENCES

[1] S. Winnerl, D. Buca, S. Lenk, Ch. Buchal, S. Mantl, D.-X. Xu, "Fast IR Si /SiGe superlattice MSM photodetectors with buried CoSi contacts", *Microelectronic Eng.* **64**, 205–209, (2002).

- [2] A. K. Okyay, A. J. Pethe, D. Kuzum, S. Latif, D. A. B. Miller, and K. C. Saraswat, " Novel SiGe Optoelectronic MOSFET," *Opt. Lett.*, **32**, 14 (2007).
- [3] A. K. Okyay, A. J. Pethe, D. Kuzum, S. Latif, D. A. B. Miller, and K. C. Saraswat, "Novel Si-based CMOS Optoelectronic Switching Device Operating in the Near Infrared," *OFC* Anaheim, California, USA, Mar 25 - Mar 29, 2007.
- [4] B Aslan, R Turan, H C Liu and J-M Baribeau, "Mechanisms of photocurrent generation in SiGe/Si HIP infrared photodetectors", *Semicond. Sci. Technol.*, **19**, 399-403, (2004).
- [5] M. Kabeer, K. Gowri, and V. Rajamani, "Three dimensional modeling and simulation of a nano MISFET photodetector," *Journal of Optoelectronics and Advanced Materials*, **9**, 2879 -2885, (2007).
- [6] K. Balasubadra, T. Thangam, V. Rajamani, K. Sankaranarayanan, "Three dimensional numerical modeling and simulation of a uniformly doped GaAs MESFET photodetector", *Journal Of Optoelectronics And Advanced Materials*, **10**, 2494-2501, (2008).
- [7] Yu Ye, Lun Dai, Xiaonan Wen, Peicai Wu, Ruomin Pen, and Guogang Qin, "High-Performance Single CdS Nanobelt Metal-Semiconductor Field-Effect Transistor-Based Photodetectors", *Applied materials and interfaces*, **2**, 2724-2727, (2010).
- [8] B K Mishra, L Jolly, K Patil, "Modeling of GaAs MESFET under Back Illumination, " *International Conference and Workshop on Emerging Trends in Technology (ICWET 2011)*, Mumbai, Maharashtra, India, 1133-1137, February 25-26, 2011.
- [9] ATLAS User's Manual: 3-D Device Simulator, SILVACO International, Version 5.14.0.R, 2010.

REDUNDANCY: A NOVEL PROPERTY OF CANTOR DIFFRACTALS

Rupesh Verma, Varsha Banerjee and Paramasivam Senthilkumaran
Indian Institute of Technology, Delhi, Hauz khas New Delhi
Email: rupeshverma.iitd@gmail.com

Abstract: Cantor diffractals are waves that have encountered a Cantor grating. Here, we report an important property of Cantor diffractals, namely that of redundancy. We observe that the fractal aperture can be reconstructed from small fragments of the diffraction pattern. Redundancy appears to be a generic feature of diffractals, especially when they emanate from deterministic fractals.

1. INTRODUCTION

Fractals are geometric objects with regular or hierarchic structure, which persists at all levels of magnification [1]. As a result, they exhibit self-similar and scale invariance properties. Because of these features, it is natural to expect that some properties of fractal objects are in sharp contrast with ordinary geometric forms. For example, diffraction of light on a fractal lattice results in a self-similar diffraction pattern.

A surprising feature of fractals is that their dimension is non-integer that is greater than their topological dimension but less than their Euclidean dimension.

Diffractals, as defined by Berry, are waves that have encountered a fractal structure [2]. They propagate in space and time to produce the diffraction pattern of the fractal aperture. We studied the redundancy in case of Cantor diffractals. Redundancy indicates superfluous information that can be omitted without loss of meaning. Redundancy appears in holography where a recorded interference pattern of light generated from reference beam and an object beam is spread all across. Therefore the entire image can still be reconstructed from scratched, dirty or fragmented holograms without serious loss of information [4, 5].

2. CANTOR GRATING

The Cantor grating is a typical example of a regular, rectangular fractal. The Cantor set is generated by removing the middle third of the unit segment (step 1). From the remaining line segments, each one third in length, the middle thirds are again removed (step 2). The middle thirds of the remaining four line segments, each one-ninth in length, are then removed (step 3) and so on to infinity. What is left is a collection of infinitely many disappearing line segments lying on the unit interval whose individual and combined lengths approach zero. This set of points is known as Cantor set.

The fractal dimension is given by the formula

$$D_f = \frac{\ln(N)}{\ln(1/\varepsilon)} \quad (1)$$

where N is the number of self-similar segments and

ε is the scaling ratio.

So in case of Cantor grating in step 1, we have $N=2$ and $\varepsilon=1/3$, so its fractal dimension is $\ln(2)/\ln(3) = 0.6309$. Similarly for step 2, we have $N=4$ and $\varepsilon=1/9$, so again the fractal dimension is $\ln(4)/\ln(9) = 0.6309$. Therefore, the fractal dimension of Cantor set is 0.6309.

Let $R_0(x)=\text{rect}(\varepsilon_0=2a, x=0)$ be a rectangle function of width w placed symmetrically about point x . Defining $R_n(x)=\text{rect}(\varepsilon_n=\varepsilon_{n-1}/3, x=0)$, the n -th generation of the Cantor grating is given by

$$G_n(x) = R_n(x) * \Delta_n(x), \quad n \geq 1 \quad (2)$$

where $\Delta_n(x) = \sum \delta(x-x_i)$ with $i = 1$ to 2^n and $x_i = \pm 2a/3 \pm 2a/3^2 \dots \pm 2a/3^n$.

A few generations of the Cantor grating obtained from Eq. (2) are shown in fig. 1.

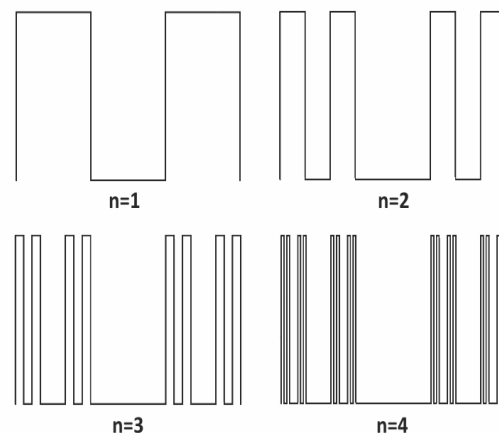


Fig.(1): Four generations of the Cantor grating.

The interaction of electro magnetic waves with it yields Cantor diffractals [6-9].

The corresponding diffraction pattern can be obtained by Fourier transformation (FT) of Eq. (2). Its amplitude is given by

$$A_n(f) = \left(\frac{2}{3}\right)^n 2a \text{sinc}\left(\frac{2\pi af}{3^n}\right) \prod_{m=1}^n \cos\left(\frac{4\pi af}{3^m}\right) \quad (3)$$

where $\text{sinc}(x)=\sin(x)/x$ and f is the spatial frequency of the scattered wave having dimensions of inverse length. The intensity is given by the square of the diffraction pattern, so for Cantor grating

$$I_n(f) = [A_n(f)]^2 \quad (4)$$

This diffraction pattern is also self-similar i.e. fractal in nature and can be employed to determine the fractal dimension of the grating itself [9, 12, 13].

In Fig. 2, we show the diffractal intensity profiles for the first four orders of the Cantor grating. These intensity profiles have been rescaled using the relation $I_n(f) = (2/3)^2 I_{n-1}(f/3)$ to illustrate the self-similarity [3, 11].

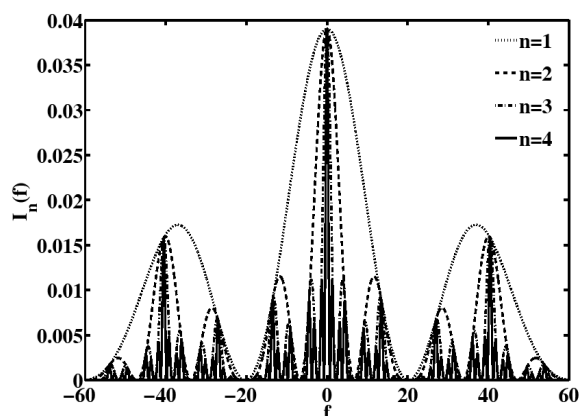


Fig.(2): Diffraction intensity profiles of the first four generations of the Cantor grating rescaled using the relation $I_{n+1}=(2/3)^2 I_n(f/3)$ to demonstrate the self-similarity.

3. RECONSTRUCTION FROM BANDS

As seen in Fig. 2, the Cantor diffractals consists of band like structures. The zeroes of the sinc function give the width of the band. For any order the width of each band is constant and increases as the order of the grating increases. The width of central band is double of the individual band and the amplitude of these bands decreases gradually according to the sinc function. The internal structure is governed by the cosine terms of Eq. (3). The number of minima and maxima in a band are given by these cos terms.

We find that each band in the diffraction pattern contains the complete information about the aperture function: an inverse FT of an arbitrary band gives back the profile of the Cantor grating employed for obtaining the Cantor diffractals. This feature is strikingly different from a similar reconstruction of conventional (non-fractal) apertures. In the later case there is a total loss of information due to edge enhancement caused by the exclusion of the zero frequency [10].

We have also observed in the case of diffraction patterns of higher order gratings that each band contains the information about all the previous orders. So we can reconstruct the previous order gratings from the same band using appropriate clipping [16].

In Fig. 3, we show the reconstruction using one band from fourth order diffraction pattern. Fig. 3(a) shows the reconstruction of the fourth order Cantor grating from the fourth order band, 3(b) shows the third order reconstruction, 3(c) shows the second order reconstruction and 3(d) shows the first order reconstruction from the same band of the fourth order diffraction profile.

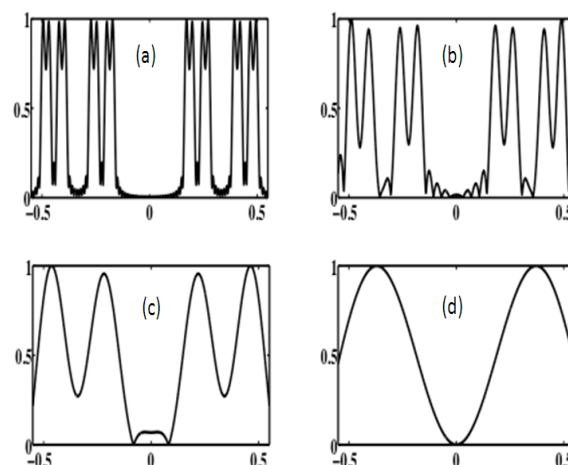


Fig.(3): Reconstruction from one band of 4th order grating. 3(a) shows the fourth order, 3(b) shows the third order, 3(c) shows the second and 3(d) shows the first order reconstruction from the same fourth order band.

4. CONCLUSION

In conclusion, we observe redundancy in Cantor Diffractals – a consequence of the aperture function being pervasive and entrenched in them. This property should be generic to diffractals, especially where they emanate from deterministic fractals. This property would be technologically useful in diverse physical problems. For example, fractal phases appear promising reduction of speckle noise in holographic reconstructions [14]. In a different context, redundancy may be potentially useful in the identification and characterization of fractal morphologies in stochastic growth phenomena [15].

ACKNOWLEDGEMENT

R. Verma would like to acknowledge financial support from CSIR Grant No. 086(0951)/09/EMR-I. V. Banerjee and P. Senthikumar would like to acknowledge the partial support of CSIR Grant No. 03(1077)/06/EMR-II.

REFERENCES

- [1] B. B. Mandelbrot, "The Fractal Geometry of Nature" (W. H. Freeman, New York, 1982).
- [2] M. V. Berry, "Diffractals", J. Phys. A Math. Gen. **12**, 781 (1979).

- [3] D. A. Hamburger-Lidar, "Elastic scattering by deterministic and random fractals: Self-affinity of the diffraction spectrum", *Phys. Rev. E* **54**, 354 (1996).
- [4] E. N. Leith and J. Upatnieks, "Wavefront reconstruction with diffused illumination and three dimensional objects", *J. Opt. Soc. Am.* **54**, 1295 (1964).
- [5] H. J. Gerritsen, W. J. Hannan and E. G. Ramberg, "Elimination of Speckle Noise in Holograms with Redundancy", *App. Opt.* **7**, 2301 (1968).
- [6] D. Bak, S. P. Kim, S. K. Kim, K. -S. Soh and J. H. Yee, "Fractal Diffraction Grating", <http://arxiv.org/abs/physics/9802007>.
- [7] Bo Hou, Gu Xu, Weijia Wen and George K. L. Wong, "Diffraction by an optical fractal grating", *Appl. Phys. Lett.* **85**, 6125 (2004).
- [8] G. Chabassier, B. Angeli, F. Heliodore and A. Le Mehaute, "Optical wave diffraction on fractal objects", *Pure Appl. Opt.* **1**, 41 (1992).
- [9] C. Allain and M. Cloitre, "Optical diffraction on fractals", *Phys. Rev. B* **33**, 3566 (1986).
- [10] J. W. Goodman, "Introduction to Fourier Optics" (McGraw-Hill, 1996).
- [11] M. Lehman, "Fractal diffraction grating built through rectangular domains", *Optics Comm.* **195**, 11 (2001).
- [12] C. Guerin and M. Holschneider, "Scattering on fractal measures", *J. Phys. A* **29**, 7651 (1996).
- [13] B. Dubuc, J. F. Quiniou, C. R.- Carmes, C. Tricot and S. W. Zucker, "Evaluating the fractal dimensions of profiles" *Phys. Rev. A* **39**, 1500 (1989).
- [14] P. Senthilkumaran and F. Wyrowski, "Phase synthesis in wave-optical engineering: mapping- and diffuser-type approaches" *Journal of Modern Optics* **49**, 1831 (2002).
- [15] A. L. Barabasi and H. E. Stanley, "Fractal Concepts in Surface Growth" (Cambridge Univ. Press, 1995).
- [15] Rupesh Verma, Varsha Banerjee and Paramasivam Senthilkumaran, "Redundancy in Cantor Diffractals", communicated.

Goos-Hanchen and Fedorov-Imbert shift for Hermite-Gauss beam

Chandra Prajapati and D.Ranganathan

Physics Department, Indian Institute of Technology Delhi, Hauz Khas, N. delhi
Chandra9.iitd@gmail.com

Abstract: We studied the lateral Goos-Hanchen and the transverse Fedorov-Imbert shift for reflection of Hermite-Gauss beams. We used the vector angular spectrum method for a three dimensional light beam in terms of a two-form angular spectrum consisting of the two orthogonal polarized components. We have done a detailed calculation of these shifts at different angles of incidence, over the whole range of angles without making the usual approximations. The shift variation with refractive index and order of the Hermite-Gauss beam are also studied.

1. INTRODUCTION

A bounded beam upon reflection and transmission from a planar interface, shifts with respect to geometric optics predictions. These shifts are called Goos-Hanchen shift (GH) (shift in lateral direction of beam propagation) [1] and Fedorov-Imbert shift (IF) (shift in transverse direction of beam propagation) [2,3]. Artmann [4] gave the theoretical predictions of GH shift using the stationary phase approximation where he interpreted GH shift as the shift of peak intensity (centroid) of beam upon reflection. Another different interpretation of the GH shift was given by Renard [5] using conservation of energy. The fact that there is an energy flow associated with evanescent wave parallel to the interface in the less dense medium, there is a shift in direction of beam propagation to ensure energy conservation. Fedorov [2] initially predicted a transverse displacement of the totally reflected beam and Imbert [3] calculated this displacement (IF) using the energy flux argument developed by Renard for GH shift and experimentally measured it. Subsequently, this has been applied to explain angular momentum conservation and Spin Hall Effect of Light [6,7] and other areas of physics [9]. Dutta Gupta et.al., studied the GH shift for Gaussian mode[10].

In our study, we used the vector angular spectrum of a three dimensional light beam in terms of the two form angular spectrum, as developed by Chun-Fang-Li [8], consisting of its two orthogonal polarizations namely s and p polarized components. The two-form angular spectrum amplitude describes the polarization state of beam in such a way that the GH shift is quantized with eigenstates being the two orthogonal linear polarizations and IF shift is quantized with eigenstates being the two orthogonal circular polarizations [8].

We considered the optical reflection from the planar interface, with incidence from the denser medium to the rarer medium near the critical angle. Finally we extended this result to study the two shifts for whole range of incident angles.

2. NUMERICAL CALCULATION OF GH SHIFT

Consider a monochromatic 3D Hermite-Gauss light beam incident in a homogeneous and isotropic medium of refractive index n from denser medium to rarer medium, which is assumed to be vacuum. So $n > 1$. The reflection interface is taken to be yz -plane. We are using the method of Chun-Fang-Li [8] to calculate GH and IF shift. The general formula to calculate GH shift is [8]

$$\langle y \rangle = \frac{\iint i \left(A^\dagger \frac{\partial A}{\partial k_y} - \frac{k_x k_y}{k(k_y^2 + k_z^2)} (A_s^* A_p - A_p^* A_s) \right) dk_y dk_z}{\iint A^\dagger A dk_y dk_z} \quad (1)$$

Consider the linearly polarized light beam for which, GH shift is maximum, and hence

$$A_s^* A_p - A_p^* A_s = 0 \quad \text{then, the GH shift is,}$$

$$\langle y \rangle = \frac{\iint i A^\dagger \frac{\partial A}{\partial k_y} dk_y dk_z}{\iint A^\dagger A dk_y dk_z} \quad (2)$$

The Incident beam is written as

$$A_i = L_i A = \begin{bmatrix} l_{i1} \\ l_{i2} \end{bmatrix} \quad (3)$$

With normalization condition

$$\iint A^\dagger A dk_y dk_z = 1. \quad (4)$$

Using the above eq. (1) and (2), we get centroid of the incident beam at reflection plane is at the origin. The reflected beam is written as,

$$A_r = L_r A = \begin{bmatrix} l_{r1} \\ l_{r2} \end{bmatrix} A,$$

where $L_r = UC_r = UR_c C_i = R_l UC_i = R_l L_i$. (5)

U is a unitary transformation matrix. For a linearly

polarized beam, $U = \begin{bmatrix} 1 & 0 \\ 0 & 1 \end{bmatrix}$. C_i is the complex

amplitude of polarization and L_i describes the state of polarization of incident beam.

$$R_l = \begin{bmatrix} R_s & 0 \\ 0 & R_p \end{bmatrix} \quad \text{with}$$

$$R_s = |R_s| \exp i\phi_s \quad \text{and} \quad R_p = |R_p| \exp i\phi_p. \quad (6)$$

so the reflected beam is $A_r = \begin{bmatrix} R_s l_{i1} \\ R_p l_{i2} \end{bmatrix}$. (7)

on calculating further we get the shift as

$$\langle y \rangle = \frac{-\iint \left(|l_{i1}|^2 \frac{\partial \phi_s}{\partial k_y} + |l_{i2}|^2 \frac{\partial \phi_p}{\partial k_y} \right) A^2 dk_y dk_z}{|l_{i1}|^2 + |l_{i2}|^2}. \quad (8)$$

For linearly polarized beam $L_i = \frac{1}{\sqrt{2}} \begin{bmatrix} 1 \\ 1 \end{bmatrix}$. (9)

Now we apply these results to the case of Hermite-Gauss beams.

Consider an arbitrarily polarized incident Hermite-Gauss beam propagating in the direction of the x -axis, making an angle θ_0 and its angular spectrum amplitude $A(k_y, k_z)$ is a positive definite symmetric function. This is sharply peaked around $(k_{y0}, k_{z0}) = (k \sin \theta_0, 0)$, and obeys the condition,

$$\iint A^2(k_y, k_z) dk_y dk_z = 1. \quad (10)$$

Where θ_0 is angle of incidence. The amplitude spectrum of the Hermite-Gauss beam is given by

$$A(k_y, k_z) = \sqrt{\frac{\omega_y \omega_z}{2^{p+q} \pi p! q!}} H_p \left(\frac{\omega_y}{\sqrt{2}} (k_y - k_{y0}) \right) H_q \left(\frac{\omega_z k_z}{\sqrt{2}} \right) \exp \left(-\frac{\omega_y^2}{2} (k_y - k_{y0})^2 \right) \exp \left(-\frac{\omega_z^2 k_z^2}{2} \right). \quad (11)$$

The Fresnel reflection coefficients for s and p

polarized beam are $R_s = \frac{n \cos \theta_1 - \cos \theta_2}{n \cos \theta_1 + \cos \theta_2}$,

and $R_p = \frac{\cos \theta_1 - n \cos \theta_2}{\cos \theta_1 + n \cos \theta_2}$. (12)

On putting $\frac{\partial \phi_s}{\partial k_y}$ and $\frac{\partial \phi_p}{\partial k_y}$ into the expression of

GH shift for s and p polarized beams, we get,

$$D_{GH}^s = \frac{1}{2} \frac{\omega_y \omega_z}{2^{p+q} \pi p! q!} \frac{2nk_x}{k^2 \sqrt{(n^2-1)(k^2-k_x^2)-k_x^2}} \iint \exp \left(-\omega_y^2 (k_y - k_{y0})^2 \right) k_y \exp \left(-\omega_z^2 k_z^2 \right) \left(H_p \left(\frac{\omega_y}{\sqrt{2}} (k_y - k_{y0}) \right) \right)^2 \left(H_q \left(\frac{\omega_z k_z}{\sqrt{2}} \right) \right)^2 dk_y dk_z,$$

and for the p -polarized beam,

$$D_{GH}^p = \frac{1}{2} \frac{\omega_y \omega_z}{2^{p+q} \pi p! q!} \frac{2nk_x}{\left((k^2 - k_x^2) n^2 - k_x^2 \right) \sqrt{(n^2-1)(k^2-k_x^2)-k_x^2}} \iint k_y \times \exp \left(-\omega_y^2 (k_y - k_{y0})^2 \right) \exp \left(-\omega_z^2 k_z^2 \right) \left(H_p \left(\frac{\omega_y}{\sqrt{2}} (k_y - k_{y0}) \right) \right)^2 \left(H_q \left(\frac{\omega_z k_z}{\sqrt{2}} \right) \right)^2 dk_y dk_z. \quad (13)$$

Now we consider the beam of the form H_{m0} . This is a Gaussian in the y -direction and makes an angle θ_0 with x -axis and the beam is such that its angular distribution function is sharply peaked around $(k \sin \theta_0, 0)$ and the integration limit is extended to $\pm\infty$ for both variables k_y and k_z . Then $q=0$ and $k_x = k \cos \theta_0$ and $\sqrt{k_y^2 + k_z^2} = k \sin \theta_0$, where

$k = \sqrt{k_x^2 + k_y^2 + k_z^2}$. Then the GH shifts becomes,

$$D_{GH}^s = \frac{1}{2} \frac{\omega_y \omega_z}{2^{p+q} \pi p! q!} \frac{2nk_x}{k^2 \sqrt{(n^2-1)(k^2-k_x^2)-k_x^2}} \iint k_y \times \exp \left(-\omega_y^2 (k_y - k_{y0})^2 \right) \exp \left(-\omega_z^2 k_z^2 \right) \left(H_p \left(\frac{\omega_y}{\sqrt{2}} (k_y - k_{y0}) \right) \right)^2 dk_y dk_z,$$

and

$$D_{GH}^p = \frac{1}{2} \frac{\omega_y \omega_z}{2^{p+q} \pi p! q!} \frac{2nk_x}{\left((k^2 - k_x^2) n^2 - k_x^2 \right) \sqrt{(n^2-1)(k^2-k_x^2)-k_x^2}} \iint k_y \times \exp \left(-\omega_y^2 (k_y - k_{y0})^2 \right) \exp \left(-\omega_z^2 k_z^2 \right) \left(H_p \left(\frac{\omega_y}{\sqrt{2}} (k_y - k_{y0}) \right) \right)^2 dk_y dk_z. \quad (14)$$

3. NUMERICAL CALCULATION OF IF SHIFT

IF shift is calculated by using the following equation of Chun-Fang-Li,

$$\langle y \rangle = \frac{\iint i \left(A^\dagger \frac{\partial A}{\partial k_z} + \frac{k_x k_y}{k(k_y^2 + k_z^2)} (A_s^* A_p - A_p^* A_s) \right) dk_y dk_z}{\iint A^\dagger A dk_y dk_z} \quad (15)$$

The IF shift of a linearly polarized beam is zero. On the other hand for the left circularly polarized beam, the unitary transformation matrix is $U = \frac{1}{\sqrt{2}} \begin{bmatrix} 1 & 1 \\ -i & i \end{bmatrix}$. For circularly polarized beam z -coordinate of centroid of incident beam is not on the origin at the reflected plane. This gives a non vanishing transverse displacement of incident beam from the plane $z=0$, this is the evidence of the translational inertial spin effect of light. This occurs when the two dimensional electromagnetic field is uniform in the transverse direction. Here we define a beam that is not transversely uniform but the expectation value of transverse wave vector is zero. Hence the IF shift is

$$\langle y \rangle = \frac{\iint i \frac{k_x k_y}{k(k_y^2 + k_z^2)} (A_s^* A_p - A_p^* A_s) dk_y dk_z}{\iint A^\dagger A dk_y dk_z} \quad (16)$$

The reflected beam is written as

$$A_r = R_t U C_i A = \frac{1}{\sqrt{2}} \begin{bmatrix} R_s (C_{i1} + C_{i2}) \\ R_p (-iC_{i1} + iC_{i2}) \end{bmatrix} A \quad (17)$$

For a circularly polarized beam $C_i = \begin{bmatrix} 1 \\ 0 \end{bmatrix}$.

Then the Imbert-Fedorov shift for beam of H_{m0} form is

$$D_{IF} = \iint \left(\frac{k_x k_y}{k(k^2 - k_x^2)} \right) \frac{\omega_y \omega_z}{2^p \pi p!} \frac{|R_s| |R_p|}{|R_s|^2 + |R_p|^2} \left(H_p \left(\frac{\omega_y}{\sqrt{2}} (k_y - k_{y0}) \right) \right)^2 \cos(\phi_p - \phi_s) \exp(-\omega_y^2 (k_y - k_{y0})^2) \exp(-\omega_z^2 k_z^2) dk_y dk_z \quad (18)$$

So the IF shift for the right circularly polarized beam is of the same magnitude as in the case of the left circularly polarized beam but with negative value.

3. RESULT AND DISCUSSION

We consider a 634 nm polarized Hermite-Gauss beam of mode of form H_{m0} , collimated at a beam waist of $\omega_0 = 20\mu\text{m}$, incident on a planar interface from a denser to rarer medium. For total internal reflection, $|R_s| = 1$, $|R_p| = 1$ and ϕ_s , ϕ_p are calculated from the Fresnel reflection coefficients, eq (12). GH shift for s -polarized beam and p -polarized beam were studied separately. It was observed that there is sharp peak at critical angle agreement with the Artmann formula and the shift decreases as the angle of incidence increases, and it vanishes at grazing incidence. For the p -polarized beam, a dip is observed at the Brewster angle. On increasing the order of the Hermite-Gauss beam, the shift decreases. It is maximum for H_{00} mode i.e. for Gaussian mode. IF shift for the HG beam is also a sharply peaked around the critical angle but peak is not symmetric. The results are presented in graphical form below.

4. FIGURES AND GRAPHS

Figure 1.

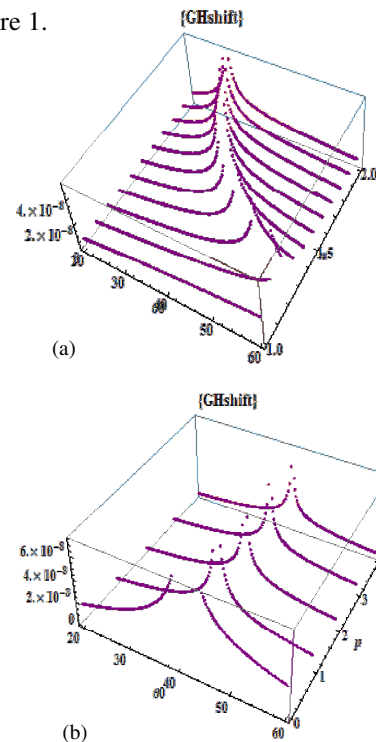


Figure 1a represents the variation of GH shift for s -polarized H_{10} mode HG beam with n and θ_0 . Figure 1b represents the variation of GH shift for s -polarized beam of modes $H_{00}, H_{10}, H_{20}, H_{30}, H_{40}$ with θ_0 at $n=1.5$. There is a sharp peak at the critical angle in both cases.

Figure 2.

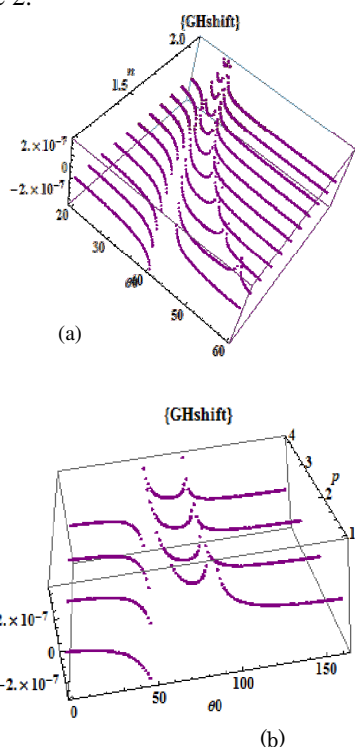
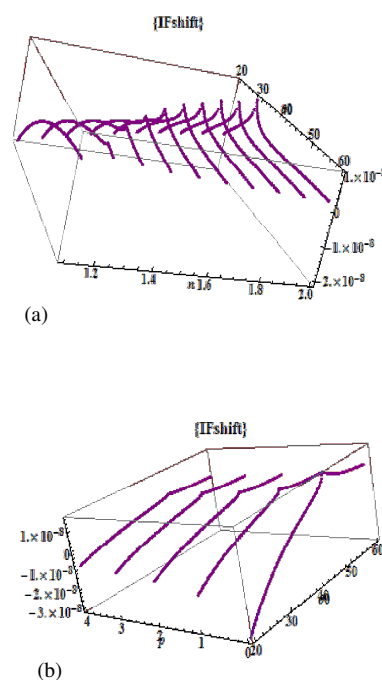


Figure 2a represents the variation of GH shift for p -polarized H_{10} mode HG beam with n and θ_0 . Figure 2b represents the variation of GH shift for p -polarized beam of modes $H_{00}, H_{10}, H_{20}, H_{30}$ with θ_0 at $n=1.5$. There is a sharp peak at the critical angle in both cases and a dip at the Brewster angle.

Figure 3a represents the variation of IF shift for left circularly polarized H_{10} mode HG beam with n and θ_0 . Figure 1b represents the variation of IF shift for same polarized beam of modes $H_{00}, H_{10}, H_{20}, H_{30}, H_{40}$ with θ_0 at $n=1.5$. There is a sharp peak at the critical angles in both cases but the graph is not symmetric about critical angle.

Figure 3.



ACKNOWLEDGEMENT

Chandra Prajapati acknowledges financial support of the UGC, Government of India.

REFERENCES

- [1] [2] F. Goos and H. Hanchen, "Ein neuer and fundamentaler Versuch zur total Reflection," *Ann. Phys.* **1**, 333 (1947).
- [2] F. I. Fedorov, Dokl. Akad. Nauk SSSR 105, 465 (1955).
- [3] C. Imbert, Calculation and Experimental Proof of the Transverse shift induced by TIR of a Circularly Polarized Light Beam *Phys. Rev. D* **5**, 787 (1972).
- [4] K. Artmann, *Ann Phys.* **2**, 87 (1948).
- [5] R. H. Renard, *J. Opt. Soc. Am.* **54**, 1190 (1964).
- [6] M. Onoda, S. Murakami, and N. Nagosa, *Phys. Rev. Lett.* **93**, 083901 (2004).
- [7] K. Yu. Bliokh and Y. P. Bliokh, *Phys. Rev. Lett.* **96**, 073903 (2006).
- [8] Chun-Fang-Li "Unified theory for Goos-Hanchen and Imbert-Fedorov effects", *Phys. Rev. A* **76**, 013811 (2007).
- [9] A. Aiello and J. P. Woerdman, "Role of beam propagation in GH and IF shifts", *Opt. Lett.*, **33**, 13, (2008).
- [10] Dheeraj Golla and S Dutta Gupta, "Goos-Hanchen shift for higher order Hermite-Gauss beams" *Pramana J. of Phys.*, **76**, 4, (2011).

OPTIMIZATION OF POWER CONFINEMENT IN A SILICON SLOT WAVEGUIDE

Kanchan Gehlot^{*}, D. M. H. Leung[†], A. Agrawal[†], and B. M. A. Rahman[†]

^{*}Department of Physics, IIT Delhi, Hauz Khas, New Delhi 110016, India, [†]School of Engineering and Mathematical Sciences, City University London, Northampton Sq, London, EC1V 0HB England
*gehlot.kanchan@gmail.com

Abstract: The modal and confinement properties of silicon-on-insulator horizontal slot waveguide structure have been investigated using full-vectorial \mathbf{H} -field finite element method. The optimization of structure parameters was carried out in order to achieve maximum field confinement in the low-index slot region. A new design for application of such structure in chemical and biochemical sensing has also been proposed.

1. INTRODUCTION

In recent years, there has been growing interest in developing silicon photonics [1] to realize nanometer size all-optical devices. Strong confinement of optical field in high index contrast Si waveguide structures allows realization of submicron optical devices, which can be fabricated at very low cost using well developed complimentary metal-oxide semiconductor (CMOS) fabrication processes. In addition to photonic structures such as silicon strip waveguide [2] and photonic crystal slab waveguides, a new type of waveguide structure, called slot waveguide [3], has attracted much attention.

A slot waveguide consists of a narrow low-index region sandwiched between two silicon waveguides. Due to the high index contrast at the interface, the normal component of electric field undergoes large discontinuity, enhancing field in the slot side with a ratio of dielectric constant. With optimization of structure parameters, very high power density can be achieved in the narrow region of low index slot.

In this paper, the case of horizontal slot waveguide grown over PEOX buffer of $1\mu\text{m}$ thickness is studied. The quasi-TM mode, which has \mathbf{H} -field parallel to the slot, forms the waveguide mode of our interest. We have carried out detailed theoretical analysis of modal and confinement properties to optimize the structure parameters of the waveguide structure to obtain maximum field confinement in air-slot region and investigated its possible application in chemical and biochemical sensing. To carry out such analysis, a very rigorous and numerically efficient vector- \mathbf{H} -field Finite Element Method (VFEM) [4] is used to calculate propagation constant and the full-vectorial modal profiles of vector \mathbf{H} -field and vector electric field (\mathbf{E}).

2. THEORY

A full-vectorial \mathbf{H} -field Finite Element Method (FEM) is used in this study to obtain propagation constant and field profile of the fundamental quasi-TM mode of asymmetric horizontal slot waveguide. The full-vectorial formulation is based on the minimization of the following functional in terms of

the nodal values of the full \mathbf{H} -field vector:

$$\omega^2 = \frac{\int [(\nabla \times \vec{H})^* \cdot \epsilon^{-1} (\nabla \times \vec{H}) + p (\nabla \cdot \vec{H})^* (\nabla \cdot \vec{H})] dx dy}{\int \vec{H}^* \cdot \mu \vec{H} dx dy} \quad (1)$$

where \mathbf{H} is the full-vectorial magnetic field, $*$ denotes a complex conjugate and transpose, ω^2 is the eigenvalue, where ω is the angular frequency of the wave, ϵ and μ are the permittivity and permeability, respectively and p is the dimensionless penalty parameter. Penalty method is incorporated in this analysis to reduce spurious solutions and improve the quality of physical solution. It is been shown in [5] that a 'p' value of the order of $1/n_g^2$ would give a satisfactory result, where n_g is the refractive index of the Si core.

3. RESULTS

3.1 Horizontal Slot Waveguide Structure

The schematic of horizontal slot waveguide structure used in the analysis is shown in Fig. 1.

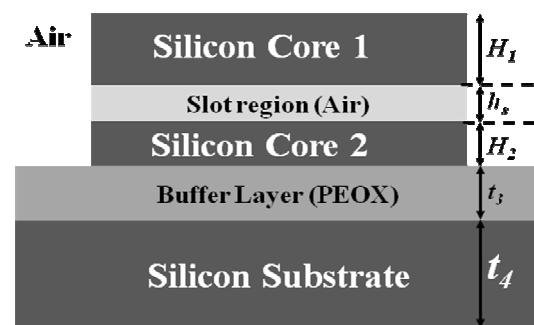


Figure 1: 2D schematic of horizontal slot waveguide structure.

The slot waveguide formed by an air slot in middle of two high index Si waveguides is placed on top of a PEOX buffer layer of $1\mu\text{m}$ thickness with air as the surrounding medium. By leaving silica buffer layer un-etched around the wider input and output section this type of slot waveguide can be fabricated. The refractive index of Si core at $1.55\mu\text{m}$ is taken as 3.50, the refractive indices of PEOX buffer and air is taken as 1.52 and 1.0 respectively. All the results shown here are computed for fundamental quasi-TM mode of

the waveguide structure at communication wavelength of $\lambda = 1.55 \mu\text{m}$.

To avoid losses, for practical purposes, horizontal slot waveguide is preferred over conventional vertical slot waveguide structure due to low scattering losses in the former structure. The field intensity is very high at the interfaces in a slot waveguide, thus the roughness of interface surface can lead to very high scattering losses. It is easier to fabricate smooth slot surfaces in horizontal structure by means of layered deposition or thermal oxidation processes. A vertical slot waveguide is created by etching a vertical slot in middle of high index waveguide, which can lead to rough slot surfaces.

3.2 Optimization of Structure Parameters

Structure parameters are optimized to achieve maximum power confinement in the air slot region of the horizontal slot waveguide structure.

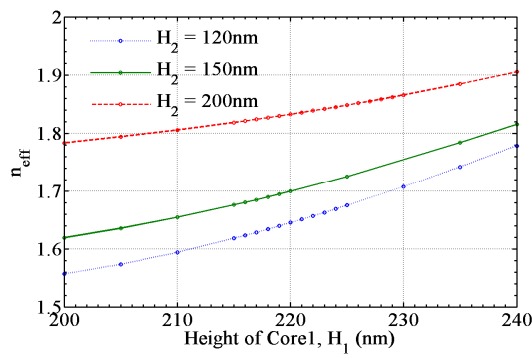


Figure 3: Variation of n_{eff} of the horizontal slot waveguide structure with core height H_1 , for $W=500\text{nm}$, $h_s = 50\text{nm}$ and $H_2 = 120 \text{ nm}$, 150 nm and 200 nm .

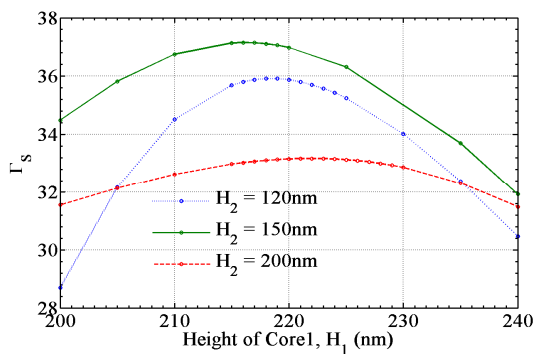


Figure 3: Variation of Γ_s in air slot with core height H_1 , for $W=500\text{nm}$, $h_s = 50\text{nm}$ and $H_2 = 120 \text{ nm}$, 150 nm and 200 nm .

To measure the fraction of power confined in the slot, the optical power confinement factor in the slot

$$\Gamma_s = \frac{\iint_{\text{Slot}} \text{Re}(\vec{E} \times \vec{H}^*) \cdot \hat{z} dx dy}{\iint_{\text{Total}} \text{Re}(\vec{E} \times \vec{H}^*) \cdot \hat{z} dx dy} \quad (2)$$

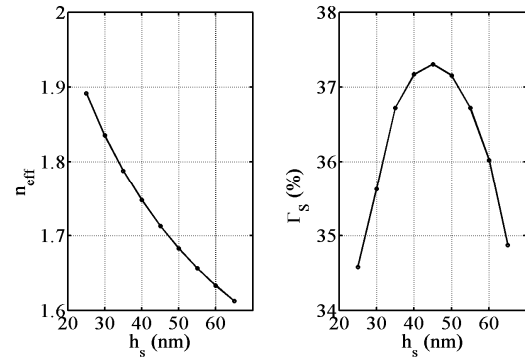


Figure 4: Variation of n_{eff} and Γ_s with slot height h_s .

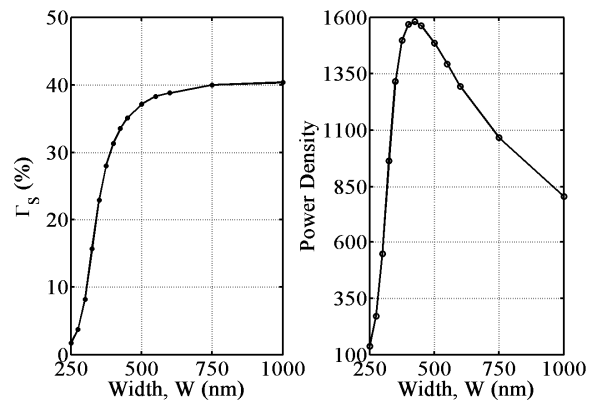


Figure 5: Variation of Γ_s and power density with slot height h_s .

region is defined as:

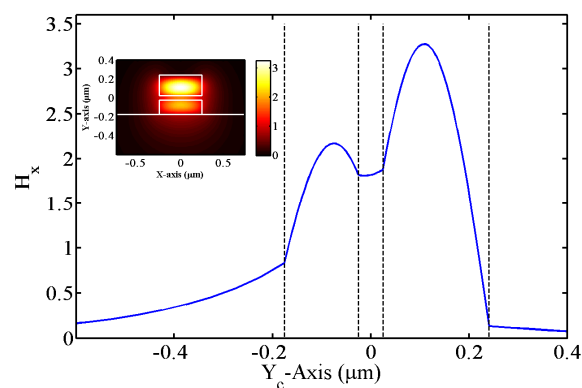
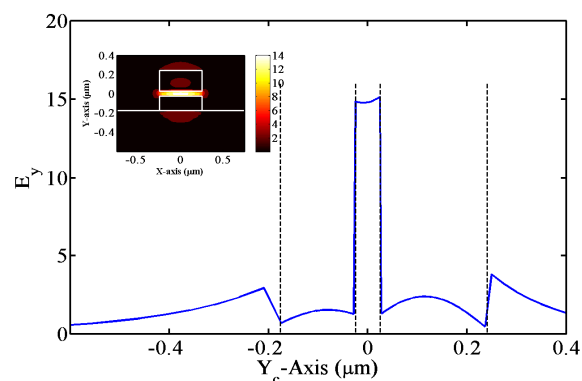
The dependence of confinement factor and effective index with various structure parameters is studied for the optimization.

The effective index, n_{eff} , of a given mode is a normalized propagation parameter, which can be defined by $n_{\text{eff}} = \beta_0/k_0$, where β_0 is the propagation constant of that mode and k_0 is the free space wavenumber defined as $k_0 = \omega (\epsilon_0 \mu_0)^{1/2} = 2\pi/\lambda$.

The lateral symmetry of the waveguide structure is kept unaltered by considering equal width W for both the silicon cores. Presence of substrate and buffer layer makes the slot waveguide structure asymmetric about horizontal axis passing the centre of slot region, so it is expected that the optimized structure will have unequal core heights H_1 and H_2 .

Variation of effective index and confinement factor with H_1 and H_2 is presented in Fig. 2 and 3, respectively, by keeping $W = 500 \text{ nm}$ and $h_s = 50 \text{ nm}$. For $W = 500 \text{ nm}$, the maximum confinement factor is achieved for $H_1 = 216 \text{ nm}$, $H_2 = 150 \text{ nm}$ and $h_s = 50 \text{ nm}$.

For larger values of H_1 and H_2 , effective index is large due to larger size of the high index region of Si cores. It can be noticed that for $H_2 = 200 \text{ nm}$, the confinement factor doesn't change much when H_1 is varied between 200-240 nm, whereas for $H_2 = 120$

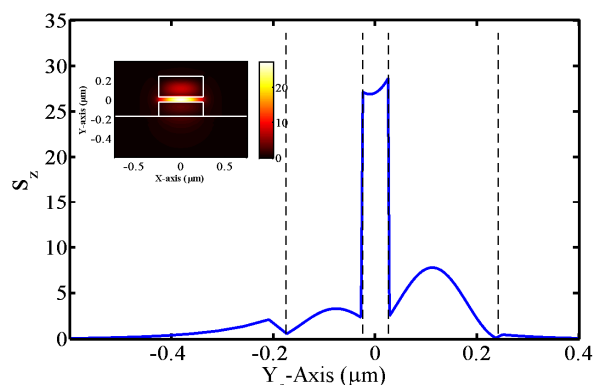
Figure 6: Variation of H_x along Y_c -axis.Figure 7: Variation of E_y along Y_c -axis.

nm, confinement factor changes substantially for the same range of H_1 . Confinement factor is sensitive to core heights H_1 and H_2 for highly asymmetric structure and symmetric structures are very less sensitive to variation in confinement factor.

Then to optimize h_s , Fig. 4 shows variation of effective index and confinement factor with h_s for width $W=500$ nm, and optimized core heights $H_1=216$ nm, $H_2=150$ nm. The effective index decreases monotonically with increase in height of low index slot region, whereas the confinement factor is peaked at $h_s = 45$ nm and decreases very fast on both side of maximum value.

Thus, for $W = 500$ nm, the maximum confinement factor, $\Gamma_s = 37\%$ is achieved for $H_1=216$ nm, $H_2=150$ nm and $h_s=50$ nm.

Finally, variation of confinement factor, Γ_s and power density with slot waveguide width, W has been plotted in Fig. 5 with keeping H_1 , H_2 and h_s constant at the optimized values for $W = 500$ nm. It should be noted that to make an exact statement about dependence of Γ_s on W , all other parameters should be optimized at each value of W . Since for broader waveguides the fundamental mode is well confined in the slot region, it can be expected that the amount of optical power guided in the slot region should increase with increase in W , but as the maximum possible confinement in the horizontal direction is achieved, it saturates and there is no further increase in Γ_s with W . In Fig. 5, Γ_s saturates to a value of 40%

Figure 8: Variation of S_z along Y_c -axis.

at around $W = 750$ nm. It should be noted that maximum power density is obtained when the width is around 500 nm.

Similar calculations were carried out for $W = 750$ nm also and the optimized confinement factor was achieved as $\Gamma_s = 42\%$ $H_1=200$ nm, $H_2=144$ nm and $h_s=50$ nm. Although the maximum power confinement is achieved when the width is around 750 nm, the power density is maximum around $W = 500$ nm. Therefore, an appropriate set of parameters should be used according to the requirement of high confinement factor or high power density.

3.3 Modal Field Analysis

In the analysis, vector \mathbf{E} -field is calculated from the vector \mathbf{H} -field obtained by the VFEM method. Specifically the fundamental quasi-TM mode has been studied which is supported by the horizontal slot waveguide structure. The quasi-TM mode has dominant H_x and E_y field. The contour plot of dominant H_x field component for the fundamental mode of optimized structure at $W = 500$ nm is shown in inset in Fig. 6. To show the variation more clearly, the H_x field along the vertical axis passing through the center of the slot region, Y_c -axis, is also plotted in the same figure.

The contour plot of dominant E_y field is shown in inset in Fig. 7. The bright region at the center shows a strong \mathbf{E} -field inside the slot. To show the variation more clearly the E_y field along the vertical axis, Y_c , passing through the center of the slot region is also plotted in the same figure. It evidences the large discontinuity at slot interfaces and high \mathbf{E} -field confinement in the slot region.

3.4 Poynting Vector Profiles

From the full vectorial \mathbf{E} and \mathbf{H} fields, the Poynting vector, S_z can be calculated. The contour plot of S_z intensity profile is shown in an inset in Fig. 8.

Variation of S_z along the vertical axis passing through the center of the slot region, Y_c , is also plotted in the same figure. It can be noticed that S_z and thus the guided power in the waveguide structure is very high in the slot region for the optimized

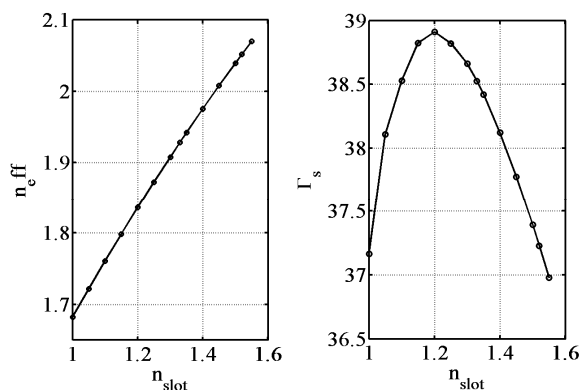


Figure 9: Variation of n_{eff} and Γ_s with refractive index of slot region

structure. Such a high power density in the easily accessible slot region would allow to design novel photonic devices.

3.5 Sensing Application

The analysis carried out to optimize the horizontal slot waveguide structure is extended to find possible sensing application. Variation in n_{eff} and confinement factor with refractive index of slot region from $n_{slot} = 1$ to 1.55 is plotted in Figure 9. In this case, waveguide width $W = 500\text{nm}$, slot height $h_s = 50\text{ nm}$ core heights, $H_1 = 216\text{ nm}$, $H_2 = 150\text{ nm}$ respectively were used which is optimized structure for horizontal waveguide with air slot for this width W . It can be noticed that the confinement factor, Γ_s doesn't change significantly for change in refractive index of the slot region in this range, but n_{eff} of the concerned mode changes linearly. The guided mode for the optimized horizontal slot waveguide structure has high confinement factor in the slot region allowing high interaction between slot material and guided light. This makes slot region very sensitive to refractive index changes. Thus a new type of sensing device can be realized where slot region acts as the sensing region.

4. CONCLUSION AND DISCUSSION

We have carried out a detailed rigorous analysis of modal properties of the horizontal slot waveguide structure for fundamental quasi-TM mode using full-vectorial H-field Finite Element Method (FEM). The structure parameters have been optimized to achieve maximum optical power confinement in the air slot region for waveguide widths of $W = 500\text{nm}$ and 750 nm . It has been found that for optimization, core heights H_1 and H_2 needs to be asymmetric.

For $W = 500\text{nm}$, maximum confinement factor, $\Gamma_{slot} = 37\%$ was obtained for asymmetric core heights, $H_1 = 216\text{ nm}$, $H_2 = 150\text{ nm}$ and slot height $h_s = 45\text{ nm}$. And for $W = 750\text{ nm}$, maximum $\Gamma_{slot} = 42\%$ is obtained for $H_1 = 200\text{ nm}$, $H_2 = 144\text{ nm}$ and slot height $h_s = 50\text{ nm}$. For even broader waveguides,

confinement factor doesn't depend on waveguide width W . It is observed that though the confinement factor is maximum for $W = 750\text{ nm}$, the power density is maximum around $W = 500\text{ nm}$. Thus according to requirement of the optical device under consideration, the suitable set of parameters should be chosen for high confinement factor or high power density.

Further, for $W = 500\text{ nm}$, variation in effective index and slot confinement factor with variation in refractive index of slot region was studied to find possible sensing application of the structure. It has been found that the effective index of the horizontal slot waveguide structure is very sensitive to refractive index of the slot region for the fundamental quasi-TM mode. Thus a new type of sensing device can be realized where slot region acts as the sensing region.

ACKNOWLEDGEMENT

Author wants to acknowledge The UK India Education and Research Initiative (UKIERI) project for project grant and support.

REFERENCES

- [1] M. Lipson, "Guiding, Modulating, and Emitting Light on Silicon—Challenges and Opportunities", *J. Lightwave Technol.* **23** (12), 4222-4238 (2005).
- [2] D. M. H. Leung, N. Kejalakshmy, B. M. A. Rahman and K. T. V. Grattan, "Rigorous modal analysis of silicon strip nanoscale waveguides", *Opt. Express* **18**, 8528 (2010).
- [3] Vilson R. Almeida, Qianfan Xu, Carlos A. Barrios, and M. Lipson, "Guiding and confining light in void nanostructure", *Opt. Lett.* **29**, 1209 (2004).
- [4] B. M. A. Rahman and J. B. Davies, "Finite Element solution of integrated optical waveguides", *J. Lightwave Technol.* **2**(5), 682-688 (1984).
- [5] B. M. A. Rahman, and J. B. Davies, "Penalty Function Improvement of Waveguide Solution by Finite Elements", *IEEE Trans. Microw. Theory Tech.* **32**(8), 922-928 (1984).

DESIGN OF COMPACT POLARIZATION ROTATOR EXPLOITING SILICON SLOT WAVEGUIDES

Ajanta Barh^{*#}, B. M. A. Rahman[†], D. M. H. Leung[†], B. P. Pal^{*} and R. K. Varshney^{*}

^{*}Department of Physics, IIT Delhi, New Delhi, India.

[†]School of Engineering and Mathematical Sciences, City University London, England.

[#]email: ajanta.barh@gmail.com

Abstract: Design approach of a compact polarization rotator (PR) exploiting power coupling through phase matching between the TM mode of a strip WG and TE mode of a vertical slot WG. Optimized cross sectional dimensions of the coupler have been achieved to use this device as a compact polarization rotator with a device length below 100 μm .

1. INTRODUCTION

Silicon photonics is emerging as a low-cost technology by exploiting well developed CMOS fabrication process [1]. Recently, silicon on insulator (SOI)-based nano sized compact slot optical WG has become a popular field of study in many research groups due to its potential applications [2]. Due to high index contrast at the interface, transverse electric field shows a very high discontinuity at the interface with very high optical confinement inside the low index slot region when the transverse dimension of the slot is less than the characteristic decay length of that electric field [2, 3, 4]. Therefore, the slot WG dimensions are small but these are also highly polarization sensitive. However, for polarization diversity systems, this problem can be sorted out by incorporating polarization splitter and polarization rotator (PR). Recently, PR made of horizontal slot and strip WG has been reported based on mode evolution [5]. It's fabrication poses difficulty as required proper control of tapered structure is not easy to realize. Moreover, it can rotate only one polarization state for one input direction. Here our proposed design of PR should be easy to fabricate as no tapering is required and the whole structure can be made with a single mask. Moreover, it can rotate both polarization states for a single input direction (i.e., at L_c , TM input in the Si nanowire will produce TE output from slot WG and TE input in slot WG will produce TM output from Si

nanowire). We have shown that in the present configuration that it is possible to match two different polarization states by exploiting coupling between a silicon nanowire (strip WG) and a air-silicon vertical slot waveguide.

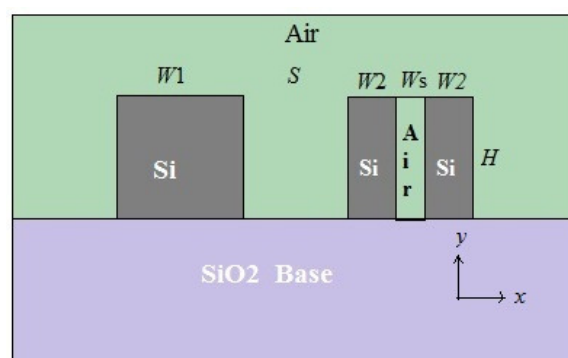


Fig. 1: Schematic cross-sectional view of a strip and slot WG coupler. Width of strip WG is $W1$, separation between two WG's is S , width of slot WG is $W2+W_s+W2$, where width of high index and low index slot regions are $W2$ and W_s , respectively. Height is H . High index region is silicon (Si) and low index region is air.

2. METHODOLOGY

Cross sectional geometry of the proposed PR is shown schematically in Fig. 1. Here two WG's are implemented on silica (SiO_2) base with air as cover and low index slot material. But we can use any low index compatible material for the slot region, such as electro-optic materials for high-speed modulators [6] or doped material to achieve gain [7]. A full vectorial finite element method was used to analyse the above mentioned 2-D structure. Abrupt refractive index change has been taken care of by optimizing the mesh. All the vector fields are studied and depending

on Hybridness, TE and TM modes are identified. Vertical slot WG is more likely to confine TE mode (E_x is the dominant component). So, here confinement of fundamental TE mode in slot WG and TM mode in strip WG (nanowire) is considered. By optimizing the cross sectional dimensions, phase matching between two orthogonal polarization states can be achieved for a PR.

3. RESULTS AND DISCUSSIONS

The refractive indices of the chosen materials are, $n_{Si} = 3.4754752$, $n_{SiO_2} = 1.4440236$ at the operating wavelength, $\lambda = 1.55 \mu m$ and $n_{air} = 1.00$.

Our chosen slot WG dimensions are $W_2 = 255 \text{ nm}$, $W_s = 90 \text{ nm}$, $H = 220 \text{ nm}$. In the absence of strip WG, the n_{eff} of fundamental TE mode inside the slot WG has been found out as $n_{eff_TE} = 1.53716$.

Now for the strip WG of same height the variation of n_{eff} of the fundamental TM mode with W_1 is studied in the absence of slot WG. The variation of n_{eff_TM} with W_1 is shown in Fig. 2.

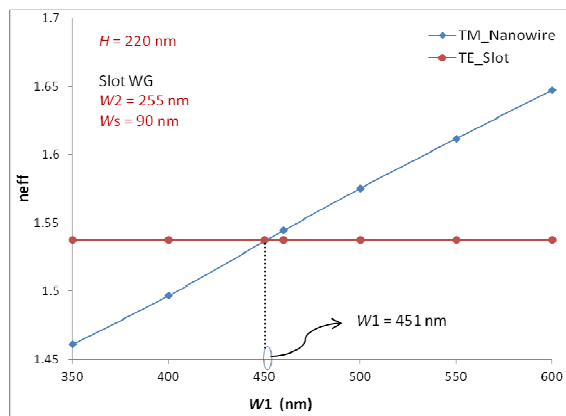


Fig. 2: Variation of n_{eff} of fundamental TM mode of strip WG with W_1 in the **absence** of slot WG. The horizontal line corresponds to the n_{eff} of fundamental TE mode inside the Slot WG ($n_{eff_TE} = 1.53716$) in the **absence** of strip WG.

This figure clearly indicates that at $W_1 = 451 \text{ nm}$, the n_{eff} of strip mode becomes equal to that of slot mode. Using these dimensions (i.e. $W_1 = 451 \text{ nm}$, $W_2 = 255 \text{ nm}$, $W_s = 90 \text{ nm}$, $H = 220 \text{ nm}$), the variation of the n_{eff} of two orthogonal polarized modes has been studied as a function of two WG separation (S) to find out the

mode exchange regime. The variation of upper n_{eff} and lower n_{eff} with S is shown in Fig. 3. Thus with our chosen WG dimensions, the phase matching condition will be achieved for WG separation (S) around 500 nm .

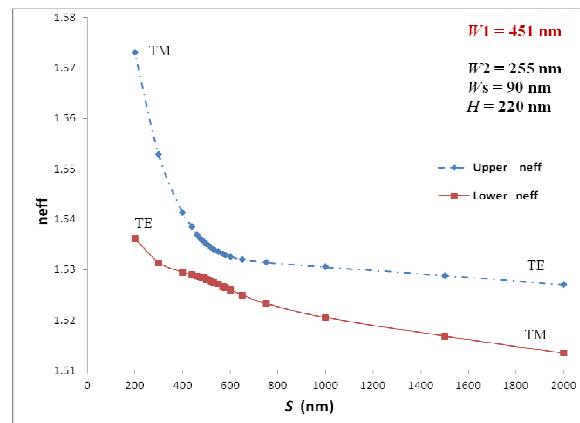


Fig. 3: Variation of TE and TM n_{eff} with S . Exact anti-crossing point is $S \approx 490 \text{ nm}$ (because which initially was the TM mode at $S = 489 \text{ nm}$ became TE mode at $S = 491 \text{ nm}$ and vice versa) where mode exchange has taken place.

The three basic parameters to study a PR are n_{eff} , hybridness and coupling length (L_c). For three different S values (450 nm , 500 nm , 550 nm), the variation of above mentioned parameters were studied as a function of strip WG width (W_1). The variation of n_{eff} with W_1 is shown in Fig. 4 for $S = 550 \text{ nm}$.

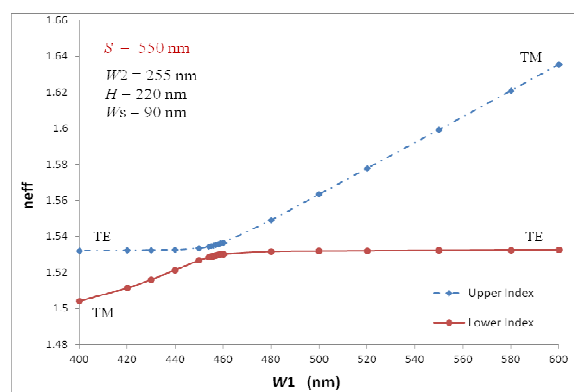


Fig. 4: Upper & lower n_{eff} variation with W_1 . Fixed $S = 550 \text{ nm}$.

In this case, we have obtained the phase matching point as $W_1 = 455 \text{ nm}$.

Variations of the n_{eff} of the TE and TM modes for three cases are shown in Fig. 5.

This figure clearly indicates that the value of $W1$ corresponding to anti-crossing point shifts towards a higher value as S increases.

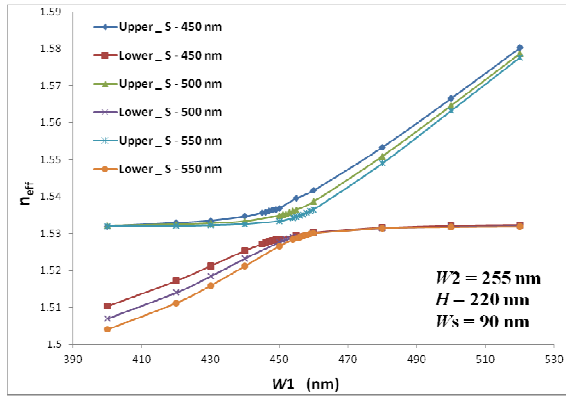


Fig. 5: Upper & Lower n_{eff} variation with strip WG width ($W1$) for three different separations, $S = 450$ nm, 500 nm, 550 nm.

Hybridness of the two modes can be defined as the ratio of the maximum values of the H_y to H_x field components for the TM and similarly H_x/H_y for the TE mode. Variation of H_x/H_y for the TE mode is shown in Fig. 6 and H_y/H_x for the TM mode is shown in Fig. 7.

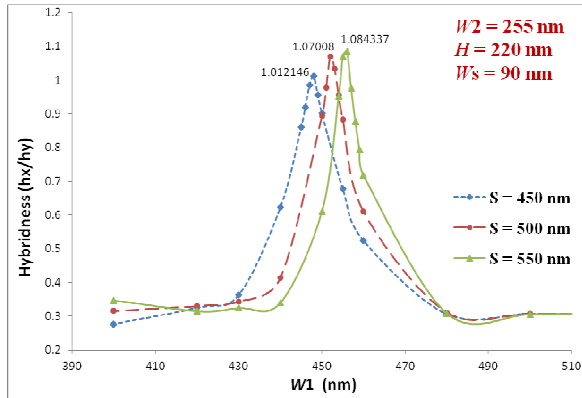


Fig. 6: Variation of modal hybridness of the TE mode with $W1$.

All the peaks appear around the mode exchange regime. For $S = 550$ nm, the peak value of hybridness is maximum for TE mode and minimum for TM mode. For TE mode (see Fig. 6), the peak exceeds 1. Since the hybridness was defined from the peak field components rather than the average field components, anomalies may appear when their profiles are very different.

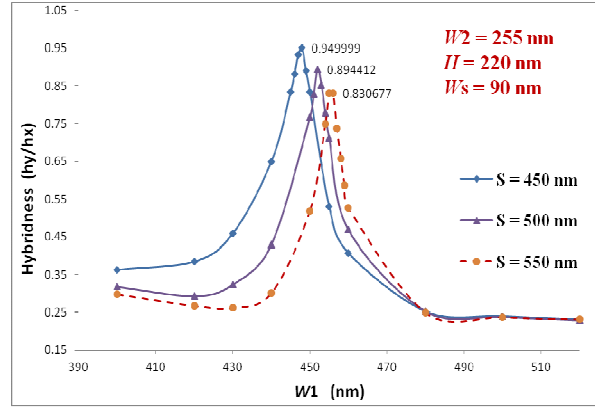


Fig. 7: Variation of modal hybridness of TM mode with $W1$.

Polarization coupling length of the two modes are defined as

$$L_c = (\pi / |\beta_1 - \beta_2|)$$

Where, β_1 and β_2 are the mode propagation constants of TE and TM modes. The variation of absolute value of L_c is shown in Fig. 8.

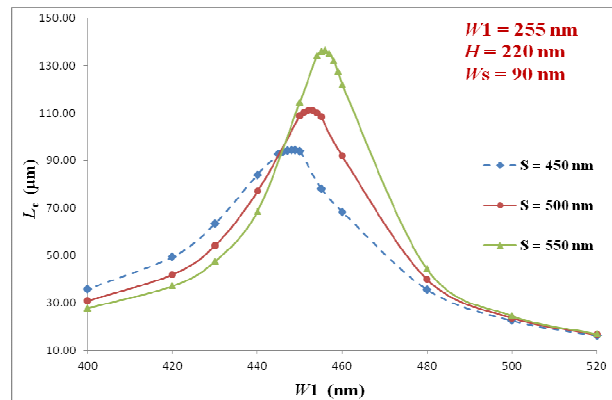


Fig 8: Variation of absolute value of coupling length (L_c) with $W1$ for three different $S = 450$ nm, 500 nm, 550 nm.

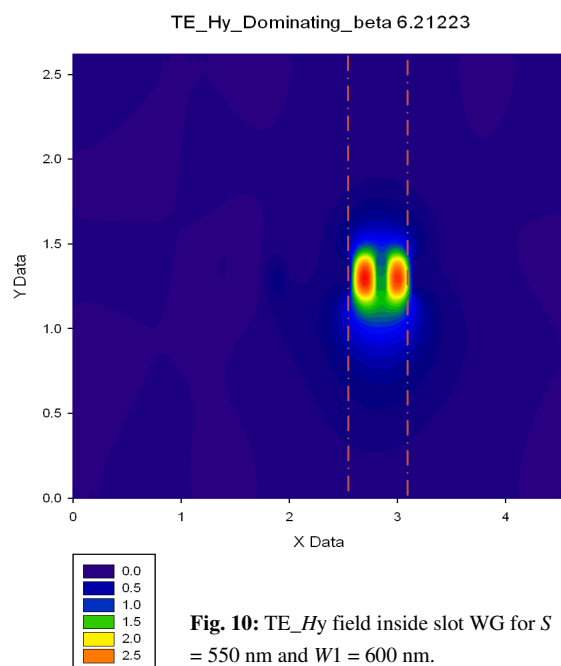
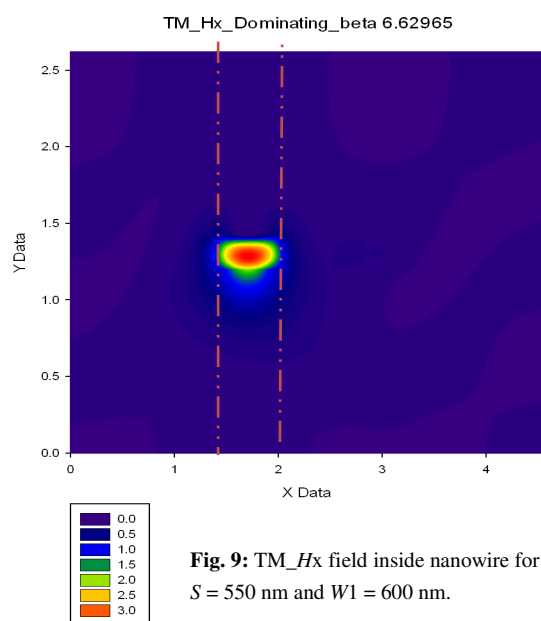
It clearly indicates that L_c has a peak value around the mode exchange regime. Values of maximum L_c and the corresponding $W1$ for different values of S are tabulated in Table-1.

Table-1: L_c and $W1$ for different S

WG separation (S) in nm	Width of nanowire ($W1$) in nm	$ L_c $ in μm
550	455	136.41
500	452	111.17
450	447	94.51

Thus for nearly 100 μm long coupler, the complete exchange of power between the two orthogonal polarized modes is possible.

Some field plots are shown below for $W_2 = 255$ nm, $H = 220$ nm, $W_s = 90$ nm, $S = 550$ nm and $W_1 = 600$ nm. Figure 9 shows the dominant H_x field for the TM mode in the silicon nanowire and Fig.10 shows the dominant H_y field for the TE mode in the slot waveguide section.



CONCLUSION

A novel design of a compact SOI polarizer incorporating slot waveguide is presented. The above results suggest that a compact 100 μm long PR can be designed by exploiting the phase matching between the orthogonally polarized modes of a silicon nanowire and that of a vertical slot silicon waveguide.

This work was supported by the ongoing Indo-UK collaboration under the UKIERI Project – RP02008. Ajanta Barh thanks UKIERI for funding her visit to City U London during the summer of 2011 and also her host Prof. Rahman for making her stay there pleasant and academically rewarding.

REFERENCES

- [1] K. K. Lee, D. R. Lim, L. C. Kimerling, J. Shin, and F. Cerrina, *Opt. Lett.* **26**, 1888 (2001).
- [2] V. R. Almeida, Q. Xu, C. A. Barrios, R. R. Panepucci, and M. Lipson, *Opt. Lett.* **29**, 1209 (2004).
- [3] Q. Xu, V. R. Almeida, R. R. Panepucci, and M. Lipson, *Opt. Lett.* **29**, 1626 (2004).
- [4] Ning-Ning Feng, Jurgen Michel and Lionel C. Kimerling, *IEEE journal of quantum electronics*, **42**, 9 (2006).
- [5] Ning-Ning Feng, Rong Sun, Jurgen Michel, and Lionel C. Kimerling, *Opt. Lett.* **32**, 15 (2007).
- [6] T. Baehr-Jones, M. Hochberg, Guangxi Wang, R. Lawson, Y. Liao, P. A. Sullivan, L. Dalton, A. K.Y. Jen, and A. Scherer, *Opt. Express*, **13**, 14 (2005).
- [7] P. Pintus, S. Faralli, and F. Di Pasquale, *IEEE photonics technology letters*, **22**, 19 (2010).

DESIGN AND DEVELOPMENT OF CCD OPTICAL SIGHT FOR TRACKING REAL TIME OBJECTS

R. Sudhakar Rao

Design & Engineering Division, Bharat Dynamics Limited,
Kanchanbagh, Hyderabad – 500 058, A.P., India
E-mail:rsrbd1@yahoo.com

and

Prof. Chandra Lingam

Dept. of Physics, College of Engineering,
JNTU, Kukatpally, Hyderabad – 500 085, A.P., India.
E-mail:chandra_lingam@yahoo.com

Abstract: Charge Coupled Devices enable instant imaging. Basing on this principle, novel CCD Optical Sight was developed. The necessity, design principles with the help of theory and development details with the help of system data, diagrams and photographs are provided in this paper. Application of the device is explained.

1. CCD IMAGING

Scientific imaging applications are expanding in to different domains [1]. Image observation through eyepiece based instruments is cumbersome and strenuous. The observation cannot be made for longer periods. Later, the imaging units were clubbed with a film for recording the image. These delivered sharp, clear pictures with plenty of details and good contrast. The hard copy print was a result of the photographic's efforts. Nevertheless, there were many drawbacks in the use of the film. The wait to see a picture was a lengthy process. It was difficult to get a film image into a computer. Storage of film based pictures consumed a lot of space, the files were difficult and time consuming to retrieve, and they degraded over time. Finally, some of the characteristics of film, such as its dynamic range, linearity at different light levels and consistency left a lot to be improved upon.

Solid State Technology helped to overcome the difficulty experienced in using the film based imaging. This technology has given, Charge Coupled Devices (CCDs). These devices have become the image-capturing platform of choice for scientific imaging, because of their ability to image in real time and ensured the accuracy of focus and exposure. This type of imaging is called CCD Imaging. Solid-state technology enabled the image on a screen as soon as it is exposed. This screen is either a Television Monitor or Computer Monitor. Storing images on standard computer media is highly efficient and there is no danger of degradation. There is no chemical processing. Solid-state imaging delivers consistent and repeatable results. Notable improvements in CCD image over a photographic image are: a) Low noise, b) Large dynamic range, c) High resolution and d) Higher quantum efficiency.

Taking advantage of the better characteristics of the CCD sensors and contemporary Optical software and hardware tools, a novel CCD Optical Sight was conceived and it was developed to function as real time video capturing unit. Following paragraphs provides the design, development, integration, evaluation and application stages of the equipment.

2. DESIRABLE FEATURES OF WEAPON SIMULATOR

A second generation Anti Tank Guided Weapon (ATGW) system consists of a Weapon and a Launcher. A pilot is required to swivel the Launcher Optical Device manually for surveillance and aiming purposes. Once a specified target is in the vicinity of attackable range, pilot is expected to acquire the target, then fire the weapon and continue to track the target until the weapon hits it. This is a complex task for a pilot considering the technology, accuracy, short flight duration of 12 to 13 s for its range, cost of the weapon and expensive drills in outdoor environments.

Therefore, a pilot needs training on a Simulator with the following desirable features:

- Actual Launcher or close to it used in battlefield conditions on actual targets in real terrain
- Immersion effect to the pilot in the battlefield environment.
- Instant feedback during and after the exercise on aiming, tracking, launching, guiding the weapon, lead, lag, hit and miss information
- Measurement of improvements made from drills and
- Equipment which is easy to install, operate and rugged.

3. DESIGN ASPECTS OF CCD IMAGER

While developing a weapon simulator, necessity arose to capture the target movements in real time to enable the instructor to assess and improve the performance of the pilot. Therefore, a novel CCD Optical Sight was conceived and developed.

Design of CCD Optical Sight started with an assessment of: a) Target Acquisition; b) Lens System; c) Image Sensor and d) Display Device parameters. Firstly application constraints, requirements and desired results are discussed. Later, the selection of the lens system, image sensor and display devices are studied.

3.1 Target Acquisition Constraints, Requirements and Desired Results

The criteria of target acquisition [2] is dependent on how much field of view supported by the optical sensor, its magnification and its ability to provide data that is meaningful for visual discrimination task. Target acquisition generally deals with detection, Recognition and Identification of the point of interest. For a weapon simulator application, targets could be military vehicles or soldiers.

The human eye has a resolving power of about one-minute of arc, which is equivalent to 291 μ rad. Comparing this resolution with the required sensor's field of view can provide an estimation of the magnification necessary for the required visual task.

As per the Johnson's criterion, there exists a relationship between observer's ability to resolve bar targets through an imaging device and their ability to detect, recognize and identify military vehicles. It was found that observers could detect a target when presented with "one cycle" of information, which in the case of a bar target is one black and one white bar. Table 1, provides the information about the "number of cycles" that is just resolvable across a target's critical dimension for various discrimination tasks. Johnson's criterion thus helped to calculate the sensor resolution necessary for any visual acquisition task at any range. With this criterion and other data shown in Table 2, it was possible to arrive at an appropriate sensor size, its field of view, resolution and other parameters.

The design criteria mainly depended on capturing a target of 1.5 m x 1.5 m located at a distance of 1000 m to 1500 m with clarity and its image must be displayed on a computer monitor. The acquired target image size displayed on a computer screen must not be less than 10 x 10 pixels out of 220 x 144 pixels. It was then the dedicated software program could recognize, process the image, analyze and provide useful data.

3.2. Lens System, Image Sensor and Display Devices Selection

Lens System was the most basic optical component. It collects light from a target and refracts/reflects that light to form a usable image of the target. Basic lens system properties are: Effective Focal Length (EFL), Aperture, Field of View (FOV) and Image Format. Required field of view was 1°. Clear Aperture of the Optical System selected was 80 mm, so that this size caters to the light gathering power in the day environment from dawn to dusk. FOV is often determined by the size of a detector.

Table 1: Target's critical dimension data for three discrimination tasks

Target	Detection (cycles)	Recognition (cycles)	Identification (cycles)
Truck	0.9	4.5	8
Jeep	1.2	4.5	5.5
Commando Car	1.2	4.3	5.5
M-48 Tank	0.7	3.5	7
Soldier	1.5	3.8	8
105 Howitzer	1	4.8	6
Average	1.0 \pm .25	4.0 \pm 0.35	6.4 \pm 1.5

Table 2: Relationship between Sensor's IFOV, Range and Resolution

Res. Capability	Detection (cycles)	Recognition (cycles)	Identification (cycles)
Range-km	4	3.8	2.5
No. of cycles (N)	0.7	3	6
Att. Factor	2	2	2
Sensor IFOV/mrad	0.38	0.1	0.07
Hor. Pixels-visible	640	640	640
Sensor FOV- Deg	14	3.7	2.8

The relation between FOV, image size and EFL is:

$$\text{FOV} = 2 \tan^{-1} \{ \text{image height} / \text{EFL} \} \quad (1)$$

Since FOV value determined was 1°, to suit the picture format on the computer, a CCD sensor of 8.0 mm (diagonal size of ½ inch CCD camera) was selected. Using the Eq. (2), EFL of the optical system was calculated and it was 458 mm. Lens System speed is a useful indicator of the brightness conditions under which it functions. Lens system speed (F-No) is related to EFL and Entrance Pupil Diameter with the following relation:

$$\text{F-No.} = \text{EFL} \div \text{Entrance Pupil Dia.} \quad (2)$$

Practically, Lens System's F-No varies from F-1, which is very fast, to a slow F-22. Image brightness is inversely proportional to the square of F-No. In the

present system, F-No varied from 5.7 to 305. An adjustable iris mechanism was used to work in varied brightness conditions. Lens system collects light from a point on the target and focuses to a corresponding point on the sensor. Ideally, the image of a point source formed by a perfect lens system would be an image of zero diameters. In the real world, even a perfect lens system gets affected from diffraction and the lens system aperture causes diffraction pattern called the *Airy pattern*. The central spot in the pattern is called the *Airy Disc*. The diameter of the Airy Disc is directly proportional to the lens system F-No and the wavelength (λ) of the light. The relation between Airy Disc spot diameter, F-No., and λ is given by the equation:

$$\text{Spot diameter} = 2.44 * \lambda * \text{F-No} \quad (3)$$

Using Eq. (3), value of the spot diameter calculated to be 8 μm . It is a well known fact that 85 % of the incident light power is focused by the lens system in to this spot. This spot size decides the individual pixel size of the sensor, as it is reasonable to match the blur size with pixel size. Therefore, the spot size assessment makes optical design calculations more meaningful. The inability of a lens system to form a perfect image is due to *lens aberrations* [3]. It is normal practice to choose a lens system with a small blur circle to give the required resolution. While choosing a lens system, the monochromatic aberrations-Spherical, Coma, Field curvature, Astigmatism, Distortion & polychromatic aberrations-Axial color, Lateral color are optimized. In order to arrive at an optimum lens system, design was carried out from the first order layout and optimized using computer aided optical design software. Sensor was selected based on the required image size.

Table 3: System Data

Optical System Data	Focal length: 458 mm; Clear Aperture: 80 mm diameter FOV (H x V x D): 0.8° x 0.6° x 1° Resolution: ~ 0.1 mil; Diff. Lim.: 8 μm Iris & Focus: Manual Control Range: 25–2000m; Day Time use
CCD Sensor Data	CCD format: ½ inch Color Sensing Area: 6.4 mm x 4.8 mm Pixels (H x V): 9 μm x 9 μm Res.:480TVL; Sensitivity: 1.5Lux(min.)
Display Devices Data:	Computer: Display size: 14 inch; Format: 320 x 200 pixels; Power:230VAC, 50 Hz ADU: CRT diagonal size: 14 inch; Resolution:480 TVL(H); Scanning: PAL 625 TVL; Power:230 VAC, 50 Hz.

Display device is desirable to have good fidelity of the image generated by the lens system and CCD sensor combination. It must support the display activity for visualizing the image by a batch of trainees, as well as to help the instructor in assessing the pilot’s performance.

4. SYSTEM DATA

Calculations were carried out to derive the System Data (Table 3), basing on the design principles and equations keeping the image quality as prime concern. System data was used in fabricating the CCD Optical Sight (Fig. 2).

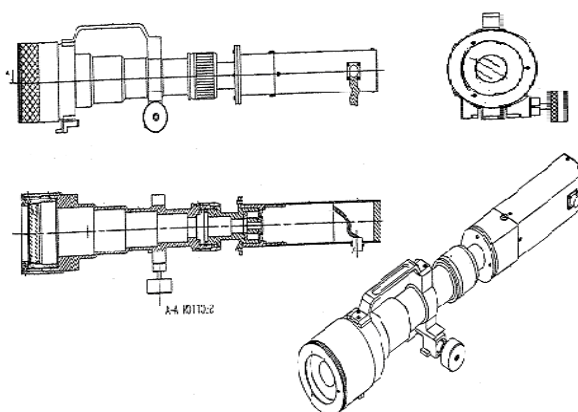


Fig. 1. CAD models of CCD Optical Sight

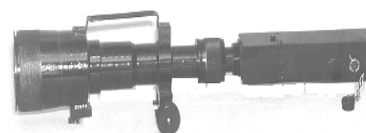


Fig. 2. Photograph of CCD Optical Sight

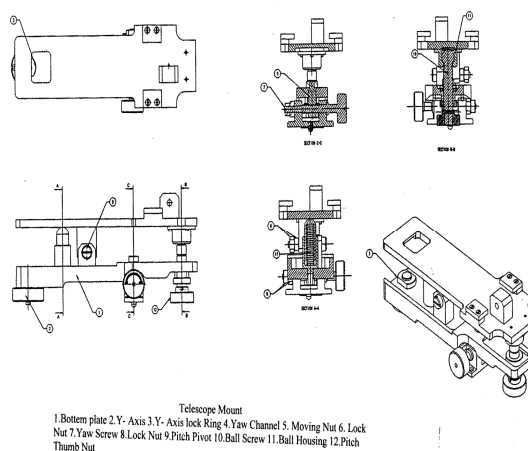


Fig.3. CAD Drawings of Mount

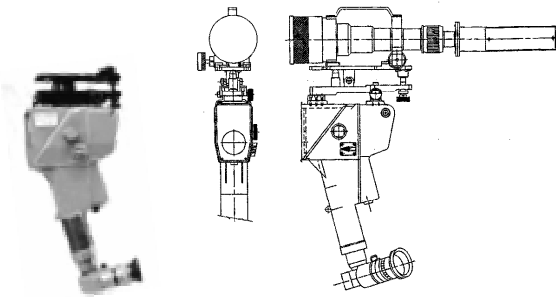


Fig. 4. Mounting arrangement on the Optical Device

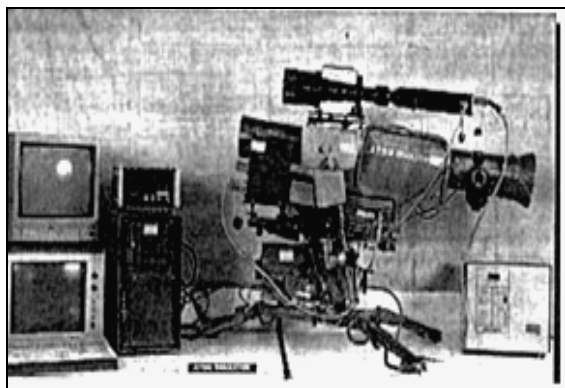


Fig. 5. Photograph of Outdoor Simulator (ODS)

Computer System and Auxiliary Display Unit (ADU) are also added. Computer System works as a Command & Control Station for the System and analysis tool to the Instructor. ADU functions as demonstrative tool to the co-pilots. CCD Optical Sight tracks a target situated in the range between 25 to 2000 m, in real time; sends analogue video image to Computer and ADU. Once the trigger is pressed, computer starts acquiring target images and continues the process till the end of weapon flight time. The analogue image from the CCD Optical Sight is converted into digital image by a frame grabber resident in the computer. The acquired image is processed and analyzed for specific purpose using dedicated motion analysis algorithms using computer hardware.

The resulting data, such as aiming, tracking, hit / miss indication and error etc., in graphic and text form, are displayed on the computer monitor. The instructor then provides a feedback to the pilot and reviews the sequence of performance of the pilot. Simultaneously, co-pilots are shown the video display on ADU. Initially few prototypes were fabricated. Rigorous field trials at different locations proved the robustness and efficacy of the system.

During the evaluation, some problems surfaced and they were corrected (Table 4).

Table 4: Problems encountered and solution provided

Problems	Long focal length lens system required a long lens barrel and so the balancing the unit on the Launcher.
	Flares were observed in the image
	Image degradation due to atmospheric turbulence and mirage effects
Solutions	Rugged mount helped to adjust the centre of gravity to suit the launcher length.
	Arrangement of decreasing steps inside the lens housing and application of dull black paint reduced the flares.
	Implementation of image processing algorithms helped to control the image degradation due to changes in atmospheric conditions, turbulence and mirage effects.

Afterwards few numbers of these items were fabricated, integrated in to the Weapon Simulators.

6. CONCLUSION

Novel concept of introducing a CCD Optical Sight on a Weapon Simulator was realized. The system was successfully put into practice in capturing the video images of the remote target moving in real terrain. The development of CCD Optical Sight gave further impetus to create a Long Range Telescope CCD System for Real Time Target & Weapon Tracking [4]. This knowledge helped us to develop, “An Outdoor Simulator for Training in Missile Launching and Guidance” in real time [5].

ACKNOWLEDGEMENTS

R. Sudhakar Rao is grateful to CMD, Directors, GM (P&A), Head – D&E, BDL for permitting to present this paper. He is also thankful to the project team colleagues who have coordinated in the design, development, integration, evaluation and application of the system.

REFERENCES

- [1] EG&G Optoelectronics - Reticon Product Data Book on “Image Sensing & Solid State Cameras”, 1994-95.
- [2] R L Lombardo Jr, “Target Acquisition: It’s Not Just for Military Imaging”, Photonics Spectra, p123, July 1998.
- [3] Rudolf Kingslake, “Lens Design Fundamentals”, Chapters 3 – 6, Academic Press, London, 1978.
- [4] R. Sudhakar Rao et al, “Design and development of a Long Range Telescope coupled with CCD Camera for Remote Detection Applications”, Jr. of Optics, Vol. 31, No. 3, Pages 145-152, 2002.
- [5] Indian Patent No. 228497 dated 5th Feb 2009.